

PROCEEDINGS OF SPIE



SPIE—The International Society for Optical Engineering

Contract F 61708-97-W0098

CSP 97-1044

ROMOPTO '97

Fifth Conference on Optics

Valentin I. Vlad
Dan C. Dumitras
Chairs/Editors

9-12 September 1997
Bucharest, Romania

Sponsored by

Romanian Ministry of Research and Technology
Romanian Academy, Division of Physics
Romanian Ministry of Education
SPIE—The International Society for Optical Engineering
SPIE/RO—SPIE Romanian Chapter
EOARD—European Office of Aerospace Research and Development
ICTP—International Center for Theoretical Physics
ICO—International Commission for Optics
EOS—European Optical Society
Institute of Atomic Physics, Bucharest



19981029 093



Volume 3405
Part One of Two Parts

DTIC QUALITY INSPECTED 4

AQF99-01-0110

REPORT DOCUMENTATION PAGE

Form Approved OMB No. 0704-0188

Public reporting burden for this collection of information is estimated to average 1 hour per response, including the time for reviewing instructions, searching existing data sources, gathering and maintaining the data needed, and completing and reviewing the collection of information. Send comments regarding this burden estimate or any other aspect of this collection of information, including suggestions for reducing this burden to Washington Headquarters Services, Directorate for Information Operations and Reports, 1215 Jefferson Davis Highway, Suite 1204, Arlington, VA 22202-4302, and to the Office of Management and Budget, Paperwork Reduction Project (0704-0188), Washington, DC 20503.

1. AGENCY USE ONLY (Leave blank)		2. REPORT DATE 8 October 1998		3. REPORT TYPE AND DATES COVERED Conference Proceedings	
4. TITLE AND SUBTITLE 5th Conference on Optics: ROMOPTO'97				5. FUNDING NUMBERS F6170897W0098	
6. AUTHOR(S) Conference Committee					
7. PERFORMING ORGANIZATION NAME(S) AND ADDRESS(ES) Institute of Atomic Physics IPTRD-Laser Department, P.O. Box MG-36 Bucharest R-76900 Romania				8. PERFORMING ORGANIZATION REPORT NUMBER N/A	
9. SPONSORING/MONITORING AGENCY NAME(S) AND ADDRESS(ES) EOARD PSC 802 BOX 14 FPO 09499-0200				10. SPONSORING/MONITORING AGENCY REPORT NUMBER CSP 97-1044	
11. SUPPLEMENTARY NOTES Came as two volumes.					
12a. DISTRIBUTION/AVAILABILITY STATEMENT Approved for public release; distribution is unlimited.				12b. DISTRIBUTION CODE A	
13. ABSTRACT (Maximum 200 words) The Final Proceedings for 5th Conference on Optics: ROMOPTO'97, 9 September 1997 - 12 September 1997 These are available as SPIE Proceedings vol 3405, parts one and two. lasers and radiation sources; lasers in material science; nonlinear, quantum and information optics; laser spectroscopy; biophotonics; optoelectronics; optical sensors and metrology; optical components; and optics in environmental research					
14. SUBJECT TERMS EOARD Adaptive Optics, Fibre Optics, Imaging, Lasers, Optical Components, Detector Technology, Non-linear Optics, Medical applications				15. NUMBER OF PAGES 1232	
				16. PRICE CODE N/A	
17. SECURITY CLASSIFICATION OF REPORT UNCLASSIFIED	18. SECURITY CLASSIFICATION OF THIS PAGE UNCLASSIFIED	19. SECURITY CLASSIFICATION OF ABSTRACT UNCLASSIFIED	20. LIMITATION OF ABSTRACT UL		

NSN 7540-01-280-5500

Standard Form 298 (Rev. 2-89)
Prescribed by ANSI Std. Z39-18
298-102

PROCEEDINGS OF SPIE



SPIE—The International Society for Optical Engineering

ROMOPTO '97

Fifth Conference on Optics

Valentin I. Vlad
Dan C. Dumitras
Chairs/Editors

9–12 September 1997
Bucharest, Romania

Sponsored by

Romanian Ministry of Research and Technology
Romanian Academy, Division of Physics
Romanian Ministry of Education
SPIE—The International Society for Optical Engineering
SPIE/RO—SPIE Romanian Chapter
EOARD—European Office of Aerospace Research and Development
ICTP—International Center for Theoretical Physics
ICO—International Commission for Optics
EOS—European Optical Society
Institute of Atomic Physics, Bucharest



Volume 3405
Part One of Two Parts

SPIE is an international technical society dedicated to advancing engineering and scientific applications of optical, photonic, imaging, electronic, and optoelectronic technologies.



The papers appearing in this book comprise the proceedings of the meeting mentioned on the cover and title page. They reflect the authors' opinions and are published as presented and without change, in the interests of timely dissemination. Their inclusion in this publication does not necessarily constitute endorsement by the editors or by SPIE.

Please use the following format to cite material from this book:

Author(s), "Title of paper," in *Fifth Conference on Optics (ROMOPTO '97)*, Valentin I. Vlad, Dan C. Dumitras, Editors, Proceedings of SPIE Vol. 3405, page numbers (1998).

ISSN 0277-786X

ISBN 0-8194-2857-4

Published by

SPIE—The International Society for Optical Engineering

P.O. Box 10, Bellingham, Washington 98227-0010 USA

Telephone 360/676-3290 (Pacific Time) • Fax 360/647-1445

Copyright ©1998, The Society of Photo-Optical Instrumentation Engineers.

Copying of material in this book for internal or personal use, or for the internal or personal use of specific clients, beyond the fair use provisions granted by the U.S. Copyright Law is authorized by SPIE subject to payment of copying fees. The Transactional Reporting Service base fee for this volume is \$10.00 per article (or portion thereof), which should be paid directly to the Copyright Clearance Center (CCC), 222 Rosewood Drive, Danvers, MA 01923. Payment may also be made electronically through CCC Online at <http://www.directory.net/copyright/>. Other copying for republication, resale, advertising or promotion, or any form of systematic or multiple reproduction of any material in this book is prohibited except with permission in writing from the publisher. The CCC fee code is 0277-786X/98/\$10.00.

Printed in the United States of America.

Contents

xxi	<i>Conference Committee</i>
xxiii	<i>Introduction</i>

Part One

SESSION 1 LASERS AND RADIATION SOURCES

- 2 **Q-switch regime of 3- μ m erbium lasers (Invited Paper) [3405-01]**
S. Georgescu, V. Lupei, C. Hapenciuc, National Institute for Laser, Plasma, and Radiation Physics (Romania)
- 10 **Stabilization of unstable states in a modulated noisy CO₂ laser (Invited Paper) [3405-02]**
V. Ninulescu, P. E. Sterian, M. A. Dumitru, M. C. Piscureanu, Politehnica Univ. of Bucharest (Romania)
- 17 **Beam optimization of a TEA-CO₂ laser [3405-03]**
T. Groß, D. Ristau, G. Wallas, Laser Zentrum Hannover eV (FRG); G. Dumitru, D. G. Sporea, C. A. Timus, National Institute for Laser, Plasma, and Radiation Physics (Romania)
- 24 **Modeling optical amplification in Er³⁺-doped LiNbO₃ waveguides [3405-04]**
N. N. Puscas, Politehnica Univ. of Bucharest (Romania); R. Girardi, CSELT (Italy); D. Scarano, Pirelli Cavi (Italy); I. Montrosset, Politecnico di Torino (Italy)
- 32 **Output beam characteristics of a Nd:YVO₄ miniature laser [3405-05]**
N. I. Pavel, National Institute for Laser, Plasma, and Radiation Physics (Romania); T. Taira, M. Furuhashi, T. Kobayashi, Fukui Univ. (Japan)
- 39 **Bound-state excitation in ion-ion collision as related to the modeling of x-ray lasers with Li-like ions [3405-06]**
V. Stancalie, National Institute for Laser, Plasma, and Radiation Physics (Romania); A. Sureau, Univ. Paris-Sud (France); V. M. Burke, DRAL Daresbury Labs. (UK)
- 45 **Nd:YAG linear resonator using an external stimulated Brillouin scattering Q-switching mirror [3405-07]**
A. Mocofanescu, National Institute for Laser, Plasma, and Radiation Physics (Romania), V. Babin, S. Miclos, A. Farcas, National Institute of Optoelectronics (Romania)
- 51 **Excitation upconversion by sensitized photon avalanche [3405-08]**
V. Lupei, E. Osiac, National Institute of Atomic Physics (Romania); T. Sandrock, E. Heumann, G. Huber, Univ. Hamburg (FRG)
- 58 **Medium-power stabilized laser diode [3405-09]**
E. Smeu, N. N. Puscas, I. M. Popescu, Politehnica Univ. of Bucharest (Romania); Gr. I. Suruceanu, Technical Univ. of Moldova; R. G. Ispasoiu, Politehnica Univ. of Bucharest (Romania)
- 65 **High-resolution spectral analysis of a pulsed CuBr laser [3405-10]**
E. Scarlat, L. Preda, C. P. Cristescu, A. M. Preda, Politehnica Univ. of Bucharest (Romania)

- 70 **Influence of active-medium properties on high-power solid state laser beam characteristics [3405-11]**
N. I. Pavel, National Institute for Laser, Plasma, and Radiation Physics (Romania); T. Taira, Fukui Univ. (Japan); T. Dascalu, V. Lupei, National Institute for Laser, Plasma, and Radiation Physics (Romania)
- 75 **Degradation effects in pulsed AlGaAs large optical cavity (LOC) structure laser diodes [3405-12]**
R. V. Ghita, National Institute of Materials Physics (Romania); E. Vasile, METAV SA (Romania); V. Cimpoca, National Institute of Materials Physics (Romania); N. Baltateanu, National Institute for Laser, Plasma, and Radiation Physics (Romania)
- 81 **Performance of a pump system for diode-pumped lasers [3405-13]**
A. Stratan, C. G. Fenic, R. V. Dabu, N. Herisanu, C. Luculescu, D. G. Sporea, G. Dumitru, National Institute for Laser, Plasma, and Radiation Physics (Romania); G. Iordache, National Institute of Materials Physics (Romania)
- 85 **Medium-power cw He-Se laser [3405-14]**
M. Ristici, I. Ristici, V. R. Medianu, National Institute for Laser, Plasma, and Radiation Physics (Romania)
- 89 **Pump distribution effects on photon avalanche in fiber lasers [3405-15]**
V. Lupei, E. Osiac, Institute of Atomic Physics (Romania)
- 99 **High-quality beam transversal gas transport cw CO₂ laser [3405-16]**
I. Gutu, V. R. Medianu, P. Cristian, National Institute for Laser, Plasma, and Radiation Physics (Romania)
- 106 **Comparison between method of lines and time domain method in evaluating the large signal responses of Fabry-Perot semiconductor lasers [3405-17]**
A. L. Braverman, Politehnica Univ. of Bucharest (Romania)
- 112 **Generalized model for cw three-micron emission in concentrated Er systems [3405-18]**
V. Lupei, S. Georgescu, National Institute for Laser, Plasma, and Radiation Physics (Romania)

SESSION 2 LASERS IN MATERIAL SCIENCE

- 122 **Synthesis, characterization, and mechanical properties of carbide and nitride films prepared by pulsed-laser-deposition method (Invited Paper) [3405-19]**
A. Kumar, H. L. Chan, Univ. of South Alabama (USA); R. Alexandrescu, National Institute for Laser, Plasma, and Radiation Physics (Romania)
- 130 **Deposition of CN thin films by reactive pulsed laser ablation (Invited Paper) [3405-20]**
A. Perrone, Univ. degli Studi di Lecce (Italy) and Istituto Nazionale per la Fisica della Materia (Italy)
- 143 **Laser diagnostics in flame deposition of diamond (Invited Paper) [3405-21]**
R. J. H. Klein-Douwel, J. J. ter Meulen, Univ. of Nijmegen (Netherlands)
- 153 **Synthesis of nanosize powders by pulsed laser ablation and related plasma diagnostics (Invited Paper) [3405-22]**
K. Yatsui, W. Jiang, K. Nishiura, T. Yukawa, Nagaoka Univ. of Technology (Japan); C. Grigoriu, I. Chiş, A. Marcu, D. Miu, National Institute for Laser, Plasma, and Radiation Physics (Romania)

- 162 **X-ray micromachining with a laser-plasma source at 1-nm wavelength (Invited Paper)** [3405-23]
I. C. E. Turcu, C. M. Mann, Rutherford Appleton Lab. (UK); S. W. Moon, Rutherford Appleton Lab. (UK) and Korea Institute of Science and Technology; B. J. Maddison, R. M. Allott, N. Lisi, S. E. Huq, Rutherford Appleton Lab. (UK); N. S. Kim, Rutherford Appleton Lab. (UK) and Kumho Information and Telecommunication Lab. (Korea)
- 174 **Preparation of metal oxides by laser versus thermal processes (Invited Paper)** [3405-24]
R. Alexandrescu, I. G. Morjan, National Institute for Laser, Plasma, and Radiation Physics (Romania); C. R. Popescu, LACECA Research Ctr. (Romania); I. N. Voicu, National Institute for Laser, Plasma, and Radiation Physics (Romania)
- 182 **New studies of reactive pulsed laser deposition (Invited Paper)** [3405-25]
I. N. Mihailescu, E. Gyorgy, National Institute for Laser, Plasma, and Radiation Physics (Romania); V. S. Teodorescu, National Institute of Materials Physics; G. Marin, National Institute for Laser, Plasma, and Radiation Physics (Romania); D. Pantelica, National Institute of Nuclear Physics and Engineering Horia Hulubei; A. Andrei, Institute of Nuclear Research (Romania); J. Neamtu, Univ. of Craiova (Romania)
- 188 **Discharge-aided reactive laser ablation for ultrafine powder production (Invited Paper)** [3405-26]
I. Chis, National Institute for Laser, Plasma, and Radiation Physics (Romania); A. Marcu, Nagaoka Univ. of Technology (Japan); D. Miu, National Institute for Laser, Plasma, and Radiation Physics (Romania); T. Yukawa, Nagaoka Univ. of Technology (Japan); D. Dragulinescu, C. Grigoriu, National Institute for Laser, Plasma, and Radiation Physics (Romania); W. Jiang, K. Yatsui, Nagaoka Univ. of Technology (Japan)
- 199 **Deposition of carbon nitride thin films by IR-laser-induced reactions in carbon-nitrogen gas-phase compounds** [3405-27]
A. Crunteanu, R. Alexandrescu, R. Cireasa, S. Cojocaru, I. G. Morjan, National Institute for Laser, Plasma, and Radiation Physics (Romania); A. Andrei, Institute of Nuclear Research (Romania); A. Kumar, Univ. of South Alabama (USA)
- 205 **Influence of thermal annealing on optical properties of porous silicon films** [3405-28]
I. Baltog, M. L. Ciurea, G. Pavelescu, E. Pentia, G. Galeata, National Institute of Materials Physics (Romania); J. P. Roger, Ecole Supérieure de Physique et de Chimie Industrielles (France)
- 211 **Optical devices with silica-gel small spheres** [3405-29]
A. M. Preda, E. Scarlat, L. Preda, I. M. Popescu, Politehnica Univ. of Bucharest (Romania)
- 218 **Growth of polycrystalline hydroxyapatite thin films by pulsed laser deposition and subsequent heat treatment in air** [3405-30]
V. D. Nelea, National Institute for Laser, Plasma, and Radiation Physics (Romania); C. Ghica, National Institute of Materials Physics (Romania); C. Martin, A. Hening, I. N. Mihailescu, National Institute for Laser, Plasma, and Radiation Physics (Romania); L. C. Nistor, V. S. Teodorescu, National Institute of Materials Physics (Romania); R. Alexandrescu, National Institute for Laser, Plasma, and Radiation Physics (Romania); J. Werckmann, Institute of Physics and Chemistry of Materials (France); E. Gyorgy, G. Marin, National Institute for Laser, Plasma, and Radiation Physics (Romania)

- 225 **Mechanisms of droplet formation in pulsed laser growth of thin oxide films [3405-31]**
V. Craciun, D. Craciun, National Institute for Laser, Plasma, and Radiation Physics (Romania); M. C. Bunesco, E. Vasile, A. Ioncea, METAV SA (Romania); R. V. Dabu, National Institute for Laser, Plasma, and Radiation Physics (Romania); I. W. Boyd, Univ. College London (UK)
- 233 **Nd:YAG laser surface texturing [3405-32]**
M. Poterasu, T. Dascalu, A. Marian, D. Buca, National Institute for Laser, Plasma, and Radiation Physics (Romania)
- 241 **Investigation of $\text{HgBr}_{1-x}\text{I}_x$ using confocal laser scanning microscopy and x-ray diffraction [3405-33]**
G. A. Stanciu, Politehnica Univ. of Bucharest (Romania); J. L. Oud, Univ. of Amsterdam (Netherlands); E. K. Polychronyadis, M. Daviti, Aristotle Univ. of Thessaloniki (Greece); A. Stanciu, National Institute of Microtechnology (Romania); C. Miu, Politehnica Univ. of Bucharest (Romania)
- 246 **Lasers for material processing [3405-34]**
A. Nichici, I. David, E. F. Cicala, Politehnica Univ. of Timisoara (Romania)
- 252 **Effects of UV laser radiation on the surface defects of NiO catalysts [3405-35]**
E. Ivana, V. Lăcătușu, M. Chelu, M. Craiu, Institute of Physical Chemistry (Romania); C. G. Fenic, A. Stratan, National Institute for Laser, Plasma, and Radiation Physics (Romania); L. C. Nistor, C. Ghica, National Institute of Materials Physics (Romania); P. Mărginean, Institute of Isotopic and Molecular Technology (Romania)
- 258 **Modeling of chalcogenide glass structures before and after laser illumination, based on mass spectroscopy data [3405-36]**
A. M. Andriesh, Ctr. of Optoelectronics (Moldova); A. I. Buzdugan, V. Dolghier, Ctr. of Metrology (Moldova); M. S. Iovu, Ctr. of Optoelectronics (Moldova)
- 262 **Ionic space-charge-limited currents in natural quartz crystal [3405-37]**
I. Enculescu, B. Iliescu, National Institute of Materials Physics (Romania)
- 267 **Compacting of metallic powder by using Nd:YAG laser [3405-38]**
A. Marian, D. Buca, T. Dascalu, M. Poterasu, National Institute for Laser, Plasma, and Radiation Physic (Romania)
- 272 **Microstructure of hydroxyapatite thin layers grown by pulsed laser deposition [3405-39]**
D. Craciun, V. Craciun, C. Martin, I. N. Mihailescu, National Institute for Laser, Plasma, and Radiation Physics (Romania); M. C. Bunesco, E. Vasile, A. Ioncea, METAV SA (Romania); I. W. Boyd, Univ. College London (UK)
- 278 **Computing coupling coefficients in transmission systems [3405-40]**
V. Calian, M. Ursache, C. Sarpe-Tudoran, M. Socaciu, Univ. of Craiova (Romania)
- 282 **Effect of pulsed-laser deposition parameters on plasma expansion studied by fast-framing photography [3405-41]**
D. Miu, A. Marcu, National Institute for Laser, Plasma, and Radiation Physics (Romania); T. Yukawa, Nagaoka Univ. of Technology (Japan); C. Grigoriu, I. Chis, National Institute for Laser, Plasma, and Radiation Physics (Romania); K. Yatsui, Nagaoka Univ. of Technology (Japan)

- 288 **Synthesis of europium-activated calcium tungstate phosphor [3405-42]**
E.-J. Popovici, F. Forgaciu, M. Nemes, Institute of Chemistry Raluca Ripan (Romania); V. Ursu, Institute of Physical Chemistry I.G. Murgulescu (Romania)
- 293 **Off-line multiresponse optimization of gas-jet-assisted CO₂ laser cutting of polymettacrylate [3405-43]**
E. F. Cicala, D. Zsivanov, A. Nichici, Politehnica Univ. of Timisoara (Romania)
- 299 **Establishing the regression polynomials for the objective function that defines dimensional accuracy in the case of laser drilling [3405-44]**
I. David, E. F. Cicala, Politehnica Univ. of Timisoara (Romania)
- 305 **Theoretical model for the reactive pulsed deposition process: application to the case of ablation of a Ti target in low-pressure N₂ [3405-45]**
J. Neamtu, Univ. of Craiova (Romania); I. N. Mihailescu, National Institute for Laser, Plasma, and Radiation Physics (Romania)
- 311 **Pulsed-laser and alpha particle irradiation effects in Fe-based glassy ferromagnets [3405-46]**
M. I. Toacsan, D. Barb, National Institute of Materials Physics (Romania); M. Sorescu, Duquesne Univ. (USA); B. Constantinescu, National Institute of Nuclear Physics and Engineering Horia Hulubei (Romania); L. Jeloica, National Institute of Materials Physics (Romania)

SESSION 3 NONLINEAR, INFORMATION, AND QUANTUM OPTICS

- 320 **Quantum optics of a single atom (Plenary Paper) [3405-47]**
H. Walther, Univ. München (FRG) and Max-Planck-Institut für Quantenoptik (FRG)
- 335 **Optical properties of quasi-periodic (self-similar) structures [3405-48]**
M. Bertolotti, C. Sibilia, Univ. degli Studi di Roma La Sapienza (Italy), Gruppo Nazionale di Elettronica Quantistica e Plasmi (Italy), and Istituto Nazionale per la Fisica della Materia (Italy)
- 353 **Novel femtosecond optical solitons in weakly excited semiconductors (Invited Paper) [3405-49]**
D. Mihalache, Institute of Atomic Physics (Romania); I. V. Mel'nikov, General Physics Institute (Russia); N.-C. Panoiu, New York Univ. (USA)
- 363 **Various approaches for optical implementation of the wavelet transform (Invited Paper) [3405-50]**
E. Marom, D. Mendlovic, Z. Zalevsky, Tel-Aviv Univ. (Israel)
- 375 **Radiation spectrum and thermodynamics of the quantum cubic cavities (Invited Paper) [3405-51]**
V. I. Vlad, N. Ionescu-Pallas, National Institute for Laser, Plasma, and Radiation Physics (Romania)
- 385 **Photoinduced phenomena in chalcogenide glasses and their application in optoelectronics (Invited Paper) [3405-52]**
A. M. Andriesh, Institute of Applied Physics (Moldova)
- 393 **Thermo-optic dispersion formula of AgGaSe₂ and its applications to thermal lensing effects (Invited Paper) [3405-53]**
E. Tanaka, Keio Univ. (Japan); K. Kato, Japan Defense Agency

- 399 **Possibility of two-photon superradiance in microcavities [3405-54]**
M. Macovei, N. A. Enaki, Institute of Applied Physics (Moldova)
- 406 **Nonlinear excitonic susceptibilities of semiconductors at high levels of excitation [3405-55]**
P. I. Khadzhi, D. V. Tkachenko, Trans-Dniester State Univ. (Moldova)
- 411 **Appearance and suppression of stochastic self-pulsations of coherent excitons and biexcitons in condensed matter [3405-56]**
V. Z. Tronciu, Technical Univ. of Moldova; A. H. Rotaru, State Univ. of Moldova
- 418 **Novel approaches in morphological correlations [3405-57]**
D. Mendlovic, A. Shemer, Z. Zalevsky, E. Marom, G. Shabtay, Tel-Aviv Univ. (Israel)
- 425 **Rotation-invariant pattern recognition using circular harmonics and synthetic discriminant functions [3405-58]**
D. Cojoc, Politehnica Univ. of Bucharest (Romania)
- 432 **Surface study of laser-induced charge gratings in $\text{Bi}_{12}\text{SiO}_{20}$ with an atomic force microscope [3405-59]**
E. Soergel, W. Krieger, Max-Planck-Institut für Quantenoptik (FRG); V. I. Vlad, Institute of Atomic Physics (Romania)
- 439 **Optical bistability in short-external-cavity DBR semiconductor lasers [3405-60]**
V. B. Guja, Politehnica Univ. of Bucharest (Romania); I. Montrosset, Politecnico di Torino (Italy); O. D. Iancu, Politehnica Univ. of Bucharest (Romania)
- 446 **Nonlinear optical properties of noncrystalline semiconductors [3405-61]**
V. N. Chumash, Institute of Applied Physics (Moldova)
- 454 **LBO optical parametric oscillator pumped by second harmonic of a Nd:YAG laser [3405-62]**
R. V. Dabu, C. G. Fenic, A. Stratan, C. Luculescu, National Institute for Laser, Plasma, and Radiation Physics (Romania); G. L. Muscalu, Pro Optica SA (Romania)
- 462 **Enhanced internal second harmonic generation in InGaAs/GaAs/AlGaAs strained single-quantum-well buried-heterostructure laser diodes [3405-63]**
R. G. Ispasoiu, N. N. Puscas, E. Smeu, C. E. Botez, Politehnica Univ. of Bucharest (Romania); V. P. Yakovlev, A. Z. Mereutza, G. I. Suruceanu, Technical Univ. of Moldova
- 469 **Resonatorless optical bistability in a thin semiconductor film [3405-64]**
S. L. Gaivan, P. I. Khadzhi, Institute of Applied Physics (Moldova)
- 473 **Nonlinear transmission of ultrashort light pulses by a thin semiconductor film in the exciton range of the spectrum [3405-65]**
P. I. Khadzhi, S. L. Gaivan, Institute of Applied Physics (Moldova)
- 477 **Cryptographic mixing transformations for image applications [3405-66]**
A. Vlad, M. Mitrea, Politehnica Univ. of Bucharest (Romania)
- 483 **Characterization of the silicon guided-wave optical couplers and Mach-Zehnder interferometers [3405-67]**
N. N. Puscas, G. Nitulescu, V. V. Gherman, A. Ducariu, Politehnica Univ. of Bucharest (Romania)

- 489 **Holographic interferometry study of interphase mass transfer [3405-68]**
L. Stefan, Univ. of Bucharest (Romania); A. Guzun-Stoica, Politehnica Univ. of Bucharest (Romania); M. Kurzeluk, Technical Univ. of Civil Engineering (Romania)
- 494 **Nonlinear processes in laser radiation absorption on metallic surfaces [3405-69]**
M. Ursache, V. Calian, M. Socaciu, C. Sarpe-Tudoran, Univ. of Craiova (Romania)
- 498 **Construction of the first-order stochastic nonlinear differential equations in the modeling of stimulated scattering of optical fields [3405-70]**
V. Babin, M. Grigore, L. Cojocaru, S. Ersen, A. Moldovan, National Institute of Research and Development for Optoelectronics (Romania)
- 504 **Spectral Jones vectors and spectral coherence matrices in analyzing modulated light [3405-71]**
T. S. Tudor, I. Vinkler, Univ. of Bucharest (Romania)
- 511 **Fidelity evaluation of the conjugated wavefront in photorefractive crystals using direct spatial phase demodulation of optical interferograms [3405-72]**
V. I. Vlad, A. Petris, A. Jianu, National Institute for Laser, Plasma, and Radiation Physics (Romania)
- 517 **Talbot moiré deflectometry with direct spatial reconstruction of optical phase [3405-73]**
A. Jianu, A. Petris, National Institute for Laser, Plasma, and Radiation Physics (Romania); C. Popa, D. Popa, Politehnica Univ. of Bucharest (Romania); V. I. Vlad, National Institute for Laser, Plasma, and Radiation Physics (Romania)

SESSION 4 LASER SPECTROSCOPY

- 524 **Competitive processes in a nonisothermal plasma by deconvolution of low-intensity spectral lines (Invited Paper) [3405-74]**
I. Iova, Gh. Ilie, M. Băzăvan, C. Biloiu, I. Gruia; I. Chera; Univ. of Bucharest (Romania); M. Cristea, T. Constantinescu, Politehnica Univ. of Bucharest (Romania)
- 533 **Formation of nonlinear optical MQD (metal quantum dot) in waveguides and modification by high-power laser irradiation (Invited Paper) [3405-75]**
G. Battaglin, Istituto Nazionale per la Fisica della Materia (Italy) and Univ. degli Studi di Venezia (Italy); E. Borsella, G. De Marchi, F. Gonella, G. Mattei, P. Mazzoldi, Istituto Nazionale per la Fisica della Materia (Italy) and Univ. degli Studi di Padova (Italy); A. Quaranta, Istituto Nazionale per la Fisica della Materia (Italy) and Univ. degli Studi di Trento (Italy)
- 541 **Optical pumping via a velocity-selective state (Invited Paper) [3405-76]**
N. Leinfellner, L. Windholz, Technische Univ. Graz (Austria); I. E. Mazets, A.F. Ioffe Institute of Physics and Technology (Russia)
- 548 **Linear and nonsaturating effects in atomic multiplets subjected to three strong electromagnetic fields of resonance (Invited Paper) [3405-77]**
F. F. Popescu, F. Marica, G. Radu, Univ. of Bucharest (Romania)

- 556 **Multicomponent trace gas analysis with a CO-laser-based photoacoustic detector: emission of ethanol, acetaldehyde, ethane, and ethylene from fruit [3405-78]**
F. J. M. Harren, J. Oomens, S. Persijn, Univ. of Nijmegen (Netherlands); R. H. Veltman, H. S. M. de Vries, Agrotechnological Research Institute (Netherlands); D. H. Parker, Univ. of Nijmegen (Netherlands)
- 563 **Spectroscopy of Yb³⁺ codoped Pr³⁺:YAG laser crystals [3405-79]**
A. Lupei, V. Lupei, A. Petraru, Institute of Atomic Physics (Romania)
- 570 **Effects of resonant electron-phonon interactions for the RE³⁺ ions in laser crystals [3405-80]**
V. N. Enaki, Chisinau State Univ. (Moldova); A. Lupei, V. Lupei, C. Presura, Institute of Atomic Physics (Romania); V. E. Ciobu, Chisinau State Univ. (Moldova)
- 578 **Laser photoacoustic detection of the essential oil vapors of thyme, mint, and anise [3405-81]**
A. M. El-Kahlout, M. M. Al-Jourani, Keele Univ. (UK); M. I. Abu-Taha, Al Quds Univ. (Israel); D. C. Lainé, Keele Univ. (UK)
- 584 **Coherent Raman scattering on light-induced optical gratings prepared by adiabatic population transfer [3405-82]**
N. Leinfellner, L. Windholz, Technische Univ. Graz (Austria); I. E. Mazets, A.F. Ioffe Institute of Physics and Technology (Russia)
- 589 **Energy transfer processes in Cr³⁺, Nd³⁺:YAG [3405-83]**
A. Lupei, V. Lupei, A. Petraru, M. Petrache, Institute of Atomic Physics (Romania)
- 596 **Infrared photochemistry of trichloroethylene in the presence of oxygen [3405-84]**
C. Ungureanu, Institute of Isotopic and Molecular Technology (Romania); M. Ungureanu, Gh. Lazar College (Romania)
- 603 **Excited xenon(1s₄) atom detection by modulation laser absorption spectroscopy [3405-85]**
Y. Sakai, Hokkaido Univ. (Japan); M. A. Bratescu, G. Musa, National Institute for Laser, Plasma, and Radiation Physics (Romania); K. Miyamoto, Hokkaido Univ. (Japan); M. Miclea, National Institute for Laser, Plasma, and Radiation Physics (Romania)
- 612 **Multiphonon transitions and heating effects in Er:YAG laser rods [3405-86]**
S. Georgescu, V. Lupei, National Institute for Laser, Plasma, and Radiation Physics (Romania)
- 619 **Determination of phase transitions in liquid crystals by optical absorption spectroscopy [3405-87]**
C. Sarpe-Tudoran, M. Socaciu, M. Ursache, J. Neamtu, G. Bratulescu, S. Radu, Univ. of Craiova (Romania)
- 623 **Photoluminescence decay in porous silicon films [3405-88]**
I. Baltog, M. L. Ciurea, G. Pavelescu, L. Mihut, M. Baibarac, National Institute of Materials Physics (Romania)
- 627 **Photoacoustic detection of ethylene released by biological samples under stress conditions [3405-89]**
S. M. Cristescu, D. C. Dumitras, D. C. A. Dutu, National Institute for Laser, Plasma, and Radiation Physics (Romania)

- 632 **Luminescence properties of some double-activated zinc-sulphide-type phosphors [3405-90]**
E.-J. Popovici, M. Aneculaese, Institute of Chemistry Raluca Ripan (Romania); V. Ursu, Institute of Physical Chemistry I.G. Murgulescu (Romania)
- 636 **Correlation of some radiative processes resulting from electronic and vibrational spectra of a CN molecule excited in an electric arc discharge [3405-91]**
I. Iova, M. Băzăvan, C. Biloiu, Gh. Ilie, M. Bulinski, Univ. of Bucharest (Romania)

Part Two

SESSION 5 BIOPHOTONICS

- 642 **Laser-based assessment of lipid peroxidation in humans (Invited Paper) [3405-92]**
G. Giubileo, ENEA (Italy)
- 654 **CO₂ laser ablation of biological tissue (Invited Paper) [3405-93]**
D. C. Dumitras, D. C. A. Dutu, C. E. Matei, National Institute for Laser, Plasma, and Radiation Physics (Romania)
- 665 **Laser method for corneal structure investigation (Invited Paper) [3405-94]**
M. L. Pascu, National Institute for Laser, Plasma, and Radiation Physics (Romania); B. Carstocea, Central Military Hospital (Romania); G. Popescu, National Institute for Laser, Plasma, and Radiation Physics (Romania); L. Gafencu, S. Apostol, Central Military Hospital (Romania); N. Moise, M. Roman, C. M. Ticos, National Institute for Laser, Plasma, and Radiation Physics (Romania)
- 673 **Electronic-beam analysis of excimer lasers used for photorefractive keratotomy (Invited Paper) [3405-95]**
C. B. Roundy, Spiricon, Inc. (USA)
- 678 **UV laser radiosensitivity of normal and tumoral chromatin [3405-96]**
L. Radu, Victor Babes Institute (Romania); I. N. Mihailescu, National Institute for Laser, Plasma, and Radiation Physics (Romania); V. Preoteasa, I. Radulescu, D. Gostian, Victor Babes Institute (Romania); A. Hening, National Institute for Laser, Plasma, and Radiation Physics (Romania); S. Radu, Polytechnia Univ. of Bucharest (Romania)
- 686 **Observations concerning the use of rMuIFN- γ -activated macrophages by intra- and peritumoral perfusion combined with laser therapy in animals with carcinosarcoma [3405-97]**
V. F. Dima, Cantacuzino Institute (Romania); V. V. Vasiliu, National Institute for Laser, Plasma, and Radiation Physics (Romania); D. Laky, Victor Babes Institute (Romania); S. V. Dima, Ctr. Medico-Chirurgico S.I.S. Hahnemann (Italy)
- 692 **Influence of the laser beam wavelength on the gonarthrosis treatment: a preliminary comparative study [3405-98]**
G. Brojbeanu, St. Suteanu, Clinical Hospital Dr. Ioan Cantacuzino (Romania); M. V. Udrea, V. V. Vasiliu, National Institute for Laser, Plasma, and Radiation Physics (Romania)
- 696 **Value of low-power lasers in the treatment of symptomatic spondilosis [3405-99]**
C. Antipa, Colțea Clinical Hospital (Romania); V. Moldoveanu, Bagdazar Clinical Hospital (Romania); N. Rușca, Genesis srl (Romania); I. I. Bruckner, M. Vlăiculescu, E. Ionescu, Colțea Clinical Hospital (Romania); V. V. Vasiliu, National Institute for Laser, Plasma, and Radiation Physics (Romania)

- 702 **Dependence of the ablative effect of nanosecond laser pulses at the surface of dentine samples on laser wavelength [3405-100]**
C. G. Fenic, I. Chiş, R. V. Dabu, A. Stratan, I. G. Apostol, R. Stoian, C. Luculescu, National Institute for Laser, Plasma, and Radiation Physics (Romania); C. Ghica, L. C. Nistor, National Institute for Materials Physics (Romania)
- 708 **Comparison of the effect of UV laser radiation and of a radiomimetic substance on chromatin [3405-101]**
I. Radulescu, L. Radu, Victor Babes Institute (Romania); R. Serbanescu, Univ. of Bucharest (Romania); V. D. Nelea, C. Martin, I. N. Mihailescu, National Institute for Laser, Plasma, and Radiation Physics (Romania)
- 713 **Laser therapy in ocular tumors [3405-102]**
B. Cârstocea, O. L. Gafencu, S. Apostol, M. Ioniţă, Central Military Hospital (Romania); A. Moroşeanu, T. Dascălu, V. Lupei, National Institute for Laser, Plasma, and Radiation Physics (Romania); V. Ioniţă-Mânzatu, Biotechnos SA (Romania)
- 717 **Laser-induced fluorescence of atherosclerotic plaques [3405-103]**
N. Moise, M. L. Pascu, National Institute for Laser, Plasma, and Radiation Physics (Romania); C. Carp, C. Volvoreanu, Institute of Cardiology (Romania)
- 722 **Determination of size-shape distribution of biological particles from light-scattering measurements [3405-104]**
N. E. Mincu, Institute of Optoelectronics (Romania); M.-A. Popovici, Politehnica Univ. of Bucharest (Romania); M. Dobre, Carol Davila Medical Univ. (Romania)
- 727 **Photodynamic therapy using hematoporphyrin derivative and He-Ne laser irradiation in Erlich tumor: an experimental study on mice [3405-105]**
M. Radu, National Institute for Research and Development of Optoelectronics (Romania); D. Ciotaru, Victor Babes Institute (Romania); M. Calin, National Institute for Research and Development of Optoelectronics (Romania); G. Savi, Victor Babes Institute (Romania); M. Bota, Univ. of Southern California (USA); C. Stroila, Victor Babes Institute (Romania)
- 733 **Comparative study of the thermal effects generated by laser irradiation for medical applications [3405-106]**
M. Calin, M. Tomescu, R. N. Radvan, M. Radu, T. Necsoiu, National Institute for Research and Development of Optoelectronics (Romania)
- 739 **Low-power laser efficacy in peripheral nerve lesion treatment [3405-107]**
C. Antipa, Colţea Clinical Hospital (Romania); M. Nacu, N. Malaxa Clinical Hospital (Romania); I. I. Bruckner, Colţea Clinical Hospital (Romania); D. Bunilă, Plastic Surgery Hospital (Romania); M. Vlaiculescu, Colţea Clinical Hospital (Romania); M. L. Pascu, National Institute for Laser, Plasma, and Radiation Physics (Romania); E. Ionescu, Colţea Clinical Hospital (Romania)
- 747 **Low-power laser use in the treatment of alopecia and crural ulcers [3405-108]**
T. Ciuchiş, Military Hospital Pitesti (Romania); M. Uşurelu, Military Hospital Cluj (Romania); C. Antipa, M. Vlaiculescu, E. Ionescu, Colţea Clinical Hospital (Romania)

SESSION 6 OPTOELECTRONICS

- 756 **Applications of infrared, heterodyne detection systems (Invited Paper) [3405-109]**
M. Strzelec, Z. Puzewicz, Institute of Optoelectronics (Poland); M. Kopica, Military Univ. of Technology (Poland)
- 762 **Characterization of integrated optical waveguides based on oxidized porous silicon (Invited Paper) [3405-110]**
M. Balucani, V. Bondarenko, Istituto Nazionale per la Fisica della Materia (Italy) and Univ. degli Studi di Roma La Sapienza (Italy); N. Kasuchits, Belarusian State Univ. of Informatics and Radioelectronics; G. Lamedica, Istituto Nazionale per la Fisica della Materia (Italy) and Univ. degli Studi di Roma La Sapienza (Italy); N. Vorozov, Belarusian State Univ. of Informatics and Radioelectronics; A. Ferrari, Istituto Nazionale per la Fisica della Materia (Italy) and Univ. degli Studi di Roma La Sapienza (Italy)
- 768 **Electronic laser beam profile measurement (Invited Paper) [3405-111]**
C. B. Roundy, Spiricon, Inc. (USA)
- 779 **Satellite remote sensing data applied for seismic risk assessment of Vrancea region (Invited Paper) [3405-112]**
M. Zoran, C. L. Braescu, C. Aiftimiei, Institute of Optoelectronics (Romania)
- 784 **Amorphous silicon photodetectors for optical integrated circuits [3405-113]**
M. Balucani, Istituto per la Fisica della Materia (Italy) and Univ. di Roma La Sapienza (Italy); V. Bondarenko, Istituto per la Fisica della Materia (Italy) and Belarusian State Univ. of Informatics and Radioelectronics; G. Lamedica, A. Ricciardelli, A. Ferrari, Istituto per la Fisica della Materia (Italy) and Univ. degli Studi di Roma La Sapienza (Italy)
- 790 **Properties of polymer compositions for recording and copying optical images [3405-114]**
V. V. Bivol, Ctr. of Optoelectronics (Moldova); N. A. Barba, S. V. Robu, B. M. Ishimov, L. A. Vlad, State Univ. of Moldova; A. M. Prisacari, G. M. Triduh, E. A. Akimova, Ctr. of Optoelectronics (Moldova)
- 796 **Electro-optic response of some chiral liquid crystals with high spontaneous polarization [3405-115]**
C. Dascalu, C. Motoc, E. Petrescu, C. Rosu, Politehnica Univ. of Bucharest (Romania); H. D. Koswig, U. Labes, Technische Univ. Berlin (FRG)
- 801 **Fluid optical components and their applications in optoelectronics [3405-116]**
R. N. Rădvan, M. Călin, R. Savastru, M. Robu, M. Radu, National Institute for Research and Development of Optoelectronics (Romania)
- 807 **Optical fiber multiplexed image transmission system [3405-117]**
S. Micloș, T. Zisu, B. Robea, Institute of Optoelectronics (Romania)
- 813 **Cylindrical piezoceramic transducer for remote optoelectronic system [3405-118]**
I. Chilibon, M. Robu, Institute of Optoelectronics (Romania)
- 819 **Optical systems for night vision devices [3405-119]**
G. Copot, R. Copot, Institute of Optoelectronics (Romania)
- 825 **Optical beacon for pointing and tracking systems for free-space communications [3405-120]**
P. E. Sterian, Politehnica Univ. of Bucharest (Romania); P. P. Digulescu, Technical Military Academy (Romania); R. V. Ivan, Politehnica Univ. of Bucharest (Romania)

- 831 **Laser treatment of a-SiC:H thin films for optoelectronic applications [3405-121]**
D. Ghica, N. E. Mincu, National Institute for Research and Development of Optoelectronics (Romania); C. A. Stanciu, G. H. Dinescu, E. Aldea, National Institute for Laser, Plasma, and Radiation Physics (Romania); V. Sandu, National Institute of Materials Physics; A. Andrei, Institute of Nuclear Research (Romania); M. Dinescu, National Institute for Laser, Plasma, and Radiation Physics (Romania); A. Ferrari, M. Balucani, G. Lamedica, Istituto per la Fisica della Materia (Italy) and Univ. degli Studi di Roma La Sapienza (Italy)
- 837 **Gamma-induced transparency loss of thick quartz fibers [3405-122]**
E. M. Gasanov, E. M. Ibragimova, B. S. Yuldashev, Institute of Nuclear Physics (Uzbekistan); M. Kh. Ashurov, I. R. Rustamov, Scientific Association Phonon (Uzbekistan)
- 846 **Electrical and optical characterization of PbTiO₃/Si heterostructures for applications in optoelectronics [3405-123]**
V. Dragoi, L. Pintilie, I. Pintilie, D. Petre, I. Boerasu, National Institute of Materials Physics (Romania); M. Alexe, Max Planck Institute of Microstructure Physics (FRG)
- 852 **Optical integrated circuits [3405-124]**
O. D. Iancu, D. Pircălăboiu, Politehnica Univ. of Bucharest (Italy)
- 860 **Optical properties of polycrystalline In_xGa_{1-x}Sb (x = 0.20) from 15 to 30 μm [3405-125]**
C. A. E. Grigorescu, Institute of Optoelectronics (Romania); S. A. Manea, National Institute of Materials Physics (Romania); M. F. Logofatu, I. I. Munteanu, B. Logofatu, Univ. of Bucharest (Romania); M. Calin, M. Radu, National Institute for Research and Development of Optoelectronics (Romania); M. F. Lazarescu, National Institute of Materials Physics (Romania)
- 865 **Verifying a model for statistical hypothesis in detection of noncoherent radiation [3405-126]**
V. Babin, S. Ersen, A. Moldovan, National Institute for Research and Development of Optoelectronics (Romania); N. Iftimia, Military Research and Development Institute (Romania)
- 873 **Characterization of ion-exchanged waveguides from near-field measurements [3405-127]**
D. Pircălăboiu, Politecnico di Torino (Italy) and Politehnica Univ. of Bucharest (Romania); G. Motta, G. Perrone, I. Montrosset, Politecnico di Torino (Italy)
- 877 **Non-Markovian effects in dissipative systems [3405-128]**
E. N. Stefanescu, National Research Institute of Microtechnology (Romania); P. E. Sterian, Politehnica Univ. of Bucharest (Romania)
- 883 **Optoelectronic micropositioning device with a piezoceramic transducer [3405-129]**
I. Chilibon, M. Robu, Institute of Optoelectronics (Romania)
- 887 **Spectroellipsometric characterization of multilayer systems containing Ni and Bi [3405-130]**
V. Hutsanu, Univ. of Bucharest (Romania); M. Gartner, C. Ghita, Institute of Physical Chemistry (Romania); V. Dolocan, Univ. of Bucharest (Romania)
- 891 **Orthorectification of radar (SAR) data: synergism and complementariness with optical (Landsat TM) data [3405-131]**
C. L. Brăescu, M. Zoran, C. Aiftimei, A. Stoica, Institute of Optoelectronics (Romania); D. Răducanu, Technical Military Academy (Romania)

- 897 **Al₂O₃ single-crystalline substrates for optoelectronic applications** [3405-132]
C. Logofatu, National Institute for Lasers, Plasma, and Radiation Physics (Romania); B. Iliescu, I. Enculescu, National Institute for Materials Physics (Romania); C. A. E. Grigorescu, Institute of Optoelectronics (Romania); S. A. Manea, National Institute of Materials Physics (Romania)
- 902 **Optical light modulation in planar As₂Se₃Sn_x waveguides** [3405-133]
A. A. Popescu, A. I. Albu, A. Tsaranu, Ctr. of Optoelectronics (Moldova)
- 906 **Approximate solutions of the eigenvalue equation near cutoff for TE_{0m} and TM_{0m} modes for a step index fiber optic: new forms and considerations** [3405-134]
C. L. Schiopu, P. Schiopu, Politehnica Univ. of Bucharest (Romania)
- 912 **Concept of WDM-HD: WDM for increasing the information capacity of fiber optic communication systems** [3405-135]
P. Schiopu, Politehnica Univ. of Bucharest (Romania); L. Dragnea, Institute of Microtechnology (Romania)
- 916 **Modeling the passive and active LiNbO₃ optical waveguides** [3405-136]
N. N. Puscas, I. M. Popescu, Politehnica Univ. of Bucharest (Romania)
- 922 **Effective index method for the computation of the propagation constant and electromagnetic field distribution in z-uniform dielectric or semiconductor waveguides** [3405-137]
M. Dumitrescu, Tampere Univ. of Technology (Finland); M. Guina, Politehnica Univ. of Bucharest (Romania)
- 926 **Real performance of image intensifier systems for night vision** [3405-138]
M. Mirzu, L. Cosereanu, M. Jurba, Army Institute for Research and Development (Romania); G. Copot, D. Ralea, R. Marginean, Institute of Optoelectronics (Romania)
- 930 **Control of laser spiking in Nd:YAG lasers with saturable absorbers** [3405-139]
M. Jurba, Army Institute for Research and Development (Romania); V. Babin, Institute of Optoelectronics; N. Baltaneanu, National Institute for Laser, Plasma, and Radiation Physics (Romania); I. Gherghina, V. Jipa, E. Popescu, L. Cosereanu, M. Mirzu, Army Institute for Research and Development (Romania)
- 936 **Optical transmission of ZnO thin films** [3405-140]
I. I. Rusu, Bacău Univ. (Romania); I. D. Bursuc, Al. I. Cuza Univ. (Romania); I. Vascan, Bacău Univ. (Romania)
- 941 **Magneto-optical behavior of ferronematics** [3405-141]
C. Motoc, E. Petrescu, C. Dascalu, Politehnica Univ. of Bucharest (Romania)
- 946 **Optical bistability using nematic liquid crystals and polymer-dispersed liquid crystals** [3405-142]
D. Manaila-Maximean, C. Rosu, R. Bena, A. M. Albu, I. M. Popescu, Politehnica Univ. of Bucharest (Romania)
- 951 **IR absorption of TiO₂ thin films** [3405-143]
M. D. Stamate, Bacău Univ. (Romania); G. I. Rusu, Al. I. Cuza Univ. (Romania); I. Vascan, Bacău Univ. (Romania)

- 955 **Computerized lateral-shear interferometer [3405-144]**
S. A. Hasegan, A. Jianu, V. I. Vlad, National Institute for Laser, Plasma, and Radiation Physics (Romania)
- 960 **Amorphous Se/CdSe and SiO_x/CdSe multilayers [3405-145]**
M. A. Popescu, F. Sava, A. Lörcinzi, National Institute of Materials Physics (Romania); E. Vateva, D. Nesheva, G. Tchaushev, Institute of Solid State Physics (Bulgaria); I. N. Mihailescu, Institute of Atomic Physics (Romania); P.-J. Koch, S. Obst, H. Bradaczek, Freie Univ. Berlin (FRG)
- 965 **Aluminophosphate glass with CdS_xSe_{1-x} microcrystallite for optoelectronics [3405-146]**
R. Rogojan, M. Elisa, MATPUR SA (Romania); P. E. Sterian, Politehnica Univ. of Bucharest (Romania)

SESSION 7 OPTICAL SENSORS AND METROLOGY

- 972 **New principle for self-calibration techniques in phase-shift interferometry (Invited Paper) [3405-147]**
A. Dobroiu, D. Apostol, V. Damian, V. Nascov, National Institute for Laser, Plasma, and Radiation Physics (Romania)
- 978 **Instruments and standard measurement procedures for laser beam characterization (Invited Paper) [3405-148]**
R. Mästle, C. Schmitz, F. Varnik, A. Giesen, H. Hügel, Univ. Stuttgart (FRG)
- 990 **Laser frequency comparisons involving Romanian length standard and traceability (Invited Paper) [3405-149]**
G. Popescu, National Institute for Laser, Plasma, and Radiation Physics (Romania); J.-M. Chartier, Bureau International des Poids et Mesures (France); F. Bertinotto, Istituto di Metrologia G. Colonnetti (Italy); F. Petru, Institute of Scientific Instruments (Czech Republic)
- 999 **All-direction localizer of pulsed optical sources [3405-150]**
P. P. Digulescu, Technical Military Academy (Romania); P. E. Sterian, Politehnica Univ. of Bucharest (Romania)
- 1007 **UV radiation sensors with unitary and binary superficial barrier [3405-151]**
V. Dorogan, T. Vieru, V. Kosyak, Technical Univ. of Moldova; I. Damaskin, Institute of Applied Physics (Moldova); F. Chirita, Technical Univ. of Moldova
- 1013 **New type of sensor of radiation in a wide range of energy [3405-152]**
A. M. Andriesh, S. A. Malkov, V. I. Verlan, M. G. Bulgaru, Institute of Applied Physics (Moldova)
- 1022 **Interference devices for noncontact diagnostics of arbitrarily shaped rough surfaces [3405-153]**
P. P. Maksimyak, Chernivtsy Univ. (Ukraine)
- 1027 **Optical studies on sedimentation of suspensions [3405-154]**
S. Anghel, Univ. of Pitești (Romania); I. Iova, Șt. Levai, Univ. of Bucharest (Romania); I. Iorga Simăn, I. Iosub, Univ. of Pitești (Romania)

- 1032 **Quadrant detector based on InGaAsP heterostructures [3405-155]**
V. Dorogan, V. Brynzari, T. Vieru, V. Kosyak, Technical Univ. of Moldova
- 1039 **Photothermal method using a pyroelectric sensor for thermophysical characterization of agricultural and biological samples [3405-156]**
A. Frandas, D. Dadarlat, M. Chirtoc, Institute of Isotopic and Molecular Technology (Romania); H. Jalink, Ctr. for Plant Breeding and Reproductive Research (Netherlands); D. D. Bicanic, Wageningen Agricultural Univ. (Netherlands); D. Paris, J. S. Antoniow, M. Egee, Univ. de Reims (France); C. Ungureanu, Institute of Isotopic and Molecular Technology (Romania)
- 1045 **Techniques for accurately measuring laser beam width with commercial CCD cameras [3405-157]**
C. B. Roundy, Spiricon, Inc. (USA)
- 1056 **Definition of a robust measurement of similarity for the localization of small shapes in scenes [3405-158]**
X. Fernández, Industrias de Optica, SA (Spain); J. Ferré-Borrull, S. Bosch, Univ. de Barcelona (Spain)
- 1063 **Light scattering in liquid crystals [3405-159]**
M. Ursache, M. Socaciu, C. Sarpe-Tudoran, Univ. of Craiova (Romania)
- 1067 **Digital laser powermeter [3405-160]**
E. Smeu, N. N. Puscas, I. M. Popescu, Politehnica Univ. of Bucharest (Romania)
- 1074 **Structured light in visual inspection [3405-161]**
C. Blanaru, V. V. Vasiliu, National Institute for Laser, Plasma, and Radiation Physics (Romania)
- 1078 **Romanian primary length standards involved in international comparisons [3405-162]**
G. Popescu, National Institute for Laser, Plasma, and Radiation Physics (Romania)
- 1083 **Calibration procedures for a 10.6- μ m laser calorimeter [3405-163]**
M. Kennedy, D. Ristau, Laser Zentrum Hannover eV (FRG); G. Dumitru, D. G. Sporea, C. A. Timus, National Institute for Laser, Plasma, and Radiation Physics (Romania)
- 1088 **Estimation of some physical characteristics of metallic powders using VIS reflectance measurements [3405-164]**
M. Nicola, E. Darvasi, D. Gomoiescu, E. Cordoş, Research Institute for Analytical Instrumentation (Romania)
- 1094 **Method for small birefringence evaluation [3405-165]**
A. M. Beldiceanu, Pro Optica SA (Romania)
- 1100 **Circularity measurement by laser triangulation [3405-166]**
V. Damian, C. Blanaru, D. Apostol, A. Dobroiu, V. Nascov, National Institute for Laser, Plasma, and Radiation Physics (Romania)

SESSION 8 OPTICAL COMPONENTS

- 1106 **Polarizing interference coatings made with anisotropic thin films (Invited Paper) [3405-167]**
F. Flory, C. Defay, Ecole Nationale Supérieure de Physique de Marseille (France)

- 1114 **Special mirrors for cw CO₂ high-power lasers (Invited Paper)** [3405-168]
R. V. Medianu, I. Gutu, G. Georgescu, National Institute for Laser, Plasma, and Radiation Physics (Romania); M. F. Lazarescu, National Institute of Materials Physics (Romania)
- 1120 **Spectrophotometry, ellipsometry, and computer simulation in thin film developments (Invited Paper)** [3405-169]
S. Bosch, Univ. de Barcelona (Spain)
- 1132 **Structure investigations of optical coatings on GaAs substrate (Invited Paper)** [3405-170]
C. A. Timus, R. V. Medianu, G. Georgescu, National Institute for Laser, Plasma, and Radiation Physics (Romania); E. Vasile, METAV SA (Romania)
- 1137 **Characteristics of a carbon/nickel multilayer structure for soft x-ray optics deposited by rf magnetron sputtering** [3405-171]
M. Ulmeanu, G. Georgescu, R. V. Medianu, National Institute for Laser, Plasma, and Radiation Physics (Romania); N. Nastase, National Institute of Microtechnology (Romania); C. Ghica, National Institute of Materials Physics (Romania); V. V. Vasiliu, National Institute for Laser, Plasma, and Radiation Physics (Romania)
- 1143 **New method for automatic optimization of glass combination in optical systems working in the visible range** [3405-172]
D. Ralea, R. Marginean, Institute of Optoelectronics (Romania); M. Marzu, Army Institute for Research and Development (Romania)
- 1150 **Interferometric characterization of GRIN lenses for ophthalmic uses** [3405-173]
J. R. de F. Moneo, I. P. Juvells, S. R. Vallmitjana, S. Bosch, A. Carnicer, I. Labastida, J. Pérez, Univ. de Barcelona (Spain)
- 1156 **Ray tracing for ophthalmic optics: specific developments for GRIN materials** [3405-174]
J. R. de F. Moneo, I. P. Juvells, S. R. Vallmitjana, S. Bosch, A. Carnicer, I. Labastida, J. Pérez, Univ. de Barcelona (Spain)
- 1162 **Solutions of single-layer synthesis with symmetrical three-layer periods** [3405-175]
A. G. Dincă, P. T. Miclea, V. Lupei, National Institute for Laser, Plasma, and Radiation Physics (Romania); M. P. Dincă, Univ. of Bucharest (Romania)
- 1167 **Yield optimization of multilayer optical coating by modeling of the monitoring process** [3405-176]
G. L. Muscalu, Pro Optica SA (Romania)
- 1173 **Interferential filter design with continuously variable refractive index** [3405-177]
A. G. Dincă, V. Lupei, National Institute for Laser, Plasma, and Radiation Physics (Romania); M. P. Dincă, Univ. of Bucharest (Romania)
- 1178 **Filters with induced transmission** [3405-178]
Gh. Honciuc, Pro Optica SA (Romania)
- 1183 **Software for optical coating design** [3405-179]
Gh. Honciuc, Pro Optica SA (Romania); Gh. Singurel, Al. I. Cuza Univ. (Romania)
- 1189 **Electrostatically driven dynamic focus system** [3405-180]
H. Țoția, M. Micluța, National Institute for Laser, Plasma, and Radiation Physics (Romania)

SESSION 9 OPTICS AND ENVIRONMENT

- 1194 **III-V compounds and piezoelectric ceramic thin films deposited by reactive PLD: application to sensor building (Invited Paper) [3405-181]**
M. Dinescu, National Institute for Laser, Plasma, and Radiation Physics (Romania); P. Verardi, F. Craciun, CNR Institute of Acoustics (Italy); C. A. Stanciu, R. Dinu, National Institute for Laser, Plasma, and Radiation Physics (Romania); C. Gerardi, L. Mirengi, PASTIS CNRSM (Italy); M. Gartner, Institute of Physical Chemistry I.G. Murgulescu (Romania); V. Sandu, National Institute of Materials Physics (Romania)
- 1202 **Laser monitoring of pesticides in water (Invited Paper) [3405-182]**
M. L. Pascu, N. Moise, L. Voicu, National Institute for Laser, Plasma, and Radiation Physics (Romania); T. Negoita, Polar Research Ctr. (Romania); G. Manolescu, Institute of Physical Chemistry (Romania); A. Smarandache, National Institute of Materials Physics (Romania)
- 1215 **Detection of atmospheric pollutants by pulsed photoacoustic spectroscopy [3405-183]**
M. Roman, M. L. Pascu, A. Staicu, National Institute for Laser, Plasma, and Radiation Physics (Romania)
- 1220 **Modeling of atmospheric effects on the angular reflectance characteristics of vegetation canopies [3405-184]**
G. Stancalie, National Institute of Meteorology and Hydrology (Romania)
- 1228 *Author Index*

Conference Committees

Conference Chair

Valentin I. Vlad, National Institute for Laser, Plasma, and Radiation Physics (Romania)

Organizing Committee Chair

Dan C. Dumitras, National Institute for Laser, Plasma, and Radiation Physics (Romania)

Scientific Committee

A. Andriesh (Moldova)
H. Arsenaull (Canada)
M. Bertolotti (Italy)
E. Borsella (Italy)
D. Botez (USA)
C. Boulon (France)
D. Cacuci (FRG)
D. Casasent (USA)
M. Cauchetier (France)
P. Chavel (France)
O. Conde (Portugal)
J. C. Dainty (UK)
G. Denardo (Italy)
G. Emiliani (Italy)
T. Fujioka (Japan)
M. Giurgea (Romania)
R. Grigorovici (Romania)
G. Huber (FRG)
F. Huysken (FRG)
O. Keller (Denmark)
A. Katzir (Israel)
F. Kneubuehl (Switzerland)
V. Konov (Russia)
A. Luches (Italy)
D. Malacara (Mexico)
E. Marom (Israel)
A. Peled (Israel)
I. I. Popescu (Romania)
D. Ristau (FRG)
P. Rastogi (Switzerland)
A. Sandulescu (Romania)
A. Sona (Italy)
S. Tamir (Israel)
T. Tschudi (FRG)
J. Tsujiuchi (Japan)
I. Ursu (Romania)
H. Walther (FRG)
K. Yatsui (Japan)

Program Committee

R. Alexandrescu (Romania)
D. Apostol (Romania)
J. M. Chartier (France)
V. Ciumas (Moldova)
T. Dascalu (Romania)
D. Dumitras (Romania)
D. Dutu (Romania)
F. Flory (France)
L. Garifo (Italy)
C. Grigoriu (Romania)
N. Ionescu-Pallas (Romania)
I. Iova (Romania)
M. Jelinek (Czech Republic)
A. Lofthus (FRG)
V. Lupei (Romania)
R. Medianu (Romania)
I. N. Mihailescu (Romania)
D. Mihalache (Romania)
I. Morjan (Romania)
I. Moya (Spain)
Th. Necsoiu (Romania)
L. Panasiuk (Moldova)
M. L. Pascu (Romania)
A. Piegari (Italy)
I. M. Popescu (Romania)
N. Sabotinov (Bulgaria)
D. Sporea (Romania)
P. Sterian (Romania)
V. I. Topa (Romania)
C. Ungureanu (Romania)
V. I. Vlad (Romania)
M. Zoran (Romania)

Technical Committee

S. Amarande (Romania)
M. Dinescu (Romania)
D. C. A. Dutu (Romania)
L. Fara (Romania)
S. Georgescu (Romania)
St. Levai (Romania)
A. Lupei (Romania)
A. Petris (Romania)
N. Puscas (Romania)
R. Radvan (Romania)
M. Robu (Romania)
D. Savastu (Romania)
R. Savastu (Romania)
D. Sporea (Romania)
C. Timus (Romania)
T. Tudor (Romania)

Organized by



Romanian Physical Society - Division of Optics and Quantum Electronics



The International Society for Optical Engineering - Romanian Chapter (SPIE / RO)

National Institute for Laser, Plasma and Radiation Physics



National Institute for Research & Development of Optoelectronics (INOE 2000)



Institute of Optoelectronics (IOEL-S.A.)

University of Bucharest - Faculty of Physics

Politehnica University of Bucharest

Sponsored by

Romanian Ministry of Research and Technology



Romanian Academy - Division of Physics

Romanian Ministry of Education



The International Society for Optical Engineering (SPIE)



European Office of Aerospace Research and Development (EOARD)



International Centre for Theoretical Physics (ICTP)



International Commission for Optics (ICO)



European Optical Society (EOS)



Institute of Atomic Physics

Introduction

The ROMOPTO '97 Conference is the fifth in a series of international conferences dedicated to optics and lasers held every three years in Bucharest. The topics of this conference are rather broad and reflect the fast evolution of optics, including lasers and their applications in material science, information science and technology, biology and medicine, sensing and metrology, as well as in environmental research.

The aims of the ROMOPTO conferences are to increase the number of meetings for the experts working in optics and lasers, where they can share experiences, discuss their newest results, stimulate interdisciplinary research, and consider the prospects of applications. The position of Romania in Central-Eastern Europe plays an important role in the promotion of scientific contacts in this part of the world, where, even since the Wall came down, many difficulties and inequalities still exist. The existence of a national research school in the field of optics and of an important optics community in Romania (in universities, national research institutes and industry, the third largest one in the Romanian physics, with approximately 300 members, according to the roster of the Romanian Physical Society) is another active element in these scientific events.

Organization of ROMOPTO '97 was possible only through the actions and support of several domestic and international organizations. We must mention the Division of Optics and Quantum Electronics of the Romanian Physical Society, which is a Territorial Committee of ICO, the Romanian Chapter of SPIE, the National Institute for Laser, Plasma, and Radiation Physics, the National Institute for Research and Development of Optoelectronics (INOE 2000 and IOEL SA), the Faculty of Physics at the University of Bucharest, and the Politehnica University of Bucharest. Thanks are due to the cosponsoring institutions for their important advice and contributions to the success of this conference: the International Society for Optical Engineering (SPIE), the United States Air Force European Office of Aerospace Research and Development (EOARD), the International Centre for Theoretical Physics (ICTP, Trieste), the International Commission for Optics (ICO), the European Optical Society (EOS), the Romanian Ministry of Research and Technology, the Romanian Academy, the Romanian Ministry of Education, and the Institute of Atomic Physics.

Through the efforts of the Scientific and Program Committees, 288 papers by authors from 23 countries have been selected for presentation at ROMOPTO '97, making this conference a truly international one. In addition, 3 plenary lectures and 44 invited lectures gave an overview of the newest and the most important results in optics. We express our gratitude to the referees, to the invited professors, and to all the participants in ROMOPTO '97 for their very high level work. Thanks are due to SPIE, which assured that most of these works are published in the present volume, having a wide distribution in the scientific world.

We would like to express our thanks to the Organizing Committee, to many colleagues and persons on the various committees, and to the secretariat for their collaboration and hard work. We hope that everyone attending ROMOPTO '97 enjoyed the scientific sessions and our country. We also hope that ROMOPTO '97 provided an opportunity to renew previous friendships and start new ones.

On behalf of the organizing institutions, we would like to extend our warmest thanks to all participants of ROMOPTO '97 and to invite them to bring their valuable contribution to our next conference in 2000.

Valentin I. Vlad
Dan C. Dumitras

SESSION 1

Lasers and Radiation Sources

Q-switch regime of 3- μm erbium lasers

Serban Georgescu, Voicu Lupei, and Claudiu Hapenciuc

National Institute for Lasers, Plasma and Radiation Physics, Bucharest, Romania

ABSTRACT

A mathematical model, based exclusively on spectroscopic data concerning radiative, non-radiative, and energy transfer processes, is proposed and used to simulate the Q-switch regime of three-micron Er: YAG laser. The connection between the main energy transfer mechanisms that make possible generation on the self-saturated transition $^4I_{11/2} \rightarrow ^4I_{13/2}$ (up-conversion from $^4I_{13/2}$, and $^4I_{11/2}$, cross-relaxation from $^4S_{3/2}$) and the giant pulse characteristics is discussed. The radiative as well as non-radiative losses during optical pumping and giant pulse generation are defined and evaluated. A particular attention is given to FTIR Q-switch which demonstrated real qualities for 3- μm Erbium lasers. The reasons responsible for experimental performances of Q-switched Er: YAG lasers inferior to those predicted by the mathematical modelling are analysed.

Keywords: mid infrared lasers; Q-switch, Er^{3+} .

1. INTRODUCTION

Laser radiation at 3- μm is of great interest in medical and biological applications because water and hydroxyapatite, which are the major constituents of soft, and, respectively, hard (bones, tooth enamel) biological tissues, have very strong absorption in this region. Furthermore, in order to produce minimal thermal damage of the adjacent tissues in surgical operations, short pulses (if possible, in the nanosecond range) are desirable.

The Er: YAG laser, working in Q-switch regime at 2.94 μm (laser transition $^4I_{11/2} \rightarrow ^4I_{13/2}$), could satisfy these requirements. Nevertheless, since this laser transition is self-saturated (i. e., the lifetime of the initial laser level is much shorter than the lifetime of the final one) efficient generation of short pulses is a quite delicate problem.

The generation of giant pulses of three-micron Erbium lasers was obtained experimentally using different Q-switches as mechanical (spinning prism), electro-optic, passive and, more recently, FTIR (from Frustrated Total Internal Reflection). Though the idea of utilisation of FTIR devices to control the emission of lasers is not new¹, only in the last years convenient Q-switches based on this phenomenon were designed^{2,3} and demonstrated real qualities for 3- μm lasers.

There are few works devoted to the mathematical modelling of the Q-switching of three-micron Er-lasers^{3,4}, where a simplified two-level model is used and the initial population inversion is taken from experiment (small signal, single pass amplification coefficient). Though the results of this modelling describe quite satisfactorily the experimental data, no connection was made between energy transfer processes governing three-micron lasing of Er laser, pumping conditions, co-doping, and the characteristics of giant pulse generation, as for cw emission⁵. In order to understand the peculiarities and the possibilities of the 3- μm Er lasers working in Q-switch regime, we have constructed and used a more general, rate equation model, based exclusively on spectroscopic data, involving the populations of Er^{3+} energy levels up to $^4S_{3/2}$ and three energy transfer processes: up-conversion from $^4I_{11/2}$ and $^4I_{13/2}$ and cross-relaxation from $^4S_{3/2}$. The necessary spectroscopic coefficients, entering the rate equations, were measured by us or were taken from literature. The Q-switch action was simulated for two cases: idealised (step function) and more realistic one, with 1.5 μs switching time, illustrating the FTIR device. The results of the simulations are then compared with data concerning the FTIR Q-switched Er: YAG lasers, for which more systematic experimental data are available in literature.

2. RATE EQUATIONS MODEL

The energy transfer processes considered in our model are presented in Fig. 1 with dashed lines. The evolution of the energy level populations and the photon density, function of pumping conditions, activator

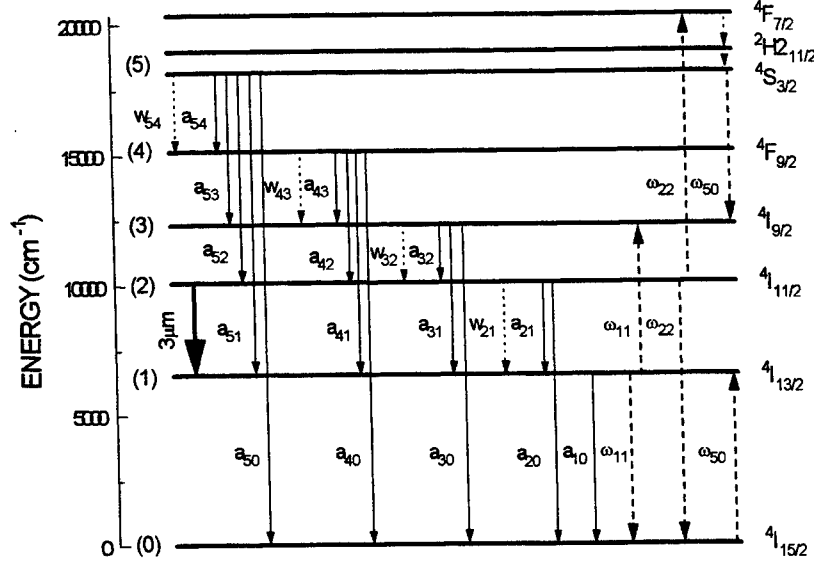


Fig. 1. Energy level scheme of Er^{3+} in YAG and the radiative (solid line), multiphonon (dotted line), and energy transfer processes (dashed line) involved in the rate Eqs. (1).

concentration, and laser resonator characteristics, is described by the non-linear system of coupled rate equations

$$\begin{aligned}
 \frac{dN_5}{dt} &= -(a_{50} + a_{51} + a_{52} + a_{53} + a_{54} + w_{54})N_5 - \omega_{50}N_5N_0 + \omega_{22}N_2^2 + R_{p5}N_0 \\
 \frac{dN_4}{dt} &= -(a_{40} + a_{41} + a_{42} + a_{43} + w_{43})N_4 + (a_{54} + w_{54})N_5 + R_{p4}N_0 \\
 \frac{dN_3}{dt} &= -(a_{30} + a_{31} + a_{32} + w_{32})N_3 + a_{53}N_5 + (a_{43} + w_{43})N_4 + \omega_{11}N_1^2 + \omega_{50}N_5N_0 + R_{p3}N_0 \\
 \frac{dN_2}{dt} &= -(a_{20} + a_{21} + w_{21})N_2 + a_{52}N_5 + a_{42}N_4 + a_{32}N_3 - 2\omega_{22}N_2^2 - c\sigma(\alpha N_2 - \beta N_1)\phi + R_{p2}N_0 \\
 \frac{dN_1}{dt} &= -a_{10}N_1 + a_{51}N_5 + a_{41}N_4 + a_{31}N_3 + (a_{21} + w_{21})N_2 - 2\omega_{11}N_1^2 + \omega_{50}N_5N_0 + c\sigma(\alpha N_2 - \beta N_1)\phi + R_{p1}N_0 \\
 \frac{d\phi}{dt} &= \frac{c\phi}{(n-1 + l'/l)} [\sigma(\alpha N_2 - \beta N_1) - \rho] + k_{se}a_{21}N_2
 \end{aligned} \quad (1)$$

where N_0 to N_5 are the populations of the $4I_{15/2}$, $4I_{13/2}$, $4I_{11/2}$, $4I_{9/2}$, $4F_{9/2}$, and $4S_{3/2}$ (thermalized, at room temperature, with $2H_{11/2}$), respectively. The coefficients a_{ij} and w_{ij} are the probabilities of radiative and, respectively, multiphonon ($i \rightarrow j$) transitions (see Fig. 1). The energy transfer processes are represented in Eqs. (1), by ω_{ij} (for an Er (50 at. %) YAG crystal $\omega_{11} = 1.3 \times 10^{-15} \text{ cm}^3 \text{ s}^{-1}$, $\omega_{22} = 3.7 \times 10^{-15} \text{ cm}^3 \text{ s}^{-1}$, and $\omega_{50} = 1.06 \times 10^{-21} \text{ cm}^3 \text{ s}^{-1}$ (Ref. 5)). Pumping is allowed in any energy level, i , with the rate R_{pi} . In Eqs. (1) σ ($= 2.6 \times 10^{-20} \text{ cm}^2$) is the emission cross-section, c , the speed of light, ϕ , the photon density inside the laser resonator, ρ - the total losses for a round trip, and α , β ($\alpha = 0.2$,

$\beta = 0.04$ for the 2.94 μm transition at room temperature) are the Boltzmann population coefficients for the Stark sub-levels involved in the laser emission. In the last of Eqs. (1) n represents the refraction index of the active medium of length l , and l' is the length of the laser resonator.

The coefficients a_{ij} entering Eqs. (1) are the sum of electric- and magnetic-dipole probabilities, given in Table 1. The probability of the multiphonon transition, between successive, levels is $w_{i,i-1} = 1/T_i^f - 1/T_i^{\text{rad}}$, where T_i^f , T_i^{rad} are, respectively, the fluorescence and the radiative lifetimes (Table 1). The last term in the 6th of Eqs. (1) represents the spontaneous emission at the laser wavelength. The electric-dipole transition probabilities were calculated with a modified Judd-Ofelt analysis ⁶.

Table 1. Spectroscopic data for Er: YAG, at room temperature.

Initial level	Terminal level	A_{ij}^{ed} (s ⁻¹)	A_{ij}^{md} (s ⁻¹)	T_i^{rad} (μs)	T_i^f (μs)	w_{ij} (s ⁻¹)
$^4\text{S}_{3/2}$	$^4\text{F}_{9/2}$	0.6	-	619	16	5.56×10^4
	$^4\text{I}_{9/2}$	60.5	-			
	$^4\text{I}_{11/2}$	31.8	-			
	$^4\text{I}_{13/2}$	446.6	-			
	$^4\text{I}_{15/2}$	1075.5	-			
$^4\text{F}_{9/2}$	$^4\text{I}_{9/2}$	0.5	3.9	629	1.5	6.65×10^5
	$^4\text{I}_{11/2}$	52.9	10.4			
	$^4\text{I}_{13/2}$	63.3	-			
	$^4\text{I}_{15/2}$	1485.7	-			
$^4\text{I}_{9/2}$	$^4\text{I}_{11/2}$	0.6	1.5	4420	0.05	2×10^7
	$^4\text{I}_{13/2}$	45.9	-			
	$^4\text{I}_{15/2}$	178.3	-			
$^4\text{I}_{11/2}$	$^4\text{I}_{13/2}$	16.2	12.49	7170	100	9.86×10^3
	$^4\text{I}_{15/2}$	110.8	-			
$^4\text{I}_{13/2}$	$^4\text{I}_{15/2}$	97.9	56.3	6484	6500	~ 0

The total loss per round trip, ρ , is expressed as $\rho = -\frac{\ln(R_1 R_2 T_Q^2)}{2l} + \rho_0$, where R_1 , R_2 are the reflectivity of the total (rear) and partial (coupling) laser mirrors, T_Q is the one-way optical transmission of the Q-switch, and ρ_0 is the total passive loss coefficient. The Q-switch operation is simulated in the Eqs. (1) by changing the optical transmission of the Q-switch from the low value, T_Q^{low} , to the high value, T_Q^{high} .

The energy of the giant pulse is calculated with the expression

$$E_{\text{pulse}} = \frac{h\nu_l c A \ln(1/R_2)}{1 + (n-1)(l/l')} \int_{\text{pulse}} \phi(t) dt \quad (2)$$

$h\nu_l$ being the energy of a laser photon and A the cross-section of the active element. The FWHM (full width at half maximum) pulsewidth, τ_{pulse} , is calculated in the so called triangular approximation, i. e. $\tau_{\text{pulse}} = \int \phi(t) dt / \phi_{\text{max}}$, where ϕ_{max} is the maximum value of the photon density.

The energy stored in the Er: YAG active medium is the sum of the "potential" energies of all energy levels populated by the optical pumping. The non-uniform (Boltzmann) population of the Stark sub-levels was taken into

account by defining the "thermal center of gravity" of the i^{th} energy level, $E_i^B \equiv \sum_j E_{ij} \frac{\exp[-(E_{ij} - E_{i1}) / k_B T]}{\sum_j \exp[-(E_{ij} - E_{i1}) / k_B T]}$,

where E_{ij} is the j^{th} Stark sub-level of the level i , k_B is the Boltzmann constant, and T is the absolute temperature. The energy stored / cm^3 of active medium at the time moment t is now

$$E_{\text{stored}}(t) = \sum_{i=1}^5 N_i(t) h\nu_i \quad (3)$$

where $N_i(t)$ is the instantaneous population of the level i and $h\nu_i$ is the photon energy corresponding to E_i^B .

We can simulate either monochromatic pumping in any level i (with rate R_{pi}) or flash lamp pumping (approximating the Xenon flash lamp with a black body). For flash lamp pumping we define the spectral pumping coefficients $k_{pi} = \int_{\text{abs. band}} g(\lambda) \sigma(\lambda) d\lambda$, with $\sum_i k_{pi} = 1$. $g(\lambda)$ contains the spectral dependence of the black body

emissivity and $\sigma(\lambda)$ is the absorption cross-section of Er^{3+} in YAG at the wavelength λ . We estimated that for black body temperature of 10000 K, approx. 78 % of the pump energy is absorbed in the 0.355 - 0.565 μm domain, and, via rapid multiphonon transitions transferred to $^4S_{3/2}$. The energy absorbed effectively by the Er: YAG crystal in eleven absorption bands (from $^4I_{15/2} \rightarrow ^4I_{13/2}$ at 1.5 μm , up to $^4I_{15/2} \rightarrow ^4G_{9/2}$, $^2K_{15/2}$, at 0.36 μm) is

$$E_{\text{abs}} = \sum_{i=1}^{11} k_{pi} h\nu_i \int_0^{\Delta t} R(t) dt \quad \text{where } h\nu_i \text{ is the photon energy associated with the } i^{\text{th}} \text{ energy level of } \text{Er}^{3+}.$$

During the optical pumping and giant pulse generation a fraction of the absorbed energy is lost as spontaneous emission (radiative loss) or as heat (non-radiative loss). The expression of the energy lost by radiative transitions / cm^3 of active medium, during the optical pumping is

$$E_{\text{rad}} = \int_0^{\Delta t} \left\{ \sum_{i=1}^5 N_i(t) \left[\sum_{j < i} a_{ij} h\nu_{ij} \right] \right\} dt \quad (4)$$

where Δt is the duration of the optical pumping and a_{ij} , $h\nu_{ij}$ are related to the radiative transition $i \rightarrow j$. The same expression can be used for the radiative losses during the generation of the giant laser pulse. For the non-radiative losses we found three main contributions. Thus, the contribution produced through normal multiphonon transition from the energy levels involved in Eqs. (1) is

$$E_{\text{nrad}}^{(1)} = \int_0^{\Delta t} \left[\omega_{22} N_2^2(t) h\nu_{65} + \sum_{i=2}^5 N_i(t) w_{i,i-1} h\nu_{i,i-1} \right] dt \quad (5)$$

where the first term in the square parentheses represents the heat generated in the rapid multiphonon transition $^4F_{7/2} \rightarrow ^4S_{3/2}$, with the energy gap between them corresponding to $h\nu_{65}$. The level $^4F_{7/2}$ is fed from $^4I_{11/2}$ by the up-conversion process with rate ω_{22} . A second contribution, due to the off-resonance of some of the energy transfer processes (an excess of 778 cm^{-1} for the up-conversion from $^4I_{13/2}$, and a deficit of 533 cm^{-1} for the cross-relaxation from $^4S_{3/2}$) is expressed as

$$E_{\text{nrad}}^{(2)} = \int_0^{\Delta t} \left[\omega_{11} N_1^2(t) h\nu_e - \omega_{30} N_0(t) N_5(t) h\nu_d \right] dt \quad (6)$$

where $h\nu_e$, $h\nu_d$, are, respectively, the excess and deficit energy per photon. For flash lamp pumping a supplementary source of heating is represented by the energy lost in the non-radiative transitions from the higher pump levels to $^4S_{3/2}$,

$$E_{nr}^{(3)} = \sum_{i=6}^{11} k_{pi} h\nu_{i5} \int_0^{\infty} R(t) N_0(t) dt \quad (7)$$

with $h\nu_{i5}$ corresponding to the energy difference between the higher pump levels and $^4S_{3/2}$. We must note that $E_{nr}^{(3)}$ is included in total non-radiative losses only during the flash pumping interval. Since, in our model, the populations of the Er^{3+} levels higher than $^4S_{3/2}$ are not taken into account, only $E_{nr}^{(1)}$ and $E_{nr}^{(2)}$ will be considered in evaluating the non-radiative losses during the giant laser pulse.

3. RESULTS AND DISCUSSION

In our simulations we have used square pump pulses 200 μs . The Q-switch is open at the end of the pump pulse, when the maximal value of the population inversion is reached. If not specified otherwise, we will consider the following parameters: a volume of the active medium ($\text{Er}(50 \text{ at. \%})$: YAG) of 1 cm^3 , with length $l = 8 \text{ cm}$ and cross-section $A = 0.125 \text{ cm}^2$ (as used in Ref. 3). The resonator length is $l' = 27 \text{ cm}$ and the mirrors reflectivities are $R_1 = 1$, $R_2 = 0.78$. The passive loss coefficient is $\rho_0 = 0 \text{ cm}^{-1}$. For an active medium of 8 cm the value of $T_Q^{\text{high}} = 0.95$ corresponds to $\rho_0 = 0.0064 \text{ cm}^{-1}$.

Two different approaches were used in calculating the energy generated during the giant laser pulse: (i) with the expression of E_{pulse} , given in the precedent section; (ii) considering the variation of the stored energy in the active medium during the giant laser pulse, ΔE_{stored} and subtracting the radiative and non-radiative losses, E_{loss} . As an illustration, we present in Fig. 2 E_{pulse} as well as ΔE_{stored} and E_{loss} , function of the absorbed energy, in the case of a FTIR Q-switch. We must note that the losses produced during the giant pulse can not be neglected, especially near laser threshold.

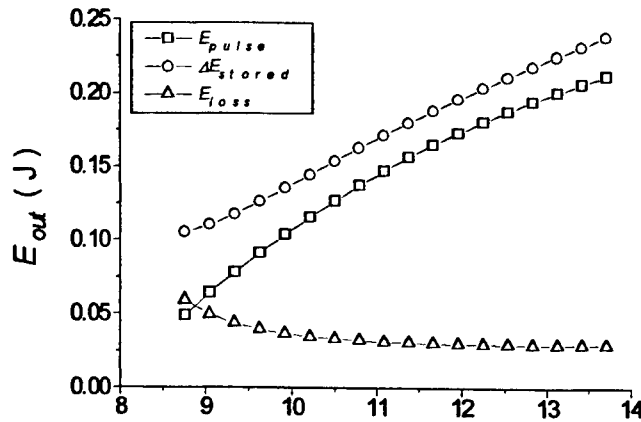


Fig. 2.. Input - output characteristics for a FTIR Q-switch with $T_Q^{\text{high}} = 0.95$, switching time $t_{Qs} = 1.5 \mu\text{s}$. The active medium has 1 cm^3 volume ($l = 8 \text{ cm}$, $A = 0.125 \text{ cm}^2$). The resonator length is $l' = 27 \text{ cm}$ and the mirror reflectivities are, respectively, $R_1 = 1$, $R_2 = 0.78$.

A comparison between FTIR and idealised-Q-switches performances, for various resonator lengths, is given in Fig. 3. The rather good performances of the FTIR Q-switch, especially for longer resonators, could be explained by the relatively low value of the emission cross-section, leading to long pulse build-up times.

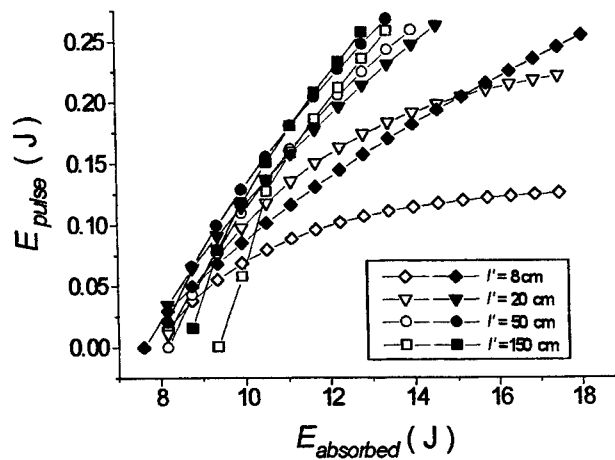


Fig. 3. Comparison between the output characteristics of FTIR (open symbols) and the idealised (solid symbols) Q-switches, for various lengths of the laser resonator. Due to a long build-up time, the efficiency difference between the FTIR and the idealised Q-switches is not drastic, especially for long resonators.

For usual pumping pulses (200 - 300 μs) our calculations show that we could still consider the levels population close to the stationary values, especially for high pump intensities. On the other hand, our analysis show that during the giant pulse generation the role of the energy transfer processes, essential for the realisation of the population inversion, is not very important. Therefore, within a rather good approximation, some of the main conclusion of the cw regime⁵ could be applied to the Q-switch regime. One of the conclusions was addressed to the effect of co-doping the Er: YAG crystal with ions as Tm^{3+} or Ho^{3+} , in order to reduce the lifetime of the terminal laser level, T_1 . Thus, according to Ref. 5, for the 2.94 μm laser transition of Er in YAG, characterised by a subunitary figure of merit $p = (\alpha / \beta) \sqrt{(\omega_{22} / \omega_{11})}$ ($= 0.43$), the value of the terminal laser level lifetime, T_1 , should be kept as large as possible for efficient cw lasing. For the Q-switch regime our simulations show the same tendency: the reduction of T_1 , though it could help the formation of the laser pulse, reduces the population inversion and the overall result is negative. On the contrary, for transitions with $p > 1$ (as for example, the emission at 2.802 μm of Cr: Er: YSGG, with $p = 1.027$ or the emission at 2.7 μm of Cr: Er: YAG, with $p = 1.85$ ⁵) the reduction of T_1 should be twice beneficial for Q-switched lasers: improves the population inversion and helps the formation of the giant pulse.

A comparison of the results of our analysis for the 2.94 μm emission of FTIR Q-switched Er: YAG laser with published experimental data^{2,3} show that, generally, the experimental giant pulses are less energetic than this mathematical model predicts. Using the FWHM pulsewidth, τ_{pulse} , versus pulse energy, E_{pulse} representation (which proved to be very convenient, being non-sensitive to the spectral composition of the pumping light and to the experimental pump efficiency), giant pulses with energy less than 100 mJ and shorter than 100 ns, for comparable laser configurations and active media, can be obtained only for passive losses $\rho_0 > 0.02 \text{ cm}^{-1}$ (Fig. 4). Taking into account the very strong absorption of the water at 2.94 μm , water vapour traces present in the atmosphere could introduce, especially for long resonators, rather high passive losses. On the other hand, the rate equation model

requires a population inversion at the laser threshold, significantly higher than the experimental value estimated (approx. $1.2 \times 10^{18} \text{ cm}^{-3}$, according to ²). Therefore, to explain the discrepancy between the experiment and theory we

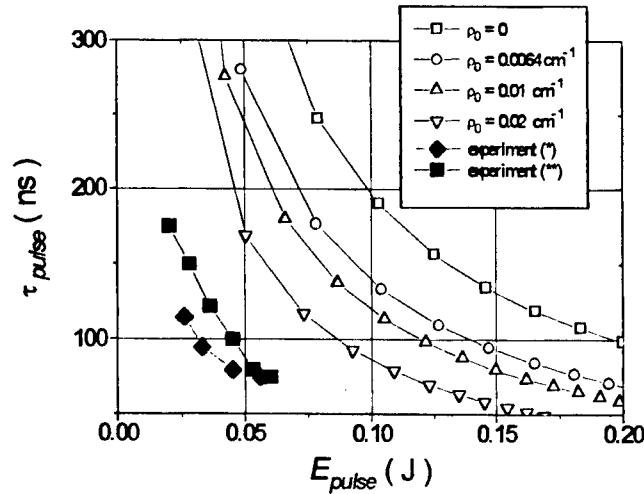


Fig. 4. Open symbols: theoretical τ_{pulse} versus E_{pulse} , curves for various passive losses, ρ_0 (FTIR Q-switch, $l' = 27 \text{ cm}$, $T_Q^{high} = 0.95$); solid symbols: experimental dependencies ³: $\blacklozenge R_2 = 0.8$; $\blacksquare R_2 = 0.73$.

should look for the possible non-homogeneity of the population inversion inside the active medium, resulting in a non-uniform distribution of the emission intensity across the emitting surface of the laser rod. In fact, hot spots in the near field image of the Er: YAG emission have been observed. This non-uniformity could be equivalent with a reduction of the effective emitting surface area.

4. CONCLUSIONS

The mathematical for the Q-switch regime of 3- μm Erbium lasers, presented in this paper, is based exclusively on spectroscopic data concerning radiative, non-radiative, and energy transfer processes. This model allows simulation of various types of Q-switches and monochromatic as well as flash lamp pumping. The FTIR Q-switch, though characterised by microsecond switching times, proves to be very convenient for 2.94 μm Er: YAG laser due to the long pulse build-up time.

The non-radiative losses, associated with various multiphonon transitions and the off-resonance of the energy transfer processes produced during the optical pumping and giant pulse generation, are defined and evaluated. Comparatively with non-radiative losses, the radiative ones are negligible. Our calculations have shown that during the giant pulse generation, the non-radiative losses can not be neglected, especially near laser threshold.

For usual pump duration (200 - 300 μs) the main conclusions for the cw generation, concerning the emission efficiency, are still valid. Thus, the figure of merit $p = (\alpha / \beta) \sqrt{(\omega_{22} / \omega_{11})}$ continues to play a crucial role. For transitions with $p < 1$ (2.94 μm in Er: YAG) the reduction of the terminal laser level lifetime, by co-doping, would reduce the population inversion and, as a consequence, the emission efficiency; on the other hand, for transitions with $p > 1$ (2.802 μm in Cr: Er: YSGG or 2.7 μm in Cr: Er: YAG) this reduction should be twice beneficial: improves population inversion and helps the formation of the giant pulse.

For comparable pulsewidths, the pulse energies, predicted by this mathematical model, are superior to the experimental ones. Possible explanations of this discrepancy could be related to possible high passive losses and the

reduction of the effective emission area, due to the non-homogeneity of the population inversion inside the active medium.

5. REFERENCES

1. I. N. Court and F. K. van Willisen, "Frustrated total internal reflection and applications of its principle to lasers cavity design," *Appl. Opt.*, vol. 3, pp. 719- 726 , 1964.
2. A. Högele, G. Hörbe, H. Lubatschowski, H. Welling, and W. Ertmer, "2.70 μm CrEr: YSGG laser with high output energy and FTIR-Q-switch," *Opt. Commun.*, vol. 125, pp. 90-94, 1996.
3. A. Högele, C. Ziolek, H. Lubatschowski, S. Lohmann, H. Welling, A. Olmes, and W. Ertmer, "FTIR-Q-switched 3 μm erbium lasers for applications in laser surgery," *Laser und Optoelektronik*, vol. 29, April, 1997.
4. Kh. S. Bagdasarov, V. I. Zhekov, V. A. Lobachev, A. A. Manenkov, T. M. Murina, A. M. Prokhorov, M. I. Studenikin, and E. A. Fedorov, in *Laser with Yttrium-Erbium-Aluminium Garnet*, T. M. Murina, Ed., in *Proc. IOFAN*, Moscow: Nauka, 1989, vol. 19, pp. 5-68.
5. V. Lupei, S. Georgescu, and V. Florea, "On the dynamics of population inversion for 3 μm Er^{3+} lasers," *IEEE J. Quantum Electronics*, vol. 29, pp. 426-434, 1993.
6. S. Georgescu, C. Ionescu, I. Voicu, and V. I. Zhekov, "A modified Judd-Ofelt analysis of Er^{3+} in YAG," *Rev. Roum. Phys.*, vol. 30, pp. 265-276, 1985.

Stabilization of unstable states in a modulated noisy CO₂ laser

V. Ninulescu, P. E. Sterian, M. Dumitru, and M. Piscureanu

"Politehnica" University of Bucharest, Splaiul Independentei 313, 77206, Romania

Electronic address: sterpisc@physics2.physics.pub.ro

ABSTRACT

The work addresses the problem of a CO₂ laser dynamics control in the presence of Gaussian white noise in the cavity losses. We improve the delayed continuous feedback method by introducing memory of the previous states. The method proves a powerful one that works for otherwise chaotic dynamics and regular dynamics equally well and it is robust with respect to noise.

Keywords: bifurcation, deterministic chaos, control of chaos, self-controlling method.

1. INTRODUCTION

It is well known now that deterministic chaos is present in the dynamics of lasers. An example of such behavior is encountered in the modulated CO₂ laser where chaos can settle down even in the vicinity of the laser threshold^{1,2}. As the applications of lasers are mainly based on the coherent radiation they furnish, the onset of chaos in lasers has to be avoided.

The control of chaos is an interesting and challenging research subject recently arisen in the field of Nonlinear Dynamics. In a pioneering work, Ott, Grebogi and Yorke³ proposed that an unstable periodic orbit can be stabilized by making small time-dependent perturbations on one of its adjustable parameters. The technique implies the preliminary analysis of the Poincaré map of the system, and the adjustment of the parameter each time the system crosses the chosen Poincaré section. Other discrete feedback methods have been developed.

The necessity of preliminary and on-line computer analysis of the system limits the use of discrete methods in the case of very fast systems, for instance, optical systems. Another drawback is related to the impact of noise: for the control of systems with large Lyapunov exponent, tiny errors introduced may move away the state of the system out of its controllable region. The continuous feedback methods are initiated by Pyragas⁴ who introduced a continuous perturbation for one of the system's variables in such a way that it does not change the unstable periodic orbit of the system, but only changes the Lyapunov exponents so that the orbit becomes stable. To achieve the stabilization, it is not necessary any information about the location of the periodic orbit. We will refer to this type of control as self-controlling method. Bielavski et al.⁵ have applied the method to the stabilization of unstable periodic cycles for a CO₂ laser with modulated losses by applying the control in the parameter of cavity losses.

An important problem concerning any method of chaos control is its robustness against external noise. This issue is very relevant in practical applications where dealing with noise and its consequences are inevitable. When perturbed away from the controlled orbit, the trajectory can leave the basin of attraction and the control fails. To increase the rate of the convergence to the desired orbit, an improved method is considered here, by including memory of the previous states.

In a recent paper, Christini and Collins⁶ prove that chaos control through small perturbations can be extended to the case of regular dynamics of the system. By means of noise externally introduced, the dynamics is perturbed from that of the regular motion. When the state variables are close enough to the interested unstable orbit, the control is initiated. We show that self-controlling technique can be applied equally well to the two kinds of dynamics: regular and chaotic.

2. PHYSICAL SYSTEM MODEL AND ITS DYNAMICS

The laser rate equations are a simple model for the description of certain laser systems, for instance, CO₂ laser. Here the polarization rate of decay is much larger than the other rates of decay in the system and polarization is excluded by setting $dP/dt=0$. Then the dimensionless intensity of radiation I and the normalized population inversion D , in the approximation of a single mode two-level laser are ruled by the set of equations^{1,2,5}:

$$\dot{I} = I \left(\frac{GD}{1+\delta^2} - 2\kappa_0 \right), \quad (1a)$$

$$\dot{D} = \gamma_1 \left(1 - D - \frac{DI}{1+\delta^2} \right). \quad (1b)$$

The parameters G , δ , γ_1 and κ_0 are the gain, cavity detuning in units of polarization relaxation rate, atomic (molecular) relaxation rate, and cavity damping rate, respectively. When laser action takes place, the system is dissipative, i.e., contracts volumes in the state space. Indeed, by introducing the coordinates $x=\ln I$ and $y=\ln D$ (I and D are always positive) we have

$$\partial \dot{x} / \partial x + \partial \dot{y} / \partial y = -\gamma_1 \exp(-y) < 0$$

at any time. Thus every volume in (x,y) space contracts as time passes by. System (1) possesses a globally attracting fixed point $(I_0, D_0) = (A-1-\delta^2, (1+\delta^2)/A)$ where we have introduced the pumping parameter of the laser $A = G/2\kappa_0$. From the linearized system at (I_0, D_0) , we infer that all nearby solutions damp oscillating with a relaxation frequency

$$f_0 = (1/2\pi) \{2\gamma_1 \kappa_0 [A/(1+\delta^2) - 1]\}^{1/2}.$$

We will study the laser at modulation frequencies close to f_0 . In such cases, nontrivial effects are expected due to the nonlinear interaction between the relaxation frequency and the modulation one. Typical values of the parameters are chosen for a waveguide CO₂ laser²: $\gamma_1 = 2.5 \times 10^5 \text{ s}^{-1}$, $\kappa_0 = 5 \times 10^7 \text{ s}^{-1}$, and $\delta=0.25$. We choose an excitation parameter close to the threshold value $A_{th} = 1+\delta^2$, namely $A=1.2$, and a modulation in the losses $\kappa_0 \rightarrow \kappa = \kappa_0 [1 + m \sin(2\pi ft)]$ where m and $f=250\text{kHz}$ are the index and the frequency of losses modulation.

Figure 1 presents two bifurcation diagrams when the index of modulation is slowly swept in the increasing direction and the reversed one. It can be seen a lot of types of time evolution: an oscillation at the period of the modulation, a route to chaos through subharmonic bifurcations, a window of regular dynamics, crises, and chaotic dynamics. The asymptotic evolution depends in some regions on the initial condition. Enlargements of the diagrams in the region of chaotic dynamics would reveal other small regions of regular evolution.

The noise is taken into account through the substitution $\kappa_0 [1 + m \sin(2\pi ft)] \rightarrow \kappa_0 [1 + m \sin(2\pi ft) + \xi]$ for the cavity damping rate, where ξ is a real Gaussian white noise with zero mean and standard deviation σ_ξ . In the numerical simulations the random variable ξ is supplied by the computer's random number generator. The dynamics of the noisy laser is concentrated around the noise free trajectory. The noise induces precursors of period-doubling, interrupts the route to chaos and induces transitions between co-existing attractors.

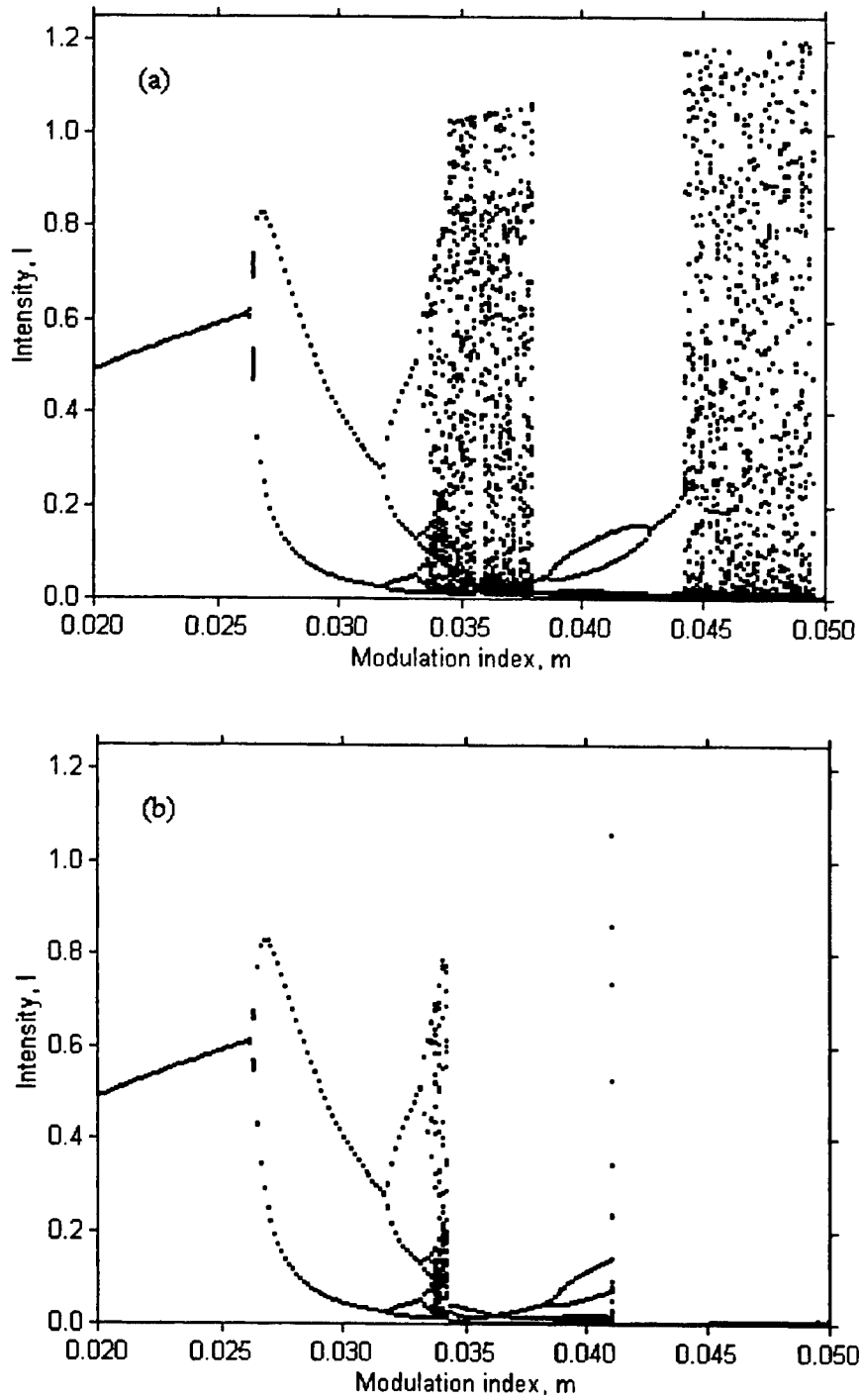


Figure 1. Bifurcation diagram of the CO_2 laser with modulated losses: (a) m is increasing, (b) m decreases. The values of the parameters are given in the text.

3. CONTROL METHOD

To overcome the difficulties of the discrete feedback methods, Bielavski et al.⁵ proposed a continuous correction of an accessible system parameter. Suppose an unstable orbit of period T exists at a value p_0 of the parameter. The continuous applied correction is of the form $\Delta p(t) = \alpha[x(t) - x(t-T)]$, where $x(t)$ is a scalar dynamical variable and α is the gain parameter of the feedback loop. Thus the strength of the perturbation is driven by the information extracted from the dynamics itself. Implementation of the scheme is based on the variability of the gain α . The method has been verified on a CO_2 laser with loss modulation using an intracavity electro-optic modulator. The cavity loss parameter $\kappa = \kappa_0[1 + m \sin(2\pi ft)]$ is changed through the control into $\kappa_0\{1 + m \sin(2\pi ft) + \alpha[I(t) - I(t-nT)]\}$ where $T = 1/f$ and nT is the period of the unstable orbit. Technical details for the implementation of the feedback loop are presented in⁵.

To improve this self-controlling procedure we propose a scheme that takes into consideration memory of the past states of the system⁷. We change the Bielavski correction into $\Delta p(t) = \alpha[x(t) - x(t-T)] - \beta \Delta p(t-T)$, where β is the gain parameter of the additional control. The supplementary control introduces another adjustable parameter that can optimize the control technique. The system equations write now:

$$\dot{I}(t) = I(t) \left\{ \frac{GD(t)}{1 + \delta^2} - 2\kappa_0[1 + m \sin(2\pi ft) + \varepsilon(t)] \right\}. \quad (2a)$$

$$\dot{D}(t) = \gamma_1 \left[1 - D(t) - \frac{D(t)I(t)}{1 + \delta^2} \right], \quad (2b)$$

$$\varepsilon(t) = \alpha[I(t) - I(t-nT)] - \beta \varepsilon(t-nT). \quad (2c)$$

These equations form an infinitely dimensional dynamical system whose analytical study is difficult. Here we will be interested in the numerical analysis of the system. Comparison to the Bielavski method will also be made.

As in the previous method, the nT -periodic orbits are not destroyed by the control which changes only the stability. If the periodic orbit is stabilized, the power in the feedback loop vanishes, but the control have to carry on: in the absence of any control, small disturbances generated by noise will increase and the system will go away from the desired orbit. Knowledge referring to the position of the unstable orbit is not necessary. We need only the periodicity and in the studied system this is determined by the modulation frequency only.

Figure 2 presents typical dynamics for the control of a CO_2 laser using Bielavski method and the proposed one in the same conditions. Both methods achieve stabilization whatever is the initial condition of the system, i.e., the basin of attraction is the whole space. This makes the self-controlling method very powerful and advantageous with respect to other procedures. It can be remarked a much larger rate of convergence in the proposed method, and this is adjusted from the parameter β . The presented method also enlarges the domain of the parameter α where the dynamics is stabilized, thus diminishing the power needed in the feedback loop.

The stabilization technique is also applicable in the case of a regular dynamics of the system. It is the case, for instance, of a system in the period-doubling route to chaos. If the motion takes place on a $2^n T$ periodic orbit, it has all $2^m T$ ($0 \leq m < n$) periodic orbits and they are all unstable. Christini and Collins⁶ disturb the initial regular dynamics through a noise externally introduced prior to the effective control. In the self-controlling method, the continuous perturbation has this task and the control is obtained. Figure 3 presents this control for a period $2T$ cycle for a value of the modulation index where the system is $4T$ periodic. Consequently, the well installed idea that it is an advantage of the chaotic dynamics only to permit control through small changes in the system has to be modified.

It can be seen a much larger rate of convergence in the proposed method. This is very important in the case of a noisy system. The perturbations are rapidly damped and the quality of the controlled dynamics is better than in the Bielavski method. Figures 4 and 5 show the control of a period T orbit and $2T$ one, where the impact of noise is included. Larger noise

levels do not destroy the periodicity of the orbit. Thus the idea of multiple Poincaré sections⁸ to diminish the time between two successive corrections not to allow errors to grow is not necessary here.

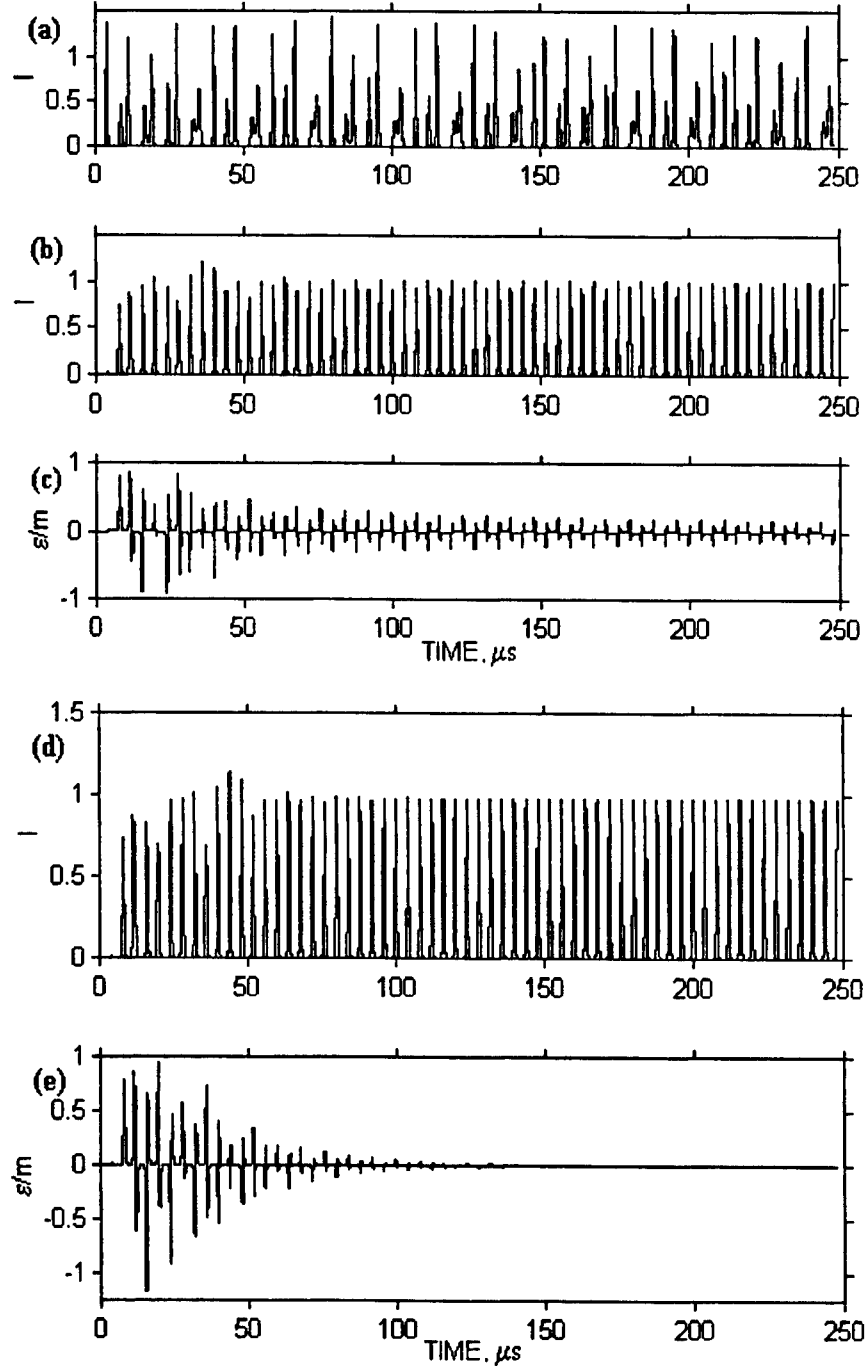


Figure 2. Control of a chaotic state through the self-controlling technique for a periodic motion of period T . (a) The uncontrolled time evolution. (b, c) Laser intensity and the applied continuous control in the case of Bielavski method. (d, e) Laser intensity and the applied continuous control in the proposed method. $m=0.037$ and $\alpha = 0.4$ in the control through both methods and $\beta=0.3$. Laser parameters are the same as in figure 1.

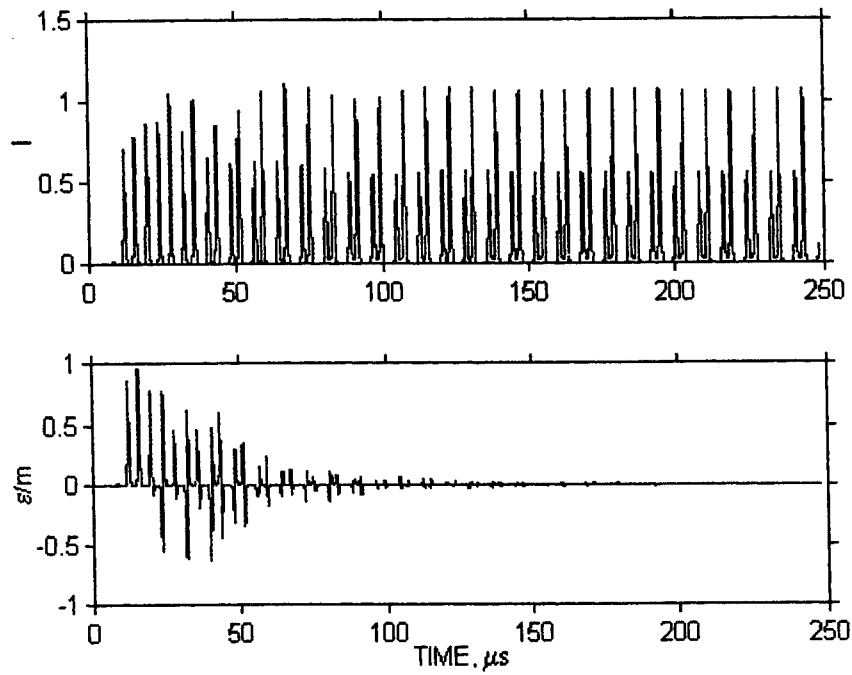


Figure 3. Control of a periodic $2T$ orbit for parameters at which the modulated laser has a $4T$ periodic stable cycle ($m=0.033$). We have chosen $\alpha=0.04$ and $\beta=-0.3$.

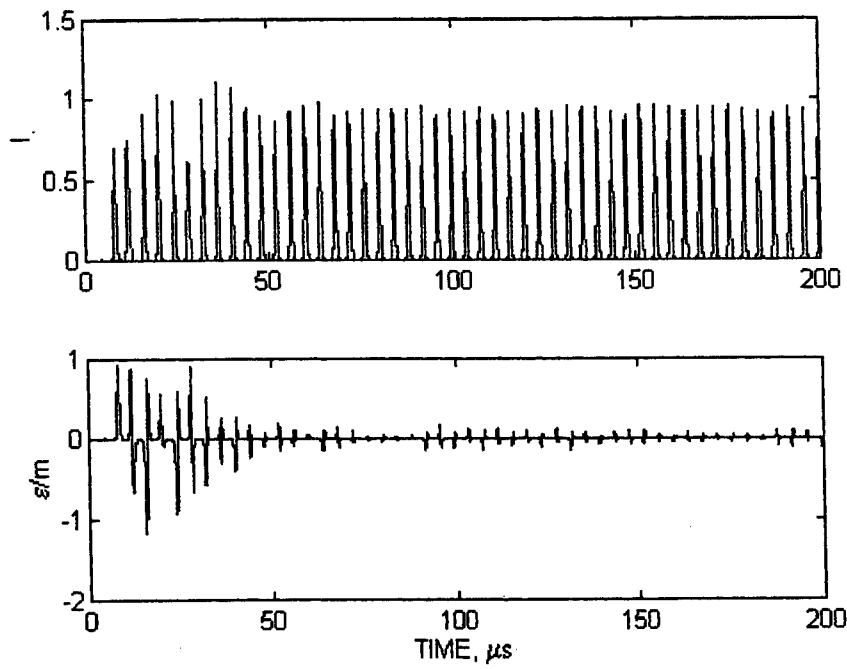


Figure 4. Stabilizing of the period T orbit in the presence of Gaussian noise. $\sigma_{\xi}=10\%m$ and other parameters the same as in figure 2d, e.

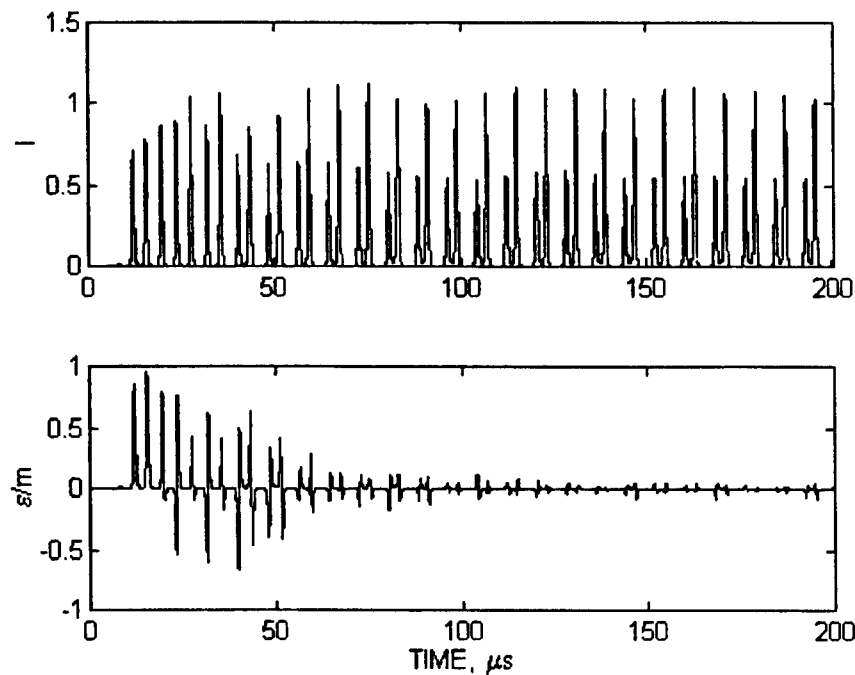


Figure 5. Stabilizing of the period $2T$ orbit in the presence of Gaussian noise. $\sigma_{\xi}=10\%m$ and other parameters the same as in figure 3.

4. CONCLUSIONS

The continuous feedback method with memory included is tested for the single mode CO_2 laser with cavity detuning and Gauss noise in the cavity losses included. Usually the method is recommended for the stabilization in systems where only one parameter variation is not sufficient for the control⁹. The investigated system has a large basin of attraction and by introducing the memory parameter the trajectory falls rapidly to the desired orbit noise effects being small.

5. REFERENCES

1. J. R. Tredicce, F. T. Arecchi, G. P. Puccioni, A. Poggi, and W. Gadomski, "Dynamic behavior and onset of low-dimensional chaos in a modulated homogeneously broadened single-mode laser: Experiments and theory", *Phys. Rev. A* **34**, No. 3, pp. 2073-2081, 1986.
2. D. Dangoisse, P. Glorieux, and D. Hennequin, "Chaos in a CO_2 laser with modulated losses: Experiments and numerical simulations", *Phys. Rev. A* **36**, No. 10, pp. 4775-4791, 1987.
3. E. Ott, C. Grebogi, and J. A. Yorke, "Controlling Chaos", *Phys. Rev. Lett.* **64**, No. 11, pp. 1196-1199, 1990.
4. K. Pyragas, "Control of chaos via extended delay feedback", *Phys. Lett. A* **206**, pp. 323-330, 1995.
5. S. Bielavski, D. Derozier, and P. Glorieux, "Controlling unstable periodic orbits by a delayed continuous feedback", *Phys. Rev. E* **49**, No. 2, pp. R971-974, 1994.
6. D. J. Christini and J. J. Collins, "Using noise and chaos control to control nonchaotic systems", *Phys. Rev. E* **52**, No. 6, pp. 5806-5809, 1995.
7. J. E. S. Socolar, D. W. Sukow, and D. J. Gauthier, "Stabilizing unstable periodic systems in fast dynamical systems", *Phys. Rev. E* **50**, No. 4, pp. 3245-3248, 1994.
8. S. R. Bishop and D. Xu, "Control of chaos in noisy flows", *Phys. Rev. E* **54**, No. 4, 3204-3210, 1996.
9. M. de Sousa Vieira and A. J. Lichtenberg, "Controlling chaos using nonlinear feedback with delay", *Phys. Rev. E* **54**, No. 2, pp. 1200-1207, 1996.

Beam optimization of a TEA-CO₂ laser

Tobias Groß, Detlev Ristau, Gordon Wallas, Gabriel Dumitru*, Dan G. Sporea*, Clementina Timus*

Laser Zentrum Hannover e.V., Department of Laser Components,
Hollerithallee 8, 30 419 Hannover, Germany

*National Institute for Laser, Plasma and Radiation Physics,
PO Box 52-36, 76900 Bucharest, Romania

ABSTRACT

The paper describes the methods used to adapt an industrial TEA-CO₂ laser to the requirements of the ISO standard 11 254-2 for a laser induced damage threshold experimental facility. The goals were to improve the pulse energy stability and the laser beam spatial profile and the methods were: (i) finding the best discharge voltage; (ii) adapting the laser cavity, (iii) using suitable apertures. There is also presented the experimental set-up for beam characterization, which included a laser beam profiler (a line of 60 pyroelectric detectors), an energy-meter to monitor the pulse energies and KCl optical components for beam splitting and beam guiding. Every beam distribution was regarded as a linear combination of normalized Gauss-Hermite functions and the fitting algorithm allows the calculation of the coefficients of this combination.

Keywords: TEA-CO₂ laser, laser induced damage, ISO standard 11 254-2, pulse energy fluctuations, energy density profile

1. INTRODUCTION

The more and more increasing laser energies that are used in various applications lead to the problem of damages induced in optical components by high levels of energy densities. At the present moment, efforts are focused on finding substrates and coatings with higher laser induced damage threshold (LIDT). Repetitive laser radiation may depreciate and damage an optical surface at irradiation levels below those measured for single shot damages. The standard ISO 11 254-2 is concerned with the influence of a repetitively pulsed laser beams and it defines a test method for determining the LIDT of optical surfaces subjected to a succession of identical laser pulses.

The standard defines the symbols and units of measurement which have to be used and it also includes a classification for the types of laser devices that are used as sources for repetitive radiation pulses: five groups, with respect to the pulse duration and seven classes after the pulse repetition rate. The LIDT S-on-1 experimental facility that is presented, had as source of laser radiation an industrial TEA-CO₂ laser, included in Group 4 and in Class C. For this type of lasers, the standard requires the following¹ maximum variations:

- pulse energy $\pm 5 \%$;
- pulse duration $\pm 5 \%$;
- effective area $\pm 6 \%$;
- power density $\pm 10 \%$.

Initially, the laser device had variations above these limits and the goal of this work was to obtain, using various optical and non-optical methods, a laser beam complying to the requirements of ISO 11 254-2 standard.

2. EXPERIMENTAL SET-UP

Two laser modules Ureenco-TEA-CO₂, type HL1000, were coupled and used to generate repetitive laser pulses; the pulse duration was in the range of 200 μ s and the maximum repetition rate was 50 Hz.. The laser gas was a combination of 10.5 % CO₂, 10.5 % N₂ and 89 % He and the discharge voltages could be varied from 28 kV to 34 kV.

In order to improve the beam quality, the laser cavity was enlarged (figure 1). At the end of the second module, the laser beam was passing through a Brewster window and it was guided by a plane copper mirror into a telescope (convex and concave copper mirrors). The beam was leaving the cavity through a coated Ge window with 30 % reflectance. Two aperture holders were introduced inside the laser cavity (at the end and between the modules), to find the diameters of the apertures that allowed the TEM₀₀ mode to oscillate and cut the higher TEM modes.

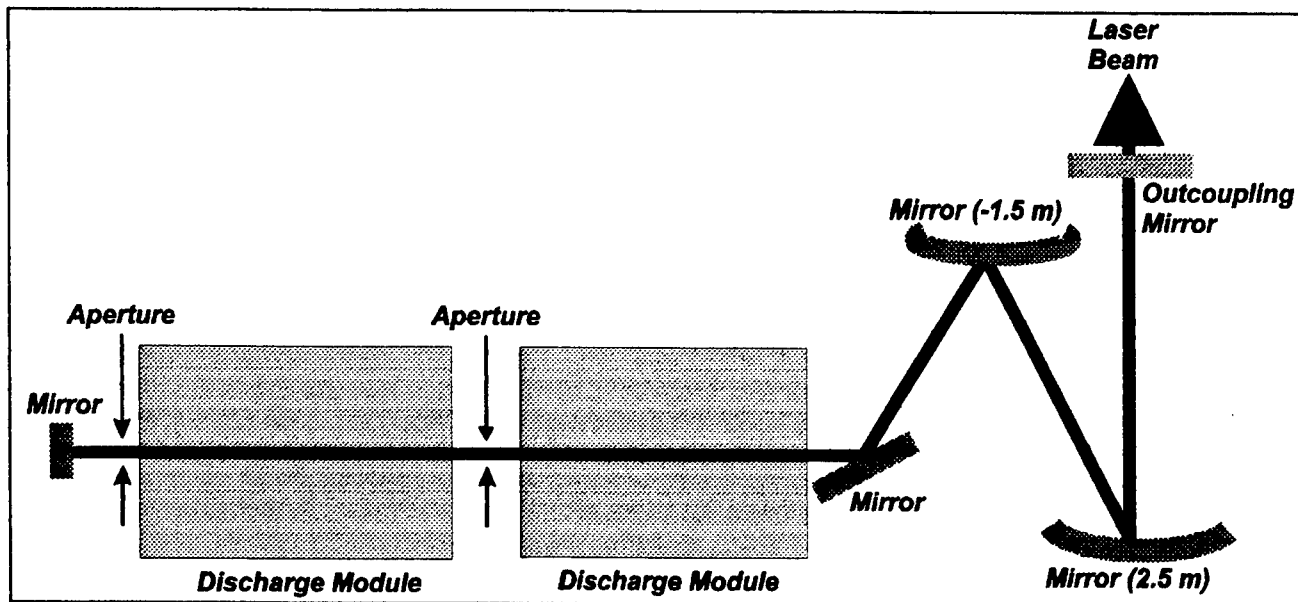


Figure 1 - The laser cavity

After leaving the cavity, the laser beam was guided to the LIDT set-up which included:

- attenuation and focusing systems - ZnSe optical components,
- sample holder - optical stage with positioning system,
- on-line visual monitoring line - microscope coupled to a CCD camera and a monitor.

The subject of the present paper is not the entire LIDT experimental facility; it is only related to the methods used to improve the beam quality, therefore to the optimization of the laser cavity. An experimental set-up (figure 2) was developed to evaluate the laser beam quality. The set-up included an energy-meter to monitor the pulse energies, a laser beam profile monitor with a line of 60 pyroelectric elements and KCl optical windows for beam delivery. The size of the pyroelectric elements² was 0.375 per 2.67 mm² and they had an optical cross-talk smaller than 0.5 % and an electrical cross-talk smaller than 1.5 %.

The laser beam profiler and the energy meter were connected to a PC compatible computer via the parallel, respectively the serial communication ports. For a given laser cavity configuration, the laser device was operated at a 5 Hz repetition rate; for every laser pulse the energy and the beam profile were acquired and stored on the computer.

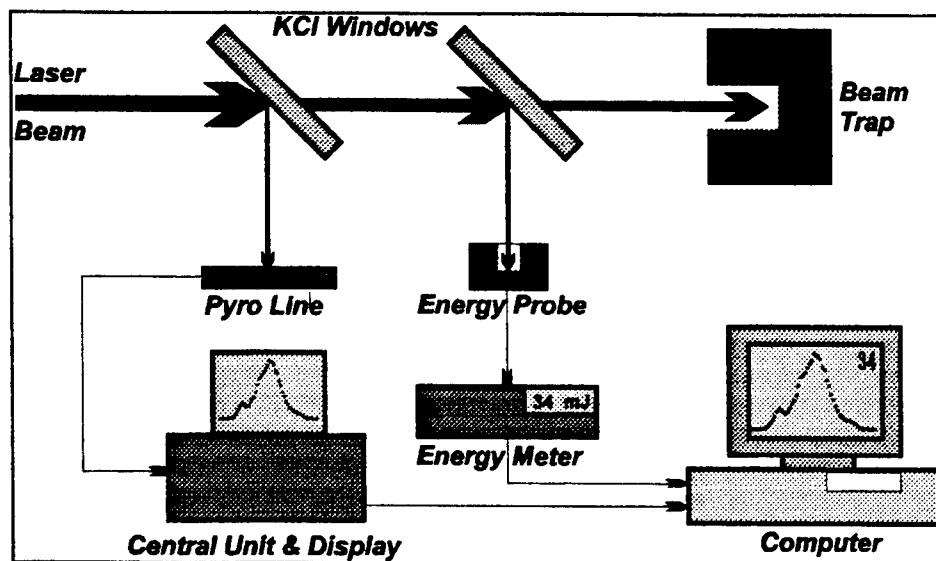


Figure 2 - Set-up for laser beam evaluation

3. CAVITY ADJUSTMENT

The design of laser cavity allowed several parameters to be adjusted, in order to obtain an optimum for the laser beam exiting the outcoupling mirror. The degrees of freedom usable in the optimization process are shown in table 1.

Table 1 - Adjustable parameters

Parameter:	Values:
• telescope length	28 cm, 29 cm, 30 cm
• discharge voltage	28 kV, 31 kV, 34 kV
• aperture at the end of the cavity	14 mm, 16 mm, 18 mm
• aperture between the modules	8 mm, 10 mm, 12 mm

The laser device operated with all the possible configurations for its cavity. For every combination, there were acquired:

- 500 laser pulses, in order to calculate the mean pulse energy and the fluctuations,
- 20 pulses to calculate the mean energy density horizontal profile,
- 20 pulses to calculate the mean energy density vertical profile.

For different laser cavity configurations, important variations of the pulse energy fluctuations and beam profile were observed. The results obtained with several combinations were selected to be shown.

Length: 29 cm, Voltage: 31 kV, End aperture: 10 mm, Middle aperture: 16 mm

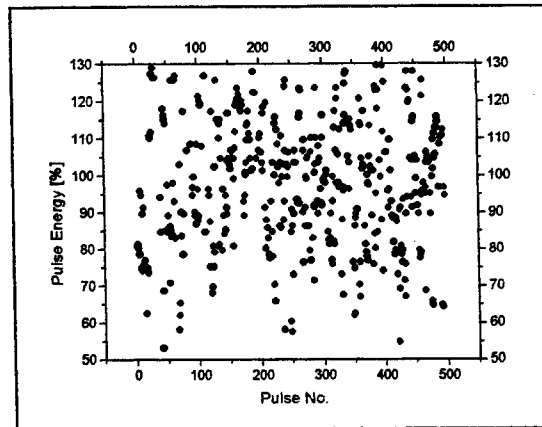


Figure 3a - The fluctuations of pulse energy

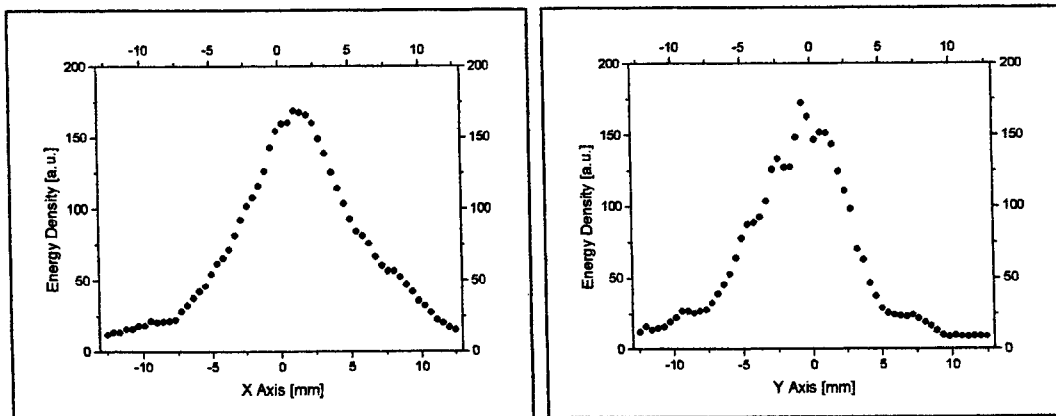


Figure 3b - The horizontal (left) and vertical profiles

For this combination (figure 3), the fluctuations for pulse energy were very large and the horizontal and vertical energy density profiles were not in a gaussian shape.

Length: 29 cm, Voltage: 28 kV, End aperture: 12 mm, Middle aperture: -

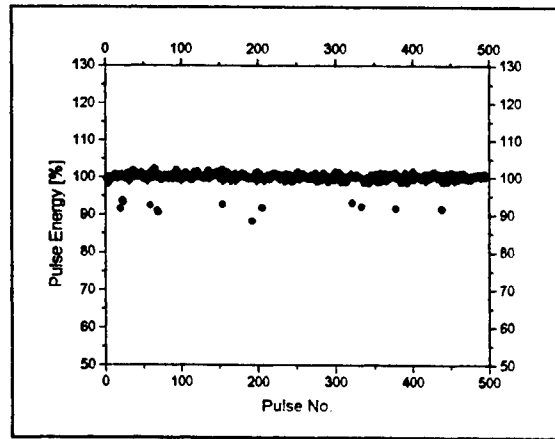


Figure 4a - The fluctuations of pulse energy

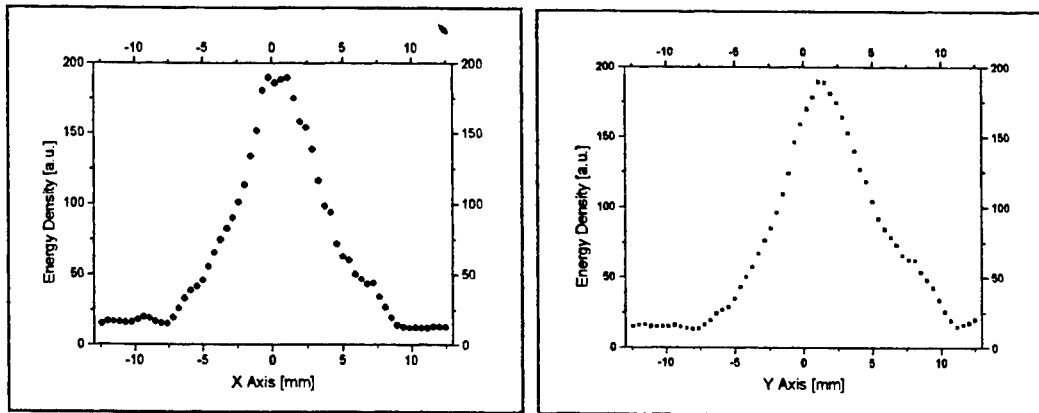


Figure 4b - The horizontal (left) and vertical profiles

The pulse energy was very stable, but the beam profiles had to be improved (figure 4).

Length: 30 cm, Voltage: 28 kV, End aperture: -, Middle aperture: 18 mm

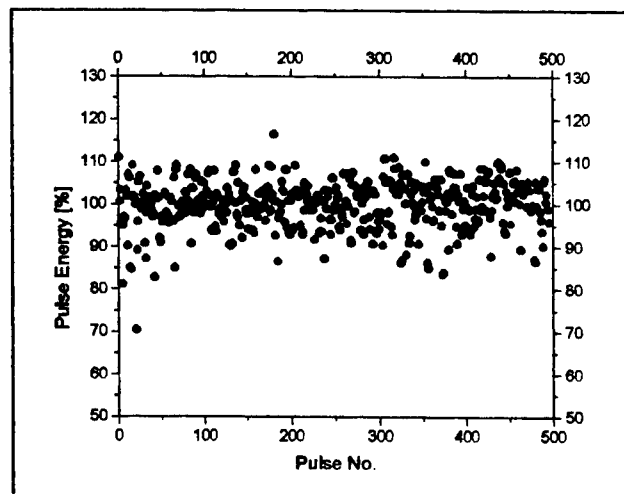


Figure 5a - The fluctuations of pulse energy

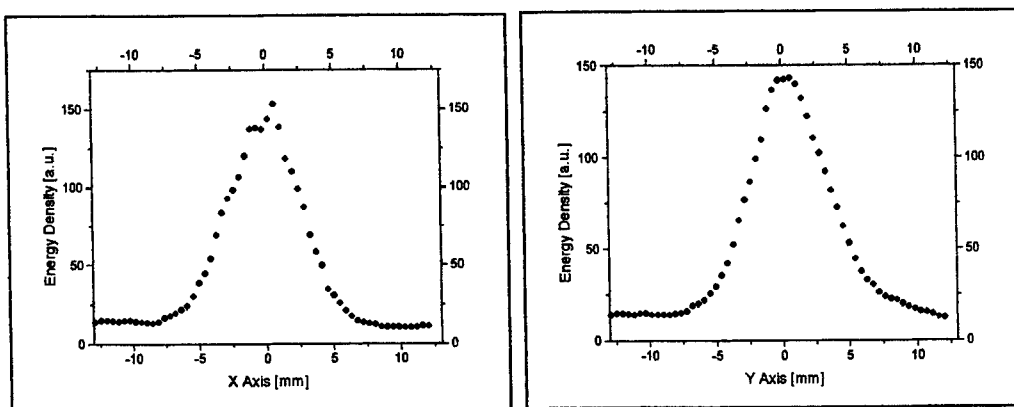


Figure 5b - The horizontal (left) and vertical profiles

The beam profiles were closed to the gaussian shape, but the variations were above the limit of $\pm 5\%$ (figure 5).

Length: 30 cm, Voltage: 31 kV, End aperture: -, Middle aperture: 18 mm

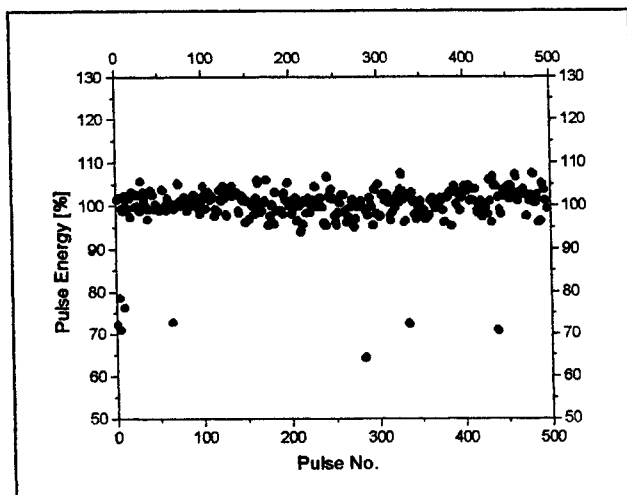


Figure 6a - The fluctuations of pulse energy

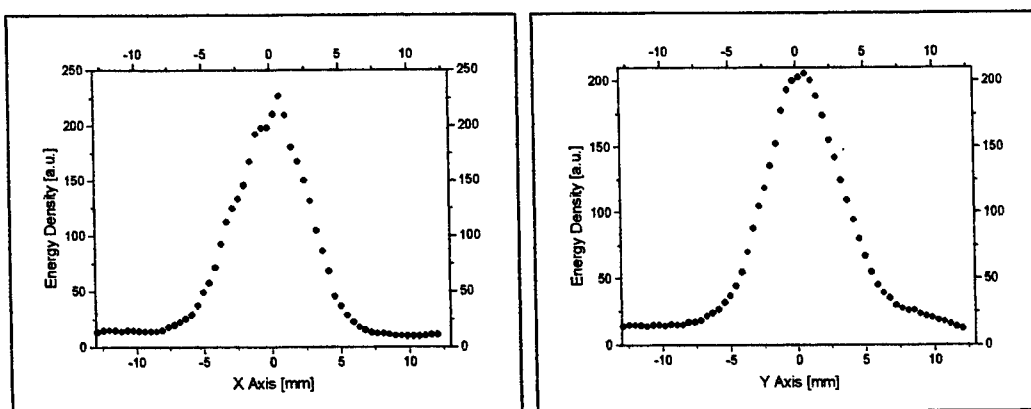


Figure 6b - The horizontal (left) and vertical profiles

This configuration yielded to appropriate (figure 6) pulse energy fluctuations and energy density profiles.

4. FITTING ALGORITHM

The goal of the fit algorithm³ is to find the analytical function which gives the closest values to the experimentally determines energy distribution profile. The solution of the paraxial equation for laser beam propagation can be written with respect to the eigenmodes:

$$\Psi_{m,n}(x, y, z) = e^{i \cdot \arg(\Psi)} \sqrt{\frac{2}{2^{m+n} m! n! \pi}} \cdot \frac{1}{\sqrt{w_x \cdot w_y}} e^{-\left(\frac{x^2}{w_x^2} + \frac{y^2}{w_y^2}\right)} \cdot H_m\left(\frac{\sqrt{2} \cdot x}{w_x}\right) H_n\left(\frac{\sqrt{2} \cdot y}{w_y}\right), \quad (1)$$

where H_m and H_n are the Hermite polynomials of m^{th} and n^{th} order, and w_x, w_y are the beam's waists.

The set of orthogonal and normalized functions:

$$u_{m,n}(x, y) = \sqrt{\frac{2}{2^{m+n} m! n! \pi}} \cdot \frac{1}{\sqrt{w_x \cdot w_y}} e^{-\left(\frac{x^2}{w_x^2} + \frac{y^2}{w_y^2}\right)} \cdot H_m\left(\frac{\sqrt{2} \cdot x}{w_x}\right) H_n\left(\frac{\sqrt{2} \cdot y}{w_y}\right), \quad (2)$$

can be used to form a linear combination for any distribution $\Psi(x, y)$:

$$\Psi(x, y) = \sum_m \sum_n C_{m,n} u_{m,n}(x, y), \quad (3)$$

Finding the coefficients $C_{m,n}$ is equivalent to find a fit for the amplitude distribution of the laser beam. The most accessible parameter to be measured is the power (energy) density profile $P(x, y)$. After the coefficients calculations:

$$C_{a,b} = \sum_i \sum_j \Psi(x_i, y_j) u_{a,b}(x_i, y_j), \quad (5)$$

and the laser power (energy) is given by:

$$P = \int_{-\infty}^{\infty} \int_{-\infty}^{\infty} Y(x, y)^2 = \sum_a \sum_b C_{a,b}^2 \int_{-\infty}^{\infty} \int_{-\infty}^{\infty} u_{a,b}^2(x, y) dx dy = \sum_a \sum_b C_{a,b}^2 P_{a,b}. \quad (6)$$

where $P_{a,b}$ as the power (energy) of the laser mode TEM_{ab} . The algorithm leads to an analytical profile for the laser beam power (energy) density and it also enables the obtaining the probable distribution of the beam, by TEM modes.

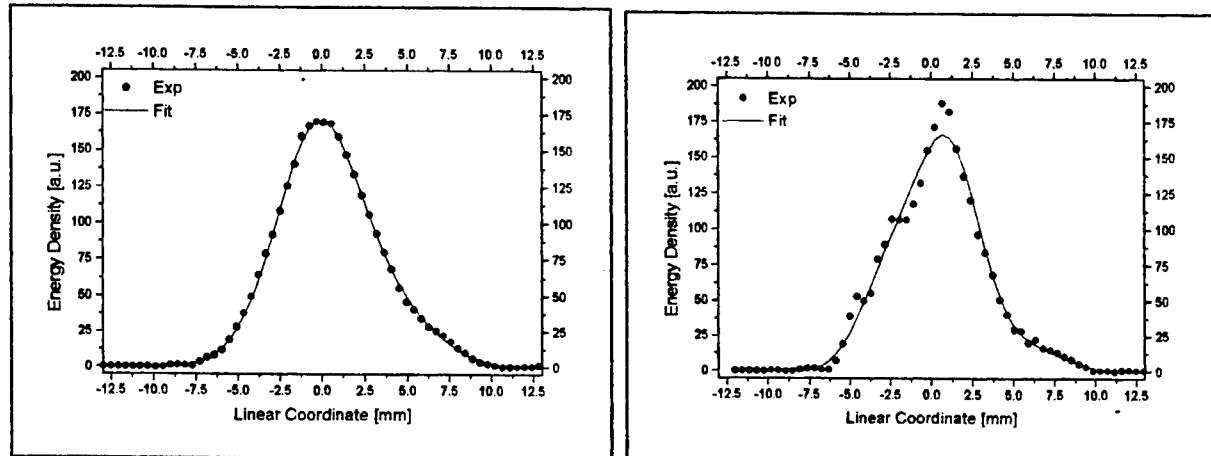


Figure 7 - Example of experimental and fitted profiles (horizontal - left)

Table 2 - Numerical⁴ results for the profiles depicted in figure 7

w_x (mm)		%	n = 0	n = 1	n = 2	n = 3	n = 4
Exp	Fit	m = 0	92.1	0	2.8	0	0.4
6.17	6.11	m = 1	0	0	0	0	0
w_y (mm)		m = 2	3.2	0	0.1	0	0
Exp	Fit	m = 3	0.3	0	0	0	0
5.91	5.83	m = 4	0.4	0	0	0	0

From the experimental set-up the linear energy profiles were obtained for both horizontal and vertical directions. The particularization of the fitting formalism to one dimension is immediate and due to the fact that in (1) variable are separable, one can calculate the fit functions for O_x and O_y , and their product represents the analytical profile of the fitted energy distribution. Using the analytical function which fits the beam profile, the 3D plot of energy density was obtained

The major draw-back of the fitting algorithm is the sampling frequency. For smooth profiles, with low spatial frequency, the fit process has a good precision, but for profiles with local peaks (high spatial frequencies), the fit curve does not resolve them. The solution might be the use of arrays with more elements (CCD camera, for instance).

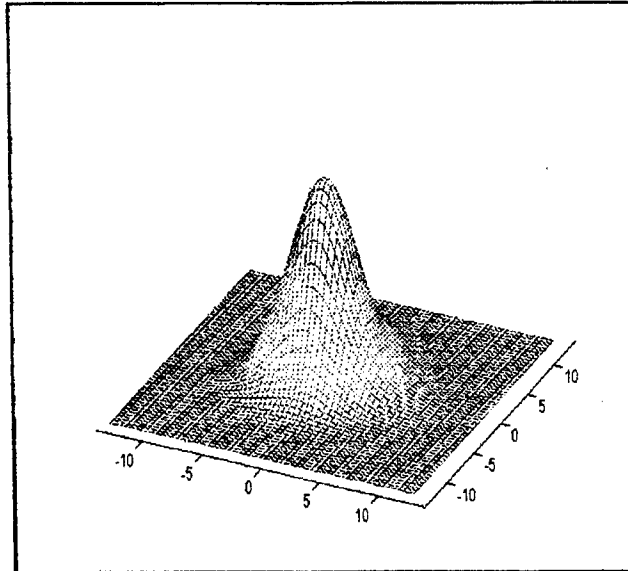


Figure 8 - 3D plot of the computed energy profile for the example.

5. ACKNOWLEDGEMENTS

The research was performed at the experimental facilities of the Laser Zentrum Hannover e.V., in the frame of the PECO project ERBCIPDT 940609.

6. REFERENCES

1. ISO 11 254-2: "Optics and optical instruments. Lasers and laser related equipment. Test methods for laser induced damage threshold of optical surfaces. Part 2: S on I test".
2. Laser Beam Profile Monitor MK IV, User Manual, Delta Developments Inc.
3. Gabriel Dumitru, Dan G. Sporea, Clementina Timus, "Computation of the 3D energy density profile using a linear array of pyroelectric detectors", 4th International Workshop on Laser Beams and Optical Components, June 14-16, 1997, Munich, Germany.
4. ISO 11 146: "Optics and optical instruments. Lasers and laser related equipment. Test methods for laser parameters".

Modeling optical amplification in Er^{3+} -doped LiNbO_3 waveguides

N. N. Puscas⁽¹⁾, R. Girardi⁽²⁾, D. Scarano⁽³⁾, I. Montrosset⁽⁴⁾

(1) University "Politehnica" Bucharest, Physics Department, Splaiul Independentei 313, 77206, Bucharest, Romania,

(2) C S E L T, Via G. Reiss Romoli 274, 10148 Torino, Italy,

(3) Pirelli Cavi, Viale Sarca 202, 20126 Milano, Italy

(4) Politecnico di Torino, Dipartimento di Elettronica, Corso Duca degli Abruzzi 24, 10129, Torino, Italy

ABSTRACT

Based on the small gain approximation in the unsaturated regime in this paper we present the derivation and the evaluation of the spectral optical gain, spectral noise figure and spectral quality factor on single and double pass configuration Er^{3+} -doped LiNbO_3 waveguide amplifier pumped near 1484 nm. The simulations show the evolution of the above mentioned parameters under various pumping regimes. In the present work we demonstrated that high gains and low noise figures are achievable in high pump regimes and double pass configuration.

The obtained results can be used to theoretically model the optical amplification around 1500 nm in Er^{3+} -doped LiNbO_3 waveguides as function of various parameters.

KEYWORDS

Er^{3+} : LiNbO_3 waveguide amplifier, double pass configuration, gain, noise figure

1. INTRODUCTION

The study of the spectral distribution of the noise figure plays an important role in obtaining amplifiers having low noise and high optical gain^{1,2,3,4,5}. The quantum theory of the amplitude noise in the optical waveguide amplifiers is based on the more general quantum theories of coherent light, coherent light/matter interaction, noise and laser emission⁴.

In this paper we report, in the small gain approximation, an accurate derivation and evaluation for single and double pass configuration of the spectral optical gain, spectral noise figure, and spectral quality factor which characterize an Er^{3+} -doped LiNbO_3 waveguide amplifier in the unsaturated regime, pumped near 1484 nm, and also their evolution under various pumping regimes.

In Sec. 2 we present the basic equations which describe the optical amplification in waveguides and a theoretical study of the spectral distribution of the above mentioned parameters. Sect. 3 is devoted to the discussion of the simulation results.

2. THEORY

The theoretical model we used to evaluate the noise characteristics of Er^{3+} -doped LiNbO_3 waveguide amplifier is closely related to EDFA model⁴ and has been modified to account for the effects of the host material. We considered a quasi two level system model and we neglected excited state absorption due to the considered pumping wavelength.

From the analysis of the interaction of the pump and signal photons with Er^{3+} ions in LiNbO_3 ^{2,3,4,5} it is possible to obtain a system of coupled differential equations for the population densities of the upper laser level and for the pump, signal, and amplified spontaneous emission (ASE) field intensity. In the case of steady state these equations are:

$$N_2(x, y, z) = N_{T0} d(x, y) \frac{\sum_{k,m} \frac{\tau}{h\nu_k} \sigma_{a,km} (P_{km}^+(z) + P_{km}^-(z)) i_m(x, y)}{1 + \sum_{k,m} \frac{\tau}{h\nu_k} (\sigma_{a,km} + \sigma_{e,km}) (P_{km}^+(z) + P_{km}^-(z)) i_m(x, y)} \quad (1)$$

$$\begin{aligned} \frac{d}{dz} P_{km}^\pm(z) = \pm \left\{ \left[(\sigma_{e,km} + \sigma_{a,km}) \int_A N_2(x, y, z) i_{km}(x, y) dx dy \right. \right. \\ \left. \left. - (\sigma_{a,km} \int_A N_T(x, y, z) i_{km}(x, y) dx dy + \alpha_{km}) \right] P_{km}^\pm(z) \right. \\ \left. + h\nu_k \Delta\nu \sigma_{e,km} \int_A N_2(x, y, z) i_{km}(x, y) dx dy \right\} \end{aligned} \quad (2)$$

where $P_{km}^\pm(z)$ represents the longitudinal distribution of the power spectral component at frequency ν_k , having the polarization denoted by the index m (m being π for the parallel or σ for the perpendicular directions to the optical axis of the crystal) in the forward (+) and backward (-) propagation directions.

The scattering losses of the integrated optical waveguides have been taken into account by the term α_{km} and the term $h\nu_k \Delta\nu \sigma_{e,km}$ represents an equivalent spontaneous emission input noise power in the frequency slot $\Delta\nu_k$ corresponding to the central frequency ν_k ⁴.

The transition rates are given in terms of the mode intensity profiles $i_m(x, y)$ and the cross-sections $\sigma_{s,km}$, s denoting the absorption (a) and emission (e) processes. Spontaneous transitions from the excited states to the ground state are described by the rate $A_{21} = \frac{1}{\tau}$, τ being the fluorescence lifetime. Further the normalized transversal intensity distribution $i_m(x, y)$ has been considered wavelength independent: $i_{km}(x, y) = i_m(x, y)$.

In Eqs. (1)-(2) we considered the following distribution of the Er^{3+} ions: $N_T(x, y) = N_{T0} d(x, y)$ with $N_{T0} = N_T(0, 0)$ and $d(0, 0) = 1$.

To consider the most general configuration we used the following boundary conditions:

$$\begin{aligned} P_{km}^+(z=0) &= (1 - R_{0,km}) P_{in0,km} + R_{0,km} P_{km}^-(z=0) \\ P_{km}^-(z=L) &= (1 - R_{L,km}) P_{inL,km} + R_{L,km} P_{km}^+(z=L) \end{aligned} \quad (3)$$

where $R_{0,km}$, $R_{L,km}$ are the mirror reflectivities in $z = 0$ (input) and $z = L$ (output) respectively and $P_{in0,km}$, $P_{inL,km}$ are the optical powers injected at the waveguide input and / or output, for the field at frequency ν_k and polarization m .

The selfconsistent numerical solution of the system of coupled first order differential equations (2), with (1) and (3), allows to calculate the longitudinal evolution of the pump, signal and amplified spontaneous emission powers.

Assuming an atom distribution density $N_1(x,y,z)$ for the ground state and $N_2(x,y,z)$ for the excited state, the rate of change for the probability for having n photons at frequency ν in a single longitudinal mode P_n , is given by the *photon statistics master equation* of the linear amplifier⁴:

$$\frac{dP_n}{dz} = \sigma_e N_2 \{nP_{n-1} - (n+1)P_n\} + \sigma_a N_1 \{(n+1)P_{n+1} - nP_n\} \quad (4)$$

where σ_a and σ_e represent the phenomenological cross sections for the absorption and emission processes that in LiNbO₃ crystal should be assumed polarization dependent.

Considering that the normalized mode intensity profiles $i_m(x,y)$ are not uniform in the transversal section of the waveguide the photon number distribution becomes $n \times i_m(x,y)$.

Multiplying (4) by $i_m(x,y)$ and integrating over the transversal section of the waveguide we obtain the following equation for the two photon polarization probability:

$$\frac{dP_n}{dz} = \gamma_e nP_{n-1} + \gamma_a nP_{n+1} - [\gamma_e(n+1) + \gamma_a n]P_n \quad (5)$$

where:

$$\begin{aligned} \gamma_e &= \gamma_e(z, \nu) = \sigma_e(\nu) \int_A N_2(x, y, z) i_m(x, y) dx dy \\ \gamma_a &= \gamma_a(z, \nu) = \sigma_a(\nu) \int_A N_1(x, y, z) i_m(x, y) dx dy. \end{aligned} \quad (6)$$

After multiplying (5) by the number of photons n and summing over n we obtain the photon mean value $\langle n(z) \rangle$ as:

$$\langle n(z) \rangle = G(z) \langle n(0) \rangle + N(z) \quad (7)$$

where:

$$G(z, \nu) = \exp \left\{ \int_0^z [\gamma_e(z', \nu) - \gamma_a(z', \nu) - \alpha(\nu)] dz' \right\} \quad (8)$$

$$N(z, \nu) = G(z, \nu) \int_0^z \frac{\gamma_e(z', \nu)}{G(z', \nu)} dz' \quad (9)$$

represent the spectral gain and the ASE photon number, respectively.

In the case of large gain (i. e. $G(z) \gg 1$) the noise figure is given by⁴:

$$F_0(z, \nu) = \frac{1 + 2N(z, \nu)}{G(z, \nu)} \quad (10)$$

where the term $2N/G$ correspond to a beat noise regime at the peak gain and the term $1/G$ to a shot noise at the spectrum tails.

Taking into account the photon statistics master equation of the linear amplifier (5) and the relations between the forward $P^+(z)$ and backward $P^-(z)$ powers:

$$\begin{aligned} P^+(z) &= P^+(0)G(z) \\ P^-(0) &= P^-(z)G(z) \end{aligned} \quad (11)$$

we calculated the net gain and the noise figure of the amplifier in the single pass ($G_{s.p.}(\nu)$, $F_{s.p.}(\nu)$, output section at $z = L$) and in the double pass configuration $G_{d.p.}(\nu)$, $F_{d.p.}(\nu)$, output section at $z = 0$) assuming signal injection at $z = 0$ and the mirror reflectivities $R(0) = 0$ and $R(L) \neq 0$; we obtained:

$$G_{s.p.}(\nu) = G(L, \nu)(1 - R(L)) \quad (12)$$

$$G_{d.p.}(\nu) = G^2(L, \nu)R(L) \quad (13)$$

$$F_{s.p.}(L, \nu) = \frac{1 + 2G(L, \nu) \int_0^L \frac{\gamma_e(z', \nu)}{G(z', \nu)} dz'}{G(L, \nu)} \quad (14)$$

$$F_{d.p.}(\nu) = \frac{R(L)G(L, \nu) \left(1 + 2G(L, \nu) \int_0^L \frac{\gamma_e(z', \nu)}{G(z', \nu)} dz' \right) + 1 - G(L, \nu) + 2 \int_0^L \gamma_e(z', \nu) G(z', \nu) dz'}{R(L)G^2(L, \nu)} \quad (15)$$

where:

$$G(L, \nu) = \exp \left\{ \int_0^L [\gamma_e(z', \nu) - \gamma_a(z', \nu) - \alpha(\nu)] dz' \right\} \quad (16)$$

is a modified version of Eq. (8) in order to account for the waveguide scattering losses.

In deriving the noise figure at the input and output of the device (Eqs. (14)-(15)) we considered an input signal with Poisson statistics ($\sigma^2(0) = \langle n(0) \rangle$).

As a measure of the gain and the noise characteristics of the waveguide amplifiers, we adopted a quality factor, $Q(z, \nu)$, defined as the ratio between the gain and the noise figure:

$$Q(z, \nu) = \frac{G(z, \nu)}{F(z, \nu)}. \quad (17)$$

At the output of the amplifier configurations considered above, the equations of the quality factor become, respectively:

$$Q_{s.p.}(\nu) = \frac{G^2(L, \nu)}{1 + 2G(L, \nu) \int_0^L \frac{\gamma_e(z', \nu)}{G(z', \nu)} dz'} \quad (18)$$

$$Q_{d.p.}(\nu) = \frac{R^2(L)G^4(L,\nu)}{R(L)G(L,\nu) \left[1 + 2G(L,\nu) \int_0^L \frac{\gamma_e(z,\nu)}{G(z,\nu)} dz \right] + 1 - G(L,\nu) + 2 \int_0^L \gamma_e(z,\nu) G(z,\nu) dz} \quad (19)$$

3. DISCUSSION OF THE SIMULATION RESULTS

The system of coupled first order differential equations (1)-(2) for the optical power components and the upper population level, can only be solved by numerical methods. We used the Runge-Kutta integration method (4th order, 4 stages).

Moreover, the presence of the boundary conditions (3) at both the extremities of the device requires an iterative procedure of integration.

The simulation of the optical amplification in Er^{3+} -doped LiNbO_3 waveguide has been performed using parameters obtained from literature^{1,2}. Using Eqs. (12)-(19), we numerically calculated the spectral dependence of the gain, noise figure, and quality factor for a single and double pass configuration of the optical amplifier with signal and pump wavelengths at 1531 nm and 1484 nm, respectively.

The spectral dependence of the cross sections has been explicitly considered, adopting for σ_a, σ_e a set of values measured at different wavelengths and dividing the emission spectrum in a number of small intervals (in these simulations 100 intervals for the wavelength range from 1450 to 1650 nm).

We used the following values for the absorption (a) and emission (e) cross sections of the pump (p) and signal (s) for TE and TM polarizations: $\sigma_{\text{TE}}^a(1484 \text{ nm}) = 5.61 \times 10^{-25} \text{ m}^2$, $\sigma_{\text{TM}}^a(1484 \text{ nm}) = 3.46 \times 10^{-25} \text{ m}^2$, $\sigma_{\text{TE}}^e(1484 \text{ nm}) = 1.92 \times 10^{-25} \text{ m}^2$, $\sigma_{\text{TM}}^e(1484 \text{ nm}) = 1.105 \times 10^{-25} \text{ m}^2$, $\sigma_{\text{TE}}^a(1532 \text{ nm}) = 17.24 \times 10^{-25} \text{ m}^2$, $\sigma_{\text{TM}}^a(1532 \text{ nm}) = 12.15 \times 10^{-25} \text{ m}^2$, $\sigma_{\text{TE}}^e(1532 \text{ nm}) = 16.36 \times 10^{-25} \text{ m}^2$, $\sigma_{\text{TM}}^e(1532 \text{ nm}) = 11.53 \times 10^{-25} \text{ m}^2$.

The Er-profile has been considered Gaussian in depth and constant in width, with a surface concentration of about $7 \cdot 10^{25} \text{ m}^{-3}$ and a diffusion depth of 20 μm .

We assumed the following values for the scattering loss and spontaneous emission lifetime: $\alpha = 3.7 \text{ dB} \cdot \text{m}^{-1}$ for TE, $\alpha = 4.8 \text{ dB} \cdot \text{m}^{-1}$ for TM, and $\tau = 2.6 \text{ ms}$, respectively.

The length of the waveguide in our simulations is $L = 5.4 \text{ cm}$ and the pump or signal assumed to be TE polarized if not explicitly stated.

The double pass gain spectra $G_{d.p.}(\nu)$ is presented in Fig. 1 for the input pump power of 150 mW (high pump regime) and 25 mW (low pump regime, near the threshold pump power, which is $P_{th} = 18.5 \text{ mW}$ for the single pass and $P_{th} = 12.5 \text{ mW}$ for the double pass configuration).

The noise figure spectra $F(z, \nu)$ can be calculated using (14)-(15) for single and double pass, respectively; results are shown in Fig. 2 for the double pass case with a mirror reflectivity at $z = L$ section $R(L) = 0.98$. As can be seen, the calculated noise figure values for Er^{3+} -doped LiNbO_3 waveguides amplifiers in double pass and high pump regime are comparable at peak values ($F_{d.p.} = 5.8 \text{ dB}$ for $\lambda = 1531 \text{ nm}$) with those obtained in optical fiber amplifiers.

When the waveguide is pumped a few times above the threshold (i. e. $P(0) = 50$ mW) the forward and backward noise figure spectra are very similar, the forward noise figure spectra being lower about 5% at peak values than the backward noise figure spectra.

In high pump regime, however, the difference between the forward and backward spectra vanishes. The same effect is obtained in the case of ASE spectra for the optical fiber amplifiers as was shown in Ref. 4.

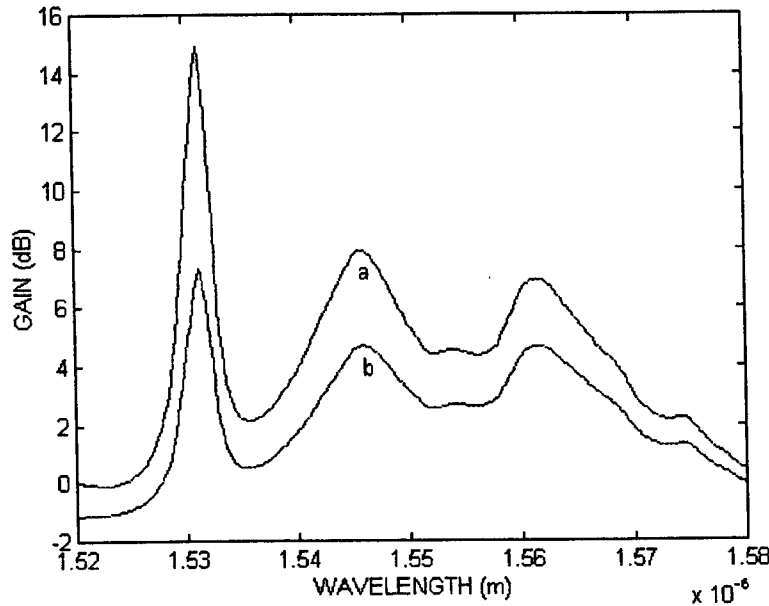


Fig. 1. The double pass gain spectra for: a) $P(0) = 150$ mW and b) $P(0) = 25$ mW; $L = 5.4$ cm

The spectra of the quality factor $Q_{d.p.}(\nu)$ for the double pass amplifier are presented in Fig. 3 while in Fig. 4 we present the dependence of the quality factor versus the pump power. In an interval of 2 nm around $\lambda = 1531$ nm the double pass configuration with high pump regime ($P(0) = 150$ mW) allows to obtain high gain (about 14.5 dB) and low noise figures (5.9 dB) for amplifier length of 5.4 cm.

From the behaviour of the above mentioned parameters under various pumping regimes we demonstrated that high gains and low noise figures are achievable in high pump regimes and double pass configuration, this allows to obtain amplifiers having high quality factors.

4. CONCLUSIONS

In this paper we present an accurate evaluation of the spectral optical gain, spectral noise figure and spectral quality factor for an Er^{3+} -doped LiNbO_3 waveguide amplifier pumped at 1484 nm with a TE pump.

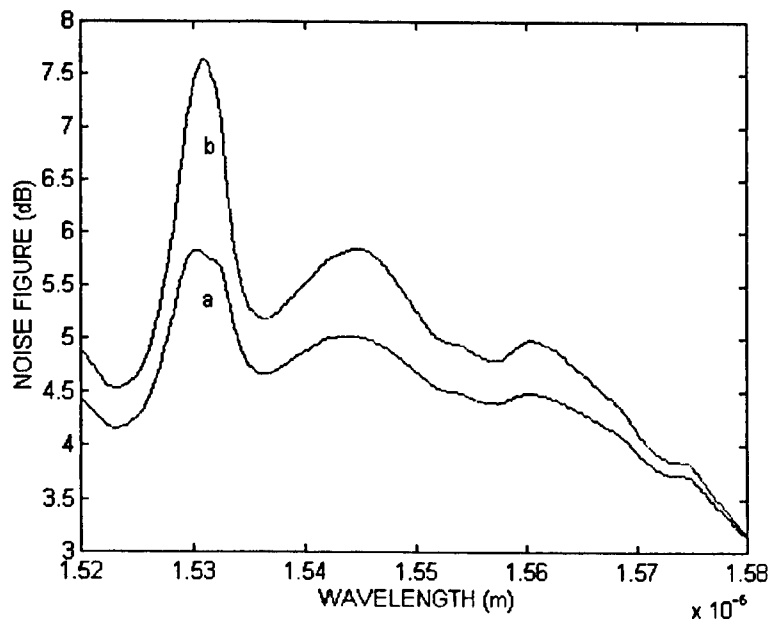


Fig. 2. Noise figure spectral behaviour as in Fig. 1

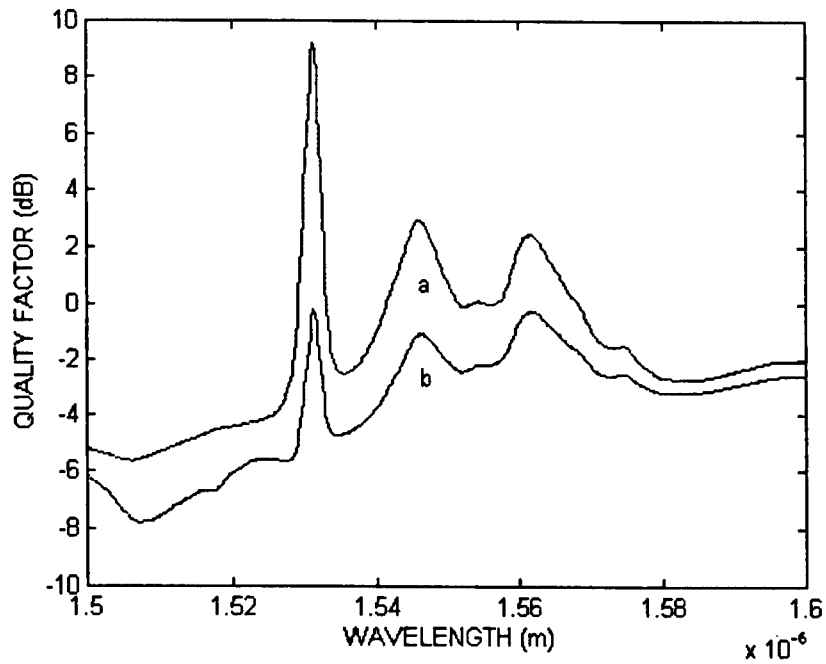


Fig. 3. Quality factor behaviour as in Fig. 1

The theoretical analysis was made using the small gain approximation in the unsaturated pump regime for both single and double pass configurations.

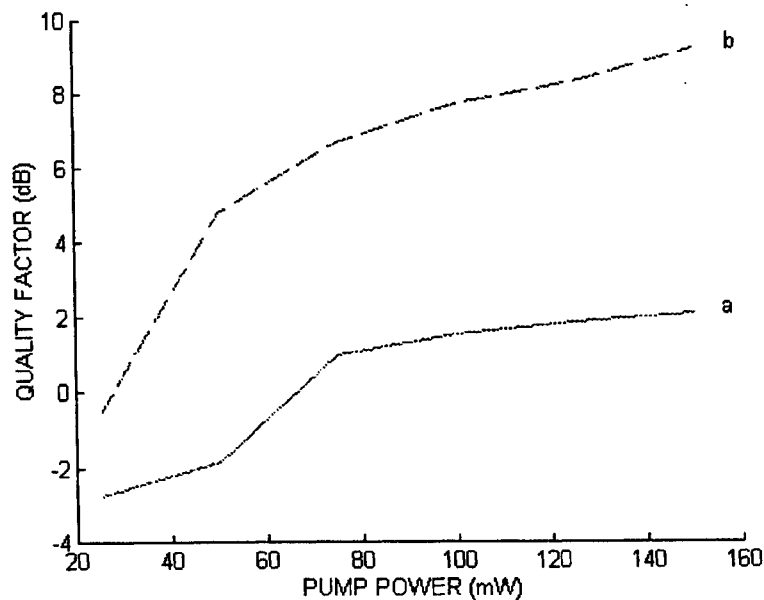


Fig. 4. Quality factor behaviour vs the pump power

We demonstrated in this theoretical analysis that high gains and low noise figures are achievable in high pump regimes and double pass configuration; this allows to obtain amplifiers having high quality factors.

5. REFERENCES

1. R. Brinkmann, W. Sohler, and H. Suche: "Broadband gain in single -mode erbium diffused Ti:LiNbO₃ -strip waveguides," in *Proceedings of the IOOC'91 International Conference on Integrated Optics and Optical Fiber Communication 9-12 September, 1991, Paris*, pp. 157-160.
2. W. Sohler: "Rare Earth Doped LiNbO₃ Waveguide Amplifiers and Lasers," in *"Waveguide Optoelectronics"*; J. Marsh and R. de la Rue (eds.), NATO ASI Series E: Applied Sciences, vol. 226, pp. 361-394, Kluwer-Academic, Dordrecht, Boston, London (1992).
3. I. Baumann, R. Brinkmann, M. Dinand W. Sohler and S. Westenhofer: "Ti:Er:LiNbO₃ Waveguide Laser of Optimized Efficiency," *IEEE J. Quant. Electr.*, **QE 32**, 1695-1706 (1996).
4. E. Desurvire, *Erbium-Doped Fiber Amplifiers*, J. Wiley & Sons, Inc. New York (1994).
5. M. J. F. Digonnet: "Closed-Form Expressions for the Gain in Three- and Four Level Laser Fibers," *IEEE J. Quant. Electr.*, **QE 26**, 1788-1796 (1990).

OUTPUT BEAM CHARACTERISTICS OF A Nd:YVO₄ MINIATURE LASER

N. PAVEL*, T. TAIRA, M. FURUHATA, and T. KOBAYASHI

Faculty of Engineering, Fukui University, 9-1 Bunkyo 3-Chome,
Fukui-shi - JAPAN

* National Institute for Laser Plasma and Radiation Physics, Bucharest - ROMANIA

e_mail: taira@kyomu1.fuee.fukui-u.ac.jp
 pavel@optele.fuee.fukui-u.ac.jp; npavel@roifa.ifa.ro

ABSTRACT

The output beam characteristics of a CW diode end-pumped miniature Nd:YVO₄ laser (1.1 at.%, 1x3x3mm³) operating in fundamental and SHG regime are presented. Using M² factor to describe the multimode pump beam's propagation from the broad-emission-area diode-laser the coupling optics was designed to obtain a high value for the mode-matching efficiency. A maximum slope efficiency of $\eta_s=58.6\%$, with $\eta_0=53.8\%$ optically efficiency at maximum pump power, characterized a laser resonator of 50mm length in transversal TEM₀₀ mode. In the SHG experiments using a KTP crystal a maximum power of 100mW was reach in a circular laser beam of 4.2 mrad half-angle divergence.

Keywords: Nd:YVO₄ laser, end pumping scheme, M² factor, SH generation.

1. INTRODUCTION

Nd:YVO₄ is one of the most efficient laser host crystal for diode laser-pumped solid-state lasers. Compared with Nd:YAG it possess the advantages of lower dependency on pump wavelength and temperature control of a diode laser, higher slope efficiency, lower lasing threshold, linearly polarized emission and single-mode output. Its large stimulated emission cross-section at lasing wavelength, high absorption coefficient and wide absorption bandwidth at pump wavelength, make Nd:YVO₄ an excellent crystal for stable and cost-effective diode laser-pumped solid-state lasers.

In this paper the output beam characteristics of an end-pumped miniature Nd:YVO₄ (1.1 at.%, 1x3x3mm³) operating in CW fundamental and SHG regime are presented. Earlier work includes reports on monolithic Nd:YVO₄ laser^[1], transversal TEM₀₀ operation^[2], longitudinal single-mode oscillation^[3] or simultaneously Q-switching and SHG by a KTP crystal of a microchip Nd:YVO₄ laser^[4]. A special attention we paid to design a less-dimension focusing optics, that to ensure in the same time an almost cylindrical pump beam in the active medium. Using M² factor, which was introduced to indicate the transverse mode beam quality of lasers, it is possible to describe the beam propagation from diode lasers as a Gaussian one^[5, 6]. Then the beam propagation after the focusing optics can be obtained and it helped us to optimize the design of Nd:YVO₄ laser. This technique has the advantage of simplicity as compared with previously ones^[7-10], but is more proper for an active medium of mm length order.

This design guideline was examined by a Nd:YVO₄ miniature laser with the coupling optics consists of a simple combination of fiber lens, rod lens and focusing lens instead of the prism beam expanders. We obtained a low threshold power and a high slope efficiency of ~58.6% in a TEM₀₀ output laser beam. A good agreement between theoretical and experimental results was observed.

2. FOCUSING OPTICS AND LASER CAVITY DESIGN

For solid-state lasers optically pumped by diode lasers two basic approaches, end- and side-pumping are used. The end-configuration is an attractive mean to obtain efficient lasers, while the side-scheme is a method for power scaling. In Fig. 1 a model of an end-pumped solid-state laser used to design our focusing line is presented. Here w_{p0} denotes the waist ($1/e^2$ definition) of the multimode pump beam in the active medium and w_{l0} is the laser resonator TEM₀₀ mode spot-size on the exit face of it. Compared with the pump beam the spot size of the laser cavity mode is approximately cylindrical on the active medium length.

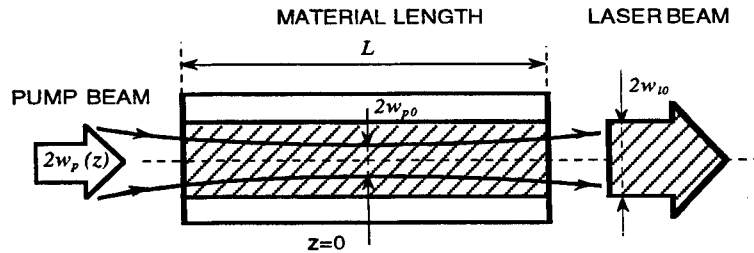


Fig. 1 Model for an end-pumped four-level solid-state laser. The laser cavity mode is almost cylindrical on the active medium length. For a quasi-three-level laser the focused pump beam radius w_{p0} has to be larger than the laser spot size w_{l0} .

The diode laser beam is multimode and characterized by a high degree of astigmatism. Considering a laser beam of M^2 factor, the spot size as a function of distance z from the beam waist w_{p0} expands as a hyperbola [5, 6]:

$$w_p(z) = w_{p0} \sqrt{1 + \left(\frac{M^2 \lambda_p z}{n \pi w_{p0}^2} \right)^2} \quad (1)$$

where n is the refractive medium index and λ_p denotes the laser wavelength. For optimum mode matching of pump and laser beams the confocal parameter $l_{cp} = (2\pi n w_{p0}^2)/(M^2 \lambda_p)$ must be longer or at least equal with the active medium length L . Usual L is one or two times the inverse active-medium absorption coefficient at the pump wavelength. As a result the minimum focused beam radius is given by:

$$w_{p0} = \sqrt{\frac{M^2 \lambda_p L}{2n\pi}} \quad (2)$$

Then the diode-laser beam's spot-size on the active medium side facing the diode can be obtained as

$w_p(L/2) = \sqrt{M^2 \lambda_p L / n\pi}$ and for a four-level-laser it should be smaller than the laser cavity spot-size $w_p(L/2) \leq w_{l0}$. Finally, the minimum focal length f of the solid-state laser coupling optics is:

$$f = \frac{n\pi}{M^2\lambda_p} w_{p0} w_0 = w_0 \sqrt{\frac{n\pi L}{2M^2\lambda_p}} \quad (3)$$

where w_0 is the light-source beam's waist-size.

Literature attests to the perfect mode overlap efficiency of the four-level-lasers when the pump beam radius is smaller than the oscillating beam radius, i.e. $w_{p0}/w_{l0} < 1$, with pump intensity^[11] few times higher than the threshold intensity. Then a relation between the fundamental mode area S_{eff} and M^2 factor of the diode laser radiation must be kept:

$$S_{eff} = \pi w_{l0}^2 \geq \pi w_p^2 (L/2) = M^2 \lambda_p L / n \quad (4)$$

Here, for a plane-concave resonator, w_{l0} result from the g_i -parameter's theory as $w_{l0}^2 = (\lambda_l / \pi) \sqrt{l_c(\rho - l_c)}$, where ρ denotes the output mirror radius and $l_c = L/n + l_{air}$.

Now will consider the input-output characteristics of the laser cavity. The active medium circulating gain g_0 can be written as:

$$g_0 = \frac{(f_a + f_b)\sigma_e \tau}{h\nu_p} I_p \quad (5)$$

where σ_e is the stimulated emission cross-section for the laser transition, τ represents the upper manifold lifetime, f_a and f_b are the fractional populations of the lower- and upper-level, respectively. The effective pump intensity is given by $I_p \equiv \eta_a P_{in} / S_{eff} = n\eta_a P_{in} / M^2 \lambda_p L$ where η_a is the pump beam's absorption efficiency in the medium and P_{in} denotes the input pump power. For the laser performances the slope efficiency η_s and the threshold pump power P_{th} are important parameters. The laser output power P_{out} can be written as function of a residual resonator loss L_i and an output mirror transmission T as^[12]:

$$P_{out} = \frac{I_s S_{eff} T}{2} \left(\frac{2g_0}{L_i + T} - 1 \right) = \eta_s (P_{in} - P_{th}) \quad (6)$$

where I_s represent the active medium saturation intensity, which is defined as $I_s = h\nu_l / (f_a + f_b)\sigma_e \tau$. The threshold pump power P_{th} can be given by:

$$I_{th} = \frac{P_{th}}{S_{eff}} = \frac{h\nu_p}{2\eta_a(f_a + f_b)\sigma_e \tau} (L_i + T) = \frac{h\nu_p}{h\nu_l} \frac{L_i + T}{2\eta_a} I_s \quad (7)$$

From condition $\partial P_{out} / \partial T = 0$ the optimum output coupler transmission is:

$$T_{opt} = \sqrt{2g_0 L_i} - L_i \quad (8)$$

with the corresponding optimum output power:

$$P_{out}^{max} = \left(\frac{I_s S_{eff}}{2} \right) (\sqrt{2g_0} - \sqrt{L_i})^2 \quad (9)$$

Equation (4) indicates the requirements for pump beam and laser material characteristics to obtain a good overlap between the active medium pumped volume and TEM₀₀ cavity mode. By eq. (8) the output coupler transmission that extracts the optimum laser output power at a given pump intensity was establish.

3. EXPERIMENTAL RESULTS AND DISCUSSION

The diode laser pumped Nd:YVO₄ miniature laser shown in Fig. 2 was designed by above method. The laser cavity consists of a Nd:YVO₄ chip and an output mirror of 100mm radius of curvature, with reflectivity of R=98.9%, 95.6% and 94.0% at 1.06mm wavelength, placed 50mm apart from the crystal. A 1.1 at.% Nd doped YVO₄ crystal (NEC Co.) with dimensions of 3x3mm² and 1mm thickness was used. The Nd:YVO₄ medium has high transmission ($\geq 95\%$) at 809 nm and high reflectivity ($>99.9\%$) at 1.06 mm on the side that face the pump diode. The opposite side has antireflection coating at 1.06mm.

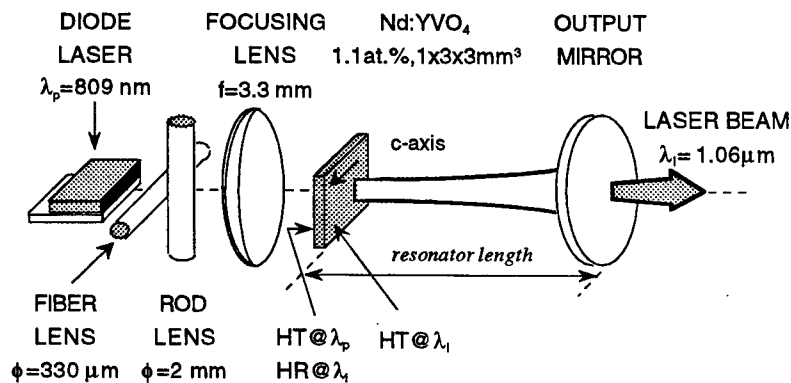


Fig. 2 Schematic of the diode-pumped Nd:YVO₄ miniature laser. A resonator of 50mm length and output couplers of 100mm radius were used.

The crystal was longitudinally pumped by a max. 1 W of 809nm light from a diode laser (Optopower Co. OPC-810-CT100) with emission area of 100mmx1mm. The diode-laser was temperature controlled to ensure an absorption coefficient maximum value of $\alpha_a = 27\text{cm}^{-1}$; then the absorption efficiency η_a was at least 93.3%. The divergence of the emitted radiation (FWHM definition) was 754 mrad perpendicular to the junction and ~117 mrad parallel to the junction and from these data the pump beam was characterized by M^2 factor of $M_x^2 = 22.7$ and $M_y^2 = 1.5$. As coupling optics a combination of a fiber lens (330 mm diameter), an antireflection coated rod lens ($\phi = 2$ mm) and a focusing spherical lens were used.

The pump beam propagation after the focusing lens is presented in Fig. 3. On Ox direction it was focused to ~60mm radius: we choose that as minimum value because at smaller focused radii the active medium can be thermal damaged. In Oy direction the minimal radius was ~9 mm, but in the middle of the active medium a circular beam was obtained. At more tightly focused beam on Oy direction the elliptical pump beam in the medium can not keep the lower transverse mode output at high pump region. One of the advantages of this simple coupling optics consists in its dimensions, namely less than 20mm. More, by proper variation of distances between the fiber- or rod-lens and the laser diode, the pump beam ellipticity in the medium can be controlled. The agreement between experimental points and theoretical curves with $M_x^2 = 27.9$ and $M_y^2 = 1.7$ of Fig. 3 indicates that it is possible to calculate the beam shapes after any complex optics of a given pump source by using ABCD matrix method.

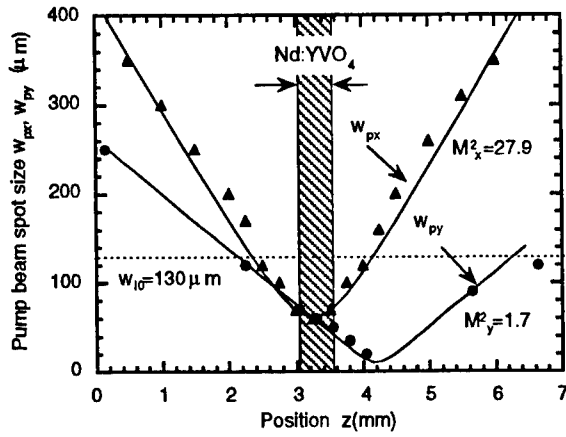


Fig. 3 Focused diode-laser beam propagating in z -direction. The curves represent the calculated beam shape with $M_x^2 = 27.9$ and $M_y^2 = 1.7$.

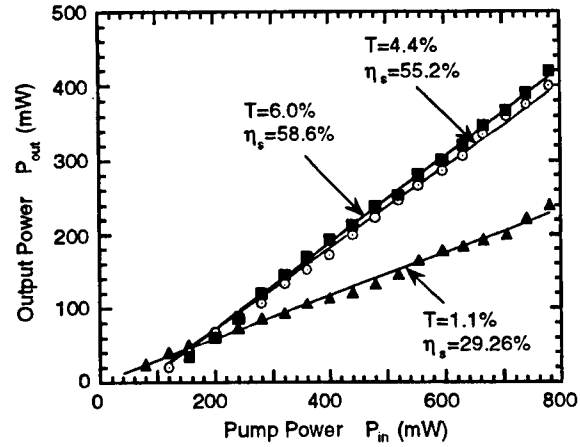


Fig. 4 Input-output power characteristics of the Nd:YVO₄ (1.1 % at., 1x3x3mm³) laser. From fit data was obtained a residual loss L_i of 1.8%.

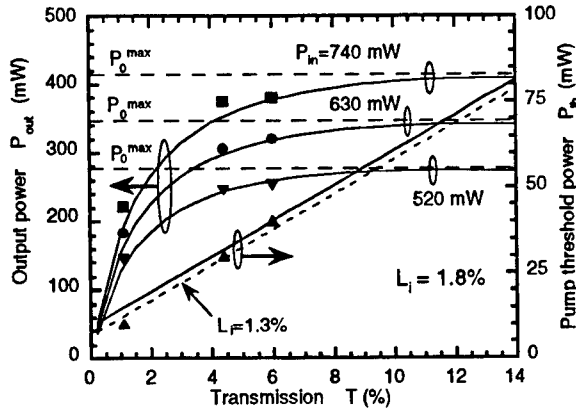


Fig. 5 Theoretical output power and threshold pump power as a function of output mirror transmission T . The experimental results are also indicated.

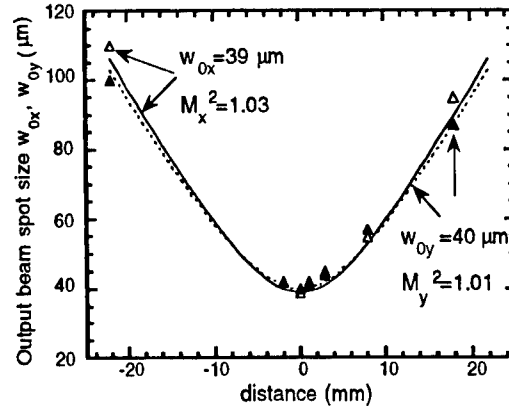


Fig. 6 Output beam spot-sizes as a function of distance from the beam's waist (knife edge method). The maximum output power was considered.

The output power as a function of pump power is presented in Fig. 4, for output mirror transmissions of 1.1%, 4.4% and 6.0%. A maximum slope efficiency value of $\eta_s = 58.6\%$, with optical efficiency of 53% at maximum pump power, characterized the laser resonator with $T = 6.0\%$. From the theoretical fit we obtain an internal loss L_i of $\sim 1.8\%$. Figure 5 shows the output power and pump threshold power as a function of the output mirror transmission. The curves and lines represent the calculated output power P_{out} from eq. (6) and the pump threshold power P_{th} from eq. (7), considering as parameters the pump power P_{in} namely 520 mW, 630 mW and 740 mW. The following values we used: $S_{eff} = 5.31 \times 10^{-4} \text{ cm}^2$ (corresponding to a laser beam radius of $w_{i0} = 130 \text{ mm}$) and $I_s = 1.36 \text{ kW/cm}^2$. From eq. (8) the optimum output-mirror's transmission values are 11.7%, 13.1% and 14.4%. Using eq. (9) the optimum output powers are 274mW, 345 mW and 414 mW; these values are also indicated on Fig. 5

(the horizontal dashed lines). Due to specific variation of the output power as function of the transmission, the experimental results for the mirror transmission of 6.0% are very closed to the optimum theoretical values. At maximum output power the output beam laser has a divergence (half angle, measured by knife-edge method) of 3.07×3.125 mrad, that correspond to an M^2 factor of 1.01×1.03 .

Finally, the SHG performances of our miniature laser were investigated. An CASIX KTP 5mm long crystal was cut for type II of phase matching and antireflection coated for fundamental and second harmonic generation. The laser resonator consists of a 50 mm output mirror's radius with 99.9% reflectivity at 1.064 μm and transmission of 99% at 532 nm. For properly phase matching condition the KTP crystal was temperature controlled. The best results on output power at 532 nm as functions of pump power are presented in Fig. 7. A maximum green power of 100 mW, that correspond to a conversion efficiency of $\eta_{2\omega} \approx 25\%$, in a circular laser beam of 4.2 mrad half-angle divergence was obtained.

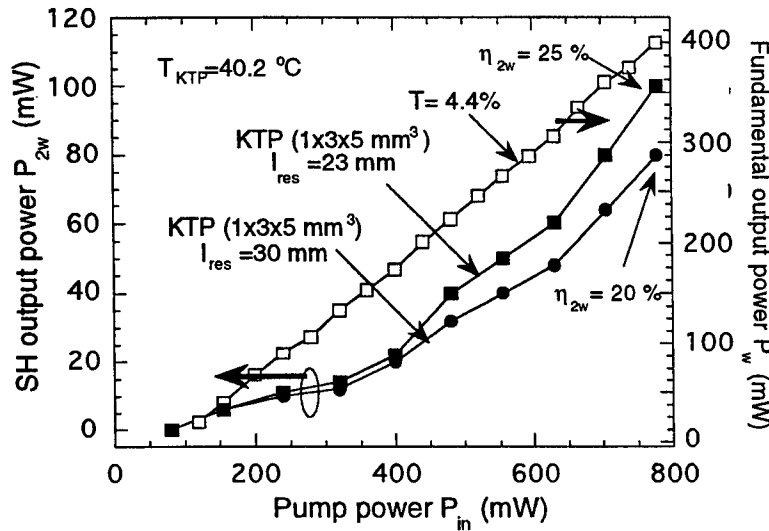


Fig. 7 Fundamental and second harmonic output power for the Nd:YVO₄ miniature laser.

4. CONCLUSIONS

The output beam characteristics of a cw diode end-pumped miniature Nd:YVO₄ laser (1.1% at., $1 \times 3 \times 3 \text{ mm}^3$) operating in cw fundamental and SHG regime are presented. The laser beam of the broad emission area diode-laser was described by M^2 factor that helped us to design a high efficiency miniature laser. A maximum slope efficiency of 58.6% was reached from an end-pumped Nd:YVO₄ miniature laser, pumped by maximum 0.8 W at 809 nm, in a TEM₀₀ laser beam of 1.01×1.03 M^2 factor. The theoretical model presented shows a good agreement with experimental data. The coupling optics we used between the laser pump diode and active medium has the advantages of simplicity: fiber lens, rod lens and spherical lens, small dimensions: less than 20 mm, and ensures an almost circular pump beam on the medium length. In the SHG experiments a maximum power of 100mW was reach in a circular laser beam of 4.2 mrad half-angle divergence.

This work was supported by the Grand-in-Aid (Project no. 09222207), the Japanese Ministry of Education, Science, Sports and Culture (MONBUSHO). Mr. N. Pavel acknowledges the support of MONBUSHO during his research-student's period at Fukui University of Japan.

5. REFERENCES

1. R. Scheps, J.F. Myers, and G. Mizell, "High-efficiency 1.06- μm output in a monolithic Nd:YVO₄ laser", *Appl. Opt.* **33**, 5546-5549 (1994).
2. G. Feugnet, C. Bussac, C. Larat, M. Schwarz, and J.P. Pocholle, "High-efficiency TEM₀₀ Nd:YVO₄ laser longitudinally pumped by a high-power array", *Opt. Lett.* **20**, 157-159 (1995).
3. T. Taira, A. Mukai, Y. Nozawa, and T. Kobayashi, "Single-mode oscillation of laser-diode-pumped Nd:YVO₄ microchip lasers", *Opt. Lett.* **10**, 1955-1957 (1991).
4. T. Taira and K. Kobayashi, "Q-switching and Frequency Doubling of Solid-State Lasers by a Single Intracavity KTP Crystal", *IEEE J. Quantum Electron.* **QE-30**, 800-804 (1994).
5. A.E. Siegman, "New developments in laser resonators", *SPIE* **1224**, 2-14 (1990).
6. M.W. Sasnett, "Propagation of multimode laser beam - the M² factor", in *The Physics and Technology of Laser Resonators*, ed. by D.R. Hall and P.E. Jackson, 133-142 (1992).
7. T.Y. Fan and A. Sanchez, "Pump Source Requirements for End-Pumped Lasers", *IEEE J. Quantum Electron.*, **QE-26**, 311-316, 1990.
8. P. Laporta and M. Brussard, "Design Criteria for Mode Size Optimization in Diode-Pumped Solid-State Lasers", *IEEE J. Quantum Electron.*, **QE-27**, 2319-2326, 1991.
9. Y.F. Chen, T.S. Liao, C.F. Kao, T.M. Huang, K.H. Lin, and S.C. Wang, "Optimization of Fiber-Coupled Laser-Diode End-Pumped Lasers: Influence of Pump-Beam Quality", *IEEE J. Quantum Electron.*, **QE-32**, 2010-2016, 1996.
10. T. Taira, J. Saikawa, T. Kobayashi, and R. Byer, "Diode-Pumped Tunable Yb:YAG Miniature Lasers at Room Temperature: Modeling and Experiments", *IEEE J. Select. Topics Quantum Electron.*, **3**, 100-104 (1997).
11. W.P. Risk, "Modeling of longitudinally pumped solid-state lasers exhibiting reabsorption losses", *J. Opt. Soc. Am. B* **5**, 1412-1423 (1988).
12. W. Koechner, in *Solid-State Laser Engineering*, Springer 4th Ed., p.97 (1995).

BOUND STATE EXCITATION IN ION-ION COLLISION AS RELATED TO THE MODELLING OF X-RAY LASERS WITH LI-LIKE IONS

V.Stancalie¹, A.Sureau², V.M.Burke³

¹National Institute for Laser, Plasma and Radiation Physics, Laser Dept., P.O.Box MG-36, Bucharest, 76900 ROMANIA

²Universite Paris-Sud, Laboratoire de Spectroscopie Atomique et Ionique, 91405 Orsay Cedex, FRANCE

³DRAL Daresbury Laboratories, Warrington, WA4 4AD, U. K

ABSTRACT

Within the framework of x-ray laser research using the recombination of heliumlike ions with free electrons to produce lithiumlike ions in expanding and cooling hot plasmas, we present a set of spectroscopic data required to improve the gain modelling. We estimate the cross section and rate for ion-impact excitation in aluminium Li-like lasing medium using the two-state approximation for transitions caused by a multipole interaction. The approximation used for atomic data calculation is presented.

Keywords: x-ray lasers, atomic data, inelastic transition probability, cross section, rate coefficients

1. INTRODUCTION

The modelling of x-ray lasers is a complex theoretical problem requiring an accurate time dependent solution of the hydrodynamic equations of the plasma coupled in a consistent way with a large number of basic atomic processes such as electron excitation and ionisation, radiative and di-electronic recombination and radiative transfer. For the particular case of x-ray lasers with Al Li-like ions, $1s^2n/$ configuration, the electronic temperature covers a wide range, between several hundreds of eV to less than 20 eV. The most frequently studied transitions, experimentally and theoretically, are the 3d-4f and 3d-5f. The evolution of the gain coefficient for these two transitions ($5/2-7/2$ component) in Al^{10+} has been computed but including only the electron-impact and decay processes in redistributing population among low-lying excited states. However some persistent discrepancies between calculated and measured absolute gain values are still to be removed. Improvements of the predicted gain values are expected within the different parts of the modelling¹⁻³. We concentrated our analyse on the last part of plasma history, when complications as such as non-Maxwellian particle distributions, radiation fields, and transient plasma conditions can be neglected, and when the plasma electrons and ions have comparable temperatures, $T_e \approx T_i$.

We have examined the probability for excitation in ion-and electron- collisions including electric-dipole and quadrupole transitions of type:



2. APPROXIMATION USED FOR ATOMIC DATA CALCULATION

The $1s^2 2l$, $1s^2 3l$, $1s^2 4l$ and $1s^2 5l$ states of Al^{10+} have been carefully considered. The target wave functions were represented by configuration interaction (C.I.) wavefunctions of the form:

$$\Phi(LS\pi) = \sum_{i=1}^N a_i \Phi_i(\alpha_i LS\pi) \quad (2)$$

where each Φ_i is constructed from one electron orbital whose angular momenta are coupled in a manner defined by α_i to form a total L and S common to all N configurations in (2). The radial part of each orbital is a sum of Slater-type functions:

$$P_n(r) = \sum_i c_i r^{p_i} \exp(-\zeta_i r) \quad (3)$$

Fifteen orthogonal one-electron orbitals 1s, 2s, 2p, 3s, 3p, 3d, 4s, 4p, 4d, 4f, 5s, 5p, 5d, 5f, 5g were used in our work. They had been calculated as part of the Opacity Project⁴. The large C.I. computer code developed by Hibbert⁵ was used in all of our bound state calculations.

Using these C.I. wavefunctions we were able to calculate the energy difference, ΔE , and transition linestrengths, $S^{(\lambda)}$, $\lambda=1, 2, 3$ (dipole, quadrupole, octupole) between all 14 states as output from RMATRIX II⁶. All these calculations have been obtained using the non-relativistic LS coupling code. In order to carry out the calculation of finestructure linestrength values we used the approximate expressions for vector-coupling coefficients and 6-j symbols⁷. The corresponding level energies included in our present work are given by direct SCF method of the numerical multiconfigurational Hartree-Fock type modified by relativistic Darwin terms of the Pauli approximation in the Hartree-Fock differential equations^{8,9}.

Part of these results are given in Table 1.

Table 1.

transition $n'l_i \rightarrow n'l_f$	mode $E\lambda$	ΔE (atomic units)	$S^{(\lambda)}$ (atomic units)
$2s_{1/2} - 3p_{1/2}$	E1	9.423787	0.035511
$2s_{1/2} - 3p_{3/2}$	E1	9.432537	0.071022
$2p_{1/2} - 3s_{1/2}$	E1	8.403088	0.007641
$2p_{3/2} - 3s_{1/2}$	E1	8.373493	0.015282
$2s_{1/2} - 3d_{3/2}$	E2	9.506180	0.1156123
$2p_{3/2} - 3p_{1/2}$	E2	8.589400	0.033190
$2p_{3/2} - 3p_{3/2}$	E2	8.598160	0.298715
$2p_{3/2} - 4f_{7/2}$	E2	11.62300	0.072640
$2p_{3/2} - 5f_{7/2}$	E2	12.98429	0.0283449

3. TRANSITIONS CAUSED BY A MULTIPOLE INTERACTION

In the usual impact parameter method, for a transition from initial state $|i\rangle$ to final state $|f\rangle$, the cross section is equal to the integral of an excitation probability P_{if} over all impact parameters, b , i.e.,

$$\sigma_{if}(v) = 2\pi \int_0^\infty P_{if}(v, b) b db \quad (4)$$

where v is the relative velocity, and P_{if} is the square of the absolute value of the transition amplitude $P_{if} = |a_{if}|^2$. The amplitudes a_{if} satisfy a set of coupled differential equations. The problem of calculating the transition probability $P_{if}(v, b)$ reduces to a system of equations for the time dependent amplitudes of the state that can be written in the form:

$$i\hbar \frac{da_k}{dt} = \sum_m V_{km}(t) \exp(i\omega_{km}t) a_m \quad (5)$$

where $\omega_{km} = E_k - E_m / \hbar$ is the energy difference between unperturbed levels, and V_{km} are the matrix elements of the interaction, depending on the parameters b and v .

We shall consider two state approximation theory¹⁰ to calculate cross section and rates for inelastic transitions of type (1) induced by Al^{10+} ion. In this case the transition probability is given by a multipole interaction at comparatively large distances, larger than atomic dimensions. The matrix element V is assumed in the form:

$$V(R) = \lambda/R^n - \exp(-\phi R) f(R) \quad (6)$$

where n is determined by the multipole order of the transition under consideration ($n = 2$ and $n = 3$ for electric dipole and quadrupole transitions, respectively) and where λ (with dimension $s^{-1}cm^n$) is the constant of the interaction related to the linestrength of the transition¹¹. In eq.(6) the function $f(R)$ is a polynomial in R^{1-n} and ϕ is constant expressed in terms of the ionisation potentials of the states involved in the transition under consideration. The trajectories of the colliding particles are considered to be rectilinear and $V(R) \rightarrow \text{cons.}$ when $R \rightarrow 0$. Two effects^{12,13} combine to reduce rate coefficients drastically at low energy: the repulsive coulomb force acting between colliding ions and the effect of the finite energy gap ω_{JT} . Accurate calculations¹⁴ over a wide range of collision parameters involved in ion-ion collisions have been reported including the collisional effects on the $2p^5 3p$ level populations in Se^{24+} lasing medium.

We used first-order perturbative theory to make some order of magnitude. The collisions have been divided according to whether b is less than or greater than b_0 . The limiting impact parameter b_0 was written as:

$$b_0 = (\alpha_n \lambda / v)^{1/(n-1)}, \quad \alpha_n = \sqrt{\pi} \Gamma(n-1/n) / \Gamma(n/2) \quad (7)$$

When $b < b_0$ the transition probability begins to oscillate rapidly about the mean value closed to the limiting value of $1/2^{15}$. When $b > b_0 > R_0$ the potential (6) can be replaced by the potential λ/R^n . In this case $R_0 = 1/\phi$ is the effective radius that must be estimated by integrating over trajectory function composed of classical trajectory integrals $I_{\lambda\mu}$. Here $(\lambda\mu)$ labels the spherical polar component μ of the multipolar interaction term of order λ . The integrals $I_{\lambda\mu}$ were originally obtained for application to nuclear excitation¹⁶. For velocities satisfying the condition $b > b_0 > R_0$, the two state approximation gives the following excitation probability and cross section formulae:

$$P_{if} = \sin^2(\alpha_n \beta_n^{n/2}) \exp(-2(2^{2/n} \beta_n \sin^2(\pi/2n) + \chi^2)^{1/2}) \quad (8)$$

$$\sigma = 2\pi (\lambda/v)^{2/(n-1)} \exp[-2^{(n+1)/n} \sqrt{\beta_n} \sin(\pi/2n)] I_n(\beta_n) \quad (9)$$

where $\beta_n = \lambda^{2/n} \omega^{2(n-1)/n} / v$, $\chi = \phi \omega / v$ are collision parameters and where:

$$I_n(\beta_n) = \int_0^\infty \sin^2[\alpha_n y^{(n-1)}] \exp\{-2\beta_n^{1/2} [(2^{2/n} \sin^2(\pi/2n) + \beta_n^{1/(n-1)} y^2) - 2^{1/n} \sin(\pi/2n)]\} y dy \text{ for } \beta_n \gg 1 \text{ and}$$

$$I_2(\beta_2) \rightarrow \pi^2 \ln(1/\beta_2), \quad I_3(\beta_3) \rightarrow \pi/2 \text{ when } \beta_n \rightarrow 0.$$

4. RESULTS

The cross sections for Al^{10+} impact excitation of the $1s^2 2l' - 1s^2 n l''$ transitions in Al^{10+} ion were evaluated using eqs.(9). We used in our calculation the general formula for the interaction constant related to the linestrength of transition under consideration:

$$\lambda = Z_0 \left(\frac{(2l+1)}{(2k+1)} \right)^{1/2} \begin{pmatrix} l_0 & l_1 & k \\ 0 & 0 & 0 \end{pmatrix} \int_0^\infty P_0(r) P_1(r) r^k dr \quad (10)$$

where $P(r)$ is the radial eigenfunction of the optical electron in the state $n l$.

For optical allowed transitions $1 \rightarrow 0$ one has a simple form¹⁷ connected with the radiative transition probability A_{10} (s^{-1}):

$$\lambda^2 = 1.55 \times 10^{-11} g_1 A_{10} Z_0^2 / (g_0 \omega^3) \quad (11)$$

In relation (11) g_1 and g_0 are statistical weights of the levels 1 and 0, respectively, and Z_0 is the charge of the incident ion. In all our calculations the incident ion is assumed structureless and the trajectory of the perturbing particles as rectilinear. To avoid fast numerical calculations the target size, r_T , has been compared with r_0 ($r_0 = Z_0 Z_T e^2 / 2E$), one-half the distance of closest approach at zero impact parameter and relative energy E ¹⁴. The results we have obtained were concentrated on the collision velocity range where the penetration of the target does not occur ($2r_0 > r_T$). The most interesting case is the dipole allowed transitions with $k = 1$. The figure 1 gives the ratio $2r_0/r_T$ for the electric-dipole transition $1s^2 2p_{3/2} - 1s^2 3d_{5/2}$ induced by Al^{10+} impact excitation as functions of collision energy. Through collisional excitation of low-lying states such as these, ion-ion collisions can increase the amount of radiation emitted by a plasma. Excitations that do not involve a change of principal quantum number ($\Delta n = 0$ transitions) usually are favoured in collisions between thermal ions. However, as the relative velocity increases, collisions can occur at velocities near the peak of some $\Delta n > 0$ cross sections. In figure 2 is shown the cross section for Al^{10+} impact excitation of the electric-quadrupole $1s^2 2p_{1/2} - 1s^2 2p_{3/2}$ transition in Al^{10+} ion.

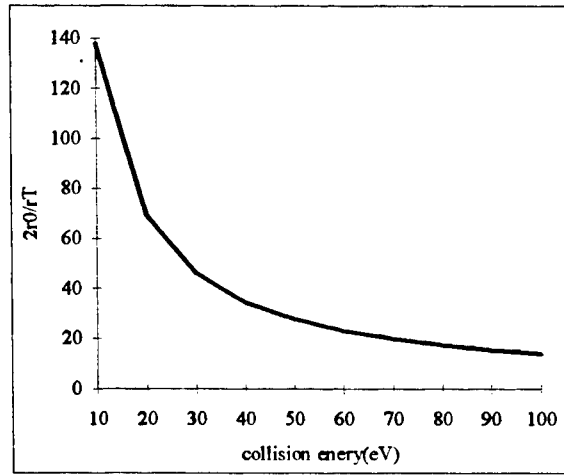


Fig. 1. The ratio of the closest approach to the target size, $2r_0/r_T$, as function of collision energy, for the $1s^2 2p_{3/2} - 1s^2 3d_{5/2}$ transition induced by Al^{10+} impact excitation in Al^{10+} ion.

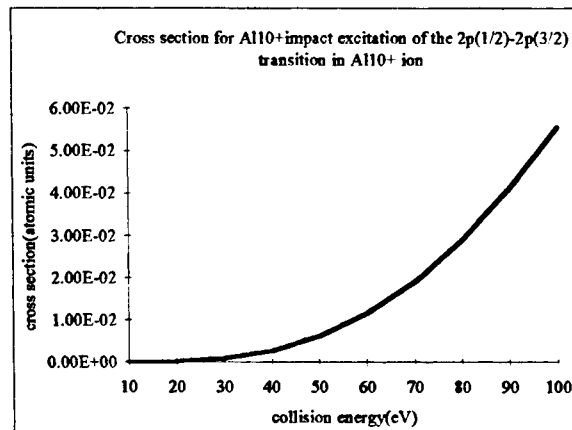


Fig. 2. Cross section (in atomic units) for Al^{10+} ion-impact excitation of the $1s^2 2p_{1/2} - 1s^2 2p_{3/2}$ transition in Al^{10+} ion as function of collision energy(in eV units)

For applications it is necessary to know the excitation rates, which can be obtained by averaging the cross section over the Maxwellian velocity distribution. We have estimated the rate coefficients for some transitions of interest induced by ion-ion and electron-ion excitation in Al^{10+} ion.

Most modern methods of calculating electron excitation rates of an ion are based on the expansion of total wave function of the electron plus ion system in terms of the wave function of the ion. The most effective method so far is the R-matrix method which was pioneered by P.G.Burke⁶. In this method one make use of the physics of the situation. At short distances from the nucleus within a sphere of radius a the exchange effects are included as well as electron-electron interaction but outside the sphere the exchange effects are neglected and the electron moves in an asymptotic field. Because so few ion-ion collisions have been investigated and in order to provide an estimation of electron-excitation rates we used the semi-empirical formula of Van Regemorter¹¹ which is currently the most frequently used. The Table 2 gives our results concerning rate coefficients for ion-impact excitation, $\langle v\sigma_i \rangle$, and for electron-impact excitation, $\langle v\sigma_e \rangle$, of some transitions of interest in eq.(1).

Table 2

Rate coefficients for Al^{10+} impact excitation, $\langle v\sigma_i \rangle$, and rate coefficients for electron-impact excitation, $\langle v\sigma_e \rangle$ of some electric-dipole and quadrupole transitions in Al^{10+} ion at different values of electronic temperature, T_e (eV)

$$\langle v\sigma_i \rangle / \langle v\sigma_e \rangle \text{ (cm}^3 \text{ s}^{-1}\text{)}$$

transition(mode)	20 eV	30 eV	40eV	50eV
$1s^2 2s_{1/2} - 1s^2 3d_{3/2}(E2)$	1.978E-11/ 0.1578E-13	4.1326E-08/ 0.1179E-12	7.4451E-08/ 0.3841E-12	4.8126E-07/ 0.8301E-12
$1s^2 2p_{1/2} - 1s^2 2p_{3/2}(E2)$	4.4009E-07/ 0.8399E-08	1.2603E-05/ 0.6679E-08	2.7085E-05/ 0.5675E-08	4.8747E-05/ 0.4999E-08
$1s^2 2p_{3/2} - 1s^2 3p_{1/2}(E2)$	1.7494E-11/ 0.1436E-15	2.4056E-09/ 0.5756E-14	3.5258E-08/ 0.3493E-13	2.0012E-07/ 0.1005E-12
$1s^2 2p_{3/2} - 1s^2 3d_{5/2}(E1)$	3.8672E-11/ 0.1373E-13	7.4009E-09/ 0.5741E-12	2.2947E-06/ 0.3558E-11	1.3789E-05/ 0.1036E-10
$1s^2 2s_{1/2} - 1s^2 3p_{3/2}(E1)$	2.5321E-10/ 0.1665E-14	6.4449E-08/ 0.9785E-13	1.3634E-06/ 0.7188E-12	0.1055E-06/ 0.2319E-11
$1s^2 2p_{1/2} - 1s^2 3d_{3/2}(E1)$	5.0951E-11/ 0.1461E-13	9.6073E-09/ 0.6186E-12	8.9837E-07/ 0.3857E-11	0.5724E-07/ 0.1128E-10
$1s^2 2p_{1/2} - 1s^2 3s_{1/2}(E1)$	3.6513E-10/ 0.7176E-15	4.5883E-08/ 0.2644E-13	8.9837E-07/ 0.1538E-12	5.7241E-06/ 0.4313E-12
$1s^2 2p_{3/2} - 1s^2 3d_{3/2}(E1)$	9.6634E-10/ 0.1532E-14	1.4667E-07/ 0.6398E-13	0.5905E-07/ 0.3963E-12	3.9706E-06/ 0.1154E-11

5. CONCLUSIONS

We have implemented the two state approximation method to evaluate cross sections and rates for inelastic transitions induced by Al^{10+} ion impact excitation in aluminum Li-like lasing medium. The previous results have been obtained using the assumption of the rectilinear trajectory of the perturbing particles and for limiting impact parameter under the conditions:

$$b_0 > R_0 \quad \text{and} \quad (2\lambda/\omega)^{2/n} \sin^2(\pi/2n) + b^2 > R_0^2.$$

where for allowed transitions the constant of the interaction was evaluated by eq.(11). The impact parameters we have used were evaluated in the range of thermal energies, between less than 10 eV and 30 eV. In the range of collision velocity of

order 10^6 cm s^{-1} the parameters β_2 and χ_2 were calculated for impact parameters less than b_0 . However, for arbitrary trajectory the internuclear distance is linked with time and the Coulomb repulsion must be included into the calculations together with the close-coupling effect. Our preliminary results ignore these effects. The method we have used yields less accurate cross section estimate in the case, where close coupling increase the likelihood of a (weaker) quadrupole transition at the slight expense of the stronger dipole transitions. The relative errors are much less for E1 transitions, and they tend to decrease with increasing collision energy, as the close-coupling effects diminish. Thus for excitation of ions together with close-coupling effect which is substantial when $\beta_2 \geq 1$, i.e. collision energy less than 25 eV for the E1 transition $1s^2 2p_{3/2} - 1s^2 3d_{5/2}$, the Coulomb repulsion is exponential in the parameter $r_0\omega/v$.

We have compared the ion-ion and electron-ion rate coefficients by integrating the ion-impact excitation cross section on the Maxwellian distribution over velocities of the particles. We used quasi-classical formulae to calculate the electron-excitation rates. We conclude from the preceding comparisons that the semi-classical method of two state problem, as we have implemented it, generally yields reliable results if strong coupling through intermediate state is neglected. Close coupling calculations are in progress.

6. REFERENCES

1. A. Klisnick, A.Sureau, H.Guennou, C. Möller, J.Virmont, "Modelling of recombination x-ray lasers", *Ann. Phys. Fr.* **15**, 529-547 (1990).
2. A. Klisnick, A.Sureau, H.Guennou, C. Möller, J.Virmont, "Effective rates for Li-like ions: Calculated XUV gains in Al^{10+} ", *Appl.Phys.B.* **50**, 153-164 (1990).
3. V.Stancalie, A.Sureau, A.Klisnick, C. Möller, H.Guennou, Y.Bérété, "Influence of dielectronic recombination on gain modelling of x-ray lasers with Li-like ions" *Laser Interaction with matter*, S.Rose ed., Int.Conf.Ser.40, 129-133, I.O.P.Publishing Ltd., Bristol, 1995.
4. J.A.Tully, M.J.Seaton, K.A.Berrington, "Atomic data for opacity calculations:XIV. The beryllium sequence" *J.Phys.B.: At. Mol. Opt.Phys.* **23**, 3811-3837 (1990).
5. P.G.Burke, H.Hibbert, W.D.Robb, "Electron-scattering by complex atoms", *J.Phys.B.: At.Mol.Opt.Phys.* **4**, 153-161 (1971).
6. P.G.Burke, K.A. Berrington, *Atomic and Molecular Processes: an R-matrix approach*, I.O.P. Publishing, Bristol, (1993).
7. A.R. Edmonds, *Angular Momentum in Quantum Mechanics*, Princeton, New Jersey Princeton University Press (1957).
8. H. Guennou, A.Sureau, "Ab initio Al XI and S XIV spectra.Transient population inversions in laser-produced plasmas", *J.Phys.B.:At. Mol.Phys.* **20**, 919-934 (1987).
9. A.Sureau, H.Guennou, M.Cornille, "A direct SCF method for low-Z atomic level structure. Application to some excited levels of the Kr isoelectronic series", *J.Phys. B.: At. Mol. Phys.* **17**, 541-553 (1984).
- 10.I.I.Sobelman, L.A. Vainshtein, E.A.Yukov, *Excitation of Atoms and Broadening of Spectral Lines*, Springer Series in Chemical Physics 7, J.P. Toennies ed., Springer Verlag Berlin Heidelberg New York (1981)
11. I.I. Sobelman *Atomic Spectra and Radiative Transitions*, 2-nd ed.,Springer Series on Atoms+ Plasmas 12, J.P. Toennies ed.,Springer-Verlag (1991).
12. R.M. Pengelly, M.J. Seaton, "Recombination Spectra", *Month.Not. Roy. Astr. Soc.* **127**, 165-175 (1963-64).
13. M.J.Seaton, "Recombination Spectra III", *Month.Not. Roy. Astr. Soc.* **127**, 178-184 (1963-64).
- 14.R.S.Walling and J.C. Weisheit, "Bound state excitation ion ion-ion collisions", *Physics Reports* **1**, 1-43 (1988).
- 15.J. N. Bahcall and R.A.Wolf, "Fine structure transitions", *Astrophys.J.* **152**, 701-729 (1968).
16. Alder, K., Bohr, A., Huus, T., Mottelson, B., and Winther, A., "Coulomb excitation" *Rev.Mod.Phys.* **28**, 4, 432-542 (1956).
17. I.Yu.Skobelev and A.V.Vinogradov, "Coulomb-Born and unitarised Coulom-Born cross sections and rates of inelastic transitions in ion-ion collisions", *J.Phys.B.:At.Mol.Phys.* **11**, 16, 2899-2905 (1978).

Nd:YAG linear resonator using an external stimulated Brillouin scattering Q-switching mirror

Anca Mocofanescu, V.Babin*, S.Miclos*, Ana Farcas

Institute of Atomic Physics, National Institute for Laser, Plasma and Radiation Physics
Bucharest 76900, P.O. Box MG-36, Romania

*Institute of Atomic Physics, National Institute of Optoelectronics
Bucharest 76900, P.O. Box MG-22, Romania

ABSTRACT

We report Q-switching of a Nd:YAG laser with a phase-conjugating mirror based on external stimulated Brillouin scattering in carbon disulphide (CS_2) using a linear resonator. Q-switching is provided by a nonlinear LiF:F_2^- crystal before the stimulated Brillouin scattering takes place. Employing proper mode selectors pulses with 6mJ minimum energy and duration of 20ns were generated, the beam divergence being 1.5 the diffraction limit. A new theoretical model of the Q-switching regime has been proposed and good agreement between experimental and theoretical data has been obtained.

Keywords : nonlinear optics, stimulated Brillouin scattering, Q-switching regime of the laser resonator

1. INTRODUCTION

For many scientific and practical applications of the high power solid-state lasers the brightness of the beam is a crucial parameter. Optical phase conjugation can be used to compensate the phase distortions of the solid-state lasers¹ greatly improving the quality of the generated laser beam. The simplest realisation of such adaptive phase conjugating mirror is based on stimulated Brillouin scattering (SBS) in gases and liquids. This leads to handy and self-pumped devices for building laser oscillators and double or multipass amplifiers.

Beside achieving a good beam quality another feature provided by the SBS interaction is the self Q-switching of the optical resonator. The approach usually adopted is to include the SBS medium inside a laser cavity with a secondary mirror employed to provide feedback at the beginning of the laser action². High intra-cavity intensities experienced by the SBS medium in this configuration can lead to poor spatial beam quality. This limits the repetition rate and peak power of the output. There has been reported also an alternative cavity configuration in which SBS medium resides outside the conventional cavity³⁻⁵. The output beam was found to have a TEM₀₀ mode and efficient energy extraction at very high repetition rate using high purity SBS media.

We have investigated theoretically and experimentally the performance of a pulsed Nd:YAG laser system utilising external stimulated Brillouin scattering for Q-switching and phase conjugation of the cavity radiation using a linear laser resonator. In our paper we have described the SBS interaction considering some particular aspects of the SBS process in the case when the duration of the laser pulse is long compared with the lifetime of the acoustic phonons and the experimental results obtained have confirmed our theoretical model.

2. THEORETICAL MODEL

The reflectivities of SBS mirrors depend on excitation conditions and material properties. Different theoretical approximations were investigated, especially the steady state case was explored in detail^{3,4}. When the duration of the pumping pulse, t_L , is long in comparison with the lifetime of the acoustic phonons, τ_B , in the nonlinear medium may appear other nonlinear processes with random character (great fluctuations of the thermal field, induced turbulence, multiplicative ionisation phenomena, shock hydrodynamic waves, etc) besides the Brillouin scattering. In this case the Brillouin gain is modulated by the random process.

The authors have written the general system of equations for the SBS interaction in the form⁶:

$$\begin{aligned}\frac{n}{c} \frac{\partial I_{Lc}}{\partial t} + \frac{\partial I_{Lc}}{\partial z} &= -\alpha I_{Lc} - (1 - \epsilon') g_B^e I_{Lc} I_S \\ \frac{n}{c} \frac{\partial I_S}{\partial t} - \frac{\partial I_{Lc}}{\partial z} &= \alpha I_S + (1 - \epsilon') g_B^e I_{Lc} I_S\end{aligned}\quad (1)$$

where ϵ' is a random variable, I_{Lc} is the pumping intensity and I_S is the Stokes intensity. The simplest case is when the random variable has a gaussian distribution. The dispersion of the process is called σ .

For calculating the Brillouin reflectivity we used the following expression for the Stokes intensity, deduced by analytical methods from the system (1):

$$I_S(t) = \frac{I_{Lo}(t) \exp \left[(g_B^e I_{Lo} - \alpha - \sigma^2 g_B^2 I_{Lo}^2) \frac{c\tau}{n} - G \right]}{1 + \exp \left[(g_B^e I_{Lo} - \sigma^2 g_B^2 I_{Lo}^2) \frac{c\tau}{n} - G \right]}\quad (2)$$

where $G \sim 25$ is related to the initial Stokes noise level, g_B is the Brillouin gain.

The passive Q-switching regime of the laser is described by the rate equations⁷:

$$\begin{aligned}\frac{dq}{dt} &= q[Bn - \gamma_{nl}(q)] \\ \frac{dn}{dt} &= -qBn \\ n(0) &= n_{th}(1 + \zeta); q(0) = q_{sp}\end{aligned}\quad (3)$$

where q is the photon density and n - the population inversion, n_{th} is the threshold inversion, B is the Einstein coefficient and $\gamma_{nl}(q)$ represents the losses which are intensity dependent because of the SBS mirror reflectivity R_B . The initial population inversion $n(0)$ has been assumed above threshold by a factor $1 + \zeta$ ($\zeta \approx 2\%$).

The threshold condition for laser oscillation is:

$$IR_1 T e^{(\gamma_a - \alpha)l_r} T_G R_2 + R_G R_B I = I \quad (4)$$

where I is the laser intensity in the resonator, R_1 is the reflectivity of the output mirror, $R_2 = 100\%$, T is the saturable absorber transmission, T_G , R_G are the transmission and the reflectivity of the Glan polarizer, l_r - the Nd:YAG rod length, γ_a - the amplification coefficient and α the losses per unit length.

The nonlinear losses are:

$$\gamma_{nl} = \left(\frac{l_r}{l_o} \right) c\alpha + \frac{c}{l_o} \ln \frac{1 - R_G R_B}{R_1 R_2 T T_G} \quad (5)$$

l_o - the length of the resonator.

By introducing the normalised variables:

$$\begin{aligned}
\xi &= t/\tau \\
R(\xi) &= I_s/I \\
y(\xi) &= n(\xi)/n(0) \\
x(\xi) &= (I + I_s)g_B L_{eff}
\end{aligned} \tag{6}$$

where I_s is the Stokes intensity and $\tau=l_0/c$ is the round trip time of the resonator and L_{eff} is an effective interaction length which depends on the radiation focusing inside the cell, we obtain the following system of equations :

$$\begin{aligned}
\frac{dR(\xi)}{d\xi} &= [A_0 y - G(R_B)]C(R_B) \\
\frac{dy(\xi)}{d\xi} &= -B_0 yx \\
\frac{dx(\xi)}{d\xi} &= [A_0 y - G(R_B)]x
\end{aligned} \tag{7}$$

The initial conditions are :

$$R_B(0) \approx e^{-G}; y(0) = 1; x(0) \approx e^{-G} \tag{8}$$

The constants and functions used in system (7) are :

$$\begin{aligned}
A_0 &= \frac{l_0}{c} Bn(0) \\
B_0 &= \frac{2 \frac{l_0}{c} B}{ch g_B \nu L_{eff}} \\
G(R_B) &= \ln \frac{1 - R_G R_B}{R_1 R_2 T T_G} \\
C(R_B) &= (1 - R_B) \left[1 - \frac{1 - R_B}{(1 - R_B) - R_B(1 - 2R_B)L_{eff}/\sigma^2 + 3R_B(1 - 2R_B)\ln\left(\frac{R_B e^G}{1 - 2R_B}\right)} \right]
\end{aligned} \tag{9}$$

The results of the numerical simulations are presented in Figure 1.

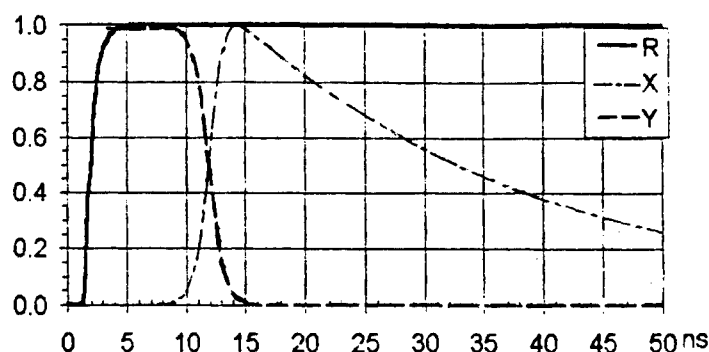


Fig.1 Plot of the SBS reflectivity R, population inversion Y, output pulse X as a function of time

Our theoretical model which has considered the quasistationary approximation for the SBS interaction proved to be good enough to explain the Q-switching regime of the linear resonator and the predicted pulse duration was 20ns.

3. EXPERIMENTAL SET-UP AND RESULTS

The experimental set-up is depicted schematically in Figure 2.

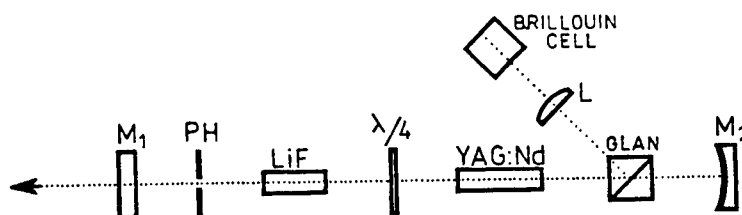


Fig.2 Schematic of the experiment

The concave mirror (3m radius) with reflectivity $R > 99.5\%$ and the plane mirror with $R = 20\%$ defined a hemispherical resonator whose length was 1.1m. The Nd:YAG rod with a 6mm diameter and a 80mm length was pumped by a flash lamp in a diffuse, liquid cooled cavity. The radiation at $1.06\mu\text{m}$ was outcoupled by a quarter-wave plate-Glan polarizer combination which provided an easy way to optimise the output energy by adjusting the coupling transmission, including the final Brillouin reflectivity. The Brillouin cell ($L = 10\text{cm}$) filled with carbon disulphide, CS_2 , was placed behind a lens (focal length = 5cm) outside the linear cavity. We choose CS_2 because of its large gain (0.06cm/MW) for SBS. This cell acted as both a phase conjugate mirror and as a Q-switch. The pinhole selected the transverse modes by limiting the Fresnel number.

The Brillouin backscattered radiation returned to the main resonator was extracted through the mirror M_1 to be analysed. A fast vacuum photodiode (rise time = 0.3ns) and a Tektronix 519 oscilloscope (bandwidth = 1GHz) was used to monitor the laser pulse duration. A TRG 102 energimeter was used to measure laser beam energies. The divergence of the output radiation was estimated by putting different apertures in the focal point of a 1m focal length lens and measuring the diameter corresponding to 80% full energy.

When the quarter-wave plate is oriented in such a way that maximum of the beam energy was outcoupled by the Glan polarizer, the energy entering the Brillouin cell was about 30mJ in the form of relaxation oscillations pulses with

duration of the order of 200-300ns. This output power proved not to be enough to onset the SBS process so we used a saturable absorber to start the Q-switching of the cavity so we put in the cavity a LiF crystal with F_2^- centres ($T_0=10\%$).

a) An output beam with an energy of 40mJ in a pulse of 15-20ns duration was obtained when the energy incident on the Brillouin cell was 25mJ. The experimental recordings of the output pulse with a width (FWHM) of 40ns and 20ns is shown in Figure 3. The divergence was smaller than 3mrad.

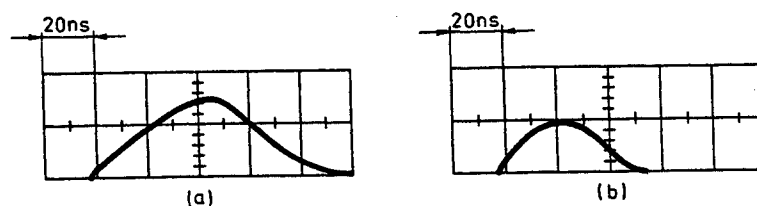


Fig.3 Pulse shape with LiF crystal Q-switching (3a) and with simultaneous LiF and SBS Q-switching (3b)

b) Introducing a pinhole (2.5mm) into the cavity the energy dropped to 5mJ, the pulse duration was the same (20ns) but the divergence became 1.5 the diffraction limit (Fig.3a and Fig.3b).

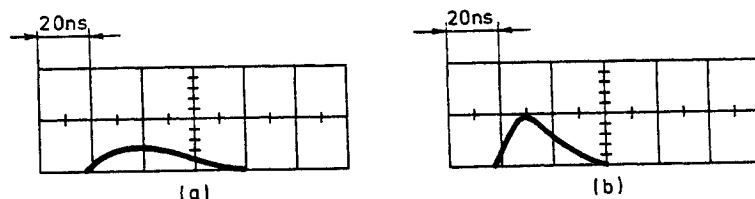


Fig.4 Pulse shape with LiF crystal Q-switching (4a) and with simultaneous LiF and SBS Q-switching (4b) when a pinhole is introduced in the resonator

The figures 3a and 4a show the output pulse without the Brillouin cell and figures 3b and 4b the case when the Brillouin cell is in action.

4. CONCLUSIONS

We demonstrated a SBS Q-switching of a linear resonator based on the gain material Nd:YAG. The power generated in the free-running regime proved to be not enough to reach the threshold of the SBS process in CS_2 . However we succeed to start operation of the laser in the Q-switching regime using a solid state saturable absorber in the form of a LiF crystal, so we think that we have improved the experimental set-up in comparison with³ because our experimental arrangement is more reliable.

For the best of the authors knowledge, there is for the first time that a theoretical description of the external SBS Q-switched resonator has been developed using the quasi-stationary approximation for the SBS interaction and introducing a random phase variable to modulate the SBS gain, in the case when the pump pulse duration is long compared with the lifetime of the acoustic phonons and good agreement between experimental data and theory was obtained. The predicted pulse was smooth since the equations modelled take no account of propagation effects within the resonator and the subsequent frequency shift which is characteristic for SBS.

5. REFERENCES

1. D.A. Rockwell, "A review of phase-conjugate solid state lasers", *IEEE J. Quantum Electronics* **24**, 1124-1140 (1988)
2. H. Meng, H.J. Eichler, "Nd:YAG laser with a phase-conjugating mirror based on stimulated Brillouin scattering in SF₆", *Optics Letters*, **16**, 569-571 (1991)
3. A. Agnesi, G.C. Reali, "Passive and self Q-switching of phase conjugation Nd:YAG laser oscillators", *Optics Communications*, **89**, 41-46 (1992)
4. P.P. Pashinin, E.I. Shklovsky, "Characteristics of a SBS self-injection locked laser", *Laser Physics*, **1**, 160-165 (1991)
5. R.A. Lamb, M.J. Damzen, "Q-switching of a Nd:YAG phase conjugate laser using external stimulated Brillouin scattering", *OSA Proceedings on Advanced Solid state lasers*, **15**, 112-116, 1993
6. V. Babin, A. Mocofanescu, V.I. Vlad "Exact analysis of stimulated Brillouin scattering using characteristic equations" *Romanian Reports in Physics*, **3-4**, 110-140 (1997)
7. A.E. Siegman, *Lasers*, University Science Book, 1986

Excitation upconversion by sensitized photon avalanche

V. Lupei¹, E. Osia¹, T. Sandrock², E. Heumann² and G. Huber²

1. Institute of Atomic Physics, 76900 Bucharest, Romania

2. Institut für Laser Physik, Universität Hamburg, 20355 Hamburg, Germany

ABSTRACT

The features of a new upconversion mechanism of excitation, the sensitized photon avalanche, are discussed on the basis of a rate equation modelling. In this process the excited state absorption (ESA) from a metastable level (reservoir) of the active ion is enhanced by a cross-relaxation between the emitting level of this ion and the sensitizer ion which is able to transfer subsequently the accepted excitation back into the reservoir level of the activator; the donor act of the cross-relaxation ends on this reservoir level too. When the efficiencies of these two energy transfer processes are larger than specific threshold values related to the intrinsic de-excitation rates of the emitting level of activator and of the excited level of sensitizer, a process of population of the reservoir level with a quantum efficiency larger than the unit for each act of de-excitation of the emitting level takes place. Further on, if the ESA rate exceeds a threshold value determined by the intrinsic de-excitation of the reservoir and by the efficiencies of the energy transfers an avalanche population of these levels could take place. This process could be used for infrared pumping of visible solid state lasers. The theory is illustrated for Yb^{3+} - sensitized visible emission of Pr^{3+} under infrared pump (835 nm).

Keywords: photon avalanche, avalanche upconversion, upconversion lasers, visible solid state lasers

1. INTRODUCTION

The photon avalanche upconversion of excitation could be an efficient means to pump high energy emitting levels when the pump quantum is too low to reach directly these levels by an one-step ground state absorption. Such devices are of great importance for upconverting the infrared radiation of pump diode lasers to visible emitting levels of rare earth ions in crystals or glasses. Photon avalanche is a strongly nonlinear process of population of the emitting level under the action of a cw radiation resonant with a high cross-section excited state transition (but non with any ground state absorption line) from an intermediate metastable level (reservoir) which is populated by a cross-relaxation process whose initial states are the emitting and the ground levels and the final states for both the donor and the acceptor act correspond to the reservoir level^{1,2}. If the efficiency of the cross-relaxation is larger than that of the intrinsic de-excitation processes of the emitting level to the ground state, it could induce an overall quantum efficiency of population of the reservoir larger than the unit for each ESA act from reservoir to the emitting level. Moreover, if the ESA rate is larger than the intrinsic rate of de-excitation of reservoir by an amount which also depends on the efficiency of cross-relaxation, an avalanche process of population of the reservoir and of the emitting levels takes place. Thus the photon avalanche is a threshold process as concerns both the efficiency of cross-relaxation and the ESA pump rate. An additional condition is a very low ground state absorption at the pump wavelength.

This scheme of avalanche produces the upconversion of excitation to a high energy level from which emission at a wavelength shorter, equal or longer than that of the pump radiation could take place. Several other avalanche schemes are also possible, which use part of the excitation quantum upconverted by ESA in a cross-relaxation which contributes to the population of the reservoir together with the radiative and multiphoton processes; usually in these schemes, although the excitation is upconverted, the emission is at a longer wavelength than that of pump. In practice, although all these schemes of avalanche involve only several (three or four, depending on scheme) significant levels, they must fit into the very complex energy level diagrams of the rare earth or transition ions. Thus the photon avalanche was reported for various three-valent rare earth ions such as Pr^{3+} , Nd^{3+} , Sm^{3+} , Er^{3+} or Tm^{3+} as well as for the transition ion Ni^{2+} . For some of the rare earth ions several avalanche schemes are possible but, as mentioned above, not all of them lead to emission at shorter wavelengths than that of pump. Of particular practical interest at the present time are the avalanche schemes leading to visible emission (especially in the ranges suitable for laser color display) under infrared diode laser pump.

As shown above, the photon avalanche implies a large cross-relaxation efficiency, i.e. a high energy transfer rate and/or a high concentration of the active ion. The first of these conditions imposes a severe selection of the potential avalanche systems while the second condition is not easily fulfilled either due to technological limitations or to the activation of other parasitic non-radiative energy transfers which could increase the global effective intrinsic de-excitation rates of the emitting and/or of the reservoir level; this leads to a corresponding increase of the threshold values for the cross-relaxation efficiency and/or for the ESA pump rate. Such a case is Pr^{3+} whose excited level $^3\text{P}_0$ is a very good emitter in all the visible ranges suitable for display (blue, green, red) on transitions terminated on various low energy levels. However, the only reported avalanche emission in crystals doped with Pr^{3+} was the red and orange $^3\text{P}_0$ emission under green excitation from $^3\text{H}_5$ level 1 , although a strong ESA in the range 800-860 nm from the metastable level $^1\text{G}_4$ to $^1\text{I}_6$ and $^3\text{P}_1$ levels could take place, followed by a fast phonon relaxation on $^3\text{P}_0$ which could then cross-relax with another Pr ion in ground state, both the donor and acceptor acts ending on $^1\text{G}_4$. Thus, although apparently all the mechanisms necessary for photon avalanche with $^1\text{G}_4$ and $^3\text{P}_0$ as reservoir and emitting level respectively, i.e. with visible emission under infrared pump, exist in case of Pr^{3+} , no such emission was reported for systems doped only with this ion. The main cause is the high value of the intrinsic de-excitation rates of these two levels which leads to high threshold values for the cross-relaxation and for the ESA pump; increasing the Pr concentration in order to assure a high efficiency for cross-relaxation activates also parasitic de-excitation processes of levels $^3\text{P}_0$ and especially of $^1\text{G}_4$ leading to a further increase of the threshold conditions.

A possibility to solve this problem could be the use of an additional ion (sensitizer) which cross-relaxes with the active ion (in such a way that the donor act ends on reservoir) and which is able to transfer the accepted excitation back to the reservoir level of the active ion. Thus the joint action of the activator-sensitizer cross-relaxation and of the back transfer in this scheme is equivalent to the role of the cross-relaxation in single activated systems, but it does not require a high concentration of the active ion. In case of Pr^{3+} visible avalanche emission of $^3\text{P}_0$ under infrared pump a very convenient sensitizer could be Yb^{3+} ; this ion has a very simple electronic structure with only two energy levels in the ground electronic configuration, which do not introduce any deleterious effects on the avalanche process.

The present paper presents the results of the mathematical modelling of the sensitized avalanche process described above. The predictions of this model are then compared with the experimental observation ^{3, 4, 5} of Yb^{3+} sensitized avalanche emission of Pr^{3+} .

2. EXPERIMENTAL DATA

The experimental investigation of Pr, Yb:YLiF₄ has been conducted along two lines: spectroscopic investigation in order to determine the parameters necessary for the modelling of the avalanche process and investigation of room temperature emission under cw pump in the range of 800-860 nm.

The spectroscopic measurements have been performed on YLiF₄ crystals single doped with Pr or Yb as well as on (Pr, Yb) co-doped samples; in the last case the Pr concentration was about 0.2 at.% while the Yb concentration was changed between 5 and 20 at.%. The optical absorption data indicate that radiation in the range 800-860 nm is not resonant with any GSA line either of Pr and Yb; however the photon tail of Yb absorption extends up to this range, although it is extremely weak, corresponding to a cross-section σ_1 of about or less than 10^{-4} times smaller than that of ESA (σ_2) from $^1\text{G}_4$ to $^1\text{I}_6$ reported for Pr^{3+} in fluoride hosts.

At the room temperature the luminescence decays of short pulse resonantly pumped $^3\text{P}_0\text{Pr}^{3+}$, $^1\text{G}_4\text{Pr}$ and $^2\text{F}_{5/2}\text{Yb}$ in YLiF₄ doped with low concentrations of Pr^{3+} or Yb^{3+} are exponential, with lifetime of about 47 μs , 18 μs and 1.8 ms respectively. The luminescence decay of resonantly pumped $^3\text{P}_0$ level of Pr^{3+} in presence of Yb confirms the existence of an efficient cross-relaxation between these two ions: the luminescence decay changes to a strongly non-exponential, Yb - concentration dependent decay, corresponding to an effective energy transfer rate s of the order of $5 \times 10^{16} \text{ cm}^3\text{s}^{-1}$.

The cross-relaxation process in this case is ($^3\text{P}_0\text{Pr}$, $^2\text{F}_{7/2}\text{Yb}$) \rightarrow ($^1\text{G}_4\text{Pr}$, $^2\text{F}_{5/2}\text{Yb}$); due to a better matching of $^3\text{P}_0\text{Pr} \rightarrow ^1\text{G}_4\text{Pr}$ emission spectrum with $^2\text{F}_{7/2}\text{Yb} - ^2\text{F}_{5/2}\text{Yb}$ absorption than with $^3\text{H}_4\text{Pr} \rightarrow ^1\text{G}_4\text{Pr}$, the transfer rate s is, as expected, larger than that of the self-quenching process p inside the system of Pr ions ($^3\text{P}_0$, $^3\text{H}_4$) \rightarrow ($^1\text{G}_4$, $^1\text{G}_4$). The existence of Pr-Yb transfer is manifested also in the presence of Yb emission at resonant pump in $^3\text{P}_0\text{Pr}$: the temporal evolution of this emission after short pulse excitation shows a risetime which reflects the lifetime of the pump level $^3\text{P}_0$.

On the other hand the presence of Pr modifies the luminescence decay of resonantly pumped Yb ions: the beginning of decay is fast and it is followed by an exponential part faster than in absence of Pr. The initial part of this decay could reflect the presence of a cooperative three-ion energy transfer by which two excited Yb ions in the nearest neighbourhood of Pr transfer simultaneously their excitation to the level 3P_0 of Pr while the slower exponential decay reflects the two - ion transfer from Yb to the reservoir level 1G_4 or Pr with an effective transfer rate r of about $1.2 \times 10^{16} \text{ cm}^3 \text{ s}^{-1}$. Both these Yb to Pr transfer processes are assisted by a fast migration of energy over the excited Yb level at the high concentrations of this ion used in our experiment,

The room temperature measurement of emission in YLiF_4 samples (3 mm thick) doped with 0.2 at.% Pr and 10 at.% Yb under Ti: sapphire-cw excitation in the range from 800-860 nm shows visible luminescence emission from ^3P_0Pr at various wavelengths from blue (480 nm) to red (720 nm). The maximum of emission is obtained with pump around 835 nm which corresponds to ESA from 1G_4 to 1I_6 . Laser emission was obtained so far only for the red (639.5 nm) transition $^3P_0 \rightarrow ^3F_4$. At the same time a strong emission from Yb^{3+} is observed. The temporal and pump intensity dependence of 3P_0 luminescence emission at various wavelengths shows clear features of an avalanche process, similar to those described for simple systems:

- at low pump intensity the emission is weak, it starts immediately after the onset of pump and reaches very soon a plateau (stationary emission) which depends quadratically on the pump power;
- with increasing of pump intensity the moment of time when the emission reaches the plateau (t_p) increases and at the avalanche threshold it reaches a maximal value of several milliseconds (in the range of 7 to 10 ms), much longer than any lifetime from the system. At the pump threshold the intensity of the stationary emission increases strongly (by several orders);
- by further increasing the pump the value of t_p decreases strongly at the beginning then much slower to a very low value, while the intensity of the stationary emission shows a saturation behavior with respect to the pump intensity.
- at high pump intensity a sharp spike is observed at the beginning of emission.

The red laser emission at 639.5 nm shows the features of avalanche too.

The emission of Yb shows also a complex temporal behavior which evolves to a stationary regime whose intensity depends linearly on the pump in the low pump region, then shows a very strong increase (at a pump intensity larger than the threshold for ^3P_0Pr emission) followed by a rapid saturation.

3. RATE EQUATION MODELLING

3.1. The physical model

The scheme of the sensitized avalanche emission is shown in figure 1, where by I is denoted the sensitizer ion S and by II the active ion A. The significant levels of these ions are denoted by (1i) and (2j) respectively and their populations are n_{1i} and n_{2j} ; thus, the emitting level is (23) and the reservoir is (22). The rates W_{1i} and W_{2j} correspond to the total intrinsic de-excitation processes (radiative and non-radiative) and b is the effective branching ratio for populating the ground level (21) of the active ion directly from level (23) by intrinsic processes.

In order to simplify the discussion we assume that the cross-relaxation can be described by a unique rate s , regardless the A-S pair and a similar assumption is made for the back S-A energy transfer r too. Due to the high concentration of the sensitizer ion, a migration - assisted cooperative sensitization (process u) of the emitting level (23) of the active ion by simultaneous transfer from two excited nearest neighbor sensitizer ions could be possible as observed for the systems Yb-Tb, Yb-Tm or Yb-Pr in various hosts, as well as an inverse three-ion $(23, 11, 11) \rightarrow (21, 12, 12)$ cross-relaxation t . We also assume that a very weak ground state absorption (of rate R_1) at the wavelength of pump takes place in the sensitizer ion and that is much smaller than the resonant ESA pump (rate R_2) in the active ion. We also assume that an internal cross-relaxation $(23, 21) \rightarrow (22, 22)$ of rate p could take place inside the system of active ions A and that a two-step S-A energy transfer composed by the process r and second step q is also possible.

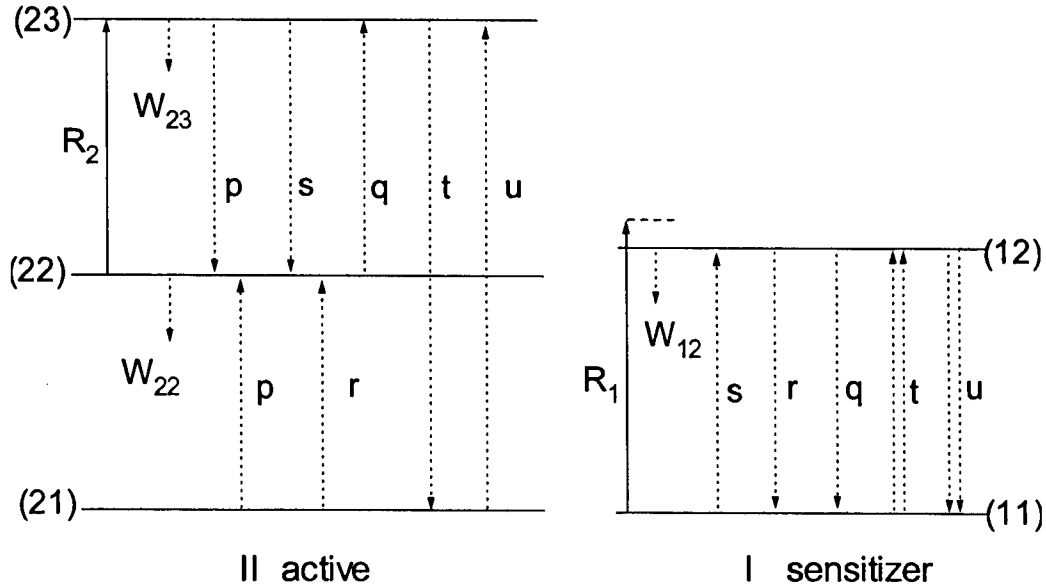


Figure 1

This scheme can be adapted to several S-A systems. Thus, in case of the system formed by Yb as sensitizer and Pr as active ion, the levels (22) and (23) correspond to 1G_4 Pr and 3P_0 Pr respectively, while (12) is the excited state $^2F_{5/2}$ of Yb. The ESA pump in this case takes place on the intense, spin-allowed (of cross-section σ_2 of the order of 0.5 to $2.5 \times 10^{20} \text{ cm}^2$ in various hosts) transition from 1G_4 to 1I_6 from which the excitation decays rapidly on 3P_0 . The three-ion process u is possible due to the favorable energy levels of Pr and Yb in various hosts. The process p has been observed, but its rate is usually smaller than that of the process p; at the same time the two-step Yb to Pr transfer process is not very likely because of the large mismatch for the second step q. The rates W_{23} and W_{22} are quite large (2 to $10 \times 10^4 \text{ s}^{-1}$ and 10^3 to $1.5 \times 10^6 \text{ s}^{-1}$ respectively in various hosts), but with increasing Pr concentration both (23) and especially (22) are quenched by cross-relaxation. In case of Pr the intrinsic de-excitation (radiative) processes end on levels placed below reservoir and thus the branching ratio b is close to the unit. In case of $\text{Ho}^{3+} - \text{Yb}^{3+}$ system the level ($^5F_4, ^5S_2$) could act as emitter and 5I_4 reservoir, while for $\text{Er}^{3+} - \text{Yb}^{3+}$, $^4S_{3/2}$ could be emitter and either $^4I_{11/2}$ or $^4I_{13/2}$ could act as reservoir.

3.2. The system of rate equations

The system of rate equations which describe the sensitized avalanche process and its competition with other upconversion processes (intrinsic avalanche determined by process p, the step-by-step (r+q) process and the energy-transfer assisted successive GSA+ESA absorption R_1 -r- R_2) is

$$\begin{aligned}\frac{dn_{11}}{dt} &= -sn_{11}n_{23} + rn_{12}n_{21} + W_{12}n_{12} + qn_{12}n_{22} - 2tn_{11}^2n_{23} + 2un_{12}^2n_{22} - R_1n_{11} \\ \frac{dn_{12}}{dt} &= sn_{11}n_{23} - rn_{12}n_{21} - W_{12}n_{12} - qn_{12}n_{22} + 2tn_{11}^2n_{21} - 2un_{12}^2n_{21} + R_1n_{11}\end{aligned}\quad (1)$$

$$n_{11} + n_{12} = n_{10}$$

$$\frac{dn_{21}}{dt} = W_{22}n_{22} + bW_{23}n_{23} - rn_{21}n_{12} - pn_{21}n_{23} + tn_{23}n_{11}^2 - un_{12}^2n_{21}$$

$$\frac{dn_{22}}{dt} = -R_2n_{22} - W_{22}n_{22} + sn_{23}n_{11} + rn_{12}n_{21} + (1-b)W_{23}n_{23} + 2pn_{21}n_{23} - qn_{22}n_{12}$$

$$\frac{dn_{23}}{dt} = R_2n_{22} - W_{23}n_{23} - sn_{23}n_{11} - pn_{23}n_{21} + qn_{22}n_{21} - tn_{23}n_{11}^2 + un_{21}n_{12}^2$$

$$n_{21} + n_{22} + n_{23} = n_{20}$$

This system of rate equation describes the evolution of the system at constant pump rates R_1 and R_2 . These rates are connected with the intensity of pump radiation I by the relation $R_k = I\sigma_k/h\nu$, where $h\nu$ is the pump quantum and $k = 1$ or 2 . In a real system the pump intensity could show local variations either due to the distribution of the intensity in the transversal section of the incident beam or/and the absorption of pump radiation along its path inside of the sample due to the GSA and ESA processes. Thus eq. (1) could be considered as valid only for punctual modelling while in a real system the variation of the pump rates must be taken into account, and the global response of the sample is obtained by integration over the pumped volume.

3.3. Analytical solution

A complete analytical solution of the system of rate equation (1) is not possible. However, an approximate analytical solution could be obtained for the stationary regime ($t \rightarrow \infty$) in case of a very weak depletion of the ground states and in absence of the three-ion processes t and u . In this case, for a simplified system which includes only the energy transfer processes s and r a quadratic algebraic equation can be obtained for the stationary population n_{23}^∞ . The positive solution of this equation is possible only when the pump rate R_2 exceeds the threshold value

$$R_{2\text{lim}} = \frac{(sn_{10} + W_{23})[W_{22}(rn_{20} + W_{12}) + R_1(W_{22} + rn_{20})]}{sn_{10}rn_{20} - b(rn_{20} + W_{12})W_{23} - R_1(rn_{10} + bW_{23})}\quad (2)$$

and if the energy transfer processes are efficient as compared to the intrinsic de-excitation

$$sn_{10} > bW_{23} + \frac{n_{10}}{n_{20}} R_1\quad (3)$$

and

$$rn_{20} > \frac{(W_{12} + R_1)bW_{23}}{sn_{10} - bW_{23} - \frac{n_{10}}{n_{20}}R_1} \quad (4)$$

For very low GSA in sensitizer the terms in R_1 in eqs. (3) and (4) could be neglected. Eqs. (2) to (4) connect the threshold values for the ESA pump rate R_2 and for the energy transfer processes to the de-excitation rates W_{22} , W_{23} and W_{12} ; it is thus evident that weak intrinsic de-excitation processes favor the avalanche process. Eq. (3) is similar to the avalanche condition in simple (activator-only) photon avalanche; however in this case it is much easier to fulfil owing to the large ground state population n_{10} of the sensitizer. A very efficient cross-relaxation reduces the threshold values for the pump rate R_2 and for the back transfer too.

The restrictive condition for analytical treatment (low depletion of the ground states) is well fulfilled up to the on-set of avalanche in case of very low GSA rates R_1 ; this indicates that the threshold rates given by eqs. (2) to (4) are correct. Indeed, eq(2) predicts in case of $\text{YLiF}_4\text{:Pr}$ (0.2 at.%), Yb (10 at.%) a threshold value for ESA rate of $6.2 \times 10^4 \text{ s}^{-1}$, in the range observed in experiment. This indicates also that the dependence of the threshold values for R_2 and of the efficiencies of the energy transfer processes on the spectroscopic parameters of the system are correct and they can be used in order to select the active systems for the sensitized avalanche.

3.4. Numerical modelling

The analytical modelling can describe only the stationary emission but not the temporal evolution of the system after the onset of the cw ESA pump. It is also limited to a very low depletion of the ground state, a condition which could be valid only up to the beginning of avalanche, and only in case of very low R_1 GSA rates. However, the complete solution of the rate equation system (1) can be obtained by numerical methods. We performed this modelling in two steps: first we used the spectroscopic data on Pr , Yb:YLiF_4 in order to explain the observed emission and to check the limits of validity for the analytical modelling then we varied the various spectroscopic parameters in large limits in order to put into evidence the effect of the interactions from system on the avalanche process.

The main results of the numerical modelling are:

- at low pump intensity, below the value corresponding to the avalanche threshold, the population of the emitting level increases steeply immediately after the onset of pump and evolves in a time t_p to a stationary value which depends quadratically on the pump power. In this region the time t_p has low values, but close to the avalanche threshold it increases strongly. The populations of the ground states of both ions are still high as far as $R_1 \ll R_2$;
- the avalanche threshold for the ESA pump rate R_2 in absence of three-ion process u is very close to the value predicted by analytical modelling; this confirms the validity of the equation for threshold value (2);
- the time necessary to reach the stationary emission has the largest value for R_2 pump rates around $R_{2\text{lim}}$; this value is much larger than any lifetime from the system and depends on the ratio of the ESA to GSA pump rates (R_2/R_1). At avalanche the temporal evolution of population n_{23} changes its shape by showing an inflexion point on the rising part.
- around the avalanche threshold a strong depletion of the ground state (21) of the active ion takes place both in favor of populations of reservoir (the largest part) and of the emitting level. The population of reservoir increases up to a pump rate R_2 of about $1.2 R_{2\text{lim}}$ to a value which is several times (up to 6.5) larger than that of the emitting level; above this rate the population of (22) is depleted in a manner similar to that of a simple two-level system, and the ratio (n_{23}/n_{22}) becomes linear in the pump rate.
- below the avalanche threshold the population of the excited level (12) of the sensitizer increases linearly with the pump intensity; however in the avalanche region a strong depletion of the ground state (11) takes place, but this is not so severe as for the active ion. This depletion could produce an inversion of population in the sensitizer ion and it is caused by the bottleneck of the energy transfer process rn_{21} due to the depletion of the ground state of the active ion.
- the cooperative sensitization of the emitting level (the three-ion process u) produces a triggering of the avalanche process manifested in the reduction of the pump threshold value $R_{2\text{lim}}$ and in the modification of the temporal dependence of the population n_{23} : it induces an early spike of emission, which depends on the rates of the

various processes and on the pump intensity. The effect of the cooperative sensitization u is similar to that of an external triggering of avalanche described in ⁶. Thus the process a is the most likely explanation for the early spike of emission observed experimentally.

- the internal cross-relaxation process p as well as the two steps $r-q$, $S-A$ energy transfer reduce the efficiency of the sensitized avalanche; however, by a proper choice of the system their effect could be minimized.

The numerical modelling at uniform pump gives a fairly good description of the dependence of stationary emission of level 3P_0 on the pump intensity in case of $Yb, Pr:YLiF_4$; however, it does not describe well the moment of apparition of the spike with respect to t_p . Moreover the observed emission of the reservoir level 1G_4 does not evidence clearly a maximum of emission at $1.2 R_{2lim}$; the emission increases with the pump then levels off. The agreement between modelling and experiment can be restored if the non-uniform distribution of pump intensity in the sample volume, due especially to the transverse distribution (Gaussian), is taken into account. This shows that for a given incident pump beam the various parts of the sample could be pumped below, around or above threshold and an integration of emission over the pumped volume modifies strongly the temporal dependence of emission (it places the spike in the right position) and the dependence of total emission on pump (especially in case of reservoir level 22).

4. CONCLUSION

The analytical and numerical modelling of the sensitized photon avalanche in $Pr, Yb:YLiF_4$ describes well the observed features of visible luminescence emission under infrared cw pump. This modelling enables a connection between the characteristics of avalanche and the spectroscopic parameters of the system, the concentration of the active ion and of the sensitizer and the conditions of pump. It is thus apparent that Yb^{3+} is a good sensitizer for the avalanche visible emission from 3P_0 level; it could be used for sensitization of cross-relaxation processes with transfer of quanta of the order of 10000 cm^{-1} in other rare earth ions such as Er^{3+} or Ho^{3+} . On the other hand, similar processes which lead to the up-conversion of excitation could be expected in the sensitization by Ce^{3+} of low quantum (around $2000\text{--}3000\text{ cm}^{-1}$) cross-relaxation processes in ions such as Nd^{3+} or Pr^{3+} .

5. REFERENCES

1. J. S. Chivian, W. E. Case and D. D. Eden "The photon avalanche: A new phenomenon in Pr^{3+} - based infrared quantum counters", *Appl. Phys. Lett.* **35**, 124 (1979)
2. M. F. Joubert, S. Guy and B. Jaquier "Model of the photon-avalanche effect" *Phys. Rev. B.* **48**, 10031 (1993)
3. T. Sandrock, E. Heumann, G. Huber, V. Lupei, B. Bejan and E. Osiac "Visible Lasing of $Pr, Yb:LiYF_4$ Pumped Via Sensitized Photon Avalanche Upconversion", *International Quantum Electronics Conference IQEC'96*, Sydney, Australia, 1996
4. T. Sandrock, E. Heumann, G. Huber, V. Lupei, B. Bejan and E. Osiac "Visible Emission under Sensitized Photon Avalanche Upconversion of Infrared Radiation", *European Quantum Electronics Conference EQEC'96*, Hamburg, Germany 1996.
5. V. Lupei, E. Osiac, G. Huber, E. Heumann and T. Sandrock "Excited state dynamics in photon avalanche processes" *J. Luminesc.* (in press)
6. F. Auzel and Y. Chen "Photon avalanche luminescence of Er^{3+} ions in $LiYF_4$ crystal", *J. Luminesc.* **65**, 45 (1995).

Medium power stabilized laser diode

E. Smeu, N. Puscas, I. M. Popescu, Gr. Suruceanu*, R. Ispasoiu

"Politehnica" University of Bucharest, Physics Department,
Spl. Independentei 313, Bucharest 77206, Romania

E-mail: pnt@physics2.physics.pub.ro

*Technical University of Moldova, Optoelectronics Research Center,
Stefan cel Mare 168, Chisinau 277012, Moldova

ABSTRACT

Power stabilized DL's represent today convenient sources for radiometric applications, as transfer laboratory standards. Stability measurements were carried out and reported by other authors for different time intervals, **but only for low optical power levels (max. 16 mW)**. For calibrating usual optical radiometers, such low emitted power DL's are useless. This paper reports stability measurements carried out on several collimated DL's with λ around 980 nm and emitted power **up to 265 mW in near-field / 150 mW in far-field**. Stabilities of the order $1e-4$ for short-time intervals (tens of seconds) and $1e-3$ for medium-time intervals (1 hour) were found for a non-thermostated structure, having the control photodiode (PD) in the same enclosure with the DL (at the rear of the structure). The corresponding stabilities for an external control PD resulted of the order $1e-5$ for both short and medium time intervals. The schematic of the optical power stabilizer is presented.

Key words: diode laser, control photodiode, optical power, stability

1. INTRODUCTION

If one has to calibrate an optical radiometer by comparison to a reference one, a transfer standard of emitted power is needed. Power stabilized laser DL's represent today convenient sources for radiometric applications, as power transfer standards. This type of laser is maybe the easiest to power-stabilize. It also allows optical power tuning, this feature being a very convenient one. A higher emitted power also becomes more and more necessary, **but only small power stabilized DL's have been reported - max. 16 mW^{1,2}**. In this paper an order of magnitude higher optical stabilized emitted power DL's are reported.

Power stabilization is achieved by a feedback loop. The control element is a PD, which can be placed in the same enclosure with the DL (internal PD), behind it (as the DL emits at both ends), or separately (external PD). The two situations are represented in Fig. 1 a and b.

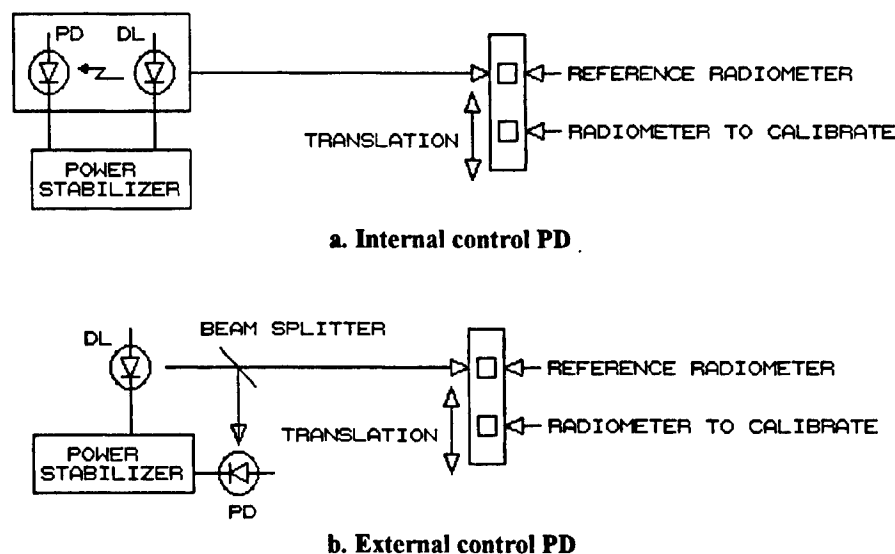


Fig. 1.

Internal control PD leads to a compact structure, but it requires structure temperature stabilization, which is usually achieved by a Peltier cooler^{1,2}, as its responsivity is temperature dependent.

External control PD is somehow more “uncomfortable”, but the DL requires only a heat sink (or even a fan for more powerful devices), if the temperature drift of the central λ is not important. This is true for flat spectral response of the reference radiometer and of the radiometer to calibrate (specific to most of thermal detectors). In this case, a control PD must be chosen with a moderate or small slope of the spectral response at the central λ of the DL. As this paper further demonstrates, these were easy tasks. The external control PD is thus more versatile, especially if a high power DL is used (up to 20 - 50 W today). For such DL's, it would be difficult to built an internal PD which would not saturate.

2. PRINCIPLE OF POWER STABILITY MEASUREMENT

As a measure of stability the standard deviation relative to the average of several power values was chosen^{1,3}:

$$SdtDev_{ST} = \sqrt{\frac{\sum_{i=1}^n (P_i - Avg)^2}{n-1}} \quad (1)$$

$$Stability_{ST} = \frac{SdtDev_{ST}}{Avg} \quad (2)$$

For short therm intervals (ST) the relation (2) is used straightforward (that is why the ST index was used). For medium time intervals (MT) several measurement equally-time spaced cycles are performed. All cycles contain the same number of values n and an average power is calculated for each cycle:

$$Avg_j = \frac{\sum_{i=1}^n P_{ij}}{n} \quad (3)$$

where $j = \overline{1, m}$ is the cycle number. The average (3) is the “representative power” for cycle j ^{1,3}. For all cycles the global average and standard deviation are finally calculated and then the MT stability:

$$Avgavg = \frac{\sum_{j=1}^m Avg_j}{m} \quad (4)$$

$$SdtDev_{MT} = \sqrt{\frac{\sum_{j=1}^m (Avg_j - Avgavg)^2}{m-1}} \quad (5)$$

$$Stability_{MT} = \frac{SdtDev_{MT}}{Avgavg} \quad (6)$$

3. EXPERIMENTAL RESULTS

We have used 3 buried heterostructure double quantum well InGaAs/InGaAsP/InGaAs DL's with the central emission λ around 980 nm. The devices could emit up to 1.3W (the most powerful) of cw radiation for an injection current of 1 A, but

the beams were divergent. As a good quality optical beam is absolutely necessary for a transfer standard, a compact optical collimator was used (it also had the function of a heat sink), but it reduced the power of the output beam. For reliability reasons, a max. current of 0.88 A was used. The used DL's and the collimator are produced at the Technical University of Moldova in Chisinau, Moldova. The experiment was performed in "Politehnica" University of Bucharest, Romania.

The power stabilization was achieved by a common electronic feedback loop. Both setups in Fig. 1 were used (i.e. internal and external control PD). The internal control PD of DL1 was reverse biased with 5 V, but the external control PD (a large area type) was not biased, for optimum noise performance. In Fig. 2 the schematic of the feedback loop is presented (with the internal control PD).

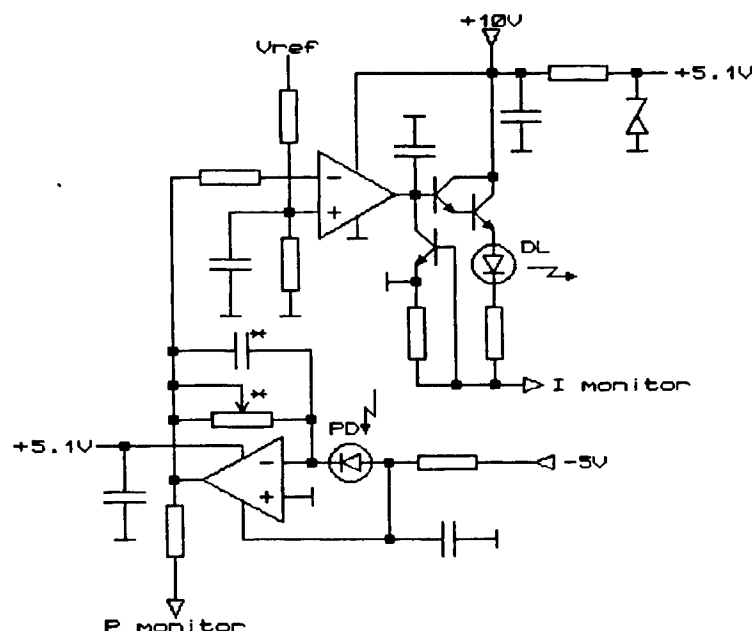


Fig. 2. Schematic of the optical power stabilization loop

The loop consists of a usual voltage stabilizer ic, a super- β opamp (as a I/U converter), a medium power transistor and some passive components. Only the values marked "*" are dependent on the used control PD. At the "P monitor" output a Keithley 6517 Electrometer interfaced with an IBM-compatible PC were used to acquire data. The electrometer was programmed for optimal noise performance. For the MT stability measurements a 1 hour interval was chosen, as it is enough for the calibration of a radiometer by comparison with a reference one (or another similar work). 21 measurement cycles were performed, each of 30 values, 3 min. time-spaced. The results are presented in Figs. 3 - 8. Output optical powers were measured in near field (NF) at 30mm of the collimator exit and in far field (FF) at 50-70 cm (only for DL3), without beam splitter. The beam splitter reduces useful power, but a high transmission one can be used.

From the graphs one can observe a ST stability (i.e. for each measurement cycle) of the order of some E-4 and a MT stability of some E-3 for internal control PD. The fan does not improve the order of magnitude for neither ST or MT stabilities (Figs. 3 and 4). The same DL, but with an external control PD, delivers a much more stable optical power (some E-5 for both ST and MT - Figs. 5 and 6). The stabilities are the same for DL 2 and 3 too (Figs. 7 and 8). DL 3 was chosen to be our transfer emission standard.

It is worth noting that other researchers reported stabilities of some E-6...E-5 for ST and of some E-4 for MT at a max. optical power of only 16 mW^{1,2}. They have used both custom and commercial DL's (Hitachi, Sharp, Philips), but the electronic power stabilizer was a home-made model (as commercial types are not made for high stability performances). The number of measurement cycles (21), values per cycle (30) and time-spacing of the cycles (3 min.) were the same with ours, so a direct comparison of the stabilities can be made.

Such power-stabilized DL's are very useful not only for calibrating radiometers, but they have been used for measuring the characteristics of optical components⁴. Radiant power stabilization at 980 nm is also important for direct pumping of Er³⁺-doped lasers⁵ and Er³⁺-doped optical fiber amplifiers⁶.

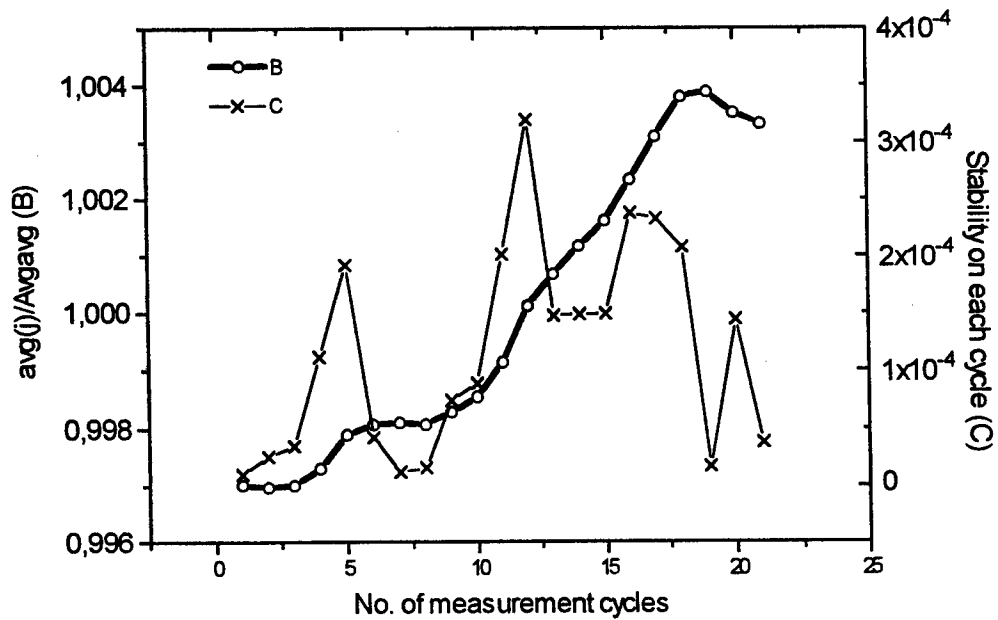


Fig. 3. DL 1, internal control PD, heat sink only, 0.74 A, 130 mW NF, 1 hour stability=2.528e-3

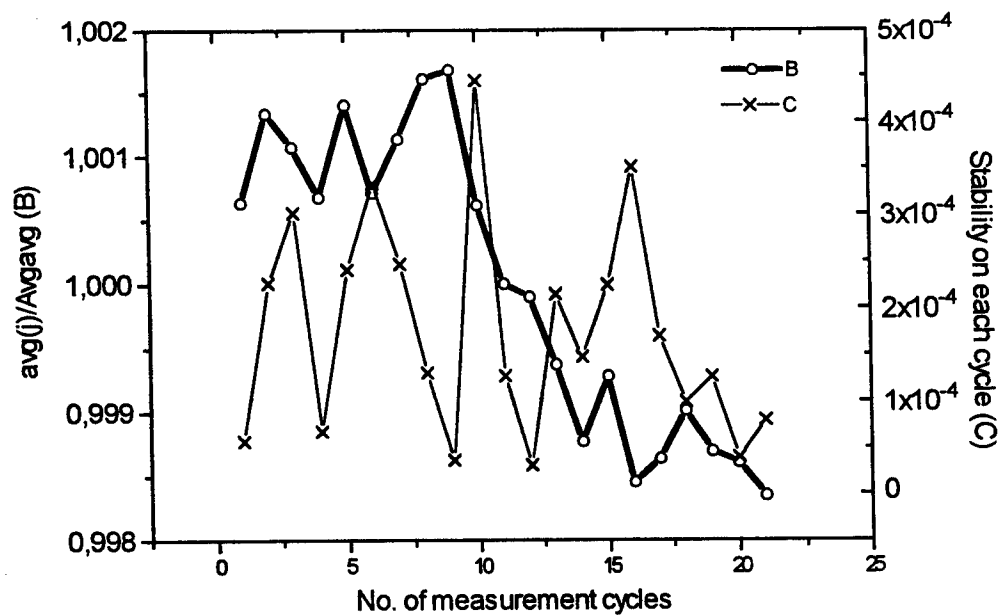


Fig. 4. DL 1, internal control PD, heat sink + fan, 0.88 A, 135 mW NF, 1 hour stability=1.169e-3

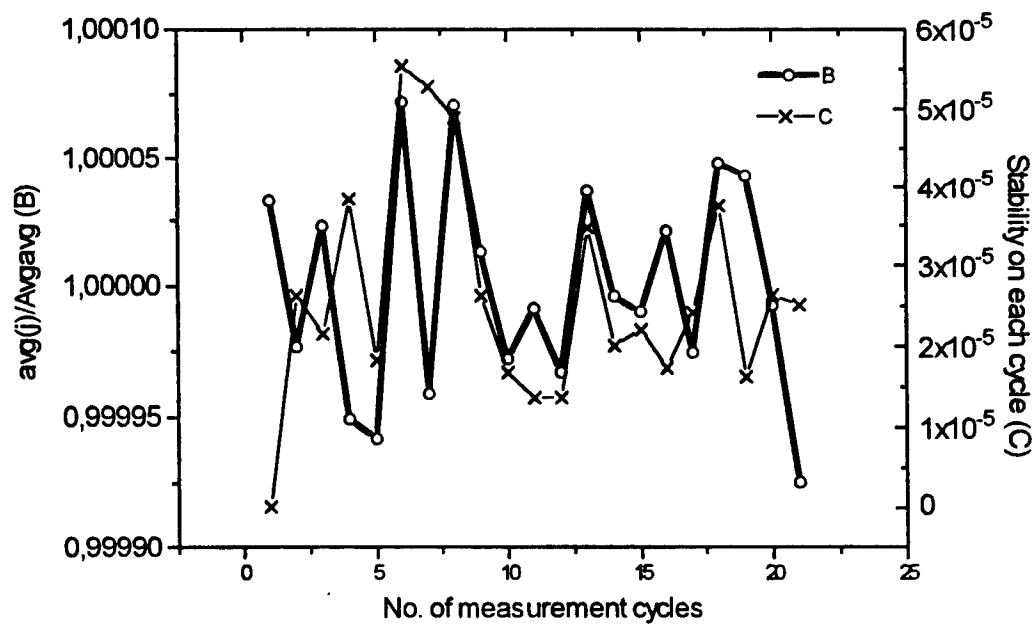


Fig. 5. DL 1, the same as in Fig. 3, but external control PD, 1 hour stability= $4.156e-5$

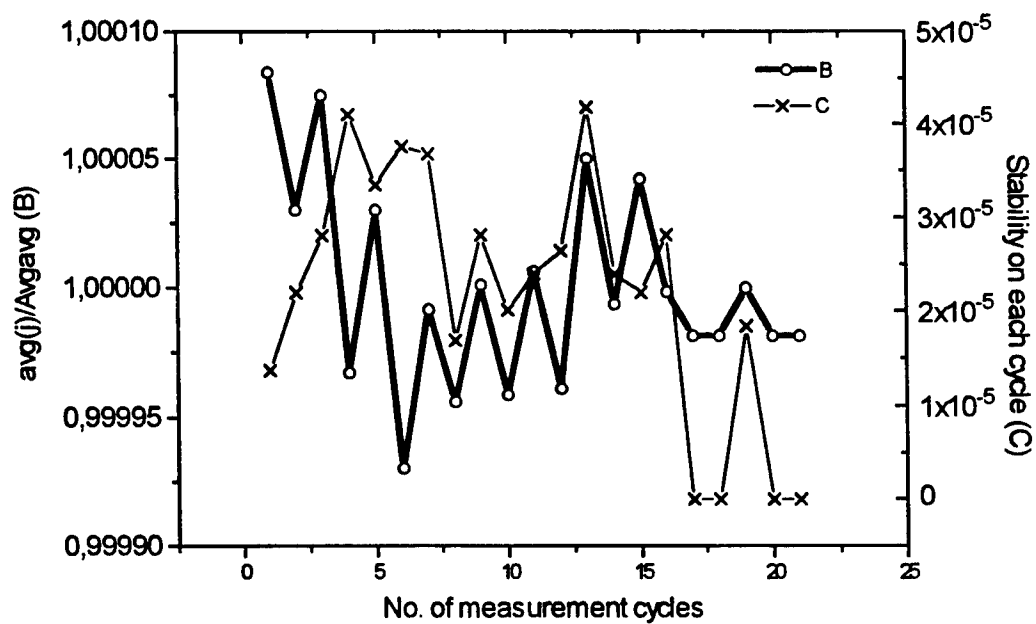


Fig. 6. DL 1, the same as in Fig. 4, but external control PD, 1 hour stability= $3.959e-5$

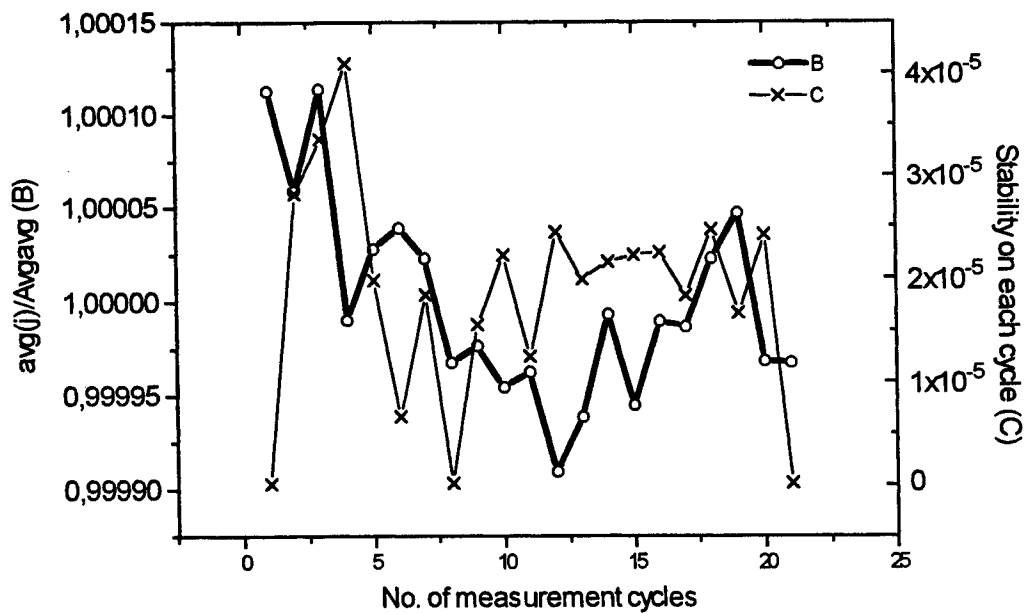


Fig. 7. DL 2, external control PD, heat sink only, 0.88 A, 130 mW NF, 1 hour stability=5.351e-5

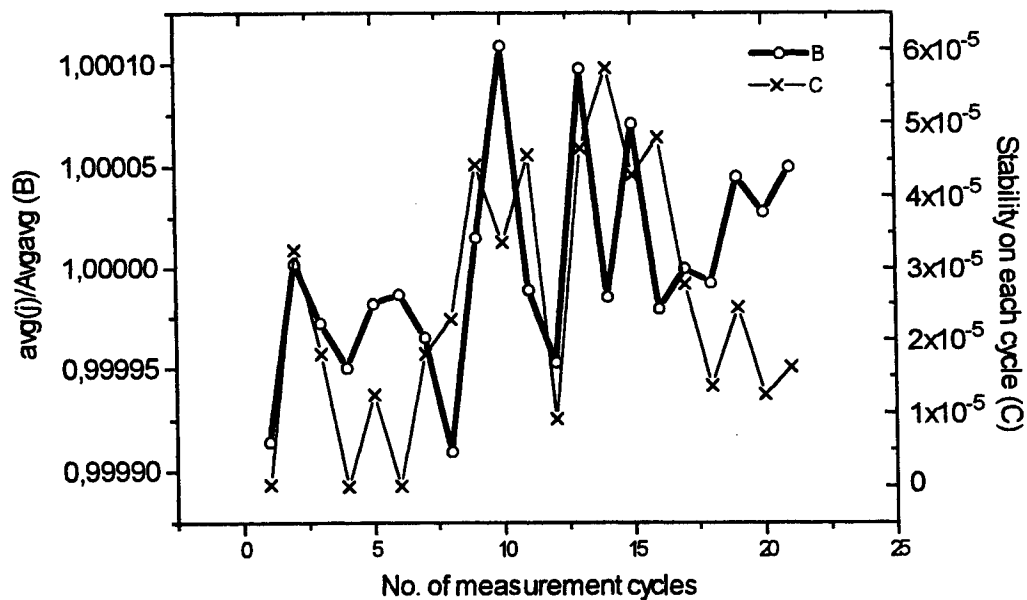


Fig. 8. DL 3, external control PD, heat sink only, 0.88 A, 265 mW NF (30 mm from output), 150 mW FF (50-70 cm from output), 1 hour stability=5.269e-5

4. CONCLUSIONS

The stabilities obtained with external control PD are better than expected. Even with an internal control PD (with the advantage of compactness) a non-thermostated DL transfer standard is good enough, but the measurement will be performed again with Peltier coolers.

5. ACKNOWLEDGEMENTS

This experiment was performed under Contract INCO COPERNICUS no. IC15 - CT96 - 0820 (DG12 - MUYS) supported by the European Community and Contract no. 689/1996 supported by the Romanian Ministry of Research and Technology.

6. REFERENCES

1. J. M. Desbancs, J. Bastie, "Caracterisation du rayonnement emis par les diodes lasers en vue de leur utilisation en metrologie des rayonnements", *Opto*, **72**, 27-34, 1993 (in french)
2. J. M. Coutin-Desbancs, O. Touayard, J. Bastie, "Mise en oeuvre de nouvelles sources de reference radiometrique a partir de diodes lasers", *Proceedings of the 7th International Metrology Congress METROLOGIE'95*, 236-241, 1995 (in french)
3. A. Allisy, "Les incertitudes des mesures. Applications pratiques.", *Bulletin BNM*, **53**, 13-15, 1983
4. J. M. Coutin-Desbancs, J. Bastie, "Measurement of high density optical filters using a laser diode", *CIE 119 - 1995 - 23rd Session, New Delhi*, Vol. 1, 98-129, 1995
5. R. C. Stoneman, J. G. Lynn, L. Esterovitz, "Direct upper-state pumping of the 2.8 μm Er^{3+} : YLF laser", *IEEE Journal of Quantum Electronics*, Vol. 28, 1041, 1992
6. S. Poole, "Fiber amplifier use expands as functionality increases", *Laser Focus World*, Oct. 1994, 111

High resolution spectral analysis of a pulsed CuBr laser

E. Scarlat, Liliana Preda, C. P. Cristescu, A. M. Preda

Dept. of Physics, "Politehnica" University Bucharest
Spl. Independentei 313, 077206 Bucharest 5, Romania
tel. 4104542/102, E-mail: lili@physics2.physics.pub.ro

ABSTRACT

A simple and inexpensive method to perform high resolution spectral studies of the green-yellow pulse shapes of a CuBr laser is presented. The radio-frequency (RF) spectrum of the temporal shape of the detected signal is called "pulse-shape spectrum" (PSS). The individual 510.6 nm (green) and 578.2 nm (yellow) PSS are studied in the range 20-500 MHz with 1 MHz resolution. The RF spectral analyses of the compound signal (the weighted sum of the two pulses, one of them being delayed with respect to the other one) reveals that the coherence properties of the spectral components are dependent both on the pulsed mode excitation and the optical modes supported by the optical cavity.

Keywords: CuBr laser, pulse shape spectrum, time separation.

1. INTRODUCTION

A large part of actual research efforts are dedicated to improve the optical transmission of information. This increase our need to understand and control the beam quality¹, as well as the modulation systems or the analysis techniques of the detected signal² in order to extract the useful information. For these purposes various methods are of interest, such as: mutual- or auto-correlation, spectral analysis, adaptive filtering etc. This paper presents a simple and low-cost method to perform studies on a pulsed CuBr laser. First, the 510.6 nm (green) and 578.2 nm (yellow) pulses are isolated and separately detected. The initial delay time between the appearances of the overlapping laser pulses may be measured by compensating it with a variable delay time given by different optical paths. On the contrary, by increasing the initial delay time up to achieve time separation, one can obtain qualitative information concerning the decrease of the coherence degree induced by the optical cavity modes.

2. EXPERIMENTAL SETUP

We use a CuBr laser working both on 510.6 nm. and 578.2 nm. copper lines at a repetition rate of 22 kHz. The CuBr laser is operated in the pulsed mode, so both spatial and temporal coherence are low^{3,4}.

The optical path 1 (fig.1) is longer than the optical path 2 and can be varied in order to obtain different delay time intervals. A 4 mm pinhole PH affects the amplified spontaneous radiation, while the lenses L1 and L2 reduce the spot diameter. The prism P separates the green and yellow radiation. PM1 and PM2 are two modified photomultipliers VA-S-968 (to improve the response time, only three dynodes are used) which detect the green and the yellow pulse.

The weighted summation of the electrical signals is delivered at the input of a 800 MHz large band (RF) amplifier (a modified TV-set amplification chain including VHF/UHF amplifiers and IF amplifier). Special cautions have to be taken to avoid the surrounding tv-signal to enter the amplifier.

The RF amplification factor is etalonated⁵ in order to keep the zeroth order spectrum as reference (i.e. unity value). The whole range is swept with a 6 MHz window given by the VHF/UHF channel selector.

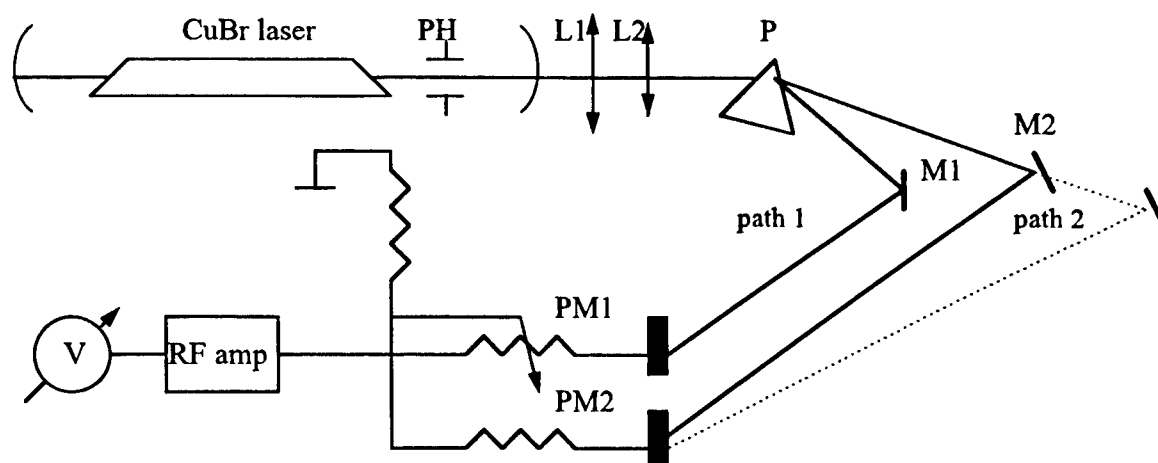


Fig. 1 Schematic diagram of the experimental setup. M1, M2- plane mirrors

The output signal is sampled with an electronic SMV 6.1/RFT r.m.s. voltmeter. The “normal” step is of 1 MHz, but we may increase the number of measuring points when necessary. Because of the significant response time of the voltmeter, it indicates a value which is proportional to the spectral component $I(\nu)$ of the periodical laser pulse intensity shape $I(\nu_o, t)$ ⁶:

$$I(\nu) \sim \left\langle \sum_{m=0}^{M-1} I_m(\nu_o, t) \right\rangle \quad (1)$$

where M is the number of round trips (RT) and $I_m(\nu_o, t)$ is the low-coherent superposition of all pulsed inhomogenous broadened optical cavity modes, as well as the fine and hyperfine line structure components of the copper neutrals^{7,8}. The brackets mean the time average. Note that ν and ν_o are the RF frequency and the optical frequency, respectively.

3. EXPERIMENTAL RESULTS AND DISCUSSION

3.1 Single color analysis.

The typical PSS is presented for each color (Fig.2 and Fig.3).

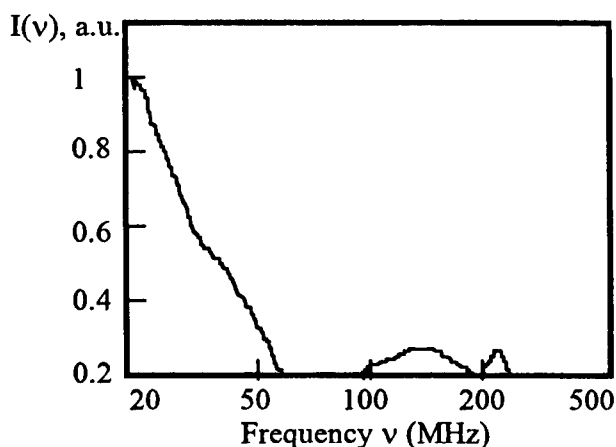


Fig.2 Green pulse spectrum

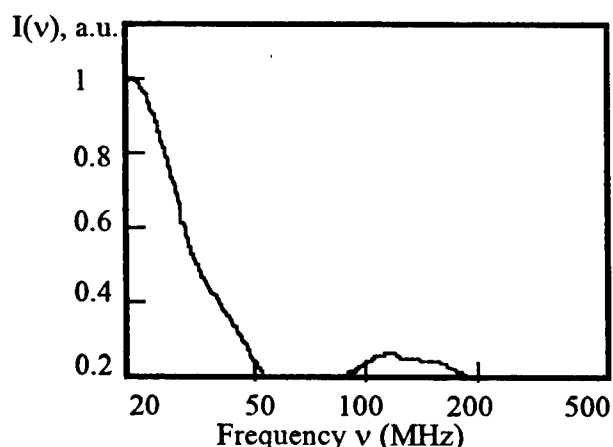


Fig.3 Yellow pulse spectrum

In this case we use the same optical path first for the green pulse and then for the yellow one. The logarithmic scale begins at 20 MHz because of the 22 kHz (and its harmonics) noise source given by the repetition rate of the pulses. The noise of the whole measuring chain was below 20% (arbitrary units). The main spectrum is of about 30 MHz wide (FWHM) for both colors, but at higher excitation pulse energy, the green one has a more complex structure, also noted by⁹.

3.2 Two color analysis, green delayed.

The green pulse propagates along the longer optical path 2, while the yellow one propagates along the other way. Our analysis indicates that the yellow pulse appears after the green one. The delay is of the order of several nanoseconds and can be compensated by the optical path difference. Relevant results of the spectral analysis are given in fig.4, where $I_s(\nu)$ is the weighted sum of the green and yellow pulses.

We introduce the following notations:

$$g(t) \leftrightarrow I_g(\nu)e^{j\varphi(\nu)} \quad (2a)$$

$$y(t) \leftrightarrow I_y(\nu)e^{j\psi(\nu)} \quad (2b)$$

$$s(t) = g(t) + y(t) \leftrightarrow I_s(\nu)e^{j\sigma(\nu)} \quad (2c)$$

the time functions describing the green, yellow and sum of the pulsed intensities, respectively, and their Fourier images. We assume also: $t=0$ the moment when the green pulse appears; $t=\tau_0$ the moment when the yellow pulse appears; $t=\tau$ the delay time of the green pulse due to the longer optical path 2. The spectrum of the compound signal $I_s(\nu)$ is

$$I_s(\nu) = \left\{ I_g^2(\nu) + I_y^2(\nu) - 4I_g(\nu)I_y(\nu) \sin^2 \left[\frac{1}{2} \varphi(\nu) - \frac{1}{2} \psi(\nu) + \pi\nu(\tau - \tau_0) \right] \right\}^{\frac{1}{2}} \quad (3)$$

Depending on the coherence degree of the PSS (i.e. the time variation of the phases φ and ψ from pulse to pulse), eq. (3) indicates the possibility to obtain interference pattern in RF domain. Theoretically, this kind of analysis have been used before in other frequency domains^{10,11}.

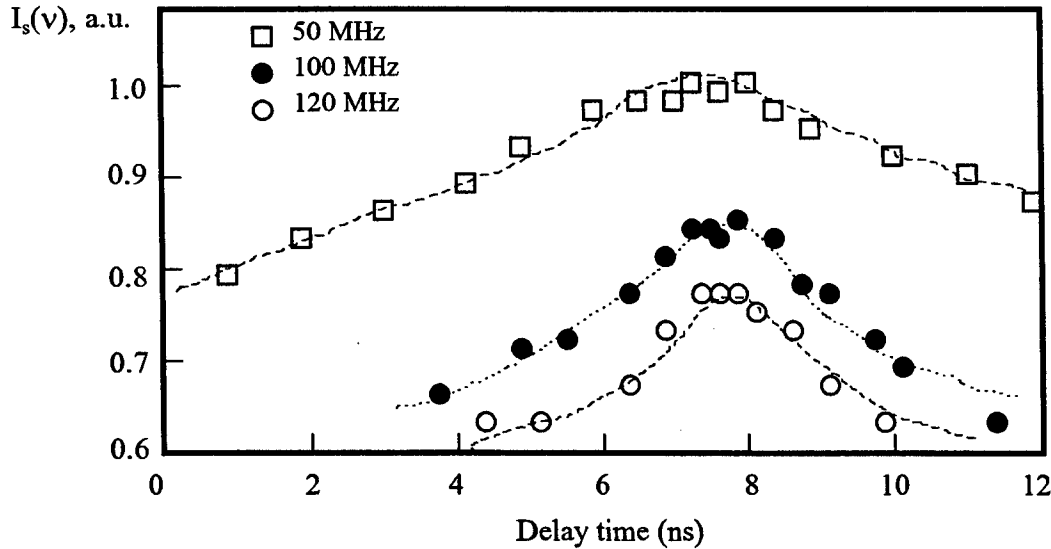


Fig.4 Compound (weighted sum) pulse spectrum I_s vs. time delay

When $\tau=\tau_0$, from (3) one can obtain maximum values for all frequencies provided that

$$\delta(\nu) = |\varphi(\nu) - \psi(\nu)| \approx 0 \quad (4)$$

especially for low voltages (3-4 kV) of the excitation pulse, when the pulse shapes are similar.

From fig.4 we conclude

$$\tau_0 \approx 8 \pm 1 \text{ ns} \quad (5)$$

Similar values are reported in⁹. In the vicinities of τ_0 , at higher frequencies is fulfilled the condition

$$\delta(\nu) \ll 2\pi\nu(\tau - \tau_0) \quad (6)$$

and, consequently, from (3), the maxima are sharper.

3.3 Two color analysis, yellow delayed

The yellow pulse propagates along the longer optical path 2 and this delay time τ is additional to the initial delay τ_0 ; consequently, we may achieve a delay time as long as the time separation between the pulses.

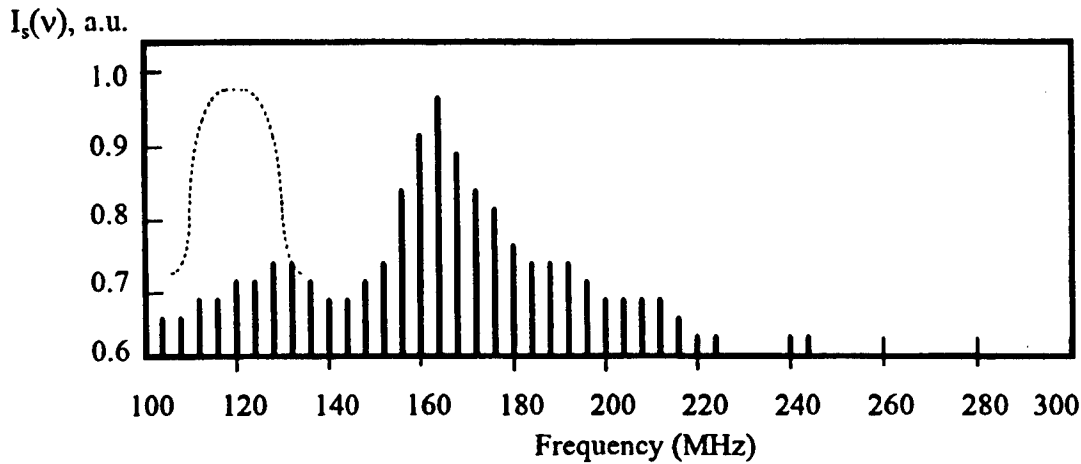


Fig.5 Compound signal spectrum I_s for an entire delay time $\tau + \tau_0 \approx 25$ ns; dashed line: the missing maximum.

Unlike the previous case, maximum values are obtained for well-defined frequencies; from (3), these are given by

$$\varphi(\nu) - \psi(\nu) + 2\pi\nu(\tau + \tau_0) = (2n + 1)\pi \quad (7)$$

where n is an integer. The greater the values of $\tau + \tau_0$, the smaller the influence of the value of $\varphi - \psi$, but the smaller the spectral components. At high values of $\tau + \tau_0$, (7) become

$$2\pi\nu(\tau + \tau_0) \approx (2n + 1)\pi \quad (8)$$

The maxima and minima are separated by a frequency interval $\Delta\nu$

$$\Delta\nu = \frac{1}{2(\tau + \tau_0)} \quad (9)$$

For an entire delay time of 25 ns, eq. (9) gives $\Delta\nu \approx 20$ MHz which “modulates” the interference RF pattern from fig. 5; consequently, there are several visible peaks. As shown in Figs. 2 and 3, these spectral components do really exist (this is not obvious for the 240 MHz component of the yellow pulse) in the individual spectra. In the range of approx. 120 MHz, the RF coherent modulation is reduced (dashed line in Fig.5), and this might be the result of the incoherence of the beating frequencies of the laser modes in the successive optical laser pulses. This supposition is sustained by the fact that the 123 MHz frequency corresponds to the $c/(2L)$ frequency shift of the longitudinal modes of our optical cavity ($L = 1.22$ m, $c \approx 3 \cdot 10^8$ m/s); modifying L , we observe that the position of the reduced components also modifies. In addition to the pulsed modulation, the beating mode frequency produces

an incoherent modulation which affects the optical carriers. Whichever the color, the frequency shift between the longitudinal modes of the optical cavity is the same and this induces a certain degree of incoherence between the modulated pulses.

4. CONCLUSIONS

We presented here a simple method to perform spectral studies on a pulsed CuBr laser. The method offers information about the green and yellow pulse shape spectra, the time delay between the green and yellow pulses, as well as about the presence of the highest spectral components in both color laser shape pulses. Despite the overlapping of the optical modes of a pulsed copper laser⁶, the spectrum of the time-separated pulse shapes qualitatively depends on the shift frequency of the longitudinal modes of the optical cavity.

5. REFERENCES

1. L. J. Peltz and B. L. Anderson, "Practical use of the spatial coherence function for determining laser transverse mode structure", *Opt. Eng.*, **34** (11), pp. 3323-3328, 1995.
2. U. Minoni, G. Scotti and F. Docchio, "Wide-range distance meter based on a frequency modulation of an Nd: YAG laser", *Opt. Eng.*, **35** (7), pp. 1949-1953, 1996.
3. V. S. Rao Gudimetla, J. F. Holmes, M. E. Fossey and P. A. Pincus, "Covariance of the received intensity of a partially coherent laser speckle pattern in the turbulent atmosphere", *Appl. Optics*, **31** (9), pp. 1286-1295, 1992.
4. B. Sotskii and M. Goncharenko, "On the relationship between the radiation coherence and the number of modes of a laser", *Opt. Spectrosc. (USSR)*, **19**, pp. 435-437, 1965.
5. M. Silisteanu, L. Cipere and C. Constantinescu, *TV-set service*, pp. 110-128, E.D.P. Bucuresti, 1981.
6. W. C. Kreye and F. L. Roesler, "High-resolution line shape analysis of the pulsed cuprous chloride-laser oscillator and amplifier", *Appl. Opt.*, **22** (6), pp. 927-936, 1983.
7. J. Tenenbaum, I. Smilanski, S. Gabay, L. A. Levin, G. Erez and S. Lavi, "Structure of the 510.6 and 578.2 nm copper laser lines", *Opt. Comm.*, **32** (3), pp. 473-477, 1980.
8. W. Yongjang, P. Bailiang, D. Xiangde, Q. Yunjun and S. Shuyi, "Multiple spectral structure of the 578.2 line for copper vapor laser", *SPIE Proc.*, **1412**, pp. 60-65, 1991.
9. K. Ouchi, M. Suzuki and K. Fujii, "Green-yellow lasers in CuBr-AgBr-Ne systems operating at 40 kHz of repetition frequency", *IEEE Jour. Q. E.*, **27** (11), pp. 2473-2482, 1991.
10. Y. N. Ning, K. T. V. Grattan, A. W. Palmer and B. T. Meggitt, "Coherence length modulation of a multimode laser diode in a dual Michelson interferometer configuration", *Appl. Optics*, **31**(9), pp. 1322-1327, 1992.
11. S. L. Chin, V. François, J. M. Watson and C. Delisle, "Spectral modulation of two coherently separated femtosecond laser pulses", *Appl. Optics*, **31** (18), pp. 3383-3384, 1992.

INFLUENCE OF ACTIVE MEDIUM PROPERTIES ON HIGH-POWER SOLID-STATE LASERS BEAM CHARACTERISTICS

N. Pavel, T. Taira*, T. Dascalu, and V. Lupei

National Institute for Laser Plasma and Radiation Physics, Bucharest - ROMANIA

*Faculty of Engineering, Fukui University, 9-1 Bunkyo 3-Chome,
Fukui-shi - JAPAN

ABSTRACT

In order to describe the transversal mode construction in a real laser resonator, a mathematical model was investigated. The analysis use Kirckhoff-Fresnel diffraction equation and amplification processes in the active medium, that was supposed as sum of thin discs with gain and losses constants on every disc's length. Influence of additional phenomenon on laser beam characteristics, as phase-shift caused by active medium thermal induced refractive power and curvature of the resonator mirrors were considered.

Keywords: stable resonator, Kirchhoff diffraction equation, thermal induced effects.

1. INTRODUCTION

Thermal effects in a laser active media are result of combination of heat generation due to pump radiation absorption and heat flow to cooling processes. These leads to a nonuniform temperature in the medium and radial variation of the refraction index. The principal distortions that arise are thermal lensing and thermally induced birefringence; in addition, optical distortions can be result of an elongation and bending of the medium. A rod active medium in which generation of heat is uniform and heat flow is radial, becomes as a thick lens with refractive power of D , proportional with the pump power.

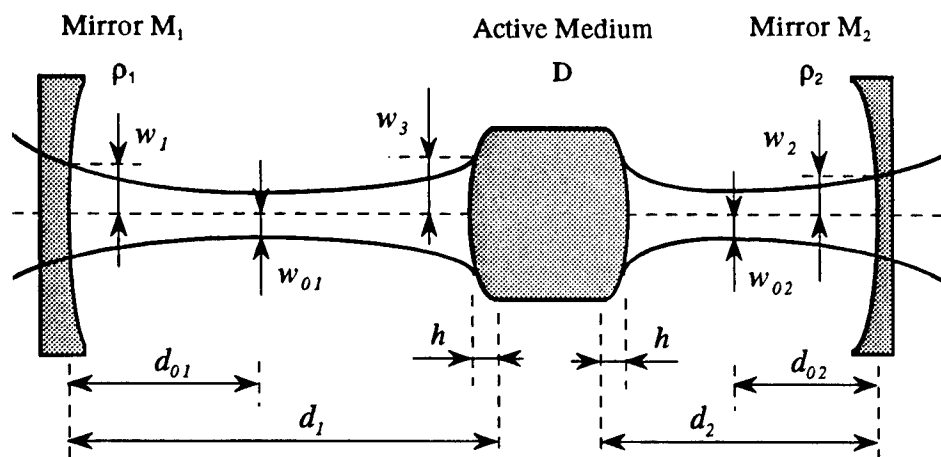


Fig. 1 Spherical resonator with the lenslike active medium.

The laser resonator (presented in Fig.1) can be described by the equivalent g_i^* -parameters $g_i^* = 1 - (d_1 + d_2)/\rho_i - Dd_j(1 - d_j/\rho_i)$, $i, j = 1, 2$ $i \neq j$ and length $L^* = d_1 + d_2 - Dd_1d_2$. It can operate in two stability zones, placed symmetrical in $g_1^* g_2^*$ plane, with the same width ΔD in terms of rod's refractive power. Inside the resonator the beam propagation can be obtained starting from the known beam-sizes on the mirrors and using ABCD-matrix formalism. Relation between stability width and laser output power is in inverse proportion: then a higher output power can be obtain on a narrow stability range. A similar relation holds for the output power and the laser beam maximum parameter-product^[1]. However, this restriction relates only the worst beam quality to a relative range of output power. Theoretically, high output power and beam-quality can be simultaneously obtained if the resonator is near to a limit of zone stability. The experimental results presented till now don't prove these assumptions and the model presented below can be used to explain that.

2. RESONATOR MODEL AND NUMERICAL SIMULATIONS

In order to find the active medium properties influence on the laser resonator transversal mode distribution a numerical model was investigated; the resonator sketch is presented in Fig. 2.

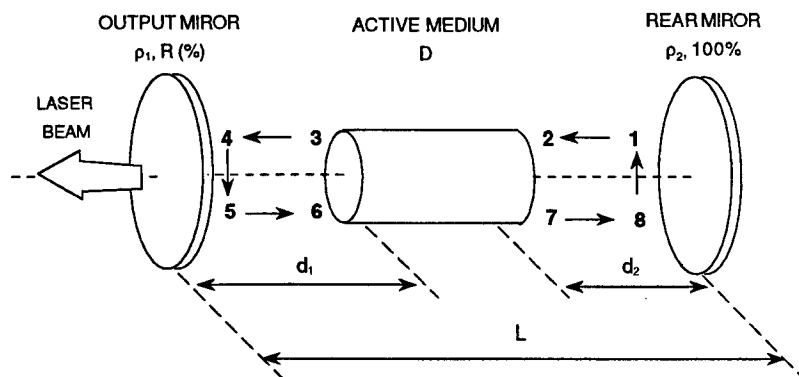


Fig. 2 Resonator model used to calculate the near-field laser beam characteristics.

For intervals between resonator's mirrors and active medium principal planes the electric fields (here denote by $U_a \rightarrow U_b$) are related by a Fresnel integral:

$$U_b = \frac{jk}{4\pi} \int_s U_a \frac{e^{-jkR}}{R} (1 + \cos \Theta) ds \quad (1)$$

The field reflection on the resonator's mirrors was described by:

$$U_{5(1)}(x, y) = \sqrt{R_{1(2)}} e^{-2jk\Delta d(x, y)} U_{4(8)}(x, y) \quad (2)$$

with R the mirror's reflectivity and $e^{-2jk\Delta d(x, y)}$ a term that take into account the phase shift induced by the mirror's radius of curvature. The active medium of length l was divided in discs with small-signal gain and losses equals on every discs^[2,3] (Fig. 3), with amplification of the electric field from disc to disc described by:

$$\begin{aligned} A_{i+1}(x_2, y_2) &= A_i(x_1, y_1) e^{(g_i - \alpha)\Delta l} \\ B_{i+1}(x_2, y_2) &= B_i(x_1, y_1) e^{(g_i - \alpha)\Delta l} \end{aligned} \quad (3)$$

Here, the signal gain g_i was recalculated at every active medium transit considering the local field as sum of the counter propagating waves:

$$g_i(x, y) = \frac{g_0}{1 + \frac{A_i^2(x, y) + B_i^2(x, y)}{I_s}} \quad (4)$$

The output beam power was obtained by relation:

$$P_{out} = (1 - R) I_s \int_A U_4(x, y)^2 dx dy \quad (5)$$

and the parameters of the laser beam, spot-size w_m and divergence ϕ_m were defined by 90% power content for rectangular and 86.5% for circular geometry.

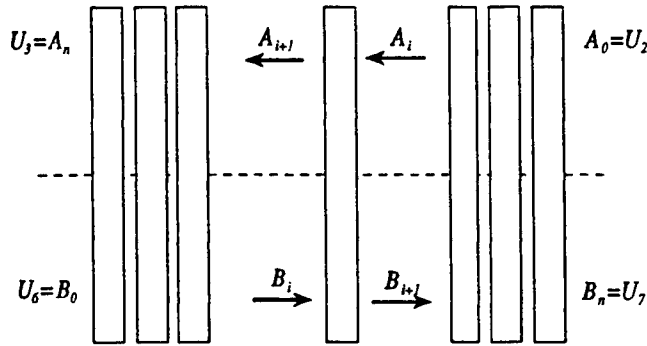


Fig. 3 Model used to describe the field amplification in the active medium.

By numerical simulations we find the active medium should be split in 20 discs for a value of small-signal gain $g_0 l$ less than 4; the field was proper described for $4 < g_0 l < 8$ when 50 discs were used to approximate the active medium. Considering only the refractive index temperature-dependent change, for a 1m plane-plane resonator the laser beam characteristics are presented in Fig. 4. Refractive powers of the Nd:YAG ($f=5$ mm) medium near the critical points of stability zones and in the middle of that were considered at small-signal gain $g_0 l=3$ and losses $\alpha_0 l=0.05$. At values of thermally induced refractive power D near zero, the resonator mode is a Gaussian one, characterized by a low beam-parameter-product and smooth phase. If the resonator moves inside the stability zone, the near-field beam distribution change to multimode operation: an increase of output power was obtained but at a lower value of the beam quality. Near the next refractive power critical point the laser beam's power decrease, the beam quality gets poorer and poorer and the resonator will pass in the unstable region.

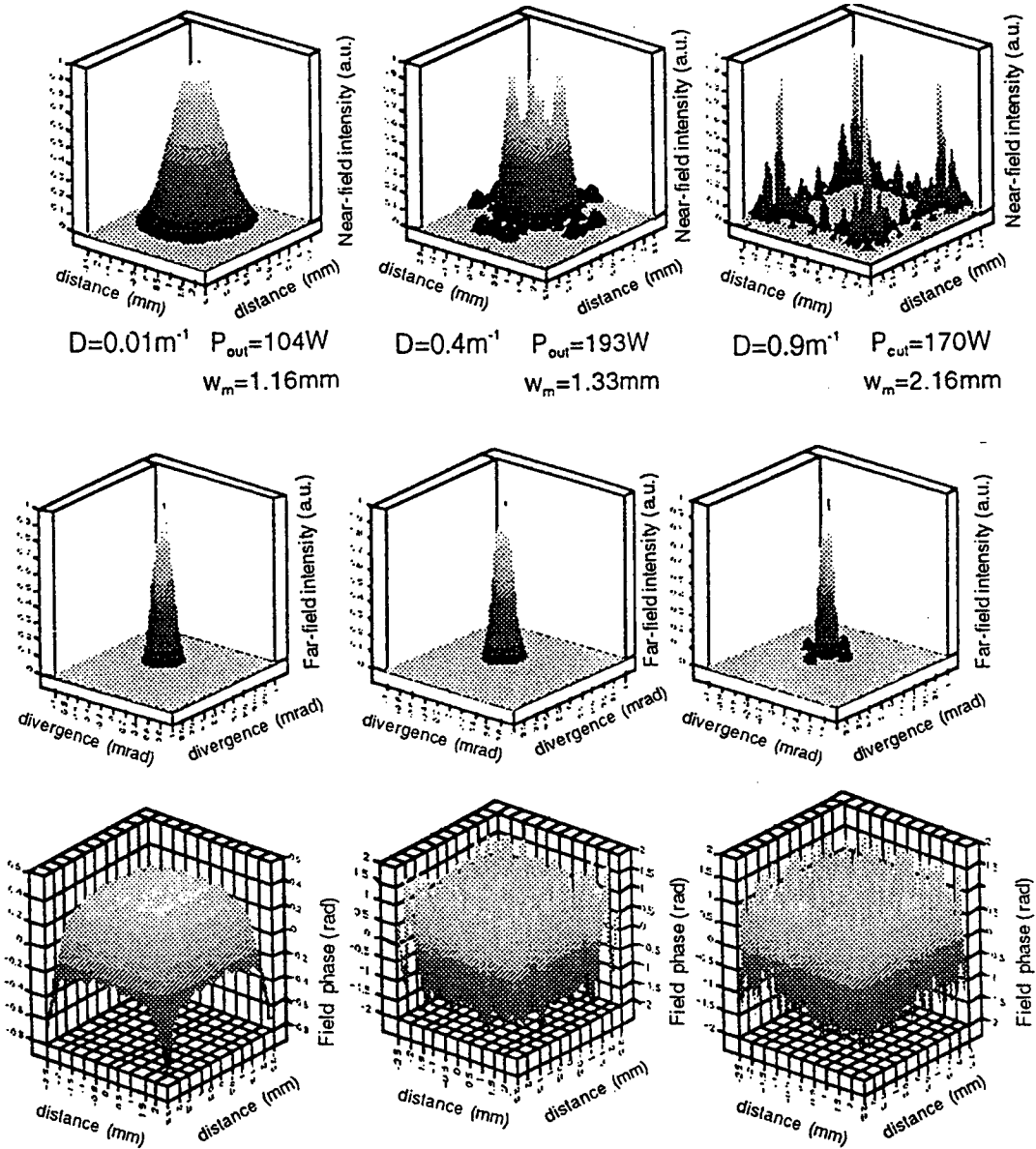


Fig. 4 Near-field (up), far-field intensity distributions (middle) and phase distribution (down) for a Nd:YAG medium ($\phi=5$ mm) placed in a 1 m resonator's length. The active medium was characterized by a small-signal gain of 3 and losses of 0.05, and different values of the thermally induced refractive power D were considered (from left to right).

In conclusion, a model that considers the Kirchhoff-Fresnel diffraction equation and amplification processes in the active medium was used to describe the transversal mode construction in a real laser resonator. Additional phenomenon, as active medium spherical aberrations^[4], thermal induced birefringence, gain distribution can be easily considered.

3. REFERENCES

1. K.P. Driedger, R.M. Ifflander, and H. Weber, "Multirod resonators for high-power solid state lasers with improved beam-quality", IEEE J. Quantum Electron. 24, 665-673 (1988).
2. D.B. Rensch and A.N. Chester, "Iterative Diffraction Calculations of Transverse Mode Distributions in Confocal Unstable Resonators", Appl. Opt. 12, 997-1009 (1973).
3. K. Yasui, M. Tanaka, and S. Yagi, "Negative-branch unstable resonator with a phase unifying output coupler for high-power Nd:YAG lasers", J. Appl. Opt. 65 (1), 17-21 (1989).
4. N. Hodgson and H. Weber, "Influence of Spherical Aberration of the Active Medium on the Performance of Nd:YAG Lasers", IEEE J. Quantum Electron. 29, 2497-2507 (1993).

Degradation effects in pulsed AlGaAs large optical cavity (LOC) structure laser diodes

R. V. Ghita*, E. Vasile**, V. Cimpoca*, N. Baltateanu***

*- National Institute for Materials Physics, P.O.Box MG 7, Magurele
76900 Bucharest, Fax: (040)-1-4231700, ROMANIA

** - METAV SA, Zapada Mieiilor 16-18, Bucharest, Fax: (40-0) 2123076, ROMANIA

***- National Institute of Lasers, Plasma and Radiation Physics, P.O.Box MG 6 Magurele,
Bucharest, Fax: (040)-1-4209391, ROMANIA

ABSTRACT

High power pulsed laser diodes are of interest due to their potential use in medicine and peculiar applications. This paper presents failure analysis for catastrophic damage in GaAs/AlGaAs LOC pulsed laser devices. There is presented failure decrease of optical power as $\lg(P/P_0) = f(t)$ where P_0 is initial power, P actual power, t -operating time. The damaged devices were investigated by optical and scanning electron microscopy (SEM) and there was performed a electron dispersion spectroscopy (EDS) analysis. These experiments advanced the idea of dividing catastrophic degradation in three types, respectively: 1-catastrophic optical mirror damage (COMD), 2- catastrophic damage due to major mechanic defects (CDMMD), 3-catastrophic damage due to metal migration (e.g. Au) (CDMM). There was established an experimental criterion to characterise catastrophic damage.

keywords: pulsed laser diodes, failure analysis, catastrophic degradation, SEM and EDS analysis

2. INTRODUCTION

The ability to fabricate high performance laser diodes with active regions close to semiconductor surface is a purpose for quantum well devices and optoelectronic integrated circuits.

For a reliable application the first problem to overcome is the degradation process. The degradation of heterostructure lasers can be divided into three types according to operation time: a-catastrophic degradation; b-rapid degradation; c-gradual degradation. This paper presents failure analysis on catastrophic damage for LOC structure GaAs/AlGaAs pulsed laser devices with a heterostructure design grown by normal high temperature liquid phase epitaxy (LPE).

The early observations of 70's suggested that catastrophic failure of injection lasers is associated with optical power density at mirrors which results in an abrupt and large temperature increase that is sufficient to cause localised melting.¹

The experiments were carried on exclusively on pulsed operation laser diodes, and that is the reason for the absence of data concerning continuous wave (cw) operation, and degradation effects on rapid and gradual degradation.

Qualitatively, the emission may be considered to result from a number of filaments, each of them with its own threshold and current density. For damaged lasers, there is no emission uniformity and at threshold the filament with the lowest current density J_{th} starts to lase. As current is increased, other filaments lase and optical distribution ceases to change markedly after the last filament is above its threshold.

There are presented output power decrease curves for devices with uncoated and dielectric coated mirrors, SEM images, optical registered image and EDS spectrum for laser devices that operated at room temperature in normal environmental conditions. The interest to study catastrophic degradation mechanisms is related to improving the high power laser diodes lifetime.

There were identified three kinds of catastrophic failure as there are proposed: 1- COMD²; 2-catastrophic damage due to major mechanic defects (CDMMD), 3-catastrophic damage due to metal migration (CDMM).

3. EXPERIMENTAL

The experiments were carried on pulsed heterostructure lasers of GaAs/AlGaAs LOC design grown by LPE at high temperature (starting growth temperature procedure : 800 °C). The principal characteristic of a LOC device is that the waveguide region is divided into a very thin recombination region of 0.1µm called active region (p-GaAs) and a relatively thick passive region of n-Al_{0.05}Ga_{0.95}As or n-GaAs where the optic field is spreading, called passive region. The structure

and the propagation condition of electromagnetic field is influenced by refractive index steps in waveguide ($n_{\text{GaAs}}=3.590$, $n_{\text{AlGaAs}}=3.554$). The MESA stripe width obtained by chemical etching was 225 μm . The epilayer structure thickness including cap layer was 20 μm , where the waveguide thickness was around 2 μm . The p-side metallization and the metal thickness were as following: Cr: 0.02 μm / Au: 0.26 μm / Ag: 0.048 μm / Au: 0.065 μm / In : 3 μm . The n-side metallization and metal thickness were : Au: 0.065 μm / Au-Ge: 0.33 μm / Ag: 0.48 μm / Au: 0.065 μm / In: 3 μm . The Au wires were bonded using an In based solder. The whole device was hermetically packed in N_2 atmosphere. Laser diodes with cleaved uncoated and coated dielectric mirrors fabricated in the same technological process were studied. The dielectric coating had the layers structure and refractive indexes as follows: antireflecting coating on front mirror: Al_2O_3 - 3 $\lambda/8$ (2086 Å), with $n_1=1.63$; reflecting coating Al_2O_3 - $\lambda/4$ (2 780 Å) , or a multilayer structure of Al_2O_3 (1 356 Å)/ a-Si (565 Å)/ Al_2O_3 (1 356 Å)/a-Si (565 Å)/ Al_2O_3 (1356 Å) with $n_1=1.63$ and $n_2=3.95$.

The operating conditions for laser diodes at room temperature were: forward current $I_f = 30$ A, forward voltage $U_f = (6-7)$ V, fill factor $ff = (10^{-5}-10^{-3})$ range until laser failed. The main optoelectronic parameters were investigated during experiment i.e: I-V curve shape, output optical power P_{out} , emission uniformity, general feature of front mirror. Catastrophic failure had been recognised as a drop in output power by more than 50% during 24 hours operating time as proposed in literature for continuous wave (cw) devices³. The degraded diodes were investigated by SEM facilities in a Philips 515 system and by EDS in a PV 9900 detection system.

4. RESULTS AND DISCUSSION

Investigated devices had at the starting operating time a uniform emission pattern in transversal junction plane as can be observed in Fig.1



Fig.1 Farfield uniform emission pattern

During operation, the presence of degradation mechanisms causes major change of emission uniformity as can be observed in Fig.2

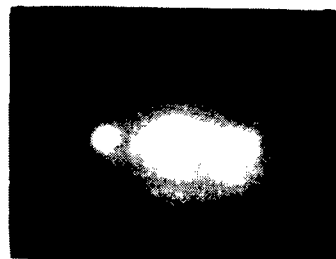


Fig.2 Degraded farfield emission pattern

Sometimes, this farfield change does not affect the I-V characteristic, so laser devices remain good electric diodes even with the drop of optical power.

In Fig.3 there are presented degradation curves $\lg (P/P_0)$ versus operating time t , where P represents actual power and P_0 the initial one, so there is a relative decrease of output power for different laser diodes fabricated in the same technology. These devices presents a catastrophic failure regarding the conditions for output power drop.

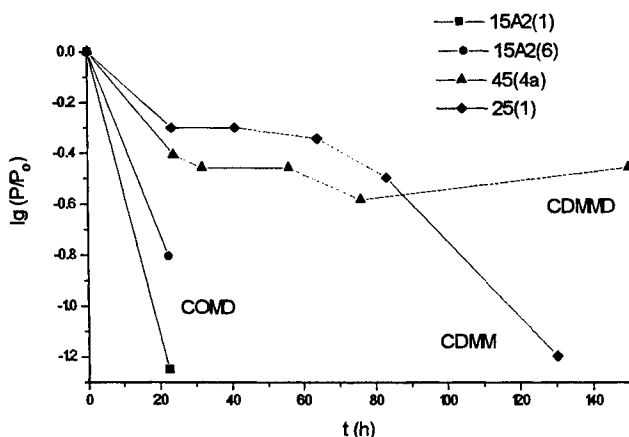


Fig.3 Decrease of optical power output during operation-catastrophic failure

The catastrophic degradation is caused by three mechanisms as we identified: catastrophic optical mirror damage (COMD), catastrophic damage due to major mechanic defect, catastrophic damage due to metal migration. The first and unpredictable mechanism that appeared during operation is COMD of laser diode. The general external feature is the presence of a melted area as can be noticed in Fig.4.



Fig.4 COMD area on pulsed laser diode front mirror

Before COMD the diodes had a good quality front mirror and a multimode emission pattern. After COMD on the whole mirror surface can be observed 'burn-in-phase' areas due to crystal overheating. In low duty cycle (10^{-4}) the device operated for few hours and as is presented in Fig.3 such a drop is announced by the presence of a slope less than: -0.025 h^{-1} . The mechanism that leads to the occurrence of COMD is not well understood and the drop in output power seems to take place without any obvious forewarnings⁴. The degradation process has microscopic origins not always well known², and in the literature⁵ the thermal model attributed the heat source to the absorption of laser light inside catastrophic damaged area.

Catastrophic failure due to major mechanic defects on mirror surface such as cracks can be observed in Fig.5.

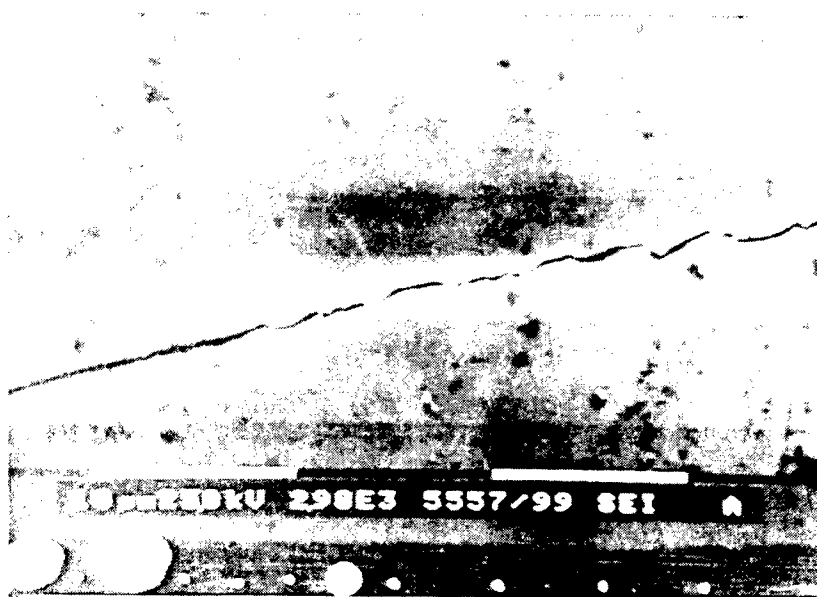


Fig.5 Major mechanic defect on front mirror surface

This failure is related with power decrease curve from Fig. 3, by the presence of a device whose power decrease curve slope is in the $(-0.025 - -0.015) \text{ h}^{-1}$ range (e.g. 45 (4a) device). In this experiment for studied devices there was not performed a heat management.

The last device on Fig.3 curves (i.e. 25(1)) had different slope changes in power decrease curve with peculiar aspect that the first one is greater than -0.015 h^{-1} . This device is susceptible to present catastrophic failure due to metal migration from p-side metallization⁶. The EDS spectrum for such kind of mechanism is presented in Fig.6. The device with an index-sample C was exposed to EDS analysis after it operated at room temperature over 200 hours in a duty cycle of 10^{-4} .

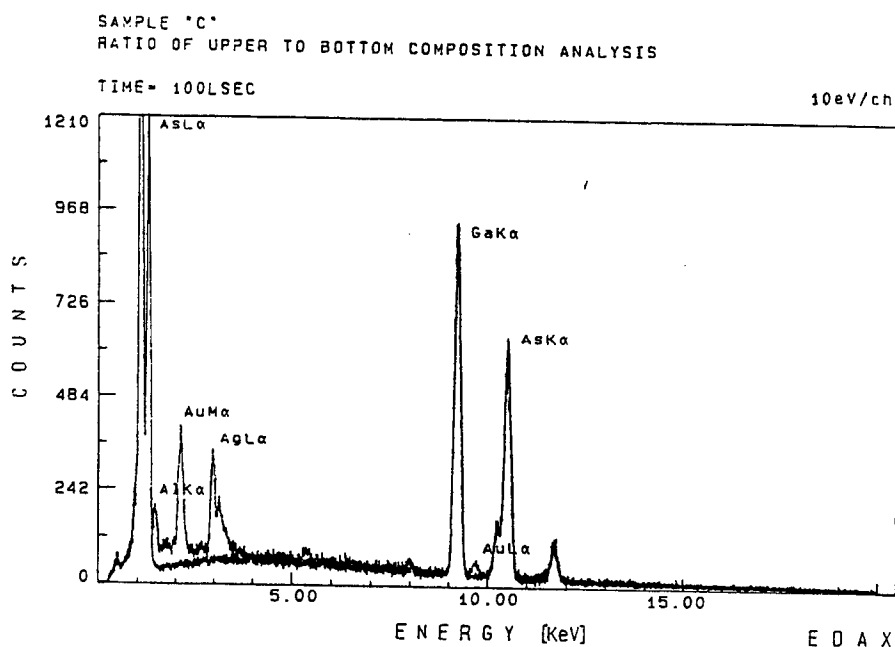


Fig.6 EDS spectrum for a catastrophic failed device

The spectrum shows the existence of two areas of laser structure, where there are located two analysing points called upper and bottom areas starting from faced surface. The initial contact annealing do not permit a mixture between metal layers, but as can be observed there exists a signal of Ag (L_{α}), Cr(K_{α}), Au(M_{α}) lines from a $0.7\mu\text{m}$ depth. During operating time occurred a diffusion of these elements (e.g. Ag is no longer a barrier for Au migration) from contact layer. Gold (Au) presence was predicted in literature⁶ and our analysis revealed metal migration from contact layer.

There was also studied the influence of dielectric coating on catastrophic degradation with a special accent on COMD one. In Fig.7 there is presented the degradation curve for a device with protected mirrors, and as can be observed there exists slow slope changes for $\lg(P/P_0)$ vs. time decrease regarding graphic scale. These observations suggest that for the present moment only dielectric coatings can be a way to overcome catastrophic and rapid degradation phenomena.

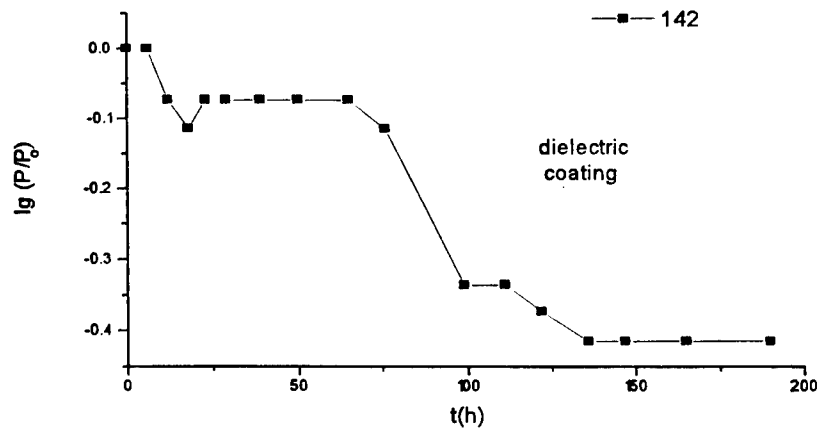


Fig. 7 Optical power decrease curve for dielectric coated mirrors

5. FINAL REMARKS

In the experiments carried on pulsed heterostructure laser diodes was studied the occurrence of catastrophic degradation process. There were identified three types of catastrophic failure with their general features as follows:

- 1- catastrophic optical mirror damage (COMD) - general presence of melted and 'burn-in-phase' areas on front mirror, accompanied by a slope less than : -0.025 h^{-1} on relative optical power decrease curves
- 2- catastrophic damage due to major mechanic defects (CDMMD)- general presence of cracks that intersects the inner active region, accompanied by a slope in $(-0.025- -0.015) \text{ h}^{-1}$ range on power decrease curve
- 3- catastrophic damage due to metal migration (CDMM) - (e.g Au) from p-side metallization during operation, accompanied by a first slope greater than: -0.015 h^{-1} on power decrease curve

For catastrophic failure caused by metal migration a EDS analysis on the device front mirror was performed with a special interest for Au diffusion depth. This is an original experimental contribution to explain catastrophic damage mechanism. On the traditional experience, the dielectric coating remains a protection against degradation mechanisms.

These results have a certain qualitative importance for passivation surface problem and contact annealing for optoelectronic integrated circuits (OEIC's).

6. REFERENCES

1. H.C.Casey and M.B.Panish, *Heterostructure Lasers*, Part B, Academic Press, New York, San Francisco,London, 1978
2. P.W.Epperlein, P.Buchmann, and A.Jakubowicz, "Lattice disorder, facet heating and catastrophic optical mirror damage of AlGaAs quantum well lasers," *Appl.Phys.Lett.* **62**(5), 455-457 (1993)
- 3.William J.Fritz, "Gradual bulk degradation in (AlGa)As laser diodes during -20°C tests due to arsenic out-diffusion,"*J.Appl. Phys.* **66**(6), 2260-2264 (1989)
4. W.C. Tang and H.J.Rosen, "Raman microprobe study of the time development of AlGaAs single quantum well laser facet temperature on route to catastrophic breakdown," *Appl.Phys.Lett.* **58**(6), 557-559 (1991)
5. Wlodzimierz Nakwaski, "Thermal model of the catastrophic degradation of high-power stripe geometry GaAs/(AlGa)As double-heterostructure diode lasers,"*J.Appl.Phys.***67**(4), 1659-1668 (1990)
6. William J.Fritz, "Correlation between forward voltage at low current and catastrophic metal migration failure mechanisms in (AlGa)As laser diodes," *J.Appl.Phys.* **66**(7), 2819-2827 (1989)

Performance of a pump system for diode-pumped lasers

A. Stratan, C. Fenic, R. Dabu, N. Herisanu, C. Luculescu, D. Sporea, G. Dumitru, G. Iordache*

National Institute for Laser, Plasma, and Radiation, Laser Department, P. O. Box MG-36, Bucharest 76900, Romania

*National Institute of Materials Physics, P. O. Box MG-7, Bucharest 76900, Romania

ABSTRACT

We have developed a laser-diode pump system for continuous-wave (CW) end-pumping of Nd:YAG lasers. The pump system includes a pair of 1 W diode-arrays mounted in coaxial enclosures, a driver unit and the pump optics. The array wavelength was temperature tuned to achieve the maximum absorption of the pump radiation in the Nd:YAG crystal. The characteristics of the pump system are presented and the pump-beam profile is investigated.

Keywords: diode-arrays, end-pumping, Nd:YAG.

1. INTRODUCTION

In this paper, we report the performance of a CW diode-array pump system developed for longitudinal pumping of Nd:YAG lasers. The driver unit provides the supply currents and a full thermoelectric cooling control for the both arrays. The beam emitted from the arrays are collimated, overlapped through a polarizing beam splitter cube and focused in a pump spot. The focused pump beam was investigated with a laser beam analyser. A method for the temperature tuning of the emission spectrum of the arrays to the absorption maximum at 808 nm of Nd:YAG is described. The pump system operation was tested using a common Nd:YAG rod made for flash-pumped operation.

2. EXPERIMENTAL AND RESULTS

The experimental setup is shown in Fig. 1. The pump laser consists of two 1W CW diode arrays mounted in coaxial enclosures¹, which preserve a dry atmosphere. Each array consists of 3 wide stripes with each aperture of 100 μm spaced 100 μm . The divergence of the beams emitted from the arrays are 10° FWHM for the horizontal component (the parallel component to the junction) and 39° FWHM for the vertical component. The arrays are mounted on a cooper heatsink attached to a thermoelectric cooler equipped with a water cooling heat exchanger.

The driver unit² provides the continuous-adjustable DC currents and a full thermoelectric cooling control for the both arrays. It also includes the diode-protection and overcurrent-limit circuits. The main driver features include:

- i). Operating current :
 - Max. 6 A for each array;
 - Line regulation : Max. $\pm 1\%$ at nominal load;
 - Ripple and noise, p-p, 15 MHz bandwidth : Max. 1% .
- ii). Temperature control :
 - Set point range : 10 - 45°C ;
 - Resolution : 0.1°C .
- iii). Power : 90-260 VAC.

The diode output beams are partially collimated by 12 mm focal length aspherical lenses having a numerical aperture (NA) of 0.75, overlapped through a polarizing beam splitter cube and focused with a 15.5 mm focal length aspherical lens in a pump spot. Using uncoated collimating and focusing lenses, approximately 68% of the diode light is collected in the pump spot. The size and the radial intensity profile of the pump spot, shown in Fig. 2., are measured with a CCD camera coupled to a laser beam analyser. The image of the pump spot was adapted to the CCD camera by using a large NA microscope-objective, a convergent lens and optical attenuators. The size of the pump spot in the focal plane of the focusing lens was measured with a calibrated circular aperture of 400 μm in diameter.

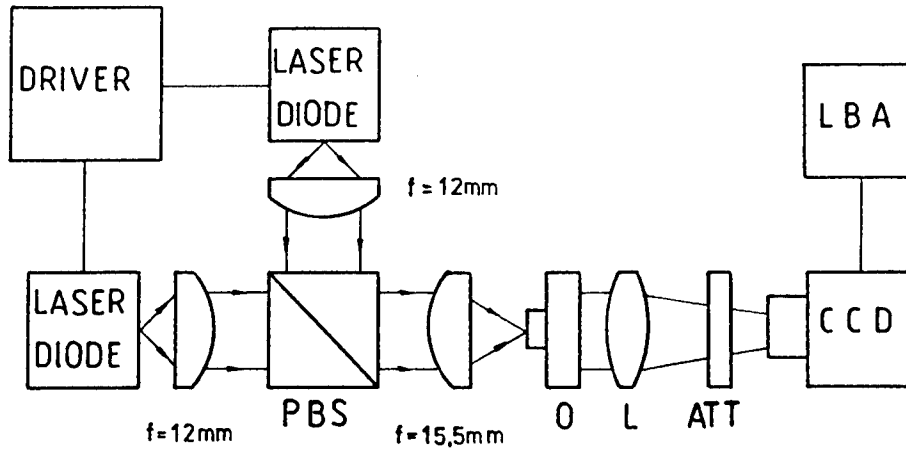


Fig. 1 Schematic of the laser-diode pump system experiment. PBS: polarizing beam splitter cube; O: microscope objective; L: convergent lens; ATT: optical attenuators; LBA; laser beam analyser

As the array wavelengths were not selected for Nd:YAG pumping, it was necessary to increase the operating temperature up to 40°C to tune the diode output to the 808 nm absorption peak of the Nd:YAG. We start testing the high temperature operation of the arrays. The array output power versus current at heatsink temperatures between 15 and 40°C is shown in Fig. 3. Starting with a slope efficiency of 0.84 W/A and a threshold current of 0.51 A at the operating temperature of 15°C, we obtained 0.79 W/A slope efficiency and 0.6 A threshold current for 40°C array temperature. We conclude the arrays can be used in this temperature range.

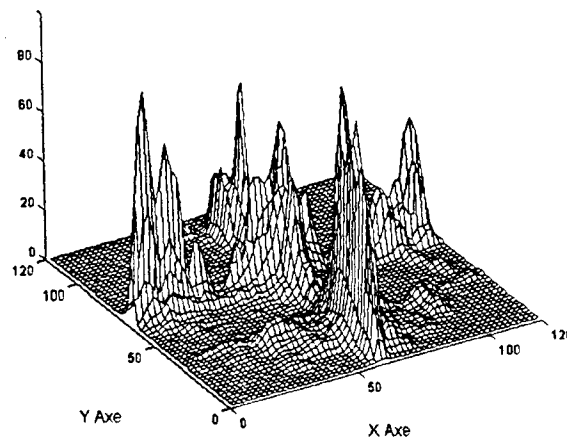


Fig. 2 Spatial beam profile of the pump spot in the focal plane of the focusing lens. X,Y dimensions: 120 pixels \approx 400 μ m.

The emission spectrum of the arrays was measured with a SPM-2 monochromator equipped with a infrared grating. The monochromator was calibrated using the 818.32 nm and 819.48 nm Na emission lines. We have measured the absorption spectrum of the Nd:YAG around the 808 nm absorption peak and we obtained a good agreement with other spectra^{1,2}. The strong absorption peak was found at a wavelength of 808.75 nm \pm 0.05 nm. The measured value for spectral linewidth of the arrays was about 2.2 nm FWHM. Fig. 4. shows the absorption spectrum of Nd:YAG and the emission spectrum of a diode

array tuned for maximum absorption in the active medium. Finally, a fine adjustment of the array wavelength was made measuring the maximum absorption of the diode radiation in a 3 mm thick Nd:YAG crystal.

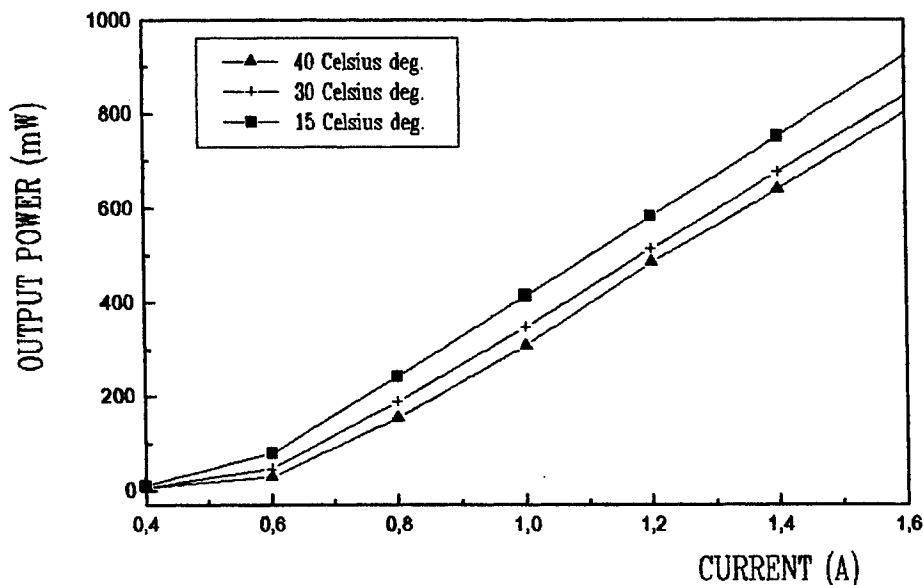


Fig. 3. Output power versus current for CW operation of 500 μm aperture GaAlAs laser-diode array at heatsink temperatures between 15 and 40 $^{\circ}\text{C}$.

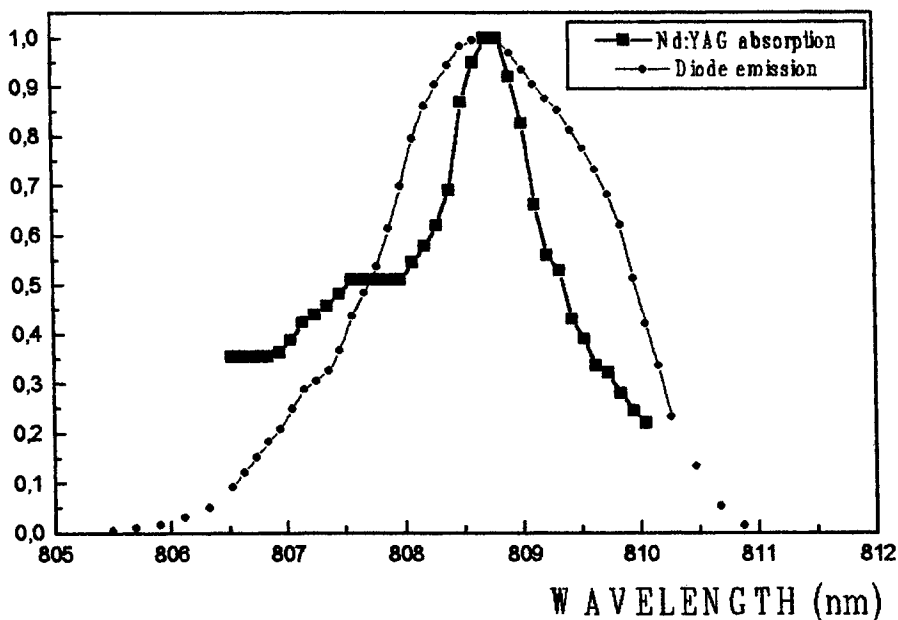


Fig. 4. Absorption spectrum of Nd:YAG (optical density) and emission spectrum of laser-diode array in operation at the temperature of 40 $^{\circ}\text{C}$.

The pump system was tested using a 30 mm long Nd:YAG rod made and coated for flash-pumped operation. One facet of the rod is high reflecting (HR) at 1064 nm wavelength and the other rod end is antireflection coated at 1064 nm. The reflectivity of the HR facet for 808 nm radiation was estimated to 10%. The Nd:YAG resonant cavity was formed by the HR

facet and a plane output mirror with 99.5% reflection at 1064 nm. The resonant cavity length was 60 mm. The pump beam was focused into the HR facet of the Nd:YAG rod and a Nd:YAG output power of 2.3 mW at 1064 nm wavelength was measured. The intensity profile of the Nd:YAG output beam is shown in Fig. 5.

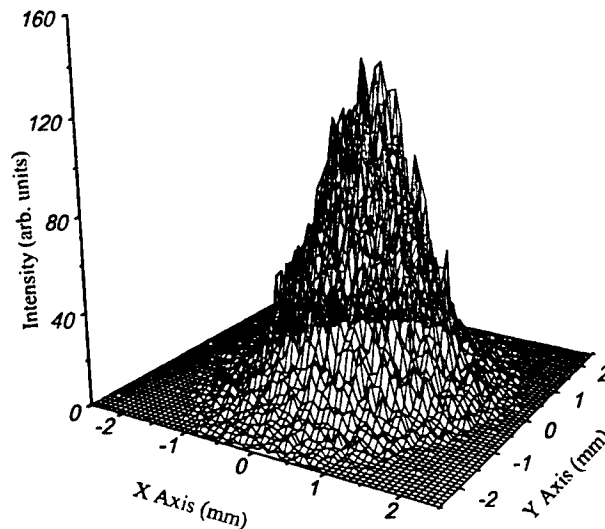


Fig. 5. Beam profile of the laser-diode array end-pumped Nd:YAG laser observed at the position 120 cm away from the output mirror.

3. CONCLUSION

Using a pair of 1W diode-arrays hermetically sealed in coaxial mounts, we have developed a CW diode pump system for end-pumped Nd:YAG lasers. The compact and easy to operate driver unit includes two low noise current sources and precise temperature control of the arrays. The pump system can use high-brightness CW diode-arrays having an output power of maximum 4W and an emitting aperture not longer than 500 μm .

The maximum absorption of the pump power in the Nd:YAG crystal was achieved by a fine adjustment of the array emission spectrum around the 808.75 nm wavelength.

The laser-diode source should be incorporated in a variety of diode-pumped solid-state lasers for scientific, medical and industrial use.

4. ACKNOWLEDGEMENTS

The authors wish to thank Prof. Dan Botez, University of Wisconsin, Madison, for helpful suggestions and support to achieve this experimental setup.

The authors would also like to express their thanks to SPIRICON Inc., Logan, Utah, for the donation of the LBA-100 laser beam analyser used in these experiments.

5. REFERENCES

1. C. Fenic, A. Stratan and R. Dabu, "Coaxial dismantling module with laser diode", Romanian Patent nr.112323 B1, 1997.
2. A. Stratan, C. Fenic and R. Dabu, "Supply and measure circuit for laser diodes", Romanian Patent nr. 112066 B1, 1997.
3. G. P. A. Molcolm, A. I. Ferguson, "Diode-pumped solid-state lasers", *Contemporary Physics*, Vol. 32, No. 5, pp. 305-319, 1991.
4. S. Yamaguchi, H. Imai, "Efficient Nd:YAG laser end-pumped by 1 cm aperture laser-diode bar with a GRIN lens array coupling", *IEEE J. Quantum Electron.*, Vol. 28, pp. 1101-1105, 1992.

A medium power cw He-Se laser

M. Ristici, Iosefina Ristici, R. Medianu
National Institute for Laser, Plasma and Radiation Physics
P.O. Box: MG -36, Bucharest, Romania

Abstract

We have developed a simple, all Pyrex, 60 cm active length laser tube in a self-heating geometry. For a He pressure of 20 Torr and a current of 120 mA, the laser power was 28 mW on seven lines in the blue-green region. By spectroscopic measurements we have determined the influence of metal vapour presence on the intensity of a helium line. Some modifications of the vapour clouds generated by a magnetic field are reported.

Keywords: lasers, metal vapours lasers

1. INTRODUCTION

Silfvast and Klein [1,2] have obtained the first cw laser oscillation in a He-Se plasma. The selenium molecules are broken in atoms by electron collisions. The collision between a selenium atom and a helium ion creates the necessary inversion of population for the laser oscillation on over sixty lines. The most powerful lines are green, blue and infrared. However, there are medium power lines in the red region, so that a white laser light can be generated.

2. EXPERIMENTAL LASER TUBE

To obtain a reasonable lifetime for He-Se laser we must consider the existence of some phenomena: He clean-up in the electrical discharge (a high rate phenomena due to condensation of the Se vapours), He losses by diffusion through the hot walls of the capillary tube, cathode sputtering by heavy Se ions and the chemical reaction between selenium and cathode metal.

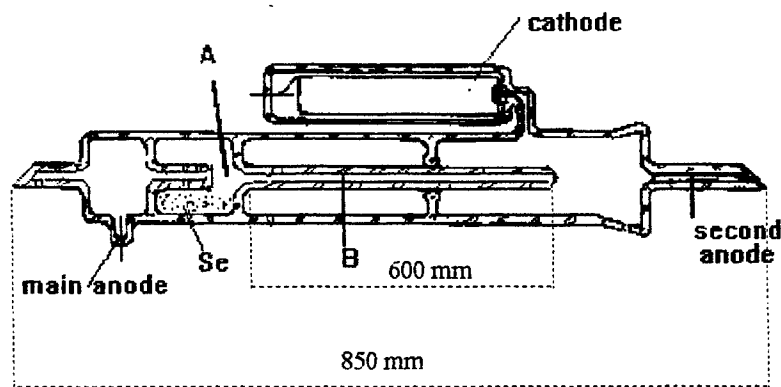


Fig. 1. Experimental He - Se laser tube.

Tube constructions that overcome partially these problems were developed by many authors [3,4]. All of them use a quartz capillary to withstand the high wall temperature of the about 300 mA laser discharge. A first He-Se Pyrex laser tube that we have developed, was presented in a previous report [5].

Fig. 1 presents the laser tube used in our experiments. A 36 mm diameter glass mantle surrounds the 2 mm ID discharge capillary so that the wall in contact with the atmosphere has a temperature under 80 °C and the permeability of glass is low enough. A selenium container is placed near the anode. Inside this container there is a small piece of capillary. The

discharge current passing through that piece increases the metal temperature to the necessary value for the evaporation process. The maximum safe current for our 2 mm Pyrex capillary is 150 mA. In this case the corresponding helium pressure must be higher than that reported by other authors. So, we have found the optimum helium pressure value in the (15 - 20) Torr range. For pressure values higher than 20 Torr, the optimum current was too low so that some metal deposition on capillary appears. Therefore the discharge parameters in our laser tube were : 20 Torr for the helium pressure, 120 mA for the discharge current. The laser resonator consists of two mirrors each two meters radius of curvature, dielectrically coated for the (450 - 550) nm spectral range. One mirror was full reflecting and the other has a transmission coefficient about 2%. A maximum power of 28 mW was measured on seven simultaneous laser radiation. For a set of full reflecting mirrors the oscillation was established on twelve wavelengths. A standard He-Ne laser mirrors set was also used and we have obtained laser oscillation on 644 nm and 649 nm lines, with 1 mW power for each of them.

For the described tube we have measured the influence of the magnetic field on some selenium spectral lines by spectroscopic methods. The measurements were made on lateral emitted light by two regions of the laser tube (Fig.1). We denote as "A" the region localised in the metal reservoir, between the end of the short capillary and the front of the long capillary. That is the place where the selenium vapours enter in the discharge, the molecules are broken and the atoms are ionised. When the discharge is on, a blue-green colour of that region points out that the metal vapours are present in the discharge. We denote as "B" a region of the long capillary where the condition for population inversion is obtained. From our spectroscopic measurements we have obtained some information about the influence of selenium vapours presence on helium plasma parameters and the perturbation induced by a magnetic field on the vapour cloud. Spectral apparatus consists of a grating monochromator with 0.1 nm resolution, an EMI 9558 QB photomultiplier and a photon counting detection electronics.

Because of our self-heating geometry we must be carefully regarding to the existence of the connection between the discharge current and the metal vapours pressure. So, we must be sure that our measurements were made for a specified vapour density corresponding to a discharge current value I . We have measured in the region "A" the influence of the discharge current on the intensity of the 501.5 nm helium line which has the metastable 2^1S as final level. The measurements were made with and without vapours (Fig.2). Curve (a) is obtained in the absence of the selenium vapours. Curve (b) is obtained for a vapour pressure corresponding to $I = 120$ mA and curve (c) is obtained when additionally, the magnetic field is applied. The behaviour shows that when the vapours are present in the discharge, the electron temperature decreases. The action of the applied magnetic field is to increase the selenium vapours density in the discharge plasma.

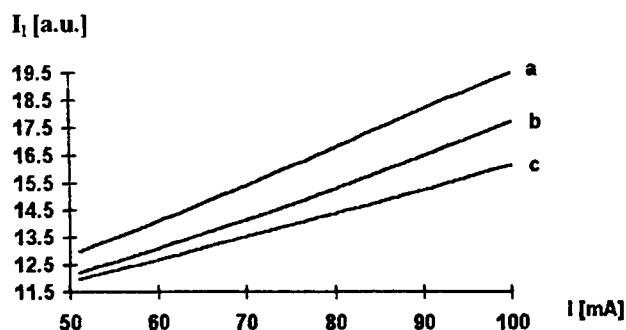


Fig. 2. Dependence of the 501.5 nm helium atom line intensity on discharge current.

Curve "a" shows the case when selenium vapours are not present,

"b" is obtained when the heating current is $I = 120$ mA and

"c" when additionally, a magnetic field is applied.

The influence of the magnetic field intensity on the selenium ion density is shown in Fig. 3, where I_l is the measured intensity of 499.3 nm selenium ion line and r is the distance between the tube axis and the magnet. The applied magnetic field in the "B" region has almost no effect.

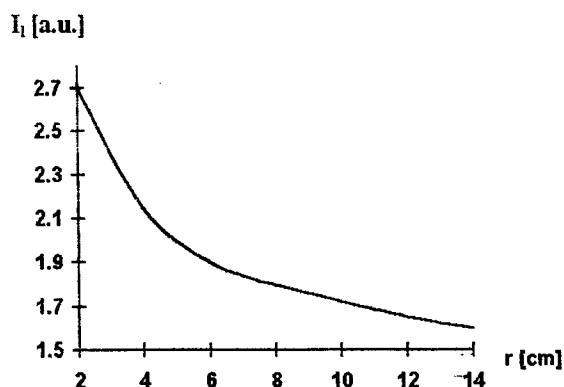


Fig. 3. Dependence of the 499.3 nm line intensity on distance r between tube axis and magnet.

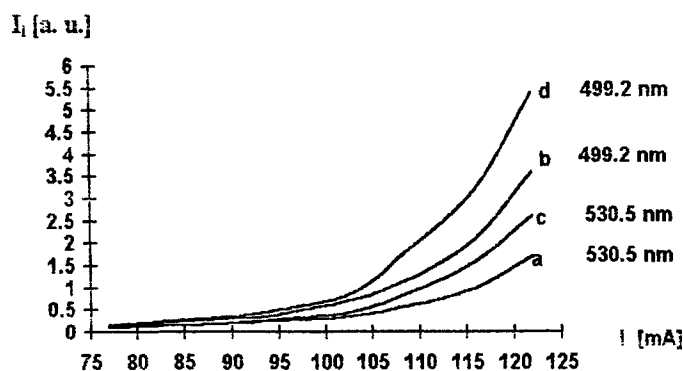


Fig. 4. Dependence of two selenium ion line intensities (530.5 nm and 499.2 nm) on discharge current without (curves "a" and "b") and with applied magnetic field (curves "c" and "d").

Fig. 4 shows the behaviour of two selenium ion laser lines when the discharge current increases. The curves "a" and "b" are for 530.5 nm and 499.3 nm, respectively, without magnetic field, and "c" and "d" are for the same lines but with applied magnetic field on the laser tube. For low current region the line intensity increases linearly, but for higher currents the growing is much abrupt due to the higher vapour density. The magnetic field influence on laser output was also observed [5].

For a steady state of the tube operation - a well defined current and metal temperature - a stable plasma region exists in the region "A" of the tube. We have determined, by spectroscopic measurements that the vapour content of that region consists mainly of selenium ions. Also, there are selenium molecules and atoms but in much smaller quantities (Fig.5).

The magnetic field is effective when it is directed perpendicularly to the tube axis (Fig.1). The density of selenium ions is not uniform around the tube axis; it is higher in the region between the surface of the metal and the tube axis. When they move to enter in the main capillary, the Lorentz force acts on them so that other vapours can lift from the metal surface. In this new steady state the ions are pumped more efficiently in the discharge.

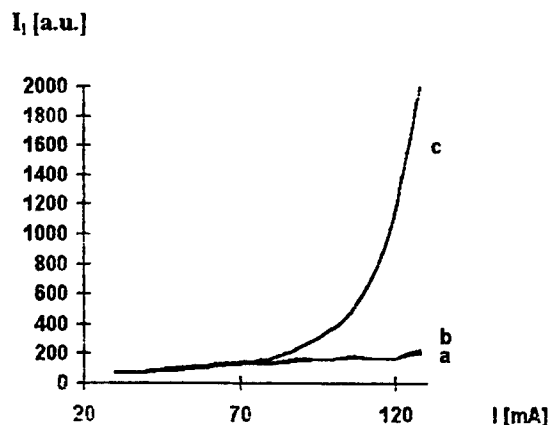


Fig. 5. Dependence of the line intensity of the selenium species on discharge current: a) - for 473.1 nm of selenium atom. b) - for 487.8 nm of selenium molecule and c) - for 499.3 nm of selenium ion

3. CONCLUSIONS

We have developed our own He-Se laser of medium power. Because of the Pyrex capillary we used, the current must not exceed 150 mA. As a consequence we have experimented unusually high helium pressure range and have concluded that for the sealed-off tube a convenient laser operation is obtained when helium pressure is 20 Torr and discharge current is about 120 mA. For an active length of 60 cm and 2 mm I.D. the maximum laser power was 28 mW on seven green and blue simultaneous laser lines.

Spectroscopic measurements showed that the dominant component of metal vapours in the discharge plasma is the Se^+ ions. A magnetic field is very effective to compel the selenium vapours to come in the main capillary where the population inversion appears.

In some preliminary experiments we have observed that the plasma developed in the metal reservoir absorbs the laser radiation.

4. REFERENCES

1. W.I. Silfvast and M.B.Klein, "CW Laser Action on Visible Wavelengths in Se II", Appl. Phys. Lett., 17, 400 (1970);
2. M.B.Klein and W.I. Silfvast, "New cw Laser Transition in Se II", Appl. Phys. Lett., 18, 482 (1971);
3. H.P. Popp, E. Schmidt, M. Neiger, F. Pfeil, "Construction, Operation and Output Characteristics of a Small, Long Life, Cathaphoretic HeSe⁺ Laser", Optics and Laser Technology, p. 321, December (1981);
4. E. Schmidt, J.Mentel and K.H.Krahn, "Three-colour He-Se⁺ with Optimised Output Power", Appl. Opt., 25, 1383 (1986);
5. M. Ristici, M.V.Udrea, R. Medianu, I. Ristici, A.I.Ciura, "A Low-power He-Se Laser", Proc. SPIE, vol. 2461, p. 18, (1995).

Pump Distribution Effects On Photon Avalanche In Fiber Lasers

V. Lupei and E. Osiac

Institute Of Atomic Physics, 76900 Bucharest, Romania

ABSTRACT

The paper discusses the effect of pump intensity variations caused by absorption in a fiber system with upconversion avalanche fluorescence or laser emission. The numerical modelling shows that in given pump conditions the initial part of the fiber (up to a distance z_{th}) is pumped above the avalanche threshold while the remaining part lies below it. This induces a strong variation of populations of the excited levels along the fiber. The characteristics of the avalanche emission are connected to the spectroscopic parameters of the system and to the conditions of pump. It is also shown that the features of the global luminescence emission at the end of fiber depend strongly on the fiber length for the short fibres ($L \leq z_{th}$) but for the long ones this dependence diminishes; thus the avalanche emission of a long fiber could be different from that predicted by a constant rate modelling. The effect of distribution of local pump intensities on laser emission in avalanche-drive upconversion fiber lasers is also discussed.

Keywords: photon avalanche, upconversion, fiber lasers.

1. INTRODUCTION

Recent studies show that the photon avalanche processes in simply activated (references in the review papers^{1,2}) or in sensitized systems³ could be an efficient driving mechanism for upconversion excitation of the high energy levels of rare earth ions in crystals or glasses under the excited state absorption (ESA) of cw infrared pump radiation. The mathematical modelling of the process is made by numerical or analytical (where possible) solution of the system of rate equations for the evolution of populations of the energy levels involved in the process; generally this modelling assumes constant cw R_2 rates in all the points of the sample. The experimental data and the rate equation modelling show that an important condition for photon avalanche is a R_2 rate larger than a threshold value R_{2th} and that the temporal evolutions of the populations and their stationary values at long times after the on-set of pump have specific and strong dependencies on R_2 ; these differences manifest differently for pump rates below, around or above threshold.

The pump rate R_2 is determined by the absorbed pump radiation intensity (power density) according to the relation $R_2 = \left(\frac{I}{h\nu} \right) \sigma_2$ where $h\nu$ is the pump quantum and σ_2 is the ESA cross-section. The pump radiation could

be also absorbed by a non-resonant ground state absorption (GSA) $R_1 = \left(\frac{I}{h\nu} \right) \sigma_1$, whose cross-section σ_1 is much smaller ($\sim 10^{-4} - 10^{-5}$) than that of ESA. Due to these two absorption processes the pump intensity I could change along the path inside the active medium, especially in the longitudinally pumped systems. Local variations of I could be also caused by the transversal distribution of intensity of the incident pump beam and by the effect of focusing. The relative importance of these factors depends on the geometry of the system: in case of core-pumped fiber lasers the first of these (absorption) is dominant, for longitudinally - pumped thin plates the transverse distribution is the main factor while for longitudinally-pumped bulk samples all these three factors could be important.

The temporal and incident pump intensity dependence of the populations at any point of the sample is described by a system of coupled rate equations for the local populations and for the local pump intensity. These solutions could be then integrated over the pumped volume in order to obtain the overall response of the system.

This paper presents the results of modelling of sensitized avalanche process in a "top hat" core - pumped fiber by taking into account the effect of pump distribution due to absorption. For modelling we use spectroscopic parameters characteristic for Yb^{3+} - sensitized visible photon avalanche emission from $\text{Pr}^{3+} {}^3\text{P}_0$ level under ESA ${}^1\text{G}_4 \rightarrow {}^1\text{I}_6$ infrared pump (830 - 850 nm). The interest for the problem was stimulated by the recent reports on visible

luminescence or laser emission in Yb, Pr - codoped fluoride fibers^{4,5} in conditions which make possible the existence of avalanche upconversion of the infrared pump.

2. PUMP RATE DEPENDENCE IN PUNCTUAL MODELLING

The scheme of sensitized photon avalanche is shown in *figure 1*; only the interactions which determine the avalanche process are taken into account. In the sensitized avalanche process the pump radiation is absorbed by ESA from an excited level (22) to the emitting level (23) of the active ion. The excited level (23) could cross-relax with the sensitizer ion (process *s*) such as the donor act ends on the level (22) while the accepted excitation of level (12) on the sensitizer could be transferred back (process *r*) in the level (22) of the active ion. Thus, for each cross-relaxation act more than one excitation can be fed in the level (22). If this condition can be kept in the competition of the process *s* with other processes of de-excitation (radiative and multiphonon relaxation) of level (23), the level (22) could accumulate population. This process of population is accomplished on the expense of the ground state (21) by the joint action of energy transfer processes *s* and *r*, which must fulfil a threshold condition with respect to the intrinsic rate W_{23} . Thus the level (22) could act as a reservoir for ESA which transposes part of its population to the emitting level: if the rate R_2 overpasses a threshold value R_{2lim} determined by its competition with the intrinsic processes W_{12} and by the efficiency of energy transfer processes, an avalanche process of population of (22) takes place, which determines then an avalanche emission from (23). A weak GSA of rate R_1 in sensitizer is assumed.

Due to the energy level diagram of ions I (sensitizer) and II (active ion), a cooperative sensitization of the emitting level (23) could sometimes take place by the simultaneous de-excitation of two excited sensitizer ions (process *u*); the efficiency of this process could be reduced by an inverse three-ion cross-relaxation process *t*. Several other energy transfer processes are possible in such systems; however, for the avalanche process of essential importance are the two-ion processes *s* and *r* and the three-ion processes *u* and *t*. The rate equation system used in modelling of the avalanche process is

$$\begin{aligned}
 \frac{dn_{11}}{dt} &= -sn_{11}n_{23} + rn_{12}n_{21} + W_{12}n_{12} - 2tn_{11}^2n_{23} + 2un_{12}^2n_{21} - R_1n_{11} \\
 \frac{dn_{12}}{dt} &= sn_{11}n_{23} - rn_{12}n_{21} - W_{12}n_{12} + 2tn_{11}^2n_{23} - 2un_{12}^2n_{21} + R_1n_{11} \\
 n_{11} + n_{12} &= n_{10} \\
 \frac{dn_{21}}{dt} &= W_{22}n_{22} + bW_{23}n_{23} - rn_{21}n_{12} + tn_{23}n_{11}^2 - un_{12}^2n_{21} \\
 \frac{dn_{22}}{dt} &= -R_2n_{22} - W_{22}n_{22} + sn_{23}n_{11} + rn_{12}n_{21} + (1-b)W_{23}n_{23} \\
 \frac{dn_{23}}{dt} &= R_2n_{22} - W_{23}n_{23} - sn_{23}n_{11} - tn_{23}n_{11}^2 + un_{21}n_{12}^2 \\
 n_{21} + n_{22} + n_{23} &= n_{20}
 \end{aligned} \tag{1}$$

The temporal evolution of populations n_{1i} and n_{2j} can be obtained only by numerical modelling. We performed the modelling by changing the spectroscopic parameters (intrinsic de-excitation rates, energy transfer rates, absorption cross-sections) in the range characteristic for the Pr^{3+} (active ion) and Yb^{3+} (sensitizer) in various crystals or glasses. This modelling puts into evidence the dependence of the characteristics of the avalanche process (the temporal evolution of populations, the time, necessary to reach the stationary emission, the stationary value of emission) on the pump rate R_2 . Thus, *figure 2* shows the dependence of the population of the reservoir level (22) and that of the emitting level on the pump rate R_2 in such a system: it is apparent that while n_{23} shows a sudden increase at the avalanche threshold, followed by a saturation behaviour, the population n_{22} shows an increase up to

$R_2 \approx 1.2 R_{2th}$, followed by a depletion regime; at the same time, the population of the ground state shows a strong depletion in the region of threshold. Strong dependencies on pump rate show the populations of the sensitizer ion too.

These dependences must be taken into account for systems where the local pump intensity I which determines the pump rates R_1 and R_2 could show local variation due to absorption or to the non-uniform transversal distribution of intensity in the pump beam. Such situation could arise in important laser active systems such as longitudinally pumped fibers, thin plates or bulk crystals.

3. PUMP INTENSITY DISTRIBUTION IN FIBERS DUE TO ABSORPTION

We assume an optical fiber doped uniformly with active and sensitizer ions and pumped longitudinally in the core. In order to put into evidence the effects of absorption we assume that the pump beam profile is top hat, i.e. the transverse distribution of the pump in the section of the fiber is uniform. In this case due to the GSA and ESA processes discussed above the intensity of the pump beam along the fiber shows a variation described by the equation

$$\frac{dI(z,t)}{dz} = [-n_{11}(z,t)\sigma_1 - n_{22}(z,t)\sigma_2]I(z,t) \quad [2]$$

where z is the variable along the fiber. Equation (2) is then coupled to the system of rate equations (1) in which the populations n_{1i} and n_{2j} as well as the rates R_1 and R_2 become dependent on z .

The numerical solution of the coupled equations (1) and (2) shows that although the pump is made in a cw regime, due to the temporal variations of populations n_{11} and n_{22} the local pump intensity at each point z shows a very complex temporal behaviour which evolves to a stationary value (figure 3). If the incident pump intensity I_0 exceeds the avalanche threshold value I_{th} corresponding to the threshold ESA rate R_{2th} , i.e. if the ratio $k = (I_0/I_{th}) > 1$, in the stationary regime of pump three z regions could be distinguished: in the pump end region the fiber is pumped above threshold, at a given distance z_{th} the pump intensity reaches the I_{th} value and the remaining part of the fiber is pumped below threshold (Figure 4). The distance z_{th} depends on k , but not linearly. As shown in figure 4, the pump intensity decreases almost linearly in the region $z < z_{th}$, then around z_{th} a sudden drop in intensity takes place up to a very low value (the variation of intensity in this region depends on the ratio $l = (R_1/R_2)$; when this is very small, the intensity of pump remains almost constant). This shows that in a pure avalanche regime (very low l) the incident pump beam cannot be absorbed completely even in very long fibers.

The variation of the local pump intensity along the fiber is accompanied by variations of populations of all the energy levels from system. Thus, the population of the emitting level n_{23} shows a complex temporal variation, dependent on z , (Fig. 5) which evolves to a stationary value. For $z < z_{th}$ these stationary values of n_{23} are high, as expected from the dependence show in figure 2; in the region of z_{th} they drop almost suddenly and subsequently decrease slowly to a constant value for $z \gg z_{th}$ (Fig. 6). The temporal dependence of the populations n_{23} for various z distances from the pump end confirms the behaviour expected from the punctual modelling under constant rate: the time t_p necessary to reach the stationary regime has the largest value when $z = z_{th}$. It is also apparent that the three-ion processes u and t induce an early spike of population n_{23} on the rising portion, similar to that of an external triggering of avalanche. The total n_{23} population in the fiber up to the point z (obtained by summing the local populations up to this point) shows also a complex temporal and z dependence (Fig. 7), while the z dependence of the stationary total n_{23} population (Fig. 8) shows clearly two distinct regions: up to z_{th} it increases almost linearly with z_{th} then at z it changes the slope and shows a tendency to a very weak linear dependence on distance.

The temporal variation of population n_{22} of the reservoir level is also dependent on distance z ; at the same time its stationary value at the pump end of the fiber, pumped above threshold, is low, it increases suddenly and reaches a maximal value at a distance z_{max} slightly shorter than z_{th} then decreases again. It is important to note that by changing the pump parameter k , the maximal stationary value of n_{22} remains constant, but its coordinate z_{max} moves inside of the fiber (Fig. 9). The total population n_{22} at various distances z depends also on time, and its

stationary value increases very slowly below z_{max} , it starts to increase more strongly at this distance and then shows a tendency to a weak dependence at long distances.

The process of population of levels (22) and (23) is accompanied by the variation of population (21): in the region pumped above threshold is almost zero but for $z > z_{th}$ it increases strongly. At the same time a strong temporal and distance dependence is manifested in the populations n_{11} and n_{12} of the sensitizer: figure 10 shows that the local population of level (12) for $z < z_{th}$ are very high but they drop almost to zero in the region of z_{th} . This can be explained by the bottleneck of the back transfer r due to the severe depletion of the ground state of active ion in region $z < z_{th}$, and it shows that an efficient inversion of population for the sensitizer ion takes place in this region.

The dependence on the pump rate of the total (22) and (23) populations in a fiber depends on its length. Thus, for a short fiber (Figure 11) these dependencies still show resemblances with the results of the punctual modelling (figure 2). In case of longer fibers (Figure 12) this dependence is different, it shows an almost linear dependence at lower rates (but which still could be over an order of magnitude larger than R_{2th}), followed by a very weak dependence. The temporal dependence of the total emission from fibers could be also different from that given by the punctual modelling. Since the most of the experiments are made with very long fibers, the features of avalanche observed in thin samples are not obvious any longer and this could sometimes lead to erroneous interpretation of mechanisms leading to upconversion in these systems. The results of this modelling show that for avalanche-driven systems the length of the fiber could be limited (due to the distance z_{th} which depends on the parameters of the system and on the pump factor k), without much loss in efficiency; moreover, this reduces the passive losses dependent on the total fiber length.

The laser emission processes from the emitting level 23 to levels below (22) (and ending practically on 21) in these fibers could be modelled by introducing a light flux rate equation and suitable additional terms in the population rate equations (1). Similar to the case without laser emission, the characteristics of avalanche-governed laser emission in the fiber are different from those predicted by the constant rate modelling owing to the absorption-induced pump intensity variation along the fiber. The numerical modelling shows also that the modification of the population dynamics due to the laser emission could influence the characteristics of emission. The local pump intensity along the fiber decreases up to a given distance from the pump end (z_{thL}) dependent on the incident pump intensity, but this distance is larger than z_{th} in absence of laser emission and the drop of intensity in this regim is not so pronounced; for $z > z_{thL}$ the local pump intensity becomes very small. As expected, the stationary values of populations n_{22} and n_{23} for $z < z_{thL}$ are smaller (by several units), but for $z > z_{thL}$ they, as well as the local pump intensity become equal to the values in absence of laser emission. However, the local values of the population n_{12} of the sensitizer are much smaller (by about two orders of magnitude), due to preventing of the bottleneck of the back transfer process r owing to the permanent repopulation of the ground state (21) of the active ion by the laser emission. The light flux shows an early spike, dependent on the incident pump intensity, due to the triggering three-ion process u . The local light flux values are zero for $z > z_{thL}$ and thus the total laser emission in these systems increases with distance z up to z_{thL} then it remains practically constant for larger z (Fig. 13). The pump dependence of the light flux in long fibers ($L \gg z_{thL}$) does not show the characteristic avalanche behavior predicted by the punctual modelling, but increases almost linearly with pump then saturates. The predictions of the rate equation modelling of laser emission in the sensitized avalanche governed systems are consistent with the experimental reports^{4,5}.

4. REFERENCES

1. M. F. Joubert, S. Gay and B. Jaquier, "Model of the photon avalanche effect" *Phys. Rev. B*, **48**, 10031 (1993)
2. Ph. Goldner and F. Pelle, "Photon avalanche fluorescence and lasers" *Opt. Mat.* **5**, 239 (1996)
3. T. Sandrock, E. Heumann, G. Huber, V. Lupei, B. Bejan and E. Osiać, "Visible Lasing of Pr:Yb:LiYF₄ Pumped via Sensitized Photon Avalanche" *Internat. Quantum Electronics Conf. IQEC*, Sydney 1996
4. P. Xie and T. R. Gosnell, "Room temperature upconversion fiber laser tunable in the red, orange, green and blue spectral regions" *Opt. Lett.* **20**, 1014 (1995)
5. T. Sandrock, H. Scheife, E. Heumann and G. Huber, "High power cw upconversion laser at room temperature" *Opt. Lett.* **22**, 808 (1997).

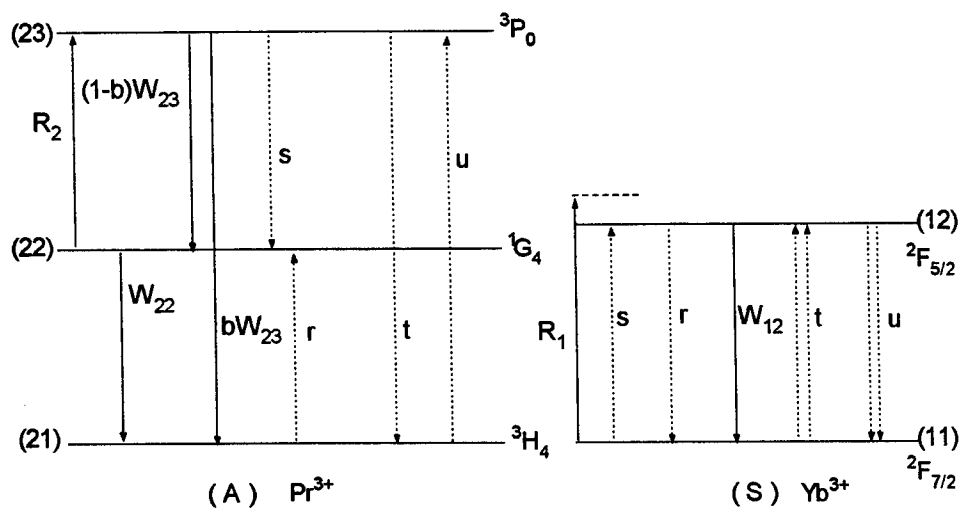


Figure 1

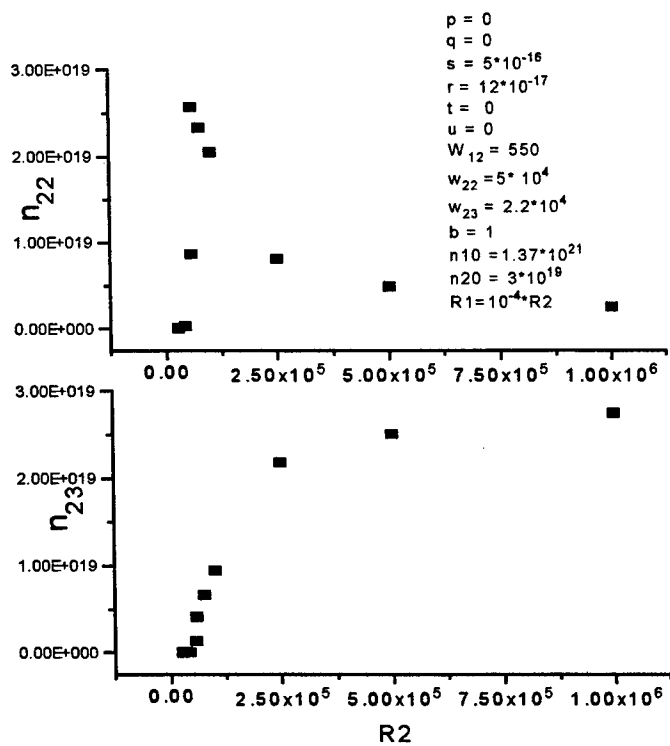


Figure 2

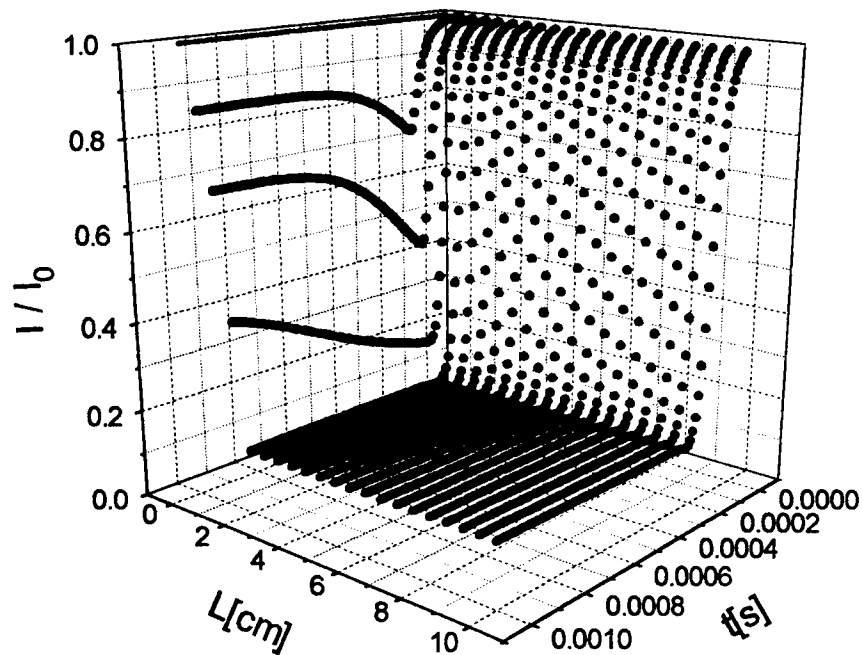


Figure 3

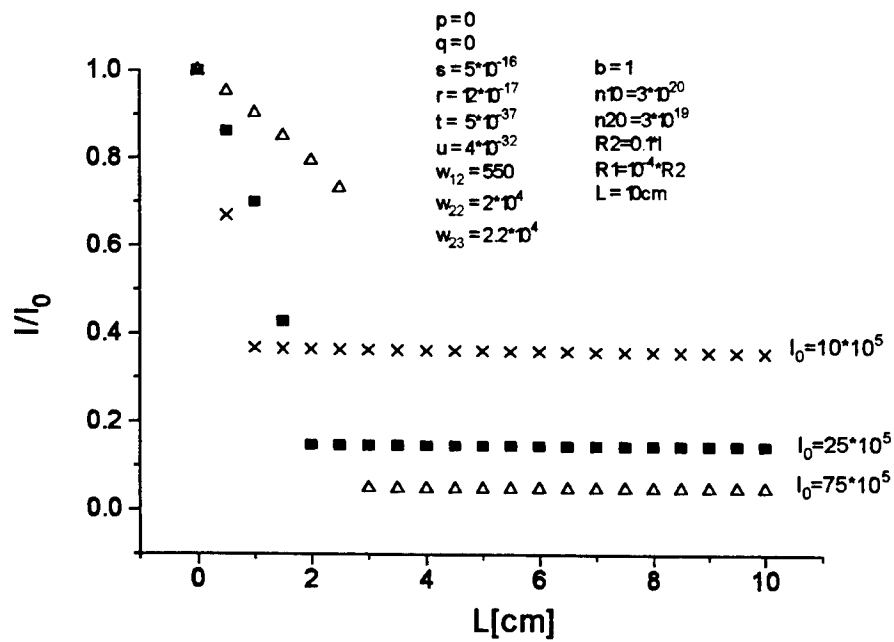


Figure 4

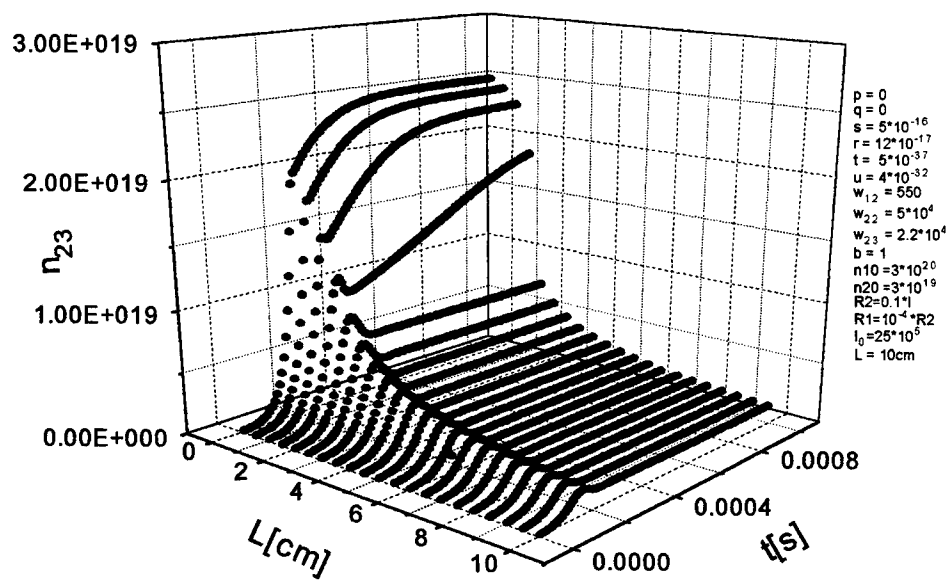


Figure 5

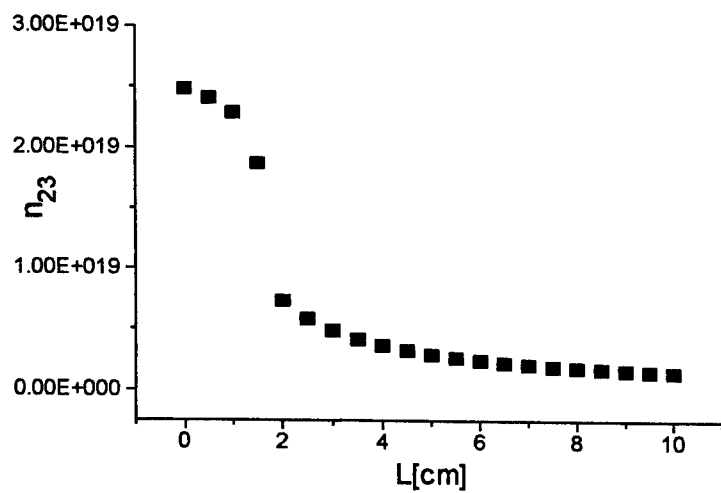


Figure 6

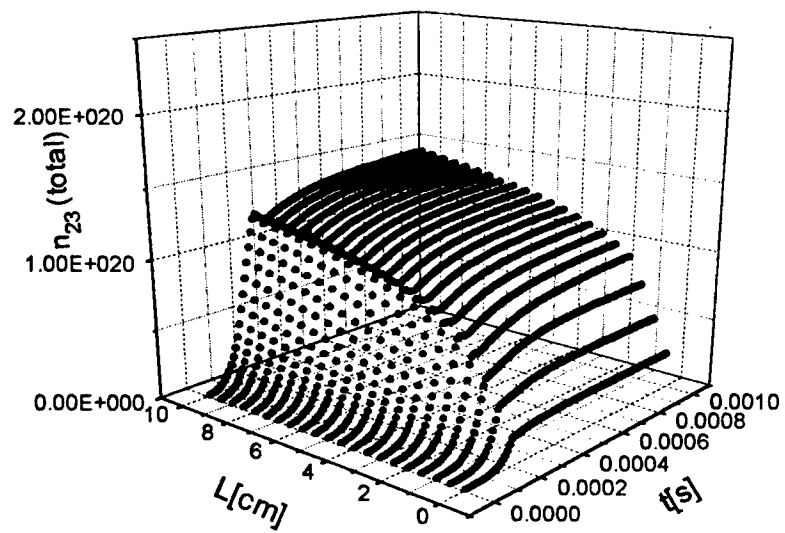


Figure 7

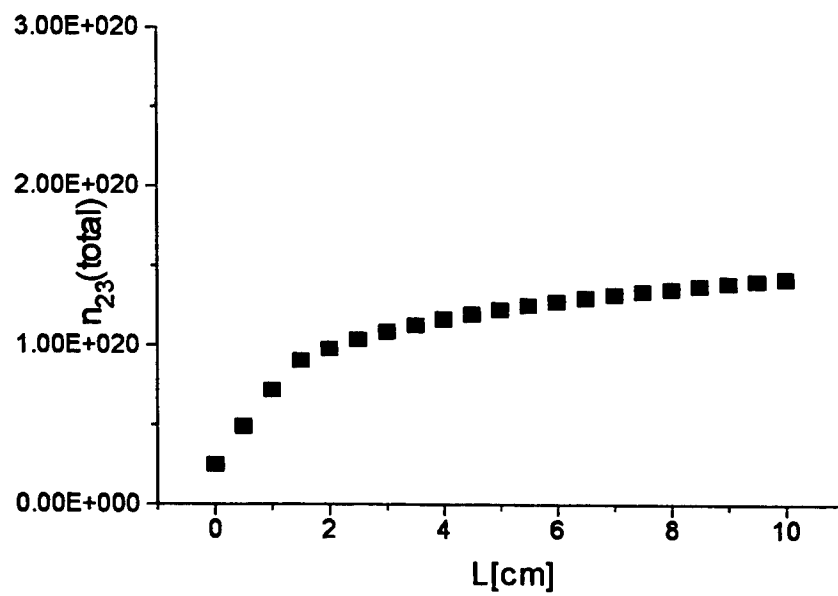


Figure 8

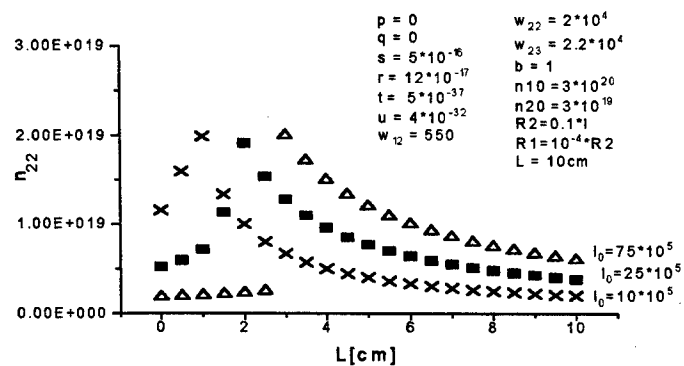


Figure 9

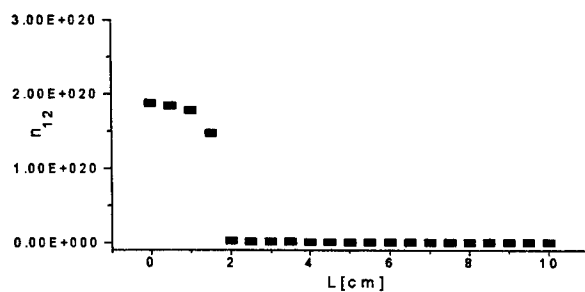


Figure 10

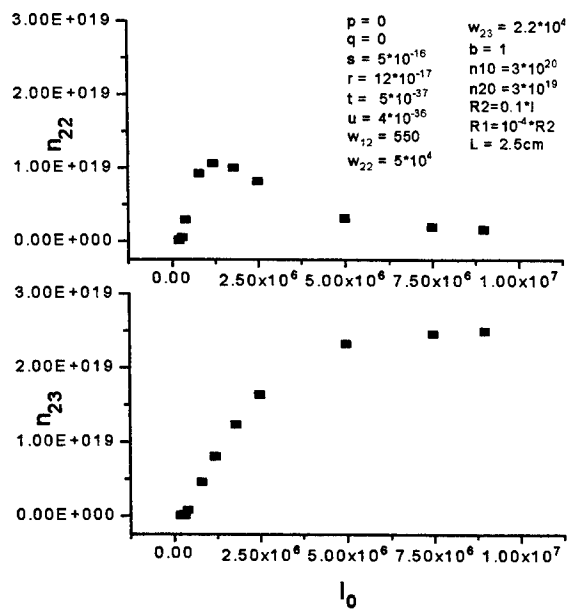


Figure 11

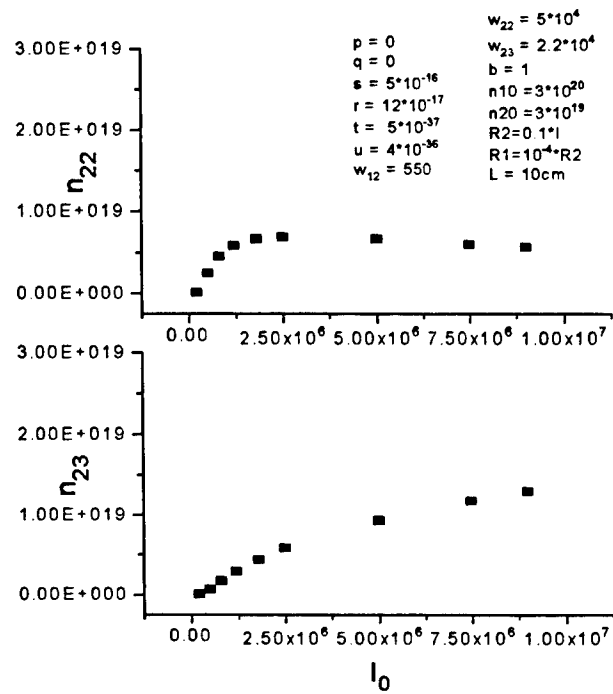


Figure 12

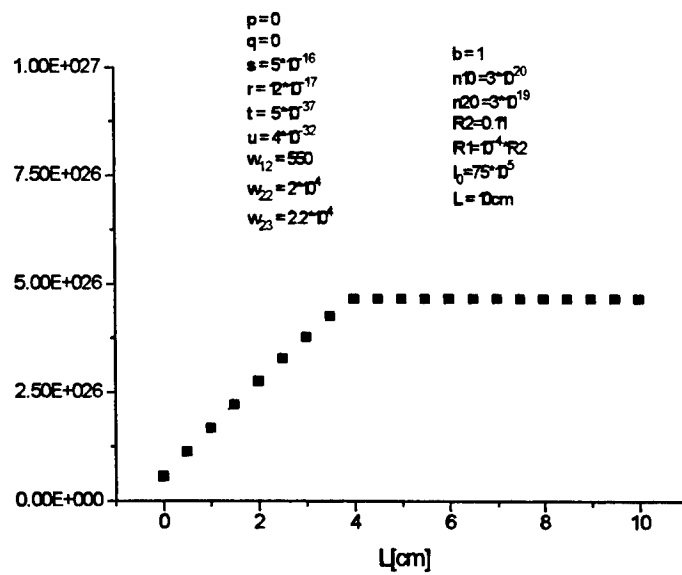


Figure 13

High quality beam transversal gas transport c.w. CO₂ laser

Iulian Gutu, Victor Rares Medianu, Petre Cristian
National Institute for Laser, Plasma and Radiation Physics, Laser Department
P.O.Box MG-36, Bucharest, Romania

ABSTRACT

A new optical resonator configuration for transverse flow CO₂ laser (TFL) was developed. A high value of the matching coefficient (the cross section of the laser beam/the cross section of the electrical discharge) - η_m , is obtained for laser beams with TEM_{00/01} intensity distribution (that corresponds to the low values of the Fresnel number - N_F of the optical resonator). Simultaneously, both types of the gain and refractive index asymmetries of the active medium (parallel and perpendicular on the flow direction) are compensated. A 90° deflection device is the main constructive element (this is built by two mirrors at 45° relative angle and offers the pentaprism properties). This deflection device reverses the wavefront in one of the two discharge channel and in addition improved the resonator stability. The main results are $\eta_m \cong 0.83$ for $N_F \cong 1.9$ and the beam pattern is independent of the power level in the range of 300 W to 1800 W.

Keywords: transverse flow, CO₂ laser, asymmetries compensation, good optical quality, high efficiency

I. INTRODUCTION

There are well known the advantages of the transverse flow CO₂ laser (TFL): relatively small dimensions and weight, reliability, compactness, low price, simplicity in the construction, high power capability, high small signal gain coefficient a.s.o.

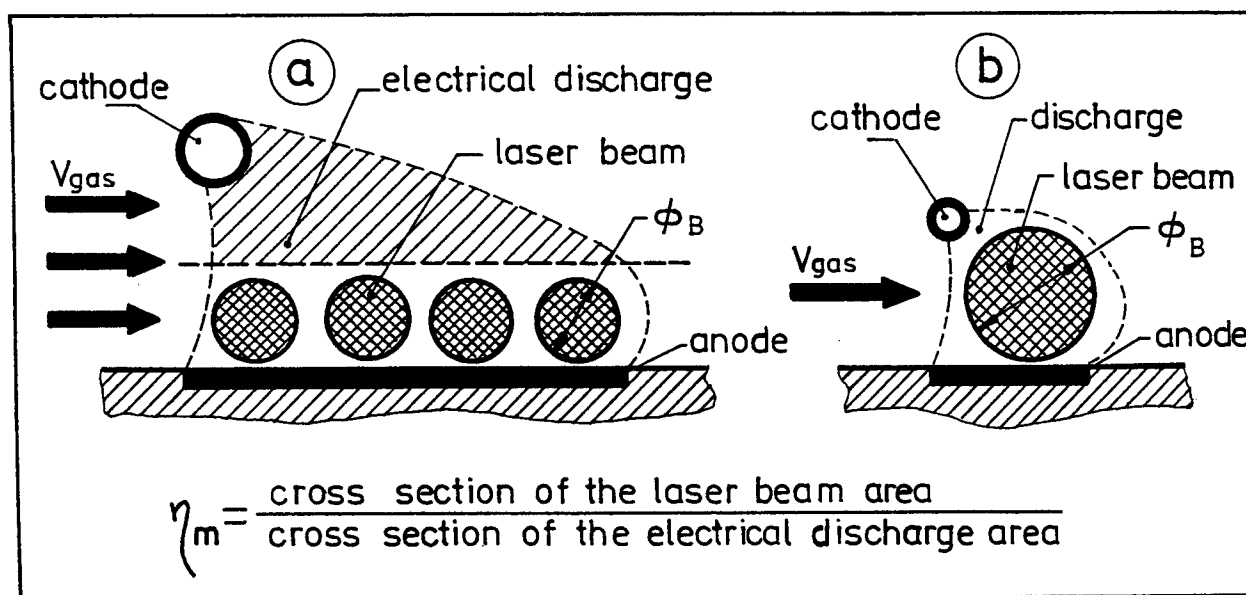


Fig.1 Typical shape of the electrical discharge in transverse flow CO₂ laser:

a) multipass resonator used for TEM_{00/01} laser beam characterized by a low value of the η_m parameter

b) single pass resonator is used for multimod laser beam with large diameter (25 - 40) mm and nonuniform intensity distribution, characterized by a high value of the η_m parameter

But, due to the fact that:

- the shape and dimensions of the discharge cross section do not identical with the shape and the dimensions of the $TEM_{00/01}$ laser beam cross-section;

- the laser beam is transversely passed both of the gas mixture flow and the electric discharge current (fig.1); there are some major disadvantages:

- in the case of laser beams with a $TEM_{00/01}$ intensity distribution (that correspond to the low values of the Fresnel number - N_F of the optical resonator - typical $N_F < 1.5(2.5)$ - for TEM_{00} respectively TEM_{01}) the matching coefficient - η_m , have a low value (fig.1 a); in the case of multimode laser beam - $N_F \gg 2$ - when $\eta_m \rightarrow 1$ (fig.1 b) the intensity distribution of the beam is nonuniform and noncircular in shape;

- the small signal gain and the refraction index profiles of the active medium on the cross section of the laser beam are asymmetrical both on the flow and anode-cathode directions¹; therefore, the intensity distribution of the laser beam is not symmetric with respect to the optical axis. The direction of the optical axis (beam pointing stability) and the beam pattern will depend on the laser power level.

In this work we try to eliminate these disadvantages by:

- compensation of the both types of the active medium asymmetries (along and perpendicular to the flow direction)

- designing of the electrical discharge region (anode length in the flow directions, anode-cathode distance) in connection with diameter of the optical resonator mode control aperture - $\phi_B(N_F)$, thus $\eta_m(N_F) \rightarrow \text{maximum}$ for a chosen N_F value ($N_F < 1.5(2.5)$ for TEM_{00} respectively TEM_{01}).

2. EXPERIMENTAL SETUP

In a previous paper² we shown that a gas circulation fluidodynamical circuit with cylindrical geometry - fig.2 - in combination with a U-type resonator can compensate the gain and refractive index profile asymmetry along the flow direction. Also we have shown that a two mirror system (M_1, M_2) - fig 3 can reverse the wave front of the laser beam in one of the two discharge channel and consequently the compensation of the anode-cathode asymmetry is assured.

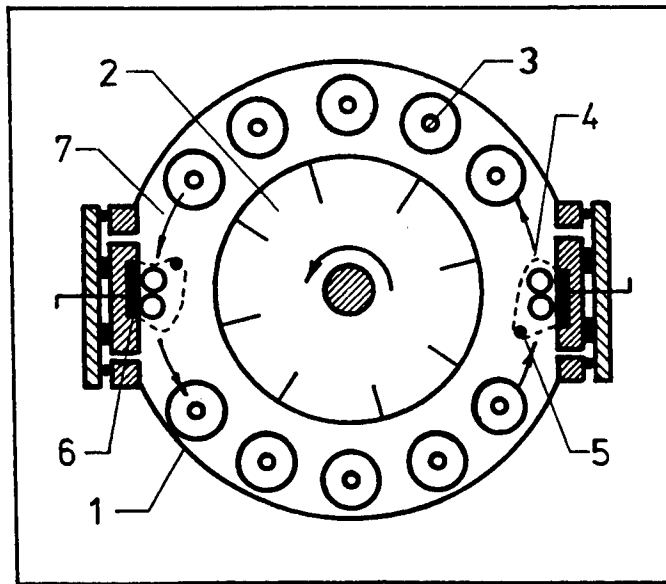


Fig.2 - Gas circulation fluidodynamical circuit used for compensation of the gain and refraction index asymmetry profile along the flow direction:

1 - metallic cylinder; 2 - blower; 3 - heat exchanger; 4 - electrical discharge; 5 - cathode; 6 - anode; 7 - gas flow direction

This experiment was made on a GT-1200 laser type³ in which: anode dimension in the low direction - $l_a = 45$ mm - fig.4 -; adjustable anode-cathode distance - $h_{a-c} = (27 - 40)$ mm; cathode diameter - $\phi_c = 10$ mm; the one discharge length - $L_d = 1.2$ m; in the optical path length U - type resonator - $L_r = 4$ m. In this case the aperture diameter - $\phi_B(N_F)$ inside the optical resonator is 14.5 mm (17.5 mm) for $N_F = 1.3$ (1.9) - that correspond to $TEM_{00}(TEM_{01})$ intensity distribution. The active medium volume - $V_m(N_F)$ enclosed in the optical resonator with $\phi_B(N_F)$ diameter will be: $V_m(N_F) =$

1.3) = 400 cm³ respectively $V_m(N_F = 1.9) = 580$ cm³. For matching coefficient we obtain very low values: $\eta_m(N_F = 1.3) = 0.17$ and $\eta_m(N_F = 1.9) = 0.25$ (for $h_{a-c} = 30$ mm).

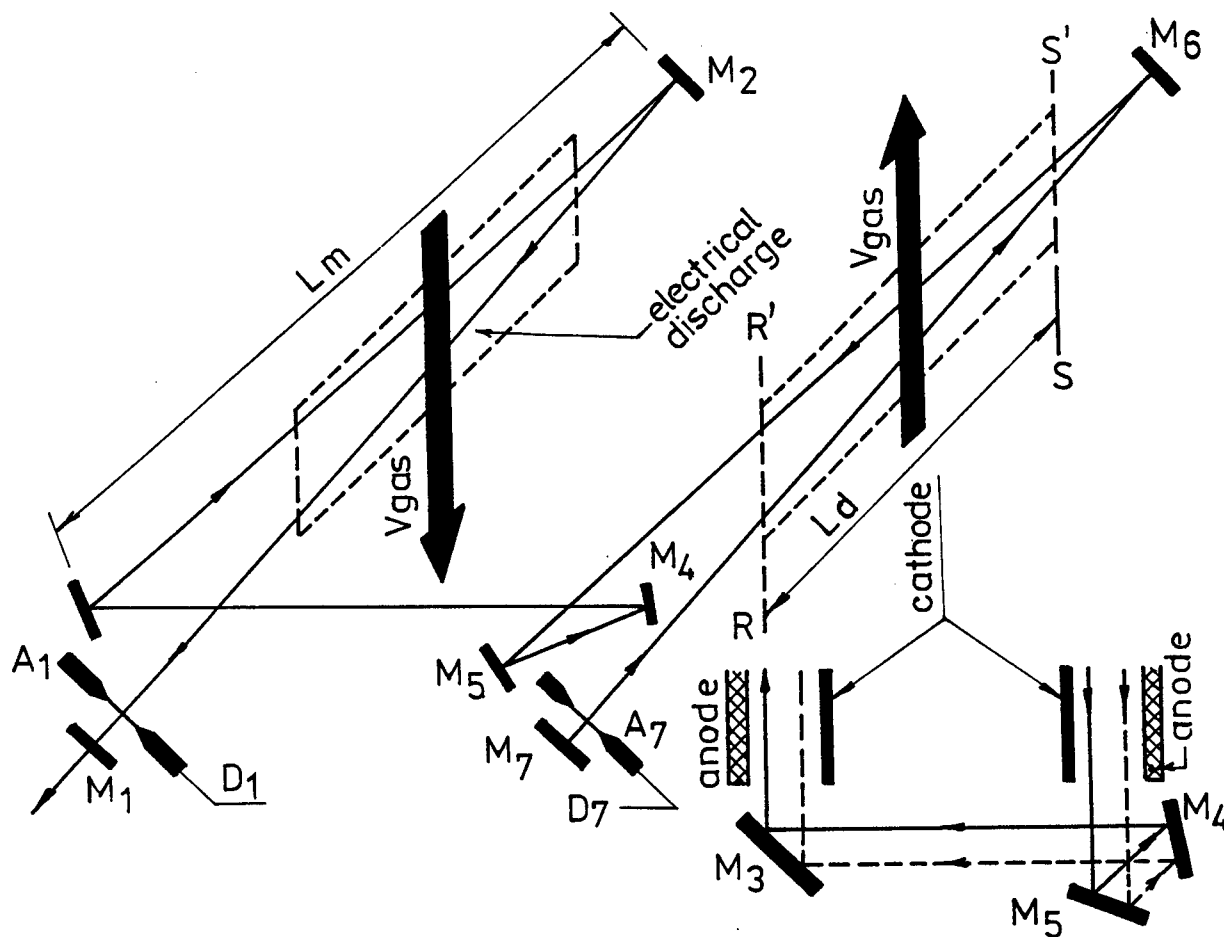


Fig.3 - Double V optical resonator with a mirrors system (M_4, M_5) used for 90° ray deflection and wave front reversal, by which is obtained:

- increasing of the matching coefficient - η_m and compensation of the asymmetry along the flow direction
- compensation of the gain and refractive index asymmetry on the anode-cathode direction

For increasing the active medium volume V_m in condition $N_F < 1.5(2.5)$, we have used a double V optical resonator - fig.3 - with 7.7 optical path length. Using the fig.4 we obtain: $\phi_B(N_F = 1.3) = 20$ mm, $\phi_B(N_F = 1.87) = 24$ mm and $V_m(N_F = 1.3) = 1500$ cm³, $V_m(N_F = 1.87) = 2000$ cm³.

For the increasing of the matching coefficient value - η_m , we have to take into account the simetrization possibility (on anode - cathode direction)⁴ of the gain and refractive index profile, offered by (M_4, M_5) mirror system. Therefore the anode - cathode distance was adjusted at the value - $h_{a-c} = 31$ mm. So, all electrical discharge - fig.4 - was enclosed in the mode volume with $\phi_B(N_F = 1.87) = 24$ mm diameter. In these conditions results a matching coefficient $\eta_m(N_F = 1.3) = 0.65$ and $\eta_m(N_F = 1.87) = 0.83$ comparable with that obtained in FAF (fast axial flow laser). The middle position of the optical axis (l_0, h_0) - on parallel and perpendicular to flow direction - was established under requirement that $\eta_m(N_F = 1.87) = \text{maximum}$ - fig.4.

In fig.5 and fig.6 it is shown a photograph of the rear and front plate of the resonator plates.

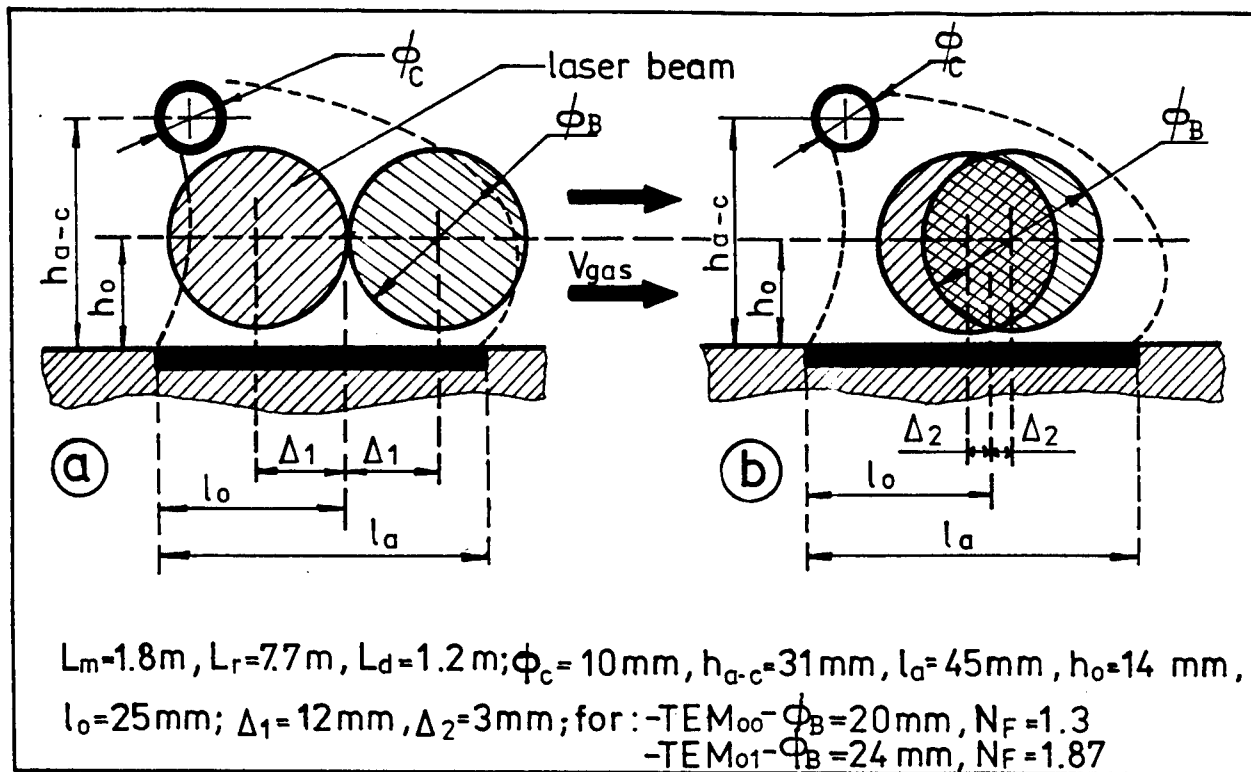


Fig.4 - Design of the discharge region (for $N_F < 1.2$ (2.5)) correspondingly to $\text{TEM}_{00/01}$)when a double V resonator - as in fig. 3 - with 7.7 m length of the optical path is used. a, b - cross section through the electrical discharge in the region (R - R') respectively (S - S'). L_r - optical path length inside optical resonator; $N_F = \phi_B^2 / 4\lambda L_r$ - Fresnel number

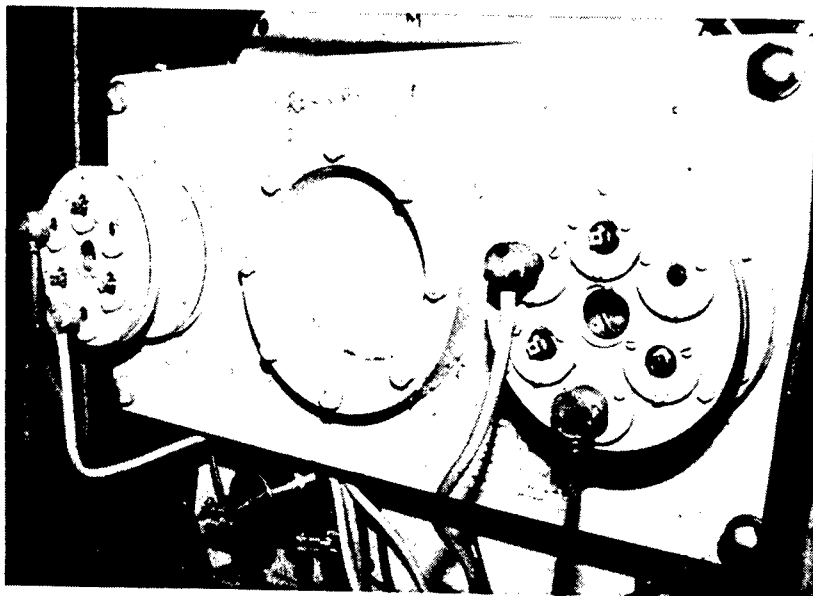


Fig.5 - Photograph of the rear plate resonator assembly (where M_2 and M_6 mirrors are placed)

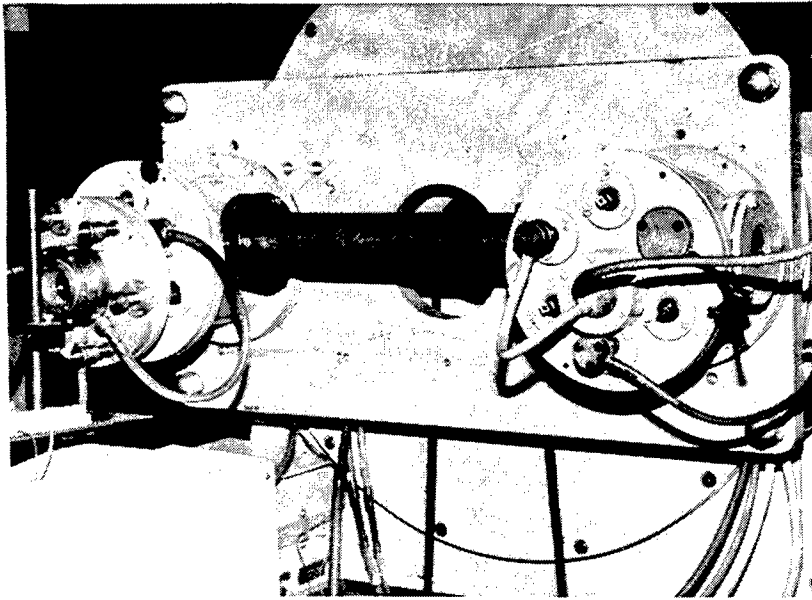


Fig.6 - Photograph of the front plate resonator assembly (where output and end mirror are externally placed and M_3 , M_4 , M_5 are inner mirrors)

3. EXPERIMENTAL RESULTS

By adjusting the A_1 and A_2 apertures - fig.3 - different optical resonator Fresnel numbers in the range of $1 < N_F < 2.5$ might be obtained. The laser beam has been analysed in near field (at 1 m distance from the output mirror) and in far field (in the focus of a mirror with $R = 3$ m curvature radius) by measuring the burning profile in a Plexiglas plate. Different coupling and end mirror have been used.

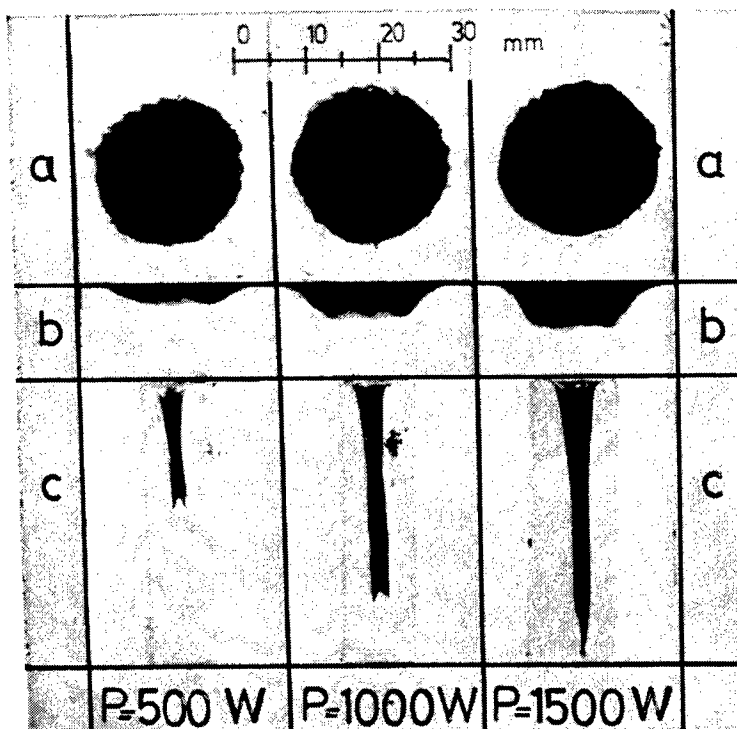


Fig.7 - Beam patterns (burning profile on a plexiglas plate) of the multimod laser beam at different laser power levels;

- a and b - near field at 1 m distance from the output mirror, front view and respectively cross section (on anode-cathode direction); the irradiation time was 4 s.

c - far field in the focus of a 3 m concave mirror; the irradiation time was approximately 1.5 s

M_1 - GaAs uncoated, transmission - $T = 72\%$, curvature radius - $R_1 = 40$ m; aperture $D_1 = 25$ mm;

M_7 - Cu mirror, gold coated, $R_7 = 16$ m, without aperture

As an example, in fig.7 (M_1 : GaAs, $T = 72\%$, $R_1 = 40$ m, $D_1 = 25$ mm; M_7 : Cu mirror, $R = 16$ m, without aperture) is shown an uniform intensity distribution with two transversal oscillation modes (observed in far field profile). To note that the intensity profile shape (in near field and far field) is unchanged for different laser power levels. The resulting laser beam - 22 mm diameter and approximately 2.5 mrad divergence - is suitable for practical purposes. A maximum 1800 W laser power has been obtained.

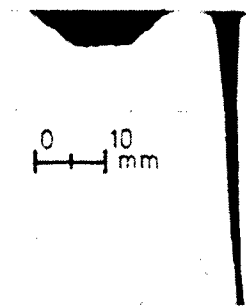


Fig.8 - Beam patterns (left - near field, right - far field; the irradiation time - 3s respectively 1.5s) of a laser beam where a 20 mm aperture at the output mirror was used; 600 W laser power; M_1 - GaAs, $R_1 = 40$ m, $T = 72\%$, $D_1 = 20$ mm; M_7 - Cu mirror, $R_7 = 16$ m, without aperture

A single mode distribution (fig.8) has been achieved by adjusting the apertures A_1 at the output mirror ($D_1 = 20$ mm, M_7 - without aperture). The laser beam which was obtained (15 mm diameter, 1.5 mrad divergence) is suitable to be focused by a $f = 5$ cm lens, which is important for our applications.

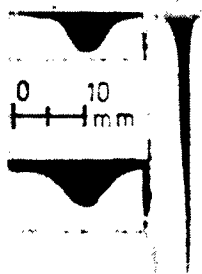


Fig.9 - Beam patterns of a laser beam when $D_1 = 20$ mm, $D_7 = 20$ mm apertures were used (at the output mirror respectively and mirror); left -near field, right far field; M_1 - GaAs, $T = 72\%$, $R_1 = \infty$, M_7 - Cu mirror, $R_7 = 16$ m (or 21 m)

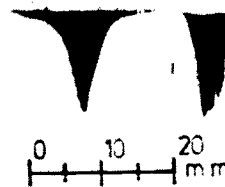


Fig.10 - Far field for the laser beam described in fig.9, at 800 W laser power level; (left - near field; right - far field; the irradiation time - approximately 2 s)

By adjusting the aperture A_7 ($D_7 = 20$ mm at the end mirror) a beam pattern of the type TEM_{00} was obtained - fig.9. In this case it was possible to continuously increase the laser power up to about 600 W. The exceeding of this limit leads to a practically useless laser beam - fig.10 - both intensity profiles (near field and far field) a strongly disturbed. This denotes an increase by a factor of four of the divergence of the laser beam. We have tried to eliminate this effect - due to the thermal deformation of the GaAs mirror (2.5% absorption in our case) by using a high radius of curvature ($R = 40$ m) on an output mirror (the results are presented in fig.7).

Also, we have to emphasise the high stability of the optical resonator (which is formed by 7 mirrors and has a 7.7 m optical path). This stability is due to the remarkable properties of the 90° deflection optical element which is made by the mirrors M_4 and M_5 (see fig.2). Constructively, this was built by a single metal piece on which the M_4 and M_5 mirrors were mounted, with a 45° relative angle. This element - fig. 11 - has properties similar with a pentaprism and we consider that it might be successfully utilised in the construction of optical resonators and in different other systems of leading and focusing of high power laser beams.

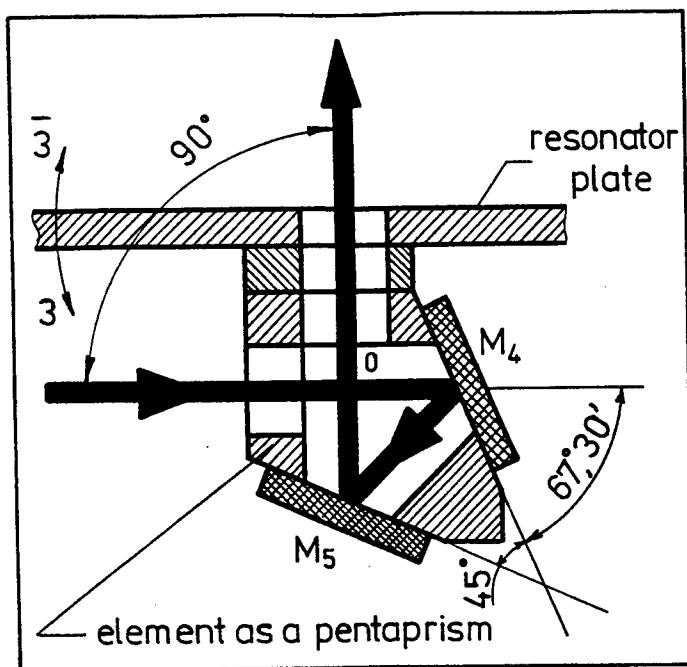


Fig.11 - One piece element for 90° deflection of the laser beam (used for mirrors assembly M_4 , M_5) that exhibit properties alike pentaprism: the same exact 90° - degree deviation angle applies to all rays transmitted by the useful aperture - regardless of the angles between these rays and the optical axis (or entrance and exit face normal).

4. CONCLUSIONS

- Was developed a new optical resonator for TFL with a matching coefficient $\eta_m \cong 0.8$ and a Fresnel number $N_F < 2$ in which the asymmetries of the active medium are compensated. This leads to the increase of the total laser efficiency for beam intensity distribution $TEM_{00/01}$ (in accordance with $N_F < 2$). Also, the shape of the laser beam profile intensity is unchanged for different laser power levels. The main elements for this resonator are:

- gas circulation fluidodynamical circuit in cylindrical geometry with two opposite discharges³;
- 90° deflection device (pentaprism alike) which reverse the wave front;

- Also, it was developed a new very stable 90° beam deflection optical element with properties alike pentaprism. This element might be used in optical resonator construction, transport and focusing systems of the laser beam, a.s.o

- The use of a GaAs uncoated mirror ($T = 72\%$) was possible (due to high value of the small signal gain characteristic to TFL and to long amplification path present in this gas circulation fluidodynamical circuit and optical resonator configuration). This is a great practical interest in the field of very intense laser beams. Also the lifetime of the output mirror will be increased.

5. ACKNOWLEDGEMENTS

The authors are indebted to Dr. D. Levhovici and M. Paraschiv from the ICPAM - Galati, which offer us the opportunity to utilise their GT-1200 laser and their facilities.

6. REFERENCES

1. A. Sona, "RF and DC excited high power CO_2 lasers", *SPIE Vol.801 High Power Lasers* (1987), p. 23
2. I.Gutu, M.L.Pascu, "A new design for high power transverse - flow CO_2 lasers", *Laser and Optoelectronik*, Vol. 24(4), p. 37 (1992)
3. I. Gutu, T. Julea, V. Draganescu, D. Dumitras, I.N. Mihailescu, R. Medianu, "Development of a high power gas transport CO_2 laser with cylindrical geometry", *Optics and Laser Technology*, Vol. 18, No.6, p. 308(1986)
4. I. Gutu, M.L.Pascu, "New design of the high power CO_2 lasers for industrial applications", *Institute of Atomic Physics - LOP-83-1992*, p.35, March (1992)

Comparison between "Method of Lines" and "Time Domain Method" in evaluating the large signal responses of Fabry-Perot semiconductor lasers

Ada Livia Braverman

University "Politehnica" of Bucharest,
Faculty of Electronics and Communications, TEF Department,
Blvd. Iuliu Maniu 1-3, 77202, Bucharest

ABSTRACT

An extensive comparison between two modeling methods: Method of Lines (ML) and Time Domain Method (TDM) in analyzing the large signal responses of Fabry-Perot (FP) semiconductor lasers is presented. The methods are implemented in two numerical codes written in FORTRAN and using DIGITAL ALPHA workstations under VAX/VMS and UNIX operating systems. The comparison shows good agreement between the simulation results under specific conditions. A special accent is placed on the advantages and drawbacks of both methods by taking into account their numerical problems and the computational effort implied by simulations.

Keywords: Fabry-Perot semiconductor lasers, large signal response, Method of Lines, Time Domain Method

1. THEORETICAL APPROACH

1.1 The mathematical model

The starting point of both numerical methods used in evaluating the large signal response of FP semiconductor lasers is a set of three equations:

$$\frac{1}{v_g} \frac{\partial A^+(z,t)}{\partial t} + \frac{\partial A^+(z,t)}{\partial z} = (g - \alpha_{int} - i\delta) A^+(z,t) + T_p^+(z,t) \quad (1)$$

$$\frac{1}{v_g} \frac{\partial A^-(z,t)}{\partial t} - \frac{\partial A^-(z,t)}{\partial z} = (g - \alpha_{int} + i\delta) A^-(z,t) + T_p^-(z,t) \quad (2)$$

$$\frac{dN(z,t)}{dt} = \frac{I}{eLwd} - \frac{N(z,t)}{\tau} - BN^2(z,t) - CN^3(z,t) - 2v_g g \frac{P}{\Gamma} \quad (3)$$

which represent the traveling wave equations for the forward and reverse optical waves in the laser cavity, (1) and (2), and the rate equation for the carrier density, (3). In these equations:

- (i) $A^+(z,t)$ and $A^-(z,t)$ are the slowly varying complex envelope amplitudes of the forward and reverse optical fields,
- (ii) v_g is the group velocity,
- (iii) t and z represent the time, respectively the space coordinate,
- (iv) g accounts for the optical gain and has the expression:

$$g(z,t) = \frac{1}{2} \Gamma \frac{\partial g}{\partial N} (N(z,t) - N_0) \quad (4)$$

where Γ is the optical confinement factor, $\partial g / \partial N$ is the differential gain (assumed constant) and $N(z,t)$ is the carrier density, (v) α_{int} represents the absorption and scattering loss in waveguide, (vi) δ is the detuning caused by changes in the refractive index due to changes in the carrier density and is given by:

$$\delta(z,t) = -\frac{\omega_0}{c} \cdot \frac{\lambda}{4\pi} \Gamma \frac{\partial g}{\partial N} \alpha_h (N(z,t) - N_0) \quad (5)$$

where ω_0 is the central pulsation, λ is the emission wavelength, α_h the linewidth enhancement factor, N_0 the carrier density at transparency and c is the light velocity in vacuum,

(vii) I is the pumping current, L the cavity length, w the width of the active region, d the thickness of the active region, τ is the carrier lifetime, B the bimolecular coefficient, C the Auger coefficient.

The optical fields are normalized to give the photon density as follows:

$$P(z,t) = |A^+(z,t) + A^-(z,t)|^2 \quad (6)$$

(viii) $T_p^+(z,t)$ and $T_p^-(z,t)$ are the spontaneous emission terms. We consider the same expression for both. The spontaneous noise source $T_p(z,t)$ is taken complex, zero mean and Gaussian distributed with the autocorrelation function given by:

$$\langle T_p(z,t) T_p^*(z,t') \rangle = \frac{\beta \Gamma B N^2(z,t)}{Lv_g} \delta(t-t') \delta(z-z') \quad (7)$$

where β is the spontaneous coupling factor, $\delta(t-t')$ and $\delta(z-z')$ are Dirac functions. The large-signal model presented above is developed in several papers^{1,2} for the evaluation of dynamics of distributed feedback (DFB) and colliding-pulse mode-locked (CPM) semiconductor lasers. We adapted this model for the study of a FP laser diode. The gain saturation effect and gain dispersion are neglected in a first approximation.

1.2 Description of the numerical methods

The first step, valid for both numerical methods is to discretize in one dimension the laser cavity along the cavity axis using equal space intervals. The uniform mesh is convenient and may be used here since no special problems appear as in the case of semiconductor lasers with different cavity regions (e.g. CPM semiconductor lasers which contain saturable absorbers). However, the problem of choosing the number of discretization points still remains. The slowly varying envelopes of the optical waves allow the fields to be sampled below the Nyquist frequency, thereby avoiding any aliasing problems. As a general consideration for both numerical methods, the number of discretization points is taken such that the beat period T_b between sequential modes must be longer than the sampling time interval. Besides, some particular aspects must be taken into account when dealing with each method.

To impose the initial conditions, the laser is considered at the beginning under the threshold operation. The values of the phases of the optical fields are initially set to zero.

1.2.1 Method of Lines

ML is a hybrid method. The space derivatives in equations (1) and (2) are approximated using the Finite Difference Method (FDM). Hence, the system composed from equations (1), (2) and (3) becomes an ordinary differential equations system in function of time. A numerical solution is obtained by using a Runge-Kutta-Verner integration method (RKVM) with adaptative step for nonstiff systems. The boundary conditions at the cleaved facets are given as:

$$\begin{aligned} A^+(0,t) &= R \cdot A^-(0,t) \\ A^-(L,t) &= R \cdot A^+(L,t) \end{aligned} \quad (8)$$

where R is the reflection coefficient, considered equal and phase independent for both facets.

When the space derivatives are approximated using (FDM), two different calculus scheme can be used. If np is the number of calculus points, the first scheme consists in approximating all the space derivatives in both equations (1) and (2) with central differences, beginning with the 2nd point and ending with the $(np-1)$ -th one. As noted in equations (8), at the left cleaved facet of the laser the value of the forward optical field is determined from the reverse optical field value. Therefore, it is sufficient to approximate in this point only the space derivative in equation (2). Obviously, a forward difference formula must be used. The same problem is for the point on the right facet, but this time the space derivative in the first equation is approximated with a backward difference formula, while the reverse optical field value in this point is determined from the value of the forward optical field. The other scheme is to use only backward differences to approximate the space derivatives in equation (1), while forward differences are used only to approximate the space derivatives in equation (2). The remark regarding the boundary points remains valid. Although the first alternative (with hybrid FDM) seems to have a higher order of accuracy, the use of forward/backward differences at the boundaries leads to a decreasing of the overall accuracy. Much more the numerical solution is instable and nonconvergent as will be seen in section 2.

1.2.2 Time Domain Method

The forward and reverse optical fields are sampled as in the case of ML along the laser cavity at a number of points separated by regular intervals Δz . The equations (1) and (2) are then used to estimate the values of the optical fields at time

$t+\Delta t$, in terms of the fields at time t , where $\Delta t=\Delta z/v_g$. The forward and reverse optical fields are thus implicitly sampled both in space and time. We do not detail here this method since it is already presented³. By introducing a "complex instantaneous frequency" updated at each time step and in each calculus point, equations (1) and (2) are written together as a typical eigenvalue and eigenvector system. It is assumed that the instantaneous frequency remains constant throughout one time step Δt which is equivalent to the sampling criteria mentioned above. The rate equation for the carrier density is separately solved at each time step and in each calculus point by a first order Newton-Raphson method, after equations (1) and (2) are solved. The boundary conditions are imposed in the same manner as in equation (8).

2. SIMULATION RESULTS

A numerical analysis of the large signal response gives information about the laser dynamics which could be very useful for example in evaluating the gain-switching operation regime. In our simulations, a generic FP semiconductor laser was used with two different sets of parameters which are given in appendix, in Tables 1 and 2. We wrote two FORTRAN codes that have been used in simulations. We will discuss first some numerical problems that occur when ML is used. The comparative simulations between ML and TDM will be presented further.

2.1 The instable solution of ML with hybrid FDM

The length of the laser cavity is 300 μm and 301 discretization points are taken. Hence, the spatial step is, $\Delta z=1 \mu\text{m}$ and the time step is $\Delta t=\Delta z/v_g$ equal to 12.3 fs. The beat period is equal to the round-trip time in the cavity: 7.5 ps. The sampling criteria is thus fulfilled, as discussed in section 1.2. The device parameters are given in Table 1. When the applied current has a step variation at $t=0$ from 0 to a value of 85 mA (three times greater than the threshold value which is ~ 28.32 mA) the laser exhibits relaxation oscillations until the steady state is reached. The carrier density has a complementary time evolution with respect to the photon density. The numerical solution is not convergent when ML with hybrid FDM is used to solve the system composed by the equations (1), (2) and (3). Fig. 1 illustrates the normalized carrier density against the number of round-trips for two calculus points, at the right facet and in the center of the cavity. The normalization constant is taken equal to 10^{24} m^{-3} . The overall profile of the carrier density in the cavity vs the number of round-trips is perfectly

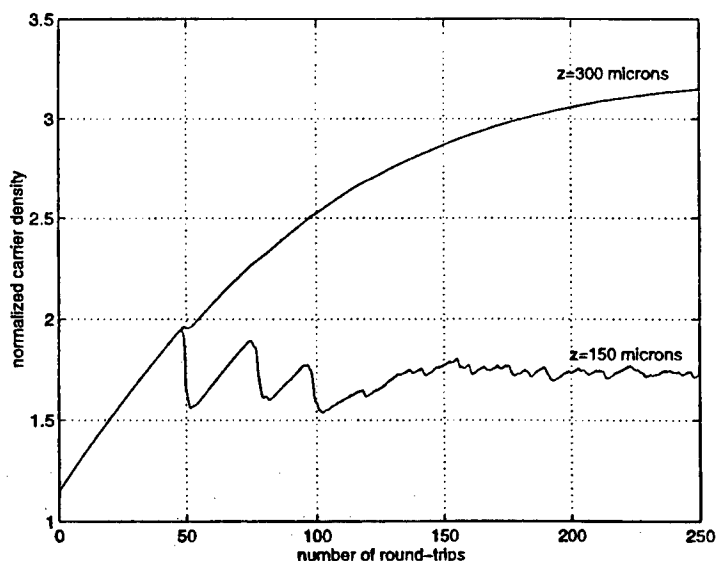


Fig. 1. Normalized carrier density for two cavity sections vs the number of round-trips.

symmetric with respect to the middle calculus point. Toward the steady state, the normalized carrier density seems to converge despite of some small discontinuities due to numerical errors, but the normalized calculated value at the steady state is slightly different (~ 1.94) from that shown in the graphic. However, this solution has no physical meaning. First, it is not possible to obtain such a great difference between the values at the facets and those in the middle section. Second, at the steady state the carrier density must be smaller at the boundaries than in the center. This is because the photon density at the facets is greater at the output than in the center of the cavity. Although we do not have an exact explanation of this numerical effect, it is clear that it is due to the instability generated by using a hybrid FDM. Much more, although the central differences are more accurate than the forward/backward ones, this scheme does not respect the causality principle. The central differences always use the "next" calculus point to estimate the value in the precedent point. According to the conventional direction of

propagation, at this time the value in the "next" point is unknown. Finally, the RKVM may contribute to the propagation of the numerical errors due to the intrinsic calculus method. Taking into account the above considerations, the simple forward/backward difference scheme is preferable.

2.2 The numerical "filtering" effect of the forward/backward difference scheme

Although less accurate, a simple forward/backward difference scheme used within ML is always stable and the numerical solution is convergent. For a 800- μm long cavity and 301 discretization points, the photon density at the right facet of the laser is presented in Fig. 2, while for 1001 calculus points is illustrated in Fig. 3. The device parameters are given in Table 2. In both cases the sampling condition is fulfilled. Here, trt is the round-trip time.

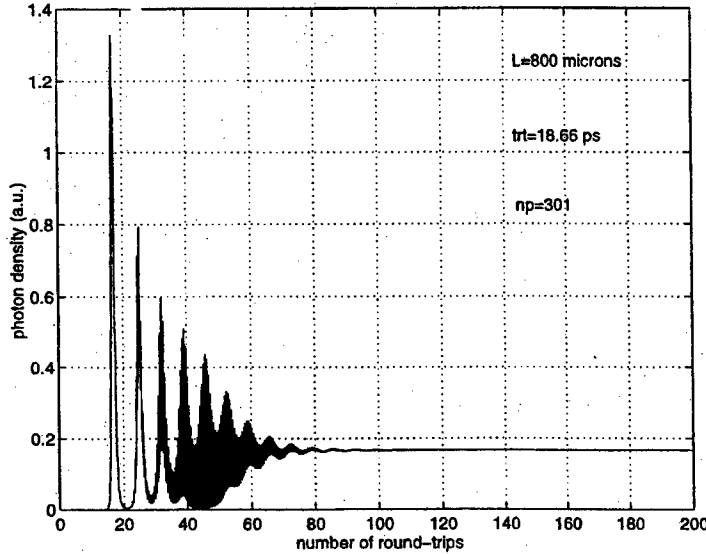


Fig. 2. Photon density at the output of the laser ($z=800 \mu\text{m}$) against the number of round-trips ($np=301$).

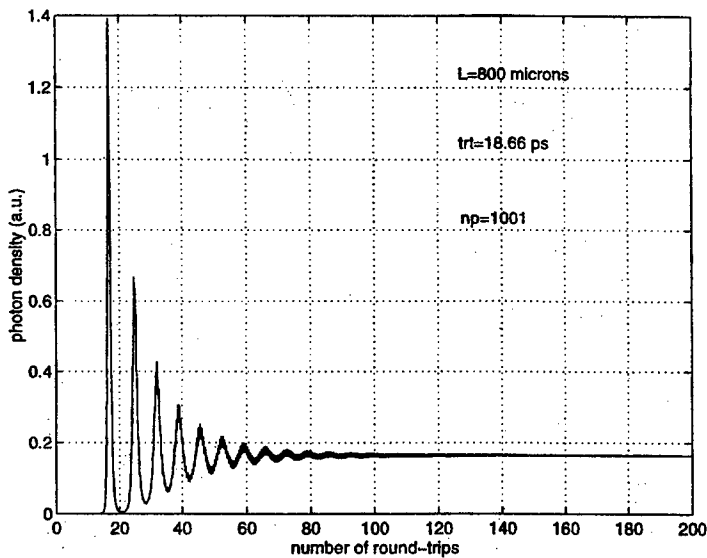


Fig. 3. Photon density at the output of the laser ($z=800 \mu\text{m}$) against the number of round-trips ($np=1001$).

The laser reaches the steady state in both cases after being pumped with a current step from 0 to 100 mA (the threshold current is 18.33 mA). No discontinuities due to numerical effects are observed as in Fig. 1. Since the forward/backward difference scheme is first order accurate a sufficiently large number of discretization points must be taken in order to obtain a correct solution. If this condition is not fulfilled, numerical errors could occur. This is the case in Fig. 2, where 301 discretization points are not enough. The dark zone when the laser is still oscillating does not represent the beats between the cavity modes but a numerical noise. Increasing the number of discretization points, the solution becomes more accurate. However, these beats are not obtained in both cases. The solution is not realistic, since a FP laser is multimodal. If one takes into account Fig. 3 and performs a spectral analysis of the photon density for the last 100 round-trips, one will see only two spectral lines: one of them on the central frequency (corresponding to the emission wavelength) and the other at small frequencies ($\sim\text{GHz}$) corresponding to the slow variable relaxation oscillations toward the steady state. In conclusion, the forward/backward difference scheme presents a numerical "filtering" effect as it cuts off the other frequencies corresponding to the cavity modes. By using this scheme it is equivalent to adding an artificial diffusion term and then using the central difference scheme to approximate the space derivatives of this new problem. For this reason the scheme will smooth out the discontinuities or the corners of the solution. This effect is usually referred to by saying that the scheme is dissipative⁴. As $\Delta z \rightarrow 0$, the approximation will converge toward the true solution. As expected, the fast variations due to the beats between the cavity modes are smoothed out. An important role is played also by the integration method (RKVM). The time integration step must be no longer than $\Delta t = \Delta z/v_g$, but may be of course smaller. The last alternative is not very convenient because it increases the computational

time. Besides, RKVM used in our simulation is a five order accurate method with adaptative step. For a single simulation 200 round-trips of transient regime, with 301 calculus points, the computational time is about 6 hours on a DIGITAL ALPHA workstation under VAX/VMS operating system. Figure 4 illustrates the normalized carrier density along the cavity axis vs the number of round-trips for $np=1001$. The normalization constant is equal to 10^{24} m^{-3} . The normalized value of the carrier density at steady state is equal to 1.55. As seen, the numerical solution tends to this value.

The carrier density profile is symmetric with respect to the middle calculus point. Near the cleaved facets the values of the carrier density decreases slightly which corresponds to the reality. In the center, the carrier density exhibits a slight curvature. The difference between the values in the center and those at the boundaries is of the order of 10^{-2} , in normalized values.

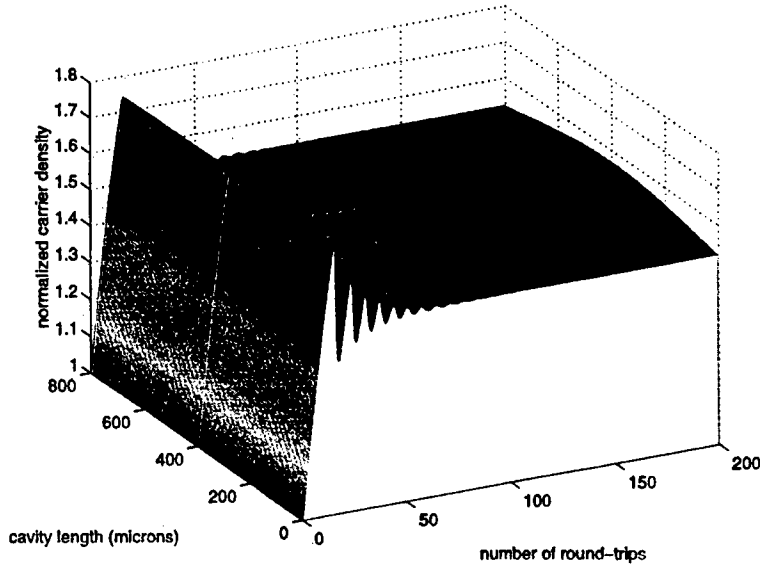


Fig. 4. Normalized carrier density along the cavity axis as a function of the number of round-trips ($n_p=1001$).

2.3 Comparative results

The device parameters are given in Table 2. In simulations using ML 301 discretization points are used, while for TDM only 40 calculus points are enough. In both cases the sampling condition is fulfilled. The amplitude of the current step is taken equal to 85 mA. As seen in Fig. 5, where the photon densities are represented vs the number of round-trips, the steady state is not yet reached. Despite of a great difference between the two numerical methods, the solutions are quite similar. In the case of TDM solution, the beats between the cavity modes are put into evidence by the dark zone under the photon density envelope (Fig. 5, (b)). As presented in section 1, the gain dispersion was neglected in a first approximation, thus all the cavity modes compete equally. The numerical effect of "filtering", due to the FDM is clearly seen in Fig. 5, (a). One can see that the photon density in this case represents the envelope of the photon density obtained with TDM. Small differences between values in both cases could appear because the numerical codes use different random generators to simulate the spontaneous emission term.

The carrier density vs the number of round-trips have similar profiles for both cases. We considered that the picture showing the photon density vs the number of round-trips is sufficiently relevant for our comparison, hence we do not illustrate the carrier densities against the number of round-trips.

The example presented above shows good agreement between both numerical methods.

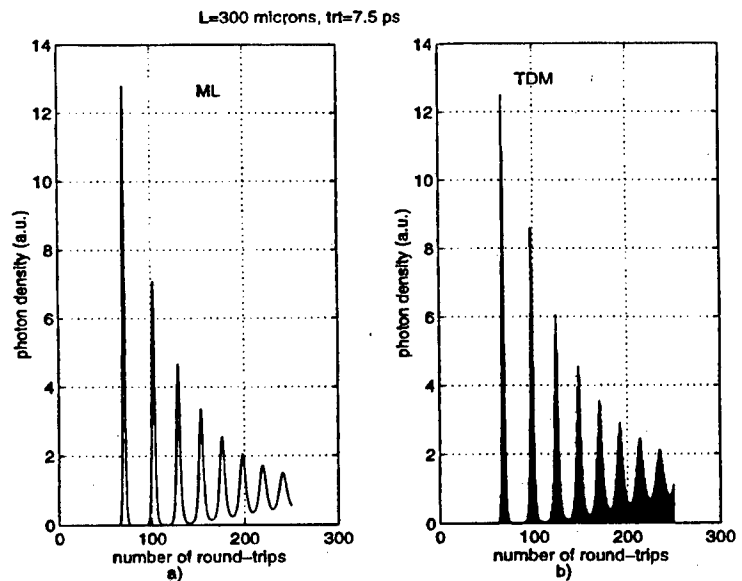


Fig. 5. Photon density at the laser output against the number of round-trips: a) solution obtained with ML; b) solution obtained with TDM.

It is possible to obtain accurate results using ML, but only with forward/backward differences and using a large number of discretization points. Moreover, an aspect which was not put into evidence until now is the possibility to obtain a more realistic solution by introducing a numerical filter to simulate the gain dispersion. A first order infinite impulse response filter was already presented³. The difference between ML and TDM in solving the system of equations, assures a very simple implementation of the digital filter in the case of TDM, but renders quite impossible its implementation in ML, due in principal to the use of an integration method. Instead, ML could solve a more complex system of equations, where second order terms due to the material and gain dispersion are taken into account. Unfortunately the system becomes stiff and special integration methods must be used. The problem becomes very difficult because of the high computational time for solving the equations.

3. CONCLUSIONS

In this paper, two numerical methods, ML and TDM are discussed. Their performances are analyzed from the point of view of the calculus time, computational effort and accuracy. A special accent is placed on the numerical problems encountered in simulations using ML, since this part was particularly developed by us. Very powerful computers are needed to solve accurately the partial differential equations system, when ML is used. Only the forward/backward difference scheme for ML provides correct solutions. On the other hand, in spite of the high computational time, ML allows a better control of the accuracy by setting the tolerance of the integration method with adaptative time step. Besides, ML allows a relative independence between the space interval and the time interval, while TDM does not have this advantage. However, the reduced computational effort and time and its simplicity, nominate TDM as an efficient simulation tool of the large signal responses of semiconductor lasers.

4. APPENDIX

TABLE 1⁵: Device parameters (model 1)

Cavity length, L	$300 \cdot 10^{-6} \text{ m}$
Cavity volume, $Vol=L \cdot w \cdot d$	$180 \cdot 10^{-18} \text{ m}^3$
Reflection coefficients, R_1, R_2	0.32
Optical confinement factor, Γ	0.35
Group refractive index, n_g	3.7
Differential gain, $\partial g / \partial N$	$2.96 \cdot 10^{-20} \text{ m}^2$
Linewidth enhancement factor, α_h	2.0
Absorption loss, α_{int}	4000 m^{-1}
Transparency carrier density, N_0	$1.2 \cdot 10^{24} \text{ m}^{-3}$
Carrier lifetime, τ	$5 \cdot 10^{-9} \text{ s}$
Bimolecular coefficient, B	$10^{-16} \text{ m}^3 \cdot \text{s}^{-1}$
Auger coefficient, C	$10^{-41} \text{ m}^6 \cdot \text{s}^{-1}$
Emission wavelength, λ	$1.55 \cdot 10^{-6} \text{ m}$
Spontaneous coupling factor, β	10^{-4}

TABLE 2: Device parameters (model 2)

Cavity length, L	$800 \cdot 10^{-6} \text{ m}$
Cavity volume, $Vol=L \cdot w \cdot d$	$96 \cdot 10^{-18} \text{ m}^3$
Reflection coefficients, R_1, R_2	0.30
Optical confinement factor, Γ	0.05
Group refractive index, n_g	3.5
Differential gain, $\partial g / \partial N$	$1.49 \cdot 10^{-19} \text{ m}^2$
Linewidth enhancement factor, α_h	2.0
Absorption loss, α_{int}	2880 m^{-1}
Transparency carrier density, N_0	$1.2 \cdot 10^{24} \text{ m}^{-3}$
Carrier lifetime, τ	$3 \cdot 10^{-9} \text{ s}$
Bimolecular coefficient, B	$1.3 \cdot 10^{-16} \text{ m}^3 \cdot \text{s}^{-1}$
Auger coefficient, C	$10^{-40} \text{ m}^6 \cdot \text{s}^{-1}$
Emission wavelength, λ	$1.51 \cdot 10^{-6} \text{ m}$
Spontaneous coupling factor, β	$3 \cdot 10^{-4}$

5. REFERENCES

1. L. M. Zhang, S. F. Yu, M. C. Nowell, D. D. Marcenac, J. E. Carroll, and R. G. S. Plumb, "Dynamic analysis of radiation and side-mode suppression in a second-order DFB laser using time-domain large-signal traveling wave model", *IEEE Journal of Quantum Electronics*, **30**(6), 1389-1395 (1994).
2. L. M. Zhang and J. E. Carroll, "Dynamic response of colliding-pulse mode-locked quantum well lasers", *IEEE Journal of Quantum Electronics*, **31**(2), 240-243 (1995).
3. D. J. Jones, L. M. Zhang, J. E. Carroll, and D. D. Marcenac, "Dynamics of monolithic passively mode-locked semiconductor lasers", *IEEE Journal of Quantum Electronics*, **31**(6), 1051-1058 (1995).
4. N. Bellomo, L. Preziosi, *Modelling Mathematical Methods and Scientific Computation*, pp. 263, CRC Press, Inc., Boca Raton, 1995.
5. P. P. Vasil'ev, *Ultrafast diode lasers (fundamentals and applications)*, pp. 56, Artech House, London, 1995.

A generalised model for cw three-micron emission in concentrated Er systems

Voicu Lupei and Serban Georgescu

National Institute for Lasers, Plasma and Radiation Physics, Bucharest, Romania

ABSTRACT

A generalised model of the cw three-micron emission in concentrated Er systems, which takes into account the whole variety of de-excitation processes is presented. The analytical equation for the flux of light enables a direct correlation of the parameters of emission (threshold, slope efficiency) with the spectroscopic parameters and pump conditions. The effect of excited state absorption is, also, put in evidence.

keywords: mid infrared lasers; Er^{3+}

1. INTRODUCTION

Despite of a much shorter lifetime of the emitting level ($^4I_{11/2}$), as compared to the terminal laser level ($^4I_{13/2}$), efficient three-micron room temperature laser emission between these two levels was obtained in concentrated Erbium systems¹⁻³. The models proposed to explain the absence of self-saturation of this transition could be grouped in two classes, one based on the excited state absorption (ESA) from the terminal laser level⁴ and the other, based on co-operative up-conversion inside the system of Er^{3+} ions⁵⁻⁷. The presence of efficient laser emission in concentrated systems favours the last model.

For the stationary regime of generation (cw or long pulse) our investigations^{8,9} show that the system of rate equations including the populations of all the Erbium energy levels involved, by pump or by energy transfer, in the three-micron emission and the photon flux density, can be solved analytically, the influence of the various energy transfer processes on the laser characteristics being expressed by specific figures of merit¹⁰.

Based on the analytical expressions obtained for the population inversion, photon flux density, and quantum efficiency, we discuss the role of the different interactions which could make possible efficient three-micron generation on the self-saturated transition $^4I_{11/2} \rightarrow ^4I_{13/2}$. This model, confirmed by a large bulk of experimental data, show that in concentrated Erbium systems, although ESA from the terminal laser level could improve the parameters of emission, the driving mechanism for three-micron generation is the co-operative up-conversion from the terminal laser level.

2. THREE-MICRON GENERATION ON THE SELF-SATURATED TRANSITION $^4I_{11/2} \rightarrow ^4I_{13/2}$

To explain the efficient three-micron room-temperature laser on $^4I_{11/2} \rightarrow ^4I_{13/2}$ transition we shall discuss first the "self-saturation condition". In fact, this condition is not $T_2 < T_1$ but $\alpha T_2 < \beta_{21} \beta T_1$ ¹¹, where α , β are the Boltzmann population coefficients of the Stark sublevels involved in the laser transition and β_{21} is the fraction of excitation from the initial laser level that reaches, radiatively or non-radiatively, the terminal laser level. The possibility to overcome this condition depends of the specific transition (via the Boltzmann coefficients α , β) and of the host crystal (T_1 , T_2 and β_{21}). For example, the 2.81 μm transition of Er: YLiF₄¹² ($\alpha=0.201$, $\beta=0.113$, $\beta_{21}\approx 0.6$, $T_1 = 10$ ms, $T_2 = 4$ ms (our measurements)), but for no transition in Er: YAG¹³, where $T_1 \approx 6$ ms and $T_2 \approx 0.01$ ms. To explain the efficient cw (or long pulse) operation of Er: YAG laser¹⁴ co-operative up-conversion or ESA from $^4I_{13/2}$ must be considered.

There are two main up-conversion (two-ion) mechanisms acting in Erbium systems at high concentrations:

(i) up-conversion from $^4I_{13/2}$ (Fig. 1a): $(^4I_{13/2} \rightarrow ^4I_{15/2}) + (^4I_{13/2} \rightarrow ^4I_{9/2})$, proposed in ¹⁴. This "positive" mechanism takes out two excitations from $^4I_{13/2}$ and adds one two $^4I_{11/2}$ (via the efficient multiphonon transition $^4I_{9/2} \rightarrow ^4I_{11/2}$);

(ii) up-conversion from $^4I_{11/2}$ (Fig. 1b): $(^4I_{11/2} \rightarrow ^4I_{15/2}) + (^4I_{11/2} \rightarrow ^4F_{7/2})$ proposed in ¹⁵. This "negative" mechanism depletes the initial laser level.

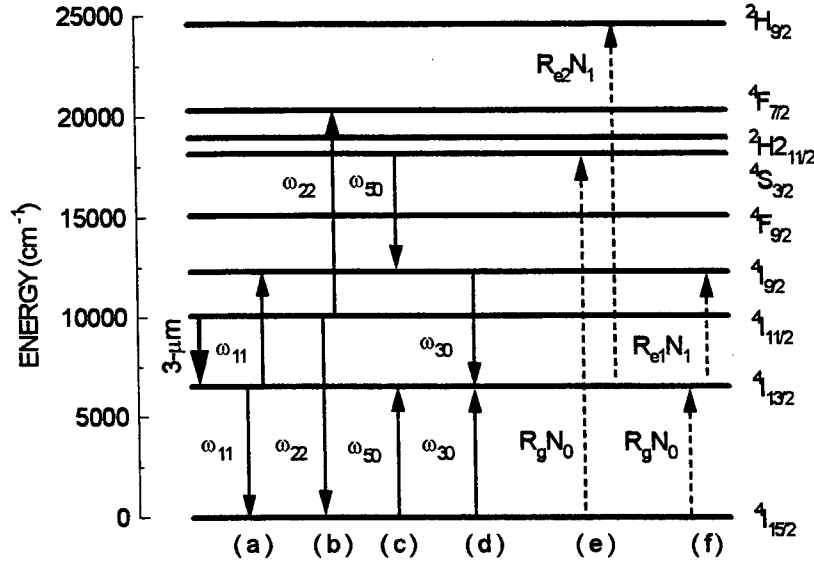


Fig. 1. Energy level scheme of Er^{3+} and the main processes responsible for three-micron lasing: (a) - co-operative up-conversion from $^4I_{13/2}$; (b) - co-operative up-conversion from $^4I_{11/2}$; (c) - cross-relaxation from $^4S_{3/2}$; (d) - cross-relaxation from $^4I_{9/2}$; (e) - ESA for pumping in $^4S_{3/2}$; (f) - ESA for pumping in $^4I_{9/2}$ (R_g is the rate for the ground state absorption).

Though the efficiency of three-micron Erbium laser depends on the rapport between the two up-conversion mechanisms, significant for cw (or long pulse) operation is not the ratio $\omega_{22} / \omega_{11}$, where ω_{11} is the rate of the up-conversion mechanism (i) and ω_{22} for (ii) but the figure of merit $p \equiv (\beta / \alpha) (\omega_{22} / \omega_{11})^{1/2}$. Besides these up-conversion mechanisms, the rate equations describing the kinetics of main metastable levels of Er^{3+} , involved in the laser transitions, must include the cross-relaxation processes from $^4S_{3/2}$ (Fig. 1c) ¹⁶ and from $^4I_{9/2}$ (Fig. 1d) ¹⁷:

$$\begin{aligned}
 \frac{dN_5}{dt} &= -\frac{N_5}{T_5} - \omega_{50} N_0 N_5 + \omega_{22} N_2^2 + R_{p5} N_0 \\
 \frac{dN_4}{dt} &= -\frac{N_4}{T_4} + \frac{N_5}{T_5} + R_{p4} N_0 \\
 \frac{dN_3}{dt} &= -\frac{N_3}{T_3} + \frac{N_4}{T_4} + \omega_{11} N_1^2 + \omega_{50} N_0 N_5 - \omega_{30} N_0 N_3 + R_{p3} N_0 \\
 \frac{dN_2}{dt} &= -\frac{N_2}{T_2} + \frac{N_3}{T_3} - 2\omega_{22} N_2^2 + R_{p2} N_0 \\
 \frac{dN_1}{dt} &= -\frac{N_1}{T_1} + \beta_{21} \frac{N_2}{T} - 2\omega_{11} N_1^2 + 2\omega_{30} N_0 N_3 + \omega_{50} N_0 N_5 + R_{p1} N_0
 \end{aligned} \quad (1)$$

where N_1, \dots, N_5 are, respectively, the populations of the levels $^4I_{13/2}$, $^4I_{11/2}$, $^4I_{9/2}$, $^4F_{9/2}$, and $^4S_{3/2}$. T_1, \dots, T_5 being their lifetimes measured at low Erbium concentrations and low pump intensities. In the rate equations (1) ω_{50} is the rate of the cross-relaxation process from $^4S_{3/2}$, and ω_{30} - the rate of the cross-relaxation from $^4I_{9/2}$. Pumping is allowed in any level i with the rate $R_i N_0$.

The cross-relaxation from $^4S_{3/2}$ (thermalized, at room temperature, with $^2H_{21/2}$) plays a very important role in the built of population of the laser levels. At moderate and high erbium concentrations the excitation from this level, populated by direct pump or by energy transfer, is equally distributed on the initial and final laser levels.

The effect of cross-relaxation from $^4I_{9/2}$, "inverse" to the up-conversion (i), is a reduction of the global efficiency and will be discussed later.

The rate equation system (1) can be simplified if we take into account the inequality $T_1, T_2 \gg T_3, T_4, T_5$, characteristic for the Erbium system and the very high efficiency of the cross-relaxation from $^4S_{3/2}$. Including the laser terms, and assuming $\beta_{21} = 1$, over the laser threshold, we have in the stationary regime, analytical solutions for the populations of the laser levels:

$$N_1 = \frac{-1 + \sqrt{1 + 4\omega_{11}T_1^2(R_1 + R_2)N_0}}{2\omega_{11}T_1}, \quad N_2 = \frac{-1 + \sqrt{1 + 4\omega_{22}T_2^2[(2R_1 + R_2)N_0 - N_1/T_1]}}{2\omega_{22}T_2} \quad (2)$$

For high pump intensities we have the approximate solutions:

$$N_1 \approx \sqrt{\frac{(R_1 + R_2)N_0}{\omega_{11}}} \quad \text{and} \quad N_2 \approx \sqrt{\frac{(R_1 + 2R_2)N_0}{\omega_{22}}}$$

The condition for population inversion, $\alpha N_2 - \beta N_1 > 0$ gives:

$$\alpha N_2 - \beta N_1 \approx \alpha \sqrt{\frac{(R_1 + 2R_2)N_0}{\omega_{22}}} \left(1 - \frac{\beta}{\alpha} \sqrt{\frac{\omega_{22}}{\omega_{11}}} \sqrt{\frac{R_1 + R_2}{R_1 + 2R_2}} \right) > 0 \quad (3)$$

Eq. (3) suggests the figure of merit (formerly introduced in ¹⁸) $p \equiv (\beta/\alpha)\sqrt{\omega_{22}/\omega_{11}}$ which expresses the condition for population inversion as

$$p \leq \sqrt{\frac{(R_1 + 2R_2)}{R_1 + R_2}} \quad (4)$$

The very interesting result is that now the condition for population inversion does not depend of the lifetime of the initial and terminal laser levels, overcoming the "bottleneck" produced by self-saturation.

The explicit effect of various parameters become apparent on examining the analytic expression of the photon flux density ϕ ⁹

$$\phi = \frac{N_0}{\rho} \left[R_1 + (R_1 + R_2)(1 - p^2) \right] - \frac{1}{\alpha\sigma T_2} - \frac{\omega_{22}\rho}{\alpha^2\sigma^2} - N_1 \left(\frac{\beta}{\rho\alpha T_2} + \frac{2\beta\omega_{22}}{\alpha^2\sigma} \right) - \frac{1 - p^2}{\rho T_1} N_1 \quad (5)$$

Thus, only the first and the last term in the right-hand side could be positive, depending on the pump rates and the figure of merit p . The first term is positive if the condition (4) is satisfied; this gives $p < \sqrt{2}$ when $R_1 = 0$ (i. e., for

pumping in one or all of the levels $^4F_{9/2}$, $^4I_{9/2}$, or $^4I_{11/2}$) and $p < 1$ for $R = 0$, i. e., for pumping only in $^4I_{13/2}$. On the other hand, the last term in (5) is positive if $p > 1$ regardless the pump wavelength. The relative magnitude of these two terms restricts the possible combinations of Stark sublevels of $^4I_{11/2}$ and $^4I_{13/2}$ for stationary laser emission for given pumping conditions.

The lifetime T_2 of the initial laser level enters only at the denominator of the negative terms in (5) and should be as large as possible.

The effect of the lifetime T_1 depends on p . If $p < 1$ the last term in (5) is negative and is desirable to have large T_1 ; by contrary, for $p > 1$ a shorter T_1 increases the photon flux density.

The up-conversion parameter ω_{22} (from $^4I_{11/2}$) appears directly in two negative terms and indirectly in the figure of merit, p . A small ω_{22} is always beneficial: it reduces the emission threshold and extend the range of the laser transitions.

The parameter ω_{11} influences the flux density by intermediate of p and N_1 . Generally, a large value of ω_{11} is beneficial. Nevertheless, for $p > 1$ there is a competition between the terms containing N_1 ; when $T_1 / T_2 < (\alpha / \beta)(p^2 - 1)$ a lower value of ω_{11} may be preferred.

We can define the quantum efficiency of the three-micron laser transition as the ratio between the number of quanta generated in the laser cavity and the number of pump quanta. The upper limit of the quantum efficiency for pumping performed in the level i is

$$\eta_i = [R_2 + (R_1 + R_2)(1 - p^2)] / R_{pi} \quad (6)$$

Thus, for pumping in $^4S_{3/2}$, $\eta = 3 - 2p^2$, in $^4F_{9/2}$, $^4I_{9/2}$, or $^4I_{11/2}$ $\eta = 2 - p^2$, and for pumping in $^4I_{13/2}$ $\eta = 1 - p^2$. It results that laser transitions with quantum efficiency higher than one are possible. This is explained by the circulation of excitation specific to the Erbium system.

ESA from the terminal laser level $^4I_{13/2}$ was considered as a possible mechanism for eliminating self saturation of the 3 μ m Erbium laser ⁴. A noticeable ESA from $^4I_{13/2}$ of the Xenon lamp pump radiation was put in evidence in Er^{3+} LuAG with a cross-section similar to ground state absorption. The effect of ESA on the 3 μ m emission depends strongly on the pump wavelength and can be taken into account by proper additional terms in the rate equations. If the pumping wavelength is smaller than 1.1 μ m ESA from $^4I_{13/2}$ excites levels up to $^4F_{9/2}$, avoiding the cross-relaxation from $^4S_{3/2}$; however, for pumping wavelengths shorter than 0.85 μ m, the cross-relaxation from $^4S_{3/2}$ is activated. Denoting by R_{e1} the ESA pumping rate for $\lambda_p > 1.1$ μ m and with R_{e2} the ESA pumping rate corresponding to $\lambda_p < 0.85$ μ m, the expression of the photon flux density becomes

$$\phi = \frac{N_0}{\rho} [R_1 + (R_1 + R_2)(1 - p^2)] - \frac{1}{\alpha\sigma T_2} - \frac{\omega_{22}\rho}{\alpha^2\sigma^2} - N_1 \left[\frac{\beta}{\rho\alpha T_2} + \frac{2\beta\omega_{22}}{\alpha^2\sigma} \right] - \frac{1 - p^2}{\rho T_1} N_1 + \frac{N_1}{\rho} [R_{e1} + (2 - p^2)] R_{e2} \quad (7)$$

ESA introduces a supplementary term in the flux density equation. An analysis of Eq. (7) shows that ESA relaxes to some extent the condition on the figure of merit p when pumping is performed in $^4I_{13/2}$ or $^4S_{3/2}$. Though ESA could improve the emission characteristics, it can not, generally, solve by itself the self-saturation problem ¹¹.

In Eq. (5) and Eq. (7) the negative influence of cross-relaxation from $^4I_{9/2}$ was not taken into account. Its effect, expressed through the "efficiency" of the relaxation process from the level labelled with "3" in the rate

equations (1), i. e. $e_3 = \frac{\omega_{30}N_0T_i}{1 + \omega_{30}N_0T} < 1$ is

$$\phi = \frac{R_p N_0}{\rho} - \frac{1}{\alpha\sigma T_2'} - \frac{\omega_{22}\rho}{\sigma^2\alpha^2} \frac{(1 - e_3)}{1 - e_3(1 + p^2)} - \frac{N_1}{\rho} \left[\frac{\beta}{\alpha T_2'} + \frac{2\omega_{22}\beta\rho}{\sigma\alpha^2} \frac{1 - e_3}{1 - e_3(1 + p^2)} \right] - \frac{N_1}{\rho T_1} \frac{1 - e_3 - (1 + e_3)p^2}{1 - e_3(1 + p^2)} \quad (8)$$

where $\frac{1}{T_2'} = \frac{1}{T_2} \left\{ 1 + \frac{(1 - \beta_{21})[1 - e_3 - (1 + e_3)p^2]}{1 - e_3(1 + p^2)} \right\}$

and the pump term, R_p , has the expression:

$$R_p = \frac{R_{p1}[1 - e_3 + (1 + e_3)p^2] + R_{p2}[2(1 - e_3) - (1 + 2e_3)p^2] + (R_{p3} + R_{p4})[2(1 - e_3) - (1 + 3e_3)p^2]}{1 - e_3(1 + p^2)} + \frac{R_{p5}[3(1 - e_3) - 2(1 + 2e_3)p^2]}{1 - e_3(1 + p^2)} \quad (9)$$

A general decrease of the quantum efficiency due to the cross-relaxation from $^4I_{9/2}$ is observed.

Another figure of merit (denoted by f in ⁹) expresses the modification of the balance of rate equations due the presence of the sensitizer Cr^{3+} . The position of Cr^{3+} levels 2E and 4T_2 in rapport with Er^{3+} levels favours the chain of processes $^4S_{3/2}(\text{Er}^{3+}) \rightarrow ^2E, ^4T_2(\text{Cr}^{3+}) \rightarrow ^4I_{9/2}(\text{Er}^{3+})$ which furnishes an alternative channel for the de-excitation of $^4S_{3/2}$. In ⁹ this figure of merit was defined as

$$f = \frac{\omega_{50} N_{\text{Er}}}{\omega_{50} N_{\text{Er}} + \omega'_{50} N_{\text{Cr}}}$$

where N_{Cr} , N_{Er} are, respectively, the Chromium and Erbium concentrations and ω'_{50} is the rate of $\text{Er}^{3+} \rightarrow \text{Cr}^{3+}$ energy transfer process. Obviously, in the absence of Chromium, $f = 1$.

In the presence of Cr^{3+} ions the analytical expression for the photon flux density (19) becomes :

$$\phi = \frac{R_{p3} N_0}{\rho} \frac{2(1 - e_3) - p^2[(1 - e_3)f + 4e_3]}{1 - e_3 + (1 - f - e_3)p^2} - \frac{1}{\alpha \sigma T_2''} - \frac{\omega_{22} \rho}{\sigma^2 \alpha^2} \frac{(1 - e_3)(2 - f)}{1 - e_3 + (1 - f - e_3)p^2} - \frac{N_1}{\rho} \left[\frac{\beta}{\alpha T_2''} + \frac{2\omega_{22} \beta \rho}{\sigma \alpha^2} \frac{(1 - e_3)(2 - f)}{1 - e_3 + (1 - f - e_3)p^2} \right] - \frac{N_1}{\rho T_1} \frac{1 - e_3 - (1 + e_3)p^2}{1 - e_3 + (1 - f - e_3)p^2} \quad (10)$$

where

$$\frac{1}{T_2''} = \frac{1}{T_2} \frac{1 + (1 - \beta_{21})[1 - e_3 - (1 + e_3)p^2]}{1 - e_3 + (1 - f - e_3)p^2}$$

and the pumping is assumed only in $^4I_{9/2}$ with the rate R_{p3} due to presence of the sensitizer Cr^{3+} . Only laser transitions that make the first term (pumping term) in (22) positive are permitted. For $e_3 \neq 0$ the efficiency and the range of possible generation wavelengths are reduced. This loss could be compensated by the presence of Cr^{3+} ($f < 1$), extending the emission towards shorter wavelengths.

3 DISCUSSION

At low Erbium concentrations, when the effects of up-conversion and cross-relaxation processes can be neglected, cw generation of Er (1 at. %): YLiF_4 at 2.81 μm for pumping in $^4F_{9/2}$ or $^4I_{9/2}$ was possible ¹⁹ due to the

combination of material parameters T_1 , T_2 , α , β , and β_{21} which overcome the self-saturation condition. Increasing the Erbium concentration the condition for population inversion (3) make the rapport between the lifetimes T_1 , T_2 becomes less important. Nevertheless, as we have seen from the inspection of the flux equation (5), a large value of the initial laser level lifetime T_2 is always beneficial. On the other hand, the effect of T_1 depends on p . For the Er: YAG crystal stable long pulse or cw generation²⁰ at room temperature was observed only for $\lambda = 2.94 \mu\text{m}$, corresponding to the transition between the second (in the order of increasing energy) Stark sublevel of $^4I_{11/2}$ and the seventh of $^4I_{13/2}$. For this transition $p = 0.43 < 1$ (using ω_{11} , ω_{22} given in⁷) making the last term in Eq. (5) negative, a larger value of T_1 being desirable. This explains the failure of the earlier attempts to improve the efficiency of the $2.94 \mu\text{m}$ Er: YAG laser by co-doping²¹ with Tm^{3+} or Ho^{3+} in order to reduce T_1 or with Nd^{3+} for simultaneous generation of Er, Nd: YAG²². On the other hand, for transitions with $p > 1$ (transition at $\lambda = 2.702 \mu\text{m}$ of Cr, Er: YSGG, with $p = 1.92$ estimated using the sublevels identification and ω_{11} , ω_{22} given in²³) the co-doping with Ho^{3+} and Tm^{3+} is beneficial²⁴.

The co-doping with Cr^{3+} , besides an overall increasing of the emission efficiency due a better absorption of the pump radiation, can modify the generation picture. In fact, a shift of the emission toward shorter wavelengths was experimentally observed²⁵ in Cr, Er: YAG, the generation taking place at $2.7 \mu\text{m}$ instead of $2.94 \mu\text{m}$. This shorter wavelength correspond to the transition between the first sublevels of both $^4I_{11/2}$ and $^4I_{13/2}$ with $p = 1.85 > 1$.

In the frame of our model lasing on transitions with $p > \sqrt{2}$ could be explained by the relaxation of this condition introduced by the presence of Chromium. In fact, the inspection of Eq. (10) for the population flux density with $f < 1$ shows that positive pump term is obtained for $p < \sqrt{2(1-e_3) / [4e_3 + f(1-e_3)]} \approx \sqrt{2/f}$, considering, as for YAG, $e_3 \approx 0$. An estimation of the figure of merit f for Cr, Er: YSGG as a function of Cr^{3+} and Er^{3+} concentration was made⁹, based on the spectroscopic data given in²³. Values for f as low as ~ 0.3 could be obtained, extending the emission range to transitions with $p < 2.58$.

According to our model the temperature dependence of the quantum efficiency is conditioned by the temperature dependence of the figures of merit p and e_3 . As we shown in²⁶, in the temperature range (20 - 100°C), usual for solid state lasers, the temperature dependence of p is given mainly by the Boltzmann population coefficients α , β ; the temperature dependence of e_3 express the concurrence between the multiphonon transition $^4I_{9/2} \rightarrow ^4I_{11/2}$ and the cross relaxation from $^4I_{9/2}$. Our estimations, based on the experimental temperature dependence of the lifetime T_3 (of $^4I_{9/2}$) measured for two crystals (Er(45 at.%): YAlO_3 and Er(25 at.%): YLiF_4), show that for Er: YAlO_3 the temperature dependence of the cross-relaxation is stronger, leading to an increase of e_3 with negative effects on the quantum efficiency; in contrast, for Er: YLiF_4 , the multiphonon process has a steeper temperature dependence, with possible positive effects on the quantum efficiency.

The role of three-ion energy transfer in $3 \mu\text{m}$ lasing of Erbium doped crystals was reviewed recently²⁷. While three-ion cross-relaxation from $^4S_{3/2}$ level merely accelerates the depletion of this level, three-ion up-conversion from $^4I_{13/2}$ could improve the laser efficiency and relax, in some extent, the restriction imposed by the figure of merit p .

4 CONCLUSIONS

Efficient $3 \mu\text{m}$ generation of Erbium lasers on the self-saturated transition $^4I_{11/2} \rightarrow ^4I_{13/2}$ is made possible by energy transfer processes, very active at high activator concentrations.

The population inversion condition which depends at low Erbium concentrations of the lifetimes of the laser levels, and can be fulfilled only in few cases (as, for example, $2.81 \mu\text{m}$ lasing in Er: YLiF_4) is replaced at higher concentrations by a new one, depending of the up-conversion rates.

For stationary regime of emission our mathematical model based on analytical formulae for population inversion, photon flux density and quantum efficiency, explains in an unitary manner the main characteristics of the Erbium lasers.

The role of various interactions with influence on $3 \mu\text{m}$ lasing in Erbium systems is expressed by specific figures of merit which can be determined from spectroscopic measurements.

This model, confirmed by a large bulk of experimental data shows that for concentrated Erbium systems though, ESA from the terminal laser level could improve the lasing efficiency, the driving mechanism for 3 μm emission is the co-operative up-conversion from the terminal laser level.

5. REFERENCES

1. Kh. S. Bagdasarov, V. A. Lobachev and T. M. Murina, "Study of generation characteristics of YAG: Er³⁺ laser ($\lambda = 2.94 \mu\text{m}$) under pulsed pump of millisecond duration," *Proc. 5th All-Union Conf., Optics of Lasers*, Leningrad, 1987, S. V. Vavilov, Ed., State Instit. Opt., p. 247.
2. P. Albers, V. G. Ostroumov, A. F. Umyskov, S. Schnell and I. A. Shcherbakov, "A high-repetition-rate low threshold three-micron YSGG: Cr, Er laser," *Kvant. Elektron.* vol. 15, pp. 871-872, 1988.
3. S. Wüthrich, W. Lüthy and H. P. Weber, "Comparison of YAG: Er and YAlO₃: Er laser crystals emitting near 2.9 μm ," *J. Appl. Phys.* vol. 68, pp. 5467-5471, 1990.
4. M. A. Andriasyan, N. D. Vardanyan and R. B. Kostanyan, "On the influence of the excitation energy absorption from ⁴I_{13/2} level of Erbium ions on the performances of laser utilising Lu₃Al₅O₁₂: Er crystals," *Kvant. Elektron.* vol. 9, pp. 1269-1271, 1982.
5. V. I. Zhekov, V. A. Lobachev, T. M. Murina and A. M. Prokhorov, "Co-operative phenomena in crystals of yttrium-erbium-aluminium garnet," *Kvant. Elektron.* vol. 11, pp. 189-192, 1984.
6. S. Georgescu, V. Lupei, I. Ursu, V. I. Zhekov, V. A. Lobachev, T. M. Murina and A. M. Prokhorov, "The role of cross-relaxation mechanisms in the quasi-stationary generation regime of YAG: Er laser," *Rev. Roum. Phys.* vol. 31, pp. 857-864, 1986.
7. V. I. Zhekov, T. M. Murina, A. M. Prokhorov, M. I. Studenikin, S. Georgescu, V. Lupei and I. Ursu, "Co-operative processes in Y₃Al₅O₁₂ - Er³⁺ crystals," *Sov. Phys. J. Quantum Electron.* vol. 16, pp. 274-276, 1986.
8. V. Lupei, S. Georgescu, and V. Florea, "The effect of terminal laser level lifetime on three-micron laser emission in Er-doped crystals," *Optics Commun.* vol. 92, pp. 67-72, 1992.
9. V. Lupei, S. Georgescu, and V. Florea, "On the dynamics of population inversion for 3 μm Er³⁺ lasers," *IEEE J Quantum Electron.* vol. 29, 426-434, 1993.
10. S. Georgescu, V. Lupei, T. J. Glynn and R. Sherlock, "Spectroscopic determination of the figures of merit for 3 μm Er³⁺ lasers," *J. Lumin.* vol. 60&61, pp. 241-244, 1994.
11. V. Lupei and S. Georgescu, "Erbium 3- μm laser as an upconversion system," *Opt. Eng.*, vol. 35, pp. 1265-1272, 1996.
12. S. Hubert, D. Meichenin, B. V. Zhou and F. Auzel, "Emission properties, oscillator strengths and laser parameters of Er³⁺ in LiYF₄," *J. Lumin.*, vol. 50, pp. 7-15, 1991.
13. S. Georgescu, V. Lupei, A. Lupei, V. I. Zhekov, T. M. Murina and M. I. Studenikin, "Concentration effects on the up-conversion from the ⁴I_{13/2} of Er³⁺ in YAG," *Optics Commun.* vol. 81, pp. 186-192, 1991.
14. Kh. S. Bagdasarov, V. I. Zhekov, V. A. Lobachev, T. M. Murina and A. M. Prokhorov, "Steady-state stimulated emission from Y₃Al₅O₁₂: Er³⁺ laser ($\lambda = 2.94 \mu\text{m}$, T = 300K)," *Kvant. Elektron.* vol. 10, pp. 452-454 1983.
15. Kh. S. Bagdasarov, V. I. Zhekov, V. A. Lobachev, A. A. Manenkov, T. M. Murina and A. M. Prokhorov, "Cross-relaxation YAG: Er laser," *Izv. AN SSSR, ser. fiz.* vol. 48, pp. 1765-1769 1984.
16. L. G. Van Uitert and L. F. Johnson, "Energy transfer between rare earth ions," *J. Chem. Phys.* vol. 44, pp. 3514-3522, 1966.
17. S. Georgescu, T. J. Glynn, R. Sherlock and V. Lupei, "Concentration quenching of the ⁴I_{9/2} level of Er³⁺ in laser crystals," *Optics Commun.* vol. 106, pp. 75-78, 1994.
18. M. A. Noginov, S. G. Semenov, V. A. Smirnov and I. A. Shcherbakov, "Effect of interaction between excited erbium ions on the formation of inverse population on the ⁴I_{11/2}→⁴I_{13/2} transition in a YAGG: Cr, Er crystal under stationary excitation," *Optika i Spektrosk.* vol. 69, pp. 120-127, 1990.
19. B. Schmaul, G. Huber, R. Clausen, B. Chai, P. LiKamWa and M. Bass, "Er³⁺: YLiF₄ continuous wave cascade laser operation at 1620 and 2810 nm at room temperature," *Appl. Phys. Lett.* vol. 62, pp. 541-543, 1993.

20. B. J. Dinerman and P. F. Moulton, "CW laser operation from Er: YAG, Er: GGG and Er: YSGG," *OSA Proc. on Adv. Solid State Lasers*, vol. 13, pp. 152-155, 1992.
21. A. A. Kaminskii, T. I. Butaeva, A. O. Ivanov, I. V. Mochalov, A. G. Petrosyan, G. I. Rogov and V. A. Fedorov, "New data on stimulated emission of crystals containing Er^{3+} and Ho^{3+} ions," *Sov. Tech. Phys Lett*, vol. 2, pp. 308-310, 1976.
22. W. Q. Shi, R. Kurtz, J. Machan, M. Bass, M. Birnbaum and M. Kokta, "Simultaneous, multiple wavelength lasing of (Er, Nd): $\text{Y}_3\text{Al}_5\text{O}_{12}$," *Appl. Phys. Lett.* vol. 51, pp. 1218-1220, 1978.
23. E. V. Zharikov, N. N. Il'ichev, S. P. Kalitin, V. V. Laptev, A. A. Malyutin, V. V. Osiko, P. P. Pashinin, A. M. Prokhorov, Z. S. Saidov, V. A. Smirnov and A. F. Shcherbakov, "Spectral-luminescent and lasing properties of a chromium- and erbium- doped yttrium-scandium-gallium garnet crystal," *Kvant. Elektron.* vol. 13, pp. 973-979, 1986.
24. G. Huber, E. V. Duczynski and K. Petermann, "Laser properties of Ho-, Tm-, Er- doped garnet lasers at room temperature," *IEEE J. Quantum Electron.* vol. 24, pp. 920-923, 1988.
25. Yu. K. Voronko, S. B. Gessen, I. V. Gribkov, V. V. Osiko, P. A. Ryabochkina, V. M. Tatarintsev, S. N. Ushakov and L. I. Tsymbal, "Sensitisation of the Er^{3+} luminescence in $(\text{YEr})_3\text{Al}_5\text{O}_{12}$ Cr^{3+} crystals and lasing at 2.7 μm wavelength," *Sov. J. Quantum Electron.* vol. 20, pp. 923-925, 1990.
26. 32. S. Georgescu, V. Lupei, T. J. Glynn and R. Sherlock, "Thermal effects on the quantum efficiency of 3 μm Er^{3+} lasers," *Radiation Effects and Defects in Solids*, vol. 136, pp. 13-27, 1995.
27. S. Georgescu and M. Micluta, "The role of two- and three-ion energy transfer processes in three-micron generation of Erbium doped crystals," *Proc. SPIE (LO'95, St. Petersburg, Russia)*, vol. 2772, pp. 37-47, 1996.

SESSION 2

Lasers in Material Science

THE SYNTHESIS, CHARACTERIZATION AND MECHANICAL PROPERTIES OF CARBIDES AND NITRIDES FILMS PREPARED BY PULSED LASER DEPOSITION METHOD

Ashok Kumar, H. L. Chan, and Rodica Alexandrescu*

Department of Electrical Engineering

University of South Alabama, Mobile, AL 36688, USA

* National Institute for Lasers, Plasma and Radiation Physics, Lasers Department

P. O. Box MG-36, R-76 900, Bucharest, Romania

ABSTRACT

Carbides and nitrides of metal have a large number of applications in modern technology owing to their interesting, and in some ways unique, physical and chemical properties. Thin film coatings of titanium carbide (TiC) and aluminum nitride (AlN) were deposited on Si (100) substrates using pulsed laser deposition (PLD) method. The structural and microstructural properties of these films have been characterized using x-ray diffraction, and Fourier transform infrared spectroscopic techniques. The mechanical properties of the films were evaluated to measure the hardness and modulus values. It has been shown that the films deposited at higher temperature have the best crystalline quality structure and also have higher hardness values compared to the film deposited at lower temperatures.

Keywords: Pulsed laser deposition, Titanium carbide, Aluminum nitride, Hardness,

1. INTRODUCTION

Transition metal of carbides and nitrides have many desirable properties for applications at elevated temperatures because of extremely high melting point, hardness, high temperature strength, good thermal shock resistance, and high thermal conductivity [1]. Titanium carbide (TiC) is an excellent material for applications where corrosion and wear resistance are important. Because of its high melting point, it is also a promising material to be used as first wall material in fusion reactors. Aluminum nitride (AlN) is a wide band gap (6.2 eV) III-V compound with desirable thermal conductivity, electrical resistivity, and acoustic properties. AlN can also be made translucent or transparent if it has sufficient density and purity, and combined with its wear resistance makes AlN attractive for some electrooptics applications. AlN films can be a promising material for applications in microelectronics and optoelectronics devices such as passivation and dielectric layers in integrated circuits, short wave length emitter, and surface acoustic devices. In addition, AlN can help extend the life of moving mechanical components due to its potential as a wear-resistant hard coating [2-4].

Many deposition techniques such as sputtering, ion beam deposition etc., have been utilized to fabricate TiC coatings [5, 6]. AlN films have been deposited in various ways, such as chemical vapor deposition (CVD), reactive sputtering, evaporation, molecular beam epitaxy (MBE), metallographic chemical vapor deposition (MOCVD), ion implantation, and

ion beam assisted deposition (IBAD) [7-8]. In the last decade, the PLD method has emerged as an excellent technique for the deposition of carbides and nitrides coatings [9-11]. The uniqueness of using PLD technique for depositing carbide and nitride thin film are as follows: (i) this process provides correct stoichiometric TiC films with unique microstructure and properties, (ii) thin film deposition is performed at relatively low temperature and, (iii) laser deposition rate is relatively high in the range of 50 to 100 Å/sec. Furthermore, it has the advantages of improving adhesion to the substrate, easier to control of composition and thickness of the film and possibility of synthesizing compounds films and growing films at room temperature. In addition, PLD provides the capability to tailor film behavior by precise control of film morphology, and crystal structure through adjustment of film deposition parameters. In this article, we report the formation of high quality TiC and AlN films with excellent mechanical properties.

2. EXPERIMENTAL

The PLD system at University of South Alabama consists of a laser, a six way cross vacuum chamber, vacuum pumps (Rotary Vane and Turbo Molecular Vacuum pumps) and other relevant instruments such as leak valves, temperature and pressure gauges. This PLD system is capable of depositing multi-layer structures composed of up to five different materials, in a vacuum of up to 10^{-8} Torr, at up to 700°C in background atmosphere of Nitrogen, Argon, and Oxygen. Figure 1 shows an overall schematic diagram of the PLD system at University of South Alabama. There are five target holders mounted on a disk which can be rotated to bring the desired target for laser irradiation. A high-energy pulsed laser beam (KrF, wavelength = 248 nm) is directed and focused on to the target's materials for the respective deposition of thin films inside the experimental chamber [9-10]. The films of aluminum nitride were deposited on Si (100) substrates at various temperatures (100°C, 200°C, 300°C, 400°C, 550°C, 600°C, 625°C, 675°C, and 725°C) and different thickness (300 nm and 600 nm) in 15 mTorr nitrogen environment with 10 J/cm² energy density. The films of titanium carbide were deposited on Si (100) substrates at different temperatures (room temperature, 300°C, 500°C and 650°C) in high vacuum with 3000 Å thickness. The laser beam was operated at the constant energy mode at repetition rates at 20 Hz. The mechanical properties such as hardness of these films were determined using Nanoindenter IIA.

3. RESULTS AND DISCUSSIONS

X-ray diffraction patterns for the TiC samples prepared under various conditions (room temperature, 300°C, 500°C, and 600°C) are shown in Fig. 2. The film structures were found to be strongly dependent on the deposition temperature. At room temperature, there were no peaks observed except Si (100). In addition, the film's quality as well as the film's adhesion were not very good. At higher deposition temperatures (600°C), the film was found crystalline. The peak can be indexed to a (200) textured TiC phase.

X-ray diffraction analysis of the AlN films that were 3000 Å in thickness, grown on Si (100) substrates, could not detect any characteristic AlN diffraction pattern, suggesting that the films are amorphous. The lack of crystallinity in these films appears to be related

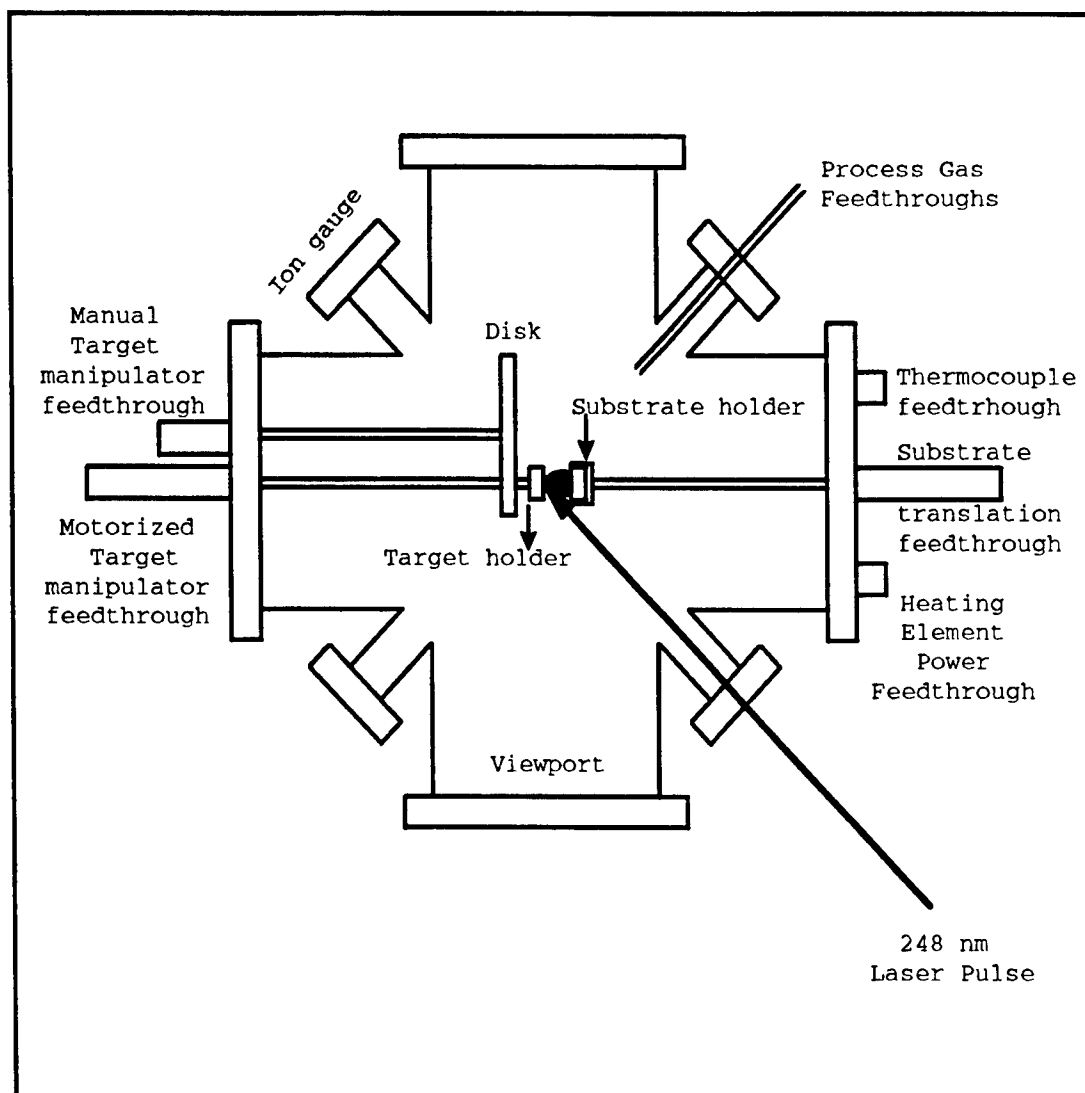


Fig. 1: Schematic diagram of the pulsed laser deposition system

to the low growth temperature, low thickness, and low repetition rate which means lower energy density. In general, it has been observed that regardless of the growth technique employed, the growth of AlN films on various substrates at temperature higher than 500°C has resulted in epitaxial or preferentially oriented films, while depositions at temperatures below 500°C have produced amorphous films. These trends strongly suggest that to achieve crystallinity in thin films, it is necessary to provide energy to the components of the film during deposition. Fig. 3 shows that films deposited at 550°C and 625°C have very low intensity peak of AlN but it shows highly c-axis oriented along normal to the substrate. The lattice constant for these films is found to be 4.97Å which is very close to the literature value of the bulk material. The AlN film deposited at 675°C, in 15 mTorr N₂ has produced the best quality thin film. This film is highly textured, having the c-axis perpendicular to Si (100) substrate. It can also be seen that the integrated intensity of (0002) peak increases as a function of substrate temperature.

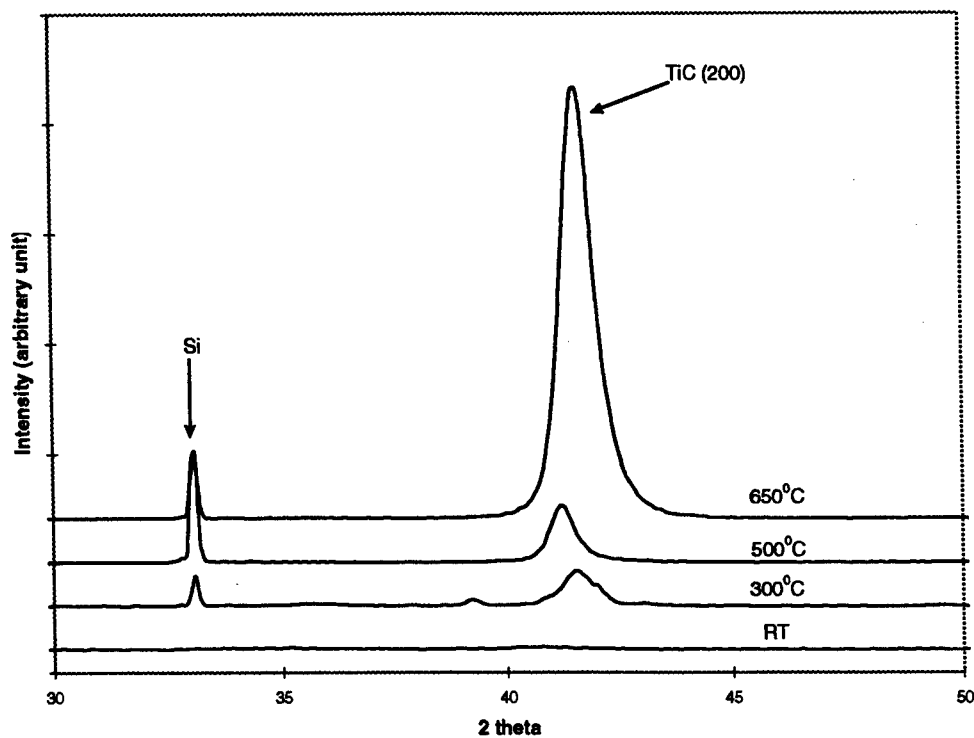


Fig. 2: X-ray diffraction pattern of TiC films on Si (100) substrates at different deposition temperatures

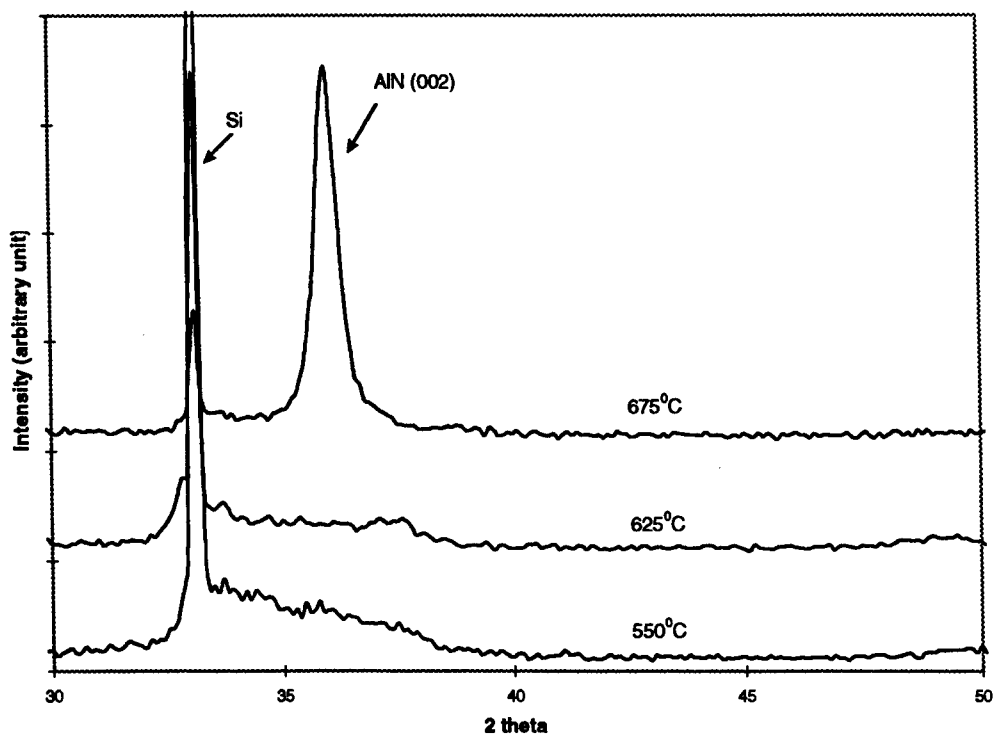


Fig. 3: X-ray diffraction pattern of AlN films on Si (100) substrates at different deposition temperatures

Fig. 3 shows the IR transmittance spectrum of AlN films deposited at 675°C in 15 mTorr nitrogen environment using Nicolet Magna IR 750. This spectrum was obtained by computer subtraction of the Si (100) substrate background. The strong absorption peak at 665 cm⁻¹ is due to the transverse optical phonon modes of AlN [12-13]. These phonon modes clearly show that the laser deposited films contain AlN phase.

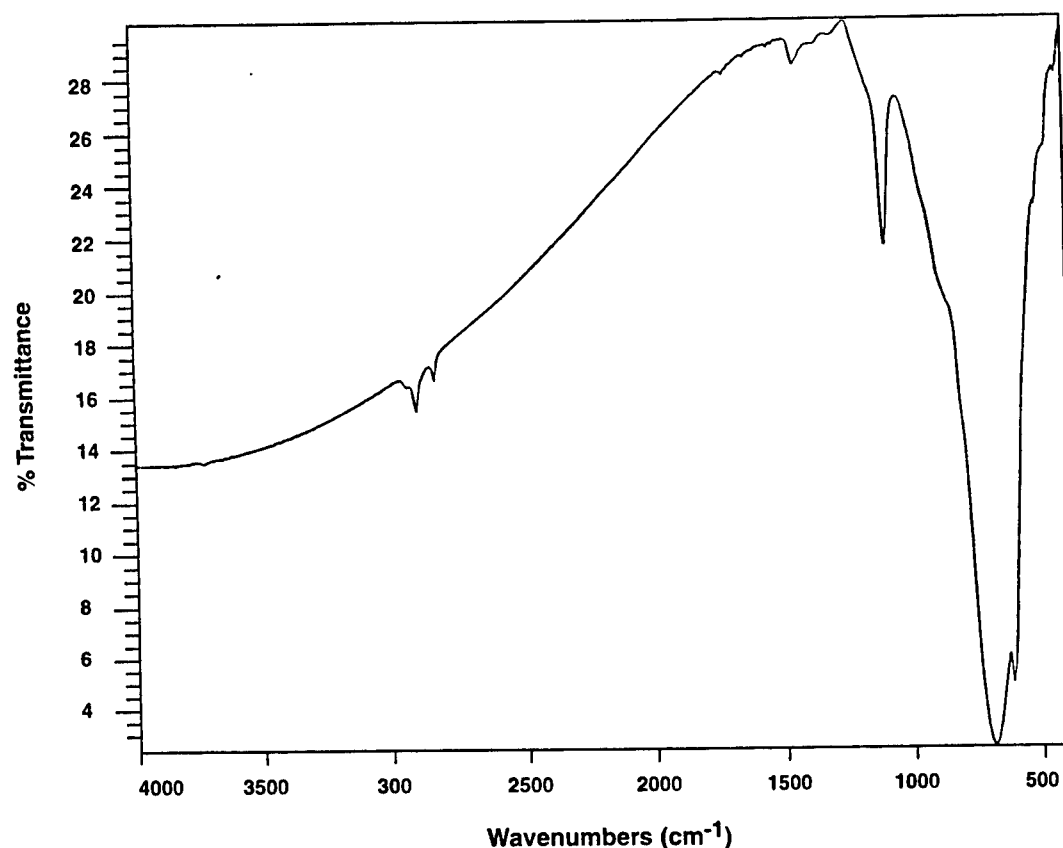


Fig. 4: FTIR Spectrum of AlN Deposited on Si (100) Substrates at Different Temperatures in 15 mTorr Nitrogen

The hardness of TiC films deposited on Si (100) substrates at different temperature (room temperature and 600°C) with 3000 Å are given in Fig. 5. as a function of penetration depth. Obviously, there was a substrate effect when the penetration was increased up to 50 nm and 100 nm so that the values of hardness and Young's modulus were decreased. There seems to be an obvious trend of slightly increasing hardness and with increasing deposition temperature, i.e. when going from amorphous to crystalline microstructure. The film deposited at a higher temperature (600°C) displays higher hardness values than the film deposited at a lower temperature (room temperature). These values are well comparable to the bulk target of the TiC [14] and no results are available to compare in the thin film form.

The hardness values of AlN films deposited on Si (100) substrates at different temperatures (675°C and 550°C) in 15 mTorr nitrogen environment are given in Fig. 6

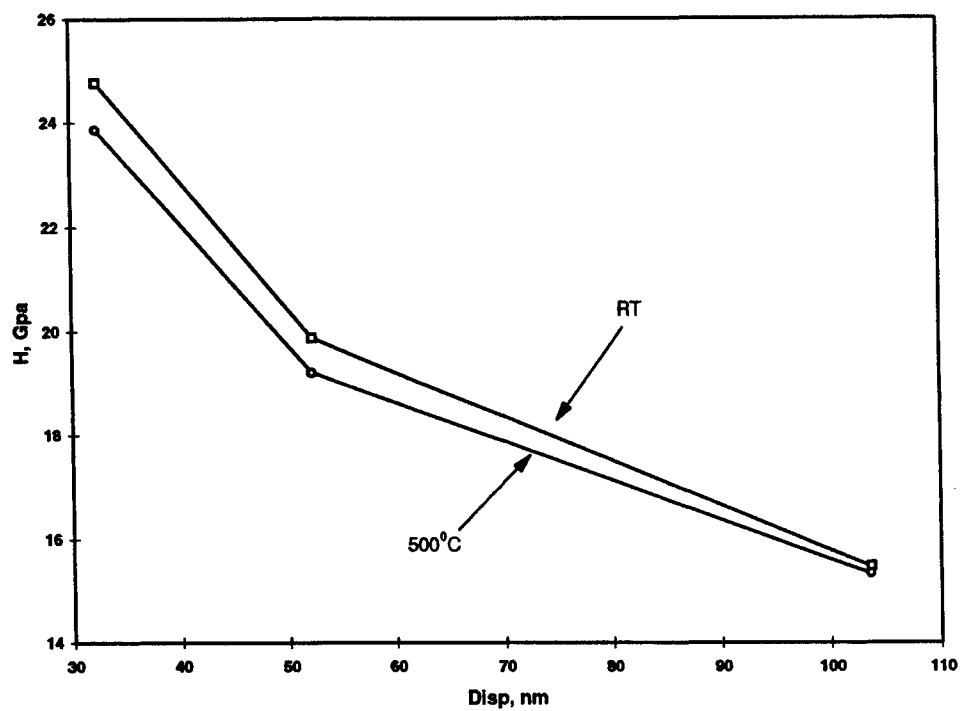


Fig. 5: Hardness of TiC films deposited on Si (100) substrates at different deposition temperatures as a function of penetration depth

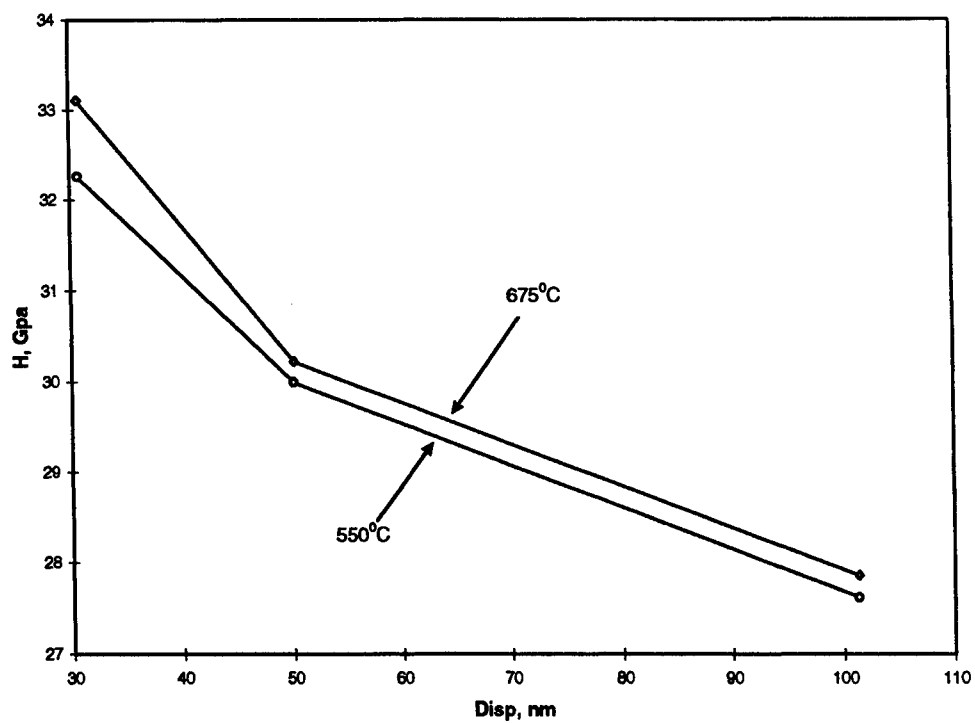


Fig. 6: Hardness of AlN films deposited on Si (100) substrates at different deposition temperatures as a function of penetration depth

as a function of penetration depth. In this case, there is no clear evidence that there is a substrate effect. There seems to be an obvious trend of slightly increasing with increasing deposition temperature, i.e. when going from amorphous to crystalline microstructure. The film deposited at higher temperature (675°C) displays higher hardness values than the film deposited at higher temperature (550°C).

4. CONCLUSIONS

The hardness value of the TiC film deposited at higher temperature (600°C) is higher than those of the film deposited at lower temperature (room temperature). The X-ray diffraction patterns show that crystalline TiC films have been made successfully. The films deposited at higher temperature have better quality crystallinity than the films deposited at lower temperatures. Thin films of AlN have been grown successfully on Si (100) substrates. The films are crystalline in nature. It was found that the film deposited at higher temperature (675°C) shows the characteristics of AlN films. The hardness values of these films also show that AlN film with higher deposition temperature (675°C) has the better hardness properties compared to the films fabricated at lower temperature (550°C) which transforms into amorphous structure.

ACKNOWLEDGMENTS

This research was supported by Alabama NASA EPSCoR program. Part of this research was also supported by NRC Twining and NSF Academic Research Infrastructure (DMR # 9512324) grants. The authors would like to thank Dr. J. Barnard for analysis of mechanical properties.

REFERENCES

- [1] Ashok Kumar, U. Ekanayake, D. Kjendal, N. Shu, R. B. Inturi and J. A. Barnard, TMS Annual Meeting High Temperature Coating II, 349 (1996)
- [2] H. Morkoc, S. Strite, G. B. Gao, M. E. Lin, B. Sverdlov, and M. Burns, J. Appl. Phys., 76, 1364 (1994)
- [3] J. H. Edgar, J. Mater. Res., Vol. 7, 235 (1992)
- [4] L. M. Sheppard, *Ceramic Bulletin.*, Vol. 69, No. 11, 1801 (1990)
- [5] W. J. Sessler, M. S. Donley, J. S. Zabinski, S. D. Walck, and V. J. Dyhouse, *Surface and Coatings Technology* 56, 125 (1993)
- [6] W. H. B. Hoondert, B. J. Thijsse, A. van Veen, and A. Van den Beukel, *Surface and Coatings Technology.*, 51, 338 (1992)
- [7] J. Yang, C. Wang, X. Yan, K. Tao and Y. Fan, J. Phys. D: Appl. Phys. 27, 1056 (1994)
- [8] M. A. Khan, J. N. Kuznia, R. A. Skogman, and D. T. Olson, Appl. Phys. Lett., Vol. 61, 2539 (1992)
- [9] Ashok Kumar, U. Ekanayake, R. B. Inturi and J. A. Barnard, MRS Symposium Proceeding Layered Materials for Structural Applications, Vol. 434, 189 (1996)

- [10] Ashok Kumar, U. Ekanayake, R. B. Inturi and J. A. Barnard, MRS Symposium Proceeding Thin Films- Stresses and Mechanical Properties VI, Vol. 436, 65 (1996)
- [11] H. L. Chan, M. S. Thesis, Department of Electrical Engineering, University of South Alabama (1997)
- [12] K. S. Seki, X. Xu, H. Okabe, J. M. Frye, and J. B. Halpern, Appl. Phys. Lett. 60, 2234 (1992)
- [13] R. D. Vispute, J. Narayan, H. Wu, and K. Jagannadham, J. Appl. Phys. 77, 4724 (1995)
- [14] J. F. Shackelford, W. Alexander and J. S. Park "CRC Practical Handbook of Materials Selection" CRC Press (1995)

DEPOSITION OF CN THIN FILMS BY REACTIVE PULSED LASER ABLATION

A. Perrone

Universita' di Lecce, Dipartimento di Fisica e Istituto Nazionale Fisica della Materia,
73100 Lecce, Italy

ABSTRACT

The effects of laser fluence on the structure and properties of the reactive pulsed laser deposited carbon nitride (CN_x) thin films prepared at different gas pressures of N₂ and NH₃ were investigated. The structure, the morphology and the chemical composition of the films were characterised by X-ray photoelectron spectroscopy (XPS), X-ray diffraction (XRD), transmission electron microscopy (TEM), scanning electron microscopy (SEM), Rutherford backscattering (RBS) and Fourier transform infrared (FTIR). The films were plane, adhesive and relatively hard, with a low droplet density. The deposition rate decreases with increasing gas pressure and laser fluence, while the N/C atomic ratio increases. The nitrogen concentration in the deposited films drops when the substrate temperature is increased, indicating a desorption process of the CN radicals. Spectroscopic studies of the plasma plume indicate an interesting correlation between the CN band emission intensity and the nitrogen concentration in the samples.

Keywords: Laser ablation; Carbon nitride thin films; Graphite; X-ray photoelectron spectroscopy; Rutherford backscattering; IR absorption; Optical emission spectra; Mass spectra.

1. INTRODUCTION

Present interest in the synthesis of carbon nitrides thin films and in particular for β -C₃N₄ phase starts from the well known theoretical work by Liu and Cohen predicting for this new compound a very large hardness nearly equal to that of diamond¹. This hard material can be used as coating for thermally unstable materials such as glasses and plastics. Many other applications are foreseen in the microelectronics, optics, and tribology industries²⁻⁵. The numerous deposition techniques that have been tried so far include plasma chemical deposition^{6,7}, ion assisted dynamic mixing method⁸, low energy ion beam deposition^{9,10}, double ion source deposition¹¹, shock wave compression¹², rf sputtering¹³, magnetron sputtering¹⁴ and laser ablation¹⁵⁻¹⁸. Up to now, the most of work reported on CN films involved low nitrogen concentrations which are much lower than that expected for stoichiometric β -C₃N₄. However, some papers reported the deposition of CN films containing microdomains of β -C₃N₄ crystallites^{17,19,20}.

We propose an approach aimed at both synthesis and deposition of high quality CN thin films in one step procedure. In order to evaluate the actual potential as well as the limits of reactive pulsed laser ablation (RPLA) in obtaining good quality thin films we continued our investigations with a parametric study in relation to the gas pressure and laser fluence.

2. EXPERIMENTAL APPARATUS

Depositions were performed using a XeCl excimer laser ($\lambda=308$ nm, $\tau_{FWHM}=30$ ns). Series of 10,000 pulses at a repetition rate of 10 Hz were directed to high purity graphite targets. The laser fluences were $F=3, 6, 12$ and 16 J/cm². The laser beam was incident on the target surface with an

angle of 45° . In order to obtain irradiation conditions as uniform as possible, the target was rotated with a 3 Hz rotation frequency during the application of the multipulse laser irradiation. The ablated material was collected either on (111) Si or KBr substrates. The substrates were placed on a support at a distance $d=4.0$ cm from the target and they could be heated up to 500°C . All the depositions were conducted inside a stainless steel high-vacuum chamber (Fig. 1).

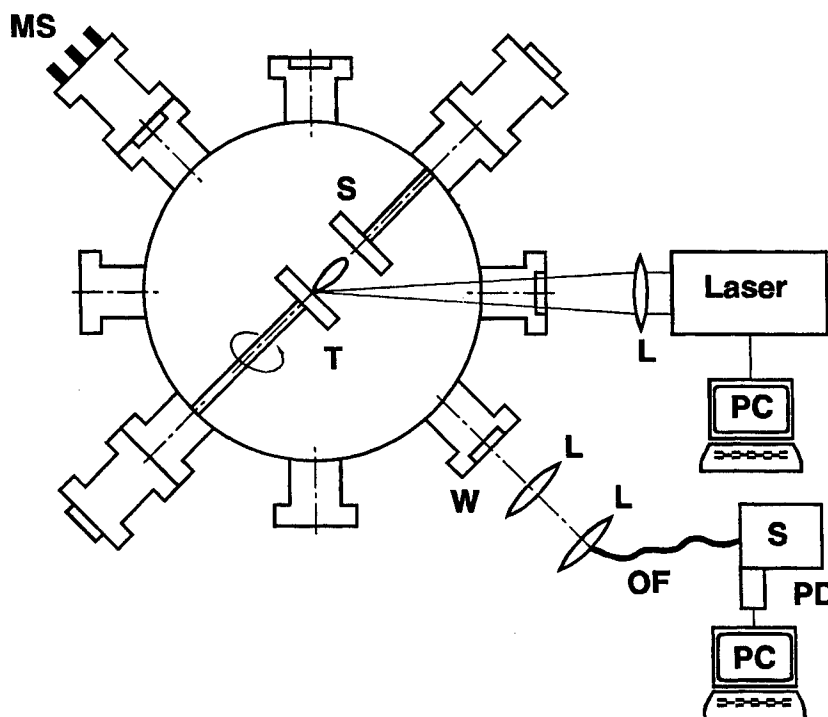


Fig. 1 Scheme of the experimental apparatus. T: target; S: substrate; L: lens; MS: quadrupole mass spectrometer; SP: optical spectrograph; PDA: photodiode array; PC: personal computer; OF optical fibre.

The chamber was first evacuated down to 10^{-5} Pa, while its walls were heated in order to facilitate the desorption of water vapour. Then, a jet of either high pure nitrogen (electronic grade) or pure NH_3 (99,99%, with less than 4 p.p.m. oxygen) was continuously blown inside the chamber which was accurately set at a chosen value in the 1 – 250 Pa range. The residual gas conditions were monitored by a quadrupole mass spectrometer.

3. EXPERIMENTAL RESULTS

Initial tests to determine suitable substrate temperatures, substrate-target distance and reactive ambient gas were performed. The tests indicated much better adhesion, uniformity and higher N/C atomic ratios at lower substrate temperatures. However, also when no intentional substrate heating was used, the film growth temperature was recorded to be approximately 60°C .

The substrate-target distance of 4.0 cm resulted to be the best compromise between high deposition rates (which decrease with increasing distance) and low droplet density on the film surface (which decreases with increasing distance).

The highest N/C atomic ratios were observed in films deposited in NH_3 atmosphere, even though they had a lower fraction of N atoms bonded to C atoms than films deposited in N_2 at the same experimental conditions. This can be due to the large quantity of N-H bonds detected by IR spectroscopy in the films deposited in NH_3 atmosphere. Moreover, the deposition rate is lower in NH_3 than in N_2 at the same ambient pressure. It means that the diffusion of ablated material by NH_3 molecules is more efficient than diffusion by N_2 molecules.

Series of CN samples were deposited at various gas pressures (1-250 Pa) and at different laser fluences (3, 6, 12 and 16 J/cm^2). Typical experimental conditions used in this study are listed in Table I.

Table I: Deposition conditions used in these experiments

TARGET	HIGH PURITY GRAPHITE
TARGET FREQUENCY	3 Hz
REACTIVE GAS	ULTRA HIGH PURITY N_2 AND NH_3
SUBSTRATES	Si (1 1 1) and KBr
SUBSTRATE TEMPERATURE	20, 250 and 500 °C
BASE PRESSURE	10^{-5} Pa (10^{-7} mbar)
GAS AMBIENT PRESSURE	1 to 250 Pa
LASER FLUENCE	3, 6, 12, 16 J/cm^2
LASER FREQUENCY	10 Hz
NUMBER OF PULSES	10,000
TARGET-SUBSTRATE DISTANCE	4.0 cm

Composition and chemical bonds of the films were studied by XPS technique. N 1s and C 1s photoelectron spectra of the CN films deposited at 16 J/cm^2 and at $p(\text{N}_2)=10$ Pa are shown in figs. 2a and 2b, respectively.

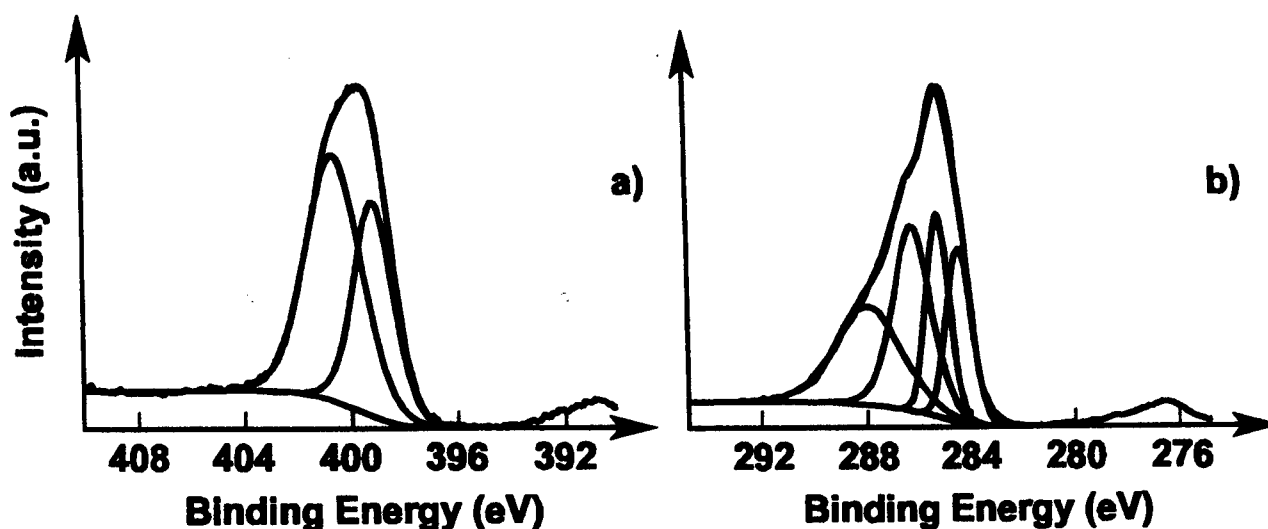


Fig. 2 Typical N 1s (a) and C 1s (b) photoelectron spectra of carbon nitride layers deposited at $F=16 \text{ J/cm}^2$ and at $p(\text{N}_2)=10 \text{ Pa}$. The data are presented after inelastic background subtraction and using gaussian fits.

To look in details, the spectra were deconvoluted using the gaussian fit. The results of the deconvolution of the broad N 1s and C 1s photoelectron peaks clearly suggest different chemical bonds both for N and for C atoms. The N/C atomic ratio of the films were calculated from the area ratio of each peak considering the sensitivity of the detector and the photoionization cross sections.

The binding energy of the N 1s centred at 400.6 eV can be associated to N atoms bonded to C atoms in the sp^2 bonding state and the one at 399.1 eV can be assigned to N atoms bonded to C atoms in sp^1 bonding state, that is to $\text{C}\equiv\text{N}$ triple bond²¹. By times the N 1s spectrum showed a tail at high energy due to N-O bond.

The four gaussian profiles of the C 1s spectrum shown in fig. 2b are peaked at 284.4, 285.2, 286.2 and 287.9 eV. The binding energies of C 1s at 284.4 and 285.2 eV can be associated to grafitic and diamond-like structures, respectively²². Instead, the peaks at 286.2 and 287.9 eV can be associated to C atoms bonded to N atoms in the sp^1 and sp^3 bonding states, respectively²³. XPS analyses of the deposited films have clearly showed that the number of N atoms covalently bonded to C atoms and the nitrogen concentration increase with laser fluence and gas pressure.

The chemical composition and thickness of the CN films were studied by RBS method using 2.2 MeV He^+ beams. Thickness and C/N atomic ratio were determined by RUMP (Rutherford Universal Manipulation Program) simulation²⁴. Figures 3a and 3b show the RBS spectra of the CN films deposited on(111) Si substrate at 16 J/cm^2 and at $p(\text{N}_2)=5$ and 10 Pa. The N/C atomic ratio increases with the laser fluence and gas pressure and it reaches the maximum value of 0.7 at 16 J/cm^2 and $p(\text{N}_2)=10 \text{ Pa}$ (see Table II). On the contrary, the deposition rate decreases with increasing laser fluence in agreement with the model suggested by Singh and Narayan²⁵. The deposition rate also decreases with increasing ambient pressure. The nitrogen concentration in the films decreased when films were deposited on substrates heated to 250°C , under identical experimental conditions (Fig. 4). At 500°C the nitrogen content decreased to not detectable level. This effect could be due to the desorption of CN radicals²⁶.

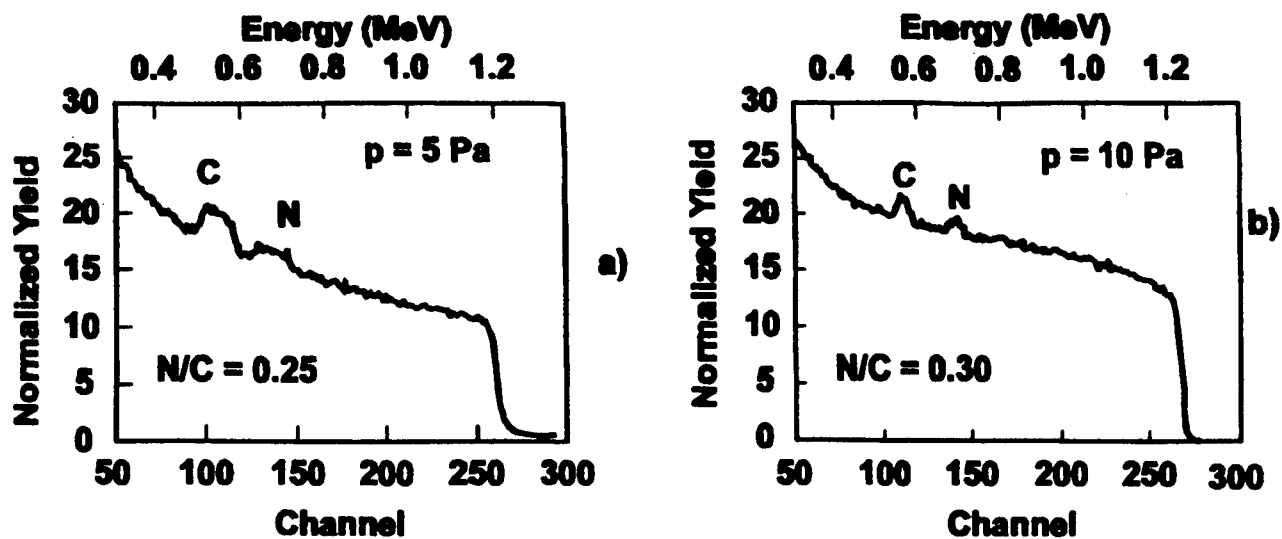


Fig. 3 RBS spectra of CN films deposited at 12 J/cm^2 and at (a) $p(\text{N}_2)=5 \text{ Pa}$ and (b) $p(\text{N}_2)=10 \text{ Pa}$

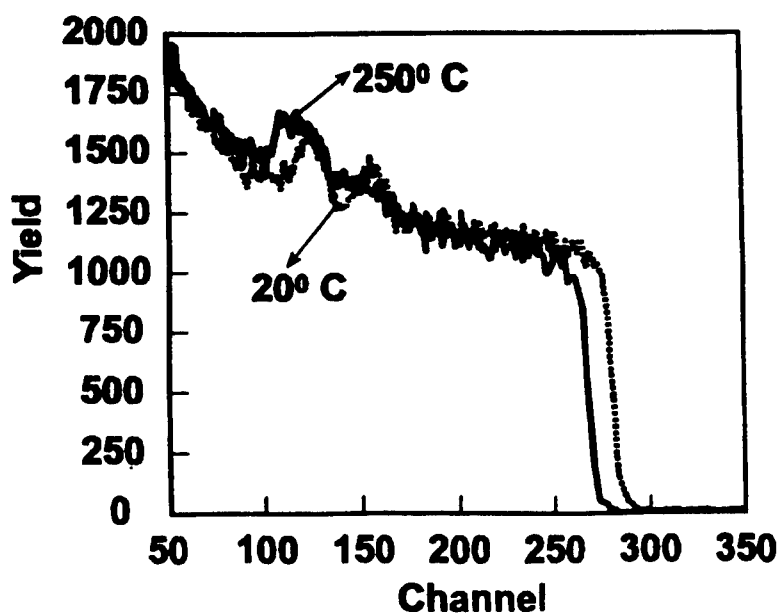


Fig. 4 RBS spectra of the films deposited at $F=12 \text{ J/cm}^2$, $p(\text{N}_2)=10 \text{ Pa}$ and substrate temperature of $T_s=20^\circ \text{ C}$ and 250° C

Table II: N/C atomic ratio and thickness inferred by RBS spectra

$p(N_2)$ (Pa)	Thickness $T_s=20^\circ\text{C}$ $F=12\text{ J/cm}^2$	N/C $T_s=20^\circ\text{C}$ $F=12\text{ J/cm}^2$	Thickness $T_s=20^\circ\text{C}$ $F=16\text{ J/cm}^2$	N/C $T_s=20^\circ\text{C}$ $F=16\text{ J/cm}^2$	Thickness $T_s=250^\circ\text{C}$ $F=16\text{ J/cm}^2$	N/C $T_s=250^\circ\text{C}$ $F=16\text{ J/cm}^2$
1	220	0.20	280	0.20	250	0.20
5	150	0.25	200	0.40	200	0.20
10	60	0.30	150	0.70	200	0.25
50	10	0.50	< 10	?	180	0.25

Further evidence in favour of the existence of CN chemical bonds was obtained by FTIR measurements. Figure 5 shows the infrared absorption spectra of CN films deposited on KBr substrate at different N_2 pressures and at 6 J/cm^2 .

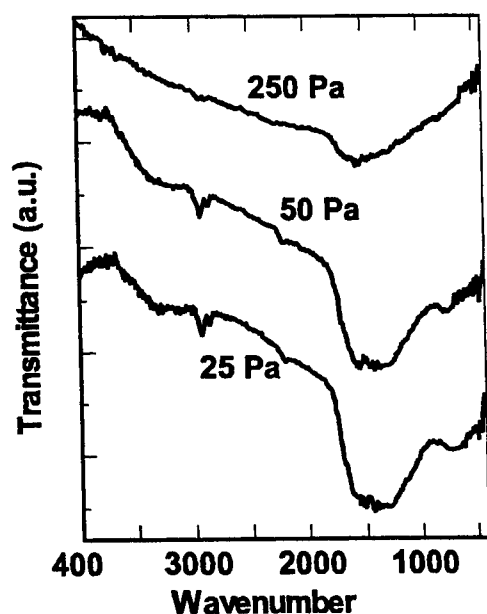


Fig. 5 FTIR transmission spectra of the samples deposited on KBr substrates under different N_2 pressures, at $F=6\text{ J/cm}^2$ and $T_s=20^\circ\text{C}$

The spectra look similar to those of the films deposited by other techniques²⁷⁻²⁸. The absorption peak centred at 2200 cm^{-1} is due to the stretching vibration of $\text{C}\equiv\text{N}$ triple bond. The broad asymmetric absorption band from 1000 to 1700 cm^{-1} can be assigned to $\text{C}=\text{N}$ double bond (1625 cm^{-1}) and to $\text{C}-\text{N}$ single bond ($1350\text{--}1500\text{ cm}^{-1}$). C.W. Ong and his collaborators associated this broad band to graphitic rings (sp^2 configuration) become infrared active because some carbon atoms in the rings are replaced by nitrogen atoms²⁹. The low intensity band feature near 700 cm^{-1}

is due to the out-of-plane bending mode in graphitic like sp^2 domains²⁹. At last, the double peak near 2900 cm^{-1} can be due to hydrocarbon contaminants.

XRD analyses have also been carried out to investigate the crystalline properties of the films. XRD profiles in glancing incident geometry ($0.5\text{--}4^\circ$) on all our films do not show any diffraction peak. This can be due to the small scattering factors of C and N atoms. The analyses carried out using $\theta - 2\theta$ Bragg geometry indicate a polycrystalline structure of the films deposited on KBr and at 12 and 16 J/cm^2 . Figure 6 shows the XRD profiles of the film deposited at 12 J/cm^2 and $p(\text{N}_2)=1$ and 10 Pa . The three peaks at 0.389 , 0.377 and 0.347 nm can not be associated neither to carbon phase nor to C_3N_4 phases. We may suppose that they could be due to a new CN_x phase.

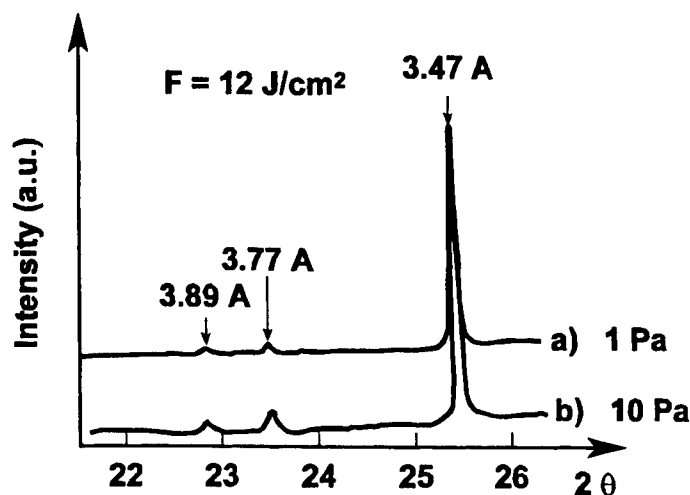


Fig. 6 XRD spectra of the samples prepared at $F=12\text{ J/cm}^2$ and $p(\text{N}_2)=1$ and 10 Pa

The narrow peaks indicate a quite large crystallite. All films deposited at 3 and 6 J/cm^2 have an amorphous structure.

The structure of the CN films has also been investigated with electron diffraction. TEM studies show that the films either exhibit poor crystallinity (12 and 16 J/cm^2) or are amorphous (3 and 6 J/cm^2). The sample deposited at room temperature, 16 J/cm^2 and $p(\text{N}_2)=1\text{ Pa}$ evidences the formation of monocrystals with an ellipsoid basis. The major axis of the ellipse ranges between 2 and $15\text{ }\mu\text{m}$, while the minor axis ranges between 1 and $5\text{ }\mu\text{m}$. These electron diffraction studies indicate that the crystals, which seem to exhibit a diamond-like structure, grew almost epitaxially on the (111) Si substrate. It is not possible to index the experimental diffraction data to diamond or graphite structures. The crystallinity of the films seems to increase with laser fluence.

SEM analyses indicate that the droplet density and dimensions decrease with increasing laser fluence and gas pressure.

Microhardness values of the samples deposited at 6 J/cm^2 were measured by using a diamond nanoindenter. The values range from 10 to 21 GPa , far lower than theoretical value of $\beta\text{-C}_3\text{N}_4$ ³⁰.

All the samples deposited at room temperature in N_2 and NH_3 atmosphere present a sheet resistivity higher than $10^9\text{ }\Omega/\text{cm}^2$. This is a further confirmation of the existence of covalent carbon-nitrogen bonds in the samples²⁹.

Mass and optical emission spectra were recorded during the laser ablation of graphite target at low pressure (up to 250 Pa) of N_2 and NH_3 atmosphere to study the role of gas-phase reactions in CN compound formation. Significant correlation with film characteristics were found.

Figure 7 shows typical time integrated optical emission spectra recorded at different N_2 pressures. The spectra are dominated by the bands due to $\Delta v = -2, -1, 0, +1, +2$ vibrational sequences (Svan system) of the C_2 ($d^3\Pi_g - a^3\Pi_u$) electron transition and by the bands due to $\Delta v = -1, 0, +1$ vibrational sequences of CN ($B^2\Sigma^+ - X^2\Sigma^+$) electronic transition. The CN radical is considered the most appropriate precursor for the deposition of C_3N_4 ³¹. The CN and C_2 bands intensities increase with nitrogen pressure at all the used laser fluences.

In figure 8 time integrated optical emission spectra recorded at different laser fluences are shown. The spectra always have the same bands and the same structures, with CN band intensities increasing with laser fluence. Optical emission studies confirm the results deduced from XPS and RBS analyses: the N/C atomic ratio in the deposited films and the CN band emission increase with laser fluence and N_2 gas pressure.

The most interesting results have been obtained from the study of the spectra recorded at different distances from the target (Fig. 9). CN violet bands, which were very weak at 1 mm, become the dominant ones at larger distances. This feature is observed at all the used laser fluences. In fig 10, the dependence of CN and C_2 emission intensity on the distance from the target, for a fluence of 12 J/cm^2 and a pressure of 100 Pa, is shown. One can see that the C_2 emission has a narrow profile which reaches the maximum near the target and exhibits a rapid decrease with the distance. The CN radical emission has a large profile which reaches the maximum at about 6 mm from the target. These results indicate that, even if the formation mechanisms of the CN radical are not still well known, the gas phase formation of CN radical seems to be very important³².

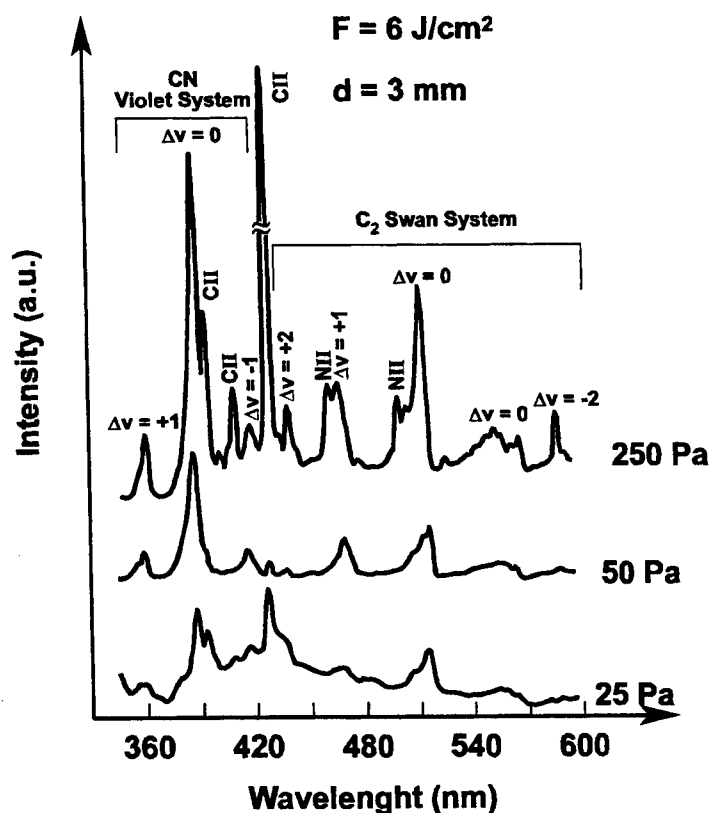


Fig. 7 Typical time integrated optical emission spectra recorded during laser ablation of graphite at different N_2 pressures and at $F=6 \text{ J/cm}^2$

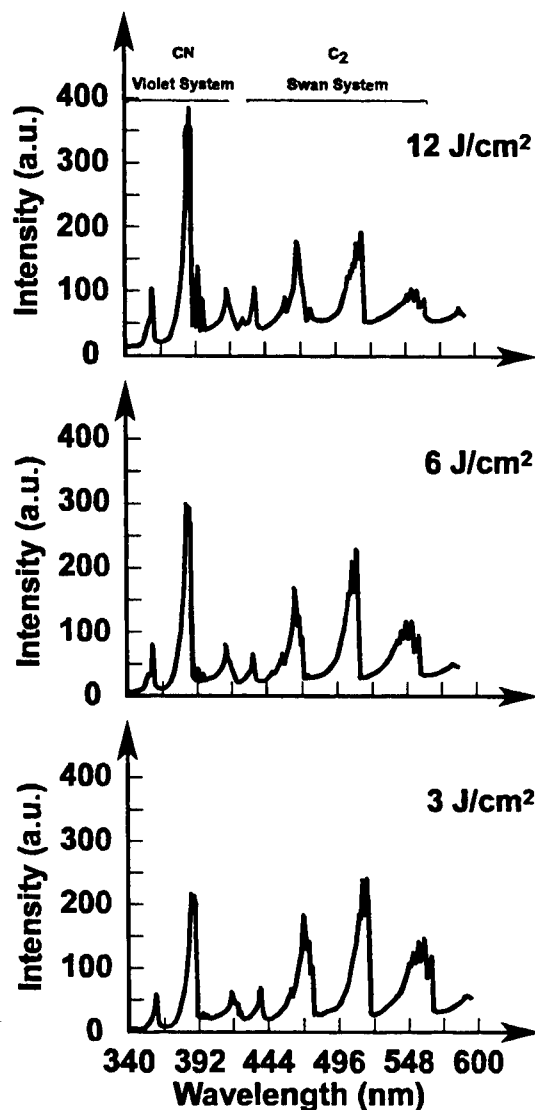


Fig. 8 Optical emission spectra of the plasma plume recorded during laser ablation of graphite at different laser fluences in N_2 at 250 Pa and at 5 mm from the target

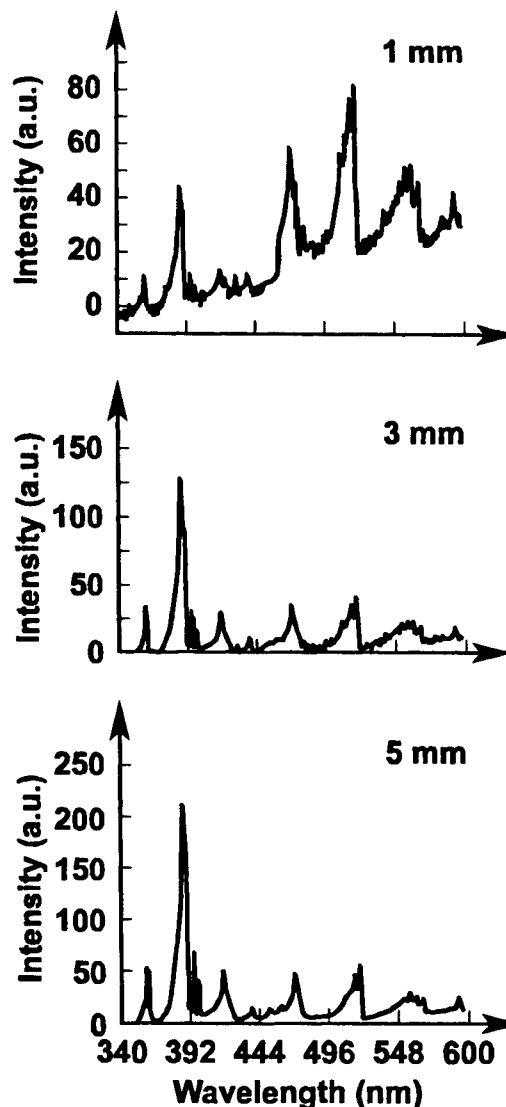


Fig. 9 Optical emission spectra recorded in N_2 at different distances from the target. The laser fluence was set at 12 J/cm^2

The spectra recorded in NH_3 had the same structures as ones recorded in N_2 , with the C_2 Swan system bands dominant. The CN violet system bands were very weak and lightly increase with NH_3 pressure and laser fluence.

The mass spectra recorded in N_2 ambient atmosphere at $p=10^{-2}$ Pa, the highest working pressure of our mass spectrometer, were full of peaks (Fig. 11a). The most interesting ones were due to C, C_2 , CN, C_2N , CN_2 and C_2N_2 . After the first 2000 pulses many peaks disappeared, but the CN mass peak didn't disappear, even if it was less intense than before (Fig. 11b). This effect was observed every time we irradiated virgin target surfaces. This behaviour could be explained with a nitridation process between carbon surface and adsorbed nitrogen leading to CN formation on the target surface.

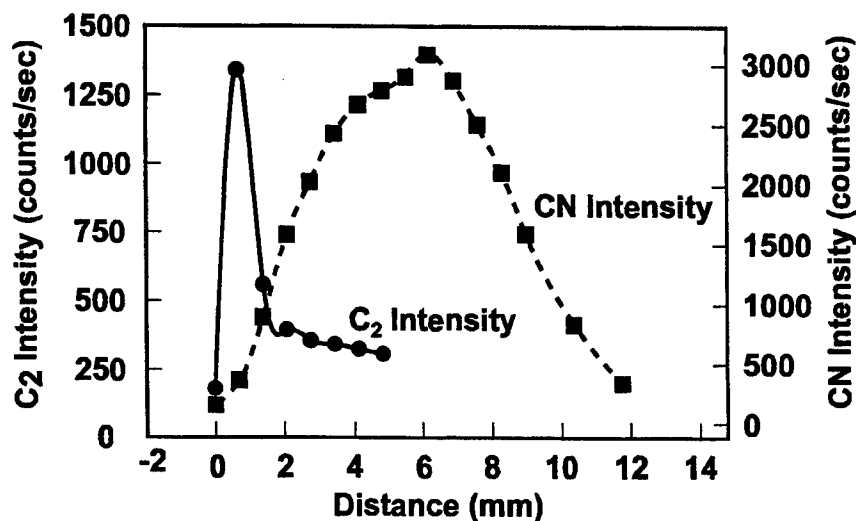


Fig. 10 Behaviour of CN and C_2 bands intensities as a function of the distance from the target with $p(N_2)=100$ Pa and $F=12$ J/cm²

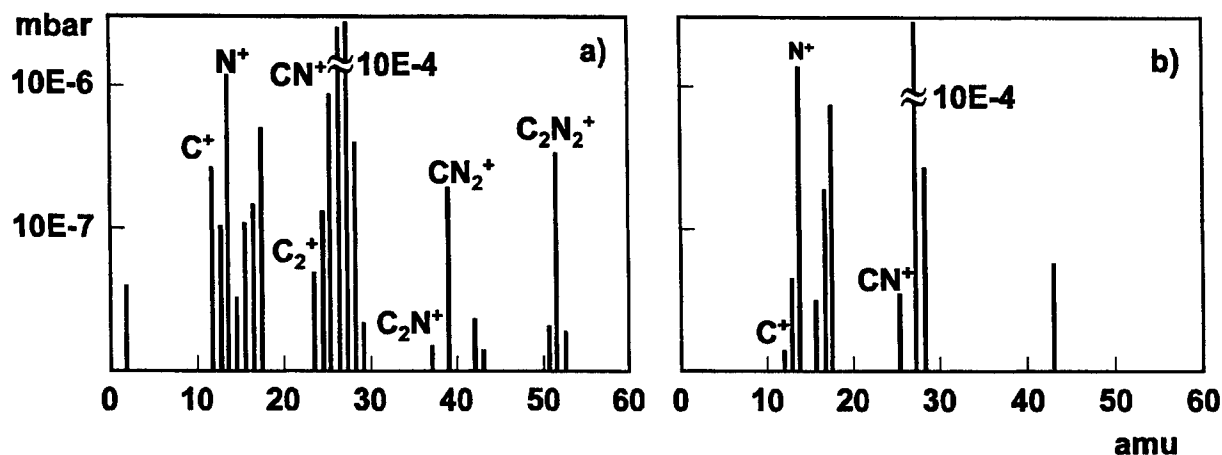


Fig. 11 Typical mass spectra recorded during pulsed laser ablation of graphite (a) in low pressure (10^{-2} Pa) of N_2 during the first pulses of ablation and (b) after 2000 laser pulses. The laser fluence was set at 6 J/cm²

4. DISCUSSION

The deposition rate of the deposited films decreases with increasing gas pressure because the number of collisions between the ablated material and the ambient gas molecules increases with gas pressure. The deposition rate also decreases with increasing laser fluence. This effect is due to the shape of the plasma created during the laser irradiation of the target. In fact, the variation of the film thickness can be expressed in the form of d^P , where d is the substrate-target distance and P is the expansion coefficient describing the nature of the expansion. The value of P corresponds to 3 for a spherical expansion and is equal to 1 for a linear expansion. The expansion coefficient is

dependent on the spot size. As the spot size is decreased (as the laser fluence increased), the plasma expansion becomes more spherical and the thickness and deposition rate decrease²⁵.

The N/C atomic ratio increases with laser fluence and gas pressure. It is higher in films deposited in NH₃ atmosphere than in N₂ at the same conditions, even if the number of atoms bonded to C atoms is lower in NH₃ than in N₂ atmosphere. This can be explained with the large quantity of N-H bonds detected by IR spectroscopy in samples prepared in NH₃ atmosphere.

The analyses of XPS and IR spectra indicate that C atoms are present in different bonding states. It is not clear why in the N 1s spectrum the gaussian peak associated to N atoms bonded to C atoms in sp³ bonding state is absent. Measurements with as high an energy resolution possible are needed in order to obtain deconvolutions as reliable as possible.

Observed peaks in the XRD spectra correspond to interplanar distances that can not be assigned neither to carbon phase nor to C₃N₄ phases. They could be due to a new CN_x phase.

Heating of substrate reduces the nitrogen content in the samples. It could be explained by the thermal desorption of CN radicals.

From spectroscopy studies we found a strong correlation between the CN band intensities and the nitrogen concentration in the deposited films, both increase with laser fluence and gas pressure. Moreover, from the study of the optical emission spectra recorded at different distances from the target, a gas-phase reaction for the CN radical formation can be guessed. On the contrary, from the mass spectra analyses a nitridation process on the target surface can be also deduced. In fact, a high CN peak intensity is observed until the already adsorbed nitrogen on the target surface is reacted, afterwards the CN signal decreased and stabilised at a value sustained only by the nitrogen adsorbed between two consecutive laser pulses³³. In case of ammonia atmosphere, even though we observed a similar behaviour, the CN mass peak was smaller and decreased just lightly with the number of laser pulses. This effect could be explained by the less amount of NH₃ molecules adsorbed on the target surface. The lower production of CN radical explains the predominance of the C₂ Swan system bands over the CN bands in the optical emission spectra recorded during laser ablation of graphite in ammonia. These experimental evidences of nitridation processes on the target surface and in gas phase do not exclude the possibility of other nitridation processes in the growing film substrate.

5. CONCLUSIONS

Carbon nitride thin films have been deposited on Si and KBr substrates by RPLA of graphite at various gas pressures and at different laser fluences. The films were relatively hard and adhesive, with a low droplet density. Furthermore, they are plane and without cracks or corrugations. Quite high values of N/C atomic ratio (up to 0.7) were measured into films. The quality of films increases with gas pressure and laser fluence. Heating of the substrates reduces the nitrogen concentration in the deposited films.

The simple method of RPLA of graphite target in low pressure of nitrogen results to be a promising technique for the deposition of good quality carbon nitride films on substrates at room temperature. We believe that the formation of polycrystalline carbon nitride is closely related to the experimental conditions. It therefore would be interesting to study the effect of even higher laser fluences (>20 J/cm²) on the CN film properties.

6. ACKNOWLEDGEMENTS

I would like to thank the group of the Physics Radiation Laboratory of Lecce University and the group of Prof. I. Mihailescu of Bucharest University. I also wish to thank Profs G. Majni and P. Mengucci of Ancona University and the Dr. J. Zemek of Czech Academy of Sciences of Prague. This work is supported by funds from the Istituto Nazionale Fisica della Materia.

7. REFERENCES

1. A.Y. Liu and M.L. Cohen, "Prediction of new low compressibility solids", *Science*, **245**, 841-842, 1989
2. R.B. Jackman and L.H. Chua, "Diamond-like carbon within microelectronics: dielectric properties on silicon and GaAs", *Diam. Relat. Mater.* **1**, 895-899, 1992
3. B. Singh, S. McClelland, F. Tams III, B. Halon, O. Mesker and D. Furst, "Use of black diamond-like carbon films as a contrast enhancement layer for liquid-crystal displays", *Appl. Phys. Lett.* **57**, 2288-2290, 1990
4. A.Z. Khan, J.A. Woollam and Y. Chung, "Interfacial effect due to the tunnelling to insulator gap states in amorphous carbon on silicon metal-insulator-semiconductor structure", *J. Appl. Phys.* **55**, 4299-4303, 1984
5. G. Zhang, L.G. Guo, Z. Liu and X. Cheng, "Application of diamond-like carbon films as protection and antireflection coatings of ZNS elements", *Opt. Eng.* **33**, 1330-1333, 1994
6. H. Han and B.J. Feldman, "Structural and optical properties of amorphous carbon nitride", *Solid State Commun.* **65**, 921-923, 1988
7. J.H. Kaufman and S. Metin, "Symmetry breaking in nitrogen doped amorphous carbon: infrared observation of the Raman-active G and D bands", *Phys. Rev.* **B39**, 13053-13060, 1989
8. F. Fujimoto and K. Ogata, "Formation of carbon nitride films by means of ion assisted dynamic mixing (IVD) method", *Jpn. J. Appl. Phys.* **32**, L420-423, 1993
9. D. Marton, A.H. Al-Bayati, S.S. Todoroc, K.J. Boyd and J.W. Rabalais, "Synthesis of carbon-nitride films using a fast switched dual-source low energy ion beam deposition system", *Nucl. Instrum. Methods, Phys. Rev.* **B90**, 277-281, 1994
10. I. Gouzman, R. Brener and A. Hoffman, "Carbon nitride formation by low-energy nitrogen implantation into graphite", *Thin Solid Films*, **253**, 90-94, 1994
11. D. Marton, K.J. Boyd, A.H. Al-Bayati, S.S. Todorov and J.W. Rabalais, "Carbon nitride deposited using energetic species: a two-phase system", *Phys. Rev. Lett.* **73**, 118-121, 1994
12. M.R. Wixom, "Chemical preparation and shock wave preparation of carbon nitride precursors", *J. Am. Ceram. Soc.* **73**, 1973-1978, 1990
13. C.J. Torng, J.M. Silversten, J.H. Judi and C. Chang, "Structure and bonding studies of the C:N thin films produced by rf sputtering", *J. Mater. Res.* **5**, 2490-2496, 1990
14. D. Li, Y.W. Chung, M.S. Wong, and W.D. Sproul, "Nano-indentation studies of ultrahigh strength carbon nitride thin films", *J. Appl. Phys.* **74**, 219-223 1993
15. A. Luches, A.P. Caricato, G. Leggieri, M. Martino, A. Perrone, G. Barucca, P. Mengucci and J. Zemek, "Laser reactive ablation deposition of carbon nitride thin films", *SPIE Proc.* **2789**, 293-304, 1996
16. E. D'Anna, A. Luches, A. Perrone, S. Acquaviva, R. Alexandrescu, I.N. Mihailescu, J. Zemek and G. Majni, "Deposition of C-N films by reactive laser ablation", *Appl. Surf. Science*, **106**, 126-131, 1996.

17. C. Niu, Y.Z. Lu and C.M. Lieber, "Experimental realisation of the covalent solid carbon nitride", *Science*, **261**, 334-337, 1993
18. Z.M. Ren, Y.C. Du, Y. Qiu, J.D. Wu, Z.F. Ying, X.X. Xiong and F.M. Li, "Carbon nitride films synthesised by combined ion beam and laser ablation processing", *Phys. Rev.* **B51**, 5274-5277, 1995
19. K.M. Yu, M.L. Cohen, E.E. Haller, W.L. Hansen, A.Y. Liu and I.C. Wu, "Observation of crystalline C_3N_4 ", *Phys. Rev.* **B49**, 5034-5037, 1994
20. J.P. Riviere, D. Texier, J. Delafond, M. Jaouen, E.L. Mathe and J. Chamount, "Formation of crystalline β - C_3N_4 phase by dual ion beam sputtering deposition", *Mater. Letters*, **22**, 115, 1995
21. W.T. Zheng, K.Z. Xing, N. Hellgren, M. Logdlund, A. Johansson, U. Gelivs, W.R. Salanek and J.E. Sundgreen, "Nitrogen 1s electron binding energy assignment in carbon nitride thin films with different structures", *Journal of Elect. Spectr. and Relat. Phenom.* (in press)
22. Y. Mizokawa, T. Miyasato, S. Nakamura, K.M. Geib and C.W. Wilmsen, "The CKLL first - derivative X-ray photoelectron spectroscopy spectra as a fingerprint of the carbon state and the characterisation of diamond-like carbon films ", *J. Vac. Sci. Technol.* **A5**, 2809-2813, 1987
23. S. Kumar, K.S.A. Butcher and T.L. Tansley, "X-ray photoelectron spectroscopy characterization of radio frequency reactively sputtered carbon nitride thin films", *J. Vac. Sci. Technol.* **A14**, 2687-2692, 1996
24. L.R. Doolittle, "Algorithms for the rapid simulation of Rutherford backscattering spectra", *Nuclear Instrum. Method*, **B9**, 344-351, 1985
25. R.K. Singh and J. Narajan, "Pulsed-laser evaporation technique for deposition of thin films: Physics and theoretical model", *Phys. Rev.* **B41**, 8843-8859, 1990
26. P. Gonzalez, R. Soto, E.G. Parada, X. Redondas, S. Chiussi, J. Serra, J. Pou, B. Leon and M. Perez-Amor, "Carbon nitride films prepared by excimer laser ablation", *Appl. Surf. Science*, **3819**, 380-383, 1996
27. Z.J. Zhang, S. Fan and C.M. Lieber, "Growth and composition of covalent carbon nitride solids", *Appl. Phys. Lett.* **66**, 3582-3584, 1995
28. P. Hammer, M.A. Baker, C. Lenardi and W. Gissler, "Synthesis and properties of carbon nitride films deposited using a dual ion beam method", *Vuoto*, **26**, 38-41, 1997
29. C.W. Ong, X.A. Zhao, Y.C. Tsang, C.L. Choy and P.W. Chan, "Effects of substrate temperature on the structure and properties of reactive pulsed laser deposited CN_x films", *Thin Solid Films*, **280**, 1-4, 1996
30. A.Y. Liu and M.L. Cohen, "Structural properties and electronic structure of low-compressibility materials: β - Si_3N_4 and hypothetical β - C_3N_4 ", *Phys. Rev.* **B41**, 10727-10734, 1990
31. S. Veprek, "Transport of carbon in non-isothermal low pressure nitrogen plasma", *Z. Phys. Chem.* **86**, 95-107, 1973
32. E. Aldea, A.P. Caricato, G. Dinescu, A. Luches and A. Perrone, "Optical emission diagnostic of laser-induced plasma during CN_x film deposition", *Jpn. J. Appl. Phys.* **36**, 4686-4689, 1997
33. S. Aquaviva, A.P. Caricato, M.L. De Giorgi, A. Luches and A. Perrone, "Spectroscopic studies during pulsed laser ablation deposition of C-N films", *Appl. Surf. Science*, **109/110**, 408-412, 1997.

Laser diagnostics in flame deposition of diamond

R.J.H. Klein-Douwel¹ and J.J. ter Meulen

Dept. of Molecular and Laser Physics, University of Nijmegen
Toernooiveld, 6525 ED Nijmegen, The Netherlands. Fax: +31-24-3653311

ABSTRACT

Combustion diagnostics by means of two-dimensional Laser Induced Fluorescence (2D-LIF) is applied to a diamond depositing oxyacetylene flame. The method and results of diamond growth are discussed, as well as the 2D-LIF technique. The distributions of atomic hydrogen, CN, and C₂ in the flame are presented together with their relations to diamond growth.

Keywords: diamond, CVD, oxyacetylene flame, Laser Induced Fluorescence, atomic hydrogen, C₂, CN, nitrogen incorporation

1. INTRODUCTION

A relatively simple method to make sufficient amounts of radicals for chemical vapour deposition (CVD) of diamond is the use of highly exothermic reactions which take place in for instance flames. Hydrocarbon flames of various structures and compositions can be used. This idea was first utilized by Hirose in 1988, who employed an oxyacetylene combustion flame to deposit diamond on a cooled substrate under atmospheric conditions¹. The oxyacetylene flame burns C₂H₂ with O₂ and is the hottest hydrocarbon flame ($\approx 3000^\circ\text{C}$)². This method was soon picked up by several other groups, and the technique is now well developed to deposit polycrystalline diamond on non-diamond substrates and single crystalline diamond layers on a diamond seed crystal^{3, 4, 5, 6}, which is either of natural origin or grown by another CVD technique.

In flame deposition of diamond the high velocity gas flow of the flame normally impinges at normal incidence on the cooled substrate. This creates a stagnation-point flow at the surface where the gas stream is deflected radially. The exact shape of the gas stream profile depends on the flow velocity beyond the flame front and on the distance between flame front and substrate. Assuming chemical equilibrium in the gas phase, its composition can be calculated from the flame feed stock gases, which shows CO, H₂, H, and C₂H₂ to be the major species beyond the flame front⁷. In these calculations the temperature is assumed to be constant throughout the flame, only decreasing linearly in a thin boundary layer above the substrate. The major species react with the other species present in the flame and the temperature profile and the transport of important species like atomic hydrogen towards the substrate can be calculated, taking hydrodynamic gas phase properties like density and viscosity into account^{8, 9}. These results are given only for one fixed set of deposition conditions, but recently species and temperature profiles and the corresponding diamond growth rate and quality have been calculated for various sets of growth conditions in the laminar oxyacetylene flame, agreeing reasonably well to empirical results^{10, 11}.

The possible mechanism of the diamond growth process on the surface is depicted in figure 1. The top layer of carbon atoms is connected to the diamond bulk below and their remaining bonds are either dangling or terminated by hydrogen atoms. These adsorbed hydrogen atoms can be etched away by gas phase atomic hydrogen, forming gas phase H₂, which leaves a free site on the surface. At such a site CH₃, which is thought to be an important growth species, may stick to one surface carbon atom and, after one or more of its hydrogen atoms have been desorbed, to a neighbouring one as well. Like hydrogen atoms, CN and OH, if present, are considered to be important for hydrogen abstraction from the surface. Apart from CH₃, the growth species may include CH, C₂, and CN, molecules often present in flames.

The exact deposition mechanism, however, is not well known and the two-dimensional Laser Induced Fluorescence (LIF) technique is used to shed some extra light on the flame processes and obtain relations between the gas phase and the diamond layer characteristics, such as growth rate, morphology, and nitrogen incorporation. The LIF method is applied because of its species specificity, high spatial resolution, non-intrusiveness, and high sensitivity. In combination with a pulsed laser and a CCD (charge coupled device) camera both laminar and turbulent flames are studied in detail. The obtained information elucidates the rôle of flame species and their importance (or

¹email: robertkd@sci.kun.nl

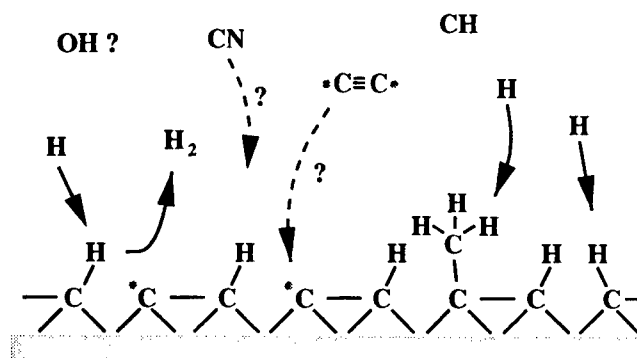


Figure 1: Schematic representation of a possible diamond growth mechanism. Some species present in the oxyacetylene flame are indicated.

unimportance) for diamond growth. The relations between diamond growth and flame characteristics can be used as a monitor in the growth process, enabling fast feedback to obtain diamond layers with properties closer to desired for industrial applications, and reveal which parameters are important for upscaling the deposition area, another (economic) aspect of industrial application of flame growth of diamond.

2. EXPERIMENTAL SETUP

The experimental setup for diamond growth combined with LIF detection during deposition is depicted in figure 2. Exact experimental details are described in previous studies on H, C₂, CH, CN, and OH^{12, 13, 14}, but important parameters and their typical values are given here. The acetylene supersaturation S_{ac} is important during diamond deposition, which is why both the oxygen and acetylene flows are regulated by mass flow controllers. The burner orifice diameter is 1.4 mm and the oxygen flow is 3.0 standard liters per minute. Diamond growth can take place on the substrate, positioned in the acetylene feather, for $0 < S_{ac} \lesssim 9\%$. For $S_{ac} \gtrsim 9\%$ the deposit will not contain diamond anymore, but mostly amorphous carbon. In most experiments $S_{ac}=5\%$ is used, resulting in an acetylene flow of ≈ 2.5 SLM.

The substrate consists of a thin (0.5 mm) molybdenum square soldered to a molybdenum holder. The substrate is cooled from below by a pulsed water nozzle, which is regulated by a thermocouple located 2.5 mm beneath the centre of the substrate surface. The thermocouple temperature T_s is kept at 900 ± 1 °C, resulting in a deposition temperature T_d at the substrate surface of 1050 ± 20 °C. Prior to deposition the molybdenum substrate is scratched with micrometre sized diamond powder to enhance nucleation and adhesion to the substrate of the diamond layer to be grown.

Apart from S_{ac} and T_d , the distance d between the tip of the flame front and the substrate (indicated in figure 2) is a main parameter in determining the characteristics of the obtained diamond layer. Typical values of d are between 0.5 and 3 mm, where short distances result in a high central maximum in the diamond growth rate v_d (which can be more than 150 $\mu\text{m/h}$) and larger distances yield a central valley surrounded by an annulus of enhanced growth. Diamond layers deposited at a distance d of 1 to 2 mm reveal in their centre a continuous area of uniform thickness and well connected randomly oriented {111} and {100} facets. The diameter of this region is 4 - 5 mm. A photograph showing an entire diamond layer, deposited with a laminar flame at the somewhat larger distance $d=4.04$ mm, is given in figure 3a². At distances d larger than about 3 mm a so called *core zone*¹⁵ of ≈ 2.0 mm ϕ develops in the centre. In this core zone the crystallites mainly reveal {111} facets and are often much smaller than in the rest of the centre. They also show a large amount of secondary nucleation, as can be seen in figure 3b, which gives a scanning electron microscope (SEM) photograph of the core zone. The large crystallites in this photograph, which are of normal size, are interspersed with many much smaller ones. This is why the core zone appears slightly darker than the surrounding central region in figure 3a.

²Photographs of diamond layers deposited at smaller distances are given in references¹² and ¹³, but the general description is identical.

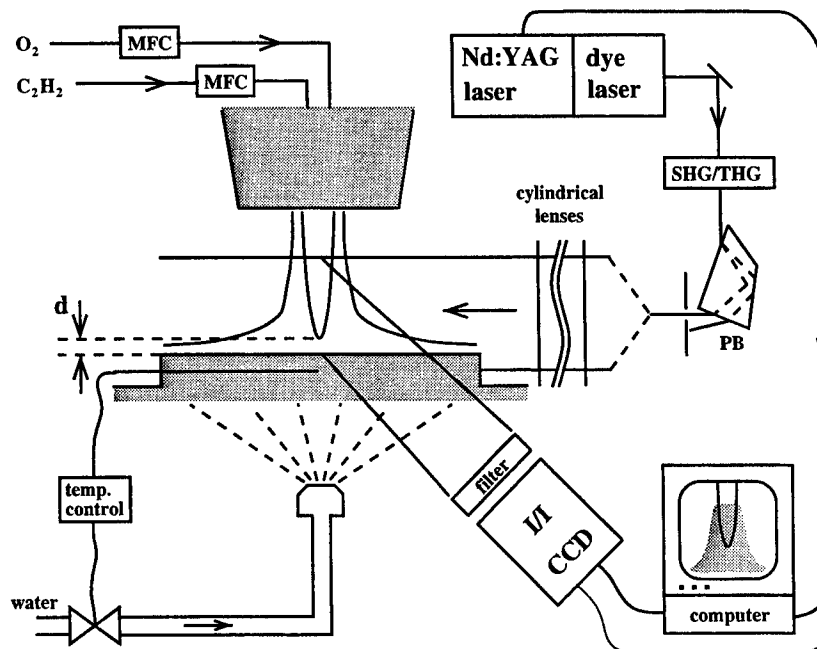


Figure 2: Schematic representation of the diamond growth and LIF detection setup. MFC = mass flow controllers, SHG/THG = second/third harmonic generation (if applicable), PB = Pellin-Broca prism, I/I = image intensifier, CCD = charge coupled device camera. The distance d between the substrate and the tip of the flame front is indicated.

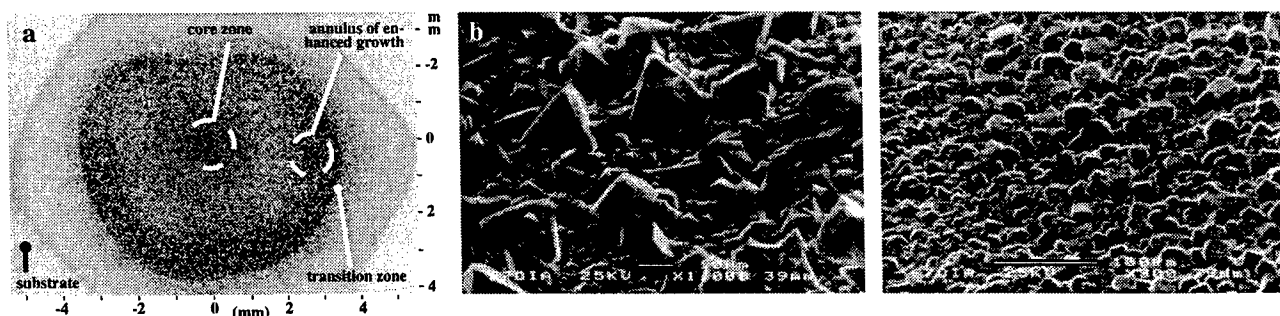


Figure 3: Photographs revealing the morphology of a diamond layer, deposited by a laminar flame at $d=4.04$ mm. (a) Normal photograph, showing the entire layer; various regions are indicated. The slight spherical asymmetry is caused by an irregularity in the burner tip. (b) SEM photograph of the *core zone*, showing normal-sized crystallites embedded in many much smaller ones. The scale bar is $10\ \mu\text{m}$ long. (c) Transition zone, revealing a highly $\{100\}$ textured region, beyond the annulus of enhanced growth (which is located outside the upper right-hand corner of the image). At the left-hand side the small crystallites of the diamond layer edge become visible. The scale bar is $100\ \mu\text{m}$ long.

Outside the centre an annular region of enhanced growth is observed, where the morphology is markedly different. This annulus typically exhibits large columnar crystallites, separated by voids or embedded in an amorphous layer, which frequently have {100} top facets almost parallel to the substrate. In figure 3a it appears darker than the centre due to a lower density of reflecting facets. Outside the annulus of enhanced growth a sharp transition zone is generally found, which is only 0.1 - 0.2 mm wide and can exhibit a continuous, highly {100} textured morphology. A SEM photograph of this is shown in figure 3c: morphologies like this are of interest to many applications of polycrystalline diamond layers. Beyond this transition zone the morphology resembles that of the central area, with the size of the crystallites rapidly diminishing towards the edge of the diamond layer. The reflectivity of the outer edge is smaller, owing to the vanishing crystallite size.

After growth the deposited diamond layers are characterized by optical differential interference contrast microscopy (DICM), scanning electron microscopy (SEM), Raman spectroscopy, and cathodoluminescence topography (CL), which technique reveals information about the incorporation of nitrogen into the diamond layer. The diamond layer thickness is determined by focusing the optical microscope with an accuracy of $\pm 2 \mu\text{m}$ at different locations of the layer.

3. LASER INDUCED FLUORESCENCE

Figure 2 depicts how the LIF technique is applied to the oxyacetylene flame during the deposition of diamond. The second or third harmonic of a Nd:YAG laser is used to pump a dye laser. The output of the dye laser (5 ns laser pulses with a repetition frequency of 10 Hz) is directed to the flame and passes through the cylindrical telescope. If necessary, the frequency of the dye laser is doubled in a birefringent crystal and can be mixed in a second birefringent crystal to obtain the third harmonic. The wavelengths are then separated in a Pellin-Broca prism and the undesired wavelengths are dumped. Fluorescence is collected by a charge coupled device (CCD) camera equipped with an image intensifier, with an appropriate filter in front of it, and the signals are digitized by and can be further processed on a personal computer. The exposure time of the image intensifier is typically 20 ns. This is long enough to capture the LIF signal and short enough to reduce the natural emission of the flame considerably, which is important when studying bright flames such as the oxyacetylene flame.

In order to select the optimum excitation and detection wavelength for making LIF images of flame species, first their excitation and dispersed fluorescence spectra have to be recorded. A useful tool for doing so is an optical multichannel analyzer (OMA). It is constructed by removing the exit slit of a monochromator (Jobin Yvon M25, 600 g/mm, resolution 1 nm) and placing the CCD camera without any optics directly behind it. A spherical lens is used to create a 1:1 image of the laser beam trajectory through the flame on the entrance slit of the monochromator. In this way a CCD image contains spatial information on one axis and dispersed wavelength information on the other. The resulting resolution is about 0.25 nm per pixel, which corresponds to a total range of 70 nm viewed in an image. An example of this is shown in figure 4, where 656 nm atomic hydrogen fluorescence (Balmer α) is visible after two-photon excitation at 205 nm, together with the second order NO fluorescence at 607 and 639 nm. This NO fluorescence stems from the one-photon $A^2\Sigma^+(v'=2) \leftarrow X^2\Pi(v''=0)$ transition of NO (γ system) at 205 nm¹⁶, which, as a pure coincidence, is excited simultaneously with the Lyman β transition in atomic hydrogen, and results in $v'=2 \rightarrow v''=6-10$ fluorescence between 263 and 320 nm. From figure 4 it is clear that atomic hydrogen is present from the centre of the flame to at least 4 mm outside, whereas NO is only present beyond 2 mm from the centre. Using the OMA it is possible to obtain an excitation spectrum and a dispersed fluorescence spectrum simultaneously during a single wavelength scan of the laser. For this purpose a column of width Δx of an OMA image (figure 4) is integrated in x -direction and stored as a single line. This is repeated continuously while the laser wavelength λ_{exc} is scanned. The resulting image gives λ_{disp} versus λ_{exc} .

A review of the species detected by LIF in the oxyacetylene flame during diamond growth is given in table 1. All transitions can be excited by a dye laser, using its second or third harmonic if necessary. Only for NO excitation at 193 nm a tunable ArF excimer laser is used. For detection of atomic hydrogen the third harmonic of 615 nm dye laser radiation is used, which is separated from the second harmonic and the fundamental frequency by the Pellin-Broca prism (see figure 2). The LIF signal is proportional to the population density in the lower state of the species of interest. Determining this proportionality constant, *id est* quantification of the LIF signal, suffers from several problems if the LIF method is used in atmospheric pressure flames. Due to collisions of the excited species with neighbouring species in the flame, part of the fluorescence is quenched.

The spatial variation of the temperature is one of the intriguing aspects of the oxyacetylene flame during diamond deposition. In order to investigate the temperature distribution in the flame, excitation spectra of the $C_2 \Delta v=2$

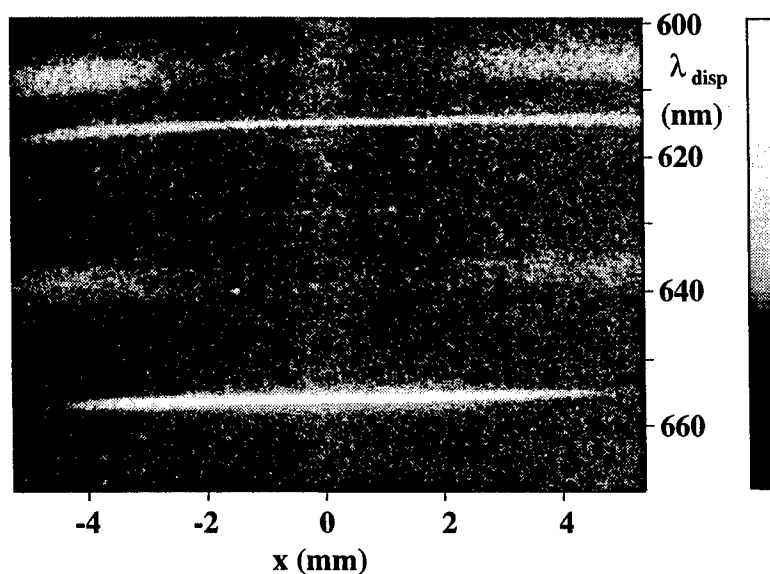


Figure 4: OMA image of atomic hydrogen fluorescence (656 nm) and second order NO fluorescence (607 and 639 nm) after excitation at 205 nm with one (NO) or two (H) photons. The line at 615 nm is due to scattered light of the dye laser fundamental wavelength. The signal around $x=0$ mm consists of natural emission of the flame and non-resonant fluorescence. Recorded with a 0.05 mm wide entrance slit. Intensities are represented on a gray scale from black to white (to make the features stand out more clearly, low intensities are suppressed in this image, whereas medium intensities are enhanced).

Species	Transition		λ_{exc} (nm)	
H	n=3	← n=1	2×205	Lyman β
NO	$D^2\Sigma^+(v'=0)$	← $X^2\Pi(v''=1)$	193	ϵ bands
	$A^2\Sigma^+(v'=2)$	← $X^2\Pi(v''=0)$	205	γ bands
OH	$A^2\Sigma^+(v'=3)$	← $X^2\Pi(v''=0)$	248	3064 Å bands
	$A^2\Sigma^+(v'=1)$	← $X^2\Pi(v''=0)$	282	
	$A^2\Sigma^+(v'=0)$	← $X^2\Pi(v''=0)$	308	
C ₂	$C^1\Pi_g(v'=2)$	← $A^1\Pi_u(v''=0)$	340	Des. - d'A. bands
CN	$B^2\Sigma^+(v'=1)$	← $X^2\Sigma^+(v''=0)$	359	Violet bands
CH	$B^2\Sigma^-(v'=0)$	← $X^2\Pi(v''=0)$	393	3900 Å bands
C ₂	$d^3\Pi_g(v'=2)$	← $a^3\Pi_u(v''=0)$	438	Swan bands
	$d^3\Pi_g(v'=0)$	← $a^3\Pi_u(v''=2)$	619	
	$d^3\Pi_g(v'=0)$	← $a^3\Pi_u(v''=3)$	686	

Table 1: Species detected by LIF during diamond growth and their excitation wavelengths

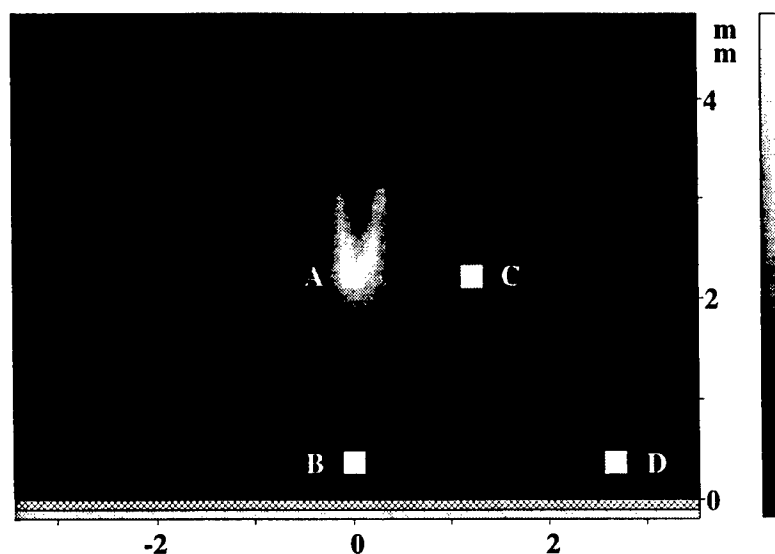


Figure 5: C_2 LIF image during diamond growth showing the locations at which excitation spectra are recorded simultaneously ($x=0$ [A, B], $x=1.22$ mm [C], $x=2.68$ mm [D], and $y=2.22$ mm [A, C], $y=0.38$ mm [B, D]). Intensities are given on a linear gray scale and dimensions are in mm.

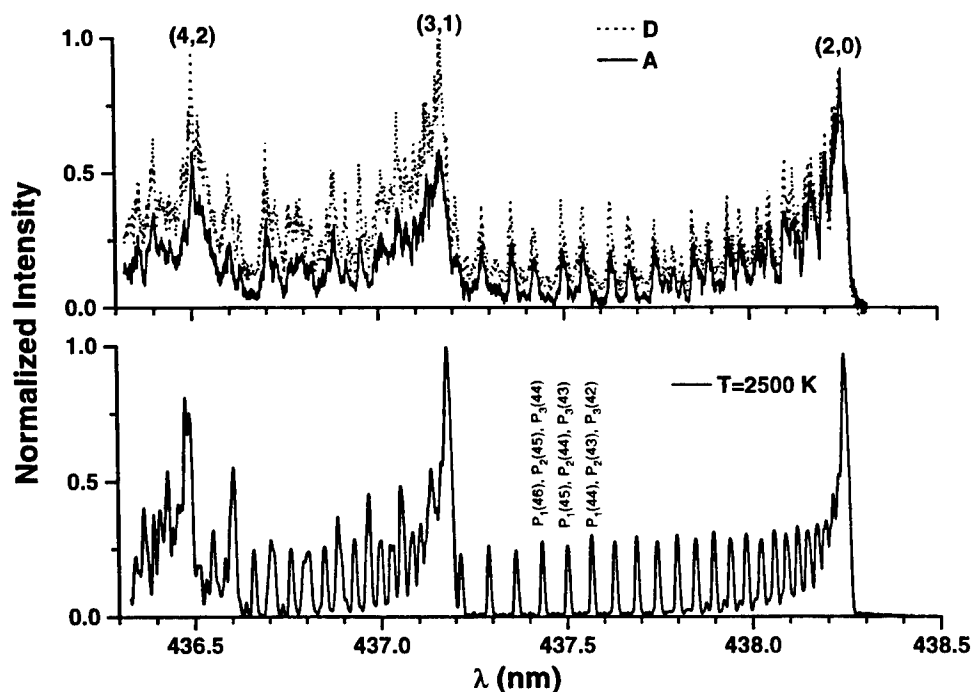


Figure 6: C_2 excitation spectra. Upper part: observed spectra A and D (from figure 5); lower part: spectrum calculated for $T=2500$ K. All spectra are normalized at the (2,0) bandhead.

Swan band have been recorded simultaneously at four different positions in the flame during diamond deposition. The spectra are collected in square areas of $0.20 \times 0.20 \text{ mm}^2$, the location of which is shown in figure 5. All spectra are normalized at the (2,0) bandhead. The relative intensities in spectrum D of higher rotational and vibrational levels are larger than in spectrum A, indicating the temperature in location D may be higher. A measure of the temperature can be obtained when the relative intensity of the (2,0) bandhead is compared to that of for instance the line consisting of the overlapping $P_1(45)$, $P_2(44)$, and $P_3(43)$, and the two neighbouring lines, as indicated in figure 6. The small background between these lines (maybe due to the R branch becoming important at elevated temperatures or to a non-resonant signal) is subtracted and the quenching of fluorescence is assumed to be independent of the rotational level involved. Spectrum A then yields a temperature of 2300K, whereas D has an apparent temperature of 2900K (spectrum B gives 2800K and spectrum C yields 2400K), with an uncertainty of about 800K. If, however, the intensity of the (3,1) bandhead is compared to that of the (2,0) bandhead, the resulting temperatures are lower: 1700, 2200, 2100, and 2500 (again $\pm 800\text{K}$) for A, B, C, and D, respectively. This may indicate that there is no thermal equilibrium between rotation and vibration, the rotational temperature being higher. In contrast to what is expected, the temperature closer to the substrate appears to be higher than at the flame front, which has the lowest apparent temperature of the recorded spectra.

From these results it may be concluded that the model which is used to derive temperatures from the observed spectra is not good enough. Apparently the quenching does depend on the rotational level the C_2 molecule is in, and this in such a way that the rotational dependence seems to invert from spectrum A to D: the quenching rate appears to increase for high rotational levels in spectrum A, whereas an apparent decrease is found in spectrum D. Yet one useful fact arises from the simultaneous spectral measurements: the spectra and apparent temperatures at the locations B and D, both close to the substrate, reveal only slight differences, indicating the lateral gas phase temperature variation just above the substrate may be small.

The effects of temperature variations within the atmospheric pressure oxyacetylene flame on the LIF signals are shown above to be complex and are therefore not taken into account in the results described below. But many results given concern relative densities in a layer parallel and close to the substrate, where the temperature is not expected to vary very much. Hence the conclusions drawn from these results will not be affected much by neglecting temperature effects.

4. RESULTS AND DISCUSSION

The distribution of C_2 in the flame during diamond deposition is shown in figure 5. The distance d between the tip of the flame front and the substrate is 2.22 mm. The laser beam extends from the substrate to about 4 mm above it. Since the background is subtracted, the upper part of the flame front (total length $\approx 6 \text{ mm}$) is not visible in figure 5. From this figure it is clear that C_2 is present in the acetylene feather and that the maximum signal is found at the flame front. In the acetylene feather the C_2 signal is more or less constant, but close to the substrate it drops markedly, yet it is still readily detectable.

An example of the CN LIF signal is given in figure 7a. If compared to figure 5, it is evident that CN is located at the edge of the acetylene feather and that it is not found at or close to the flame front. This may be explained by a mechanism in which the CN is formed from carbon containing species from inside the flame and nitrogen containing species from outside the flame. Because the flame is fuel-rich, the acetylene combustion is incomplete and species containing one or more carbon atoms are ubiquitous at and beyond the flame front. N_2 from the ambient air is entrained by the gas flow of the flame and diffuses into the acetylene feather, where it may be decomposed by thermal dissociation or reactions with radicals in the acetylene feather.

Figure 7b shows the distribution of atomic hydrogen LIF signal in the first two millimetres above the substrate. Comparison with figures 5 and 7a reveals H to be present inside as well as outside the acetylene feather. Measurements at various heights of the laser beam in the flame¹⁴ show that H LIF signal is also found at the flame front, where it is created. Atomic hydrogen diffuses rapidly throughout the flame and is consumed outside the acetylene feather by reactions with ambient air. Both the images of C_2 and H LIF are recorded at relatively large distances d and in both cases a central minimum can be discerned in the LIF signal close to the substrate.

In order to study the species distribution close to the substrate in more detail, horizontal profiles are taken from LIF images obtained at various distances d . Figure 8 shows horizontal profiles of the C_2 , CN, and H LIF signals, for each species, one at a relatively small distance d and one at a relatively large distance. Also shown in this figure is the lateral variation of the growth rate v_d of the corresponding diamond layers, which is measured along the path of the laser beam. The behaviour of the H and C_2 profiles is similar: for small distances d a clear central

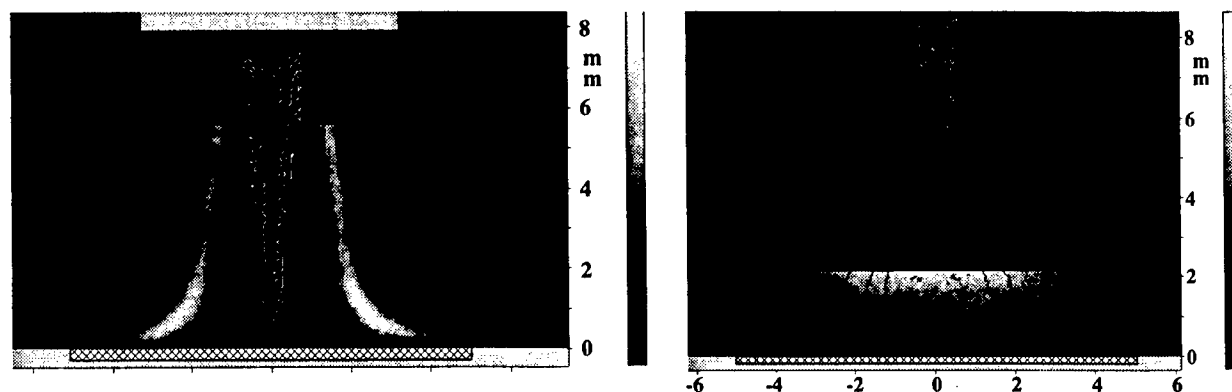


Figure 7: (a) CN LIF signal and (b) H LIF signal during diamond deposition in the flame (linear gray scale in arbitrary units, ranging from black (zero) to white (maximum)). Natural emission of the flame is superimposed (isophotes, representing equal intensity difference steps). The distance between flame front and substrate is $d=0.55$ mm (a) and $d=3.05$ mm (b). The images are corrected for the vertical intensity distribution of the laser beam (the noisy uppermost part is removed for reasons of clarity). The substrate and the burner tip are indicated in gray, the crosshatched area depicts the diamond deposition region, and dimensions are in mm.

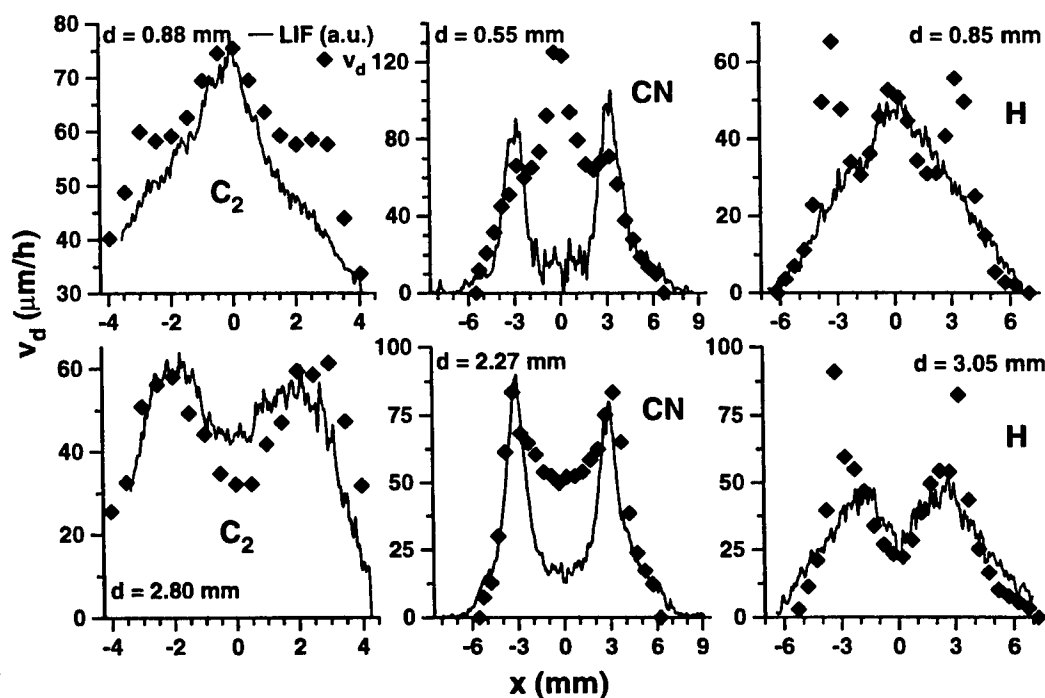


Figure 8: Horizontal profiles of the C_2 (left), CN (centre), and H (right) LIF signals (solid lines) compared to the variation of the growth rate v_d (diamonds) of the corresponding diamond layer, as measured along the path of the laser beam.

maximum is found and the LIF signal decreases more or less linearly with radial distance, and for large distances the central maximum is substituted by a central minimum, as already discussed above. The presence of atomic hydrogen, however, extends radially further than that of C_2 .

The general behaviour of v_d as a function of d is already discussed above. In figure 8 the annulus of enhanced growth is clearly visible in the variation of v_d . When v_d is compared to the radial distribution of H LIF signal close to the substrate, it is striking that both show a very similar radial behaviour from the centre all the way to the edge of the diamond layer, if the annulus of enhanced growth is not taken into account. The good agreement between the H distribution close to the substrate and v_d (apart from the annulus of enhanced growth) indicates the importance of atomic hydrogen to the deposition rate of the diamond layer, which has already been studied elaborately in theory 9, 17, 18, 19, 20, 21, 22. At the edge of the diamond layer atomic hydrogen is still found in measurable quantities, but diamond growth here is limited by the lack of carbon containing species. The correspondence between the C_2 profiles and v_d is similar to that of atomic hydrogen, although it is limited to a smaller area. The resemblance indicates that C_2 may be important for the diamond growth rate in the centre of the deposited layer¹², which agrees to the rôle of C_2 as a diamond precursor, as put forward by Gruen and co-workers^{23, 24, 25, 26, 27}.

Inspection of figure 8 shows that v_d drops much less rapidly with increasing distance d in the annulus of enhanced growth than in the centre of the diamond layer. In addition to this, the annulus of enhanced growth and the transition zone just outside it reveal a large fraction of {100} facets parallel to the substrate, compared to the centre and the outer edge of the diamond layer, as described above and in 6, 13, 15. These observations are strong indications that the growth mechanism in the annulus is different from elsewhere in the deposited diamond layer. The fact that the maxima in the horizontal CN profiles coincide with the annulus of enhanced growth therefore indicates that CN or a closely related species (only one or two reaction steps away) may be important in the diamond growth process in the annulus, regarding both the morphology and the local growth rate. The influence of CN (or a closely related species) on the growth rate may be explained by the possibilities of CN and HCN to abstract adsorbed hydrogen from the growing diamond surface^{28, 29}, which creates free growth sites and may increase the local growth rate. The preferential formation of {100} facets parallel to the substrate in and close to the annulus of enhanced growth may also be related to the presence of CN or a closely related species, since similar morphologies have been observed upon nitrogen addition to flame and other diamond growing CVD systems^{28, 30, 31, 32, 33, 34}, in which studies also the positive effect of nitrogen addition to the diamond growth rate is described.

After growth the diamond layers are examined by CL to study the incorporation of nitrogen as nitrogen-vacancy pairs into the diamond lattice. Depending on the distance d between flame front and substrate and the exact composition of the acetylene and oxygen source gases, the nitrogen incorporation in the centre of the diamond layer is medium to completely absent, but in the annulus of enhanced growth always a maximum nitrogen incorporation is found^{13, 15}. This can be explained by diffusion and subsequent thermal decomposition of ambient N_2 in the flame: outside the acetylene feather the temperature is too low for N_2 decomposition and close to the flame axis the diffusion of nitrogen decreases, resulting in a maximum amount of reactive nitrogen at the location where CN is found, *id est* above the annulus of enhanced growth. The CN LIF signal can therefore be used as an indicator for nitrogen incorporation into the diamond layer during the flame growth process.

5. CONCLUSIONS

Flame deposition of diamond by the oxyacetylene flame is a relatively simple and fast technique to grow diamond layers. Yet the exact growth mechanism is not well known and therefore the method of (two-dimensional) Laser Induced Fluorescence is applied to the flame during diamond growth. LIF is a powerful and highly sensitive technique to obtain information about molecular density distributions in combustion processes, allowing visualization of one or more species during a single laser pulse. Although quantification of the LIF signal is hampered by collisional quenching, the obtained signals of H, C_2 , and CN reveal much information about the diamond growth process. Relations are observed between the distributions of these three species in the flame and the growth rate, morphology, and nitrogen incorporation of the diamond layers. These relations may also be used for upscaling and real-time control of the flame deposition process.

ACKNOWLEDGMENTS

The authors wish to thank Ir. J.J. Schermer, Ir. M. Okkerse and Dr. W.J.P. van Enckevort for many useful discussions. This work has been made possible by financial support of the Stichting voor Technische Wetenschappen (Technology Foundation).

REFERENCES

- ¹ Y. Hirose and N. Kondo, Extended Abstracts, 35th Jpn. Appl. Phys. Spring Meeting, March 1988, p. 434
- ² A.G. Gaydon and H.G. Wolfhard, *Flames, their structure, radiation and temperature*, Chapman & Hall, London, 1979.
- ³ Y. Matsui, A. Yuuki, M. Sahara, and Y. Hirose, Jpn. J. Appl. Phys. **28**, 1718 (1989).
- ⁴ G. Janssen, W.J.P. van Enckevort, J.J.D. Schaminée, W. Vollenberg, L.J. Giling, and M. Seal, J. Cryst. Growth **104**, 752 (1990).
- ⁵ L.M. Hanssen, K.A. Snail, W.A. Carrington, J.E. Butler, S. Kellogg, and D.B. Oakes, Thin Solid Films **196**, 271 (1991).
- ⁶ J.J. Schermer, J.E.M. Hogenkamp, G.C.J. Otter, G. Janssen, W.J.P. van Enckevort, and L.J. Giling, Diamond Rel. Mater. **2**, 1149 (1993).
- ⁷ Y. Matsui, H. Yabe, and Y. Hirose, Jpn. J. Appl. Phys. **29**, 1552 (1990).
- ⁸ D.G. Goodwin, Appl. Phys. Lett. **59**, 277 (1991).
- ⁹ D.G. Goodwin, J. Appl. Phys. **74**, 6895 (1993).
- ¹⁰ M. Okkerse, R.J.H. Klein-Douwel, M.H.J.M. de Croon, C.R. Kleijn, J.J. ter Meulen, G.B. Marin, and H.E.A. van den Akker, Proceedings of the 14th international CVD symposium - 11th EUROCVD Conference, Paris, August 31 - September 5 (1997), accepted for publication, (1997).
- ¹¹ M. Okkerse, private communication (1997).
- ¹² R.J.H. Klein-Douwel, J.J.L. Spaanjaars, and J.J. ter Meulen, J. Appl. Phys. **78**, 2086 (1995).
- ¹³ R.J.H. Klein-Douwel, J.J. Schermer, and J.J. ter Meulen, submitted to Diamond Rel. Mater., (1997).
- ¹⁴ R.J.H. Klein-Douwel and J.J. ter Meulen, submitted to J. Appl. Phys., (1997).
- ¹⁵ J.J. Schermer, W.A.L.M. Elst, and L.J. Giling, Diamond Rel. Mater. **4**, 1113 (1995).
- ¹⁶ K.P. Huber and G. Herzberg, *Molecular Spectra and Molecular Structure. IV. Constants of Diatomic Molecules*, Van Nostrand Reinhold Company, New York, 1979.
- ¹⁷ G. Janssen, W.J.P. van Enckevort, and L.J. Giling, Proc. First Int. Symp. on Diamond and Diamond-like Films, J.P. Dismukes (ed.), The Electrochemical Soc., Pennington, 508 (1989).
- ¹⁸ M. Frenklach and K.E. Spear, J. Mater. Res. **3**, 133 (1988).
- ¹⁹ M. Frenklach, J. Appl. Phys. **65**, 5142 (1989).
- ²⁰ M. Frenklach and H. Wang, Phys. Rev. B **43**, 1520 (1991).
- ²¹ S.J. Harris and D.G. Goodwin, J. Phys. Chem. **97**, 23 (1993).
- ²² A. Ohl, J. Röppcke, and W. Schleinitz, Diamond Rel. Mater. **2**, 298 (1993).
- ²³ D.M. Gruen, S. Liu, A.R. Krauss, and X. Pan, J. Appl. Phys. **75**, 1758 (1994)
- ²⁴ D.M. Gruen, S. Liu, A.R. Krauss, J. Luo, and X. Pan, Appl. Phys. Lett. **64**, 1502 (1994)
- ²⁵ D.M. Gruen, C.D. Zuiker, A.R. Krauss, and X. Pan, J. Vac. Sci. Technol. A **13**, 1628 (1995).
- ²⁶ D.A. Horner, L.A. Curtiss, and D.M. Gruen, Chem. Phys. Lett. **233**, 243 (1995).
- ²⁷ P.C. Redfern, D.A. Horner, L.A. Curtiss, and D.M. Gruen, J. Phys. Chem. **100**, 11654 (1996).
- ²⁸ S. Bohr, R. Haubner, and B. Lux, Appl. Phys. Lett. **68**, 1075 (1996).
- ²⁹ A. Badzian, T. Badzian, and S.-T. Lee, Appl. Phys. Lett. **62**, 3432 (1993).
- ³⁰ R. Locher, C. Wild, N. Herres, D. Behr, and P. Koidl, Appl. Phys. Lett. **65**, 34 (1994).
- ³¹ J.J. Schermer and F.K. de Theije, in preparation.
- ³² W. Müller-Sebert, E. Wörner, F. Fuchs, C. Wild, and P. Koidl, Appl. Phys. Lett. **68**, 759 (1996).
- ³³ S. Jin and T.D. Moustakas, Appl. Phys. Lett. **65**, 403 (1994).
- ³⁴ G.Z. Cao, J.J. Schermer, W.J.P. van Enckevort, W.A.L.M. Elst, and L.J. Giling, J. Appl. Phys. **79**, 1357 (1996).

Synthesis of nanosize powders by pulsed laser ablation and related plasma diagnostics

K. Yatsui, W. Jiang, K. Nishiura and T. Yukawa
Laboratory of Beam Technology, Nagaoka University of Technology
Nagaoka, Niigata 940-21, Japan

C. Grigoriu, I. Chis, A. Marcu* and D. Miu
National Institute for Laser, Plasma and Radiation Physics, Laser Department
Bucharest-Magurele, P. O. Box MG 36, Romania

ABSTRACT

Nanosize powders of AlN was successfully synthesized by pulsed laser ablation. The target can be either Al or AlN , with ambient gas nitrogen. With Al targets, typical powder diameters were in the range of 2.5 ± 25 nm. In order to study the process of powder formation, we have used a high-speed camera and a time-resolved spectrum analyzing system to investigate the behaviour of the ablation plasma and the ion species in the plasma. For the diagnostic experiments, the target was Al and the ambient gas was oxygen.

Keywords: nanosize powder, pulsed laser ablation, aluminum nitride, ablation plasma, plasma spectroscopy, high-speed photography, ceramics, specific surface-area

1. INTRODUCTION

Nanosize powders have a very large specific surface area. For this reason, nanosize powders of many kinds of material have specific magnetic, optical, chemical and sintering properties.¹ These properties have made nanosize powders very interesting in applications such as magnetic media, catalysts, gas sensors, and other industrial fields.

Aluminum nitride (AlN) powders are industrially interesting since AlN is expected to be used as the substrate material for semiconductor circuits, replacing the presently used aluminum oxide (Al_2O_3). AlN is advantageous compared to Al_2O_3 because it has a higher thermal conductivity and a thermal expansion coefficient closer to that of silicon. However, AlN is more difficult to sinter than Al_2O_3 . This problem is expected to be solved by using AlN nanosize powders.

Nanosize powders can be produced by using the chemical method.² With this method, nanosize powders can be produced in large amounts, but the purity is rather poor. It has been realized that the purity of nanosize powders obtained by this method is hardly improved due to its reliance on chemical reactions. In recent years, physical methods such as pulsed laser ablation^{3,4} and pulsed ion beam evaporation⁵⁻¹¹ have been developed for the production high purity nanosize powders.

In this paper we report our recent results on nanosize powder production by using pulsed laser ablation and the results of related plasma diagnostics. The characteristics of AlN powders are analyzed by XRD (x-ray diffraction), TEM (transmission electron microscope) and surface area measurement. The plasma diagnostics are also carried out by using a high-speed camera and a time-resolved spectrum analyzing system.

*Present address: Laboratory of Beam Technology, Nagaoka University of Technology, Nagaoka, Niigata 940-21, Japan

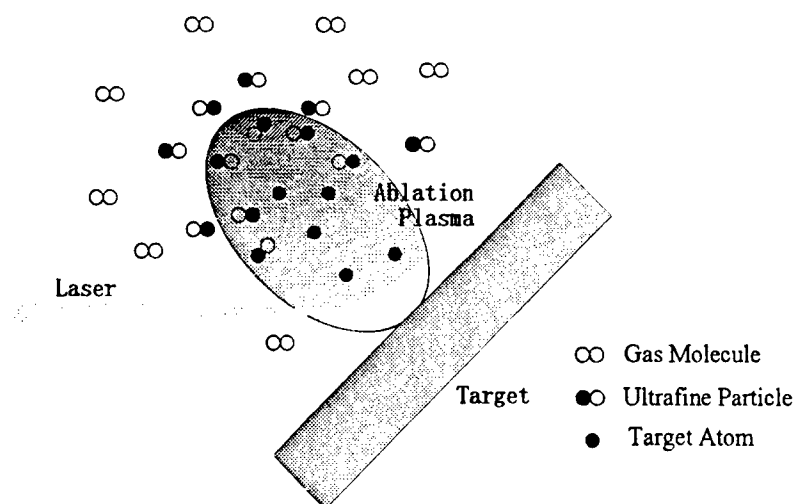


Fig. 1 Principle of nanosize powder production.

2. EXPERIMENTAL SETUP

Figure 1 shows the basic principle of synthesizing nanosize powders by using the pulsed laser ablation method. When the high power laser beam is irradiated on the target, the target surface is heated to high temperature due to very high energy density of the laser beam. It is vaporized, partially ionized and expands into the surrounding space. If the surrounding space is filled with gas, the ablated materials

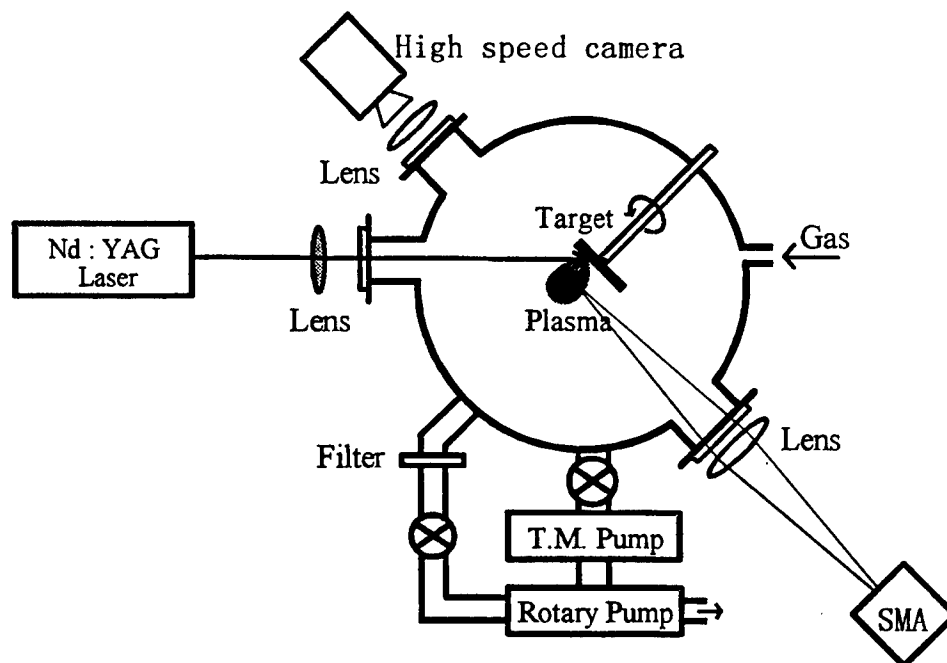


Fig. 2 Experimental setup.

will be cooled by the interaction with the gas molecules. The uniform solidification of the materials results in nanosize powders.

Figure 2 shows the schematic of experimental setup. A Q-switched Nd:YAG laser ($1.064\text{ }\mu\text{m}$, 7 ns, $10\sim 16\text{ J/cm}^2$) was used to ablate the aluminum target with an angle of 45 degree to the target surface. Throughout the experiments, the ambient gas was flowing with the speed of $1\text{ N}\ell/\text{min}$ (2.0 kg/cm^2) and the target was being rotated to avoid the concentrated damage. At the outlet of the gas flow, a membrane filter is located to collect the powder produced.

3. EXPERIMENTAL RESULTS

3.1 Production of AlN nanosize powders

Nanosize powders was produced by pulsed laser ablation method. The target was aluminum (99.5 % in purity) and the ambient gas was nitrogen (99.9999 % in purity). The pressure of the ambient gas was varied from 10 to 500 Torr.

Figure 3 shows FE-SEM (field-emission scanning electron microscope) photographs of the powders. Figures 3(a), 3(b), and 3(c) show the samples obtained with nitrogen pressure of 60, 200, and 500 Torr, respectively. It is seen from these photographs that the produced particles are smaller than $1\text{ }\mu\text{m}$.

Figure 4 shows the typical result of XRD. In Fig. 4, the diffraction peaks of SUS (stainless steel) originate from the steel mesh that was used as the supporter of the particles in the XRD analysis. We see from Fig. 4 that, with nitrogen pressure lower than 60 Torr, the particles are aluminum or a mixture of aluminum and aluminum nitride. When the pressure is higher than 100 Torr, however, the particles are pure aluminum nitride.

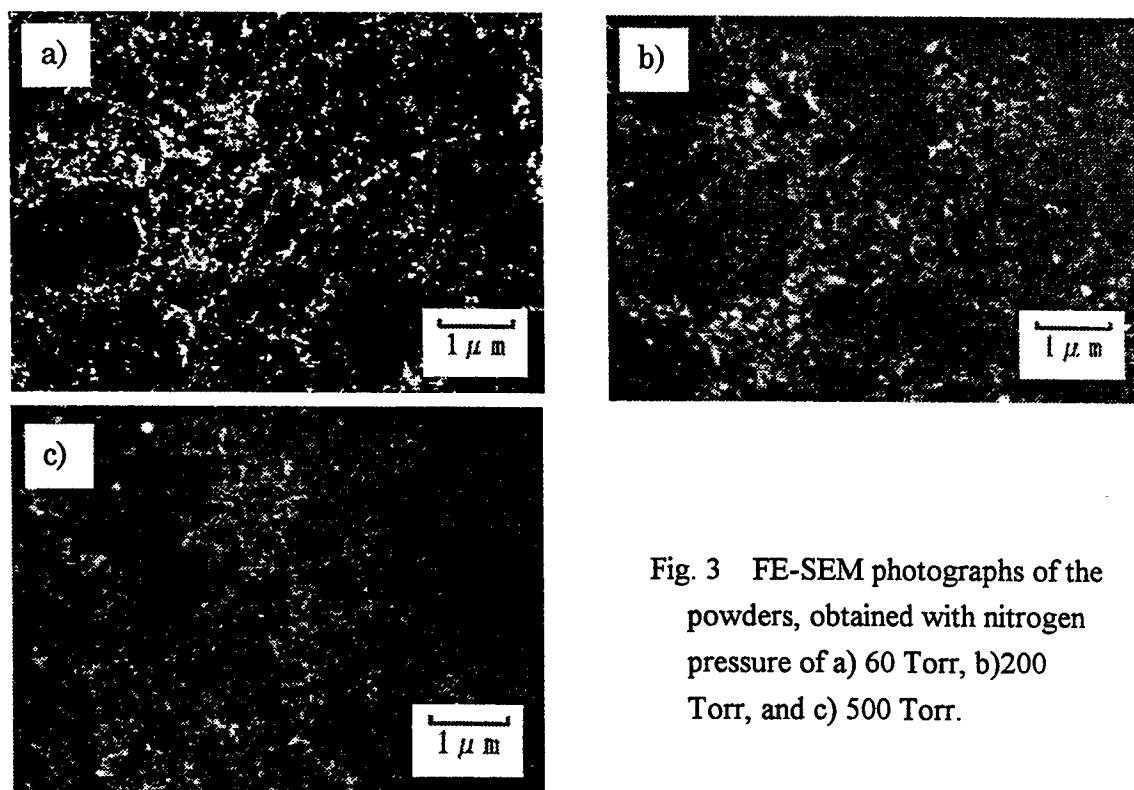


Fig. 3 FE-SEM photographs of the powders, obtained with nitrogen pressure of a) 60 Torr, b) 200 Torr, and c) 500 Torr.

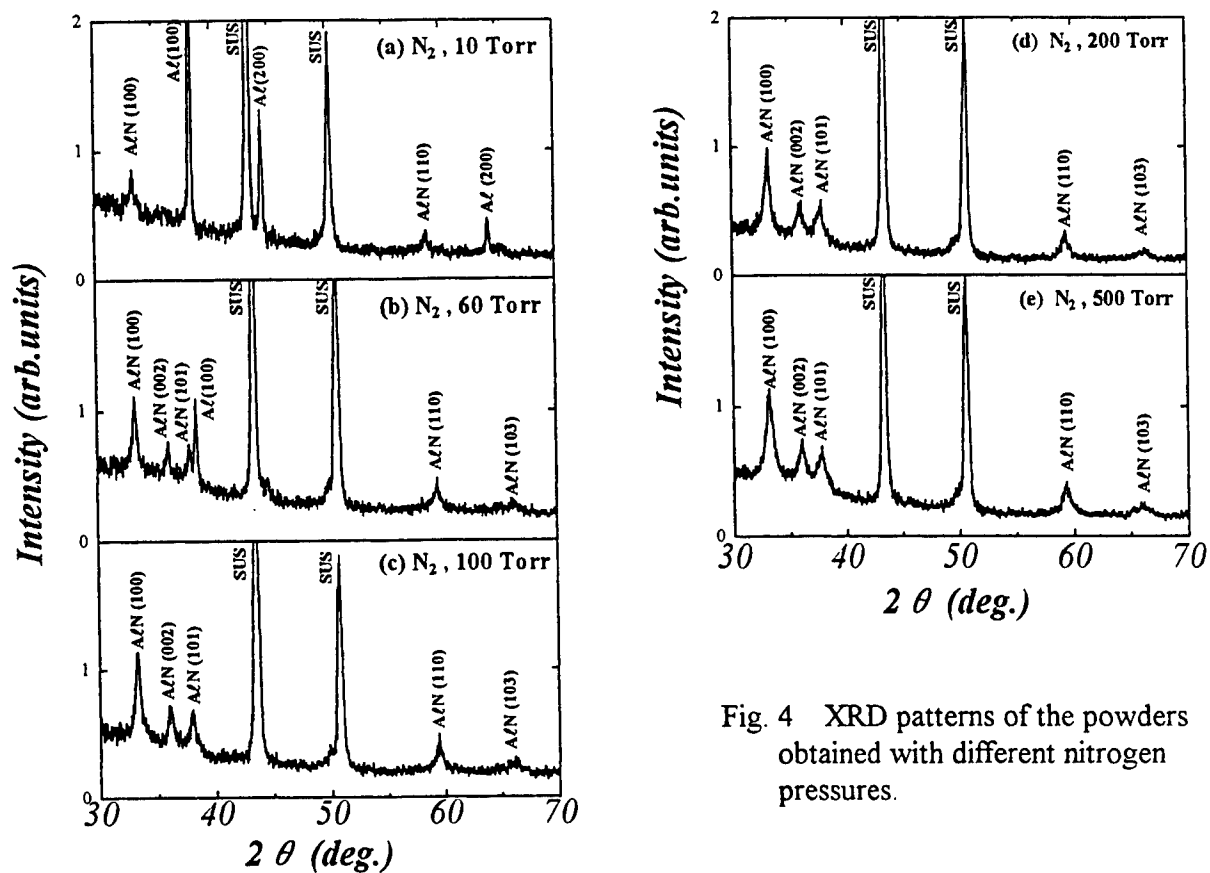


Fig. 4 XRD patterns of the powders obtained with different nitrogen pressures.

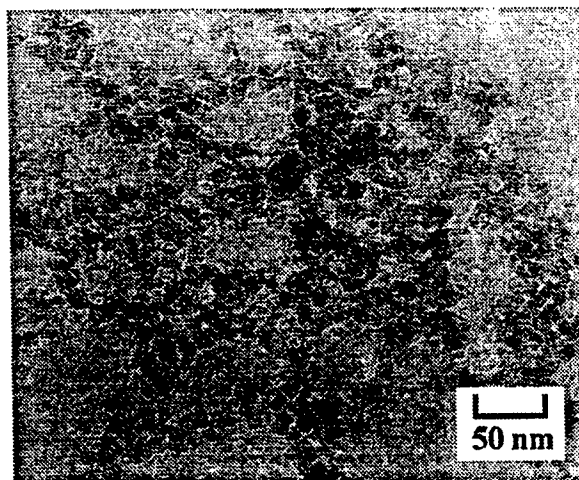


Fig. 5 TEM photograph of particles obtained at nitrogen pressure of 200 Torr.

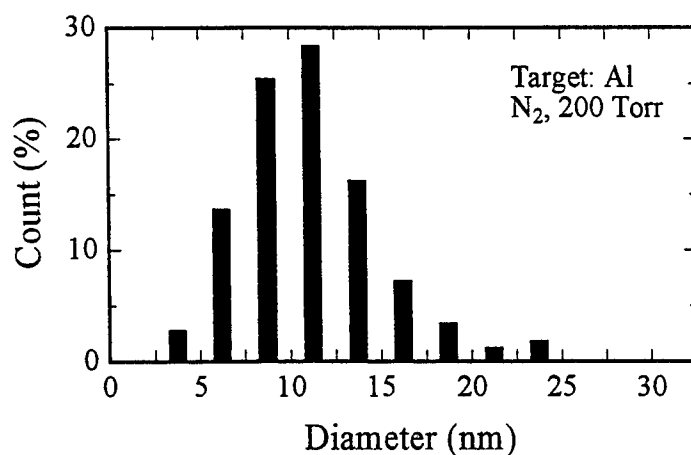


Fig. 6 Particle size distribution obtained from Fig. 5.

Figure 5 shows the TEM photograph of the particles obtained at nitrogen pressure of 200 Torr. The particle sizes are seen to be ~ 10 nm. Furthermore, some particles are seen to be hexagonal, which is consistent with the hexagonal structure of the AlN crystal.

Figure 6 shows the particle size distribution obtained from Fig. 5. It is seen that all particles are smaller than 25 nm, and the average particle size is ~ 11 nm.

Figure 7 shows the dependence of the average particle size on the pressure of the ambient nitrogen gas, where the AlN bulk was used as the target. The average particle sizes were obtained from the

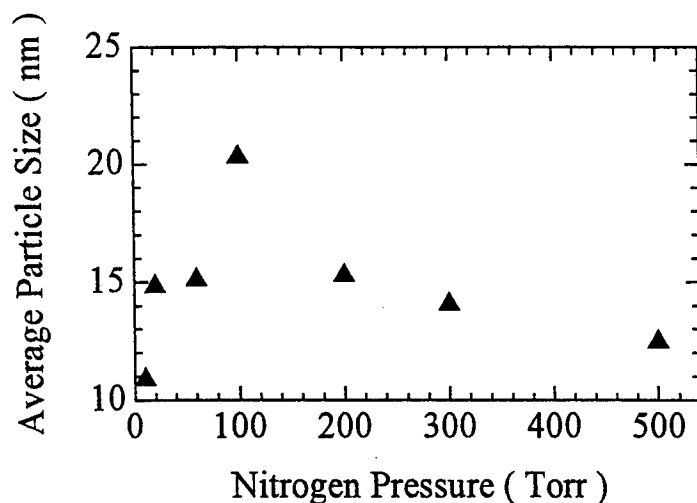


Fig. 7 Dependence of average particle size on nitrogen pressure.

results of surface area measurement. All powders obtained at different pressures were identified as AlN by XRD. It is seen from Fig. 7 that the particle size increases with the nitrogen pressure when the pressure is below 100 Torr and decreases when the pressure is between 100 and 500 Torr.

3.2 Diagnostics of Ablation Plasma

3.2.1 High-Speed Photography

The expansion process of the ablated plasma was observed by a high-speed camera. Figure 8 shows the framing photographs obtained with laser energy density of 16 J/cm^2 and oxygen pressure of 200 Torr. The time of exposure and interframe were 40 ns and 200 ns, respectively. In Fig. 8, the number indicates the sequence of the photographs, where the first photograph was taken 200 ns after the laser pulse. It is seen from Fig. 8 that the shape of the ablated plasma is initially spherical, and later changes to a mushroom with decreasing luminosity.

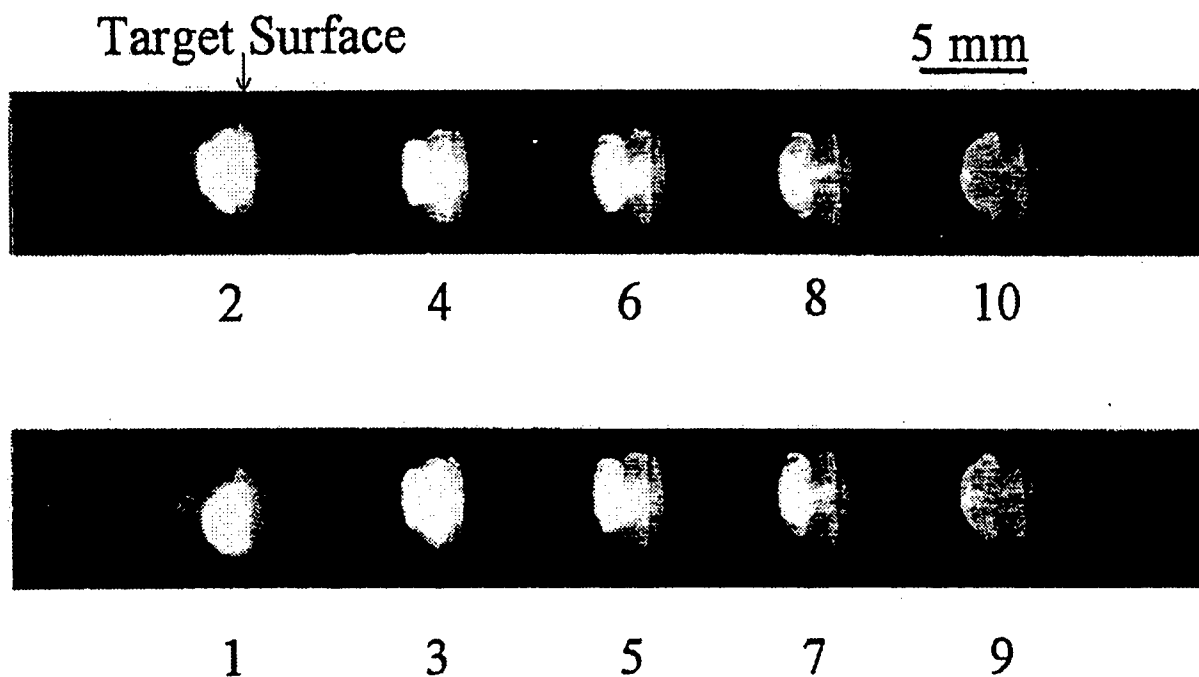


Fig. 8 Framing photographs of ablated plasma at $F \approx 16 \text{ J/cm}^2$, $P_{\text{oxygen}} = 200 \text{ Torr}$.

3.2.2 Spectroscopic measurement

The light emission from the ablated plasma was studied by using a spectrum analyzing system. Figure 9 shows the time-integrated spectroscopy photograph obtained with laser energy density of 10 J/cm^2 and gas pressure of 200 Torr, where aluminum was used as the target and oxygen was used as the ambient gas. The spectrum measured is limited to be above 300 nm due to ultraviolet absorption of the lens. From Fig. 9, we see the spectral lines of aluminum atoms, Al^+ ions, Al^{++} ions, oxygen atoms, and O^+ ions. The strong lines are observed for Al II at 358.7 nm and Al I at 394.4 nm and 396.1 nm.

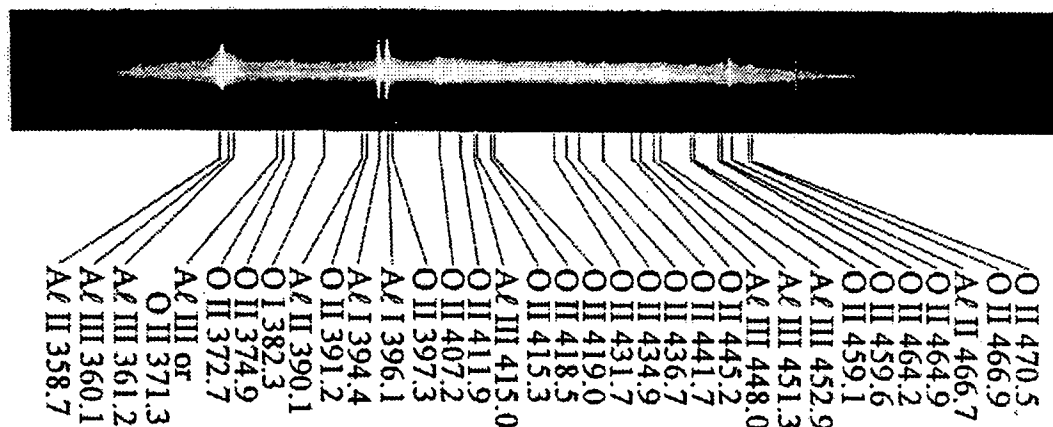


Fig. 9 Spectrum of light emission from ablation plasma.

Besides the above lines, a continuous spectrum is also seen in Fig. 9, which is probably caused by recombination and bremsstrahlung.

3.2.3 SMA Measurement

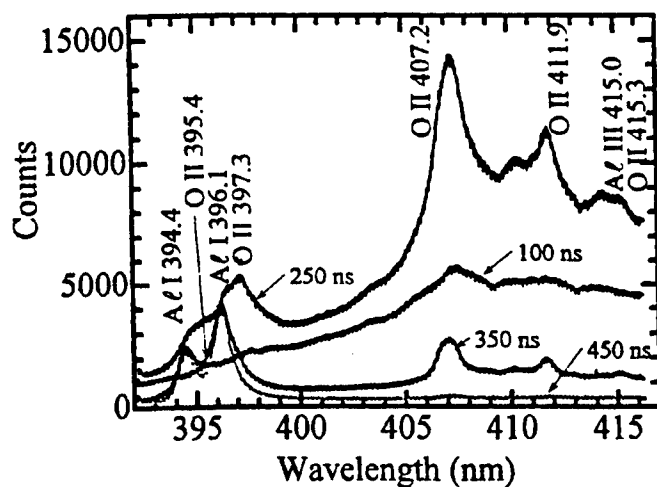
The spectra of the ablated plasma have also been studied by using SMA in time-resolved mode. Figure 10 shows the time-resolved spectra obtained by SMA with delay times from 100 ns to 2,050 ns. The laser energy density and oxygen pressure were 10 J/cm^2 and 200 Torr, respectively. The slit of the spectrometer was parallel to the target surface and the position of the observation was 1 mm from the target surface. The gate pulse was 100 ns. It is seen from Fig. 10 that the initial light emission consists of continuous spectrum and oxygen lines. At 250 ns after the laser pulse, the continuous spectrum and oxygen lines reach the peak and the aluminum lines appear. The oxygen lines disappear at about 450 ns and the aluminum lines last for a few microseconds.

4. CONCLUSIONS

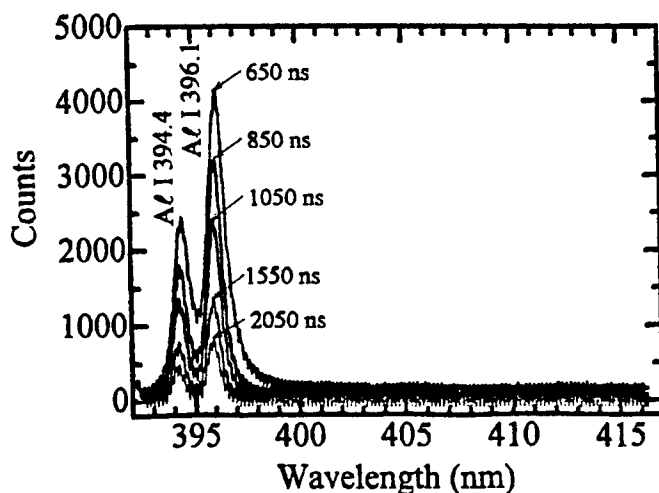
From the results of XRD and TEM analysis of the aluminum nitride powders, we have obtained the following conclusions:

- 1) When Al was used as the target, with nitrogen pressure lower than 60 Torr, the produced powders were Al or a mixture of Al and AlN. With nitrogen pressure higher than 100 Torr, the produced powders are pure AlN. The average powder size obtained with nitrogen pressure of 200 Torr was ~ 11 nm.
- 2) When AlN was used as the target, all the powders obtained with different nitrogen pressures were pure AlN. The average powder size increased with the nitrogen pressure when the pressure was lower than 100 Torr and decreased when the pressure was between 100 and 500 Torr.

From the results of plasma diagnostics experiments under the same condition as the nanosize powder production by with oxygen ambient gas, we have obtained the following conclusions:



(a) 100 - 450 ns delay



(b) 650 - 2050 ns delay

Fig. 10 Time-resolved spectra of ablation plasma at $F \approx 10 \text{ J/cm}^2$, $P_{\text{oxygen}} = 200 \text{ Torr}$.

- 1) The ablation plasma expands in a spherical shape.
- 2) The ablation plasma consists of aluminum atoms, Al^+ ions, Al^{++} ions, oxygen atoms, and O^+ ions.
- 3) The strong light emissions are seen due to Al II at 358.7 nm and Al I at 394.4 nm and 396.1 nm.
- 4) The light emission starts with continuous spectrum and oxygen lines that last for about 450 ns. The aluminum lines start at about 250 ns and last for a few microseconds.

References

- [1] A. Kato and H. Arai : "Nanosize powder" Asakura Syoten (1993) Ch.1 [in Japanese].
- [2] T. Yoshino : "Nanosize powder and materials", Nippon Zairyou Kagaku Kai (1993) Ch.1 [in Japanese].
- [3] A. Matsunawa and S. Katayama : Transaction of JWRI, **19**, 137 (1990).
- [4] G. P. Johnston, R. E. Muenchausen, D. M. Smith, and S. R. Foltyn : J. Am. Ceram. Soc., **75**, 3465 (1992).
- [5] Y. Shimotori, M. Yokoyama, S. Harada, H. Isobe, K. Masugata and K. Yatsui : J Appl. Phys., **63**, 968 (1988).
- [6] Y. Shimotori, M. Yokoyama, S. Harada, K. Masugata and K. Yatsui : Jpn. J. Appl. Phys., **28**, 468 (1989).
- [7] K. Yatsui : Laser & Particle Beams, **7**, 733 (1989).
- [8] K. Yatsui, X. Kang, T. Sonogawa, T. Matsuoka, K. Masugata, Y. Shimotori, T. Satoh, S. Furuuchi, Y. Ohuchi, T. Takesita and H. Yamamoto : Phys. Plasmas, **1**, 1730 (1994).
- [9] K. Yatsui, C. Grigoriu, H. Kubo, K. Masugata and Y. Shimotori : Appl. Phys. Lett., **67**, 1214 (1995).
- [10] C. Grigoriu, Y. Nakagawa, E. P. A. Chamdani, T. Sonogawa, K. Nishiura, K. S. Nathan, K. Masugata and K. Yatsui : in Proceedings of Physics, Diagnostics, and Application of Pulsed High Energy Density Plasma as an Extreme State, ed. by S. Ishii, NIFS-PROC-26, p.25, (1996).
- [11] K. Yatsui, C. Grigoriu, K. Masugata, W. Jiang and T. Sonogawa: Jpn. J. Appl. Phys., **36**, 4928 (1997).

X-ray micromachining with a laser-plasma source at 1nm wavelength

ICE Turcu^a, CM Mann^a, SW Moon^{a,b}, BJ Maddison^a, R Allott^a, N Lisi^a, SE Huq^a, NS Kim^{a,c}

^a Rutherford Appleton Laboratory, Chilton, Didcot, Oxfordshire, OX11 0QX, UK.

^b Korea Institute of Science and Technology, PO Box 131, Cheongnyang, Seoul, 130-650, Korea.

^c Kumho Information and Telecommunication Laboratory, 527, Sangam-dong, Kwangsan-ku, Kwangju, 506-303 Korea.

Abstract

A picosecond excimer laser-plasma source has been constructed which generates an x-ray average power of 2.2 Watt and 1.4 Watt at the wavelengths required for proximity x-ray lithography: 1.4nm (steel target) and 1nm (copper target), respectively. The plasma source could be scaled to the 50 - 75W x-ray average power required for industrial lithographic production by scaling the total average power of the commercial excimer laser system up to 1kW. The 1nm x-ray source is used to micromachine a 2.5THz microwave waveguide-cavity package with a 48 μ m deep, three-dimensional structure, using the LIGA technique.

Keywords: MEMS, x-ray lithography, microstructures, laser-plasma x-ray sources, optical waveguides, waveguides, LIGA, chemically amplified photoresist.

1. Introduction

Microlithography benefits from both characteristics of soft x-ray radiation, high resolution printing and penetration of thick photoresist:

(i) the short wavelength, $\lambda \approx 1\text{nm}$ which allows the printing of 180nm, 130nm, 100nm ... feature sizes, required by the semiconductor industry to manufacture the 1Gbit, 4Gbit, 16Gbit memory chips;

(ii) the $t_e \sim 5\mu\text{m}$ penetration of the $h\nu \approx 1.2\text{keV}$ photon in photoresist is beneficial in the production of semiconductor devices and can also be used in conjunction with the LIGA technique to generate $48\mu\text{m}$ deep three-dimensional structures, i.e. for "x-ray micromachining".

The paper demonstrates both applications using novel techniques and a compact, laboratory sized, high average power laser-plasma x-ray source, which can be scaled for industrial production of microchips and MEMS. In particular, a 2.5THz microwave cavity and waveguide structure¹ is constructed using this technique.

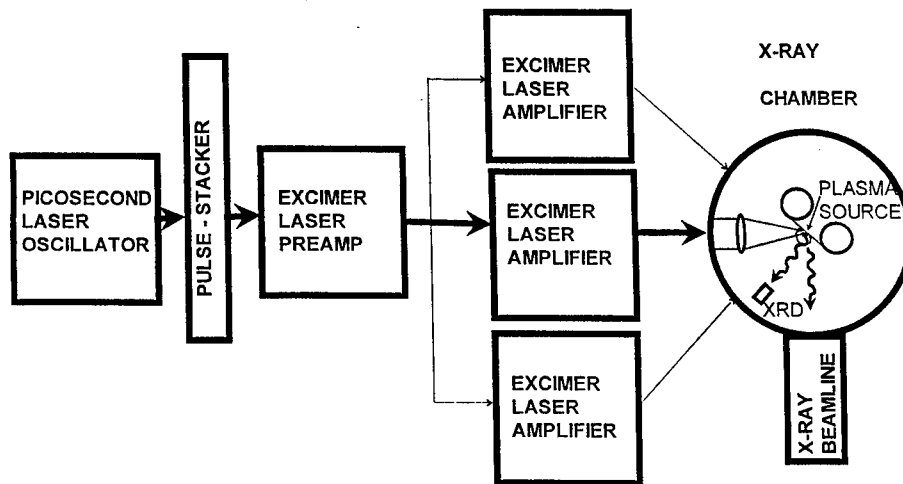


Fig. 1. Concept of the high average x-ray power laser-plasma source. When generating 1nm wavelength x-rays, the source operates in atmospheric pressure helium gas and the plasma is formed by the laser focused on a thin copper tape target.

2. Laser-plasma x-ray source

At RAL we have constructed a picosecond excimer laser system which is used to generate a plasma x-ray source. A high laser to x-ray energy conversion efficiency is obtained in a copper plasma² formed by single, 4ps long, KrF laser pulses with energies on target of up to 13mJ focused to $10\mu\text{m}$ focal spots and power densities of up to $4 \times 10^{15} \text{ W/cm}^2$. A maximum conversion efficiency of 11% (or per unit solid angle: $1.75\% \text{ sr}^{-1}$) is obtained for Cu plasmas². The emission spectrum of this Cu plasma is centred at 1nm wavelength² and therefore is ideally suited for x-ray lithography: good absorption in the gold

absorber on the x-ray mask, good transmission through the mask substrate (if required), and good absorption in a reasonable thickness of photo-resist. This high x-ray conversion efficiency constitutes the basis for the construction of a high x-ray average power excimer laser-plasma source for x-ray lithography. Fig. 1 shows a schematic of the high average power 1nm x-ray plasma source driven by a high peak and average power excimer laser system. All the lasers used (picosecond oscillator and excimers) are commercial lasers, which can be bought "off the shelf". Using a single Lambda Physik 210iF (70W output power with stable cavity at 100Hz) excimer laser final amplifier a record x-ray average power has been demonstrated at RAL³: 2.22 Watt for steel targets @ 1.4nm wavelength; and 1.37W for copper targets @ 1nm wavelength. In the US, similar results are obtained by JMAR⁴.

A combination of four factors renders the x-ray beamline virtually debris free: use of helium gas at atmospheric pressure in the x-ray chamber in order to stop the atomic debris; circulate the helium gas to remove the debris gas generated in front of the target; a thin tape target such that the shock wave generated by the creation of the hot plasma breaks through the target and ejects the cluster debris away from the focusing lens and x-ray beam-line and exposure apparatus; a train of picosecond KrF pulses each laser shot instead of a 25ns laser pulse: the picosecond pulse train irradiates the target over a much shorter time interval and therefore ablates less material, generating less debris in the first place.

3. New technique for soft x-ray micromachining

Traditional x-ray micromachining (LIGA) technique uses a short x-ray wavelength $\sim 0.2\text{nm}$ in order to increase the x-ray penetration of the resist, as well as relatively insensitive PMMA photoresist resulting in long exposure times on synchrotron (SRS) beam-lines. The short wavelength also requires very thick gold absorber features on the x-ray mask (typically $15\mu\text{m}$ or more) which are expensive and time-consuming to manufacture, resulting in a long turn-around of the manufactured product from the design stage, and this constitutes a problem especially for prototyping.

The present work describes, a new method of performing deep lithography, with: (a) softer x-rays of 1nm wavelength, generated by a compact laser-plasma x-ray source; (b) more sensitive, chemically amplified photoresist (even more so for $\lambda \sim 1\text{nm}$ compared to $\lambda \sim 0.2\text{nm}$); (c) thinner, $2\mu\text{m}$ thick gold

absorber features on the x-ray mask; (d) integral surface and embedded x-ray mask for generating deep 3D structures without the need of an aligner; (e) a sequence of x-ray exposures, each penetrating 12 μ m deep in resist, followed by exposed resist removal (by developing) and re-exposure until the desired depth is reached; (f) reduction of total x-ray exposure times to 10 minutes for a 48 μ m deep structure; (g) successful application of the technique to fabricate 2.5 THz waveguides for microwave detector research.

4. X-ray beamline and exposure cell

The picosecond excimer laser-plasma source of 1nm x-rays is used to expose the lithographic cell containing the wafer, such that the distance between the point-like (10 μ m diameter) source and the wafer is 23mm, and the exposed area on the wafer is 0.5cm². The plasma source is operated at 20Hz repetition rate, with a copper tape target in atmospheric pressure helium, and the lithographic cell is fitted with 10 μ m thick beryllium window/filter, which allows only the \sim 1nm wavelength x-rays (copper L-shell emission) emitted by the plasma to expose the resist. The exposure cell like the rest of the x-ray chamber is at atmospheric pressure helium. The absence of vacuum exposure has beneficial effects on the chemically amplified photoresist and allows fast injection of the exposure cell into the x-ray chamber, through a helium purge pipe. No contamination with target material is observed on the Be filter or wafer.

The silicon wafer is spray coated in several layers (each \sim 5 μ m thick) to build up the required thickness of 48 μ m. AZ PF514 (Hoechst) chemically amplified x-ray resist is used because it has a \sim 30 times higher sensitivity (@1nm) than PMMA, and very good etching and mechanical properties. The very high resolution of AZ PF514 allows the printing of 180nm long transistor gates, as will be shown in the next Section. The 2 μ m thick gold absorber x-ray mask is directly deposited on the resist, using an inexpensive, standard mask-making machine, and therefore can be mass produced as part of the lithographic process performed on the wafer. This **integral mask** arrangement is chosen in order to simplify the realignment of the mask after each exposure/development step which, in the present experiment, was repeated four times.

5. Repeated exposure method

The x-ray exposures are measured absolutely by means of a calibrated p-i-n x-ray diode filtered with the same thickness of beryllium foil as the lithographic exposure cell. A fluence of $I_1 = 200 \text{ mJ/cm}^2$ of 1nm wavelength x-rays allows the development and removal of $12 \mu\text{m}$ thick resist each exposure step. The exposure time is 2 minutes/step for a laser-plasma repetition rate of 20Hz. This exposure dose/step is 10 times the surface fluence ($I_s = 20 \text{ mJ/cm}^2$) required for exposing AZ PF514 photo-resist for manufacturing transistor gates (see next Section). This is consistent with an x-ray penetration of $\ln(10) = 2.3$ times the $1/e$ absorption depth at 1nm wavelength, which is $t_e \sim 5 \mu\text{m}$ (the inverse of the resist absorption coefficient). Because of the severe overexposure of the photoresist, tone reversal occurs in a thin “skin” at the top of the resist. This thin, top layer is removed by ashing before wet development of the resist.

By using four repeated exposures, the total x-ray fluence required to penetrate $48 \mu\text{m}$ of resist is ~ 330 times smaller (and total exposure time shorter) compared to a single continuous exposure. Using Beer’s law for calculating the irradiation fluence $I(t_1)$ needed for a selected exposure depth t_1 :

$$I(t_1) = I_s \exp(-t_1 / t_e), \quad \text{with the above notations.}$$

The fluence $I(t_n)$ required for a depth of $t_n = n t_1$ is:

$$I(t_n) = I_s \exp(-n t_1 / t_e), \quad \text{in a continuous exposure, but also}$$

$$I(t_n)^* = n I(t_1) = n I_s \exp(-t_1 / t_e),$$

when the $I(t_1)$ is repeated n times, and the resist removed (developed) after each exposure. With the values used in the present experiment, the ratio of x-ray fluence for continuous and repeated exposure/development is:

$$I(t_n) / I(t_n)^* = (1/n) \exp[(n-1) t_1 / t_e] = (1/4) \exp[(4-1) 12 \mu\text{m} / 5 \mu\text{m}] = 334.9$$

If the ratio of the resist sensitivities, AZPF514 chemically amplified versus PMMA, is taken into account, the improvement in exposure time at this x-ray wavelength is $\sim 10,000$ times. This great reduction in exposure time allows the use of the plasma sources, to demonstrate deep x-ray lithography with reduced exposure times. Synchrotrons ($\lambda \sim 1 \text{ nm}$) would further reduce exposures.

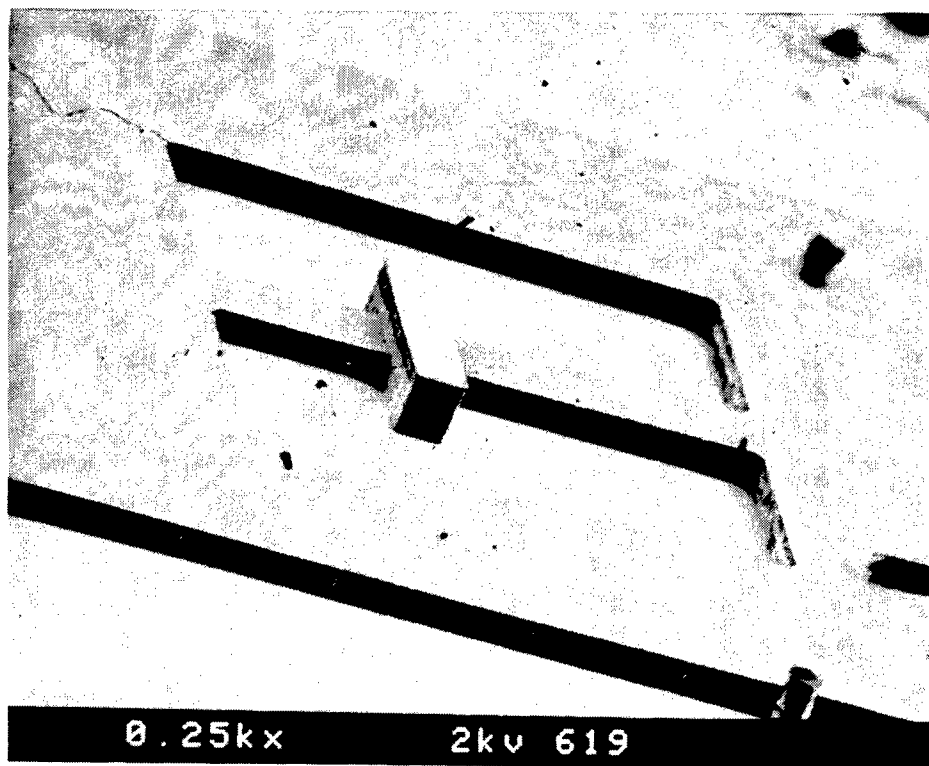


Fig. 2. Scanning electron micrograph of a three-dimensional, $48\mu\text{m}$ deep structure patterned by 1nm wavelength x-ray lithography into AZ PF 514 chemically amplified resist, using: a <10 minute total exposure time from a compact, laser-plasma x-ray source; $3\mu\text{m}$ thick gold absorber integral mask as well as embedded mask; four repeated resist exposure and etching stages, each removing a $12\mu\text{m}$ resist thickness. The structure is a 2.5 THz waveguide former. (Courtesy Dr CM Mann, SSD at RAL).
Fig. 2.

6. Deep, three dimensional structures

Fig. 2 shows a $48\mu\text{m}$ structure patterned by 1nm wavelength x-rays generated by the RAL plasma source. The quality of the etching is good, the striations on the vertical walls being due to imperfection in the edges of the gold absorber, which can be readily remedied. The imprints of the four exposure/development stages can be seen on the central element of the structure. A special technique in mask configuration, the **embedded mask** (Fig. 3), is used to obtain the **true three-dimensional**

structure: (a) the gold absorber (embedded mask) defining the large rectangles was deposited on a first layer of resist, $24\mu\text{m}$ thick, (b) after which another layer of resist, $24\mu\text{m}$ thick, was coated on top of it, (c) and finally the top gold absorber (integral mask) is deposited to generate the central feature of the structure. The central structure is $100\mu\text{m}$ long, $25\mu\text{m}$ wide and $48\mu\text{m}$ high. A higher aspect ratio cylindrical structure can be observed near side of Fig. 2. It was accidentally generated, by a mask imperfection.

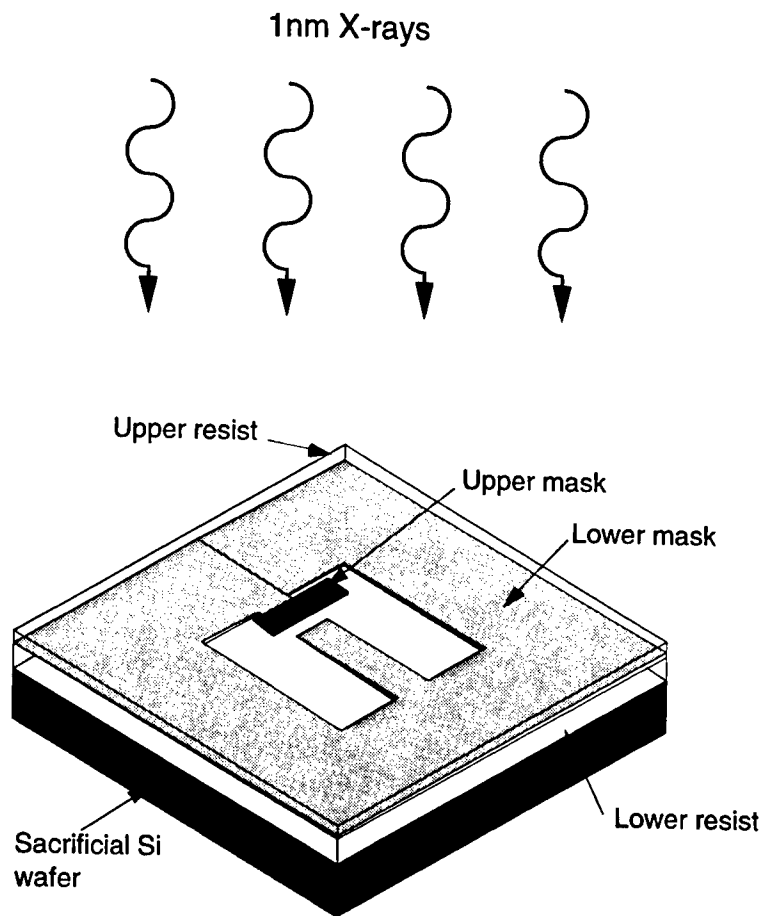


Fig. 3. The multilayer resist composite used to generate the 3D structures. Two integral x-ray masks are used at the surface of and embedded in the resist, at half its thickness.

7. Cavity and waveguide structure for 2.5THz microwaves

The next step in the LIGA technology is the metal plating of the resist structure. The resist structure is covered with a $2\mu\text{m}$ thick layer of sputtered gold, and further electroplated to a gold thickness of $20\mu\text{m}$. The substrate is mounted upside down onto another sacrificial wafer and the first sacrificial wafer is removed by backlapping and chemical etching. The resist is dissolved in acetone to complete the fabrication process. Fig. 4 shows the complete cavity-waveguide structure which is the mirror image in gold, of the structure printed in photoresist. It constitutes a new method of fabricating high precision waveguide structures operating at the $\nu \approx 2.5$ THz microwave frequency or $\lambda \approx 120\mu\text{m}$ wavelength. Fig. 5 shows the schematic of the complete microwave detector designed in the Space Science Department at RAL, with the micromachined cavity-waveguide package fabricated in the present work (Fig. 4) by deep x-ray lithography shown below the diode detector section.

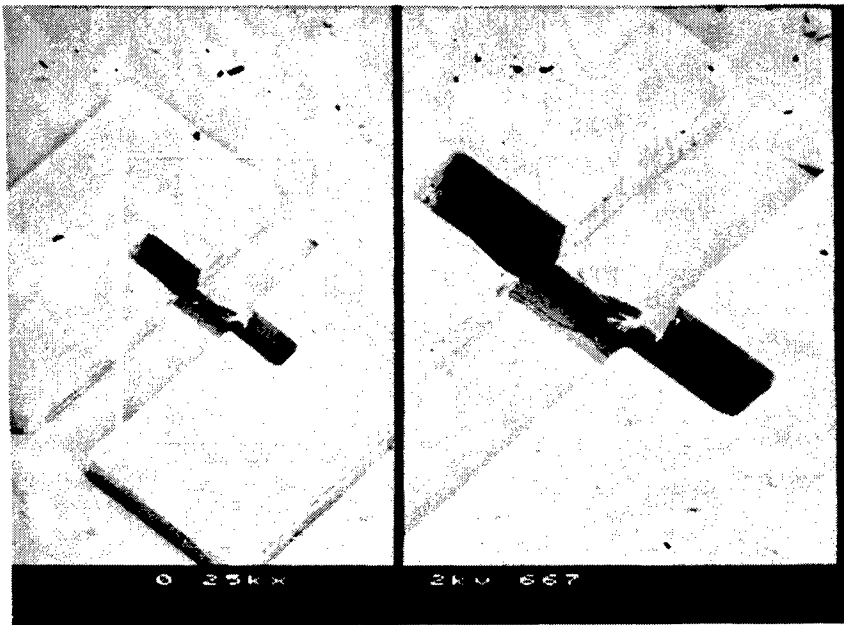


Fig. 4. Scanning electron micrograph of the 2.5 THz microwave cavity and waveguide structure fabricated in gold, by plating the photoresist structure of Fig. 2.

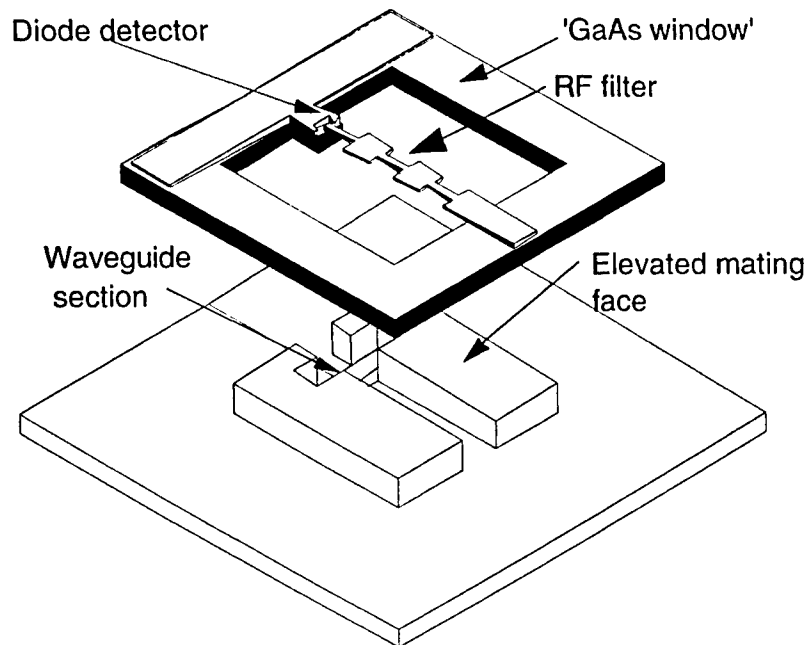


Fig. 5. The 2.5THz microwave detector package designed in Space Science Department at RAL.

8. Fast x-ray LIGA for prototyping

In conclusion, deep 3D structures can be generated with ~10 minute total exposure time, in chemically amplified resist, using compact laser-plasma x-ray source generating 1nm wavelength radiation. The use of repeated exposure/etching of the photoresist together with the higher sensitivity of the chemical amplified resist results in a ~10,000 fold reduction of exposure time compared with a continuous (single) exposure of PMMA resist at the same wavelength

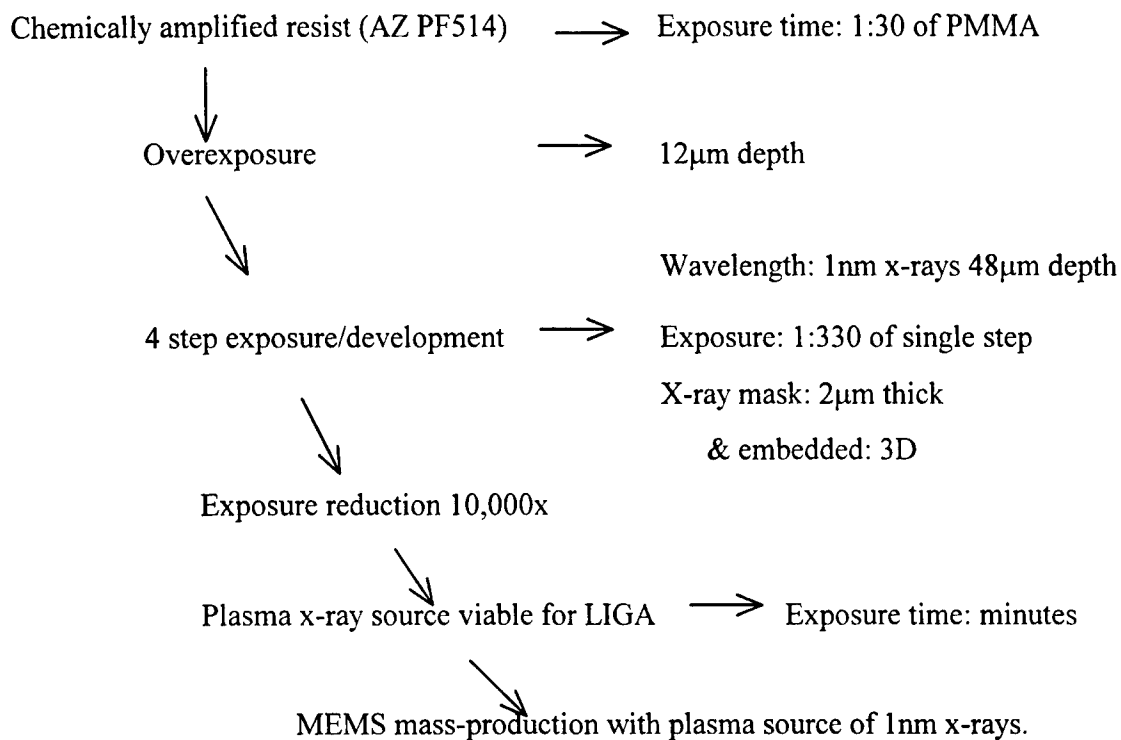
The use of 1nm wavelength x-rays, and the repeated exposure/etching technique, reduces dramatically the thickness (to a few micrometers) of the gold absorber required to mask the x-rays, compared to the standard LIGA exposures carried out at ~0.2nm wavelength, which require gold absorber thickness of tens of micrometers, and make the masks expensive and time consuming to manufacture. The thinner gold absorber allows the use of integral (surface and embedded)masks which do not require realignment

during several exposure/etching processes. The integral x-ray mask survives, unaffected, the repeated process: exposure, postbake, ashing, wet developer. Thinner absorber features on the mask have smaller aspect ratio and therefore allow high resolution x-ray lithography in deep structures. True three-dimensional structures with straight walls, can be generated using integral surface and embedded masks. The resist structures can be replicated in solid gold to fabricate high precision 2.5 THz waveguide structures.

The process could be automated to take full advantage of the short (~minute) x-ray exposure times. A robot could be loaded with e.g. 20 exposure cells, such that while one cell is irradiated, the one after it undergoes post exposure baking etc., with the 19th preceding cell ready for the next x-ray exposure. This technique could open up new applications for the LIGA technique, in high volume, cost efficient, mass production of micro-components, compared to the present use of LIGA restricted to low volume, high added value tool-making, which tools, in their turn are used for mass production. There are many aspects in which the two techniques are complementary. The standard LIGA generates very high structures, ~1mm, but requires long mask fabrication and exposure time, and the availability of a synchrotron beam. The new LIGA technique, presented in this work (but also adequate for synchrotrons), could be extended to a few tenth of mm structures, but has fast turn-around (simple/low cost mask process, fast exposure and processing), and the manufacturer can afford to own the compact plasma x-ray source. The SRS beam-line has the advantage of parallel illumination. When the point x-ray source is used, the exposure time depends on the wafer area: a larger wafer is placed at a larger distance to avoid image distortion at the edges, due to the spherical exposure geometry. For example, if a 3° wall angle is acceptable at the edge of the exposure field, the plasma source, operated at 1W (220mW/sr) power will require 20min/step to expose a $3 \times 3 \text{ cm}^2$ wafer, placed at 30cm from the plasma source. The present source can be scaled to 50-75W average power (Section 2) reducing the exposure to a few seconds/step, with depth of $12 \mu\text{m}/\text{step}$. For fast turn-around prototype runs of only a few tens of devices, the exposure geometry used in the present work is adequate.

If reduced resolution is required, other sources of radiation, e.g. UV can also use the techniques of multiple exposure/development and integral surface and embedded masks to generate 3D structures.

The technique allows integration on one chip, of deep, $>50\mu\text{m}$, three dimensional structures, with ultrahigh resolution, $\sim 100\text{nm}$ structures, because both fabrication methods use the same: x-ray wavelength (1nm), plasma source, photoresist (chemically amplified), and basic process. These Micro-Electro-Mechanical-Devices (MEMS) or even Micro-Electro-(Opto-)Mechanical-Devices (ME(O)MS) are one of the key technologies of the future. The diagram below summarises the breakthrough achieved by this new technique of “soft x-ray LIGA” :



6. Conclusions and discussion

In conclusion, deep structures can be generated with < 10 minute total exposure time, in chemically amplified resist, using compact laser-plasma x-ray source generating 1nm wavelength radiation. By using the RAL plasma x-ray source at its full 1Watt power the total exposure times can be reduced further by an order of magnitude. This would allow the exposure cell to be moved further away from the point-like plasma source (say to 5cm or 10cm) to allow a larger wafer area to be exposed to x-rays with reasonable radiation divergence angle.

The use of repeated exposure/etching of the photoresist together with the higher sensitivity of the chemical amplified resist results in a ~10,000 fold reduction of exposure time compared with a continuous (single) exposure of PMMA resist at the same wavelength.

The LIGA technique described in the present work could be used, to generate on the same substrate, both deep, three dimensional structures, typically of hundreds of micrometer in size, as well as ultrahigh resolution: in previous work described in Ref. 5, 180nm gate-length MOSFET working devices have constructed using the RAL laser-plasma x-ray source. This has very exciting implications in integrating micro-mechanical, -optical, and -electrical devices. Both devices can be printed on the same chip because they use the same: photoresist and development process, x-ray wavelength (1nm) and exposure process, same plasma x-ray source.

References

1. BN Elison, ML Oldefield, DN Matheson, BJ Maddison, CM Mann, S Marzita, TW Crowe, P Maaskant, WM Kelly, "First results for a 2.5THz Schottky diode waveguide mixer", in Proc. 7th Symp Space Terahertz Technology, Univ Virginia, March 1996.
2. ICE Turcu, IN Ross, GJ Tallents, "Efficient keV x-ray emission from plasmas generated with 4ps KrF excimer laser pulses", Appl Phys Lett **63**, 3046-8, 1993.
3. ICE Turcu, IN Ross, "1 Watt plasma x-ray source for lithography at 1nm wavelength", Rev Sci Instrum **67**, 3245-7, 1996.
4. H Shields, M Powers, ICE Turcu, IN Ross, JR Maldonado, PG Bruckhalter, DA Newman, "High power excimer laser-generated plasma source for x-ray microlithography", in "Applications of laser-plasma radiation II", MC Richardson, GA Kyrala, Eds, Proc Soc Photo-Opt Instrum Eng **SPIE 2523**, 295-8 (1995).
5. CM Reeves, ICE Turcu, PD Prewett, AM Gundlach, JT Stevenson, AJ Walton, AWS Ross, RA Lawes, P Anastasi, R Burge, P Mitchell, "Fabrication of 200nm field effect transistor by x-ray lithography with a laser-plasma x-ray source", Electronics Lett. **31**, 2218-9 (1995).

Preparation of metal oxides by laser versus thermal processes

R. Alexandrescu, I. Morjan, C. Popescu*¹, I. Voicu

National Institute for Lasers, Plasma and Radiation Devices
P. O. Box MG-36, Magurele-Bucharest, Romania

* LACECA Research Centre,
Str. Siret Nr. 95, RO-78308, Bucharest, Romania

ABSTRACT

The study of producing metal based oxides has become increasingly interesting because of several specific features which make them extremely attractive for various uses, e.g.: catalysts, pigments, magnetic records, sensors, etc. In the present paper we report the synthesis of various iron, copper and nickel oxides by the IR laser processing of different salts. X ray diffraction technique was used in order to characterise the reaction products. An analysis of the differences between these oxides and those obtained from the same salt by thermal means is presented. It was found that the oxides obtained by laser processing show specific characters concerning the crystallinity and chemical composition.

Keywords: metal oxides, thermal analysis, crystallite size, mixed oxides

1. INTRODUCTION

During recent years much effort has centred on the production and characterisation of metal oxides due to several specific features which make these oxides attractive for various uses, e.g. catalysts, pigments, magnetic recordings, sensors, etc. It was observed that both the synthesis methods and the choice of precursors strongly influence the morphology and the stoichiometry of the obtained oxides.

Most common precursors for preparation of metal oxides are the parent metal salts. Compared to the merely chemical methods for the processing of inorganic salts (thermal decomposition, precipitation, etc.) laser methods are characterised by a strong localised action of the light beam, which imposes specific features to the process. Moreover the laser synthesis of new materials may offer interesting alternatives for controlling the properties of the reaction products by handling the experimental parameters^{1,2}.

In previous papers concerning metal oxides synthesis by CO₂ laser irradiation of inorganic salts^{3,4}, we have shown that copper and nickel oxides exhibited peculiarities concerning their morphology and stoichiometry, and these features depend on the precursors absorptivity to the wavelength of laser radiation. These properties were distinct from those of oxides obtained by conventional thermal controlled heating.

Following the previous reported results, in this work we aim to present the data about the metal oxides obtained by IR laser processing of different metal parent salts and to discuss the differences, revealed by X ray diffraction technique, between these oxides and those obtained from the same salts by thermal means. Some results concerning the production of mixed oxides by the help of laser irradiation are also presented.

2. EXPERIMENTAL

2.1 Materials

Two nickel salts (carbonate and nitrate), two copper salts (carbonate and chloride) and two iron salts (ferrous sulphate and ferric - ammonium alum), were used for the experiment and all of them were of analytical purity. Their IR absorbency values are given in Table 1, together with the codes used throughout the paper.

2.2 Laser experiments

A cw CO₂ laser, which produces a 10.6 μ m radiation, has been used for inducing the decomposition of the inorganic salts. The laser experiments have been performed in an experimental arrangement described elsewhere⁵. The cell with the

¹ Corresponding author

inorganic salt which underwent the laser treatment was weighed after each passage through the laser beam until its weight was recorded as constant. The speed of the cell through the laser beam, of 0.3, 0.55 and 1.3 mm sec⁻¹ and the power of the laser source, of 15, 20, and 25 w, were the parameters of the laser experiments.

TABLE 1. Absorptivity values of nickel, copper and iron salts at 10.6 μ m

Substance	Code	Absorptivity (%)
Nickel		
NiCO ₃ Ni(OH) ₂ H ₂ O	K1	42
Ni(NO ₃) ₂ 6H ₂ O	A1	2
Copper		
CuCO ₃ Cu(OH) ₂	K2	15
CuCl ₂ 2H ₂ O	C	1-2
Iron		
FeSO ₄ 7H ₂ O	S	14
FeNH ₄ (SO ₄) ₂ 12H ₂ O	A2	31

2.3 Thermal experiments

The thermal experiments were conducted in a Derivatograph Q 1500 D, type Paulik, Paulik and Erdey, produced by MOM Budapest. The device records the weight loss, as thermogravimetry (TG) curve, and the thermal effect, as differential thermal effect (DTA) curve, when the temperature is changed according to the heating programme, from 20 to 1000°C. Air atmosphere, alumina as reference material and heating rates of 10 and 20 K min⁻¹ have been used as thermal experiments parameters.

2.4 X-ray diffraction (XRD) measurements

The obtained oxide crystals were investigated by the help of a Phillips diffractometer, with CuK α radiation for the nickel and copper oxides, and CrK α radiation for the iron oxides, respectively, in order to measure their size and isotropy.

3. RESULTS AND DISCUSSIONS

We have assumed, based on our previous researches⁵, that during the laser induced process the decomposition reactions follow the same paths as during the thermal induced process, and that one of the basic differences between the two types of processes is due to the high heating rates which develop within the impact area of the laser beam. In other words the laser induced decomposition might be modelled, with good approximation, as a fast thermal induced decomposition.

A sample of a thermal induced decomposition curves, recorded by the Derivatograph as TG one, is given in Fig. 1a, and a sample of a laser induced decomposition curve, as inferred by us from the recorded weight after each passage, is given in Fig. 1b.

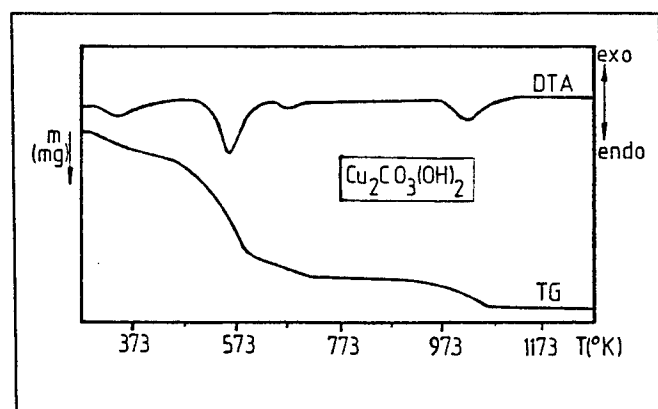


Figure 1a. The weight loss of the metal salt heated with a constant heating rate

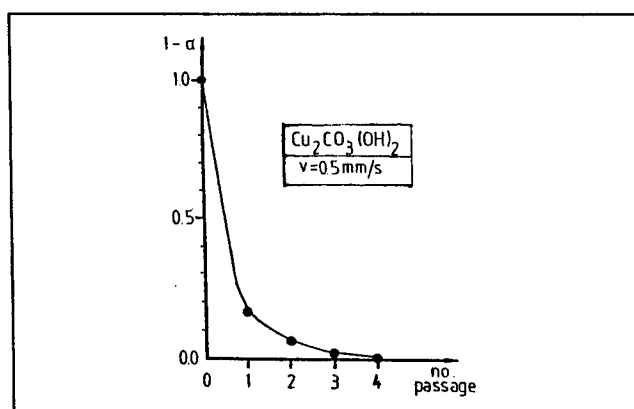


Figure 1b. The weight loss of the metal salt irradiated by laser, over number of passages through the laser beam

One may notice, from any of the TG curves, that the salts decompose thermally in several steps, producing oxides as end product, according to the weight loss. On the other side the laser induced decomposition seem to occur in one step only and again the end product is the corresponding oxide, according to the total weight loss. According to our above mentioned assumption, this curve is the overlapping result of the steps observed on TG curve.

The end products obtained by both types of experiments were analysed by XRD in order to compare their crystallite sizes and isotropy. The measured dimensions were D111 and D200 for nickel and copper oxides, and D011 and D104 for iron oxides. Their values were used in order to investigate the differences between thermal and laser obtained crystallites in terms of their size and isotropy. We consider this "isotropy" to be related to the difference between the value of D104/D011 ratio and unity.

3.1 Kinetic study of the decomposition processes

The weight loss versus time recorded curves allow to perform some kinetic calculus for a better description of the decomposition process.

Table 2 gives the reaction steps which might occur, according to the recorded weight loss, for all the thermal induced processes. The kinetic analysis of each of the identified steps is done by using an integral methods discussed previously². It is based on the equation:

$$\int_0^{\alpha} \frac{dx}{f(x)} = \int_{T_0}^T \frac{A}{\beta} \cdot \exp\left(-\frac{E}{R \cdot y}\right) \cdot dy \quad (1)$$

where α is the conversion degree, $f(\alpha)$ is the conversion function, T_0 is the initial temperature, T is those recorded at that moment, A is the pre-exponential factor, E is the activation energy, R is the gas constant and β is the heating rate. The conversion degree, α , is defined by:

$$\alpha = (m_t - m_0)/(m_f - m_0) \quad (2)$$

m_t standing for the weight at time t , m_f is the final weight and m_0 is the initial weight of the sample.

Based on the recorded weight loss over time, i.e. the TG curve, the values of the conversion degree are calculated and equation (1) may be used in order to calculate, for each reaction, its kinetic parameters, namely: the activation energy, E , the pre-exponential factor, A , and the analytical form of the kinetic function, $f(\alpha)$. The obtained values are included also in Table 2.

As it was mentioned, the laser induced decomposition occur in one step which is, presumably, the result of an overlapping of the several steps recorded during the thermal experiments. This overlapping phenomenon may be explained by the high heating rate developed within the laser impact area. An equation developed previously for relating the maximum value reaction rate temperature shift with the heating rate states that⁶:

$$\ln(\beta_2/\beta_1) = E/R \cdot (1/T_{m1} - 1/T_{m2}) \quad (3)$$

Taking into account values of heating rate of about 10000 K min⁻¹ within the laser beam impact area one may calculate (based on the values of the kinetic parameters from Table 2) the maximum reaction rate temperatures during the laser experiments. The results are given in Table 3.

It can be seen that the calculated temperatures are almost within the same range in all the cases, demonstrating that for each salt the identified thermal decomposition steps occur almost simultaneously. This fact may explain why an apparent one step decomposition reaction is recorded during the laser experiments.

The weight loss recorded during laser experiments for each passage through the laser beam of the cell allows to calculate, also, the degree of conversion, according to eqn. (2), and a kinetic analysis may be also initiated.

The kinetic analysis of laser induced processes should take into account that during the laser experiments we have measured the weight after the salt has passed through the laser beam. Because of this, one may consider that the recording of weights has been done under quasi-isothermal conditions. Therefore the integral form of the reaction rate can be re-written:

$$\int_0^{\alpha} \frac{dx}{f(x)} = A \cdot \exp\left(-\frac{E}{R \cdot T_1}\right) \cdot \int_{t_0}^t dt \quad (4)$$

where T_1 is the temperature recorded within the laser beam impact area, t_0 is the time at the beginning of the reaction and t is the time at the moment of the weighting.

TABLE 2. Reaction steps and the inferred kinetic parameters for thermal and laser induced decomposition processes

Decomposition reaction stages	Thermal			Laser	
	n	E (kJ mole ⁻¹)	A (s ⁻¹)	n	k(T) (s ⁻¹)
<u>Ni₂CO₃(OH)₂·H₂O in thermal regime</u>					
1. Ni ₂ CO ₃ (OH) ₂ ·H ₂ O - NiCO ₃ ·NiO + 2H ₂ O	1	35.5	10 ²		
2. NiCO ₃ ·NiO - 2NiO + CO ₂	1	129.2	10 ⁹		
<u>Ni₂CO₃(OH)₂·H₂O in laser regime</u>				3	7.776
Ni ₂ CO ₃ (OH) ₂ ·H ₂ O - 2NiO + CO ₂ + 2H ₂ O					
<u>Ni(NO₃)₂·6H₂O in thermal regime</u>					
1. Ni(NO ₃) ₂ ·6H ₂ O - Ni(NO ₃) ₂ + 6H ₂ O	*	*	*		
2. Ni(NO ₃) ₂ - NiO + 2NO + 1/2 O ₂	3/2	263	8.7 10 ²¹		
<u>Ni(NO₃)₂·6H₂O in laser regime</u>				1.27	3.6 10 ⁻²
Ni(NO ₃) ₂ ·6H ₂ O - NiO + 2NO ₂ + 1/2 O ₂ + 6H ₂ O					
<u>Cu₂CO₃(OH)₂ in thermal regime</u>					
1. 2Cu ₂ CO ₃ (OH) ₂ - 2CuCO ₃ ·CuO·Cu(OH) ₂ + H ₂ O	2.2	73.1	2.1 10 ¹⁰		
2. 2Cu ₂ CO ₃ ·CuO·Cu(OH) ₂ - 2Cu ₂ O ₃ + CO ₂ + H ₂ O	0	85.7	10 ⁷		
3. 2Cu ₂ O ₃ - 2CuO·Cu ₂ O ₃ + 1/2 O ₂	2	222.8	4.0 10 ¹⁷		
4. 2CuO·Cu ₂ O ₃ - 4CuO + O ₂	0.2	203.6	2.0 10 ⁹		
<u>Cu₂CO₃(OH)₂ in laser regime</u>				1/3	1.02 10 ⁻²
Cu ₂ CO ₃ (OH) ₂ - 2CuO + 2H ₂ O + CO ₂					
<u>CuCl₂·2H₂O in thermal regime</u>					
1. CuCl ₂ ·2H ₂ O - CuCl ₂ ·H ₂ O + H ₂ O	1	79.0	3.6 10 ⁹		
2. CuCl ₂ ·H ₂ O - CuCl ₂ + H ₂ O	0.6	76.1	1.7 10 ⁶		
3. CuCl ₂ + H ₂ O - CuO + 2HCl	1.2	206.5	3.0 10 ¹³		
<u>CuCl₂·2H₂O in laser regime</u>				1/3	3.2 10 ⁻³
CuCl ₂ ·2H ₂ O - CuO + H ₂ O + 2HCl					
<u>FeSO₄·7H₂O in thermal regime</u>					
1. FeSO ₄ ·7H ₂ O → FeSO ₄ ·0.84 H ₂ O + 6.16 H ₂ O	1	93.2	3.3 10 ¹¹		
2. FeSO ₄ ·0.84H ₂ O → FeSO ₄ ·0.72H ₂ O + 0.12 H ₂ O	*	*	*		
3. FeSO ₄ ·0.72H ₂ O → FeSO ₄ ·0.48 H ₂ O + 0.24 H ₂ O	*	*	*		
4. FeSO ₄ ·0.48H ₂ O → FeSO ₄ + 0.48 H ₂ O	2/3	259.7	3.0 10 ¹⁴		
5. FeSO ₄ → FeO + SO ₃	*	*	*		
<u>FeSO₄·7H₂O in laser regime</u>				0.61	4.7 10 ⁻³
FeSO ₄ ·7H ₂ O → FeO + SO ₃ + 7 H ₂ O					
<u>FeNH₄(SO₄)₂·12H₂O in thermal regime</u>					
1. 2 FeNH ₄ (SO ₄) ₂ ·12H ₂ O → Fe ₂ (SO ₄) ₃ (NH ₄) ₂ SO ₄ + 24 H ₂ O	1	55.6	4.5 10 ⁶		
2. Fe ₂ (SO ₄) ₃ (NH ₄) ₂ SO ₄ → Fe ₂ (SO ₄) ₃ + 2NH ₃ + H ₂ O + SO ₃	2/3	200.4	6.4 10 ¹⁵		
3. Fe ₂ (SO ₄) ₃ → Fe ₂ O ₃ + 3SO ₃	1/3	209.7	2.0 10 ¹⁰		
<u>FeNH₄(SO₄)₂·12H₂O in laser regime</u>				0.09	2.37
2 FeNH ₄ (SO ₄) ₂ ·12H ₂ O → Fe ₂ O ₃ + 2NH ₃ + 4SO ₃ + 24H ₂ O					

“*”: the kinetic parameters have been not calculated, because the resolution of the process on TG curve did not allow

TABLE 3. The value of the temperatures of maximum rate, T_m , for the reactions from Table 2 when the heating rate, β , is of 10^4 K min^{-1} order

Reaction (see Table 2)	Measured T_m for $\beta = 10 \text{ K min}^{-1}$	Calculated T_m for $\beta = 10^4 \text{ K min}^{-1}$
Nickel carbonate - reaction (1)	363	566
- reaction (2)	582	902
Nickel nitrate - reaction (2)	643	973
Copper carbonate - reaction (1)	337	460
- reaction (2)	559	893
- reaction (3)	680	825
- reaction (4)	1054	1500
Copper chloride - reaction (1)	406	576
- reaction (2)	535	897
- reaction (3)	773	984
Ferrous sulphate - reaction (1)	459	690
- reaction (4)	678	797
Ferric alum - reaction (1)	428	767
- reaction (2)	630	770
- reaction (3)	825	1065

The time interval $(t - t_0)$ may be calculated by considering the number, N , of passes through the laser beam of the cell of length " l ", with speed " v ", as given by equation:

$$t - t_0 = (N \cdot l)/v \quad (5)$$

By noting the left-side integral of equation (4) as $F(\alpha)$, and by substituting equation (5) into equation (4) followed by logarithmisation and re-arranging the terms this becomes:

$$\ln[F(\alpha)] = \ln(N) + \ln(l/v) + \ln[A \cdot \exp(-E/RT_1)] \quad (6)$$

From eqn. (6) one may calculate, with a certain approximation, the kinetic form of $f(\alpha)$, and the value of the rate constant, $k(T_1) = A \cdot \exp(-E/RT_1)$, at the temperature of the experiment. The calculated values have rather informative than kinetic meaning and are listed in Table 1, together with the results of the kinetic analysis of the thermal induced decomposition.

3.2 The effect of experiment type on the oxide crystallites

The values of crystallite dimensions for the oxides obtained by both laser (coded "L") and thermal (coded "T") routes are shown in Fig. 2.

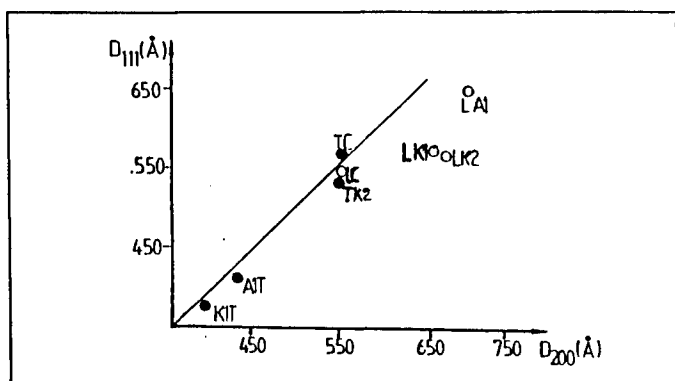


Figure 2a. Crystallite dimensions of nickel and copper oxides

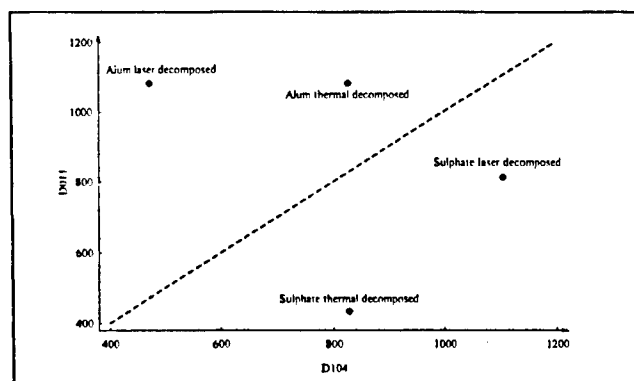


Figure 2b. Crystallite dimensions of iron oxides

It can be seen that the laser experiments produce larger and more anisotropic crystallites than those obtained by thermal methods. This is in full agreement with our previous results^{3,4}, which showed that the final oxides differs from those obtained by thermal means, provided the initial salt has a significant absorbency value of the laser radiation.

3.3 The effect of the laser energy

The study of the influence of laser supplied energy on the crystallites obtained has also been investigated by us in a previous paper³. For this we have taken into account that from the definition of energy:

$$W = P \cdot t \quad (7)$$

where W is the energy and P is laser power, by replacing time t with equation (5) and rearranging the terms one obtains:

$$W/l = NP/v \quad (8)$$

Equation (8) shows a linear relationship between the supplied energy per length unit and the ratio P/v , of two parameters we may control. The influence of energy supplied by laser on the physical form of the end products may be investigated by modifying the laser power and the speed of the cell through the laser beam whilst keeping constant the number of passages, N . Figure 3 shows the dependence of the crystallite dimensions (D_{111} and D_{200} in Fig. 3a, and D_{104} and D_{011} in Fig. 3b respectively) on the value of P/v , for a constant number of passages $N = 2$.

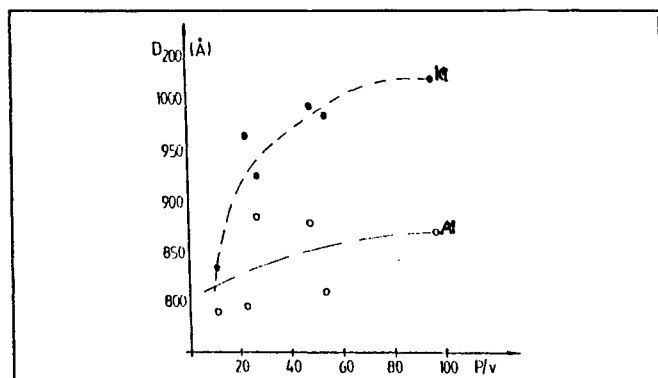


Figure 3a. The influence of supplied energy on the crystallite size of CuO

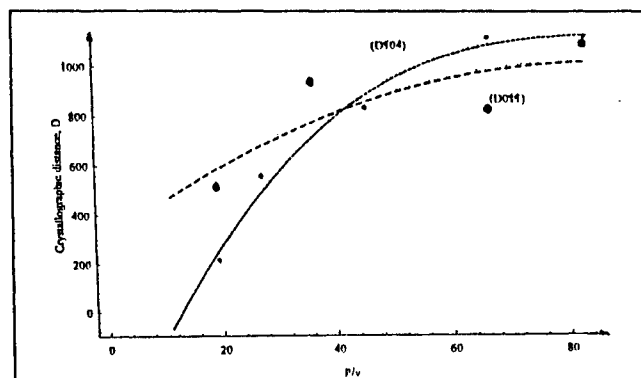


Figure 3b. The influence of supplied energy on the crystallite size of FeO

From Fig. 3 it can be seen that crystallite size is dependant on the amount of energy supplied, which, in turn, is related to the absorbcy of the initial salt decomposed. An empirical relationship to give account of the results from Fig. 4 is proposed:

$$D = K (P/v)^a \quad (8)$$

where D is crystallite dimension, " K " and " a " being two constants. The values of " K " and " a " for the two salts are given in Table 4.

TABLE 4. The values of parameters " K " and " a " from fitting experimental data with the relationship (8)

Salt	Crystallographic distance	"K" value	"a" value
FeSO ₄ 7H ₂ O	D011	0.00	1.72
	D104	0.19	0.84
FeNH ₄ (SO ₄) ₂ 12H ₂ O	D011	0.02	1.20
	D104	31.64	0.02
CuCl ₂ 2H ₂ O	D111	764	0.02
	D200	723	0.04
Cu ₂ CO ₃ (OH) ₂	D111	567	0.13
	D200	695	0.09
Ni ₂ (OH) ₂ CO ₃	D200	91	0.52
NiNO ₃ 6H ₂ O	D200	592	0.01

These experiments conclude that the use of laser decomposition to produce metal oxides again shows the influence of the initial salt absorbency value on the final physical form of the obtained oxide. We have termed this phenomenon the "laser effect" and our data indicates that it is related to the value of P/v , e.g. the higher are the values of P/v , larger crystallites are obtained (see Figure 4). However it has to be stressed that the experimental data suggest that the influence of P/v ratio upon the size of the resultant crystallites reduces after a certain value, related to the parent salt chemistry. In other words the curve described by eqn. (8) seems to reach a plateau, which may be noticed from the curves exhibited in Fig. 3.

3.4 Mixed oxides

We have performed also a laser decomposition of a mixture of copper and nickel carbonates in ratio $K2:K1 = 2.8:1$, related to their absorbency values. The same mixture was decomposed under controlled heating and the resulted oxides were investigated by IR transmission and XRD.

The crystallite dimensions for the thermal and laser obtained oxides are given in Table 5, in terms of the values calculated for CuO and NiO phases.

TABLE 5. The size D (Å) of crystallites in laser and thermal obtained oxides

Sample/Phase	CuO	NiO
Thermal	337	427
Laser	210	142

Results in Table 5 show that the dimensions of crystallites obtained from thermal experiment are higher than those produced by laser. This is quite opposite to the results obtained with single salt decomposition, where the crystallites obtained in laser experiments were larger than those obtained by thermal means (see also Fig. 2). A possible explanation of this reversing might be the growth of the forming oxides which, due to the high thermal gradients induced by laser radiation, takes place simultaneously and leads to a competitive growing. The rather low heating rates experienced by thermal treated samples allow, probably, an oxide to grow before the other one starts growing too. As a consequence, the two methods for synthesising the blend of copper and nickel oxides lead to different textures of the final product.

The results of X-photon spectroscopy (XPS) investigations supported the above conclusions, pointed out that:

i) the oxygen content of laser samples is higher than those of thermal obtained ones; ii) the laser samples seem to contain, beside CuO and NiO as major phases, other copper and nickel oxides like Cu_2O , and Ni_2O_3 . These facts can be related to the competitive growing process and to larger surface of the laser obtained crystallites which may absorb more atmosphere oxygen.

An IR analysis of the products has been also performed, the recorded spectra being shown in Fig. 4.

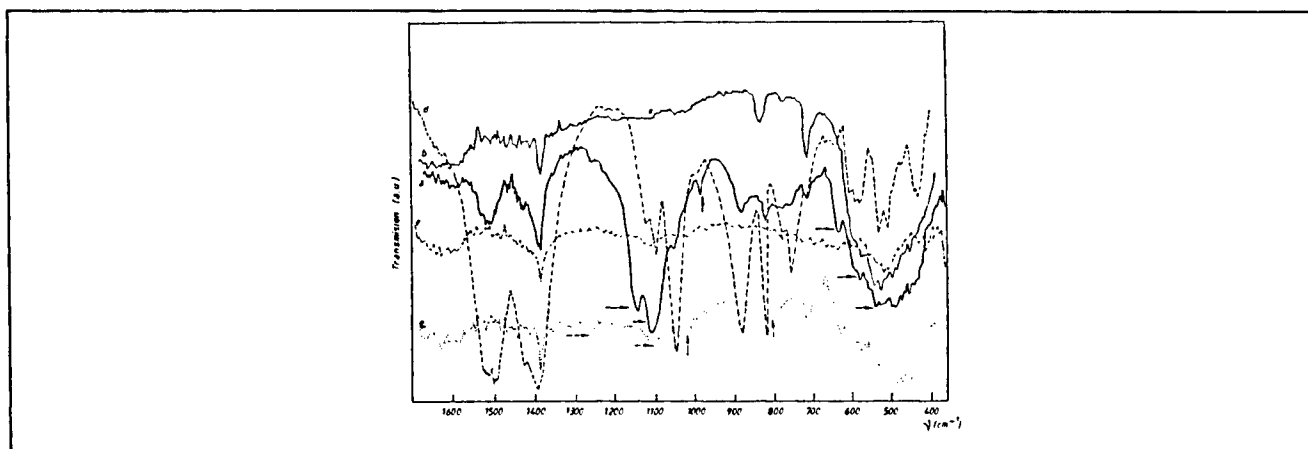


FIGURE 4. IR spectra of copper/nickel salts mixture, and obtained oxides

Curve (a) is recorded for thermally treated mixture, curve (b) is for laser irradiated mixture, curve (c) is for a blend of NiO_x and CuO_x oxides obtained by laser processing and mixed subsequently, curve (d) belongs to copper carbonate and curve (e)

to nickel carbonate respectively. It appears that the peaks from 1220, 1140 and 980 cm^{-1} characterise the oxide obtained from the mixture irradiated with laser only. Although their identification is not fully clarified we assume that they indicate some carbon-oxygen bonds.

The results of all the investigations pointed out that the two methods of obtaining the copper/nickel oxides lead to solid phases with different textures, and partly, to differences of their chemical compositions. The laser oxides showed higher degree of crystallisation and smaller crystallites than those obtained by thermal means. Also the laser oxide chemical composition has a high relative oxygen content and some metal suboxides were detected. Possible carbon-based impurities, resulted from a low conversion of carbon into CO_2 during laser irradiation might be also trapped in the obtained material.

4. CONCLUSIONS

Several metal oxides were prepared comparatively by laser and thermal decomposition of parent salts. In all the cases we have noticed that laser obtained oxides crystallites are larger and more anisotropical than those obtained by thermal experiments. It appears that the differences are larger when the parent salts absorbs better laser radiation and a qualitative relationship, equation (8), was proposed to describe this "laser effect".

Quite different results are obtained when mixture of well absorbing parent salts is also decomposed comparatively by laser and thermal meanings. The end products have different textures, but the crystallite dimensions are smaller for laser material. Also chemical composition of the end products is different; the laser contains metal suboxides and more oxygen than thermal products. No confirmation of the existence of a Ni-Cu bond could be obtained and, as a consequence, one cannot state that mixed oxides could be obtained by this method.

5. REFERENCES

1. E. Borsella, S. Botti, M. Cesile, S. Martelli, R. Alexandrescu, R. Giorgi, C.A. Nametti, S. Turtu and G. Zappa, *Nanostructured Materials*, **6**, 341-346 (1995).
2. R. Alexandrescu, R. Cireasa, B. Dragnea, I. Morjan, I. Voicu, A. Andrei, F. Vasiliu, C. Popescu and D. Fatu, "IR and UV laser-assisted deposition from titanium tetrachloride: a comparative study," *Advanced Mat. Optics Electronics*, **5**, 19-30 (1995).
3. C. Popescu, D. Fatu, R. Alexandrescu, I. Voicu, I. Morjan, M. Popescu and V. Jianu, "Copper oxides obtained by CO_2 laser irradiation of copper salts," *J. Mater. Res.*, **9**, 1257-1262 (1994).
4. R. Alexandrescu, C. Popescu, I. Morjan, I. Voicu and D. Dumitras, "IR laser chemical processing of metal salts for preparation of oxides and metal-containing layers," *Infrared Phys. Technol.*, **36**, 1-13 (1995).
5. C. Popescu, R. Alexandrescu, I. Morjan and M. Popescu, "Solid decomposition reactions induced by laser: the use of a non-isothermal kinetics model," *Thermochim. Acta*, **184**, 73-80 (1991).
6. C. Popescu and E. Segal, "Variation of the maximum rate of conversion and temperature with heating rate in non-isothermal kinetics. Part II," *Thermochim. Acta*, **82**, 387-389 (1984).

New studies of reactive pulsed laser deposition

I. N. Mihailescu, Eniko Gyorgy, V. S. Teodorescu*, G. Marin, D. Pantelica**, A. Andrei***, J. Neamtu****

National Institute of Laser, Plasma and Radiations Physics, P.O.Box MG-54, Bucharest-76900, Romania

* National Institute for Materials Physics, Bucharest, Romania

**National Institute for Nuclear Physics and Engineering "Horia Hulubei", Bucharest - 76900, Romania

***Institute of Nuclear Research, Pitesti, Bucharest, Romania

****Department of Natural Science, University of Craiova, Romania

ABSTRACT

We report the synthesis and deposition of TiC films by reactive pulsed laser deposition. Ti targets have been submitted to multipulse UV laser action in low pressure CH_4 . The thin films were grown on a collector placed parallel to the target. The films were characterized by electron microscopy, electron spectroscopy and nuclear techniques.

Keywords: reactive pulsed laser deposition, titanium carbide thin films

1. INTRODUCTION

The pulsed laser deposition (PLD) has recently emerged as a promising film growth technique¹. PLD permits the use of metallic targets in combination with oxygen, nitrogen or hydrocarbon ambient for the growth of oxides, nitrides or carbides⁴⁻⁸. This method is also called reactive PLD (RPLD). We report herewith new results obtained by RPLD of Ti samples in low pressure methane.

As is known, TiC is a ceramic with many applications in high technology. This is the consequence of an attractive set of physical and chemical characteristics: a high melting point (3260 °C), a high hardness (3200 kg/mm²), a low density ($4.9 \times 10^3 \text{ kg/m}^3$), a good wear to corrosion and oxidation.

2. EXPERIMENTAL

We used a KrF* excimer laser source (Lambda Physik LPX200), ($\lambda = 248 \text{ nm}$, $\tau_{\text{FWHM}} = 30 \text{ ns}$) operated at a repetition rate of 10 Hz. The laser fluence incident onto the Ti target was set at 5 J/cm^2 . A series of 10^4 subsequent laser pulses were applied for the deposition of one film. The experiments were conducted in a cylindrical stainless steel chamber, evacuated down to $2 \times 10^{-3} \text{ Pa}$ and then filled with high purity CH_4 at working pressure in the range (10^{-3} -1) Pa. We used a titanium target having a purity of about 99.9%. The ablated material was collected on $\langle 100 \rangle$ or $\langle 111 \rangle$ single crystalline Si wafers. Prior to the introduction into the chamber, the collectors were carefully cleaned with acetone and 10% HF in distilled water. The distance between target and collector, z_s , was set at 30, 40 and 70 mm.

The morphology and the composition of the deposited films was studied by Transmission Electron Microscopy (TEM) and Selected Area Electron Diffraction (SAED) with a Jeol TEMSCAN 200 CX electron microscope. The films were also characterized by X-Ray Photoelectron Spectroscopy (XPS) with an ESCALAB MK II (VG Scientific) instrument. The K_{α} radiation of Al (1486.6 eV) was chosen for excitation. During analysis the residual pressure inside the installation was below 10^{-7} Pa. A detailed scan of the zones corresponding to the $2p_{3/2}$ peak of titanium was carried out with a step resolution of 0.1 eV.

The formation of titanium carbide was also studied by Rutherford Backscattering Spectrometry (RBS) and Elastic Recoil Detection Analysis (ERDA). For RBS measurement, the samples were mounted in a small reaction chamber which was evacuated down to 10^{-3} Pa. The investigations were conducted with a ${}^7\text{Li}^{++}$ beam of 4.5 MeV. The typical current was (3-5) nA. The beam was produced by a Tandem Van de Graaf accelerator at the Bucharest Institute of Physics and Nuclear Engineering (B.I.P.N.E.). The backscattered particles were detected with a surface barrier silicon detector, placed at 147° with respect to the ${}^7\text{Li}^{++}$ beam. In order to get information about the thickness of the thin films, the recorded RBS spectra were analyzed with a simulation computer code⁹.

For the ERDA measurement the samples were mounted in a large scattering chamber and were placed at 10° with respect to the Cu atom beam. We used a ${}^{63}\text{Cu}$ beam of 80 MeV, delivered by a Tandem Van de Graaf accelerator at B.I.P.N.E.. The light recoil nuclei were detected in an (E- Δ E) telescope configuration consisting of a gas Δ E detector and of a silicon state E detector. The (E- Δ E) telescope was mounted inside the scattering chamber at 30° with respect to the Cu atom beam. For the normalization of the ERDA spectra we used the pulses of the Si E detector¹⁰.

3. RESULTS

In TEM observation the films look uniform and homogenous. We notice crystallites with dimensions in the range 10-20 nm. The corresponding SAED patterns have revealed a cubic f.c.c. structure characteristic to TiC (with the lattice parameter $a_0 = 0.436$ nm).

The positions of the Ti $2p_{3/2}$ peak in the spectra recorded for different samples clearly indicates a composition close to TiC (fig. 1). From Fig. 1 one notices that the Ti $2p_{3/2}$ peak is shifted from its normal position in pure Ti ($E_{b0}=454.0$ eV) to $E_b=455.0$ eV. This value is close to 454.6 eV, the energy of the Ti $2p_{3/2}$ peak in pure TiC.

This small deviation from 454.6 eV could be the effect of the presence in the films of a certain amount of nitrogen or of contamination with oxygen. This slight contamination with oxygen (in form of a nonstoichiometric oxide) could be due to the samples handling in atmosphere after deposition.

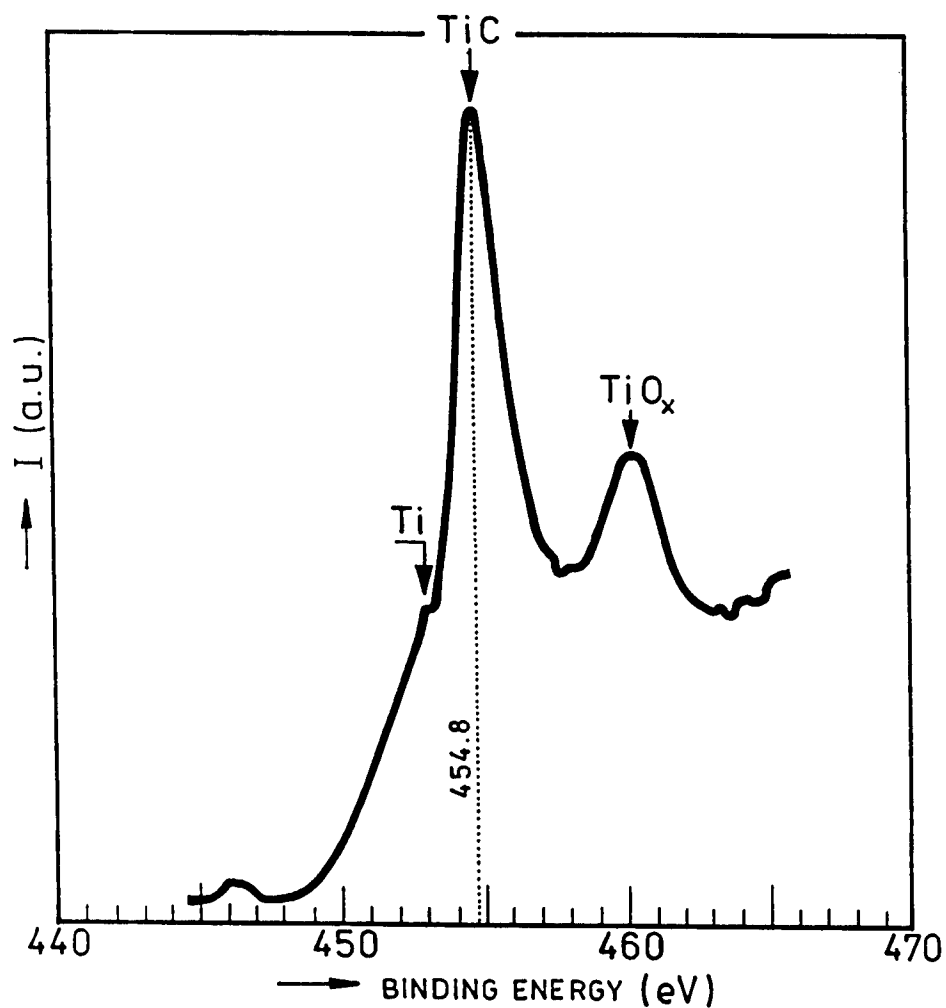


Fig. 1. A portion of the XPS spectrum recorded in the case of the film deposited at 1 Pa CH_4

In the RBS spectra the Ti signal is visible as an intense peak, but no signal coming from C has been detected. The thickness evaluated with the numerical code is 350 nm for thin films prepared at 10^{-1} Pa (fig. 2).

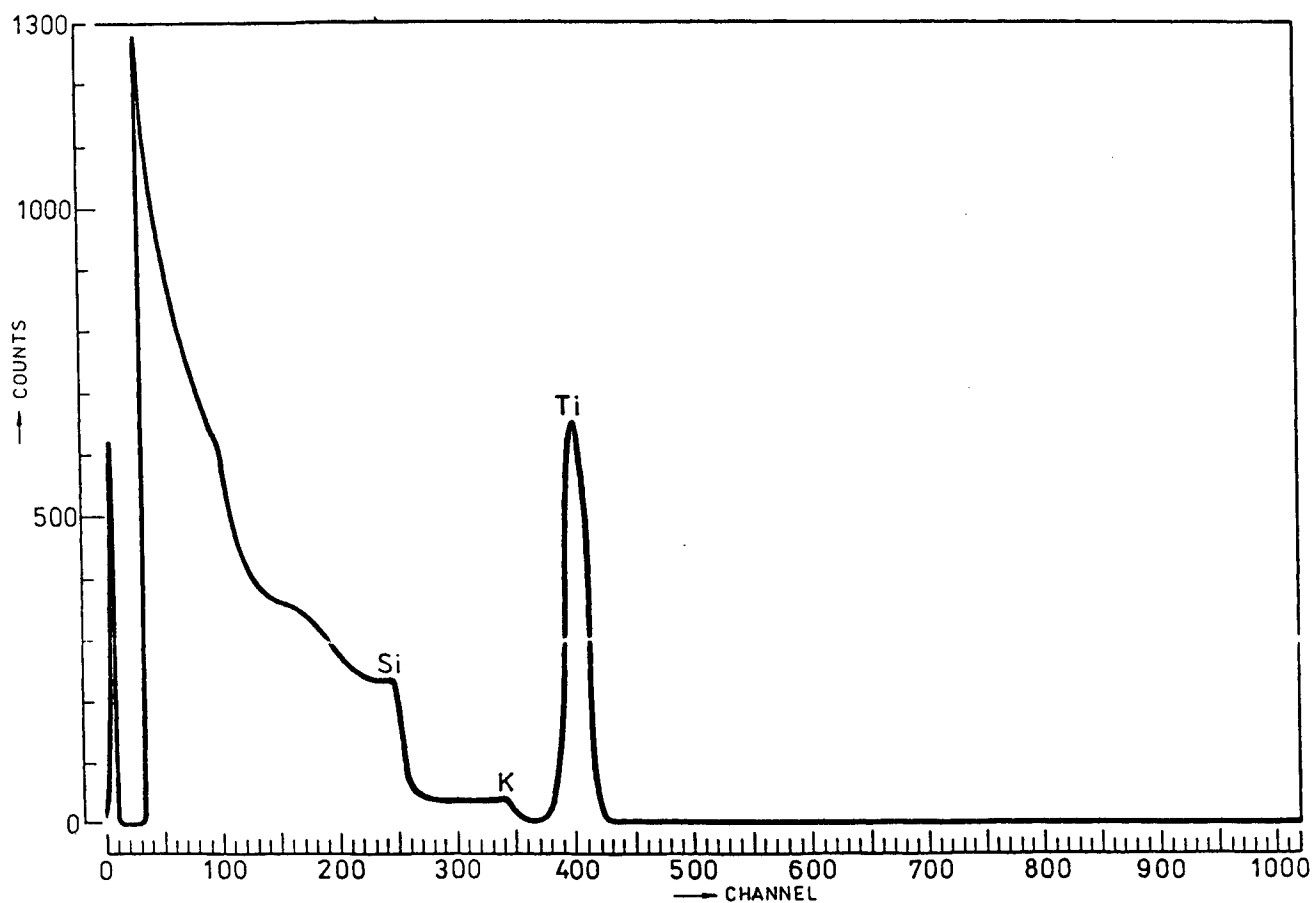


Fig. 2. The RBS spectrum recorded for the film deposited at 10^{-1} Pa CH_4

The signal corresponding to ^{12}C is clearly visible in the ERDA spectra (fig. 3) of the same sample. Other visible signals are due to ^{16}O and ^{28}Si respectively and are originating from the substrates.

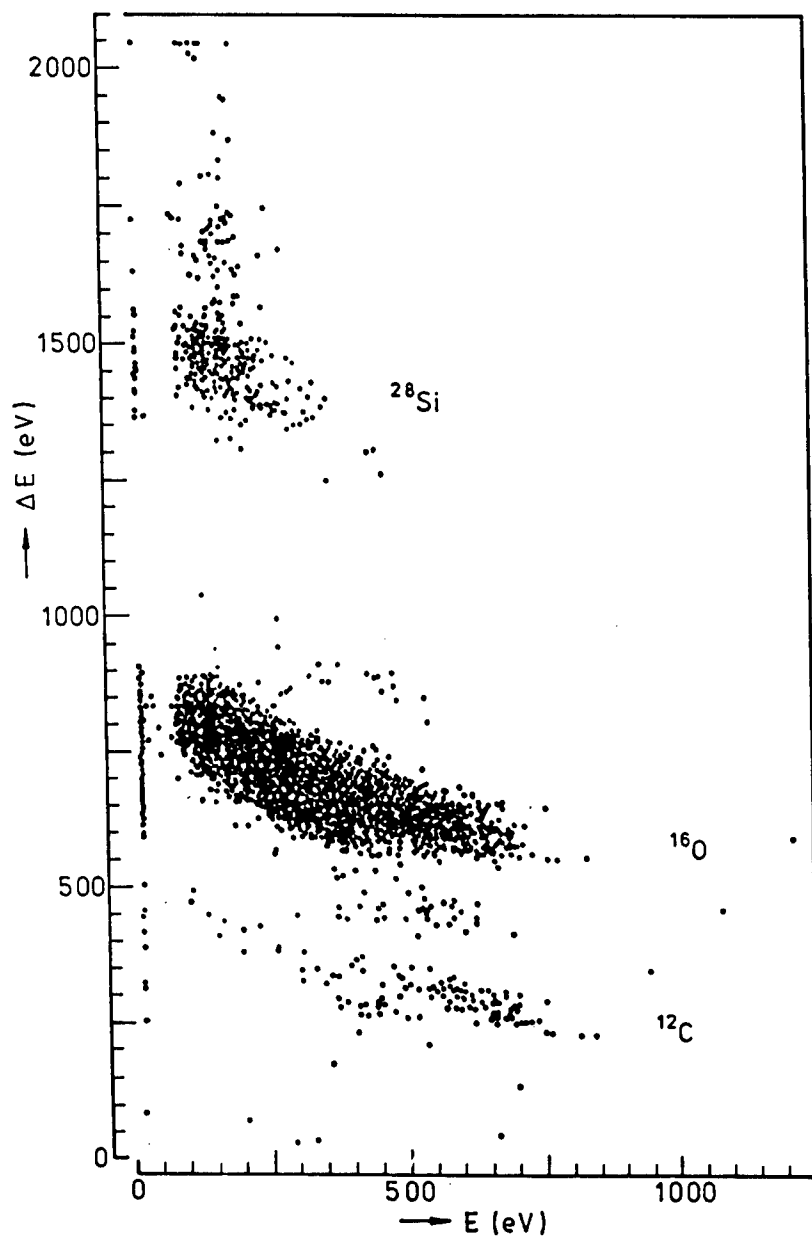


Fig. 3. ERDA spectra recorded for the films deposited at 10^{-1} Pa CH_4

4. CONCLUSIONS

We obtained good quality thin films on cool (room temperature) collectors by RPLD of Ti targets in low pressure methane. The films are adherent to the substrates and hard. The contamination with oxygen is low and is entirely restricted to a top layer (of a

few nm of the deposited films). A deposition rate of 3.5×10^{-2} nm/pulse was obtained for a target-collector distance of 70 mm.

5. REFERENCES

1. D. G. Chrisey, G.K. Hubler, Eds., "Pulsed Laser Deposition of Thin films" (J. Wiley, New York, 1994).
2. D. Bauerle, "Laser Processing and Chemistry", Springer Verlag, 1996 (second edition)
3. M. von Allmen, A. Blatter: Laser-Beam Interactions with Materials, 2nd ed., Springer Ser. Mater. Sci., (1995)
4. I. N. Mihailescu, N. Chitica, L.C. Nistor, M. Popescu, V.S. Teodorescu, I. Ursu, A. Andrei, A. Barborica, A. Luches, M. Luisa de Giorgi, A. Perrone, B. Dubreuil, J. Hermann, *Journal of Applied Physics*, **74** (9), pp. 5781-5789, (1993)
5. I. N. Mihailescu, N. Chitica, L. C. Nistor, M. Popescu, V. S. Teodorescu, I. Ursu, A. Andrei, A. Barborica, A. Luches, M. Luisa De Giorgi, A. Perrone, B. Dubreuil, J. Hermann, *J. Appl. Phys.* **74** (9), (1993) 5781
6. I. N. Mihailescu, N. Chitica, V. S. Teodorescu, M. Luisa De Giorgi, G. Leggieri, M. Martino, A. Perrone, B. Dubreuil, *J. Vac. Sci. Technol. A* **11**(5), (1993) 2577
7. M. L. De Giorgi, G. Leggieri, A. Luches, M. Martino, A. Perrone, G. Majni, P. Mengucci, J. Zemek, I. N. Mihailescu, *Appl. Phys. A* **60**, (1995) 275
8. G. Leggieri, A. Luches, M. Martino, A. Perrone, G. Majni, P. Mengucci, I. N. Mihailescu, *Thin Solid Films* **258**, (1995) 40
9. L. R. Doolittle, *Nucl. Instr. Meth. B9* (1985) 344
10. M. Petrascu, *Nucl. Instr. Meth. B4* (1984) 396

Discharge aided reactive laser ablation for ultrafine powder production

I. Chis*, A. Marcu**, D. Miu*, T. Yukawa**, D. Dragulescu*, C. Grigoriu*, W. Jiang**, K. Yatsui**

* National Institute for Laser, Plasma & Radiation Physics, Magurele, Bucharest, Romania

** Laboratory of Beam Technology, Nagaoka University of Technology, Nagaoka, Japan

ABSTRACT

Ultrafine alumina powder was produced by aluminium target ablation with a Nd:YAG laser beam (1064 nm wavelength; 340 mJ/pulse energy; 7 ns pulse duration; 10 pps repetition rate), in a 120 Torr O₂ atmosphere. A theoretical approach for the ablation process, based on laser energy absorption and energy balance in the target, is used for comparison with the experimental production rate. Three experimental irradiation conditions were chosen: (a) energy density of 5 J/cm², considered reference (**RDE**), (b) lower energy density of 2.5 J/cm² (**LDE**) and (c) RDE with auxiliary discharge between an auxiliary electrode and target, triggered by the ablation plume (**RDA**). Calculated and experimental data of target weight loss show good agreement (135 ng/pulse, calculated, and 100, 110, 120 ng/pulse, experimentally, for RDE, LDE, RDA conditions, respectively). The X-Ray Diffraction (XRD) spectra of alumina show formation of γ -alumina particles only, especially in LDE and RDA conditions. From Scanning Electron Microscopy (SEM) size analysis, a decrease of particle size, in LDE and RDA irradiating conditions, is observed. The decrease of laser beam fluence or aiding of ablation using an auxiliary discharge is both favourable for the production of high quality powder, without diminishing the production rate. This can be a good basis for future improvement of the ultrafine powder production process.

Keywords: nanotechnology, ultrafine powder, reactive laser ablation, electrical discharge, gas-plasma interaction, nanosize powder characterisation

1. INTRODUCTION

UltraFine Powders (UFP) are part of a large class of materials, consisting of particles with tens or hundreds of atoms or molecules, ordered in different arrangement types. Ultrafine clusters, with dimensions between those of molecules and the bulk material, have different physical and chemical properties in comparison with above-mentioned state of matter limits. This led to their being named a new kind of material and more courageously, "the fifth state of matter"[1]. Interest in this field began approximately thirty years ago, with gaseous clusters (aerosols) and has grown explosively in the last few years. "Nanotechnology", now a common word, refers to the production and properties of these particles. Frequently used alternate names are nanosize or nanophase particles and clusters.

Today, great interest is shown for pure metallic or alloys and oxides, nitrides or carbides of Al, Ti, Fe, Ni, Cr, Zr, Ta, Mo, W, Si powders.

Many methods for UFP production¹⁻⁵ are similar with those used for thin films deposition⁶⁻⁷, but conditions regarding process finality are different, i. e. low adhesion to collector for UFP and high adhesion to substrate for thin films. Pulsed laser ablation (PLA) method has some advantages, such as the possibility of operation at high gas pressures and the good control of UFP quality parameters. In the case of Reactive Laser Ablation (RLA) powder production, the high ambient gas pressure (> 10 kPa) is necessary, on one hand, to assure complete reaction of ablation particles, for high powder purity, and on the other hand, to decrease their speed, in order to exclude adhesion to the collecting filter. For dimensional powder characterisation very high resolution microscopy instruments are used. The obtaining of high quality powder requests good control of RLA process stages. The use of additional techniques can also improve the PLA process.

This study presents alumina (Al₂O₃) synthesis by RLA, improved using an electrical discharge between an auxiliary electrode and target, triggered (ignited) by the ablation plasma. Alumina powder production was chosen, being representative for the difficulties of ceramic UFP production by RLA of a metallic target (Aluminium) in a high ambient gas pressure (Oxygen). Three RLA operation conditions were used to reveal the influence of laser fluence and auxiliary discharge on powder quality parameters.

2. GENERAL REMARKS

2.1. Ultrafine clusters

The cluster is an aggregate of atomic or molecular species in a low potential energy order, such as crystalline structure. General properties G of the cluster, such as the ionization potential, binding energy, lattice parameter, free energy, entropy, melting temperature, specific electrical resistance, mass density, etc., are dependent on cluster radius R , in respect to the Quantum Chemical Analytic Cluster Model (QACM)⁸,

$$G(R) \cong c_0 + c_{-1} R^{-1}. \quad (1)$$

where c_0 , c_{-1} are coefficients. Considering the evolution of properties between c_0 for bulk and $c_0 + c_{-1}$, it is possible to establish a correlation between the size of the particles and the value of the property G , that is to predict property value for a given powder size or to produce a powder size for a requested property value.

In many situations, properties close to those of the molecular state, i.e. smaller particles, are desirable. Since the powder is a collection of particles, the quality parameters of a UFP are determined by the chemical composition of the particles, their size and size differences. Therefore, the quality parameters for an ultrafine powder are:

- average size of particles - $R(\text{nm})$
- dispersion of sizes - $\delta R(\text{nm})$
- purity - percentage of the desired particles with same constitutive molecule in all powder particles.

It is desirable for R and δR to have lower values, and for the phase purity to assure a higher percentage of stoichiometric composition.

Recently, many studies have been dedicated to metallic¹⁻² and ceramic UFP^{2-5, 9-10}, due to enhanced chemical (catalysis, reactivity), mechanical (sinterizability, plasticity¹¹, etc) and electric or magnetic properties.

The obtaining of nanosize particles¹² is mainly possible through:

- a) condensation by adiabatic expansion of supersonic vapour or gas jets.
- b) surface erosion of a target (ablation) through interaction with beams (photons, electrons, ions) or through an electrical discharge (the target being one electrode).

Using method a), mainly gaseous particles are obtained. In case b), the ablation can be produced in the presence of a chemically active or inert gas atmosphere. In the case of a chemically active gas environment, the particles are the final product of reactions between species in the target plasma and the gas molecules; this is known as reactive ablation. Ablation using beams is expensive in comparison with that using electrical discharges, but the control of particle quality parameters is better. Using laser systems as photon sources has some advantages in the production of ultrafine powders, such as: the process is clean, good control of the ablated region and the speed of the particles is possible, the plume has a well-directed expansion, operation at high gas pressures is possible, which implies the possibility of high quality powders. A shortcoming, though, is the lower production rate.

2.2. UFP production through reactive laser ablation

Reactive laser ablation (RLA), used for ultrafine ceramic powder production, is based on thermal (generally) or chemical (rarely) ablation of a target in a reactive gas atmosphere. The overall production process consists of several localised processes: laser beam energy absorption in the target, thermal evaporation, plasma plume expansion, gas-phase reactions and particle collection. In many aspects, the initial process is very similar to those for thin film deposition, but there are differences in the subsequent plasma evolution for the two cases, due to the much higher gas pressure used for UFP production.

A part of the laser beam photons are absorbed by the atoms or molecules in the target¹³. The amount of energy absorbed depends on laser beam and target parameters through the reflectivity R . The reflectivity is related to the wavelength and polarisation of the laser beam, the nature, surface state and temperature of the target, and the incidence angle of the beam on the target. The energy E_{abs} absorbed from the incident laser energy on the target surface E is:

$$E_{\text{abs}} = E(1 - R) \quad (2)$$

The absorbed energy is dissipated in depth of target according to the exponential Beer law, with an absorption coefficient $\alpha[\text{cm}^{-1}]$, dependent on material nature and laser beam wavelength. A more important parameter is the absorption length $l_\alpha[\text{cm}]$, given by:

$$l_\alpha[\text{cm}] = 1/\alpha \quad (3)$$

representing the depth where the major part of energy is absorbed.

Among the laser ablation mechanisms, direct ablation, that is, photochemical desorption of the species which constitute the target (atoms, molecules, ions) by bond breaking with high energy photons (from UV laser beam), is possible for very limiting materials only. In most cases, thermal evaporation produces ablation.

The species are excited by photon absorption from laser beams. Excited species lose energy by photon emission, which can reexcite other species, or nonradiative transition, thermally. Finally, almost all absorbed energy is transferred to heating energy of target. In this manner, the laser beam is a heat source for the target material and this thermal behaviour is submitted to the heat equation. The absorbed energy is consumed for irradiated zone heating, melting and latent heats of vaporisation. A part of this energy is lost by heat diffusion, convection and thermal radiation. If the irradiated zone temperature rises above vaporisation threshold, ablation occurs by free vapour species emission. The excess vaporisation energy is transferred to the vapour plume particles as internal and translational energy. The convection and thermal radiation are negligible in the energy heat balance for RLA conditions. Energy loss by diffusion is directed by a material parameter, the thermal diffusivity $D[\text{cm}^2/\text{s}] = k/\rho c_p$ and thermal diffusion length $l_T = 2(D \tau_l)^{1/2}$, where $k[\text{W/cm K}]$ is the thermal conductivity, ρ - material density, c_p - specific heat and τ_l is the laser pulse duration. To characterise the ablation phenomenology, the relationship between l_α and l_T is of great importance.

If $l_\alpha \gg l_T$ surface absorption of the radiation exists and the material is ablated layer by layer. For this case, applicable for almost all metallic targets, an approximate solution of the heat equation is possible, which gives the threshold laser fluence, the temperature rise of the target surface and the material removal rate. Some acceptable approximations are necessary, such as: temperature independence of interaction and material parameters, neglecting of melted layer in the ablation zone, and temperature gradient in the target.

In order for ablation to take place, a temperature rise above the vaporisation temperature is necessary. This implies a laser irradiance I greater than the threshold irradiance I_{th} ,

$$I_{th} \cong \rho \Delta H_v / \alpha(1 - R) \tau_l \quad (4)$$

If the threshold energetic condition is fulfilled, the estimated temperature rise for an irradiance $I > I_{th}$ is

$$\Delta T \cong I l_T / \pi^{1/2} K \quad (5)$$

For moderate intensities, I near I_{th} , which lead to very convenient powder quality parameters, laser energy absorbed or scattered in the plasma, and energy losses by diffusion outside the ablated zone and thermal convective losses can be neglected. In these conditions, the mass released from the target m_a , upon interaction with a laser pulse having energy E , representing the ablated mass rate per pulse, is:

$$m_a \cong E(1-R) / (c_p \Delta T + \Delta H_m + \Delta H_v) \quad (6)$$

where ΔH_m and ΔH_v are melting and vaporisation enthalpies.

The target material is released in the form of particles, molecules, atoms (neutral or charged) and electrons, which constitute a plasma plume evolving in ambient atmosphere. The plasma plume evolves in a direction normal to the target, with speed and directionality parameters depending on the interaction geometry and coupling. The pressure and nature of the ambient gas have a great influence on plume expansion and reactivity.

The expansion model for the motion of an ablation plume in a high pressure atmosphere, specific for the UFP process, seems to be the effusion or the recondensation model¹⁴ rather than the outflow model. According to this model, the ejected species have a planar motion¹⁵⁻¹⁶ oriented normal to the target. After thermalization by a few collisions in the Knudsen Layer (KL), the species acquire a Maxwellian velocity distribution. This is followed by an unsteady adiabatic expansion (UAE) when their pressure is above the ambient gas pressure, and deceleration after the formation of a shock wave in the ambient gas, when the two pressures become equal. The best conditions for reaction between the ejected species and the gas environment are present in this last stage of evolution.

During plasma evolution, the ejected species undergo elastic or inelastic collisions among themselves (proportional to their density), leading to thermalization (in the KL), or recondensing in larger particles which evolve in the forward plume direction towards the collector or backward towards the target.

Another essential collision in ceramic UFP processes is the reaction collision with ambient gas species to obtain the desired molecular clusters. The reaction probability¹⁷ is governed in this case by the reaction cross section between plume and gas species. The reaction cross section is dependent on the nature of the reactants, the interaction energy and geometry. In most cases, atomic, ionic or excited species and higher relative collision velocities lead to increased reaction cross section.

Considering target plume species of density n_t and gas species of density n_g interacting in the volume V with a relative velocity $v = |v_t - v_g|$, the reaction rate for powder molecules production is given by:

$$N_p = n_t n_g V v S(v), \quad (7)$$

where $S(v) = \int \sigma(v, \Omega) d\Omega$ is total reactive cross section, Ω being solid angle in interaction space.

For higher powder purity, which means the absence of unreacted target species, (7) implies that excess gas density is favourable. But a higher gas pressure means a higher density of species at the contact front when the shock wave is created, a greater probability of large cluster formation, and thus low quality parameters for powder. For lowering ambient gas pressure and plume density, desirable for smaller particles, it is favourable to obtain a higher production rate by increasing the species reactivity $S(v)$ and collision velocity.

Once powder particles are produced by chemical reaction, their subsequent collisions with the gas atmosphere cool and scatter them. If cooling is desired, so that their kinetic energy does not permit collector heating and thus lowering of adhesion, then scattering means loss of particles. In order to avoid powder losses, a suitable gas flow rate is used to direct particles towards the collecting filter.

2.3. Methods of UFP production process improvement

How the above-mentioned UFP production process is similar to thin film deposition, as well as many aspects of the quality parameters request for dimensionality and stoichiometry, are the same. A higher ambient gas pressure influences the last part of the UFP production process. For such a process, a quantitative analysis is very difficult, but establishing of the qualitative correlation in process phenomenology can lead to improvement.

Fluence has a major influence on the dimension, energy, nature and density of species ejected from the target. As already shown, in order for ablation to occur, the fluence must be greater than the threshold value¹³. A moderate fluence above threshold has a beneficial effect on the decrease of ejected species dimension and density, which is favourable for powder finesse. At the same time, a lower ionization degree and energy is expected.

Because many pulses are necessary to ablate a significant amount of material from the target, although the target is rotated, surface erosion produces craters that are responsible for the ejection of large agglomerates¹⁸⁻²⁰. The value of the ambient gas density is very important for decelerating (in the case of an inert gas) and to completely react (for a reactive gas) with plume particles. On the other hand, a high pressure means a higher density of species in the plume-gas contact front and a higher collision probability, thus a greater probable particle size.

Auxiliary techniques aiding UFP production process can improve some process conditions to obtain a better quality powder. Such techniques can be: electrical discharge²¹, electric or magnetic²² fields and UV photons. While electric or

magnetic fields mainly influence plume parameters, and UV photons dissociate or excite gas molecules to increase reaction capability at lower pressures, an electrical discharge acts both on plume and ambient gas parameters.

An auxiliary electrical discharge, triggered by the ablation laser plasma, improves laser-target coupling, plume expansion and gas reactivity. With a negatively biased electrode placed near the grounded target, the electrical field and discharge which appear after the ignition of ablation can accelerate and annihilate plume ions, which means lowering of ion density in the path of the laser beam, reduction of beam photon absorption in the plasma and increase of laser energy absorption in the target. The discharge can dissociate, ionize or excite molecules, increasing the reactive cross section of gas species.

3. EXPERIMENTAL PROCEDURE

3.1. Experimental premises

For the Aluminium target ablation by Nd:YAG laser beam, threshold values for irradiance and fluence can be calculated using relation (5). They are of 70 MW/cm² and 0.5 J/cm² (for 7 ns pulse duration), respectively. In order to find the best ways to improve the UFP production process, three main experimental irradiation conditions were established;

- a) fluence of 5 J/cm², considered reference density of energy (RDE),
- b) low fluence of 2.5 J/cm², and corresponding low density of energy (LDE),
- c) reference fluence of 5 J/cm² with an auxiliary electrical discharge, between an electrode and target, triggered by the ablation plume (RDA).

Among other methods of producing ultrafine ceramic powders, based on evaporation of metal target in a gas atmosphere, reactive laser ablation (RLA) has several advantages: it is a clean, controllable method that produces the desired powder stoichiometry; a lower production rate is a shortcoming. RLA can prepare extremely fine powders, the energy density and gas pressure being the main factors for decreasing particles size.

Some of these dependencies and a possible method of improving the process with an auxiliary electrical discharge are described.

Ultrafine alumina ceramic powder production was chosen as being representative for other UFP ceramics produced by RLA. Ultrafine alumina sintered ceramics also exhibit enhanced mechanical properties, such as superplasticity¹¹. Alumina powder was produced by aluminium target ablation using a Nd:YAG laser beam in 15.8 kPa (120 torr) oxygen atmosphere.

3.2. Experimental arrangement

Alumina UFP is produced by RLA in a stainless steel irradiation vacuum chamber connected to a preliminary vacuum pump and turbomolecular pump, reaching a base pressure of 10⁻³ Pa (8x10⁻⁶ torr). An oxygen pressure of 15.8 kPa was maintained in the chamber at a flow rate of 1 l/min, by preliminary pump operation and a continuum adjustable connecting valve. The target was high purity Aluminium, smoothed using fine emery paper and ultrasonically cleaned. In order to avoid the formation of large craters by superposition of two consecutive pulses, the target is rotated at 40 rot/min.

The Gaussian Nd:YAG laser beam (BM Industries, Model 501 DNS Compact; 1064 nm wavelength; 350 mJ pulse energy; 7 ns pulse duration, 10 pps repetition rate) (fig. 1) is focused by a lens (focal length $l = 600$ mm), and interacts with the target at a 45° incidence angle in the horizontal plane. Alumina powder was collected on 50 µm stainless steel grids and .1mm nylon filters (Nihon Millipore Ltd) placed along a direction normal to the target, in vacuum path. The target-collector distance is 300 mm approximately.

The aluminium electrode for the auxiliary electrical discharge was placed in a vertical plane 5 mm from the beam impact zone centre. The fluence on the target was varied by changing the distance between focusing lens and target, from 425 mm in RDE and RDA to 345 mm for the LDE regime.

The impact spot area was established by microscope examination of the target surface morphology after 20 superposed pulses and a geometrical calculation, considering the beam diameter before focusing, focal length, lens-target distance and incidence angle. Within the limit of 3% differences, 7 mm² and 14 mm² spot area on target were considered, that is 5 J/cm² and 2.5 J/cm² fluence.

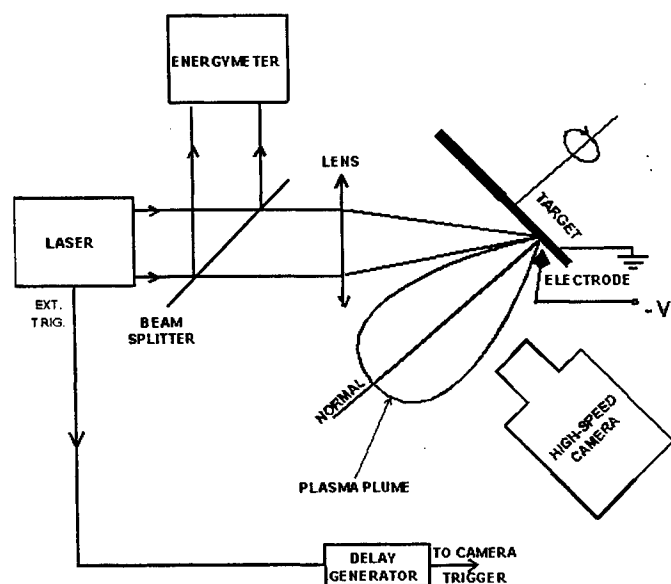


Figure 1. Experimental setup

Outside the chamber, in a plane parallel to the target surface, a High Speed Framing Camera (IMCO Electro-Optics Ltd, model FS 501) was placed to study the spatial and temporal evolution of the ablation plume.

3.3 Electrical discharge circuit

The scheme of the electrical circuit is shown in fig. 2. A 20 nF capacitor battery (10x2 nF) charged at 450 V voltage in 3 ms from a DC voltage supply (Hamamatsu HTV C752) is discharged, by the ablation plume, in the space between electrode and target. The electrode material was chosen to be the same with that of the target to avoid impurification.

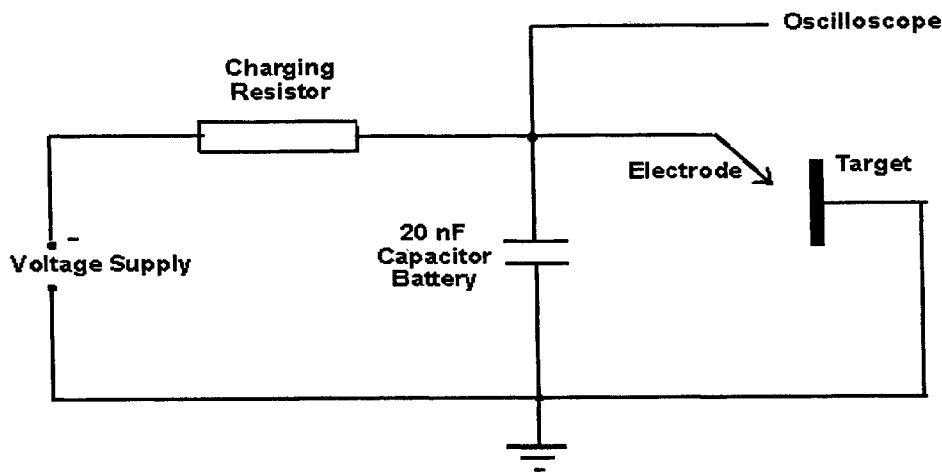


Figure 2. Electrical discharge circuit

The electrode tip was placed in a vertical plane containing the plume direction, 3 mm above this direction and 4 mm from the target, leading to an angle of approximately 40° between the electrical discharge and plume expansion. A capacitor battery energy of 2 mJ is completely introduced in discharge, in a 500 ns discharging time, measured with a Hewlett Packard digital oscilloscope (HP 54111D). The linear slope of the capacitor discharging voltage suggests a constant flow rate of electrons.

4. EXPERIMENTAL RESULTS

These results attempt to evidence the effect of the fluence on target reducing and influence of an auxiliary discharge in alumina powder process by RLA. We follow these effects regarding to target morphology, plume evolution and powder characterisation.

4.1. Target morphology

Target track profile determination and surface microscope examination are indirect methods to characterise the influence of fluence and electrical discharge on powder parameters. We determined the depth profile of reference fluence with and without auxiliary discharge.

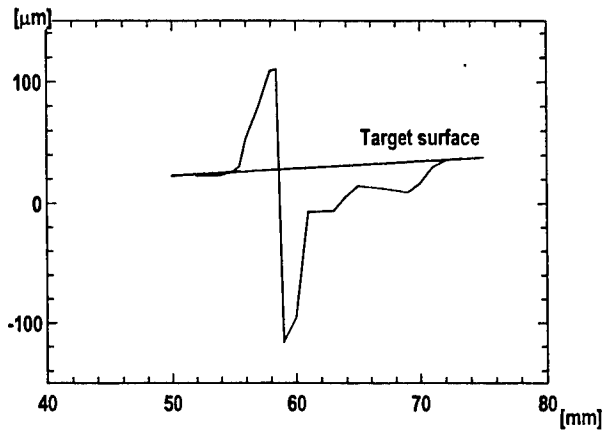


Figure 3. Track profile of RDE irradiation

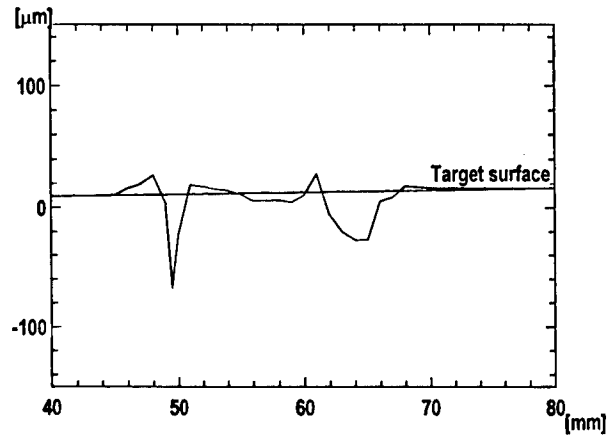


Figure 4 Track profile of RDA irradiation

Profile determination was made by focusing depth (± 1 mm precision), while moving in a radial direction on the ablation track ring. Average pulse density on circumference length was the same, approximately 1200 pulses/min for both cases. Profile examination shows that while without an electrical discharge (fig 3) there is a 150 μm ditch followed by a 70 μm ridge, when an electrical discharge is present (fig. 4) there are two ditches, 42 and 75 μm , followed by 25 and 24 μm ridges. This last profile with smaller morphological changing can be a sign that finer particles are ejected from the target in the case of laser ablation aided by an electrical discharge.

Microscopic target morphology examination outside of the circular track reveals a deposition area with big recondensed particles having velocities opposite to the plasma expansion velocity, as shown above. The dimension of the particles depends on the operation regime. While in the RDE regime, the cluster size is $40 \div 100 \mu\text{m}$, for the LDE and RDA regimes, the sizes decrease 4 and 6 times, respectively, being in $10 \div 25 \mu\text{m}$ and $7 \div 15 \mu\text{m}$.

The examination of the target morphology, in the above described manner, offers information on processes close to the target and on the influence of auxiliary techniques in improving them. In the presence of an electrical discharge, an improvement of powder finesse can be expected.

4.2. Plasma Evolution

To study spatial and temporal evolution of plasma in a high pressure ambient medium conditions a High Speed Framing Camera was used for photoimage registration. Camera triggers simultaneously with laser discharge. For every experimental regime (RED, LED, RDA) 8 frames are given for plume evolution. The most interesting image was registered in the presence of electrical discharge, because symmetry, specific in RDE and LDE regimes for all frames, is affected during expansion. This image, computer scanned and 2.5 times magnified, is given below in figure 5.

Sequence of frames is in order:

1		4	→	5		8
↓		↑		↓		↑
2	→	3		6	→	7

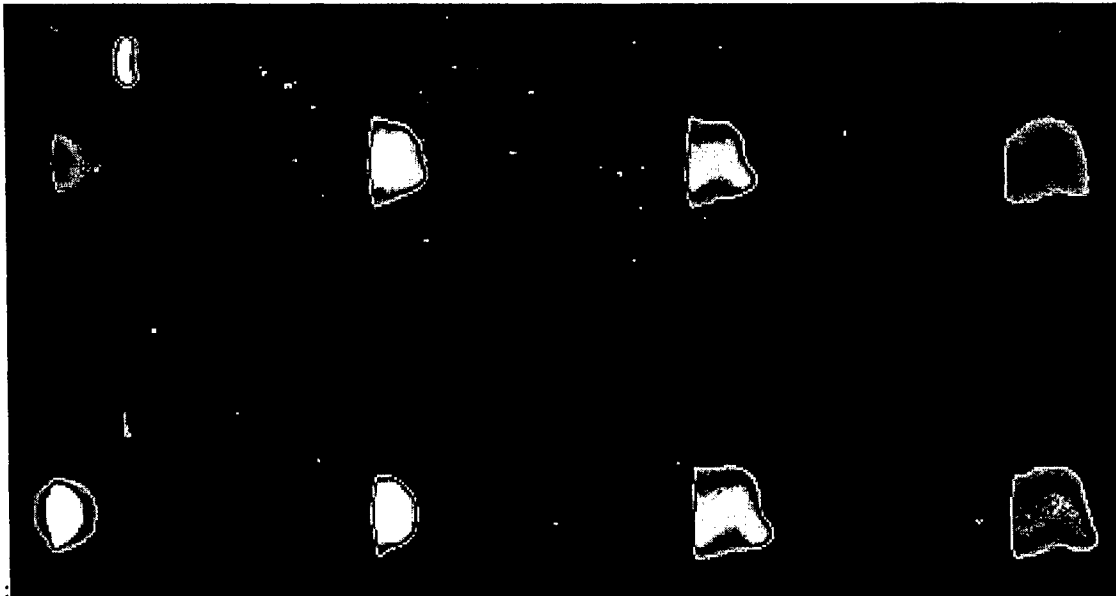


Figure 5. The frames of plasma expansion for RDA irradiating regime

Delay and exposure time, controlled by NEC-PC9801nv, of each frame was chosen to obtain the best exploring of the plume evolution, being given below:

Delay[μ s]/(Exposure time[ns]): 0.5/(60) - 0.8/(60) - 1.3/(60) - 2/(100) - 2.9/(170) - 4.1/(400) - 6.1/(700) - 8.6/(1200)

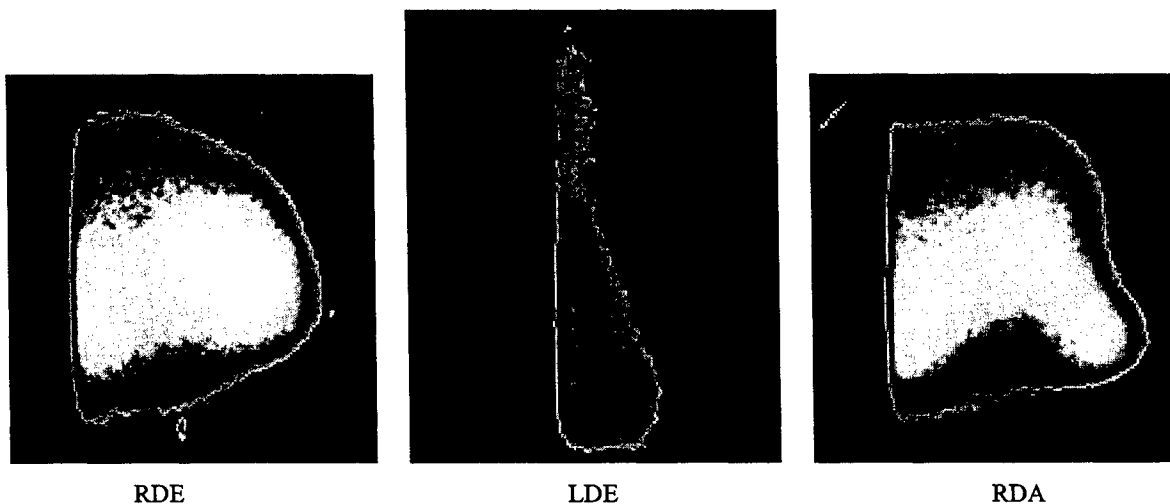


Figure 6. The 6th frame of plasma expansion for RDE, LDE and RDA regimes

Differences which appear between the three operation regimes, for the 6th frame, computer scanned and 8 times magnified, are shown in figure 6. A summary analysis of plume expansion reveals that :

- the plume remains coupled to target up to the last frame (8.6 μ s), because expansion is decelerated by high pressure ambient gas
- the expansion velocity is much more reduced in comparison with free expansion (in vacuum), being of 0.8×10^3 m/s in RDE or RDA regimes and 40×10^3 m/s for vacuum expansion
- the expansion symmetry, appearing in regimes without discharge, is disturbed in regime with discharge presence, 1.3 μ s from plasma initiation
- low brightness and rapid quenching of emission in LDE regime appear, 0.5 μ s from plasma initiation
- plasma expansion can be characterised, for each experimental regime, in the following manner:

- spherical expansion with law²³⁻²⁴ $R(t) \sim t^\beta$, for RDE regime, R being distance of plasma front to target, t is time from plasma initiation and β -expansion parameter
- planar expansion in the case of LDE regime
- initial spherical expansion ($<1.3\mu s$) is changed to approximate planar expansion, for RDA regime.

5. POWDER CHARACTERISATION

The main quality parameters for powder characterisation are particle size and chemical composition. These parameters give powder finesse and purity.

5.1. Dimensional characterisation

To determine particle dimensions a Scanning Electron Microscopy (SEM) with JEOL Superprobe 733 ($\times 10\,000$ magnification) was used. A part of the registered micrographs, computer scanned, is shown in figure 7, for every operation regime.

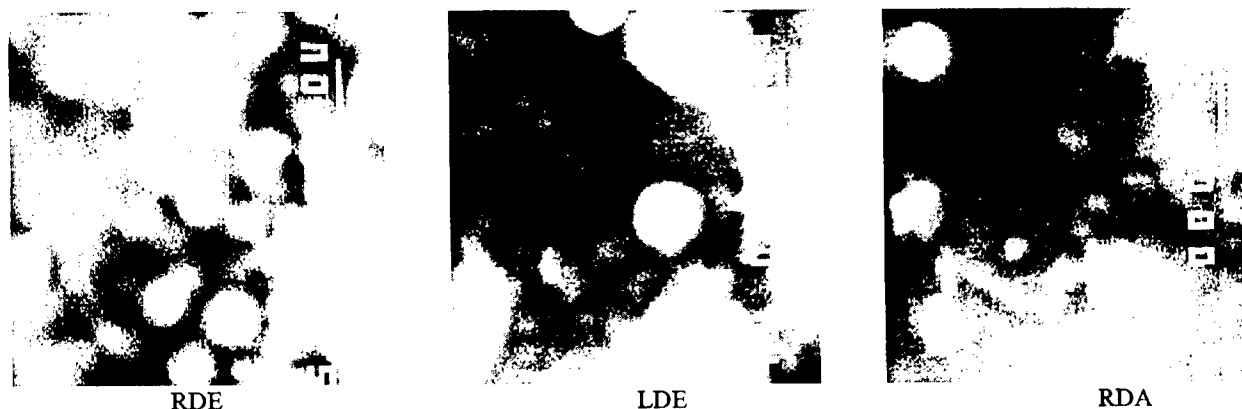


Figure 7. The powder micrographs for RDE, LDE and RDA regimes

Significant differences appear between powder images of the reference regime (RDE) and LDE or RDA regime. While in RDE conditions, most of the observed particles are submicronic, spherical and with sharp edges for 10 000 times magnification, in LDE and RDA micrographs, the “fuzzy” images which appear, at the same magnification, signify the presence of much smaller particles, with dimension much lower than the microscope resolution limit.

As observed, the presence of an electrical discharge in a plasma generated at high fluence has a favourable effect in size decreasing the size of the powder, similar to fluence reduction.

5.2. Purity characterisation

The physical and chemical properties of a powder have a strong dependence on the chemical composition. In the case of RLA, if a high purity target and gas are used, unreacted target ejected species can impurify the powder composition. In respect to this, X-Ray Diffraction (XRD) spectra for every irradiation regime, in a θ -2 θ scan and $30\div 80^\circ$ angular interval, was traced.

Spectra analysis show that:

- spectra shape is quite similar, with γ -alumina lines being stronger for crystalline orientations (400) or (440) and less intense for (311) or (222),
- the powder spectrum of alumina produced in RDE regime seems to have a very small line of Al(111), signifying possible presence of low amount of unoxidized metal,
- the spectra of powder produced in the LDE or RDA regime present γ -alumina lines only, indicating obtaining of a very high purity powder.

Regarding to the above considerations, one may conclude that the presence of an electrical discharge improves powder purity obtained in high fluence irradiating conditions.

6. POWDER PRODUCTION RATE

The process powder production rate is given by the collected mass of powder for a laser pulse. It depends on the ablation rate and powder collection efficiency.

The target ejected mass is related to the interaction parameters (laser beam pulse characteristics, nature and surface state of target, etc.). Using the calculated ablation rate (6), in our conditions it is 135 ng/pulse. In the same conditions, measured target mass losses are 100 ng/pulse for RDE regime, 110 ng/pulse for LDE and 120 ng/pulse for RDA regime. Differences between measured rates are not significant enough to conclude favourable regimes. Also, calculated and experimental data of target mass loss show good agreement, meaning that approximations used in the theoretical model were justified.

The collection efficiency is defined as the ratio of deposited powder mass on filter and mesh to obtainable powder mass by total reaction of ejected species from target. In our case, the difference between both masses is insignificant, meaning that flow gas rate is able to collect all ceramic particles.

Because of low powder production rate, long laser operation ($>10^5$ pulses) was necessary for all three irradiating conditions to obtain a significant amount of powder.

7. CONCLUSIONS

As is known, fluence reduction has a favourable effect on improving the quality parameters of powders. Our experiments confirm this. Electrical discharge presence in the plasma produced with a high fluence, described in this paper, assures obtaining of a higher quality powder in comparison to the absence of discharge case. The effect of electrical discharge presence in plasma is similar to fluence reduction.

The influence of the electrical discharge on laser-target coupling and plasma evolution, show that powder parameters depend on all RLA process steps, and electrical discharge presence (with negative biased electrode) in plasma gives a favourable modification of target irradiation and plume expansion parameters.

Although the powder characterisation methods used (SEM and XRD) mainly give qualitative information on powder quality, the good role of discharge presence is evidenced.

In conclusion, this work confirms that using a low laser beam fluence for target ablation is favourable for reducing the particle size and obtaining a correct stoichiometry of the powder. The presence of an auxiliary discharge in the ablation plume for a higher energy density leads to the same results as the low energy density case, namely the production of high quality powders.

We consider that the method of reactive laser ablation aided by an auxiliary discharge, can be a good basis for future improvement of the ultrafine powder production process.

8. ACKNOWLEDGEMENTS

This research was performed as part of the collaboration between the Institute of Atomic Physics in Romania and the Nagaoka University of Technology in Japan. The authors want to thank Professor Yasuzo Uchida for supporting this cooperation.

We also want to thank Consuela Matei for computer scanning of the photoimages.

9. REFERENCES

1. A. Matsunawa, S. Katayama, A. Susuki and T. Ariyasu, "Laser Production of Metallic Ultra-Fine Particles", *Transactions of JWRI* **15**(2), 61-72 (1986).
2. A. Matsunawa and S. Katayama, "Laser Production of Ultra-fine Particles", *Transactions of JWRI* **14**(2), 197-201 (1985).
3. A. Matsunawa and S. Katayama, "Laser Production of Ultrafine Particles of Ceramics and Ceramic-Metal Mixtures", *Transactions of JWRI* **19**(1), 137-148 (1990).
4. G.P. Johnston, R. Muenchausen, D.M. Smith, W. Fahrenholtz and S. Foltyn, "Reactive Laser Ablation Synthesis of Nanosize Alumina Powder", *J. Am. Ceram. Soc.* **75** (12), 3293-3498 (1992).
5. G.P. Johnston, R. E. Muenchausen, D.M. Smith, and S. Foltyn, "Reactive Laser Ablation Synthesis of Nanosize Aluminum Nitride", *J. Am. Ceram. Soc.* **75** (12), 3465-3468 (1992).
6. V. Sandu, A. Crisan, Dana Grigorescu, L. Miu, I. Chis, G. Aldica, E. Cruceanu, C. Grigoriu and D. Dragulinescu, "TEA-CO₂ laser deosited YBa₂Cu₃O_{7-x} superconducting thin films", *J. Mater. Sci. Lett.* **8**, 509-510 (1989).
7. V. Sandu, J. Jaklovsky, Dana Miu, D. Dragulinescu, C. Grigoriu and M. C. Bunesu, "LaAlO₃ thin films deposited on silicon and sapphire as buffer layers for YBa₂Cu₃O_{7-x}", *J. Mater. Sci. Lett.* **13**, 1222-1225 (1994).
8. H. Muller, H.-G. Fritsche and L. Skala, "Analytic Cluster Models and Interpolation Formulae for Cluster Properties", *Cluster of Atoms and Molecules I : Theory, Experiment, and Clusters of Atoms*, ed. H. Haberland, pp. 114-140, Springer-Verlag, Berlin, 1995.
9. S. Rajendran, "Production of ultrafine alpha alumina powders and fabrication of fine grained strong ceramics", *J. Mater. Sci.* **29**, 5664-5672 (1994).
10. G. Soucy, J. W. Jurewicz and M. I. Boulos, "Parametric study of the plasma synthesis of ultrafine silicon nitride powders", *J. Mater. Sci.* **30**, 2008-2018 (1995).
11. I.-W. Chen, L.A. Xue, "Development of Superplastic Structural Ceramics", *J. Am. Ceram. Soc.* **73** (9), 2585-2609 (1990).
12. H. Haberland, "Experimental Methods", *Cluster of Atoms and Molecules I : Theory, Experiment, and Clusters of Atoms*, ed. H. Haberland, pp. 207-252, Springer-Verlag, Berlin, 1995.
13. D. Bauerle, *Laser Processing and Chemistry*, 2nd edition, Springer Verlag, Berlin, 1996.
14. R. Kelly and B. Braren, "On the Direct Observation of the Gas-Dynamics of Laser-Pulse Sputtering of Polymers, Part I: Analytical Considerations", *Appl. Phys. B* **53**, 160-169 (1991).
15. B. Braren, K. G. Casey and R. Kelly "On the gas-dynamics of laser-pulse sputtering of polymethyl metacrylate", *Nuclear Instruments and Methods in Physics Research B*, **58**, 463-472 (1991).
16. Dana Miu, C. Grigoriu, D. Dragulinescu and I. Chis, "Characterization of pulsed-laser deposition plasmas using ion probes", *Opt. Eng.* **35**(5), 1325-1329 (1996).
17. I. G. Murgulescu, Tatiana Oncescu and E. Segal, *Introduction to Physical Chemistry*, Vol. II, part 2 : *Chemical Kinetics and Catalysis*, Ed. Academiei RSR, Bucharest, 1981, (in Romanian).
18. D. S. Misra and S. B. Palmer, "Laser ablated thin films of YBa₂Cu₃O_{7-δ} : the nature and origin of the particulates", *Physica C* **176**, 43-48 (1991).
19. S. R. Foltyn, R. C. Dye, K. C. Ott, E. Peterson, R. E. Muenchausen, X. D. Wu, K. M. Hubbard, W. Hutchinson and R. C. Estler, "Target Modification in the Excimer Laser Deposition of YBa₂Cu₃O_{7-x} Thin Films", *Preprint LA-UR-90-2873*, Los Alamos National Laboratory, 1990.
20. J. A. Greer and M. D. Tabat, "Large-area pulsed laser deposition: Techniques and applications", *J. Vac. Sci. Technol. A* **13**(3), 1175-1181 (1995).
21. D. Fried, T. Kushida, G. P. Reck and E. W. Rothe, "The effects of the electric field associated with a laser-induced pulsed discharge on the ablation-generated plumes of YBa₂Cu₃O_{7-x}", *J. Appl. Phys.* **72**(3), 1113-1125 (1992).
22. L. Dirnberger, P. E. Dyer, S. R. Farrar and P. H. Key, "Observation of magnetic-field-enhanced excitation and ionization in the plume of KrF-laser-ablated magnesium", *Appl. Phys. A* **59**, 311-316 (1994).
23. Y. A. Zeldovitch and Yu. P. Raizer, *Physics of Shock Waves and High Temperature Hydrodynamic Phenomena*, Vol. 1, Academic Press, New York, 1967.
24. P. E. Dyer, A. Issa and P. H. Key, "An investigation of laser ablation and deposition of Y-Ba-Cu-O in an oxygen environment", *Applied Surface Science* **46**, 89-95 (1990).

Deposition of carbon nitride thin films by IR laser-induced reactions in carbon-nitrogen gas-phase compounds

A. Crunteanu, R. Alexandrescu, R. Cireasa, S. Cojocaru, I. Morjan, A. Andrei*
A. Kumar**

National Institute for Lasers, Plasma and Radiation Physics

P.O. Box MG-36, R-76900, Bucharest, Romania

*) Institute for Nuclear Reactors, Pitesti, Romania

**) University of South Alabama, Mobile, AL 36 688, USA

ABSTRACT

Since the theoretical studies of Liu and Cohen who predicted the existence of a superhard phase of carbon nitride, a great deal of effort was undertaken in order to synthesise this hypothetical material with a nitrogen content as high as the 57% present in a β - C_3N_4 structure. This study presents an attempt to produce CN_x thin films using the laser-induced CVD technique. CW CO_2 laser was used for irradiating various carbon-nitrogen containing mixtures such as $C_2H_4/N_2O/NH_3$. The CN_x films were grown alternatively on bare alumina (α - Al_2O_3) substrates and on pre-deposited Ti films. A comparative analysis of nitrogen incorporation in the films obtained in different experimental conditions was performed by means of the X-ray photoelectron spectroscopy (XPS). The same method was used to identify the chemical states of the CN system.

Keywords: laser pyrolysis, carbon nitride, thin films, XPS analysis

1. INTRODUCTION

In the last few years, the synthesis of carbon-nitride films has been the subject of numerous experimental [1-5] and theoretical [6-8] studies. The prediction of its extreme hardness, high thermal conductivity and a high elastic modulus for a covalent C_3N_4 material [6,7] has raised a great interest in the scientific world, in order to obtain and to study this new material. Different methods for obtaining CN_x thin films, such as ion beam assisted deposition, magnetron sputtering laser reactive ablation, shock compression and cyclotron resonance plasma assisted vapour deposition have been applied.

In a previous work [5] we first demonstrate the possibility of a laser-CVD method to produce CN_x thin films by using different carbon/nitrogen gas precursors and substrates. In this report we have studied the dependence of the chemical content of films obtained by IR irradiation on some deposition parameters such as gas-mixture composition and nature of the substrate. Using ethylene/nitrous oxide/ammonia precursor system, the partial concentration of NH_3 was successively varied in order to enhance nitrogen incorporation in CN_x thin films. Irradiation was made alternatively on bare alumina (α - Al_2O_3) and pre-deposited Ti substrates. The various C-N bond configurations, identified by XPS analysis are discussed.

2. EXPERIMENTAL

The experimental set-up for laser-CVD has been described in [5]. Briefly, it consisted of a glass reaction cell (base pressure 10^{-3} torr) into which the gases/vapours and the substrate are introduced. A medium power CW CO_2 laser (maximum output power 50 W) has been used. The incident laser energy could be varied by modifying the irradiation time and by using an electrical chopper with variable pulse length (ms) and frequency (Hz). The IR radiation of the CO_2 laser was penetrating the cell through a NaCl window and was focused through a NaCl lens ($f=15$ cm), perpendicularly to the substrate (2 cm behind it). The incident laser energy onto the substrate was maintained at about 1337 J in all cases. Alternatively the film were grown on bare α - Al_2O_3 and pre-deposited Ti layers. For obtaining pre-deposited Ti films, $TiCl_4$ dissociation by means of the CO_2 laser radiation was performed at room temperature and at a $TiCl_4$ vapour pressure of ~ 10 torr. The thickness of the deposited Ti films was measured by interference microscopy (approximate accuracy level 1/20 of the visible light wavelength). Prior to each CN_x deposition on a Ti substrate, the Ti films were thoroughly degassed and kept under vacuum.

The CN_x films were deposited by irradiating mixtures of ethylene/nitrous oxide/ammonia, with variable partial concentrations of NH_3 ($C_2H_4:N_2O:NH_3=1:2:3, 1:2:5, 1:2:8$ and $1:2:10$), at a total pressure of ~ 80 torr. When using a pre-deposited substrate, the relative concentration of gases was $C_2H_4:N_2O:NH_3=1:2:8$.

The chemical and morphological properties of the produced films were characterized by X-ray photoelectron spectroscopy (XPS) and scanning electron microscopy (SEM). Photoelectron spectra were obtained with a VG ESCALAB MK II spectrometer (base pressure $\sim 9 \times 10^{-10}$ mbar). For XPS, Al $K\alpha$ radiation ($h\nu = 1486.6$ eV) was used. Spectral calibration was performed by means of the Ag $3d_{3/2}$ ($h\nu = 368.26$ eV) line, with the Fermi level as an energy reference. A "flood gun" was used for the correction of surface charging effects.

3. RESULTS AND DISCUSSIONS

3.1 Deposition of titanium substrates

In the IR wavelength range, $TiCl_4$ is transparent to the CO_2 laser radiation. In a perpendicular geometry of irradiation the Ti film grows on Al_2O_3 surface due to thermal decomposition of reactant molecules adsorbed on the laser heated surface. The variation in film thickness with increasing effective irradiation time is shown in Figure 1.

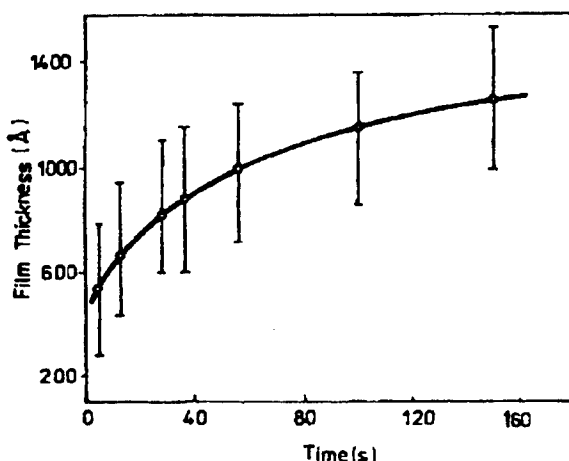


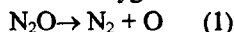
Figure 1. The dependence of Ti film thickness on effective irradiation time, in case of CO_2 laser pyrolysis of $TiCl_4$ vapor

The plot was obtained by combining the results of the IR transmission measurements with those given by the interferential microscopy method. In case of CN_x film, a Ti thickness of ~ 1000 Å was used for the pre-deposited substrate.

We should note that the catalytic effect of a Ti substrate for enhancing photo-deposition was observed earlier [9]. However, it was shown [10] that the high reactivity of Ti with many functional groups (among which CN_x at a surface may shift preferentially the reaction routes leading finally to titanium compounds.

3.2. CN_x thin film deposition

If we refer to the induced decomposition of the gas precursors involved in the present deposition process, we observe that N_2O has the lowest dissociation energy ($D[N_2-O] = 1.67$ eV), as compared to C_2H_4 ($D[H_2C-CH_2] = 7.2$ eV) and NH_3 ($D[NH_2-H] = 4.3$ eV). On another hand, it is known that N_2O dissociation promotes an oxidizing atmosphere through the release of native oxygen



which favors ethylene depletion (at high temperatures) with partial conversion to acetylene. It was indeed observed that C_2H_2 was the main gas product in laser reactions involving N_2O and C_2H_4 [11]. At the same time, when the precursor mixture has a high N_2O relative concentration (at low NH_3 partial pressure), carbon incorporation in films increases, resulting in low nitrogen-to-carbon ratio in films. This will be discussed below.

During CN_x deposition, different $C_2H_4/N_2O/NH_3$ gas mixtures for which the NH_3 relative concentration was progressively increased were studied. The experimental parameters are listed in Table 1, for samples CN20-CN23, respectively.

Also presented in Table 1 is the sample labeled CN25, for which the laser deposition occurred on a pre-deposited Ti substrate. During each run, the nitrogen incorporation and the chemical bonds in films were analyzed by XPS.

The N/C atomic ratio for the as-deposited CN_x films on $\alpha-Al_2O_3$ and pre-deposited Ti substrate is presented in Table 1. Due to the fact that the elemental composition indicates the usual carbon contamination in the ambient, the N/C values in parentheses were obtained by subtracting the contribution of adventitious carbon (at 284.6 eV in Table 1). At the same time, the detected oxygen contamination for samples handled in air suggests a higher degree of surface oxidation for the film grown on a pre-deposited Ti substrate. A higher N/C ratio in films was obtained by using precursor mixtures with intermediate partial concentrations of NH_3 (samples CN21 and CN22).

Table 1.

Mixture composition and XPS results for CN_x films obtained by IR irradiation(1337 J incident laser energy) The mixture total pressure was 80 torr.

Run	Mixture $C_2H_4:N_2O:NH_3$	N/C* (at%), as deposited films (calculated from XPS data)
CN20	1:2:3	0.04 (0.14)
CN21	1:2:5	0.1 (0.35)
CN22	1:2:8	0.11 (0.29)
CN23	1:2:10	0.06 (0.18)
CN25 [†]	1:2:8	0.04 (0.09)

[†]) Films grown on pre-deposited Ti layers.

*) The values in parenthesis were obtained by subtracting the contribution of the adventitious carbon from the C overall concentration in films.

Following the analysis of carbon and nitrogen XPS lines performed by Wu [2], there are four characteristic peaks in the $C1s$ spectrum and three in the $N1s$ spectrum which characterise thin CN_x films. These peaks were also analysed by Marton et al. [3]. In Figure 2 and Figure 3 are shown typical $C1s$ and respectively $N1s$, spectra of films deposited on $\alpha-Al_2O_3$. The spectra a (Fig. 2 and Fig. 3) and b (Fig. 2 and Fig. 3) were obtained from $C_2H_4:N_2O:NH_3 = 1:2:8$ and $C_2H_4:N_2O:NH_3 = 1:2:10$ gas mixtures, respectively (samples CN22 and CN23, respectively).

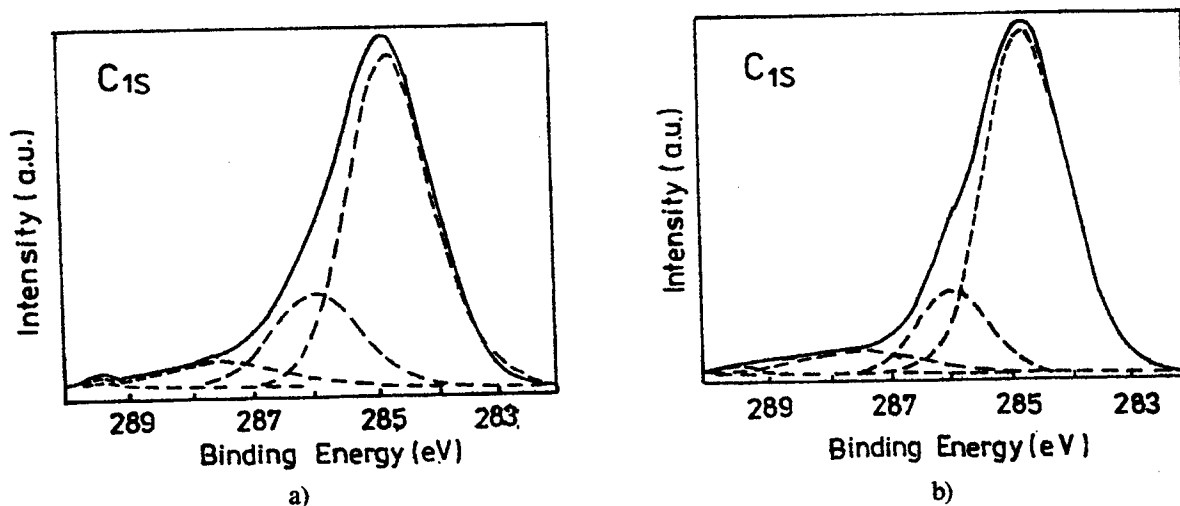


Figure 2.

Carbon XPS deconvoluted spectra of films obtained from $C_2H_4/N_2O/NH_3$ mixtures with relative concentrations: $C_2H_4:N_2O:NH_3 = 1:2:8$ (a) and $1:2:10$ (b) on $\alpha-Al_2O_3$ substrates. The spectra a and b correspond to samples CN22 and CN23, respectively, in Table 1.

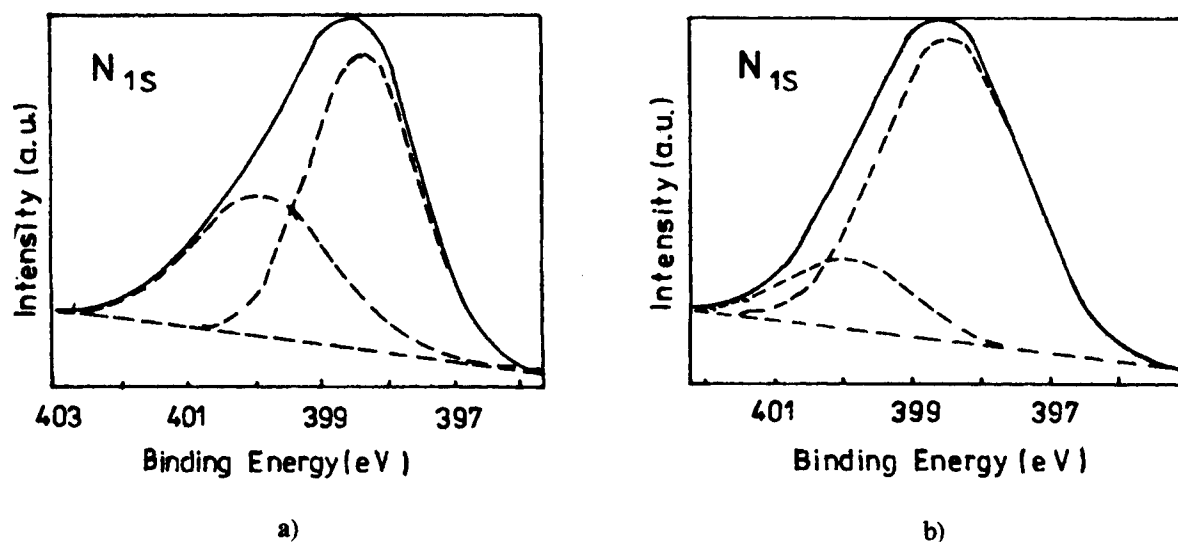


Figure 3.

Nitrogen XPS deconvoluted spectra of films obtained from $C_2H_4/N_2O/NH_3$ mixtures with relative concentrations: $C_2H_4:N_2O:NH_3 = 1:2:8$ (a) and $1:2:10$ (b) on $\alpha-Al_2O_3$ substrates. The spectra c and d correspond to samples CN22 and CN23, respectively, in Table 1.

Characteristic peaks [2] at 284.6, 285.9, 287.5 and 289.5 eV of the C1s photoelectrons and 398.4, 399.8 and 402.1 eV for the N1s photoelectrons were chosen, in order to obtain the deconvolution of spectra, and the best gaussian fits. Their relative % atomic concentrations expressed as ratios areas of the peaks areas, are presented in Table 2 and calculated relatively to the total C and N atomic concentrations. Accordingly, the results of the deconvolution of C1s and N1s spectra imply the presence of different types of chemical bonding in the films. Thus, the C1s peak at 284.6 eV is near the value usually assigned to adventitious carbon but may contain contributions from amorphous carbon, graphite and surface carbon which have lost their nitrogen due to reactions with O_2 [8]. However, this peak was also associated with the N1s peak at 402.1 eV for describing a carbon nitride phase with a very low nitrogen incorporation [4]. This last nitrogen peak (402.1 eV) was also identified as coming from free nitrogen atoms [2]. The C1s peak at 289.5 eV was attributed to CO-type bonds.

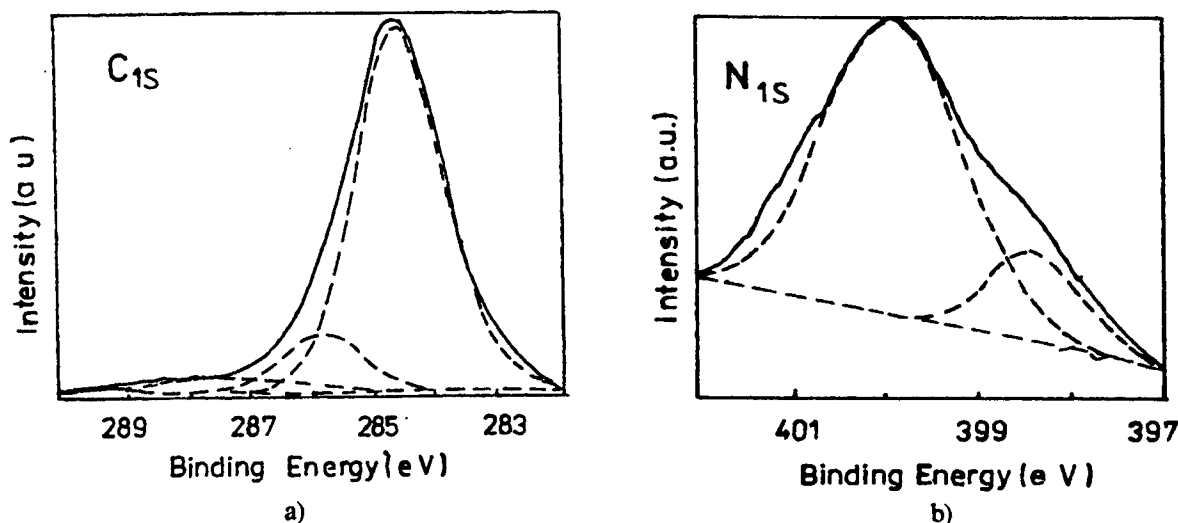


Figure 4.

Carbon (a) and nitrogen (b) XPS deconvoluted spectra of films obtained in IR irradiation from $C_2H_4/N_2O/NH_3$ mixture with relative concentration: $C_2H_4:N_2O:NH_3 = 1:2:8$ on pre-deposited Ti substrates (sample CN25 in Table 1)

The remaining C1s and N1s peaks were selected in two pairs, each of them reflecting different binding states between carbon and nitrogen: i) the pair 287.5 and 398.4 eV was assigned to a phase 1 (C¹ and N¹), reflecting a tetrahedrally (sp³) bonded carbon phase which should resemble the β -C₃N₄ phase [2]; ii) the pair 285.9 and 400.1 eV was ascribed to a phase 2 (C² and N²) resembling to sp² bonded C and comprising a lower N incorporation, this composition supporting variations from C₅N to C₄N₂ and beyond [3]. We should note that the phase ascribed to sp³ bonded C was identified by Sharma et al. [12] with the C1s and N1s peaks at 286.1 and 398.6 eV, respectively.

Based on the relative % atomic concentration of C¹, C², N¹ and N² phases, as determined in Table 2, the N/C composition for phases 1 and 2 ($(N^1+N^2)/(C^1+C^2)$), for phase 1 ($(N^1)/(C^1)$), as well as the fractional concentration of phase 1, $(N^1+C^1)/((N^1+N^2)+(C^1+C^2))$ may be obtained [3]. The results suggest that intermediate partial pressures of ammonia seem to favor the composition of phase 1 and 2 (samples CN21 and CN22). At the same time, the composition of phase 1 seems to be almost independent on ammonia content in precursor mixtures. We also observe that most of the nitrogen bonds characterized by a binding energy of 402.1 eV are missing. The process through which the relative concentration of N-containing gas-phase precursors could influence nitrogen incorporation in a specific bonding state are presently not clear but they will be studied by further investigations.

Table 2.

XPS results for CN_x films obtained by IR (1337 J incident laser energy) The mixture total pressure was 80 torr.

Run	XPS data									
	Relative % atomic concentration**							N/C composition***		
	C1s				N1s					
	289.5 (eV)	287.5 (eV)	285.9 (eV)	284.6 (eV)	402.1 (eV)	399.8 (eV)	398.4 (eV)	$(N^1+N^2)/(C^1+C^2)$	N^1/C^1	$\frac{N^1+C^1}{N^1+C^1+N^2+C^2}$
CN20	0.8	6.3	20.4	68.6	0	0.8	3.1	0.14	0.50	0.30
CN21	0.3	8.3	10.0	74.8	0.1	1.3	5.2	0.35	0.50	0.54
CN22	0.4	7.3	18.3	66.4	0	2.9	4.7	0.30	0.64	0.36
CN23	0.7	7.3	14.9	72.8	0	0.7	3.6	0.20	0.49	0.41
CN25 [†]	0.9	5.2	11.5	80.7	0	1.4	0.3	0.10	0.06	0.30

**) Calculated on the basis of total C and N atomic concentration.

***) Ascribed according to Ref. [2] (see also text).

As observed before, in the case of our pyrolytic processes an enhanced CN film deposition by using Ti layers as substrates was not evident. The effects of both nitrogen incorporation and the formation of CN structures assigned to phases 1 and 2 are lower than those obtained in case of a bare α -Al₂O₃ substrate. In this respect, it is possible that in a thermal process, the temperature should activate the interaction between titanium atoms and freshly deposited CN groups, with the subsequent formation of titanium carbides/nitrides. The tailing effect observed in the C1s spectra towards 283 eV (see, for instance Figure 2c) could represent a contribution from TiC. It was shown that the high reactivity of Ti at a surface may lead finally to titanium oxides with various oxidation states [10]. In our case we observed indeed that the Ti 2p_{3/2} peak of the sample obtained on a pre-deposited Ti substrate (CN25) was located towards the characteristic binding energy of TiO₂ (towards 458 eV).

4. CONCLUSIONS

In this work we performed a study on the chemical composition of CN_x thin films prepared by the CO₂ laser CVD method. Using a perpendicular geometry of irradiation, two substrates (α -Al₂O₃ and Ti pre-deposited layer) and different partial concentrations of NH₃ in ternary precursor system: ethylene/nitrous oxide/ammonia were chosen, in order to

investigate the degree of nitrogen incorporation in the deposited CN_x films. The overall stoichiometry of films was N-deficient relatively to the predicted C_3N_4 form but the N/C ratio in films increases for precursor mixtures with intermediate partial pressures of NH_3 , which seem to favour also the composition of the phase in which C is tetrahedrally bonded to N (sp^3).

The high C content in films obtained with low ammonia partial pressure could be explained by the enhanced hydrocarbon decomposition in presence of native oxygen (released by N_2O) dissociation.

The pre-deposited Ti substrates has demonstrated a negative effect of CN_x film nucleation and growth probably due to subsequent titanium compound formation by the interaction between reactive atoms and CN groups on surface.

5. ACKNOWLEDGEMENTS

Part of this research was supported by the National Research Council (NRC) USA under Twinning Program.

6. REFERENCES

1. Y. Zhang, Z. Zhou, and H. Li, "Crystalline carbon nitride films formation by chemical vapor deposition" *Appl. Phys. Lett.* **68**(5), 634-636 (1996)
2. Z. Wu, Y. Yu, and X. Liu, "Characteristics of carbon nitride films synthesized by single-source ion beam enhanced deposition system" *Appl. Phys. Lett.* **68**, 1291 (1996)
3. D. Marton, K.J. Boyd, A.H. Al-Bayati, S.S. Todorov and J.W. Rabalais, "Carbon Nitride Deposited Using Energetic Species: A Two Phase System" *Phys. Rev. Lett.* **73**, 118 (1994)
4. S. Kumar, K.S.A. Butcher and T.L. Tansley, "X-ray photoelectron spectroscopy characterization of radio frequency reactively sputtered carbon nitride thin films" *J. Vac. Sci. Technol. A* **14**(5), 2687-2692 (1996)
5. R. Alexandrescu, R. Cireasa, G. Pugna, A. Crunteanu, S. Petcu, I. Morjan, I.N. Mihailescu and A. Andrei, " CN_x thin films obtained by laser induced CVD in different gas-substrates system" *Appl. Surf. Sci.* **109/110**, 544-548 (1997)
6. A.Y. Liu and M.L. Cohen, "Prediction of New Low Compressibility Solids" *Science* **245**, 841 (1989)
7. A.Y. Liu and M.L. Cohen, "Structural properties and electronic structure of low-compressibility materials: $\beta\text{-Si}_3\text{N}_4$ and hypothetical $\beta\text{-C}_3\text{N}_4$ " *Phys. Rev. B* **41**, 10727-10733 (1990)
8. V. Guo and W.A. Goddard III, "Is carbon nitride harder than diamond? No, but its girth increases when stretched (negative Poisson ratio)" *Chem. Phys. Lett.* **237**, 72 (1995)
9. M. Hanabusa and A. Komatsu, "Catalytic and Photoinduced Effects of Ti and TiO_2 layers on Al film growth by Chemical Vapor Deposition" *J. Appl. Phys.* **65**, 1826 (1994)
10. K. Konstantinidis, P. Zhang, K.L. Opila and D.L. Allara, "An in-situ X-ray photoelectron study of the interaction between vapor-deposited Ti atoms and functional groups at the surfaces of self-assembled monolayers" *Surface Science* **338**, 300-312 (1995)
11. A. Crunteanu, R. Cireasa, R. Alexandrescu, I. Morjan, V. Nelea, I.N. Mihailescu, A. Andrei and F. Vasiliu, "Influence of the surface treatment of the substrate in the LCVD of CN_x films", *Proceedings of the E-MRS Spring Meeting 1997, Strasbourg, France*, to be published in *Carbon* (1998)
12. A.K. Sharma, P. Ayyub, M.S. Multani, K.P. Adhi, S.B. Ogale, M. Sunderaraman, D.D. Upadhyay and S. Banerjee, "Synthesis of crystalline carbon nitride thin films by laser processing at a liquid-solid interface" *Appl. Phys. Lett.* **69**(6), 3489-3491 (1996)

The influence of the thermal annealing on optical properties of porous silicon films

I. Baltog, M.L. Ciurea, G. Pavelescu, E. Pentia, G. Galeata

National Institute of Materials Physics, P.O. Box MG 7, Bucharest, Romania

J.P. Roger

Laboratoire d'Optique Physique, ESPCI, 10 rue Vauquelin, 75005, Paris, France

ABSTRACT

The influence of the thermal annealing on the optical properties of the porous silicon (PS) films was revealed by photoluminescence (PL) and spectroellipsometric (SE) measurements. As result of 200°C annealing small changes of the dielectric functions could be understood by desorption process of some molecules from Si skeleton surface. Strong changes of PL and dielectric function spectra after the thermal annealing at high temperatures (up to 800°C) were explained by the change of the passivation from hydrogen to oxygen and then the beginning of the oxidation process. This oxidation process produces the disappearance of the PL slow component, an important enhancement of PL (2-3 orders of magnitude) and a shift of maximum position to higher energies, corresponding to the thinning of the nanocrystallites from the Si skeleton.

Keywords: porous silicon, photoluminescence, ellipsometry

1. INTRODUCTION

It is well known the considerable interest of the scientific community for porous silicon (PS) field because of potential applications in silicon-based optoelectronics. In spite of the large research efforts spent, many problems remain open.

According to the quantum confinement mechanism, the peak wavelength of photoluminescence of PS is closely related with the size of Si wires and dots¹. It has been found that some post treatment such as oxidation in air, in water or by others electrochemical processes²⁻⁴, can reduce the size of the Si skeleton, and thus it causes a blue shift of the luminescence spectrum.

The aim of this paper is the investigation of changes in optical properties induced by the thermal annealing. Photoluminescence (PL) and spectroellipsometric (SE) measurements on as prepared and thermal annealed samples in air (200°C, 400°C, 600°C and 800°C) were performed. PL spectra were taken at room (RT) and liquid nitrogen temperatures (LNT). The effects of the oxidation on the optical properties of PS sample due to storage duration and thermal annealing are compared.

2. EXPERIMENTAL

PS samples were prepared by the electrochemical etching of 5 --7 Ωcm p-type (100) Si wafers in HF based electrolyte under constant current conditions⁵. This process was followed by another one for PL activation. It is already well known that the etching duration determines the layer thickness and also strongly influences the microstructure of PS layers. Four types of samples, etched for different durations were studied: S₁₀, S₃₀, S₉₀, S₁₅₀ anodized for 10, 30, 90 and 150 min, respectively. All sample has the same average porosity of about 72-76%, gravimetrically determined. They were measured after a storage in air for more than 3 weeks. These samples will be named in the following "as prepared".

The optical characterization of PS films was made in the energy range from 1.5 to 4.5 eV by SE measurements using SOPRA ES4G ellipsometer.

The PL spectra under pulsed excitation have been recorded by means of a monochromator and a BURLE C 31034 photomultiplier interfaced with a computer. For PL measurements under pulsed excitation a BOXCAR AVERAGER was also used. A TEKTRONIX TD 320 oscilloscope interfaced with a computer allows to study the luminescence decay of PS samples.

3. RESULTS AND DISCUSSION

3.1 Ellipsometric investigations

Spectroellipsometric technique yields a complex picture of the optical response of the materials and a valuable information on the material structural characteristics. From SE measurements the complex dielectric function $\epsilon(\omega) = \epsilon_r(\omega) + i\epsilon_i(\omega)$ or the complex refractive index $\tilde{n} = n + ik$ results. For a given wavelength, if the film thickness is less than the respective penetration depth of light, information from film as well as the substrate is obtained. Consequently, the measured dielectric function corresponds to the pseudodielectric function $\langle \epsilon(\omega) \rangle$ (or pseudorefractive index $\langle \tilde{n} \rangle$) of the film substrate system. For samples thicker than the penetration depth, SE provides directly the complex dielectric function of the film, without any contribution from the substrate.

The real and imaginary parts of the pseudodielectric function for samples S_{90} and S_{150} , anodized for 90 and 150 min, respectively, are illustrated in Fig.1. The overall reduction of the $\epsilon_r(\omega)$ with the increasing of the etching duration is explained by the increase of the layer porosity. Rossow et. al.⁶ have shown that the increase of the porosity during the electrochemical etching process is more pronounced in the top part of the film, but the variation in the porosity is small enough to consider the PS layers as homogeneous over the light penetration depth. For a longer etching time the spectral position of the broad feature in $\epsilon_i(\omega)$ is shifted to higher energies, indicating that the crystallites diameters of Si skeleton are reduced⁶. Similar results were obtained by Thönissen et al.⁷ from Raman measurements.

As a conclusion, the etching time changes the microstructure of the PS layers, causing an increasing of the porosity and a thinning of the silicon skeleton, mainly in the top part of the film, because the topmost layers remain for a longer time in contact with the electrolyte.

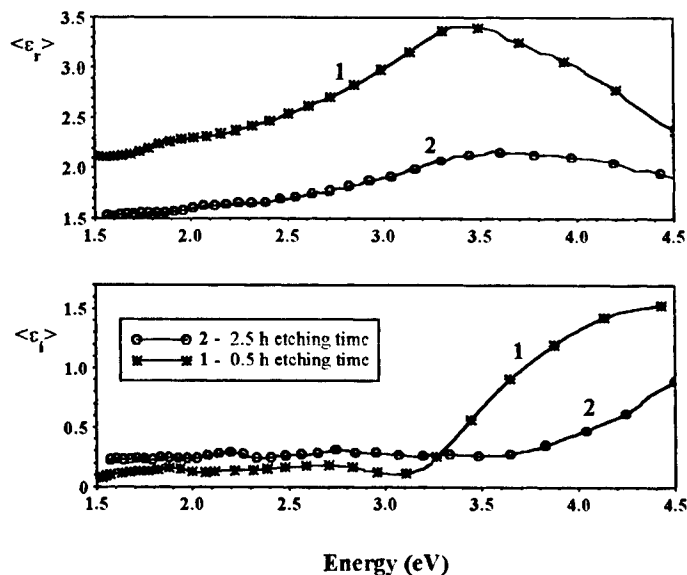


Fig.1 Spectral dependence of pseudodielectric function for different etching times
1 -- S_{90} sample
2 -- S_{150} sample

The aging effects in air of PS films produce the growing of an oxide layer (SiO_x) overall the internal surface that results in a change of the microscopic structure with depth. Fig.2 shows typically $\langle n \rangle$ and

$\langle k \rangle$ spectra for PS samples stored in air for different time periods: 7 weeks (sample 1), 12 weeks (sample 2) and 12 months (sample 3), respectively. A progressive decrease in $\langle n \rangle$ and $\langle k \rangle$ values as a result of the increasing duration of storage (under normal conditions) was obtained. The relative small decrease in $\langle n \rangle$ values, observed despite the large increase in the oxygen content after a long storage time can be explained by the pore filling due to the oxidation-induced expansion and by other species chemisorbed from the humid ambient air⁸.

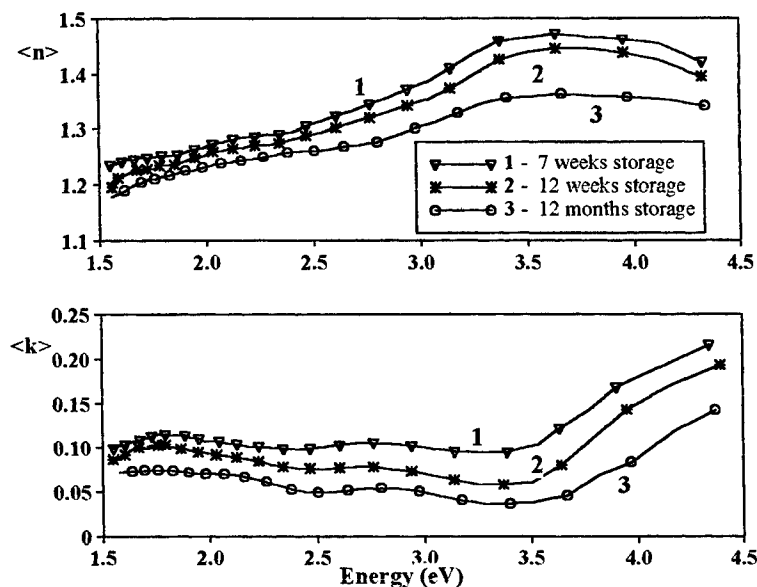


Fig. 2. $\langle n \rangle$ and $\langle k \rangle$ spectra of S_{90} PS film after storage in air
1 -- 7 weeks
2 -- 12 weeks
3 -- 12 months

In Fig. 3 it is illustrated the dispersion of the pseudodielectric constants for S_{30} PS film (as prepared and annealed at 200°C, 600°C and 800°C). Up to 200°C the oxidation or/and desorption from surface modifies the $\langle n \rangle$ curve in the same way as that obtained after storage. More drastically change on the pseudorefractive function was observed, when the thermal annealing is performed at temperatures higher

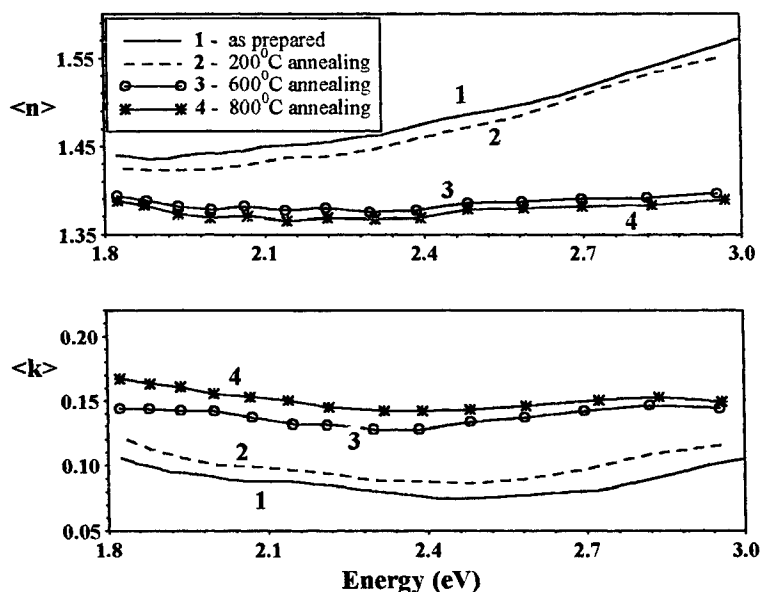


Fig. 3. $\langle n \rangle$ and $\langle k \rangle$ spectra of S_{30} PS film
1 - as prepared; annealed at
2 - 200°C, 3 - 600°C, 4 - 800°C

than 600°C (curves 1,2 compared with 3,4). The important decrease of $\langle n \rangle$ values and the change of the shape of $\langle n \rangle$ curve suggests that a higher oxidation process followed by a significant change in surface morphology takes place.

The curves of the energy dependence of $\langle k \rangle$ are parallel within the investigated range (1.8 - 3.0 eV). An increase of $\langle k \rangle$ values with the raise of annealing temperature was observed.

The differences in behaviour of the pseudodielectric function, related with the storage duration and the annealing temperature, may be explained as follows: during storage, the whole internal surface of the PS films is oxidized and a thin layer of SiO_x is formed. After thermal annealing above 600°C, a more pronounced oxidation process takes place and thus it can cause the isolation and decoupling of the nanocrystallites from the Si matrix by interrupting the Si wire.

3.2 Photoluminescence results

PL spectra taken at LNT and RT ($\lambda_{\text{excitation}}=337.1\text{nm}$) on S_{150} PS film (as prepared and annealed at 400°C and 800°C) are shown in Fig.4. The curve 1 provides typical behaviour of PS films prepared under experimental conditions described above⁵. It presents one maximum situated at 2.2 eV and two shoulders situated at approximately 1.75 eV and 1.5 eV, respectively. The first step of annealing (30 min at 400°C) produces an increasing with about one order of magnitude (curve 2) of the PL signal and a shift of the maximum to lower energies. As it can be seen in Fig. 4b, a new shoulder appears at about 2.75 eV. The second step of annealing (at 800°C) drastically increases the PL signal (curves 1 and 4 compared with 3 and 6, respectively) and maintains the positions of maxima and shoulders. This step of annealing also changes the relative intensities of maxima and shoulders, enhancing the blue emission band (2.75 eV).

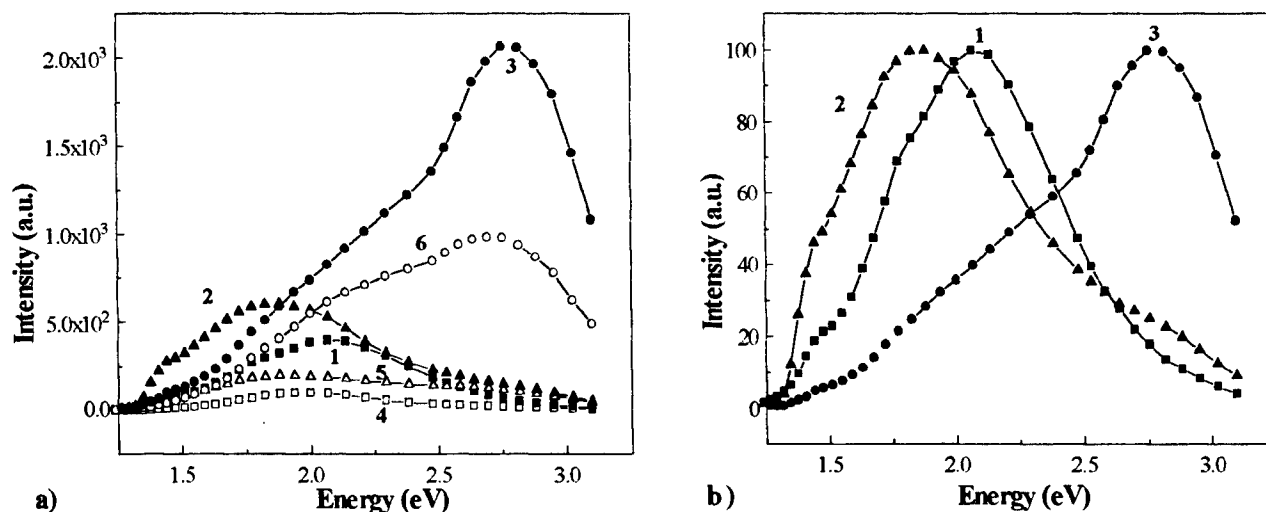


Fig.4. PL spectra of S_{150} PS films before and after thermal treatment as prepared (1,4); thermal annealing at 400°C (2,5); thermal annealing at 800°C (3,6) 1,2,3 - performed at LNT, 4,5,6 - performed at RT
a) unnormalized and b) normalized curves

The PL spectra for S_{30} PS film are presented in Fig.5. An enhancement with about 3 orders of magnitude of PL intensity can also be observed after annealing at 800°C. The new emission band in the blue spectrum range appeared after the thermal treatment has the same position as that for thick sample (S_{150}).

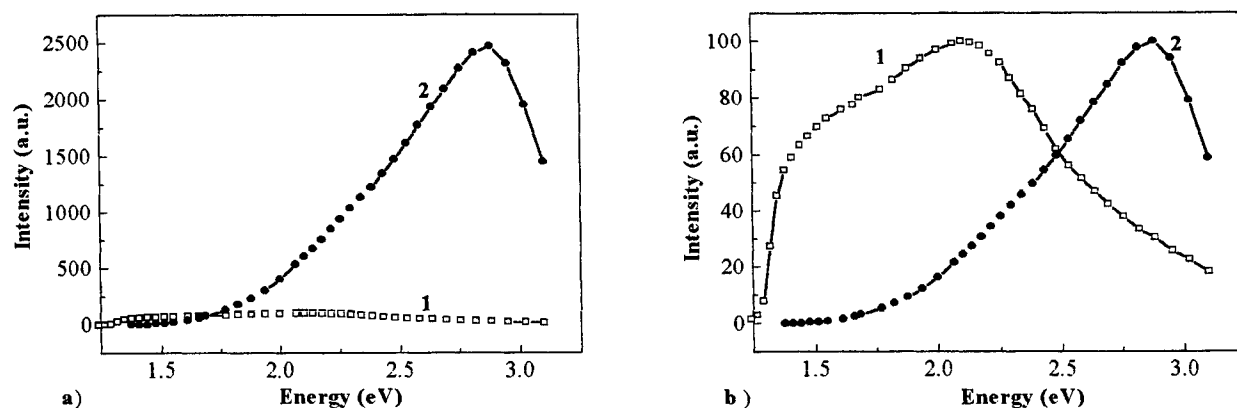


Fig. 5. PL spectra of S_{30} PS films taken at LNT: 1 - as prepared, 2 - annealed at 800°C
a) unnormalized and b) normalized curves

It is interesting to observe the following experiment, performed on very thin layers. Thus, the sample S_{10} , stored 12 months in air under normal conditions has PL spectrum (Fig.6) very similar to these illustrated in Figures 4 and 5, curves 2, for thicker samples. This fact shows that the storage in air for a long time, as well as the thermal annealing at temperatures, higher than 600°C has mainly the same effect: the formation of SiO_x layer on the whole internal surface of PS films. The difference is that oxidation by

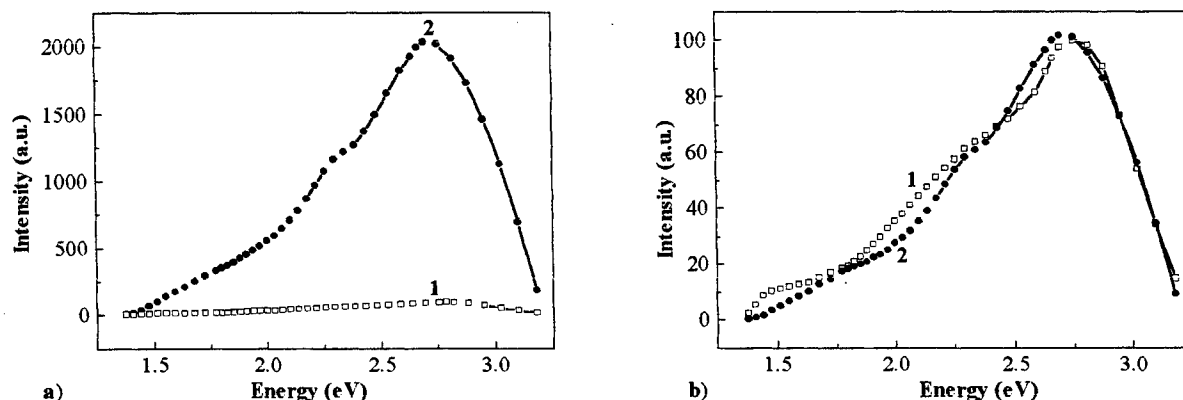


Fig. 6. PL spectra of S_{10} PS film taken at LNT: 1- stored 12 months in air, 2- annealed at 800°C
a) unnormalized and b) normalized curves

thermal annealing produces a more intense effect resulting in isolation of nanocrystallites from the Si skeleton. The formation of nanodots in SiO_x matrix reduces the electron-hole pair migration and thus it diminished the nonradiative recombination probability. This leads to an enhancement of the PL emission.

The influence of the thermal treatment at successive temperatures 400°C and 800°C for 15 min in air on the decay time of PL for S_{150} film is illustrated in Fig.7. It can be observed that before annealing, the slow component weight monotonically increases to the red edge of the emission spectrum up to the wavelength at which the maximum on PL emission was achieved (650 nm). After the annealing at 400°C , the slow component weight reaches also a maximum at wavelength corresponding to the shifted red maximum (Fig.4). The next step of annealing at 800°C for 15 min practically destroys the slow component. The PL decay is characterized on the whole emission spectrum by the fast component only, with the decay time of tens of ns.

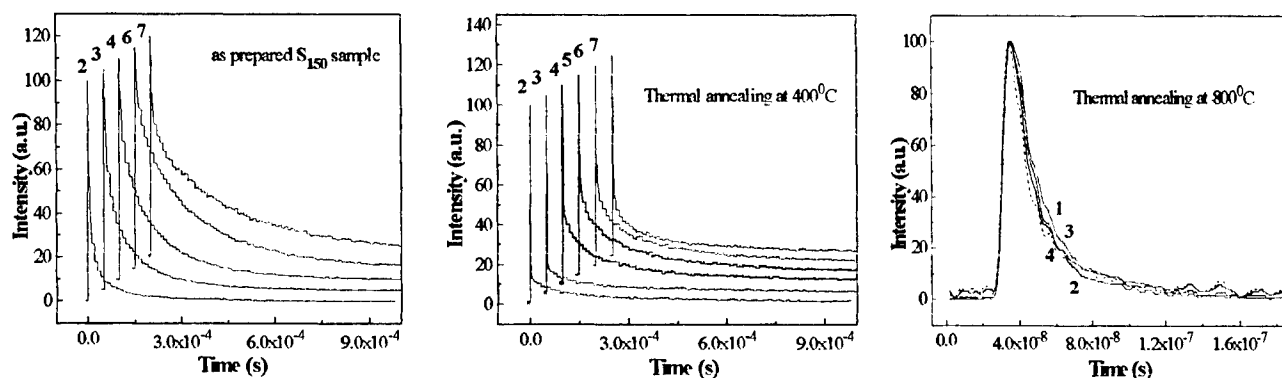


Fig. 7 Decay time at LNT for S_{150} sample at different emission wavelengths
1- 450 nm; 2- 550 nm; 3- 650 nm; 4- 700 nm; 5- 760 nm; 6- 800 nm; 7- 860 nm

In our opinion the slow PL component (10^{-4} - 10^{-6} s) is due to the surface contribution. In the above explanation, the SiO_x layer growth by annealing up to 600°C changes the surface configuration and/or passivation. The second step ($T > 800^\circ\text{C}$) induces the disappearance of the surface contribution and thus the radiative recombination process inside the isolated nanodots takes place.

4. CONCLUSIONS

The annealing of PS samples at low temperatures induces mainly changes in the passivation of PS layer, while the high temperatures annealing produce a SiO_x layer on the internal surface of PS films, leading to the isolation of nanocrystallites in Si skeleton. This oxidation process causes the disappearance of the PL slow component, an important enhancement of PL and a shift of maximum position to higher energies, corresponding to the thinning of the Si skeleton.

The storage in air also produces an oxide layer on the internal PS surface, causing the decreasing of the optical constants and a less PL enhancement compared with that due to the high temperature annealing.

5. REFERENCES

1. T. Canham, "Silicon quantum wire array fabrication by electrochemical and chemical dissolution of wafers", *Appl. Phys. Lett.* **57**(10), 1046-1048 (1990)
2. Hideki Tamura, Markus Ruckschloss, Thomas Wirschem, and Stan Veprek, "Origin of green/blue luminescence from nanocrystalline silicon", *Appl. Phys. Lett.* **65** (12), 1537-1539 (1994).
3. D. R. Tallant, M. J. Kelly, T. R. Guilinger, and R. L. Simpson, "Porous silicon photoluminescence: Implications from in situ studies", *J. Appl. Phys.* **80**(12), 7009-7017 (1996).
4. K.-H. Li, C. Tsai, J. C. Campbell, B. K. Hance, and J. M. White, "Investigation of rapid-thermal oxidized porous silicon", *Appl. Phys. Lett.* **62** (26), 3501-3503 (1993).
5. M. L. Ciurea, E. Pentia, A. Manea, A. Belu-Marian, and I. Baltog, "Visible Photoluminescence in porous silicon prepared in different conditions", *Phys. Stat. Sol. (b)* **195**, 637-645 (1996)
6. U. Rossow, U. Frotscher, M. Thonissen, M. G. Berger, S. Frohnhoff, H. Munder, W. Richter, "Influence of the formation conditions on the microstructure of porous silicon layers studied by spectroscopic ellipsometry", *Thin Solid Films* **255**, 5-8 (1995).
7. M. Thonissen, S. Billat, M. Kruger, H. Luth, M. G. Berger, U. Frotscher, and U. Rossow, "Depth inhomogeneity of porous silicon layers", *J. Appl. Phys.* **80**(5), 2990-2993 (1996).
8. L.T. Canham, M. R. Houlton, W. Y. Leong, C. Pickering, and J. M. Keen, "Atmospheric impregnation of porous silicon at room temperature", *J. Appl. Phys.* **70**(1), 422-431 (1991)

Optical devices with silica-gel small spheres

A. M. Preda, E. Scarlat, Liliana Preda and I. M. Popescu

“Politehnica” University, Department of Physics,
313 Spl. Independentei, 077206, Bucharest 5, Romania
E-mail: lili@physics2.physics.pub.ro.

ABSTRACT

Some inexpensive optical devices using small silica-gel spheres are presented. The silica-gel spheres of good quality are investigated under the microscope. These sphere presents some particularities which make them very useful in applications like interferometry, hygrometry and optical microscopy. Such small spheres may be doped with microcrystals or dye solution in order to study a large range of nonlinear phenomena. Experimental studies have been performed on the silica spheres as alternative media for laser action using a pulsed CuBr laser as excitation source.

Keywords: silica sphere, interferometry, hygrometry, optical microscopy, random active laser media.

1. INTRODUCTION

Recently, there has been a great deal of interest in investigation the optical properties of dielectric spheres. Latest papers have reported lasing phenomena and/or stimulated Raman scattering using the very high quality factor (Q value) of the electromagnetic whispering-gallery mode (WGM) provided for these small spheres¹. Investigations on the liquid droplets, dye-doped solid polystyrene spheres, as well as on the Nd-doped glass small spheres were also performed^{2,3}. In this paper we report several spherical silica-gel optical devices.

2. PREPARATION OF THE SILICA SPHERES

“Silica” is used as a short convenient designation for silicon dioxide in all its crystalline, amorphous, and hydrated or hydroxylated forms. The term “polymerization” means a linking together of monomer units to form a polymer of same composition, but in silica system the monomer, $\text{Si}(\text{OH})_4$, condenses to form polymer that ultimately has the composition $(\text{SiO}_2)_n$.

Formation and growth of spherical particles is one kind of polymerization that takes place under certain conditions. In most densely packed gels, each sphere is touched by 12 surrounding spheres, and the volume fraction of spheres, S , is 0.745. In a more open regular network, each sphere is connected to three others and S is only 0.05. Formation of silica spheres occurs by coacervation. The term “coacervation” means the formation of a “liquid precipitate” by the coagulation of colloids. If one of the components in a silica-organic coacervate is undergoing polymerization just as the liquid coacervate droplets come out of the aqueous phase, the droplets solidify into small spheres. Under special conditions, when the organic material is burnt out, very uniform porous spheres are obtained.⁴ Spherical particles can be made from silicon esters. The polyethoxysiloxane is an oil which forms an emulsion in more water-alcohol and solidifies to gel beads of 0.2-0.5 mm in diameter with a pore diameter of 2 nm.

New types of gels like silica gel is formed in a liquid medium, usually aqueous. The terms alcogel and xerogel are gels in which the pores are filled with the corresponding liquid, that is alcohol or water. A xerogel is a gel from which the liquid medium has been removed, the structure being compressed and

the porosity reduced to a certain value by surface tension forces when the liquid is removed. An aerogel is a special type of xerogel from which the liquid has been removed in such a way as to prevent any collapse or change in the structure when the liquid is removed.

Owing to their high hygroscopicity, the silica-gel small spheres are packed under pharmaceutical control to avoid water absorption. Then, using a standard optical microscope, these spheres were fixed on the head of a needle. Some silica-gel small spheres were impregnated with water solutions of rhodamine 6G, fluorescein or microcrystals as CdS, CuCl and CuBr.

3. INTERFEROMETER WITH SILICA-GEL SMALL SPHERE

In order to obtain two coherent waves it is necessary to divide the beam of incident rays in two different ways, and then recombine them to observe the interference. In the interferometer described, the beams are separated by a small sphere with good transmission factor, as can be seen from figure 1.

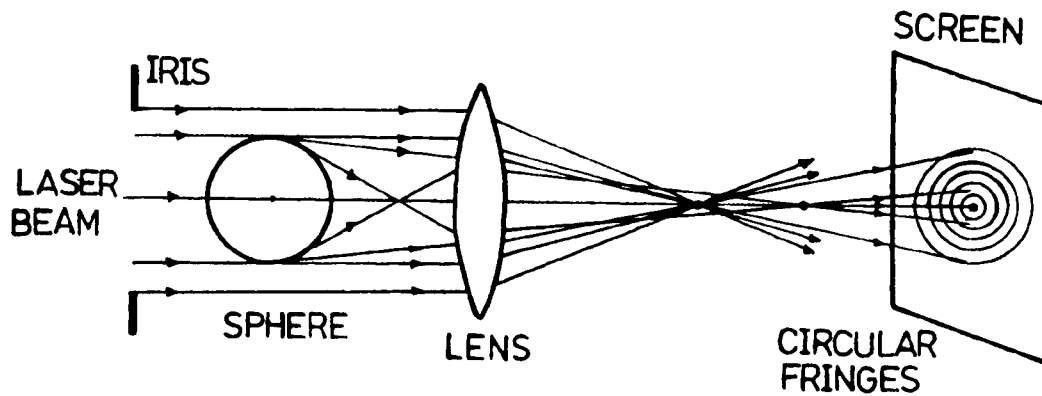


Fig.1: Experimental setup of interferometer using a small sphere

Such kind of interferometer have been reported by⁵. In that case laser beam intercepts an opaque sphere, and light diffracted by the surface of sphere will interfere with the direct laser light passing near the sphere. In our case, the phenomenon is illustrated in figure 1. The circular fringes on the screen results from the diffracted light from the neighborhood of the spherical surface and the transmitted light through the transparent sphere, with a diameter of 1 mm.

The edge of the sphere and the edge of the iris act as the annular aperture. Suppose that the annular aperture is bounded by two concentric circles of radii a and ϵa , where a is the radius of the sphere and ϵ is some positive number less than unity. The light distribution in the Fraunhofer pattern is given by⁶:

$$U = C\pi a^2 \left[\frac{2J_1(kaw)}{kaw} \right] - C\pi \epsilon^2 a^2 \left[\frac{2J_1(k\epsilon aw)}{k\epsilon aw} \right] \quad (1)$$

C being a constant so that $I_0 = |C|^2 \pi^2 a^2 (1 - \epsilon^2)^2$ is the intensity at the center $w=0$ of the pattern, where w represents the sine of the angle θ which the current direction (p, q) makes with the central direction $p=q=0$, $w=(p^2+q^2)^{1/2}$ and $|U|^2$. $J_1(x)$ is the Bessel functions defined by

$$J_1(x) = \frac{i^{-1}}{2\pi} \int_0^{2\pi} e^{ix \cos \alpha} e^{i\alpha} d\alpha \quad (2)$$

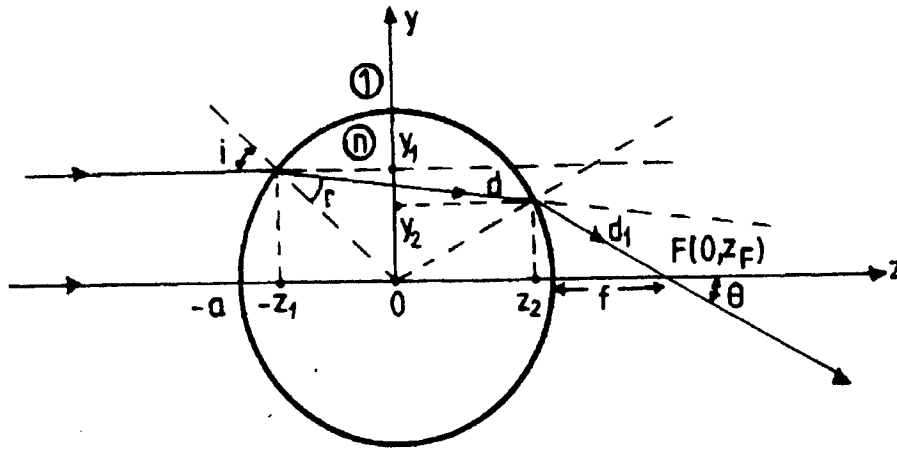


Fig. 2: Optical paths of the rays

Consider a plane wave incident on a spherical surface of the silica medium with the complex amplitude at $z=-a$ (see Fig.2) given by

$$U_i = A_i e^{ika} \quad (3)$$

where $k=2\pi/\lambda$. If y_1 is the height above the axis oz at which a ray meets the first surface of the sphere, then the transmitted wave at z_F may be represented by

$$U_e(\theta, a, n) = A(\theta, n) e^{-ik(2an+f-\delta)} \quad (4)$$

where $A(\theta, n) = A_i(1-R)(1-R') e^{-\alpha d}$, R and R' are reflection coefficients at the air-sphere interfaces, α is the absorption coefficient and d is the distance between the points $(y_1, -z_1)$ and (y_2, z_2) (see Fig.2).

The optical path δ is given by

$$\delta = a \left[2(1-n) + 2 \left(n^2 + 1 - 2n \cos \frac{\theta}{2} \right)^{\frac{1}{2}} - \frac{n \sin \frac{\theta}{2} \tan \frac{\theta}{2}}{\left(n^2 + 1 - 2n \cos \frac{\theta}{2} \right)^{\frac{1}{2}}} \right] \quad (5)$$

and the focal length

$$f = z_F - a = \frac{na}{2 \cos \frac{\theta}{2} \sqrt{n^2 + 1 - 2n \cos \frac{\theta}{2}}} - a \quad (6)$$

In (4), (5) and (6) δ and f may be regarded as a function of a , n and θ , and one can easily derive expressions for the phase change $\phi=k(2an+f-\delta)$, and for the intensity $I_e(\theta) = |U_e(\theta, a, n)|^2$ in the current direction.

According to (1) and (4), the resultant intensity distributions of the interference pattern is

$$I = |U + U_e|^2 \quad (7)$$

i.e. the intensity variations are circles with the bright and dark fringes. The radii of the fringes may be regarded as a function of θ , n and a . The principle of this interferometer is similar to the Linnik interferometer. In addition to its simplicity, the advantage of this interferometer is its low sensitivity to vibrations so that the interference pattern can be photographed without taking special precautions.

4. DEVELOPMENT OF HUMIDITY SENSORS BASED ON POROUS SILICA SPHERE

Conventional humidity sensors are typically based on the electrical properties of the sensing materials. These can be divided in two categories, the resistive and capacitive types. The electrical conductivity or impedance of the sensing material is enhanced by adsorption of surrounding water vapor. In recent years, there has been great interest in the development of humidity sensors based on porous optical fibers⁷. Optic fiber sensors can be also divided in two categories, the dew point hygrometer and humidity sensors based on porous optical fibers. For the former, the dew detecting unit is a fiberglass reflectometer. For the latter, the porous sensing section of the glass fiber is immersed into an aqueous solution of chromophoric material. The absorption or fluorescence changes depend on the hydrated and dehydrated states of material⁷.

In this work, we report a new moisture sensor based on the difference of the optical transmittance between the hydrated and dehydrated states of porous silica sphere.

As a dew point hygrometer model can be utilized the interferometer shown in figure 2. In the experimental set-up the porous sphere was seated in a testing chamber. During running, the air to be tested flows around the sphere cooled from a freon container. The sphere temperature is thus always the dew point temperature. At this point the transmittance of the sphere will change quickly when the concentration of water molecule into sphere will increase.

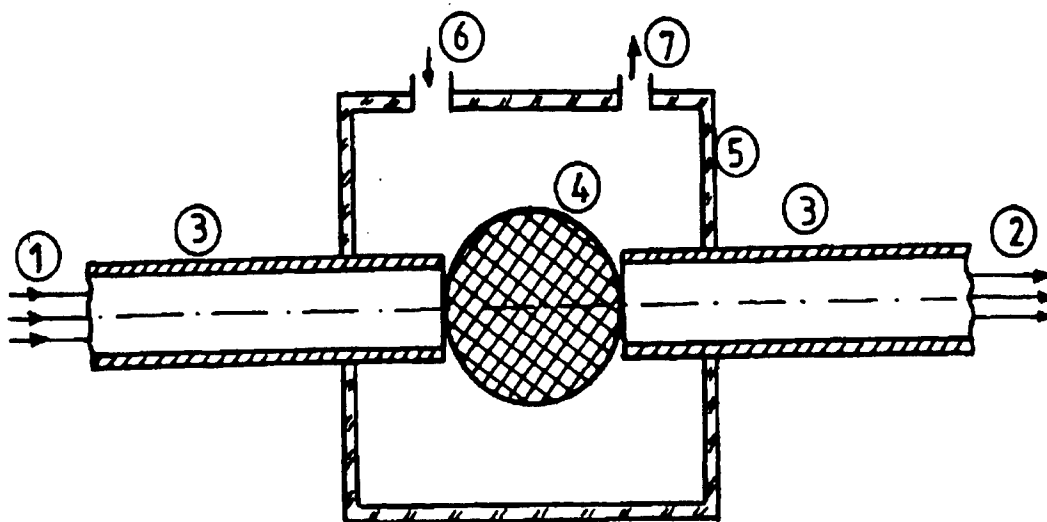


Fig. 3 Configuration of a porous silica sphere hygrometer. 1- light in; 2-light out; 3- optical fibers; 4- porous silica; 5- test chamber; 6- water-vapor entrance; 7- vapor exit

Water absorption will cause the change of the refractive index of the silica-gel small sphere and consequently this leads to modifications of fringe pattern. Using a microscope with a micrometric ocular one can examine the position of the dark fringes and plot the refractive index dependence of the water absorption rate.

In figure 3 is shown another configuration of a porous silica sphere optical sensor. The porous silica sphere can be impregnated with cobalt salts which react with gaseous water molecules permeating into the porous sphere to form hydrated complexes. The response of the porous sensors is affected by the pore size, concentrations of hydrated material and moisture, temperature and the flow rate of introduced air. A response time of 1-2 min. was observed. This configuration of a porous silica sphere sensor is operating in high temperature environments.

5. MICROSCOPE MICRO-OBJECTIVE

In recent work⁸ has been developed a micro-objective manipulated with optical tweezers. This micro-objective has made from a polystyrene sphere with a diameter of 0.25 μm . The silica small sphere covered with a monomolecular layer of polyvinyl alcohol are highly transparent in the visible spectrum region.

The angular magnification M of a sphere of radius a and refractive index n is

$$M = \frac{2l}{a} \left(1 - \frac{1}{n} \right) \quad (8)$$

where l is the nearest point of distinct vision. For $l=25$ cm., $a=1$ mm. and $n=1.5$, from eq. (8) we obtain $M \approx 167$.

The resolution of any optical system can be discussed in terms of its numerical aperture, $\sin \alpha$. Following the principle used by Rayleigh for a circular aperture, the transverse resolution is given by

$$\delta_t = \frac{0.61 \cdot \lambda}{\sin \alpha} \approx \frac{0.61 \cdot \lambda f}{a} \quad (9)$$

If we consider the focal spot produced at a distance f from the sphere with a radius $a \approx f$, at $\lambda=0.65 \mu\text{m}$, $\delta_t \approx 0.4 \mu\text{m}$. By combining a silica small sphere, a standard microscope and a laser diode source one obtains a modern research microscope⁸.

6. SILICA POROUS SPHERE AS ALTERNATIVE SOURCE OF COHERENT LIGHT

Recently, much attention has been paid to the study of optical properties of nanometer-sized particles dispersed in glass and polymer matrices from the viewpoint of scientific interest and their applications to nonlinear optical devices^{9,10}. Most commonly considered materials are made of nonlinear particles embedded in a linear host. The nonlinearities of such materials may be strongly enhanced relative to bulk samples of the same materials.

Despite the high porosity, silica gel, if it is properly made, is highly transparent in the visible spectrum region. At $\lambda=630$ nm the specific extinction coefficient is of the order of 0.1 m^2/kg . Toward the blue and ultraviolet strong Rayleigh scattering is observed which is expected for a material with pore structures in the 1 to 100 nm size range.

In this paper, we present the silica porous spheres as alternative media for laser action. We have employed the rhodamine 6G, rhodamine B and fluorescein dyes in water solvent with the concentration in the range 10^{-5} to 10^{-3} M. In these dye solutions we have introduced the silica porous spheres during 24 hours. An hour later the impregnated spheres has fixed on the tip of a needle and has pumped with a pulsed CuBr laser. The pumping CuBr laser beam, which has approximately 25 ns full width at half maximum, $\lambda=510.6$ nm, 2 kW peak-power output and 10 kHz repetition rate, is focused on the impregnated sphere by a spherical quartz lens after beam-shaping through a circular aperture.

We have measured the fluorescence intensity at the peak wavelength ($\lambda=620$ nm) from these spheres in the direction perpendicular to the excitation beam with a system consisting of a monochromator, a phototube and a storage oscilloscope.

Figure 4 represents the fluorescence intensity at peak wavelength (for rhodamine 6G) as a function of the pump intensity on a logarithmic scale. We see that there is a threshold at the position at which the slope of the curve has a sharp change (the arrow indicates the position of the threshold). The laser oscillation takes place in the whispering gallery modes of sphere.

The silica porous spheres doped with dye make up a random active laser media. The behavior of an amplifying random medium is expected to be totally different from that of a passive one^{11,12}.

To explain the microscopic mechanism of the laser activity, as well as the coherence properties of light emission, we assume that the main characteristics of this medium are a result of the following processes: 1) the multiple scattering; 2) the packing arrangement in regular network of the silica microspheres, each of them being characterized by a certain coordination number; 3) the local electric field can be increased above its ambient or average value in the vicinity of the dye inclusions which are embedded in silica medium; 4) the dye active medium from silica pores might have some properties of the quantum wells; 5) strong feedback effects arising from radiation of the WGM of silica microspheres.

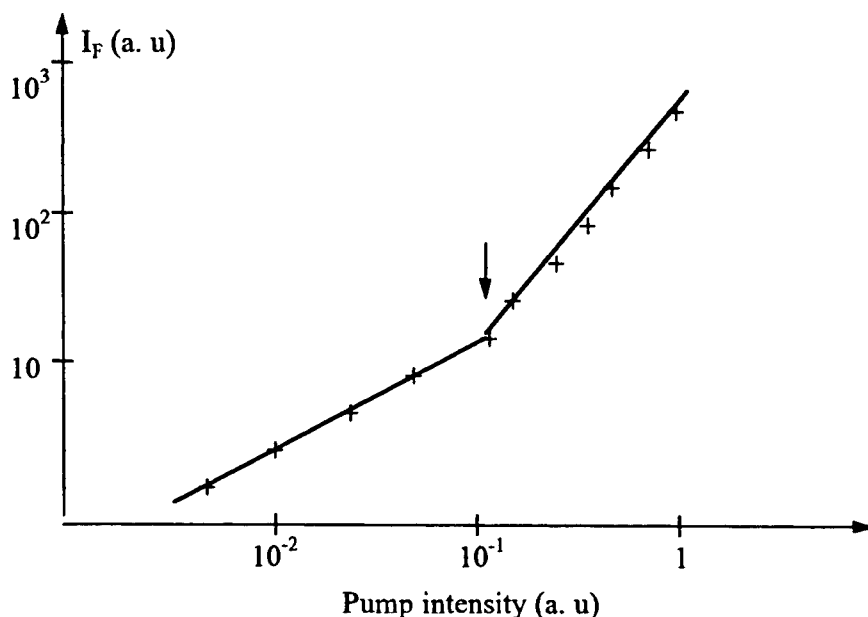


Fig.4 Fluorescence intensity at $\lambda=620$ nm vs. pump intensity

7. CONCLUSIONS

We have shown some optical applications of the silica porous spheres. These spheres present some characteristics which make them very useful in interferometry, optical hygrometry and microscopy.

We have demonstrated that these spheres doped with dye solution have good WGM lasing qualities with an adequate CuBr laser pump. The silica spheres doped with microcrystals may be useful for nonlinear phenomena experiments.

8. REFERENCES

1. V. Sandoghdar, F. Treussat, J. Hara, V. Lefevre, A. Seguin, J. M. Raimond, and S. Haroche, "Very low threshold whispering-gallery mode microsphere laser", *Phys. Rev.*, **54 A**, pp. R1777-R1779, 1996.
2. H. Taniguchi, H. Tomisava, "Simple arrangement for liquid-droplet experiments due to morphology dependent resonance", *Rev. Sci. Instrum.* **64**, pp. 3594-3598, 1993.
3. A. M. Preda, C. P. Cristescu, I. M. Popescu, A. G. Toma, "The fluorescence of liquid microspheres induced by laser irradiation", *Appl. Surface Sci.* **106**, pp. 517-522, 1996.
4. R. K. Iler, "The chemistry of silica", chap. 3, John Wiley & Sons, New York, 1981.

5. H. H. Chuaqui and E. S. Wyndham, "An example of the use of point diffraction interferometry", *J. Phys. E, Sci. Instrum.* **17**, pp.268-272, 1984.
6. M. Born, E. Wolf, "*Principles of optics*", pp. 416-424, Pergamon Press, Oxford, 1970.
7. J.Y. Ding, M. R. Shahriari, G. H. Sigel Jr., "Development of high temperature humidity sensors based on porous optical fibers", *Internat. Journ. of Optoelect.*, **6** (4), pp. 385-393, 1991.
8. M. Sasaki, T. Kurosawa and K. Hane, "Micro-objective manipulated with optical tweezers", *Appl. Phy. Lett.* **70**, pp. 785-786, 1997.
9. C. W. Bates Jr., "Factors affecting the optical properties of metal-semiconductor composites", *J. Appl. Phys.*, **81** (3), pp. 1457-1481, 1997.
10. Y. Hosoya, T. Suga, T. Yanagawa, Y. Kurokawa, "Linear and nonlinear properties of sol-gel - derived Au nanometer-particle-doped alumina", *J. Appl. Phys.*, **81** (3), pp. 1475-1479, 1997.
11. S. John G. Pang, "Theory of lasing in a multiple-scattering medium", *Phys. Rev.*, **54 A**, pp. 3642-3652, 1996.
12. D. S. Wiersma, A. Lagendijk, "Light diffusion with gain and random lasers" *Phys. Rev.*, **54 E**, pp. 4256-4265, 1996.

Growth of polycrystalline hydroxyapatite thin films by pulsed laser deposition
and subsequent heat-treatment in air

V. D. Nelea, C. Ghica*, C. Martin, A. Hening, I. N. Mihailescu,
Leona C. Nistor*, V. S. Teodorescu*, Rodica Alexandrescu,
J. Werckmann**, Eniko Gyorgy, G. Marin

National Institute for Lasers, Plasma and Radiation Physics,
Department of Lasers

Bucharest, Magurele, Romania, MG-36, 76900

*National Institute of Materials Physics

Bucharest, Magurele, Romania, MG-6, 76900

**Institute of Physics and Chemistry of Materials, Strasbourg, France

ABSTRACT

Hydroxyapatite (HA), $\text{Ca}_{10}(\text{PO}_4)_6(\text{OH})_2$, is the primary constituent of the human bone and one of the best biocompatible materials. In this work we developed a simple method for the deposition of polycrystalline HA thin films onto various collectors including substrates of medical interest (e.g. Ti). We proceeded by the pulsed laser deposition of HA targets onto parallel collectors placed at (2-5) cm in vacuum. After deposition the films were heated in air at 500 °C for 30 minutes. The heated film has a structure which appears in electron diffraction as identical to the structure of the base material. The obtained films are uniform and very adherent to the substrate. The P/Ca atomic ratio, determined by energy dispersive X-ray analysis, was found to be close to that characteristic to HA, for the post-depositing heated films.

Keywords: pulsed laser deposition, biocompatible materials, hydroxyapatite thin films

1. INTRODUCTION

The pulsed laser deposition (PLD) method is a fast-developing technique for the growth of performant thin films.^{1,2} PLD is based upon the physical processes taking place during and immediately after the multipulse irradiation of an appropriate target with a high-intensity laser beam. The ablated substance flux is frequently modified by the presence of an ambient gas and plasma. Large progress was obtained in the last few years in the development of PLD by a careful parametric study of the key process parameters such as the substrate temperature, the plasma flux density, the ionisation degree and/or the geometrical arrangement in the deposition chamber.²⁻⁶ PLD ensures the stoichiometric transfer of any chemical compound from target to collector.

Hydroxyapatite (HA), $\text{Ca}_{10}(\text{PO}_4)_6(\text{OH})_2$, is the primary constituent of the human bone and one of the best biocompatible materials. It was demonstrated that HA encourages the ingrowth of natural bone inside the prosthetic devices.¹ We note however that HA is brittle and cannot be used as bulk-ceramic for the prostheses manufacturing. As a coating on a metallic implant (e.g. Ti or Ti alloys), HA takes over the mechanical integrity of the metallic device and ensures in the same time a high biocompatibility due to the natural mineral bone composition. The coating prevents the ingress into living tissue of extraneous substances which may induce inflammation and other immune reactions.

Many techniques for HA deposition on substrates of biomedical interest have been already reported in literature. We mention here: ion sputtering⁷, plasma spraying⁸, electrophoretic deposition⁹, diffusion bonding¹⁰ and high velocity oxyfuel deposition¹¹. There are still many difficulties related to the impurities present in the depositions obtained by these techniques and especially to their adherence to the substrates. PLD presents the following potential advantages in comparison with the afore-mentioned techniques: the photodeposited films are expected to exhibit good stoichiometry, very low content of impurities and to be strongly adherent to the substrate.

We report herewith the extension of PLD to the deposition of HA thin films on various substrates. After the deposition, the films were submitted to a heat-treatment in air in order to promote recrystallization.

2. EXPERIMENTAL

Our experimental setup is schematically depicted in Fig. 1.

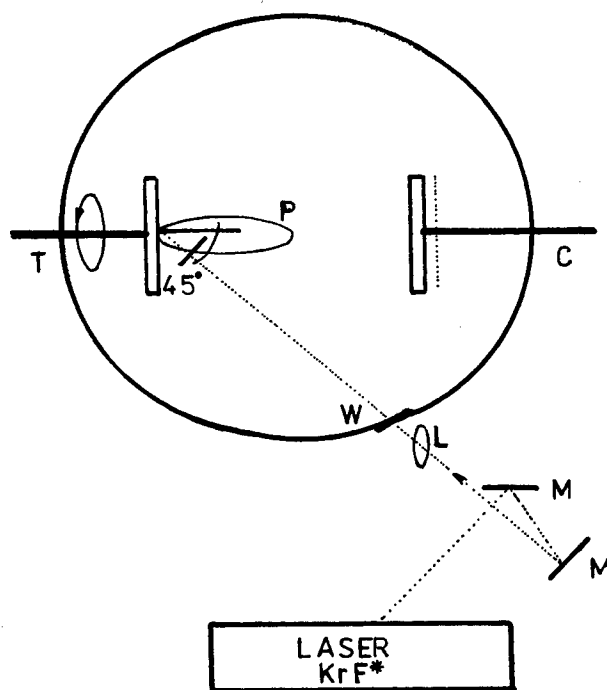


Fig. 1 Experimental setup

(T = target, C = collector, P = plasma plume, W = quartz window, L = focusing lens, M = mirrors)

We used a KrF excimer laser source ($\lambda = 248 \text{ nm}$, $\tau_{\text{FWHM}} \geq 20 \text{ ns}$). The laser beam was incident onto the surface of a HA target at an incidence angle of $\cong 45^\circ$. The laser radiation was focused with the aid of an external MgF_2 cylindrical lens. The targets were prepared by hot-pressing of high-purity polycrystalline HA powder in form of pellets of (15-25) mm diameter and (2-3) mm thickness. Series of

10^4 subsequent laser pulses were applied for the deposition of a single film. A plasma spark was generated and evolved in front of the target surface under the action of every laser pulse. In order to avoid piercing, the target was rotated during the multipulse laser treatment.

The plasma was oriented normally to the target surface. The plasma intersected a collector of KCl, KBr or Ti placed parallel to the target at a separation distance of (2-5) cm. Prior to the deposition, the Ti collectors were carefully cleaned with solvents in an ultrasonic bath. The KCl and KBr plates were freshly cleaved just before the introduction into the irradiation chamber. We set the level of the incident laser fluency within the range (1-2) J/cm².

The collectors could be heated at controlled temperatures up to 600° C. The stainless steel irradiation chamber was evacuated at 10^{-3} Pa. After deposition the samples were firstly allowed to cool to the ambient temperature in vacuum. Then, the irradiation chamber was slowly filled with air up to the atmospheric pressure. Some of the as deposited collectors were heated in air at 500 °C for 30 minutes.

The deposited films were studied by electron microscopy with the aid of a JEOL TEM-SCAN 200 CX apparatus. The films were investigated by scanning electron microscopy (SEM), transmission electron microscopy (TEM) and selected area electron diffraction (SAED). The IR spectrophotometry investigation of the thin films, within the (4000-500) cm⁻¹ spectral range, was performed with an IR SPECORD Karl Zeiss Jena instrument. For a compositional characterisation, energy dispersive X-ray spectroscopy (EDS) analysis was performed with a Topcon 2000 electron microscope operating at 200 kV and using an 8.8 nm electron probe.

3. RESULTS

3.1. Electron microscopy studies

Figure 2 shows a TEM micrograph (a) and a typical diffraction pattern (b) obtained in the case of HA base powder.

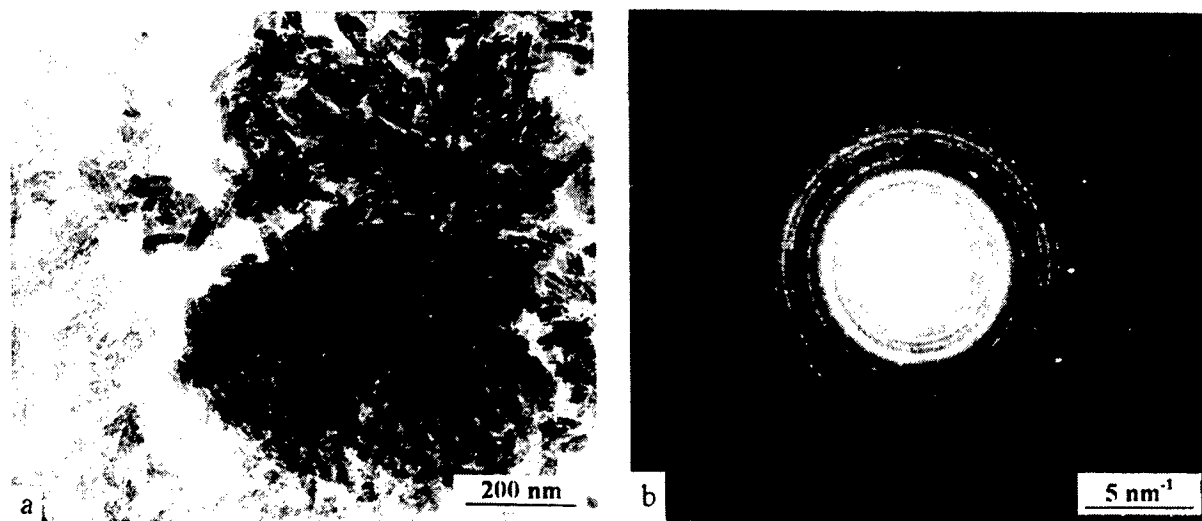


Fig. 2 The characteristic features of the HA powder precursor
(a) TEM micrograph (b) SAED pattern

We notice a hexagonal polycrystalline structure with cell parameters $a = 9.4 \text{ \AA}$ and $c = 6.9 \text{ \AA}$. The powder consists of small crystalline grains of about 60 nm long and 20 nm wide.

In view of further simpler TEM preparation, some of the films were deposited onto freshly cleaved single crystalline KCl slides. The deposited films were then simply floated on the microscope grids by submersion in distilled water.

The TEM micrograph and the corresponding SAED pattern of a film deposited in vacuum (10^{-3} Pa) at room temperature on KCl substrate are presented in Fig. 3. The film is amorphous and its surface is covered by small particles which are the most probably ejected in liquid phase from the laser action zone on the target surface under the recoil pressure of the vapours and plasma. The particles density usually reaches $5 \times 10^9 \text{ cm}^{-2}$.

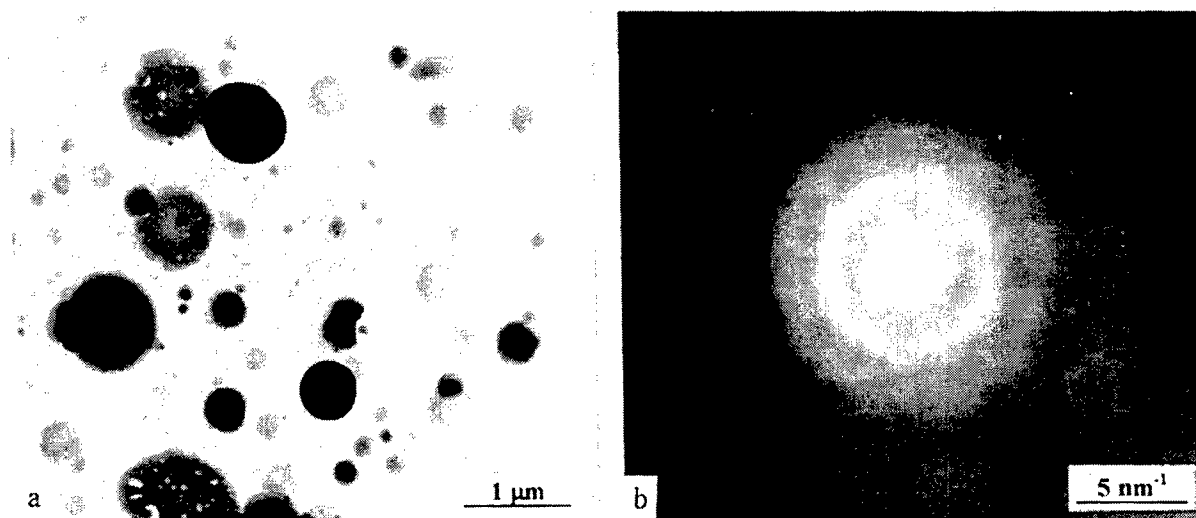


Fig. 3 The characteristic features of the film deposited in vacuum at room temperature
(a) TEM micrograph (b) SAED pattern

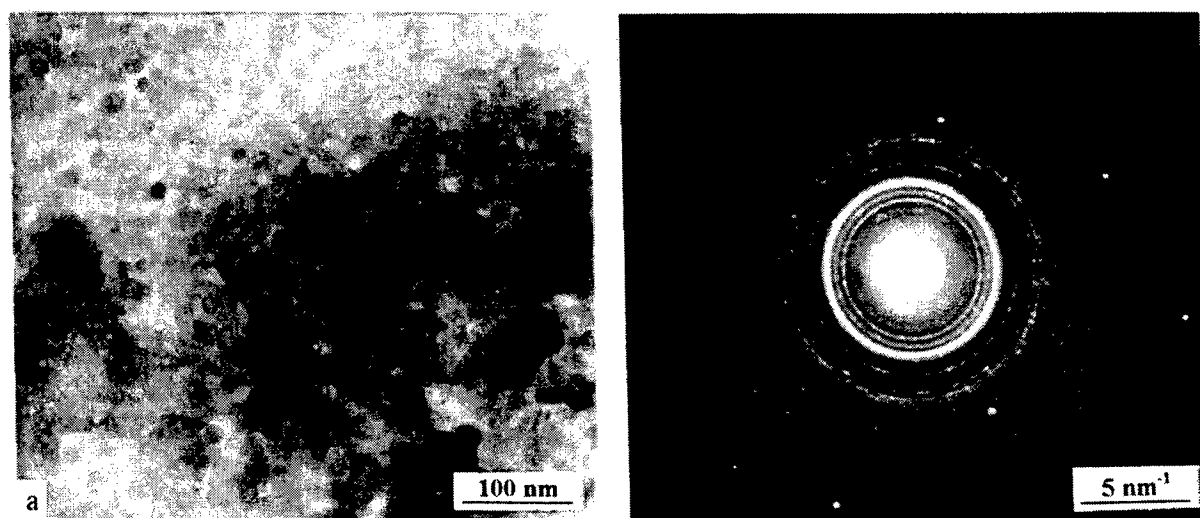


Fig. 4 The film deposited in vacuum and submitted to a heat-treatment in air at 500 °C for 30 minutes
(a) TEM micrograph (b) SAED pattern

The complete recrystallization of the films is obtained as an effect of a heat-treatment in air at 500 °C for 30 minutes. The films become polycrystalline with grains mean size of 20 nm (Fig. 4 a). As visible in Fig. 4 b, the corresponding diffraction pattern is identical to the diffraction pattern of the HA base material (Fig. 2).

3.2. IR spectrophotometry investigations

A typical IR transmission spectrum in the (400-1400) cm^{-1} range of the HA thin film deposited at room temperature in vacuum (10^{-3} Pa) on a KBr substrate is shown in Fig. 5, curve b. For comparison,

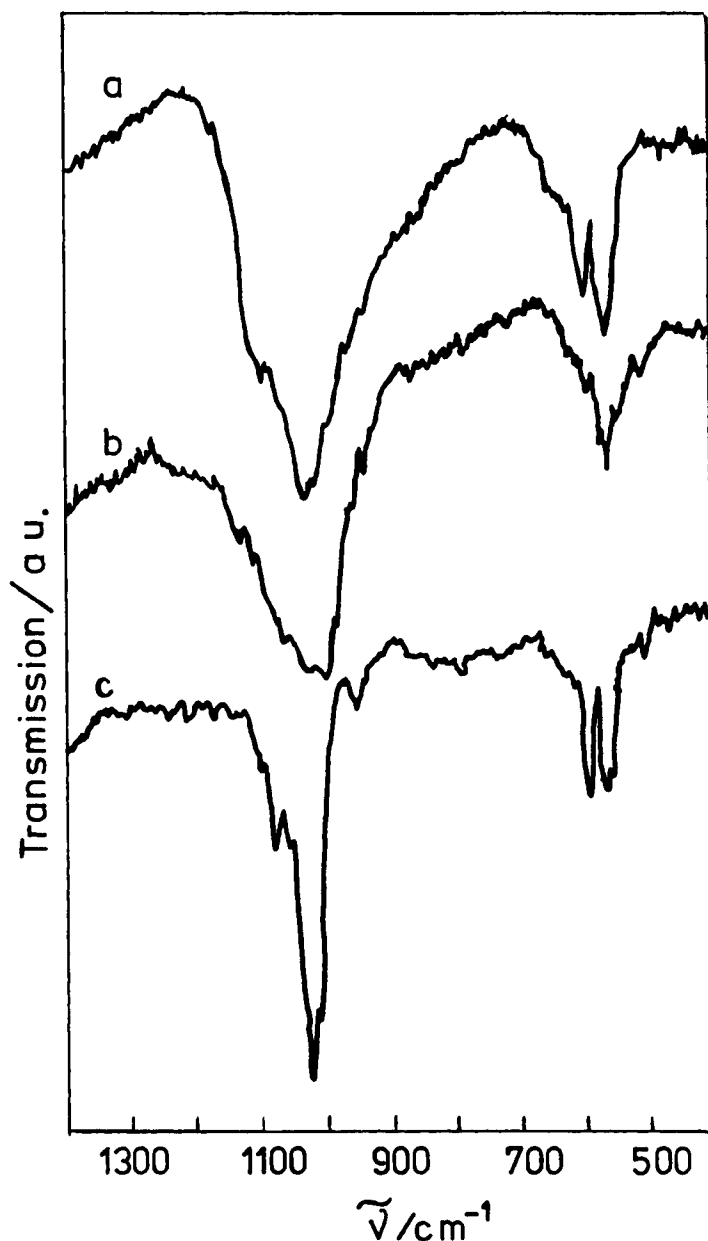


Fig. 5 IR transmission spectra for the HA film deposited in vacuum at room temperature (a), the base powder precursor (b) and the film deposited in vacuum and heat-treated in air (c), respectively

the IR spectrum of the HA base powder precursor, pressed in a KBr pellet is also presented in Fig. 5 (curve a). The curve c in the same figure is the spectrum of the HA film submitted to a heat-treatment in air after deposition. The main absorption band of HA is visible in the (1200-900) cm^{-1} spectral range¹³. It is ascribed to the P-O bonds of the ortophosphoric (PO_4)³⁻ groups¹⁴. The characteristic absorption peaks due to the P-O bonds should appear at 1080, 1010, 600 and 560 cm^{-1} . We note however important differences between the three spectra presented in Fig. 5 concerning the location and the band-width of the main absorption maxima. The as-deposited film shows a broad peak between 1025 and 1000 cm^{-1} (curve b). For the same sample the maxima at 1080 and 600 cm^{-1} are missing. The peaks resolutions and intensities notably increase for the thermally treated film (curve c). Specifically, the main peak is shifted towards higher wavenumbers (at $\approx 1035 \text{ cm}^{-1}$) as compared to the as-deposited films and to the HA target powder. For the thermally treated sample the half width value of the above mentioned peak is about one third of that of the same peak in the IR spectrum of the untreated film (compare curve b and c). This line narrowing may be directly related to a strong increase of the crystallinity of the sample. This assumption is sustained by the sharp peaks at 1080 and 600 cm^{-1} , which are also present in the HA powder precursor. However, the shift of the main band of the thermally treated sample should be explained by the manner in which the vibrational frequencies of the functional groups are affected by the presence of other substitute groups or compounds¹⁵. Indeed, the position of a band is dependent on the electronegativity of the attached group, which tends to move the frequency towards more stable stoichiometric forms. We may suppose that, during heating in air, a substantial oxygen absorption occurs, which causes an increase of the O_2 bonds in the sample lattice. The increased electronegativity of these groups, simultaneously with the crystalline grain growth, may supplementary shift the absorption maximum to higher energies.

3.3. Energy dispersive X-ray spectroscopy studies

EDS measurements of the HA base powder have revealed values of the P/Ca atomic ratio in the (0.56-0.63) range. We observe that the variation of the recorded ratio around the stoichiometric value of 0.6 keeps within the typical apparatus accuracy of $\pm 2.5\%$. An important confirmation of the results presented in the previous sections is that the EDS investigation of the HA thin films deposited in vacuum and submitted to a heat-treatment in air showed a P/Ca atomic ratio almost within the same range (i.e. 0.55-0.65).

We may therefore conclude that the crystalline films have the same structure and stoichiometry as the HA base powder.

4. DISCUSSION

We developed a rather simple method to obtain HA polycrystalline depositions on various substrates. The coatings were very adherent to substrates and they successfully passed both the "finger" and the "scotch" tests. The method makes no use of corrosive (e.g. water vapours, oxygen) or other gases. We note that, according to previous reports in literature^{1,12}, the deposition of crystalline HA coatings was possible only assisted by water, oxygen and argon fluxes in parallel with the collector heating up to (400-600) $^{\circ}\text{C}$. The simple heating of the collector in vacuum proved to be insufficient to promote the total recrystallization of the film. The recrystallization was obtained by heating in atmospheric air.

The films are covered by a large number of particles. We consider that the presence of particles is beneficial with respect to the practical application of the films. Indeed, the particles have the same polycrystalline structures as the base powder material. Secondly, the presence of these small protuberances on the surface of the films are similar to the imperfections of the human bone contributing to a better biacceptance of the deposited pivots or prostheses inside the human body.

REFERENCES:

1. D. B. Chrisey and G. K. Hubler (eds.), "Pulsed Laser Deposition of Thin Films", Wiley, New York, 1994
2. D. Bauerle, "Laser Processing and Chemistry", Springer Verlag, 1996 (second edition)
3. I. N. Mihailescu, Adriana Lita, V. S. Teodorescu, Eniko Gyorgy, and Rodica Alexandrescu, A. Luches and M. Martino, A. Barborica, *J. Vac. Sci. Technol. A* **14**(4), 1986-1994 (1996)
4. V. S. Teodorescu, I. N. Mihailescu, Eniko Gyorgy, A. Luches, M. Martino, Leona C. Nistor, J. van Landuyt, J. Hermann, *Journal of Modern Optics* **43**(9), 1773-1784 (1996)
5. I. N. Mihailescu, Eniko Gyorgy, N. Chitica, V. S. Teodorescu, G. Marin, A. Luches, A. Perrone and M. Martino, J. Neamtu, *Journal of Materials Science* **31**, 2909-2915 (1996)
6. N. Chitica, Eniko Gyorgy, Adriana Lita, G. Marin, I. N. Mihailescu, D. Pantelica, M. Petrascu, A. Hatzia Apostolou, C. Grivas, N. Broll, A. Cornet, Codruta Mirica, A. Andrei, *Thin Solid Films* **301** 71-76 (1997)
7. R. Stevenson, H. S. Legg, and K. O. Legg, *Mater. Res. Soc. Symp. Proc.* **110**, 715-720 (1989)
8. A. Campbell, H. C. Gledhill, S. R. Brown, and I. G. Turner, *J. Vac. Sci. Technol. A* **14** (1996)
9. S. Ducheyne, S. Radin, M. Haughebeart, and J. C. Haughebeart, *Biomater.* **11**, 44 (1994)
10. B. Bourne, C. H. Rorabeck, B. C. Burkaart, and P. G. Kirk, *Clin. Orthopaed. Relat. Res.* **21**, 1375 (1987)
11. J. Thorpe and M. L. Thorpe, Proceedings of the 1993 National Thermal Spray Conference, Anaheim, CA (unpublished)
12. M. Jelinek, V. Olsan, L. Jastrabik, V. Studnicka, V. Hnatowicz, J. Kvitek, V. Havranek, T. Dostalova, I. Zergioti, A. Petrakis, E. Hontzopoulos, and C. Fotakis, *Thin Solid Films*, **257**, 125-129 (1995)
13. R. A. Niquist and R. O. Kagel, "Infrared spectra of inorganic compounds", Academic Press, London, 1971
14. L. Torrisi, *Thin Solid Films*, **237** 12 (1994)
15. G. Socrates, "Infrared characteristic group frequencies", John Wiley and Sons, Chichester, New York, Brisbane, Toronto, 1985

Mechanisms of droplets formation in pulsed laser growth of thin oxide films

V. Craciun, D. Craciun, M. C. Bunescu*, E. Vasile*, A. Ioncea*, R. Dabu, and I. W. Boyd**

Laser Department, National Institute for Laser, Plasma and Radiation Physics, PO Box MG-36, Bucharest V, Romania

*METAV SA, 16-18 Zapada Micilor, Bucharest I, Romania

**Electronic and Electrical Engineering, University College London, London WC1E 7JE, United Kingdom

ABSTRACT

The role of the sub-surface explosive boiling mechanism for droplet formation during the pulsed laser deposition (PLD) of thin films has been examined. For photons with an energy lower than the target optical band-gap, $h\nu < E_g$, a highly perturbed target surface morphology exhibiting micrometer sized round-shaped cavities always formed, whereas for $h\nu > E_g$ the surface was much less perturbed. Depth-profile estimations of the temperature profiles inside the laser irradiated targets were also quite different for these two cases. For low optical absorption coefficient (OAC) values, $\alpha < 5 \times 10^4 \text{ cm}^{-1}$, a thick layer of liquid formed whose maximum temperature was located at some point below the surface. Simultaneous to the cavity formation, the droplet density on the surface of the grown films was found to increase by orders of magnitude, indicating a clear connection between the target OAC, the temperature profile, the presence of the cavities and a high droplet density. The decrease of the OAC value during prolonged laser ablation could also explain the gradual increase of the droplet density observed when growing $\text{La}_{0.5}\text{Sr}_{0.5}\text{CoO}_3$ films. Based on these results, we suggest that an important fraction of the droplets on the surface of films grown under laser irradiation conditions where the OAC is smaller than $5 \times 10^4 \text{ cm}^{-1}$ is caused by an explosive sub-surface boiling mechanism.

KEY WORDS: pulsed laser deposition, thin films, zinc oxide, cerium oxide, $\text{La}_{0.5}\text{Sr}_{0.5}\text{CoO}_3$, droplet formation, temperature simulations, sub-surface boiling.

1. INTRODUCTION

Some of the highest quality thin films yet reported such as high temperature superconductors, giant magneto-resistance films, and hard and optical coatings¹⁻³ have been grown using the pulsed laser deposition (PLD) technique. The most important drawback of the method seems to be the presence of micrometer sized droplet on the surface of the grown films. The surface density of these can be reduced by employing special deposition geometries⁴, velocity filters⁵, shorter wavelength lasers⁶, or high density targets⁷. However, their complete elimination, which will extend the application area of PLD grown films in microelectronics, would be possible only after more fully understanding their formation mechanisms which are still a subject of debate. There have been several mechanisms of droplet formation suggested so far⁸⁻¹¹. Taking into account the experimental results obtained when depositing ZnO , CeO_2 and $\text{Pb}(\text{Ti}_{0.5}\text{Zr}_{0.5})\text{O}_3$ (PZT) thin films by PLD, we tentatively suggested in our previous studies^{12, 13}, following the initial idea of Gagliano and Paek⁸ that the majority of these droplets observed on the surface of films grown using longer wavelength lasers ($h\nu < E_g$, E_g being the target material optical band-gap) were caused by explosive boiling due to a sub-surface super-heating (SSSH) effect. Further on we have shown that under identical laser irradiation conditions, the droplet density is dramatically reduced when increasing the value of the target optical absorption coefficient (α or OAC) at the laser wavelength¹⁴. Complementary to this finding are new results presented here which show that the decrease of the α during the laser ablation process caused by preferential evaporation of one component is responsible for increased droplet emission when depositing films for long time. Scanning electron microscopy (SEM) investigations of various target surface morphologies induced by the laser ablation process and numerical estimations of the temperature profile for irradiation conditions used which support the occurrence of a SSSH effect causing this volume boiling mechanism are also presented here.

2. EXPERIMENT

Targets of ZnO , CeO_2 , PZT, apatite, and $\text{La}_{0.5}\text{Sr}_{0.5}\text{CoO}_3$ (LSCO) were prepared by cold pressing high purity powders into 1 cm diameter pellets which were afterwards sintered in air at 1100 °C for several hours. The targets were then irradiated in air or different oxygen pressures from 10^{-7} to 10^{-2} mbar with two Nd:YAG lasers emitting Gaussian beams and having full width at half maxima (FWHM) time durations of 15 (8) ns, 11 (6) ns and 7.5 (4) ns at 1064 nm, 532 nm and 266 nm, respectively. The peak fluence was varied from 1 to 8 J/cm², values usually employed to grow thin films¹²⁻¹⁵. Some

irradiations were also performed with an excimer laser (KrF, $\lambda=248$ nm, 20 ns pulse duration) at similar fluences. The quantity of material ablated was measured with a quartz crystal microbalance (QCM) situated at around 4 cm in front of the irradiated target.

The structural, electrical and optical properties of the films grown by PLD under optimum conditions have been presented in detail elsewhere^{12, 13, 15} and only optical transmission data recorded with a double beam spectrophotometer in the 1100-190 nm range, which are relevant for the temperature simulations, are shown here. Investigations of the surface morphology of the targets before and after laser irradiation were performed using SEM. Energy and wavelength dispersive X-ray analysis (EDX and WDS) were also performed to assess the chemical composition changes of the irradiated areas with respect to the as-prepared values. The crystalline structure of the grown films and droplet characteristics were also investigated by depositing some films on Si₃N₄ membranes and analysing in a transmission electron microscope (TEM).

3. RESULTS AND DISCUSSION

Optical transmission spectra of ZnO and CeO₂ films deposited using the KrF laser under optimised conditions are shown in Fig. 1, whereas some of their optical parameters estimated from the recorded transmission spectra¹⁶ are presented in Table 1. One can notice that these films are highly transparent from the near infrared region down to 400 nm. Regardless of the PLD conditions employed, the use of the 532 nm or 1064 nm laser radiation failed to produce similar high quality results. Not only did the X-ray diffraction (XRD) patterns exhibit wider peaks than those recorded from films grown with the KrF or fourth-harmonic Nd:YAG lasers (248 nm and 266 nm, respectively), but the surface morphology also showed a 10²-10⁴ fold increase in droplet density¹²⁻¹⁵. TEM investigations of the grown films strongly indicated that the deposited particles most likely had originated from the target. In Figs. 2 a and b, TEM micrographs of a region of a ZnO film containing such a particle and also a droplet free region, together with their corresponding electron diffraction patterns are shown. Whereas the film grown on the substrate is highly textured exhibiting only the (002) and (004) diffraction rings, the droplet exhibits all the characteristic ZnO rings, similar to the target material.

An SEM micrograph of the surface of a typical as-prepared ZnO target is shown in Fig. 3, and in Fig. 4 a micrograph of the ZnO target surface after irradiation by 100 laser pulses of

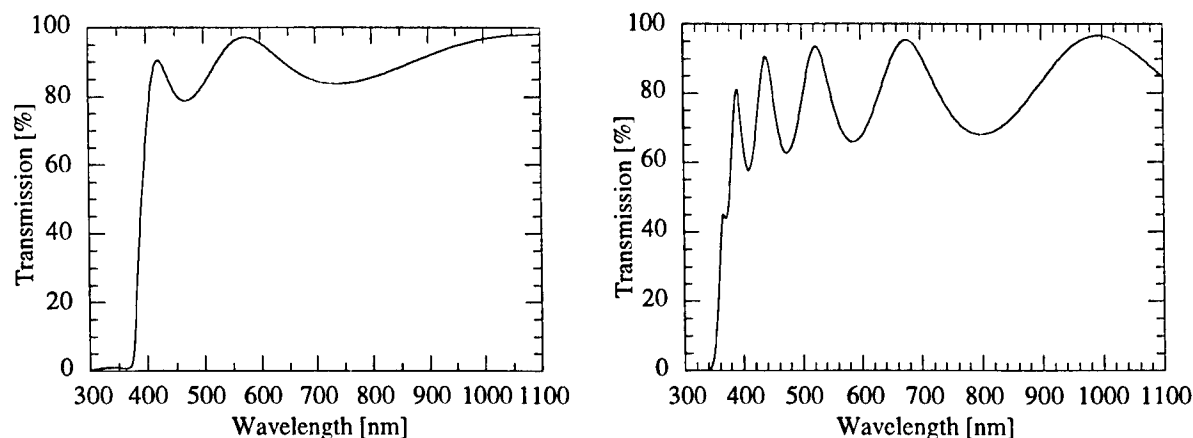


Figure 1. Typical optical transmission spectra of ZnO and CeO₂ thin films deposited by PLD

Table 1. Optical parameters of the PLD grown ZnO and CeO₂ grown layers

	λ [nm]	n refraction index	k extinction coefficient	α [cm ⁻¹]	thickness [nm]	R [%]
ZnO	572	2.0	$4.3 \cdot 10^{-3}$	$9.5 \cdot 10^2$	290	11.0
	1083	1.9	$5.6 \cdot 10^{-3}$	$6.5 \cdot 10^2$	290	9.3
CeO ₂	524	2.5	$5.6 \cdot 10^{-3}$	$1.3 \cdot 10^3$	430	18
	995	2.3	$5.6 \cdot 10^{-3}$	$7.0 \cdot 10^2$	430	16

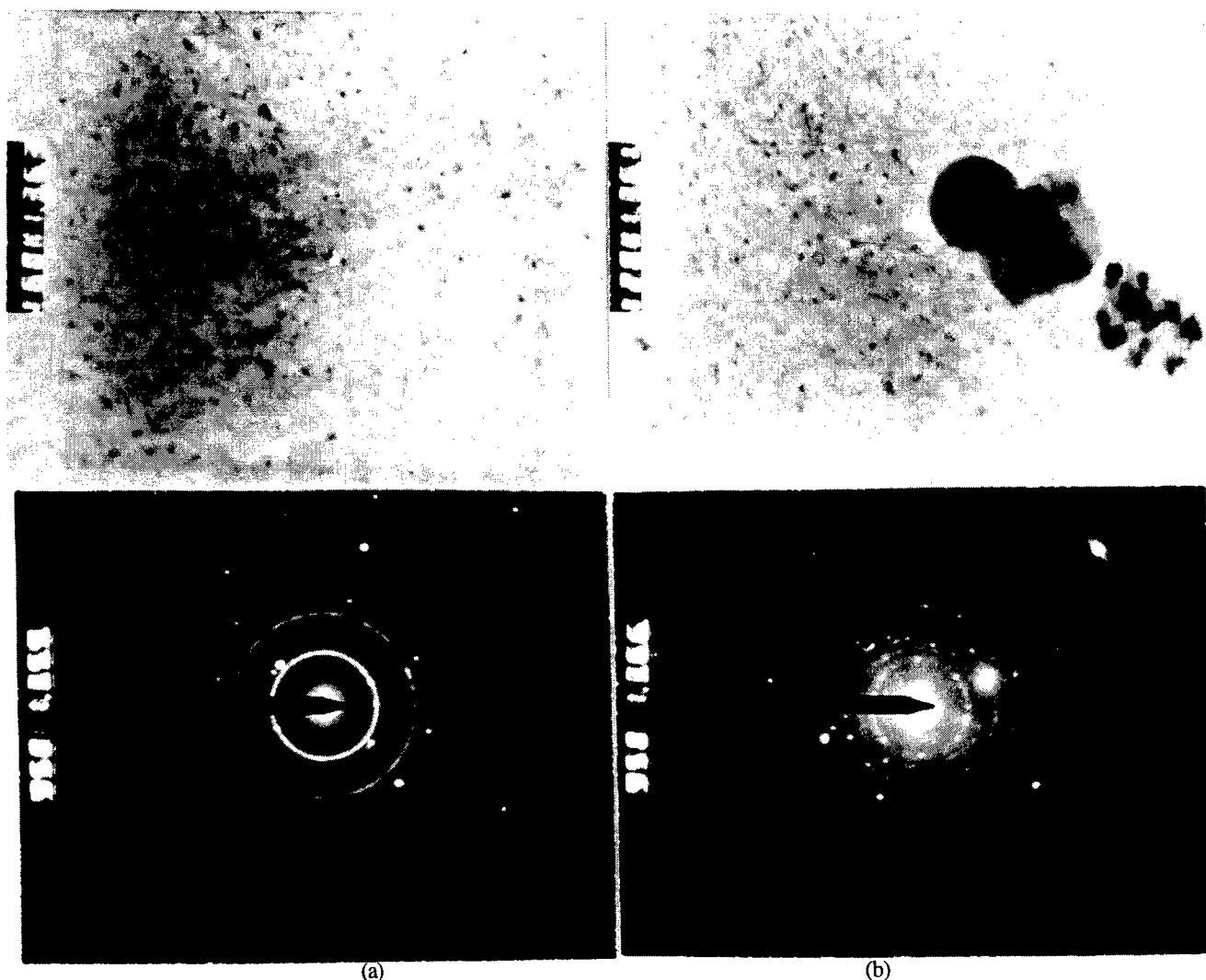


Figure 2. TEM micrographs (x250 000 magnification) and SAED patterns of an area of a thin ZnO film deposited by PLD without droplet (a) and of an area containing droplet and other debris material (b).

the 1064 nm Nd:YAG laser at a fluence of 4 J/cm^2 (above the ablation threshold of only 0.5 J/cm^2) is displayed. The laser irradiated target exhibits clear evidence of surface melting. It is worth noting the presence of micrometer-sized cavities on the surface of the target. Their circular shape suggests that they were most likely caused by the release of gas from beneath the surface when the region was molten.

SEM investigations also showed that when using laser wavelengths where the photon energy was lower than the target optical band-gap, i.e. $h\nu < E_g$, these cavities were always formed on the target surface. As one can clearly see in Fig. 5, where a surface micrograph of a ZnO target irradiated by the KrF laser (248 nm, 2.1 J/cm^2) is shown, the surface morphology was quite different. Morphological features associated with surface melting, like the rounded shape of the crystallites, are present, but the surface is generally quite flat, without any cavities.

There might be several mechanisms which can account for the cavity formation. For example, the presence of an initial cavity-type defect on the target surface will increase the local absorption, A , of the incoming laser radiation up to the value of $A=1$ (or, alternatively, reflectivity $R=0$), when it is completely trapped due to multiple reflection and absorption processes. This will lead to a higher quantity of energy being absorbed in this location, thus resulting in the ablation of a larger amount of material. In turn, this higher removal rate will further deepen the initial cavity through a positive feed-back reaction. However, according to our temperature estimations (shown later), once the material melts, it will remain molten for tens of nanoseconds allowing enough time for the liquid material to flow into and partly fill the holes, so that the surface can regain its more or less flat morphology. Moreover, it has been observed that such cavities can form after the action of only one or two pulses, when this or indeed other feedback operations^{9, 17} could have not occurred. It is also very unlikely



Figure 3. SEM micrograph of an as-prepared ZnO target surface.



Figure 4. SEM micrograph of a ZnO target irradiated at 1064 nm and 4 J/cm² by 100 laser pulses

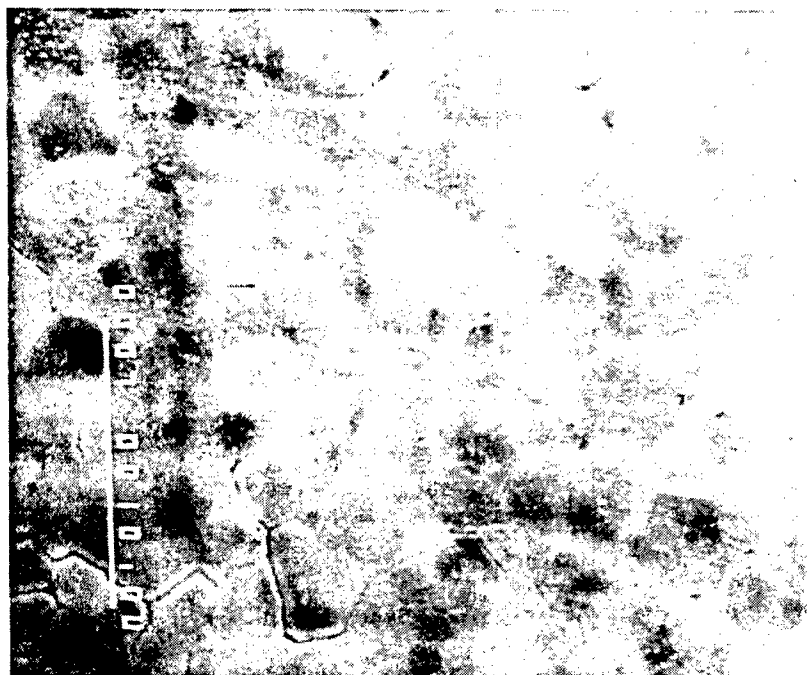


Figure 5. SEM micrograph of a ZnO target surface irradiated by 100 laser pulses at 248 nm and 2 J/cm².

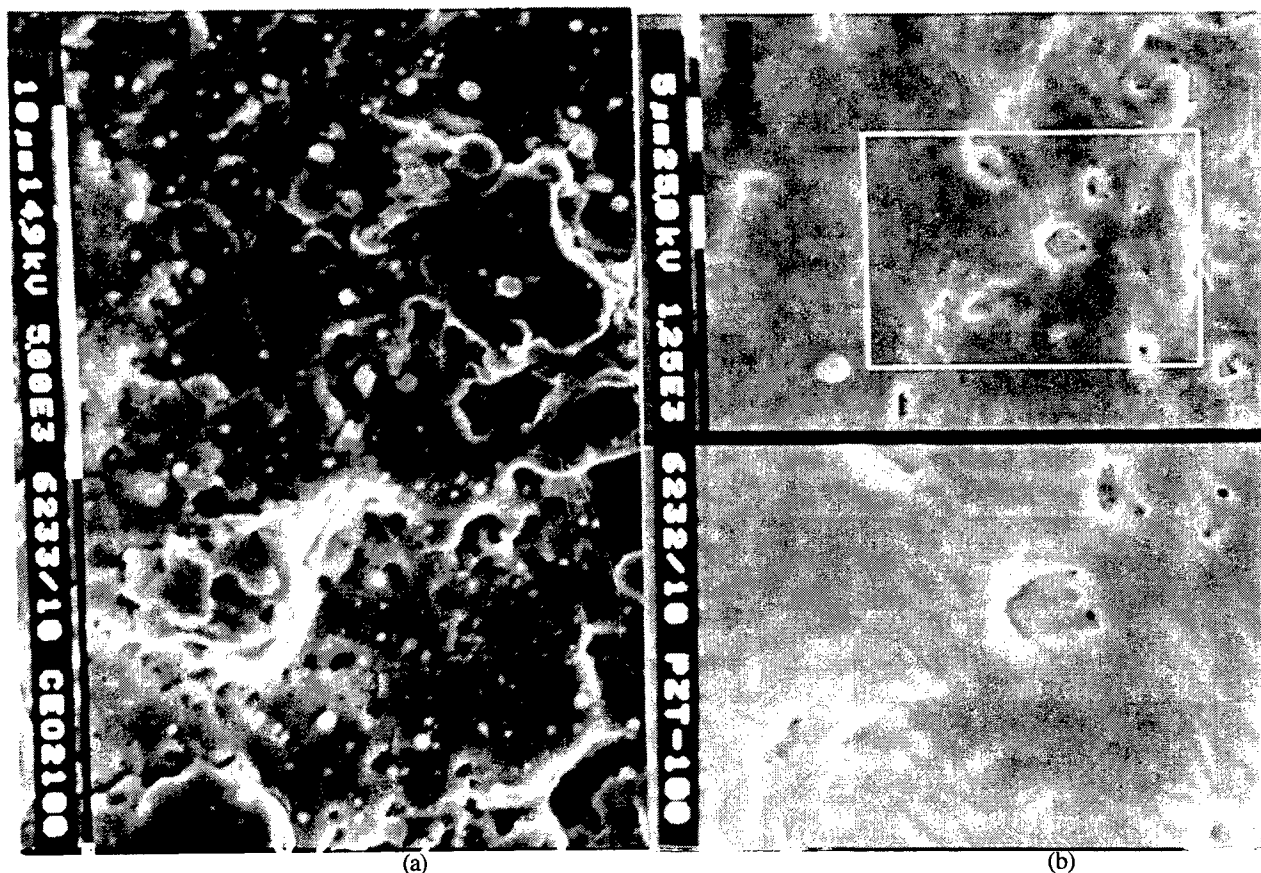


Figure 6. SEM micrographs of CeO₂ (a) and PZT (b) targets irradiated by 100 laser pulses at 1064 nm and 2 J/cm².

that these cavities were caused by the initial presence of defects or contaminants on the target surface, as they were not formed when using highly absorbed radiation such as the 248 or 266 nm wavelengths.

Another mechanism which can explain the formation of these circular cavities is the release of trapped or dissolved gases inside the target. Similar cavities have been observed when lime glass, a material known to contain dissolved gases at a level of several percentages, was irradiated by a CO₂ laser (10.6 µm)¹⁸. However, Fig. 4 shows that such holes are still present on the surface of a ZnO target even after 100 laser pulses on the same location. This makes it rather difficult to believe that in our case dissolved gases are still released after such a long irradiation time.

An alternative explanation for the cavity formation in ZnO could be the thermal decomposition of the target material in the liquid phase¹⁹. The fact that the cavities were not observed when using a shorter laser wavelength ($h\nu > E_g$) and similar incident fluences (see Fig. 5) rules out this proposition. Furthermore, EDX analysis performed on the rim and bottom of such cavities did not reveal any significant change in chemical composition.

Very similar surface morphology features can be seen in Figs. 5 a and b, where micrographs of CeO₂ and PZT laser irradiated targets under essentially identical conditions to those employed for the ZnO target ablation are shown. Neither CeO₂ nor PZT are known to easily dissociate when in the liquid phase. These materials have similar wavelength-dependent OACs, to ZnO. As in the ZnO case, the cavities were no longer present when the irradiation laser wavelength was changed to the high absorption spectral region, i.e. 266 nm or 248 nm.

A very important finding revealed by these SEM investigations was that the droplet density on the surface of the grown films was directly associated with the presence of these surface topographical modifications. Whenever the cavities were formed on the target during the laser ablation process, a significant increase by 2 to 4 orders of magnitude of the droplet density on the surface of the grown films was also noticed.

Valuable information about the cavity formation mechanism was obtained by estimating the temperature depth-profile inside the laser irradiated target. For this aim, the usual one-dimensional heat diffusion equation²⁰, which is appropriate for the nanosecond pulsed laser processing, was numerically solved by a finite difference technique²¹:

$$\rho(T)C(T)\frac{\partial T}{\partial t} = \frac{\partial}{\partial x} \left(\kappa(x, T) \frac{\partial T}{\partial x} \right) + (1 - R(T))I(t)\alpha \exp(-\alpha x) \quad (1)$$

Here T , C , ρ , κ , R , I , and α are, respectively, temperature, specific heat, mass density, thermal conductivity, reflection coefficient, laser intensity and absorption coefficient. The boundary conditions for the surface, initial time and deep inside of the sample (the semi-infinite sample) were, respectively¹¹:

$$\left(\frac{\partial x}{\partial t}\right)_{x=0} \approx \beta p_b \exp\left[\frac{\Delta H_v m}{k_b} \left(\frac{1}{T_b} - \frac{1}{T}\right)\right] \times (2\pi m k_b T)^{-1/2} (m / \rho) \quad (2)$$

$$T(x, t = 0) = 300 K \quad (3)$$

$$T(x \rightarrow \infty, t) = 300 K \quad (4)$$

β is the vaporisation coefficient (with a value from 0.8 to 0.9¹¹), p_b is the boiling pressure (0.1 MPa), T_b is the corresponding boiling temperature, k_b is the Boltzmann constant, m is the mass of a ZnO molecule and ΔH_v is the heat of vaporisation^{19, 22}.

Typical temperature depth-profiles precisely when 1 nm of ZnO was removed from the target surface after ablation by 532 nm and 248 nm laser radiation, respectively, at a fluence of 2.1 J/cm² are shown in Fig. 7. For the irradiation with the weakly absorbed light one can notice a very mild thermal gradient in the surface region with maximum temperature situated around 30 nm inside the target, whereas for the strongly absorbed radiation the temperature profile is much steeper and the maximum temperature is very close to the surface. It should be pointed out that, because molten ZnO is metallic¹⁹ and has a high electrical conductivity, the corresponding value of α was also chosen to be high, $5 \times 10^5 \text{ cm}^{-1}$, and independent of wavelength. The differences between these two temperature profiles are thus solely due to the value of α for the solid phase material.

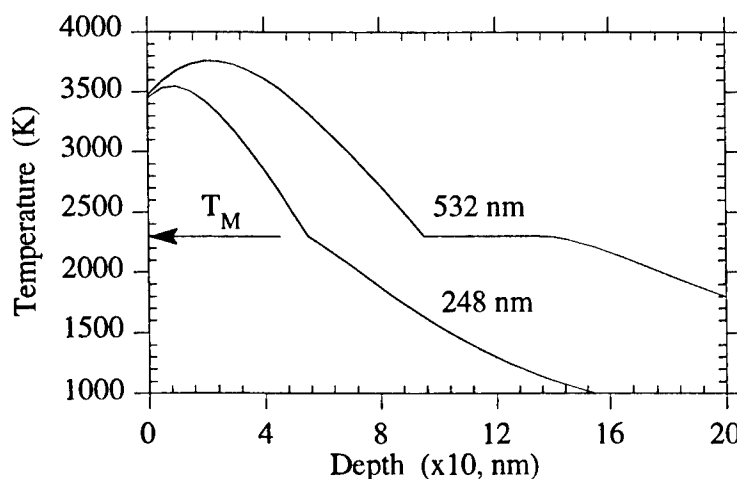


Figure 7. Temperature depth profiles inside ZnO targets during the action of a laser pulse with a fluence of around 2.0 J/cm² and a wavelength of (a) $\lambda=248 \text{ nm}$ and (b) $\lambda=532 \text{ nm}$; T_M is the melting temperature.

Another interesting observation from Fig. 7 is that the thickness of the liquid layer increases when α decreases. The number of nucleation sites for boiling will depend on the nucleation rate, which in turn depends on the temperature and volume of the liquid. It is thus obvious that a low α value simultaneously increases both factors which could cause sub-surface explosive boiling processes similar to microexplosions to occur and thus explain the high droplet density observed on the surface of the grown films. However, it should be stressed that the sub-surface or explosive boiling process does not solely depend on the value of the super-heating temperature. Even if the maximum temperature is located at the surface, volume boiling could occur provided a thick layer of molten material having a temperature higher than that corresponding to the normal boiling temperature exists. The cavities observed on the surface after the ablation process with poorly absorbed photons, are caused by these microexplosions.

Confirmation of the direct correlation between the value of α and the droplet density was provided by the results obtained when growing apatite films by PLD. This material has a low $\alpha < 5 \times 10^4 \text{ cm}^{-1}$, even at 266 or 248 nm, the laser wavelengths used for ablation. Confirming our expectations, the surface of the grown films was covered by a high density of micrometer-sized droplets¹⁴. However, when the α value was significantly increased either by doping with Mn or as an effect of a reducing annealing treatment in a H₂ atmosphere, the surface density of the droplets was reduced by orders of magnitude¹⁴.

It is important to note that Dat et al.²³, when growing LSCO thin films by PLD (KrF, $\lambda=248$ nm, fluences around $1-3$ J/cm²), observed a sudden increase in the droplet density for prolonged deposition times. The authors have suggested that the loss of oxygen due to preferential evaporation could cause the modification of the thermal and mechanical properties of the target making the material more brittle and thus inducing splashing. We believe that this is yet another example of the OAC role in the droplet formation.

To study the effect of the oxygen content on the OAC value, LSCO films were grown on quartz substrates at a base vacuum of 10^{-7} torr or under an oxidising atmosphere (N_2O , from 10^{-2} to 10^{-4} torr) using a KrF laser and similar fluence values to those employed in ref.²³. The optical transmittance of the films grown in vacuum and under the oxidising atmosphere, measured from 220 to 280 nm, around the laser wavelength employed for ablation, is shown in Fig. 8. Taking into account the thickness of identical films grown on Si substrates, the OAC values were calculated to be 1.8×10^4 cm⁻¹ and 2.4×10^5 cm⁻¹, respectively. It was found by Rutherford backscattering spectroscopy that films grown under vacuum were oxygen deficient with respect to those grown under an oxidising atmosphere.

Numerical estimations of the temperature depth-profiles for the two OAC values, based on the one dimensional heat diffusion equation previously shown were also performed. Unfortunately, thermo-physical data for LSCO material are not well documented. To circumvent this difficulty, the ablation threshold was determined by measuring with a QCMB the dependence of the deposited mass on the laser fluence. As the deposited mass was found to be linearly dependent on the laser fluence, it was also inferred that the plasma absorption could be neglected in these numerical simulations. Where the remaining necessary thermo-physical data for LSCO were not available those of LaO_3 were used instead, adjusted to yield a similar laser ablation threshold value.

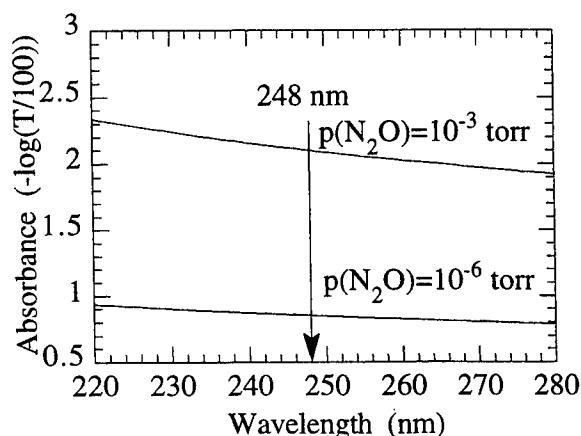


Figure 8. Optical absorptivity of LSCO films deposited under an oxidising atmosphere and in vacuum.

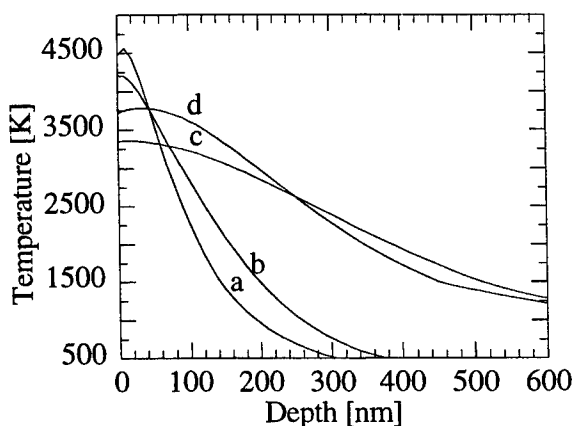


Figure 9. Temperature depth profiles inside a LSCO target during the action of a laser pulse with a 1.5 J/cm² fluence and 248 nm wavelength for different OAC, α (cm⁻¹), and thermal

conductivities, κ (W/cmK): a) $\alpha=2.4 \times 10^5$, $\kappa=0.05$, b) $\alpha=2.4 \times 10^5$, $\kappa=0.05-0.13$, c) $\alpha=1.8 \times 10^4$, $\kappa=0.05$, and d) $\alpha=1.8 \times 10^4$, $\kappa=0.05-0.13$.

The temperature depth-profiles for the two OAC values experimentally measured are displayed in Fig. 9. Also shown for each OAC value is another temperature depth-profile estimated with a reduced value of thermal conductivity. It can be noticed that although the thermal conductivity variation affects the data, the major contribution comes from the value of the OAC. It is clear that for films having a low OAC value, the laser radiation induced a volume heating, with a thick melted layer which reached temperatures in excess of the normal boiling temperature. Under such conditions, sub-surface explosive boiling is very likely to occur, which can explain the appearance of the splashing effects observed when growing LSCO films for long time durations.

4. CONCLUSIONS

The surface morphology of laser irradiated targets under conditions usually employed for PLD has been investigated. For irradiation with photons whose energies are lower than the target material band-gap energy, the presence of circularly-shaped cavities, most likely formed by the release of gas (vapour) from beneath the surface caused by the sub-surface boiling, was always observed, regardless of the target material. Whenever these holes appeared on the target surface, the droplet

density on the surface of the film deposited from such targets significantly increased. This investigation suggests that the sub-surface or volume boiling is at least partially responsible for the large density of droplets seen on the surface of grown films using a laser wavelength that is not strongly absorbed by the target. Even when the initial optical absorption coefficient is high and the droplet density very small, laser irradiation can induce target modifications which decrease the absorption and, consequently, increase the droplet density. A non-negligible SSSH effect in laser irradiated targets is predicted according to heat-diffusion simulation results provided the initial α value is below $5 \times 10^{-4} \text{ cm}^{-1}$. However, we believe that this SSSH value is not solely responsible for the volume boiling, but also the thicker liquid layer formed under these conditions. It should be also clearly stated that sub-surface volume boiling is not the only mechanism responsible for droplet emission, as droplets, although fewer in number, were also found on the surface of films grown using highly absorbed laser wavelengths.

5. REFERENCES

1. D. B. Chrisey and G. K. Hubler, *Pulsed laser deposition of thin films*, Wiley, N. Y. (1994).
2. W. Zhang, I. W. Boyd, N. S. Cohen, Q.-T. Bui, Q. A. Pankhurst, "Giant magnetoresistance behaviour in in-situ $\text{La}_{0.6}\text{Sr}_{0.4}\text{MnO}_3$ films grown on Si substrates by pulsed laser deposition", *Appl. Surf. Sci.* **109-110**, 350-353 (1997).
3. D. Craciun and V. Craciun, "Reactive pulsed laser deposition", *Appl. Surf. Sci.* **54**, 75-77 (1992).
4. B. Holzapfel, B. Roas, L. Schultz, P. Bauer, and G. Saemann-Ischenko, "Off-axis laser deposition of $\text{YBa}_2\text{Cu}_3\text{O}_{7-\delta}$ thin films", *Appl. Phys. Lett.* **61**, 3178-3180 (1992).
5. D. Lubben, S. Barnett, K. Suzuki, S. Gorbatiukin, and J. Green, "Laser-induced plasmas for primary ion deposition of epitaxial Ge and Si films", *J. Vac. Sci. Technol.* **B3**, 968-974 (1985).
6. G. Koren, A. Gupta, R. J. Baseman, M. I. Lutwyche, and R. B. Laibowitz, "Laser wavelength dependent properties of $\text{YBa}_2\text{Cu}_3\text{O}_{7-\delta}$ thin films deposited by laser ablation", *Appl. Phys. Lett.* **55**, 2450-2452 (1989).
7. R. K. Singh, D. Bhattacharya, and J. Narayan, "Control of surface particle density in pulsed laser deposition of superconducting $\text{YBa}_2\text{Cu}_3\text{O}_7$ and diamondlike carbon thin films", *Appl. Phys. Lett.* **61**, 483-485 (1992).
8. F. P. Gagliano and U.-C. Paek, "Observation of laser-induced explosion of solid materials and correlation with theory", *Appl. Opt.* **13**, 274-279 (1974) and F. W. Dabby and U.-C. Paek, "High-intensity laser-induced vaporization and explosion of solid material", *IEEE J. Quant. Electr.* **8**, 106-111 (1972).
9. T. D. Bennett, C. P. Grigoropoulos, and D. J. Krajnovich, "Near-threshold laser sputtering of gold", *J. Appl. Phys.* **77**, 849-864 (1995).
10. A. B. Brailovsky, S. V. Gaponov, and V. I. Luchin, "Mechanisms of melt droplets and solid-particle ejection from a target surface by pulsed laser action", *Appl. Phys. A* **61**, 81-86 (1995).
11. A. Miotello and R. Kelly, "Critical assessment of thermal models for laser sputtering at high fluences", *Appl. Phys. Lett.* **67**, 3535-3538 (1995).
12. V. Craciun, J. Elders, J. G. E. Gardeniers, and I. W. Boyd, "Characteristics of high-quality ZnO thin films deposited by pulsed-laser deposition", *Appl. Phys. Lett.* **65**, 2963-2965 (1994).
13. V. Craciun, S. Amirhaghi, D. Craciun, J. Elders, J. G. E. Gardeniers and I. W. Boyd, "Effects of laser wavelength and fluence on the growth of ZnO thin-films by pulsed-laser deposition", *Appl. Surf. Sci.* **86**, 99-106 (1995).
14. O. Guillot-Noel, R. Gomez-San Roman, J. Perriere, J. Hermant, V. Craciun, C. Boulmer-Leborgne, P. Barboux, "Growth of apatite films by laser ablation: Reduction of the droplet areal density", *J. Appl. Phys.* **80**, 1803-1808 (1996).
15. S. Amirhaghi, F. Beech, V. Craciun, A. Sajjadi, M. Vickers, S. Tarling, P. Barnes, and I. W. Boyd, "Growth of cerium oxide buffer layers and superconducting thin-films", *Mater. Res. Soc. Proc.* Vol. 275, 501--506 (Pittsburg 1992).
16. R. Swanepoel, "Determination of the thickness and optical constants of amorphous silicon", *J. Phys. E: Sci. Instrum.* **16**, 1214-1222 (1983).
17. E. van de Riet, C. J. C. M. Niellensen, and J. Dieleman, "Reduction of droplet emission and target roughening in laser ablation and deposition of metals", *J. Appl. Phys.* **74**, 2008-2012 (1993).
18. G. Allcock, P. E. Dyer, G. Elliner, and H. V. Snelling, "Experimental observation and analysis of CO_2 laser-induced microcracking of glass", *J. Appl. Phys.* **78**, 7295-7304 (1995).
19. Landolt-Bornstein New Series, Volume 17b, Ed. O. Madelung (Springer Verlag, Berlin, Heidelberg, New York, 1982).
20. H. S. Carslaw and J. C. Jaeger, *Conduction of heat in solids*, 2nd ed. (1959)
21. J. Crank, *Free and moving boundary problems* (Oxford University Press, Oxford 1984).
22. D. Craciun and V. Craciun, "Mechanism of droplet formation in laser ablation", *Science and Technology of Electroceramic Films*, O. Auciello and R. Waser eds., NATO ASI Series E, vol. 284, 67- 73 (1995).
23. R. Dat, O. Auciello, D. J. Lichtenwalner, and A. I. Kingon, "Pulsed laser ablation-deposition of $\text{La}_{0.5}\text{Sr}_{0.5}\text{CoO}_3$ for use as electrodes in nonvolatile ferroelectric memories", *J. Mater. Res.* **11**, 1514-1519 (1996).

Nd:YAG Laser Surface Texturing

M.Poterasu, T.Dascalu, A. Marian, D. Buca

National Institute for Laser Plasma and Radiation Physics
Bucharest PO Box MG36 76900
e_mail: dascalu@roifa.ifa.ro

ABSTRACT

Obtaining sharp and sometimes special patterns on hard materials surfaces (texturing) is rather difficult by conventional procedures, which made the laser an attractive choice in this matter. Absorption of Nd:YAG's 1.06 μm radiation in most steels and ceramics, which are the common materials for textured surfaces, is good such that average power lasers can be used.

In this paper we are concerned with the principal phenomena involved in the texturing process and with the sought of a simple mathematical model that will allow to choose right working regime, and make estimations about the system performances (speed, power consumption, etc.). Experimental data were obtained by using both a Electro-Optically Q-switched CW laser with an average power of up to 100W and a pulsed free running laser with an average power of up to 100 W and pulse energy of up to 10J. The experimental set-up includes an X-Y stage and two gold deflectors used to cover the entire surface.

Keywords: texture, Nd:YAG laser, Q-switch

1. INTRODUCTION

Surface texturing consist in creating a microscopic relief on technical surfaces. The necessity of such structured surfaces comes from different applications that require improvement of adhesion, friction or ink and paint uniformity. Such relief, which are made by digging closed or overlapped small groves are usually made on metallic surfaces or ceramic coatings and most of these materials interact well enough with the Nd:YAG laser beam.

Some parts in printing industry require a special kind of texture in which the profile is not perpendicular to the surface. With conventional techniques like chemical , electro-chemical, sandblasting this is almost impossible to achieve. One of the advantages of laser texturing is that such holes in material can be obtained using an average power (in range of tenths or hundreds Watts) laser that can penetrate the material at different angles.

Besides the aspects of material removal by laser which is the main phenomena involved in the process some considerations must be taken in order to determine the quality of the textured surface. Formerly we will be concerned with the two main aspects of this technique in a proper order.

2. THEORETICAL

2.1 Laser ablation

Given available lasers today the radiation must be focused on the surface in order to obtain interaction. This leads to a most used cylindrical geometry and the texture by material removed will be obtained from ablated craters which may or may not be overlapped.

Thus the processing problem will be reduced to the geometry of the craters obtained by laser irradiation of the surface. Shape of craters will depend on optical and thermophysical properties of the material and the characteristics of laser pulses used. Depending on the laser power density (energy per unit time and unit area) used, two different situations occur. First one corresponds to irradiation with short pulses in case of which the main phenomenon is vaporisation and the other one is a regime with long laser pulses (smaller power density) which leads to another removal mechanism. In the second case the material; is expelt from the substrate both in liquid and vapour phase due to recoil shocks determined by the boiling of the melt.

2.1.1 Ablation with short laser pulses

When a short laser pulse (in fs -ps range) reaches a material surface it will be quickly absorbed by it. Compared to thermal relaxation times the irradiation is fast and heat conduction losses are small. In this case almost the entire amount of energy provided will be used to vaporise the material so that simple computations will give the volume of material removed. This is a saturation situation in which the efficiency of the process is maximum. Actually this efficiency varies rapidly at lower power density when conduction losses occur and plasma cloud is not removed fast enough. When not considering absorption in plasma cloud a relationship for ablation depth was obtained[1] (eq.1)

$$L_e \approx \frac{1}{\alpha} \ln \left(\frac{I}{I_{th}} \right) \quad (1)$$

where L_e is the crater depth, I is laser intensity and I_{th} is a threshold value given by condition from eq. 2

$$I_{th} \approx \rho \frac{\Omega}{\alpha \tau_e}, \quad (2)$$

where Ω is vaporisation specific heat, τ_l is laser pulse duration, α the exponential absorption coefficient and ρ is the mass density. Equations above are correct if an approximate condition that requests the heat losses to be small, is satisfied. (eq.3).

$$I_{th} \leq I \leq I_{th} \exp \left(\frac{\Omega^{1/2}}{D\alpha} \right) \quad (3)$$

The above relations were in good agreement with experiments and they are also used for modelling the laser drilling process.

2.1.2 Ablation with long laser pulses at low fluencies

When irradiation time is long enough that heat penetrates beyond the interaction zone then a significant amount of heat is lost by conduction. In this regime when vaporisation occurs, there is already a large amount of melted material. Furthermore when vaporisation has begun pressure of vapours quickly generated blow out melted material which will be found around the crater. However, in this regime significant vaporisation that actually starts the process will occur only if a threshold laser intensity is reached (eq.4), otherwise there will be only melted and re-solidified material.

$$I > I_{th} \approx \frac{\rho \Omega D^{1/2}}{\tau_l^{1/2}} \quad (4)$$

In this case it is more difficult to find relationship that gives the ablation depth. However some mathematical models have been developed[2]. The main reason is that the ratio between melted and vaporised material varies with material thermal properties and laser intensity. There is an important aspect of the process that concerns the laser texturing with long laser pulses. Besides the crater formed, additionally relief is obtained from the debris of expelt material (photo 2). In some situations this will substantially increase the quality of the texture.

2.2 Texturing degree

The analysis of the textured surface regardless the processing method, may be often necessary in order to be able to measure the efficiency of a certain method or to compare two or more textured surfaces. For this propose we must relate to each one a numerical value which corresponds to a physical greatness which can be measured directly or to be calculated from the values corresponding to the measurable properties of the surface. The physical greatness introduced should carry sufficient information about the properties of the investigated surface.

It is obvious that it only a physical greatness that cannot be measured directly can be considered being actually derived from results of statistical measurements or computations of about the surface. We must first see if an order relationship is consistent by answering to ourselves to the following question: *What means a more textured surface than another?* As we saw, it may depend on the application that requires a textured surface. For example let us consider the case of improving paint adhesion to a certain substrate. Paint adherence can be considered as the force per unit area necessary to unstuck it from the substrate. For a planar surface related to molecules or small particles involved, this force depends upon the resultant of cohesion, forces between paint molecules (particles) and substrate. Given a certain surface the total unstuck force is proportional to surface area, i.e. the effective contact surface. If from a macroscopically point of view the examined surface remains the same but it is not smooth then the effective contact area will be larger and the corresponding adherence will be greater than when smooth (figure 1).

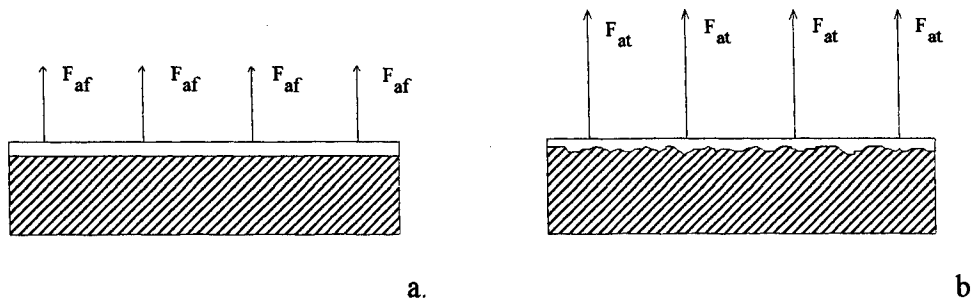


Figure 1 The necessary unstuck force for smooth (a) and rough (b) surfaces

Thus the first criteria we may introduce for texturing characterisation can be the effective free area resulted which can be put without difficulty in direct correspondence with paint adherence. But it is not sufficient in this case because we may want to know which is the medium size of the textured relief

because the total free area resulted might not be completely used. This happens when relief size is comparable with particles size or anti-capillarity can occur (in case of non wetting liquids - figure 2).

We have established so far at least two parameters that should characterise a textured surface which are the microscopically times macroscopically area and medium hole size. Some authors [3] are concerned with the random aspect of the texture which is given by an autocorrelation spectrum, uniformity of the texture given by profile departure density and from a simple Fourier profile spectrum one can verify the absorptivity and adhesion of thick fluids.

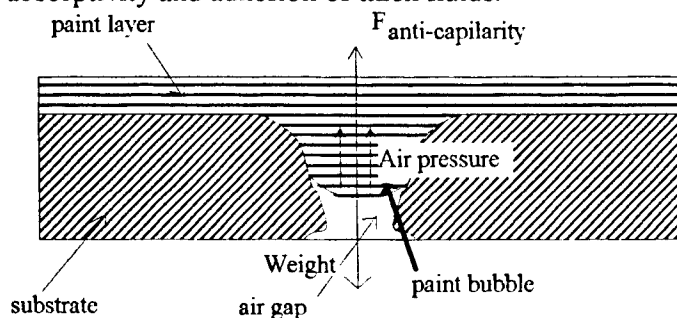


Figure 2 Typical forces that determine the penetration of paint in texture depth

One practical method of investigation is laser scan of the surface followed by a numerical processing of obtained data. A focused laser beam is scanned along the investigated surface and scattered light feeds into an optical detector. Analogue data is converted to digital and fed to a computer which also controls the scanning process.

There are two ways of handling with digital data. One is averaging the spectrum and autocorrelation obtained in one dimension over the entire surface and the other one is to perform directly a two-dimensional analysis. Handling and discussing one dimensional data is a bit simpler than in two dimensions and it is preferred this way. However variations of depth over the averaging direction is lost or, in other words, if the scan is made on a new direction, perpendicular to the first one, then the spectrums may differ considerably.

From the former paragraphs we saw that it is possible to determine the geometry of the texture obtained when knowing the irradiation regime and periodicity of the scan. It is possible then to calculate parameters of the textured surface in the ideal case, in which the geometry is exactly as predicted. An integral relation can be found that gives the total microscopic area:

$$A_{micro} = \iint \left(1 + \left(\frac{\partial h(x, y)}{\partial x}\right)^2\right) \left(1 + \left(\frac{\partial h(x, y)}{\partial y}\right)^2\right) dx dy \quad (5)$$

where $h(x, y)$ is the function of depth of the relief. Also the formula can be used for experimental data resulted from laser scanning or microphotography. Additional information are given by a Fourier Transform of the depth function:

$$H(\omega) = \iint h(x, y) \exp(-i\omega(x + iy)) dx dy \quad (6)$$

In some simplified situations we are able to calculate both spectrum and microscopically area theoretically for a given geometry. Let us consider the most common case in which texture consists in

closed cylindrical groves of diameter D and depth h and density g (groves /cm²). Simple considerations will lead us to the formula below:

$$A_{micro} = A_{tot}(1 + \pi Dhg) \quad (7)$$

Thus we may expect paint adherence to grow linearly with groves density or diameter in some limits (not overlapped). From this point of view we may conclude that the surface will be better textured if we have a larger groves density and diameter which means that the groves must be very close to each other. This is a limit case in which eq. 7 has only one parameter, D as the groves density is maximum:

$$A_{micro} = A_{tot}(1 + \pi h / D) \quad (8)$$

Equation 8 shows that we expect an improvement of the texture (from paint adhesion point of view) as groves diameter decreases. Of course this is true only in some limits as discussed formerly. An approximate formula can be established for textured surfaces obtained with long pulse laser assuming an hemispherical shape of the crater.

Besides the parameters above some applications require computation of means like roughness, profile bearing part, profile departure density or auto-correlation spectrum.

3. EXPERIMENTAL

Two types of laser were used in order to obtain texture in a wide range of laser intensity working regime. The first one was a short E-O (Electro-Optically) Q- switched pulse pumped laser and the second one was a long pulse laser. A texture pattern like the one presented in photo 1 was obtained using a μ m step X-Y stage to move the sample in the focal plane of the focusing lens.

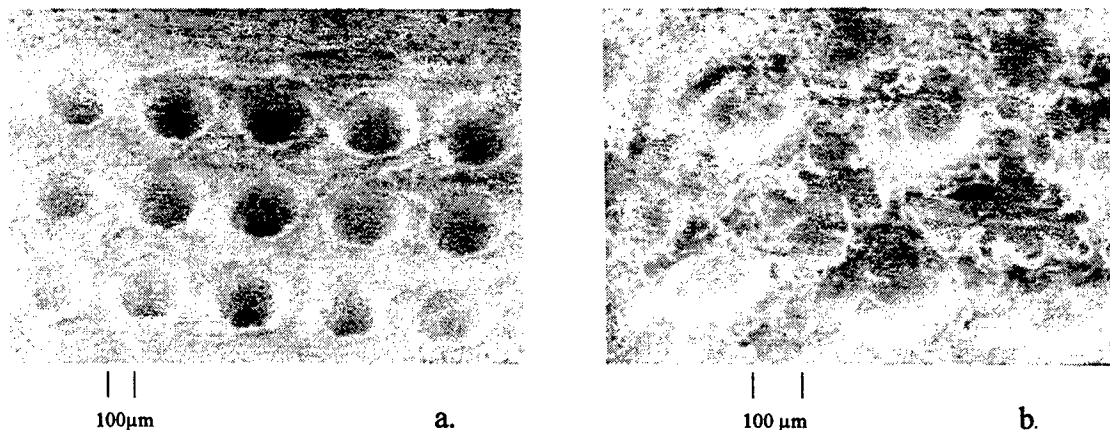


Photo 1. a. Detail of textured surfaces of Aluminium sample with E-O Q-Switched pulses (220 mJ, 56 ns); b. Detail of textured surfaces of Stainless Steel sample with long free running pulses (1.6J, 0.5ms)

For the E-Q Q-Switched laser energy per pulse ranged between 70 and 250 mJ while pulse duration was 30 to 70 ns. Table 1 presents experimental results obtained on Stainless-Steel, Aluminium and Brass. The depth of the craters was measured with an optical microscope and the diameter was measured with an electronic microscope.

Table 1

Laser Characteristics				Stainless steel	Aluminium	Brass
Pulse Energy (mJ)	Pulse Duration (ns)	Spot Diameter (μm)	Laser Intensity (GW/cm^2)	Crater depth (μm)	Crater depth (μm)	Crater depth (μm)
79	70	250	2.5	14	32	3
130	64	280	3.5	26	72	-
180	60	280	4.8	39	130	8
220	56	280	5.86	53	173	-

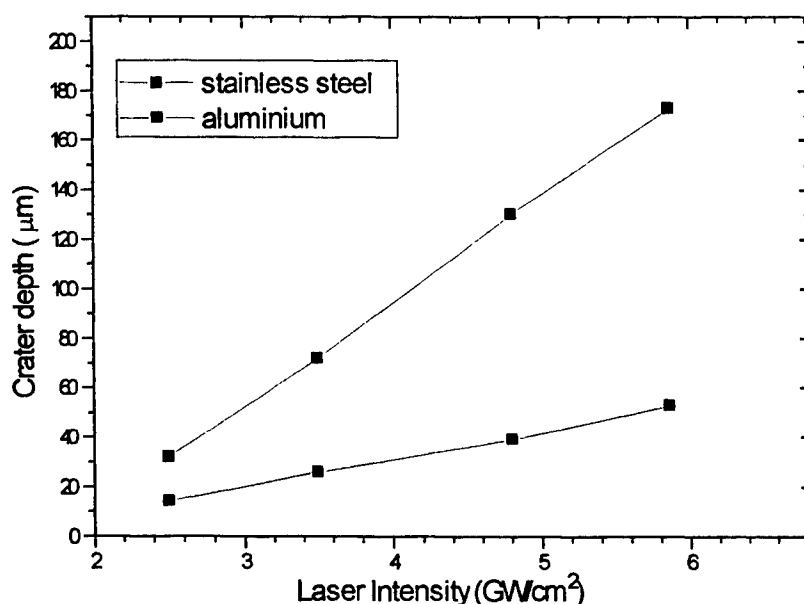


Figure 3. Variation of crater depth in aluminium and stainless steel when irradiated with E-O Q-Switched laser pulses.

Figure 3 presents variation of craters depth obtained with E-O Q-switched pulses vs. Laser intensity. A very good linear fit matched the two plots. Equation 4 from section 2 gives the threshold condition for ablation with laser pulses in ns - μs range. Although the discussion referred at low laser fluencies ($0.1\text{-}10 \text{ J}/\text{cm}^2$) the same relationship can be used for higher fluencies because it is a threshold condition and we can consider that the process is not initiated. As the laser fluency is increased further variations will depend on the dynamics of the process. Assuming an average pulse duration of 60 ns we obtained from the linear fit the threshold fluency for stainless steel $78 \text{ J}/\text{cm}^2$ and for aluminium $108 \text{ J}/\text{cm}^2$.

In the case of long pulse laser (0.5 to 4 ms) when laser intensity ranged from 1 to 4 MW/cm² the effect on metals was small because a small amount of material could be vaporised. However, we were able to obtain grooves with depth in range of 5 to 12 μm with a threshold of 1 to 2.5 MW/cm². When working with short laser pulses an alumina sheet weakly interacts with the laser beam but with long laser pulses it could be textured with non constant depth of the craters. Moreover, it was noticed that for small power densities the process does not always start-up. Figure 4 shows the ignition probability (relative frequency) obtained in our experiments.

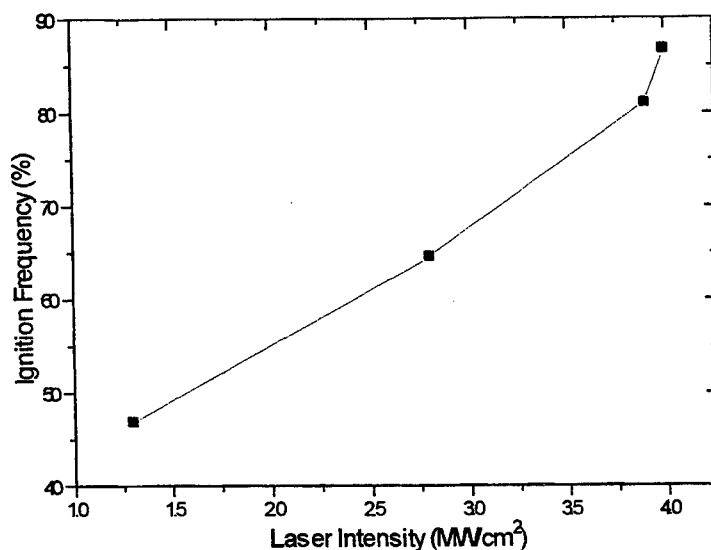


Figure 4. Ignition probability of interaction of an alumina plate with long laser pulses (0.5 to 4ms) vs. laser intensity.

It is believed that such a behaviour comes out from the fact that the laser beam was focused into a spot which is comparable with the dimensions of the domains that dictate the overall reflectivity. Some absorption centers may be located on small areas that are not always "found" by the laser beam. From figure 5 it results that one can expect a good texture if the power density exceeds 4-4.5 MW/cm², while crater depth can be controlled by correlating power density with laser fluency and pulse duration.

4. CONCLUSIONS

Theoretical considerations and experimental results presented in this paper aimed to help in fulfilling the task of surface texturing with Nd:YAG laser. First of all one must start from the requirements of the texture, which will depend on applications of the textured surface. Thus the material and the parameters of the texture to be obtained must be known. Once the texture requirements are set, a certain pattern will be chosen depending on the available laser capabilities (spot geometry and size, correlation of spot size with working regime). Paragraph 2.2 gives an example of computing texture parameters in a common geometry obtained in our experiments. Furthermore the texturing process is not set until the type of material is known. Laser Intensity and pulse duration are practically the most important parameters in the process. Thus it was shown that metallic surfaces will be efficiently textured with short laser pulses (50-70 ns) corresponding to high intensities and a linear dependence was found

between crater depth and power density in this case. Meanwhile ceramic materials like Alumina can be processed with long laser pulses with a laser intensity that exceed 4 MW/cm^2 .

Only when the working regime is known the last parameters of the scan can be set and the process can be started. Sometimes preliminary experiments are required in order to determine the differences between the parameters of the texture calculated ideally and the obtained ones. Experiments on alumina and metallic surfaces showed that a good texture can be obtained using intermediate laser intensities ($0.01\text{-}1 \text{ GW/cm}^2$) with longer laser pulses ($0.1\text{-}200\mu\text{s}$) corresponding to relaxation regime of pulsed laser or A-O (Acusto-Optically) Q-Switched lasers. In this case mathematical models require numerical solving complicated systems of differential equations for predicting crater shape and dimensions.

5. REFERENCES

1. Carsten Momma, Boris Chichkov, Stefan Nolte, "Short-pulse laser ablation of solid targets", *Optics Communications* **129** (1996) 134.
2. A. Kar and J. Mazumder, "Two-dimensional model for material damage due to melting and vaporisation during laser irradiation", *J. Appl. Phys.*, **68** (8), (1990).
3. Ho. K. Tonshoff, M. Sturmee, L. Overmeyer, "Strukturieren technischer Oberflächen mittels Laserstrahlung", *Laser und Optoelectronik* **25**(2) (1993)
4. Echard Meiners, "Mikrostrukturierung von Makrooberflächen Laseranwendungen in der Druckformerherstellung", *Proc. ECLAT'96*, p.663 (1996).

Investigations on $\text{HgBr}_x\text{I}_{2-x}$ using Confocal Laser Scanning Microscopy and X-ray diffraction

G. A. Stanciu*, J.L. Oud**, E.K. Polychroniadis***, Maria Daviti***, Angelia Stanciu****, Catalin Miu*

*University "Politehnica" Bucharest, **University of Amsterdam, ***University Aristotle of Thessaloniki,

****National Institute of Microtechnology.

ABSTRACT

The compound Mercuric Bromoiodide ($\text{HgBr}_x\text{I}_{2-x}$) belongs to the HgI_2 - HgBr_2 system. It is promising for the same applications as HgI_2 , that is as solid state X and γ detector, operating at room temperature since it exhibits a number of properties which are necessary for such applications, i.e. large atomic number, large band gap (2.4-3.4 eV) and high resistivity.

Using a Confocal Laser Scanning Microscope we made some investigations regarding topographical distribution of impurities or related defects. Analysis of chemical composition of $\text{HgBr}_x\text{I}_{2-x}$ crystals were performed on a SEM model Phillips 515 equipped with Energy Dispersive X-ray Analysis (EDAX).

Keywords: semiconductors, detectors, confocal microscopy, X-ray diffraction

1. INTRODUCTION

The compound Mercuric Bromoiodide ($\text{HgBr}_x\text{I}_{2-x}$) belongs to the HgI_2 - HgBr_2 system crystallizes in the orthorhombic system with space group C_{2v}^{12} and lattice parameters $a=7.716$ Å, $b=13.106$ and $c=6.044$ Å¹. It is promising for the same applications as HgI_2 , that is as X and γ -ray solid state radiation detector, operating at room temperature² since it exhibits a number of properties which are necessary for such applications, i.e. large atomic number, large bandgap (2.8 eV) and high resistivity (10^{12} $\Omega\cdot\text{cm}$). It is reported in literature that it can be grown from solution, from the vapour phase and from the melt.

The ability to control the distribution of impurities in grown materials depends on which methods we measure the appropriate variable with sufficient sensitivity. The detection of optical inhomogeneities in semiconductors can be easily explained considering the interaction between the electromagnetic radiation and the semiconductor.

A knowledge of the topographical distribution or related defects is equally desirable in order to select materials of uniform optical and consequently electrical properties. The Scanning Laser Infrared Microscopy was designed to observe the spatial distribution of optical inhomogeneities in semiconductors³⁻⁸. This technique insured high speed and high contrast observations in real-time. The main disadvantage of this method was connected with the resolution. That disadvantage was eliminated by using Confocal Laser Scanning Microscope (CLSM), which assures a better resolution⁹⁻¹⁴.

The chemical composition of the samples was determined using a non-destructive method by scanning electron microscopy (SEM) equipped with a X-ray analyzer (EDAX).

Using CSLM and EDAX techniques we investigated several $\text{HgBr}_x\text{I}_{2-x}$ crystals. Using the both techniques we obtained details regarding the homogeneity of the crystals as well as information about chemical composition.

2. MATERIAL AND METHODS.

2.1. Material.

$\text{HgBr}_x\text{I}_{2-x}$ crystals were grown by the vertical moving vapour transport method. The starting material was polycrystalline HgBrI which was prepared by us.

The ampoule containing HgBrI was then placed in a vertical transparent tube furnace in such a way that its whole length was at a temperature $\sim 230^\circ\text{C}$, which is above the melting point of HgBrI ($\sim 190^\circ\text{C}$) but below the melting points of HgI_2 and HgBr_2 . The ampoule was left to this position for 24 hours and then it was pulled up inside the furnace at a rate of 1.5 cm/day, towards the upper cooler part of the furnace. When the upper tip of the ampoule reached a temperature below the melting point of the compound, condensation of the gas phase occurred there and finally a small transparent orange-colored crystal appeared, which grew in size in 1-2 days till all the starting material was deposited. The cooling rate around solidification point was 0.11°C/h . After the crystal was formed, the pulling continued for at least 10 days. The resulting ingot, after cooling at room temperature, was yellow, visually homogeneous and consisted of few large single-crystalline grains. The transparent and yellowish crystals were easily cleaved, so it was easy to obtain single crystalline thin plates with a surface of about 2 cm^2 .

2.2. Methods of investigation.

It is very well known that unlike light microscopy, CSLM allows for higher resolution due to ability to scan images in a single focal plane. The CSLM can record a series of optical sections through relatively thick specimens, that can be individually viewed in two dimensions (2D) or in three dimensions (3D).

In our case the images were acquired through a CSLM Leica (Fig. 1) with a special intermediate tube for laser coupling x/y mirror scanner and detector unit with two independent channels (photomultipliers) for confocal reflection and/or fluorescence microscopy. the system is equipped with an Kr-Ar laser (488nm/514nm), with an output power of 2-50mW, which is used as illuminating source. The detector has a variable pinhole. In our experiments the data have been acquired on the two channels in fluorescence and in reflection.

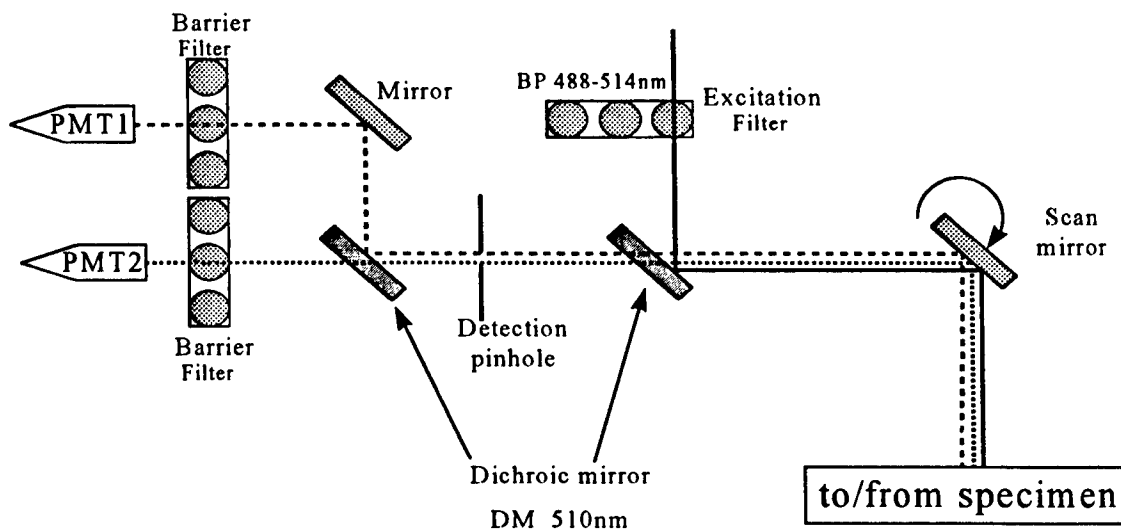


Fig.1. Schematic diagram of Confocal Laser Scanning Microscope

The images were acquired by using a Leica confocal laser scanning microscope (Leica Lasertechnik, Heidelberg, Germany), with a special intermediate tube for laser coupling x/y mirror scanner and a detector unit with two independent channels (photomultipliers) for confocal reflection and/or photoluminescence microscopy. The system is equipped with an Argon-Krypton laser (488 nm/514 nm), with an output power of 2-50 mW, which is used as illuminating source. For investigations based on photoluminescence two filters were used, one for the radiation with $\lambda > 488$ nm and another for photoluminescence radiation having $\lambda > 550$ nm.

The detector has a variable pinhole ($\Phi 20\text{--}500\mu\text{m}$). The small pinhole size offers a better lateral and axial resolution, but also the lower the intensity of the photoluminescence light that reaches the photomultiplier.

In our experiments the data have been acquired on two channels, in photoluminescence and in reflection. The format was 256x256 pixels or 512x512 pixels per slice. To increase the magnification level a variable electronic zooming factor acquisition was used. The original image data set was transferred from the CLSM Leica system to the SPARC station running Open Windows system. Each image of the various sequences was interactively displayed by using a special software.

Analysis of chemical composition of $\text{HgBr}_x\text{I}_{2-x}$ crystals were performed on SEM model Phillips 515 equipped with EDAX.

3. RESULTS AND DISCUSSION

3.1. Compositional analysis.

The chemical composition of the samples was determined using a non-destructive method by scanning electron microscopy (SEM) equipped with an energy dispersive X-ray analyzer (EDAX). The analyses were done on a Phillips Model 505 unit within 1% accuracy. Fig.2 illustrates the EDAX spectrum profile on a sample of. It can be seen the presence of the three peaks assignment to individual elements Hg, Br and I respectively and then an approximate composition can be evaluated from the peak intensity ratios.

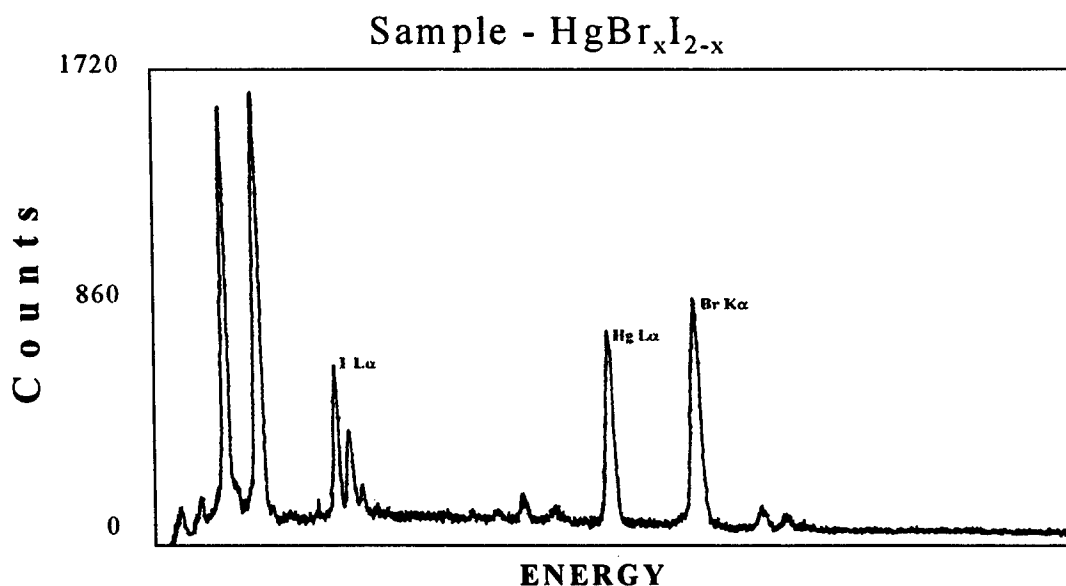


Fig. 2. EDAX analysis on $\text{HgBr}_x\text{I}_{2-x}$ semiconductor

3.2. Investigation by CLSM

The Fig. 3 shows the images obtained by photoluminescence for different penetration depths in the crystal. We used green radiation (514nm) of the Kr-Ar laser. The images represent different sections of the crystal, the distance between two successive sections being of 5 μm . The image 1 represents the crystal surface. It can be observed that in the images 3, 4 and 5 a strong photoluminescence appeared. The three focal planes are placed at 15 μm , 20 μm (fig. 4) and 25 μm under surface. We can conclude that in the bulk of the crystal there is a inhomogeneity in the crystal. Due to the fact that wavelength of the photoluminescence crystal is much more then 550nm we can suppose that the inhomogeneity represent a accumulation of $\text{HgBr}_x\text{I}_{2-x}$, where x next to zero (it is know that HgI_2 have a bandgap of 2,4eV corresponding with a wavelength of 516nm).

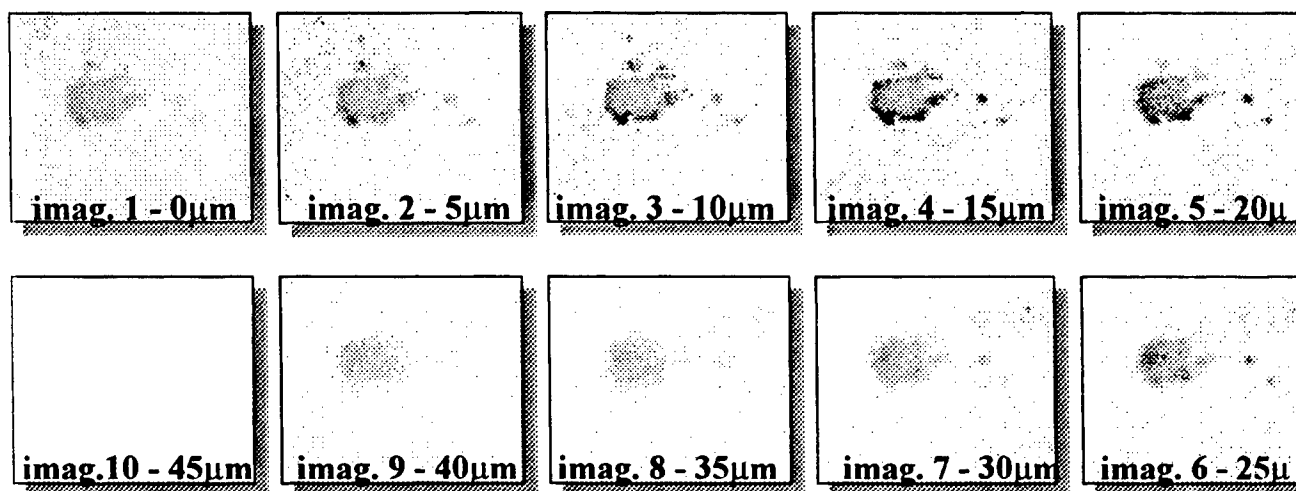


Fig. 3. Confocal images obtained by photoluminescence for different penetration depths

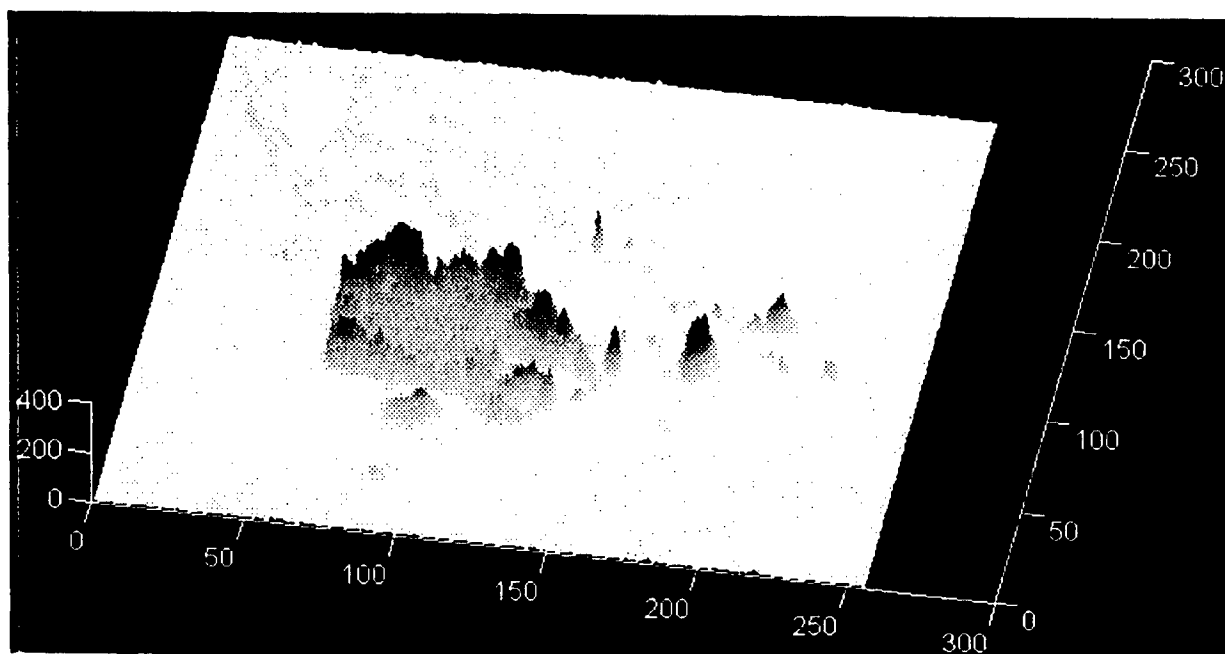


Fig. 4. 3D representation of image 4

4. CONCLUDING REMARKS

Using CLSM we made several non-destructive characterizations of the HgBr₂ crystals. The signal generated by photoluminescence offers a better possibility to know the exact position of the inhomogeneity placed on the surface and in the volume of the crystal as well as the nature of inhomogeneity.

5. ACKNOWLEDGEMENTS

This work has been made possible by the NATO Collaborative Research Grant 960157, Grant #4001 CNSCU, and MCT Research Contract #836.

6. REFERENCES

1. ICDD Powder Diffraction File No:30-835
2. "Semiconductors for Room Temperature Nuclear Applications", Semiconductors and Semimetals, Vol.43, ed.by T.Schlessinger and R. James, Academic Press, N.Y. 1995
3. Jungbluth, E.D., Review of bulk and process-induced defects in GaAs semiconductors, Metallurgical Transactions,1,pp. 575-586,1970.
4. Sherman, B. and Black, J.F., Scanned Laser Infrared Microscope, Appl. Optics,9, pp.802-809, 1970.
5. Gupta, D.C., Sherman, B., Jungbluth, E.D., Black, J.F., Non-destructive semiconductor testing, using scanned laser technique, Solid State Tech., pp. 44-50,1971.
6. Jungbluth, E.D., Metal Trans., Scanning laser infrared imaging of normally opaque pure InAs, Technical GTE Report, TR 71-151.7, 1975.
7. Sherman, B. and Black, J.F., Appl. Optics,9, 802-809 , 1973.
8. Jungbluth, E.D. and Black, J.F., Scanning Laser Infrared microscopy of doping inhomogeneities in InAs single crystals, Solid State Comm., 13, pp.1099-1105, 1973.
9. Minsky M., U.S. Patent #3013467, Microscopy Apparatus (1957).
10. Sheppard, C.J.R., Choudhury, A. Image formation in the scanning microscope, Optica Acta, 24, pp. 1051-1073, 1977
11. McCarthy, J.J., Walker J.S., Scanning confocal optical microscopy, EMSA Bulletin 18(2), 75-79, (1988).
12. Guidotti, D., Batchelder J.S., Van Vechten J.A., Finkel A., Appl. Phys. Lett.48, pp.68 (1986).
13. Wilson, T., Pester, P.D., Analysis of photoluminescence generated in a semi-infinite semiconductor slab by a time-varying focused laser beam, J.Appl.Phys,63, 871-877, 1988.
14. Sah, K.K., Moy, L.M., Zhang, J., Olsner, F., Lund, J.C., Squillante,M.R., Nucl. Instrum. and Meth. A322,509(1992).

ABSTRACT

The selection of the best laser for a given application is a common problem of laser users. However, a direct relationship between laser intrinsic characteristics and a potential application, risks to make the laser source selection process unilateral and partially mistaken. In fact, the best processing technology for a given application must be chosen. Therefore, the present paper proposes an indirect, more realistic selection process. This process starts from a general laser application definition. Then, it passes through the analysis of the needed laser beam - workpiece material interaction and of the necessary laser technological system. Finally, the selection process ends with the laser processing technology definition, where the choice of the most suitable laser source becomes in fact possible.

Keywords: laser sources selection, laser technological systems, material processing

1. INTRODUCTION

Laser material processing is achieved by a specific technological system action. In such action, adequate energetic transformations, induced by laser irradiation, are utilised for accurate accomplishment of some expected physical, chemical and/or geometrical modification of workpiece material and shape.

The performance of the technological action are mainly determined, on the one hand, by the structure and the long time functionality of laser system and, on the other hand, by the workpiece defining features.^{1,2}

In this complex situation, the choice of the best laser source for a given technological application has a primordial importance.

Establishment of a direct relationship between laser intrinsic characteristics and a potential technological application is very difficult and risks to make the laser source choice unilateral and partially mistaken. In fact, the number and the variety of laser selection criteria is very large. These criteria may be intrinsic (relating to the laser oneself) or extrinsic (relating to a laser integrated in a technological system) and also, as in any machine tool system, they can be functional, constructive, technological, economic and ergonomic.

The selection of the best laser for a given application, requires a knowledge of all these (and even other) criteria.

The present paper proposes a laser selection process based on a technological point of view.³ By practical reasons the paper, keeping its generality, refers to the choice of the best laser source for a laser cutting process.

2. LASER SOURCE SELECTION PROCESS

The structure and the functionality of a laser cutting system can be characterised by a lot of elements, factors and parameters (figures 1 and 2).

The fulfilment of material processing objectives imposes the initiation and the upkeep of some well determined interaction phenomena between the laser beam and the workpiece material, in the frame of requirements defined by the general laser application.

The selection and the characterization of these phenomena have in mind both the workpiece initial and final features, as well as the processing technology to be applied.

On this basis it becomes possible to structure the laser technological system, able to materialize the desirable effects and modifications.

A possible logical schema of a laser manufacturing technology design, which implies the choice of the best laser source, incorporable in a new laser cutting system is given in figure 3.

It must be underlined that for a certain application all laser system main components - laser source, optical, mechanical and assist gas systems etc. - are more or less simultaneously involved.

Thus, in the idealized situation in which different laser sources would have the same or near functional parameters, quality and reliability, the main criteria to choose the best one would become those connected to the integration of lasers in a technological system.

Unfortunately, for a long period of time and so far the commercial lasers for material processing were, in fact, incomparable because their main functional features - power, intensity profile, wavelength and temporal mode have been very different. Therefore, an actual selection process of the best laser for a given application was impossible.

The existing situation can be illustrated by data in tables 1 and 2.^{4,5}

Figure 1

Laser system structural elements	
MAIN	PERIPHERICAL
Laser source	Assist material
Beam guiding systems	Workpiece handling
Laser working head	Process control
Workpiece mounting	Optics cooling system
Manipulating system	Optics protection devices
NC control unit	Safety system

From the functional point of view, the most important differences between disposable lasers for material processing concern the laser beam wavelength (which is not or only partially adjustable), the laser mean power (which is passed over ten kW only for the flowing CO₂ lasers) and the operating mode (cw or/and pw).

Only in the last some years, by the important progress in laser physics and engineering, became obvious a convergency trend of above mentioned main functional features for a limited number of representative high power industrial lasers.

Table 1

CHARACTERISTICS	CO ₂	Nd:YAG	DIODE LASER
Power, [kW]	≤ 20	≤ 3	multi - kW
Watts/Lasing Volume [W/cm ³]	1	50	1000
Efficiency [%]	5-10	1-3	30-60
Price/Watt [DM/W]	200-400	300-1000	200-400
Wavelength [μm]	10,6	1,064	0,78-0,83
Voltage [V]	< 10000	< 1000	< 100
Lifetime [h]	10000	10000	20000-100000
Maintenance [h]	each 500	each 200 (lampe)	free
Fiber Delivery	not possible	possible	possible

Figure 2

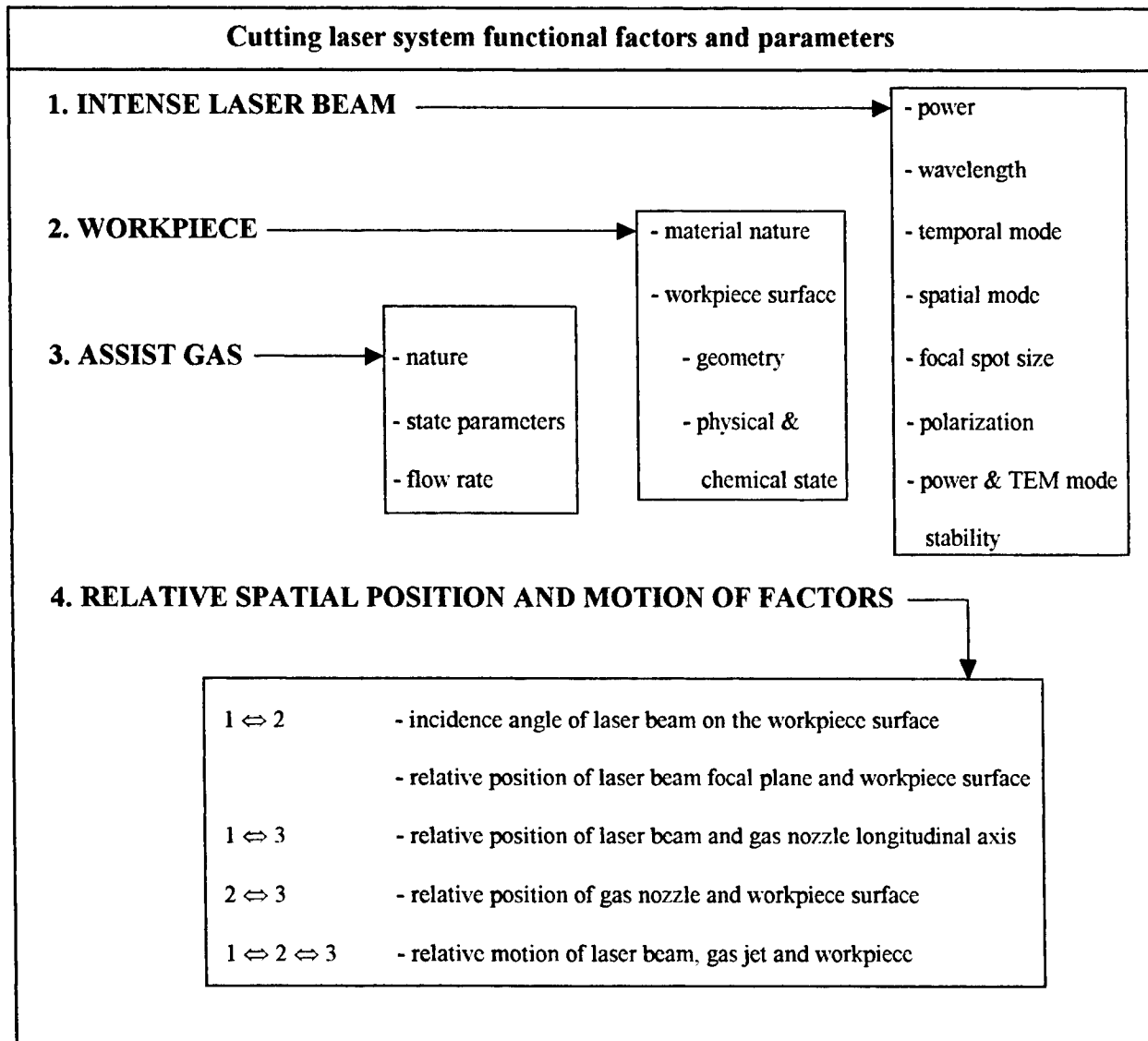


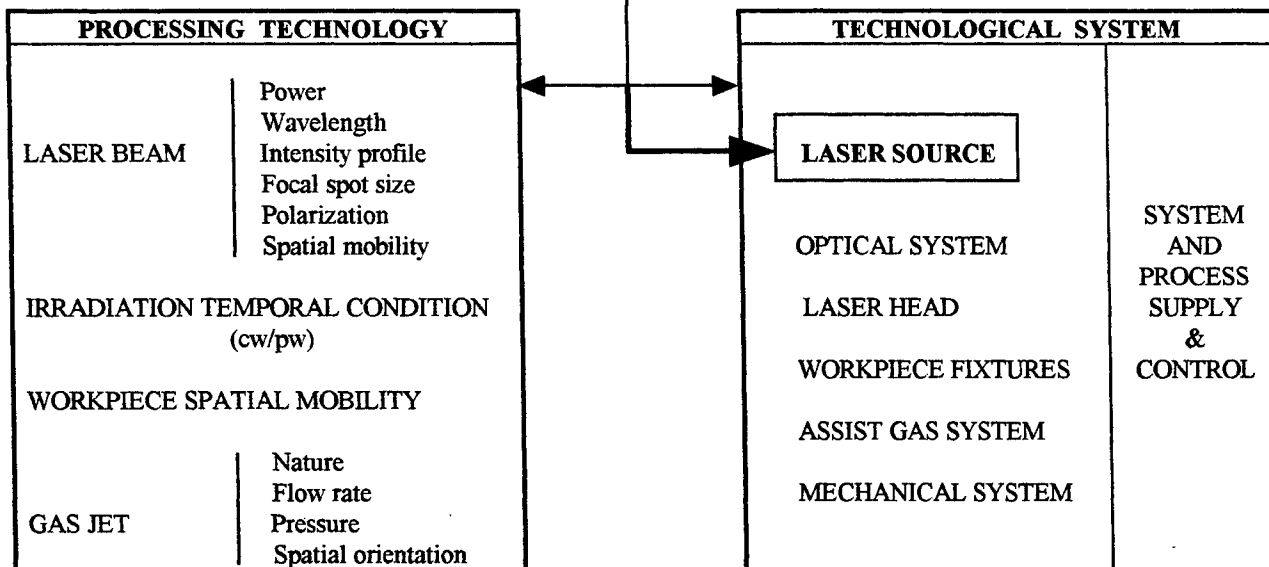
Table 2

CHARACTERISTICS	CO ₂		Nd: YAG		Excimer
	cw	pw	cw	pw	pw
AVERAGE POWER	10 kW	100W	2 kW	20 W	200 W
PEAK POWER	10 kW	100 MW	2 kW	100 MW	40 MW
PULSE DURATION	cw	10 ⁻⁸ s	cw	10 ⁻⁸ s	10 ⁻⁸ s
REPETITION RATE	cw	100 Hz	cw	20 Hz	500 Hz

Figure 3

GENERAL LASER APPLICATION					
MANUFACTURING TYPE		WORKPIECE		IMPOSED TECHNOLOGICAL PERFORMANCES	ADMISSIBLE SPECIFIC COSTS/ CONSUMPTIONS
		MATERIAL	GEOMETRY		
-Job - lot -Batch -Mass	production	-Metal -Ceramics -Plastics -Composite	-Workpiece length, breadth, thickness; - Cutting spatial trajectory	-Kerf's depth and breadth - Kerf's wall quality - Cutting speed/material removal rate	-Equipment -Consumables -Energy -Labour

LASER BEAM - MATERIAL INTERACTION PHENOMENOLOGY			
LASER BEAM-MATERIAL COUPLING PARAMETERS	PHYSICAL & CHEMICAL EFFECTS INDUCED BY IRRADIATION	EXPECTED LASER CUTTING PHYSICAL MECHANISM	THRESHOLD/ OPTIMUM ENERGY ACTIVATION FOR AN EXPECTED TECHNOLOGICAL ACTION
Reflectivity, absorbtivity & thermal properties of material, in given conditions	-Heating -Melting -Vaporization -Ablation -Oxidation -Thermal decomposition -Erosion	-Vaporization -Melting and blowing -Burning in reactive gas -Controlled fracture -Scribing -"Athermal" cutting	-Laser beam intensity/ fluence -Irradiation duration -Linear energy -Gas flow rate & pressure



A such situation (excepting the wavelength) is now specific to industrial CO₂ and Nd:YAG lasers. In this and similar cases, as it was told before, the main laser source selection criteria become the extrinsic ones (for example, those indicated in table 3 for comparison of CO₂ and Nd-YAG laser manufacturing systems).⁶

Table 3

COMBINATION LASER/ HANDLING SYSTEM	Nd: YAG/ ROBOT	CO ₂ / GANTRY
Investment costs	low	high
Running costs (laser)	high	low
Floor space required	less	much
Accuracy	low	high
Beam guiding system	easy	complex
Accessibility	good	bad
Workroom	small	big

Carbon dioxide (CO₂) and solid state (Nd:YAG) lasers retain a preferential status because their power, adjustability, quality of engineering and existing technological information, permitting their large and efficient use.

However, the increasing number of applications, especially in new advanced technologies (semiconductor and microelectronic processing as well as rapid prototyping, desktop manufacturing and micromachining) may require nontraditional laser sources, the most representative being excimer, diode and diode pumped solid state lasers.

The development of such nontraditional laser sources could assure a better matching of output properties of the disposable lasers with the technological, economic and environmental factors of industry. More powerful, smaller, better performing, more efficient, more cost effective and more user-friendly lasers now compete directly in new materials-related processes.

It appears that lasers for material processing have been and are continuing to move towards a today's ideal laser source, characterised by⁷ a high power, a short wavelength, an excellent beam quality, a good optical fiber delivery, a big enough conversion efficiency and a cheap, ecological active medium.

In this context, it is very important to underline the capability of mentioned above new laser sources to run at shorter wavelength (predominant under 1 μm) and to allow, by this way, a higher spatial resolution of laser beam-target interaction. This capability, associated with the high resolution of nowadays imaging systems and precision motion-control devices make possible relatively easy acces to micromanufacturing feature sizes in the 1...100 μm range and even under 1 μm (such feature sizes are typically, by example, to high density ICs manufacturing).

3. CONCLUSION

The selection of a suitable laser source must be carefully matched with:

- the laser source adaptability to the real needs of processing technology, synthetically expressed by an optimum laser beam power/quality rate;
- the laser source capability to achieve, for a given laser power/quality rate and by its own intrinsic characteristics (lasing medium, wavelength, spatial and temporal modes etc.), the best irradiation technology for a considered specific application;

- the laser source parameters stability, the most important condition for the technological effects reproductibility;

- the investment and the running costs of laser source itself and of the laser technological system, incorporating the chosen laser source.

Mentioned above criteria for the choice of a particular laser source are extremely restrictive. A detailed analysis of the actually state in this field, prove the today's very limited number of disposable technological laser types. At same time, a such analysis shows potential significative mutations in the scientific and commercial offer of new technological lasers. These mutations could have a favorable impact on laser processing applications future development.

REFERENCES

1. M. Bass, *Laser materials processing*, chapter 1, North-Holland Publishing Company, New York, 1983.
2. G. Chryssolouris, *Laser machining*, Springer Verlag, New York, 1991.
3. A. Nichici, E. Cicala, "Criterii pentru selectia asistata a laserilor pentru aplicatii tehnologice", *Analele Universitatii din Oradea*, Fasc. Mecanica, pag.527-536, 1992,.
4. E. Beyer, V. Krause, P. Loosen, "Recent developments in new laser systems used for material processing", *Journal de Physique IV*, Colloque C4, vol. 4, pag. C4-13-C4-23, avril,1994.
5. D. Basting, "The Excimer laser - a New Tool for Industrial Material Processing", *Material Processing Technology*, pag. 3-13,1991.
6. M. Geiger, A. Gropp, P. Hoffmann, "Technological comparison of CO₂ - and Nd:YAG - laser manufacturing systems", *Laser Applications in Automotive Industry*, Proceedings of ISATA'92, pag.511-518,1992.
7. G. Boulon, "Les lasers de puissance de l'avenir", *Laser de puissance et traitements de matériaux*, Chap.8, pag.153-174, 1991

Effects of the UV laser radiation on the surface defects of the NiO catalysts.

E. Ivana, V. Lăcătușu, M. Chehu, M. Craiu, C. Fenic*, A. Stratan*, L. Nistor**, C. Ghica**, P. Mărginean***

Institute of Physical Chemistry, Spl. Independentei 202, 77208 Bucharest, Romania

*National Institute for Laser, Plasma and Radiation Physics, Bucharest, Romania.

**National Institute for Materials Science, Bucharest, Romania.

***Institute of Isotopic and Molecular Technology, Cluj-Napoca, Romania.

ABSTRACT

NiO is a metal-deficient p-type semiconductor with surface defects which are correlated with the non-stoichiometry. The dissociative H₂ adsorption on the NiO surface takes place on oxygen-excess sites (over equilibrium). The H₂ TPD spectra vary significantly with calcination temperature (stoichiometry) and chemical treatment. UV laser radiation enhances H₂ adsorption on the defective surfaces (non-stoichiometric) as compared with the stoichiometric ones, even chemically treated.

The fourth harmonic (FH) of a Q-switched Nd:YAG laser is used for the NiO samples irradiation. The wavelength of the UV laser radiation is 266nm, under the band-gap of the semiconductor.

Keywords: NiO, nonstoichiometry, surface defects, H₂ adsorption, UV radiation, Nd:YAG laser.

1. INTRODUCTION

In the future, the requirements of reducing the greenhouse effect could be met by a technology based upon the photocatalytic hydrogenation of CO₂ on semiconductor oxides. The effectiveness of the reaction at room temperature, is increased by UV irradiation of the catalyst surface¹⁻³.

The degree of non-stoichiometry of NiO is an important factor in controlling its adsorptive and catalytic properties. NiO is a metal-deficient p-type semiconductor with cation vacancies and electron holes as the primary lattice point defects which are correlated with the non-stoichiometry⁴⁻⁹. The pretreatment of the oxide (thermal and chemical) induces differences in the stoichiometry and surface perfection.

The purpose of this study is to reveal the effect of UV laser radiation on the defects at the semiconductor oxide surface, as reflected by changes in the TPD spectra following the adsorption of H₂ molecules. This way, the H₂ TPD spectra are a relevant tool of investigation of the different types of NiO defects.

2. EXPERIMENTAL

NiO samples and chemically treated NiO samples, calcinated at different temperatures have been studied. The preparation condition and the characteristics of the samples are given in the Table.1.

Table 1. The preparation conditions and samples characteristics

Sample	Preparation conditions			Characteristics	
	precursor	calcination temperature (°C)	calcination duration (h)	Crystallite size (TEM) (nm)	BET surface (m ² /g)
NiO ₄₅₀	Ni(OH) ₂	450	6	30	38.4
NiO ₉₀₀	NiO ₄₅₀	900	6	299	0.96
NiO ₁₂₀₀	NiO ₉₀₀	1200	6	700	0.15
NiO ₉₀₀ *	NiO ₄₅₀	900	6	294	1.14
NiO ₁₂₀₀ *	NiO ₉₀₀	1200	6	~700	0.19

* chemically treated sample

The chemical treatment consisted in 1N HNO_3 washing at 60°C , for 25,5h, for the NiO_{900} sample, and 50h for the NiO_{1200} sample, respectively. After the washing, the samples were dried at 120°C , for 4h and subsequently calcinated at 400°C , in air, for 1h. By chemical washing, $2,3 \times 10^{-4}$ moles Ni/1g NiO_{900} are dissolved, in the case of NiO_{900} sample and $0,32 \times 10^{-4}$ moles Ni/1g NiO_{1200} , in the case of NiO_{1200} sample, respectively.

The experimental methods used in this work: Transmission Electron Microscopy (TEM), Brunauer-Emmett-Teller method (BET), Temperature Programmed Desorption (TPD), Temperature Programmed Reduction (TPR) have been described previously¹⁰. UV irradiation of the samples was performed with the fourth harmonic of a Q-switched Nd:YAG laser, operating in oscillator-amplificator configuration. The laser oscillator with dynamic stable resonator is electrooptically Q-switched by a longitudinal electrooptic modulator. The SHG is obtained with a KTP II crystal. The fourth harmonic (266nm) is obtained with a 27mm long ADP I quadrupler. The 4H beam is separated from the fundamental and SH beams with two fused silica prism transparent in UV range. The UV laser beam, passing a quartz beam splitter and a divergent quartz lens, is deflected by a silver mirror on the quartz cell containing the semiconductor sample. This is the same quartz cell used for the adsorption-desorption experiments. For irradiation uniformity, the sample, in powder form, was stirred after a number of laser pulses and rearranged to fit the same area. The irradiated area is marked by a rectangular diaphragm centred on the laser beam. The beam deflected by the beam-splitter is registered with a calibrated pyroelectric detector in order to count the irradiated energy on the sample surface. The overall energy on the cell surface is about 500mJ, the same for every sample, accumulated from the laser pulse train. The UV laser wavelength is under the band gap of the material (3,8eV).

3.RESULTS AND DISCUSSION

The TEM images of some NiO samples are presented in fig. 1. The corresponding electron diffraction patterns are given in the insets. For the NiO_{450} sample, it shows the characteristic ring of a face centred cubic structure (fig. 1a). The dimensions of the NiO_{450} particles are very small, 30nm on average, giving rise to a very large access surface for the adsorbed gases, namely $38,4 \text{ m}^2/\text{g}$, as measured by BET. The TEM images of the NiO_{900} samples (untreated and chemically treated), in the figs.1b and 1c reveal the presence of the crystallites which are 10 times larger than those of the NiO_{450} sample. This fact corresponds to the reduction of the BET surfaces, as compared to NiO_{450} sample. But, the number of the crystallinity defects is increased by the chemical treatment and also, an increase of the BET surface is noticed for the NiO_{900} and NiO_{1200} chemically treated samples (Table1).

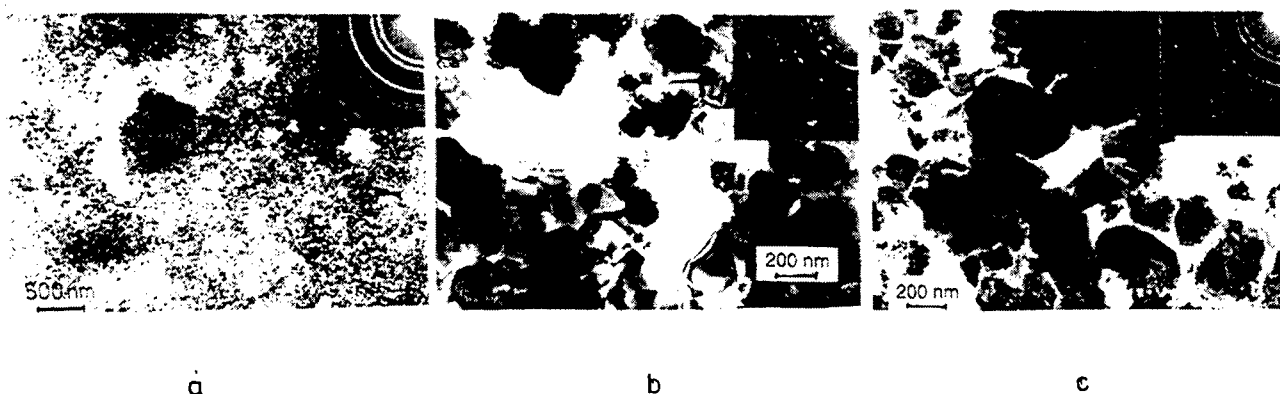


Fig.1 TEM images and electron diffraction patterns (inset) for the NiO samples: (a) NiO_{450} ; (b) NiO_{900} untreated; (c) NiO_{900} chemically treated.

The H_2 adsorption on NiO samples has been performed as mentioned in the reference 10. The desorption spectra after H_2 exposure, from room temperature to 450°C , for NiO_{450} , and from room temperature to 700°C , for NiO_{900} and NiO_{1200} are given in figs. 2 and 3. The TPD spectra of the NiO_{450} samples, both non-irradiated and irradiated, exhibit four very well

resolved peaks, I-IV, with maxima located at 120°C, 210°C, 300°C and 380°C (fig. 2a, b). The UV radiation enhances the intensity of the peaks II and III by ~ 100%, but has no influence on peaks I and IV. A three peaks structure spectra are obtained for the NiO_{900} samples, untreated (fig. 2c) and chemically treated (fig. 2d), with maxima at 120°C, 250-275°C and 450°C. The desorption amounts are about two times larger for the chemically treated NiO_{900} sample, in the second and third peaks, than for the untreated sample. The TPD spectra of the NiO_{1200} samples, untreated and treated, show no peaks in the temperature domain 0-400°C. One important peak, at 450°C is obtained for both samples, slightly increased for the chemically treated one. The UV radiation has no influence on the TPD spectra obtained after room temperature H_2 adsorption on these samples (fig. 2c, d).

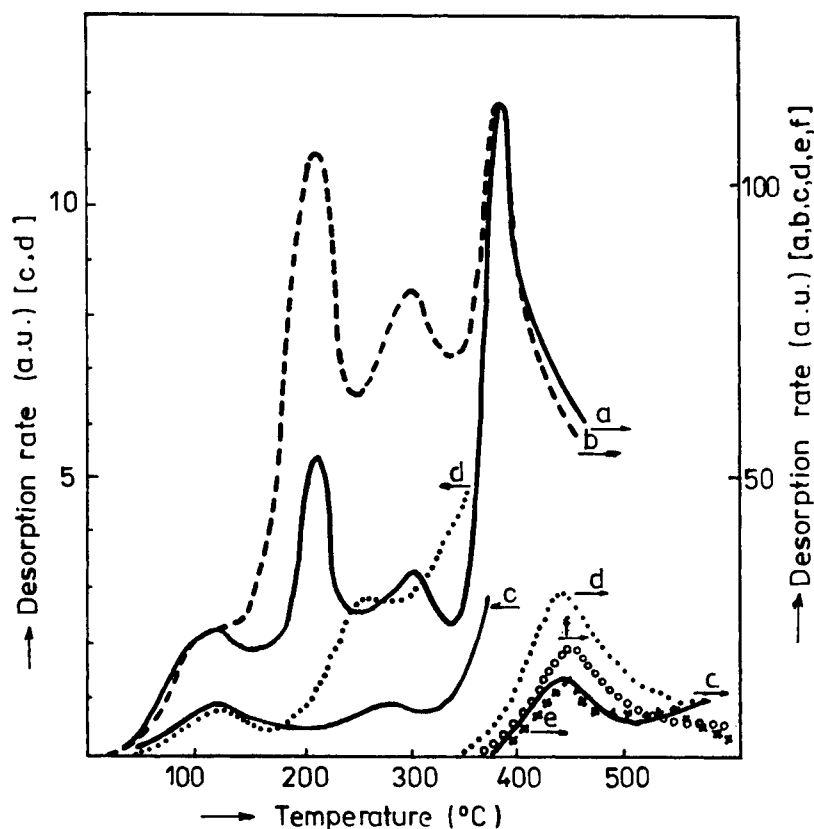


Fig.2 TPD spectra after room temperature H_2 adsorption on the NiO samples: (a) NiO_{450} , non-irradiated; (b) NiO_{450} sample, irradiated; (c) NiO_{900} sample, untreated; (d) NiO_{900} sample, chemically treated; (e) NiO_{1200} sample, untreated; (f) NiO_{1200} sample, chemically treated.

A second room temperature H_2 adsorption is performed on all the mentioned samples, in the same conditions, after cooling to room temperature, with no laser irradiation (fig. 3). A general characteristic of the resulted TPD spectra is the reduction of the peaks intensities and the disappearance of the 200°C peak. In the resulting TPD spectra of the NiO_{450} sample, only peaks I and III are present, but diminished by a factor of ~10. Also, peak III for the previously irradiated sample, is still higher than the peak III for the non-irradiated NiO_{450} sample. The 450 peak in the TPD spectra of NiO_{900} and NiO_{1200} samples diminishes by a factor of ~2 for the chemically treated sample (fig. 3d, e), and the 250°C peak is practically absent in the TPD spectrum of the NiO_{900} treated sample (fig. 3d).

Additional experiments were carried out on a non-irradiated NiO_{450} fresh sample. The sample is Temperature Programmed Degassed (TPDeg) in vacuum, from room temperature to 450°C , and a four peaks spectrum is obtained (not shown), with maxima at 100°C , 210°C , 300°C and 365°C . The subsequent TPDegassings reveal the complete disappearance of the 100°C and 210°C peaks and the presence of the 300°C peak, which diminishes more and more, after each TPDegassing. The H_2 consumption ratio obtained from the TPR data for NiO_{900} chemically treated and NiO_{900} untreated samples is 1,08. The TPR experiments have been carried out on dehydroxylated surfaces.

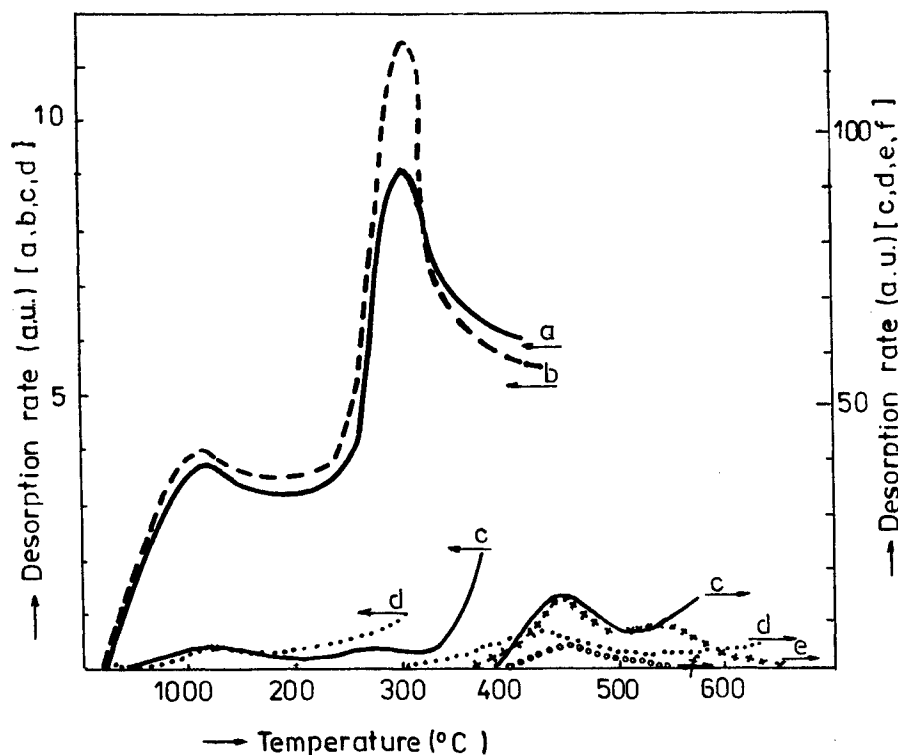


Fig.3 TPD spectra after the second room temperature H_2 adsorption on the NiO samples: (a) NiO_{450} sample, non-irradiated previously; (b) NiO_{450} sample, irradiated previously; (c) NiO_{900} sample, untreated; (d) NiO_{900} sample, chemically treated; (e) NiO_{1200} sample, untreated; (f) NiO_{1200} sample, chemically treated.

Oxides surfaces are generally hydroxylated to varying degrees, even for the oxides calcinated over 1000°C , due to the dissociative adsorption of ambient H_2O ^{11,12}. Upon heating in vacuum, the oxides typically dehydroxylate over a range of temperatures as a function of site heterogeneity and the relative proximity of adjacent hydroxyl groups. Smart and Roberts¹¹ consider that hydroxylation of surface oxide ions occurs at defect sites (e.g. sites with less than five-fold coordination) and that the dehydroxylation, after heating the oxide in vacuum, leaves O^- species and Ni vacancies at the surface. The concentration of such sites is greatly increased from the NiO calcinated at high temperatures surfaces to those calcinated at lower temperatures. Langell and Nassir¹², in their X-ray Photoelectron Spectroscopy (XPS) study, attribute the hydroxylation of the NiO surface to hydroxyls adsorbed at regular surface Ni^{2+} lattice sites. The dehydroxylation, as evidenced by the substantial decrease of the hydroxyl $\text{O}1\text{s}$ peak ($531,2\text{eV}$) in the XPS spectrum, is almost completed until 330°C . The oxide peak ($529,4\text{eV}$) also decreases in intensity as the substrate is heated, with the effect being most pronounced for substrate temperature 330°C . However, the hydroxyl peak decreases in intensity more rapidly than does the oxide peak as the substrate is heated to higher temperatures. Cooling the surface to room temperature does not

regenerate the 531,2eV hydroxyl peak and only causes a slight increase of the 529,4eV NiO lattice oxygen peak. Thus, the decrease in O 1s intensity represents a permanent loss in near-surface oxygen.

The behaviour of peak II in the TPD spectra (fig. 2a, b) and in the TPDeg (as described) of the NiO_{450} sample is consistent with these results. The H_2 adsorption on the corresponding surface sites is strongly influenced by UV radiation, but completely disappears in the second TPD run (fig. 3a). It is possible that this species, as indicated by the High Resolution Electron Loss Spectroscopy (HREELS), possesses substantial ionic character and is singly coordinated to a Ni^{2+} surface site and it is primarily in an atop, non-hydrogen bonding configuration¹². It looks like this OH adsorption confers to the Ni^{2+} sites, on the nonstoichiometric NiO_{450} surface, some Ni^{3+} character and that explains the enhancement of H_2 adsorption under UV irradiation.

The peak III in the TPD spectra of NiO_{450} sample (fig. 2b), which also shows an important increase due to UV irradiation, is still present in the second TPD spectrum (fig. 3b), indicating a remanent effect of UV irradiation. Its intensity decreases in the subsequent TPDegassings and we believe that it is correlated with the presence of the $|\text{O}^-, \text{Ni}^{3+}|$ nonstoichiometry defects as suggested by previous results¹⁰⁻¹³. The nature of the peak IV, considered to be due to the leaving of residual OH upon heating, and that of the peak I, has been commented elsewhere¹⁰.

The TPD spectra of the higher nonstoichiometry samples, NiO_{900} and NiO_{1200} , (fig. 2 and 3) change significantly after the chemical treatment. On the untreated samples the H_2 adsorption leads to the increase of stoichiometry¹⁰. Hydrogen adsorbs on the surface of chemically treated samples on the same low-coordination sites (450°C peak), but the desorbed amounts are ~2 times higher. The presence of a second peak at some lower temperature for the chemically treated NiO_{900} sample than for the untreated one (fig. 2c, d) is due to the presence of a small amount of NiO_{400} as a result of calcination at 400°C, after chemical attack. This NiO_{400} is in a too small amount in the sample NiO_{1200} to manifest itself in the TPD spectrum. The increase of the desorbed amount in the 450°C peak, for both chemically treated samples, NiO_{900} and NiO_{1200} , in the first TPD run, suggests that more low-coordination sites exist on the surface, which are revealed and even created by the chemical attack, producing more crystallinity defects. The H_2 adsorption on these sites is not affected by UV irradiation. This fact is in accordance with the TEM results (fig. 1b, c), BET data (tab.1) and H_2 consumption from TPR data. The ratio of the 450°C peak intensities for NiO_{900} chemically treated sample and the untreated one (fig. 2 d, c) is higher than the corresponding BET surfaces ratio, because the chemical attack does not create a number of low-coordination sites proportionally with their surface increase. The dissolved Ni amounts and the duration of the chemical attack are in accordance with the results of Jones and all.¹⁴ and shows that the phenomenon is more accelerated for the NiO_{900} sample than for the NiO_{1200} sample. It proves that, on the NiO_{900} sample surface the number of low-coordination are higher than on the surface of NiO_{1200} sample. This fact is in agreement with the TPD results (450°C peaks in fig. 2d, f).

The defective NiO surfaces are active surfaces for gases adsorption and chemical reactions. UV radiation is an effective factor in discerning between the two types of defects of NiO samples: nonstoichiometry (over equilibrium) surface defects and crystallinity defects. UV irradiation strongly enhances the H_2 adsorption on the nonstoichiometry (over equilibrium) surface defects, but does not influence the crystallinity defects (low-coordination sites).

4. ACKNOWLEDGEMENTS

The authors are grateful to Mr. Valeriu Paunescu for assistance in sample preparation.

5. REFERENCES

1. K. Ogura, M. Kawano and D. Adachi, "Dark catalytic reduction of CO_2 over photopretreated NiO/Ksgr catalyst", *J. Molec. Catal.*, **72**, 173-179, (1992).
2. H. Yamashita, N. Kamada, H. He, K. Tanaka, S. Ehara and M. Anpo, "Reduction of CO_2 with H_2O on $\text{TiO}_2(100)$ and $\text{TiO}_2(110)$ single crystals under UV irradiation", *Chem. Lett.*, 855-858, (1994).
3. S. Ichigawa and R. Doi, "Hydrogen production from water and conversion of carbon dioxide to useful chemicals by room temperature photoelectrocatalysis", *Proceedings of the First World Conf. "Environmental Catalysis"*, Pisa, Italy, pp 179-182, SCI Publisher, Rome, May 1995.
4. A. Boudriss and L.C. Dufour, *Non-stoichiometric compounds surfaces, grain boundaries and structural defects*, pp 311-320, Kluwer Academic Publishers, Dordrecht, 1989.

5. H. B. Charman, R. M. Dell and S. S. Teale, "Chemisorption on metal oxides. Part 1. Nickel oxide", *Trans. Faraday Soc.* **59**, 453-469 (1963).
6. W. Carrillo-Cabrera and D. J. Smith, "HRTEM study of the surface and bulk of nickel oxide: Influence of annealing and quenching", *Solid State Ionics*, **32/33**, 749-758 (1989).
7. E. R. S. Winter, "Adsorption upon pure and lithium-doped nickel oxide. I. Oxygen", *J. Catal.*, **6**, 35-49 (1966).
8. B. De Rosa and L. C. Dufour, "Nickel monoxide-oxygen interaction between 20 and 1000°C and its impact on the nickel monoxide reduction mechanism", *Reactivity of Solids*, **4**, 53-72 (1987).
9. B. De Rosa and L. C. Dufour, *Physical chemistry of the solid state: Application to metals and their compounds*, pp 37-45, Elsevier Science Publishers B.V., Amsterdam, 1984.
10. E. Ivana, V. Lacatusu, M. Craiu, M. Chelu, C. Fenic, R. Dabu, A. Stratan, L. Nistor, D. Dragulinescu, I. Chis, P. Marginean, "Laser enhanced H₂ chemisorption on Ni_{1-y}O catalysts for CO₂ reduction", *Appl. Surf. Sci.*, **106**, 198-204 (1996).
11. M. W. Roberts and R. St. C. Smart, "The defect structure of nickel oxide surfaces as revealed by Photoelectron Spectroscopy", *J. Chem. Soc., Faraday Trans. I*, **80**, 2957-2968 (1984).
12. M. A. Langell and M.H. Nassir, "Stabilisation of NiO(111) thin films by surface hydroxyls", *J. Phys. Chem.*, **99**, 4162-4169 (1995).
13. A.R. Gonzáles - Elipe, J.P. Holgado, R. Alvarez and G. Munuera, "Use of factor analysis and XPS to study defective nickel oxide", *J. Phys. Chem.*, **96**, 3080-3086 (1992).
14. C. F. Jones, R. L. Segall, R. St. Smart and P.S. Turner, "Semiconducting oxides. The effect of prior annealing temperature on dissolution kinetics of nickel oxide", *J. Chem. Soc. Faraday Trans. I*, **73**, 1710-1719 (1977).

The modelling of the chalcogenide glasses structures before and after laser illumination,
based on the mass spectroscopy data

A. Andriesh^b, A. Buzdugan^a, V. Dolghier^a, and M. Iovu^b

^aCenter of Metrology, Automation & Scientific Research Work, Academy of Sciences of Moldova,
3/2, Academiei str. MD-2028, Chisinau, Moldova (Rep.)

^bCenter of Optoelectronics, Academy of Sciences of Moldova.

ABSTRACT

In this communication we present the results of computational modelling of molecular units as As_mS_n registered by mass spectrometry in the $As_2S_3:Sn_x$ glasses before and after laser illumination. Using HyperChem Computational Chemistry program we obtained 3D structures, with global minimum energy conformation for following molecules : As_4 (3.47); S_8 (4.44); As_4S_3 (11.87); As_2S_5 (14.36); As_2S_4 (17.62); As_2S_6 (19.11); As_4S_4 (21.88); As_4S_5 (24.98); As_2S_3 (25.81); As_4S_6 (43.13).

The model of the $As_2S_3:Sn_{0.1}$ glasses, using 200 As atoms, 300 S atoms and 10 Sn atoms for computational modeling, is presented too. Such model shows that a tin atom may be bonded in two ways: when the tin atom are common for two rings with 12 atoms and when the tin atom are bonded between the layer of the glassy network. When the tin atom are insert in the network rings for 12 atoms the structural model shows the more compact packing of the atoms.

Keywords: chalcogenide glasses, clusters, doping, mass spectrometry, modelling, structure, thin films,

1. INTRODUCTION

The interaction of radiation with vitreous materials leads to irreversible and reversible changes of atomic and electronic structures. These changes in their term manifest themselves in the experiment through changes of their mechanical, thermal, optical, photoelectrical and other characteristics. Under the radiation the structure of vitreous materials changes, new defects appear, film crystallization or amorphization take place, phase transition or transition from one unstable state to another unstable state are observed¹.

In this paper we suggest that a study of the composition of condensed molecules by means of mass spectrometry may yield complementary information helpful in building structural models of chalcogenide glasses and explaining the mechanism of the photostructural changes in the vitreous semiconductors^{2,3}.

2. EXPERIMENTAL

The alloys of high purity As, S, Se and Sn components were synthesised. Thin films were obtained by thermal deposition in a vacuum on the preliminary cleaned glass substrates and capillaries.

The measurements were made using the MX 1320 mass spectrometer at ionizing electron energy $V=70$ eV and vaporization at about 453K.

The mass spectra of bulk material and thin films is investigated, respectively, with fine grained samples of the initial alloys and the above mentioned capillaries, which were placed into vaporizer. For the illumination the Ar- laser ($\lambda=514$ nm) was used.

Using HyperChem Computational Chemistry program were built the sketch of the molecules and for 3D representation of the molecules measured Bond Distances, Bond Angles, Torsion Angles and Nonbonded Distances. Performing a Single Point Calculation we obtained the total energy of the molecule configurations and the rootmean-square (RMS) gradient of

the current configuration of atoms. By performing a molecular mechanics optimization, using Polak-Ribiere minimization algorithm we obtain 3D structures of the molecules with global minimum energy conformation⁴.

3. RESULTS

More stability forms we obtained for the following molecules :

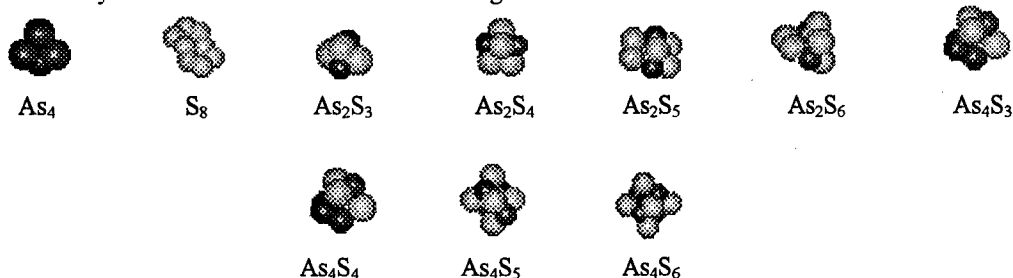


Table 1 gives the results of the mass spectrometric analysis of vaporization from thin films of $As_2S_3:Sn_x$ for $x=0.1$, before and after Ar-laser radiation and the parameters of the molecules such as maximum distances from the atoms, bond angles and the minimum of the potential energy of the molecules.

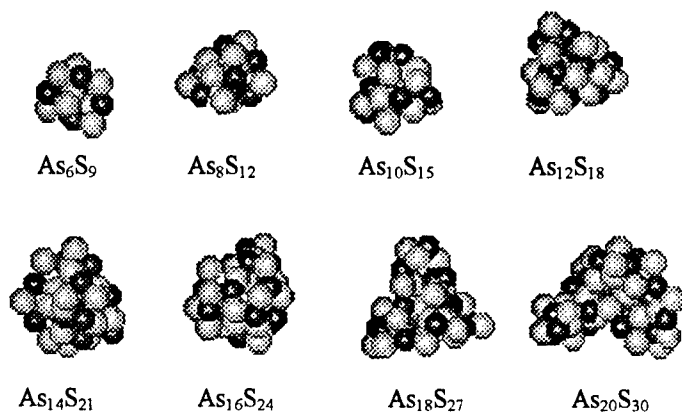
The identification of the species is made according to the relative abundance of the sulphur isotopes they contain. The intensity of peaks were measured with an error of $\sim 10\%$.

Table 1

Molecule	m/z	I Before	I After	Distance from atoms	D(A)	Angle	ϕ_{max}	Energy Kcal/mol
As_4	300	4.5	24.0	As-As-As-As	2.40	As-As-As	60.03	3.47
S_8	256	-	33.0	S-S-S-S	4.29	S-S-S	103.51	4.44
As_2S_3	246	18.0	-	S-As-S	3.01	S-As-S	83.92	25.81
						As-S-As	79.96	
As_2S_4	278	26.0	-	S-As-S-S	3.60	S-As-S	107.12	17.62
						As-S-As	97.69	
						As-S-S	82.30	
As_2S_5	310	7.5	-	S-As-S-S	4.42	S-As-S	107.93	14.36
						As-S-As	84.35	
						As-S-S	95.97	
As_2S_6	342	-	3.0	S-As-S-S	4.24	S-As-S	136.48	19.11
						As-S-S	97.59	
As_4S_3	396	10.5	42.0	S-As-As-S	3.81	S-As-S	125.28	11.87
						As-S-As	93.01	
						As-As-S	110.52	
As_4S_4	428	33.0	21.0	S-As-As-S	4.78	S-As-S	99.47	21.88
						As-S-As	91.21	
						As-As-S	108.52	
As_4S_5	460	21.0	1.0	S-As-As-S	4.99	S-As-S	138.37	24.98
						As-S-As	95.25	
						As-As-S	107.57	
As_4S_6	492	-	-	S-As-S-As-S	5.23	S-As-S	137.32	43.13
						As-S-As	99.09	
SnS	152	-	2					
SnS_2	184	2	-					

The following results are deduced from table 1:

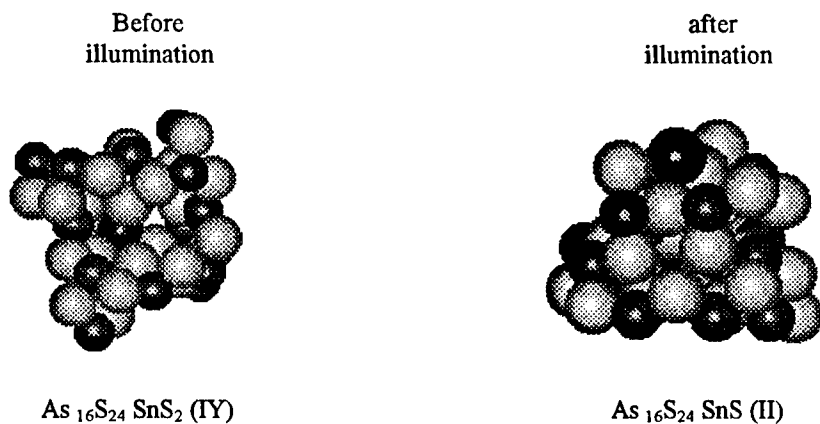
1. The fragments of the form $[As_nS_n]^+$ for the samples before illumination differ from the same after illumination.
 2. After illumination increased the intensities of the peaks, corresponding to the fragments As_n^+ ; S_n^+ ;
 3. Before illumination are registered the fragments of the form SnS_2^+
 4. After illumination didn't registered the fragments SnS_2^+ but are registered the fragments of the forms SnS^+
 5. The bond distances and the bond angles are in correlation with experiments⁵⁻⁷.
 6. The minimum of the potential energy of the molecules are in correlation with the mass spectrometry data.
- The big molecules as $As_{2n}S_{3n}$ were built and calculated.



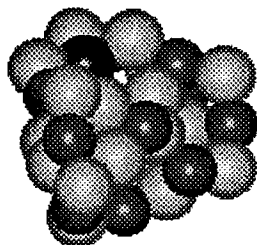
The structure of such molecules contains the rings of 8 and 6 atoms with the angle atoms S-As-S 1180 and As-S-As 1080 . The maximum distance from the atoms is 6 Å for As_6S_9 . It is known that the molecule As_6S_9 was registered experimentally by mass spectrometry⁸.

4. DISCUSSION

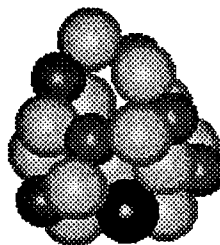
The model of the glassy network for $As_2S_3:Sn_{0.1}$ was built taking into account that the tin atom is four coordinated and is bonded only with the chalcogenide atoms Sn-S. Modeling shows that tin atoms are included in the glasses network in the following modes:



Such clusters are formed when the alloys contain about 2% of tin atoms.



As₁₂S₁₈ SnS₂ (IV)



As₁₂S₁₈ SnS (II)

Such clusters are formed when the alloys contain about 3% of tin atoms.

The distance from tin atoms is maximum 16 Å for As₂S₃:Sn_{0.1} for network. Bond distances in this model are respectively: Sn-S 2.43 Å; As-S 2.22 Å. Bond angles are respectively: S-Sn-S 110°. Such model shows that a tin atom may be bonded in two ways: when the tin atom are common for two rings with 12 atoms and when the tin atom are bonded between the layer of the glassy network. When the tin atom are insert in the network rings for 12 atoms the structural model shows the more compact packing of the atoms.

That behaviour may be connected with the peculiarities of the structure of the As-S and As-S-Sn thin films. So, as a result of photostructural transformation under illumination the tin doping change their valence from IV to II. In the same way the illumination change the coordination number of tin and that make the structure of the doped thin films more stable. That permit us to conclude that the As-S-Sn alloys are more perspective for holographic and optical recording than the chalcogenide glass alloys without tin.

5. CONCLUSIONS

Thus, we conclude that as a result of laser radiation of chalcogenide glasses, the photostructural changes take place at the molecules and clusters level. The molecules transformations are responsible for the irreversible photostructural changes and the clusters transformations are responsible for the reversible photostructural changes.

6. REFERENCES

1. A.M. Andriesh, "Photoinduced phenomena in chalcogenide glass semiconductors", Physics and Applications of Non-Crystalline Semiconductors in Optoelectronics, Edited by Andrei Andriesh and Mario Bertolotti, NATO ASI Series, **36**, 17-30 (1997).
2. V.T. Dolghier, "Mass spectrometric investigation of photostructural changes in chalcogenide glasses", Physics and Applications of Non-Crystalline Semiconductors in Optoelectronics, Edited by Andrei Andriesh and Mario Bertolotti, NATO ASI Series, **36**, 457 (1997).
3. A.A. Popescu, A.I. Buzdugan, V.T. Dolghier, I.I. Vataman, C.M. Indrichian, "Mass spectrometric investigation of the photostructural transformation in As₂B₃Sn_x systems, (B=S, Se), Proceedings of the 8th International conference on Ternary and Multinary Compounds, Kishinev, USSR, **2**, 111-114 (1990)
4. Hypercube, Inc., "HyperChem Computational Chemistry", 1994.
5. M. Popescu, "Medium range order in chalcogenide glasses", Physics and Applications of Non-Crystalline Semiconductors in Optoelectronics, Edited by Andrei Andriesh and Mario Bertolotti, NATO ASI Series, **36**, 215-232 (1997).
6. K. Tanaka, "Stress-induced anisotropy in chalcogenide glasses", J. Non-Cryst. Solids **119**, 254 (1990).
7. J.M. Lee, M.A. Paesler and D.E. Sayers, "Kinetic X-ray absorption studies and computer structural modelling of photo-darkening in amorphous arsenic sulphide", J. Non-Cryst. Solids **123**, 295 (1990).
8. T.P. Martin, "Arsenic sulfide clusters", Solid State Communications, **47**, 111-114, (1983).

Ionic space charge limited currents in natural quartz crystal

Ionut Enculescu and Brandusa Iliescu

National Institute of Materials Physics, 76900 Bucharest-Magurele, PO Box MG-7, Romania

ABSTRACT

Arrhenius plots and current-voltage characteristics were studied for natural quartz samples, in different conditions of air-sweeping time, of temperature, of electrodes (with or without any source of positive ions). Some observations about the influence of the ionic space charge limited current are made. Some dependencies of ionic current versus voltage were found.

1. INTRODUCTION

Transport phenomena in electric field for quartz crystals are strongly related to the punctual defects from the lattice, specially the Al^{3+} substitutional for Si^{4+} and the corresponding monovalent ion compensators (Li^+ , Na^+ , H^+) but also to the channels present in the structure parallel with its optical axis¹.

Studies of conductivity as a function of temperature, electric field, crystallographic orientation and time tried to explain the transport mechanism². Due to the great number of unknown parameters as: other point defects, the strong dependence on time, the influence of the electrodes' material, a general theory was not presented yet.

Four components of the direct current have been suggested to contribute to the electric conductivity of quartz crystals³:

- a) the normal dielectric charging current
- b) the anomalous charging current
- c) the surge current
- d) the steady direct current.

a) The normal dielectric charging current (displacement current) is a result of the capacitor formed by the electrodes. In dc measurements this mechanism is of no practical importance because the relaxation time is of 10^{-2} - 10^{-1} s.

b) The anomalous charging currents are small currents which make their appearance whenever the potential is changed. These currents have a relaxation time of the order of a few minutes and are superposed on the current resulting from other modes of conduction.

c) The surge current (impurity transport current) is the one which constitutes the largest part of the total current for several hundred hours after applying the potential. Upon application of a potential, for the first time at any given temperature, current rises rapidly to a maximum, reaching peak values in less than three minutes. Thereafter, current decreases with passage of time. The decrease is rapid for the first hour, generally to one percent of the initial peak current.

d) The steady state current, the fourth part of the current, becomes manifest only after the disappearance of the short term effects. It is attributed to electrolytic dissociation of the quartz.

Interesting for the applications is the current given by the movement of the impurities because the change of the monovalent impurities, using the possibility of transport along the channels parallel to the optical axis, leads to an important increase in the quality of the crystal (commercially employed and known as "quartz sweeping" process). The study of this type of currents is complicated by the existence of the space charge polarization. This was observed studying the appearance of an anomalous contrast on the X-ray topographies when an electric field is applied on the quartz sample^{4,5}.

The space charge polarization was also observed using the depolarization currents and thermally stimulated depolarization currents^{4,6}. Calamitrou⁴ proved that the blocking activity of both electrodes appears to create the necessary spatial field inhomogeneity which is required to explain through piezoelectricity the reduction in extinction observed by X-ray topography.

In the present paper we report the influence of space charge polarization on the current-voltage characteristics for the case of impurity transport current for natural quartz crystals.

2. EXPERIMENTAL

The specimens employed were natural clear quartz from Brazil, Z-cut, twin free. The dimensions of the samples were $15 \times 15 \times 2 \text{ mm}^3$ and the surfaces were polished.

There were measured current-voltage characteristics, for different temperatures, with the voltage varying between 10-600V and the temperature range 250-500°C. The electrodes used were made of graphite with the surface dimensions of $1 \times 1 \text{ cm}^2$. There were also made measurements with a LiCl layer at the anode as a source of Li^+ ions.

The current voltage characteristics were measured for different air-sweeping times between 1h and 100h in the impurity transport time region. To avoid the errors caused by the anomalous polarization currents, there was a time interval of a few minutes after every change of the applied potential before recording the data.

3. RESULTS AND DISCUSSIONS

In figure 1 the Arrhenius plots after 1 hour of air electrodiffusion are presented in two cases: a) using a positive ions source at the anode (a LiCl layer) and b) without the compensators ion source for different applied voltages. The activation energies calculated for the two cases are equal and do not depend on the applied voltage, their value being 1.1eV.

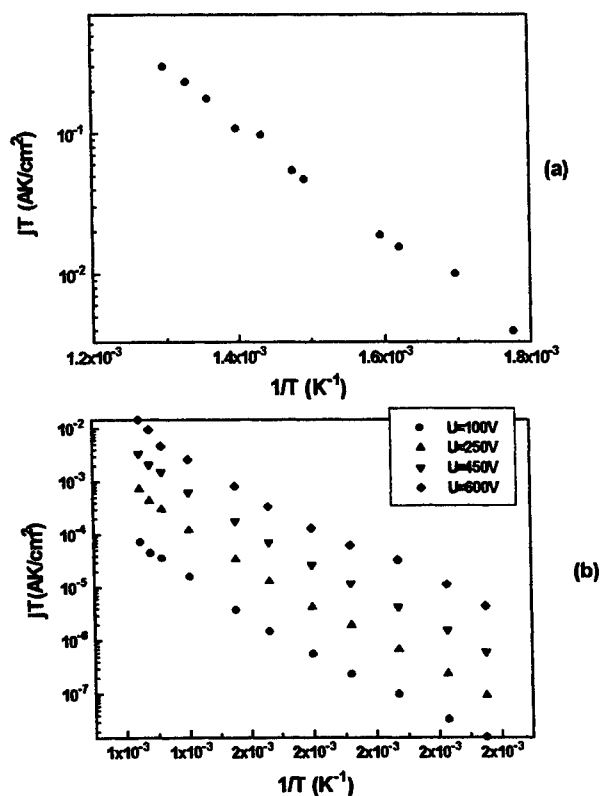


Figure 1. Arrhenius plots of a quartz sample air-swept for an hour: a) with a LiCl layer as a source of Li^+ ions at the anode and b) without any source of positive ions

If for the Arrhenius plots there is no difference between the two cases: with or without positive ions source at the anode, for the current-voltage (I-V) representations the situation is quite different. We have represented in figure 2 the I-V characteristics for the case of LiCl layer present at the anode (figure 2a) and for the case in which the LiCl layer it is not present at the anode (figure 2b and 2c) for different temperatures.

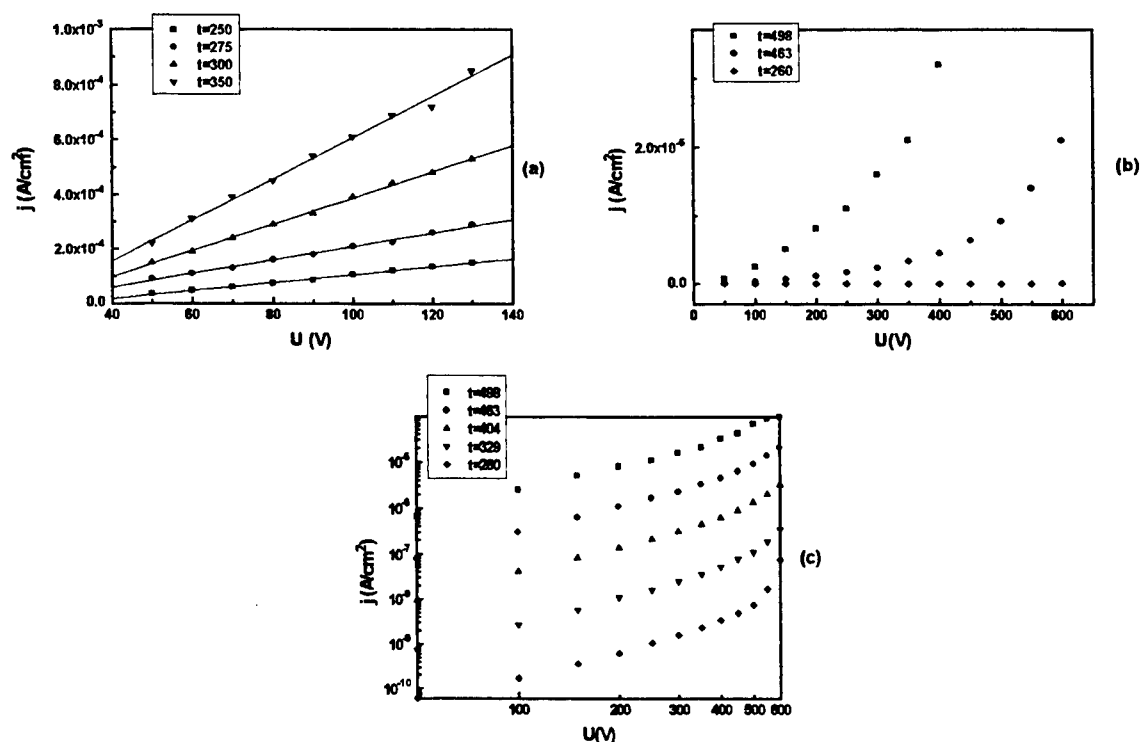


Figure 2. Current-voltage characteristics after 1h sweeping for different temperatures: a) with LiCl at the anode, b) without LiCl at the anode and c) the data from b) in logarithmed coordinates

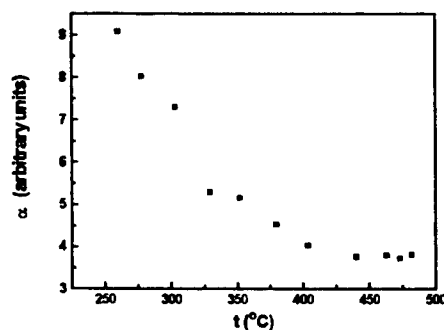


Figure 3. The dependence of α as a function of temperature

One can observe that the characteristics represented in figure 2a) are ohmic and in the second case (figure 2b) the characteristics are no longer linear. Representing these last characteristics in logarithmic coordinates (figure 2c) two types of dependencies of the current with the applied voltage are observed: for voltages under 350 V, the current density $j \sim U^2$ and for the applied voltage higher than 350 V, the current density $j \sim U^\alpha$.

The dependency of α as a function of temperature is represented in figure 3. Fitting the data from figure 3 we have obtained $\alpha \sim 1/t^{3/2}$.

The change of the current-voltage characteristics shape with the time of sweeping for a sample with no positive monovalent ions source at the anode is presented in figure 4.

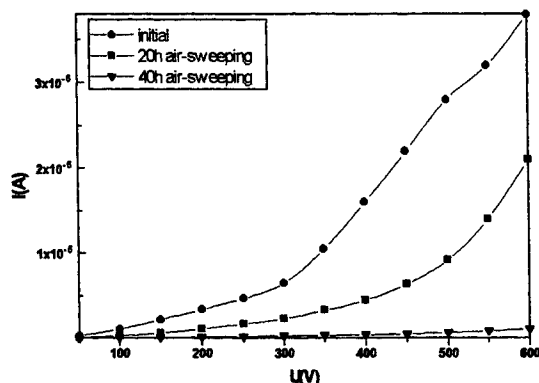


Figure 4. The change of the current voltage characteristics with the sweeping time

It is easy to observe the decrease of the current value with the time of sweeping. In the same time the dependency of the intensity with the applied voltage changes, after 40 hours of sweeping being $I \sim U^{3/2}$; this behavior of the current remains the same till the experiments' end (100 hours). The activation energy calculated from the Arrhenius increases with the time of sweeping, reaching 1.5 eV at 100 hours sweeping.

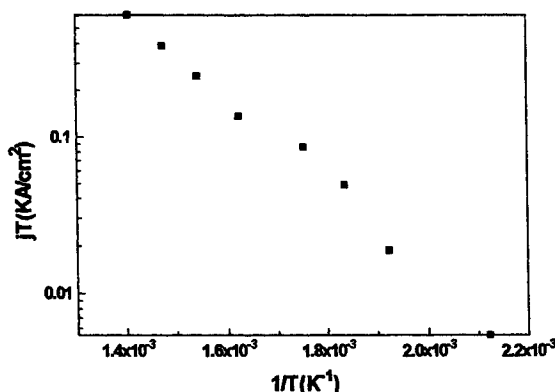


Figure 5. Arrhenius plot for a natural quartz sample 100 hours air-swept

Figure 5 represents the Arrhenius plot for a sample swept for 100 hours without Li^+ source at the anode and measured with a LiCl layer at the anode. The activation energy determined from the slope is 0.44eV, being equal with the migration energy of the Li^+ ion along the structural channels determined by conductivity measurements made on irradiated samples by Nowick and Jain⁷.

All these experimental results allow us to made the following observations:

- The non linearity of the current voltage characteristics in the case of air sweeping (without other monovalent positive ions source at the anode, excepting the hydrogen from the atmosphere) proves the existence of the space charge polarization in the sample.

- The linearity of the current voltage characteristics in the case of a monovalent positive ions source present at the anode proves that the space charge is produced by the unassociated Al^{3+} ions from the anode region (in good concordance with the X-ray topographies observations).

- The evolution of the current voltage characteristics and the change of the activation energy with the time of sweeping lead us to make the following hypothesis: during the sweeping the type of the charge carriers that gives the current is modified. This is in good concordance with the measurements of depolarization currents made by now, where it was proved that at least three types of charge carriers are present.

-The fact that after 100 hours of air-sweeping the activation energy of the Li^+ ions is equal with the migration energy (the term of the dissociation energy of the pair $\text{Al}^{3+}\text{-Li}^+$ disappears) proves that the major part of the charge carriers are not produced by the dissociation reaction $\text{Al}^{3+}\text{-Li}^+ \rightleftharpoons \text{Al}^{3+} + \text{Li}^+$ but by carriers injected from the anode.

4. CONCLUSIONS

The current voltage studies at different temperatures and the conductivity measurements made with or without monovalent ionic sources at the anode permit a better understanding of the conduction mechanism in quartz crystals.

The correlation between the activation energies calculations from the Arrhenius representations and the dependencies of the current intensity with the applied field intensity, crystallographic orientation and time can lead to a general theoretical model for the charge transport phenomena in quartz crystals.

5. REFERENCES

1. J.J. Martin, "Acoustic loss in cultured quartz", *Proc. of IEEE International Frequency Control Symposium*, 170-177, (1996)
2. H. Jain and A.S. Nowick, "Electrical Conductivity of synthetic and natural quartz crystals", *J. Appl. Phys.* **53**(1), 477-484 (1982)
3. H.E. Wenden, "Ionic diffusion and the properties of quartz. I. The direct current resistivity", *Am. Mineral.*, **42**, 859-888 (1957)
4. M. Calamioutou, V. Psicharis, S.E. Filippakis and E. Anastassakis, "Space charge polarisation and extinction reduction in α -quartz", *J. Phys. C: Solid State Phys.* **20**, 5641-5653 (1987)
5. M.T. Sebastian and H. Klapper, "Space-charge polarisation and X-ray diffraction extinction reduction in synthetic and natural quartz crystals", *Phys. Stat. Sol. (b)*, **186**, 341-353 (1994)
6. C. Poignon, G. Jeandel and G. Morlot, "Mobility of ionic impurities in quartz", *J. de Phys. III*, **4**, C2-159-C2-167 (1994)
7. A.S. Nowick and H. Jain, "Electrical conductivity and dielectric loss of quartz crystals before and after irradiation", *J. Appl. Phys.*, **53**, 477-482 (1982)

Compacting of metallic powder by using Nd:YAG laser

A.Marian, D.Buca, T.Dascalu, M.Poterasu

National Institute for Laser Plasma and Radiation Physics
Bucharest PO Box MG36 cod 76900
e_mail: dascalu@roifa.ifa.ro

ABSTRACT

The processes involved in the melting and solidification of powders have been studied, in order to obtain 3D pieces. The experiments have been performed with a CW Nd:YAG laser, but the Q-switched regime has been also used. Measurements about compacting rate for different parameters (scanning speed, thickness of layer) and a comparison between the two regimes have been made.

Keywords: Nd:YAG laser, powder compacting, Q-switch, sintering.

1. INTRODUCTION

The rapid prototyping represents a new and a very useful technique, with a large field of applications. One of the methods of this technique is Selective Laser Sintering (SLS). With this method, using a laser beam, we can build from metallic or nemetallic powders, 3D models of various forms. Mainly, the process consists in the melting and the compacting of successive layers of powder by scanning a laser beam over the powder following a pre-established contour, until the model is completely build. The advantages of SLS are both the short time for building of the 3D pieces and the possibility to obtain complex forms by precise control of the laser beam moving over the powder bed. Nevertheless, the pieces obtained in this mode have not a high density and a very good mechanical resistance. Therefore, for the practical use, the density must be increased by infiltration [1].

There are two methods for compacting the powders by SLS: the direct and the indirect method. In the indirect method, the powder is mixed with a polymer; during the interaction with the laser beam the polymer is melted and the particles of powder will be linked together. The direct method uses the laser beam to interact directly with the powder. Depending on the nature of the powder, we can distinguish the case of multicomponent powder, when the component with the lowest melting point is the liant which links all others particles and the case of unicomponent powder.

By melting, the powder particles tend to link together. Due to superficially forces they form little spheres whose dimensions depend on the melted powder volume, but mainly have the dimension equal with the laser beam spot. These spheres will link each other tangential therefore the prototype has a porous structure (and consequently a low mechanical resistance) and the surface has a frayed aspect. Also, due to nonhomogenous heating during the building process of the piece, mechanical strains will occur which decrease the hardness of the piece [2].

In order to obtain a high density prototype it is necessary that the powder to be completely melt, because, in this case, appear a significant condensation (compacting). Compacting of powders is a very complex process depending of many parameters. Some parameters, (like dimension of powder particles, the kind of material, the debit of powder delivered) are invariable during the process, while other parameters (like laser output power, diameter of laser spot, power density, scanning velocity, the degree

of surface covering) can be varied and controlled during the process. By a really importance is the understanding of the interdependence of all these parameters and the behaviour of the melting. Also, it is necessary to isolate the working zone from the atmospheric oxygen that can cause the apparition of an oxide layer which worse the compacting process. This protection is usually made by using nitrogen or argon.

An other important parameter is the thickness of the powder's layers. By decreasing of this thickness, we can improve the quality of the surface. The first layer is decisive for the building of entire piece. This layer must adhere and link to the underlying substrate, otherwise, due to the instability of the first layer, the particles of next layers are spread. Therefore, we must adopt a special regime (power density, scanning speed) for the first layer of the piece.

2. EXPERIMENTAL

Experiments were performed on an unicomponent metallic (Fe) powder with average radius of $200\text{ }\mu\text{m}$ ($60\text{ }\mu\text{m}$ - $400\text{ }\mu\text{m}$) using a CW pumped Nd:YAG laser. SLS was obtained both in CW and acousto-optically Q-switched laser regime with average power up to 20 W. General schematics of the experimental set-up is shown in figure 1.

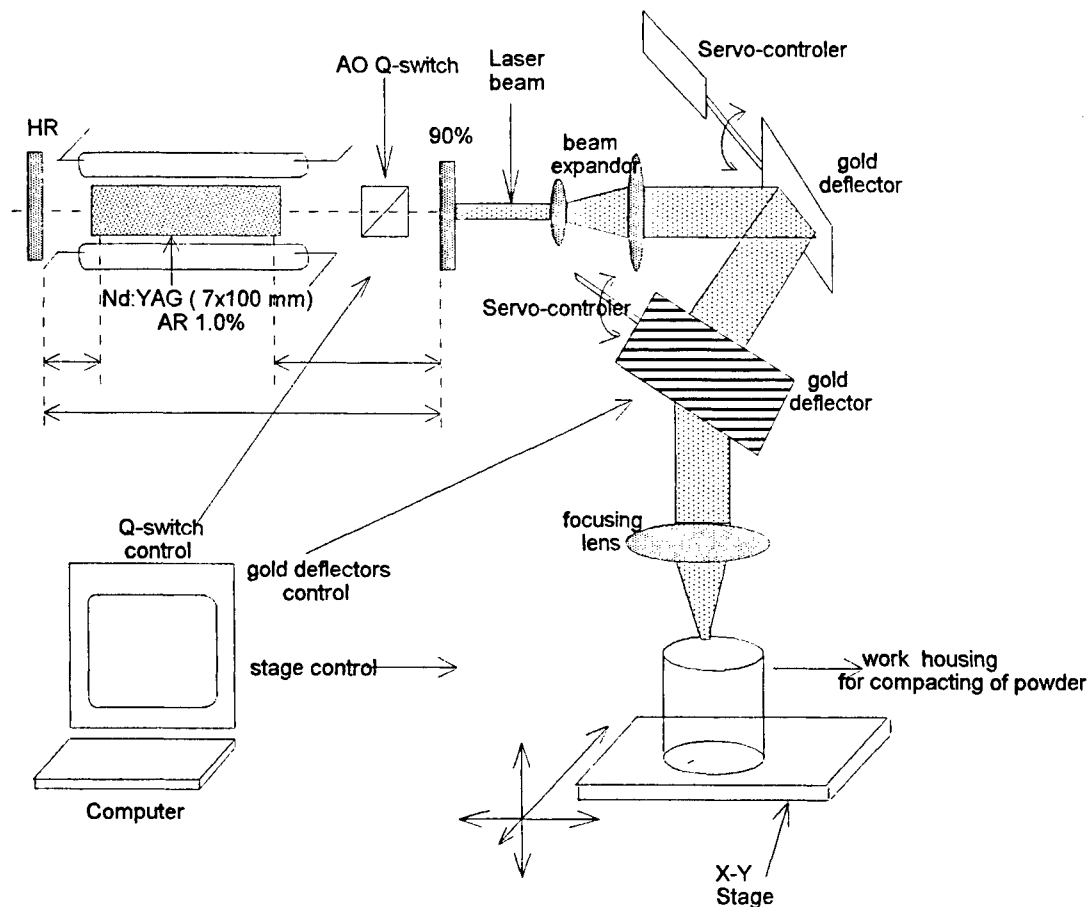


Fig. 1 The experimental set-up

Figure 2 shows the work housing in detail.

In our experiments we used a low speed beam deflections in order to build a 3-D form. The scanning speed was correlated with the laser power, layer thickness and focal spot.

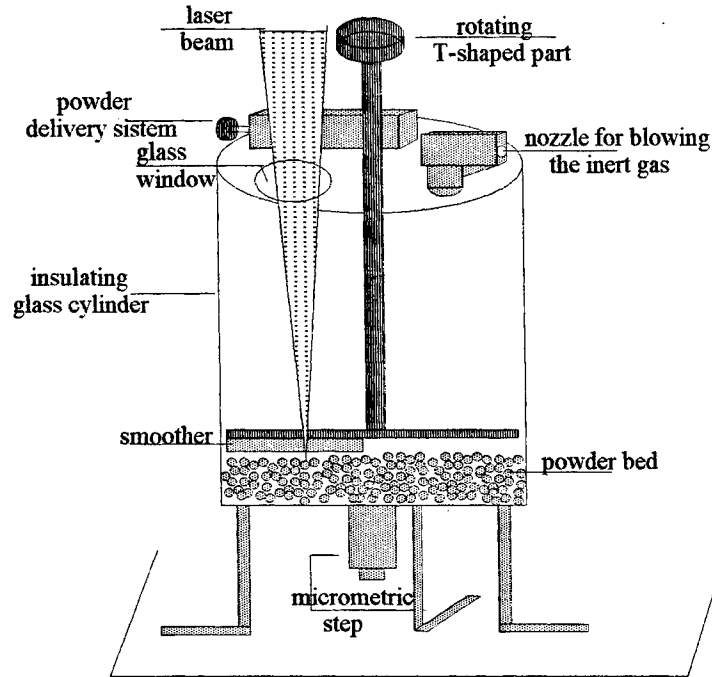


Fig. 2 The experimental device used for compacting the powder

3. RESULTS AND DISCUSSION

Experiments were performed in two stages. The first stage was dedicated to the sintering of the first powder layer. As mentioned, the first layer is partly sintered and partly allied to a tin cover of the substrate. Studying the uniformity of the successive layer the spot size must be a few times larger than average particle size.

Successive layers' thickness was an important parameter from two reasons; first of all, a thick layer would not allow the heat to penetrate till the underlying layer so the joint between layers will be poor. A simple energy conservation law shows that there must be a correlation between scanning speed and the thickness desired. So if the power was maintained constant and the layer thickness increased there had to be a decrease of scanning speed because the energy per unit-time must be larger. From this point of view a simple condition that dictates the scanning speed can be founded.

$$\Delta t = f(P_{laser}, \Delta h, characteristics, prototyping \cdot geometry) \quad (1)$$

$$\Delta t \approx \frac{1}{P_{laser}} \cdot \Delta h \approx const \cdot \frac{\Delta h}{P_{laser} / d_{spot}^2} \quad (2)$$

$$V_x = \frac{dx}{dt} \Rightarrow V_x = const \cdot \frac{P_{laser}}{\Delta h \cdot d_{spot}} \quad (3)$$

where Δt represents the irradiation time, V_x is the scanning speed under x direction, P_{laser} is the average laser power, d_{spot} is the spot diameter on the work piece and Δh is the thickness of the layer.

The threshold condition of SLS is that the interactions time should be long enough enough (Δt) to allow the melting front to penetrate to the underlying compacted powder bed. The constant above depends on the thermal properties and the geometry of material. However, equations 3 shows that because of layer thickness the speed of the process is limited high.

First experiments were performed in order to determine the SLS approximate process parameters. The optimum thickness of the successive layers Δh was establish at 200 μm (the average radius of powder particles). For the scanning speed we studied both CW regime and Q-switched regime. At the same length of the piece (l), the resolution on X-axis $R(x)$ (the number of stops which covers the entire length on X direction) has been varied. Therefore, using simple relations, we can estimate the scanning speed on X-axis, V_x :

$$V_x = \frac{l \cdot f_{stop}}{R(x)} \quad \text{for CW regime} \quad (4)$$

$$V_x = \frac{l \cdot f_{rep}}{R(x) \cdot N_{p/stop}} \quad \text{for Q-switched regime} \quad (5)$$

where f_{stop} is the frequency of stops in CW regime (we divided the CW regime in discrete intervals and so we estimated an average scanning speed), f_{rep} is the frequency of stops in Q-switched regime and $N_{p/stop}$ is the-number of pulses at each stop.

In CW regime we obtained the best results for a scanning speed of 3.3 mm/s ($f_{stop}=30$ Hz, $R(x)=100$). For Q-switched regime the compactation was obtain with discrete X-axe displacement ($f_{rep}=3$ kHz) using 10^3 laser pulses at each stop. In Q-switched regime, with a 0.33 mm/s speed (ten times slower) we obtained similar results. These results consist in a compacting degree (the ratio between the density of compacted piece and the density of the metallic powder) up to 90%.

Pictures of upper surfaces of compacted slabs are shown in figure 3.

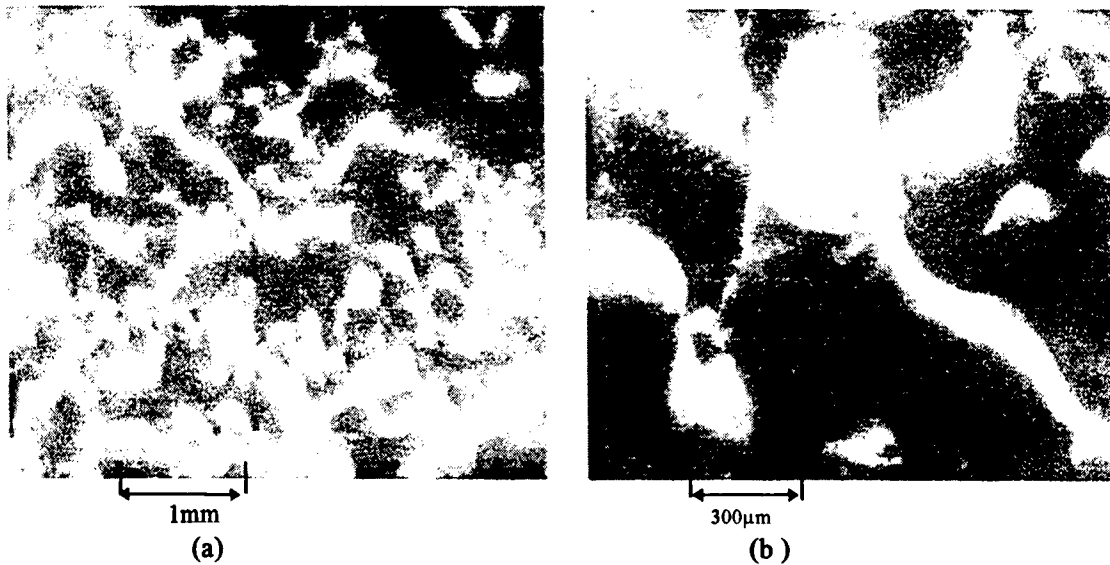


Fig. 3 The structure of upper surfaces of compacted slabs (a). Figure (b) presents a detail

4. CONCLUSIONS

Our experiments proved that the compacting of powder is a very efficiently method for realise in a short time 3-D pieces with various and complex forms.

Experimental results proved that iron powder can be efficiently compacted with Nd:YAG laser in both CW or Q-switched operation modes. It was shown that the compacting speed must be correlated with laser intensity and thickness of the successive powder layers in order to obtain a good compacting in both vertical and horizontal directions. With an CW average power of 20 W the iron powder was compacted at a rate of 15.6 mm³/min.

5. REFERENCES

1. William M. Steen, "Laser Material Processing", Springer Verlag London Limited (1991).
2. W.Meiners, K.Wissenbach, R.Poprawe, Mit Selektivem Laser Sintern zu metallischen Prototypen aus seriennahen Werkstoffen, Proc. ECLAT'96, p.879-886.

Microstructure of hydroxyapatite thin layers grown by pulsed laser deposition

D. Craciun, V. Craciun, C. Martin, and I. N. Mihailescu

Laser Department, National Institute for Laser, Plasma and Radiation Physics, PO Box MG-36, Bucharest V, RO-76900, Romania

M. C. Bunesco, E. Vasile and A. Ioncea

METAV SA, 16-18, Zapada Micilor, Bucharest I, Romania

I. W. Boyd

Electronic and Electrical Engineering, University College London, London WC1E 7JE, United Kingdom

ABSTRACT

Thin films of hydroxyapatite (HAp) have been grown on Si, quartz, Ti, and Ge substrates by the pulsed laser deposition (PLD) method employing a KrF excimer laser (wavelength $\lambda=248$ nm, pulsed duration $\tau_{FWHM}=20$ ns). The influence of the laser deposition parameters on the properties of the grown layers was investigated in order to optimise the Ca/P ratio and the crystalline structure. It was found that the optimum conditions for preserving the Ca/P ratio i.e. high oxygen pressures and low substrate temperatures do not coincide with those for obtaining adherent and crystalline layers i.e. low oxygen pressures and high substrate temperatures. For films deposited onto Ti substrates it was also found that high substrate temperatures promote the diffusion of Ti through the depositing film up to the surface where it gets oxidised. Further investigations are required before high quality HAp-coated Ti implants by PLD can be obtained.

KEY WORDS: hydroxyapatite, pulsed laser deposition, thin films, Fourier transform IR spectroscopy

1. INTRODUCTION

The use of bioceramic materials for orthopaedic devices is hampered by their low tensile strength. Metals, which possess superior mechanical properties are, however, corroded by the body fluids, causing irritation or inflammation. Another problem is the poor attachment of bone to the metallic parts. The solution to these problems is to coat the metallic parts with a bioceramic material which will both protect the protease from body fluids and promote bony ingrowth. Amongst the calcium phosphate-based bioceramics, calcium hydroxyapatite, $\text{Ca}_{10}(\text{PO}_4)_6(\text{OH})_2$ (HAp), is the closest to the natural bone composition and therefore, extremely biocompatible. Crystalline HAp has been reported to be the most stable form of calcium phosphate in contact with the body fluids, with amorphous HAp and β -tri-calcium phosphate being less stable and more readily resorbed by the body. Being such a complex molecule, the growth of thin films of HAp by plasma or thermal spraying, rf-sputtering, or hydrothermal methods proved to be rather difficult.

Recently, the pulsed laser deposition method (PLD), which is very useful for the growth of materials with complex stoichiometry, has been employed to deposit thin films of HAp¹⁻³. The studies have shown that the deposition conditions can greatly change the crystalline structure and stoichiometry, namely the Ca/P ratio of the grown layers. Moreover, the surface of the grown films has a rough morphology, being covered with a high density of droplets. We have shown that most of these droplets are ejected by a sub-surface explosive boiling mechanism because the HAp target does not strongly absorb the laser radiation⁴. We have further proposed several methods for increasing the optical absorption coefficient at the laser wavelength used for ablation and, based on this, obtained a dramatic reduction of the droplet density on the surface of grown films. In this article new investigations aimed at improving the crystallinity of PLD grown HAp films are presented.

2. EXPERIMENT

Targets of HA were prepared by cold pressing high purity powders in 1 cm diameter pellets which were afterwards sintered in air at 1100 °C for several hours. The targets were then mounted in a holder inside the ablation chamber which was rotated at a frequency of 0.2 Hz in order to avoid very fast target erosion during the laser ablation process. The chamber was first evacuated down to 10^{-7} mbar, purged, and then backfilled with N_2O , known to be a better oxidising agent than pure O_2 , at various pressures from 10^{-5} to 10^{-2} mbar. Irradiation was performed with a KrF laser having a full width at half maximum

(FWHM) time duration of 20 ns at fluences from 1 to 6 J/cm². Single crystalline Si and Ge, quartz and highly polished Ti substrates were placed at 4 cm in front of the target on a holder which could be resistively heated up to 800 °C.

The structural properties of the films grown on Si substrates were investigated by Fourier transform IR spectroscopy (FTIR), while the optical transmission data of films deposited on quartz were recorded with a double beam spectrophotometer in the 1100-190 nm range. Investigations of the film surface morphology were performed using a scanning electron microscope (SEM) equipped with energy and wavelength dispersive X-ray analysis (EDX and WDS) systems to assess the chemical composition. As the EDAX system has a limited energy resolution which precluded a very clear separation between the Si and P signals, some films were grown on single crystalline germanium substrates. For preliminary transmission electron microscopy (TEM) and selected area electron diffraction (SAED) some films were deposited on 10 nm thick Si₃N₄ membranes.

3. RESULTS AND DISCUSSION

SEM investigations of the HAp layers revealed a highly perturbed morphology with a high density of droplets and other debris material. The main formation mechanism of these droplets is the sub-surface explosive boiling caused by the low optical absorption coefficient which promotes a volume heating resulting in the formation of a thick layer of molten material which favours sub-surface boiling^{4, 5}. As one can notice from Fig. 1 where the optical transmission of a HAp film deposited on quartz is displayed, the film is quite transparent down to 190 nm. The absorption seen below 200 nm is probably caused by the formation of a compound at the quartz-film interface as the absorption increases with the increase of the deposition time, and not by the material itself.

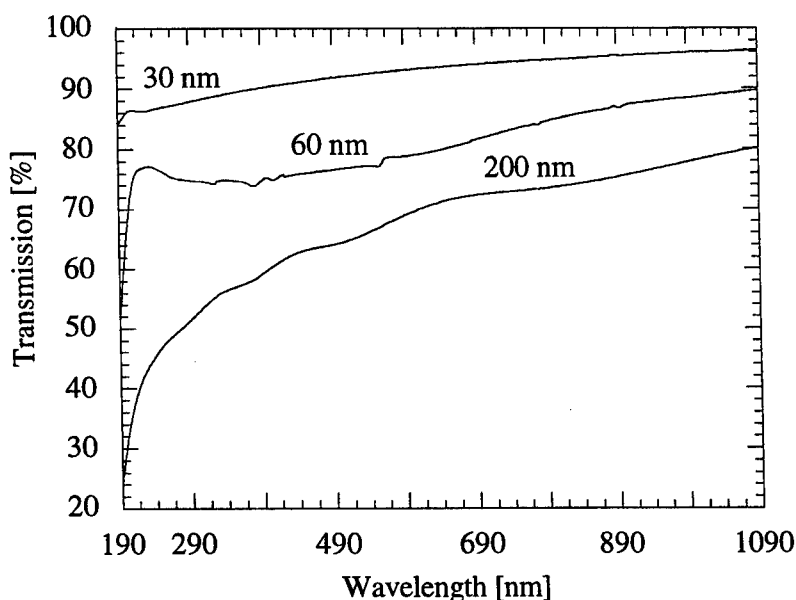


Figure 1. Optical transmission of HAp thin films deposited at 700 °C with 2.5 J/cm².

In Fig. 2, where a micrograph of a film surface deposited on Ti is displayed, a large 30x20 μm² crystallite is visible. We suggest that such crystallites, although fewer than the number of droplets, were also expelled from the target by such micro-explosions caused by the sub-surface boiling mechanisms. The shock-wave caused by these micro-explosions can displace loosely bound crystallites which are thus deposited on the surface of the grown film. It is interesting to note that the film morphology improves when using targets which were sintered for longer periods of time, as one can see in Fig. 3, where micrographs of films deposited from targets which were sintered for 4 and 14 hours are displayed. The small (less than 1 μm), irregularly-shaped and very bright powder-like particles seen in Fig. 3a were found by EDAX to be very rich in Ti. Their bright colour suggests that the Ti, which diffused from the underlying substrate up to the surface, is oxidised.



Figure 2. SEM micrograph of a crystallite directly expelled from the target.

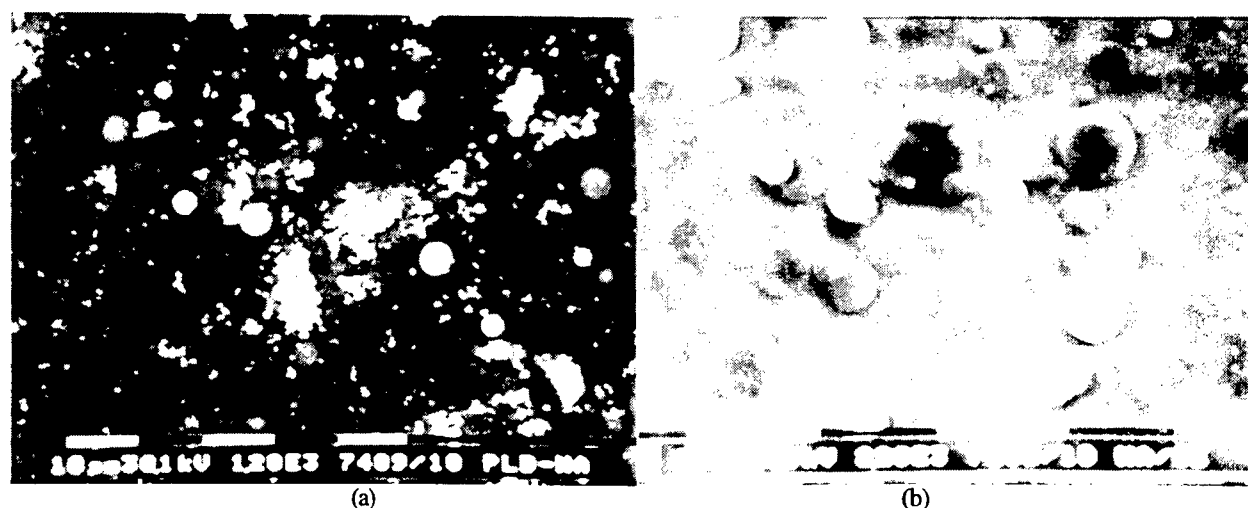


Figure 3. SEM micrographs of HAP films grown from targets sintered for 14 hrs (a) and 4 hrs (b).

The Ca/P value determined by EDAX of the film deposited at temperatures below 300 °C was around 1.40, being quite close to that of 1.51 measured for the as-sintered targets. Increasing further the substrate temperature increases also the Ca/P value. For example, a Ca/P value of around 1.91 was measured for a film deposited at 400 °C. However, values around 1.50, very similar to the target value were found on several analysed droplets, implying that these were directly expelled from the target when in liquid phase.

The fact that the material transfer from target to film is more or less stoichiometric can also be seen from Fig. 4 where the FTIR spectra of a film deposited at 650 °C under 4×10^{-3} mbar of N₂O and of the as-received HAP powder are shown. Clearly, all the important absorption bands of HAP⁶ were also present with the grown film.

The substrate temperature was found to play a key role on the structural properties of the grown layers. From room temperature up to values of around 300 °C, the films were amorphous according to SAED investigations. Films deposited at 400 °C start to exhibit some faint electron diffraction rings, an indication of a polycrystalline structure with very small grain sizes. However, as one can notice in Fig. 5 where the TEM micrograph of a very thin HAP film deposited on a Si₃N₄ membrane is shown, it is difficult to assess whether the diffraction rings originated from the small crystallites or the large droplet. It is also interesting to observe that the crystallites are better formed in the area surrounding the droplet.

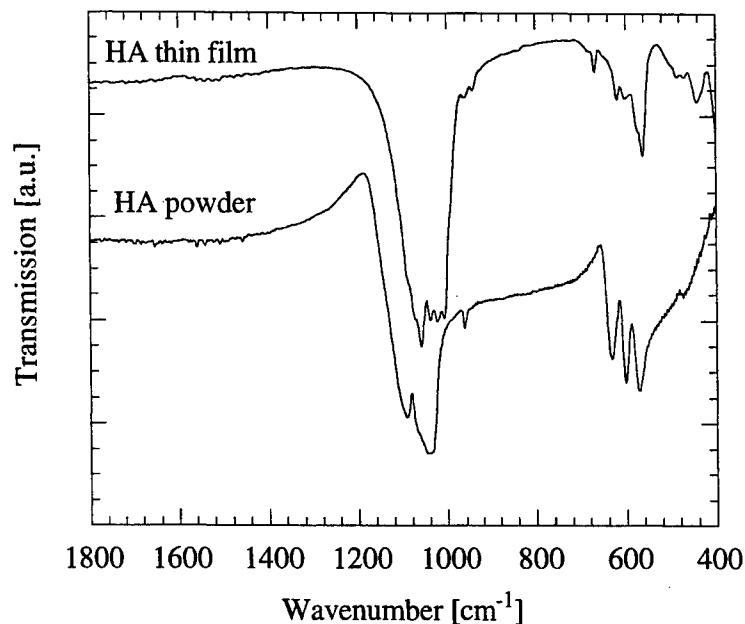


Figure 4. FTIR spectra of a typical HAp film grown by PLD and of an as-received powder.

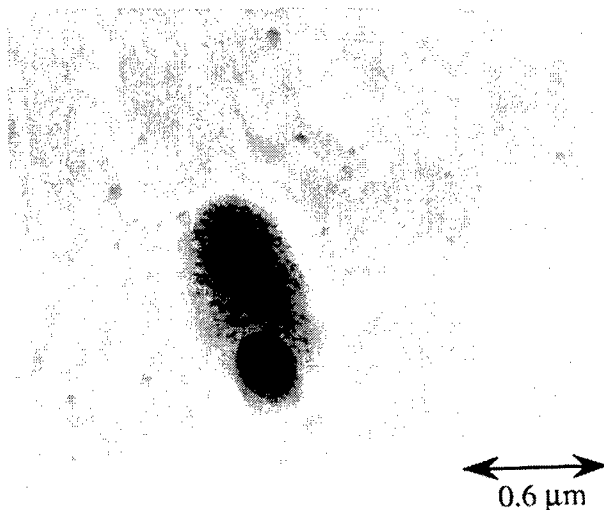


Figure 5. TEM micrograph of the initial growth stage of a HAp thin film.

For substrate temperatures above 600 °C, the grown films begin to exhibit a good crystalline structure, as inferred from the FTIR spectra shown in Fig. 6 which were recorded from two films deposited at 400 °C and 650 °C, respectively, substrate temperatures. One can note that the intensity of the IR absorption band at around 1000 cm^{-1} is higher for the 650 °C deposited film, its width is narrower.

The oxidising gas pressure was another important deposition parameter as one can note from Fig. 7 where the FTIR spectra of two films deposited at 4×10^{-2} and 4×10^{-4} torr of N_2O , respectively, are shown. The film deposited at higher pressure is thicker because the deposition time was longer. Nonetheless it is evident that the film deposited at a lower pressure has narrower FTIR absorption bands, which suggests that it possesses a better crystallinity.

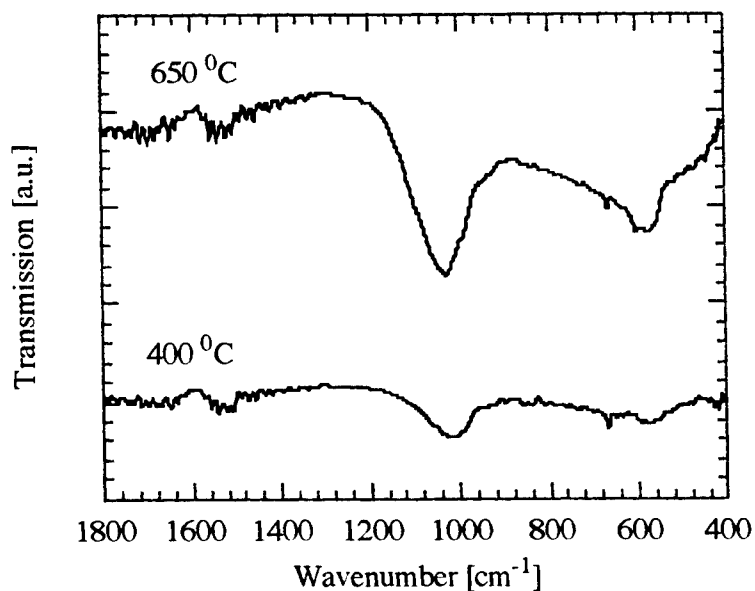


Figure 6. FTIR spectra of films grown at different substrate temperatures.

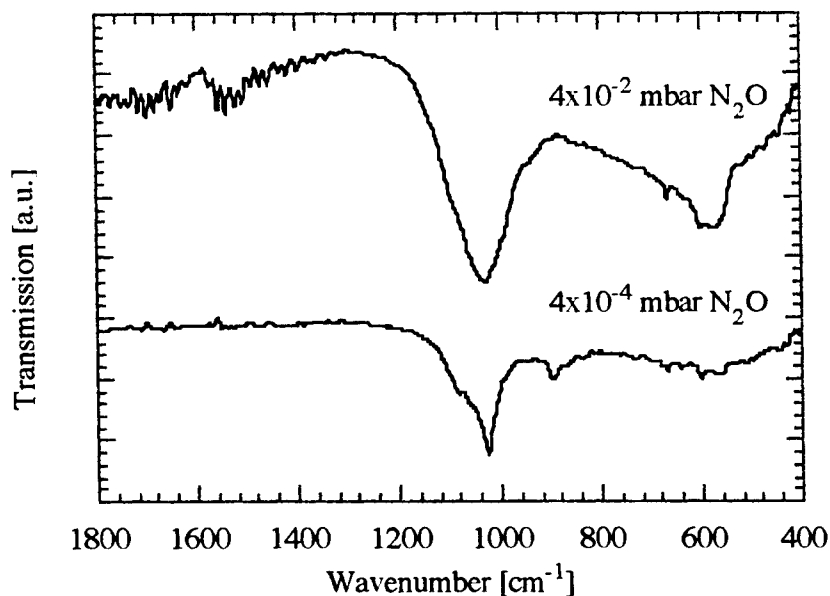


Figure 7. FTIR spectra of HAp thin films deposited at different N₂O gas pressures.

We have thus found that the optimum PLD conditions for stoichiometric transfer, i.e. low substrate temperature and high oxygen pressure are not conducive to good crystallinity as assessed from FTIR investigations. Moreover, a high

substrate temperature induces Ti diffusion across the grown film, up to the surface where it gets oxidised. This process will create bio-compatibility problems when Ti-based orthopaedic prostheses alloys are coated by HAp films deposited at such high temperatures. It appears that, at least for the initial stages of growth, the surface temperature should be kept below 400 °C, sacrificing the crystallinity but preserving the HAp stoichiometry (Ca/P ratio) and avoiding Ti diffusion. Investigations aimed at improving the crystalline structure of low-temperature deposited films are in progress.

4. CONCLUSIONS

The growth and properties of thin HA films by PLD under various deposition conditions has been investigated. Ca/P values close to those of the as-prepared targets were obtained for films grown at modest substrate temperatures and high oxidising pressures. However, the crystallinity of such films, as assessed by FTIR analysis is poor. Further treatments to promote the crystallisation of these films without perturbing the Ca/P ratio would be highly desirable. New investigations trying to achieve this are underway.

5. REFERENCES

1. C.M.Cotell, "Pulsed laser deposition and processing of biocompatible Hydroxylapatite thin films", *Appl. Surf. Sci.* **69**, 140-148 (1993)
2. L.Torrisi and R.Setola, "Thermally assisted hydroxyapatite obtained by pulsed-laser deposition on titanium substrates", *Thin Solid Films* **227**, 32-36 (1993)
3. S.Hontsu, T.Matsumoto, J.Ishii, M.Nakamori, H.Tabata, T.Kawai, "Electrical properties of hydroxyapatite thin films grown by pulsed laser deposition", *Thin Solid Films* **295**, 214-217 (1997).
4. O.Guillot-Noel, R.Gomez-San Roman, J. Perriere, J.Hermann, V. Craciun, C. Boulmer-Leborgne, P.Barboux, "Growth of apatite films by laser ablation: Reduction of the droplet areal density", *J. Appl. Phys.* **80**, 1803-1808 (1996).
5. V. Craciun, D. Craciun, M.C.Bunescu, R.Dabu, I.W.Boyd, "Growth of highly transparent oxide layers by pulsed laser deposition: reduction of droplet density", *Appl. Surf. Sci.* **109/110**, 354-358 (1996).
6. I. Rehman and W.Bonfield, "Characterization of hydroxyapatite and carbonated apatite by photo acoustic FTIR spectroscopy", *J. Mat. Sci.: Mat. in Med.* **8**, 1-4 (1997).

Violeta Calian, Marcela Ursache, C. Sarpe-Tudoran, Margareta Socaciu

University of Craiova, Department of Physics, 13 .A. I. Cuza,
Craiova 1100, Romania. email: violeta@oltenia.ro

ABSTRACT

A numerical method for simulating realistic problems of mode coupling in optical transmission systems is described. The conclusion concerning waveguided propagation of the electromagnetic field in complex structures, selective mode excitation and the power transfer may become an important factor in designing and connecting devices used in optical signal processing. The numerical method is based on an extension of the "Orthogonal Collocation Method" to the case of coupled systems of differential equations with an infinite range of independent variables.

Keywords: coupling coefficient, optical transmission system, waveguided propagation.

1. INTRODUCTION

The characteristics of the linear and nonlinear waveguided propagation of electromagnetic field in optical transmission systems have a crucial importance due to their potential use in the domain of optical signals processing.

If a proper mode of a transmission system component (a laser for instance) is injected into another component of the same system (as an optical waveguide) then a set of the communication system modes are excited.

The coupling of the different proper modes and the power transfer can be described and evaluated using numerical methods which all present difficulties or limiting features.

The paper presents an original method for the numerical simulation of realistic problems which include two specific waveguiding structures having rectangular and circular symmetries.

The numerical methods used to solve this kind of problems based on the finite-element technique³, the "averaged index" method², the "beam propagation" method¹, are well known, as well as their disadvantages or accomplishments.

This paper will describe in detail the numerical method used by us, which is an extension of the so-called "orthogonal collocation method" to the case of *coupled* differential equations and of an infinite set of independent variables and improved by harmonical analysis techniques.

2. NUMERICAL METHOD AND DISCUSSION

The starting point is the Helmholtz equation for the 3-dimensional propagation:

$$\frac{\partial^2 \psi}{\partial x^2} + \frac{\partial^2 \psi}{\partial y^2} + \frac{\partial^2 \psi}{\partial z^2} + k^2 n^2(x, y, z) \psi(x, y, z) = 0 \quad (1)$$

The symmetry of the guiding structure is the key part in choosing the suitable expansion orthogonal functions.

For the two analysed cases (rectangular and circular structures) we used Laguerre-Gauss and Hermite-Gauss functions respectively, and the *coupled* equations for the fields. Our work generalises the known collocation method to the case of coupled differential equations and an infinite range of independent variables.

For the three - dimensional case, the solution of the equation (1) is written as a double linear combination over sets of appropriate orthogonal functions::

$$\Psi(x, y, z) = \sum_{n=1}^{N_1} \sum_{m=1}^{N_2} K_{nm}(z) \psi_n(x) \psi'_m(y) \quad (2)$$

where $\psi_n(x)$, $\psi'_m(y)$ are Hermite-Gauss functions or Laguerre-Gauss functions, according to the circular or rectangular symmetry of the waveguiding structure:

$$\Phi_n(x) = N_{n-1} H_{n-1}(\alpha x) \exp\left\{-\frac{1}{2}\alpha^2 x^2\right\} \quad (3)$$

$$\eta_m(y) = M_{m-1} H_{m-1}(\gamma y) \exp\left\{-\frac{1}{2}\gamma^2 y^2\right\} \quad (4)$$

and N_{n-1} , M_{m-1} are the normalisation constants, α and γ are two parameters which can be arbitrarily fixed.

Choosing α , γ and N_1 , N_2 values is a crucial step for the accuracy of the solution. This is certainly increased as a function of the collocation points numbers (N_1 , N_2) while α and γ are established in correlation with the accurate division of the domain.

The collocation points are calculated from the condition:

$$H_{N_1}(\alpha x_j) = 0, \quad j = \overline{1, N} \quad (5)$$

$$H_{N_2}(\gamma y_l) = 0, \quad l = \overline{1, N} \quad (6)$$

thus from the well-known zeroes of Φ_{N_1+1} and η_{N_2+1} respectively.

The main point in solving the coupling problem is then the remark that the wavefunction is written as a combination of two kinds of quantized modes:

$$\Psi(x, y, z) = \sum \bar{K}_{nm}(x, y, z) \varphi(\alpha x) \varphi'(\alpha' y) \quad (7)$$

and that the coupling coefficients may be expressed as:

$$C(\varphi_1, \varphi'_1, \varphi_2, \varphi'_2) = \int H(\varphi_1, \varphi'_1; x, y) H(\varphi_2, \varphi'_2; x, y) dx dy \quad (8)$$

in terms of the cross-correlation functions:

$$H(\varphi_1, \varphi'_1; x, y) = \langle U(x, y, 0) \varphi_1 | \varphi'_1 \rangle. \quad (9)$$

Requiring that the wavefunction (7) must satisfy *exactly* the equation (1) in all the collocation points means that we generate a matrix differential equation having the solution $\Psi(x_i, y_j, z)$:

$$\frac{d^2\Psi}{dz^2} + A\Psi + \Psi B^t + R(\Psi) = 0 \quad (10)$$

where: $\Psi(x_i, y_j, z)$ is now a $N_1 \times N_2$ matrix defining the field $\psi(x, y)$ at the collocation points. is defined by:

$$A = DP^{-1} \quad (11)$$

with:

$$D_{ij} = \left. \frac{\partial^2}{\partial x^2} \varphi_j \right|_x \quad (12)$$

$$P_{ij} = \varphi_j(x_i) \quad (13)$$

$$B = D'(P')^{-1} \quad (14)$$

$$D'_{ij} = \left. \frac{\partial^2}{\partial y^2} \varphi'_j \right|_y \quad (15)$$

$$P'_{ij} = \varphi'_j(y_i) \quad (16)$$

while $R(\Psi)$ is a $N_1 \times N_2$ matrix with the elements defined as:

$$(R(\Psi))_{ij} = k^2 n^2(x_i, y_j, z) \Psi(x_i, y_j, z) \quad (17)$$

We are thus lead to a simple problem: a matrix differential equation which may be solved by any standard method (like a Runge-Kutta method).

Having the wavefunctions for the two waveguides, the last step of the study is devoted to the calculation of the coupling coefficient with the relation (8), in the coupling plane $z = \text{const.}$ transversal to the propagation direction.

We first checked that:

a) for the circular symmetry, with $m = p$; $m - n = l$; $m' = p'$; $m' - n' = l'$, we have:

$$C_{n,m,n',m'} = 0$$

b) for the rectangular symmetry, with $m + m' = 1(\text{mod } 2)$ and $n + n' = 1(\text{mod } 2)$, we obtain a similar result.

By contrast, for the rest of the values:

a) $l = l'$

b) m, m', n, n' - odd or even,

nonzero values of the coupling coefficient were computed and compared with the available data¹.

In order to realize this comparative study our numerical results were fitted with the calculations performed by harmonic analysis¹, which had given the following formula:

a)

$$C_{nmn'm'} = \left(\frac{2}{w w' / q} \right)^{m+1} M_{nn'}^c \cdot K_n \left(n', \frac{(q-\alpha)(q-\alpha')}{q(q-\alpha-\alpha')}, n + n' + m \right) \quad (18)$$

b)

$$C_{mnm'n'} = \left(\frac{2}{ww'/q} \right) M_{mm'n'n'}^r \cdot K_{m/2} \cdot K_{n/2} \quad (19)$$

where α, q are the Gaussian beam parameters⁵, the Krawtchouk polynomials depend on the modes as:

$$K_{m/2} = K_{m/2} \left(m'/2, \frac{(q-\alpha)(q-\alpha')}{q(q-\alpha-\alpha')}, (m+m'-2)/2 \right) \quad (20)$$

while the coefficients $M_{mm'n'n'}^r, M_{nn'}^c$ are computed according to:

$$M_{nn'}^c = \frac{(n+n'+1)!}{[n!n'!(n+1)!(n'+1)!]} \left(1 - \frac{\alpha}{q} \right)^n \left(1 - \frac{\alpha'}{q} \right)^{n'} \quad (21)$$

$$M_{mm'n'n'}^r = \left(-\frac{1}{2} \right)^{(m+m'+n+n')/2} \frac{(m+m')!(n+n')!}{((m+m')/2)!((n+n')/2)! \sqrt{m!m'!n!n'!}} P_{mnm'n'} \quad (22)$$

with:

$$P_{mnm'n'} = \left(1 - \frac{\alpha}{q} \right)^{\frac{m+n}{2}} \left(1 - \frac{\alpha'}{q} \right)^{\frac{m'+n'}{2}} \quad (23)$$

if the even numbers were considered, and with similar forms of the coupling coefficients for the odd number case.

The main conclusions we derived may be summarized now:

- a) there is no coupling between quantized transversal eigenmodes of different angular moments, for the circular case;
- b) only the even and odd quantized transversal eigenmodes are coupled in the rectangular case, i.e. the parity is preserved.

Moreover, our results are easily verified with the data in ⁵.

Therefore these properties may be of major importance in designing and optimising the devices used in optical communication systems while the memory and time consume of the described numerical method are very low and the degree of generality quite extended.

3. REFERENCES

- [1] Feit, M.D., Fleck, J.A., J. Opt. Soc. Am. A, 7, 73-79, 1990.
- [2] Hock, J.B., Burns, W.K., Appl. Opt., 16, 113-118, 1987.
- [3] Cvetkovic, R.S., Zhao, A.P., J. Opt. Soc. Am. B, No8, Vol. 10, 1401-1407, 1993.
- [4] Sharma, A., LAMP /93/4.
- [5] Schempp W., Int. Series of Num. Math., vol. 81, 1987, Birkhauser Verlag Basel.

The effect of Pulsed Laser Deposition Parameters on plasma expansion studied by fast-framing photography

Dana Miu*, A. Marcu*, T. Yukawa**, C. Grigoriu*, I. Chis*, K. Yatsui**

* National Institute for Laser, Plasma and Radiation Physics, Laser Department, P.O. Box MG-36, Bucharest-Magurele, Romania

**Nagaoka Technical University, Laboratory of Beam Technology, Nagaoka, Niigata 940-21, Japan

ABSTRACT

Fast-framing photography was used to study the effect of various parameters on the expansion of the visible plasma plume produced by KrF laser irradiation of a $\text{YBa}_2\text{Cu}_3\text{O}_{7-x}$ (YBCO) target. The ambient gas pressure has a considerable effect on the evolution and structure of the plasma. In vacuum, the visible emission is strongly forward-directed and has a relatively short duration. In the presence of an oxygen atmosphere, a long-lived, highly luminous front is formed, whose expansion may be well described by a drag model or a shock model (spherical or plane shock). Ahead of the luminous front there is weak emission, which for pressures over about 700 mTorr evolves into a highly emissive "tip". The decrease of energy density on the target by increase of the laser spot (defocusing) leads to a more forward-directed motion of the visible species. Larger energy densities obtained by increasing the energy/pulse lead to a sharper, "V" shaped front. The effect of a biased ring electrode placed 0.5 cm to 2 cm in front of the target was also studied. The emission characteristics in the electrode's presence change greatly. The effect of ring-target distance, voltage magnitude and polarity, and pressure were observed.

Keywords: laser deposition, plasma expansion, fast-framing photography.

1. INTRODUCTION

Many characteristics of Pulsed Laser Deposition (PLD) plasmas, such as the energy of the species, the ion properties and the presence of oxides, have a great effect on the quality of the deposited thin films [1].

Fast-framing photography is a convenient method to study plasma expansion under various experimental conditions, with very good temporal resolution. We studied the time evolution of the plasma obtained upon laser irradiation of various targets, at pressures from vacuum (10^{-5} Torr) to 20 Torr, in oxygen, nitrogen and argon atmospheres.

2. PLASMA EXPANSION IN THE PRESENCE OF A GAS ATMOSPHERE

Laser deposition of many high-quality thin films requires the presence of a gas atmosphere. For example, deposition of High Temperature Superconducting (HTSC) thin films is made in the presence of an oxygen atmosphere, at a pressure of 100 - 300 mTorr. In the presence of a gas, the expansion of the species is influenced by two types of processes: hydrodynamic and chemical.

For relatively low pressures (of the order tens of mTorr) or during the initial stages of expansion at higher pressures, the plasma plume propagates through the background gas in accordance with a drag model [2]. According to this model, the ablation products are slowed according to

$$x = x_f [1 - \exp(-\beta t)], \quad (1)$$

where x is the distance travelled along the target normal, x_f is the stopping distance, and β is the slowing coefficient (proportional to the ambient gas density).

For pressures over 100 mTorr (the exact value depending on other parameters as well, such as laser energy density), after a given time a shock wave forms in the gas. This considerably slows down the ablation products and produces behind it a region of high target species density. In the case of a spherical expansion, the propagation of the shock wave in the gas is described by:

$$R(t) \sim (E_0/\rho_0)^{1/5} t^{2/5}, \quad (2)$$

where R is the distance to the target, ρ_0 - the ambient gas density (proportional to the pressure), and E_0 is the energy released explosively in the gas [3]. In the case of a plane expansion, the $R(t)$ dependence is [4]

$$R(t) \sim (E_0/\rho_0)^{1/3} t^{2/3}. \quad (2')$$

For pressures over about 1 Torr, a turbulent flow of the plasma can be observed [5].

3. EXPERIMENTAL DETAILS

We used a Hadland Imacon model 792 high-speed camera in framing mode to obtain photographs of the plasma generated by irradiation of a stoichiometric $\text{YBa}_2\text{Cu}_3\text{O}_{7-x}$ (YBCO) target with a KrF laser (fig. 1). The laser has a pulse duration of 20 ns, and an energy per pulse which varies between 70 and 200 mJ. The beam is incident at an angle of 45° from the target normal. Focusing of the beam on the target leads to energy densities between 0.3 and 1.5 J/cm^2 , depending on the energy per pulse and the spot dimensions. The energy/pulse was monitored using a Gen-Tec ED500 energymeter connected to a HP54512B digital oscilloscope (300 MHz).

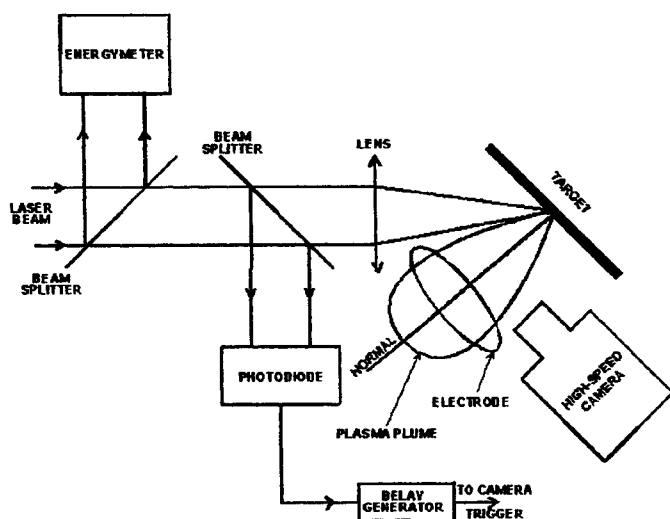


Fig. 1. Experimental set-up

The camera is triggered by the signal from a photodiode onto which a fraction of the laser beam is incident; the time reference for the photos is thus the incidence of the beam on the target. The interval between two successive photographs is 200 ns (exposure time 41.2 ns), and the delay between the incidence of the laser pulse on the target and the first photograph in the series obtained for one laser pulse is variable between 200 ns and $1 \mu\text{s}$. The sequence of photographs is:

2	4	6
1	3	5

In some cases a copper ring shaped electrode was placed at distances of 0.5, 1 or 2 cm in front of the target, parallel to its surface. The copper wire electrode has a diameter of 2.5 cm. dc voltages of different magnitudes (240 V, 450 V, 725 V) and polarities were applied on the electrode; the target was connected to the source ground. The presence of a biased electrode in the plasma improves film quality, presumably through additional plasma activation [6].

We studied the effect of several parameters on the expansion of the plasma. We will present here the effects of the following:

- ambient gas pressure,
- nature of the ambient gas,
- laser energy density on target
- presence of substrate
- presence of an electrode:
 - target-electrode distance,
 - voltage polarity,
 - voltage magnitude.

4. PLASMA EXPANSION AT VARIOUS PRESSURES AND LASER ENERGY DENSITIES

In vacuum, the plasma has a forward-directed motion (motion predominantly along the target normal), without any visible structure. The visible emission has a relatively short duration of $1.2 \div 1.6 \mu\text{s}$ (fig. 2a). In the presence of a gas atmosphere (pressures from about 60 mTorr to about 1 Torr), the behavior of the expanding species in the vicinity of the

target (< 5 mm) is the same as in vacuum, but at larger distances (of the order of several cm) a highly luminous front is formed (figure 2b, 2c). The duration of the emission is longer than in the vacuum case (> 3 μ s) due to this front.

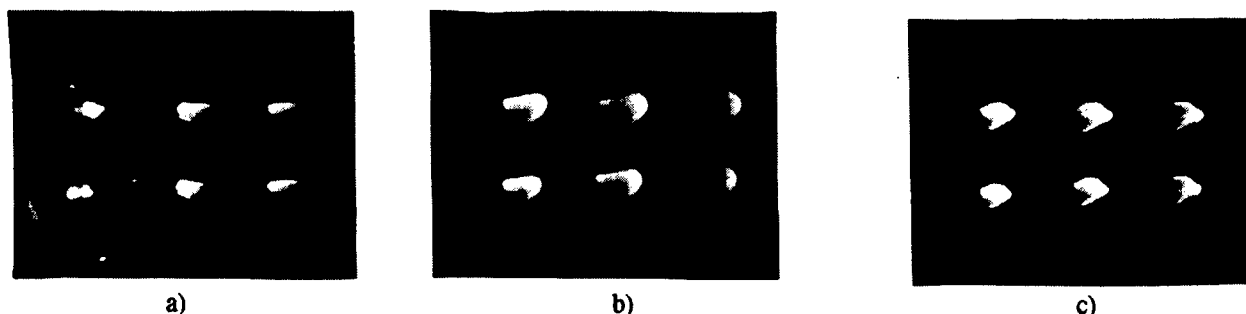


Fig. 2. Plasma evolution at various oxygen pressures. a) vacuum (10^{-5} Torr), b) 190 mTorr, c) 1.52 Torr. The first picture in each series is delayed 1 μ s from the laser pulse.

This luminous front is the region of high target species density formed behind the shock front. Many authors consider that luminescent oxide-forming reactions are responsible for this high luminosity [7]. Spectroscopic results obtained by us, however, indicate that in our experimental conditions only a small part of the emission is due to such reactions, the majority resulting from collisional excitation among the target species themselves.

The motion of the species in the presence of a gas is less forward-directed than in the vacuum case, due to the collisions of the target species with the ambient gas molecules. As the pressure increases, the extension of the plasma parallel to the target surface becomes larger. For pressures over about 700 mTorr, the "tip" of the front becomes more luminous, and propagates with a velocity greater than the rest (fig. 2c). The phenomenon could be linked to weak emission ahead of the front which is visible for lower pressures upon scanner examination of the photos (fig. 3). This indicates the existence of species moving ahead of the front. The behavior has been observed before [8] and explained using Monte Carlo simulations of collisions between target species and ambient gas molecules [9]. These faster components are eventually slowed down in another high density luminous front ahead of the first. For even higher pressures (> 1.5 Torr) the front takes on an irregular shape which indicates turbulence.



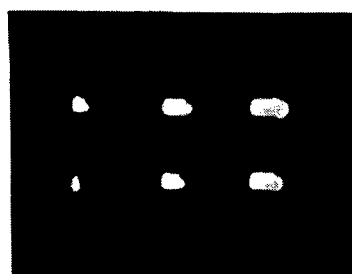
Fig. 3. Scanner image of fast-framing photo obtained in 190 mTorr oxygen, for a delay of 600 ns. Weak emission is visible ahead of the highly luminous front

The behavior of the ablated species in the presence of an ambient gas proved, in our case, to be independent of the nature of the gas used (oxygen, as in deposition conditions, nitrogen or argon), which confirms that the visible emission is due to hydrodynamic effects, and not to luminescent oxidation reactions. Due to the small difference between the molecular masses of oxygen and nitrogen and the atomic mass of argon, the former effects are expected to lead to similar expansions.

Defocusing of the laser beam on the target leads to a modification of the energy density through the change in spot size. By increasing the spot size from 13.3 mm² to 23 mm², at a constant energy/pulse of about 100 mJ, the plasma expansion becomes more forward-directed (fig. 4) (the corresponding energy densities are .75 J/cm² and .45 J/cm², respectively). The luminous front becomes less curved and has a smaller extent in the direction parallel to the target surface. The effect is noticeable for pressures of 100 + 760 mTorr. This effect could be tentatively explained by the increase of the number of collisions/particle as the spot size, and therefore the time spent by the species in the near-target region, increases. Theoretical models indicate that a greater number of collisions/particle leads to particle motion predominantly along the target normal [10].



a)



b)

Fig. 4. Effect of laser beam defocusing on the evolution of the plasma. Spot size a) 13.3 mm^2 , b) 23 mm^2 . Energy per pulse 100 mJ. Oxygen pressure 190 mTorr. Delay of first photo $1 \mu\text{s}$.

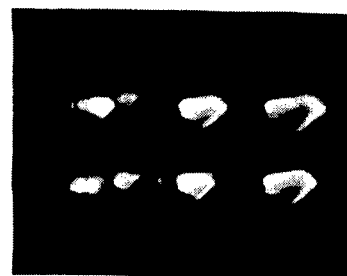


Fig. 5. Plasma evolution at large energy density (1.5 J/cm^2). 190 mTorr. Delay $1 \mu\text{s}$.

An increase of the energy density to larger values (about 1.5 J/cm^2) through an increase of laser energy/pulse leads to a characteristic "V" shape of the front instead of the rounded one obtained for lower energies (fig. 5). The amount of material removed from the target is larger, which produces a plasma of higher luminosity, both in vacuum and in an oxygen atmosphere.

Our results indicate that the plasma expansion depends both on pulse energy and on spot size, and not just on their ratio (energy density) which confirms other authors' results [10]. The relationship between the expansion along the direction parallel to the target surface and that perpendicular to it is decided mainly by the laser spot size on the target.

The results presented above are without any substrate. In the presence of a cold substrate placed 1.5 cm from the target, an intense emission is visible on its surface. This is most probably due to collisions between plasma particles reflected on the substrate and the incoming ones. The long duration of emission ($> 4 \mu\text{s}$) proves that particles are being released from the target at later times; in the absence of the substrate, however, they are not visible, since they are not in an excited state.

5. MODELLING OF LUMINOUS PLASMA FRONT PROPAGATION

As the pressure increases, the front boundary in our photos becomes sharp enough to determine the propagation law $R(t)$, where the R is the distance from the target, measured along the target normal, for the part of the front which moves with the greatest velocity, and t is the time, measured from the incidence of the laser beam on the target. This allows modelling of the phenomena.

At low pressures, the species move with a constant velocity, which results in a linear $R(t)$ dependence with a corresponding velocity of about 10^6 cm/s ; this is in accordance with the model for propagation in vacuum [11]. As the pressure increases, the interaction of target species with the ambient gas molecules (through collisions) becomes more important. For the first moments (and close to the target), the linear $R(t)$ dependence corresponding to vacuum propagation well describes the propagation. After 600 ns - $1 \mu\text{s}$ the front is slowed. Its motion can then be described using either the drag model (1) or the shock model (2, 2').

The above-mentioned models provide good fits for our experimental data. The moment when the linear $R(t)$ changes because of slowing of the species depends on pressure and energy density: for higher pressures or lower energy densities, this slowing occurs at earlier moments (fig. 6, 7). This behavior agrees with hydrodynamic theories of plasma evolution: the slowing effects produced in the presence of an atmosphere appear once the target species density equals that of the ambient gas which has been "swept up". This is to be expected to happen sooner at high gas densities (pressures) and low ablated species density (low laser energy densities).

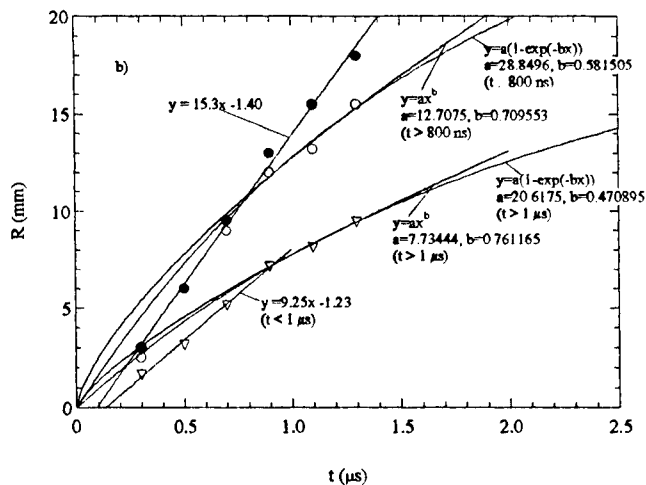


Fig. 6. $R(t)$ fit of experimental data for an oxygen pressure of 100 mTorr and a laser energy density of: .31 J/cm² (∇), .74 J/cm² (o), 1.34 J/cm² (\bullet). When the fit is not made using all the data, the interval used is the one in the parentheses.

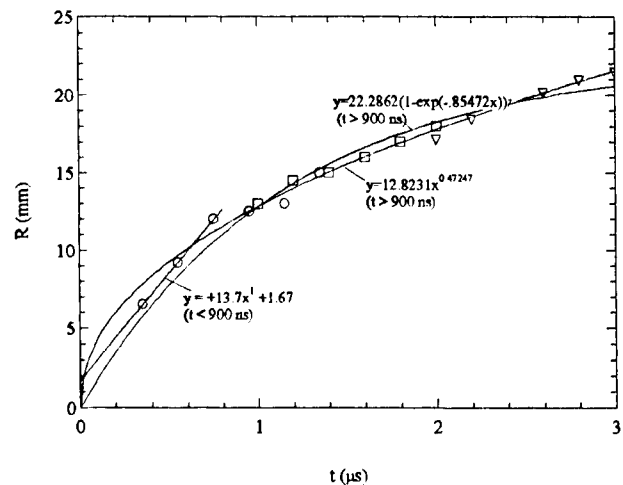


Fig. 7. $R(t)$ fit of experimental data for an oxygen pressure of 190 mTorr. Different symbols correspond to different laser pulses, all having the same energy density (1 J/cm²).

Whether the propagation of the front is best described by a plane or a spherical shock depends on pressure and energy density. In the pressure domain used in our experiments, at low pressures (< 100 mTorr) the expansion is closer to plane ($b = 0.67 \pm 0.76$), and at higher pressures (> 500 mTorr), closer to spherical ($b = 0.38 \pm 0.51$). For a given pressure of 190 mTorr, the expansion can be modelled by a spherical shock for 1 J/cm², and by a plane one for 0.7 J/cm². These results coincide with the qualitative observations of the relationship between plasma motion and irradiation parameters mentioned above.

6. PLASMA EXPANSION IN THE PRESENCE OF AN ELECTRODE

The presence of a ring electrode in the plasma leads to an increase of both emission intensity and duration, especially in vacuum (fig. 8). The differences between the situation with and without electrode appear from the moment when the plasma reaches the ring, for all target-electrode distances investigated. This indicates that the observed effects are due to the discharge current initiated through the plasma between target and ring (and not to the electric field in this region).

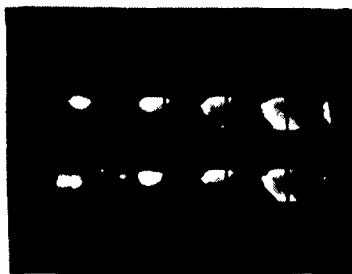
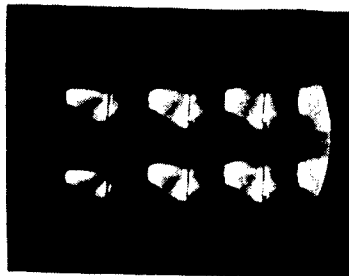
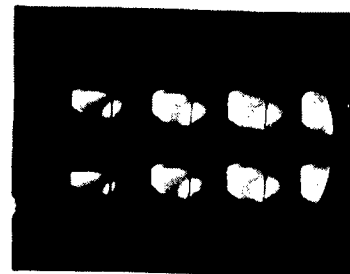


Fig. 8. Plasma evolution in the presence of an electrode, in vacuum. Electrode 9 mm from target. Voltage + 450 V. Delay 200 ns.



a)



b)

Fig. 9. Plasma evolution in vacuum for + 725 V a) and - 725 V b). Delay for first photo in sequence 1 μ s.

The emission on the target surface has a greater duration in the presence of an electrode, both in vacuum and 190 mTorr oxygen. The probable explanation is that the release of particles from the target is longer than that observed in the absence of an electrode, but the species removed from the target later emit visible radiation only in the presence of the

electrode. This could also explain the less forward-directed motion of the plasma observed in vacuum with the electrode. If true, this implies that species which are only excited when a voltage is applied to the ring have a less forward-directed motion than those excited even in its absence.

In vacuum, with the increase of electrode voltage, both the intensity of the emission and its spatial extent become larger. For a negative ring bias, the emission on the target is over a greater surface than for a positive voltage (fig. 9). A simple model could be proposed, according to which the regions where the electrons have been accelerated to greater velocities in the discharge are the ones where the area of increased emission is larger. In a 190 mTorr oxygen atmosphere, the increase of plasma emission is less visible and more uniform spatially.

For a relatively large target-electrode distance (2 cm), the dimensions of the visible plasma emission along the target normal is greater (at a given moment) than when the ring is placed close to the target, which suggests that the species are excited more efficiently in this case.

The effect of the presence of the ring electrode is to increase plasma excitation by collisions between the electrons in the discharge initiated through the plasma, and the ablated species. The increased species excitation leads to greater reactivity, which is important for applications.

7. CONCLUSIONS

Our results confirm the strong dependence of PLD plasma expansion on ambient gas pressure and laser energy density. An interesting phenomenon is the weak emission observed ahead of the luminous front, which for pressures over 700 mTorr evolves into a luminous "tip". This indicates species moving ahead of the shock front. A conclusion of fundamental as well as practical importance is the fact that plasma expansion is dictated both by pulse energy and spot size, not just by their ratio. The nature of the ambient gas proved to have no effect on plasma evolution, which suggests that hydrodynamic effects and not oxidation reactions lead to visible emission in our experimental conditions.

The movement of the luminous front boundary is well described by the drag or shock model. Whether the model for a plane shock or that for a spherical one gives a better fit for the experimental data depends on the pressure and laser energy density. To our knowledge, this is the first time such modelling has been used to establish the dependence of the expansion's character on these two parameters.

The presence of an electrode in the PLD plasma increases the duration and spatial extent of the plasma. The effects depend on voltage magnitude and polarity.

BIBLIOGRAPHY

1. A. Gupta, "Novel Pulsed Laser Deposition Approaches", in *Pulsed Laser Deposition of Thin Films*, eds. D. B. Chrisey, G. K. Hubler, p. 265-291, Wiley (1994).
2. D. B. Geohegan, *Appl. Phys. Lett.* **60** (22), p. 2732-2734 (1992).
3. Y. B. Zeldovich, Y. P. Raizer, "Physics of Shock Waves and High-Temperature Phenomena", Chapter I, Academic Press, New York (1996).
4. D. B. Geohegan, "Diagnostics and Characteristics of Pulsed Laser Deposition Plasmas", in *Pulsed Laser Deposition of Thin Films*, eds. D. B. Chrisey, G. K. Hubler, p. 115-254, Wiley (1994).
5. K. Scott, J. M. Huntley, W. A. Phillips, J. Clarke, J. E. Field, *Applied Phys. Lett.* **57** (9), p. 922-924 (1990).
6. D. Fried, G. P. Reck, T. Kushida, E. W. Rothe, *Journal of Phys. D: Appl. Phys.* **24**, p. 1065-1071 (1991).
7. D. Fried, T. Kushida, G. P. Reck, E. W. Rothe, *Journal Appl. Phys.* **73** (11), p. 7810-7817 (1993).
8. D. B. Geohegan, A. A. Puretzky, *Applied Phys. Lett.* **67** (2), p. 197-199 (1995).
9. J. C. S. Kools, *Journal Appl. Phys.* **74** (10), p. 6401-6406 (1993).
10. K. L. Saenger, "Angular Distribution of Ablated Material", in *Pulsed Laser Deposition of Thin Films*, eds. D. B. Chrisey, G. K. Hubler, p. 199-227, Wiley (1994).

Study on the synthesis of europium activated calcium tungstate phosphor

Elisabeth-Jeanne Popovici*, Flavia Forgaciu*, Miloslava Nemes*
and Veronica Ursu**

*Institute of Chemistry "Raluca Ripan", str. Fântânele 30, 3400-Cluj-Napoca

**Institute of Physical Chemistry "I.G. Murgulescu" of the Romanian Academy,
Splaiul Independentei 202., Bucuresti, ROMANIA.

ABSTRACT

The purpose of this study is to establish the way in which different synthesis conditions influence on the structural and luminescent characteristics of europium activated calcium tungstate powder phosphor. $\text{CaWO}_4:\text{Eu}^{3+}$ samples were prepared by thermal synthesis from mixtures consisting of precipitated- CaWO_4 , equivalent amounts of Eu_2O_3 and WO_3 (activating system) and CaCl_2 or Na_2WO_4 as flux. Calcination was performed at 800-1000 °C for 2 h, in air. The crystalline structure (XRD-patterns) and luminescent characteristics (emission and excitation spectra of phosphor samples were determined and interpreted.

Keywords: phosphors, luminescence, calcium tungstate, europium, $\text{Eu}(3+)$,

1. INTRODUCTION

Calcium tungstate phosphors are very sensitive to roentgen radiation so that they are largely used for the manufacture of X-Ray Intensifying Screens. Being sensitive to UV-radiation as well, they could be utilised in Plasma Display Panels on condition that their luminescence should be appropriate in colour and brightness.¹

The well-known self- or lead activated tungstate phosphors ($\text{CaWO}_4:\text{W}$ or $\text{CaWO}_4:\text{Pb}$) exhibit blue or blue green luminescence that is related to some tetrahedral WO_4 -groups of the scheelite host lattice.² When rare earth ions such as Eu^{3+} and Tb^{3+} are used as activators, new luminescence centres are formed and the characteristic red or green emission could be generated.^{3,4}

Most of the rare earth ions were tested as activators for scheelite lattice but the literature refers mainly to the luminescence of single crystals which are materials of great interest for solid state lasers.⁵ No information referring to the corresponding powder state phosphor was found.

The present paper reports some of our results concerning the synthesis of europium activated calcium tungstate phosphor powder. The purpose of this study is to establish the way in which different synthesis conditions influence on the structural and luminescent characteristics of $\text{CaWO}_4:\text{Eu}$ samples.

2. EXPERIMENTAL PART

Phosphor samples were synthesised from homogeneous mixtures consisting of luminescent grade (l.g.) CaWO_4 , CaCl_2 (l.g.) or Na_2WO_4 (l.g.) as flux and WO_3 (l.g.) and Eu_2O_3 (99.99 % Jansen Chemica) as activating system. All luminescent grade substances were prepared in our laboratory, by original procedures.

Calcium tungstate used in phosphor synthesis was prepared at room temperature, from highly purified CaCl_2 and Na_2WO_4 solutions.⁶

The synthesis mixtures contained 10 % wt.flux and equivalent amounts of WO_3 and Eu_2O_3 corresponding to $0.0025 \div 0.06 \text{ mol \% Eu}_2(\text{WO}_4)_3$. The thermal synthesis was conducted at 800 -1000 °C, in covered alumina crucibles, for 2 h. All samples were washed, dried and sieved.

Phosphor samples were characterised by crystalline structure (Philips PW 1050 Diffractometer; $\text{CuK}\alpha$) and luminescent properties. These ones were estimated on the basis of emission and excitation spectra registered on Perkin Elmer 204 Spectrofluorimeter. The excitation was performed with a 254 nm UV radiation and a self-activated calcium tungstate phosphor (N61, Bad Liebenstein) was taken as standard.

3. RESULTS AND DISCUSSION

One of the first steps in phosphor synthesis is the choice of a proper mineralising agent. With this purpose in mind, a preliminary sample series without flux and with Na_2WO_4 or CaCl_2 was prepared at 1000 °C with 1 mol % Eu and was characterised.

$\text{CaWO}_4:\text{Eu}$ samples prepared without flux or with Na_2WO_4 show red aparent luminescence whereas the sample obtained with CaCl_2 as flux does not exhibit red luminescence. In fact, under 254 nm excitation, $\text{CaWO}_4:\text{Eu}(\text{CaCl}_2)$ is almost nonluminescent. The emission spectra of $\text{CaWO}_4:\text{Eu}$ (no flux) and $\text{CaWO}_4:\text{Eu}(\text{Na}_2\text{WO}_4)$ consist mainly of two bands namely a weak one at 610-615 nm (Eu^{3+} -band) and a stronger one at 395-400 nm (self-activated band).

Taking into account that the self-activated samples prepared with CaCl_2 and Na_2WO_4 show comparable luminescence emissions (98 % and 112 %, respectively), this CaCl_2 influence on europium incorporation was rather unexpected. In fact, CaCl_2 is known as a very effective flux and is currently used in phosphor processing.

The X-ray diffraction (XRD) patterns offer an explanation. Whereas all phosphor samples prepared without flux or with Na_2WO_4 present pure, crystalline lattices with scheelite (tetra- CaWO_4), the corresponding sample prepared with CaCl_2 contain europium trioxide phase. It seems that, during the high temperature treatment, the WO_3 from the synthesis mixtures was consumed by CaCl_2 and eventually converted into calcium tungstate. As a result, europium atoms do not enter into the host lattice. Mention must be made that, in our previous work on synthesis of activated calcium tungstate phosphors, sodium nitrate was also tested as flux and gave very poor results, too.⁷

Besides the flux nature and concentration, there are many other factors that could influence on the europium incorporation and consequently on the luminescent characteristics of phosphor samples.

In order to study the influence of the firing temperature, four samples series were prepared as follows:

A1, A2, A3 - samples of $\text{CaWO}_4:\text{W}$ prepared with no flux, at 800 ; 900 and 1000 °C, respectively;

B1, B2, B3 - samples of $\text{CaWO}_4:\text{W}$ (Na_2WO_4) prepared with flux, at 800 ; 900 and 1000 °C, respectively;

C1, C2, C3 - samples of $\text{CaWO}_4:\text{Eu}$ prepared with no flux, at 800 ; 900 and 1000 °C, respectively;

D1, D2, D3 - samples of $\text{CaWO}_4:\text{Eu}$ (Na_2WO_4) prepared with flux, at 800 ; 900 and 1000 °C, respectively;

In our working conditions, the incorporation of trivalent rare earth ions into the CaWO_4 lattice could proceed in two ways: 2Eu^{3+} replace 3Ca^{2+} ions, and so a calcium vacancy is generated, and a pair $\text{Eu}^{3+} + \text{Na}^+$ replace 2Ca^{2+} ions. Samples from the C series are prepared without flux and correspond to the presumed phosphor formula $\text{Ca}_{1-3x}\text{Eu}_{2x}\square_x\text{WO}_4$, where \square represents calcium vacancy and $x=0.0526$. Samples from the D series are prepared in the presence of a large amount of melted sodium tungstate ($T_m=698^\circ\text{C}$) and consequently correspond to the phosphor formula $\text{Ca}_{1-2x}\text{Eu}_x\text{Na}_x\text{WO}_4$ where $x=0.1$.

XRD-patterns show that all samples possess a well formed scheelite structure with the same cell parameters ($a = 5.24$ c = 11.38). No unreacted Eu_2O_3 or WO_3 phases were observed.

Figure 1 presents the emission and excitation spectra for $\text{CaWO}_4:\text{Eu}$ phosphor samples prepared at 1000 °C (C3 and D3) in comparison with the self-activated phosphor $\text{CaWO}_4:\text{W}$ obtained in the same conditions (B3). The emission spectrum of $\text{CaWO}_4:\text{W}$ consists of one strong and large emission band at 395 nm generated by the WO_4 group centres from the host lattice (figure 1a). Incorporation of europium ions brings about the diminution of this self-activated band (with about 70 %) and the formation of many relatively narrow bands visible at about 325; 355; 365; 395; 465; 590; 615 and 650 nm. These bands are rather weak so that their exact position is difficult to estimate. Most of these bands are in the blue-green region and are covered by the much more intensive self-activated band. The Eu^{3+} characteristic bands are in the red region, the most intense being at 610-615 nm.

Emission spectra show that, at 254 nm excitation, both types of luminescence centres contribute to the observed luminescence namely, WO_4 -centres of the lattice and Eu^{3+} -centres.

The observed luminescence colour is determined by the ratio between the self-activated band (~ 395 nm) and the most intense Eu^{3+} characteristic band (~ 615 nm). This ratio depends on the preparative conditions.

The excitation spectra for the 615 nm band consist of many narrow bands situated at 295; 315; 370; 390; 400; 420; 470 and 540 nm. The strongest excitation bands are between 370 and 400 nm, domain where the self-emission of the host lattice is strong. This shows that a mechanism of energy transfer is involved into the excitation step.

Figure 2 presents the intensity of these two main bands versus the firing temperature. One can see that, in general, the increase of the firing temperature helps the formation of WO_4 -centres (in $\text{CaWO}_4:\text{W}$) and Eu^{3+} centres (in $\text{CaWO}_4:\text{Eu}$). In the latter case, the contribution of the lattice to the observed luminescence decreases slowly with the temperature. It seems also that the brightness of the characteristic Eu^{3+} emission is slightly improved by the flux utilization (900°C) and the increase of the firing temperature (1000°C)

The luminescent properties are also influenced by the activator concentration. Eight phosphor samples were prepared at 900°C with Na_2WO_4 as flux and with variable europium amounts. The resulting E1-E8 samples correspond to the phosphor formula $\text{Ca}_{1-2x}\text{Eu}_x\text{Na}_x\text{WO}_4$ where $x=0.000$; 0.005; 0.010; 0.025; 0.050; 0.075; 0.100 and 0.120, respectively. The emission spectra presented in figure 3 show that the specific Eu-band is well formed at only 0.5 mol % and that the self activated band decrease continuously in intensity and becomes more structured with the Eu-concentration increase.

Figure 4 presents the calculated intensity of these two main emission bands versus the europium concentration. One can see that, for 0.5 ÷ 2.5 mol% Eu, the self activated band decreases rapidly to reach a constant value representing about 30 % from the initial value. The Eu-red emission band increases slowly to an almost stationary value, either. The maximum of the red emission is obtained at 5÷7 mol% , the degree of europium incorporation being maximum.

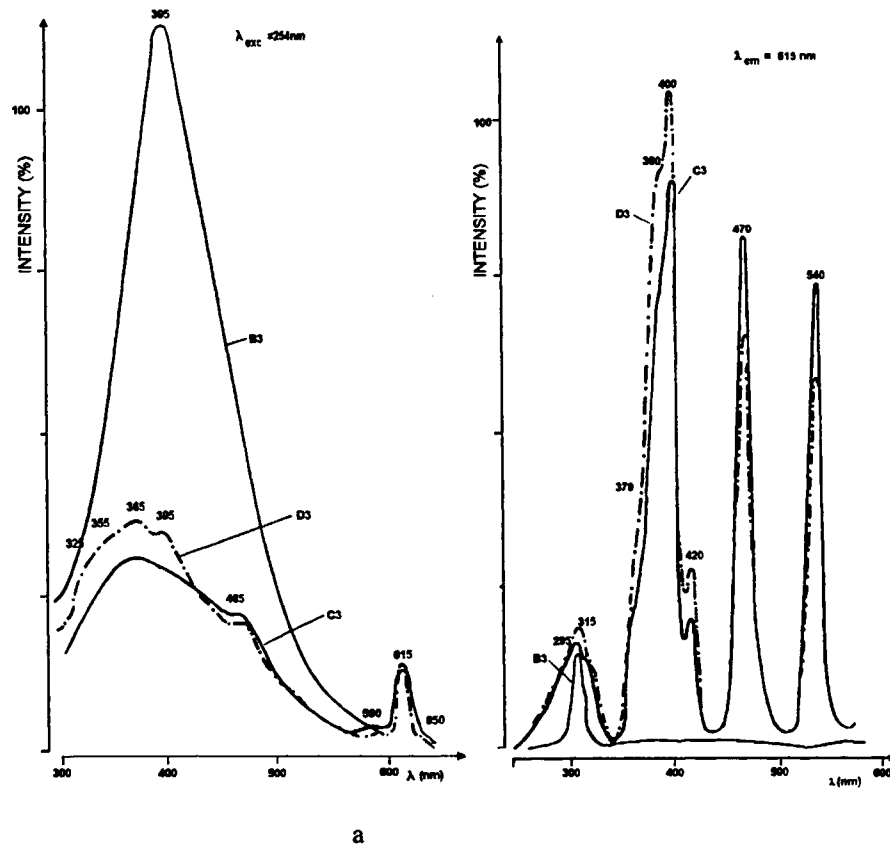


Figure 1. Emission and excitation spectra of some activated calcium tungstate phosphors prepared at 1000 °C.

B3- $\text{CaWO}_4:\text{W}(\text{Na}_2\text{WO}_4)$; C3: $\text{CaWO}_4:\text{Eu}$ (no flux); D3- $\text{CaWO}_4:\text{Eu}(\text{Na}_2\text{WO}_4)$;

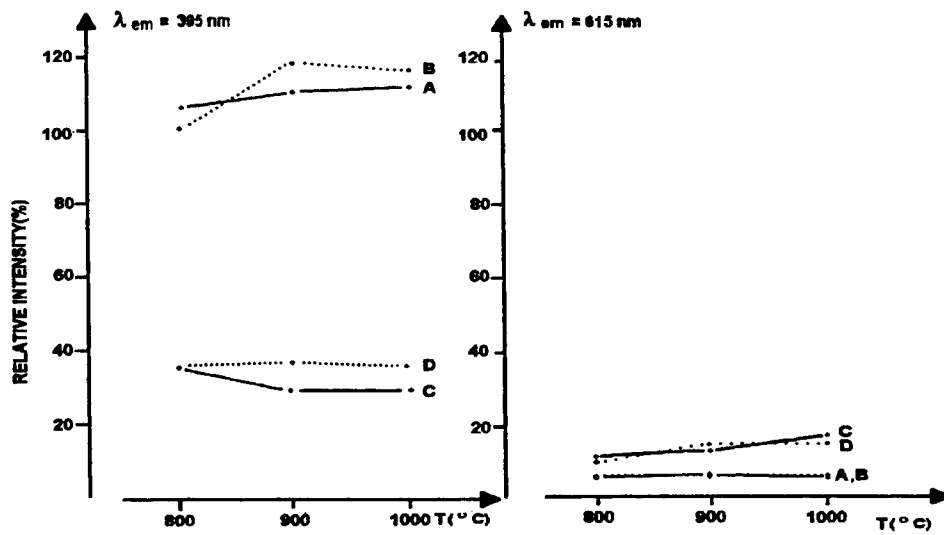


Figure 2. Relative intensity of self activated (I_{395}) and Eu-characteristic (I_{615}) versus firing temperature

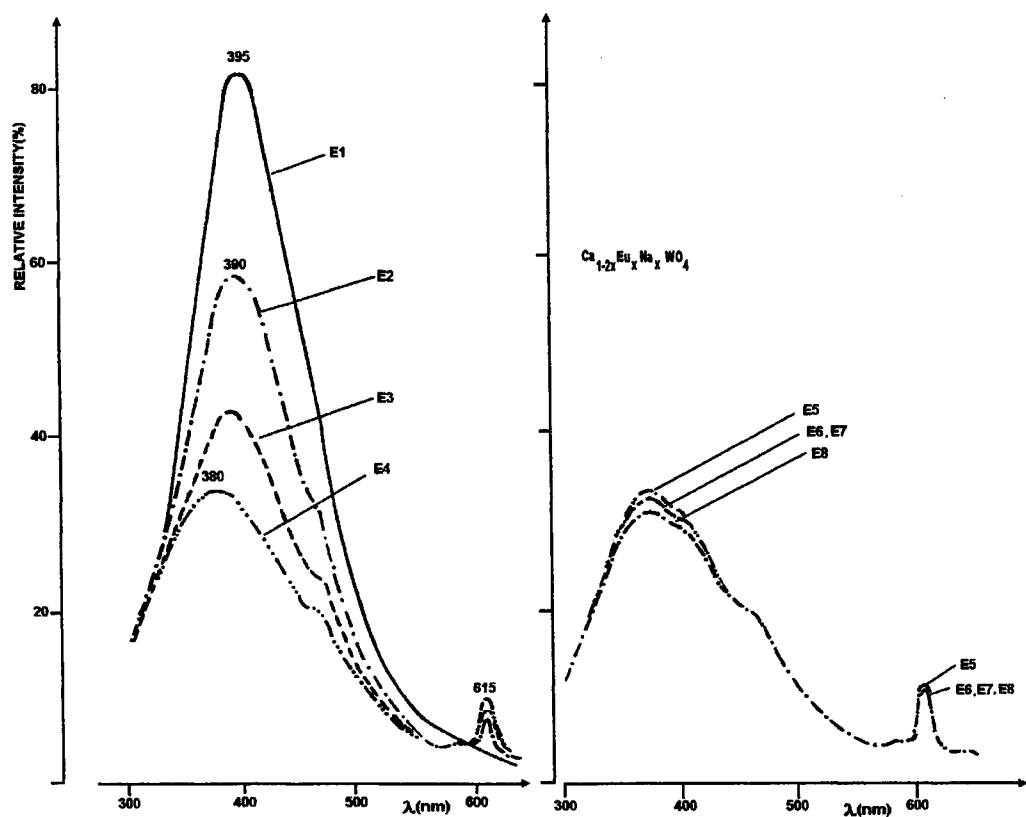


Figure 3. Emission spectra of $\text{CaWO}_4:\text{Eu} (\text{Na}_2\text{WO}_4)$ samples prepared with various activator concentrations.

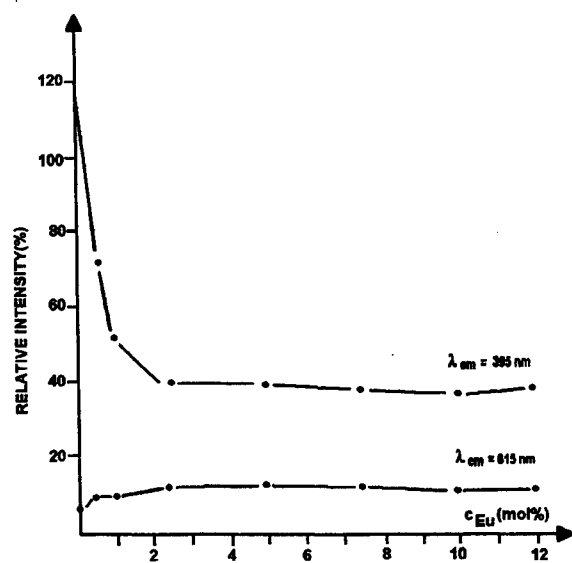


Figure 4. Relative intensity of the self-activated (I_{395}) and Eu- band (I_{615}) versus the europium concentration.

4.CONCLUSIONS

Red emitting $\text{CaWO}_4\text{:Eu}$ phosphor powder was obtained with sodium tungstate as flux and 5-7 mol% europium, at 900-1000°C. Both WO_4^- and Eu-centres contribute to the apparent luminescence. The well evidenced composite structure of emission and excitation spectra and the uniform, well formed scheelite lattice, suggest a good europium incorporation.

REFERENCES

1. W.Stern, "Colour plasma display by UV-excited phosphors", *Beitr.Plasmaphys.*, **25**(1), 57-75 (1985);
2. K.W.Butler, *Fluorescent Lamp Phosphors. Technology and Theory*, Pennsylvania State University Press, 1980.
3. G.Blasse and B.C.Grabmayer, *Luminescent Materials*, Springer Verlag, Berlin, 1994;
4. L.G.Uitert and R.R.Soden, "Multiple emission spectra of trivalent europium in the scheelite structure", *J.Chem.Phys.*, **32**(6), 1687-1689;
5. L.G.Uitert, "Luminescence of insulating solids for optical Massers", *Luminescence of Inorganic Solids* (Ed.P.Goldberg), Academic Press, 1966;
6. F.Forgaciu, M.Nemes, E.J.Popovici, V.Ursu and D.Macarovici, "Influence of precipitation conditions on the quality of calcium tungstate used in phosphor synthesis", *Studia Univer. Babes-Bolyai, Chemia*, **XL**(1-2), 47-54 (1995);
7. E.J.Popovici, F.Forgaciu, M.Nemes, V.Ursu and D.Macarovici, "Attempts on the synthesis of some activated calcium tungstate phosphors", *Rom.J.Optoelectronics*, **5**(1), 85-88 (1997);

Off line multiresponse optimization of
gas jet assisted, CO₂ laser cutting of polymetacrylate

Eugen Cicala, Delia Zsivanov, Alexandru Nichici

"Politehnica" University of Timisoara
Piata Victoriei 2, 1900, Timisoara, Romania

ABSTRACT

From the phenomenological point of view, laser cutting processes are complex, weakly organised and diffuse systems. Off line optimization of such processes demands relative simple, but accurate enough models, which could be obtained by experimental way. The article presents the results of a large factorial designed experiment, having three main objectives: to identify which factors are statistically important, to build a quantitative model relating the important factors to the response functions, to optimize these response functions and particularly the material removal rate, the kerf walls parallelism deviation and the specific energy consumption. The obtained results allow the choice of laser cutting optimal parameters.

Keywords: polymetacrylate, CO₂ laser cutting, factorial experiments, off-line optimization

1. INTRODUCTION

From the phenomenological point of view, laser cutting processes are complex, weakly organised and diffuse systems.¹ Their theoretical modelling is possible on the basis of heat conduction, mass-and energy-balance equations, but the developed mathematical models are very complicated and with difficulty utilisable in technological purposes.

By practical reasons, the off line optimization of such processes demands more simple, but accurate enough models, which could be obtained by experimental way.

The article presents the results of a large factorial designed experiment,² having three main objectives:

- to identify which factors are statistically important;
- to build a quantitative model relating the important factors to the response functions;
- to optimize these response functions and particularly the material removal rate, the kerf walls parallelism deviation and the specific energy consumption.

2. EXPERIMENTAL RESULTS AND THEIR INTERPRETATION

All trials of the experiment were performed on a laser cutting system CILAS 2000, having a 2000W, CO₂ laser and a two-axis numerical control NUM 750.³

The workpiece material was polymetacrylate ($\rho=1186 \text{ kg/m}^3$, $K=0.2 \text{ W/m.K}$, $C=1.4 \cdot 10^3 \text{ J/kg.K}$).

The hierarchic differentiation of factors influencing gas jet assisted, CO₂-cw laser cutting of polymetacrylate was made by a random balance experiment, having 16 trials.

By this way, the relationships among eight factors, namely:

- X₁- laser power P_L (with 4 levels: 100; 200; 300 and 400 W);
- X₂- cutting speed v (with 4 levels: 1; 2; 3 and 4 m/min);
- X₃- laser spot/workpiece surface distance (with 4 levels: 0.6; 0.8; 1.0 and 1.2 mm);
- X₄- workpiece thickness s (with 4 levels: 1.6; 2.6; 3.1 and 5 mm)
- X₅- assist gas pressure (with 2 levels: 1 and 3 bar)
- X₆- assist gas nature (with 2 levels: O₂ and N₂)
- X₇- gas nozzle diameter (with 2 levels: 1 and 1.5 mm)
- X₈- cutting path curvature radius (with 2 levels: 120 and ∞ mm)

and two response functions, namely: kerf width at the top B [mm] and respectively at the bottom of workpiece b [mm] were analysed.

The program matrix of the random balance experiment is given in the table 1.

Table 1

Trial number	Variation levels of influence factors								Kerf width	
	X ₁ [W]	X ₂ [m/min]	X ₃ [mm]	X ₄ [mm]	X ₅ [bar]	X ₆ [-]	X ₇ [mm]	X ₈ [mm]	B [mm]	b [mm]
1.	400	4	0.8	1.6	1.0	N ₂	1.0	20	0.26	0.26
2.	300	1	0.6	2.6	1.0	N ₂	1.0	∞	0.21	0.19
3.	200	1	0.6	2.6	3.0	N ₂	1.0	∞	0.23	0.24
4.	100	1	1.2	3.1	3.0	N ₂	1.0	∞	0.55	0.26
5.	400	3	0.8	3.1	3.0	O ₂	1.0	∞	0.53	0.42
6.	300	2	1.2	5.0	3.0	O ₂	1.0	20	0.39	0.16
7.	200	4	1.0	5.0	1.0	O ₂	1.0	20	0.32	0.00
8.	200	3	1.0	5.0	1.0	O ₂	1.0	∞	0.34	0.00
9.	100	2	1.2	5.0	1.0	N ₂	1.5	20	0.30	0.00
10.	300	4	0.8	1.6	1.0	N ₂	1.5	20	0.27	0.26
11.	400	1	1.0	1.6	3.0	N ₂	1.5	∞	0.34	0.28
12.	400	2	0.8	2.6	3.0	N ₂	1.5	∞	0.21	0.42
13.	300	4	0.6	2.6	3.0	O ₂	1.5	20	0.40	0.00
14.	200	2	1.2	3.1	3.0	O ₂	1.5	∞	0.51	0.27
15.	100	3	0.6	3.1	1.0	O ₂	1.5	20	0.24	0.00
16.	100	3	0.6	1.6	1.0	O ₂	1.5	20	0.19	0.14

The statistical treatment of experimental results has demonstrated the most important factors, from the point of view of the studied response functions, are: laser power, cutting speed, workpiece thickness, laser spot/workpiece surface distance and assist gas pressure. The influence of cutting path curvature radius, assist gas nature and gas nozzle diameter was negligible, in the given conditions.

On this basis, a complete factorial experiment CFE 2⁵ having N=2⁵=32 trials, was designed, realised and statistically analysed. The main objective of this experiment was the building of some linear polynomial models relating the 5 significant factors, selected previously by the random balance experiment and 3 response functions of the technological system, considered as the most representative for an efficient industrial cutting process, namely:

- material removal rate Y₁ [mm³/min]:

$$Y_1 = \frac{b+B}{2} \cdot s \cdot v \cdot 10^3 \text{ [mm}^3\text{/min]} \quad (1)$$

- kerf walls parallelism deviation Y₂ [-]:

$$Y_2 = 1 - \frac{b}{B} \quad (2)$$

- specific energy consumption Y_3 [J/mm³]:

$$Y_3 = \frac{120 \cdot P_L}{(b + B) \cdot s \cdot v \cdot 10^3} \text{ [J/mm}^3\text{]} \quad (3)$$

The general shape of the linear polynomial model is:

$$Y_j = b_{0j} + \sum_{i=1}^5 b_{ij} \cdot X_{ij} + \sum_{n,j=1}^5 b_{ijn} \cdot X_{ij} \cdot X_{nj}, \dots j = 1 \dots 3, i \neq n \quad (4)$$

where Y_j are response functions, X_{ij} , X_{nj} – influence factors and b_{0j} , b_{ij} , b_{ijn} – regression coefficients.

The central point (basic levels) and variation intervals of the factors involved in the factorial experiment (table 2) were established using previous theoretical and experimental results.

Table 2

Factor parameters	Codified values of factors	Natural values of factors				
		X_1 [W]	X_2 [m/min]	X_3 [mm]	X_4 [mm]	X_5 [bar]
Upper level	+1	400	3	1.2	5	3
Lower lever	-1	200	1	1.0	2.6	1
Central point (basic level)	0	300	2	1.1	3.8	2
Variation interval	ΔI	100	1	0.1	1.2	1

The estimated values of linear regression coefficients in equation (4), obtained on the basis of STATGRAPHICS software, are given in table 3.

Table 3

Regression coefficients symbols	Linear regression coefficients values corresponding to natural values of factors:		
	Material removal rate Y_1 [mm ³ /min]	Kerf walls parallelism deviation Y_2 [-]	Specific energy consumption Y_3 [J/mm ³]
b_0	-671.838	-1.21596	59.5229
b_1	-3.459	0.00534	0.0622
b_2	-369.094	0.35747	-10.2917
b_3	1411.300	Insignificant	-35.4375
b_4	242.943	0.09135	-8.4896
b_5	Insignificant	Insignificant	Insignificant

The estimation accuracy of regression coefficients values is very high (from 84.45 to 99.11%).

Using the same STATGRAPHICS software, the polynomial models corresponding surfaces, relating the above response functions to most important pair combinations of existing influence factors, were represented (fig. 1, 2 for Y_1 , fig. 3, 4 for Y_2 , fig. 5, 6 for Y_3). In all these figures, unrepresented influence factors are maintained on the basic levels (see table 2).

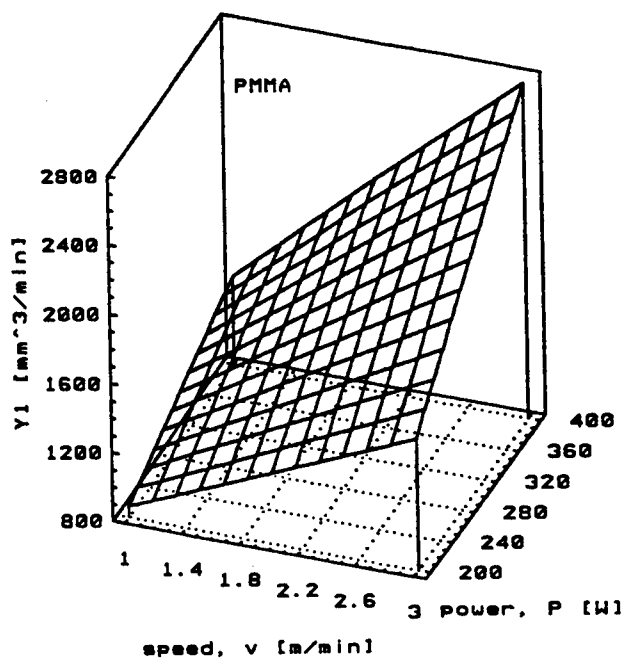


Fig.1

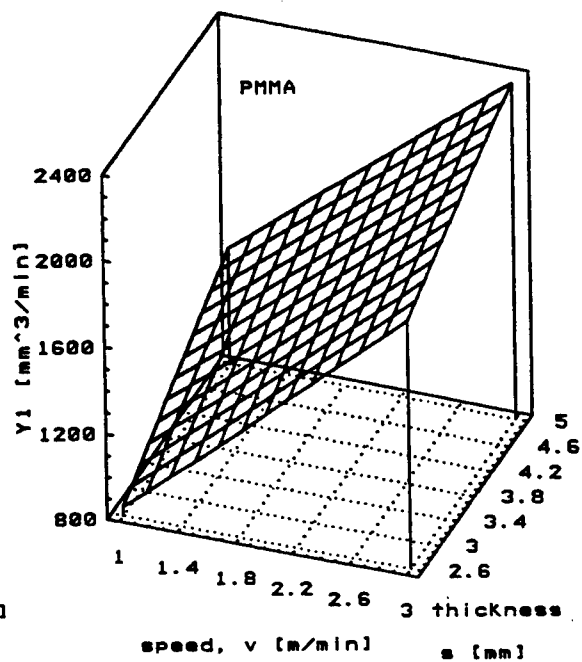


Fig.2

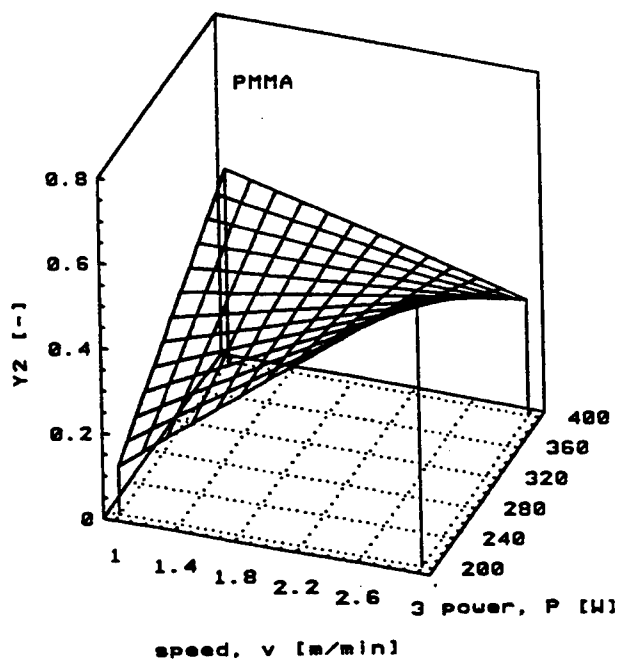


Fig.3

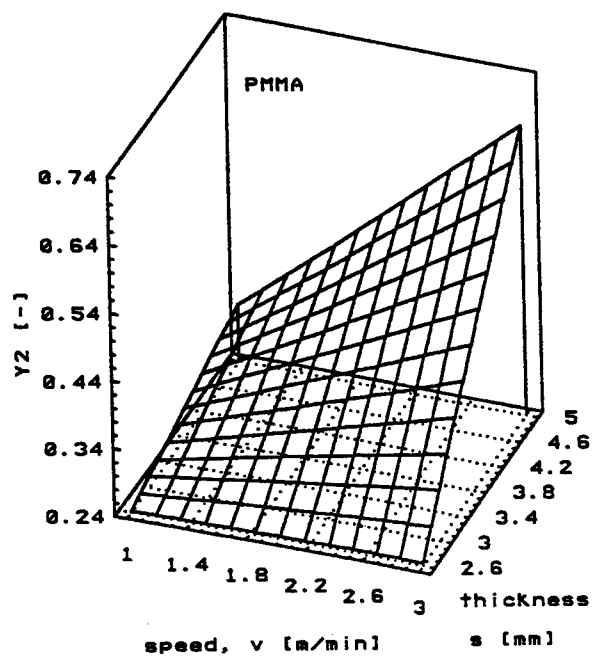


Fig.4

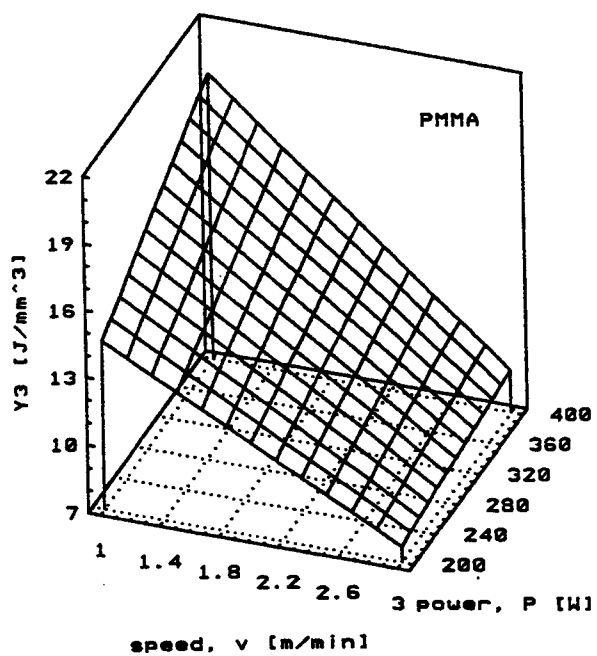


Fig.5

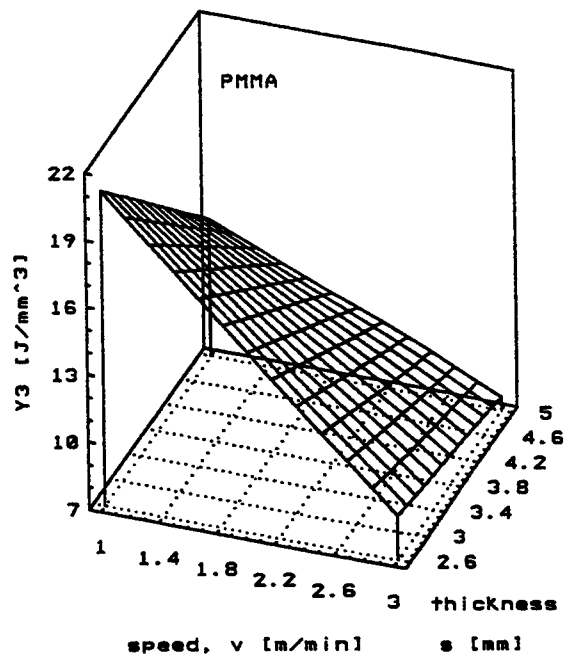


Fig.6

3. CONCLUSIONS

Analyzing the obtained results from the point of view of polymettacrylate gas jet assisted, CO₂-cw laser cutting optimization,³ the ensuing conclusions could be drawn:

- a major importance for all studied response functions have laser power, cutting speed and workpiece thickness factors;
- the developed algebraic polynomial models of the laser cutting could be utilized to looking for and to find out the maximum and minimum domains of given response functions;
- the conditions for an ideal laser cutting process – maximum values of the material removal rate and minimum values of kerf walls parallelism deviation and specific energy consumption could not be simultaneously reached.

However, generally speaking, the obtained results show ways to optimize the main laser cutting performance criteria:

- to maximize the material removal rate (the experimental mean value was 1625 mm³/min, the maximum one – 3300 mm³/min), cutting speed and laser power must be increased;
- to minimize the kerf walls parallelism deviation, (the experimental mean value was 0.375, the minimum one – zero), cutting speed and laser power must be decreased;
- to minimize the specific energy consumption, (the experimental mean value was 12.7 J/mm³, the minimum one – 6.7 J/mm³), cutting speed and laser power must be decreased.

Moreover, to optimize simultaneously material removal rate and specific energy consumption, the laser beam focal point must be put above the working surface and the workpiece thickness must be as big as possible. On the contrary, best kerf quality, with minimum kerf walls parallelism deviation, correspond to smaller values of workpiece thickness.

The obtained linear polynomial models, which are only locally adequate, could be also used as departure basis for exploring multifactorial space with extreme searching methods (such as steepest ascent methods). By this way, the accurate detection of extreme coordinates become possible.

4. ACKNOWLEDGEMENTS

The authors would like to gratefully acknowledge CALFA Laboratories of University Technological Institute, Bethune, France, where the experimental research was performed. They wish to thank also Robert Mee, Tennessee University, Knoxville, U.S.A., for his assistance in the application of STATGRAPHICS software.

5. REFERENCES

1. A. Nichici and others, *Machining by erosion in Mechanical Technology*, Facla Publ., Timisoara, 1983.
2. A. Nichici, E. F. Cicala, R. Mee, *Experimental Data Processing*, Politehnica Press, Timisoara, 1997.
3. E. F. Cicala, *Laser Material Cutting Processes Optimization*, Ph. D. thesis, "Politehnica" University, Timisoara, 1997.

Establishing the regression polynoms for the objective function that define the dimensional accuracy in case of laser drilling

Ion David, Eugen Cicala

"Politehnica" University of Timisoara
Piata Victoriei 2,1900, Timisoara, Romania

ABSTRACT

The aim of the paper is to optimise the microholes machining, in the case of laser drilling. The laser used for experiments was a Neodim-15 laser. The material used for drilling was 41MoCr11 austenitic stainless steel with a 1,5 mm thickness. As parameters of the laser drilling process were considered: diaphragm diameter, focal point position, focal length of the lens and laser pulse power. The objective functions were the diameter of the microhole in the area of the laser beam entrance in material (D_i), the diameter of the microhole in the area where the laser beam exit the material (D_e), respective their tolerances (T_i and T_e). It was used an complete factorial experiment 2^4 . The established mathematical models are useful in finding the optimum values of the parameters in various combinations, such as the hole diameter to be closer to the required diameter.

Keywords: laser drilling, experimental design, laser process optimisation

1. EXPERIMENTAL CONDITIONS

The aim of the paper is to optimise the process which realise microholes broke through stainless steel 41MoCr11 and obtention of some orifices whom effective sizes will got smaller deviations from nominal quotation.

For these experiments we used Neodim 15 laser instalation which functioned in pulses. This instalation have possibility to regulate the pulse power in range of 2,5-12 J.

The material used for drilling was austenite stainless steel, in sheets with a 1,5 mm thickness. Every experiment was repeated five times, for a better investigation.

The extreme values were eliminated and the arithmetic average of the remaining three values was used for the next stage of results processing.

The impulse power (X_1),the diaphragm diameter (X_2), the focal point position (X_3),and the focal lenght of focus objective (X_4),were considered like parameters of laser drilling process.

The following objective functions were: the diameter of the microhole in the area of laser beam entrance in material (D_i), the diameter of the microhole in the aria were the laser beam exit the material (D_e),respective their tolerances (T_i and T_e).¹

2. EXPERIMENTAL DESIGN

To avoid the measurement errors caused by melted material deposd on the microholes edges , the samples were first grinded and later cleaned in an ultrasonic bath.

It was used an complet factorial experiment 2^4 with 16 measurements. For every parameter of the process were considered two levels.The values of these two levels were established in a preliminary set of experiments.²

Matrix program structure

Tab.1

Nr.exp.	X_1	X_2	X_3	X_4	Nr.exp.	X_1	X_2	X_3	X_4
1	-1	-1	-1	-1	9	-1	-1	-1	+1
2	+1	-1	-1	-1	10	+1	-1	-1	+1
3	-1	+1	-1	-1	11	-1	+1	-1	+1
4	+1	+1	-1	-1	12	+1	+1	-1	+1
5	-1	-1	+1	-1	13	-1	-1	+1	+1
6	+1	-1	+1	-1	14	+1	-1	+1	+1
7	-1	+1	+1	-1	15	-1	+1	+1	+1
8	+1	+1	+1	-1	16	+1	+1	+1	+1

In this sense for the laser pulse power, estimated by voltage (U) applied to condensers battery, the values were 2000V and 2800V; for diaphragm diameter 6 and 9 mm; for focal point position: 0,15 and 0,75 (g- material thickness) and for focal length: 30 and 60 cm.

The matrix program structure with codificated values. is presented in table 1 and the arithmetic average of the response functions values, determined like above, are presented in table 2.

Measurement results

Tab.2

Nr.exp.	Di [mm]	Ti [mm]	De [mm]	Te [mm]	Nr.exp	Di [mm]	Ti [mm]	De [mm]	Te [mm]
1	0,234	0,100	0,060	0,040	9	0,375	0,186	0,105	0,068
2	0,229	0,100	0,127	0,130	10	0,417	0,190	0,159	0,117
3	0,273	0,097	0,110	0,083	11	0,437	0,050	0,152	0,095
4	0,357	0,103	0,132	0,123	12	0,345	0,150	0,224	0,070
5	0,410	0,125	0,151	0,105	13	0,307	0,100	0,095	0,070
6	0,338	0,170	0,117	0,123	14	0,396	0,150	0,096	0,085
7	0,370	0,150	0,162	0,057	15	0,408	0,073	0,160	0,038
8	0,478	0,225	0,218	0,115	16	0,502	0,200	0,246	0,085

3. EXPERIMENTAL RESULT AND THEIR INTERPRETATION

The measurements results, were analysed with STATGRAPHICS program.

Firstly, this program gave the hierarchy of processing parameters, according to their influence on objective functions (Tab.3).

The process parameters hierarchy

Tab.3

Imp. order	Di	De	Ti	Te	Imp. order	Di	De	Ti	Te
1	X ₃	X ₂	X ₁	X ₁	6	X ₁ X ₃	X ₄	X ₁ X ₂	X ₂
2	X ₄	X ₁	X ₃ X ₄	X ₄	7	X ₂ X ₃	X ₂ X ₄	X ₁ X ₃	X ₁ X ₂
3	X ₂	X ₃ X ₄	X ₂ X ₃	X ₁ X ₄	8	X ₁ X ₂	X ₁ X ₂	X ₁ X ₄	X ₃
4	X ₃ X ₄	X ₃	X ₂ X ₄	X ₂ X ₃	9	X ₂ X ₄	X ₁ X ₃	X ₂	X ₂ X ₄
5	X ₁	X ₂ X ₃	X ₃	X ₃ X ₄	10	X ₁ X ₄	X ₁ X ₄	X ₄	X ₁ X ₃

Using the general formula of regression polynomial, which defined the response function:

$$y_i = b_0 + b_1x_1 + b_2x_2 + b_3x_3 + b_4x_4 + b_{12}x_1x_2 + b_{13}x_1x_3 + b_{14}x_1x_4 + b_{23}x_2x_3 + b_{24}x_2x_4 + b_{34}x_3x_4 \quad (1)$$

STATGRAPHICS make possible the regression coefficients calculation, and also polynoms determination for each of this four response functions.

The values of these regressions coefficients and also the precision of mathematical model estimation, established with a confidence of 95%, are presented in table 4.

Analysing this results, it can be formulated the following conclusions:

- for entering diameter of laser beam in material, the greatest influence is caused by focal parameters: focal point position (X₃) and focal length (X₄).

- for exit diameter (De) of laser beam, the maximum influence is caused by those parameters, which define laser beam from energetically point of view.

The microhole geometry (in transversal section) is influenced, firstly, by the laser beam power. This thing results from the tolerance size of the entrance and the exit diameters of laser beam in material. Interaction between processing parameters, has also a semnificative influences on these two response functions (Ti and Te).

For objective functions which were analyzed, it may be represented :

-histograms of effects;

-3D or 2D dependences vs. different influence factors.

Fig. 1,..., Fig. 12 present these dependences, for De, Di, Te, Ti.

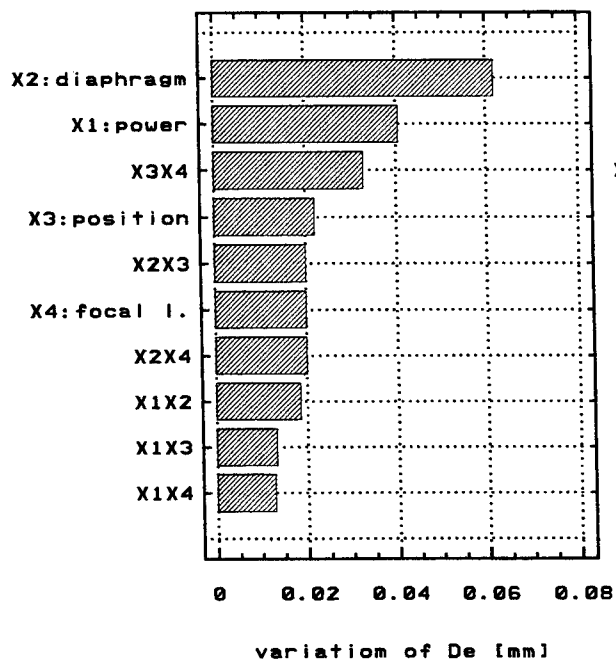


Fig. 1

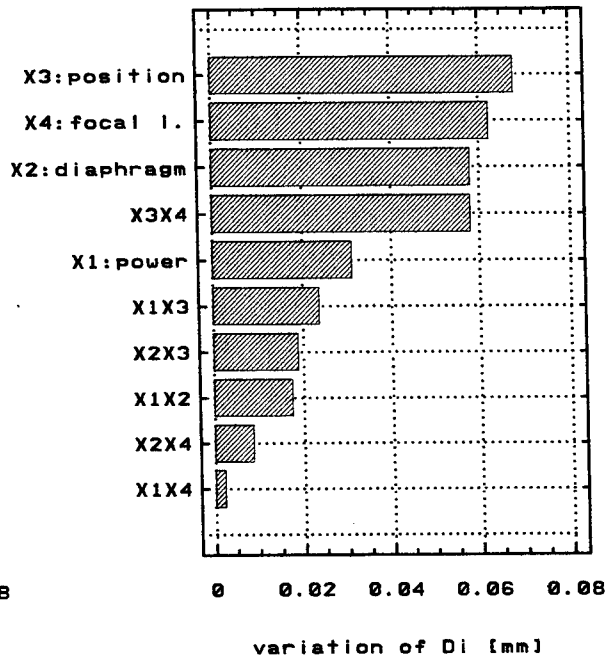


Fig. 2

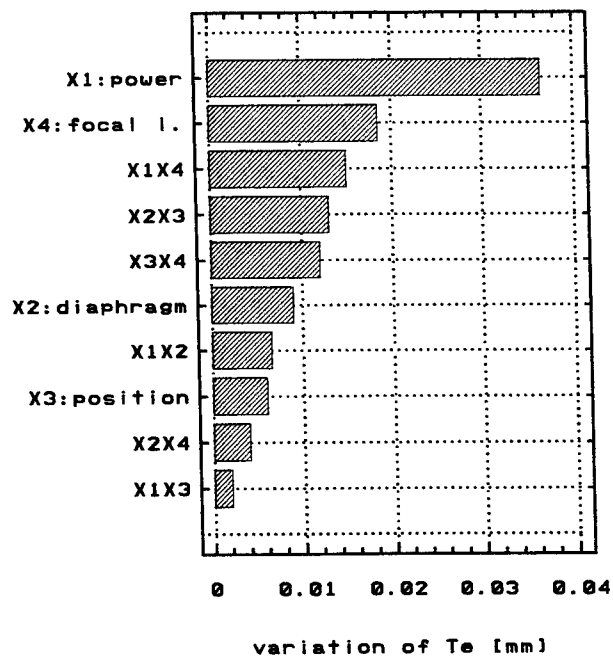


Fig. 3

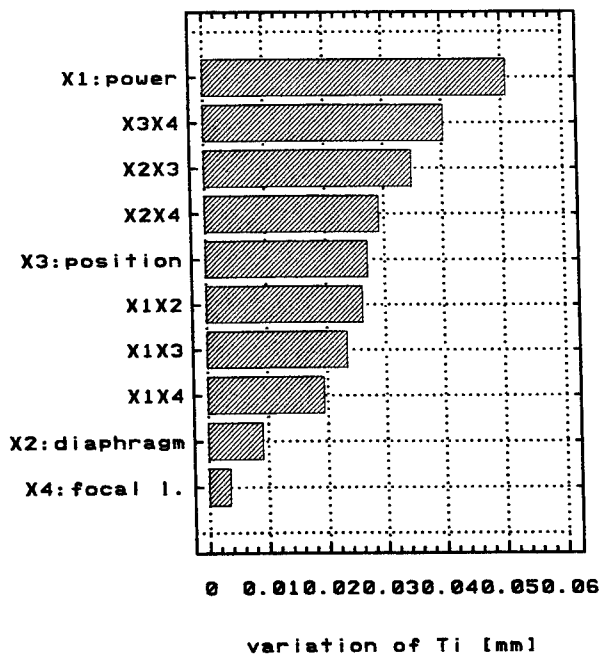


Fig. 4

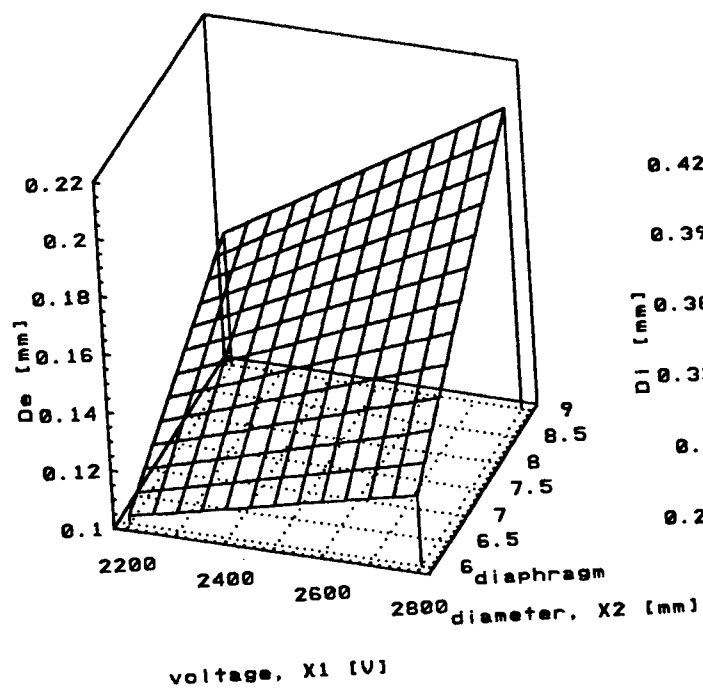


Fig.5

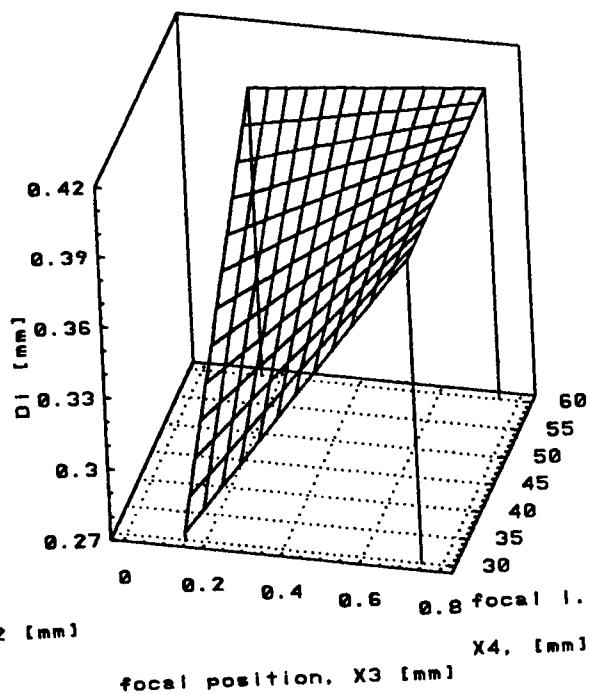


Fig.6

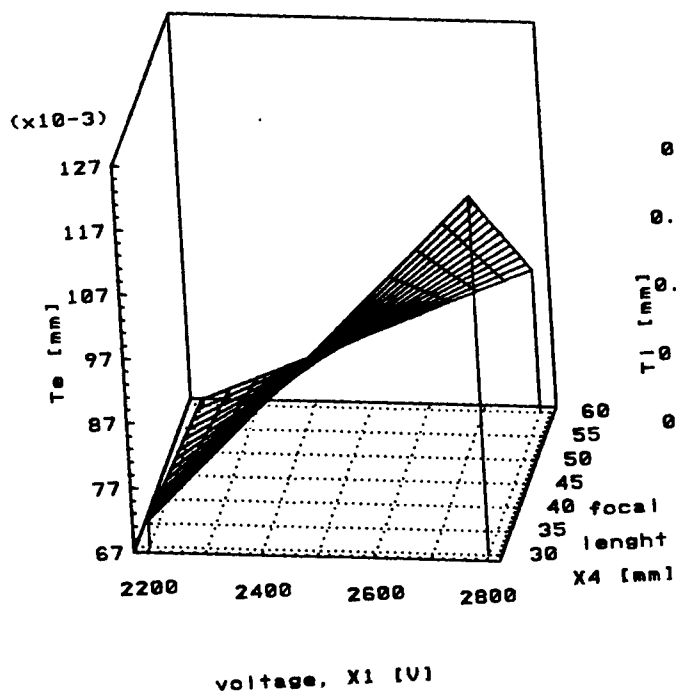


Fig.7

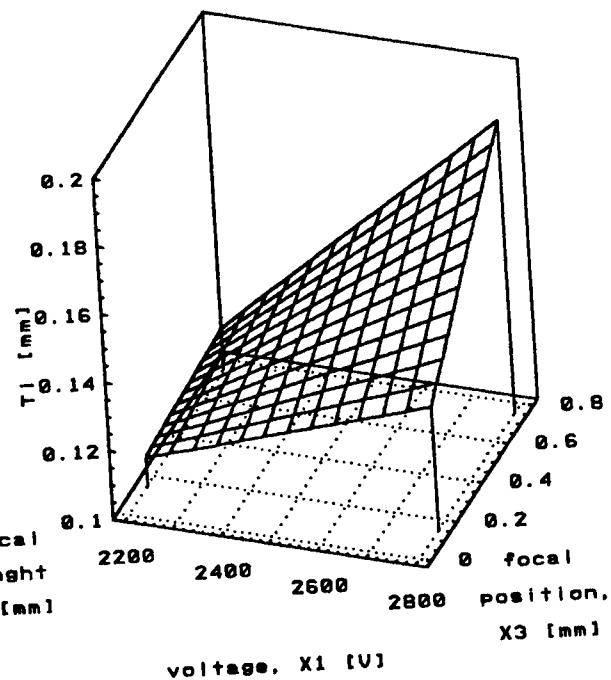


Fig.8

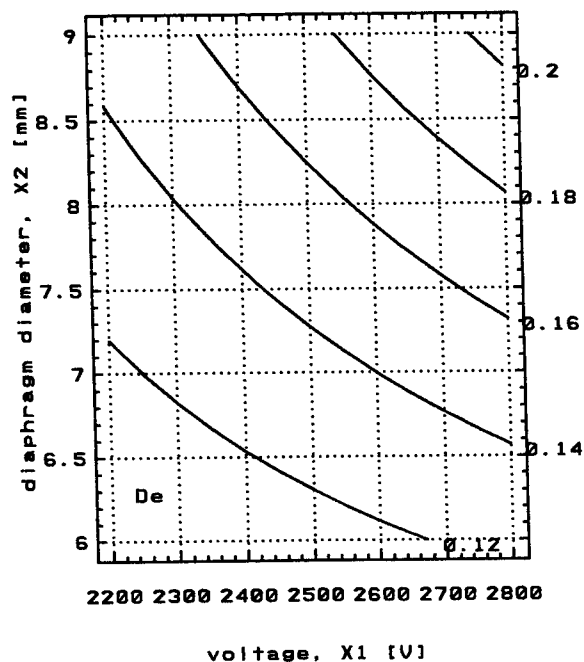


Fig. 9

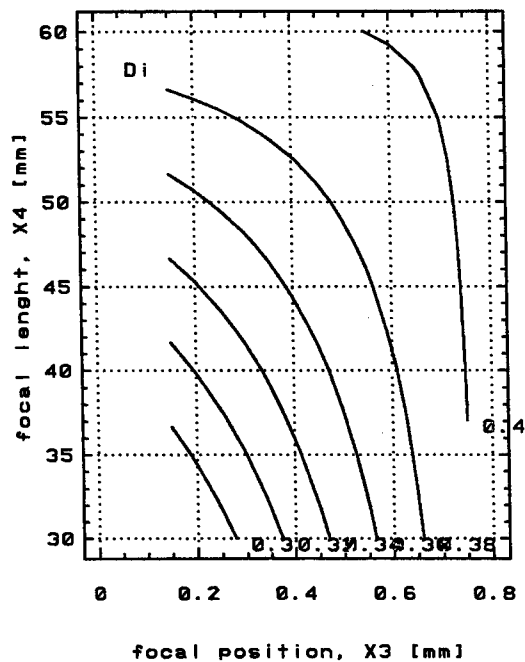


Fig. 10

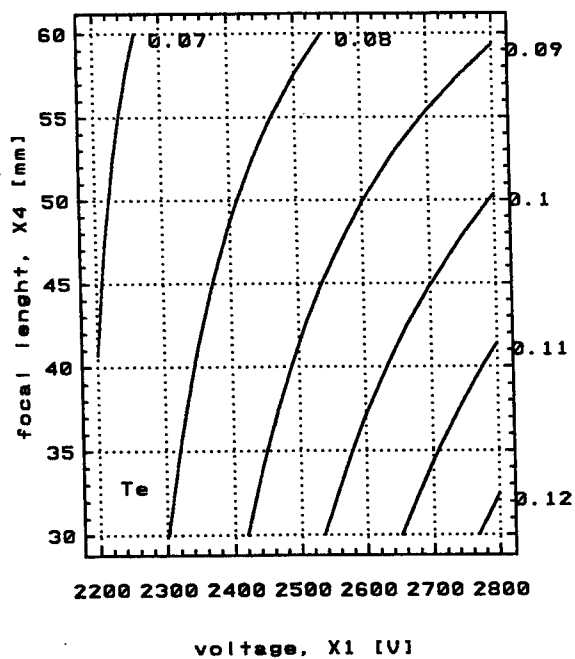


Fig. 11

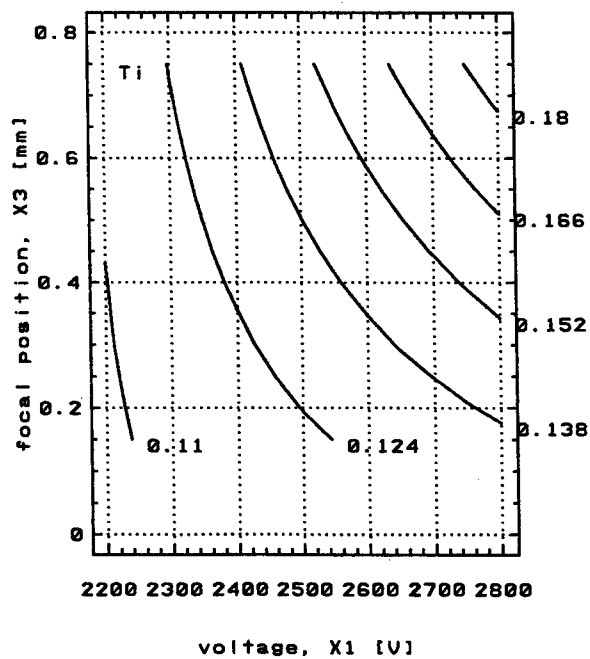


Fig. 12

The regression coefficients values

Tab.4

Coefficient	Response function			
	Di (Y1)	De(Y2)	Ti(Y3)	Te(Y4)
b_0	0,367250	0,144625	0,135563	0,08775
b_1	0,015500	0,020250	0,025437	0,01825
b_2	0,029000	0,030875	-0,004562	0,00450
b_3	0,033875	0,011000	0,013562	0,00300
b_4	0,031125	0,010000	0,001812	0,00925
b_1b_2	0,008750	0,009250	0,013062	0,00325
b_1b_3	0,011875	-0,006625	0,011687	0,00100
b_1b_4	0,001125	0,006375	0,009687	0,00750
b_2b_3	0,009375	0,010000	0,017437	0,00650
b_2b_4	-0,004375	0,010000	-0,014562	0,00200
b_3b_4	-0,029000	-0,016375	-0,020187	0,00600
Precision of estimation	75,11 [%]	91,67 [%]	93,86 [%]	73,72 [%]

4. CONCLUSIONS

The laser beam drilling process is used in processing of metallic materials and ceramics. The established mathematical models, are useful in finding the optimum values of the objective functions.

Will be preferred those processing systems which lead us to a high productivity.

This calculus methodology may be used (without any difficulty) for any interval of processing parameters variation, changing the processing materials or processing parameters.

5. ACKNOWLEDGEMENTS

The authors would like to thank prof. Robert Mec, from Tennessee University, Knoxville, U.S.A., for his assistance in the application of STATGRAPHICS software.

REFERENCES

1. I. David, "Precizia dimensionala si de forma geometrica la prelucrarea cu laser a microalezajelor", *A III-a Sesiune anuala "Progrese in fizica"*, fasc.IV, pag.173, Timisoara, 1981.
2. I.David, "Modèle mathématique simplifié pour le calcul des paramètres qui définissent la précision des orifices obtenus a faisceau laser focalisé", *Buletin Stiintific I.P.T., fasc. Mecanica*, 33, pag.43, 1988.

Theoretical model for the Reactive Pulsed Deposition Process:
application to the case of the ablation of a Ti target in low pressure N₂

J. Neamtu

Department of Physics II, Faculty of Science
University of Craiova, Str.A.I.Cuza 13, Craiova 1100, Romania

I. N. Mihailescu

National Institute for Laser, Plasma and Radiation Physics, Bucharest, Romania

ABSTRACT

We introduce a theoretical model to describe all the phenomena implied in the interaction process between the high intensity UV laser radiation and a solid target in the ambience of a low-pressure chemically active gas. The action of the laser radiation upon the solid surface is simulated by solving the 1-D heat equation. A hydrodynamical one-dimensional model was further applied to describe the interaction between the laser radiation and the plasma expanding in front of the target. The absorption of the laser radiation in the vapour plasma could be considered with the aid of a multifluid model. The transit of the ablated atoms and/or of the new formed chemical compound was approached with a Monte-Carlo method. We could compute time and space distribution of the main plasma parameters (e.g. the plasma density and temperature). We could finally predict the thickness distribution of a film deposited on a collector placed parallel to the target at a distance of (1.5-3) cm range. The calculus was conducted for the case of a Ti target in low pressure nitrogen.

KEYWORDS : pulse laser deposition, laser generated plasmas, TiN

1. INTRODUCTION

The model developed by us allows for the simulation of the whole laser reactive ablation process. The phenomena occurring during this process were simulated by solving equations governing the heating, melting and vaporising of the target.

The ionisation and heating process of the vapour plasma was modelled by considered gasodynamic equations. The ambient gas influence on laser-target-vapour interaction was considered by using a multifluid hydrodynamic code.

The analysis of these phenomena was conducted on laser time pulse condition simplifying the approaching of this question by taking into account the 1-D case.

The profile of the film on a substrate placed at a distance z_s from the initial target surface was further determined by solving the equation governing 3-D vacuum adiabatic expansion.

2. LASER PLASMA INTERACTION

Target heating, melting and vaporisation process was simulated in the same condition as reported in Ref. ¹. The phenomena occurring in these regions are governed by 1-D heat equation connected with the two Stefan conditions for the melting and vaporisation fronts, respectively. We assume the existence of a Knudsen diffusion layer between the vaporising front and the initial target surface across which the state variables are discontinuous.

The simplest and frequently used model for the simulation of this interaction is the gasodynamic one. It supposes that the plasma is an electrically neutral gas, which contains neutral atoms, ions and electrons in a local thermodynamique equilibrium.

For a time elapse of a few ns duration, one can consider that the temperatures of all components are equal, i.e. $T_e = T_i = T_a = T$. The laser radiation absorption is produced especially by inverse Bremsstrahlung, a process in which an electron placed in the field of an ion or neutral atom absorbs one photon and is accelerated.

The absorption coefficient of the plasma is K_p ² :

$$K_p = 3.69 * 10^8 (Z^3 N_i^2 / T^{0.5} \nu^3) (1 - \exp(-h\nu / KT)) \quad (\text{cm}^{-1}), \quad (1)$$

where Z , N_i , and T are the average charge, ionic concentration and plasma temperature, respectively. Here h , k are the Planck and Boltzmann constants while ν stands for the laser radiation frequency.

The laser radiation local intensity $I_l(z, t)$ is calculated assuming the absorption law in the form of the type:

$$I(z, t) = I_0(t) \exp\left(-\int_{z_i}^z K_p dz\right) \quad (2)$$

where z_i is the plasma- ambient gas boundary.

Under these conditions it seems more attractive to use a multifluid hydrodynamic code that allows to calculate the time evolution of the boundary.

Unlike other similar numerical simulations, in the depicted model, we took into account the ambient gas influence in which the laser irradiation is conducted, thus using a multifluid numerical code CEL (Coupled Euler Lagrange Code).

We assume that during of the laser pulse (in the ns range) the plasma motion has a plan 1-D character. We introduce an additional term $\dot{\Phi}$ in the energy variation equation, which represents the absorbed energy per unit of time and per unit of volume by inverse Bremsstrahlung absorption. Than the hydrodynamical differential equation system ³ becomes:

$$\begin{aligned} (mz_a)_t + (m\omega + P)_a &= 0, \\ (\rho z_a)_t + (\rho\omega)_a &= 0, \\ (Ez_a)_t + (E\omega + Pu)_a &= z_a \dot{\Phi}, \end{aligned} \quad (3)$$

where: $m = \rho u$; $\omega = u - z_t$; $z_a = \frac{\partial z}{\partial a}$; $z_t = \frac{\partial z}{\partial t}$; ρ , u , P are the gas density, velocity and pressure, respectively.

3. THE ADIABATIC EXPANSION OF THE VAPOUR PLASMA

This regime starts after the end of the laser pulse. The thermal energy of the plasma is transformed in the kinetic energy of a 3-D expansion. As our analyses extends over a time elapse much longer than the laser pulse duration, one may consider that the two phases of the process are entirely independent from each other. The expansion process is supposed to be 1-D till t_u for which $z_i(t_u)$ keeps the order of magnitude of the laser spot dimension. From this moment, we suppose that the species emerging from plasma transit to the collector. The transit of the ablated atoms and/or of the new formed chemical compound molecules was described through the intermediary of a Monte-Carlo simulation.

4. RESULT AND DISCUSSION

We developed a programme which simulates the interaction process between the laser radiation and metal target in an ambient gas at different pressures. We focus our analysis to the case of a Ti target in an N₂ atmosphere. The laser pulse considered in our simulation with the total duration $t = 20$ ns (FWHM) has a linearly-increasing front of 7.5 ns followed by a plateau of 9 ns and a linear-decreasing tail. After the installation of the vaporisation regime the spatial distribution of the target vapour density presents a maximum in the close neighbourhood of the initial target surface, i.e. for $z \approx 30 \mu m$. In Fig.1 we present the velocity and the atomic concentrations distribution, at the end of the laser pulse. We note the following trends: (i)-the maximum vapour concentration is confined in a zone close to the target surface vicinity, while the vapour plasma- ambient gas border is pushed up to (125-140) μm from the target surface (depending on the gas pressure), and (ii)-the compress gas is put into motion up to a distance of approximate (250-300) μm from the target (depending on the gas pressure). The influence of the ambient gas pressure upon the processes which developed inside the target is insignificant. This is because the only quantity which may be influenced by the pressure of the ambient gas in case of our model is the laser intensity effectively reaching the target surface. This represents a confirmation of the fact that in the case of UV laser irradiation the largest part of the pulse energy is spent in thermal processes within the target while the absorption in vapour plasma keeps much lower. From the study of Fig. 2, we observe the existence of important gradients in the spatial distribution of the electron temperature and density. This forbids the application of any models based upon the hypothesis of an uniform plasma density and/or temperature. The vapour plasma is characterised by a maximum temperature which is placed at the plasma- ambient gas border position. This border is moving far a part from the initial target surface along with the increase of the gas pressure. Such an evolution is the effect of to the confinement action exerted by the surrounding gas upon the vapour plasma. The influence of the ambient gas ((a) $P_a = 0.05$ mbarr; (b) $P_a = 1$ mbarr) upon the zone in the close vicinity of the target keeps insignificant. The temperature of the ambient gas in front of the plasma border increases till a maximum value which is reached at the interface between the moving gas-resting gas.

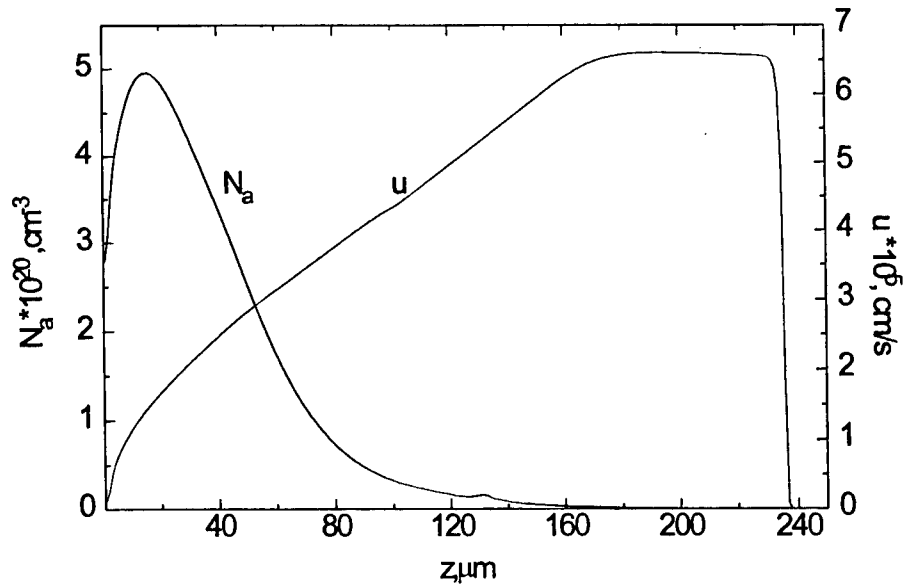


Fig. 1 The spatial distributions of the atom velocity, u , and of the concentration, N_a , of the system plasma-gas ambient, at the end of laser pulse ($P_a=1$ mbar), ($E=5\text{J/cm}^2$).

The increase of the gas pressure affects in similar manner the electron density - i.e. its maximum is placed in the close vicinity of the ambient gas - plasma border. Unfortunately, the plasma ionisation phase is not accessible to the spectroscopic investigations, because the initial vapour plasma layer is in the same time quite small and opaque. It is there for practically impossible to compare the theoretical predictions at the end of the laser pulse to direct experimental data (which become generally available a few μs latter on).

On the other hand, the numerical simulation becomes very difficult at time duration of ms order of magnitude, due to the very small time discretisation step chosen in our computation scheme. In deed, when continuing the analysis for longer time duration the round-off errors are amplified and numerical instabilities develop which make unreliable the results of the computation.

Unfortunately, the plasma ionisation phase is not accessible to the spectroscopic investigations, because the initial vapour plasma layer is in the same time quite small and opaque. It is there for practically impossible to compare the theoretical predictions at the end of the laser pulse to direct experimental data (which become generally available a few μs latter on). On the other hand, the numerical simulation becomes very difficult at time duration of ms order of magnitude, due to the very small time discretisation step chosen in our computation scheme. Indeed, when continuing the analysis for longer time duration the round-off errors are amplified and numerical instabilities develop which make unreliable the results of the computation. These shortcomings can be avoided using an implicit discretisation scheme. The data obtained in this case are in good accordance with the data obtained with other methods either analytical or numerical.

Thus in case of laser incident fluences in the $(1-10)\text{J/cm}^2$ range, the vapour plasma generated under the action of the UV laser radiation has an electron temperature lower than 1.5 eV . Let us note that such temperature are significantly smaller than those reached under the action of IR laser radiation at similar levels of the incident laser fluence.

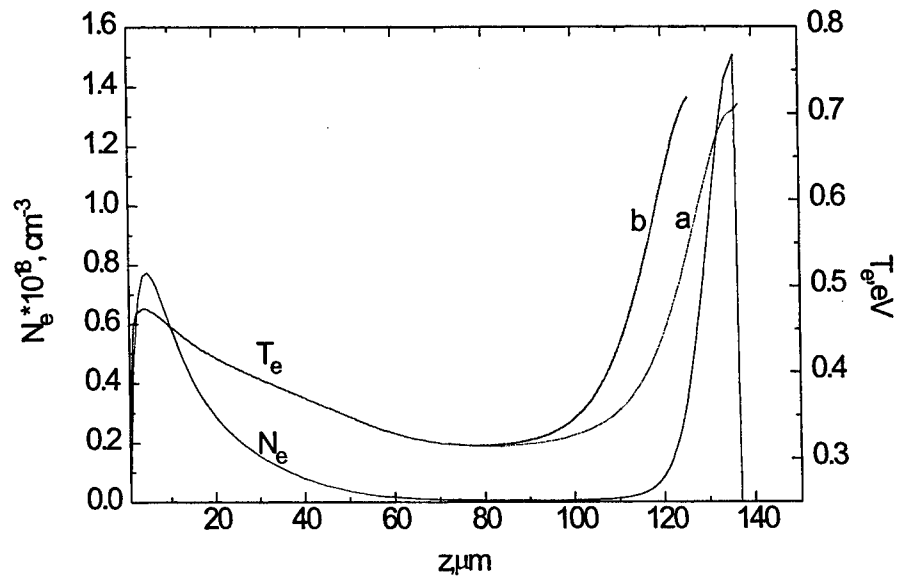


Fig. 2 The spatial distribution of electronic temperature, T_e , for (a) $P=0.05$ mbar, (b) $P=1$ mbar and the electron density, N_e , ($P=1$ mbar) at the end of laser pulse ($E=5\text{J/cm}^2$).

We further notice that the depth of the layer ablated from the target, which is predicted to be about 0.4 mm, is in reasonable agreement with experimental determinations. This concordance is remarkable in the condition we did not take into account the energy losses by conduction, convection and radiation. We further conducted Monte Carlo simulation in order to obtain an estimation of the thickness of the deposited layer (in particular TiN) in case of the pressure of the ambient gas in the range distance in the range of (1.5-3) cm. We inferred the spatial profile of the deposited film. A key parameter strongly influencing the interaction process between the molecules and atoms in the ablated flux with the molecules of the ambient gas is the corresponding collision cross-section. Details about the synthesis of the TiN molecule can be found elsewhere. If one assumes that all the Ti atoms in the ablated flux would effectively enter into a chemical reaction ending with the formation of a TiN molecule, we expect deposition rates of 0.25 nm/pulse for $P_a=50$ mbar and $z_s=1.5$ cm, and 0.04 nm/pulse for $P_a=50$ mbar and $z_s=3$ cm, respectively. Those values are no more than two times higher than the values determined experimentally by electron microscopy in cross-section. This more discrepancy may be due to the supplementary losses due to the energy leaving the interaction zone after reflection on the target surface and twice crossing the vapour-plasma cloud (which are not considered in our energy balance). Also, the velocities (i.e. the kinetic energies) of the species in the plasma are slightly overestimated because of the 1-D expansion symmetry assumed in our computation. Indeed, a radial expansion (which is a realistic assumption) causes a decrease of the overall thickness of the deposited layer. As we observe from Fig.3, the thickness of the deposited layer strongly decreases with the increase of the target-collector separation distance, the most probably according to a $h(z_s) \sim z_s^{-2.5}$ law.

We finally point out that the deposition profile was the best fitted by $(\cos\theta)^n$, with $n=5$ distribution law. Let us observe that the value $n=5$ is in fact an intermediate value between the values $n=9-12$ characteristic to the plasma expansion in vacuum and $n=2-3$ for the plasma evolution in a gas at low pressure ((1-10) Pa).

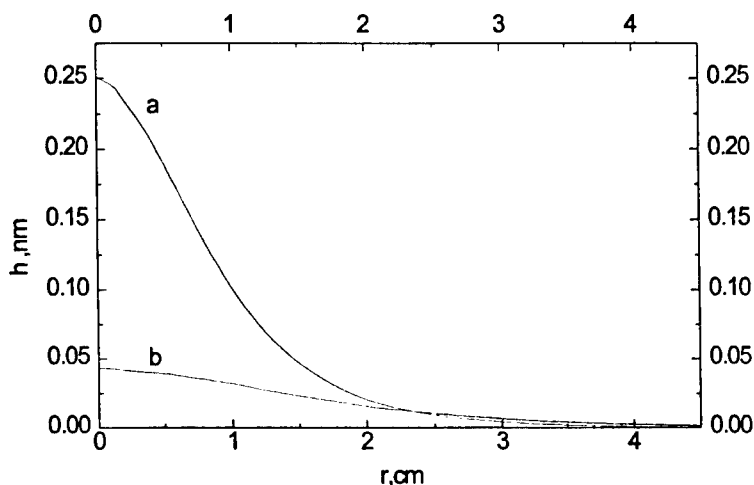


Fig. 3 The distribution profile of the deposited layer at a separation distance target- collector of $z_s=1.5$ cm (a) and $z_s=3$ cm (b), ($E=5\text{J}/\text{cm}^2$).

5. CONCLUSIONS

We developed a model which allows for the description of the PLD basic processes by taking into account both the phenomena in the target under irradiation as well as in the vapour- plasma evolving in front of it. The plasma expansion in gas was investigated with the aid of a Monte Carlo simulation in order to obtain predictions of the deposition rate for a given pressure of the ambient gas and for a chosen value of the target- collector separation distance.

6. REFERENCES

1. J. Neamtu, I. N. Mihailescu, "Hydrodynamic model for the description of the reactive pulse laser deposition", *J.Appl.Phys.* (to be submitted ,1997).
2. R. K. Singh, J. Narayan, "Pulsed-laser evaporation technique for deposition of thin films ", *Phys.Rev. B* **41** (13) 8843-8859 (1990).
3. W. F. Noh, *Methods in computational Physics*, Vol. 3, 117-179 (1964).
4. I. N. Mihailescu, E. Gyorgy, N. Chitica, V. S. Teodorescu, G. Mavin, A. Luches, A. Perrone, M. Martino, J. Neamtu, "A parametric study of the deposition of the TiN thin films by laser reactive ablation of titanium targets in nitrogen: the role of the total gas pressure and the contamination with oxides", *Journal of Materials Science* **31**, 2909-2915 (1996).

Pulsed - laser and alpha particle irradiation effects in Fe - based glassy ferromagnets

M.I.Toacsan, D.Barb, M.Sorescu*, B.Constantinescu**, L. Jeloica

National Institute for Materials Physics, Bucharest-Magurele
POB MG-7, R -76900, Romania

*Duquesne University, Physics Department, Pittsburgh, Pennsylvania 15282

**National Institute "IFIN-HH", Bucharest-Magurele, POB MG- 6
R - 76900, Romania

ABSTRACT

A comparatively study of pulsed - laser and alpha particle irradiation effects in metallic glasses has been performed in order to understand the relationship between magnetic behaviour and select variations in the structural characteristics of alloy phases. Samples of $\text{Fe}_{78}\text{B}_{13}\text{Si}_9$ and $\text{Fe}_{66}\text{Co}_{18}\text{B}_{15}\text{Si}$ metallic glasses were irradiated with a pulsed excimer laser ($\lambda=308\text{nm}$, $\tau=10\text{ns}$) and alpha particle beams ($W = 2.8 \text{ MeV}$) using radiation doses of 10^{16} and 10^{17} cm^{-2} . Irradiation - driven changes in the magnetic anisotropy and phase equilibrium of alloy samples were studied by Mössbauer Spectroscopy and scanning electron microscopy. The evolution of phases and microstructure during the radiation-induced amorphous-to-crystalline transformations or revitrification depend on the specific irradiation and sample composition.

Keywords: pulsed-excimer-laser and α -particle irradiation, metallic glasses, amorphous alloys, Mössbauer Spectroscopy, SEM, magnetic anisotropy, phase equilibrium.

1.INTRODUCTION

Recent investigations of irradiation-induced effects in metallic glasses have been performed concerning to the potential use of amorphous alloys as radiation-resistant materials. Thermal treatments and electron beam irradiation studies have shown that structural modifications in radiation-exposed alloys determine changes in their soft magnetic properties^{1,2,3}. Cw laser irradiation has been found to promote structural relaxation and/or crystallisation in amorphous ferromagnetic ribbons. Different stress distributions have been obtained in metallic glasses as a result of unhomogeneous heat flows produced by local laser annealing. Pulsed-excimer-laser irradiation has been suggested as an intriguing means the controlling of magnetic anisotropy and phase equilibrium in amorphous materials. Similar α -particles beam irradiation has been used as a means of understand the fundamentals of nucleation and growth in amorphous magnets.

The present study was carried out in order to investigate the effect of pulsed excimer laser irradiation on Fe-based amorphous alloys and compare it with the effect of α -particle beam irradiation on our materials.

In order to understand the relationship between dielectric parameters and structural characteristics of alloy phases, a promising approach is to address the phase evolution and microstructure development during various irradiation treatments. Because of its local-probe character Mössbauer spectra copy was used to monitor the changes in magnetic anisotropy and phase composition, induced by employing different values of the irradiation parameters in both treatments performed. Related morphological changes were examined by Scanning Electron Microscopy (SEM). Irradiation driven property changes are discussed in terms of phenomenological models in which the underlying alloy microstructure played an essential role.

Amorphous alloys $\text{Fe}_{78}\text{B}_{13}\text{Si}_9$ (Metglas 2605 TCA) and $\text{Fe}_{66}\text{Co}_{18}\text{B}_{15}\text{Si}$ (Metglas 2605 CO) was supplied by Allied Signal Inc., in the form of (20-40) μm thick ribbons with the magnetostriction values 30 and 35 ppm.

Square samples (2 x 2 cm) were cut from foils and exposed on the shiny side to the $\lambda=308\text{nm}$ radiation generated by a XeCl excimer laser (Lambda Physik), with the pulse width $\tau=10\text{ns}$, capable of giving an energy $W_p = 75 \text{ mJ/pulse}$. A single-pulse energy density of $3 \text{ J} \times \text{cm}^{-2}$, corresponding to a laser fluency $\Phi_L = 5 \times 10^{18} \text{ photons} \cdot \text{cm}^{-2}$ was achieved by focusing with a cylindrical fused-silica lens to a spot size of 0.5 x 5 mm. Samples were irradiated with 2, 5, 10 laser pulses/spot at a repetition rate of 1Hz, at room temperature.

Thermally treated Fe- and FeCo- alloys were prepared by annealing the amorphous specimens at 648K and 723K for 1h. These samples were further exposed to pulsed-excimer laser irradiation ($N=2$).

A different set of Fe- and FeCo- based amorphous magnets were subjected to radiation doses of 10^{16} and 10^{17} cm $_2$ generated by the 2.8 MeV alpha-particle beam at the National Institute "IFIN-HH", Bucharest-Magurele cyclotron facility.

Room temperature transmission Mössbauer spectra were recorded with the γ -ray perpendicular to the ribbon plane using a constant acceleration spectrometer (Ranger Scientific). The 25-mCi γ -ray source was ^{57}Co diffused in Rh matrix. Least squares fitting of the Mössbauer spectra corresponding to the amorphous, annealed and irradiated samples was performed with the NORMOS DIST program⁴ in the assumption of Lorentzian line shapes. The program uses the constrained Hesse-Rübarsch method to extract the hyperfine field distributions and can analyse superpositions of the field distributions and crystalline sites. The relative areas of the outer : inner line pairs of the amorphous component were constrained to the ratio 3 : 1. The relative intensities of lines one, two and three for each pattern were correlated to be the same for all crystalline subspectra.

SEM investigations were performed without further surface preparation, with JEOL electron microscope at 25 keV, operating in the secondary electron emission mode.

2.RESULTS AND DISCUSSIONS

Room temperature transmission Mössbauer spectra of the $\text{Fe}_{78}\text{B}_{13}\text{Si}_9$ samples, in the amorphous as-quenched state and after pulsed-excimer-laser irradiation ($\lambda=308$ nm, $\tau=10\text{ns}$) with 2, 5 and 10 laser pulses per spot as a laser fluency of 5×10^{18} photons/cm $_2$ and a repetition rate of 1Hz are shown in Figs. 1(a)-1(d). The corresponding hyperfine magnetic field distributions extracted from these spectra are shown in Figs. 1(A)-1(D). The referred values of the hyperfine parameters corresponding to the as-quenched and pulsed laser treated samples are listed in Table 1.

Room temperature Mössbauer data show that a rotation of the average magnetic moment direction from in-plane to an out-of-plane orientation has taken place, and maintains a upon increasing the number of applied pulses during excimer-laser irradiation. RT Mössbauer spectra shows no significant variation during laser treatment performed, suggesting the absence of crystallisation effects.

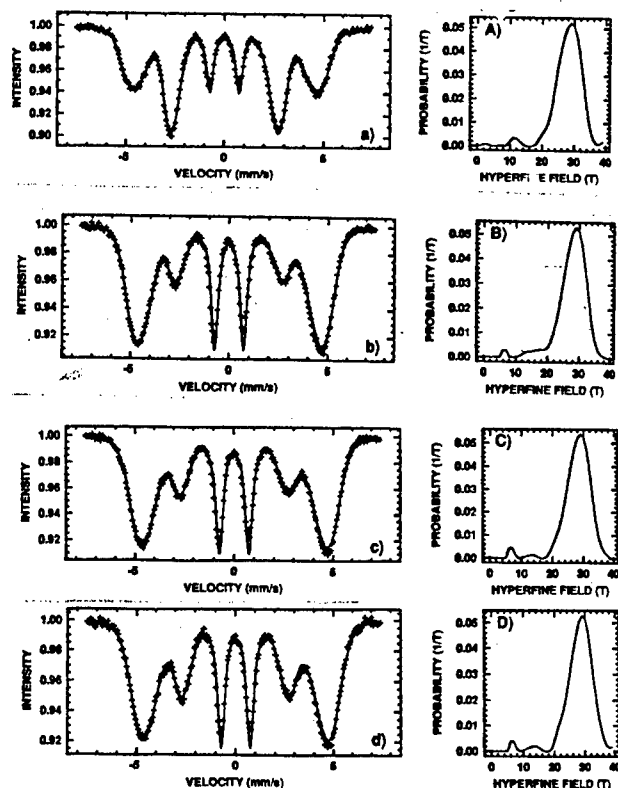


Fig. 1: Room temperature transmission Mössbauer spectra of the $\text{Fe}_{78}\text{B}_{13}\text{Si}_9$ samples:

- (a) in the amorphous as-quenched state and after pulsed excimer-laser irradiation $\lambda = 308$ nm, $\tau=10\text{ns}$, $\Phi_L = 5 \times 10^{18}$ photons/cm $_2$, repetition rate 1Hz with
- (b) 2 laser pulses/spot
- (c) 5 laser pulses/spot
- (d) 10 laser pulses/spot

The corresponding hyperfine magnetic field distributions are shown in (A)-(D).

Table1. Relative intensity of lines R_{21} , average hyperfine magnetic field $\langle H_{hf} \rangle$, mean hyperfine field $(H_{hf})_m$, width of the hyperfine magnetic field distribution ΔH_{hf} and total absorption area in the Mössbauer spectra of the $Fe_{78}B_{13}Si_9$ samples as function of the number of applied laser-pulses N .

N (laser pulses)	R_{21}	$\langle H_{hf} \rangle$ (kOe)	$(H_{hf})_m$ (kOe)	ΔH_{hf} (kOe)	Resonant area (a.u.)
0	1.11	251.1	255.2	45.5	0.219
2	0.26	249.5	255.1	45.7	0.220
5	0.41	253.2	257.3	46.5	0.178
10	0.43	251.3	256.9	47.6	0.208
Errors	± 0.02	± 2.5	± 2.5	± 2.5	± 0.005

Figs. 2(a)-2(d) and Table 2 present room temperature transmission Mössbauer spectra and corresponding data for $Fe_{66}Co_{18}B_{15}Si$ samples. We can observe a similar behaviour of Fe-Co system with $Fe_{78}B_{13}Si_9$ samples, but we found a hyperfine magnetic splitting of 362.1 kOe, corresponding to α -(FeCo) crystalline phase.

Table2: Relative intensity of lines R_{21} , average hyperfine magnetic field $\langle H_{hf} \rangle$, mean hyperfine field $(H_{hf})_m$, width of the hyperfine magnetic field distribution ΔH_{hf} and total absorption area in the Mössbauer spectra of the $Fe_{66}Co_{18}B_{15}Si$ samples as function of the number of applied laser-pulses N .

N(laser pulses)	R_{21}	$\langle H_{hf} \rangle$ (kOe)	$(H_{hf})_m$ (kOe)	ΔH_{hf} (kOe)	Resonant area (a.u.)
0	1.10	278.8	283.6	45.1	0.496
2	0.25	276.9	284.5	47.4	0.495
5	0.31	277.8	284.2	49.6	0.513
10	0.39	279.7	285.8	49.7	0.502
Errors	± 0.02	± 2.5	± 2.5	± 2.5	± 0.005

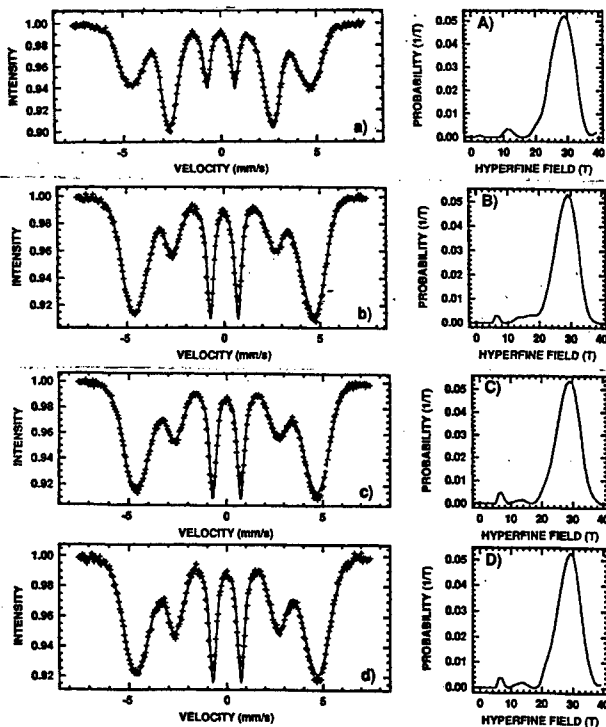


Fig. 2: Room temperature transmission Mössbauer spectra of the $Fe_{66}Co_{18}B_{15}Si$ samples:

(a) in the amorphous as-quenched state and after pulsed excimer-laser irradiation $\lambda = 308 \text{ nm}$, $\tau = 10 \text{ ns}$, $\Phi L = 5 \times 10^{18} \text{ photons/cm}^2$, repetition rate 1Hz with

(b) 2 laser pulses/spot

(c) 5 laser pulses/spot

(d) 10 laser pulses/spot

The corresponding hyperfine magnetic field distributions are shown in (A)-(D).

The partially crystallised samples (by thermal annealing at 648K for 1h) were further exposed to $\Phi_L = 5 \times 10^{18}$ photons/cm², $N = 2$. The bulk Mössbauer measurements show that the composition of the irradiated Fe-based specimens is entirely amorphous with a pronounced out-of-plane reorientation of the magnetic moment directions (laser induced magnetic anisotropy), as indicated by R_{21} values variations from 0.82 for as-annealed samples to 0.33 for the same sample annealed and laser irradiated.

A typical region as an effect of excimer laser revitrification is shown in the SEM photograph (Figs. 3(a)-(b)).

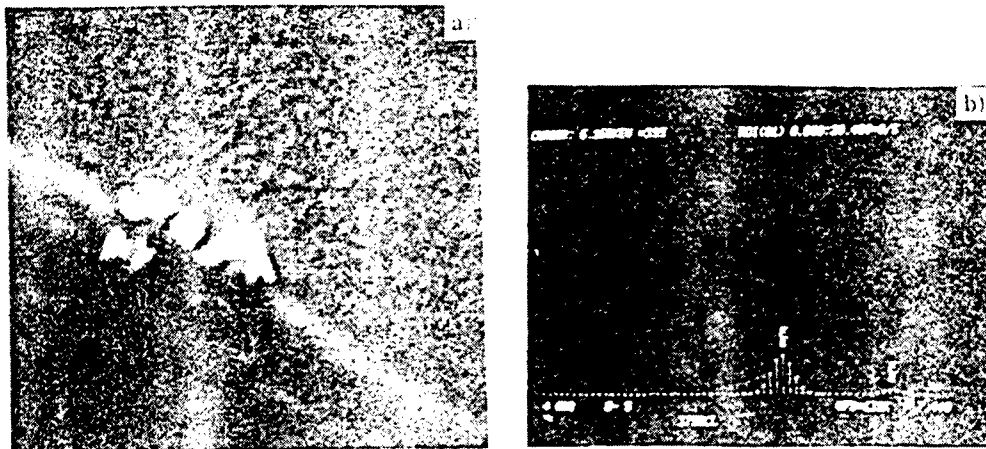


Fig.3: (a) SEM photograph (x 2000) and (b) EDX examination of the $\text{Fe}_{78}\text{B}_{13}\text{Si}_9$ sample after thermal annealing at 648 K, 1h, followed by pulsed-excimer-laser treatment ($\lambda=308$ nm, $\tau=10$ ns, $\Phi_L=5 \times 10^{18}$ photons/cm²).

By annealing at 648K for 1h, the Fe-Co based alloys we found α -(FeCo) and $(\text{FeCo})_3(\text{BSi})$ crystalline phases. After laser irradiation only α -(FeCo) phase is present in the amorphous matrix (Figs. 4(a)-4(b)).

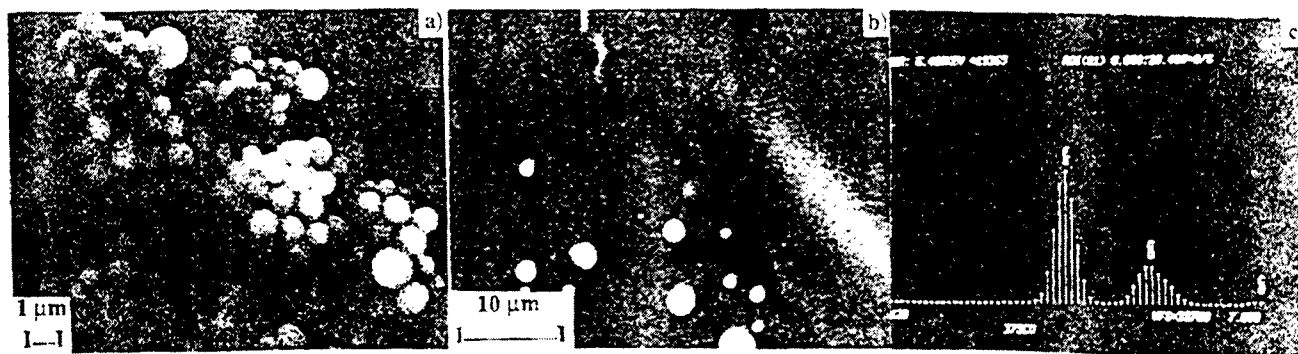


Fig. 4 (a) SEM micrograph of the $\text{Fe}_{66}\text{Co}_{18}\text{B}_{15}\text{Si}$ sample, after thermal annealing at 648K/1h; (b) SEM examination of the sample after thermal annealing at 648K for 1h and subsequent pulsed-excimer laser irradiation ($\lambda=308$ nm, $\tau=10$ ns, $\Phi_L=5 \times 10^{18}$ photons/cm², repetition rate 1Hz); (c) EDX analysis of the crystalline precipitates observed in the SEM photograph of the thermal annealed $\text{Fe}_{66}\text{Co}_{18}\text{B}_{15}\text{Si}$ sample.

On the grounds of the values obtained for room temperature Mossbauer parameters for Fe- based glassy alloys, by alpha-particle beam irradiation we found α -(FeSi), Fe_3B and Fe_2B crystalline phases in equilibrium with a dominant amorphous component. The amorphous phase was found to be even more abundant in specimens subjected to higher irradiation doses. That means that the lowest irradiation dose employed was more effective in inducing amorphous-to-crystalline transformations in glassy ferromagnets (Table 3 and Figs. 5(a)-5(c)).

Table3: Hyperfine magnetic field H_{hf} , isomer shift δ , and relative areas corresponding to the component patterns in the Mössbauer spectra for the $\text{Fe}_{78}\text{B}_{13}\text{Si}_9$ metallic glass, as a function of the radiation dose Φ employed in α -particle irradiation.

Sample treatment	Φ (cm^{-2})	H_{hf} (kOe)	δ (mm/s)	Rel.areas (%)	Assignment of sites
as-quenched	0	247.0	0.022	100.0	amorphous
irradiated	10^{16}	331.5	0.002	7.8	α -(FeSi)
		272.1	0.105	10.9	Fe_3B
		236.1	0.110	39.8	Fe_2B
		289.7	0.044	41.5	amorphous
irradiated	10^{17}	331.5	0.002	6.1	α -(FeSi)
		272.1	0.105	6.1	Fe_3B
		236.1	0.110	39.3	Fe_2B
		295.0	0.015	48.5	amorphous

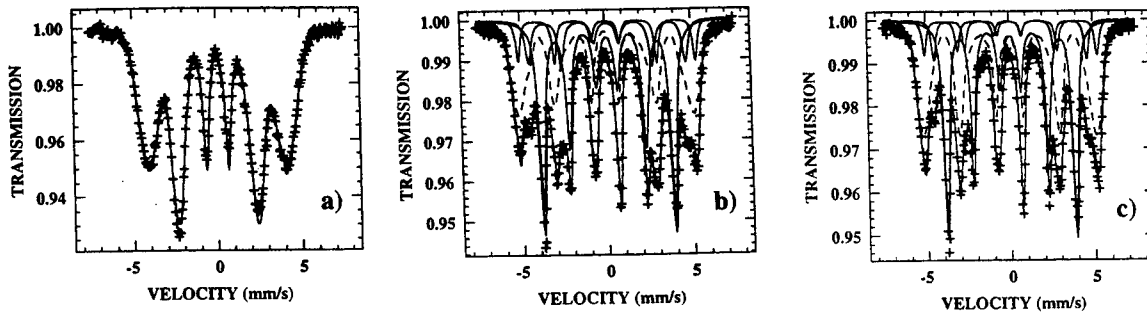


Fig. 5: Room temperature transmission Mössbauer spectra of the $\text{Fe}_{78}\text{B}_{13}\text{Si}_9$ samples: (a) in the as-quenched state and (b), (c) after irradiation with α -particle beams at doses of 10^{16} and 10^{17} cm^{-2} , respectively.

We found a complete crystallisation of FeCo based samples in α -(FeCo), $(\text{FeCo})_2$, (BSi) and $(\text{FeCo})_3$ (BSi) crystalline phases, respectively, in agreement with the results on the phase transformation by thermal and pulsed laser annealing.

Mössbauer data are presented in Table 4 and room temperature transmission Mössbauer spectra are shown in Figs. 6(a)-6(c).

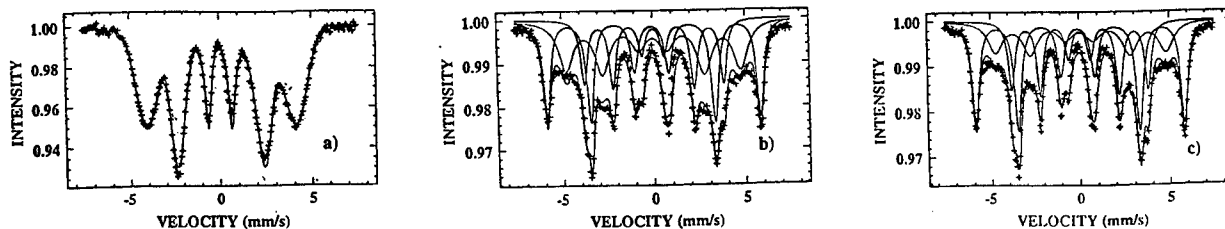


Fig. 6: Room temperature transmission Mössbauer spectra of the $\text{Fe}_{66}\text{Co}_{18}\text{B}_{15}\text{Si}$ samples: (a) in the as-quenched state and (b), (c) after irradiation with α -particle beams at doses of 10^{16} and 10^{17} cm^{-2} , respectively.

Table4: Hyperfine magnetic field H_{hf} , isomer shift δ , and relative areas corresponding to the component patterns in the Mössbauer spectra for the $Fe_{66}Co_{18}B_{15}Si$ metallic glass, as a function of the radiation dose Φ employed in α -particle irradiation.

Sample treatment	Φ (cm^{-2})	H_{hf} (kOe)	δ (mm/s)	Rel. areas (%)	Assignment of sites
as-quenched	0	278.8	0.03	100.0	amorphous
irradiated	10^{16}	362.9	0.05	37.9	α -(FeCo)
		295.9	0.11	38.7	$(FeCo)_2(BSi)$
		235.5	0.08	23.4	$(FeCo)_3(BSi)$
		362.9	0.05	45.2	α -(FeCo)
irradiated	10^{17}	296.7	0.11	27.2	$(FeCo)_2(BSi)$
		234.1	0.08	27.6	$(FeCo)_3(BSi)$

The SEM micrographs exhibit spatial formation upon α irradiation consisting in islands of crystalline precipitates depending on samples composition, with spherical shape for Fe-based alloys (Fig. 7a) and dendritical nucleation and growth for FeCo specimens (Fig. 7b).

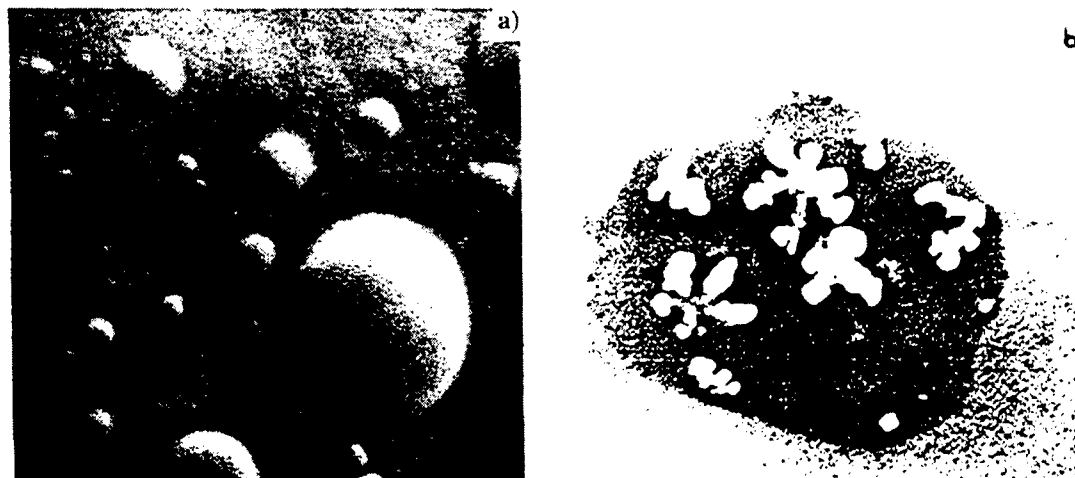


Fig. 7: SEM examination of surface morphology and crystalline phases produced by α -particle beam irradiation at irradiation dose $10^{16}/cm^2$.

(a) $Fe_{78}B_{13}Si_9$ metallic glass, magnification $\times 160$.

(b) $Fe_{66}Co_{18}B_{15}Si$ sample, magnification $\times 1800$.

3. CONCLUSIONS

In addition to inducing controlled magnetic anisotropy the pulsed-laser-eximer irradiation was shown to cause re vitrification of partially crystallised Fe and FeCo based metallic glass.

In totally crystallised $Fe_{66}Co_{18}B_{15}Si$ specimens, laser-induced partial amorphisation was shown to exhibit phase selectivity relative to the crystalline components in the alloy system.

The evolution of phases and microstructure during the irradiation amorphous to crystalline transformations in iron-based and iron-cobalt based metallic glasses exposed to α -particle beams was found to depend on the irradiation dose and sample composition.

The interaction of pulsed-lase-eximer and α -particle beams with glassy ferromagnets offer unique opportunities to understand the fundamentals of nucleation and growth in amorphous magnets, due to excitation of nonconventional path ways for the crystallisation process.

4.ACKNOWLEDGEMENTS

This work has been supported by the Roumanian Academy contract 3134/1997.

5.REFERENCES

1. M. Miglierini and I. Skorvanek, *Mater. Sci. Eng.*, **A 147**, 101 (1991).
2. I. T. Collier, M. R. J. Gibbs and N. Seddon, *J. Magn. Magn. Mater.*, **111**, 260 (1992).
3. L. Lanotte, C. Luponio and F. Porreca, *J. Magn. Magn. Mater.*, **61**, 225 (1986).
4. R. A. Brand, L. Lauer and D. M. Herlach, *J. Phys.*, **F13**, 675 (1983).

SESSION 3

Nonlinear, Information, and Quantum Optics

Quantum optics of a single atom

H. Walther

Sektion Physik der Universität München and
Max-Planck-Institut für Quantenoptik
85748 Garching, Fed. Rep. of Germany

ABSTRACT

In this paper recent experiments performed in our laboratory are reviewed dealing with the investigation of quantum phenomena in the radiation interaction of single atoms. The first part describes experiments in single mode cavities using the one-atom maser or micromaser and in the second part experiments with ion traps are summarized. The latter experiments concentrate on the investigation of resonance fluorescence. In addition new experimental proposals using ultracold atoms in cavities and traps are discussed. In those future experiments the interplay between atomic waves and light waves is important and leads to new phenomena in radiation-atom interaction.

Keywords: Cavity quantum electrodynamics, micromaser, microlaser

1. INTRODUCTION

Laser spectroscopy techniques allow today to observe quantum phenomena in radiation-atom interaction on the basis of single atoms. The most suitable systems in this connection seem to be single atoms in cavities and also single atoms in traps. The studies in cavities allow to select one interacting mode and thus represent the ideal system with respect to a quantum treatment. In high Q cavities a steady state field of photons can be generated displaying non-classical photon statistics. It thus gets possible to study the interaction also in the limit of non-classical or sub-Poissonian fields. Single trapped ions allow to observe among other phenomena quantum jumps and antibunching in fluorescence radiation. In general the fluorescent channel represents an interaction with many modes, however, it is also possible to combine single mode cavities with trapped atoms as it is e.g. the case in the proposed ion-trap laser. In such a setup many new phenomena not observable in the one-atom maser get accessible.

A new and interesting twist in radiation-atom interaction can be added when ultracold atoms are used in both cavities and traps. In this case the distribution of the matter wave plays an important role besides the standing electromagnetic wave in the cavity and their interaction is determined by their respective overlap leading to new effects.

In the following we will review experiments of single atoms in cavities and traps performed in our laboratory. Furthermore new proposals for experiments with ultracold atoms will be discussed. We start with the discussion of the one-atom maser.

2. EXPERIMENTS WITH THE ONE ATOM MASER

The one-atom maser or micromaser uses a single mode of a superconducting niobium cavity.¹⁻⁴ In the experiments values of the quality factor as high as 3×10^{10} have been achieved for the resonant mode, corresponding to an average lifetime of a photon in the cavity of 0.2 s. The photon lifetime is thus much longer than the interaction time of an atom with the maser field; during the atom passes through the cavity the only change of the cavity field that occurs is due to the atom-field interaction. Contrary to other strong coupling experiments in cavities (optical or microwave), see e.g. H. J. Kimble et al.⁵ for a comparison between the different setups, it is possible with our micromaser to generate a steady state field in the cavity which has nonclassical properties so that the interaction of single atoms in those fields can be investigated. Furthermore the generation process of those fields has been studied and is well understood. The experiment is quite unique in this respect; this also holds in comparison with the one-atom laser⁶ which has been omitted in the survey given in Table 1 of Ref. 5.

The atoms used in our micromaser experiments are rubidium Rydberg atoms pumped by laser excitation into the upper level of the maser transition, which is usually induced between neighboring Rydberg states. In the experiments the atom-field interaction is probed by observing the population in the upper and lower maser levels after the atoms have left the cavity. The field in the cavity consists only of single or a few photons depending on the atomic flux. Nevertheless, it is possible to study the interaction in considerable detail. The dynamics of the atom-field interaction treated with the Jaynes-Cummings model was investigated by selecting and varying the velocity of the pump atoms.² The counting statistics of the

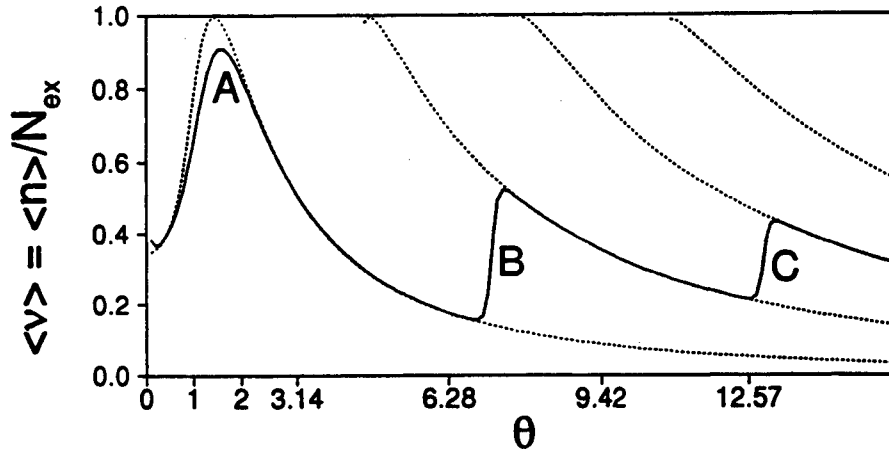


Fig. 1. Mean value of $v = n/N_{\text{ex}}$ versus the pump parameter $\Theta = \Omega t_{\text{int}} \sqrt{N_{\text{ex}}} / 2$, where the value of Θ is changed via N_{ex} . The solid line represents the micromaser solution for $\Omega = 36$ kHz, $t_{\text{int}} = 35$ μs , and temperature $T = 0.15$ K. The dotted lines are semiclassical steady-state solutions corresponding to fixed stable gain=loss equilibrium photon numbers.¹⁴ The crossing points between a line $\Theta = \text{const}$ and the dotted lines correspond to the values where minima in the Fokker-Planck potential $V(v)$ occur.

pump atoms emerging from the cavity allowed us to measure the non-classical character of the cavity field^{3,4} predicted by the micromaser theory. The maser field can be investigated in this way since there is entanglement between the maser field and the state in which the atom leaves the cavity.^{7,8} It also has been observed that under suitable experimental conditions the maser field exhibits metastability and hysteresis.⁹ The first of the maser experiments have been performed at cavity temperatures of 2 or 0.5 K. In the more recent experiments the temperature was reduced to roughly 0.1 K by using an improved setup in a dilution refrigerator.⁹ For a review of the previous work see Raithel et al.¹¹

In the following we give a brief review of recent experiments which deal with the observation of quantum jumps of the micromaser field⁹ and with the observation of atomic interferences in the cavity.¹⁰ New experiments on the correlation of atoms after the interaction with the cavity field will be briefly mentioned. We will also discuss new possibilities opened up when ultracold atoms are used for the experiments.

2.1 Quantum jumps and atomic interferences in the micromaser

Under steady-state conditions, the photon statistics $P(n)$ of the field of the micromaser is essentially determined by the pump parameter, $\Theta = N_{\text{ex}}^{1/2} \Omega t_{\text{int}} / 2$.¹¹⁻¹³ Here, N_{ex} is the average number of atoms that enter the cavity during τ_{cav} , Ω the vacuum Rabi flopping frequency, and t_{int} is the atom-cavity interaction time. The quantity $\langle v \rangle = \langle n \rangle / N_{\text{ex}}$ shows the following generic behavior (see Fig. 1): It suddenly increases at the maser threshold value $\Theta = 1$, and reaches a maximum for $\Theta \approx 2$ (denoted by A in Fig. 1). At threshold the characteristics of a continuous phase transition^{12,13} are displayed. As Θ further increases, $\langle v \rangle$ decreases and reaches a minimum at $\Theta \approx 2\pi$, and then abruptly increases to a second maximum (B in Fig. 1). This general type of behavior recurs roughly at integer multiples of 2π , but becomes less pronounced with increasing Θ . The reason for the periodic maxima of $\langle v \rangle$ is that for integer multiples of $\Theta = 2\pi$ the pump atoms perform an almost integer number of full Rabi flopping cycles, and start to flip over at a slightly larger value of Θ , thus leading to enhanced photon emission. The periodic maxima in $\langle v \rangle$ for $\Theta = 2\pi, 4\pi$, and so on can be interpreted as first-order phase transitions.^{12,13} The field strongly fluctuates for all phase transitions being caused by the presence of two maxima in the photon number distribution $P(n)$ at photon numbers n_l and n_h ($n_l < n_h$).

The phenomenon of the two coexisting maxima in $P(n)$ was also studied in a semiheuristic Fokker-Planck (FP) approach.¹² There, the photon number distribution $P(n)$ is replaced by a probability function $P(v, \tau)$ with continuous variables $\tau = t/\tau_{\text{cav}}$ and $v(n) = n/N_{\text{ex}}$, the latter replacing the photon number n . The steady-state solution obtained for $P(v, \tau)$, $\tau \gg 1$, can be constructed by means of an effective potential $V(v)$ showing minima at positions where maxima of $P(v, \tau)$, $\tau \gg 1$, are found. Close to $\Theta = 2\pi$ and multiples thereof, the effective potential $V(v)$ exhibits two equally attractive minima located

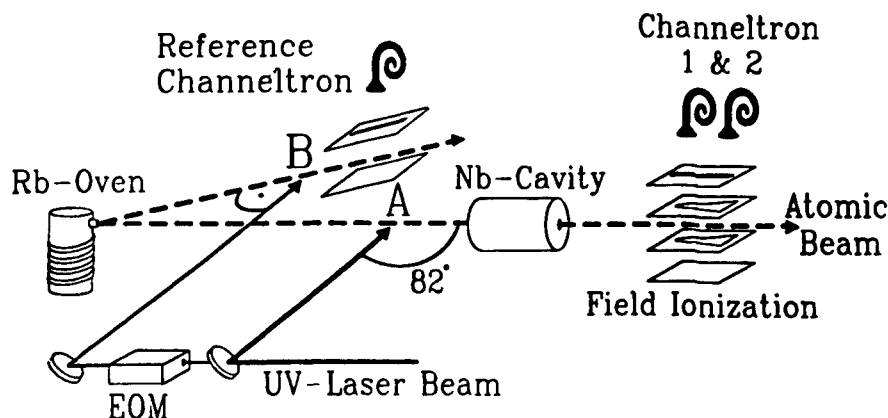


Fig. 2. Sketch of the experimental setup. The rubidium atoms emerge from an atomic beam oven and are excited at an angle of 82° at location A. After interaction with the cavity field, they enter a state-selective field ionization region, where channeltrons 1 and 2 detect atoms in the upper and lower maser levels, respectively. A small fraction of the UV radiation passes through an electro-optic modulator (EOM), which generates sidebands of the UV radiation. The blueshifted sideband is used to stabilize the frequency of the laser onto the Doppler-free resonance monitored with a secondary atomic beam produced by the same oven (location B).

at stable gain-loss equilibrium points of maser operation¹⁴ (see Fig. 1). The mechanism at the phase transitions mentioned is always the same: A minimum of $V(v)$ loses its global character when Θ is increased, and is replaced in this role by the next one. This reasoning is a variation of the Landau theory of first-order phase transitions, with \sqrt{v} being the order parameter. This analogy actually leads to the notion that in the limit $N_{ex} \rightarrow \infty$ the change of the micromaser field around integer multiples $\Theta = 2\pi$ can be interpreted as first-order phase transitions.

Close to first-order phase transitions long field evolution time constants are expected.^{12,13} This phenomenon was experimentally demonstrated in Ref. 9, as well as related phenomena, such as spontaneous quantum jumps between equally attractive minima of $V(v)$, bistability, and hysteresis. Some of those phenomena are also predicted in the two-photon micromaser,¹⁵ for which qualitative evidence of first-order phase transitions and hysteresis is reported.

The experimental setup used is shown in Fig. 2. It is similar to that described by Rempe and Walther⁴ and Benson, Raithel and Walther.⁹ As before, ^{85}Rb atoms were used to pump the maser. They are excited from the $5S_{1/2}$, $F = 3$ ground state to $63P_{3/2}$, $m_J = \pm 1/2$ states by linearly polarized light of a frequency-doubled c.w. ring dye laser. The polarization of the laser light is linear and parallel to the likewise linearly polarized maser field, and therefore only $\Delta m_J = 0$ transitions are excited. Superconducting niobium cavities resonant with the transition to the $61D_{3/2}$, $m_J = \pm 1/2$ states were used; the corresponding resonance frequency is 21.506 GHz. The experiments were performed in a $^3\text{He}/^4\text{He}$ dilution refrigerator with cavity temperatures $T \approx 0.15$ K. The cavity Q values ranged from 4×10^9 to 8×10^9 . The velocity of the Rydberg atoms and thus their interaction time t_{int} with the cavity field were preselected by exciting a particular velocity subgroup with the laser. For this purpose, the laser beam irradiated the atomic beam at an angle of approximately 82° . As a consequence, the UV laser light (linewidth ≈ 2 MHz) is blueshifted by 50-200 MHz by the Doppler effect, depending on the velocity of the atoms.

Information on the maser field and interaction of the atoms in the cavity can be obtained solely by state-selective field ionization of the atoms in the upper or lower maser level after they have passed through the cavity. For different t_{int} the atomic inversion has been measured as a function of the pump rate by comparing the results with micromaser theory,^{12,13} the coupling constant Ω is found to be $\Omega = (40 \pm 10)$ krad/s.

Depending on the parameter range, essentially three regimes of the field evolution time constant τ_{field} can be distinguished. Here we only discuss the results for intermediate time constants. The maser was operated under steady-state conditions close to the second first-order phase transition (C in Fig. 1). The interaction time was $t_{int} = 47 \mu\text{s}$ and the cavity decay time $\tau_{cav} = 60$ ms. The value of N_{ex} necessary to reach the second first-order phase transition was $N_{ex} \approx 200$. For these parameters, the two maxima in $P(n)$ are manifested in spontaneous jumps of the maser field between the two maxima with

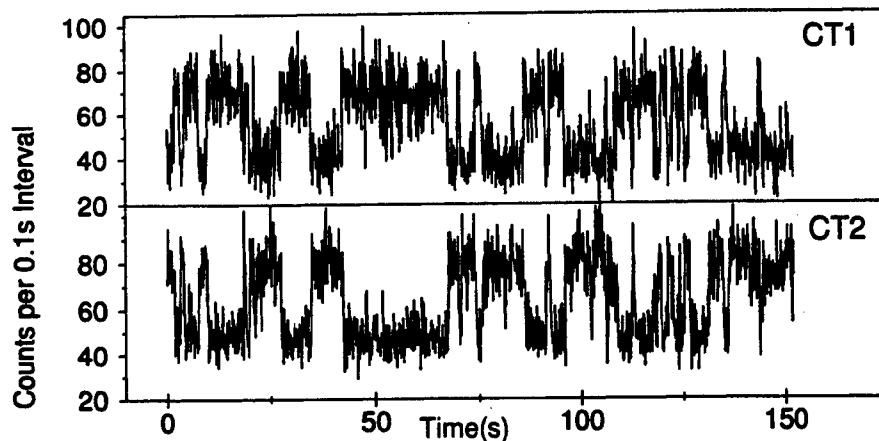


Fig. 3. Quantum jumps between two equally stable operation points of the maser field. The channeltron counts are plotted versus time (CT1 = upper state and CT2 = lower state signals). The signals of the two different detectors show a counter-phase behavior; this makes it easy to discriminate between signal and noise.

a time constant of ≈ 5 s. This fact and the relatively large pump rate led to the clearly observable field jumps shown in Fig. 3. Because of the large cavity field decay time, the average number of atoms in the cavity was still as low as 0.17. The two discrete values for the counting rates correspond to the metastable operating points of the maser, which correspond to ≈ 70 and ≈ 140 photons. In the FP description, the two values correspond to two equally attractive minima in the FP potential $V(v)$. If one considers, for instance, the counting rate of lower-state atoms (CT2 in Fig. 3), the lower (higher) plateaus correspond to time intervals in the low (high) field metastable operating point. If the actual photon number distribution is averaged over a time interval containing many spontaneous field jumps, the steady-state result $P(n)$ of the micromaser theory is recovered.

In the parameter ranges where switching occurs much faster than in the case shown in Fig. 3 the individual jumps cannot be resolved, therefore different methods have to be used for the measurement. Furthermore hysteresis is observed at the maser parameters for which the field jumps occur. Owing to lack of space these results cannot be discussed here. For a complete survey on the performed experiments it is referred to Ref. 9.

As next topic we would like to discuss the observation of atomic interferences in the micromaser.¹⁰ Since a non-classical field is generated in the maser cavity, we were able for the first time to investigate atomic interference phenomena under the influence of non-classical radiation; owing to the bistable behavior of the maser field the interferences display quantum jumps, thus the quantum nature of the field gets directly visible in the interference fringes. Interferences occur since a coherent superposition of dressed states is produced by mixing the states at the entrance and exit holes of the cavity. Inside the cavity the dressed states develop differently in time, giving rise to Ramsey-type interferences¹⁶ when the maser cavity is tuned through resonance.

The setup used in the experiment is identical to the one described before.⁹ However, the flux of atoms through the cavity is by a factor of 5 - 10 higher than in the previous experiments, where the $63\text{ P}_{3/2} - 61\text{ D}_{5/2}$ transition was used. For the experiments the Q-value of the cavity was 6×10^9 corresponding to a photon decay time of 42 ms.

Figure 4 shows the standard maser resonance in the uppermost plot which is obtained when the resonator frequency is tuned. At large values of N_{ex} ($N_{\text{ex}} > 89$) sharp, periodic structures appear. These typically consist of a smooth wing on the low-frequency side, and a vertical step on the high-frequency side. The clarity of the pattern rapidly decreases when N_{ex} increases to 190 or beyond. We will see later that these structures have to be interpreted as interferences. It can be seen that the atom-field resonance frequency is red-shifted with increasing N_{ex} , the shift reaching 200 kHz for $N_{\text{ex}} = 190$. Under these conditions there are roughly 100 photons on the average in the cavity. The large red-shift cannot be explained by AC Stark effect, which for 100 photons would amount to about one kHz for the transition used. Therefore it is obvious that other reasons must be responsible for the observed shift.

It is known from previous maser experiments that there are small static electric fields in the entrance and exit holes of the cavity. It is supposed that this field is generated by patch effects at the surface of the niobium metal caused by rubidium deposits caused by the atomic beam or by microcrystallites formed when the cavities are tempered after machining. The

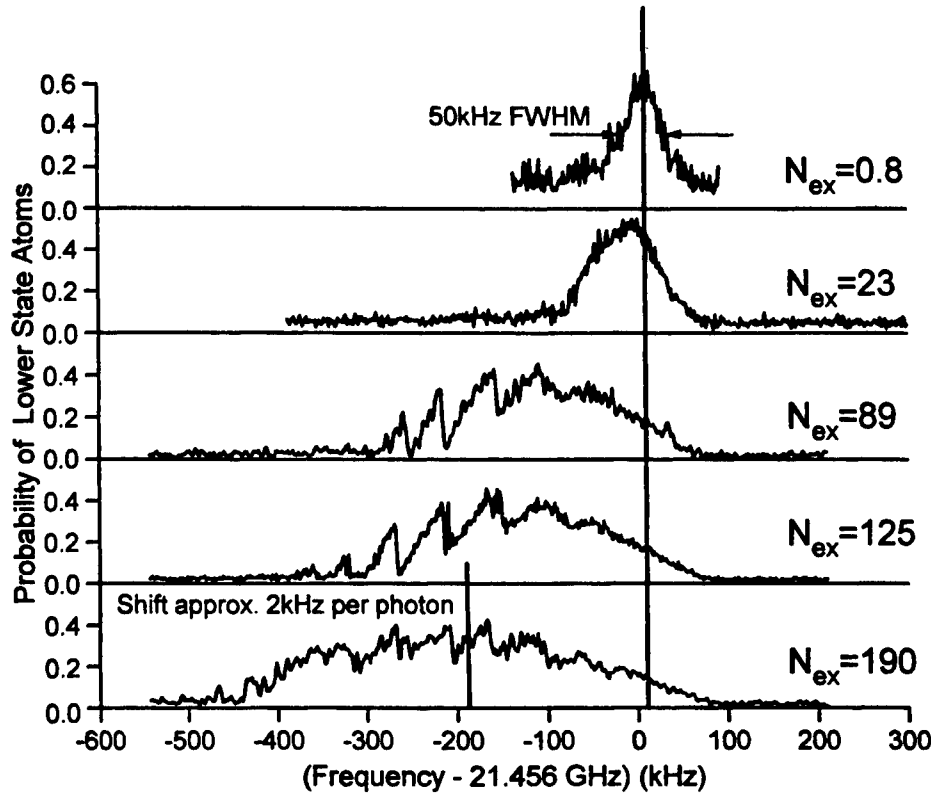


Fig. 4. Shift of the maser resonance $63\text{ P}_{3/2} - 61\text{ D}_{5/2}$ for fast atoms ($t_{\text{int}} = 35\text{ }\mu\text{s}$). The upper plot shows the maser line for low pump rate ($N_{\text{ex}} < 1$). The FWHM linewidth (50 kHz) sets an upper limit of $\approx 5\text{ mV/cm}$ for the residual electric stray fields in the center of the cavity. The lower resonance lines are taken for the indicated large values of N_{ex} . The plots show that the center of the maser line shifts by about 2 kHz per photon. In addition, there is considerable field-induced line broadening which is approximately proportional to $\sqrt{N_{\text{ex}}}$. For $N_{\text{ex}} \geq 89$ the lines display periodic structures, which are discussed in the text.

tempering process is necessary to achieve high quality factors. The influence of those stray fields is only observable in the cavity holes; in the center of the cavity they are negligible owing to the large atom-wall distances.

When the interaction time t_{int} between the atoms and the cavity field is increased the interference structure disappears for $t_{\text{int}} > 47\text{ }\mu\text{s}$.¹⁰ This is due to the fact that there is no non-adiabatic mixing any more between the substates when the atoms get too slow.

In order to understand the observed structures, the Jaynes-Cummings dynamics of the atoms in the cavity has to be analyzed. This treatment is more involved than that in connection with previous experiments, since the higher maser field requires detailed consideration of the field in the periphery of the cavity, where the additional influence of stray electric fields is more important.

The usual formalism for the description of the coupling of an atom to the radiation field is the dressed atom approach,¹⁷ leading to splitting of the coupled atom-field states, depending on the vacuum Rabi-flopping frequency Ω , the photon number n , and the atom-field detuning δ . We face a special situation at the entrance and exit holes of the cavity. There we have a position-dependent variation of the cavity field, as a consequence of which Ω is position-dependent. An additional variation results from the stray electric fields in the entrance and exit holes. Owing to the Stark-effect these fields lead to a position-dependent atom-field detuning δ .

The Jaynes-Cummings-Hamiltonian only couples pairs of dressed states. Therefore, it is sufficient to consider the dynamics within such a pair. In our case, prior to the atom-field interaction the system is in one of the two dressed states. For parameters corresponding to the periodic substructures in Fig. 4 the dressed states are mixed only at the beginning of the atom-field interaction and at the end. The mixing at the beginning creates a coherent superposition of the dressed states.

Afterwards the system develops adiabatically, whereby the two dressed states accumulate a differential dynamic phase Φ which strongly depends on the cavity frequency. The mixing of the dressed states at the entrance and exit holes of the cavity, in combination with the intermediate adiabatic evolution, generates a situation similar to a Ramsey two-field interaction.

The maximum differential dynamic phase Φ solely resulting from dressed-state coupling by the maser field is roughly 4π under the experimental conditions used here. This is not sufficient to explain the interference pattern of Fig. 4, where we have at least six maxima corresponding to a differential phase of 12π . This means that an additional energy shift differently affecting upper and lower maser states is present. Such a phenomenon can be caused by the above mentioned small static electric fields present in the holes of the cavity. The static field causes a position-dependent detuning δ of the atomic transition from the cavity resonance; as a consequence we get an additional differential dynamic phase Φ . In order to interpret the periodic substructures as a result of the variation of Φ with the cavity frequency, the phase Φ has to be calculated from the atomic dynamics in the maser field.

The quantitative calculation can be performed on the basis of the micromaser theory. The calculations reproduce the experimental finding that the maser line shifts to lower frequencies when N_{ex} is increased.¹⁰ The mechanism for that can be explained as follows: the high-frequency edge of the maser line does not shift with N_{ex} at all, since this part of the resonance is produced in the central region of the cavity, where practically no static electric fields are present. The low-frequency cutoff of the structure is determined by the location where the mixing of the dressed states occurs. With decreasing cavity frequency those points shift closer to the entrance and exit holes, with the difference between the particular cavity frequency and the unperturbed atomic resonance frequency giving a measure of the static electric field at the mixing locations. Closer to the holes the passage behavior of the atoms through the mixing locations gets non-adiabatic for the following reasons: firstly, the maser field strength reduces towards the holes. This leads to reduced repulsion of the dressed states. Secondly, the stray electric field strongly increases towards the holes. This implies a larger differential slope of the dressed state energies at the mixing locations, and therefore leads to a stronger non-adiabatic passage. At the same time the observed signal extends further to the low frequency spectral region. Since the photon emission probabilities are decreasing towards lower frequencies their behavior finally defines the low-frequency boundary of the maser resonance line. With increasing N_{ex} the photon number n increases. As for larger values of n the photon emission probabilities get larger, also an increasing N_{ex} leads to an extension of the range of the signal to lower frequencies. This theoretical expectation is in agreement with the experimental observation.

In the experiment it is also found that the maser line shifts towards lower frequencies with increasing t_{int} . This result also follows from the developed model: the red-shift increases with t_{int} since a longer interaction time leads to a more adiabatic behavior in the same way as a larger N_{ex} does.

The calculations reveal that on the vertical steps displayed in the signal the photon number distribution has two distinctly separate maxima similar to those observed at the phase transition points discussed above. Therefore, the maser field should exhibit hysteresis and metastability under the present conditions as well. The hysteresis indeed shows up when the cavity frequency is linearly scanned up and down with a modest scan rate.¹⁰ When the maser is operated in steady-state and the cavity frequency is fixed to the steep side of one of the fringes we also observe spontaneous jumps of the maser field between two metastable field states.

The calculations also show that on the smooth wings of the more pronounced interference fringes the photon number distribution $P(n)$ of the maser field is strongly sub-Poissonian. This leads us to the conclusion that we observe Ramsey-type interferences induced by a non-classical radiation field. The sub-Poissonian character of $P(n)$ results from the fact that on the smooth wings of the fringes the photon gain reduces when the photon number is increased. This feedback mechanism stabilizes the photon number resulting in a sub-Poissonian photon distribution.

2.2 Entanglement in the micromaser

Owing to the interaction of the Rydberg atom with the maser field there is an entanglement between field and state in which a particular atom is leaving the cavity. This entanglement was studied in several papers, see e.g. Refs. 18 and 8. Furthermore there is a correlation between the states of the atoms leaving the cavity subsequently. If, e.g. atoms in the lower maser level are studied¹⁹ an anticorrelation is observed in a region for the pump parameter Θ where sub-Poissonian photon statistics is present in the maser field. Recently measurements²⁰ of these pair correlations have been performed giving a rather good agreement with the theoretical predictions by Briegel et al.²¹ The pair correlations disappear when the time interval between subsequent atoms get larger than the storage time of a photon in the cavity.

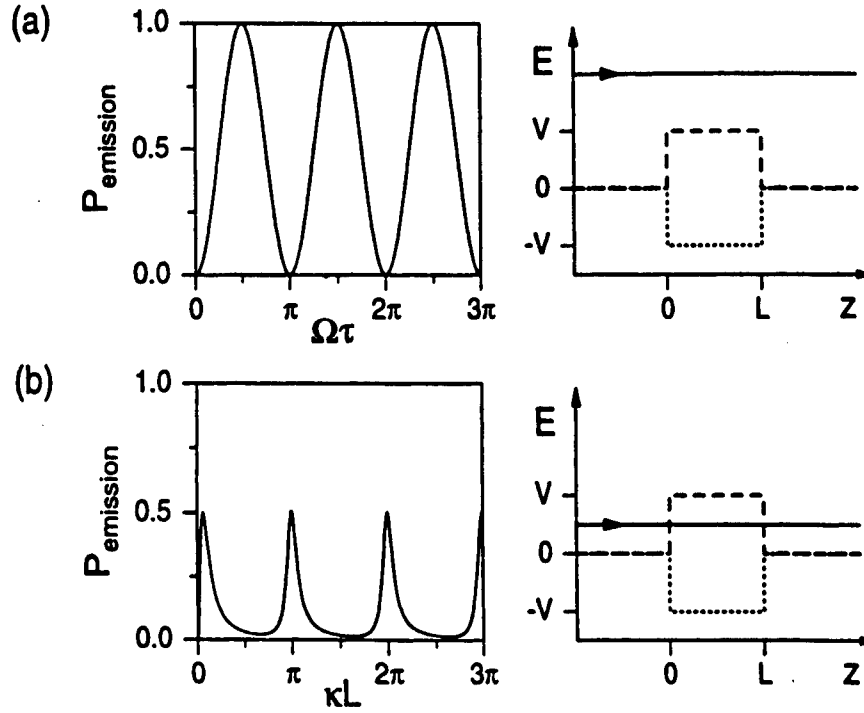


Fig. 5. Emission probability for (a) thermal atoms with $k/\kappa = 10$ versus the interaction time $\Omega\tau$ and (b) ultracold atoms with $k/\kappa = 0.1$ versus the interaction length κL , and the corresponding repulsive (dashed) and attractive (dotted) atom-field potential. The constant κ is defined by $(\hbar\kappa)^2 / 2m = \hbar\Omega$.

2.3 The one-atom maser and ultracold atoms

In the following chapter we discuss the case that the micromaser is pumped by ultracold atoms; in this limit the center of mass motion has to be treated quantum mechanically, especially when the kinetic energy $(\hbar k)^2 / 2M$ of the atoms is of the same order or smaller than the atom-field²² interaction energy $\hbar\Omega$.

For simplicity, we here consider the situation where an atom in the excited state $|e\rangle$ is incident upon a cavity that contains n photons so that the combined atom-field system is described by the state $|e, n\rangle = (|\gamma_{n+1}^+\rangle + |\gamma_{n+1}^-\rangle) / \sqrt{2}$. The dressed-state components $|\gamma_{n+1}^+\rangle$ and $|\gamma_{n+1}^-\rangle$, which are the eigenstates of the atom-field interaction Hamiltonian, encounter different potentials giving rise to different reflection and transmission of the atom. Appropriate relative phase shifts between the dressed-state components during the atom-field interaction may result in the state $(|\gamma_{n+1}^+\rangle - |\gamma_{n+1}^-\rangle) / \sqrt{2} = |g, n+1\rangle$, which corresponds to the emission of a photon and a transition to the lower atomic level $|g\rangle$. Likewise, changes in the relative reflection and transmission amplitudes may lead to a de-excitation of the atom.

For thermal atoms, the emission probability shown in Fig. 5 displays the usual Rabi oscillations as a function of the interaction time τ . For very slow atoms, however, the emission probability is a function of the interaction length L and shows resonances such as the ones observed in the intensity transmitted by a Fabry-Perot resonator. The resonances occur when the cavity length is an integer multiple of half the de Broglie wavelength of the atom inside the potential well.

Figure 6 illustrates the reflection and transmission of the atom for a cavity whose mode function is a mesa function, which approximates the lowest TM mode of a cylindrical cavity. For very cold atoms, the dressed-state component that encounters the potential barrier is always reflected. In general, the other dressed-state component is also reflected at the well. The situation changes dramatically if the cavity length is an integer multiple of half the de Broglie wavelength. In this case, the $|\gamma_{n+1}^-\rangle$ is completely transmitted, which implies a 50 % transmission probability for the atom. A detailed calculation²² shows that in such a situation the emission probability for a photon is 1/2 for each of the two dressed-state components, yielding an overall emission probability $P_{\text{emission}} = 1/2$.

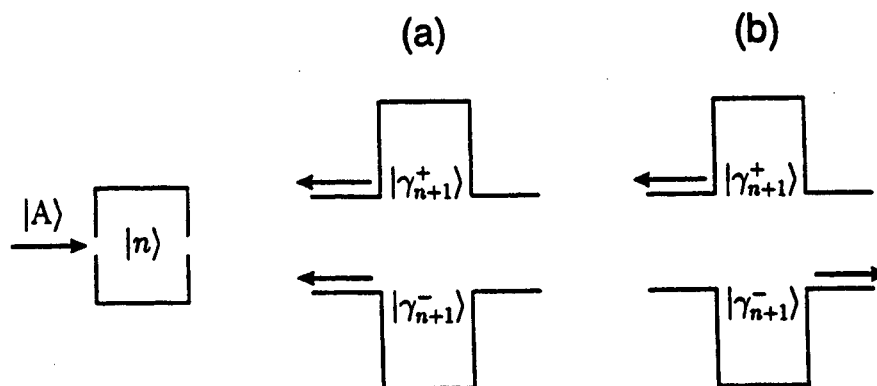


Fig. 6. Reflection and transmission of the atoms at the potential barrier for the $|\gamma_{n+1}^+\rangle$ and at the potential well for the $|\gamma_{n+1}^-\rangle$ component (a) out of the mazer resonance and (b) on resonance.

So far, we have discussed the motion and atom-field interaction of a single atom incident upon the cavity. Due to the unusual emission probability, a beam of ultracold atoms can produce unusual photon distributions such as a shifted thermal distribution. For details about this microwave amplification by z-motion induced emission of radiation (mazer), the reader is referred to the trilogy.²³⁻²⁵

In order to see the mazer resonances for atoms with a certain velocity spread, the interaction length L has to be small. Whereas in the usual cylindrical micromaser cavities the smallest cavity length is given by half the wavelength of the microwaves, cavities of the reentrant type, as depicted in Fig. 7, allow for an interaction length much smaller than the wavelength. With such a device, an experiment with realistic parameters seems possible.²⁴

3. ION TRAP EXPERIMENTS

Besides the experiments performed with atoms in a cavity the trapped ion techniques provide another way to investigate quantum phenomena in radiation atom interaction. In the following recent experiments and new proposals for experiments will be reviewed.

3.1 Resonance fluorescence of a single atom

Resonance fluorescence of an atom is a basic process in radiation-atom interactions, and has therefore always generated considerable interest. The methods of experimental investigation have changed continuously due to the availability of new experimental tools. A considerable step forward occurred when tunable and narrow band dye laser radiation became available. These laser sources are sufficiently intense to easily saturate an atomic transition. In addition, the lasers provide highly monochromatic light with coherence times much longer than typical natural lifetimes of excited atomic states. Excitation spectra with laser light using well collimated atomic beam lead to a width being practically the natural width of the resonance transition, therefore it became possible to investigate the frequency spectrum of the fluorescence radiation with high resolution. However, the spectrograph used to analyze the reemitted radiation was a Fabry-Perot interferometer, the resolution of which did not reach the natural width of the atoms, but was insufficient to reach the laser linewidth, see e.g. Hartig et al.²⁶ and Cresser et al.²⁷ A considerable progress in this direction was achieved by investigating the fluorescence spectrum of ultra-cold atoms in an optical lattice in a heterodyne experiment.²⁸ In these measurements a linewidth of 1 kHz was achieved, however, the quantum aspects of the resonance fluorescence such as antibunched photon statistics cannot be investigated under these conditions since they wash out when more than one atom is involved.

Thus the ideal experiment requires a single atom to be investigated. Since some time it is known that ion traps allow to study the fluorescence from a single laser cooled particle practically at rest, thus providing the ideal case for the spectroscopic investigation of the resonance fluorescence. The other essential ingredient for achievement of high resolution is the measurement of the frequency spectrum by heterodyning the scattered radiation with laser light as demonstrated with many cold atoms.²⁸ Such an optimal experiment with a single trapped Mg^+ ion is described in this paper. The measurement of the spectrum of the fluorescent radiation at low excitation intensities is presented. Furthermore, the photon correlation of the fluorescent light has been investigated under practically identical excitation conditions. The comparison of the two

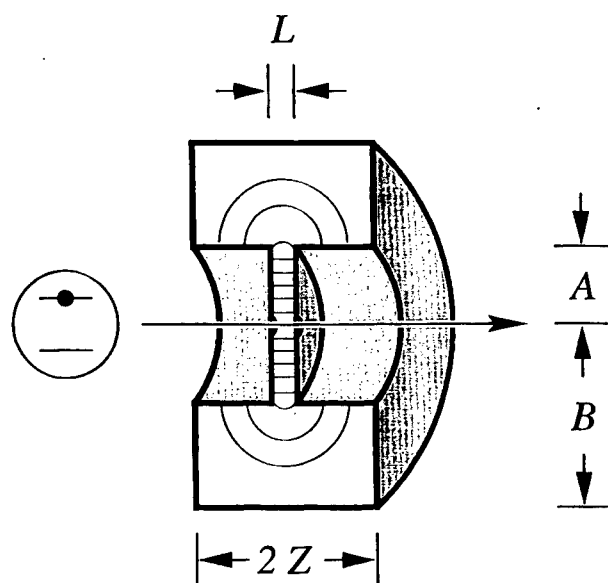


Fig. 7. Possible experimental setup with a reentrant cavity.

results shows a very interesting aspect of complementarity since the heterodyne measurement corresponds to a „wave“ detection of the radiation whereas the measurement of the photon correlation is a „particle“ detection scheme. It will be shown that under the same excitation conditions the wave detection provides the properties of a classical atom, i.e. a driven oscillator, whereas the particle or photon detection displays the quantum properties of the atom. Whether the atom displays classical or quantum properties thus depends on the method of observation.

The spectrum of the fluorescence radiation is given by the Fourier transform of the first order correlation function of the field operators, whereas the photon statistics and photon correlation is obtained from the second order correlation function. The corresponding operators do not commute, thus the respective observations are complementary. Present theory on the spectra of fluorescent radiation following monochromatic laser excitation can be summarized as follows: fluorescence radiation obtained with low incident intensity is also monochromatic owing to energy conservation. In this case, elastic scattering dominates the spectrum and thus one should measure a monochromatic line at the same frequency as the driving laser field. The atom stays in the ground state most of the time and absorption and emission must be considered as one process with the atom in principle behaving as a classical oscillator. This case was treated on the basis of a quantized field many years ago by Heitler.²⁹ With increasing intensity upper and lower states become more strongly coupled leading to an inelastic component, which increases with the square of the intensity. At low intensities, the elastic part dominates since it depends linearly on the intensity. As the intensity of the exciting light increases, the atom spends more time in the upper state and the effect of the vacuum fluctuations comes into play through spontaneous emission. The inelastic component is added to the spectrum, and the elastic component goes through a maximum where the Rabi flopping frequency $\Omega = \Gamma/\sqrt{2}$ (Γ is the natural linewidth) and then disappears with growing Ω . The inelastic part of the spectrum gradually broadens as Ω increases and for $\Omega > \Gamma/2$ sidebands begin to appear.^{27, 30}

The experimental study of the problem requires, as mentioned above, a Doppler-free observation. In order to measure the frequency distribution, the fluorescent light has to be investigated by means of a high resolution spectrometer. The first experiments of this type were performed by Schuda et al.³¹ and later by Walther et al.,³² Hartig et al.²⁶ and Ezekiel et al.³³ In all these experiments, the excitation was performed by single-mode dye laser radiation, with the scattered radiation from a well collimated atomic beam observed and analyzed by a Fabry-Perot interferometer. Experiments to investigate the elastic part of the resonance fluorescence giving a resolution better than the natural linewidth have been performed by Gibbs et al.³⁴ and Cresser et al.²⁷

The first experiments which investigated antibunching in resonance fluorescence were also performed by means of laser-excited collimated atomic beams. The initial results obtained by Kimble, Dagenais, and Mandel³⁵ showed that the second-order correlation function $g^{(2)}(t)$ had a positive slope which is characteristic of photon antibunching. However,

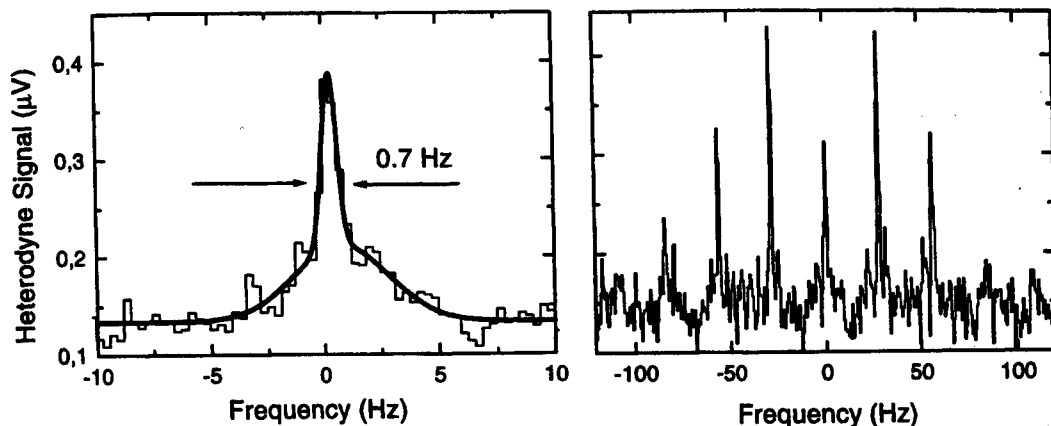


Fig. 8. Heterodyne spectrum of a single trapped 24 Mg^+ -ion. Left side: Resolution bandwidth 0.5 Hz. The solid line is a Lorentzian fit to the experimental data; the peak appears on top of a small pedestal being 4 Hz wide. The latter signal is due to random phase fluctuations in the spatially separated sections of the light paths of local oscillator and fluorescent light; they are generated by variable air currents in the laboratory. Right side: Heterodyne spectrum of the coherent peak with sidebands generated by mechanical vibrations of the mount holding the trap. The vibrations are due to the operation of a rotary pump in the laboratory. For details see Ref. 44.

$g^{(2)}(0)$ was larger than $g^{(2)}(t)$ for $t \rightarrow \infty$ due to number fluctuations in the atomic beam and to the finite interaction time of the atoms.^{36,37} Further refinement of the analysis of the experiment was provided by Dagenais and Mandel.³⁷ Rateike et al.³⁸ used a longer interaction time for an experiment in which they measured the photon correlation at very low laser intensities (see Cresser et al.²⁷ for a review). Later, photon antibunching was measured using a single trapped ion in an experiment which avoids the disadvantages of atom number statistics and finite interaction time between atom and laser field.³⁹

As pointed out in many papers photon antibunching is a purely quantum phenomenon (see e.g. Cresser et al.²⁷ and Walls⁴⁰). The fluorescence of a single ion displays the additional nonclassical property that the variance of the photon number is smaller than its mean value (i.e. it is sub-Poissonian).^{39,41}

The trap used for the present experiment was a modified Paul-trap, called an endcap-trap.⁴² The trap consists of two solid copper-beryllium cylinders (diameter 0.5 mm) arranged co-linearly with a separation of 0.56 mm. These correspond to the cap electrodes of a traditional Paul trap, whereas the ring electrode is replaced by two hollow cylinders, one of which is concentric with each of the cylindrical endcaps. Their inner and outer diameters are 1 and 2 mm, respectively and they are electrically isolated from the cap electrodes. The fractional anharmonicity of this trap configuration, determined by the deviation of the real potential from the ideal quadrupole field is below 0.1 % (see Schrama et al.⁴²). The trap is driven at a frequency of 24 MHz with typical secular frequencies in the xy-plane of approximately 4 MHz. This required a radio-frequency voltage with an amplitude on the order of 300 V to be applied between the cylinders and the endcaps.

The measurements were performed using the $3^2\text{S}_{1/2} - 3^2\text{P}_{3/2}$ transition of the 24 Mg^+ -ion at a wavelength of 280 nm. The heterodyne measurement is performed as follows. The dye laser excites the trapped ion while the fluorescence is observed in a direction of about 54° to the exciting laser beam. However, both the observation direction and the laser beam are in a plane perpendicular to the symmetry axis of the trap. A fraction of the laser radiation is removed with a beamsplitter and then frequency shifted (by 137 MHz with an acousto-optic modulator (AOM)) to serve as the local oscillator. An example of a heterodyne signal is displayed in Fig. 8. The signal is the narrowest optical heterodyne spectrum of resonance fluorescence reported to date. Thus our experiment provides the most compelling confirmation of Weisskopf's prediction of a coherent component in resonance fluorescence. The linewidth observed implies that exciting laser and fluorescent light are coherent over a length of 400 000 km. Further details on the experiment are given in Refs. 43 and 44.

Investigation of photon correlations employed the ordinary Hanbury-Brown and Twiss setup. The setup was essentially the same as described by Diedrich and Walther.³⁹ The results are shown and discussed in Ref. 43 also.

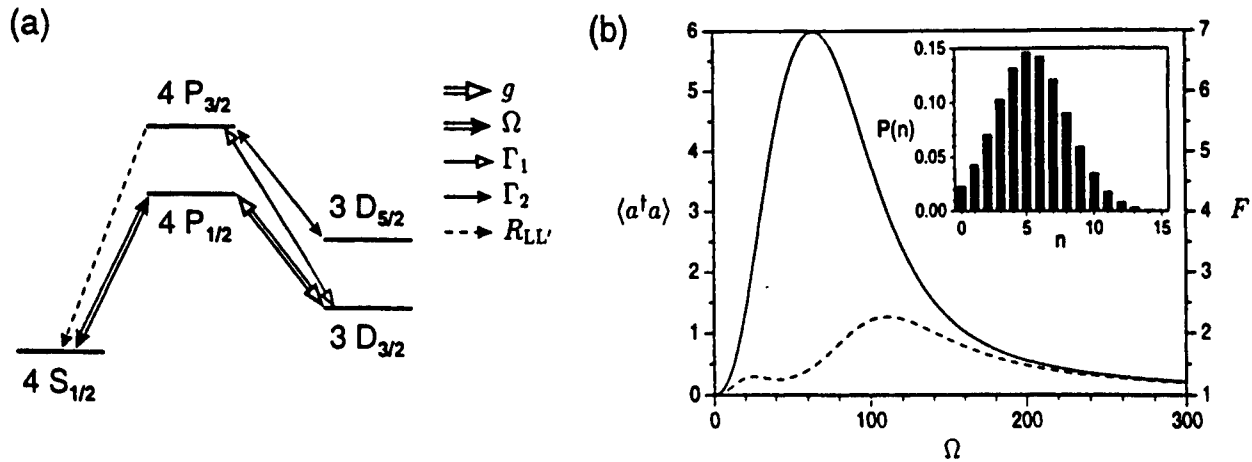


Fig. 9. (a) Schematic representation of the Ca^+ scheme for the ion-trap laser. (b) Mean photon number $\langle a^\dagger a \rangle$ (solid) and Fano factor F (dashed) versus the coherent pump strength Ω . The parameters are $A = 1$, $g = 14.8$, $\Gamma_1 = 40$, and $\Gamma_2 = 100$. The inset shows the photon distribution for $\Omega = 50$. All rates are in MHz.

The presented experiment describes the first high-resolution heterodyne measurement of the elastic peak in resonance fluorescence of a single ion. At identical experimental parameters we have also measured antibunching in the photon correlation of the scattered field. Together, both measurements show that, in the limit of weak excitation, the fluorescence light differs from the excitation radiation in the second-order correlation but not in the first order correlation. However, the elastic component of resonance fluorescence combines an extremely narrow frequency spectrum with antibunched photon statistics, which means that the fluorescence radiation is not second-order coherent as expected from a classical point of view.⁴⁵ The heterodyne and the photon correlation measurement are complementary since they emphasize either the classical wave properties or the quantum properties of resonance fluorescence, respectively.

3.2 The ion-trap laser

There have been several theoretical papers on one-atom lasers in the past.^{46-49, 56} This system provides a testing ground for new theoretical concepts and results in the quantum theory of the laser. Examples are atomic coherence effects⁵⁰ and dynamic (i.e. self-generated) quantum-noise reduction.^{51,52,49} All these aspects are a consequence of a pump process whose complex nature is not accounted for in the standard treatment of the laser. So far there is one experiment where laser action could be demonstrated with one atom at a time in the optical resonator.⁶ A weak beam of excited atoms was used to pump this one-atom laser.

A formidable challenge for an experiment is to perform a similar experiment with a trapped ion in the cavity. Mirrors with an ultrahigh finesse are required, and a strong atom-field coupling is needed. After the emission of a photon, the ion has to be pumped before the next stimulated emission can occur. Similar as in the resonance fluorescence experiments which show antibunching,^{35,39} there is a certain time gap during which the ion is unable to add another photon to the laser field. It has been shown⁴⁹ that this time gap plays a significant role in the production of a field with sub-Poissonian photon statistics.

We have investigated the theoretical basis for an experimental realization of the ion-trap laser. Our analysis takes into account details such as the multi-level structure, the coupling strengths and the parameters of the resonator. It has been a problem to find an ion with an appropriate level scheme. We could show that it is possible to produce a laser field with the parameters of a single Ca^+ ion. This one-atom laser displays several features, which are not found in conventional lasers: the development of two thresholds, sub-Poissonian statistics, lasing without inversion and self-quenching. The details of this work are reported in Ref. 53,54. In a subsequent paper⁵⁵ also the center-of-mass motion of the trapped ion was quantized. This leads to additional features of the ion trap laser, especially a multiple vacuum Rabi-splitting is observed.

The Ca^+ scheme, which is sketched in Fig. 9(a). It contains a Λ -type subsystem: the ion is pumped coherently from the ground state to the upper laser level $4P_{1/2}$, stimulated emission into the resonator mode takes place on the transition to $3D_{3/2}$ at a wavelength of 866 nm. Further pump fields are needed to close the pump cycle and to depopulate the metastable levels.

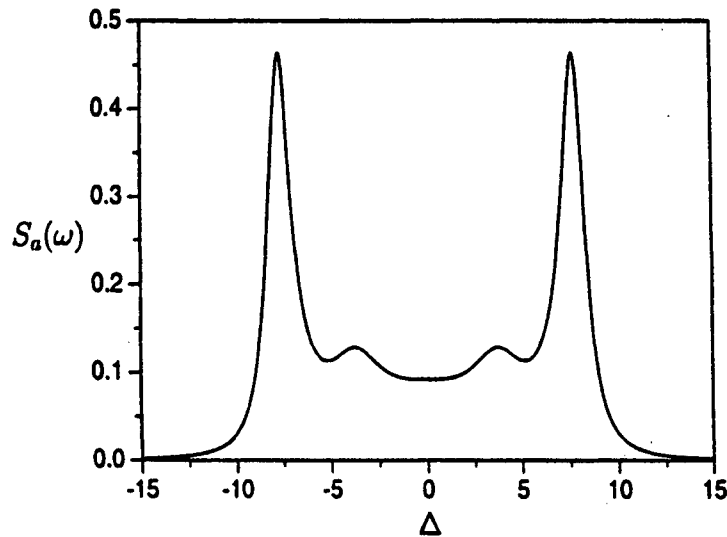


Fig. 10. Multiple vacuum Rabi splitting in the output spectrum $S_a(\omega)$ for the two-level atom with quantized CM motion. The parameters are $A = 0.1$, $B = 0.05$, $\mu = 0.5$, $R_{AB} = 0.1$, $R_{BA} = 0.001$, and $\eta = 0.7$. All rates are in units of g_0 .

Although spontaneous relaxation from the upper laser level to the ground state takes place at a relatively large rate of 140 MHz and suppresses the atomic polarization on the laser transition, laser light is generated for realistic experimental parameters due to atomic coherence effects within the Λ subsystem. The occurrence of laser action is demonstrated in Fig. 9(b) for a resonator with a photon damping rate $A = 1$ MHz and a vacuum Rabi frequency $g = 14.8$ MHz on the laser transition. For the numerical calculation of the realistic scheme, the Zeeman substructure and the polarizations of the fields have to be taken into account. With increasing coherent pump Ω , the mean photon number inside the resonator first increases and then decreases. Both the increase and decrease of the intensity are accompanied by maxima in the intensity fluctuations, which can be interpreted as thresholds. Laser action takes place in between these two thresholds. This is confirmed by the Poissonian-like photon distribution given in the inset of Fig. 9(b). In addition, the linewidth of the output spectrum is in the laser region up to ten times smaller than below the first and beyond the second threshold.⁵⁴ Note that for a thermal distribution the solid and dashed curves in Fig. 9(b) for the intensity and the intensity fluctuations would coincide.

For a nonvanishing Lamb-Dicke parameter η , higher vibrational states will be excited during the pump and relaxation processes; the amplitude of the atomic motion will increase. Therefore, the ion will in general not remain at an antinode of the resonator mode, and the strength of the atom-field coupling will decrease. However, the atom can be prevented from heating up by detuning a coherent pump field. The coupling strength is given by the product of a constant g_0 and a motion-dependent function⁵⁵ that is determined by an overlap integral involving the motional wave function of the atom and the mode function of the field.

In a simple two-level laser model with decay rate R_{AB} and pump rate R_{BA} , the cooling process may be incorporated by coupling the atomic motion to a thermal reservoir with cooling rate B and thermal vibron number μ . Already in such a simple model, the discrete nature of the quantized motion shows up below threshold in a multiple vacuum Rabi splitting of the output spectrum.⁵⁵ This is illustrated in Fig. 10. The pairs of peaks correspond to different vibrational states with different atom-field coupling.

The cooling mechanism is most transparent in the special case of resolved-sideband cooling. The coherent pump may be detuned to the first lower vibrational sideband so that with each excitation from $4S_{1/2}$ to $4P_{1/2}$ one vibron is annihilated and the CM motion is cooled. Eventually, all the population will collect in the motional ground state of the atomic ground state $4S_{1/2}$ and cannot participate in the lasing process. The coherent pump strength is now given by Ω_0 times a motion-dependent function. In order to maintain laser action in the presence of the cooling, an additional broadband pump field Γ may be applied to the cooling transition. Figure 11 indicates that a field with a mean photon number $|a^\dagger a\rangle = 2.3$ is generated while the mean vibron number is restricted to a value of $|b^\dagger b\rangle = 0.5$. If a larger mean vibron number is acceptable, the

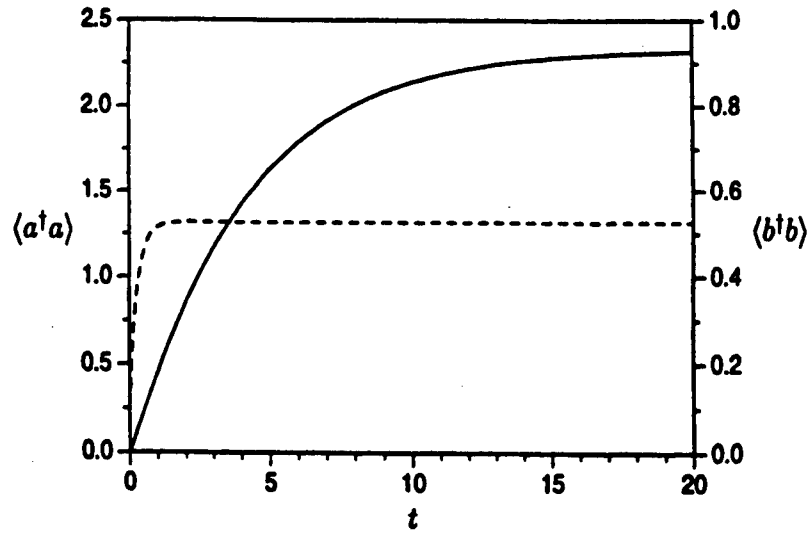


Fig. 11. Time evolution of the mean photon number (solid) and the mean vibron number (dashed) in the Ca^+ ion-trap laser with sideband cooling. The parameters are $A = 0.5$, $g_0 = 14.8$, $\Omega_0 = 100$, $\Gamma = \Gamma_1 = 40$, $\Gamma_2 = 100$, and $\eta = 0.1$ on the laser transition. Initially, the atom is in the ground state and the vibronic distribution is thermal with $|b^\dagger b\rangle = 0.1$. All rates are in MHz.

pump rate Γ can be increased and more population takes part in the laser action. This leads to considerably larger mean photon numbers. The calculation shows that it is possible to incorporate a cooling mechanism in a multilevel one-atom laser scheme and to obtain significant lasing also for nonperfect localization of the atom. Although it is difficult to reach the resolved-sideband limit in an experiment, cooling may still be achieved in the weak-binding regime by detuning a coherent pump field.

4. CONCLUSIONS

In this paper recent experiments with single atoms in cavities and traps are reviewed. It is especially pointed out that using ultracold atoms will lead to new and interesting aspects in atom-matter interaction. The possibility that now ultracold atoms are available bring such experiments into reach in the near future.

The quantum-mechanical CM motion of the atoms incident upon a micromaser cavity is equivalent to a scattering problem that involves both a repulsive and an attractive potential. The emission probability for an initially excited ultracold atom exhibits sharp resonances when the de Broglie wavelength fits resonantly into the cavity. These resonances may be observed experimentally with the help of a reentrant cavity. Whereas the eigenstates of the atomic motion are continuously distributed for the maser, the motion is confined to a trapping potential in the one-atom laser. The discrete nature of the CM motion in the trap is reflected below threshold by multiple vacuum Rabi splitting. In order to prevent the atom from being continuously heated by the pump and relaxation processes, sideband cooling has been incorporated into the model. The recently proposed Ca^+ ion-trap laser is used to illustrate the possibility of one-atom lasing in the presence of a cooling mechanism.

There is one very interesting application of the „mazer“ which should be briefly mentioned here: the device can act as a filter for matter waves and can thus be used to increase the coherence length of an atomic beam; in the same way as a Fabry-Perot can be used to increase the coherence length of a light wave. This application will be discussed in a forthcoming paper.⁵⁷

5. REFERENCES

1. D. Meschede, H. Walther and G. Müller, „The one-atom maser,“ *Phys. Rev. Lett.* **54**, 551-554 (1985).
2. G. Rempe, H. Walther and N. Klein, „Observation of quantum collapse and revival in the one-atom maser,“ *Phys. Rev. Lett.* **58**, 353-356 (1987).

3. G. Rempe, F. Schmidt-Kaler and H. Walther, „Observation of sub-Poissonian photon statistics in a micromaser,” *Phys. Rev. Lett.* **64**, 2783-2786 (1990).
4. G. Rempe and H. Walther, „Sub-Poissonian atomic statistics in a micromaser,” *Phys. Rev. A* **42**, 1650-1655 (1990).
5. H.J. Kimble, O. Carnal, N. Georgiades, H. Mabuchi, E.S. Polzik, R.J. Thompson and Q.A. Turchette, *Atomic Physics*, edited by D.J. Wineland, C.E. Wieman, S.J. Smith, Vol. 14, p. 314 American Institute of Physics, New York, 1995.
6. K. An, J.J. Childs, R.R. Dasari, M.S. Feld, „Microlaser: a laser with one atom in an optical resonator,” *Phys. Rev. Lett.* **73**, 3375-3378 (1994).
7. C. Wagner, R.J. Brecha, A. Schenzle and H. Walther, „Phase diffusion, entangled states and quantum measurements in the micromaser,” *Phys. Rev. A* **47**, 5068-5079 (1993).
8. M. Löffler, B.-G. Englert and H. Walther, „Testing a Bell-type inequality with a micromaser,” *Appl. Phys. B* **63**, 511-516 (1996).
9. O. Benson, G. Raithel and H. Walther, „Quantum jumps of the micromaser field - dynamic behavior close to phase transition points,” *Phys. Rev. Lett.* **72**, 3506-3509 (1994).
10. G. Raithel, O. Benson and H. Walther, „Atomic interferometry with the micromaser,” *Phys. Rev. Lett.* **75**, 3446-3449 (1995).
11. G. Raithel, C. Wagner, H. Walther, L.M. Narducci and M.O. Scully, „The micromaser: a proving ground for quantum physics,” *Advances in Atomic, Molecular, and Optical Physics*, Supplement 2, edited by P. Berman, Academic Press, New York, 1994, p. 57-121.
12. P. Filipowicz, J. Javanainen and P. Meystre, „Theory of a microscopic maser,” *Phys. Rev. A* **34**, 3077-3087 (1986).
13. L.A. Lugiato, M.O. Scully and H. Walther, „Connection between microscopic and macroscopic maser theory,” *Phys. Rev. A* **36**, 740-743 (1987).
14. P. Meystre, „Cavity quantum optics and the quantum measurement process,” *Progress in Optics*, edited by E. Wolf, Elsevier Science Publishers, New York, 1992, Vol. 30, p. 261-355.
15. J.M. Raimond, M. Brune, L. Davidovich, P. Goy and S. Haroche, „The two-photon Rydberg atom micromaser,” *Atomic Physics* **11**, 441-445 (1989).
16. N.F. Ramsey, *Molecular Beams*, Clarendon Press, Oxford, 1956, p. 124-134.
17. C. Cohen-Tannoudji, J. Dupont-Roc and G. Grynberg, *Atom-Photon Interactions*, John Wiley and Sons, Inc., New York, 1992, p. 407-514.
18. C. Wagner, A. Schenzle and H. Walther, „Atomic waiting-times and correlation functions,” *Optics Communications* **107**, 318-326 (1994).
19. H. Walther, „Experiments on cavity quantum electrodynamics,” *Phys. Reports* **219**, 263-281 (1992).
20. M. Weidinger, O. Benson and H. Walther, to be published.
21. H.J. Briegel, B.-G. Englert, N. Sterpi and H. Walther, „One-atom maser: statistics of detector clicks,” *Phys. Rev. A* **49**, 2962-2985 (1994).
22. M.O. Scully, G.M. Meyer and H. Walther, „Induced emission due to the quantized motion of ultra-cold atoms passing through a micromaser cavity,” *Phys. Rev. Lett.* **76**, 4144-4147 (1996).
23. G.M. Meyer, M.O. Scully and H. Walther, „Quantum theory of the maser: I. general theory,” *Phys. Rev. A*, in print.
24. M. Löffler, G.M. Meyer, M. Schröder, M.O. Scully and H. Walther, „Quantum theory of the maser: II. extensions and experimental conditions,” *Phys. Rev. A*, in print.
25. M. Schröder, K. Vogel, W.P. Schleich, M.O. Scully and H. Walther, „Quantum theory of the maser: III. spectrum,” *Phys. Rev. A*, in print.
26. W. Hartig, W. Rasmussen, R. Schieder and H. Walther, „Study of the frequency distribution of the fluorescent light induced by monochromatic excitation,” *Z. Physik A* **278**, 205-210 (1976).
27. J.D. Cresser, J. Häger, G. Leuchs, F.M. Rateike and H. Walther, „Resonance fluorescence of atoms in strong monochromatic laser fields,” *Topics in Current Physics* **27**, 21-59 (1982).
28. P.S. Jessen, C. Gerz, P.D. Lett, W.D. Philipps, S.L. Rolston, R.J.C. Spreeuw and C.I. Westbrook, „Observation of quantized motion of Rb atoms in an optical field,” *Phys. Rev. Lett.* **69**, 49-52 (1992).
29. W. Heitler, *The Quantum Theory of Radiation*, Third Edition, University Press, Oxford, 1954, p. 196-204.
30. B.R. Mollow, „Power spectrum of light scattered by two-level systems,” *Phys. Rev.* **188**, 1969-1975 (1969).
31. F. Schuda, C. Stroud, Jr. and M. Hercher, „Observation of the resonant Stark effect at optical frequencies,” *J. Phys. B*, **L198-L202** (1974).
32. H. Walther, „Atomic fluorescence induced by monochromatic excitation,” *Lecture Notes in Physics* **43**, 358-369 (1975).

33. F.Y. Wu, R.E. Grove and S. Ezekiel, „Investigation of the spectrum of resonance fluorescence induced by a monochromatic field,” *Phys. Rev. Lett.* **35**, 1426-1429 (1975); R.E. Grove, F.Y. Wu and S. Ezekiel, „Measurement of the spectrum of resonance fluorescence from a two-level atom in an intense monochromatic field,” *Phys. Rev. Lett.* **A 15** 227-233 (1977).
34. H.M. Gibbs and T.N.C. Venkatesan, „Direct observation of fluorescence narrower than the natural linewidth,” *Opt. Comm.* **17**, 87-94 (1976).
35. H.J. Kimble, M. Dagenais and L. Mandel, „Photon antibunching in resonance fluorescence,” *Phys. Rev. Lett.* **39**, 691-695 (1977).
36. E. Jakeman, E.R. Pike, P.N. Pusey and J.M. Vaughan, „The effect of atomic number fluctuations on photon antibunching in resonance fluorescence,” *J. Phys.* **A 10**, L257-L259 (1977).
37. H.J. Kimble, M. Dagenais and L. Mandel, „Multiatom and transit-time effects in photon correlation measurements in resonance fluorescence,” *Phys. Rev.* **A 18**, 201-207 (1978); M. Dagenais and L. Mandel, „Investigation of two-atom correlations in photon emissions from a single atom,” *Phys. Rev.* **A 18**, 2217-2218 (1978).
38. F.M. Rateike, G. Leuchs and H. Walther, results cited in Ref. 21.
39. F. Diedrich and H. Walther, „Non-classical radiation of a single stored ion,” *Phys. Rev. Lett.* **58**, 203-206 (1987).
40. D.F. Walls, „Evidence for the quantum nature of light,” *Nature* **280**, 451-454 (1979).
41. R. Short and L. Mandel, „Observation of sub-Poissonian photon statistics,” *Phys. Rev. Lett.* **51**, 384-387 (1983).
42. C.A. Schrama, E. Peik, W.W. Smith and H. Walther, „Novel miniature ion traps,” *Opt. Comm.* **101**, 32-36 (1993).
43. J.T. Höffges, H.W. Baldauf, T. Eichler, S.R. Helmfrid and H. Walther, „Heterodyne measurement of the fluorescent radiation of a single trapped ion,” *Opt. Communications* **133**, 170-174 (1997).
44. J.T. Höffges, H.W. Baldauf, W. Lange and H. Walther, „Heterodyne measurement of the resonance fluorescence of a single ion,” *Journal of Modern Optics*, in print.
45. R. Loudon, „Non-classical effects in the statistical properties of light,” *Rep. Progr. Phys.* **43**, 913-949 (1980).
46. Y. Mu and C.M. Savage, „One-atom lasers,” *Phys. Rev.* **A 46**, 5944-5954 (1992).
47. C. Ginzler, H.J. Briegel, U. Martini, B.-G. Englert and A. Schenzle, „Quantum optical master equations: the one-atom laser,” *Phys. Rev.* **A 48**, 732-738 (1993).
48. T. Pellizzari and H.J. Ritsch, „Photon statistics of the three-level one-atom laser,” *Mod. Opt.* **41**, 609-623 (1994); „Preparation of stationary Fock states in a one-atom Raman laser,” *Phys. Rev. Lett.* **72**, 3973-3976 (1994); P. Horak, K.M. Gheri and H. Ritsch, „Quantum dynamics of a single-atom cascade laser,” *Phys. Rev.* **A 51**, 3257-3266 (1995).
49. H.-J. Briegel, G.M. Meyer and B.-G. Englert, „Dynamic noise reduction in multilevel lasers: nonlinear theory and the pump-operator approach,” *Phys. Rev.* **A 53**, 1143-1159 (1996); „Pump operator for lasers with multi-level excitation,” *Europhys. Lett.* **33**, 515-520 (1996).
50. For a recent review see E. Arimondo, „Coherent population trapping in laser spectroscopy,” *Progress in Optics*, edited by E. Wolf, Elsevier, Amsterdam 1996, vol. **XXXV**, 257-354.
51. A.M. Khazanov, G.A. Koganov and E.P. Gordov, „Macroscopic squeezing in three-level laser,” *Phys. Rev.* **A 42**, 3065-3069 (1990); T.C. Ralph and C.M. Savage, „Squeezed light from a coherently pumped four-level laser,” *Phys. Rev.* **A 44**, 7809-7814 (1991); H. Ritsch, P. Zoller, C.W. Gardiner and D.F. Walls, „Laser light by dynamic pump-noise suppression,” *Phys. Rev.* **A 44**, 3361-3364 (1991).
52. K.M. Gheri and D.F. Walls, „Squeezed lasing without inversion or light amplification by coherence,” *Phys. Rev.* **A 45**, 6675-6686 (1992); H. Ritsch and M.A.M. Marte, „Quantum noise in Raman lasers: effects of pump bandwidth and super- and sub-Poissonian pumping,” *Phys. Rev.* **A 47**, 2354-2365 (1993).
53. G.M. Meyer, H.-J. Briegel and H. Walther, „Ion-trap laser,” *Europhys. Lett.* **37**, 317-322 (1997).
54. G.M. Meyer, M. Löffler and H. Walther, „Spectrum of the ion-trap laser,” *Phys. Rev.* **A 56**, R1099-R1102 (1997).
55. M. Löffler, G.M. Meyer and H. Walther, „One atom laser with quantized centre-of-mass motion,” to be published.
56. M. Löffler, G.M. Meyer and H. Walther, „Spectral properties of the one-atom maser,” *Phys. Rev.* **A 55**, 3923-3930 (1997).
57. M. Löffler and H. Walther, to be published.

OPTICAL PROPERTIES OF QUASIPERIODIC (SELF-SIMILAR) STRUCTURES

M. Bertolotti and C. Sibilio

Dipartimento di Energetica, Universita' di Roma "La Sapienza", Roma, Italy and

GNEQP of CNR and INFM, Italy

Abstract

The optical properties of layered materials of a fractal quasiperiodic structure are reviewed considering both the case of wavelength smaller than the thickness of the thinner layer and the reverse case in which the whole structure is much smaller than the wavelength.

1. INTRODUCTION

Interest in the optical properties of fractal structures has been growing in recent years¹. There are several categories of optical fields to which research activities are devoted related to fractals. One is image science². In this field fractals are considered as objects to be processed with various image processing techniques. Another domain of investigation is the study of the properties of optical fields produced when waves are incident over fractal structures. Scattering³ and diffraction⁴ by fractal objects have been most studied also with the aim of evaluating the fractality or because through the interaction new types of wave fields are created that may lead to the development of new optical techniques or to obtain better results than the ones obtained with conventional structures.

Here we want to focus on transmission properties of an optical field (a plane wave for the sake of simplicity) propagating through self-similar structures. Because of the aspect related to optical localization of waves appearing in fractals, there is also an increasing interest into the nonlinear optical properties of these structures.

The results will show the greater flexibility and richness of fractals with respect to traditional periodic structures.

2. A FEW INFORMATIONS ON FRACTALS

The concept of a fractal was popularised by Mandelbrot already in the 1960s^{5,6}. The term "fractal" was introduced by him to describe geometrical objects with no integer dimension. Several types of fractals are treated in physical optics. The most popular objects are **self-similar** fractals. The definition given by Mandelbrot claims that a self-similar fractal is a set whose dimension is different from the topological dimension, invariant with respect to a change of scale. An object is therefore said to be self-similar when a part of it is similar to its whole. Self-similar fractals are generated mathematically by means of a recursive operation of a generator on an initiator⁶. This is illustrated in fig. 1, where two typical self-similar fractals are shown together with their generation processes: Cantor triadic set and Koch triadic curve. Looking at the distribution of segments of the Cantor distribution, one may see that it is quasi-periodic. A property shared by many other fractal structures. One may note that any physical fractal is incomplete in the sense that the development level N is always finite. The objects that are the

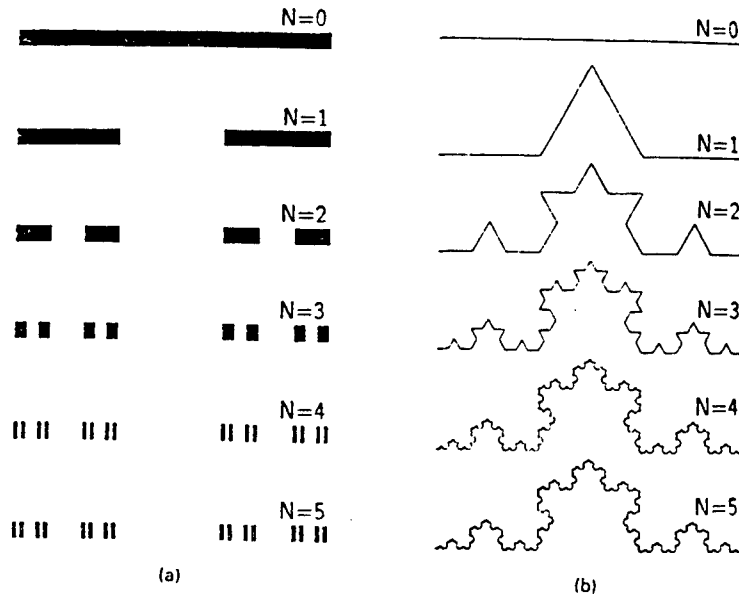


Fig.1 a) Cantor triadic set. One starts from a segment of length L (initiator, $N=0$), divide it into three equal parts and stripe out the central part (generator, $N=1$). The same procedure is then applied to all remaining segments; b) Koch triadic curve. The initiator is still a line of length L . The central segment is erased and an equilater triangle of side $L/3$ without basis is built (generator, $N=1$). The operation is repeated on each segment.

product of finite levels are sometimes called **prefractals** but because a true fractal does not exist in real world, we shall omit the distinction, bearing however this circumstance in mind.

The most prominent property of fractals is their dimensional behaviour. Different definitions are given for fractals dimensions. For example, in the case of regular self-similar fractals, in which the generator is composed of m segments of length $1/\mu$, the **similarity dimension** is defined as

$$D = \log m / \log \mu \quad (1)$$

The similarity dimension of the Cantor triadic set is $D = \log 2 / \log 3 = 0.631$. For the Koch curve, it is $D = \log 4 / \log 3 = 1.262$. It means that the Cantor set has a dimensionality between a point and a line. The Koch curve between a line and a surface. Some fractals, as the two discussed here, exhibit only one value of D (**monofractals**), other show a distribution of D values (**multifractals**).

If L_N is the length of the fractal at the N -th step and $l_N = 1/\mu_N$ is the length of each link one has

$$m = L_N / l_N \quad (2)$$

and

$$D = (\log L_N / \log \mu_N) + 1.$$

It means that, if we drop the index N ,

$$m \propto l^{-D} \quad (3)$$

It is easily seen from fig.1 that the identical construction, but at a reduced scale, is performed at each step N. For this reason, any fragment of the structure can be obtained by simply increasing any of its components up to the required scale. This circumstance is formally reflected in eq.(3). Indeed, if the length l of an elementary section is reduced by ζ^{-1} times, then the number of segments m will increase. From eq.(3) we have

$$m(\zeta l) = \zeta^{-D} m(l) \quad \zeta < 1 \quad (4)$$

If in eq.(4) the similarity parameter ζ is fixed by the condition $\zeta l=1$, eq.(3) is immediately found. Using this condition in eq.(2) we may redefine D as

$$D = 1 + \log L / N \log \zeta. \quad (5)$$

The dimension is independent of the level N of the structure.

3. SELF-SIMILAR RESONATOR

In the following we want to study the transmission properties of a fractal superlattice composed by alternating layers of refractive indices n_1 and n_2 . The optical thickness of the layers follows the Cantor triadic set (s.fig.2).

Two possible constructions can be realized: case A in which the central part is made with a material of refractive index n_2 . Case B in which the central part is made with a material with index n_1 . The structure can be studied through the transfer matrix method ⁷. The expression of the transmission of TE and TM fields is given by

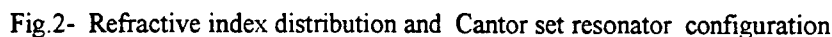
$$t(k_0, L) = \frac{2}{T_{22}^{(N)}(k_0, L) - \frac{T_{21}^{(N)}(k_0, L)}{i\beta} - i\beta T_{12}^{(N)}(k_0, L) + T_{11}^{(N)}(k_0, L)} \quad (6)$$

where i is the imaginary unit, $\beta = k_0 n$ for TE and $\beta = n_h/k_x$ for TM, $k_{xh} = k_0 \sqrt{n_h^2 - n_{eff}^2}$, where n_h is the refractive index of the n -th layer, $n_{eff} = n \sin \theta$, and θ is the input incidence angle, $T_{hk}^{(N)}$ are the elements of the $T^{(N)}$ matrix that is obtained by the N -th iteration of the recursive relation

$$T^{(k)}(l) = T^{(k-1)}(l) T_1(3^{k-1}l) T^{(k-1)}(l), \quad k = 1, 2, \dots, N \quad (7)$$

with $T^{(0)}(l) = T_2(l)$

and



(8)

Transmission spectra for normal incidence as a function of the Cantor level N are given in fig.3. The two possibilities A and B are shown. Small differences are clearly visible, especially for the case of low N level. The differences occur because the resonances of the single layers are obviously different if they are made with index n_1 or n_2 . It may be of interest to compare with the transmission of a periodic resonator with the same total optical path as the fractal one for $N=4$ (s.fig.3c). The magnitude of the transmission is a symmetric function of frequency, for a fixed optical path L of the generator, and it is periodic with the period $\varphi_p = 3\pi$. The smallest components resonate when $\varphi_p/3 = m\pi$ where m is an integer.

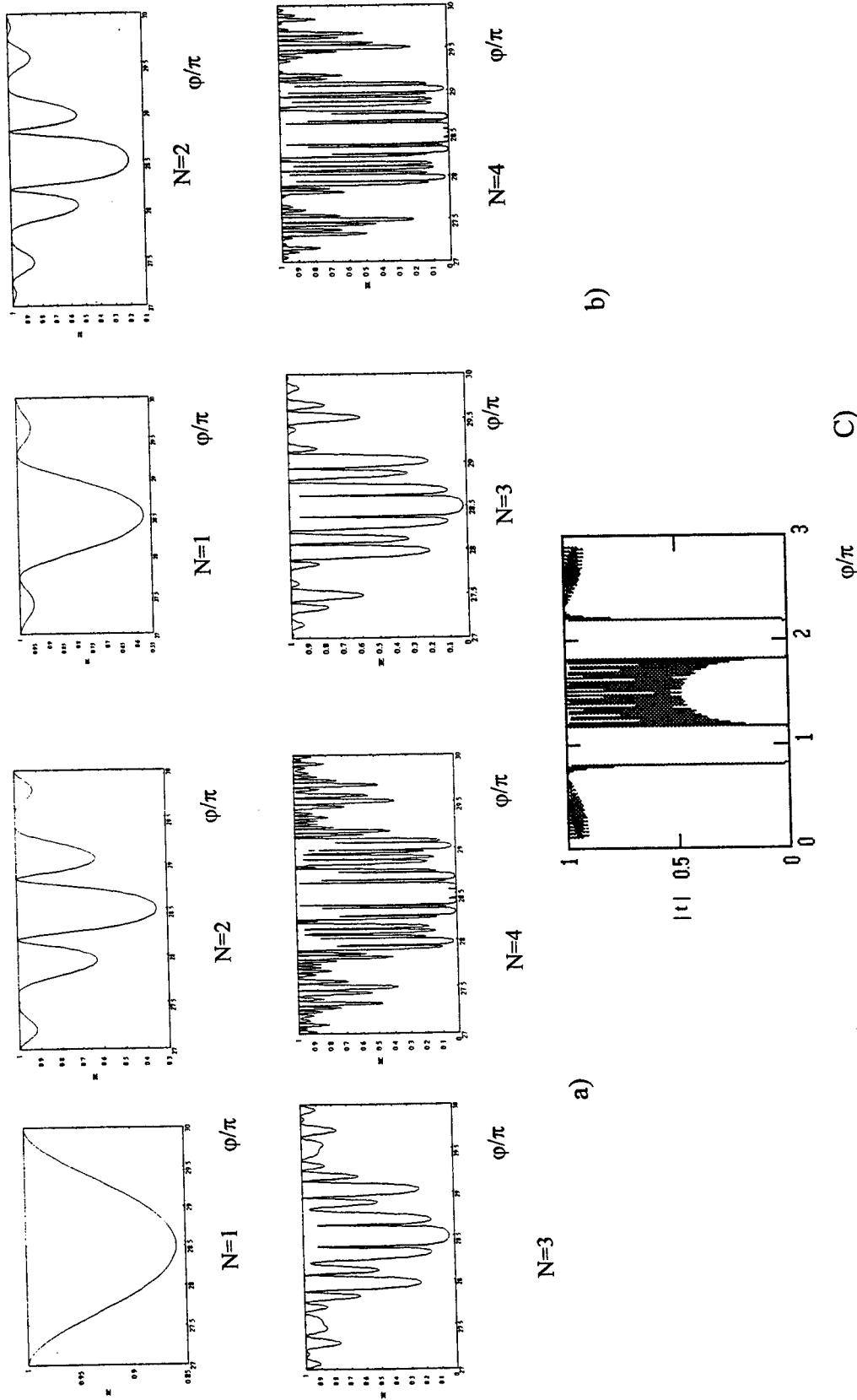


Fig.3 Transmission spectrum magnitude v.s. ϕ/π for the Cantor set, a) case A, b) Case B), c) periodic case

One of the most interesting properties of these spectra, already for level $N=3$, is the appearance of sharp isolated peaks in the forbidden gap of frequencies, for which the transmission is zero. This behaviour is quite different from the one of a periodic structure and is very important for nonlinear or time filtering applications.

The self similar behaviour is shown in figs 4.

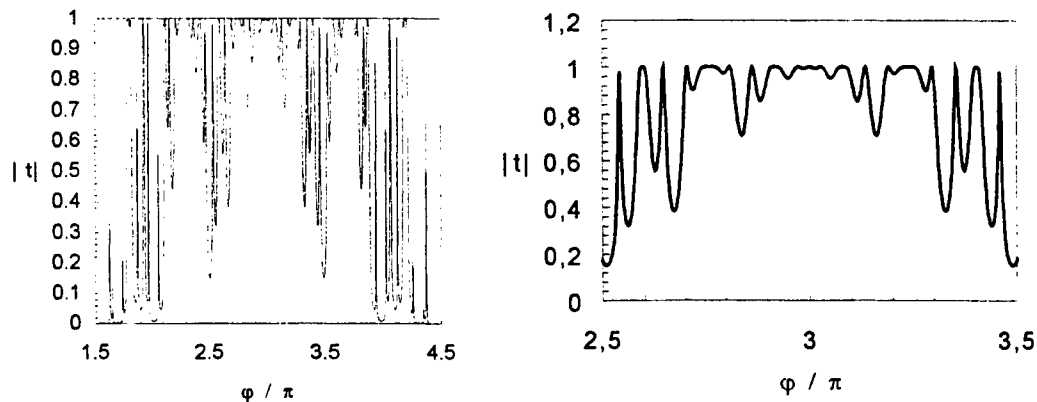


Fig 4 Transmission spectrum magnitude versus ϕ/π around $\phi_p = 3\pi$ for $N=4$, a) one period bandwidth, b) magnified central third of (a).

For oblique incidence the transmission loses the symmetry and the transmission at a fixed wavenumber is a strong function of the incidence angle (s.fig.5) because the optical path of the two basic dielectric layers is no more the same.

Localization of modes is also present, which depends on frequency ⁸.

The difference in transmission between TE and TM modes can be used to built filters (see fig 6). The same treatment can be used also to describe a corrugated waveguide ^{10,11}.

Most interesting results are obtained in the case that one of the two materials with which the resonator is made is nonlinear. This case is somehow more difficult than the linear case but can still be treated by using a matrix method. In this case it is necessary to start with the description of the behaviour of each single layer, writing the electric and magnetic fields of the wave as a superposition of forward and backward waves which contain the changes produced by the nonlinearity. The link between the fields in the h -th and in the $(h+1)$ -th medium is given by applying the boundary conditions for the electric and magnetic fields and may be written by using a transfer matrix for the layer. The nonlinear response is then obtained by the use of a generalization of the dummy-variable method starting from the last layer for which there is no reflection.

The most interesting result is that if a third-order nonlinearity is used, the optical length of the nonlinear layers is a function of the input intensity. This means that if the wavelength is chosen so to be on one of the sharp peaks of the linear transmission spectrum, a small variation of the refractive index, produced by a change of the input intensity, may drive the system from a low to a high transmission state or, viceversa, in a way which obviously depends from the form of the spectrum, and on the sign of the nonlinearity, giving bistability or even multistability.

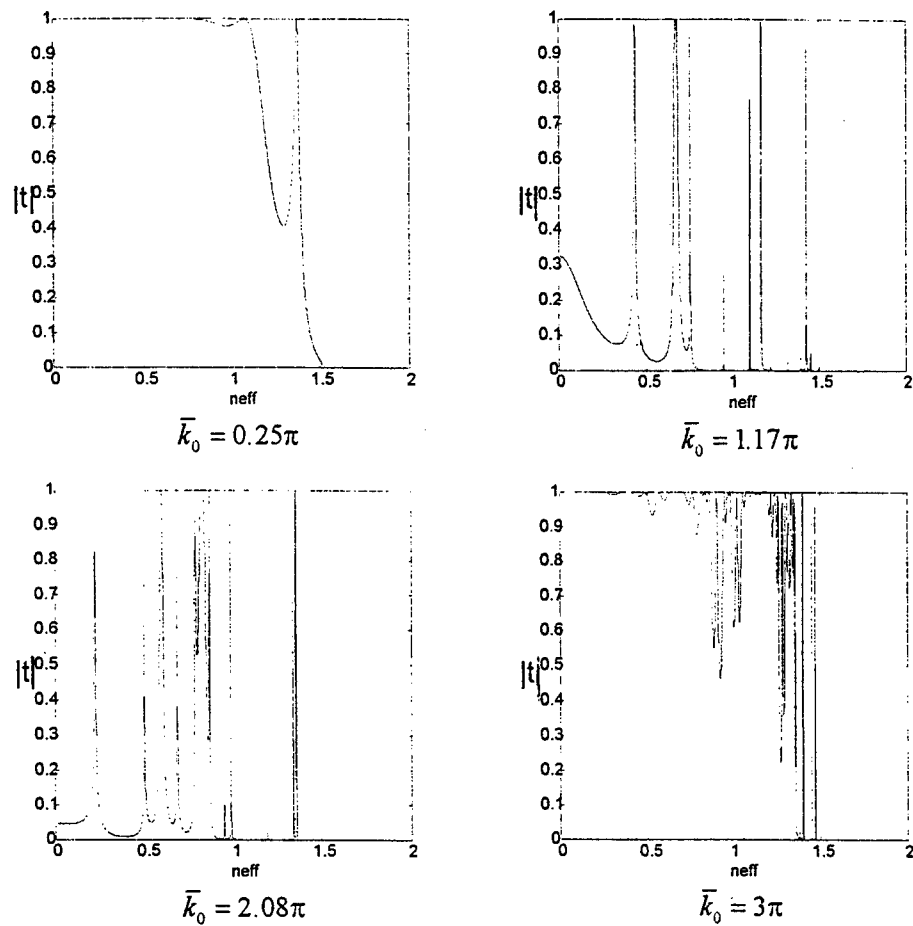
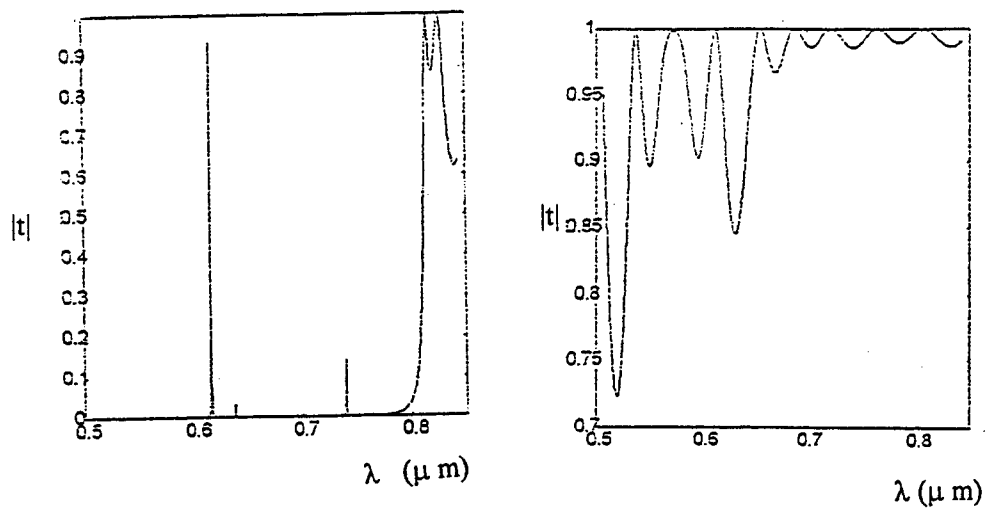


Fig.5 - Angular spectrum for different values of normalized wavevector , for $N = 4$



Fi.6 Transmission spectrum for TE (a), and TM(b) modes at a given angle of 62° .

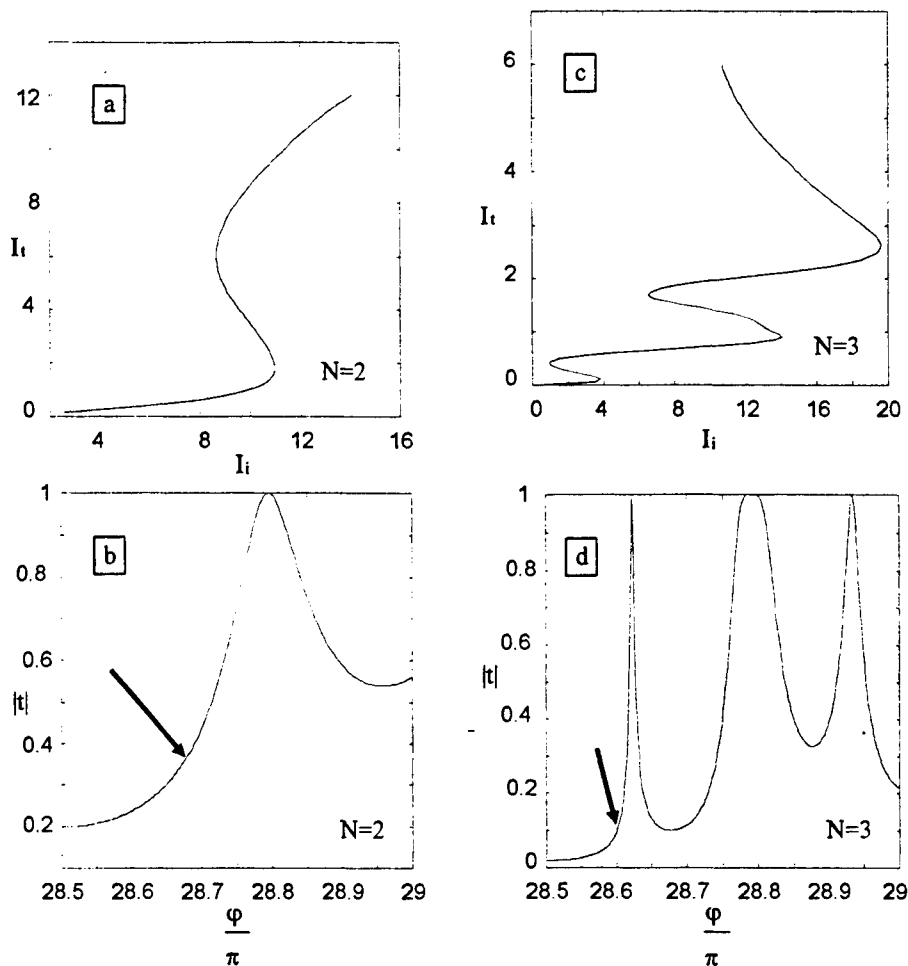


Fig. 7 Output Input Intensity for a Cantor multilayer for $N = 2$ e $N = 3$

This is very well illustrated in fig.7 where single and multiple bistability cases are shown. Hysteresis loops are best found in correspondence of the transmission shoulder as already said and depend on the initial "detuning" from a minimum. An increasing of the Cantor level produces a multistable behaviour. This behaviour can be associated to the number of the transmission oscillations in the linear spectrum. Spectra with many fast oscillations give lower thresholds of the hysteresis and may exhibit multistability. On the contrary, spectra with a few transmission oscillations have higher thresholds, give bistability, and have larger hysteresis loops.

Although a comparison with competing regular structures such as an interference filter or a periodic structure or other fractal sequences as for example a Fibonacci structure, is not easy because how the comparison should be made is questionable, one may say that the bistability exhibited by the Cantor sequence seems better, with lower thresholds and larger bistability loops (s.fig.8). The fractal case seems indeed to offer also more practical possibilities. Figs. 9 show, for ex., the behaviour of I_t vs I_i for a filter with $N=3$, that suggest to use it as a power limiter. A similar periodic structure as shown in the figure does not present that behaviour.

Third order nonlinearities are usually characterized by absorption and this limit the quantity of nonlinear material that can be contained in the structure and dissimmetrizes the two possible

configurations in which the central third part of the structure is made with the nonlinear (absorbing) or the linear material. In the first case increasing the level N increases the absorption so that devices with $N > 4$ are not feasible. In any case, because the smaller layer in the structure shall have a thickness equal or larger than a quarter of the operation wavelength, by increasing the level N , the total thickness of nonlinear material increases anyhow and therefore in any case Cantor levels greater than 4 are no more interesting.

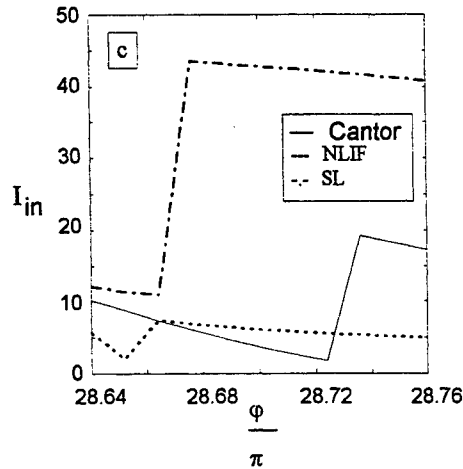


Fig. 8 Intensity threshold for bistability v.s ϕ/π : comparison between Cantor multilayer, periodical multilayer and inferential filter. NLIF is nonlinear interferential filter, SL is the periodic structure.

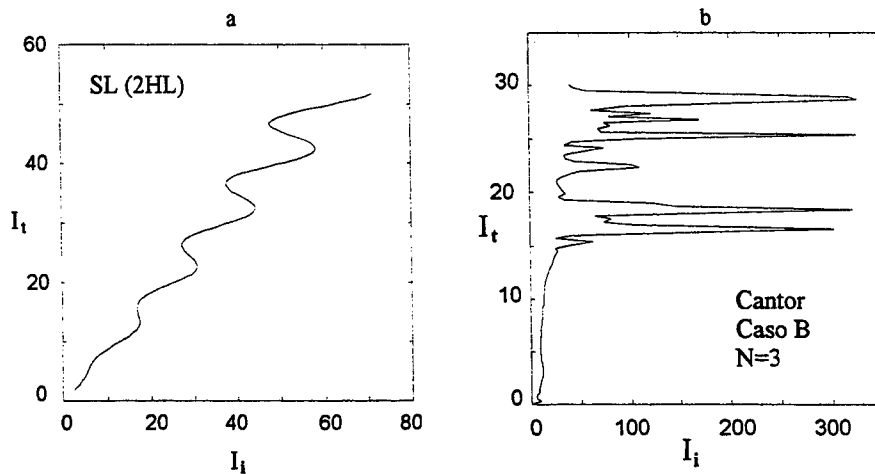


Fig.9 - Multistability of a periodical (a) and Cantor multilayer ($N=3$), (b) of equal optical path.

The presence of the sharp transmission peaks of the Cantor structure can also be used to time compress short pulses. When the pulse passes through a filter, its shape remains unchanged only if the filter has a bandwidth as large as the frequency spectrum of the pulse. The more the bandwidth is narrow with respect to the spectrum of the pulse, the more the pulse becomes

larger, because the higher spectral components are stopped by the filter. If the filter is characterized by a more complex transmission function, the shape of the pulse can deeply change because of the attenuation of some spectral components, that are not necessarily the higher ones.

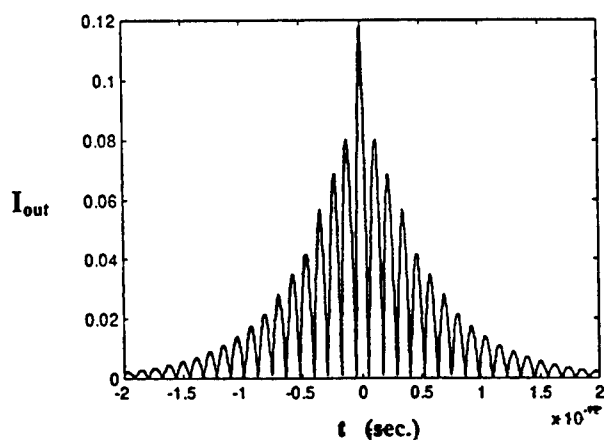
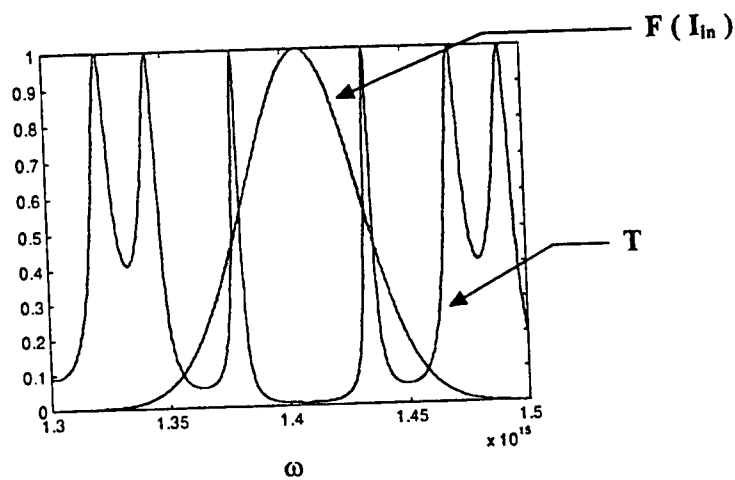


Fig.10 a) transmission spectrum of the Cantor filter $N=4$, b) output pulse

There can even result a modulation of the original pulse, if most frequencies are attenuated except a particular frequency or a group of frequencies centred around a narrow transmission peak. This is shown in fig. 10. In this case the output pulse is composed by a train of narrow pulses with a total temporal extension larger than the duration of the original pulse but the time extension of each single pulse is shorter than the length of the original pulse. The central pulse has an amplitude that is almost twice the amplitude of the first lateral pulse. After a proper filtering action to eliminate the undesired output components, a compression of the input pulse results, even if a sensible part of the energy has been reflected back to the input.

The presence of a nonlinearity changes the transmission spectrum in a very complex way as a function of input intensity and may result in a compression of the pulse for high enough peak power of the pulse. A shift of the carrier frequency of the pulse may also occur. Figs.11 show some examples in which one has assumed that the change in the spectrum of the filter is produced by a constant intensity. A periodic filter is not able to give any appreciable compression.

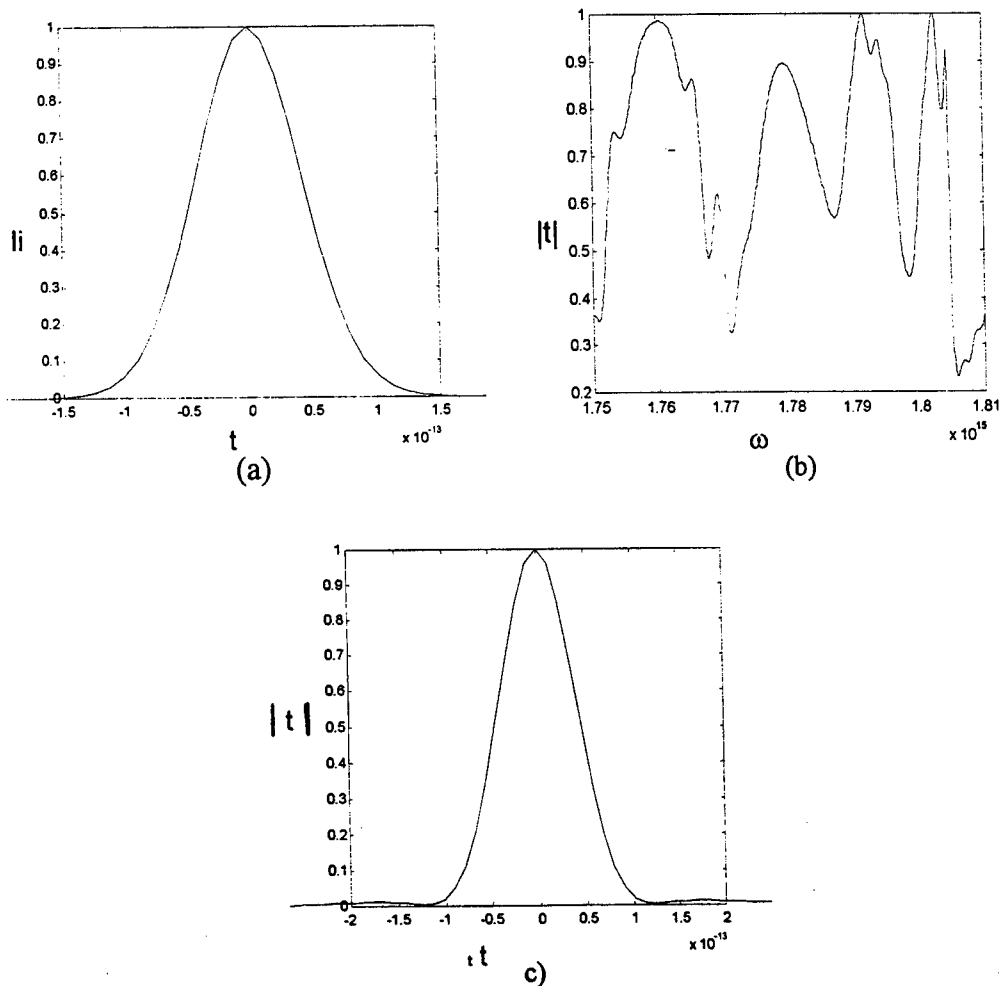
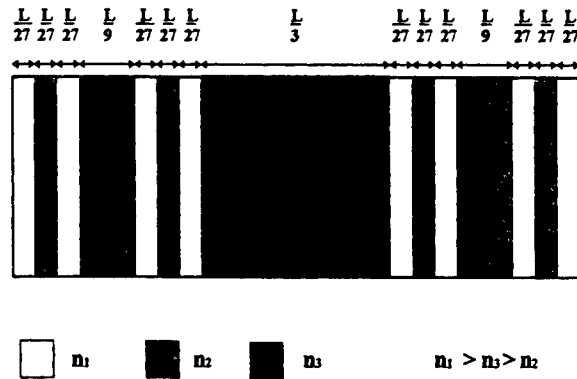


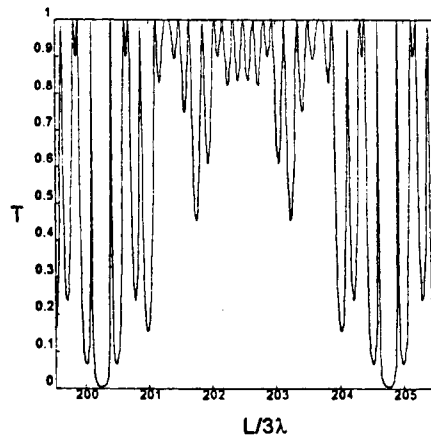
Fig.11 a- Input pulse (in time) centered at $\omega = 1.78 \times 10^{15} \text{ s}^{-1}$, b) Nonlinear transmission spectrum of a N=4 Cantor multilayer with GaAsAl / GaAl, c) Transmitted pulse in time domain.

4. SELF-SIMILAR RESONATOR WITH A SECOND-ORDER MATERIAL

A number of studies^{12,13} have discussed and demonstrated various methods of obtaining a large nonlinear phase shift in second-harmonic generation. Such a pulse shift is the outcome of alternate upconversion and downconversion (cascading effects) of energy between the fundamental frequency and the produced wave. The processes are coherent and in most cases nonresonant in nature so that are accompanied by a very low absorption. To be more specific the nonlinear effects that arise from the intensity-dependent phase distortion that affects the fundamental field in a second-harmonic generation process, are produced in the interaction between two propagating waves (at ω and at 2ω) in condition of phase mismatching. Under such conditions, in fact, a portion of the energy converted to second harmonic is down converted into the fundamental with a phase shift that depends on the two fields intensities and on mismatching. The response of layered structures in the presence of cascading can be studied using the formalism of transmission line already used for treating third-order nonlinearities suitably modified¹⁴. Here we consider a quasi-periodic structure bounded by two low order ($N=2$) Cantor sets, shown in fig. 12.



a)



b)

Fig.12 Geometric configuration and linear transmission spectrum for the Cantor multilayer ($N=2$)

It includes a nonlinear central layer between linear dielectric multilayer mirrors with fractal sequence. It is therefore a structure with three kinds of materials. The linear transmission spectrum (that is the spectrum at very low power) is shown in the figure. The nonlinear response depends in this case also from the new parameters that are the phase mismatch between the fundamental and the harmonic fields and their intensities. The transmission spectrum when the nonlinearity is working is somewhat distorted relative to the linear one; it loses part of its symmetry but maintains the same global shape. Bistability curves are shown in figs.13. The greater the detuning δ between the pump signal frequency and the resonance frequency of the filter, the more the bistability is emphasized. For detuning values below some critical detuning, bistability is absent. The phase mismatch $\Delta K l$ is the parameter that determines the position of the transmission peaks in the spectrum (s.fig.14). An increase in the number of layers reduces the input intensity threshold for bistability.

5. OPTICAL PROPERTIES OF LAYERED MESOSCOPIC FRACTAL STRUCTURES

Until now we have considered structures in which interference is predominant, that means layer thicknesses larger than a quarter of wavelength. We want now to discuss very briefly the case in which the thickness of the whole structure is less than a wavelength. In this case the multilayer structure can be considered as a uniform effective medium and the propagation of the light through the structure can be described in terms of effective linear and nonlinear susceptibilities¹⁵. The results depend critically on the direction of polarization of the incident beam. In particular, for TE polarization, the electric field is spatially uniform within the composite material and the optical constants of the composite become simple averages of those of the constituent materials weighted by their fractional content. So for a structure made with two materials a and b one has

$$\begin{aligned} n_{\text{eff}}^2 &= f_a n_a^2 + f_b n_b^2 \\ \chi_{\text{eff}}^{\text{NL}} &= f_a \chi_a^{\text{NL}} + f_b \chi_b^{\text{NL}} \end{aligned} \quad (8)$$

where

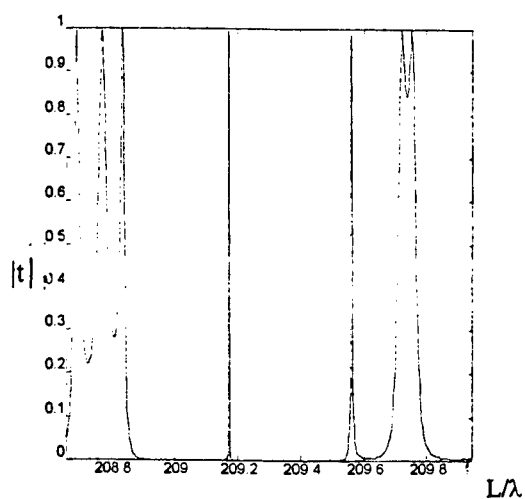
$$n_{\text{eff}}^2 = f_a n_a^2 + f_b n_b^2$$

is the effective refractive index, n_a and n_b are the refractive indices of materials a and b, respectively, and

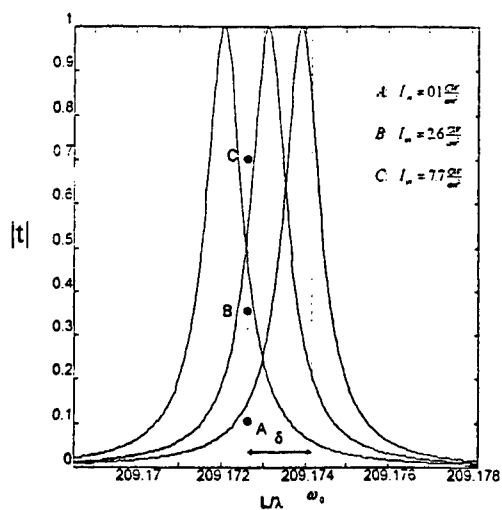
$$\begin{aligned} f_a &= \frac{d_{\text{tot}|a}}{d_{\text{tot}}} \\ f_b &= \frac{d_{\text{tot}|b}}{d_{\text{tot}}} \end{aligned} \quad (9)$$

being d_{tot} the total thickness and $d_{\text{tot}|a}$ and $d_{\text{tot}|b}$ the total thickness of material a and b, respectively.

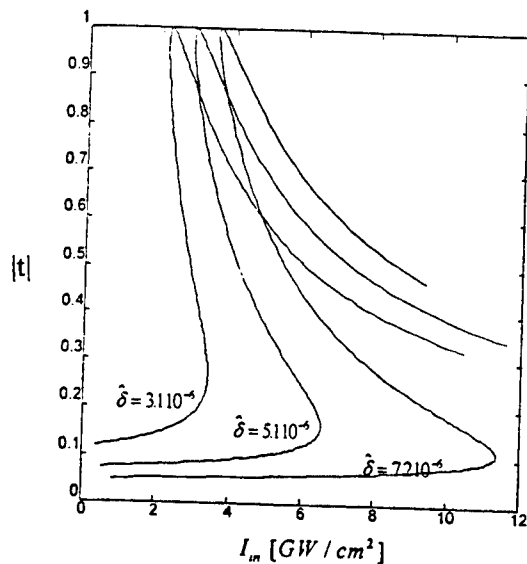
On the other hand, if the electric field is polarized TM, it becomes nonuniformly distributed inside the layers of the composite and taking advantage from the boundary conditions at each layer, the effective linear optical constants are given by



a)



b)



c)

Figs.13 - Cantor multilayer filter ($N=4$) a) transmission spectrum at low intensity, b) change of the transmission spectrum near 209 as a function of the input intensity ,the points A) $I=0.1 \text{ GW/cm}^2$ B) $I=2.6 \text{ GW/cm}^2$, C) $I=7.7 \text{ GW/cm}^2$,c) Change of the transmission spectrum v.s. input pump intensity for different cavity detuning

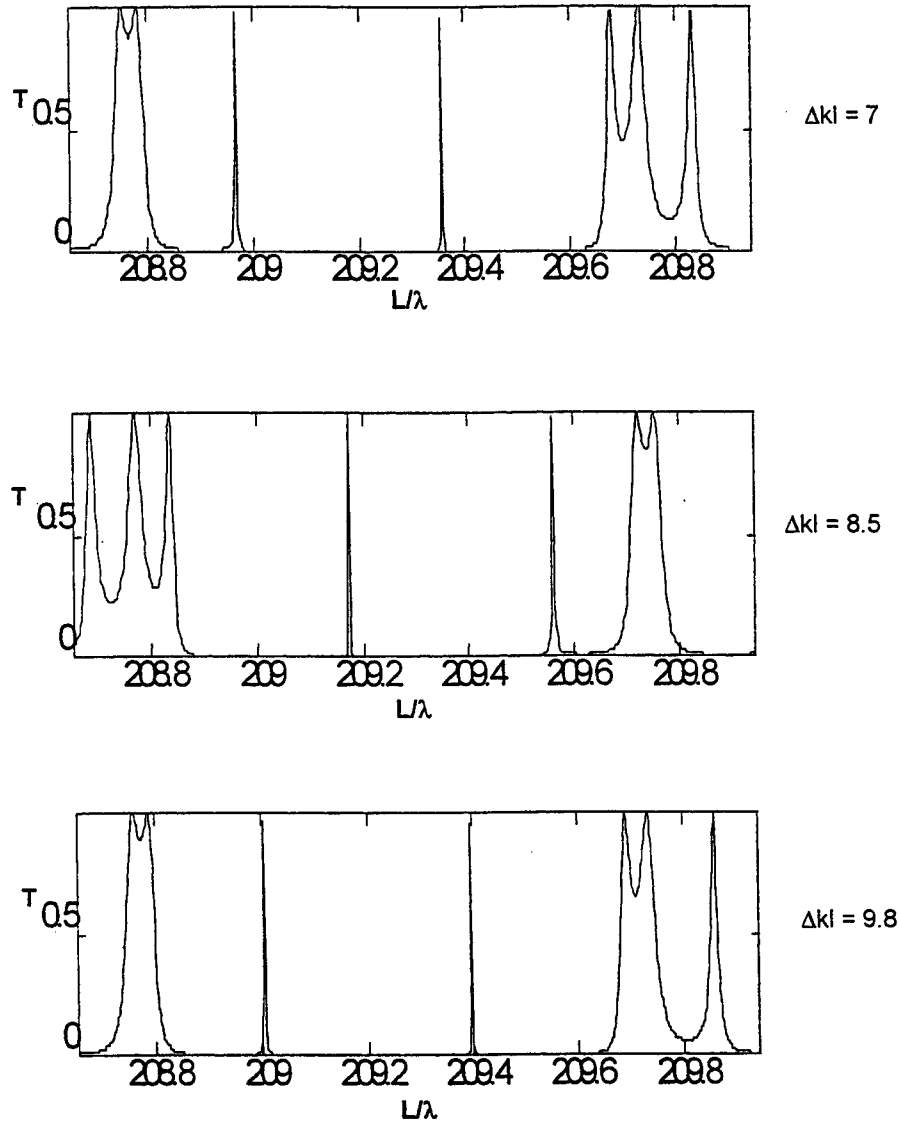


Fig 14 Cantor transmission spectrum: effect of the phase mismatch for the second harmonic generation process

$$\frac{1}{n_{\text{eff}}^2} = \frac{f_a}{n_a^2} + \frac{f_b}{n_b^2} \quad (10)$$

The effective nonlinear susceptibilities of second and third order are given by

$$\chi_{\text{eff}}^{(2)}(2\omega = \omega + \omega) = \frac{\frac{f_a \chi_a^{(2)}}{n_a^2(2\omega) n_a^4(\omega)} + \frac{f_b \chi_b^{(2)}}{n_b^2(2\omega) n_b^4(\omega)}}{\left[\frac{f_a}{n_a^2(\omega)} + \frac{f_b}{n_b^2(\omega)} \right]^2 \left[\frac{f_a}{n_a^2(2\omega)} + \frac{f_b}{n_b^2(2\omega)} \right]}$$

$$\chi_{\text{eff}}^{(3)}(\omega = \omega + \omega - \omega) = \frac{\frac{f_a \chi_a^{(3)}}{|n_a^2(\omega)|^2 n_a^4(\omega)} + \frac{f_b \chi_b^{(3)}}{|n_b^2(\omega)|^2 n_b^4(\omega)}}{\left| \frac{f_a}{n_a^2(\omega)} + \frac{f_b}{n_b^2(\omega)} \right|^2 \left[\frac{f_a}{n_a^2(\omega)} + \frac{f_b}{n_b^2(\omega)} \right]^2}$$
(10)

for the materials a and b, respectively.

If a triadic-Cantor structure is considered, the above formula remain valid but the fractional content changes as

$$f_a = \frac{d_{\text{tot}}|_a}{d_{\text{tot}}} = \frac{2^N d_a}{2^N d_a + (3^N - 2^N) d_b}$$

$$f_b = \frac{d_{\text{tot}}|_b}{d_{\text{tot}}} = \frac{(3^N - 2^N) d_b}{2^N d_a + (3^N - 2^N) d_b}$$
(11)

where d_a and d_b are the thickness of the smaller layers of the structure. Figs.15 and 16 show for example the increase of n_{eff} for two possible Cantor realizations .

6. CONCLUSIONS

A discussion about different kind of properties of quasiperiodic multilayer structures is presented. Different geometrical regimes have been studied , including also the nonlinear properties of each layer.

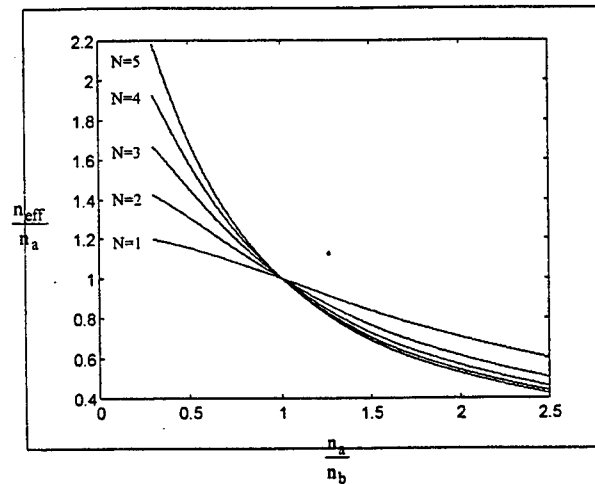


Fig.15 - Enhancement of the refractive index, for Cantor sets with layers of equal thickness

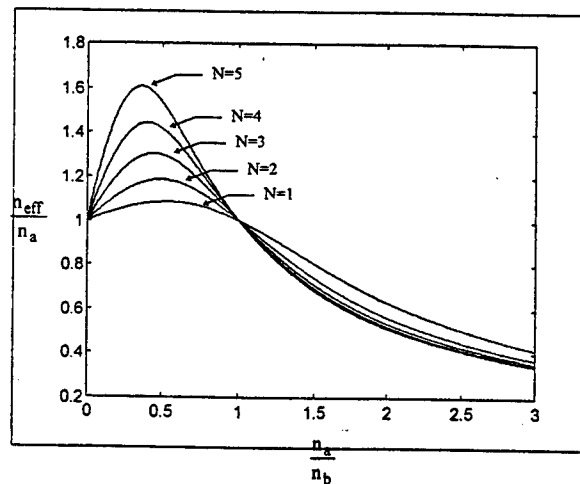


Fig.16 .The same as fig.15 but for layers of equal optical path.

7. REFERENCES

1. see, for ex., M. V. Berry, *Diffractals*, J. Phys. A12, pp. 781-797 (1979);
C.Allain and M. Cloitre, *Optical diffraction on fractals*, Phys. Rev. B33, pp. 3566-3569 (1986);
Y.Sakurada, J. Uozumi, T.Asakura, *Fresnel diffraction by one-dimensional regular fractals*, Pure Appl. Opt. 1, pp.29-40 (1992);
O.V.Angelsky, P.P.Maksimyak, and T.O.Perun, *Dimensionality in optical fields and signals*, Appl. Opt. 32, pp. 6066-6071 (1993);

- J.Uozumi, T.Asakura, in *Current Trends in Optics*, ed. by J.C.Dainty (Academic Press, San Diego, 1994) pp.54-58;
2. D.A.Zimnyakov and V.V.Tuchin, Scale properties of the diffraction fields induced by pre-fractal random screens, in *Fractal Frontiers*, M.M.Novak and T.G.Dewey eds. World Scientific, Singapore 1997, pp. 281-290;
- D.A.Zimnyakov and V.V.Tuchin, "Fractality of speckle intensity fluctuations *Appl. Opt.* 35, pp. 4325-4333 (1996);
- Y. Sakurada, J. Uozumi, T.Asakura, Scaling properties of Fresnel diffraction fields by regular fractals, *SPIE vol.1983*, pp.638- 642 (1993);
- P.W.Schmidt, X.Dacai, *Phys. Rev. A*33, pp.560-566 (1986);
- E.Jakeman, Fresnel scattering by a corrugated random surface with fractal slope, *J.Opt.Soc.Am.* pp.72, 1032-1041 (1982);
- J.M.Elson and J.M.Bennett, Relation between the angular dependence of scattering and the statistical properties of optical surfaces, *J.Opt. Soc.Am.* 69, pp.31-49 (1979);
4. J. Uozumi, T. Asakura, *Fractal Optics in Current Trends in Optics*, ed. J.C. Dainty, Academic Press, N.Y. 1994, pp. 83-93;
- Y.Kim, H.Gra bel, D. L.Jaggard, Diffraction by fractally scattered apertures, *J.Opt.Soc.Am.* A8,pp. 20-26 (1991);
- J.Uozumi, H.Kimura, T. Asakura,Fraunhofer diffraction by Koch fractals *J.Mod.Opt.* 37, pp.1011- 1020 (1990);
- D.L. Jaggard, Y.Kim, Diffraction by band limited fractal screens , *J.Opt.Soc.Am.* A4, pp.1055-1064 (1987);
- G.Chabassier, B. Angeli, F.Heliodore, A.Le Mehaute, Optical wave diffraction on fractal objects, *Pure Appl. Opt.* 1, pp.41-47 (1992);
5. B.B.Mandelbrot, *Science* 155, pp. 636- 700 (1967);
6. B.B.Mandelbrot, *The Fractal Geometry of Nature*, Freeman, San Francisco 1982;
7. M. Bertolotti, P.Masciulli, C.Sibilia, Spectral Transmission properties of a Self-Similar optical Fabry-Perot resonator, *Opt. Lett.* 19, pp.779 -781 (1994);
- 8.C. Sibilia, P. Masciulli and M. Bertolotti, Nonlinear optical properties of quasiperiodic (self-similar) structures, in *Notions and Perspectives of Nonlinear Optics*, O.Keller ed. (World Scientific, Singapore 1996) pp. 458-486;
9. M. Bertolotti, P. Masciulli, C. Sibilia, Transmission properties of a multilayer filter realized with Cantor-like code, *SPIE vol.2776*, pp.19- 26 (1996);
10. M.Bertolotti, P.Masciulli, C.Sibilia, F.Wijnands, H.Hoestra, Transmission properties of a Cantor corrugated waveguide, *J. Op. Soc. Am.* B13, pp.628-634 (1996);
11. M.Bertolotti, P.Masciulli, P.Ranieri, C.Sibilia, Optical bistability in a nonlinear Cantor corrugated waveguide, *J. Op. Soc. Am.* B13,pp. 1517-23 (1996);
12. L.Lefort and A. Barthelemy, Intensity dependent polarization rotation associated with type II phase matched second-harmonic generation: application to self-induced transparency, *Opt.Lett.* 20, pp.1749 -52 (1995);
13. A. Re, C. Sibilia, E. Fazio, M. Bertolotti, Field dependent effect in a quadratic nonlinear medium, *J.Mod. Opt.* 42, pp. 823-831 (1995);
14. L.Caleo, C.Sibilia, P.Masciulli, and M.Bertolotti, Nonlinear- optical filters based on the cascading second-order effect, *J. Opt. Soc. Am.* B14,pp. 2315-2324 (1997);
15. J.E.Sipe, R.W.Boyd, *Phys.Rev.* A46, Nonlinear susceptibility of composite optical materials in the Maxwell Garnett model ,pp.1614-1629(1992);
- R.W.Boyd and J.E.Sipe, *J.Opt.Soc.Am.* B11, Nonlinear optical susceptibilities of layered composite materials , pp. 297-303 (1994);
16. C.Sibilia, P.Masciulli, M.Bertolotti " Nonlinear Optical Properties of Quasiperiodic Self-Similar Structures ", In press on JEOS.

Novel femtosecond optical solitons in weakly excited semiconductors

D. Mihalache

Institute of Atomic Physics, Department of Theoretical Physics,
PO Box MG-6, Bucharest, Romania

I. V. Mel'nikov

General Physics Institute, Russian Academy of Sciences, 117942 Moscow, Russia

N. -C. Panoiu

Department of Physics, New York University, New York 10003, USA

ABSTRACT

We apply the quasiadiabatic approximation for the femtosecond pulse propagation in a collection of excitons in the case of weak interaction between the optical pulse and the semiconductor medium. Using the semiconductor Maxwell-Bloch equations beyond the slowly varying envelope approximation we show that the dynamics of femtosecond pulse propagation is described by the modified Korteweg-de Vries equation. Bright solitons superimposed on a continuous wave background are found and their stability against low amplitude perturbations is investigated. Possible experiments in semiconductor systems such as GaAs/AlGaAs are discussed.

Keywords: femtosecond optical solitons, weakly excited semiconductors, quasiadiabatic following

1. INTRODUCTION

Over the last decade, the fast development of colliding-pulse mode-locked lasers¹ and self-started solid-state lasers² has been crowned with the generation of 6 - 10 femtosecond (fs) pulses for wavelengths ranging from the blue-green to the near infrared. Subsequently, such short pulses have been widely exploited to generate a unipolar single-cycle electromagnetic pulse in a variety of nonlinear media³. The spectroscopic implementation of such pulses has been rather straightforward, but it has also resulted in theoretical studies in order to determine whether it is possible to describe correctly the dynamics of such pulses within the traditional framework of the slowly varying envelope approximation (SVEA) operating with a quasi-monochromatic field. From this point of view, the recent observation, pertaining to a Kerr self-focusing⁴, that SVEA loses its justification long before the pulse duration approaches an optical cycle is of great importance.

The physical reasons underlying potential difficulties in applying the SVEA to fs pulse dynamics can be easily seen. Both the wide spectrum of the pulse and its intense field increase the number of harmonics that have to be included into the expansion of the polarization in powers of the field and phase-matching conditions must be adjusted for all harmonics simultaneously. This violates the SVEA basic assumptions of a weakly nonlinear and strongly dispersive medium. The superposition principle does not apply, preventing one from reducing the problem to a finite number of interacting

waves. And what is more, quantum-mechanical effects come into action at the subwavelength scale. These factors imply that adequate insight into the nonlinear evolution of optical pulses of a few cycles should be obtained in terms of a real field and polarization governed by a self-consistent set of equations⁵.

A number of different approaches have been proposed to account for fs-pulse dynamics in nonlinear media. In the first approach, one replaces a quantum-mechanical description of the medium by a nonlinear permittivity or fit-based response function that is then used in extensive simulations by the finite-difference time domain method^{6,7}. This rather practical model has the advantage that the fs induced polarization is described by a single-valued function rather than a set of differential equations and thus the computational requirements are considerably reduced. It demonstrates numerically the possibility of propagation and interaction of soliton-like objects. The problem with this approach is that it is not *a priori* clear which features are genuine and which are merely artifacts of the model. For example, this model has the property that the Kerr-soliton collision is of qualitatively different behavior⁶ than that found both analytically and numerically within the framework of the SVEA based integrable partial differential equation (PDE)⁸. The second class contains methods based on an analytical treatment of a Boussinesq equation rather than of Maxwell-Bloch equations (MBEs)⁹. Although it incorporates propagation effects such as dispersion, second- and third-order nonlinearities, this approach, however, does not identify a proper physical link among them. The method in the third class makes use of a complete set of semiclassical MBEs for a two-level medium model, trying to extend the soliton phenomenology to the fs domain. The existence of exact soliton-like solutions to the MBEs for a unipolar pulse has been shown analytically¹⁰ and numerically¹¹. A comprehensive mathematical treatment of the exact steady-state solution to the MBEs for a carrier wave of given frequency is given in the recent works by Branis *et al*¹² and more recently by Andreev¹³. The general approach, used in Refs. 12-13, is the reduction of the hyperbolic wave equation to an elliptic problem. The use of sophisticated techniques and the aspiration to give an extensive review of all previous methods of approximating the soliton-like solutions did not allow the authors of Refs. 12-13 to classify the range of existence and stability of the solutions they found, even briefly. In particular, the relationship with the exact solution¹⁰ was missing in their analysis. More importantly, these solutions imply an effective energy exchange between the pulse and the medium. This raises the problem that it is not clear how to interpret, say, the behavior of a semiconductor laser/amplifier for which a gap renormalization, band filling, etc., have been shown to play an important role in such a parameter regime¹⁴. Furthermore, it has been found that those solutions are not exact solitons because they do not possess the common feature of an elastic collision¹⁵. This is the reason we have concentrated in this work only on the opposite case of the weak excitation of the medium. By means of formal use of quasiadiabatic following method¹⁶, we are able to find in explicit form and to classify all the solutions in this restricted class. Notice that preliminary studies have been reported recently^{5,17}.

In this work, we apply a quasiadiabatic approximation for the fs pulse propagation in a collection of excitons. This means we restrict our analysis to the case of weak interaction between the pulse and semiconductor that, in turn, dictates the pulse width $\tau_p \gg \hbar/\epsilon_g^0$, where ϵ_g^0 is the forbidden bandgap. The purpose of this paper is to go beyond the SVEA to show the advantages of the self-consistent description based on the coupled semiconductor Maxwell-Bloch system and to impose proper relationships among nonlinearity, dispersion, dissipation (or amplification), and backward-scattering effects. We derive an asymptotic analytic solution for the induced polarization of an ensemble of excitons at low density. It will be shown that the low density limit is connected

to the situation in which one can apply the quasiadiabatic following without the use of the SVEA and the rotating-wave approximation (RWA). The predicted quasiadiabatic propagation is a principally new type of soliton, which does not obey such off-resonance soliton equations as the nonlinear Schrödinger equation or its modifications. Its temporal form is shown here to be quite unique. Nevertheless, it shares several common features with the previous extensively studied solitons or with ultrashort electromagnetic pulses in electrooptic crystals.

2. BASIC EQUATIONS

In this section we present the basic equations that govern the interaction between a propagating fs pulse and a semiconductor medium. The light-matter interaction is treated semiclassically by solving the coupled set of semiconductor MBEs. No impurities, finite temperature effects, or sample boundary effects are included. If one takes fields which are x and y independent then the classical wave equation becomes

$$\frac{\partial^2 E}{\partial z^2} - \frac{1}{c^2} \frac{\partial^2 E}{\partial t^2} = \frac{4\pi}{c^2} \frac{\partial^2 \mathcal{P}}{\partial t^2}, \quad (1)$$

where E is the electric field, \mathcal{P} is the total macroscopic polarization obtained by summing over all wavevectors \mathbf{k} , $\mathcal{P} = 2 \sum_{\mathbf{k}} d_{vc} P_{\mathbf{k}}$, and d_{vc} is the interband dipole matrix element. In the summation, the factor 2 counts for the spin degeneracy. The time dependence of $P_{\mathbf{k}}$ is given in a two-band semiconductor limit by the semiconductor Bloch equations¹⁴:

$$\begin{aligned} i\hbar \frac{\partial}{\partial t} P_{\mathbf{k}} = & (\epsilon_{c,\mathbf{k}} - \epsilon_{v,\mathbf{k}} + \epsilon_g^0) P_{\mathbf{k}} \\ & + (n_{e,\mathbf{k}} + n_{h,\mathbf{k}} - 1) d_{cv} E - \sum_{\mathbf{q}} V_{|\mathbf{k}-\mathbf{q}|} P_{\mathbf{q}}, \end{aligned} \quad (2)$$

$$\begin{aligned} i\hbar \frac{\partial}{\partial t} n_{e,\mathbf{k}} = & d_{vc} E P_{\mathbf{k}} - d_{cv} E P_{\mathbf{k}}^*, \\ n_{e,\mathbf{k}} = & n_{h,\mathbf{k}}, \text{ with } \epsilon_{c,\mathbf{k}} = \frac{\hbar^2 k^2}{2m_e}, \epsilon_{v,\mathbf{k}} = \frac{\hbar^2 k^2}{2m_v}. \end{aligned} \quad (3)$$

Here, c labels conduction band states and v denotes valence band states, m_{α} is the effective carrier (electron or hole) mass in the crystal, $n_{\alpha,\mathbf{k}}$ is the carrier density in the \mathbf{k} -space. The summation in the right-hand side of Eq. (2) is conventionally termed a Coulomb hole and is given by the departure of the screened Coulomb potential from its unscreened value. $V(\mathbf{k})$ is given by

$$V_{\mathbf{k}} = \frac{e^2}{\epsilon_0 \hbar^2 \pi^2} \left[1 + \frac{\kappa^2}{k^2 + \kappa^2 (\hbar^2 k^2 / 2m_r \omega_{pl})^2} \right]^{-1}, \quad (4)$$

with the inverse screening length κ , the plasma frequency ω_{pl} , the reduced mass of an electron-hole pair m_r , and the dielectric constant of the crystal ϵ_0 . For simplicity the collision terms in Eqs. (2) and (3) are neglected; this places an upper limit of 60 fs on the pulsewidth τ_p which can give rise to the quasiadiabatic following¹⁸. Since we are interested in low carrier densities, the contribution dominated by changes in the chemical potential (i.e., phase-space filling), conventionally called screened exchange, can be neglected¹⁹, and the summations $\sum_{\mathbf{q}} V_{\mathbf{k}-\mathbf{q}} P_{\mathbf{q}} n_{\mathbf{q}}$, $\sum_{\mathbf{q}} V_{\mathbf{k}-\mathbf{q}} n_{\mathbf{q}} P_{\mathbf{q}}$, and $\sum_{\mathbf{q}} V_{\mathbf{k}-\mathbf{q}} P_{\mathbf{q}} P_{\mathbf{k}}^*$, can be also omitted in Eqs. (2) and (3).

Following the steps used to calculate the macroscopic polarization \mathcal{P} we apply the Fourier transformation to Eqs. (2) and (3),

$$i\hbar \frac{\partial}{\partial t} P(\mathbf{R}, t) = \hat{H}_{ee} P(\mathbf{R}, t) + d_{cv} E(t) [2n(\mathbf{R}, t) - \delta(\mathbf{R})], \quad (5)$$

$$i\hbar \frac{\partial}{\partial t} n(\mathbf{R}, t) = -d_{cv} E(t) P^*(-\mathbf{R}, t) + \text{c.c.}, \quad (6)$$

where c.c. means complex conjugate and the screened Hamiltonian is given by:

$$\hat{H}_{ee} = \epsilon_g^0 - \frac{\hbar^2}{2m_r} \Delta_{\mathbf{R}} - V(\mathbf{R}), \quad (7)$$

where \mathbf{R} is the coordinate of the electron-hole pair to a lattice site.

Let us now make use of the fact that the solution ψ_λ of the Wannier equation for a hydrogen-like atom

$$\left[-\frac{\hbar^2}{2m_r} \Delta_{\mathbf{R}} - V(\mathbf{R}) \right] \psi_\lambda(\mathbf{R}) = \epsilon_\lambda \psi_\lambda(\mathbf{R}) \quad (8)$$

is known¹⁴, $\psi_\lambda \sim \exp(-R/a_B)$, where a_B is the excitonic Bohr radius and λ labels the discrete exciton energy states. The solutions of this equation form a complete orthonormal set of functions. We can use them to find the polarization

$$\int d\mathbf{R} \psi_\lambda(\mathbf{R}) P(\mathbf{R}, z, t) = P_\lambda(z, t), \quad (9)$$

and the carrier density

$$\int d\mathbf{R} \psi_\lambda(\mathbf{R}) n(\mathbf{R}, z, t) = n_\lambda(z, t). \quad (10)$$

Also, we can represent the Bloch equations as follows,

$$i\hbar \frac{\partial}{\partial t} P_\lambda(z, t) = \epsilon_\lambda P_\lambda + d_{cv} E [2n_\lambda - \psi_\lambda(R=0)], \quad (11)$$

$$i\hbar \frac{\partial}{\partial t} n_\lambda(z, t) = -d_{cv} E P_\lambda^* + d_{cv}^* E P_\lambda. \quad (12)$$

In its most logical definition, the polarization P_λ and the excitation density n_λ scales with the wave function defined in the lattice site, i.e.,

$$P_\lambda = \psi_\lambda(R=0) \tilde{P}_\lambda, \quad (13)$$

$$n_\lambda = \psi_\lambda(R=0) \tilde{n}_\lambda. \quad (14)$$

With the aid of these relationships, the following equivalent pair of semiconductor Bloch equations may be derived,

$$i\hbar \frac{\partial}{\partial t} \tilde{P}_\lambda = \epsilon_\lambda \tilde{P}_\lambda + d_{cv} E (2\tilde{n}_\lambda - 1), \quad (15)$$

$$i\hbar \frac{\partial}{\partial t} \tilde{n}_\lambda = -d_{cv} E \tilde{P}_\lambda^* + d_{cv}^* E \tilde{P}_\lambda. \quad (16)$$

Correspondingly, the macroscopic polarization \mathcal{P} may be written as follows:

$$\mathcal{P}(t) = 2d_{cv} \sum_{\lambda} |\psi_{\lambda}(R=0)|^2 \tilde{P}_{\lambda} + \text{c.c.} \quad (17)$$

For weak electric fields, the electrons are predominantly in the valence band and the classical Lorentz limit of harmonically oscillating charges is accessible via linearization of Eqs. (1), (15) and (16). Correspondingly, the solution is a mixture of the photon and the exciton, called a *polariton*^{12,14}. Its dispersion relation is given by

$$\left(\frac{cK}{\omega}\right)^2 = 1 + \frac{8\pi\mathcal{N}d_{cv}^2}{\hbar(\omega_g - \omega)}, \quad (18)$$

where $\mathcal{N} = 2/\pi a_B^3$ is the Sommerfeld factor. The dispersion varies steeply near ω_g and shows a polariton gap for semiconductors of width $\omega_{LT} = 8\pi\mathcal{N}d_{cv}^2\hbar^{-1}$ in which propagation is forbidden, and where the field is strongly absorbed. At stronger fields, the nonlinearity described by Eqs. (15) and (16) comes into action, and a pulse propagation might occur in the gap. It is notable that the strength of the interaction between the optical field and the nonlinear medium is characterized by the dimensionless parameter $\alpha = \omega_{LT}/(\omega_{\lambda} - \omega_p)$, where ω_p is the carrier frequency of the pulse¹². At low densities $\alpha \ll 1$, the backward-scattering can be neglected, and the wave equation can, in turn, be decomposed into a set of two PDEs of the first order describing the propagation of a forward- and backward-running waves. In the case of $\alpha \simeq 1$, the backward-scattering can not be neglected and might affect essentially the dynamics of the pulse even though it propagates outside the gap.

3. QUASI-TRANSPARENT REGIME OF SOLITON PROPAGATION

In this section, we show how to extend the framework of the adiabatic following¹⁶ beyond the SVEA by using a method which generalizes the recursive approach developed by Crisp. Eq. (15) is a first-order differential equation for \tilde{P}_{λ} , and one can formally integrate it to obtain

$$\begin{aligned} \tilde{P}_{\lambda}(z, t) = & \frac{id_{cv}}{\hbar} \int_{-\infty}^t [1 - 2\tilde{n}_{\lambda}(z, \tau)] \\ & \times E(z, \tau) \exp[-i\omega_{\lambda}(t - \tau)] d\tau \end{aligned} \quad (19)$$

where $\epsilon_{\lambda} = \hbar\omega_{\lambda}$. This equation shows that if one knows a functional relation $\tilde{P}_{\lambda} = \tilde{P}_{\lambda}(\tilde{n}_{\lambda}, E)$ among the induced polarization, excitation density, and the pulse field, then $\tilde{n}_{\lambda}(E)$ may be determined. Furthermore, if both $\tilde{n}_{\lambda}(E)$ and $\tilde{P}_{\lambda}(\tilde{n}_{\lambda}, E)$ are known, then one can derive, at least formally by resolving the semiconductor Bloch equations (16) and (19), the functional relation $\mathcal{P} = \mathcal{P}(E)$. This turns the wave equation into a nonlinear PDE for $E(z, t)$ alone. On pursuing such an algorithm, one can start with the following ansatz used for the integral (19):

$$\begin{aligned} \int_{-\infty}^t [1 - 2\tilde{n}_{\lambda}(z, \tau)] E(z, \tau) \exp[-i\omega_{\lambda}(t - \tau)] d\tau \\ = \frac{1}{i\omega_{\lambda}} \sum_0^m \frac{(-1)^k}{(i\omega_{\lambda})^k} \frac{\partial^k}{\partial t^k} [(1 - 2\tilde{n}_{\lambda})E], \end{aligned} \quad (20)$$

which presumes that the dependence $n(E)$ is a power series in E and $\partial E/\partial t$. The convergence of the series (20) is a rather difficult problem to solve and, in principle, an infinite hierarchy of coupled equations is generated. Thus the best one can hope to do is to truncate this expansion, i.e. to find an expansion parameter which makes such a truncation meaningful. In general, this means long pulses, i.e. $\omega_\lambda \tau_p \gg 1$, which is essentially the approach first introduced by Crisp whose expansion parameter was $s = 1/(\omega_g - \omega_p)\tau_p \ll 1$. This condition is, obviously, a restriction imposed on τ_p because the pulsewidth could have any ratio to ω_λ . However, this restriction allows us to find a novel solution in an analytical form.

In the linear approximation, when the excitation density remains constant $\tilde{n}_\lambda \simeq \tilde{n}_\lambda(t = -\infty)$, Eq. (20) gives the macroscopic polarization

$$\mathcal{P}(E) \simeq \frac{4d_{cv}r_0}{\pi\epsilon_\lambda a_B^3} \left(1 - \frac{\hbar^2}{\epsilon_\lambda^2} \frac{\partial^2}{\partial t^2} + \dots \right) E(z, t). \quad (21)$$

where $r_0 = [1 - 2\tilde{n}_\lambda(t = -\infty)]$. It is readily seen that the differential operator in the right-hand side of Eq. (21) describes the linear dispersion of the ensemble of excitons. It should be noted that such a linear response can be also obtained by means of expansion of the SVEA linear susceptibility of excitons, defined as

$$\chi_l(\omega) = \frac{4\epsilon_{exc}}{\pi\epsilon_\lambda} \frac{\omega_\lambda^2}{\omega_\lambda^2 - \omega^2}, \quad (22)$$

in the low frequency limit $\omega_\lambda \gg \omega_p$, where $\epsilon_{exc} = e^2/\epsilon_0 a_B$ is the exciton binding energy.

So far, we were interested in linear properties of the medium. We now allow nonlinear effects to occur by solving Eq. (16) which has the driving term in the form of the expansion (20). As in the traditional approach of Crisp, who used both SVEA and RWA, the excitation density evolution may be classified as a transition saturation. To simplify the derivation, we assume that the pulse field is smaller than the saturation strength $\sim \epsilon_\lambda/2d_{cv}$, which can be estimated as having a value around 10^9 V/cm for wavelengths from the visible up to the infrared. Then the excitation density takes the form:

$$\tilde{n}_\lambda(t) = \frac{1}{2} + \frac{r_0}{2} \left(1 + \frac{1}{2} \frac{E^2}{E_\lambda^2} \right), \quad (23)$$

where $E_\lambda = \epsilon_\lambda/2d_{cv}$.

In deriving this equation we used the first-order term of the $(1/\epsilon_\lambda \tau_p)$ -expansion for \tilde{P}_λ . Thus the first nonlinear term contributing at the polarization is proportional to E^3 as should be expected in a non-centrosymmetric medium.

From Eqs. (21) and (23), one can derive the relation

$$\mathcal{P}(z, t) = \frac{4\epsilon_{exc}r_0}{\pi\epsilon_\lambda} \left(E - \frac{\hbar^2}{\epsilon_\lambda^2} \frac{\partial^2 E}{\partial t^2} - \frac{1}{2} E \frac{E^2}{E_\lambda^2} \right). \quad (24)$$

Note that we dropped all terms of order higher than two in the expansion (20), and that both amplifying and absorbing semiconductors are described by Eq. (24). It is also of particular importance for the analysis below that the nonlinearity and dispersion contribute to the polarization (24) with the same sign. Its substitution into the wave equation (1) leads to

$$\frac{\partial^2 E}{\partial z^2} = \frac{1}{c^2} \frac{\partial^2}{\partial t^2} \left[1 + 16r_0 \frac{\epsilon_{exc}}{\epsilon_\lambda} \left(1 - \frac{\hbar^2}{\epsilon_\lambda^2} \frac{\partial^2}{\partial t^2} \right) - 8r_0 \frac{\epsilon_{exc}}{\epsilon_\lambda} \frac{E^2}{E_\lambda^2} \right] E. \quad (25)$$

This can be further simplified by means of the following argument. Assume that spatio-temporal change of the field $E(z, t)$ is caused by fast transfer of the pulse along the characteristic $(t - z/c)$ assisted by slow change along the longitudinal coordinate²⁰. That is,

$$\frac{\partial E}{\partial t} + c \frac{\partial E}{\partial z} \approx \frac{\partial E}{\partial t}, \quad (26)$$

thus the backward-scattered wave is accounted on the spatial scale longer than the pulse length. But more remarkable consequence of this assumption is that it eliminates secularly growing forced terms that come in at higher order perturbation theory, where $(\epsilon_\lambda \tau_p)^{-1}$ is the perturbation parameter. Under these circumstances, Eq. (25) becomes

$$\frac{\partial E}{\partial z} + \frac{1}{v_g} \frac{\partial E}{\partial t} + c_1 E^2 \frac{\partial E}{\partial t} + c_2 \frac{\partial^3 E}{\partial t^3} = 0, \quad (27)$$

where the following set of parameters is used

$$v_g = c[1 + 4\pi r_0 \chi_l(0)]^{-1/2}, \quad c_1 = \frac{6\pi v_g}{c^2} r_0 \chi_{nl}(0),$$

$$c_2 = r_0 \frac{\pi v_g}{c^2} \left[\frac{\partial^2 \chi_l}{\partial \omega^2} \right]_{\omega=0}, \quad \text{and} \quad \chi_{nl}(0) = \frac{1}{4\pi} \frac{\hbar \omega_{LT}}{\epsilon_\lambda} \frac{1}{E_\lambda^2}.$$

The latter parameter relates to the traditional cubic susceptibility of the semiconductor as follows,

$$\chi_{nl}(0) = \frac{4}{3} \chi^{(3)}(3\omega, \omega, \omega, \omega) |_{\omega=0} = 4\chi^{(3)}(\omega, \omega, \omega, -\omega) |_{\omega=0}.$$

Equation (27) is the modified Korteweg - de Vries equation (mKdV) which belongs to the class of PDEs integrable by the inverse scattering transform²¹⁻²³. It has appeared in various branches of physics as anharmonic lattices and as Van Alfvén waves in a collisionless plasma. Moreover, it is needed to eliminate secularly growing terms in a formal asymptotical expansion over a small parameter²⁴. Recently, the detection of mKdV solitons in a paraelectric, along with the relevant analysis have been reported by Ikezi *et al*²⁵.

The general solutions of Eq. (27) are governed by the relative sign between the nonlinear and dispersion terms, the asymptotic values of the field (the boundary condition) and by the pulsewidth. Calling $E(z = \pm\infty) = E_\infty$, the general single soliton solution takes the form

$$E(z, t) = E_\infty \left[1 - \frac{4e^{-\beta}(1 - E_d/E_0)}{(1 - E_d/E_0 - 2\delta^2 e^{-\beta})^2 + 2\delta^2 e^{-2\beta}} \right]. \quad (28)$$

Here

$$\beta = (t - z/v)/\tau_p + \beta_0, \quad E_d^2 = 2E_\infty^2 + E_0^2, \quad \delta = E_\infty/E_0,$$

$$\frac{1}{v} = \frac{1}{v_g} \left[1 + \frac{2\pi v_g^2}{c^2} r_0 \chi_{nl}(0) (3E_\infty^2 + E_0^2) \right], \quad \text{and} \quad \tau_p = \sqrt{\frac{[\partial^2 \chi_l / \partial \omega^2]_{\omega=0}}{2E_0^2 \chi_{nl}(0)}},$$

where E_0 labels the maximum amplitude of the bright soliton whose displacement from E_∞ is given by E_d that, in turn, is to be found for a given set of boundary conditions. It turns out that

the solutions $E(z, t)$ lie in the range $E_\infty \leq E \leq \sqrt{2}E_d - E_\infty$. They describe either a hump-like pulse superimposed on a continuous wave background, i.e. a unbound soliton, or a hyperbolic-secant solitary pulse; the behavior depends on the value of E_∞ . The transition between bound and unbound solitons is at $E_\infty > 0$, which may occur when the semiconductor is biased by a dc electric field. Exactly at this condition, the unbound soliton (28) is excited and will propagate through the medium of excitons.

A number of interesting special cases can be identified. In the limiting case $E_\infty = 0$, one can expect that the general solution (28) converges into the hyperbolic-secant form

$$E(z, t) = \frac{1}{\tau_p} \sqrt{\frac{[\partial^2 \chi_l / \partial \omega^2]_{\omega=0}}{\chi_{nl}(0)}} \operatorname{sech} \left(\frac{t - z/v}{\tau_p} \right), \quad (29)$$

which is determined exclusively by the given pulsewidth τ_p ; its velocity is

$$\frac{1}{v} = \frac{1}{v_g} \left(1 + \frac{\pi r_0}{\tau_p^2} \frac{v_g^2}{c^2} \left[\frac{\partial^2 \chi_l}{\partial \omega^2} \right]_{\omega=0} \right). \quad (30)$$

This leads to the expected result that the soliton (29) has a lower velocity than that of a low-frequency electromagnetic wave in the inverted medium ($r_0 = 1$) and a greater velocity than that of a low-frequency electromagnetic wave in the absorbing one ($r_0 = -1$).

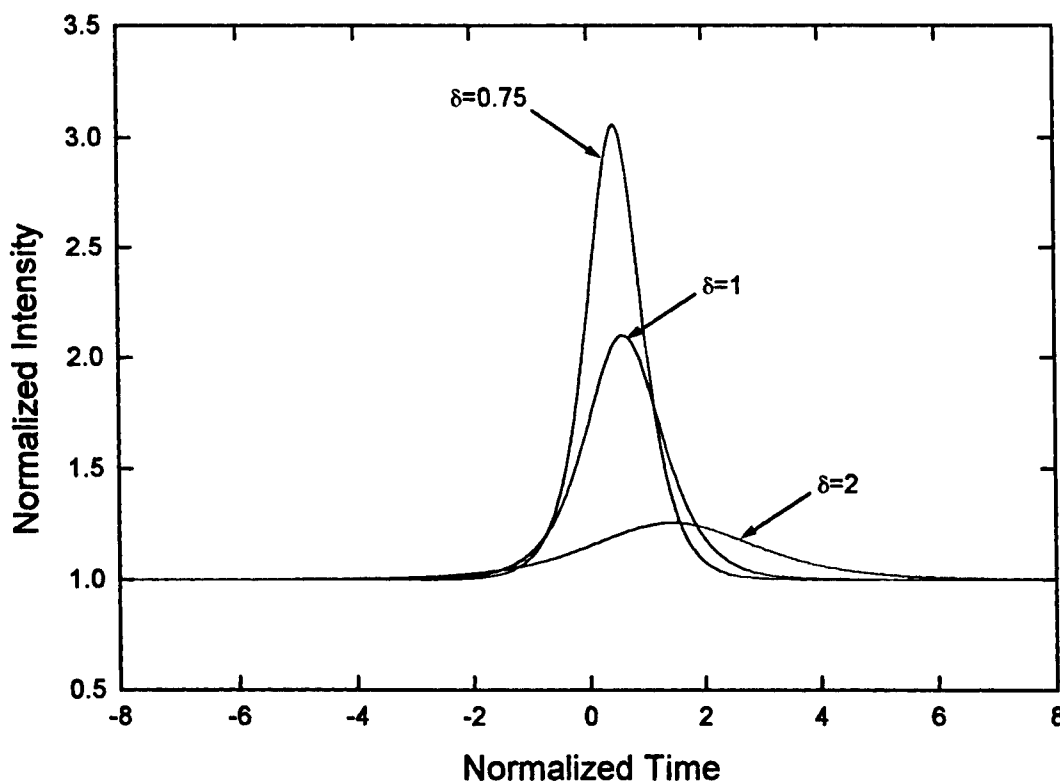


Fig. 1. Normalized intensity versus normalized time for single bright solitons on a continuous wave background.

In Fig. 1, we plot the intensity of the unbound soliton (28) for different ratios δ . There is a typical spreading out of hump amplitudes for values of $\delta \geq 1$. Consider now the interaction of two single solitons (28). Although both of them are true solitons, and the collision is not expected to change their shapes, the presence of a dispersive wave may change soliton parameters, such as velocity, position within a sequence, etc. In terms of underlying physics, this may arise from spontaneous emission noise in an illuminated semiconductor structure or from residual cw radiation in a biased semiconductor. Since the excitation of the medium by a long pulse is relatively weak, the cumulative effect of the nonsoliton component can be observed in the collision of co-propagating solitons rather than in the case of counter-propagating ones. The results of our numerical simulation of the collision of two solitons having different amplitudes in the presence of the non-soliton component, taken in the form of stochastic function, show that the non-soliton component causes negligible small perturbations to the soliton amplitudes, but has a significant effect on the rate of the decay of coupled solitons and results in considerable temporal shift of the solitons. Note that the interaction length reveals a well-defined stochastic oscillatory behavior and that the amplitude of these oscillations depends on the amplitude of the non-soliton component.

4. CONCLUSIONS

The experimental observation of quasiadiabatic following of fs optical pulses in semiconductors was reported by Harten *et al*²⁶ using a 0.37 mm-long GaAs/AlGaAs guiding structure at room temperature. The experiment showed that powerful below-resonance pulses ($\sim 1 - 10 \text{ GW/cm}^2$) of a 100-fs pulsewidth can be driven out of adiabatic following prescribed for two-level atoms¹⁶; the pulse breakup and significant delay, exceeding the pulsewidth, were observed. These features of the propagation-induced escape were identified with carrier density oscillations in the semiconductor.

It would be of interest to verify our results experimentally for semiconductor systems like that one. It is anticipated in our study that the effects of phase-space filling and exciton screening may be quasiadiabatically ruled out, and pulses of a given shape, duration, and velocity can propagate within the gap (see Eq. (18)). Thus line broadening can be neglected. On the other hand, the regime of quasiadiabatic following requires that the pulse contain several optical cycles, and hence sets a window for the pulsewidth used in experiments. In addition, one must have a structure as long as several soliton interaction lengths in order to ensure the soliton formation. To the best of our knowledge, there have not been to date snap-shots of steady-state shapes and measurements of velocities. The first step is thus to do shape measurements to see if the pulse reaches the steady-state shape corresponding to the given pulsewidth and the material parameters. If the soliton is observable, its shape can be changed by a seeding dc-field, and this provides a further test on the theoretical predictions. Summarizing over all these demands, the above referenced semiconductor structure of a 1 cm length may yield the predicted behavior upon a 10 GW/cm^2 excitation by a Ti:sapphire laser generating 20-60 fs pulses at $\lambda = 850 - 940 \text{ nm}$. Regarding possible applications, the sensitivity to boundary conditions on the pulse width and pulse shape can make the predicted bright soliton on a continuous background an effective tool for semiconductor signal processing.

5. REFERENCES

1. R. L. Fork, C. H. Brito Cruz, P. C. Becker, and C. V. Shank, *Opt. Lett.* **12**, 483 (1987); R. W. Schoenlein, J.-Y. Bigot, M. T. Portella, and C. V. Shank, *Appl. Phys. Lett.* **58**, 801 (1991).

2. A. Stingl, M. Lenzner, Ch. Spielmann, F. Krausz, and R. Szipöcs, *Opt. Lett.* **20**, 602 (1995).
3. D. H. Auston and M. C. Nuss, *I.E.E.E. J. Quantum Electron.* **QE-24**, 255 (1988); R. R. Jones, D. You, and P. H. Bucksbaum, *Phys. Rev. Lett.* **70**, 1236 (1993); A. Bonvalet, M. Joffre, J. L. Martin, and A. Migus, *Appl. Phys. Lett.* **67**, 2907 (1995).
4. J. E. Rothenberg, *Opt. Lett.* **17**, 1340 (1992).
5. N. N. Akhmediev, I. V. Mel'nikov, and A. V. Nazarkin, *Sov. Physics - Lebedev Inst. Reports No.* 2, 66 (1989).
6. P. M. Goorjian and A. Taflove, *Opt. Lett.* **17**, 180 (1992); R. M. Joseph, P. M. Goorjian, A. Taflove, *Opt. Lett.* **18**, 491 (1993).
7. S. Radic and N. George, *Opt. Lett.* **19**, 1789 (1994).
8. C. Desem and P. L. Chu, in: *Optical Solitons - Theory and Experiment*, J. R. Taylor, ed., (Cambridge University Press, Cambridge, 1992).
9. L. Xu, D. H. Auston, and A. Hasegawa, *Phys. Rev. A* **45**, 3184 (1992); K. Hayata and M. Koshiba, *J. Opt. Soc. Am. B* **11**, 2581 (1994).
10. R. K. Bullough and F. Ahmad, *Phys. Rev. Lett.* **27**, 330 (1971); J. C. Eilbeck, J. D. Gibbon, P. J. Caudrey, and R. K. Bullough, *J. Phys. A* **6**, 1337 (1973).
11. R. W. Ziolkowski and J. B. Judkins, *J. Opt. Soc. Am. B* **10**, 186 (1993); R. W. Ziolkowski, J. M. Arnold, and D. M. Gogny, *Phys. Rev. A* **52**, 3082 (1995).
12. S. V. Branis, O. Martin, and J. L. Birman, *Phys. Rev. Lett.* **65**, 2638 (1990); *idem*, *Phys. Rev. A* **43**, 1549 (1991).
13. A. V. Andreev, *Phys. Lett. A* **179**, 23 (1993).
14. W. W. Chow, S. W. Koch, and M. Sargent III, *Semiconductor-Laser Physics*, (Springer-Verlag, Berlin, 1994).
15. P. J. Caudrey and J. C. Eilbeck, *Phys. Lett. A* **62**, 65 (1977).
16. E. B. Treacy, *Phys. Lett. A* **27**, 421 (1968); D. Grishkowsky, *Phys. Rev. Lett.* **24**, 866 (1970); D. Grishkowsky, E. Courtens, and J. A. Armstrong, *Phys. Rev. Lett.* **31**, 422 (1973); M. D. Crisp, *Phys. Rev. A* **1**, 1604 (1970); R. H. Lehmberg and J. Reintjes, *Phys. Rev. A* **12**, 2574 (1975).
17. I. V. Mel'nikov, D. Mihalache, F. Moldoveanu, and N.-C. Panoiu, *JETP Lett.* **65**, 380 (1997).
18. R. Binder, D. Scott, A. Paul, M. Lindberg, K. Heneberger, and S. W. Koch, *Phys. Rev. B* **45**, 1107 (1992).
19. M. Sheik-Bahae, D. C. Hutchings, D. J. Hagan, and E. W. Van Stryland, *I.E.E.E. J. Quantum Electron.* **27**, 1296 (1991).
20. This approximation has been used on reducing Boussinesq equation to a Korteweg - de Vries equation, see, e.g., F. Calogero and A. Degasperis, *Spectral Transform and Solitons*, vol. 1, chapt. 1 (North Holland Publishing, Amsterdam, 1982) and references therein.
21. M. Wadati, *J. Phys. Soc. Jpn.* **32**, 1681 (1972).
22. K. Lonngren and A. Scott, eds. *Solitons in Action* (Academic, New York, 1978).
23. G. L. Lamb, Jr. *Elements of Soliton Theory* (Wiley, New York, 1980).
24. see, e.g., M. J. Ablowitz and H. Segur, *Solitons and the Inverse Scattering Transform*, chapt. 4 (SIAM, Philadelphia, 1981) and references therein.
25. H. Ikezi, *J. Appl. Phys.* **64**, 3273 (1988); H. Ikezi, J. S. de Grassie, and J. Drake, *Appl. Phys. Lett.* **58**, 986 (1991).
26. P. A. Harten, A. Knorr, J. P. Sokoloff, F. B. de Colstoun, S. G. Lee, R. Jin, E. M. Wright, G. Khitrova, H. M. Gibbs, S. W. Koch, and N. Peyghambarian, *Phys. Rev. Lett.* **69**, 852 (1992).

Various Approaches for Optical Implementation of the Wavelet Transform

Emanuel Marom, David Mendlovic and Zeev Zalevsky

Tel-Aviv University, Faculty of Engineering, 69978 Tel-Aviv, ISRAEL

Abstract

The Wavelet transform is a very common and useful tool for image processing and compression, however, it requires heavy computations. Optics is useful for rapid computation of parallel information channels. In this paper various important approaches for the optical implementation of 2-D Wavelet transform as well as the optical Wavelet processor are presented and discussed.

1 Introduction

Fourier processing of transient signals having short temporal or spatial extent, is usually corrupted by high frequency noise coming from periodic mode contributions outside the short temporal or spatial extent. To overcome this obstacle, a new type of transformations was defined. One premier solution was the windowed Fourier transforms, or the Gabor transform [1]. In this approach the Fourier transform is applied over the product between the input signal and a fixed window. The window's position may be shifted however its width remains constant. Such transform overcame some problems but created others as instabilities when noisy transient signals were analyzed (for instance for seismic signals analysis) [2]. A different solution was the Wavelet transform (WT) [3]. This transform includes a decomposition of a function according to scaled and shifted versions of a basic function called "mother Wavelet function" [4, 2]. This solution handled successfully not only the processing of transient noisy signal but was also well adapted for handling data compression and bandwidth reduction [5], optical pattern recognition [2, 4], sound analysis [6], representation of fractal aggregates [7] etc.

Section 2 provides the mathematical background on WT. Sections 3-8 illustrate various approaches for the optical implementation of the 2-D WT. Those approaches include time multiplexing, recycled 2-D WT, lenslet array, multi-reference matched filter, and finally multichannel and wavelength multiplexing approaches.

2 Mathematical Background

The 2-D Wavelet transform (WT) of the signal $f(x, y)$ is defined as:

$$W(\vec{a}, \vec{b}) = \int_{-\infty}^{\infty} \int_{-\infty}^{\infty} f(x, y) h_{\vec{a}, \vec{b}}^*(x, y) dx dy \quad (1)$$

where $h(x, y)$ is the "mother Wavelet" function which is a typical window function carrying a modulation term, and $h_{\vec{a}, \vec{b}}(x, y)$ the generated scaled and shifted function coined "daughter Wavelet":

$$h_{\vec{a}, \vec{b}}(x, y) = \frac{1}{\sqrt{a_x a_y}} h\left(\frac{x - b_x}{a_x}, \frac{y - b_y}{a_y}\right) \quad (2)$$

where \vec{b} is the shift amount, \vec{a} is the scale parameter and $\sqrt{a_x a_y}$ is the normalization factor. In many practical applications a global scaling factor is used $a = a_x = a_y$ instead of a vector \vec{a} . Thus, one may deal only with a 3-D distribution:

$$W(a, \vec{b}) = \int_{-\infty}^{\infty} \int_{-\infty}^{\infty} f(x, y) h_{a, \vec{b}}^*(x, y) dx dy \quad (3)$$

where

$$h_{a, \vec{b}}(x, y) = \frac{1}{a} h\left(\frac{x - b_x}{a}, \frac{y - b_y}{a}\right) \quad (4)$$

Since Eq. 3 represents a correlation integral the WT may also be written in the frequency domain as

$$W(a, \vec{b}) = a \int_{-\infty}^{\infty} \int_{-\infty}^{\infty} F(u, v) H^*(au, av) \exp[2\pi i(ub_x + vb_y)] du dv \quad (5)$$

which is an inner product between $F(u, v)$, the Fourier spectrum of the signal and $H(au, av)$ the Fourier transform of the scaled Wavelet function. Eq. 5 is the basis for the optical implementation using an optical correlator and a bank of Wavelet filters.

Using its WT components a signal may be reconstructed, based on the inverse Wavelet transform (IWT) which for the 2-D signal is defined as:

$$f(x, y) = C^{-1} \int_{-\infty}^{\infty} \int_{-\infty}^{\infty} \int_{-\infty}^{\infty} \frac{1}{a^2} W(a, \vec{b}) h_{a, \vec{b}}(x, y) da db_x db_y \quad (6)$$

where C is a constant (known as the admissible factor) needed to be finite in order to obtain the reconstruction of the signal out of its Wavelet components.

For digital calculation of the WT, the discrete version of the Wavelet is used. This version treats in a discrete way both the scale and the shift variations. In optics, it is common to perform a hybrid WT, e.g discrete scales but continuous shifts, therefore using a discrete dilation factor a . With the selection of $a = 2^n$ where $n = -\infty, \dots, -1, 0, 1, \dots, \infty$, the discretization generates an orthogonal basis. Equation 6 now becomes:

$$f(x, y) = C^{-1} \sum_{n=-\infty}^{\infty} \int_{-\infty}^{\infty} \int_{-\infty}^{\infty} \frac{1}{2^{2n}} W(2^n, \vec{b}) h_{2^n, \vec{b}}(x, y) db_x db_y \quad (7)$$

Thus, the input signal will be expressed as a linear combination of the orthogonal Wavelets. Similar to the WT, the inverse Wavelet transform is a correlation between the daughter Wavelet and the signal's WT. Therefore, it can be implemented by an optical correlator as well.

3 Time multiplexing 2-D WT

Since the 2-D WT can be interpreted as a correlation between the mother Wavelet $h(x, y)$ scaled by a dilation factor a and the input function $f(x, y)$, the most direct approach for optically achieving the 2-D WT is to use the Vander Lugt correlator [7]. The necessary matched filter is essentially the Fourier spectrum of the daughter Wavelet. However, since each daughter Wavelet requires the whole 2-D plane, it was impossible to create a matched filter that contains a bank of daughter Wavelets at one location. Instead, the proposed architecture was based on time multiplexing different matched filters (temporal representation of the matched filter), where each matched filter contains a Fourier spectrum of a different daughter Wavelet. Therefore, the major disadvantage of the suggested setup consists of not being a real time configuration.

4 Recycled 2-D WT

Another approach for achieving a 2-D WT, that keeps the real time ability of optics, was based on recycling the input through an optical correlator and using the magnification and minifying ability of optics to scale it while keeping the mother Wavelet at same scale [8]. Fig. 1 describes the above setup. The straight path proceeding from IN to OUT convolves the input with $h(x, y)$ using the standard Vander Lugt correlator. The feedback loop that appears at the upper side of the two polarizing beam splitters (PBS), scales and shifts the input function by the factor a each time it circulates through the loop. This approach has several disadvantages. First, it is against the pure spirit of the WT to scale the input instead of the mother Wavelet. Second, the recycled correlator requires very high stability, hence making the system robust and expensive. Third, its number of cycles is limited to 5-7 as reported by the proposers of this system.

5 Lenslet array 2-D WT

Another approach for performing the 2-D discrete Haar WT [9], can be realized by applying a lenslet array, where the Haar's mother Wavelet is a bipolar step function:

$$h(x, y) = \left\{ \text{rect} \left[2 \left(x - \frac{1}{4} \right) \right] - \text{rect} \left[2 \left(x - \frac{3}{4} \right) \right] \right\} \left\{ \text{rect} \left[2 \left(y - \frac{1}{4} \right) \right] - \text{rect} \left[2 \left(y - \frac{3}{4} \right) \right] \right\} \quad (8)$$

A set of 8×8 discrete Wavelets, each of which consists of 8×8 discrete values, are indexed by translation factors from (1, 1) to (8, 8) with one fixed dilation factor, and are shown on the video monitor. An 8×8 array of lenslets is designed so that each lens images a specific Wavelet submatrix

onto the input function $f(x, y)$ which is represented on the SLM. The submatrices of the Wavelets are superposed upon the input image, and the transmitted beam from the SLM is collected to form an 8×8 pixel array, which represents the 8×8 products of the 2-D Wavelet submatrices with the 2-D processed image. In input plane, each pixel (x_i, y_k) , corresponds to the WT of the input image with one daughter Wavelet of a specific dilation factor, and a matching translation factor (x_i, y_k) .

The above approach has some very apparent disadvantages. The output result has discrete translation factors and a fixed dilation factor. The WT for different daughter Wavelet functions with different dilation factors can be only computed sequentially. Moreover, here the spatial resolution is limited by the possible number of channels at the input plane.

6 Multi-reference matched filter 2-D WT

A recent approach [10] for implementing a real time 2-D WT is based on the Vander Lugt $4 - f$ configuration with a multi-reference matched filter, where each daughter Wavelet is encoded with a different reference beam. Fig. 2 shows a magnification of the matched filter. One can recognize the four different rings due to the four daughter Wavelets. In the experiment [10], a full separation between the different orders was obtained. The system provides several daughter Wavelets responses simultaneously, at different locations, in real time. Similar to the last system (section 5), this is also a spatial multiplexing of the 3-D data. However, it requires full separation between the spectra of the different daughter Wavelet functions. Thus, cases where the Fourier transforms of two daughter Wavelets are not mutually exclusive will produce cross talk and practically have no usefulness. Therefore most of the popular mother Wavelets functions can not be realized efficiently by this system.

7 2-D multichannel WT

Once again for optical implementation the well known Vander Lugt $4 - f$ configuration may be used, where the matched filter is a bank of Wavelet functions in the Fourier domain. For simultaneously displaying the whole 2-D WT daughter Wavelet set, one needs to replicate the input function or its Fourier transform, and to process each replica with a different daughter Wavelet, i.e, to use different channels spatially separated per each daughter Wavelet [11].

The first step towards such a multichannel system is to replicate the spectrum of the input object into different channels. This can be achieved by the use of Dammann gratings. By multiplying the input signal $f(x, y)$ with a Dammann grating in the input plane of a conventional Vander Lugt $4 - f$ correlator (Fig. 3), a 2-D array of equally spaced replicated spectrum, $F(u, v)$ is realized at the focal plane of the correlator (see Fig. 4). Since each image has to be processed with a different daughter Wavelet, a specifically designed matched filter is introduced at the Fourier plane. The matched filter consists of an array of channels, each corresponding to the Fourier transform of a different daughter Wavelet scaled with a different dilation factor a (but without the shift vector,

$\vec{b} = 0$). The attained matched filter may be described as:

$$MF(u, v) = \sum_{m=-N}^{m=N} \sum_{n=-N}^{n=N} H^*[a_{m,n}(u - nu_0, v - mv_0)] \quad (9)$$

The matched filter is designed so that the location of each daughter Wavelet spectra matches the exact location of the replicated input image spectrum from the Dammann grating, and therefore the array of the input's Fourier spectrum is superimposed on the matched filter's array of Wavelets spectra. Fig. 5 sketches the locations of the different Wavelet spectra, and one can easily compare them to the locations of input's replicated spectra described in Fig. 4. At the second half of the correlator a second Fourier transform is performed, thus exhibiting correlations signals in the output plane. Each correlation corresponds to the WT of the input signal with the given daughter Wavelet function. Therefore, a 2-D WT for each of the daughter Wavelets have been realized at the output plane. However, since the output plane is an image of the input plane, all the transforms will appear as a zero order diffraction and hence will be superposed upon each other. Therefore, in order to simultaneously and separately display the Wavelet decomposition, each daughter Wavelet should be encoded with a different reference beam and different incident angle $\vec{\alpha}$, thus producing a multi-reference matched filter (MRMF). The impulse response of the MRMF forms an array according to the different reference beams (and the required locations of the final WT orders) and thus, achieves spatial multiplexing in the output plane. Naturally, the MRMF is based on the matched filter described in Eq. 9 with the addition of the reference beam $\vec{\alpha}$. For $(2N+1) \times (2N+1)$ WTs the MRMF is defined by

$$MRMF(u, v) = \sum_{m=-N}^{m=N} \sum_{n=-N}^{n=N} (H^*[a_{m,n}(u - nu_0, v - mv_0)] + \exp(-i\alpha_m u - i\alpha_n v)) \quad (10)$$

where $H(u, v)$ is the Fourier transform of the mother Wavelet $h(x, y)$ and $a_{m,n}$ is the different dilation factor. One should note that α_m and α_n are the horizontal and the vertical components of the vector $\vec{\alpha}_{m,n}$, hence producing two tilt directions to the reference beam. In order to ensure the separation of the different WT orders at the output plane, $|\vec{\alpha}_{m,n}|$ has to be larger than a minimum value $|\vec{\alpha}_{min}|$ which is determined according to the maximal frequency present in $H[a_{m,n}(u, v)]$.

8 2-D continuous WT with wavelength multiplexing

In this approach the Wavelet components for the different scale factors are achieved with different wavelengths [12, 13]. The suggested optical setup is illustrated in Fig. 6. When illuminated by a white light point source, the field distribution of the input pattern obtained in the Fourier plane can be written as:

$$u_F(u, v, \lambda) = \frac{S(\lambda)}{\lambda f} \int_{-\infty}^{\infty} \int_{-\infty}^{\infty} u_{in}(x, y) \exp\left(\frac{2\pi i(xu + yv)}{\lambda f}\right) dx dy = \frac{S(\lambda)}{\lambda f} U_{in}\left(\frac{u}{\lambda f}, \frac{v}{\lambda f}\right) \quad (11)$$

where $S(\lambda)$ is the spectral distribution of the input white light point source, U_{in} is the Fourier transform of u_{in} and a constant phase factor was omitted. Thus, after passing through the spatial filter, the resulted distribution is $u_F(u, v, \lambda)H(u, v)$, where $H(u, v)$ denotes the Fourier transform of the mother Wavelet. The field distribution obtained in the output plane, is:

$$\begin{aligned} u_{out}(b_1, b_2, \lambda) &= \frac{1}{\lambda f} \int_{-\infty}^{\infty} \int_{-\infty}^{\infty} u_F(u, v, \lambda) H(u, v) \exp \left[\frac{2\pi i(b_x u + b_y v)}{\lambda f} \right] dudv \\ &= \left(\frac{1}{\lambda f} \right)^2 \int_{-\infty}^{\infty} \int_{-\infty}^{\infty} U_{in} \left(\frac{u}{\lambda f}, \frac{v}{\lambda f} \right) H(u, v) \exp \left[\frac{2\pi i(b_x u + b_y v)}{\lambda f} \right] dudv \end{aligned} \quad (12)$$

A simplification of the last expression results with:

$$u_{out}(b_x, b_y, \lambda) = S(\lambda) \int_{-\infty}^{\infty} \int_{-\infty}^{\infty} u_{in}(x, y) h \left(\frac{b_x - x}{\lambda f}, \frac{b_y - y}{\lambda f} \right) dx dy \quad (13)$$

Assuming that the spectrum of the illumination source $S(\lambda)$ is uniform, one obtains:

$$W(\lambda f, b_x, b_y) = u_{out}(b_x, b_y, \lambda) = \int_{-\infty}^{\infty} \int_{-\infty}^{\infty} u_{in}(x, y) h \left(\frac{b_x - x}{\lambda f}, \frac{b_y - y}{\lambda f} \right) dx dy \quad (14)$$

where $W(\lambda f, b_x, b_y)$ is the Wavelet decomposition expression. A comparison between Eq. 14 and the definition of the 2-D WT (see Eq. 3) shows complete agreement. If in the output plane a color filter is placed, then each Wavelet decomposition may be seen separately. Note that since the wavelength spectrum is continuous the obtained WT is also continuous. Nevertheless, since the wavelength domains of a typical white light point source is between 300nm and 700nm, the possible continuous scalings is limited within this range.

9 The optical Wavelet processor

The 2-D Wavelet processor is based on two steps in cascade. The first is the implementation of the 2-D WT, which may be implemented by one of the methods previously discussed. The second step is the realization of the IWT and the reconstruction of the 2-D signal from it's Wavelet components. Fig. 7 proposes a setup that implements the Wavelet processor, based on the multichannel approach. The Dammann grating replications generates highly efficient channels per each different daughter Wavelet. By applying a simple computer generated multi-reference matched filter, a 2-D WT set of the input signal is simultaneously generated halfway into the setup. After applying a second computer generated multi-reference match filter, the input signal is reconstructed from its WT components and displayed in the output plane. In between the two steps (in the intermediate plane), filtering in the Wavelet plane can be performed for Wavelet processing. The reconstruction is based only on the chosen Wavelet components, and therefore the whole setup serves as a flexible analysis Wavelet processor. Interesting experimental results of the discussed setup have been demonstrated by Ref. [14], as for instance a Wavelet processing of a "Lenna" picture by a Mexican-hat mother Wavelet.

10 Conclusions

This paper has reviewed various approaches used for optical implementation of the 2-D Wavelet transform. The approaches included the time multiplexing approach that temporally replaced the Wavelet functions, the recycling approach which consists of recycling the input through an optical correlator and using the magnification and minification ability of optics, the lenslet array approach that uses a lenslet array to implement a 2-D Haar WT, the multi-reference matched filter approach that encodes each daughter Wavelet with a different reference beam, the multichannel approach that replicates the spatial spectrum of the input signal in order to process it simultaneously by different daughter Wavelets and eventually the wavelength multiplexing approach where the different scales of the mother Wavelet are achieved by using a white light point source. Finally, using the multichannel method a 2-D Wavelet processor was discussed and implemented.

References

- [1] D. Gabor, "Theory of communication," J. Inst. Elec. Eng. **93**, 429-457 (1946).
- [2] H. Szu, Y. Sheng and J. Chen, "Wavelet Transform as a bank of matched filters," Appl. Opt. **31**, 3267-3277 (1992).
- [3] J. M. Combes, A. Grossmann, and Ph. Tchamitchian, eds., *Wavelets: time frequency methods and phase space*, 2nd ed., Springer-Verlag, Berlin (1990).
- [4] X. J. Lu, A. Katz, E. G. Kanterakis, and N. P. Cavaris, "Joint transform correlation using Wavelet transforms," Opt. Lett. **18**, 1700-1703.
- [5] J. Caulfield and H. Szu, "Parallel discrete and continuous Wavelet transforms," Opt. Eng. **31**, 1835-1839 (1992).
- [6] R. K. Martinet, J. Morlet, and A. Grossmann, "Analysis of sound patterns through Wavelet transforms," Int. J. Patt. Rec., Artificial Intell. **1** (2), 273-302 (1987).
- [7] E. Freysz, B. Pouligny, F. Argoul and A. Arneodo, "Optical Wavelet transform of fractal aggregates," Phys. Rev. Lett. **64** 7745-7748 (1990).
- [8] M. O. Freeman, K. A. Duell and A. Fedor, "Multi-scale optical image processing," IEEE proc. International Symposium on Circuits and Systems, June 1991, Singapore.
- [9] P. X. Wang, J. W. Tai and Y. X. Zhang, "Two dimensional optical Wavelet transform in space domain and its performance analysis," Appl. Opt. **33**, 5271-5274 (1994).
- [10] D. Mendlovic and N. Konforti "Optical realization of the Wavelet transform for two dimensional objects," Appl. Opt. **32** 6542-6546 (1993).

- [11] D. Mendlovic, I. Ouzieli, I Kiryushev and E. Marom "Two dimensional Wavelet transform achieved by computer generated multi-reference matched filter and Dammann grating," Appl. Opt. **34** 8213-8219 (1995).
- [12] D. Mendlovic, "A continuous two dimensional on axis Wavelet transformer and Wavelet processor with white light illumination" Appl. Let. (submitted).
- [13] Z. Zalevsky, "Experimental implementation of a continuous two dimensional on axis Wavelet transformer with white light illumination," Opt. Commun. (submitted).
- [14] I. Ouzieli and D. Mendlovic, "A 2-D Wavelet processor," Appl. Opt. **35**, 5839-5846 (1996).

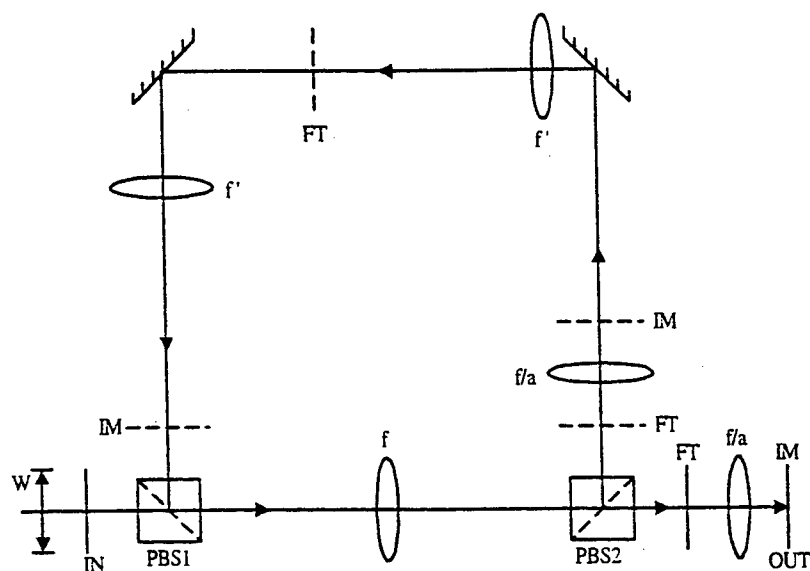


Figure 1: An optical system for computing the 2-D Wavelet decomposition of an input image.

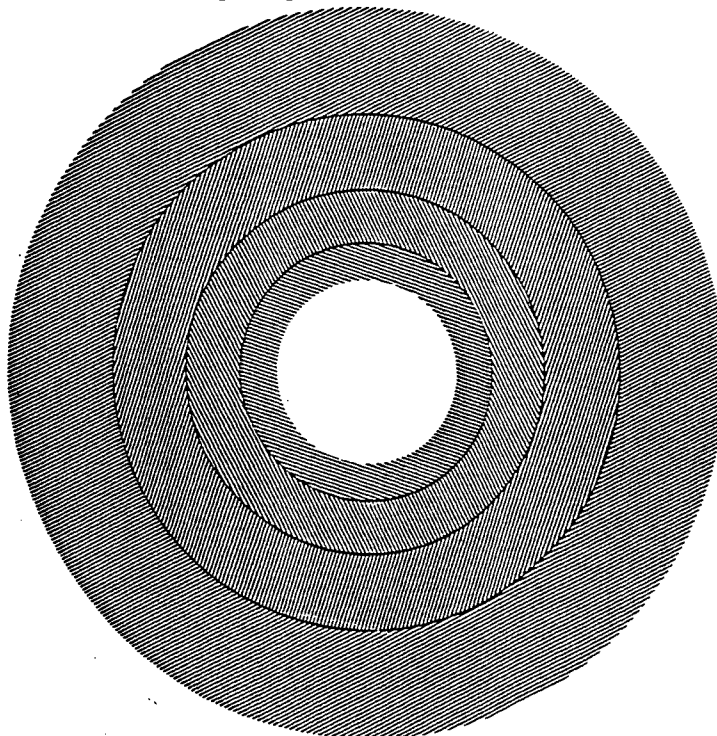


Figure 2: A magnification of the multireference matched filter with four daughter Wavelets, each encoded with different reference beam.

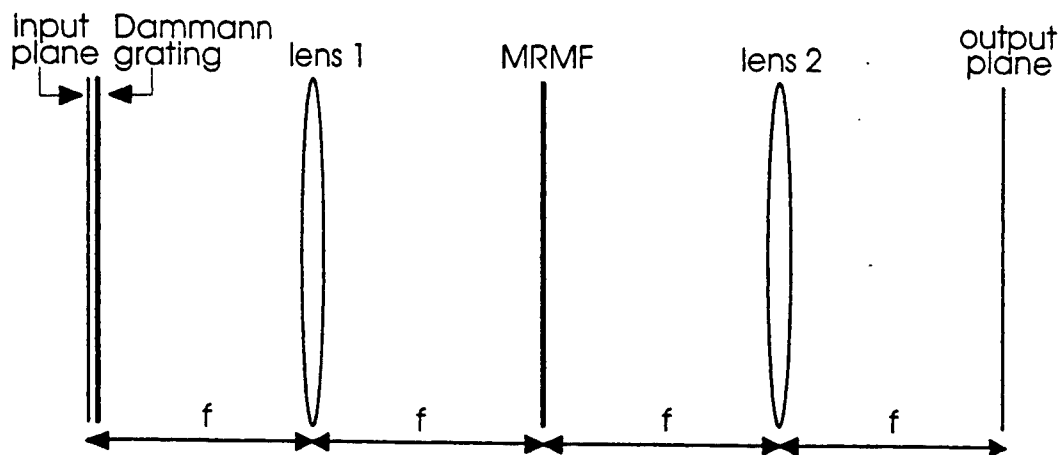


Figure 3: Optical correlator with Dammmann gratings for a 2-D WT.

$F(u + u_0, v - v_0)$	$F(u, v - v_0)$	$F(u - u_0, v - v_0)$
$F(u + u_0, v)$	$F(u, v)$	$F(u - u_0, v)$
$F(u + u_0, v + v_0)$	$F(u, v + v_0)$	$F(u - u_0, v + v_0)$

Figure 4: A 2-D array of replicated spectra, $F(u, v)$ is realized at the focal plane of the correlator.

$H[a_7(u+u_0, v-v_0)]$	$H[a_8(u, v-v_0)]$	$H[a_9(u-u_0, v-v_0)]$
$H[a_4(u+u_0, v)]$	$H[a_5(u, v)]$	$H[a_6(u-u_0, v)]$
$H[a_1(u+u_0, v+v_0)]$	$H[a_2(u, v+v_0)]$	$H[a_3(u-u_0, v+v_0)]$

Figure 5: The location of each Wavelet spectra in the filter matches the exact location of the replicated spectra of the input function.

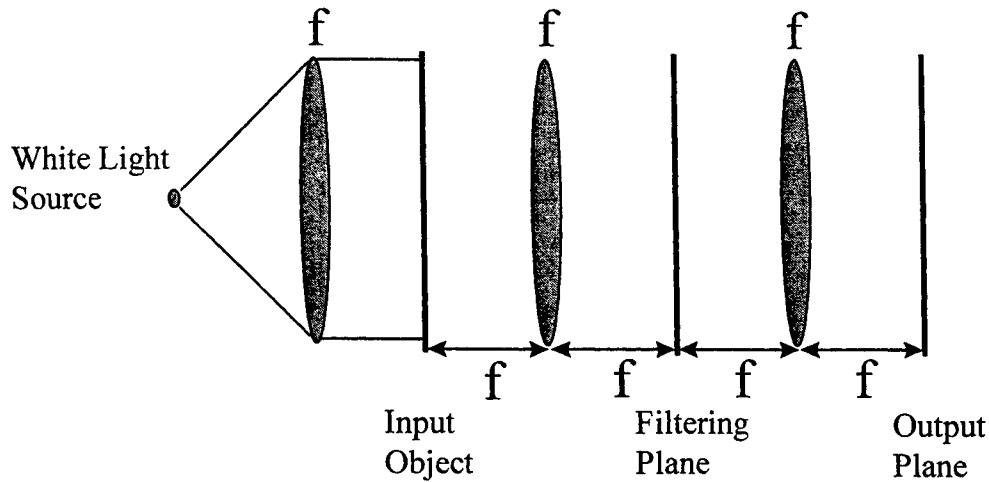


Figure 6: The suggested setup for the implementation of the 2-D continuous WT with wavelength multiplexing.

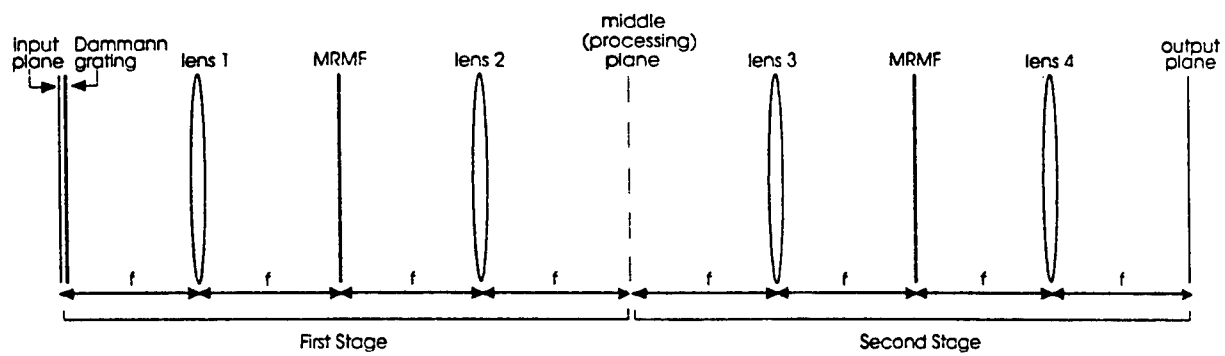


Figure 7: The suggested setup for the implementation of the 2-D Wavelet processor.

The radiation spectrum and the thermodynamics of the quantum cubic cavities

Valentin I. Vlad and Nicholas Ionescu-Pallas

Institute of Laser and Plasma Physics, Dept. of Lasers
P.O. Box MG - 36, R - 76900 Bucharest, Romania
E-mail: vlad@roifa.ifa.ro; vlad@nio.ifa.ro

ABSTRACT

In this paper, the density of modes in quantum cubic cavities is calculated taking into account the small number of modes. Then the "spatial quantisation" fluctuations, which appear as a correction factor in the mode density, are introduced in the Planck law. The discrete form of the Planck radiation spectrum is demonstrated and the limits of this double-quantum regime of the cubic cavity are set for the product of cavity size by temperature, $LT \in (0.1, 1)$. A reciprocity rule for the cavity size and the temperature is shown. Calculating the total energy in the quantum cubic cavities (QCC), we found out a "corrected" Stefan-Boltzmann law for the double-quantum regime. Furthermore, the corrections for all thermodynamic functions of the photon gas in QCC are given.

Keywords: quantum cubic cavity, discrete Planck spectrum, thermodynamics of photon gas

1. ELECTROMAGNETIC MODES IN A CUBIC CAVITY

In a box-shaped (parallelepiped) cavity with the dimensions l_x, l_y, l_z , filled with a linear, homogeneous, isotropic medium, the standing waves (normal modes, states) can be adequately described using the Hertz vector, $\mathbf{z}_k = \mathbf{a}_k(t) \exp(i\mathbf{k}_k \mathbf{r})$, whose amplitude satisfies the harmonic oscillator equation¹⁻¹⁰:

$$\ddot{\mathbf{a}}_k(t) + 4\pi^2 f^2 \mathbf{a}_k(t) = 0, \quad (1)$$

while the phase satisfies periodicity conditions over the box size L . In eq.(1), $k_x = 2\pi m_x / l_x$, $k_y = 2\pi m_y / l_y$, $k_z = 2\pi m_z / l_z$ are the components of the wave number vector, (m_x, m_y, m_z) are integers and zero and f - the temporal frequency. We consider the case of cubic cavity ($l_x = l_y = l_z = L$, without any condition on L). The frequencies of the normal modes, f_q , form a discrete spectrum defined by the equations:

$$f_q = (v/L) \sqrt{q}, \quad (E_q = hf_q = (hv/L) \sqrt{q} = (hv/2\pi) |\mathbf{k}_q|), \quad (2)$$

with v - the wave propagation speed in the cavity and q - the integer level number, which satisfy the "spatial quantisation" condition:

$$q = (m_x)^2 + (m_y)^2 + (m_z)^2 \quad (3)$$

The allowed triplets of integers of this Diophantine equation in the case of the cubic cavity (Gauss solution) are all numbers which *do not lead* to level numbers of the form: $q(p, 1) = 4p(81 + 7)$, (p and 1 positive integers)¹¹.

Lord Rayleigh and Jeans have demonstrated that the *asymptotic number* of the allowed cavity modes (for $m_k \geq 0$, ($k = x, y, z$) and two polarisations) is ¹⁻¹⁰:

$$N_q = (8\pi L^3/3 v^3) f_q^3 = \frac{8\pi}{3} (q\sqrt{q}) \quad (4)$$

The mean density of the allowed cavity modes (in the frequency unit interval and unit volume) has the form:

$$D_q = (1/V)(dN_q/df) = 8\pi f_q^2 / v^3. \quad (5)$$

The result (5) may be shown to be generally valid whatever the shape of the box².

We have observed that the number of degenerate modes in the cavity spectrum (modes with same q , frequency and energy) or *the weight of the cavity levels*, $g(q)$, is *strongly and randomly fluctuating, for small q* . (Fig. 1). We found out the asymptotic value of the weight (for a single polarisation) as:

$$g(q) \approx 2\pi\sqrt{q}. \quad (6)$$

Eq.(6) shows that *the weight of the successive levels increases linearly with their frequency*.

There are combinations of integers which did not satisfy the eq.(3) leading to "antiresonances" in the spectrum. (These modes carry the zero-point energy only).

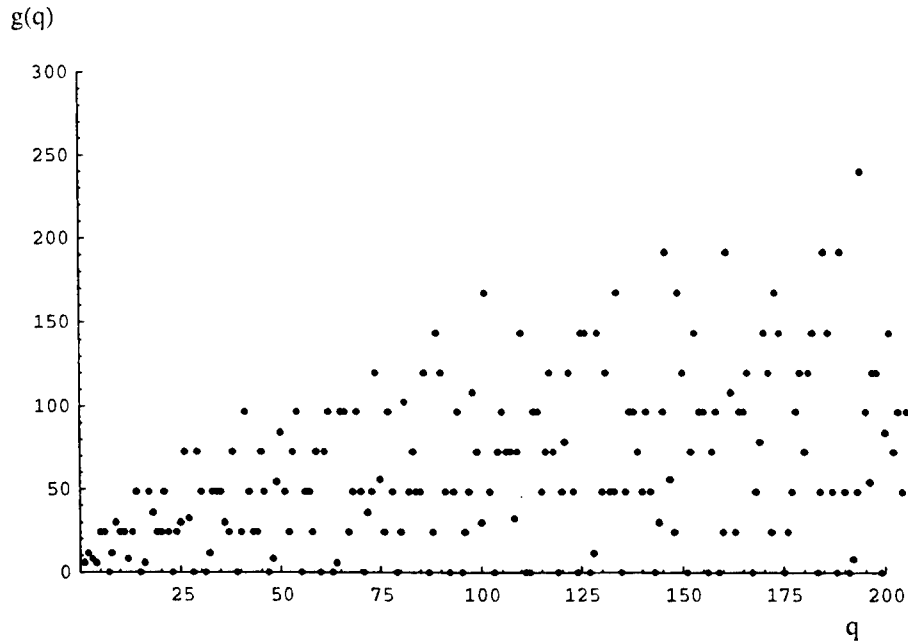


Fig. 1. The weights of the cubic cavity levels, $g(q)$ for $q \leq 200$. This distribution is strongly and randomly fluctuating. The average of the distribution $g(q)$ follows the asymptotic trend $2\pi\sqrt{q}$. The antiresonance frequencies can be identified as points on the q -axis ($g(q) = 0$). In QCC, there are maximum 16 antiresonances.

Thus, we had the first problem of deriving a more general formula for the density of modes of the cubic cavity, dN_q/df , taking into account the degeneracy fluctuations (for small number of levels). From the general expression of the weight, we can write (for 2 polarisations):

$$\begin{aligned} \frac{dN_{q1}}{df} &= \frac{dN_{q1} / dq}{df / dq} = (L/v)2\sqrt{q} \cdot \frac{dN_{q1}}{dq} = (L/v)2\sqrt{q} \cdot \frac{\Delta N_{q1}}{\Delta q} = \\ &= 2 \cdot (L/v)2\sqrt{q} \cdot g(q) = 4(L/v)^2 f \cdot g(q) \end{aligned} \quad (7)$$

and

$$\begin{aligned} D_{q1} &= \frac{1}{V} \frac{dN_{q1}}{df} = 4 \frac{1}{V} (L/v)^2 f \cdot g(q) = 4 \frac{1}{V} (L/v)^2 f \cdot 2\pi\sqrt{q} \cdot \frac{g(q)}{2\pi\sqrt{q}} = \\ &= 8\pi v^{-3} \cdot f^2 \cdot \frac{g(q)}{2\pi\sqrt{q}} = 8\pi v^{-3} \cdot f^2 \cdot \zeta(q) = D_q \cdot \zeta(q), \quad \zeta(q) = \frac{g(q)}{2\pi\sqrt{q}} \end{aligned} \quad (8)$$

The formula (8) is different from the classical one by the strongly fluctuating factor $\zeta(q)$ (around 1), which includes the mode degeneracy (spatial quantum effects) (Fig.3).

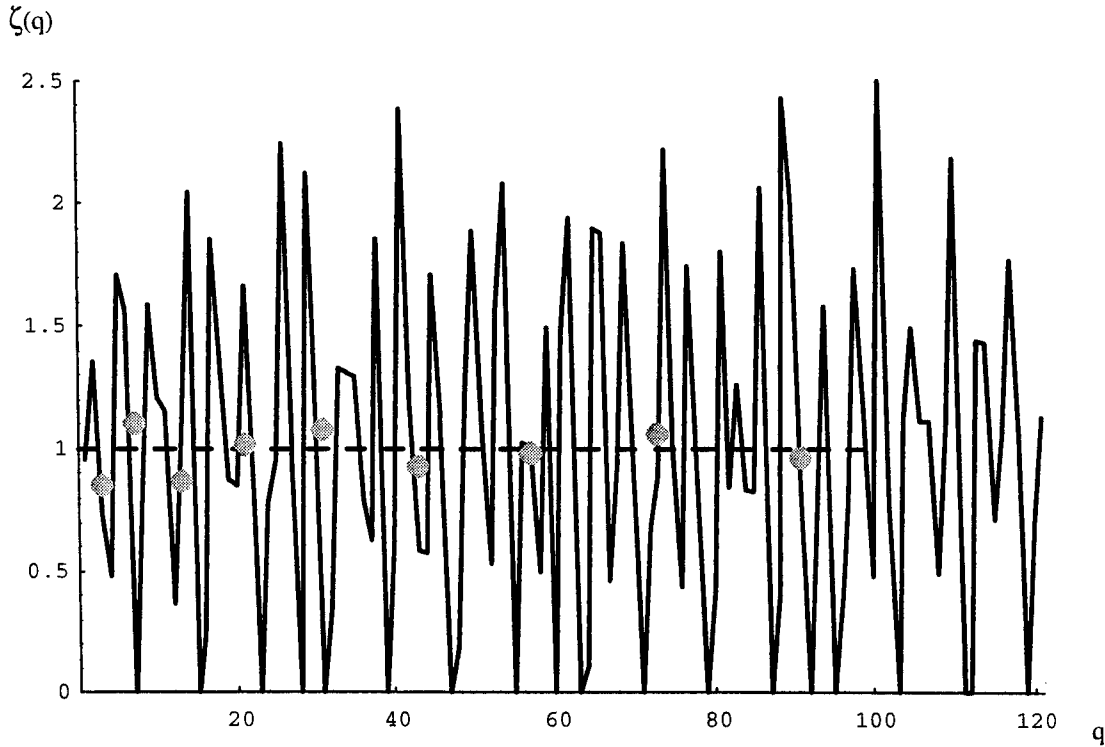


Fig. 2. The random fluctuation of the factor $\zeta(q)$ around the unit value (graph with jointed points); the dots represent the calculated average number of modes on constant frequency intervals and show that the classical (asymptotic) mode density can be reached when $q > 100$, by the averaging of the actual mode density.

We define *quantum cubic cavities* (QCC) as the cavities with a small number of levels (and modes), more precisely, with a special upper limit on the highest significant level (HSL) in the cavity: $q_T < 100$. In this case, the degeneracy fluctuations play a significant role in QCC leading to the *discrete Planck spectrum*. For $q_T > 100$, the classical mean density formula can be safely used and the continuum Planck spectrum can be derived and observed.

2. PLANCK DISCRETE RADIATION SPECTRUM IN A CUBIC CAVITY.

Max Planck quantified the linear harmonic oscillator in order to avoid the divergence of the Rayleigh and Jeans radiation spectrum at high frequencies (ultraviolet catastrophe)¹. The mean energy of the quantum oscillator for any temperature T inside the cavity is: $\epsilon_l = hf [\exp(hf/kT) - 1]^{-1}$, (9) (where h is the Planck constant). With this mean energy and the mode density found by us in eq.(8), the Planck radiation law for a cubic cavity can be written in a more complete form ($v = c$):

$$\begin{aligned} u_l(f,T) df &= D_{q1} \epsilon_l df = [8\pi h f^3 / c^3] \zeta(q) [\exp(hf/kT) - 1]^{-1} df \\ &= 8\pi h L^{-3} q^{3/2} \zeta(q) [\exp(hc/kLT) \sqrt{q} - 1]^{-1} df. \end{aligned} \quad (10)$$

The Planck spectrum is discrete for small number of levels in the cavity. (Fig.3). Consequently, for $LT = 1.35$, in the position of the Planck spectrum peak, one can find the first antiresonance of the cubic cavity, thus, the corresponding zero-point energy only (Fig.4).

We can find a reasonable superior limit of the number of levels in the cavity, q_T . Observing that, in eq.(10), the exponential dominates at high frequencies, one can write:

$$u_l(f,T) \approx [8\pi h f^3 / c^3] \zeta(q) \exp(-hf/kT) = 8\pi h L^{-3} q^{3/2} \zeta(q) \exp[-(hc/kLT) \sqrt{q}] \quad (11)$$

As $\zeta(q)$ fluctuates around 1, this function has the form: $u_l(N) = A.N^3 \exp(-N)$, with $N = hc\sqrt{q}/kLT$ and $A = \text{constant}$.

$$\text{If } u_l(N)/A \leq 10^{-3}, \text{ i.e. } N \geq 15, \quad (12)$$

the higher levels bring a negligible effect and one can truncate the Planck distribution at the highest significant level (HSL) in the cavity:

$$q_T = 108.69 (LT)^2 \quad [\text{CGS}] \quad (13)$$

In the particular case: $L = 1\text{cm}$ and $T = 1\text{K}$, eq. (13) leads to: $q_T \approx 109$.

If we rewrite the Wien displacement law as:

$$q_M \approx 3.8454 (LT)^2 \quad [\text{CGS}], \quad (14)$$

the ratio between the level numbers of HSL (from eq. 13) and of the Planck distribution peak (from eq. 14) can be derived immediately:

$$q_T / q_M \approx 28 \quad (15)$$

In this case, the ratio between the corresponding frequencies is $f_T / f_M \approx 5.3$. Thus, one can assert that the significant bandwidth of the black body radiation is $B \approx 5.3 f_M$.

3. TOTAL ENERGY DENSITY IN QCC. CORRECTION OF STEFAN-BOLTZMANN LAW

The classical Stefan-Boltzmann law provides the total energy density in the cavity:

$$u(T) = \int_0^\infty u(f,T) df = (8\pi^5 k^4 / 15h^3 v^3) T^4 = \sigma T^4 \quad (\text{Stefan-Boltzmann law}) \quad (16)$$

If we use the Planck discrete spectrum in QCC, $u_l(f,T)$, the integral from (16) can be written as a sum (with $v = c$, $\alpha = hc/k = 1.4388 \text{ cm.K}$ and with relationship between the Planck and Stefan-Boltzmann constants $\sigma = (4/c) \sigma_{SB}$):

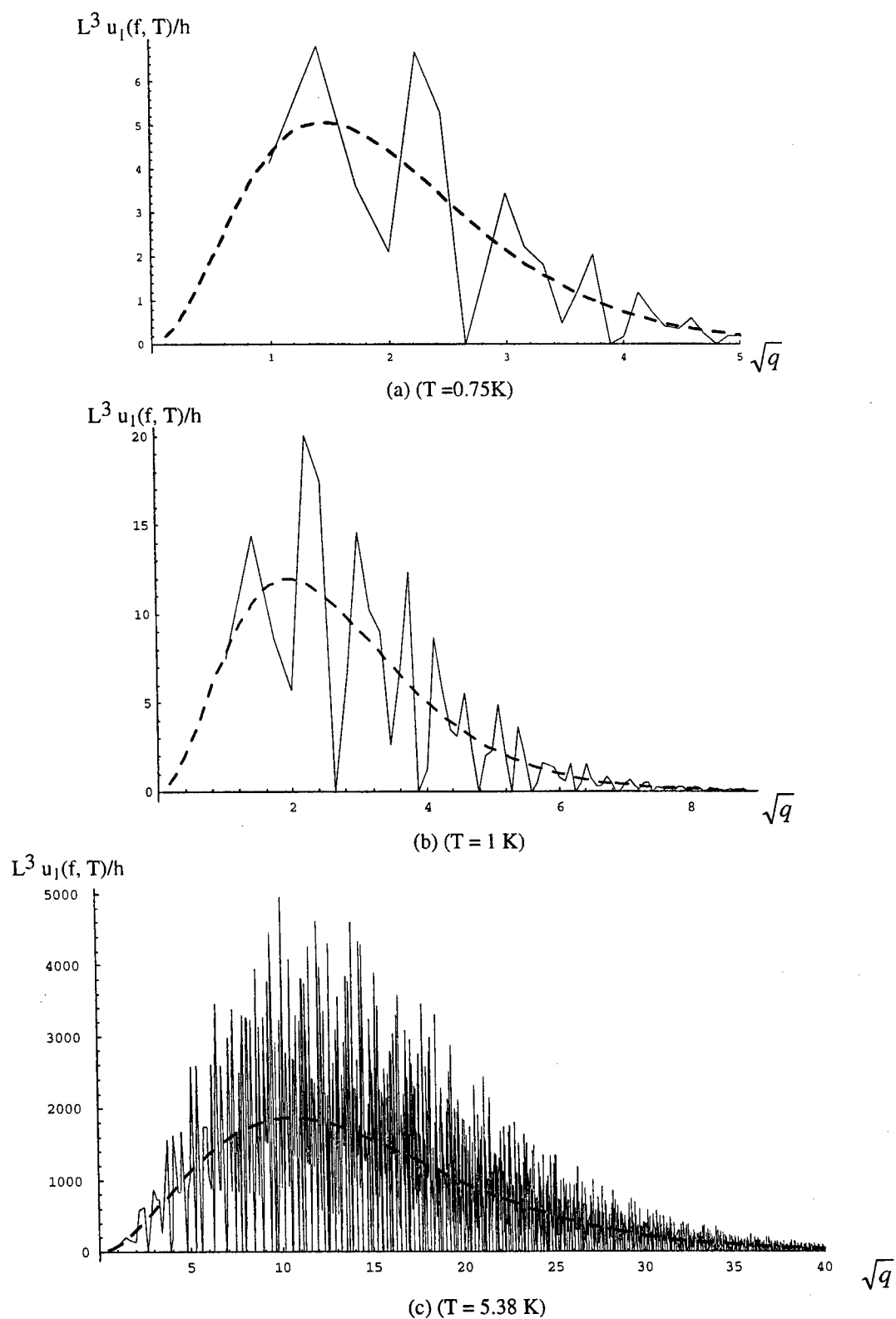


Fig. 3. Some conventional Planck distributions (dashed lines) and "quantized" distributions (solid lines), for $L = 1 \text{ cm}$ and three low temperatures: (a) $T = 0.75 \text{ K}$; (b) $T = 1 \text{ K}$; (c) $T = 5.38 \text{ K}$.

$L^3 u_1(f, T)/h$

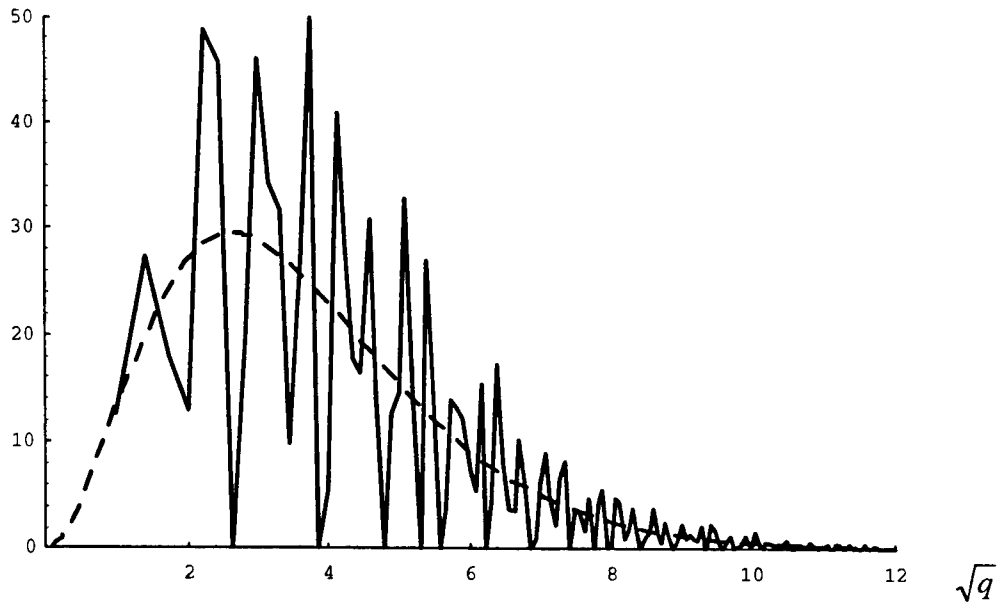


Fig. 4. The conventional Planck (dashed lines) and the "quantified" (solid lines) spectrum of a QCC with $L = 1$ cm, which hold in its maximum the first antiresonant singlet, $q_M = 7$ (at $T = 1.35$ K).

$$\begin{aligned}
 L^3 u_1(T) &= \sum_{q=1}^{q_T} 2g(q) [\exp(hf/kT) - 1]^{-1} \cdot hf = \sum_{q=1}^{q_T} 2g(q) [\exp(\alpha \sqrt{q}/LT) - 1]^{-1} (hc/L) \sqrt{q} = \\
 &= \frac{4\pi hc}{L} \sum_{q=1}^{q_T} [\exp(\alpha \sqrt{q}/LT) - 1]^{-1} q \zeta(q) = \frac{4\pi k \alpha}{(LT)^4} VT^4 \sum_{q=1}^{q_T} [\exp(\alpha \sqrt{q}/LT) - 1]^{-1} q \zeta(q) \\
 &= \sigma_1 VT^4
 \end{aligned} \tag{17}$$

Our calculations show that the total energy density $u_1(T)$ can be written as in the eq.(16), but with the corrected Planck "constant", σ_1 :

$$\frac{\sigma_1}{\sigma} = \frac{15}{4\pi^5} \left(\frac{\alpha}{LT} \right)^4 \sum_{q=1}^{q_T} \frac{\sqrt{q} g(q)}{e^{\frac{\alpha}{LT} \sqrt{q}} - 1} = 5.2515 \cdot 10^{-2} (LT)^{-4} \sum_{q=1}^{109(LT)^2} \frac{\sqrt{q} g(q)}{e^{\frac{\alpha}{LT} \sqrt{q}} - 1} = F\left(\frac{\alpha}{LT}\right) \leq 1 \tag{18}$$

When $\zeta(q)$ goes to 1 (by averaging, for very close and numerous modes), σ_1/σ tends to 1, i.e. one arrives to the conventional formalism (Fig. 5). We found also a convenient approximation of Planck constant from (18) by the formula:

$$\sigma_1/\sigma \approx \exp[0.06041/LT - 0.08193/(LT)^2]. \tag{18'}$$

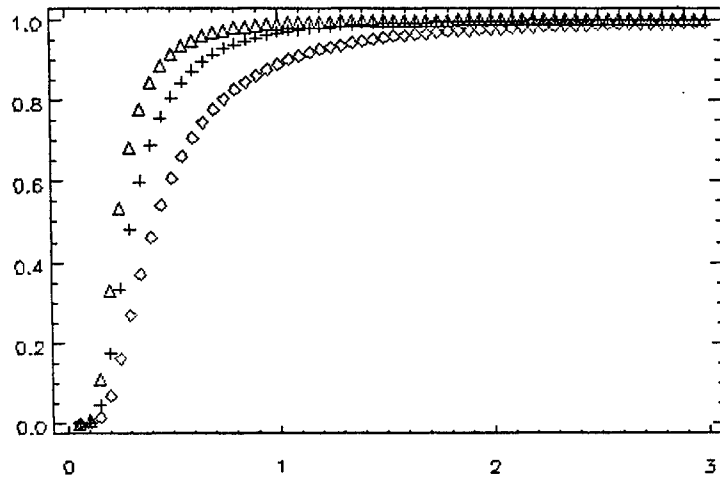
The corrected Planck "constant" σ_1 is down limited by the lowest cavity mode to the value:

$$\sigma_1 = 0.00178 \sigma = 0.00178 \cdot 7.565 \cdot 10^{-15} = 1.346 \cdot 10^{-17} \text{ [erg cm}^{-3} \text{ K}^{-4}]$$

The upper limit of the quantum regime of the QCC can be considered $LT \approx 1$, for which Planck constant takes the value

$$\sigma_1 = 0.9703 \sigma = 0.9703 \cdot 7.565 \cdot 10^{-15} = 7.340 \cdot 10^{-15} \text{ [erg cm}^{-3} \text{ K}^{-4}].$$

$F(\alpha/LT)$, $G(\alpha/LT)$, $H(\alpha/LT)$



LT (cm K)

Fig. 5. The correction factors of the thermodynamic functions in QCC: $F(\alpha/LT)$ (marked with +), $G(\alpha/LT)$ (marked with \diamond) and $H(\alpha/LT)$ (marked with Δ) (defined in section 5)

It is interesting to evaluate the effect of actual degeneracy, $g(q)$, of the small number of levels existing in QCC. Calculating the ratio σ/σ_1 from (18) with the actual degeneracy provided by the Diophantine eq. (3) and by the asymptotic relation $g(q) \approx 2\pi\sqrt{q}$, we found out differences in the order of $\approx 5 \cdot 10^{-3}$, which are negligible in these calculations. We can conclude that:

the small number of levels up to HSL in cavity (i.e., the small $P_q = LT$) play the key role in the calculation of the total energy density of QCC and in the LT dependence of the S-B "constant".

4. THE RECIPROCITY RULE FOR CAVITY SIZE AND TEMPERATURE IN QCC

The positions of the energy density peak and of HSL depend on the product $P_q = LT$:

$$q_T \approx 28q_M \approx 109 (LT)^2 \quad (19)$$

The calculations with (18) and the figure 5 show that $F(\alpha/LT)$ becomes smaller than 1, for P_q smaller than $P_{qmax} \sim 1$ [cm.K], i.e. $q < 100$. On the other hand, the lowest cavity mode (1,0,0) imposes an inferior limit to the level number at $q_T = 1$ (the smallest frequency in the cavity) and consequently, one can introduce the inferior limit $P_{qmin} = 0.1$ [cm.K].

Thus, we can define *the quantum regime of the cubic cavity (or the double quantised cubic cavity)* in the range:

$$1 < q < 100 \quad (20)$$

$$\text{or} \quad 0.1 < LT < 1 \quad [\text{cm.K}] \quad (21)$$

Moreover, we can introduce the following reciprocity rule: *the cavity size and the temperature are reciprocal parameters in the QCC, i.e. the same effects (as the total energy) can be obtained either by varying L or by varying T, if their product remain constant (in the range $LT \in [0.1, 1]$).*

One can observe that, in eq.(21), it is implicitly assumed that the cavity size should be larger than the longest wavelength in discussion. In order to point out some important numerical data, we give the following examples:

- 1) QCC with $L = 1\text{cm}$ emits radiation in the frequency band $f \in [30, 300]\text{ GHz}$, at $T \in [0.1, 1]\text{K}$;
- 2) For $L = 1\text{mm}$, QCC radiation has temperatures including the liquid He one: $1 < T < 10$.
- 3) For $L = 20\text{ }\mu\text{m}$, the quantum regime of QCC includes the room temperature, $50 < T < 500$ ($f_M \approx 17.7\text{ THz}$; $\lambda_M \approx 0.6\text{c}/f_M \approx 10\mu\text{m}$).

At the lowest limit, $T = 0.1/L$, we can conclude that $T \rightarrow 0$ implies $L \rightarrow \infty$, which means cooling to 0K an infinite cavity; this is physically impossible. Therefore, the condition (21) can be regarded as a *proof of the validity of the Nernst-Planck principle (unattainability of the absolute zero for the photon gas in QCC)*.

5. THE THERMODYNAMICS OF THE PHOTON GAS IN QCC

The total energy of the photon gas in QCC is (as in eq.(17)):

$$E = L^3 u_f(LT) = \sigma V T^4 F(\alpha/LT) \quad (V = L^3) \quad (22)$$

The free energy, F_E , which equals the grand potential, Ω , (for the chemical potential $\mu = 0$) can be obtained as:

$$F_E = -(\sigma/3)VT^4 G(\alpha/LT) = \frac{45}{4\pi^5} (\alpha/LT)^3 \sum_{q=1}^{\infty} g(q) \ln(1 - e^{-(\alpha/LT)\sqrt{q}}) \quad (23)$$

For the specific heat of the photon gas, one can calculate:

$$C_v = (\delta E / \delta T) = 4\sigma VT^3 H(\alpha/LT) = \frac{15}{16\pi^5} (\alpha/LT)^5 \sum_{q=1}^{\infty} qg(q) e^{(\alpha/LT)\sqrt{q}} \left[e^{(\alpha/LT)\sqrt{q}} - 1 \right]^{-2} \quad (24)$$

One can remark that the specific heat of the photon gas tends to zero, when $T \rightarrow 0$.

The correction factors F , G , H of the thermodynamic functions are shown in the Fig. 6. We remark that, in the first approximation, all these factors can be considered almost equal.

The entropy is:
$$S = \sigma VT^3 [F(\alpha/LT) + (1/3)G(\alpha/LT)] \quad (25)$$

This expression for the entropy of the photon gas verifies the Nernst-Planck principle. From Fig. 5, one can see that $S \rightarrow 0$, when $LT \rightarrow 0$, but absolute zero can never attained (by the arguments for QCC given in the previous section).

The free enthalpy is:
$$\Phi \equiv E + pV - TS = (1/3) \sigma VT^4 [F(\alpha/LT) - G(\alpha/LT)] \quad (26)$$

The photon pressure can be calculated from the classical arguments up to the proportionality constant :

$$P = -(\delta F / \delta V)_T = (E/3V). \quad (27)$$

Then, one can write:
$$PV = E/3. \quad (28)$$

6. CONCLUDING REMARKS

In a cubic cavity, we have found *the discrete Planck radiation spectrum* for a quantum regime, defined by the level numbers $q \in [1, 100]$. In the quantum regime, the Planck spectrum is strongly dependent on the product of the cavity size by temperature $LT \in [0.1, 1]$ (CGS). The parameters L and T are *reciprocal*, in the sense that the same effects are obtained either by varying L or by varying T , if their product remains constant.

In QCC, there are a number of “antiresonant” (empty) levels, in which, only the zero-point energy is present. This effect can be measured (e.g. $L = 1\text{cm}$; $T = 1.35\text{K}$; $f = 79.3\text{ GHz}$; $Q = 465$).

The quantum effects could be observed for cubic cavities with macroscopic (but small) sizes, at temperatures around the liquid helium one.

The quantum regime is produced by the decrease of the cavity size (and temperature) to the limit where the size and geometry (i.e. the boundary conditions) are “felt” by the temporal spectrum of the cavity radiation. (In the continuous Planck spectrum, this effect is excluded by the assumption of the large cavity, implying the validity of Kirchhoff laws). In the discrete case, the quantum counting of the mode (state) number, taking into account the level degeneracy, is essential; thus, QCC could be called also *double-quantised cubic cavity*, as it allows *an entire number of energy quanta* to each mode and *some entire level numbers* (spatial orientations of the wavevectors).

In QCC, all thermodynamic functions of the photon gas are strongly modified by the discrete spectrum. We have demonstrated that the total energy does not respect any longer the Stefan-Boltzmann (S-B) law; particularly, the S-B “constant” becomes a function of LT and tends to zero, when LT tends to zero. The entropy and the specific heat tend to zero, when LT tends to zero, verifying the Nernst-Planck principle.

The quantum regime of the cubic cavity could be interesting for the interaction of a single atom with a single cavity mode, the microcavity light emitters, the quantum boxes and so on¹²⁻²⁴.

7. ACKNOWLEDGMENTS

One of the authors (V.I.V.) thanks to Professor Herbert Walther for the visits at the Max-Planck Institute of Quantum Optics, Garching (Germany) and to International Centre for Theoretical Physics, Trieste (Italy) for the visits as an Associate Member. These visits offered the optimum conditions for thinking and writing this paper.

8. REFERENCES

1. M. Planck, Ueber das Gesetz der Energieverteilung im Normalspektrum, Ann. d. Physik, **4**, 533-563 (1901); The Theory of Heat Radiation (Wärmestrahlung, 1913), Dover Publ. Inc., N.Y., 1959.
2. F. Reif, Fundamentals of Statistical and Thermal Physics, Mc Graw Hill, N.Y., 1965, p.373.
3. P. Morse and H. Feshbach, Methods of Theoretical Physics, Mc Graw Hill, N.Y., Part II, 1953, p.1434
4. Ch. Kittel and H. Kroemer, Thermal Physics, 2nd Ed, W.H. Freeman, San Francisco, 1980, p.92
5. H.M. Rosenberg, The Solid State, Oxford Univ. Press, 3d Ed., Oxford, 1992, p.83.
6. L. Landau and E. Lifschitz, Physique Statistique, Ed. Mir, Moscou, 1967, p.203-205
7. P.C. Reidi, Thermal Physics, 2nd Ed., Oxford Univ. Press, Oxford, 1988, p.241-243.
8. L. Pauling and E. Bright Wilson, Introduction to Quantum Mechanics, Mc Graw Hill, Tokyo, 1953, p.98-100.
9. J.-M. Levy-Leblond and F. Balibar, Quantics, North Holland Publ., Amsterdam, 1990, p.306.
10. B.E.A. Saleh and M.C. Teich, Fundamentals of Photonics, J. Wiley, N.Y., 1991, p.452.
11. W. Sierpinski, Elementary Theory of Numbers (A. Schintzel, Ed), North Holland Publ. & PWN, Amsterdam, 1988, p.391
12. K. Huang, Statistical Mechanics, 2d Ed, J. Wiley, N.Y., 1987
13. P. Stehle, Phys. Rev. A **2**, 102 (1970)

14. D. Meschede, H. Walther and G. Muller, Phys. Rev. Lett. **54**, 551(1985)
15. P. Filipovicz, P. Meystre, G. Rempe and H. Walther, Optica Acta, **32**, 1105(1985)
16. S. Haroche and J. Raimond, in "Adv. in Atomic and Molecular Physics", Vol.20, B. Bederman and D.R. Bates, Eds., Academic Press, N.Y., 1985;
17. P. Goy, J.M. Raimond, M. Gross and S. Haroche, Phys. Rev. Lett., **50**, 1903(1983)
18. F. De Martini, G. Innocenti, G.R. Jacobowitz and P. Mataloni, Phys. Rev. Lett., **59**, 2955(1987)
19. D.J. Heinzen, J.J. Child, J.E. Thomas and M.S. Feld, Phys. Rev. Lett., **58**, 1320(1987)
20. S.D. Brorson, H. Yokohama and E.P. Ippen, IEEE J. Quant. Electr. **QE-24**, 1492(1990)
21. G. Bjork, S. Machida, Y. Yamamoto and K. Igeta, Phys. Rev. A, **44**, 669(1991); and Ch.13 in "Coherence, Amplification and Quantum Effects in Semiconductor Lasers", Y. Yamamoto, Ed., J. Wiley, N.Y., 1991.
22. M. Yamanishi, Progr. Quant. Electr., **19**, 1-39(1995)
23. V.I. Vlad and N. Ionescu-Pallas, Ro. Repts. Phys., **48**, 1(1996)
24. V.I. Vlad and N. Ionescu-Pallas, ICTP Preprint IC/97/28, Miramare-Trieste, April 1997.

Photoinduced phenomena in chalcogenide glasses and their application in optoelectronics

Andrei Andriesh

Centre for Optoelectronics, Institute of Applied Physics, Academy of Sciences of the Republic of Moldova
1 Academiei str., MD-2028 Chisinau, Moldova Republic

ABSTRACT

The interaction of radiation with vitreous materials provokes irreversible and reversible changes of atomic and electronic structures. These changes in their turn manifest themselves in the experiment through changes of mechanical, thermal, optical, photoelectrical and other characteristics. Under the radiation influence the structure of vitreous materials changes, new defects appears, film crystallization or amorphization takes place, phase transition or transition from one unstable state to another.

It is evident that such changes radically influence the optical and photoelectrical properties of the material: the refraction index and other optical material constants change; reflection and absorption of light as well as photoelectric parameters. Of no less importance is the appearance of new possibilities for application of vitreous materials as optical and photoelectrical recording media, fibers and planar waveguides, active and passive elements of optoelectronics, including non-linear elements and sensors of different physical quantities. This paper covers a survey of works dedicated to the research of various photoinduced phenomena in bulk, thin-film and fiber samples of chalcogenide glassy semiconductors.

Keywords: chalcogenide glasses, photoconductivity, photoinduced absorption, localized states.

1. INTRODUCTION

The interaction of optical radiation with noncrystalline materials based upon chalcogenide glasses leads to modifications of their atomic and electronic structure which can bear both reversible and irreversible character. These modifications manifest themselves through changes in the materials' mechanical, thermic, electric, photoelectric, optical, etc., properties. As a result of optical radiation action, refraction index, reflection coefficient, absorption coefficient, etc., are changed. This permits to use the results of this kind of studies for both investigations connected with noncrystalline materials physics and multiple applications in optoelectronics.

The aim of the present paper is to demonstrate certain results achieved in the studies of reversible photoinduced phenomena such as photoinduced conductivity, photoinduced absorption, etc.

The models of explanation of these phenomena will be discussed, taking into consideration the multiple captivity of light-excited samples. The photoinduced phenomena in thin films and chalcogenide glass fibers are widely used in different photoelectric and optical appliances.

Certain photoinduced phenomena in optical planar or fiber waveguides will be demonstrated. The mechanism of photoinduced absorption in optical fiber will be analysed.

The photoinduced optical phenomena were also observed in the case when optical waveguides were excited by short-length laser pulse. Possible models of photoinduced phenomena resulting from ultra-short length laser pulse action are discussed.

2. PHOTOINDUCED CONDUCTIVITY

The effect of preliminary excitation on the value of conductivity in chalcogenide glasses was observed in the 1960s. The author [1] described the conditions of obtaining photoinduced conductive memory in Tl-As-Se-Te glasses. If the temperature of the samples was low enough to exclude thermal transitions of carriers from localized states to free bands, the excess of conductivity was observed for a long period of time after the illumination was stopped (Fig.1). In order to restore conductivity it is necessary to heat the sample or to expose it to infrared light. In the first case we deal with thermostimulated currents [2] and in the second case we deal with photostimulated currents [3].

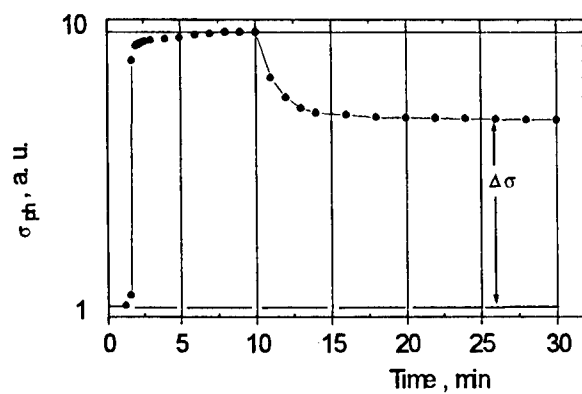


Fig.1. The change of photoconductivity of Tl-Se-As₂Te₃ during and after illumination (I~500.lux, T=105 K).

Of course, the major role of light excitation is manifested in the process under illumination. For example, spectral distribution of photoconductivity changes drastically when photoconductivity is measured in the conditions of constant illumination of the sample (Fig.2). These phenomena, as well as the numerous particulars of kinetics of photoconductivity convinced the authors [4] that the model of multiple trapping of carriers is very important for the explanation of the photoinduced conductivity in such materials.

In fact, in the process of light excitation a part of carriers are immediately captured by traps. This changes the values of conductivity, photoconductivity, and, in general, all transport phenomena. For example, a change of the drift mobility in the conditions of constant illumination of chalcogenide glasses was observed in As₂S₃ thin films by the authors [5].

3. PHOTOINDUCED ABSORPTION IN FIBERS

Taking into account our Conference's sphere of interests, the most important is the study of changes in the optical parameters of materials due to optical excitation. Due to a longer optical path, it is more favourable to study photoinduced absorption in fiber or planar waveguides.

The fibers made of As₂S₃, As-S-Se, As-Ge-S, As-Ge-Se chalcogenide glasses were fabricated. The probing light with a photon energy $h\nu < E_g$ was launched into the input face of the fiber. The intensity of the probing light transmitted through the fiber was measured at the output of the fibers. In the process of measuring of the output intensity of the probing light the

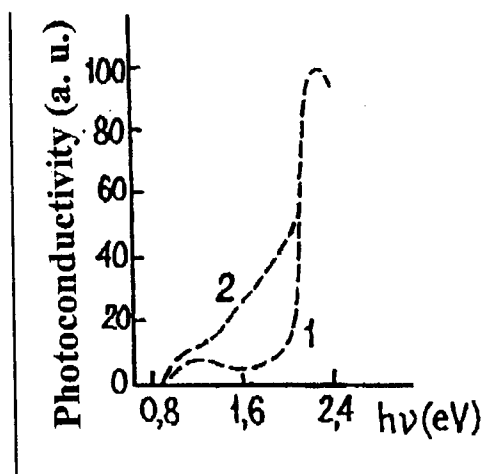


Fig. 2. Spectral distribution of photoconductivity of As_2S_3 thin films: 1 - without and 2 - with supplementary illumination.

fiber was exposed to lateral light (Fig.3). When the fiber was illuminated with bandgap light the intensity of the probing light at the output of the fiber decreased from its initial value (in the darkness) I_0 to a new one I because of photoinduced absorption manifestation. After the lateral illumination was stopped, a complete restoration of the initial optical transmittance of the fiber was observed [6].

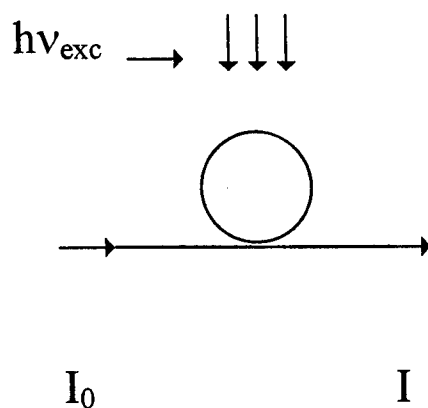


Fig. 3. Illustration of experimental set-up.

The restoration rate depends on the illumination conditions and glass composition. The spectral distribution of the photoinduced absorption measured in the range of the probing light 0.6-1.6 eV is presented in Fig.4 for As_2S_3 fibers. Similar dependencies were observed for As-S-Se and As-Ge-Se fibers.

We should note the exponential character of the spectral distribution of photoinduced absorption. Such a dependence is expected from the model with multiple trapping carriers in localized states distributed exponentially in the gap (Fig.5). The model explains other peculiarities of photoinduced absorption: the increase of photoinduced absorption depending on

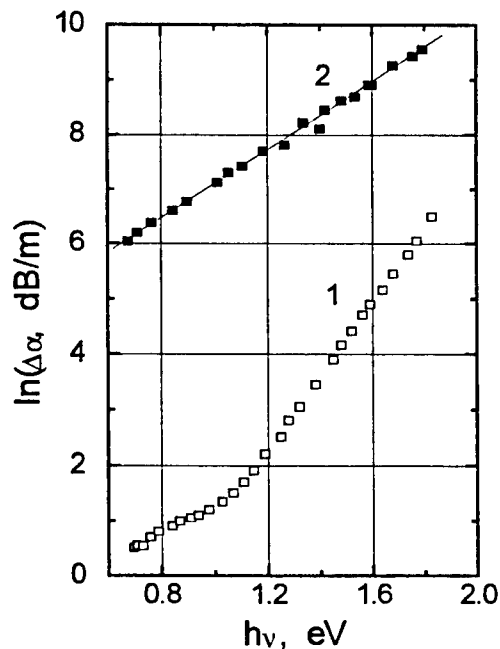


Fig.4. Spectral distribution of PA steady-state coefficient $\Delta\alpha$ in As_2S_3 fibers after irradiation with Ar laser

($\lambda_{\text{exc}} = 0.46 - 0.52 \mu\text{m}$). The intensity of exciting light $P_{\text{exc}} = 10 \text{ mW cm}^{-2}$.

The temperature T , K: 1 - 300; 2 - 77.

temperature decrease, as well as the increase of photoinduced absorption depending on the increase of lateral light intensity. As was shown in the paper [6] this could be confirmed by solving the kinetic equations which take into account all optical transitions occurring in accordance with the model with multiple trapping carriers (Fig.5).

The fact that the dependence of the steady-state photoabsorption coefficient has a power-law character, $\Delta\alpha \approx p^n$ ($n = 0.4-0.5$), which is very close to a square-root function, is of great interest. This could be used as the argument that photoabsorption excitations are recombined by a bulk bimolecular mechanism. Such a mechanism of recombination was confirmed by experiments for photoconductivity, too. In the process of photoinduced absorption, the excited carriers can contribute to conductivity. So there should exist relations between photoabsorption and conductivity. Orenstein and Kastner [7] have demonstrated that photoabsorption and drift mobility are related to the same localized carriers.

Following O'Connor and Tauc [8], Orenstein and Kastner [9], the authors [10], using the relations between photoinduced absorption and bimolecular coefficient, have determined the temperature dependence of the bimolecular coefficient ($b(T)$). At high temperatures the $b(T)$ coefficient exhibits an exponential character with activation energy equal to 0.6 eV at room temperature and 0.07 eV at low temperatures.

Taking into account the relation between the bimolecular coefficient and drift mobility

$$b = \frac{e}{\epsilon\epsilon_0} (\mu_n + \mu_p),$$

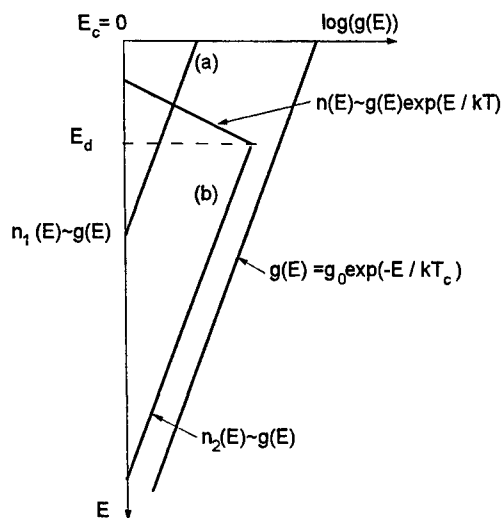


Fig. 5. The model with multiple trapping carriers in localized states.

as well as the fact that in chalcogenide glasses $\mu_n \ll \mu_p$, the authors [10] found out that the drift mobility has the same temperature dependence as the bimolecular coefficient (Fig.6). This character of the temperature dependence $\mu_p(T)$ correlates with experimental results obtained by Marshall and Owen [11] on the mobility of photoinduced holes in As_2Te_3 glasses.

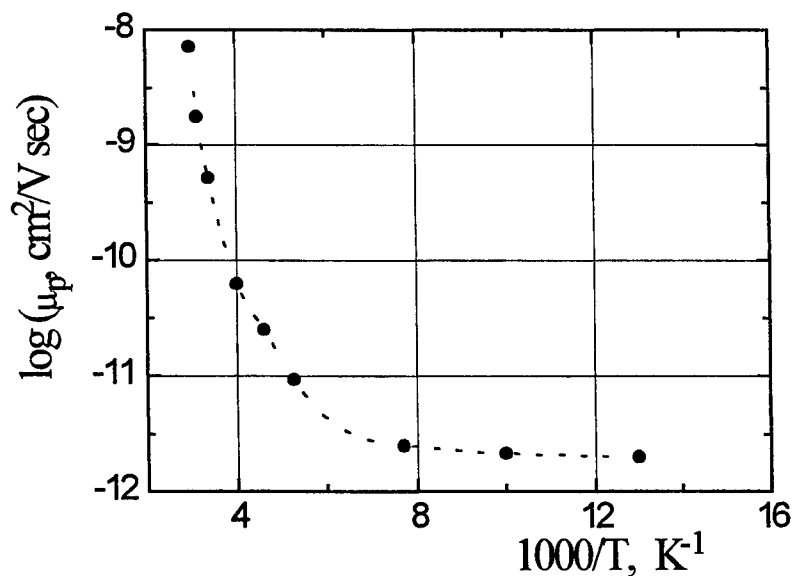


Fig. 6. Temperature dependence of drift mobility in AsS_3 glass.

The above-mentioned method of determining the temperature dependence of drift mobility is very important in the case of high-resistivity semiconductors for which traditional measurements are not acceptable, except for those conducted under high temperatures [10].

4. PHOTOINDUCED ABSORPTION IN THIN FILMS

In the above-mentioned experiments, the kinetics of photoinduced absorption of fibers was studied in the second range. Of course, in many cases there is the necessity to dispose of active optical elements for high-speed optical operations, which implies the need to study photoinduced phenomena in the range of short-time light exposition. This was done by the authors [12] who studied non-linear absorption in chalcogenide glass films in the femtosecond region for different conditions of the experiment using pump and probe light with the energy of kwants more or less than the energy gap. In this paper, only one case will be mentioned from the paper [12], when the energy of pump and probe light was less than the energy gap.

As₂S₃ films were used for the experiment, with the energy gap $\sim 2.4\text{eV}$, while pumping light was at 2.0 eV and probing light at 1.43 eV (Fig.7). After the sharp pulses with the 100 Fsec. duration which follow the shape of incident pulses, the flat part of the curves is observed which could be described by the time constants equal to 54 ps and 61 ps for high and low pumping energy, respectively.

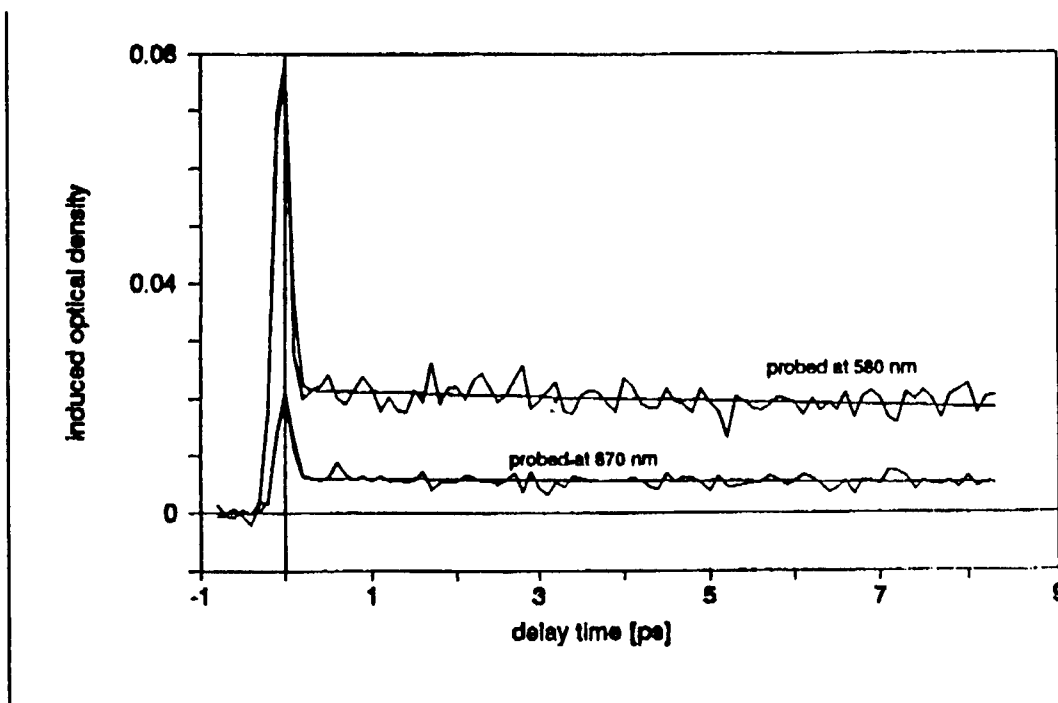


Fig.7. Absorption changes induced by 2.0 eV pulses on As₂S₃ and probed by 1.43 eV pulsed. The curves correspond to two different pumping energies 1.5 and 0.75 μJ .

The possible optical transitions are shown in Fig.8 which represents a three-level model. In this case there is a competition between two-photon and two-step absorption. The pumping can be excited by two-photon absorption carriers to level 1, but also to level 2 by one-photon transitions. Probe light can be absorbed by non-degenerate two-photon absorption to level 1 or through the 1 \rightarrow 2 or 1 \rightarrow higher energy transitions.

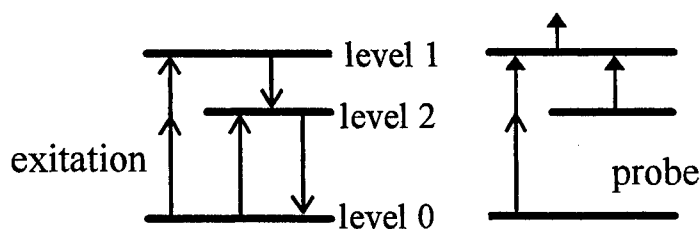


Fig.8. Scheme of the three-level system model.

The almost flat part of the curves confirms that the depletion of levels 2 occurs in a lengthy period of time (longer than 1 psec.), which allows carriers localized on the deep enough levels 2 to participate in the process of photoinduced absorption. Interpreting these results, the authors [12] suggested a bimolecular mechanism of recombination to be the case. The latter confirms that the suggestion as to the bimolecular mechanism of recombination made in order to determine the drift mobility characterized in the first part of the present paper was correct.

5. APPLICATION

A lot of devices based on the use of photoinduced phenomena in chalcogenide glasses were proposed. Only some of them will be mentioned in this paper. Photoinduced phenomena in chalcogenide glasses stimulated the interest of industry in the development of new informative multimedia technologies and systems for storage and treatment of great masses of information. These technologies are based on the holographic processes in thin films obtained from chalcogenide glasses. In order to increase the photosensitivity of the recording media, the layer-structure metal-thin film of chalcogenide glass-metal was proposed by the authors [13], which permits to produce the recording of optical information simultaneously at lighting and applying the electrical field to the recording structure. Application of an electrocontrolled process of the recording gives a possibility to considerably raise the photosensitivity of the media and diffraction efficiency of holograms. The recording process is carried out by the effects of electrostimulated deformation of the surface and electrostimulated chemical interaction of the chalcogenide glass thin film with a metal electrode when electrical field was applied under illumination.

Photoinduced phenomena in chalcogenide glassy fibers were utilized in order to propose a novel type of a variable fiber-optic attenuator [14]. It can be used in the visible and near infrared range of the spectrum in order to produce a continuous change of light intensity in fiber-optic circuits. If the lateral side of chalcogenide glass fiber is illuminated by the light with photon energy near the glass bandgap, a strong decrease of fiber-attenuating light at the output end of the fiber occurs changing the optical signal from its initial value I_0 (in the darkness) to a new one $I:I = I_0 \exp(\Delta\alpha L)$, where L is the length of the illuminated segment of the fiber and $\Delta\alpha$ is the photoabsorption coefficient. The proposed fiber-optic attenuator provides for attenuation in the range of 0÷20 dB in the 0.8÷1.8 μm wavelength range.

The chalcogenide glass thin films are promising materials for integrated optical devices, such as lenses, gratings, optical filters, multiplexors and demultiplexors, optical scanners and printer heads, multiple-output logic elements, etc. [15].

6. CONCLUSIONS

In the paper, some reversible photoinduced phenomena are described. First of all, photoinduced conductivity and photoconductivity were observed in chalcogenide glassy thin films. This allows to propose experiments aimed at the study of photoinduced absorption in fibers and thin films made of chalcogenide glasses. The latter, in their turn, permit to propose new optical devices, such as fiber attenuators, fiber sensors, planar waveguides, planar optical elements for integrated optics, etc.

7. REFERENCES

1. Andriesh A.M. (1968). Influence of the trapping levels on the decay of photoconductivity in vitreous $\text{Ti}_2\text{Se-As}_2\text{Te}_3$. In: Issledovania po poluprovodnikam. Kishinev, 105-108.
2. Andriesh A.M., Kolomiets B.T. (1964). Thermostimulated current in vitreous $\text{Ti}_2\text{Se-As}_2\text{Te}_3$. - Izvestia AN SSSR, seria fizicheskaya, 28, 1291-1292.
3. Kolomiets B.T., Mamontova T.N., Stepanov G.I. (1965) The fluctuation levels in vitreous semiconductor $\text{Ti}_2\text{Se-As}_2\text{Te}_3$. -Fiz.Tverd.Tela, 9, 27-32.
4. Arkhipov V., Rudenko A., Andriesh A., Iovu M., Shutov S. Nestatsionarnye inzhektionskiye toki vi neuporiadoceni materialah, Kishinev, 1983.
5. Andriesh A.M., Iovu M.S., Kolomeiko E.P., Tsiulyanu D.I., Shutov S.D. Investigation of hole transport in vitreous As_2S_3 .- Journal of Non-Crystalline Solids, 35 and 36 (1980), 981-986.
6. Andriesh A.M., Culeac I.P., Loghin V.M. Photoinduced changes of optical absorption in chalcogenide glass fibers. - Pure Appl.Opt., 1 (1992), 91-102.
7. Orenstein J., Kastner M., Phys.Rev.Lett., 43 (1979), p. 161.
8. O'Connor, J.Tauc. Photoinduced midgap absorption in tetrahedrally bounded amorphous semiconductors. - Physical Review B, vol.25, No 4, 1982, p.2748.
9. Orenstein J., Kastner M.A., Vaninov V. Transient photoconductivity and photoinduced optical absorption in amorphous semiconductors.Phil.Mag. B, 1982, vol.46, No 1, p.23.
10. Andriesh A.M., Culeac I.P., Ewen P.J.S., Owen A.B. The temperature dependence of time-averaged drift mobility in As_2S_3 glass derived from PA measurement. - Abstracts of the 17th International Conference on Amorphous and Microcrystalline Semiconductors. Budapest (Hungary), 25-29 August, 1997.
11. Marshall J.M., Owen A.E., Phil.Mag. 31 (1975), p.1341.
12. Fazio E., Hulin D., Chumash V., Michelotti F., Andrieah A.M., Bertolotti M. On-off resonance femtosecond non-linear absorption of chalcogenide glassy films.- Journal of Non-Crystalline Solids, 168 (1994), 213-222.
13. Andriesh A.M., Iovu M.S., Bivol V.V., Khanchevskaya E.G. Holographic Recording in Light-Sensitive Field Control Structures on Chalcogenide Vitreous Semiconductor Basis. - Optical Memory and Neural Networks. Vol.4, No 1, 1995.
14. Abashkin V., Andriesh A., Culeac I., Ponomar V. Method for light intensity control. Pat.USSR No.1336758 (08.05.1987).
15. Andriesh A.M., Ponomar V.V., Smirnov V.L., Mironos A.V. The use of chalcogenide glasses in the integrated and fiber optics (a review article).- "Kvantovaya elektronika", 13, No 6 (1986).

Thermooptic dispersion formula of AgGaSe₂ and its applications to thermal lensing effectsEiko Tanaka¹ and Kiyoshi Kato²¹Department of Computer Science, Keio University, Hiyoshi 3-14-1, Kohoku, Yokohama, Japan²Second Research Center, Japan Defence Agency, Ikejiri 1-2-24, Setagaya, Tokyo, Japan

ABSTRACT

The thermooptic constants of AgGaSe₂ have been measured at 2.052, 3.3913, 5.2955, and 10.5910μm. These results combined with the literature values were used to construct the thermooptic dispersion formula which correctly reproduces the temperature dependent phase-matching conditions for second-harmonic generation (SHG) and sum-frequency generation (SFG) of a CO₂ laser as well as the thermally induced lensing effects for the 2.05μm pumped parametric oscillators (OPO).

Keywords: AgGaSe₂, Sellmeier's equations, thermooptic constants, thermal conductivity, CO₂ laser, parametric oscillator.

1. INTRODUCTION

Although AgGaSe₂ has been used for high average power harmonic generation of a CO₂ laser¹ and parametric oscillation pumped by 2.05μm lasers^{2,3}, a large variation in the refractive indices caused by the residual absorption of the interacting wavelengths produces noticeable phase-mismatch and thermal lensing effects which prohibit ideal operation of harmonic generation and parametric oscillation. In worst case, these thermally induced effects lead to the catastrophic damage to the crystals. But no systematic study has so far been made for this deleterious effect. In addition, there has been considerable confusion over the published values of the thermooptic constants of this crystal⁴⁻⁷. Barnes et al^{4,5} reported

$d(n_o - n_e)/dT = -1.1 \times 10^{-6} \text{ } ^\circ\text{C}^{-1}$ for second-harmonic generation (SHG) of a CO₂ laser at 10.5910μm and

$d(n_o - n_e)/dT \cong +30 \times 10^{-6} \text{ } ^\circ\text{C}^{-1}$ at 3.3913μm. While Bhar et al^{6,7} reported the nondispersive value of

$d(n_o - n_e)/dT = -2.6 \times 10^{-6} \text{ } ^\circ\text{C}^{-1}$. In order to reconcile this large discrepancy encountered for the same compound, we have remeasured the thermooptic constants of this crystal at 2.052, 3.3913, 5.2955, and 10.5910μm using the well-established minimum deviation technique. Here we report the thermooptic dispersion formula of AgGaSe₂ which correctly reproduces the temperature dependent phase-matching conditions for second-harmonic generation (SHG) and sum-frequency generation (SFG) in the 2.65 - 5.30μm range as well as thermally induced lensing effect for the 2.05μm pumped parametric oscillators (OPO)^{2,3}.

2. EXPERIMENTS AND DISCUSSION

Using a Ho:YLF laser at 2.052μm, a He-Ne laser at 3.3913μm, and the fundamental and SHG of a CO₂ laser at 10.5910μm, we measured dn_o/dT and dn_e/dT between 20.0 and 120.0°C. The AgGaSe₂ prism used in this experiment was cut at an apex angle of 20.00° with a hypotenuous area of 10x15mm². The results obtained are shown in Fig.1 together with the data points at 3.3913μm presented by Barnes et al⁵ and those at 9.2824 - 10.5910μm given by Bhar et al^{6,7}. Note that there is an appreciable difference between the data points of Barnes et al⁵ and the present authors for the extraordinary ray at 3.3913μm. The origin of this discrepancy is not known. However, our data points lie on the smooth lines connecting several experimental points given by Bhar et al^{6,7}.

As in the case of KTiOPO₄ (KTP)⁸ and LiB₃O₅ (LBO)⁹, we have adjusted these raw data to give the best fit to the temperature phase-matching band-widths (FWHM) for SHG and SFG of the CO₂ laser tabulated in Table 1, in which we have also listed the published values of Barnes et al⁴ and Bhar et al^{6,7} at the corresponding wavelength. The phase-matching angles and the acceptance angles (FWHM) were calculated using the Sellmeier's equations of the present authors.^{10,11}

$$\begin{aligned} n_o^2 &= 6.8507 + \frac{0.4297}{\lambda^2 - 0.1584} - 0.00125\lambda^2 \\ n_e^2 &= 6.6792 + \frac{0.4597}{\lambda^2 - 0.2122} - 0.00126\lambda^2 \end{aligned} \quad (1)$$

where λ is in μm . The temperature phase-matching bandwidths (FWHM) were subsequently calculated using the following best-fitted thermo-optic formula:

$$\begin{aligned} dn_o/dT &= (0.046\lambda + 7.514) \times 10^{-5} (^\circ\text{C}^{-1}) \\ dn_e/dT &= (0.061\lambda + 7.984) \times 10^{-5} \end{aligned} \quad (2)$$

where λ is in μm . Agreement between theory and experiment is excellent. In addition, these two formulas correctly reproduce the temperature dependent phase-matching conditions for SHG of the CO_2 laser radiation at 10.1946 - 10.6114 μm above room temperature given by Bhar et al^{6,7} when their phase-matching angles at 24°C were amended with our index formula. However, since we were unable to reproduce precisely the data points of these authors at 9.2824 - 9.6039 μm , we have remeasured both the temperature variation of the SHG wavelengths at fixed crystal orientation and the phase-matching angles for doubling 9.2824, 9.5039 and 9.6036 μm . The results are shown in Figs.2 and 3 together with the amended values of Bhar et al^{6,7}.

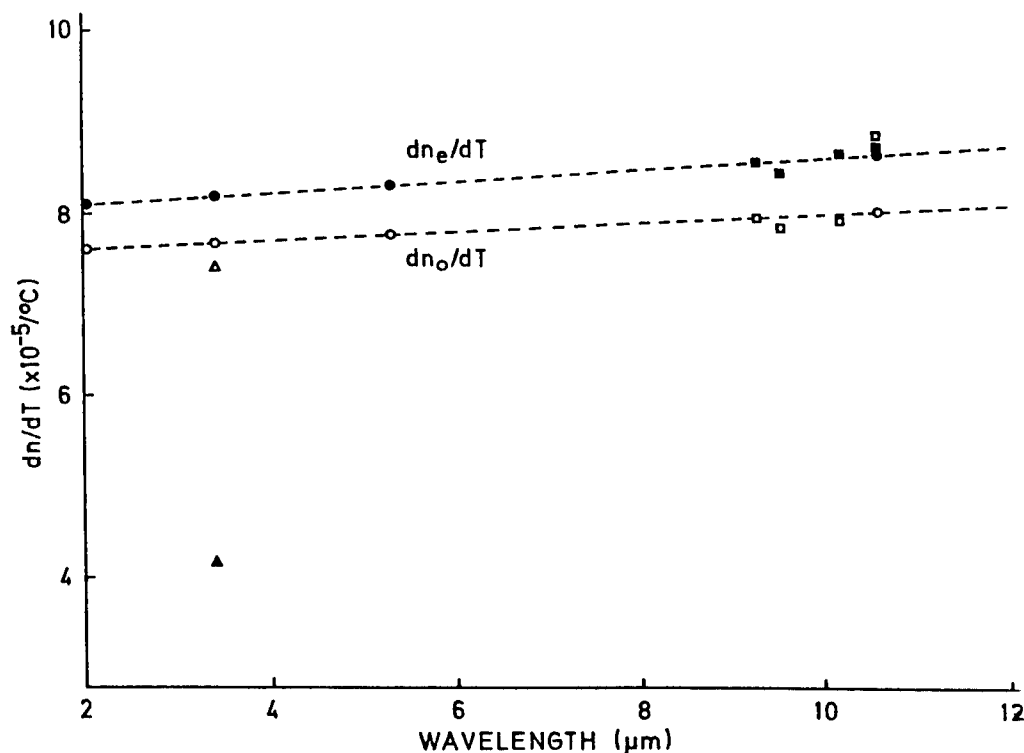


Fig. 1. Thermo-optic constants of AgGaSe_2 at room temperature.

Δ, \blacktriangle : experimental points given in Ref.5.

\square, \blacksquare : experimental points given in Refs. 6 and 7.

\circ, \bullet : experimental points.

Table 1. Temperature phase-matching bandwidths (FWHM) for second-harmonic and sum-frequency generation of the CO₂ laser frequency at 10.5910 μm in AgGaSe₂.

	λ_1 (μm) ^(a)	λ_2 (μm)	λ_3 (μm)	Phase-matching angle (deg)	$\Delta\theta_{\text{ext}} \cdot \ell$ (deg.cm)	$\Delta T \cdot \ell$ ($^{\circ}\text{C} \cdot \text{cm}$)		Ref.
SHG	10.5910	10.5910	5.2955	$\theta_{\text{ooo}}=55.5$	2.29	cal	obs	(5) (6),(7)
						351	350	
							428	
							364	
SFG	5.2955	5.2955	2.6478	$\theta_{\text{ooo}}=41.3$	1.11	225	230	
				$\theta_{\text{eoe}}=72.2$	3.94	254	260	
	10.5910	5.2955	3.5303	$\theta_{\text{ooo}}=42.4$	1.44	390	390	
				$\theta_{\text{eoe}}=56.6$	2.41	541	550	
	10.5910	3.5303	2.6478	$\theta_{\text{ooo}}=41.3$	1.11	225	220	
				$\theta_{\text{eoe}}=50.4$	1.53	257	260	

Note: (a) $1/\lambda_1 + 1/\lambda_2 = 1/\lambda_3$. (b) The subscripts of the phase-matching angle represent the polarization directions of the interacting wavelengths, in order.

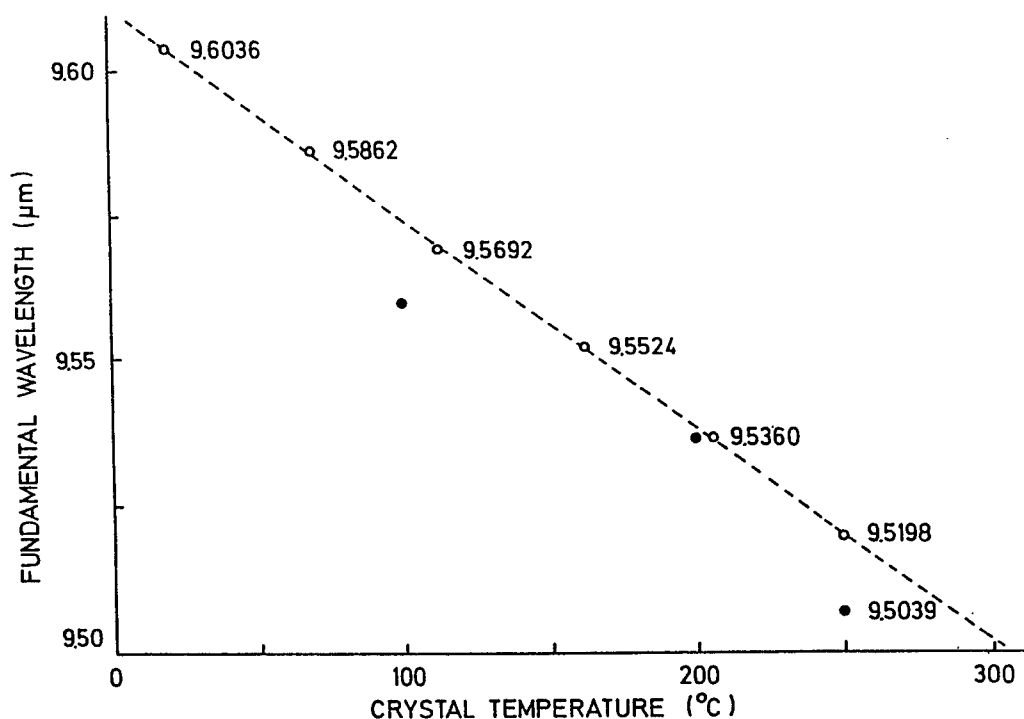


Fig. 2. Temperature variation of the phase - matching wavelength for SHG of a CO₂ laser at 9.5039 - 9.6039 μm in AgGaSe₂. The crystal is oriented at $\theta = 49.8^{\circ}$. The dashed line is calculated with the Sellmeier's equation and thermooptic dispersion formula presented in the text. ● : experimental points given in Ref.6. ○ : experimental points.

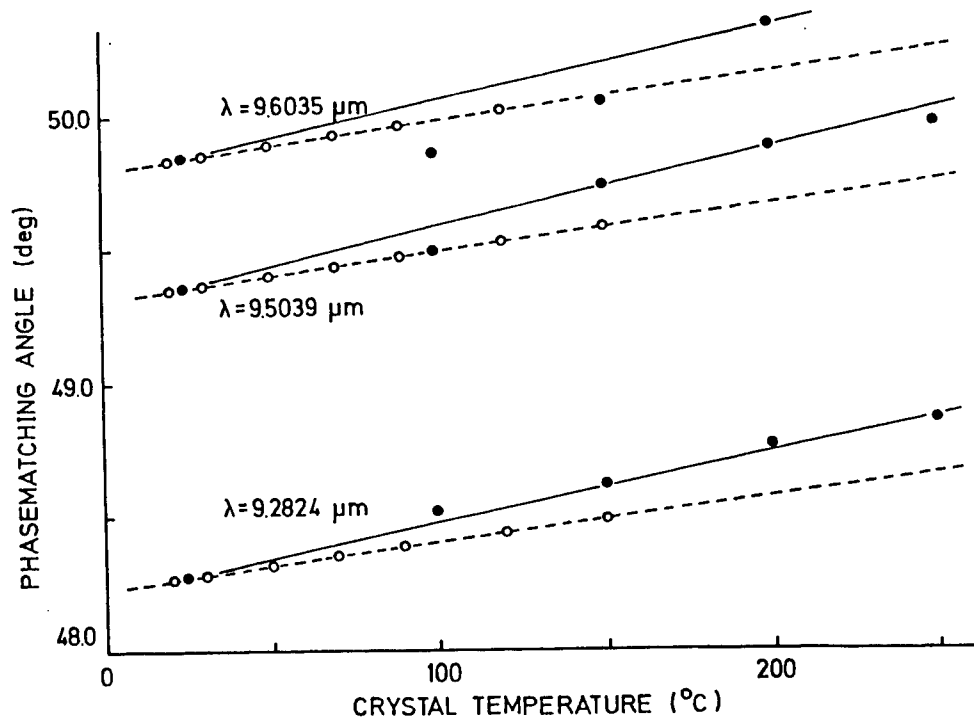


Fig. 3. Temperature variation of the phase-matching angle for SHG of a CO₂ laser at 9.2824, 9.5039, and 9.6039μm in AgGaSe₂. The dashed lines are calculated with the Sellmeier's equations and thermo-optic dispersion formula presented in the text. ● : experimental points given in Ref. 7. ○ : experimental points. These real lines are taken from Ref.7 and are inserted only for comparison.

The marginal disparity between these two experimental values may account for the tight focusing and the pump wavelength uncertainty of the previous measurements^{6,7}. For instance, the 10.2604μm point plotted in Fig.2 of Ref.6 should read 10.2744μm. Likewise, 9.56μm should read 9.5692μm as shown in Fig.2 of this paper. The present experiments were carried out with a well-defined, unfocused pump beam¹ to minimise the systematic error.

Although Barnes et al⁵ reported that both $\frac{dn_o}{dT}$ and $\frac{dn_e}{dT}$ decrease rapidly below about 150K by maintaining a constant $\frac{dB}{dT} = \frac{d(n_o - n_e)}{dT}$ the data points at 100K predict $\frac{d(n_o^1 - n_e^2(65.3^\circ))}{dT} = +(28 \pm 4) \times 10^{-5} \text{ } ^\circ\text{C}^{-1}$ for SHG of 10.5910μm, which contrasts sharply with their original value of $\frac{d(n_o^1 - n_e^2(\theta))}{dT} = -1.1 \times 10^{-6} \text{ } ^\circ\text{C}^{-1}$.⁴ Our calculated value of $\frac{d(n_o^1 - n_e^2(55.0^\circ))}{dT} = -1.36 \times 10^{-6} \text{ } ^\circ\text{C}^{-1}$ is in much closer agreement with the latter and a 15% decrease in both $\frac{dn_o}{dT}$ and $\frac{dn_e}{dT}$ at 10.5910 and 5.2955μm can settle this most important data for SHG at low temperature.

The amended phase-matching angle of $\theta_{pm} = 55.05^\circ$ at 100K reproduces correctly Barnes et al's data⁴ of

$$\Delta\theta_{pm} = \theta_{pm}(298K) - \theta_{pm}(100K) = 0.41^\circ \text{ and } \Delta T \cdot \ell = 428^\circ \text{C} \cdot \text{cm (Table 1).}$$

In order to verify further the validity of our index thermo-optic dispersion formulas, we next have calculated the focal length of the thermal lens for the 2.05 μm pumped OPO. In contrast to the thermally induced phase-mismatch that depends on the difference in the thermo-optic constants of ordinary and extraordinary polarization, the thermally induced lensing can depend on one of these parameters.

The focal length of the nonlinear crystal for radial heat extraction is given by the following expression¹².

$$f = \frac{\pi \omega_p^2 K_s}{\alpha \ell P (dn/dT) \ln 2} \quad (3)$$

where α is the absorption coefficient at the pump wavelength, ℓ is the crystal length, $K_s (= 0.011 \text{ W/cm K})$ ¹³ is the thermal conductivity at room temperature, dn/dT is the thermo-optic constant at the pump wavelength, P is the pump power, and ω_p is the pump beam radius.

Using our calculated thermo-optic constant of $dn_e(\theta = 49.1^\circ)/dT = 7.90 \times 10^{-5} ^\circ\text{C}^{-1}$ at 2.05 μm and the other physical parameters given by Budni et al² and Marquart et al³ for two separate experiments, we found $f = 3.2 \text{ cm}$ for the former and $f = 25 \text{ cm}$ for the latter, which are in excellent agreement with the observed values of $f \cong 3.0 \text{ cm}^2$ and $f = (24 \pm 3) \text{ cm}^3$ at 21 $^\circ\text{C}$, respectively.

Since the thermo-optic constants given by Bhar et al^{6,7} and the present authors exhibited no measurable temperature variation in the 2.052 - 10.5910 μm range above room temperature, the alleviation of the thermal lensing observed below room temperature³ might be largely attributed to the rapid increase in the conductivity¹⁴ rather than the decrease in dn/dT ⁵ as the temperature is lowered. If we assume the thermal conductivity of AgGaSe_2 changes as

$$K_s = 9.8 \times 10^{-2} T^{-1/2} \exp[\theta/T] \text{ (W/cm} \cdot \text{K)} \quad (4)$$

where $\theta = 193 \text{ K}$ is the Debye temperature at 298K inferred from the calculated values of Abrahams and Hsu¹⁵, we found $f = 41 \text{ cm}$ at 195K and $f = 298 \text{ cm}$ at 77K, which are in close agreement with the experimental values given by Marquart et al³. In addition, the aforementioned 15% decrease in dn/dT can assess a perfect agreement between theory and experiment.

Finally, we note that the absorption coefficient of AgGaSe_2 is nearly temperature independent at 2.05 μm ¹⁶, but it is highly temperature dependent for the ordinary polarization at 10.5910 μm ⁷ and hence the high-quality crystals are essential for the stable operation of high average power SHG and third-harmonic generation (THG) of the CO_2 laser¹ to avoid the abrupt heating and subsequent crack and/or fracture due to the highly anisotropic thermal expansion¹⁷.

3. CONCLUSIONS

We have reported the high-accuracy Sellmeier's equations and the thermo-optic dispersion formula of AgGaSe_2 which correctly reproduce the temperature dependent phase-matching conditions for harmonic generation of the CO_2 laser as well as the thermally induced lensing effect for the 2.05 μm pumped OPO at 77 - 294K^{2,3}. We believe that these two formulas are highly useful for designing the temperature stable, high average power frequency conversion system based on AgGaSe_2 .

4. ACKNOWLEDGEMENT

The authors wish to thank David Roberts for his valuable discussions on AgGaSe₂.

5. REFERENCES

1. A.Harasaki, J.Sakuma, T.Itoh, T.Satoh, M.Sugii, T.Sakuma, and K.Kato, "High-average-power mid-IR laser obtained by frequency-doubling a TEA-CO₂ MOPA system by using AgGaSe₂ crystals", *Dig.Tech.Papers. CLEO'95*, paper CTuO3. We recently generated an average output power of 3.9W for SHG and 2.2W for THG at a fundamental pump power of 22W(360mJ/pulse at 60Hz).
2. P.A.Budni, M.G.Knights, E.P.Chicklis, and K.L.Schepler, "Kilohertz AgGaSe₂ optical parametric oscillator pumped at 2 μ m", *Opt. Lett.*, **18**, 1068 - 1079 (1993).
3. C.L.Marquardt, D.G.Cooper, P.A.Budni, M.G.Knights, K.L.Schepler, R.DeDomenico, and G.C.Catella, "Thermal lensing parametric oscillator crystals", *Appl.Opt.*, **33**, 3192 - 3197 (1994).
4. N.P.Barnes, R.C.Eckardt, D.J.Gettemy, and L.B.Edgett, "Absorption coefficients and the temperature variation of refractive index difference of nonlinear optical crystals", *IEEE J.Quantum Electron.*, **15**, 1074 - 1076 (1979).
5. N.P.Barnes, D.J.Gettemy, J.R.Hietanen, and R.A.Iannini, "Parametric oscillation in AgGaSe₂", *Appl.Opt.*, **28**, 5162 - 5168 (1989).
6. G.C.Bhar, S.Das, U.Chatterjee, A.M.Rudra, R.K.Route, and R.S.Feigelson, "Temperature effects in second harmonic generation in AgGaSe₂ crystals", *J.Appl.Phys.*, **74**, 5282 - 5284 (1993).
7. G.C.Bhar, S.Das, U.Chatterjee, A.M.Rudra, R.K.Route, and R.S.Feigelson, "Evaluation of AgGaSe₂ temperature - dependent nonlinear devices", *J.Phys.D*, **27**, 231 - 234 (1994).
8. K.Kato, "Temperature insensitive SHG at 0.5321 μ m in KTP", *IEEE J.Quantum Electron.*, **28**, 1974 - 1976 (1992).
9. K.Kato, "Temperature - tuned 90° phase - matching properties of LiB₃O₅", *IEEE J.Quantum Electron.*, **30**, 2950 - 2952 (1994).
10. K.Kato, H.Komine, J.M.Fukumoto, W.H.Long Jr., and E.A.Stappert, "Noncritically phase matched mid - infrared generation in AgGaSe₂", *IEEE Select.Topics in Quantum Electron.*, **1**, 44 - 49 (1995).
11. A. Harasaki and K.Kato, "New data on nonlinear optical constant, phase-matching, and optical damage in AgGaSe₂", *Jpn.J.Appl.Phys.*, **36**, 700 - 703 (1997).
12. N.P.Barnes and J.Williams - byrd, "Average power effects in parametric oscillator and amplifiers", *J.Opt.Soc.Am.B*, **12**, 124 - 131 (1995).
13. J.D.Beasley, "Thermal conductivities of some novel nonlinear optical materials", *Appl.Opt.*, **33**, 1000 - 1003 (1994).
14. A.S.Borshchevskii, N.A.Goryunova, F.P.Kesamanly, and D.N.Naslenov, "Semiconducting A^{III}B^{IV}C^V₂ compounds", *Phys. Status Solidi*, **21**, 9 - 55 (1967).
15. S.C.Abrahams and F.S.L.Hsu, "Debye temperature and cohesive properties", *J.Chem.Phys.*, **63**, 1162 - 1165 (1975).
16. G.C.Catella, L.R.Shiozawa, J.R.Hietanen, R.C.Eckardt, R.K.Route, and R.S.Feigelson, "Mid - IR absorption in AgGaSe₂ optical parametric oscillator crystals", *Appl.Opt.*, **32**, 3948 - 3951 (1993).
17. D.Eimerl, J.Marion, E.K.Graham, H.A.McKinstry, and S.Haussuhl, "Elastic constants and thermal fracture of AgGaSe₂ and d - LAP", *IEEE J.Quantum Electron.*, **27**, 142 - 145 (1991).

The possibility of two-photon superradiance in microcavities

M. Macovei and N. Enaki

Institute of Applied Physics, Academy of Sciences of Moldova,
Academiei str. 5, Kishinev MD-2028, Moldova

ABSTRACT

We analyze the two-photon cooperative emission of excited atoms in microcavities with dimensions of the order of the emission wavelength. Here the two-photon dipole-forbidden transitions between the upper and the ground states of the three-level system are possible through the intermediate level that is off resonance with microcavity modes. In this situation one obtains the powerful pulse of two-photon highly correlated light. The superbunching phenomenon in radiated field is also discussed.

Keywords: quantum optics, Born-Markoff approximation, spontaneous emission in microcavities

1. INTRODUCTION

The radiative decay of atoms in the cavity is one of the central problems in quantum optics. In the recent years many interesting quantum effects have been studied such as the photon antibunching and squeezing for a single atom in a resonant cavity¹, stationary two-level atomic inversion in a quantized cavity field², suppression of spontaneous emission by squeezed light in a cavity³ and cavity - modified spontaneous emission⁴. It is well known that spontaneous emission inside a cavity brings its own surprises. The emission rate is inhibited in a cavity with dimensions small compared to the transition wavelength and enhanced in a resonant cavity.

In Refs. 5-7 it has been investigated for the first time the quantum oscillator working on a two-photon stimulated emission of radiation between Rydberg levels. Recently the enhanced two-photon decay has been observed in an electric dipole transition between two Rydberg levels coupled to a single mode of a strongly driven microwave cavity⁸.

In this article, we study the cooperative emission of an ensemble of N Rydberg atoms in microcavities. We consider a three - level atomic system in a cascade configuration with the intermediate level arbitrarily detuned from the microcavity modes (see Fig. 1a). In this situation, the amplification of two-photon spontaneous emission of Rydberg atoms inverted with respect to the dipole-forbidden $|2\rangle \rightarrow |1\rangle$ ($d_{21} = 0$) transitions occurs. Because we study the superfluorescence in microcavities we put here the problem of possibility of using the Born-Markoff approximation. We use the Born-Markoff approximation in the bad cavity limit and we suppose that the number of cavity modes is large and are off resonance with the intermediate level. These conditions are fulfilled when the biphotons pairs leave the cavity very quickly. In this approximation the time-behaviour of inverted system of radiators relative to dipole-forbidden transition $|2\rangle \rightarrow |1\rangle$ is similar to two-photon superradiance of Λ -type three level atomic system in free space. But the intensity of cooperative emission strongly depends on the coupling of atomic system with microcavity modes.

2. MASTER EQUATION

We study an inverted three-level atomic system interacting with cavity modes. At the initial time $t = 0$ all atoms are excited in the $|2\rangle$ state. In this model one consider that the intermediate level $|3\rangle$ is off resonant with the cavity modes (see Fig. 1a).

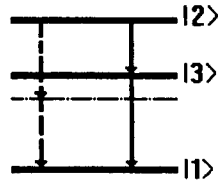


Fig. 1a Indication of two one-photon emission (solid lines) and two-photon dipole forbidden transitions (broken lines) in a cascade three-level system. Here the microcavity mode is plotted by the dash-dotted line.

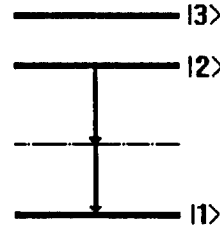


Fig. 1b The two-photon transitions in the Λ -type three level system in a microcavity.

The master equation for the density operator of the cavity electromagnetic field (EMF) modes and inverted atoms is obtained by utilizing standard techniques described in Ref. 9.

$$\frac{\partial \rho(t)}{\partial t} = -\frac{i}{\hbar}[H, \rho(t)] + \Lambda \rho(t), \quad (1)$$

where the Hamiltonian H describes the interaction of the atoms with cavity modes and can be written as

$$H = \sum_{\kappa} \hbar \omega_{\kappa} a_{\kappa}^{\dagger} a_{\kappa} + \sum_{\alpha=1}^3 \sum_{j=1}^N \hbar \omega_{\alpha} U_{j\alpha}^{\alpha} + i \sum_{\beta=1}^2 \sum_k \sum_{j=1}^N (\vec{d}_{3\beta}, \vec{g}_k) (a_k e^{i\vec{k}\vec{r}_j} - h.c.) (U_{j3}^{\beta} + U_{j\beta}^3); \quad (2)$$

$$\Lambda \rho(t) = \sum_{\kappa} G(\kappa) \{ [a_{\kappa} \rho(t), a_{\kappa}^{\dagger}] + h.c. \}. \quad (3)$$

Here the first and second term in Eq. (2) are the free cavity EMF and the free atomic Hamiltonians, respectively. The third term describes the interaction between the atomic system and cavity EMF. The loss of photons from microcavity modes is described by Eq. (3). We have introduced the

following notations in Eqs. (1-3): $\hbar\omega_\alpha$ ($\alpha = 1, 2, 3$) is the energy of level α , $d_{3\beta}$ is the dipole moment of the transition between the states $|3\rangle$ and $|\beta\rangle$ ($\beta = 1, 2$), a_κ^+ and a_κ are the creation and annihilation operators for cavity photons with momentum $\hbar\vec{\kappa}$, energy $\hbar\omega_\kappa$ and polarization λ , $\vec{g}_\kappa = (2\pi\hbar\omega_\kappa/V)^{1/2}\vec{e}_\lambda$, \vec{e}_λ is the photon polarization vector ($\lambda = 1, 2$), V is the cavity volume, $U_{j\beta}^3$ is the corresponding operator of the transition between states $|3\rangle$ and $|\beta\rangle$ of the j -th atom, $K(\kappa)$ is the energy relaxation rate from κ cavity mode, N is the number of atoms in the microcavity. The operators of the atomic subsystem and the EMF operators satisfy the commutation relations

$$[U_{j\beta}^\alpha, U_{l\alpha'}^{\beta'}] = \delta_{j,l}[\delta_{\beta\beta'}U_{j\alpha}^\alpha - \delta_{\alpha\alpha'}U_{j\beta}^{\beta'}], \quad [a_\kappa, a_{\kappa'}^+] = \delta_{\kappa\kappa'}, \quad [a_\kappa^+, a_{\kappa'}^+] = [a_\kappa, a_{\kappa'}] = 0.$$

Next we are interested in the time-behaviour of an arbitrary atomic operator $O(t)$ in the process of spontaneous emission. Using the master equation (1) one can obtain the following Heisenberg equation for the mean value of the operator $O(t)$

$$\begin{aligned} \frac{d}{dt} \langle O(t) \rangle &= \frac{i}{\hbar} \sum_{\alpha=1}^3 \sum_{j=1}^N \hbar\omega_\alpha \langle [U_{j\alpha}^\alpha(t), O(t)] \rangle \\ &- \sum_{\kappa} \sum_{j=1}^N \sum_{\beta=1}^2 \frac{(\vec{d}_{3\beta}, \vec{g}_\kappa)}{\hbar} \langle a_\kappa^+ [U_{j\beta}^3(t) + U_{j3}^\beta(t), O(t)] \rangle e^{-i(\vec{\kappa}, \vec{r}_j)} + h.c., \end{aligned} \quad (4)$$

The formal solution for a_κ, a_κ^+ cavity field operators can be obtained from the Heisenberg equation:

$$a_\kappa(t) = a_\kappa^v(t) + a_\kappa^s(t), \quad a_\kappa^+(t) = (a_\kappa(t))^+, \quad (5)$$

where $a_\kappa^v(t) = a_\kappa^v(0)e^{-i(\omega_\kappa - iK(\kappa))t}$ and

$$a_\kappa^s(t) = \sum_{j=1}^N \sum_{\beta=1}^2 \frac{(\vec{d}_{3\beta}, \vec{g}_\kappa)}{\hbar} e^{-i(\vec{\kappa}, \vec{r}_j)} \int_0^t d\tau e^{-i(\omega_\kappa - iK(\kappa))\tau} (U_{j\beta}^3(t-\tau) + U_{j3}^\beta(t-\tau))$$

are the vacuum and source parts of the operator $a_\kappa(t)$. If we substitute Eq. (5) for $a_\kappa(t)$ and $a_\kappa^+(t)$ in Eq. (4) one obtains the following equation for the mean value of the operator $O(t)$

$$\begin{aligned} \frac{d}{dt} \langle O(t) \rangle &= i \sum_{\alpha=1}^3 \sum_{j=1}^N \omega_\alpha \langle [U_{j\alpha}^\alpha(t), O(t)] \rangle - \sum_{\kappa} \sum_{j,l=1}^N \sum_{\alpha,\beta=1}^2 \frac{(\vec{d}_{3\beta}, \vec{g}_\kappa)(\vec{d}_{3\alpha}, \vec{g}_\kappa)}{\hbar^2} (e^{-i(\vec{\kappa}, \vec{r}_j - \vec{r}_l)} \\ &\times \int_0^t d\tau e^{i(\omega_\kappa + i\gamma_\kappa)\tau} \langle (U_{l\alpha}^3(t-\tau) + U_{l3}^\alpha(t-\tau)) [U_{j\beta}^3(t) + U_{j3}^\beta(t), O(t)] \rangle + h.c.) \end{aligned} \quad (6)$$

As the level $|3\rangle$ is off from resonance with the cavity mode, the transitions from the upper state $|2\rangle$ to the ground state $|1\rangle$ take place through the virtual state $|3\rangle$. To take into account such transitions we express the atomic operators $U_{l\alpha}^3(t-\tau)$ and $U_{3l}^\alpha(t-\tau)$ via atomic operators U_1^2 and U_2^1 :

$$\begin{aligned} U_{l\alpha}^3(t-\tau) &= U_{l\alpha}^3(t) e^{-i\omega_{3\alpha}\tau} + \sum_{\kappa} \sum_{\beta=1}^2 \frac{(\vec{g}_\kappa, \vec{d}_{3\beta})}{\hbar} \int_0^\tau d\theta e^{-i\omega_{3\alpha}\theta} \\ &\times \{ a_\kappa^+(t-\tau+\theta) e^{-i(\vec{\kappa}, \vec{r}_l)} - a_\kappa(t-\tau+\theta) e^{i(\vec{\kappa}, \vec{r}_l)} \} U_{l\alpha}^\beta(t-\tau+\theta) \end{aligned} \quad (7)$$

After substitution of Eq. (7) in Eq. (6) we obtain the two kind of transitions: (a) through the real state $|3\rangle$, and (b) through the virtual state $|3\rangle$. The transition through the real level $|3\rangle$ is described by the first term of Eq. (7), and the virtual transition is described by the second term of the same expression. In the bad cavity limit ($K(\kappa) > \tau_{ex}^{-1}$, τ_{ex}^{-1} is the atomic decay rate) and the relatively large number of cavity modes one can use the Born-Markoff approximation. In this case we obtain the following equation for the operator $O(t)$:

$$\begin{aligned}
\frac{d}{dt} \langle O(t) \rangle &= i \sum_{j=1}^N \sum_{\alpha=1}^3 \omega_{\alpha} \langle [U_{\alpha}^{\alpha}(t), O(t)] \rangle \\
&- \left(\frac{1}{\hbar^2} \sum_{j,l=1}^N \sum_{\kappa} e^{-i(\vec{\kappa}, \vec{r}_j - \vec{r}_l)} \{ (\vec{g}_{\kappa}, d_{32})^2 \frac{K(\kappa) + i(\omega_{\kappa} - \omega_{23})}{K^2(\kappa) + (\omega_{\kappa} - \omega_{23})^2} \langle U_{l3}^2(t) [U_{j2}^3(t), O(t)] \rangle \right. \\
&+ (\vec{g}_{\kappa}, \vec{d}_{31})^2 \frac{K(\kappa) + i(\omega_{\kappa} + \omega_{31})}{K^2(\kappa) + (\omega_{\kappa} + \omega_{31})^2} \langle U_{l3}^1(t) [U_{j1}^3(t), O(t)] \rangle \} \\
&+ \frac{1}{\hbar^4} \sum_{j,l=1}^N \sum_{\kappa_1 \kappa_2} e^{-i(\vec{\kappa}_1 + \vec{\kappa}_2, \vec{r}_j - \vec{r}_l)} \\
&\times \left\{ \frac{(\vec{g}_{\kappa_1}, \vec{d}_{31})(\vec{g}_{\kappa_2}, \vec{d}_{32})}{\omega_{23} - \omega_{\kappa_2}} - \frac{(\vec{g}_{\kappa_1}, \vec{d}_{32})(\vec{g}_{\kappa_2}, \vec{d}_{31})}{\omega_{31} - \omega_{\kappa_2}} \right\}^2 \frac{K(\kappa_1) + i(\omega_{\kappa_1} + \omega_{\kappa_2} - \omega_{21})}{K^2(\kappa_1) + (\omega_{\kappa_1} + \omega_{\kappa_2} - \omega_{21})^2} \\
&\times \langle U_{l1}^2(t) [U_{2j}^1(t), O(t)] \rangle + h.c. \quad (8)
\end{aligned}$$

The second and the third term describe the two one-photon cascade emission and two-photon dipole-forbidden transition in cavity modes, respectively.

3. TWO-PHOTON AND TWO ONE-PHOTON COOPERATIVE EMISSION

In Eq. (8) one can neglect the last term in case when the cavity modes are in resonance with the level $|3\rangle$. In this case it is possible to obtain the Dicke solvable model of superradiance¹⁰. When $\omega_{23} = \omega_{31} = \omega_0$, $d_{23} = d_{31} = d$, the behaviour of the atomic system in microcavity can be described by more simple operators of the $SU(2)$ algebra:

$$D_{zj} = U_{2j}^2 - U_{1j}^1, \quad D_j^+ = \sqrt{2}(U_{3j}^2 + U_{1j}^3), \quad D_j^- = \sqrt{2}(U_{2j}^3 + U_{3j}^1).$$

Here D_j^+ and D_j^- are the excitation and deexcitation operators of the j -th atom in the process of cascade transitions; D_{zj} is the population difference between the levels $|2\rangle$ and $|1\rangle$. The following chain of equations can be obtained from Eq. (8):

$$\begin{aligned}
\frac{d}{dt} \langle D_z(t) \rangle &= - \sum_{\kappa} \sum_{l,j=1}^N \frac{(\vec{g}_{\kappa}, \vec{d})^2}{\hbar^2} e^{-i(\vec{\kappa}, \vec{r}_j - \vec{r}_l)} \langle D_l^+(t) D_j^-(t) \rangle \frac{K(\kappa)}{K^2(\kappa) + (\omega_{\kappa} - \omega_0)^2} \\
\frac{d}{dt} \langle D_j^+(t) D_n^-(t) \rangle &= \sum_{\kappa} \sum_{l=1}^N \frac{(\vec{g}_{\kappa}, \vec{d})^2}{\hbar^2} \{ e^{-i(\vec{\kappa}, \vec{r}_j - \vec{r}_l)} \frac{1}{i(\omega_{\kappa} - \omega_0 - iK(\kappa))} \langle D_l^+(t) D_{zj} D_n^-(t) \rangle \\
&+ e^{i(\vec{\kappa}, \vec{r}_n - \vec{r}_l)} \frac{1}{-i(\omega_{\kappa} - \omega_0 + iK(\kappa))} \langle D_j^+(t) D_{zn} D_l^-(t) \rangle \}. \quad (9)
\end{aligned}$$

Neglecting the fluctuations of the operators $D_{zj}(t)$ in the case of concentrated atomic system (the dimension L of the atomic system is much less than the emission wavelength λ) the solution of the decoupled chain (9) is

$$D_z(t) = -N \tanh\left(\frac{t - t_0}{2\tau_r}\right).$$

Here τ_r and $t_0 = \tau_r \ln N$ are the cooperative emission time and the delay time, respectively:

$$\frac{1}{\tau_r} = 2N \sum_{\kappa} \frac{(\vec{g}_{\kappa}, \vec{d})^2}{\hbar^2} \frac{K(\kappa)}{K^2(\kappa) + (\omega_{\kappa} - \omega_0)^2}.$$

With increasing the detuning $(\omega_{\kappa} - \omega_0)$, the two one-photon cascade emission is substantially inhibited.

If the cavity modes are off resonance with the state $|3\rangle$ and the energy distance between the different energy modes is larger than the natural width of the level $|3\rangle$, the contribution of two one-photon emission is negligible and true two-photon transition occurs. In this situation we obtain another chain of equations for the atomic subsystem:

$$\begin{aligned} \frac{d}{dt} \langle R_z(t) \rangle &= -\frac{1}{\hbar^4} \sum_{\kappa_1 \kappa_2} \sum_{j,l=1}^N e^{-i(\vec{\kappa}_1 + \vec{\kappa}_2, \vec{r}_j - \vec{r}_l)} \left\{ \frac{(\vec{g}_{\kappa_1}, \vec{d}_{31})(\vec{g}_{\kappa_2}, \vec{d}_{32})}{\omega_{23} - \omega_{\kappa_2}} - \frac{(\vec{g}_{\kappa_1}, \vec{d}_{32})(\vec{g}_{\kappa_2}, \vec{d}_{31})}{\omega_{31} - \omega_{\kappa_2}} \right\}^2 \\ &\times \frac{K(\kappa_1)}{K^2(\kappa_1) + (\omega_{\kappa_1} + \omega_{\kappa_2} - \omega_{21})^2} \langle R_l^+(t) R_j^-(t) \rangle + h.c. \\ \frac{d}{dt} \langle R_i^+(t) R_j^-(t) \rangle &= \frac{2}{\hbar^4} \sum_{\kappa_1 \kappa_2} \sum_{l=1}^N \left\{ \frac{(\vec{g}_{\kappa_1}, \vec{d}_{31})(\vec{g}_{\kappa_2}, \vec{d}_{32})}{\omega_{23} - \omega_{\kappa_2}} - \frac{(\vec{g}_{\kappa_1}, \vec{d}_{32})(\vec{g}_{\kappa_2}, \vec{d}_{31})}{\omega_{31} - \omega_{\kappa_2}} \right\}^2 \\ &\times \left\{ \frac{e^{-i(\vec{\kappa}_1 + \vec{\kappa}_2, \vec{r}_i - \vec{r}_l)}}{i(\omega_{\kappa_1} + \omega_{\kappa_2} - \omega_{21} - iK(\kappa_1))} \langle R_l^+(t) R_{zi}(t) R_j^-(t) \rangle \right. \\ &+ \left. \frac{e^{i(\vec{\kappa}_1 + \vec{\kappa}_2, \vec{r}_j - \vec{r}_l)}}{-i(\omega_{\kappa_1} + \omega_{\kappa_2} - \omega_{21} + iK(\kappa_1))} \langle R_i^+(t) R_{zj}(t) R_l^-(t) \rangle \right\} \end{aligned} \quad (10)$$

where $R_j^+ = U_{1j}^2$, $R_j^- = U_{2j}^1$, and $R_{zj} = (U_{2j}^2 - U_{1j}^1)/2$ ($R_z = \sum_j R_{zj}$) satisfy the commutation relations for spin operators.

We wish to study the cooperative emission of two atoms in microcavities. In this case one obtains a closed system of equations for the variables $Z(t) = \langle R_{z1}(t) \rangle + \langle R_{z2}(t) \rangle$, $V(t) = \langle R_2^+(t) R_1^-(t) \rangle + \langle R_1^+(t) R_2^-(t) \rangle$, and $Y(t) = \langle R_{z1}(t) R_{z2}(t) \rangle$:

$$\begin{aligned} \frac{d}{dt} Z(t) &= -\frac{1}{\tau_0} \{1 + Z(t)\} - \frac{1}{\tau_1} V(t), \\ \frac{d}{dt} V(t) &= -\frac{1}{\tau_0} V(t) + \frac{1}{\tau_1} Z(t) + \frac{4}{\tau_1} Y(t), \\ \frac{d}{dt} Y(t) &= -\frac{2}{\tau_0} Y(t) - \frac{1}{2\tau_0} Z(t) + \frac{1}{2\tau_1} V(t). \end{aligned} \quad (11)$$

Here $Z(t)$, $V(t)$ and $Y(t)$ are the inversion of atoms, the cooperative rate of emission and the correlation function of inversions, respectively.

Using the initial conditions for the above variables $Z(t=0) = 1$, $V(t=0) = 0$, and $Y(t=0) = 1/4$, we obtain the following solution of the system (11):

$$\begin{aligned} Z(\tau) &= -\frac{4n^2}{1-n^2}e^{-2\tau} + \frac{1-n}{1+n}e^{-(1-n)\tau} + \frac{1+n}{1-n}e^{-(1+n)\tau} - 1, \\ V(\tau) &= -\frac{4n}{1-n^2}e^{-2\tau} - \frac{1-n}{1+n}e^{-(1-n)\tau} + \frac{1+n}{1-n}e^{-(1+n)\tau}, \\ Y(\tau) &= \frac{1+n^2}{1-n^2}e^{-2\tau} - \frac{1-n}{2(1+n)}e^{-(1-n)\tau} - \frac{1+n}{2(1-n)}e^{-(1+n)\tau} + 1/4. \end{aligned} \quad (12)$$

where $n = \tau_0^b/\tau_1^b$, $\tau = t/\tau_0^b$.

The biphoton spontaneous and cooperative decay times τ_0^b and τ_1^b can be found from the relations:

$$\begin{aligned} \frac{1}{\tau_0^b} &= \frac{2}{\hbar^4} \sum_{\kappa_1 \kappa_2} \frac{K(\kappa_1)}{K^2(\kappa_1) + (\omega_{\kappa_1} + \omega_{\kappa_2} - \omega_{21})^2} \left\{ \frac{(\vec{g}_{\kappa_1}, \vec{d}_{31})(\vec{g}_{\kappa_2}, \vec{d}_{32})}{\omega_{23} - \omega_{\kappa_2}} - \frac{(\vec{g}_{\kappa_1}, \vec{d}_{32})(\vec{g}_{\kappa_2}, \vec{d}_{31})}{\omega_{31} - \omega_{\kappa_2}} \right\}^2 \\ \frac{1}{\tau_1^b} &= \frac{2}{\hbar^4} \sum_{\kappa_1 \kappa_2} \cos(\vec{\kappa}_1 + \vec{\kappa}_2, \vec{r}_{21}) \frac{K(\kappa_1)}{K^2(\kappa_1) + (\omega_{\kappa_1} + \omega_{\kappa_2} - \omega_{21})^2} \left\{ \frac{(\vec{g}_{\kappa_1}, \vec{d}_{31})(\vec{g}_{\kappa_2}, \vec{d}_{32})}{\omega_{23} - \omega_{\kappa_2}} - \frac{(\vec{g}_{\kappa_1}, \vec{d}_{32})(\vec{g}_{\kappa_2}, \vec{d}_{31})}{\omega_{31} - \omega_{\kappa_2}} \right\}^2 \end{aligned}$$

We observe that the two-photon forbidden transitions achieve the maximum value when $\omega_{\kappa_1} + \omega_{\kappa_2} = \omega_{21}$. Such transitions decrease in inverse proportion to the square of detuning of the level $|3\rangle$ from resonance Δ_κ^2 , where $\Delta_\kappa = |\omega_{23} - \omega_\kappa|$. One mention here that the probability of two-photon transitions in microcavities are higher than the similar transitions for Λ -type three level systems (see Fig. 1b) in free space¹¹. It is not difficult to observe that in free space $\omega_{32} + \omega_\kappa$ is larger than Δ_κ for the microcavity.

For a large number of atoms the two-photon cooperative emission substantially increases. This follows from the chain of equations (10) which is analogous to that for the two-photon cascade emission (Eq. (9)). As the photons are generated in pairs the radiation intensity of the biphotons (photon pairs) becomes proportional to N^2 and the second-order photon correlation function remains much greater than the squared first-order correlation function during the entire collective decay process. In this situation the superbunching phenomenon is possible.

4. CONCLUSIONS

In this paper we have studied the possibility of cooperative two-photon dipole-forbidden transitions in microcavities for the inverted three level system in the cascade configuration. We have shown that when the cavity modes are far from resonance with the intermediate level $|3\rangle$, so that $\Delta_\kappa \gg N/\tau_0$, the cooperative dipole-forbidden emission stimulated by the discrete cavity modes can take place. In this case the resonance between the biphoton belonging to the two cavity modes and the same parity levels $|2\rangle$ and $|1\rangle$ is possible. The probability of two-photon dipole-forbidden transitions in a microcavity is larger than that in a free space¹¹. In order to observe the cooperative emission of biphotons in the bad cavity limit $N/\tau_0^b \ll K(\kappa)$ it is necessary to inhibit the two one-photon cascade emission.

5. REFERENCES

1. H. J. Carmichael, Phys. Rev. Lett. **55**, 2790 (1985).
2. C. M. Savage, Phys. Rev. Lett. **60**, 1828 (1988).
3. J. I. Cirac and L. L. Sanchez-Soto, Phys. Rev. A **44**, 1948 (1991).
4. H. Gieben *et al*, Phys. Rev. A **53**, 2816 (1996).
5. M. Brune, J. M. Raimond, and S. Haroche, Phys. Rev. A **35**, 154 (1987).
6. L. Davidovich, J. M. Raimond, M. Brune, and S. Haroche, Phys. Rev. A **36**, 3771 (1987).
7. M. Brune, J. M. Raimond, P. Goy, L. Davidovich, and S. Haroche, Phys. Rev. Lett. **59**, 1899 (1987).
8. W. Lange, G. S. Agarwal, and H. Walther, Phys. Rev. Lett. **76**, 3293 (1996).
9. C. W. Gardiner, *Quantum Noise*, Springer-Verlag, Berlin, 1990.
10. R. H. Dicke, Phys. Rev. **93**, 99 (1954).
11. N. A. Enaki, Zh. Eksp. Teor. Fiz. **94**, 135 (1988) [Sov. Phys. JETP **67**, 2033 (1988)].

P.I.Khadzhi, D.V.Tkachenko

Trans-Dniester State University, 25 October str., 128,
Tiraspol, Moldova, 278000

ABSTRACT

The hysteretical behaviour of imaginary and real parts of the semiconductor susceptibility in the exciton range of spectrum taking into account the exciton-photon and elastic exciton-exciton interaction in the pump-probe regime depending on the intensity and frequency of the strong pump laser pulse and on the frequency of the test pulse is studied. The conditions of the emergence of the damping suppression and test pulse gain are determined. The abrupt red and blue shifts of the spectral position of the exciton absorption band depending on the intensity of the pump pulse are predicted.

Keywords: dispersive and absorptive susceptibilities, exciton, absorption band, gain band, red and blue shifts

1. INTRODUCTION

It is well known that the physical properties of the atoms can be modified by their interaction with the strong electromagnetic radiation. For instance the virtual emission and reabsorption of nonresonant photons lead to a shift of the atomic energy levels. A similar situation might also be found in the solids for intrinsic transitions like excitons. Therefore the electromagnetically induced changes in the optical properties of the semiconductors at high level of laser excitation have attracted a great attention in the recent years due to its possible practical applications for the construction of ultrafast all-optical devices such as bistable or logic elements with on and off switching times in the picosecond or even subpicosecond domain.

The field induced transparency, optical Stark-effect, blue and red shifts of the atomic and exciton resonances and other nonlinear optical effects have proved to be important and the number of experiments have demonstrated these effects. A very large high-energy shift of the lowest exciton resonance in GaAs multiple-quantum-well structures is observed¹ during irradiation of the sample with femtosecond laser pulses. These effects were explained in terms of the excitons "dressed" by photons. The experiments and theoretical description of large optical Stark-effect in the exciton range of spectrum of semiconductors are presented². The possibility of a media with a very large refractive index and vanishing absorption has also been demonstrated³. It was shown⁴ that the field-induced transparency effect, the changes in the dispersive characteristics and possibility of the probe gain to the presence of the pump laser exist in the system of high-density excitons modelled as a system of anharmonic oscillators. For the first time we have demonstrated the hysteretical changes and jumps in the spectral behaviour of the dispersive and absorptive susceptibilities of semiconductors due to elastic exciton-exciton interaction⁵. A similar problem was discussed^{6,7} for a system of Bose-condensed excitons in the presence of pump and probe fields.

2. THE MAIN RESULTS

In this paper we present the main results of the theoretical study of the bistable and spectral peculiarities of the dispersive and absorptive susceptibilities of semiconductors in the exciton range of spectrum taking into account the exciton-photon and elastic exciton-exciton interactions in the presence of the pump and probe pulses of laser radiation. We suppose that the strong (pump) electromagnetic wave with the amplitude E_0 and frequency ω_c and the weak (probe, test) wave with the amplitude E and frequency ω incident on the crystal. The photons of the strong electromagnetic wave, being close to the resonance to the 1s-exciton state with the self-frequency ω_0 propagate in the crystal, induce the transitions from the ground state of the crystal to the exciton state and thus excite the high density of coherent excitons. The spectral changes in the optical properties of semiconductor are probed by photons of the weak pulse. The Hamiltonian of the system of coherent excitons interacting with the external fields in the frame rotating with the frequency ω_c of the strong field has the form

$$H = \hbar \Delta \alpha^+ \alpha + \hbar v \alpha^+ \alpha^+ \alpha / 2 + \hbar g (E_0^+ \alpha^+ + \alpha E_0^-) - \hbar g (\alpha^+ E e^{-i\delta t} + \alpha E e^{i\delta t}), \quad (1)$$

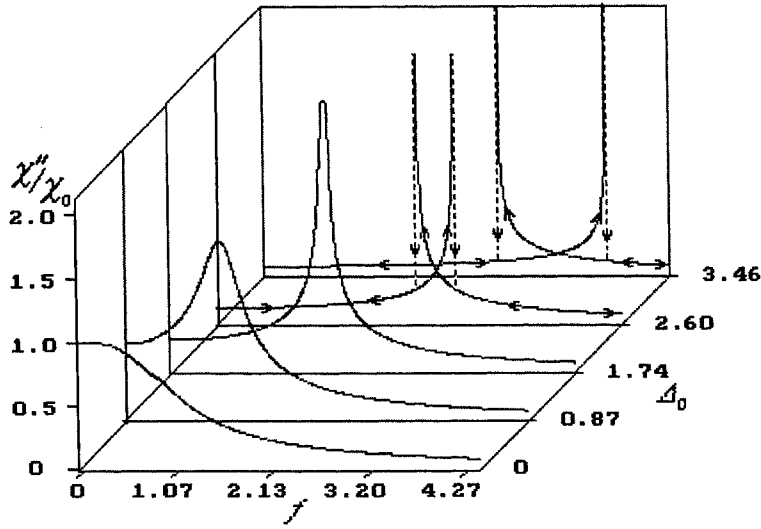


Fig.1. Absorptive susceptibility χ''/χ_0 dependence on the normalized pump amplitude f for different values of the pump detuning Δ_0 .

where $\Delta = \omega_c - \omega_0$ and $\delta = \omega - \omega_c$ are detunings, α is the amplitude of the exciton wave, g is the exciton-photon coupling constant and v is the elastic exciton-exciton interaction constant. In accordance with (1) the semiclassical equation for the exciton wave amplitude α is

$$i \frac{\partial}{\partial t} \alpha = -\Delta \alpha - i\gamma \alpha + v \alpha^+ \alpha - g E_0^+ - g E^+ e^{i\delta t}, \quad (2)$$

where γ is the phenomenological damping constant of the exciton. Then having calculated the response of the exciton system to all orders in strong field E_0 and to the first order in weak field E it is easy to obtain the following expressions for the dispersive χ' and absorptive χ'' susceptibilities of the crystal:

$$\chi'/\chi_0 = \left[\delta_0 + \Delta_0 - 2z + z^2 \cdot \frac{(\delta_0 - \Delta_0 + 2z)}{1 + (\delta_0 - \Delta_0 + 2z)^2} \right] \cdot F^{-1}, \quad (3)$$

$$\chi''/\chi_0 = \left[1 - \frac{z^2}{1 + (\delta_0 - \Delta_0 + 2z)^2} \right] \cdot F^{-1}, \quad (4)$$

where

$$F = \left[1 - \frac{z^2}{1 + (\delta_0 - \Delta_0 + 2z)^2} \right]^2 + \left[\delta_0 + \Delta_0 - 2z + z^2 \frac{\delta_0 - \Delta_0 + 2z}{1 + (\delta_0 - \Delta_0 + 2z)^2} \right]^2, \quad (5)$$

$\chi_0 = \hbar g^2 / \gamma$, $\Delta_0 = \Delta / \gamma$, $\delta_0 = \delta / \gamma$, $X = \Delta_0 + \delta_0 = (\omega - \omega_0) / \gamma$, $z = v n_0 / \gamma$, n_0 is the density of coherent excitons, excited by the field of the strong pulse, which is expressed by a nonlinear equation

$$z[(z - \Delta_0)^2 + 1] = f^2. \quad (6)$$

Here $f = E_0 / E_s$, the normalized amplitude of the strong field, where $E_s^2 = \gamma^3 / v g^2$. It follows from (6), that the density of coherent excitons z undergoes the bistable behaviour depending on f for the fixed values of Δ_0 if $\Delta_0 > 3^{1/2}$ and depending on Δ_0 for the fixed values of f if $f > f_c = (4/3)^{3/4}$. It is known⁸ that the susceptibilities under the action of only the pump pulse can also undergo the bistable behaviour depending on f and Δ_0 . Taking into consideration this conclusion we have studied the behaviour of the real (dispersive) χ' and imaginary (absorptive) χ'' parts of susceptibility depending on the pump Δ_0 and test δ_0 detunings and on the level of the pump excitation f .

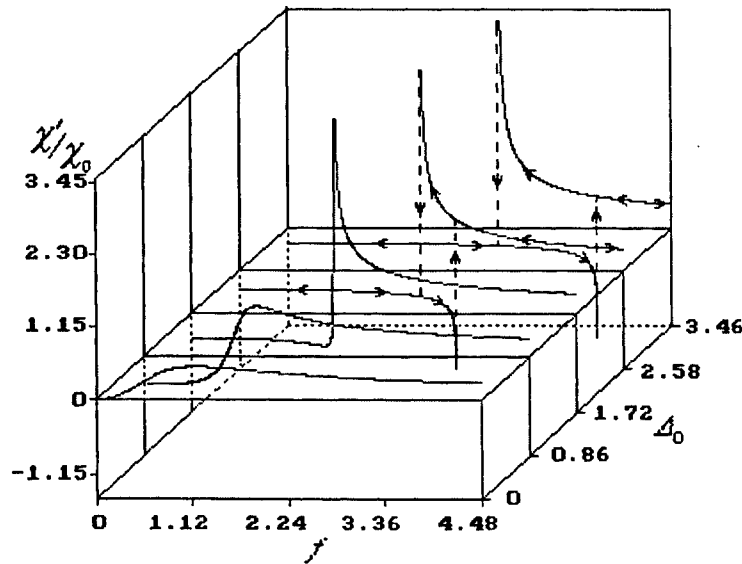


Fig.2. Dispersive susceptibility χ''/χ_0 dependence on the normalized pump amplitude f for different values of the pump detuning Δ_0 .

3. DISCUSSION OF RESULTS

It follows from (3)-(6) that χ' and χ'' are the complex function of Δ_0 , δ_0 and f . In Fig.1 the absorptive susceptibility χ'' is plotted as a function of normalized pump amplitude f for different values of pump detuning Δ_0 and fixed value of probe detuning $\delta_0=0$. The absorption monotonously decreases with the increase of the pump amplitude f if pump detuning $\Delta_0 \leq 0$, that is if the frequency of pump photons is smaller than the self-frequency of excitons. It is due to the fact that the self-frequency of excitons shifts to the fundamental frequency of crystal with the increase of the density of excitons. If the pump detuning $0 < \Delta_0 < 3^{1/2}$ the absorption at first increases with the increase of the pump amplitude f , reaches its maximum, $\chi''_{\max}/\chi_0 = (1 - \Delta_0^2/3)^{-1}$ at $f^2 = 2\Delta_0(9 + \Delta_0^2)/27$, then monotonously decreases. Since the function $z(f)$ is a threevalued one for $\Delta_0 > 3^{1/2}$ in the region $f_+ < f < f_-$ this multivaluedness displays in the behaviour of $\chi''(f)$. Therefore if $\Delta_0 > 3^{1/2}$ the function $\chi''(f)$ exhibits the bistable behaviour depending on the pump amplitude f for the fixed values of Δ_0 and undergoes the jumps at the different values of f when the field amplitude f increases then the susceptibility χ'' increases too in the interval $0 < f < f_-$. Approaching the amplitude $f=f_-$ the function $\chi''(f)$ at first infinitely increases, then it undergoes the jump to the finite value $\chi''/\chi_0 = (\Delta_0^2 - 3)^{-1}$ and further this function monotonously decreases. However if the pump amplitude decreases from the values $f > f_+$ the function $\chi''(f)$ at first monotonously increases, approaching the value $f=f_+$ it achieves infinity and undergoes the jump to the finite value of $\chi''/\chi_0 = (\Delta_0^2 - 3)^{-1}$ and at last monotonously decreases in the interval $0 < f < f_+$. Here the values f_{\pm} depend only on the detuning Δ_0 and are determined by the expressions

$$f_{\pm} = \frac{1}{3} \sqrt{\frac{2}{3}} \sqrt{\Delta_0(\Delta_0^2 + 9) \pm (\Delta_0^2 - 3)^{3/2}}, \quad (7)$$

These behaviour peculiarities of the absorptive susceptibility χ'' are due to the elastic exciton-exciton interaction which gives rise to the exciton resonance shifting.

In Fig.2 the dependence $\chi'(f)$ is plotted for different values of the pump detuning Δ_0 when the frequency of the test field is in the resonance with the exciton frequency ($\delta_0=0$). It follows from Fig.2 that the corresponding peculiarities take place in the behaviour of the dispersive susceptibility χ' too depending on the level of excitation. We can see that

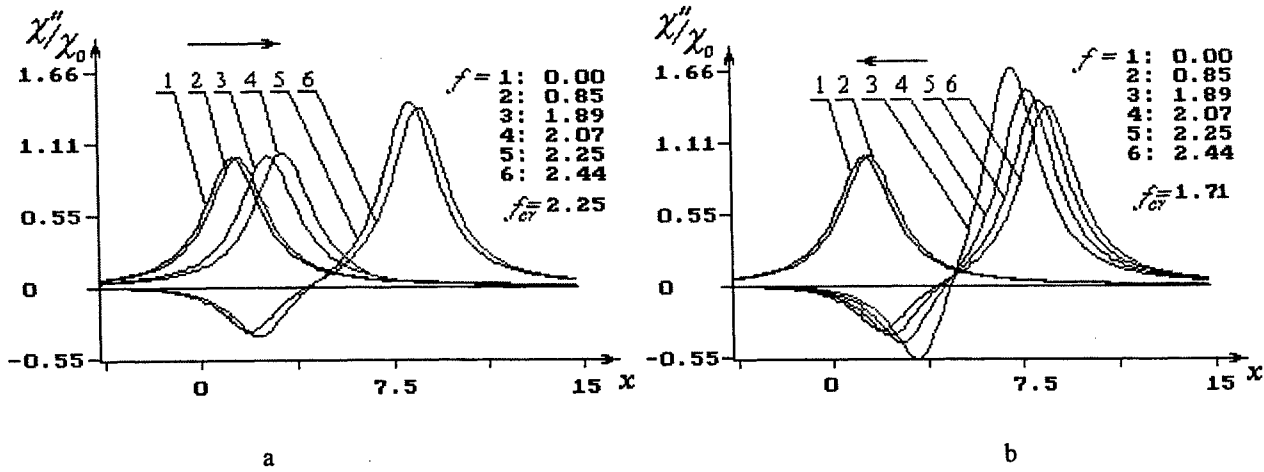


Fig.3. Absorptive susceptibility χ''/χ_0 dependence on the normalized test detuning x for pump detuning $\Delta_0=3$ and different values of the pump amplitude f for the cases, when pump amplitude increases (a) and decreases (b).

there are the different behaviours of $\chi'(f)$ for the different values of pump detunings Δ_0 , especially for the critical values of Δ_0 , when the shapes of the function $\chi'(x)$ undergo the abrupt changes.

χ' and χ'' versus $x=(\omega-\omega_0)/\gamma$ (x is the normalized detuning of the test pulse frequency ω concerning to the exciton self-frequency ω_0) are plotted correspondingly in Figs.3-4 for $\Delta_0=3$ and different values of pump amplitude f for the cases, when pump amplitude f increases (Figs.3a,4a) or decreases (Figs.3b,4b). It follows from Fig.3a that the absorption band of the test field gradually shifts to the short-wave side, when the value f increases from zero to the value $f=f_-$. It is due to the monotonous concentration shifting of the excitonic level. However in the case of a small increase of f above f_- , that is with the passage through the value $f=f_-$, the abrupt (jump) shift of the peak of the absorption band takes place in the significance distance concerning to its position at $f \leq f_-$ and simultaneously in the long-wave region band of negative absorption or the gain band of the test field arises. With further increase of $f > f_-$ only monotonous shifting of the absorption and gain bands takes place again to the short-wave side. The abrupt change of the peak position of the absorption band in the region of $f \approx f_-$ in case of increase of the pump amplitude f is due to the fact, that at this value of the pump amplitude the exciton density undergoes the jump change which is bigger, when the pump detuning Δ_0 is large. The physical reason of the gain effect is due to the processes of leaving of the excitons in pairs from the coherent state, which are excited by the strong (pump) laser field, and to its transitions to the long-wave and short-wave regions of both polariton branches in accordance with the energy and momentum conservation laws. The radiative recombination of transited excitons is the main reason of the arising of the damping suppression effect and hence of the gain band formation. The gain band as well as the absorption band undergoes the blue shifts when the pump amplitude increases. The gain effect of the test pulse arises only in the long-wave tail of the absorption band and is bounded by the spectral region of the test detuning

$$2(\Delta_0 - Z) - \sqrt{Z^2 - 1} \leq x \leq 2(\Delta_0 - Z) + \sqrt{Z^2 - 1}. \quad (8)$$

The width of this region $\Delta x = 2(Z^2 - 1)^{1/2}$ is determined only by the amplitude and frequency of the pump field f .

If now we begin to decrease the pump amplitude f from the value $f > f_-$ then, at first the monotonous shifting of the peaks of gain and absorption bands takes place up to the value $f=f_+ < f_-$ (Fig.3b). When the pump amplitude f passes through the value $f=f_+$ the gain vanishes and the absorption band peak abruptly changes its position to the long-wave side. With the further decrease of f only the monotonous shifting of the absorption band to the long-wave side takes place. Thus, the absorption band of the test radiation and the gain band undergo the abrupt (jump) spectral change of its spectral forms positions, when the pump amplitude f approaches the critical values $f=f_+$ and $f=f_-$, which are consistent with the positions of jumps of the function $z(f)$.

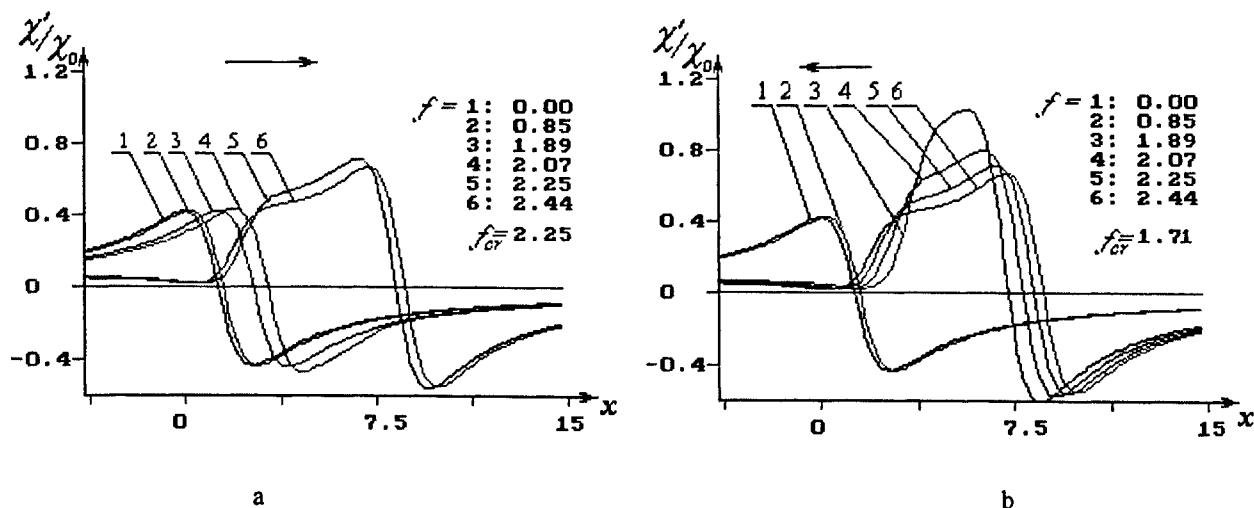


Fig.4. Dispersive susceptibility χ'/χ_0 dependence on the normalized test detuning x for pump detuning $\Delta_0=3$ and different values of the pump amplitude f for the cases, when pump amplitude increases (a) and decreases (b).

It will be noted that presented in Fig.3-4 results refer to the case when the pump detuning $\Delta_0=3$, that is when the developed bistability takes place in the dependence of the coherent excitons density $z(f)$ on the pump amplitude f . Namely in this case ($\Delta_0 > 3^{1/2}$) the abrupt (jump) changes of the shape and position of the absorption and gain bands appear. These changes are determined by the amount and direction of variation of pump field amplitude. If the pump detuning $\Delta_0 < 3^{1/2}$ the function $z(f)$ is a nonlinear single-valued one and then the shapes and positions of the absorption and gain bands peaks depend on the Δ_0 and f , but do not depend on the direction of variation of the pump amplitude.

From Figs.3b,4b we can see that the analogous peculiarities are manifested also in the behaviour of the real part of susceptibility $\chi'(x)$ for different values of the pump field amplitude.

4. REFERENCES

1. A. Mysyrowicz, D. Hulin, A. Antonetti, A. Migus, W.T. Masselink, H. Morkoc, "Dressed excitons" in a multiple-quantum-well structure: evidence for an optical Stark-effect with femtosecond response time," *Phys. Rev. Lett.*, **56**(25), 2748-2751, (1986).
2. M. Combescot, "Semiconductors in strong laser fields: from polariton to exciton optical Stark effect," *Phys.Reports*, **221**(4),167-249, (1992).
3. M.O. Scully, "Enhancement of the index of refraction via quantum coherence," *Phys. Rev. Lett.*, **67**(14),1855-1858, (1991).
4. G.S. Agarwal, "Electromagnetic-field-induced transparency in high-density exciton system," *Phys. Rev.*, **A51**(4), R2711-R2714, (1995).
5. P.I. Khadzhi, D.V. Tkachenko, "Excitonic nonlinearity of semiconductors at high level of laser excitation," Conference Digest of International Symposium on Non-Linear Electromagnetic Systems (ISEM), Braunschweig, Germany, PMB2-16, (12-14 May 1997).
6. S.A. Moskalenko, V.R. Misko, V.Gh. Pavlov, *Bose-Einstein condensation of excitons in the presence of laser radiation, Physics and Applications of Non-Crystalline Semiconductors in Optoelectronics*, Edited by A. Andriesh and M. Bertolotti, NATO ASI Series, Kluwer Academic Publishers, **36**, 431-444, (1997).
7. S.A.Moskalenko, V.G. Pavlov, "Exciton absorption and gain band in the presence of laser radiation," *Jetp*, **111**(6), 1-13, (1997).
8. P.I. Khadzhi, Y.D. Slavov, "Hysteresis of optical functions of the crystal in the exciton range of spectrum at high level of excitation," *Ukr. Fiz. Journ.*, **33**(6), 824-827, (1988).
9. P.I. Khadzhi, G.D. Shibarshina, A.Kh. Rotaru, *Optical bistability in the system of coherent excitons and biexcitons in semiconductors*, Shtiintsa, Kishinev, p.121, (1986).

Appearance and suppression of stochastic self-pulsations of coherent excitons and biexcitons in condensed matter

V.Z.Tronciu¹, A.H. Rotaru²

¹Technical University of Moldova Stefan cel Mare av. 168,
Chisinau MD-2012, MOLDOVA, ²State University of Moldova

ABSTRACT

The theory of regular and chaotic self-pulsations in a *CuCl* crystal with the participation of coherent excitons and biexcitons is elaborated. The method of chaotic self-pulsation suppression in the system of coherent excitons and biexcitons is proposed. This method consists in action of external periodical turbulence upon a stochastic system. The range of amplitude values and frequencies of external harmonic pump were found at which the chaotic oscillation regime becomes nonlinear periodic by transformation of strange attractor into a limit cycle. The feasibility of observing the predicted effects in experiment is discussed.

Keywords: self-pulsations, strange attractor, controlling of chaos, exciton-biexciton system

1.INTRODUCTION

Much attention is being paid recently to the study of cooperative processes in the exciton region of the spectrum. Since optical nonlinearities in semiconductors are particularly large in the exciton region of the spectrum, nonlinear interaction of light with matter is most strongly pronounced just in this frequency region. In Refs.1-4 using generalized Keldysh equations⁵ that describe coherent excitons and photons that are weakly inhomogeneous in space and in time, a theory was constructed of optical bistability (OB) in the exciton region of the spectrum, and optical switchover between optical-bistability modes was investigated. It was shown, for the first time ever, that regular and stochastic self-pulsations can appear on the long-wave edge of the proper absorption of a crystal, the possibility was predicted of observing and suppression of spatial turbulence in a system of coherent excitons and photons. Above-mentioned phenomena present interest because it is one of the most striking examples of optical self-organization of a system, far from thermodynamic equilibrium, and offers tremendous prospects of practical application, primarily for optical information processing and for the development of computers with optical logic.

The notion of a biexciton, whose existence was predicted by Moskalenko⁶ and Lampert⁷, is widely invoked to interpret new absorption and fluorescence bands in semiconductors. At present, convincing experimental proofs of the existence of biexcitons in *CuCl* crystal are available. These proofs are based on the observation of the M-band resulting from biexciton radiative recombination^{8,9} and two-photon excitation of biexciton from the crystal ground state¹⁰. In the work of Gogolin, Rashba, and Hanamura¹¹⁻¹³, the corresponding transitions are shown to feature giant oscillator strengths favoring the most pronounced manifestation of nonlinear phenomena in this frequency range. A theory of stationary and nonstationary OB and of self-organization of regular and random time structures was developed in Refs.14,15 for exciton-biexciton transitions.

In a *CuCl* crystal, the biexciton bond energy is of the order of 40 meV, and the exciton absorption band and the M-band of biexciton recombination are well separated from each

other in essential contrast to the situation in *CdS* and *CdSe* crystals where the biexciton bond energy is small, 3 meV. A correct study of the OB, self-pulsations and suppression phenomena in a *CuCl* crystal necessitates simultaneous action of two independent optical pulses each being in resonance with a definite transition. In addition, exciton-exciton quantum transitions are known to be characterized by giant oscillator strengths. Recognizing furthermore that the characteristic relaxation times of excitons and biexcitons are very short ($\tau \approx 10^{-10} - 10^{-12}$ s), it becomes obvious that they will play a decisive role in the design of optoelectronic instruments, where ultrafast switchover is necessary. Owing to these proprieties, optical self-organization of excitons and biexcitons is extensively investigated.

This paper presents a theoretical investigation of regular and chaotic self-pulsations in a *CuCl* crystal with the participation of coherent excitons and biexcitons. We proposed the method of chaotic self-pulsation suppression in the system of coherent excitons and biexcitons. The method consists in action of external periodical turbulence $\tilde{Y} = Y + \alpha \sin(\omega\tau)$ upon a stochastic system. The range of amplitude values and frequencies of external harmonic pump were found at which the chaotic oscillation regime becomes nonlinear periodic by transformation of strange attractor into a limit cycle.

2. DYNAMIC EQUATIONS IN THE MEAN FIELD APPROXIMATION

We use the three-level model, as applied to a *CuCl* crystal, in which the energies of the "crystal ground state-exciton" and "exciton- biexciton" transitions differ by the biexciton bond energy. It is supposed that photons of the first pulse with energy $\eta\omega_1 = E_g - I_{ex}$ are in resonance with a transition in the exciton spectral range, and photons of the second pulse with energy $\eta\omega_2 = E_g - I_{ex} - I_{biex}$ are in resonance with the region of the fluorescence M-band of a *CuCl* crystal (E_g is the band gap, I_{ex} (I_{biex}) is the exciton (biexciton) bond energy). We consider one macrofilled mode of coherent excitons and biexcitons and one macrofilled mode of coherent photons of every pulse. The full Hamiltonian of the problem consists of the sum of Hamiltonians of free excitons, biexcitons, and fields, as well as the interaction Hamiltonian which in the model adopted has the form

$$H_{int} = -\eta g(aE_1^+ + a^+ E_1^-) - \eta gG(a^+ bE_2^- + ab^+ E_2^+)$$

where a^+ and b^+ are the creation operator of exciton and biexciton, g is the constant of exciton-photon interaction, G is the exciton-biexciton optical conversion coefficient and $E^{+(-)}$ is the positive (negative)-frequency component of the electric field of the electromagnetic wave of the j^{th} pulse ($j=1,2$).

The equations of motion for the exciton and biexciton amplitudes have the form

$$i \frac{\partial a}{\partial t} = \omega_{ex} a - i\gamma_{ex} a - gE_1^+ - gGbE_1^- \quad (1)$$

$$i \frac{\partial b}{\partial t} = \omega_{biex} b - i\gamma_{biex} b - gGE_2^+ a \quad (2)$$

where $\eta\omega_{ex}$ and $\eta\omega_{biex}$ are the energies of exciton and biexciton formation, respectively, and γ_{ex} and γ_{biex} are the decay constants of excitons and biexcitons determining the rate of quasiparticle escape from coherent modes to incoherent. These constants were inserted

phenomenologically into the equations of motion. Note that these equations can be derived rigorously in terms of the quantum theory of fluctuations and decays from the flow part of the corresponding Fokker - Planck equation¹⁶.

The equations for the positive-frequency field component have the form

$$c_1^2 \frac{\partial^2 E_1^+}{\partial z^2} - \frac{\partial^2 E_1^+}{\partial t^2} = 4\pi \hbar g \frac{\partial^2 a}{\partial t^2} \quad (3)$$

$$c_2^2 \frac{\partial^2 E_2^+}{\partial z^2} - \frac{\partial^2 E_2^+}{\partial t^2} = 4\pi \hbar g G \frac{\partial^2 a^+ b}{\partial t^2} \quad (4)$$

Here c_1 and c_2 are the velocities of field propagation in the medium.

Let us represent the solution of Eqs. (1) - (4) in the form of a product of slowly-varying envelopes and rapidly oscillating components with carrier frequencies ω_1 and ω_2 and wave vectors k_1 and k_2 :

$$\begin{aligned} a &= \tilde{A} \exp(-i\omega_1 t + ik_1 z) \\ E_1^+ &= e_1^+ \exp(-i\omega_1 t + ik_1 z) \\ b &= \tilde{B} \exp(-i(\omega_1 + \omega_2)t + i(k_1 + k_2)z) \\ E_2^+ &= e_2^+ \exp(-i\omega_2 t + ik_2 z) \end{aligned} \quad (5)$$

Let us consider further the nonlinear effects in the ring cavity geometry. A sample of length L be placed between the input and the output cavity mirrors which are characterized by a transmission coefficient T . The two remaining mirrors are considered to be totally reflecting (see Fig. 1). The boundary conditions for the ring cavity have the form

$$\begin{aligned} E_j^+(0, t) &= T^{1/2} E_{I,j} + R e^{i\beta_{0,j}} E_j^+(L, t - \Delta t) \\ E_{T,j}(t) &= T^{1/2} E_j^+(L, t), \end{aligned} \quad (6)$$

where $E_{T,j}$ and $E_{I,j}$ are the amplitudes of the fields incident on the cavity input mirror and transmitted through the cavity, $R=1-T$ is the reflection coefficient of the cavity mirrors 1 and 2, $\Delta t = (2l + L)/c_0$ is the retardation time introduced by the feedback, c_0 is the velocity of light in vacuum, and $\beta_{0,j}$ is the phase increment in the cavity.

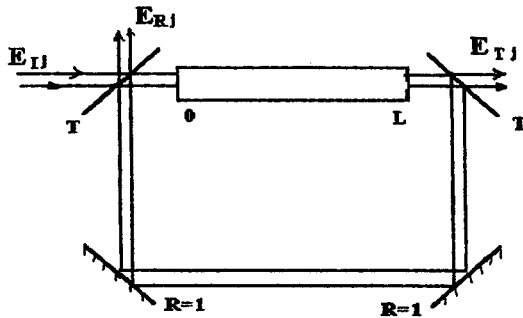


Fig. 1. Ring cavity diagram. $E_{I,j}$, $E_{R,j}$ and $E_{T,j}$ are the amplitudes of incident, reflected and transmitted fields, respectively.

Substituting (5) in Eqs. (1)-(4) in the slowly-varying envelope approximation^{17,18} and the mean-field approximation^{17,19} with allowance for the boundary conditions (6), we get

$$\frac{dX_1}{d\tau} = \sigma_1(-X_2 - 2C_1AB + Y_1) \quad (7)$$

$$\frac{dX_2}{d\tau} = \sigma_2(-X_2 - 2C_2AB + Y_2) \quad (8)$$

$$\frac{dA}{d\tau} = -dA - d(X_1 + X_2B) \quad (9)$$

$$\frac{dB}{d\tau} = -B + X_2A \quad (10)$$

where Y_1, Y_2 and X_1, X_2 are the normalized incident and transmitted field amplitudes, A and B are the normalized exciton and biexciton amplitudes, τ is the dimensionless time, and $C_1, C_2, \sigma_1, \sigma_2$ are the constants, defined by the expressions:

$$\begin{aligned} X_j &= \frac{e_{\tau,j}}{e_s}, \quad Y_j = \frac{e_{I,j}}{e_s}, \quad A = i \frac{\tilde{A}}{A_s}, \quad B = \frac{\tilde{B}}{B_s}, \\ e_s &= \frac{\sqrt{T\gamma_{ex}\gamma_{biex}}}{gG}, \quad B_s = G^{-1}, \quad A_s = \frac{\sqrt{\gamma_{ex}}}{\sqrt{\gamma_{biex}}}, \\ \tau &= \gamma_{biex}t, \quad d = \frac{\gamma_{ex}}{\gamma_{biex}}, \quad C_j = \frac{\alpha_j L}{4T}, \quad \sigma_j = \frac{c_j T}{\gamma_{biex} L}, \\ \alpha_j &= \frac{4\pi n g^2 \omega_j}{\gamma_{ex} c_j}, \quad j = 1, 2. \end{aligned}$$

Equations (7)-(10) describe temporal evolution of coherent excitons, biexcitons, and electromagnetic fields in the ring cavity and are the basis for following studying.

3.COMPUTER EXPERIMENT AND CONCLUSION

The criteria for the existence of stationary and nonstationary optical bistability and optical switching was studied in Refs. 20. The nonlinear dependence of the output radiation amplitudes X_1 and X_2 on the input radiation Y_2 amplitudes in the steady-state case is shown in fig.2.

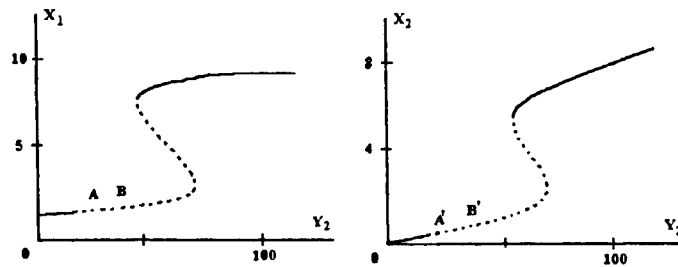


Fig.2. Steady-state OB. $X_1, X_2(Y_2)$ in the ring cavity at $Y_1=10, C_1=20, C_2=19$.

It is of great interest to investigate the stability of the curve in connection with the possible development of self-pulsations in unstable sections of the OB curves. The investigation of stability of optical hysteresis steady states with respect to small perturbations is determined by the characteristic equation for the Jacobian of the system:

$$|J - \lambda E| = \begin{vmatrix} -\sigma_1 - \lambda & 0 & 2C_1 & 0 \\ 0 & -\sigma_2 - \lambda & 2C_2 B & -2C_2 A \\ d & dB & -d - \lambda & -dX_2 \\ 0 & A & X_2 & -1 - \lambda \end{vmatrix} = 0 \quad (11)$$

where E is the unit matrix. If the real parts of all the roots of the characteristic equation (11) are negative, the corresponding steady states are stable with respect to small perturbations. Using the Routh-Hurwitz criterion, stability of steady states at values of the parameters was investigated for $C_1=20$, $C_2=19$, $Y_1=10$, $d=0.7$, $\sigma_1=0.4$, $\sigma_2=0.7$. The upper parts of the curves are stable as before, whereas a part of the lower branches becomes unstable. Near the point $A(A')$ (Fig. 2) corresponding to the initial point of instability regions, nonlinear periodic self-oscillations appear in the system, and the phase trajectory goes into a limit cycle in the shape of a figure eight curve. As the imaging point moves towards the window center, the oscillations become more complicated, new harmonics appear in their spectrum, and finally, stochastic self-oscillation and an optical turbulence mode develops in the point $B(B')$. The projections of the phase trajectories of the stochastic self-modulation process is shown in Fig. 3^a. In contrast to the famous Lorenz chaos^{21,22}, where stochastic oscillations and strange attractor creation are associated with jumps between the corresponding equilibrium states, in our case, stochasticity is related to the creation of a chaotic attractor in the four-dimensional phase space which is filled with phase trajectories in a complicated manner.

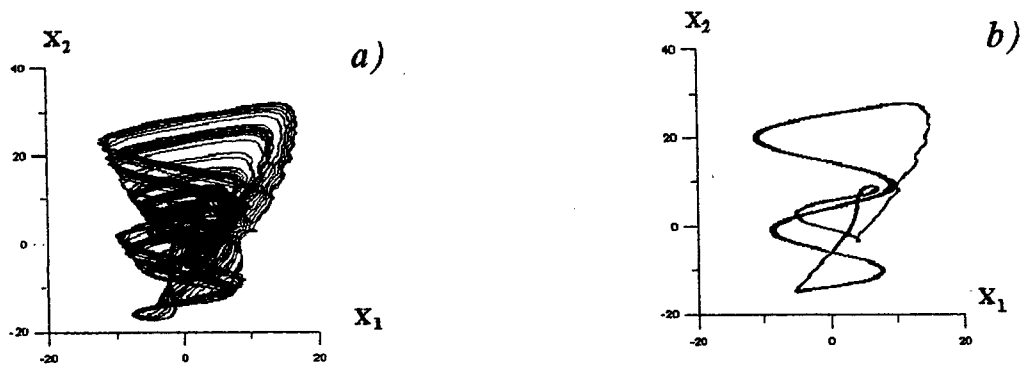


Fig.3. The strange attractor trajectories in the plane $X_2 - X_1$ a) and the projection of the phase portrait under the influence of an external periodic pump of the form $\tilde{Y}_2 = Y_2 + \alpha \sin(\omega\tau)$ b)

There is of interest the studding of dynamical chaos suppression. One of the methods consists in action of external periodical pump of form $\tilde{Y}_2 = Y_2 + \alpha \sin(\omega\tau)$ upon a stochastic system. The amplitude values α and frequencies ω of external harmonic pump were found at which the chaotic oscillation regime becomes nonlinear periodic by transformation of strange attractor into a limit cycle. The synchronization process are shown in Fig.3^b at $\alpha = 1$, $\omega = 0.9$. Power spectrum for strange attractor is shown in fig.4^a. The spectrum is continuous as we see from the figure. The spectrum is discrete in the case of the limit cycle. Three harmonics are dominant (see Fig.4^b). The increase of the parameter α leads to institution of forced oscillations in the system that are out of our interest. Deviation of the parameter ω from the critical value ($\omega = 0.9$) leads to more chaotisation. It follows that the values $\alpha = 1$, $\omega = 0.9$ corresponds to synchronization region when strange attractor transforms into limit cycle. Critical intensity under which is possible to observe the abovementioned phenomena is 2 MW/cm^2 . The concentration of excitons and biexcitons are 10^{14} 1/cm^3 and 10^{17} 1/cm^3 , respectively. The following values of the system parameters $C_1=20$, $C_2=19$, $Y_1=10$, $d=0.7$, $\sigma_1 = 0.4$, $\sigma_2 = 0.7$ correspond to these values of intensities and concentrations.

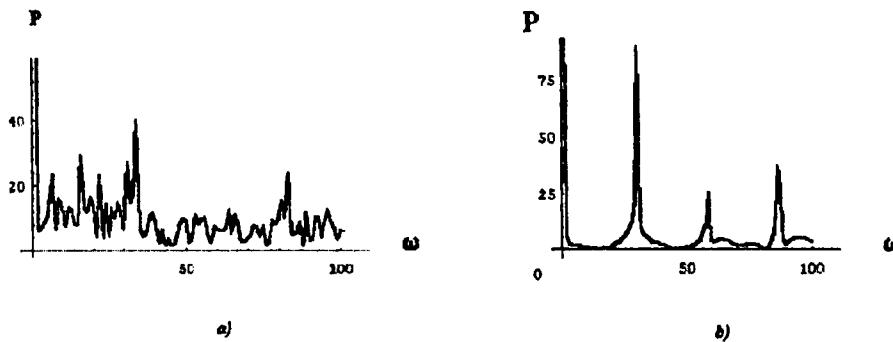


Fig.4. Power spectrum of strange attractor a) and power spectrum of limit cycle b).

In conclusion we discuss the feasibility of observing the predicted effects in experiment. The model studied by us is most valid for crystals such as CuCl , in which the exciton-binding energy is $I_{\text{biex}} \approx 40 \text{ meV}$ and $L=750 \text{ \AA}$; $\hbar\gamma_{\text{ex}} \approx 10^{-5} \text{ eV}$; $\hbar\gamma_{\text{biex}} \approx 10^{-4} \text{ eV}$; $\hbar g \approx 0.3 \text{ eV} / (\text{cm}^{1/2} \cdot V)$; Our numerical estimates allow us to conclude that it is really possible to observe self-pulsations and dynamic chaos suppression in a system of coherent excitons and biexcitons in condensed media.

4. REFERENCES

1. A. Moskalenko, A.H. Rotaru, V.M. Shvera, and V. A. Zaloj, "Quantum fluctuation and time structures of high density polaritons," *Phys. Stat. Sol. (b)* **149**, 187-194 (1988).
2. S.A. Moskalenko, A.H. Rotaru, and V.A. Zaloj, "Periodic and stochastic self-pulsation in the system of coherent exciton, photon and biexciton", *Phys. Stat. Sol. (b)* **150**, 401-406 (1988).
3. B. Sh. Parkanskii and A. Kh. Rotaru, "Nonlinear, stationary and nonstationary light spreading in semiconductors at resonant excitation of excitons", *Fiz. Tverd. Tela* **33**, 2250-2256 (1991) [*Sov. Phys. Solid State* **33**, 1268-1272 (1991)].

4. A.H.Rotaru and V.Z.Tronchu "Suppression of stochastic self-pulsation of coherent excitons and photons in semiconductor", *Fiz. Tverd. Tela* **36**, 20-24 (1994) [*Sov.Phys.Solid.State* **36**, 10-12 (1994)].
5. L. V. Keldysh, *Problems of Theoretical Physics*, Nauka, Moscow (1972) [in Russian].
6. S. A. Moskalenko, "On the theory of Mott exciton in alkali-halides crystals", *Opt. Spektrosk.* **5**, 147-155 (1958).
7. M. A. Lampert, "Mobile and immobile effective -mass-particle complexes in nonmetallic solids", *Phys. Rev. Lett.* **1**, 450-453 (1958).
8. Nikitine, A.Mysyrowicz and J.B.Grun, "Observation de la recombinaison radiative dans CuCl aux basses temperatures at aux excitations tres intenses. Tentative d'interpretation faisant intervenir la decomposition de biexcitons." *Helvetica .Physica. acta* **41**, 1058-1063 (1968).
9. A.Mysyrowicz, J.B.Grun, R.Levy, A.Bivas and S.Nikitine, "Excitonic molecule in CuCl", *Phys.Lett. A*, **26**, 615-616 (1968).
10. G. M. Gale and A. Mysyrowicz, "Direct creation of excitonic molecules in CuCl by gain two-photon absorption", *Phys. Rev. Lett.* **32**, 427-430 (1974).
11. A. A. Gogolin and E. I. Rashba, "Influence of exciton interaction on exciton spectrum", *JETP Lett.* **17**, 690-693 (1973).
12. E. Hanamura, "Gain two-photon absorption to excitonic molecule", *Solid State Commun.* **12**, 951-953 (1973).
13. E. Hanamura, "Excitonic molecule. Electronic structure. Optical properties" *J. Phys. Soc. Japan* **39**, 1506-1524 (1975).
14. V.A.Zalozh, A.Kh.Rotaru and V.Z.Tronchu, "Optical hysteresis, switchover, and self-pulsation of excitons and biexcitons in condensed media", *Zh.Eksp.Teor.Fiz.* **103**, 994-1009 (1993) [*Sov.Phys.JETP* **76**, 487-496 (1993)].
15. P.I.Bardetskii, V.A.Zalozh, A.H.Rotaru and V.Z.Tronchu, "Optical bistability and switching of coherent quasiparticles in condensed media", *Fiz. Tverd. Tela* **34**, 3143-3154 (1992) [*Sov.Phys.Solid.State* **34**, 1681-1686 (1992)].
16. S.A.Moskalenko, A.H.Rotaru, V.M.Shvera, "The Fokker-Planck equation and taking into account of quantum fluctuations in the theory of excitons and biexcitons of large density", *Teor.Mat.Fiz.* **75**, 295 - 305 (1988).
17. H. M. Gibbs, *Optical Bistability. Controlling Light with Light*, Acad. Press, Orlando, FL, 1985.
18. V. A. Zalozh, S. A. Moskalenko, and A. Kh. Rotaru, "Self-pulsation at longwave edge of fundamental absorption of a crystal", *Zh. Eksp. Teor. Fiz.* **95**, 601-612 (1989) [*Sov. Phys. JETP* **68**, 338-345 (1989)].
19. B. Sh. Parkanskii and A. Kh. Rotaru, "Optical hysteresis, switching and self-pulsations on resonant excitation of excitons in semiconductors", *Zh. Eksp. Teor. Fiz.* **99**, 899-909 (1991) [*Sov. Phys. JETP* **72**, 499-502 (1991)].
20. V.A.Zalozh, A.Kh.Rotaru and V.Z.Tronchu, "The theory of optical bistability and self-pulsation in a CuCl crystal", *Zh.Eksp.Teor.Fiz.* **105**, 260-270 (1994) [*Sov.Phys.JETP* **78**, 138 -143(1994)].
21. E.N.Lorentz, "Strange attractor" M, Mir 1981.
22. H.Haken, "Synergetics", Springer-Verl., Berlin, 1977.

Novel Approaches in Morphological Correlations

David Mendlovic, Amir Shemer, Zeev Zalevsky, Emanuel Marom
and Gal Shabtay

Tel-Aviv University, Faculty of Engineering
Department of Physical Electronics, 69978 Tel-Aviv, ISRAEL

ABSTRACT

Morphological correlation is a novel method for obtaining high discrimination ability in pattern recognition applications. It provides also important abilities for image compression and image analysis. The concept is based on slicing the input image and the reference filter into many binary slices, eg. 255, and correlating them. The morphological correlation is defined as the summation of these correlations. The morphological correlation is characterized by a sharp correlation peak narrower than that exhibited by matched filter. The disadvantages are the requirements of performing many correlations and its very high sensitivity to noise added to the reference image. In this presentation we suggest two methods to solve both drawbacks. First, instead of 255 correlations we suggest to utilize only 8, by representing the grey level of each pixel by its 8 bit binary representation. Then, 8 binary masks are constructed according to the binary representation. In order to address the problem of severe sensitivity to noise, we suggest to sum the 255 correlations of the morphology slices while each slice is multiplied by a weighting factor which equals the correlation peak of that specific slice with noise divided by its correlation peak value when no noise is added. The solutions suggested here were examined by computer simulations demonstrating considerable improvements in the performance of the morphological correlator.

1. INTRODUCTION

Morphological correlation plays an important role in the field of image matching and pattern recognition. Considerable part of the projects on image detection has been based on minimizing the mean square error (MSE) between two image functions and thus maximizing their cross correlation¹ when they represent the same object. In order to understand morphological correlation consider two real valued discrete functions $f(x,y)$ and $g(x,y)$ which will represent our images. The linear cross correlation between these functions has the form :

$$\gamma_{fg}(x,y) = \sum_{u,v \in R} f(u+x, v+y) \cdot g(u,v) \quad (1)$$

This linear correlation has been found to be useful for detection of a reference image in an input scene embedded by an additive gaussian noise^{2,3}. However, for changes in the nature of the gaussian noise, other methods yield better results. One of these methods is the Mean Absolute Error (MAE) defined as:

$$MAE(x,y) = \sum_{u,v \in R} |f(u+x, v+y) - g(u,v)| \quad (2)$$

Since,

$$|f - g| = f + g - 2 \cdot \min[f, g] \quad (3)$$

Equation 2 can be expressed as:

$$MAE(x,y) = \sum_{u,v \in R} \{f(u+x, v+y) + g(u,v) - 2 \min[f(u+x, v+y), g(u,v)]\} \quad (4)$$

Hence, minimizing^{2,4} MAE is equivalent to maximization of the non linear cross correlation term, i.e.

$$\mu_{fg}(x,y) = \sum_{u,v \in R} \min[f(u+x, v+y), g(u,v)] \quad (5)$$

The morphological correlation provides higher discrimination capabilities compared to the linear correlation in pattern recognition. However, it needs much more computational efforts to obtain the final result. This is the major reason why Morphological correlation is not widely in use.

Optoelectronic systems may solve this disadvantage. One way to achieve that is to use the well known joint transform correlator^{7,8} (JTC) as depicted in figure 1, which exhibits the cross correlation of two functions via a parallel optical computation.

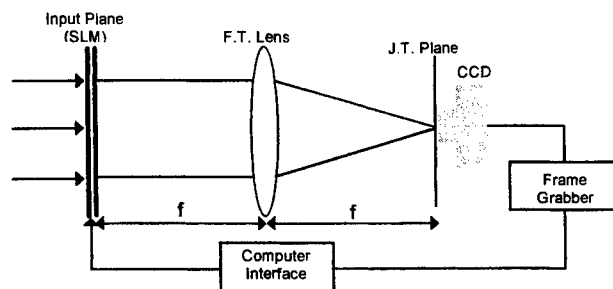


Figure 1: The Joint Transform Correlator scheme .

The JTC is used in this case to correlate binary slices that were obtained by thresholding each image separately. The result of this correlation is saved on a computer which will also be used to calculate the weighting coefficients as described in section 2. The sum of the weighted joint power spectra is fed back at the input plane for a second fourier transform to produce the final morphological correlation.

Morphological correlation is very sensitive to noise and provides a very poor detection in its presence. This sensitivity is also noticed when slight changes in the intensity of the image or their background illumination are made. Therefore, it is desirable to develop a good method to overcome these drawbacks. In this paper we present a method that uses an independent weighting coefficient to each slice and by that allow to decide which weight should be attached to each slice, as described in section 2.

In addition, in section 3 we present a way to reduce the number of correlated slices by using a binary representation of the image's grey levels. This algorithm reduces dramatically the computation complexity of the morphological correlation operation. Section 5 provides some computer simulations that demonstrate the capability of the proposed methods.

2. ADAPTIVE MORPHOLOGICAL CORRELATION.

As was mentioned in the introduction section, conventional morphological correlation was based on the assumption that all slices are equally important. In this paper the conventional morphological correlation is extended and a weighting coefficient to each correlated slice is introduced. The new definition for the morphological correlation becomes :

$$\mu_{fg} = \sum_{q=1}^Q c_q \cdot \mu_{f_q g_q} \quad (6)$$

where μ_{fg} denotes the morphological correlation and $\mu_{f_q g_q}$ denotes the correlation between slice q of image f with slice q of image g . The maximal number of grey levels that exist in the image is denoted by Q and C_q is the weighting coefficient of slice number q . This method has some advantages in comparing to the conventional morphological correlation due to the fact that it may take in consideration noise characteristics and thus improve the noise robustness.

The questions that come up are how to consider the effect of noise and which weighting coefficient should be assigned to each correlated slice. The answer is not absolute and several methods for determining those coefficients were considered. In all of those methods, information from the reference image was used, thus making the proposed algorithm adaptive. One of the most known characteristics of an image is the intensity histogram. If we denote by $I(q)$ the number of pixels with grey level q , the grey level histogram yields that summation from a certain level q to the maximum level 255, is equal to the energy of the binary slice q since it corresponds to all 1's in that slice as can be

seen from fig. 2. The histogram thus provides information regarding the number of one's in an image slice, which will be called M . We will assign to each slice a coefficient defined as:

$$C_q = \exp(k \cdot \Delta x_q) \quad \text{where} \quad \Delta x_q = |M_q - N_q| \quad (7)$$

whereby N_q , M_q are the number of ones in the reference and input slice number q , respectively. Constant k is a negative coefficient that controls the weight that each slice provides to the overall correlation and thus controls the noise robustness. These coefficients are determined such that slices with large Δx will contribute less and slices with small Δx and thus, more similarity, will contribute more.

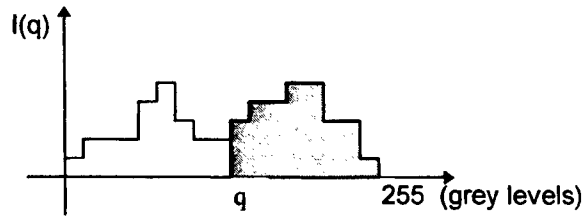


Figure 2: An example of an intensity image histogram.

Another approach was to increase the noise robustness by considering the difference between peaks of correlation or their ratio. The first peak was obtained from the "autocorrelation" generated with two reference slices. Each slice was normalized by its energy so that this peak value is one. The cross-correlation denoted as $\mu(f,g)$ represents the correlation between the normalized reference slice and the normalized input slice. It's maximum peak value is smaller than one. The corresponding weight coefficient in this case is either

$$C_q = \text{Max}[\mu_q(f,g)] \quad \text{or} \quad C_q = \exp(k \cdot |1 - \text{Max}[\mu_q(f,g)]|) \quad (8)$$

The logic behind this is the same as that of the histogram method: correlation that has small correlation peak will contribute less and vice versa.

Another way of increasing the robustness of the system is to incorporate also correlation of slices from the reference image with slices from the input image which are not from the same level of thresholding. It can be defined as:

$$\mu_{f_q g_p} = f_q * g_p \quad (9)$$

where q, p are slices from different threshold levels. This method can be very useful when considering functions with different intensities. There the morphological correlation fails to detect and one can refer to it as adding bias into the reference image.

3. BINARY MORPHOLOGICAL CORRELATION

After defining techniques for improving the noise robustness of the morphological correlation, we need also to reduce the computation complexity in order to make the morphological correlation a useful and efficient tool for image detection and pattern recognition.

The method suggested in this section is to perform morphological correlation with small computational complexity by using a binary representation of the intensity levels. For instance, image having an intensity level of 100 can be represented as binary value of 01100100. Hence, it is equivalent to eight binary masks having the value one on the seventh, sixth, and third masks and zero on the rest (see Fig.3).

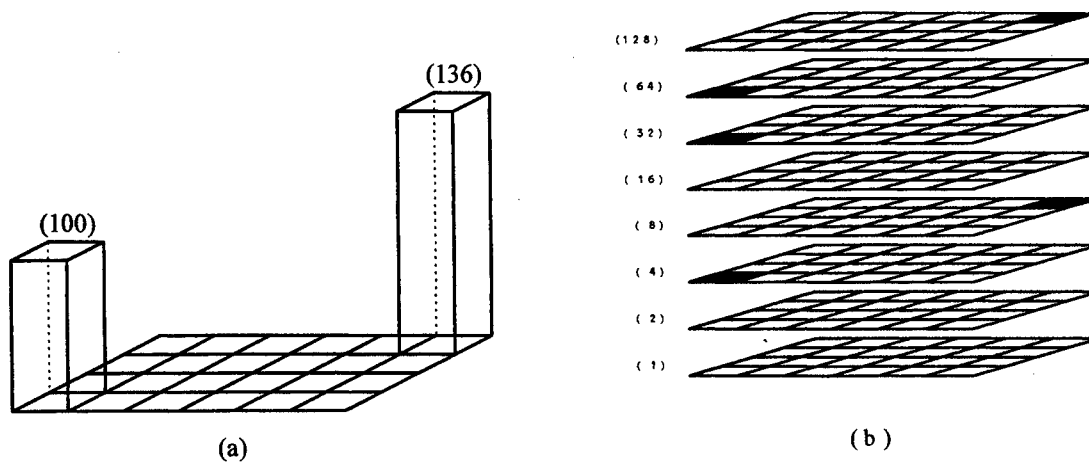


Figure 3: (a) The reference image. (b) The corresponding masks of the reference image.

This representation causes the computing complexity to be drastically reduced since only eight regular correlation operations are used instead of 256. Adding the weighting coefficient method to the binary morphological correlation, will also increase the noise robustness as in the case of the standard morphological correlation. The ways to determine the weighting coefficients are similar to the approaches presented for the conventional morphological correlator.

4. COMPUTER SIMULATIONS

In this section computer simulations investigating some of the approaches suggested in this paper are presented. In addition, tables which compare cases with different noise power levels are shown. For the simulated experiment, an image containing 256 grey levels presented in Fig. 4a, was used as the reference image. The noise matrix was based on a uniform distribution noise with different noise power levels in each simulation. Each pixel was changed by adding a noise value to it and by doing so, the grey level of that pixel was changed. This noise matrix was added to the original image producing the input image for the simulation whose results are shown in Fig. 4. The regular linear correlation, as depicted in Fig.5,6, was also normalized to obtain maximum peak value equal to one. The normalization was made according to the following expression:

$$g'_q(x,y) = \frac{g_q(x,y)}{\sqrt{\sum_{x,y=1,1}^{X,Y} g_q(x,y)^2}} \quad (10)$$

where X,Y denotes the image matrix dimension.

For this analysis the weighting coefficients were chosen to be:

$$C_q = \text{Max}[\mu_{fg}] \quad (11)$$

where $\text{Max}[\mu_{fg}]$ is the crosscorrelation maximum peak value as defined before.

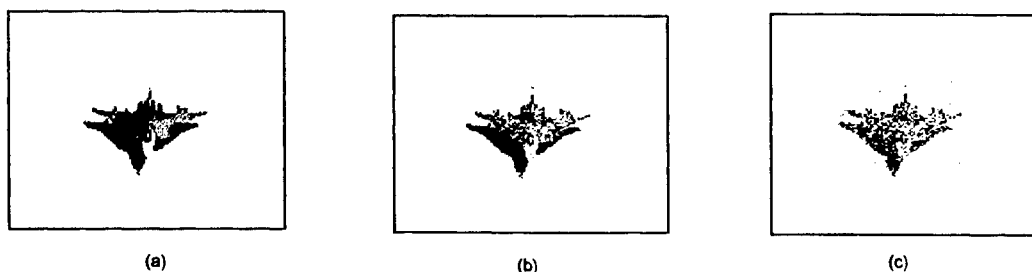


Figure 4: (a) Airplane image with no noise. (b) Airplane image with SNR equal to 2.9116 .(c) Airplane image with SNR equal to 1.294.

In order to compensate for the energy loss caused by the multiplication with the weighting coefficients we multiplied the morphological correlation by a factor defined as:

$$\text{Norm} = \frac{1}{256} \cdot \left(\sum_{n=1}^{256} 1/C_q \right) \quad (12)$$

where C_q is the weighting coefficient. This compensating factor is greater than one when noise is applied and is equal to one when the noise power reduce to zero.

Tables 1 and 2 summarize the various simulation results. Each table contains values which represent the ratio between the crosscorrelation maximum peak and the corresponding autocorrelation peak. The first table presents the simulation results without weights. It can be seen that the results are very good when regular correlation is used. When we consider the morphological and the binary correlation the maximum peak is less then 50%. The second table shows the results using the weighting on each slice. It can be seen that the morphological correlation provides better peak than the regular correlation (92% vs. 66%) when the noise is not too strong. This result shows the improvement that the weighting coefficient using the peak correlation method can give. In figure 5 and 6 some of the graphical results of the correlation are presented.

Coef =1	Regular	Morphological	Binary
Noise Amp =0	1	1	1
SNR = 5.1764	0.6592	0.4859	0.0583
SNR = 2.9116	0.5470	0.3910	0.0534
SNR = 1.294	0.3947	0.2470	0.0417

Table .1: Computer results when no weighting was applied.

Coef =1/max peak	Regular	Morphological	Binary
Noise Amp =0	1	1	1
SNR = 5.1764	0.6592	0.9198	0.0766
SNR = 2.9116	0.5470	0.7951	0.0714
SNR = 1.294	0.3947	0.4641	0.0505

Table .2 : Computer results when weighting is applied .

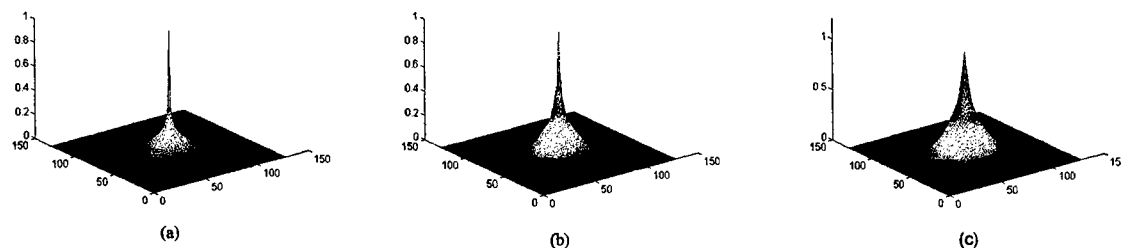


Figure 5: (a) Binary correlation without noise. (b) Morphological correlation without noise. (c) Regular correlation (Matched filter) without noise.

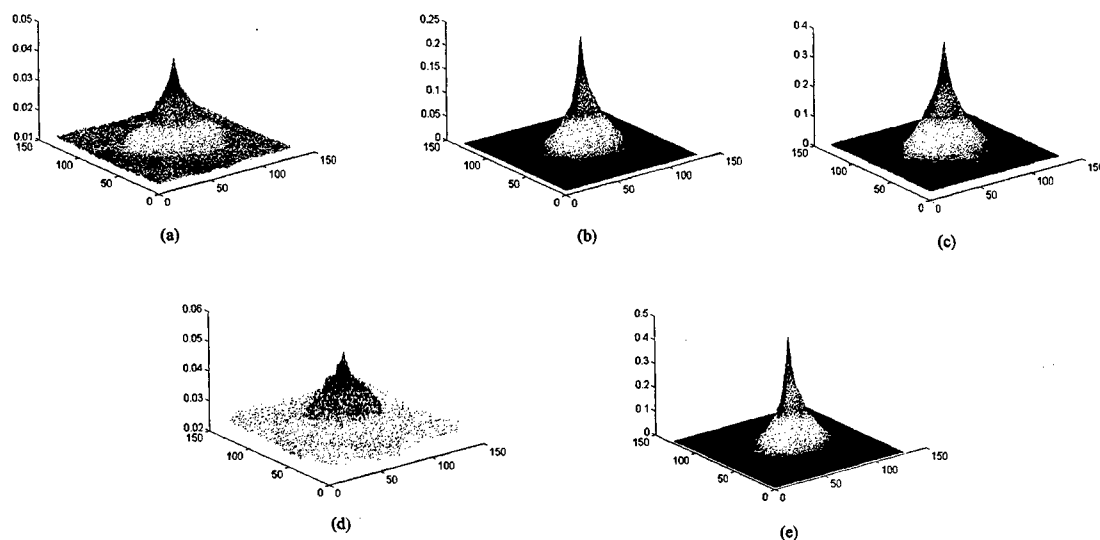


Figure 6: Computer simulations for $SNR = 1.294$:
Without weighting - (a) Binary correlation. (b) Morphological correlation. (c) Regular correlation
With weighting - (d) Binary correlation. (e) Morphological correlation.

5. CONCLUSIONS

In this paper, two new approaches for morphological correlation have been presented and demonstrated: The adaptive coefficient morphological correlation and the binary representation methods. The first becomes less sensitive to noise after using the weighting coefficients but it still preserves its discrimination capabilities. In the simulation results it was shown that the morphological correlation with adjusting coefficients yields better results in compare to the regular correlation. The second approach reduces the computing complexity but has a high discrimination and noise sensitivity. Its performances are very similar to the inverse filter but due to the fact that it is a non linear correlation it is still sensitive to multiplication by a constant.

6. ACKNOWLEDGMENT

We would like to thank Drs. Carlos Ferreira, Javier Garcia and Pascuala Garcia-Martinez for their introduction to the morphological correlation analysis.

7. REFERENCES

1. R. O. Duda and P. E. Hart, *Pattern Classification and Scene Analysis*, Chap. 7, p. 279, Wiley, New York, (1973).
2. P. Maragos, 'Morphological correlation and mean Absolute Error Criteria', *Proc. of IEEE International Conference on Acoustics, Speech and Signal Processing*, Glasgow, Scotland, (1989).
3. G. L. Turin, 'An introduction to matched filters', *IRE Trans. On Information Theory*, IT-6, 311, (1960).
4. P. Maragos, *Proceedings 2nd International Conference on Computer Vision*, Florida, p. 695, (1988).
5. J. Serra, *Image Analysis and Mathematical Morphology*, Academic, London, (1982).
6. P. Maragos and R. W. Schafer, 'Morphological Systems for Multidimensional Signal Processing', *Proc. of the IEEE* 78, p. 690, (1990).
7. C. S. Weaver and J. W. Goodman, 'A technique for optically convolving two functions', *Appl. Opt.* 5, p.1248 (1966).
8. J. E. Rau, "Detection of differences in real distributions", *JOSA* 56, 1490-1494 (1996)

Rotation invariant pattern recognition using circular harmonics and synthetic discriminant functions

Dan Cojoc

University "Politehnica" of Bucharest, Applied Optics Laboratory
Spl. Independetei 313, RO-77206, Romania
E-mail: dca@physics2.physics.pub.ro

ABSTRACT

The use of circular harmonics to design correlation filters represents one of the most powerful approach in one-target recognition with in-plane rotation invariance. Recognition of more than one target can be achieved, on the other hand, using synthetic discriminant functions. In this paper we describe how can be combined these two techniques to design a filter which ensures rotation invariant recognition of multiple targets in parallel. The usefulness of the filter is demonstrated, for the case of two targets, by experimental results obtained from computer simulations.

Keywords: rotation invariance, circular harmonics, multiclass pattern recognition, synthetic discriminant functions

1. INTRODUCTION

Optical pattern recognition has been long considered a very useful tool in machine vision, robotics and automation. However, conventional matched filter (CMF) schemes (also known as VanderLugt correlators¹) allow only shift invariance. For many applications it would be highly desirable to design filters that provide not only shift invariance but rotation and scale invariances as well. Various approaches have been proposed to achieve two invariances simultaneously. One way to extend the capabilities of the CMF so that one invariant parameter could be added, is to match the filter to only part of the input information. This added parameter could be in-plane angular orientation of an object, when recognition is obtained by restricting the correlation to only a single harmonic out of the circular harmonic (CH) decomposition² or scale variations when the MF consists of a single harmonic out of the Mellin radial harmonics decomposition.³ A common feature of the harmonic decomposition (circular or radial) is that relies on selecting a single harmonic associated with one of the orthogonal coordinates of an object. The harmonic set consists of $\{\exp(im\theta)\}$ for a circular harmonic decomposition and $\{\exp(\ln(r))\}$ for a radial harmonic decomposition. In regard to in-plane rotation invariance, the use of CHs has been shown to be one of the most convenient solution.^{2,4}

Another approach to achieve distortion invariant pattern recognition is based on synthetic discriminant functions (SDFs).⁵ The shift-and-distortion invariant SDF is synthesised as a linear combination of a basis function set to achieve a constant correlation output for in-class images. This algorithm can handle any distortion parameters as rotation⁶ and scale. CMFs are not able to perform multiclass detection; also this limitation can be surpassed using SDF's algorithm. In this paper we propose to combine two algorithms: CHs decomposition to allow rotation invariance and SDFs for parallel multiclass recognition. The choose of the optimum harmonic order for each class of objects is demonstrated to have a crucial importance in this regard. Even if the SDF algorithm is used in its simplest form, the filter which results is shown to be good enough for the case of two-class detection.

A short review of these two approaches is presented in section 2 and 3 respectively. Section 4 contains the description of the combined algorithm used for rotation invariant multiclass recognition. Section 5 discusses the results obtained from computer simulations, for the case of two objects to be detected in parallel.

2. CIRCULAR HARMONIC FILTER

In this section we derive the expression of the CHF and demonstrate its ability to allow rotation invariance. This filter belongs to the class of filters that use partial information from the target. The main idea is to develop the object function in series of orthogonal functions and to keep only one harmonic. The filter function is then calculated following the classical procedure of CMF.

Let us consider that $f(\rho, \theta)$ is the object function expressed in polar coordinates and $\{\exp(im\theta)\}$ a set of orthogonal functions called circular harmonics. Following the circular harmonic decomposition, f can be written:

$$f(\rho, \theta) = \sum_{m=-\infty}^{\infty} f_m(\rho) \exp(im\theta) \quad (1)$$

where:

$$f_m(\rho) = \frac{1}{2\pi} \int_0^{2\pi} f(\rho, \theta) \exp(-im\theta) d\theta \quad (2)$$

We denote the filter function to be calculated by $H=F_1^*$ (the impulse response is $h=f_1^*(\rho, \theta)$). Using the harmonic expansion one gets:

$$f_1(\rho, \theta) = \sum_{n=-\infty}^{\infty} f_{1n}(\rho) \exp(in\theta) \quad (3)$$

where $f_{1n}(\rho)$ is defined in the same manner as f_m in eq. (3). Introducing the object described by function f in the input plane of an optical correlator, the correlation function between the filter and the input can be written:

$$\begin{aligned} R_{f,f_1}(\rho', \theta') &= \iint_{\rho, \theta} f(\rho, \theta) f_1^*(\rho - \rho', \theta - \theta') (\rho - \rho') d\rho d\theta = \\ &= \sum_n \sum_m \iint_{\rho, \theta} f_m(\rho) f_{1n}^*(\rho - \rho') (\rho - \rho') \exp[i(m - n)(\theta - \theta')] d\rho d\theta \end{aligned} \quad (4)$$

where (ρ', θ') identifies the polar coordinates in the correlation plane. The corresponding correlation value in the centre of the correlation plane will be:

$$\begin{aligned} R_{f,f_1}(0,0) &= \sum_n \sum_m \iint_{\rho, \theta} f_m(\rho) f_{1n}^*(\rho) \rho \exp[i(m - n)\theta] d\rho d\theta = \\ &= \sum_n \sum_m \int_{\rho} f_m(\rho) f_{1n}^*(\rho) \rho d\rho \int_{\theta} \exp[i(m - n)\theta] d\theta \end{aligned} \quad (5)$$

Using the orthogonality of the set $\{\exp(im\theta)\}$ in the above equation, we obtain:

$$R_{f,f_1}(0,0) = 2\pi \sum_m \int_{\rho} f_m(\rho) f_{1m}^*(\rho) \rho d\rho \quad (6)$$

Let us now consider the rotated version of the initial object (for simplicity we consider that it is centred on the origin and the angular orientation α is performed around this point). Let denote by g the function that describes the rotated object. Due to the use of polar coordinates, the relationship between f and g can be easily expressed:

$$g(\rho, \theta) = f(\rho, \theta - \alpha) \quad (7)$$

Using the change of variable: $\beta = \theta - \alpha$, the 'm' order in the circular harmonic expansion of function g can be written:

$$\begin{aligned} g_m(\rho) &= \frac{1}{2\pi} \int_0^{2\pi} g(\rho, \theta) \exp(-im\theta) d\theta = \frac{1}{2\pi} \int_0^{2\pi} f(\rho, \theta - \alpha) \exp(-im\theta) d\theta = \\ &= \frac{1}{2\pi} \int_{\alpha}^{\alpha+2\pi} f(\rho, \beta) \exp[-im(\beta + \alpha)] d\beta = \exp(-im\alpha) f_m(\rho) \end{aligned} \quad (8)$$

The corresponding correlation value in the centre of the correlation plane will be:

$$R_{g,f_1}(0,0) = 2\pi \sum_m \exp(-im\alpha) \int_{\rho} f_m(\rho) f_{1m}^*(\rho) \rho d\rho \quad (9)$$

Rotation invariance will be provided if the same correlation values are provided in the centre of the correlation plane for functions f and g :

$$|R_{f,f_i}(0,0)| = |R_{g,f_i}(0,0)| \quad (10)$$

If we take into account eqs. (6) and (9) immediately results that using a single harmonic the condition expressed by eq. (10) is satisfied. This means that only a part of the information contained by the target is used to build up the filter that allows rotation invariant pattern recognition. Therefore it is obvious that the performances of the filter will be reduced with respect to those of CMFs. This is the cost CHs approach has to pay for rotation invariance.

At least two questions arise from the above condition: where is the optimum centre to perform the harmonic circular decomposition and which is the best harmonic?. There were already reported rigorous methods to determine the proper expansion centre.⁸ However they imply huge amount of calculus; in our opinion this step can be skipped choosing the weighting centre or a point in its vicinity to start the harmonic decomposition with. This observation has been raised from numerous experiments and discussion with other researchers working in this field. The choice of the best harmonic depends, also in our opinion, of every particular application. The second harmonic seems to be the most indicated but this does not represent a rule. In section 3 we will discuss an example that outlines this problem.

3. SYNTHETIC DISCRIMINANT FUNCTION

This section contains a description of the SDF approach, which is used to design correlation filters able to perform multiclass pattern recognition. For the case of distortion invariant pattern recognition, the distorted versions of the target can be considered to define different classes. The filter is designed then to match to a function obtained as a linear combination of these distorted versions. This function is calculated so that the same peak response will be obtained for any version of the distorted object. However, this algorithm requires a high number of training images to reduce the filter's sensitivity to object distortions. This is why we try to use the SDF approach in combination with that of CH: SDF will be used to build up a filter that matches to a linear combination of circular harmonics that belong to a limited number of different objects.

Let consider a set $\{f_i\}$ of different object functions to be recognised. Our purpose is to find a suitable response impulse function h , which can be described by:

$$h = \sum_{i=1}^N a_i f_i \quad (11)$$

where N is the number of the object functions, a_i is the appropriate coefficient, and h denotes the SDF. This function is then used to obtain a certain type of CMF (i.e. a phase-only-filter). The main problem is to determine the set $\{a_i\}$ of the linear combination coefficients.

We denote by f the matrix which contains all the object functions (the objects described by functions f_i are first represented in the vectorial form f_i), and by a the column vector containing the coefficients $\{a_i\}$ of the linear combination. Assuming that c is the correlation vector of all the imposed values $\{c_i\}$ for the correlation peaks (e.g. c_i is the value of the correlation peak obtained from the correlation between the impulse response h and the object function f_i), it can be written:

$$c = f^+ h \quad (12)$$

where f^+ represents the transpose of the complex conjugate.

Combining eqs (11) and (12) we obtain:

$$h = f(f^+ f)^{-1} c \quad (13)$$

From the above equation one can see that the coefficients set $\{a_i\}$ of the linear combination are determined by the cross-correlations between every pair of objects and the correlation vector c .

SDF has to pay a cost for multiclass detection. For CMF, when the correct image is present at the input, the output of the correlator is the autocorrelation function. Thus locating an image with its CMF is simple, since the peak of the autocorrelation is easy to identify. However the SDF filters lack a sharp correlation peak, since the input image cross-correlates with all images in the training set. This often produces sidelobes of high intensity and degrades correlation plane peak-to-sidelobe and peak-to-correlation energy ratios. To avoid this problem, minimum average correlation filters

have been proposed.⁷ These filters minimise the average correlation plane energy as the first step in filter synthesis. In an attempt to optimise the signal-to-noise ratio, a SDF with minimum variance has been also introduced.⁹

4. CH-SDF FILTER SYNTHESIS

The use of CHs has been proved to be very useful to design correlation filters that ensure rotation invariance. The main advantage of this approach is that it does not need a training set of images to start the algorithm. In consequence, the filter function is quite easy to be calculated. Rotation invariance can be also achieved using SDF, but this method requires a large set of training images to obtain performances comparable with CH filter. The training set should contain a lot of rotated samples of the target to ensure a 'fine tuning' of the rotation invariance. This leads to a huge amount of calculus to calculate the filter function. On the other hand, if there is a limited number of images, SDF can be successfully used to perform multiclass pattern recognition. We suggest to combine the two techniques mentioned above to design a filter which provides rotation invariant pattern recognition for a limited number of images (targets). The filter that results is called CH-SDF filter.

The algorithm includes the following steps:

- Cartesian to polar coordinates transform for each image of the training set
- the circular harmonic decomposition for each image
- select the most representative harmonic for each image
- establish the images to be detected from the training set
- set the values of the correlation vector (1- for objects to be detected, 0- otherwise)
- compute the filter function using the SDF
- extract only the phase

Once the filter function being calculated, follows the evaluation step in correlator. Note that, if the correlation signals differ from those expected, some parameters of the algorithm specified above should be changed. The third and fifth step of the algorithm are the most important in this regard. The choose of the most representative harmonic depends on the particularities of the images in the training set and therefore there is very difficult to predict from the beginning the best harmonic. CH-SDF filter obtained from the above algorithm is a phase-only-filter (POF) because phase extraction provides sharper correlation peaks. Nevertheless, if we adopt POF, the correlator does not possess the same peak response for the inputs belonging to the training set. Therefore the coefficients in eq. (11) should be modified for the POF version. This implies a modification of the correlation vector.

5. EXPERIMENTAL RESULTS

For an evaluation of the performances of CH, SDF and CH-SDF filters we have considered a three-class problem. The objects of interest are depicted in figure 1: 'wrench', 'screw' and 'nut'. Each image is then inserted in a matrix of 256x256 pixels.

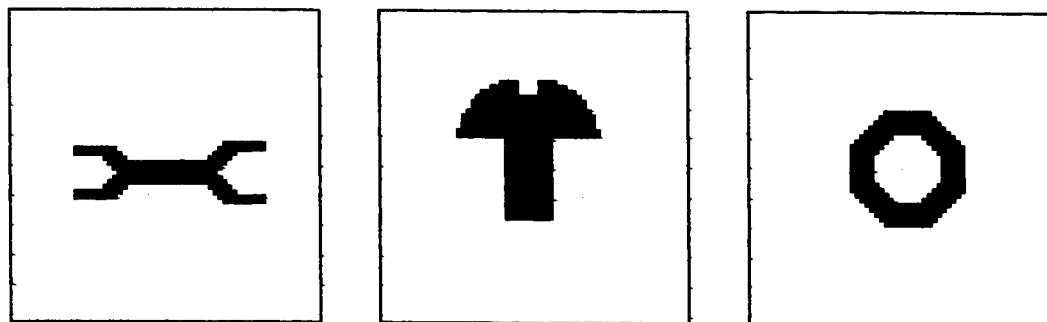


Figure 1 Test objects: 'wrench', 'screw' and 'nut'

First, we have designed the CH and SDF filters matching to the wrench. To build up the CH filter, the second harmonic has been used. For the SDF filter we have established a set of three images according to the angular orientation of the wrench: 0° , $+40^\circ$, and -40° . A set of 19 images, having different angular orientations, has been prepared for each class (the range of the rotation: $[-90^\circ, +90^\circ]$, sampled at every 10°). Each image has been introduced in the input of the correlator and spatial filtering has been performed with the two above mentioned filters. The corresponding performance of the two filters has been evaluated using the criterion of the 'correlation peak Intensity' by 'Peak-to-correlation energy' product (IP) and is depicted in figure 2.

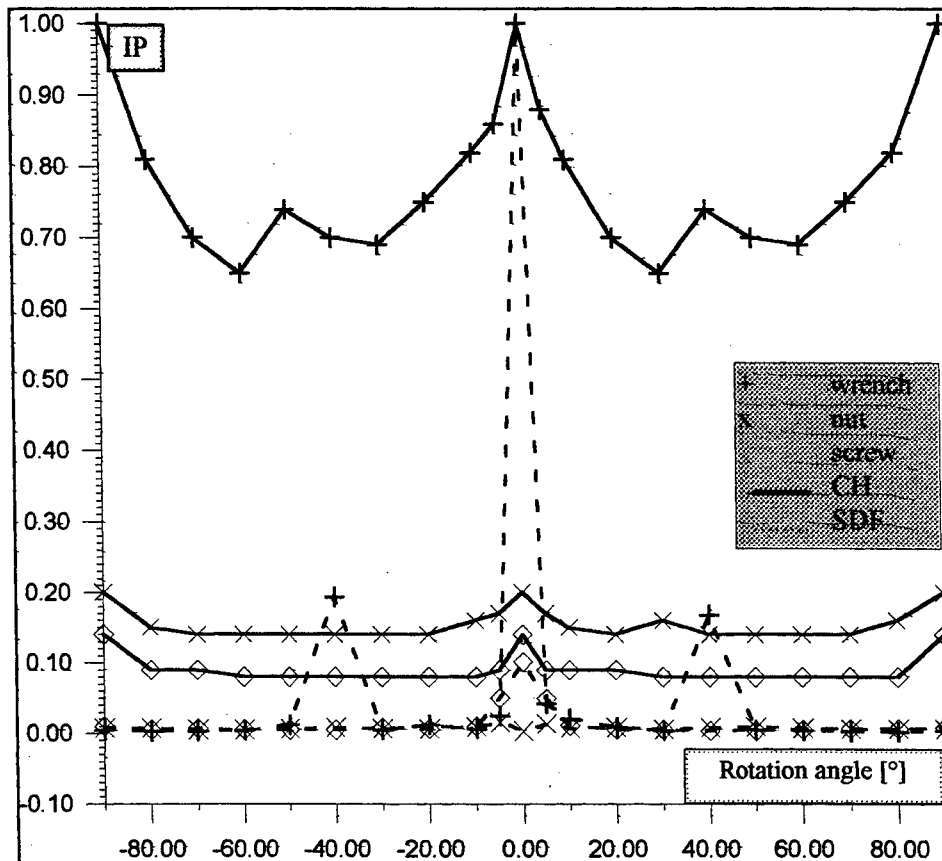


Figure 2 PI ('corellation peak intensity' x 'peak-to-correlation energy') versus the rotation angle

One can see that CH filter allows the correct detection of the target (wrench) for all angular orientations. A threshold situated between 20% and 63% will remove the signals belonging to the 'nut' and 'screw'. The correlations with SDF filter can not be used to perform rotation invariant pattern recognition. Even for the versions considered to build up the SDF filter the level of the signals are very low (only 20% of the case without rotation). However this does not mean that SDF can not provide rotation invariance; we have to evaluate again the correlation vector considering much more samples (at least 19) and this leads to a huge amount of calculus.

The use of CH filter also provides information about the angular orientation of the object. This information is very important in many applications where a robot has to handle a certain object after detection. This property of the CH filter is illustrated in figure 3 (a,b,c). Figure 3-a contains the input scene, figure 3-b the intensity distribution in the correlation plane, and figure 3-c the intensity distribution after a 50% thresholding. Thus, not only the presence of the wrench but also its orientation is accessible.

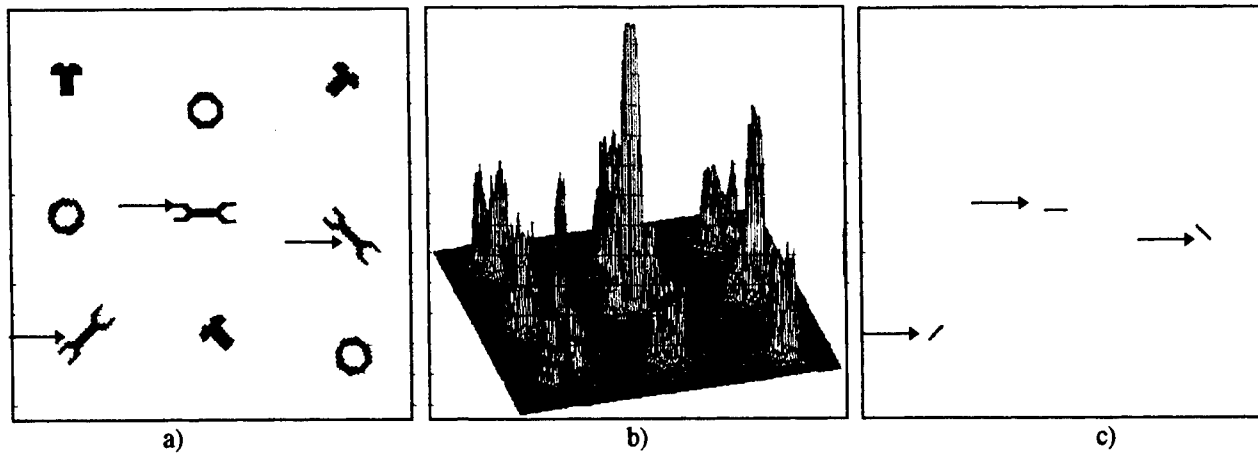


Figure 3 Detection of the angular orientation of the wrench

a) Input scene; b) Intensity distribution in the correlation plane; c) Intensity distribution after 50% thresholding

Following the algorithm described in section 4, we have calculated the CH-SDF filter. The objects to be detected are: 'wrench' and 'screw'. To evaluate the performance of CH-SDF filter we have used the criterion of 'correlation peak Intensity' (I). The choose of the proper harmonic order from the circular harmonic decomposition of each object plays a crucial role in this case. Using the second harmonic for 'wrench' and 'nut' and the third harmonic for 'screw' we have obtained much more useful correlation signals than using the second harmonic for all the three objects.

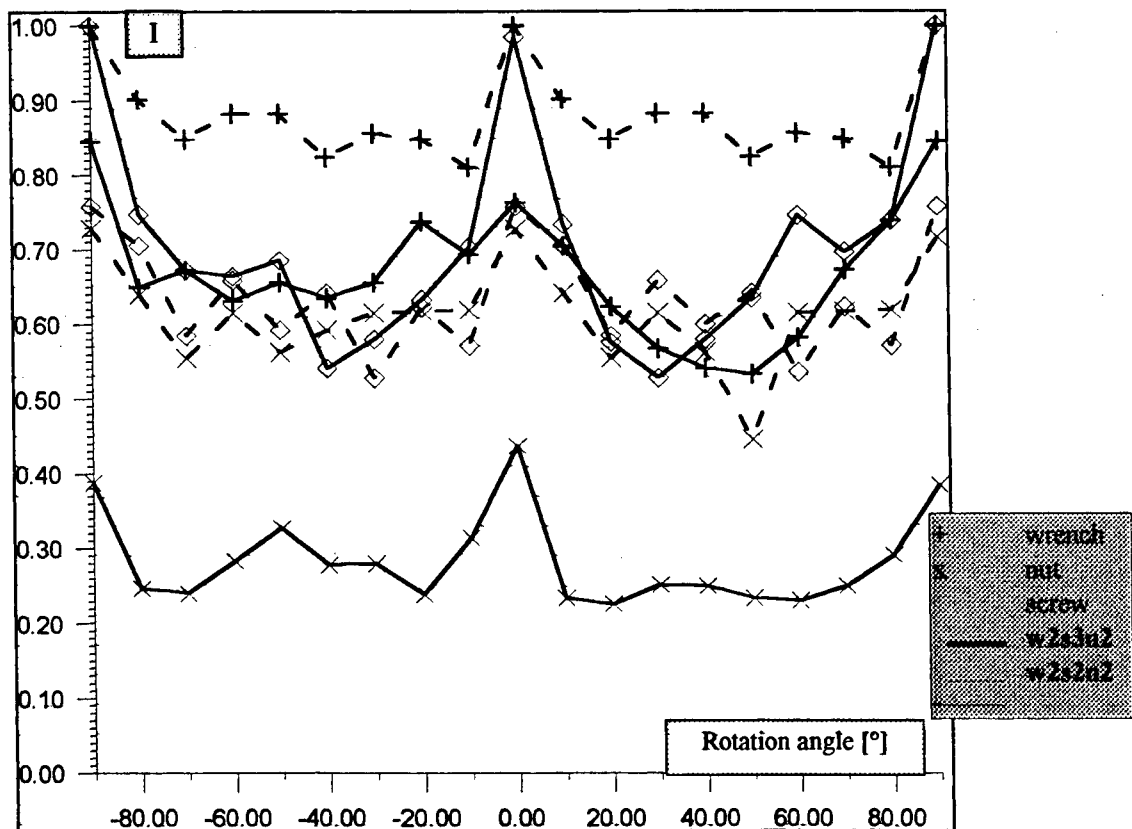


Figure 4 Correlation peaks intensity versus the rotation angle (w2s3n2- second harmonic for 'wrench' and 'nut' and third harmonic for 'screw', w2s2n2- second harmonic for all the three objects)

The results are depicted in figure 4. The intensities of the correlation peaks are higher than 52% from the maximum intensity for 'wrench' and 'screw' as well, while those corresponding to the 'nut' are lower than 47%. Even if the

discrimination interval is quite tight, a 50% threshold still allows the localisation of the two objects of interest. For the case when the second harmonic has been used for all the three objects, the signals corresponding to 'screw' and 'nut' are too close and therefore they can be confounded.

An example of two objects detection, independent of the angular orientation, is depicted in figure 5. The objects are introduced in the input scene shown in figure 5a (the objects of interest are indicated by arrows). The intensity distribution in the correlation plane is represented in figure 5b. Figure 5c represents the intensity distribution after a 50% thresholding.

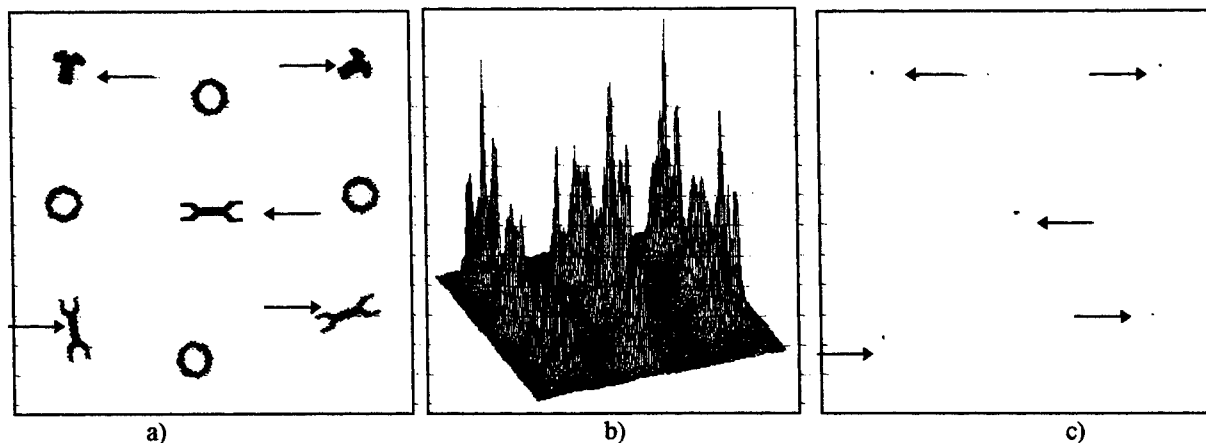


Figure 5 Two-class rotation invariant pattern recognition

a) Input scene; b) Intensity distribution in the correlation plane; c) Intensity distribution after 50% thresholding

6. CONCLUSIONS

In this paper we present some results obtained from the use of two different approaches: circular harmonics and synthetic discriminant functions, for rotation invariant pattern recognition. It is shown that for the case of only one object, circular harmonics represents the most convenient solution to ensure rotation invariance. In this case we show that CH filter can provide also the angular orientation of the object. This represents an important advantage in robotics because allows the robot with information it needs to handle the object after detection. Synthetic discriminant functions approach is, on the other hand, very useful for multiclass parallel detection. Therefore we suggest to combine the two approaches mentioned above: circular harmonics for rotation invariance and synthetic discriminant functions for multiclass detection. The filter which results is called CH-SDF filter. The ability of this filter to perform rotation invariant detection for two objects in parallel is demonstrated by experimental results obtained from computer simulations. The range of the angular orientation is $[-90^\circ, +90^\circ]$.

7. REFERENCES

1. A. VanderLugt, "Signal detection by complex filtering", *IEEE Trans. Inf. Theory*, IT-10, 139-146 (1964)
2. Y.N. Hsu, H.H. Arsenault, "Optical pattern recognition using circular harmonic expansion", *Appl. Opt.*, **21**, 4016-4021 (1982)
3. D. Mendlovic, E. Marom and N. Konforti, "Shift and scale invariant pattern recognition using Mellin radial harmonics", *Opt. Commun.*, **67**(3), 172-176 (1988)
4. D. Cojoc, E. Curatu, L. Taloi, F. Vasilescu, "Shift-and-rotation-invariant pattern recognition through optical correlation", *Optoelectronica*, **4**(3), 3-13 (1996)
5. D.P. Casasent, "Unified synthetic discriminant function computational formulation", *Appl. Opt.*, **23**, 1620-1626, (1984)
6. G. Ravichandran, D.P. Casasent, "Generalized in-plane rotation invariant minimum average correlation filter", *Opt. Eng.*, **30**, 1601-1607 (1991)
7. A. Mahalanobis, D. Casasent, "Performance evaluation of minimum average correlation energy filters", *Appl. Opt.*, **30**, 561-572 (1991)
8. Y. Sheng, H. H. Arsenault, "Method for determining expansion centres and predicting sidelobe levels for circular-harmonic filters", *J. Opt. Soc. Am.*, **A4**, 1793-1797 (1987)
9. B.V.K. Vijaya Kumar, "Minimum Variance Synthetic Discriminant Functions", *J. Opt. Soc. Am.*, **A 3**, 1579-1585 (1986)

A surface study of laser-induced charge gratings in $\text{Bi}_{12}\text{SiO}_{20}$ with an atomic force microscope

E. Soergel¹, W. Krieger¹, V. I. Vlad²

¹ Max-Planck-Institut für Quantenoptik, Hans-Kopfermann-Straße 1, D-85748 Garching, Germany

² Institute for Atomic Physics, Department of Lasers, R-79600 Bucharest, Romania

Abstract

Light-induced charge gratings at the surface of a photorefractive $\text{Bi}_{12}\text{SiO}_{20}$ crystal are investigated using electrostatic force detection with an atomic force microscope. The gratings with periods of 2.7 μm and 0.22 μm are generated by two intersecting Ar^+ -laser beams at 514 nm. The dark decay times of the stored gratings are determined. Saturation processes are directly observed by a change of the profile of the charge gratings. The polarity of the charge carriers in the material is obtained using a simultaneous measurement of the light-intensity grating.

Keywords: AFM, surface charge detection, photorefractivity, $\text{Bi}_{12}\text{SiO}_{20}$

Introduction

The photorefractive effect which shows a rich nonlinear behavior at low light intensities, offers an important potential in optical information processing and storage.¹ Increasingly, photorefractive phenomena are investigated and exploited in quantum wells, thin film structures, and fibers.² A surface-specific study of the optical recording and erasing phenomena therefore becomes necessary and important. In the conventional methods of investigation light is used to probe the light-induced refractive-index gratings in the material. Usually averages over large volumes are taken and, as a consequence, bulk phenomena cannot be separated from surface phenomena.

It is well known that scanning probe microscopy allows the investigation of a large variety of different surface effects. Using electrostatic force microscopy,³ charges on insulating surfaces can be investigated with a sensitivity sufficient for single-electron detection.⁴ This method is ideal for the study of light-induced charge distributions on photorefractive materials. In addition, the possibility of detecting evanescent light fields with the AFM,⁵ allows a determination of the phase shift between the light-intensity grating and the charge grating generated by it.

A first recording of a charge grating on BaTiO_3 was recently reported.⁶ In detailed experiments we studied charge gratings in $\text{Bi}_{12}\text{SiO}_{20}$ (BSO) and BaTiO_3 , and compared the photorefractive parameters obtained from these measurements.⁷

The aim of this paper is to demonstrate the numerous possibilities of electrostatic force imaging for the study of photorefractivity. The photorefractive material chosen is BSO. The dark decay of stored gratings is studied by measurements of the amplitude of the charge gratings. Grating

profiles recorded at different writing fluences, directly show the effects of saturation. The polarity of the charge carriers is determined.

Experimental Setup

The optical setup for the generation of charge gratings in the BSO crystal is shown in Fig.1. An argon-ion laser at $\lambda = 514 \text{ nm}$ is used. This wavelength excites photocarriers in the material very efficiently. The beam path was adjusted to provide interference patterns with maximum contrast and fringe spacings between $1.5 \text{ }\mu\text{m}$ and $3 \text{ }\mu\text{m}$. In order to obtain a smaller fringe spacing of $\approx 0.2 \text{ }\mu\text{m}$ an additional mirror M is used for backreflection. The mirror M2 can be shifted with the help of a piezoelectric transducer in order to move the grating across the crystal. The polarisation direction is parallel to the plane of incidence. The BSO crystal (undoped, size $7 \times 8 \times 2 \text{ mm}^3$, cut in transverse configuration) is optically contacted to a BK7 prism as shown in Fig.1(b).

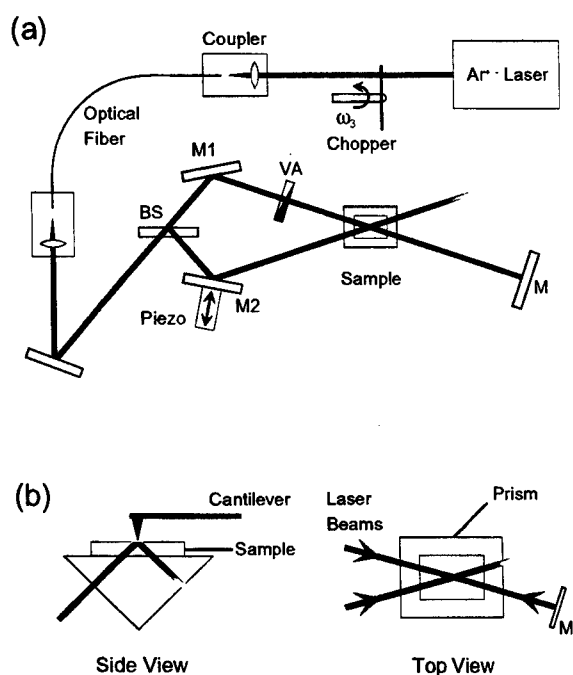


Fig.1 (a) Optical setup for the generation of charge gratings in a photorefractive sample (M1, M2 = mirrors, M = optional mirror, BS = beamsplitter, VA = variable attenuator). (b) Enlarged view of the total-internal-reflection geometry.

In atomic force microscopy a fine tip attached to a tiny cantilever is approached to a sample with the help of a piezodrive. The force between tip and sample is detected by measuring the bending of the cantilever. An image of the sample surface is obtained by scanning the tip over the sample while keeping the interaction force constant.

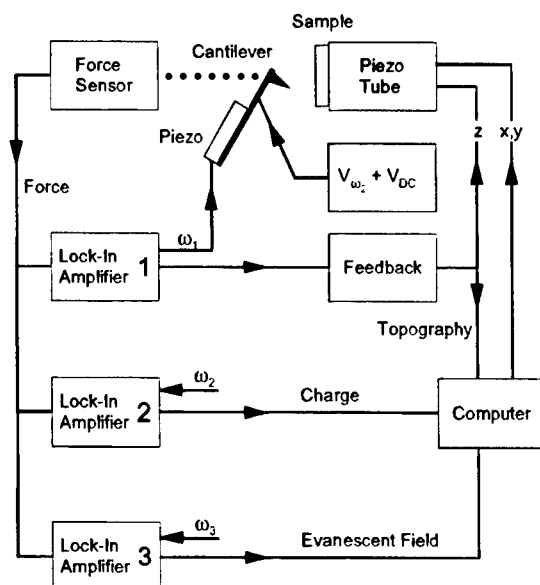


Fig.2 Experimental setup for the measurement of electrostatic forces (charge signal and evanescent field signal) with the atomic force microscope.

The experimental setup for the measurement of electrostatic forces with our home-built AFM is shown in Fig.2. The bending of the cantilever is detected with a laser beam ($\lambda = 670$ nm) which is reflected from the cantilever and falls on a position-sensitive detector. Since this laser radiation can also erase the charge gratings, the back of the silicon cantilever is covered with an aluminium layer of 60 nm thickness. In addition, the laser focus which is smaller than the width of the cantilever of 30 μm , is positioned at a distance of ≈ 50 μm from the tip. These precautions avoided any measurable effects of the sensor laser radiation on the stored charge gratings in the scanned area of the BSO crystal.

The AFM is operated in the non-contact mode at a tip-sample distance of 10 nm. The cantilever is excited at its resonance frequency ($\omega_1 \approx 60$ kHz) by a piezoelectric transducer and the oscillation amplitude, which is proportional to the force gradient, is measured by lock-in amplifier 1. A feedback module maintains a constant amplitude. Scanning the surface with a piezotube and recording the feedback signal leads to a constant-force-gradient map ("topography").

For charge detection a dc bias voltage and a low frequency signal ($V_0 = 2.5$ V, $\omega_2 = 2$ kHz) are applied to the conducting tip. The force between the surface charge and this periodically induced charge in the tip is measured with lock-in amplifier 2 at frequency ω_2 . The phase of this lock-in amplifier is set to give a positive output signal (bright area in the image) when the tip is above a negative surface charge, and a negative output signal (dark area) for a positive charge. This adjustment was controlled using small charged surface areas produced by applying voltage pulses of typically 10 V, 20 ms of both polarities to the tip (corona discharge). In this way charge images are obtained, with bright areas corresponding to electron accumulation domains. A charge image and a topography are acquired simultaneously.

Since the front end of the tip has a distance of only 10 nm from the sample it is immersed in the evanescent field of the writing beams. This field is detected via the surface-photovoltage effect in the silicon tip, i.e. the separation of excited photocarriers in the space-charge region near the surface.^{5,8}

The additional surface charges give rise to an electrostatic force which is measured by chopping the writing beams at a frequency $\omega_b = 800$ Hz and using a third lock-in amplifier. For a simultaneous measurement of the evanescent field and the charge field the tip remains fixed at a crystal position and the light grating is moved across the crystal. Alternatively, we have scanned the complete cantilever - and - force sensor assembly with additional piezoelectric transducers.

The AFM and the optical setup are fixed on a vibrationally isolated table inside a light-tight box. The laser radiation is coupled into the system using an optical fiber. In order to lower the humidity in the box, it is flooded with dry nitrogen.

Experimental Results and Discussion

In Fig.3 we show a charge image (left) and a surface topography (right) of the BSO crystal which were simultaneously obtained. The image size is $5\text{ }\mu\text{m} \times 5\text{ }\mu\text{m}$. The topographical image shows scratches in various directions which are caused by the polishing process. The maximum depth of these scratches is 5 nm. In order to demonstrate the capabilities of electrostatic force imaging, two superimposed charge gratings were written into the material.

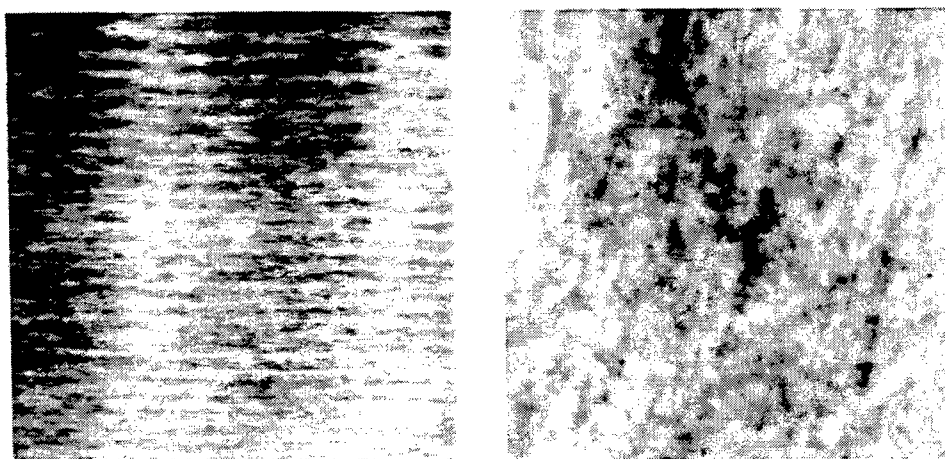


Fig.3 Electrostatic force image (left) and simultaneously recorded topography (right) of a BSO crystal. The image size is $5\text{ }\mu\text{m} \times 5\text{ }\mu\text{m}$ and the acquisition time was 8 minutes.

The two charge gratings are clearly observed in the left image. The two vertical grating lines have the expected fringe spacing of $2.7\text{ }\mu\text{m}$, and the horizontal lines have a distance of only $0.22\text{ }\mu\text{m}$. The bright spot in the center of the image is caused by the AFM tip which - during the writing process - remains at this position in the evanescent field, and locally reduces the field in the crystal by frustrated total internal reflection.

The grainy structure of the charge image is only partly due to noise. As observed in many images, it is connected with crystal inhomogeneities. Some of these charge structures were found to correlate with topographical features like adsorbed particles or scratches. Some may have its origin in crystal inhomogeneities close to the surface.

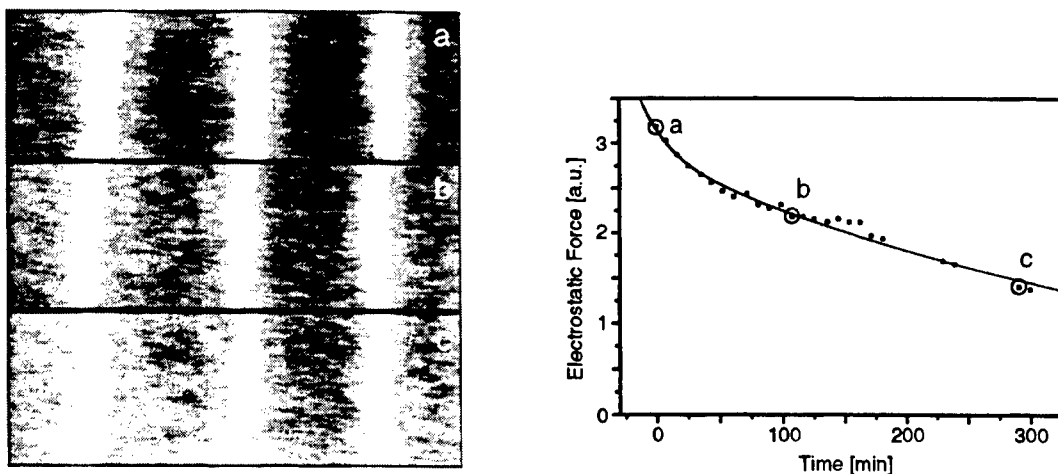


Fig.4 (left) Three images of the same charge grating at different times after the recording process. (Image size $8\ \mu\text{m} \times 2.6\ \mu\text{m}$. A slight drift is noticeable between the images). (right) Plot of the electrostatic force amplitude of the charge grating as a function of time. The data points a, b, c were obtained from the corresponding images on the left.

The most outstanding properties of electrostatic force imaging are the high lateral resolution and the surface specificity. From measurements of the distance dependence of the electrostatic force we estimate that charges can be observed with the AFM up to a depth of $\approx 10\ \text{nm}$. Therefore the values of crystal parameters obtained by a force measurement are actually surface values, in contrast to the bulk values which are measured by the conventional optical methods. These surface values may differ from the bulk values due to adsorbed layers, diffused particles and the effects of surface preparation.

The lateral resolution of the charge detection is given by the radius of curvature of the tip.⁴ New tips have a radius of $\approx 10\ \text{nm}$. This value increases by frequent use of the tips. A lateral resolution of a few $10\ \text{nm}$ is therefore easily obtained.

Measurements of the amplitude of the charge gratings can be used to study the process of recording and erasure. This is demonstrated in Fig.4 where we show a measurement of the dark decay of a charge grating. A grating with a fringe spacing of $2.7\ \mu\text{m}$ was recorded in the crystal using a laser intensity of $135\ \text{mW/cm}^2$ in each beam and a recording time of 2 seconds. Immediately afterwards a series of charge images were acquired at fixed time intervals. Three of these images are shown on the left of Fig.4. On the right we have plotted the amplitude of the charge gratings as obtained from averaged line scans, versus time. The images on the left correspond to the data points identified by a, b, c. The solid line is a double-exponential decay curve fitted to the data points. The decay times obtained are $t_1 = 23\ \text{min}$ and $t_2 = 450\ \text{min}$. These times were found to grow with the time the sample was kept in dry nitrogen. The above values correspond to an exposure time of two weeks. A double exponential decay is often found in photorefractive materials. It is related to a two-species model of donors and acceptors.⁹

Similarly, saturation processes are studied by measuring the amplitude of the charge grating versus the writing fluence.⁷ The effects of saturation can, however, also be directly observed as a change of the shape of the grating. This is shown in Fig.5. On the left, three images of charge gratings are displayed, written at different laser intensities during a time interval of 100 ms. Averaged line scans obtained from the images are shown in the right. A sinusoidal line shape - as expected

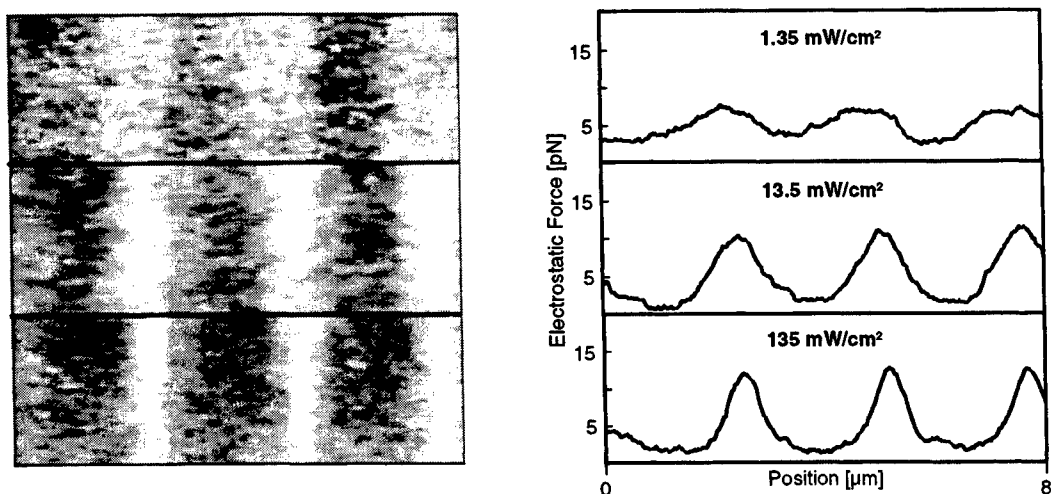


Fig.5 (left) Electrostatic force images for different laser intensities with an exposure time of 100 ms. Each image size is $8\ \mu\text{m} \times 2.6\ \mu\text{m}$. (right) Averaged line scans of the corresponding images.

for the linear regime - is only observed at the smallest laser intensity of $1.35\ \text{mW}/\text{cm}^2$. The gratings at higher intensities show profiles typical for saturation.

In a final example we make use of the fact that electrostatic force imaging allows us to distinguish between positive and negative charges. Using a simultaneous measurement of the evanescent field of the writing beams and of the light-induced charge grating generated, it becomes possible to determine the polarity of the charge carriers excited in the BSO crystal. This measurement was done by moving the light grating past the tip which remains at a fixed position. To obtain a static value for the phase shift between the light grating and the charge grating the grating velocity has to be so small that the measured phase shift becomes independent of the grating velocity.

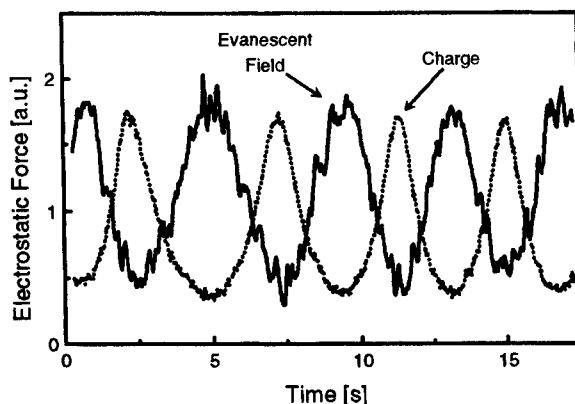


Fig.6 Simultaneous measurement of the charge signal (dotted line) and the evanescent-field signal (solid line) as a function of time. A voltage ramp applied to the piezo of mirror 2 moves the light grating across the crystal.

The results of the experiment are shown in Fig.6. The electrostatic force signals due to the evanescent field and to the charge are plotted versus the time. A voltage ramp moves the grating at a velocity corresponding to 1 fringe in 4 s. The resulting phase shift between the two gratings is $(9 \pm 3)^\circ$. This value did not change when the grating velocity was increased by a factor of 4. From Fig.6 we conclude that negative charges (corresponding to positive charge signals) accumulate at the darker grating lines, i.e. the charge carriers excited in the BSO crystal used for the measurements, are predominantly electrons. This was also found for other BSO crystals in bulk experiments.^{10,11}

Conclusions

Light-induced charge gratings in a BSO crystal were studied using electrostatic force microscopy. The amplitude, the shape, the polarity, and the relative phase of the grating lines were evaluated in order to obtain data on the polarity, the generation, the transport, and the recombination of the photocarriers in the material. Owing to the high lateral resolution, electrostatic force imaging allows to detect crystal inhomogeneities and to study their photorefractive properties. The extreme surface specificity makes this method especially suitable for the study of thin photorefractive films.

References

1. C.Medrano and G.Günther, in "Optical Phase Conjugation", M.Grower and D.Proch, Eds., Springer Verlag, Heidelberg (1994)
2. D.D.Nolte and M.R.Melloch, in "Photorefractive Effects and Materials", D.D.Nolte Ed., Kluwer Academic Publ., Dordrecht (1995)
3. B.D.Terris, J.E.Stern, D.Rugar and H.J.Marmin, Phys.Rev.Lett., 63, 2669 (1989)
4. C. Schönenberger, Phys. Rev. B45, 3861 (1992)
5. J.Mertz, M.Hipp, J.Mlynek and O.Marti, Appl.Phys.Lett.64 (18) (1994)
6. M.Hipp, J.Mertz, J.Mlynek and O.Marti, in "Photons and Local Probes", O.Marti and R.Moeller, Eds., Kluwer Academic Publ., Dordrecht (1995)
7. E.Soergel, W.Krieger and V.Vlad, submitted to Appl. Phys. B
8. D.G. Cahill and R.J.Hamers, Phys.Rev.B44, 1387 (1991)
9. G.C. Valley, Appl. Opt., 22, 3160(1983) and 23,1131(1984)
10. G.C. Valley and M.B.Klein, Opt.Eng.,22, 21(1983)
11. L.Arizmendi, J.M.Cabrera and F.Agnello, Intl. J. Optoelectronics, 7, 149(1992)

Optical bistability in short external cavity DBR semiconductor lasers

Victor Guja¹, Ivo Montrosset², Ovidiu Iancu³

¹ "Politehnica" University of Bucharest; now he is with Politecnico di Torino. GUJA@EALPHA.POLITO.IT

² Politecnico di Torino. MONTROSSET@POLITO.IT

³ "Politehnica" University of Bucharest. OPTO@JOE.TEHFI.PUB.RO

ABSTRACT

The bistability that we are describing results from designing properly the cavity of a Distributed Bragg Reflector (DBR) laser realized with an external fiber grating and is based on longitudinal mode competition. The analysis of the output power bistability is done with a simulation of the static behavior of the laser. An accurate and fast computing algorithm has been implemented to solve the steady state rate equations for photon and carrier density. The used model is based on multimode analysis and includes gain saturation.

Keywords: bistability, DBR, external cavity, fiber grating, mode competition, semiconductor lasers

1. INTRODUCTION

Optical bistability is a very interesting phenomenon for applications in the field of optical switching devices. These are important for the evolution of high speed optical signal processing and optical communications. The bistable devices based on laser diode nonlinearities have the advantage of the optical gain that permit low input switching power, high on-off ratio and large fan-out.

There are three main types of bistable effects in the output characteristics of a laser diode; these are related with changes in polarization, in wavelength and in optical output power. There are also three types of input control signals: optical, electrical and a combination of them. An overview description of the nonlinear mechanisms and structures with bistable characteristics can be found in the literature.^{1,2}

In our paper we present theoretical results for the optical output power bistability in a short external cavity DBR semiconductor laser realized using a fiber grating. The cavity was designed to obtain longitudinal mode switching with the increase of the injection current; this is obtained when the spectral reflectivity of the Bragg reflector overlaps just one longitudinal cavity mode. Variations in the injection current determine changes in the mode wavelength permitting to turn off and on the laser diode. There are a few mechanisms operating together to make this behavior possible. Increasing the injection current the carrier density changes mainly for gain saturation effects; it results a variation of the effective refractive index and of the cavity resonance wavelengths. This effect in a DBR with a properly designed grating reflectivity allows bistability as already experimentally observed and described for an integrated two section DBR structure without external cavity.³

The continuous wave laser characteristics have been obtained using a multiple longitudinal mode approach.

2. THEORETICAL MODEL OF THE STRUCTURE

The cavity we have considered is presented in Fig. 1. The left facet of the active waveguide is covered with a High Reflectivity Coating (HRC) while the right one with an AntiReflection Coating (ARC).

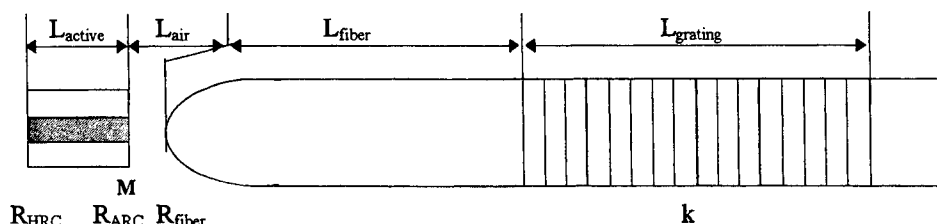


Fig. 1 Structure of the investigated external cavity DBR laser;
M, reference section for cavity effective reflectivity

To describe the steady state behavior of such a laser we used a mean field multimode rate equations approach.⁴ This is based on the equations (1), (2) written as for a usual Fabry Perot (FP) laser but with the assumption of a wavelength dependent reflectivity,

$$\frac{dN}{dt} = \frac{J}{ed} - \frac{N}{\tau_s} - \frac{c}{n_{eff}} \sum_m g_m S_m, \quad (1)$$

$$\frac{dS_m}{dt} = \Gamma \frac{\beta_m N}{\tau_s} + \frac{c}{n_{eff}} \Gamma g_m S_m + \frac{S_m}{\tau_m}. \quad (2)$$

The material gain expression for each mode (λ_m) is given by,

$$g_m = \frac{G_0 \ln\left(\frac{N}{N_t}\right) - \frac{\gamma_0 (\lambda_m - \lambda_{p0} + \lambda_{pN} N)^2}{1 + \frac{\gamma_0 N_t}{G_0} \lambda_{pN}^2 N}}{1 + \epsilon S_m}, \quad (3)$$

where we have considered logarithmic dependence with the carrier density N and parabolic dependence with the wavelength while the gain saturation effect is represented with the self saturation factor $(1 + \epsilon S_m)^{-1}$; cross saturation terms have not been considered because the described laser behavior is mainly determined by selfsaturation. Other symbols are defined in Table 1.

The model considered for the change in the refractive index due to the carrier density was assumed of the form,

$$n_{eff} = n_{active} + n_N \Gamma N, \quad (4)$$

where n_N is the coefficient for the carrier induced refractive index change.

The analysis of the structure takes into account the residual reflectivity of the ARC at the fiber tip as well as the coupling losses between the laser and the fiber. For this reason all the parts of the structure have been characterized with their proper transmission matrix.

The modal light powers at the fiber output have been obtained from the modal photon densities in the active region by evaluating the total S_{21} coefficient of the structure from the active waveguide to the output of the grating,

$$P_m = \frac{|S_{21}|^2}{1 - R_{ARCeff}} \frac{1 - R_{ARCeff}}{1 - \sqrt{R_{ARCeff}} \sqrt{R_{HRC}}} \left[-\ln\left(\sqrt{R_{ARCeff}} \sqrt{R_{HRC}}\right) \right] \frac{1}{1 + \sqrt{R_{ARCeff}}} \frac{S_m}{\lambda_m \Gamma} h c^2 \frac{dw}{n_g}. \quad (5)$$

In the presented case we neglected the effect of the unwanted residual multiple reflections inside the external cavity.

Table 1 List of the symbols used in the equations

β_m	modal spontaneous emission factor	n_{eff}, n_g	effective and group refractive index
d	active layer thickness	n_N	coefficient for the carrier induced change of the refractive index
ϵ	gain saturation coefficient	N	carrier density
g_m	nonlinear material gain	N_{tr}	carrier density at transparency
G_0	gain fitting parameter	R_{ARCeff}	modal effective power reflectivity at the right part of the M section (external cavity)
γ_0	gain curvature	R_{HRC}	modal power reflectivity of the HRC
Γ	modal confinement factor	S_m	modal photon density
J	injected current density	τ_m	modal photon lifetime
λ_m	modal wavelength	τ_s	carrier lifetime
λ_{p0}	gain's peak wavelength "without injection"	w	active layer width
λ_{pN}	derivative of gain peak wavelength with N	$\phi_{leftARC}$	effective reflectivity coefficient' phases to the left and right of the M section
		$\phi_{rightARC}$	

3. NUMERICAL ANALYSIS

To determine the main static characteristics one must solve selfconsistently the carrier and photon density equations with the longitudinal cavity resonance equation; the last allows to determine the longitudinal mode wavelengths. The most natural numerical procedure consists in setting the value of the injection current density J and in finding the carrier density N and the modal photon densities using an iterative method. In this case for each iteration is necessary to evaluate the wavelengths of the lasing modes; we found this approach inefficient due to the repeated evaluation of the resonant wavelengths and with a lot of convergence problems.

We found more efficiently an algorithm that set the value of N and finds the current density and all the other parameters, as shown in Fig. 2.⁴ This procedure has the advantage to need only once, for each N value, the computation of the resonant wavelengths and the selfconsistent solution for J and S_m . With the assumed value for the carrier density the active's effective refractive index is computed using (4); the lasing wavelengths are found numerically solving the resonance phase equation for the multiple cavity structure,

$$\phi_{\text{leftARC}}(N) + \phi_{\text{rightARC}} = 2\pi m \quad m \in \mathbb{Z} \quad (6)$$

The search to find all the existing solutions, in a given wavelength interval, determines first, with a quite complex algorithm, the subintervals in which each solution is located and then proceeds to its accurate evaluation. The obtained operation wavelength of each mode allows to determine the corresponding photon lifetime; the values for S_m and J , just for the physical solution, are found through the analytical solution of the photons (2) and carriers (1) rate equations. The output power for each mode is then obtained with (5). We found this method very stable and accurate for all the considered structures.

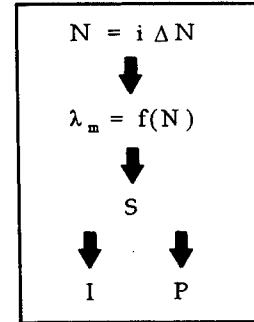


Fig. 2
Algorithm

4. SIMULATION RESULTS

In order to obtain the desired bistable behavior we consider a cavity with a Free Spectral Range (FSR) greater than the grating's Stop Band (SB). In our simulation we have considered two cases: SB almost equal to the FSR and SB much smaller than the FSR. We discuss in detail the first case while we report only the results for the second.

In Table 2 we present the most important characteristics of the structure in the first considered case. The total output optical power in fiber and the carrier density curves versus the injected current, at the constant temperature of 300K, have been reported in Fig. 3 and Fig. 4. In Fig. 6 we report the effective power reflectivity at the right end of the active section versus wavelength. The mode 1A is the fundamental one and it is lasing above the threshold current while mode 2A, the following longitudinal mode, is below threshold. Increasing the injected current the cavity modal wavelengths are moving to the left with respect to the reflectivity peak because of the change in the refractive index of the active region as a consequence of the increased carrier density due to the gain saturation. The device is designed such that the reflectivity of mode 1 is falling down while that of mode 2 is rising. This wavelength shift (Fig. 6) with a corresponding jump in the carrier density (Fig. 4) determines the bistable behavior shown in the output optical power (Fig. 3) and in the photon density (Fig. 5) versus the injected current.

The previously described behavior, varying the injected current, is represented in detail by the sequence of icons in Fig.7. This reports for increasing (Fig. 7 a-d) and decreasing (Fig. 7 d-f) current the resonance frequency position of the competing modes with respect to the curve of effective reflectivity.

Table 2 Structure parameters considered to obtain bistable behavior

HRC	0.89	power reflect.
L_{active}	750	μm
ARC	0.0001	power reflect.
L_{air}	10	μm
R_{fiber}	0.001	power reflect.
L_{fiber}	0.5	cm

k	0.4	cm ⁻¹
L_{grating}	2	cm
SB	0.015	nm
FSR	0.019	nm
I_{thr}	9.799	mA
ε	$4 \cdot 10^{-17}$	cm ³

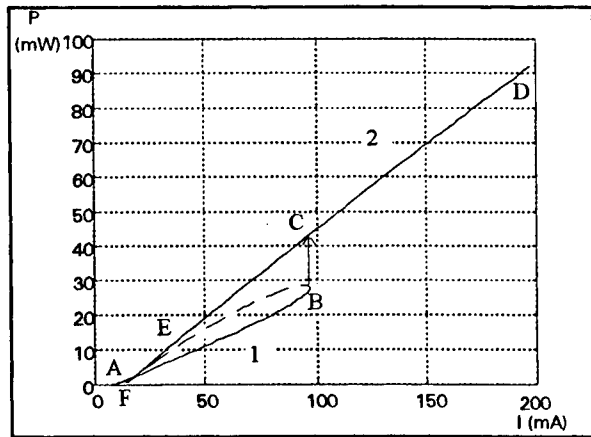


Fig. 3

P vs. I characteristic, for the structure defined in Table 2.

1 and 2 indicate the branches of the characteristics when the fundamental and the competing mode are lasing.

The dashed branch corresponds to an unstable solution.

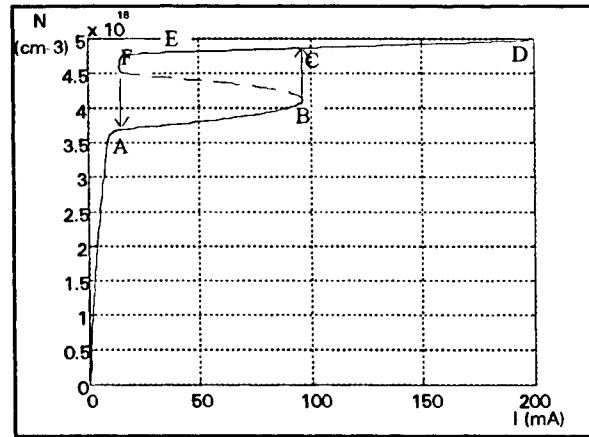


Fig. 4

Carrier density N vs. I characteristic, for the structure defined in Table 2.

The dashed branch corresponds to an unstable solution.

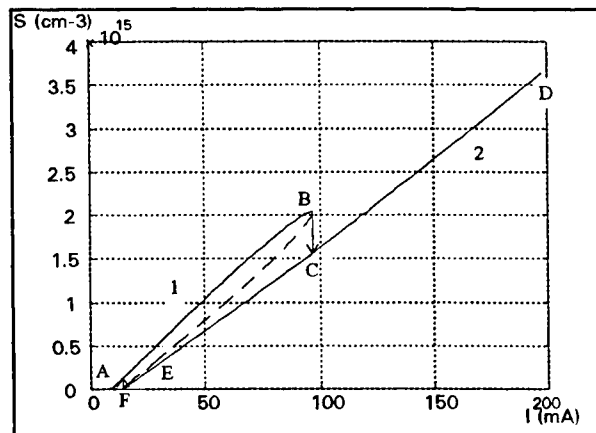


Fig. 5

Total photon density S vs. I characteristic, for the structure defined in Table 2.

1 and 2 indicate the branches of the characteristics when the fundamental and the competing mode are lasing.

The dashed branch corresponds to an unstable solution.

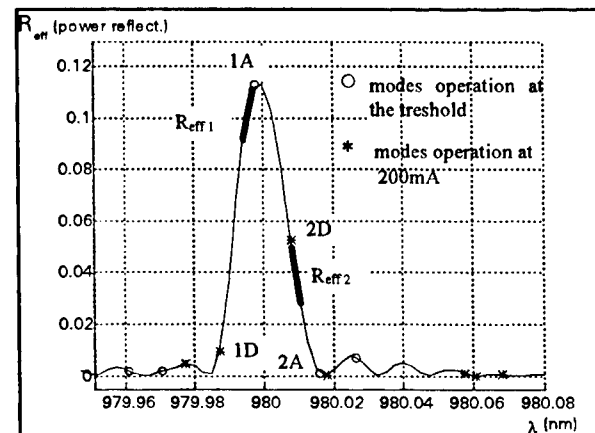


Fig. 6

Effective reflectivity R_{ARCEff} vs. wavelength characteristic, for the structure defined in Table 2.

A and D indicate the correlation with the points A, D in Figs. 3-5.

1 and 2 indicate the competing modes, mode 1 and mode 2.

Figures 7 (e-f) show that in the branch 2 the gain saturation effects are such that mode 2 is lasing even if its cavity losses are greater than those of mode 1 ($R_{eff1} \geq R_{eff2}$).

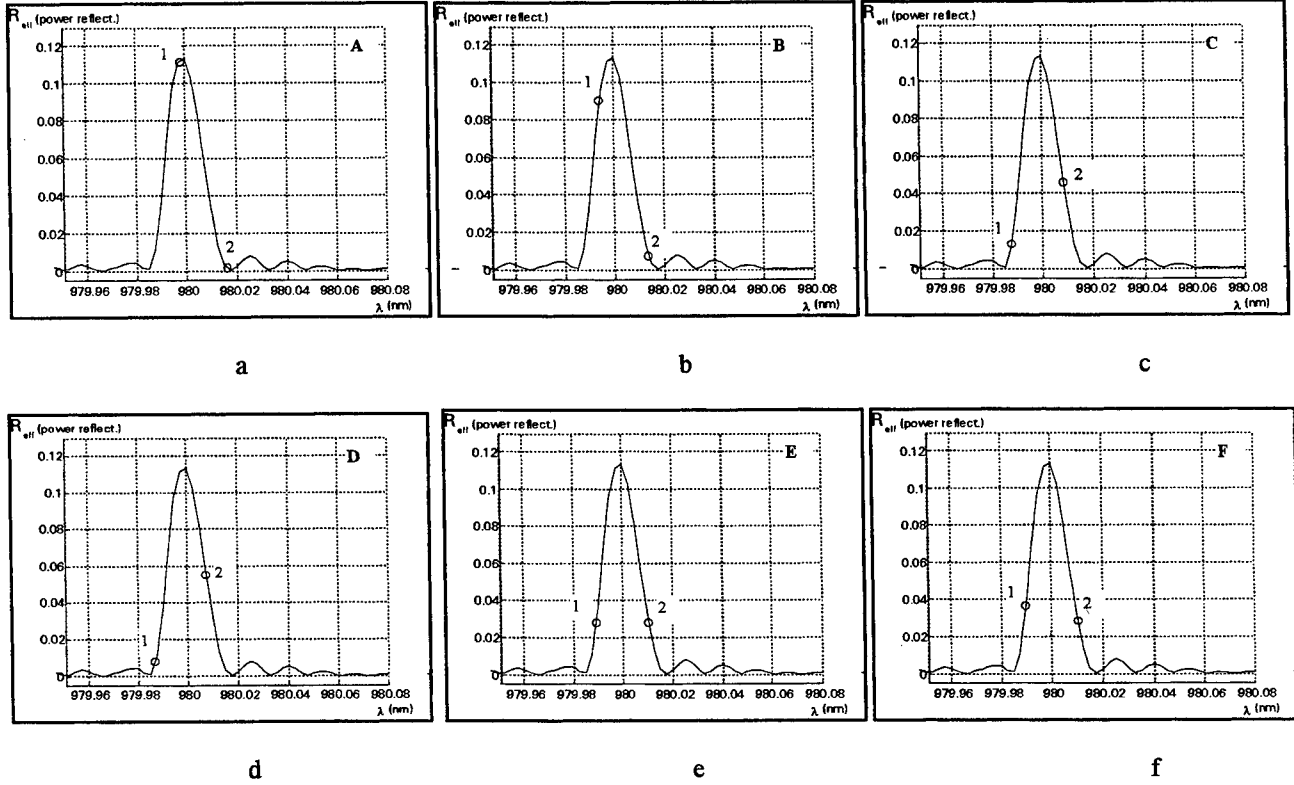


Fig. 7

Position of the fundamental 1 and competing mode 2 for different injection currents;

A : just above threshold; B : just before switching from mode 1 to mode 2; C : just after switching to mode 2; D : for high injection current; E : in the upper branch of the hysteresis loop; F : just before switching to mode 1.

A-F indicate the correlation with the points A-F in Figs. 3-5.

Details of the lower part of the optical power versus injection current characteristic are reported in Fig. 8. The characteristic's jump is associated with the corresponding transition in the carrier density shown in Fig. 4. The swallow tail behavior of the hysteresis is due to the different external quantum efficiency ($R_{eff1} > R_{eff2}$ in Fig. 6) of the two competing longitudinal modes when lasing.

The second case considered in our simulations is a structure with the grating SB much smaller than the FSR of the overall cavity. In Table 3 we present the most important characteristics for this structure. The total output optical power in fiber and the carrier density curves versus the injected current, at 300K, are shown in Fig. 9 and Fig. 10. In Fig. 11 we report the effective power reflectivity at the right end of the active section versus wavelength and the position of the modes for threshold injection current and for 200 mA. The Side Mode Suppression Ratio (SMSR) vs current curve presented in Fig. 12 creates an

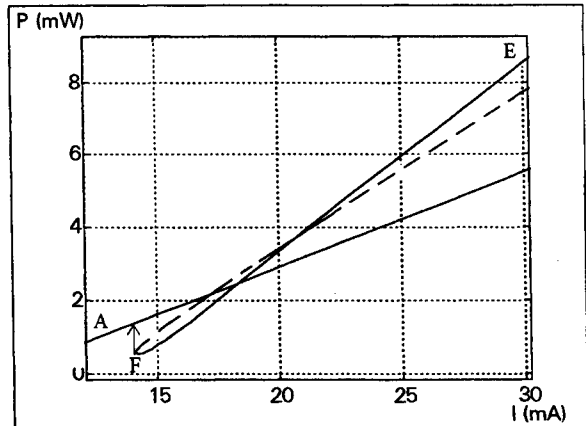


Fig. 8 Detail of the lower part of Fig. 3

image of the relative wavelength movement with respect to the effective power reflectivity curve of the two competing modes that are generating the bistability.

Table 3 Structure parameters considered to obtain bistable behavior

HRC	0.1	power reflect.
L_{active}	750	μm
ARC	0.0001	power reflect.
L_{air}	10.1225	μm
R_{fiber}	0.001	power reflect.
L_{fiber}	0.5	cm

k	0.05	cm^{-1}
$L_{grating}$	4	cm
SB	0.007	nm
FSR	0.01199	nm
I_{thr}	62.519	mA
ε	$4 \cdot 10^{-17}$	cm^3

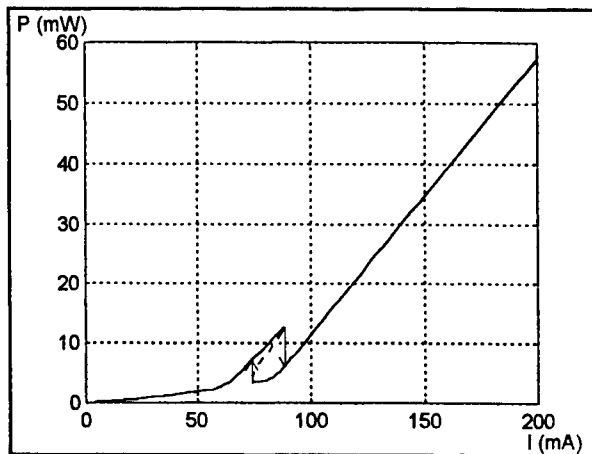


Fig. 9

P vs. I characteristic, for the structure defined in Table 3.

The dashed branch corresponds to an unstable solution.

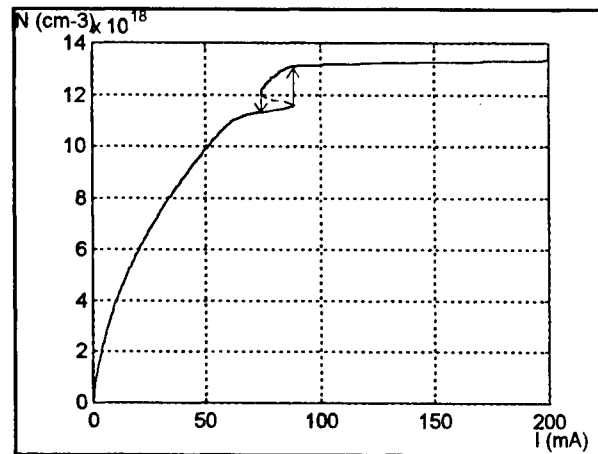


Fig. 10

Carrier density N vs. I characteristic, for the structure defined in Table 3.

The dashed branch corresponds to an unstable solution.

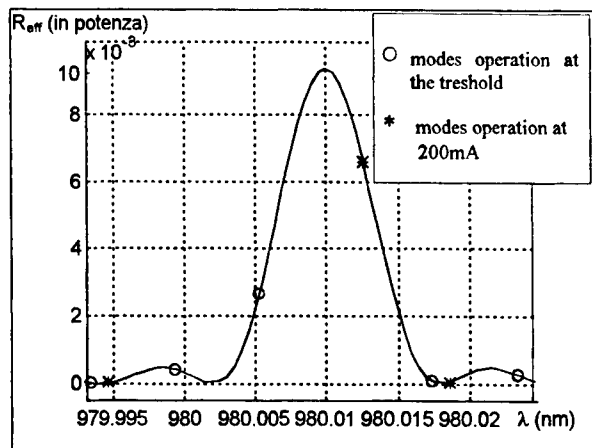


Fig. 11

Effective reflectivity R_{ARCeff} vs. wavelength characteristic, for the structure defined in Table 3.

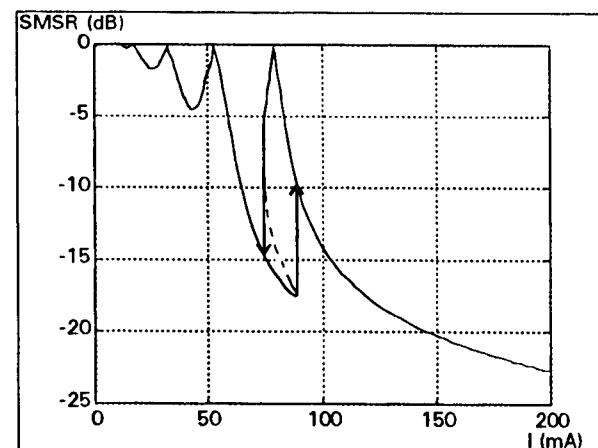


Fig. 12

SMSR vs. current characteristic, for the structure defined in Table 3.

SMSR is for the highest secondary mode with respect to the fundamental mode.

The dashed region corresponds to an unstable solution

5. DESIGN CONSIDERATIONS

The previous analysis allows to deduce some hints relevant for the design of an optical power bistable DBR external cavity laser diode.

In what concerns the active material characteristics, being the device based on the wavelength shift due to gain saturation effects, becomes important to choose materials with low saturation power and/or high linewidth enhancement factor.

The cavity characteristics should be such that the grating's SB be smaller than the FSR of the overall cavity (from the left air-semiconductor interface to the fiber grating). The swallow tail effect is related to the grating's SB dimensions. To obtain an optical switch, with a minimal classic hysteresis, the SB must take a much lower value with respect to the FSR.

In the case of a narrow SB exists the possibility of lasing, with high threshold current, when the Bragg wavelength is at the center with respect to two consecutive longitudinal FP modes. In this case, an adjustment of the air gap length or at a current control section integrated with the FP could bring the laser to have a characteristic that switches off with increasing current.

The case in Figs. 3-8 presents a behavior typically observed when the SB is little less than the FSR and the fundamental mode at low current operates at a wavelength located at the left side of the reflectivity peak.

The case in Figs. 9-12 presents a behavior typically observed when the SB is much less than the FSR and the reflectivity peak's wavelength is situated between two consecutive modes of the cavity, at low injection current.

6. REFERENCES

- 1.H.Kawaguchi, *Bistabilities and Nonlinearities in Laser Diodes*, Artech House, 1994.
- 2.H.M.Gibbs, *Optical Bistability: Controlling Light with Light*, Academic Press, 1985.
- 3.M.Margalit, N.Nagar, N.Tessler, G.Eisenstein and others, "Bistability and optical control of a distributed-Bragg-reflector laser", *Optics Letters*, vol.18, pp.610, April 1993.
- 4.K.J.Ebeling, *Integrated Optoelectronics*, pp.303, Springer Verlag, 1992.
- 5.L.A.Coldren and S.W. Corzine, *Diode Lasers and Photonic Integrated Circuits*, pp.189, John Wiley & Sons, 1995.
- 6.G.R.Gray and R.Roy, "Bistability and mode hopping in a semiconductor laser", *J.Opt.Soc.Am. B*, vol.8, pp.632, March 1991.

Nonlinear optical properties of noncrystalline semiconductors

Valentin Chumash

Center of Optoelectronics, I. A. P., Academy of Sciences of Moldova
Academiei Str. 1, Chisinau, MD-2028, Moldova

ABSTRACT

The paper summarizes the peculiarities of the nonlinear interaction of short laser pulses with the noncrystalline semiconductors (chalcogenide glasses, a-Si:H), showing that noncrystalline semiconductors (NS) are an interesting material for high speed optoelectronics. The physical mechanisms, which can contribute to the nonlinear light absorption in NS under pulsed excitation, are reviewed.

Keywords: noncrystalline semiconductors, chalcogenide glasses, a-Si:H, optical hysteresis, nonequilibrium phonons, localized vibrational excitations.

1. INTRODUCTION

Nonlinear optical effects in semiconductors are studied to a much less extent in the noncrystalline than in the crystalline state. The interest to the study of the nonlinear propagation of laser radiation in NS is determined not only by the new fundamental physical mechanisms present in these materials, but also by a wide spectrum of possible applications in optoelectronic devices and photonic switching. NS are attractive candidates for the fabrication of all-optical passive and active devices in the same medium. In recent years a variety of both passive (fibers, planar waveguides, lenses, gratings) and active (nonlinear devices mainly based on Fabry-Perot interference, optical bistability and optical hysteresis) elements have been demonstrated.^{1,2}

Special attention is paid to the phenomena that can be observed at relatively low levels of light intensity, in connection with their possible use in active elements of integrated optics and optoelectronics. The nonlinear change of the optical constants may be reached in the NS at much lower irradiation intensity than in the crystalline ones, when interband transitions with the participation of nonequilibrium phonons and nonequilibrium localized vibrational excitations play an important role.^{3,4} The capture of nonequilibrium phonons by structure inhomogeneities in NS leads to the increase of their effective lifetime.^{4,5} Promising effects are optical bistability and optical hysteresis, on the basis of which it is possible to build fast-response, all-optical switching and logical elements.^{6,7}

In a number of works some of the light induced reversible changes of the NS optical constants were studied considering the nonlinear transmission of focused CW laser radiation through thin film samples. Three types of nonlinear interaction of CW laser radiation with NS were observed: the nonlinear change of the light transmission of NS samples; the periodic oscillations in time of the photocurrent, of the transmission and of the reflection coefficients of NS films; and the light transmission bistability. In spite of a considerable number of works up to now there are no reliable data about the physical processes, describing adequately the nonlinear interactions of the CW laser radiation with noncrystalline semiconductors. The peculiarities of the nonlinear transmission of CW and pulsed laser radiation through thin NS films are reviewed in ^{1,2}.

The aim of this work is to illustrate the present state of knowledge and some unresolved problems of the nonlinear interaction of laser pulses with NS (chalcogenide glasses: As_2S_3 , As_2Se_3 , AsSe , GeSe_2 , $\text{As}_{22}\text{S}_{33}\text{Ge}_{45}$, and a-Si:H). Attention is primary given to those nonlinear phenomena that are characteristic of the NS and, as a rule, have no analogous in crystalline phase. The results of a systematic investigation of the optical hysteresis and nonlinear absorption at interband excitation of thin film samples (0.2 - 5 μm thick) of a-Si:H , a-SiC:H , As_2S_3 , As_2Se_3 , AsSe , GeSe_2 , $\text{As}_{22}\text{S}_{33}\text{Ge}_{45}$ with short laser pulses (300 K, 77 K) are briefly discussed in section 2. The physical mechanisms, which can contribute to the nonlinear light absorption in NS under pulsed excitation, are discussed in the next section. A model of the physics of the nonlinear interaction of powerful light with NS, taking into account the light interaction with nonequilibrium phonons and localized vibrational excitations, is considered for the explanation of the experimental results.

2. NONLINEAR ABSORPTION OF LASER PULSES IN NS

When the input light (with $h\nu \geq E_g$) pulse intensity was relatively low, the transmission of the NS films decreases with the thickness according to the usual Beer law (Fig. 1). However, increasing the incident light intensity over some threshold value (I_t) leads to a nonlinear light transmission by the NS films.^{1, 2, 8, 9} The characteristic value of the threshold light intensity depends on the NS film composition, wavelength of excitation, temperature and laser pulse duration. For example, for As_2S_3 , at 570 nm, the I_t values were equal: $\sim 2 \text{ MW/cm}^2$ for laser pulses with the 7 ns duration and $\sim 4 \text{ kW/cm}^2$ for laser pulses with 1 μs duration (300 K). As a result of the nonlinear light absorption a change of the time profile of the laser pulses was recorded at the output of the amorphous semiconductors. The change of the time profile of the laser pulses leads to hysteresis-like dependencies of the output light intensity (passed through the sample) on the corresponding value of the input (Fig. 2). The extension of the optical hysteresis loop increases (changing its shape) with the input light intensity up to the damage of the sample surface.

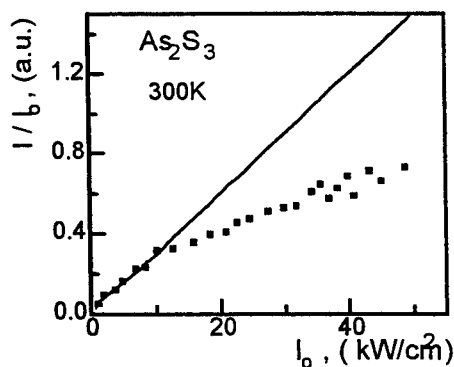


Fig. 1. Full line: continuation of low intensity light transmission. Symbols: nonlinear light transmission of $\text{a-As}_2\text{S}_3$ film (thickness 2.6 μm) versus input pulse intensity; $\hbar\omega = 2.58 \text{ eV}$.

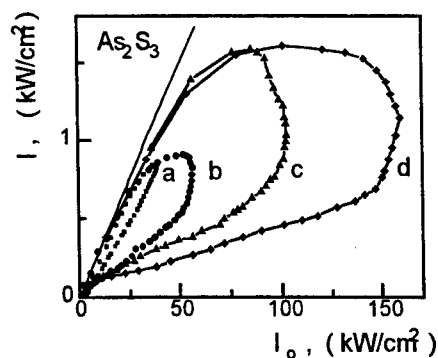


Fig. 2. Hysteresis dependencies of output light intensity versus input one. Incident pulse peak intensity (I_0): 40 (a), 55 (b), 105 (c), and 160 kW/cm^2 (d). Film thickness - 2.6 μm , $\hbar\omega = 2.58 \text{ eV}$.

The kinetics of the NS films induced darkening in the field of laser pulses has been determined. Fig. 3 presents the curves of the transmission change (in per cents) during the NS film irradiation by a laser pulse of microsecond duration. The characteristic times of establishing the new NS light absorption quasiequilibrium state (corresponding to the horizontal part in Fig. 3) in the field of laser pulses are less than the duration of the laser pulses.

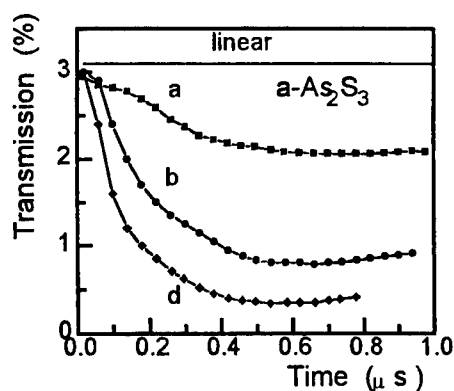


Fig. 3. Kinetics of the a-As₂S₃ darkening during the pulse irradiation. The parameter values - the same as in the Fig. 2.

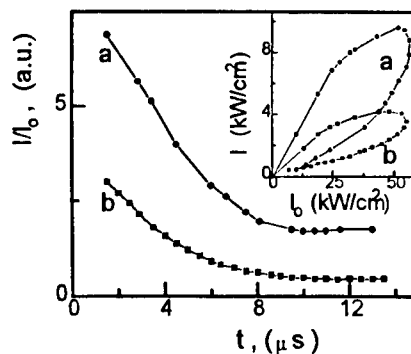


Fig. 4. Kinetics of the As₂Se₃ photodarkening during 7 ns pulse irradiation at 77K (a) and 300K. Insertion: Hysteresis loops at 77K (a) and 300K.

The photoinduced increase of the NS light absorption coefficient in the field of the laser pulses has a reversible character, i.e. the medium fully restores to its initial transmission state after the ending of the laser pulse, and if the same place of the sample is irradiated with another laser pulse the effect can be completely repeated. The restoration of the NS initial absorption state was measured by a low intensity probing light at the exciting light wavelength. The time values after which the light transmission completely restored its initial value lie in the interval from several microseconds up to several dozens of microseconds and depend on the NS film composition, its thickness, the substrate material, and the excitation intensity.¹⁰

The cooling of the NS samples leads to a considerable increase of the surface surrounded by the optical hysteresis loop (Fig. 4). It was ascertained that by cooling the samples from 300 K to 77 K the light intensity threshold values I_t does not change. The temperature behavior of the linear and nonlinear optical absorption in amorphous semiconductors points to the important role which phonons play in the process of the interband light absorption. In fact the characteristics times of the NS photoinduced transition into the new quasi-equilibrium state (corresponding to the horizontal part of the curves in Figs. 3 and 4) do not change during the sample cooling, from 300 K to 77 K. Thus, we can come to the conclusion, that the quasi-stationary value of the light absorption coefficient in the laser pulse field is determined first of all by the light intensity in the medium.

The dependence of the NS nonlinear light absorption characteristics on the laser radiation wavelength (higher than E_g up to 0.4 eV and lower than E_g up to 0.2 eV) were investigated. It was established that in this spectral range the nonlinear absorption characteristics were maintained. However, the pulse intensity threshold values I_t change with the wavelength inversely as the change of the linear absorption coefficient of the medium.

By reducing the laser pulse duration down to picoseconds or femtoseconds, it is possible to exclude or to lower the influence of some processes, for example, the laser heating of the sample, and to investigate the mechanism of the nonlinear or nonstationary interaction of light with the NS. Nonlinear light absorption of 100 femtosecond pulses in the case of inter- and intraband excitation of As₂S₃ and As₂Se₃ thin films with the pump-probe technique was measured in ^{11, 12}. Different behavior of time evolution of induced nonlinear absorption in As₂S₃ and As₂Se₃ was revealed, that can be explained by different mechanisms of interaction of powerful light with amorphous semiconductors in these two cases.

3. PHYSICAL MECHANISMS OF THE NONLINEAR LIGHT ABSORPTION IN NS

The main peculiarities of the nonlinear light transmission in NS thin films are the following: a nonlinear increase of the light absorption coefficient; a nonlinear refractive index change, whose magnitude depends strongly on the excitation intensity; the threshold character of the nonlinear transmission; the change of the time profile of the laser pulses, leading to a hysteresis transmission dependence; the characteristic time constants of the sample photoinduced darkening, which does not exceed the laser pulse duration; the independence of the nonlinear transmission character on the light beam diameter, on the film thickness, and on the substrate material; the weak dependence from the laser pulse wavelength; the successive step character of restoration of light transmission initial state; the full restoration of light transmission initial state in a microsecond time interval; the temperature behavior of the parameters of the nonlinear interaction (the invariance of the light intensity threshold values and of the transient time into the nonlinear light absorption state); the correlation with the photostructural transformations.

The different viewpoints of the physical mechanisms that can explain the peculiarities of the nonlinear light absorption in NS are discussed briefly in ^{1, 2, 9, 12}. In the case of the chalcogenide glasses (ChG) photoinduced darkening under laser pulses is accompanied by photostructural transformations of the medium. These photostructural transformations (with the E_g shift) are noticed only in freshly prepared (previously not illuminated) samples and are irreversible after the ending of the exciting pulse. The photoinduced ChG darkening in the laser field, which was described previously have another physical nature than the ChG photostructural transformations, because, first of all, it is reversible (the initial ChG light transmission sets completely in during 1-100 μ s) and, then, the photoinduced darkening has been found in materials, which, as a result of the photostructural transformations, have a different sign of the E_g shift, that is, give bleaching (GeSe_2 , $\text{As}_{22}\text{S}_{33}\text{Ge}_{45}$) or darkening (As_2S_3 , AsSe , As_2Se_3). It was experimentally shown that the peculiarities of the laser pulse nonlinear absorption are the same in annealed or in previously darkened (by other light sources) ChG films.

The saturation of the interband light absorption (the Burstein-Moss dynamic shift of the fundamental absorption edge in semiconductors, connected with the generation of a sufficient number of electron-hole pairs, and consequently, with the Fermi level shifts into the conduction band (the absorption edge shifts towards higher photon energies) cannot explain the recorded behavior of the excited amorphous semiconductor, which is connected with a considerable increase of the light absorption coefficient.¹³

In the described experiments the measurements of the behavior of the reflected light from the surface of the NS films in a regime of laser pulse nonlinear transmission were done as well. It was ascertained that the oscillograms of the reflected pulses from the NS repeat the incident ones. This points to the real increase of the NS light absorption and to the impossibility of its explanation by "metallization" effects, connected with a carrier concentration increase in the exciting region and by melting of the material on the surface of this region.

A distinctive peculiarity of the amorphous semiconductors is the presence of a high ($10^{16} - 10^{19} \text{ cm}^{-3}$) density of the localized states in the optical band gap.² In the literature the light absorption peculiarities in the NS transparent region are connected with carrier occupation and redistribution on these states.¹⁴ In a number of works this mechanism is also proposed for the explanation of the laser pulse nonlinear absorption at the NS interband excitation.¹⁵ The hot carriers, created as a result of the NS light excitation with $h\nu \geq E_g$, relax (during a period shorter than 10^{-12} s, 300 K), giving as a rule the excess energy to the phonons and being captured on the localized states. Such localized carriers may be excited by light, giving their contribution to the light absorption. However, the laser pulse nonlinear absorption at NS interband excitation, described in this work, cannot be explained on the basis of the occupancy and redistribution of the carriers on the localized states with their next excitation in the conduction band. It is conditioned by the fact that the probability of the transitions "localized state-band" (from $10^{16} \div 10^{19} \text{ cm}^{-3}$ to $\sim 10^{23} \text{ cm}^{-3}$) is some orders lower than the interband optical transitions probability (from $\sim 10^{23} \text{ cm}^{-3}$ to $\sim 10^{23} \text{ cm}^{-3}$) and, it is rather difficult to experimentally distinguish such a low contribution to the

absorption (at the same light wavelength) from the interband absorption.¹⁶ This is even more difficult because the optical absorption spectrum of the investigated compounds and the energy dependence of the density of states in the optical band gap have a monotonous dependence in energy.

It is impossible to explain the laser pulse nonlinear transmission by the homogeneous heating of the NS films. The temperature coefficient of the optical absorption edge shift in these compounds² (dE_g/dT) is about $5 \cdot 10^{-4}$ eV K⁻¹. Therefore, in order to change the absorption light coefficient in the absorption edge region, by an amount equal to the one revealed in the experiment (~ two times), it is necessary to heat the NS sample to a temperature considerably exceeding the temperature of the material softening. More rigorous experimental demonstration was done, when an analogous laser pulse nonlinear absorption has also been registered at light quantum energies, considerably exceeding the NS optical band gap (E_g), where the contribution of the temperature shift of the absorption edge on the light transmission change is smaller.

The contribution of the sample temperature increase on the light pulse nonlinear absorption may be revealed from the dependence of this absorption on the size of the excitation region, on the NS films thickness, and on the substrate material (with different heat conductivity). The investigations of the laser pulse nonlinear transmission dependence on the excitation region size was carried on. As a result of measurements no dependence of the optical hysteresis transmission curves from the diameters of the exciting beam (from 80 to 700 μm) was revealed. The influence of the substrate material (with a different heat conductivity κ) and of the sample thickness on the characteristics of the laser pulse transmission has been studied. Substrates of glass ($\kappa = 0.7 \text{ W m}^{-1} \text{ K}^{-1}$), mica ($\kappa = 0.24 \text{ W m}^{-1} \text{ K}^{-1}$) and lavsan ($\kappa = 0.17 \text{ W m}^{-1} \text{ K}^{-1}$) were used. Within the experimental error (< 20%) no influence of the substrate heat conductivity, on the curves of the optical hysteresis transmission, has been revealed. Neither influence of the NS film thickness on the nonlinear absorption (while changing the thickness from 0.1 μm to 3 μm) has been revealed.

The impossibility to explain the laser pulse nonlinear transmission by the homogeneous heating of the NS films was demonstrated by femtosecond spectroscopy measurements also.^{11, 12} Laser pulses with ~ 1,5 μJ energy were used, which can not provide a substantial heating during probe excitation with 100 fs pulses at 300 K.

The temperature behavior of the linear and nonlinear optical absorption in NS points to the important role which phonons play in the process of the interband light absorption. The temperature dependence of the light absorption coefficient is conditioned by strong electron-phonon interaction.¹⁶ A new physical model of the nonlinear interaction of powerful light with NS, taking into account the light interaction with nonequilibrium phonons and localized vibrational excitations was proposed for the explanation of the experimental results. Structure inhomogeneities in NS may lead to some spatial localization of the phonon vibrational modes, which leads to the increase of their effective lifetime.^{5, 6, 7} This, in turn, leads to a change of the light absorption coefficient as a result of the appearance (or disappearance) of additional optical transitions channels between the earlier forbidden (or less probable) band states. Consequently, a considerable role in the amorphous semiconductor interband light absorption is played by the transitions with a simultaneous participation of light quanta and phonons.^{1, 2} With such considerations in mind the coefficient of the interband light absorption may be thought to consist of two parts: $\alpha = \alpha_o + \beta N_a$, where α_o does not depend on the temperature, while the second part depends on the concentration of N_a phonons. The second part of the light absorption coefficient may change considerably by generating additional phonons as a result of the hot carrier (created by the light) energy dissipation with their consequent capture on localized states in the NS optical band gap. The kinetic equations, describing the exciting and relaxation processes of electrons and phonons in NS have been written in [9]. Equations describe: the laser energy loss during the interaction with the medium, the medium polarization decay, the transition of the carriers (under the laser field) from the valence to the conduction band and vice versa, the carrier concentration changes in the conduction and in the valence band under the action of the external laser field and carrier relaxation with the emission of optical phonons, the generation of optical and acoustic phonons, the

optical phonon decay process into acoustical phonons. The nonlinear change of the light absorption coefficient may be reached in the NS at much lower irradiation intensity than in the crystalline ones. This is possible when transitions with the participation of local acoustic phonons play an important role. The kinetic equations were solved numerically for parameter values and initial conditions, corresponding to the experimental situation. The results of the numerical solution fit reasonable well the experimental dependencies.⁹ In support of the proposed model for the explanation of the laser pulse nonlinear absorption of ChG may also serve the fact that with the same parameter values the calculated curves coincide satisfactorily with the experimental ones in spite of the changing of the laser pulse duration or amplitude in the wide range.

An additional experiment was performed, in order to demonstrate the adequacy of the proposed model. The main point of the physical model of the nonlinear interaction of powerful light with NS, taking into account the light interaction with nonequilibrium phonons and localized vibrational excitations, is the phonon localization. So, the demonstration can be the investigation in the same conditions of the peculiarities of pulse transmission in the medium with the localization possibilities (NS) and without localization (crystalline semiconductor). Such a medium is As_2S_3 : which exists in crystalline and amorphous state. The main peculiarities of the nonlinear light transmission in amorphous As_2S_3 thin films were confirmed.

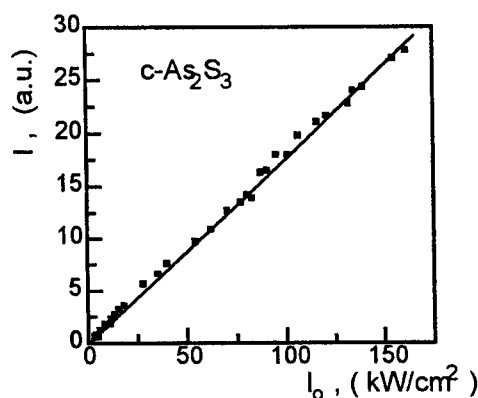


Fig. 5. The output laser pulses peak intensity versus input peak intensity in c- As_2S_3 film (thickness 5 μm), $\hbar\omega = 2.75$ eV.

The peculiarities of the pulse absorption in crystalline As_2S_3 films were measured in the similar excitation conditions (the wavelength of the laser generation was changed to $\lambda = 450$ nm). The orientation, corresponding to the minimum of the light transmission of c- As_2S_3 thin film (the light electric vector \mathbf{E} is directed in the middle between a and c axes of the crystal) was chosen to get the absorption coefficient $\alpha = 7.3 \cdot 10^3 \text{ cm}^{-1}$, comparable with amorphous material one. Fig. 5 shows the dependence of the output laser pulses peak intensity versus input one. As a result of measurement no dependence (in limits of experimental error $< 20\%$) of light absorption in crystalline As_2S_3 from pulse intensity was revealed. These measurements indicate that the clue to understand the physical mechanism lying at its base, is connected with the amorphous nature of the material. This fact additionally confirms the possibility of the application of physical model of the nonlinear interaction of powerful light with NS, taking into account the light interaction with nonequilibrium phonons and localized vibrational excitations.

The experiment, which confirm the possibility of application of the proposed physical model, is the measurements of nonlinear laser pulse absorption in a-Si:H and a-SiC:H thin films.¹⁸⁻²⁰ It is well known, that the localized state electronic spectrum in the band gap of a-Si:H is different from the one of the chalcogenide glasses.²

So, if light generation and redistribution of the carriers on the localized states with their next excitation in the conduction band play an important role, we should have different peculiarities of laser pulse absorption in a-Si:H and in chalcogenide glasses.

The peculiarities of the pulse absorption in a-Si:H and a-SiC:H films were measured in the similar excitation conditions as in the case of chalcogenide glasses. The qualitative behavior of the characteristics of the nonlinear light absorption and, as well as, of the kinetics of the sample photoinduced darkening in the field of the laser pulses (at 300K) is the same as in the case of chalcogenide glasses. For example, in figure 6 the hysteresis-like dependencies of the output light intensity (passed through the a-Si:H sample) on the corresponding value of the input is shown and, figure 7 presents the characteristic times of the setting in of the new light absorption quasiequilibrium state (corresponding to the horizontal part) in the field of 7 ns laser pulses. The most characteristic peculiarities of the investigated nonlinear light transmissions in a-Si:H thin films are the following: a nonlinear increase of the light absorption coefficient; the threshold character of the nonlinear transmission; the change of the time profile of the laser pulses, leading to a hysteresis transmission dependence; the characteristic time constants of the sample photoinduced darkening, which does not exceed the laser pulse duration; the weak dependence on the laser pulse wavelength; the restoration of light transmission initial state in a microsecond time interval. These peculiarities of nonlinear light absorption can be understood in terms of a picture of generation of the nonequilibrium localized lattice vibrations with the emission of the extended phonons, created as a result of the a-Si:H light excitation with $\hbar\omega \geq E_g$.

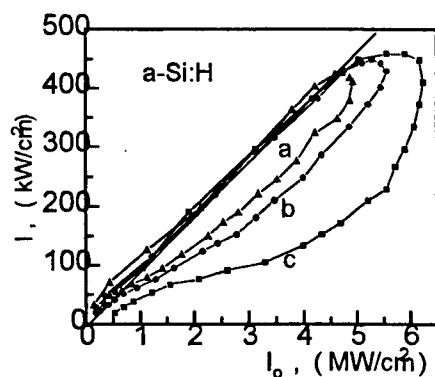


Fig. 6. Hysteresis dependencies of output light intensity versus input one. Incident peak pulse intensity: 6.3 (a); 5.7 (b) and 4.9 MW/cm^2 (c); pulse duration 7 ns, $\hbar\omega = 2.07 \text{ eV}$.

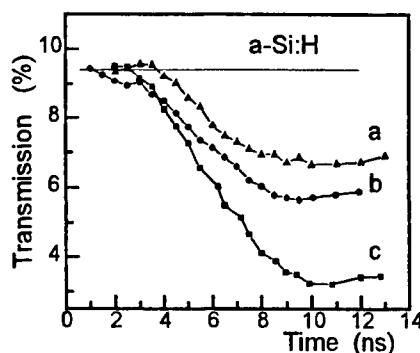


Fig. 7. Kinetics of film darkening during pulse irradiation. The parameter values - the same as in the Fig. 7.

4. CONCLUSIONS

Nonlinear interaction of short and ultrashort laser pulses with NS have shortly been described. It was shown that these characteristics do not find a satisfactory explanation in the limits of the existing physical models proposed in the literature. A new mechanism of a nonlinear light absorption in NS, taking into account the interaction with nonequilibrium phonons and localized vibrational modes is briefly discussed. A reasonably agreement of the calculated dependencies with the experimental ones is obtained. An additional experiment was performed, in order to demonstrate the adequacy of the proposed model. It is not really difficult to estimate that the number of created phonons and localized vibrational modes due to the energy dissipation of hot carriers is of

the same order as the number of the equilibrium phonons using laser pulse energy density in the range 1-10 mJ cm⁻².

5. REFERENCES

1. V. Chumash, I. Cojocaru, E. Fazio, F. Michelotti, and M. Bertolotti, "Nonlinear propagation of strong laser pulses in chalcogenide glass films", *Progress in Optics*, **36**, 1-47 (1996).
2. M. Popescu, A. Andries, V. Ciumas, M. Iovu, S. Sutov and D. Tiuleanu, *Fizica Sticlelor Calcogenice*, Ed. Stiintifica, Bucuresti & I. E. P. Stiinta, Chisinau, 1996, 486 pag.
3. V. K. Malinovskii, Iu. E. Nesterihin, V. N. Novikov, and A. P. Sokolov, "Local phonons in mediums with spatial dispersion properties", *Avtometria*, **2**, 3-9 (1986).
4. R. Orbach, "Phonon localization and transport in disordered systems", *J. Non-Crystall. Solids*, **164-166**, 917-922 (1993).
5. R. Baumgartner, M. Engelhardt, F. F. Renk, "Spatial distribution of high-frequency phonons generated by nonradiative transitions", *Phys. Lett.*, **94A**, 55-58 (1983).
6. H. M. Gibbs, *Optical Bistability: Controlling Light with Light*, Academic Press, Inc., N-Y, 1985.
7. M. Bertolotti, V. Chumash, E. Fazio, A. Ferrari, and C. Sibilia, "Nonlinear Fabry-Perot cavity of chalcogenide glass thin films", *Inst. Phys. Conf. Ser.*, **115**, 169-172 (1991), *idem J. Appl. Phys.*, **74**, 3024-3027 (1993).
8. A. M. Andriesh, N. A. Enaki, I. A. Cojocaru, N. D. Ostafeichuk, P. G. Cherbari, and V. N. Chumash, "Optical hysteresis in amorphous semiconductor", *Sov. J.T.F. Lett.*, **14**, 1985-1989 (1988).
9. A. M. Andriesh, O. I. Bogdan, N. A. Enaki, I. A. Cojocaru, and V. N. Chumash, "Optical hysteresis and nonlinear absorption of short laser pulses in chalcogenide glasses", *Bulletin Ross.Acad.Sci., Phys. Ser.*, **56**, 96-109 (1992).
10. M. Popescu, A. Andriesh, V. Chumash, N. Enachi, I. Cojocaru, and A. Grozescu, "Non-archimedian model for the relaxation process of the photoinduced darkening in amorphous chalcogenide films", *J. Non-Cryst. Solids*, **137-138**, 973-976 (1991).
11. A. Andriesh, V. Chumash, I. Cojocaru, M. Bertolotti, E. Fazio, F. Michelotti and D. Hulin, "Optical hysteresis and ultrafast transmission switching in chalcogenide glasses", *Photonic Switching, SPIE Proceed.*, **1807**, 126-135 (1992).
12. E. Fazio, D. Hulin, V. Chumash, F. Michelotti, A. M. Andriesh and M. Bertolotti, "On-off resonance femtosecond non-linear absorption of chalcogenide glassy films", *J. Non.-Cryst. Solids*, **168**, 213-222 (1993).
13. D. A. B. Miller, C. T. Seaton, M. E. Prise, and S. D. Smith, "Band-gap-resonant nonlinear refraction in II-V semiconductors", *Phys. Rev. Lett.*, **47**, 197-200 (1981).
14. M. A. Kastner, *Physical Properties of Amorphous Materials*. Eds. D. Adler, B. B. Schwartz, M. C. Steele, Plenum Press, N-Y. and London, 1985, 381 pag.
15. Z. Vardeny, "Transient induced absorption in amorphous semiconductors from picoseconds to milliseconds", *J. Non-Cryst. Sol.*, **59-60**, 317-324 (1983).
16. V. L. Bonch-Bruevichi, I. P. Zveaghin, R. Kaiber, A. G. Mironov, R. Anderlain, and B. Esser, *The Electronic Theory of Disordered Semiconductors*, Moscow, Nauka, 1981, 384 p.
17. V. Chumash, I. Cojocaru, G. Bostan, P. Cerbari, and N. Mincu. "Nonlinear absorption of laser pulses in amorphous and crystalline As₂S₃ thin films", *Optical Diagnostics of Materials and Devices for Opto-, Micro-, Quant. Electronics - OPTDIM'95, SPIE Proceed.*, Kiev, **2648**, 221-225 (1995).
18. G. N. Bostan, I. A. Cojocari, E. Carbunescu, and V. N. Ciumas, "Optical transmission hysteresis in a-Si:H films", *Buletin Academy of Sciences of Moldova, Physics & Technics*, **2**, 60-63 (1992).
19. A. Andriesh, V. Chumash, E. Carbunescu, I. Cojocaru, and G. Bostan, "Nonlinear absorption of short laser pulses in a-Si:H thin films", *Romanian Journal of Physics*, **38(9&10)**, 897-902 (1993).
20. V. Chumash, I. Cojocaru, G. Bostan, G. De Cesare, S. La Monica, G. Maiello, and A. Ferrari. "Optical hysteresis and nonlinear light absorption in a-Si:H and a-Si:C:H thin films", *Optical Diagnostics of Materials and Devices for Opto-, Micro- and Quantum Electronics- OPTDIM'95, SPIE Proceedings*, Kiev, **2648**, 23-28 (1995).

LBO optical parametric oscillator pumped by second harmonic of a Nd:YAG laser

R. Dabu, C. Fenic, A. Stratan, C. Luculescu, L. Muscalu*

National Institute for Laser, Plasma and Radiation Physics, Laser Department, P. O. Box MG-36, Bucharest 76900, Romania

*Prooptica, Bucovina Street 4, 74404 Bucharest, Romania

ABSTRACT

We describe a pulsed doubly resonant LiB_3O_5 (LBO) optical parametric oscillator (OPO) pumped with a frequency doubled Q-switched Nd:YAG laser amplifier. The threshold power density near degeneracy was found to be 29 MW/cm^2 . The OPO was continuously tuned from 970 nm to 1175 nm by rotation of the LBO crystal. The linewidth of the signal radiation at 998 nm, and idler radiation at 1136 nm wavelength, were found to be 10 nm, and 13 nm respectively. The OPO output pulse energy of signal and idler near degeneracy was 1.51 mJ for 18 mJ pump energy.

1. INTRODUCTION

If a pump radiation with frequency ω_p is incident on a nonlinear material, then a signal frequency ω_s may be amplified. In the process a third frequency ω_i , termed as the idler frequency, and such that $\omega_s + \omega_i = \omega_p$ is generated. In order to achieve significant parametric amplification it is required that at each of these frequencies the generated polarization travel at the same velocity as a freely propagating electromagnetic wave. This is the case if the refractive indices of the material are such that the wave vectors \vec{k} satisfy the momentum matching condition $\vec{k}_s + \vec{k}_i = \vec{k}_p$. For collinearly propagating waves this may be written $\omega_s n_s + \omega_i n_i = \omega_p n_p$, where n_m is the refractive index at frequency ω_m . Once the pump radiation is chosen, and thus ω_p fixed, then if the refractive indices at the signal, idler or pump frequencies are varied, the signal and idler frequencies generated in an OPO will tune. In a laser pumped singly resonant OPO (SRO) only the signal (or idler) wave is resonated. In a doubly resonant OPO (DRO) both signal and idler waves are resonated.

Several pulsed OPO's were demonstrated that use LBO as the nonlinear crystal with pump sources as excimer laser¹, frequency doubled Nd:YAG laser², frequency tripled Nd:YAG laser³, frequency quadrupled Nd:YAG laser⁴, frequency doubled all-solid state Q-switched Nd:YLF laser⁵, self mode-locked Ti:sapphire laser⁶, frequency doubled diode-pumped mode-locked Nd:YVO₄ laser⁷.

In this paper we describe the operation of a pulsed LBO DRO pumped by an electro-optically Q-switched frequency doubled Nd:YAG laser amplifier.

2. THEORY

2.1. Single pulse pumped OPO oscillation threshold

We consider an OPO with plane-parallel two mirror optical cavity. In the slowly varying envelope approximation, for collinear interaction of Gaussian waves along the z axis, assuming no pump depletion and field absorption in nonlinear material, the equations describing the parametric growth of the signal and idler field amplitudes E_s , E_i in the presence of a pump field amplitude E_p are^{8,9}

$$\frac{dE_s}{dz} = j\kappa_s E_p E_i^* \exp(j\Delta kz) \quad (1a)$$

$$\frac{dE_i}{dz} = j\kappa_i E_p E_s^* \exp(j\Delta kz) \quad (1b)$$

Here $\Delta k = k_p - k_s - k_i$ is the wave vector mismatch. The interaction coefficients κ_m ($m = s, i$) are given by

$\kappa_m = \frac{\omega_m d_{\text{eff}}}{n_m c}$, where d_{eff} is the effective nonlinear coefficient, and c is the speed of light.

For a phase matched interaction ($\Delta k = 0$) the expressions for the signal and idler field amplitudes, after propagation through an effective gain interaction length l_g are given by⁹

$$E_s(l_g) = E_s(0) \cosh(\Gamma l_g) + j \frac{\kappa_s E_p}{\Gamma} E_i^*(0) \sinh(\Gamma l_g) \quad (2a)$$

$$E_i(l_g) = E_i(0) \cosh(\Gamma l_g) + j \frac{\kappa_i E_p}{\Gamma} E_s^*(0) \sinh(\Gamma l_g) \quad (2b)$$

The parametric amplitude gain Γ is given by

$$\Gamma = \left(\kappa_s \kappa_i |E_p|^2 \right)^{1/2} = \left(\frac{2 \omega_s \omega_i d_{\text{eff}}^2}{n_p n_s n_i \epsilon_0 c^3} I_p \right)^{1/2} \quad (3)$$

where $I_p = \frac{1}{2} n_p c \epsilon_0 |E_p|^2$ is the pump peak power density, and ϵ_0 is the permittivity of free space.

The oscillation threshold condition for a DRO is that the single pass parametric gain be sufficient to offset the round trip cavity losses α_s, α_i for both E field of the signal and idler frequencies¹⁰

$$\frac{1}{1 - \alpha_s} E_s(0) = E_s(0) \cosh(\Gamma l_g) + j \frac{\kappa_s E_p}{\Gamma} E_i^*(0) \sinh(\Gamma l_g) \quad (4a)$$

$$\frac{1}{1 - \alpha_i} E_i(0) = E_i(0) \cosh(\Gamma l_g) + j \frac{\kappa_i E_p}{\Gamma} E_s^*(0) \sinh(\Gamma l_g) \quad (4b)$$

Taking the complex conjugate of (4b) and setting the determinant of the resulting two simultaneous equations to zero, we obtain the threshold condition

$$\left(\cosh(\Gamma l_g) - \frac{1}{1 - \alpha_s} \right) \left(\cosh(\Gamma l_g) - \frac{1}{1 - \alpha_i} \right) - \sinh^2(\Gamma l_g) = 0 \quad (5)$$

$$\cosh(\Gamma l_g) = 1 + \frac{\alpha_s \alpha_i}{2 - \alpha_s - \alpha_i}$$

For low loss resonators ($\alpha_s, \alpha_i \ll 1$) the oscillation threshold condition becomes

$$\Gamma^2 l_g^2 \cong \alpha_s \alpha_i \quad (6)$$

In a SRO only signal (or idler) is resonant, $\alpha_i = 1$ (or $\alpha_s = 1$), and for small α_s

$$\Gamma^2 l_g^2 \cong 2 \alpha_s \quad (7)$$

The threshold pump peak intensity I_p^{th} of a continuously operated (CW pumped) or synchronously pumped DRO (the length of the OPO optical cavity is adapted to the frequency of the ultrashort pulses generated by the pump mode-locked laser) results from (3) and (6). The ratio of the threshold pump power for SRO, given by (3) and (7), as compared to DRO is $2/\alpha_i$.

In the case of OPO pumped with single pulse Q-switched lasers, the pump intensity is usually big enough to satisfy the threshold condition. The apparent threshold of the oscillator will be a pump power producing during pump pulse a sufficient gain for the oscillation to build out of the noise.

The threshold of a SRO was calculated⁸ by assuming:

- Gaussian time profile for the incident pump intensity which yields a time dependent gain coefficient Γ described by

$$\Gamma = \Gamma_0 \exp\left(-\frac{t^2}{\tau^2}\right), \text{ where } \tau \text{ is the } 1/e^2 \text{ intensity halfwidth of the pump pulse, and } \Gamma_0 \text{ is the peak gain coefficient;}$$

- constant pump intensity during a single cavity transit ($\tau \gg \frac{n_p l_c}{c}$), where l_c is the nonlinear crystal length;

- time independent gain profile of $\bar{\tau} = 2\tau$ width, and $\bar{\Gamma}$ magnitude given by $\bar{\Gamma} \cong 1.34\Gamma_0$.

Under the same conditions we deduced the apparent threshold pump peak intensity of a single pulse pumped SRO

$$I_p^{\text{th}}(\text{SRO}) = \frac{18 \left[\ln(\sigma + \sqrt{\sigma^2 - 1}) \right]^2}{\frac{8\pi^2 d_{eff}^2 g_\lambda g_\alpha}{n_p n_i n_o \epsilon_0 c \lambda_s \lambda_i} l_s^2 (1 + \gamma)^2} \quad (8)$$

Here $\sigma = \frac{\exp(\beta)}{\sqrt{R_1 R_2 (1 - \alpha)}}$, where $\beta \cong \frac{25L}{c\tau_p}$; L is the optical cavity length given by $L = L_0 + l_c(n_p - 1)$, L_0 is the

cavity physical length; τ_p is full width at half maximum (FWHM) pulse duration; R_1 , R_2 are the signal reflectances of the OPO input and output mirrors; α is the round trip attenuation of the signal power; γ is the pump reflectance of the OPO output mirror; λ_s , λ_i are the signal and idler wavelengths; g_s is the signal spatial mode coupling coefficient⁸ defined by

$$g_s = \frac{w_p^2}{w_p^2 + w_s^2}, \text{ where } w_p, w_s \text{ are the Gaussian mode electric field radii of pump and signal radiation beams; } g_\lambda \text{ is the}$$

reduction factor in parametric gain that results from use of a pump of bandwidth $\Delta\lambda_p$ over that for a pump of negligible bandwidth⁹; g_α is the reduction in parametric gain from an ideal pumping with a collimated beam⁹; l_s is given by by⁸

$$l_s = l_w \operatorname{erf}\left(\frac{\sqrt{\pi} l_c}{2 l_w}\right), \text{ where } l_w \text{ is the walk-off length } l_w = \frac{\sqrt{\pi} w_p}{2 \rho} \sqrt{\frac{w_p^2 + w_s^2}{w_p^2 + w_s^2/2}}, \rho \text{ is the double refraction walk-off angle. Threshold power to noise power was considered } \ln\left(\frac{P_m}{P_0}\right) \cong 40.$$

For a single pulse pumped DRO, near degeneracy ($\lambda_s = \lambda_i$), assuming $\alpha_s = \alpha_i$ and the same signal and idler reflectance of the OPO mirrors, the equations to determine the apparent threshold becomes

$$\sigma E_s(0) = E_s(0) \cosh(\bar{\Gamma} l_s) + j \frac{\kappa_s E_p}{\Gamma} E_i^*(0) \sinh(\bar{\Gamma} l_s) \quad (9a)$$

$$\sigma E_i(0) = E_i(0) \cosh(\bar{\Gamma} l_s) + j \frac{\kappa_i E_p}{\Gamma} E_s^*(0) \sinh(\bar{\Gamma} l_s) \quad (9b)$$

The threshold pump peak intensity of a single pulse pumped DRO is given by

$$I_p^{\text{th}}(\text{DRO}) = \frac{1.8[\ln \sigma]^2}{\frac{8\pi^2 d_{\text{eff}}^2 g_s g_\lambda g_a}{n_p n_i n_o \epsilon_0 c \lambda_s \lambda_i} l_s^2 (1 + \gamma)^2} \quad (10)$$

With $\sigma \gg 1$ approximation we obtain the threshold relations used in references^{8,11}. Under our experimental conditions this approximation is not correct due to the relatively short L and long τ_p .

2.2. Resonated waves spot size.

We calculated the signal (idler) spot size of DRO near degeneracy. Assuming a Gaussian profile for the electric fields, near degeneracy ($w_s \cong w_i$), the driving polarization for the signal wave has the radius \bar{w}_s , given by^{8,9}. The radius of the signal (idler) polarization after a round trip through the optical cavity is

$$\frac{1}{\bar{w}_s^2} = \frac{1}{w_i^2} + \frac{1}{w_p^2} \cong \frac{1}{w_s^2} + \frac{1}{w_p^2} \quad (11)$$

$$\frac{1}{\bar{w}_s^2} = \frac{1}{w_s^2} \left[1 + \left(\frac{2L\lambda_s}{\pi w_s^2} \right)^2 \right] \quad (12)$$

By letting $\bar{w}_s = w_s$, after several round trips, the steady state signal (idler) spot size is given by the following equations

$$\left(\frac{\pi}{2L\lambda_s}\right)^2 \frac{-6}{w_s} + \frac{-2}{w_s} - w_p^2 = 0 \quad (13)$$

$$\frac{1}{w_s^2} = \frac{1}{w_s^2} - \frac{1}{w_p^2}$$

2.3. Signal (idler) linewidth

The OPO frequency linewidth is given by¹⁰ $|\Delta f| \approx \frac{1}{b l_s}$, where $b = \frac{\partial k_i}{\partial \omega_i} - \frac{\partial k_s}{\partial \omega_s}$ is a dispersive parameter. LBO is a crystal with small b , large tuning rate, and correspondingly with large parametric linewidth. The expression of the full half-power gain linewidth at signal (idler) wavelength

$$\Delta \lambda_{s,i} = \frac{\lambda_{s,i}^2}{l_s} \frac{0.886}{\left| n(\lambda_s) - n(\lambda_i) - \lambda_s \frac{\partial n}{\partial \lambda} \Big|_{\lambda_s} + \lambda_i \frac{\partial n}{\partial \lambda} \Big|_{\lambda_i} \right|} \quad (14)$$

where $n(\lambda)$ is the refractive index given by Sellmeier equations.

3. EXPERIMENTAL RESULTS

The optical cavity of the OPO, 35 mm length, is formed by a pair of plane parallel mirrors, as shown in Fig. 1.

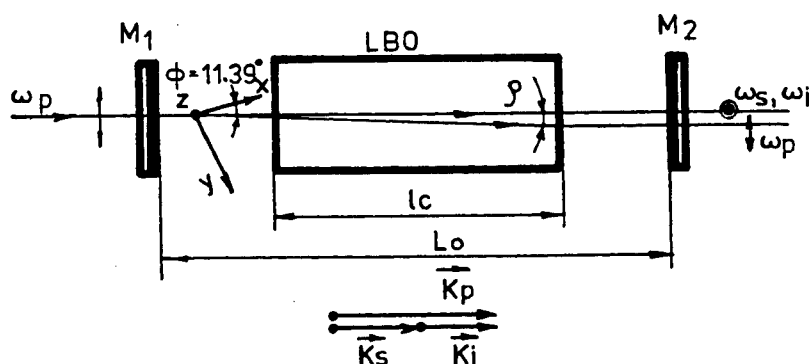


Fig.1. Schematic of LBO DRO optical cavity.

The LBO crystal used in the present device was cut for type I phase matching ($e \rightarrow oo$) in the xy crystallographic plane, $\theta = 90^\circ$, $\phi = 10^\circ$, and was 12 mm in length with 4mm x 4mm aperture. Both faces were antireflection coated at 532/1064 nm. The pump laser was a non-focused frequency doubled Q-switched TEM₀₀ Nd:YAG laser amplifier, with pulse duration 10.5 ± 1 ns, and variable output pulse energy up to 40 mJ at 532 nm. This laser system was described elsewhere¹². The main spectral characteristics of the OPO mirrors are:

- M₁ (input mirror) - high reflective (99.8%) at 1064 nm and > 99% over the range 980-1175 nm, 95% transmission at 532 nm;
- M₂ (output mirror) - 95% reflective at 1064 nm, 88-96% reflective over the range 970-1175 nm, 96% reflective at 532 nm.

Due to high reflectance at pump radiation of M_2 we obtained parametric gain on both forward and backward transits through LBO crystal. The output energy of the signal and idler radiation near degeneracy versus pump pulse energy is shown in Fig. 2.

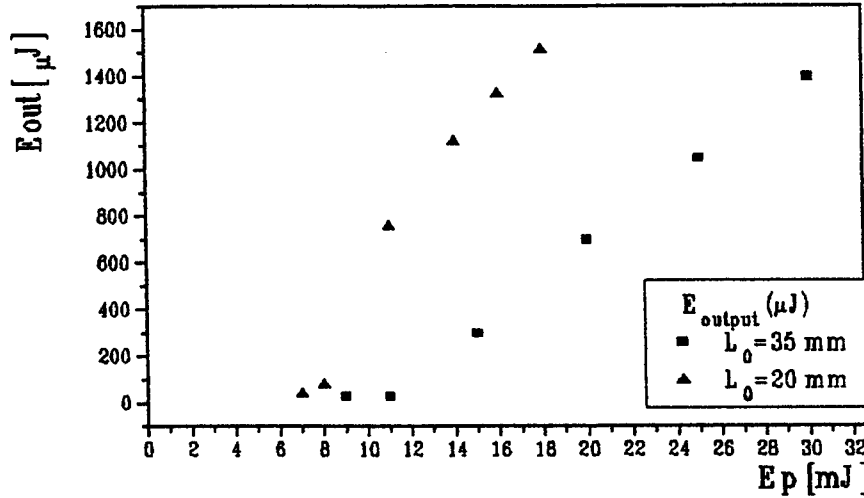


Fig. 2. OPO output energy of the signal and idler radiation as function of pump energy.

Output energy of 1.4 mJ with 30 mJ pump pulse energy for 35 mm OPO optical cavity length, and 1.51 mJ with 18 mJ pump energy for 20 mm optical cavity length was obtained. We observed an oscillation threshold of ~ 10 mJ pump energy, corresponding to a peak power density of 47 MW/cm^2 on the input mirror, and 44 MW/cm^2 on the LBO input face ($L_0 = 35$ mm), and an oscillation threshold of ~ 7 mJ, 32 MW/cm^2 , and 29 MW/cm^2 respectively, for $L_0 = 20$ mm. The level of the pump intensity is restricted by the damage of M_1 . We observed the M_1 damage after about 100 pulses at 17 mJ pump energy (82 MW/cm^2 peak power density) and after 2-5 pulses at 20 mJ pump energy (97 MW/cm^2 peak power density). The low level of the measured damage threshold is determined by the overlapping on M_1 of the forward propagating pump radiation with the backward propagating pump radiation reflected by M_2 (the round trip propagation time of the OPO resonator is much shorter than the pump pulsewidth).

We calculated the apparent oscillation threshold for pulse pumped SRO and DRO using (8), (10) relations:

$I_p^{\text{th}}(\text{SRO} - \text{LBO}) = 16 \text{ MW/cm}^2$, $I_p^{\text{th}}(\text{DRO} - \text{LBO}) = 85 \text{ MW/cm}^2$. The parameters for OPO threshold calculation are: $L = 43$ mm, $\alpha = 0.06$, $R_1 = 1$, $R_2 = 0.95$, $\gamma = 0.9$, $l_g = 11.9 \text{ mm}^{11}$, $n_p = n_s = n_i = 1.6055$, $\epsilon_0 = 8.854 \times 10^{-12} \text{ F/m}$, $c = 3 \times 10^8 \text{ m/s}$, $d_{\text{eff}} = 0.82 \times 10^{-12} \text{ m/V}^{13}$, $g_s = 0.92$, $g_\lambda = 0.97$ ($\Delta\lambda = 1.55 \text{ nm}^{12}$, $\Delta\lambda_p = 0.33 \text{ nm}$), $g_\alpha = 1$.

Tuning of the OPO was achieved by rotation of the LBO crystal in the xy crystallographic plane. The output signal and idler energy, measured at fixed pump energy, decreases with the rotation of the LBO crystal from the degeneracy angle, as shown in Fig.3. This result and the following ones were obtained with a pump pulse energy of 15 mJ (a factor of ~ 1.35 above threshold).

The calculated radius of the signal (idler) wave near degeneracy, as results from (13), was $w_s = 0.32 \text{ mm}$ ($L_0 = 35$ mm), and $w_s = 0.275 \text{ mm}$ ($L_0 = 20$ mm), significantly less than the radius of the Gaussian pump wave $w_p = 1.1 \text{ mm}$ on LBO crystal. The

calculated full divergence angle of a corresponding Gaussian signal (idler) beam is $\theta_s = \frac{2\lambda_s}{\pi w_s} \cong 2.12 \text{ mrad}$, in good agreement with the experimentally measured signal spot of 5 mm at ~ 2 m distance from the OPO output mirror.

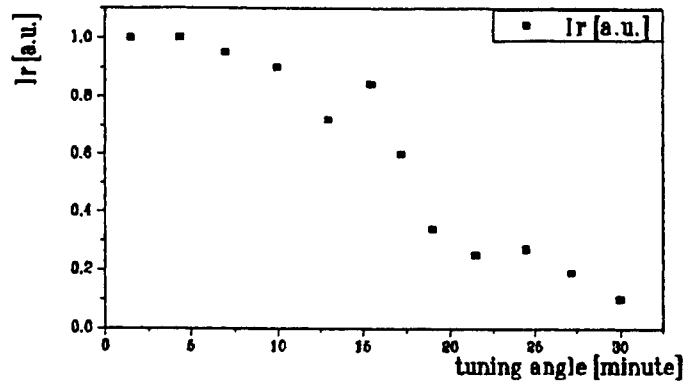


Fig.3. Normalized OPO output energy of the signal and idler radiation versus tuning angle from degeneracy.

The wavelength of the signal and idler waves versus tuning angle were measured over the tuning range 985-1155 nm. The experimental data points, compared with the calculated curve using the Sellmeier equations for LBO crystal, are shown in Fig.4.

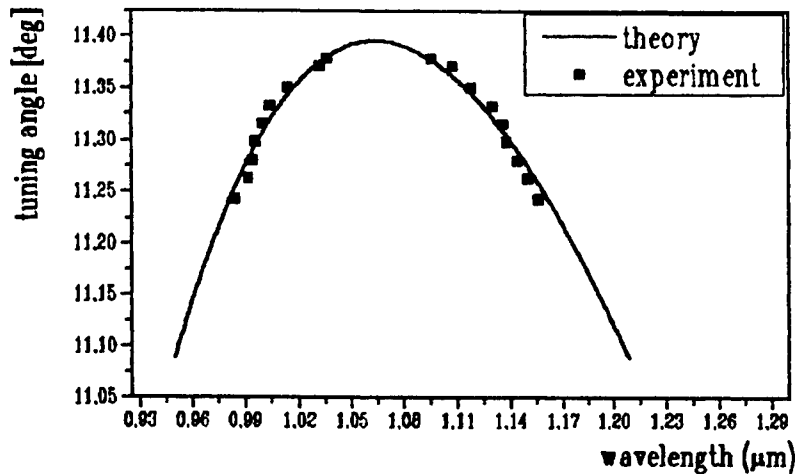


Fig.4. Tuning range of LBO DRO. Experimental data points compared with calculated curve. Calculated angle of degeneracy $\phi_d \cong 11.39^\circ$.

The OPO emission spectrum for signal and idler radiation was taken by use of a grating monochromator with a resolution of better than 0.1 nm and was averaged over a train of pump pulses. We observed a double structure for each spectrum, probably due to the "cluster effect", characteristic for DRO's (Fig.5).

The FWHM linewidth of the signal wave with 998 nm central wavelength was ~ 10 nm, and ~ 13 nm for the corresponding idler wave with 1136 nm wavelength, as shown in Fig. 5. The calculated linewidths with (14) at $\lambda_s = 998$ nm ($\lambda_i = 1136$ nm), and $\lambda_s = 900$ nm ($\lambda_i = 1301$ nm) were $\Delta\lambda_s = 32$ nm ($\Delta\lambda_i = 41$ nm), and $\Delta\lambda_s = 9$ nm ($\Delta\lambda_i = 19$ nm), respectively. The expression (14) gives correct results if the shift of the central wavelength of the signal (idler) line the degeneracy wavelengths is much larger than the signal (idler) linewidth.

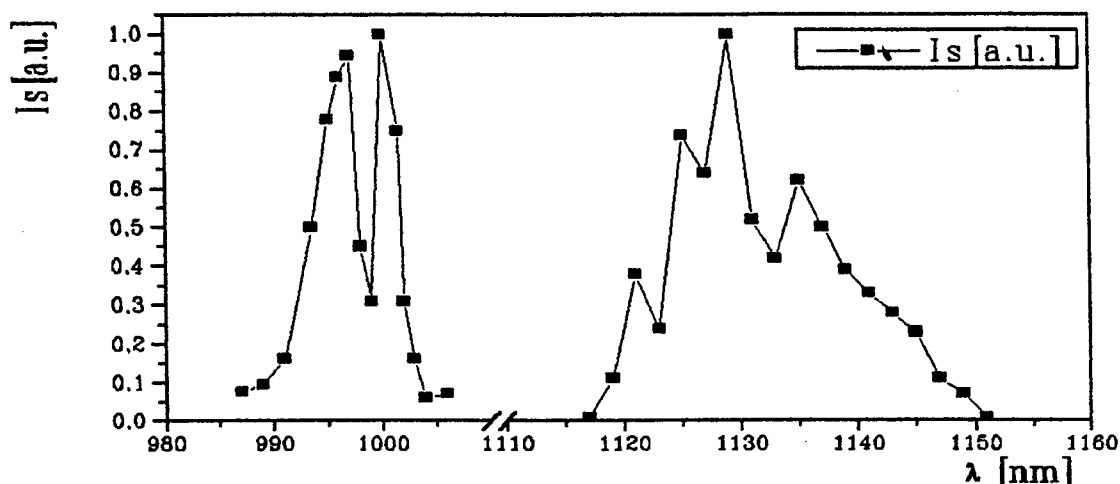


Fig.5. Spectrum of LBO DRO ($\lambda_s = 998$ nm, $\lambda_i = 1136$ nm).

4. CONCLUSIONS

- Analytical expressions of the pump peak power density at the oscillation threshold for single pulse pumped SRO and DRO, DRO signal (idler) wave spot size, and signal (idler) linewidth were calculated.
- Tunable doubly resonant OPO with LBO crystal was built.
- Experimentally measured oscillation threshold pump intensity was 44 MW/cm^2 for 35 mm length optical cavity, and 29 MW/cm^2 for 20 mm length optical cavity.
- Signal and idler output energy of 1.4 mJ at 30 mJ pump pulse energy ($L_0 = 35$ mm), and 1.51 mJ at 18 mJ pump pulse energy ($L_0 = 20$ mm) was obtained.
- Diameter of the OPO signal wave near degeneracy was 0.32 mm ($L_0 = 35$ mm), and 0.275 mm ($L_0 = 20$ mm).
- Data points of signal and idler wavelength over the tuning range (970-1175 nm) were in good agreement with the calculated curve by using Sellmeier equations.
- Linewidth of the signal (idler) radiation at 998 nm (1136 nm) wavelength was 10 nm (13 nm).

REFERENCES

1. G. Robertson, A. Henderson, and M. H. Dunn, *Appl. Phys. Lett.* **60**, 271 (1992).
2. K. Kato, *IEEE J. Quantum Electron.* **QE-26**, 2043 (1990).
3. F. Hanson, and D. Dick, *Opt. Lett.* **16**, 205 (1991).
4. Y. Tang, Y. Cui, and M. H. Dunn, *Opt. Lett.* **17**, 192 (1992).
5. G. J. Hall, and A. I. Ferguson, *Opt. Lett.* **18**, 1511 (1993).
6. M. Ebrahimzadeh, S. French, and A. Miller, *J. Opt. Soc. Am. B* **12**, 2180 (1995).
7. J. D. Kafka, M. L. Watts, and J. W. Pieterse, *J. Opt. Soc. Am. B* **12**, 2147 (1995).
8. S. J. Brosnan, and R. L. Byer, *IEEE J. Quantum Electron.* **QE-15**, 415 (1979).
9. M. J. McCarthy, and D. C. Hanna, *J. Opt. Soc. Am. B* **10**, 2180 (1993).
10. S. E. Harris, *Proceedings of the IEEE* **57**, 2096 (1969).
11. L. R. Marshall, and A. Kaz, *J. Opt. Soc. Am. B* **10**, 1730 (1993).
12. R. Dabu, C. Fenic, A. Stratan, and L. Muscah, *Optica Applicata* **26**, 171 (1996).
13. S. P. Velsko, M. Webb, L. Davis, and C. Huang, *IEEE J. Quantum Electron.* **QE-27**, 2182 (1991).

Enhanced internal second harmonic generation
in InGaAs/GaAs/AlGaAs strained single quantum well buried
heterostructure laser diodes

R. G. Ispasoiu, N. N. Puscas, E. Smeu, C. E. Botez

Physics Department, "Politehnica" University of Bucharest, Bucharest,
Splaiul Independentei, 313, 77206, Bucharest, Romania

V. P. Yakovlev, A. Z. Mereutza, G. I. Suruceanu

Optoelectronics Laboratory, Technical University of Moldova, Chisinau,
Moldova 168 Stefan cel Mare St. Chisinau 277012, Moldova

ABSTRACT

In this paper we report an indirect method based on photomultiplier response calibration to measure the radiant power of the internal second harmonic generation (ISHG) from InGaAs/GaAs/AlGaAs strained single quantum well buried heterostructure laser diodes (SQW BH LDs).

We observed enhanced ISHG radiant power, of the order of magnitude of 10^{-8} W. This phenomenon represents a signature of the beginning of the process of catastrophic optical degradation (COD) of the LD mirror facet layers, where the nonlinear optical interaction occurs.

KEYWORDS

internal second harmonic generation, InGaAs/GaAs/AlGaAs laser diodes

1. INTRODUCTION

In the thin semiconductor layers adjacent to the mirror facets of high power laser diodes the nonlinear optical phenomenon of internal second harmonic generation (ISHG) takes place.

Two major mechanisms share their contribution to the cause of this phenomenon: counterpropagating nonlinear optical interaction¹ and waveguiding² in the laser diode active region.

The efficiency of ISHG by the waveguiding effect is mainly limited by the absorption of the shorter wavelength second harmonic wave.

ISHG in InGaAs/GaAs/AlGaAs strained single quantum well buried heterostructure laser diodes (SQW BH LDs), emitting around 950 nm, received much attention^{2,3} for the fact that the second harmonic (SH)

radiation originating from the LD mirror layers could offer some important information regarding the mirror facet temperature and risk of mirror catastrophic optical degradation in conditions of high output power laser operation.

In Sec. 2 we present some theoretical considerations concerning the efficiency and the mechanisms of ISHG in the case of second order nonlinear optical processes for III - V semiconductor compounds.

Sec. 3 is dedicated to sample details and experimental setup while in Sec. 4 we report the conclusions of this paper.

2. THEORY

It was experimentally observed and theoretically confirmed³ that two counterpropagating light waves incident on the interface between a linear and a nonlinear optical medium, in a total internal reflection geometry, determine the formation of a layer of nonlinear polarization, adjacent to that interface, having the thickness of the order of the radiation wavelength.

By this effect, two half-wave harmonics are generated as emerging into and out of the substrate. This phenomenon, termed as counterpropagating nonlinear optical interaction, was also studied for the particular situation when the nonlinear medium is a semiconductor⁴.

In the case of a laser diode, such a nonlinear optical interaction occurs at the interface provided by the mirror facet.

According to the theory of counterpropagating nonlinear optical interaction, the thickness of the semiconductor material, close to the LD mirror facet, should be of the order of magnitude of the fundamental wavelength (i.e. $\sim 1 \mu\text{m}$ for our LD's).

On the other hand, another efficient mechanism for second order nonlinear optical processes in III - V semiconductor compounds (that have almost zero birefringence) is the waveguiding effect for quasi-phase-matching⁵.

The efficiency of ISHG by waveguiding is limited mainly by the absorption of the shorter wavelength second harmonic wave.

As a known fact of SHG theory, the dependence of the SH irradiance $I_{2\omega}$, on the fundamental wave irradiance, I_{ω} , is quadratic:

$$I_{2\omega}(L) = \frac{(2\omega)^2}{8\epsilon_0 c^3} \cdot \frac{|\chi^{(2)}(-2\omega; \omega, \omega)|^2}{n_{\omega}^2 n_{2\omega}} \cdot I_{\omega}^2(L) \cdot L^2 \cdot \left[\frac{\sin\left(\frac{\Delta k L}{2}\right)}{\frac{\Delta k L}{2}} \right]^2 \quad (1)$$

where ω is the fundamental wave angular frequency, ϵ_0 is the vacuum dielectric constant, c is the speed of light in vacuum, $\chi^{(2)}(-2\omega; \omega, \omega)$ is the

second order nonlinear optical interaction susceptibility, n_ω and $n_{2\omega}$ are the refractive indices for the fundamental and the second harmonic wave, respectively; L is the nonlinear interaction length, Δk is the phase mismatch between the second harmonic and the two input fundamental waves involved in the process.

The irradiances of the second harmonic and fundamental waves are expressed as:

$$I_{\omega,2\omega} = \frac{P_{\omega,2\omega}}{A} \quad (2)$$

where P is the radiant power and A is the area of the laser cavity cross section of overlap between the interacting waves.

For the experiments with our LD's, the comparison of the measured ISHG radiant power with the theoretically predictable values is made according to equation (1).

In our analysis we assume that the phase matching condition $\Delta k \rightarrow 0$ is fulfilled.

The key factor for the enhancement of ISHG emission is the design of a LD resonant cavity with material and geometry parameters that contribute to the increase of the interaction length L , according to the nonlinear optical mechanisms that determine the ISHG emission.

3. SAMPLE DETAILS AND EXPERIMENTAL SETUP

The InGaAs/GaAs/AlGaAs SQW BH LD melt etching and regrowth⁴, starting from a basic wafer first grown by molecular beam epitaxy. An In_{0.2}Ga_{0.8}As quantum well having a width of 80 Å was sandwiched between 100 Å wide GaAs spacer layers followed by AlGaAs graded index regions and cladding layers. The InGaAs/GaAs active medium buried stripe had a width of ~ 10 μm. The transversal area A for the laser wave and second harmonic propagation is evaluated to be of $20 \times 10^{-12} \text{ m}^2$.

The laser cavity length is of 740 μm and the corresponding fundamental emission wavelength is of 952 nm.

To evaluate the order of magnitude of the ISHG radiant power $P_{2\omega}$ we chose a simpler measurement method based on the calibration of the response of a cooled photomultiplier tube (PMT), around the wavelength of 476 nm, instead of the standard photon counting system.

The PMT used had a bialkali photocathode with maximum responsivity around 420 nm. The calibration light source was a scientific water cooled Ar⁺ laser tuned to lase at the 476.6 nm line.

The radiant power of the Ar⁺ laser light was first measured with a Laser Probe Rm-6600 universal radiometer equipped with the RkP-575

thermal detector head having flat response in the spectral domain from 0.4 μm to 3 μm .

Care was taken to work in the linear response regime of the PMT, at incident radiant powers around 10^{-8} W (Figs. 1, 2).

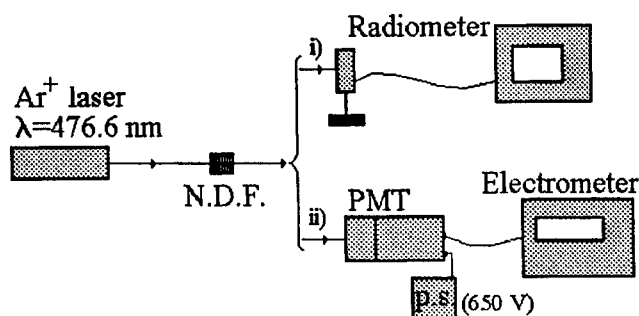


Fig. 1: Setup for PMT response calibration around 476 nm; N. D. F. is a set of neutral density filters; p. s. is the power supply for PMT

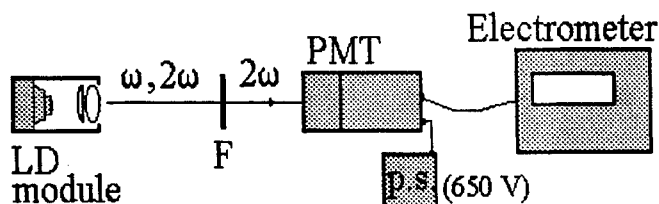


Fig. 2. Arrangement for the measurement of ISHG radiant power with calibrated PMT; the LD module is figured with heat sink and collimation optics; F is a wide-band filter for visible radiation

The electric signal from the PMT was measured with a Keithley 6517 electrometer. The background dark signal was properly subtracted in our experiments.

We observed quite high $P_{2\omega}$, of the order of 10^{-8} W, as compared to previously reported 10^{-11} W values for other configurations of LD's using the same semiconductor materials.

The power of the second harmonic, $P_{2\omega}$, higher than the values theoretically expected occurs at relatively increased injection currents as presented in Fig. 3.

Up to 70 mW of fundamental wave (FW) power $\sqrt{P_{2\omega}}$ varies close to the linear theoretical dependence, whereas for P_{ω} above 70 mW $\sqrt{P_{2\omega}}$ shows an upward displacement from theory, as can be seen from Fig. 4. This has been previously proved³ to be accompanied by an alteration of the near-field ISHG pattern and it indicates various changes occurring to the LD mirror facet, of which the most important to evaluate is the undesired temperature increase.

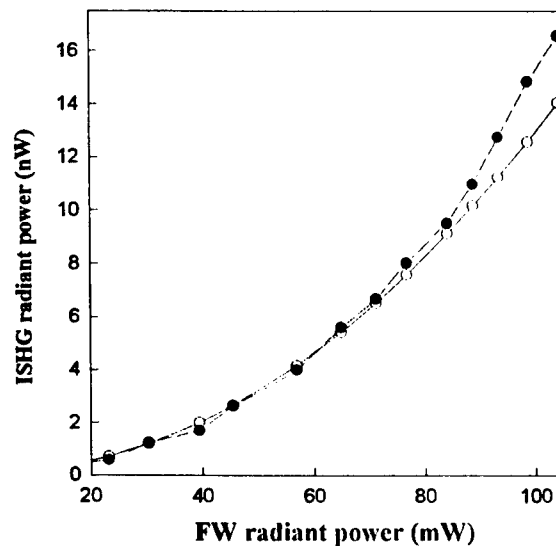


Fig. 3. The dependence of the measured (dashed line, full circles) $P_{2\omega}$ on P_{ω} , compared to the theoretical curve (solid line, hollow circles) calculated for an interaction length of 1.15 μm

For the type of LD we studied, mirror temperatures were measured³ as being always in excess with respect to the active layer temperature for injection currents above threshold.

The mirror temperature approaches a linear dependence on the injection current.

It was found that the excess mirror temperature gets higher for a narrower active domain stripe. This is the case of the LD's here presented, which have an active layer width of about 10 μm .

The results we present in Figs. 2 and 3 complete the picture on the mechanisms that determine the degradation of LD mirrors during high current injection operation.

Increased injection current determines a higher excess mirror temperature which results in a local increase of absorption in small area within the mirror layer.

This fact leads to a reduction of reflectivity in that domain and, consequently, to an increase of fundamental wave radiant power density, as a beginning for the conditions of catastrophic optical degradation; the increase of optical power density is closely monitored by a increase of fundamental wave-to-second harmonic conversion efficiency in the small area on the end-mirror-facet.

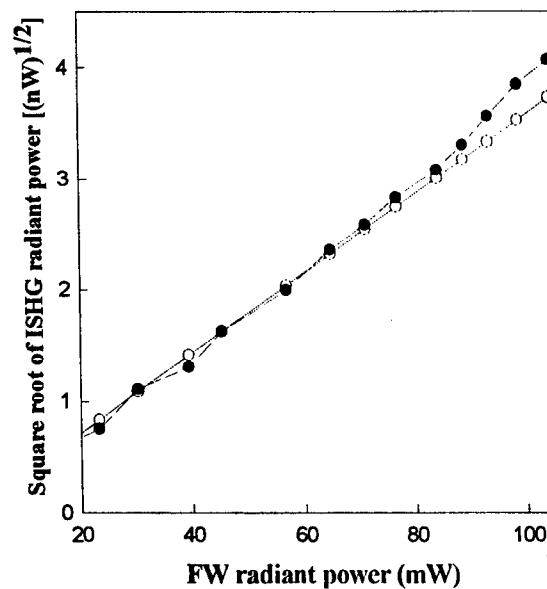


Fig. 4. Representation of $\sqrt{P_{2\omega}}$ versus P_{ω} from both measurement data (dashed line, full circles) and theoretical calculation (solid line, hollow circles)

4. CONCLUSIONS

The observed deviation of the experimental radiant power of the internal second harmonic generation from InGaAs/GaAs/AlGaAs strained single quantum well buried heterostructure laser diodes with respect to the

values theoretically expected (Figs. 3, 4), for injection currents higher than ~ 600 mA, is a signature of the excess of mirror-facet temperature increase.

The excess of internal second harmonic generation radiant power, measured by a relatively simple method, gives us information about the beginning of optical power density increase on the mirror and, at the same time, about the injection current values that enhance the risk of catastrophic optical degradation.

5. ACKNOWLEDGEMENTS

This research was performed under contract ERBIC 15 CT 960820 of the European Commission.

6. REFERENCES

1 D. Vakshoori, "Analysis of visible surface-emitting second-harmonic generators," *J. Appl. Phys.*, **70**, 5205-5217, (1991);

2 D. S. Chemla and J. Jerphagon, "Nonlinear optical properties of semiconductors", in *Handbook on Semiconductors*, T. Moss (ed.), Vol. 3, p. 546, North-Holland (1980).

3 A. V. Syrbu, A. Z. Mereutza, G. I. Suruceanu, V. P. Yakovlev, A. Caliman, A. T. Lupu, S. Vieru, M. Predescu, I. M. Popescu, and R. G. Ispasoiu, "Fabrication, characterization and applications of high performances AlGaAs-based buried-heterostructure diode lasers," *Optical Engineering*, **35**, p. 1278 (1996).

4 N. Chang, S. N. G. Chu, N. K. Dutta, J. Lopata, M. Geva, A. V. Syrbu, A. Z. Mereutza, V. P. Yakovlev, "Growth and fabrication of light performances 980 nm strained InGaAs quantum well laser for Er-doped fiber amplifiers," *IEEE J. of Quantum Electron.* **QE. 30**, p. 424 (1994).

5. P. N. Butcher and D. Cotter, *The elements of nonlinear optics*, Cambridge University Press, Cambridge, 1991.

Resonatorless optical bistability in a thin semiconductor film

S. L. Gaivan and P. I. Khadzhi

Institute of Applied Physics, Academy of Sciences of Moldova
Academia Str. 5, Kishinev MD2028, Moldova

ABSTRACT

A theoretical investigation is reported of steady-state nonlinear transmission of resonant laser radiation by a thin semiconductor film under the conditions of two-pulse generation of excitons and biexcitons. The equations of state are derived for the description of bistable behavior of the amplitudes of the transmitted pulses and of the quasiparticle concentration, depending on the parameters of the exciting fields. The criteria of existence of an optical bistability are determined.

Keywords: thin films, optical bistability, excitons

1. INTRODUCTION

It is known¹ that a wide spectrum of nonlinear optical effects, including cavity-free optical bistability, can appear in a thin film consisting of two-level atoms. Since a variety of nonlinear mechanisms can occur in semiconductors, and since their relaxation times are short and their nonlinear susceptibilities are high, one can expect striking manifestations of such effects specifically in semiconductor films.

We shall report a theoretical study of resonatorless optical bistability observed in the transmission by a thin semiconductor film (TSF) under the conditions of generation of coherent excitons and biexcitons by photons belonging to two different pulses. We shall consider simultaneously two quantum transitions (two channels), in the exciton range of spectrum and in the region of the *M*-band, which occur under the influence of photons from two different pulses. The *M* luminescence band is the result of optical exciton-biexciton conversion and is shifted towards longer wavelengths relative to the exciton absorption band by an amount equal to the biexciton binding energy.² In CuCl-type crystals, the biexciton binding energy is of the order of 40 meV, so that a transition in the *M*-band region is characterized by a considerable detuning of a resonance from a transition in the exciton range of spectrum. Moreover, the giant oscillator strength of the exciton-biexciton conversion process² may favor the appearance of optical nonlinearities even at moderate levels of excitation of a crystal. Therefore, we shall ignore the interparticle interaction effects.

2. HAMILTONIAN AND BASIC EQUATIONS

We shall assume that a TSF, located in vacuum, is exposed to two normally incident monochromatic laser pulses with the electric field envelopes E_{01} and E_{02} varying slowly with time and with the photon frequencies ω_1 and ω_2 , respectively. Photons from one of the pulses are in resonance with the frequency of an exciton transition and the photons from the other pulse are in resonance with the frequency of a transition in the *M*-band region. We shall also postulate that the film thickness L is considerably less than the incident radiation wavelength. We shall consider one macroscopically filled mode of coherent photons for each of the pulses and one mode each of coherent excitons and biexcitons, with their own wave vector and frequency. The interaction of the radiation fields with the excitons and biexcitons in a semiconductor can be described by the Hamiltonian³

$$H = -\hbar g(a^+ E_1^+ + a E_1^-) - \hbar \sigma(a^+ b E_2^- + a b^+ E_2^+), \quad (1)$$

where a and b are the amplitudes of the exciton and biexciton waves, respectively; E_i^+ and E_i^- are, respectively, the positive- and negative-frequency components of the electric field of the i -th pulse ($i = 1, 2$); g is the constant of the interaction excitons with the field; σ is the constant of the optical exciton-biexciton conversion process.

The Hamiltonian (1) yields readily the Heisenberg (material) equations for the amplitudes a and b :

$$i\dot{a} = \omega_0 a - i\gamma_e a - g E_1^+ - \sigma b E_2^-, \quad i\dot{b} = \Omega_0 b - i\gamma_m b - \sigma a E_2^+, \quad (2)$$

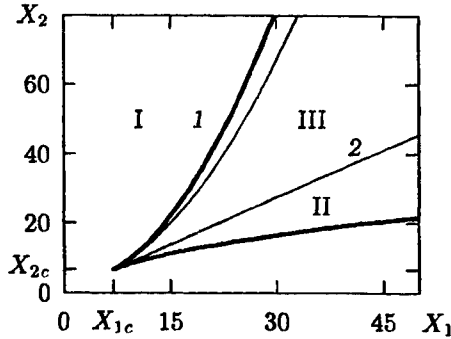


Fig. 1. Bifurcation curves in the parametric space (X_1, X_2) calculated for $C_1 = C_2 = 10$.

where ω_0 and Ω_0 are the self-frequencies of the exciton and biexciton states, respectively; γ_e and γ_m are the phenomenologically introduced damping constants of the exciton and biexciton modes, respectively.

Our task is to determine the amplitudes of the fields of the pulses transmitted by the film, E_1 and E_2 , when the amplitudes of the pulses incident on the TSF, E_{01} and E_{02} , are given. We find from the Hamiltonian (1) and from the boundary conditions postulating constancy of the tangential components of the fields at the film-vacuum interface that

$$E_1^+ = E_{01} \exp(i\omega_1 t) + i\alpha_1 g a, \quad E_2^+ = E_{02} \exp(i\omega_2 t) + i\alpha_2 \sigma a^+ b, \quad (3)$$

where $\alpha_1 = 2\pi\hbar\omega_1 L/c$; $\alpha_2 = 2\pi\hbar\omega_2 L/c$. The set of equations (2) and (3) solves the problem formulated above.

3. MAIN RESULTS AND DISCUSSION

Next, we shall introduce dimensionless quantities $Y_1 = \sigma E_1/\gamma$, $Y_2 = \sigma E_2/\gamma$, $X_1 = \sigma E_{01}/\gamma$, $X_2 = \sigma E_{02}/\gamma$, $C_1 = \alpha_1 g^2/\gamma$, $C_2 = \alpha_2 g^2/\gamma$. For simplicity, we assume here that $\gamma_e = \gamma_m = \gamma$. Equating to zero the derivatives \dot{a} and \dot{b} , under the conditions of exact resonance, $\omega_1 = \omega_0$ and $\omega_1 + \omega_2 = \Omega_0$, we obtain the following steady-state equations of state:

$$X_1^2 = n \left[1 + C_1 + \frac{X_2^2}{(1 + C_2 n)^2} \right]^2, \quad N = \frac{X_2^2}{(1 + C_2 n)^2 n}, \quad (4)$$

$$X_1 = Y_1 \left(1 + \frac{C_1}{1 + Y_2^2} \right), \quad X_2 = Y_2 \left(1 + \frac{C_2 Y_1^2}{(1 + Y_2^2)^2} \right), \quad (5)$$

where $n = (\sigma/g)^2 |a|^2$ and $N = (\sigma/g)^2 |b|^2$ are the normalized densities of coherent excitons and biexcitons, respectively.

We shall determine the range of values of the pump amplitudes X_1 and X_2 in which the densities of excitons n and biexcitons N , as well as the amplitudes of transmitted pulses Y_1 and Y_2 , can be multivalued functions of X_1 and X_2 . The boundaries of saddles in the parametric space (X_1, X_2) are defined by the following system of parametric equations:

$$X_1^2 = n \left[\frac{4C_2 n(1 + C_1)}{3C_2 n - 1} \right]^2, \quad X_2^2 = \frac{(1 + C_1)(1 + C_2 n)^3}{3C_2 n - 1}, \quad (6)$$

(curve 1 in Fig. 1). We shall now consider the stability of our steady-state solutions. A system of parametric equations

$$X_1^2 = n \left[\frac{(2 + C_1)(1 + C_2 n)}{C_2 n} \right]^2, \quad X_2^2 = \frac{(2 + C_1 + C_2 n)(1 + C_2 n)^2}{C_2 n}, \quad (7)$$

determines the stability boundary of nonsaddle singularities (curve 2 in Fig. 1). The resultant bifurcation curves split the parametric space (X_1, X_2) into three regions. In region I there is one singularity, namely, a stable focus; in region II there are three singularities, one of which is stable and the other two unstable; finally, in region III there are two stable solutions and a saddle-type singularity. The vertex of the "peak" in Fig. 1 has the coordinates $X_{1c} = 2(1 + C_1)/\sqrt{C_2}$, $X_{2c} = 2\sqrt{1 + C_1}$.

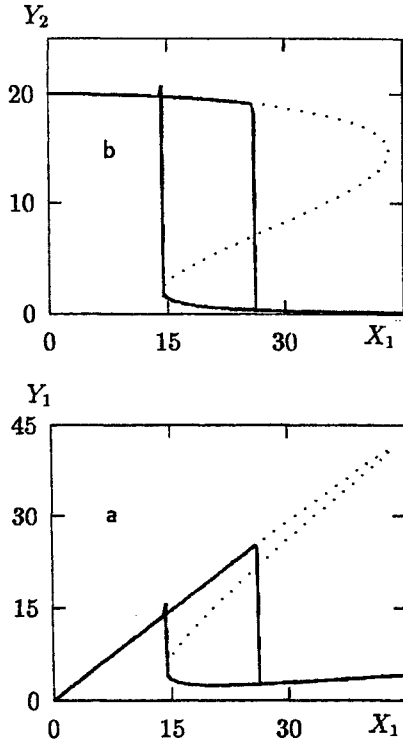


Fig. 2. Hysteretic dependencies of the amplitude Y_1 of the output radiation in the exciton part of spectrum (a) and of the amplitude Y_2 of the output radiation in the M -band region (b) on the pump amplitude X_2 in the M -band region, calculated for $X_1 = 20$ and $C_1 = C_2 = 10$.

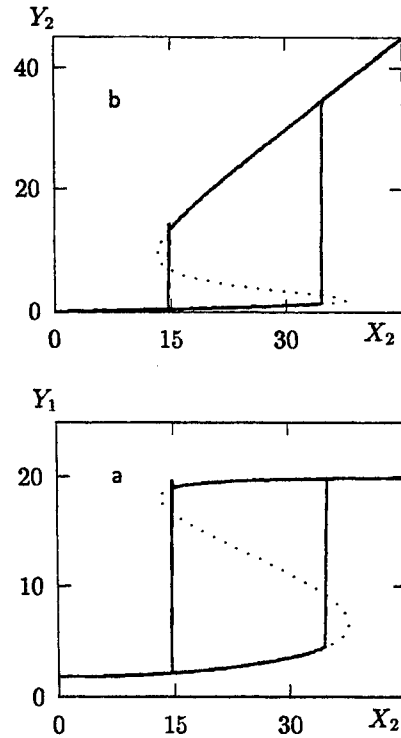


Fig. 3. Hysteretic dependencies of the amplitude Y_1 of the output radiation in the exciton part of spectrum (a) and of the amplitude Y_2 of the output radiation in the M -band region (b) on the pump amplitude X_1 in the exciton range of spectrum, calculated for $X_2 = 20$ and $C_1 = C_2 = 10$.

It therefore follows that hysteretic dependencies of the amplitudes of the transmitted fields and of the quasiparticle concentrations on the pump amplitudes are observed when excitons and biexcitons generated resonantly. An important factor is that, apart from the constant quantities C_1 and C_2 , the bistability parameters are the actual amplitudes X_1 and X_2 of the incident pulses. When one of these pump amplitudes is fixed, a change in the pump amplitude in the second channel makes it possible to control nonlinear transmission in both channels.

Let us now consider possible types of hysteretic dependencies. We shall begin with the behavior of the functions $Y_1(X_2)$ and $Y_2(X_2)$ at a fixed value of X_1 . We shall transform Eqns (5) to the equations of state relating the amplitudes of the input fields X_1 and X_2 to one of the output amplitudes:

$$X_2 = \sqrt{\frac{(1+C_1)Y_1 - X_1}{X_1 - Y_1}} \left[1 + \frac{C_2}{C_1^2}(X_1 - Y_1)^2 \right], \quad X_2 = Y_2 \left(1 + \frac{C_2 X_1^2}{(1+C_1+Y_2^2)^2} \right), \quad (8)$$

The dotted curves in Fig. 2 represent expressions (8) and the solid lines obtained by numerical solution of a relevant system of equations on the assumption that $X_1 = 20$ and that X_2 is a triangular pulse with a maximum normalized amplitude $X_{20} = 45$ and of width $500\gamma^{-1}$. The values of the pump amplitude X_2 in the M -band region, where switching takes place from one branch to another, can be found graphically from Fig. 1. The behavior of the function $Y_1(X_2)$ and $Y_2(X_2)$ has a simple physical explanation. At $X_2 = 0$ the transitions occur only in the exciton range of spectrum (first channel) and this determines the output amplitudes $Y_1 = X_1/(1+C_1)$ and $Y_2 = 0$. An increase in the pump amplitude X_2 in the M -band region results in conversion of an increasing proportion of excitons into biexcitons and, at the of switching to the upper branch, the number of excitons in the TSF falls to zero and the biexciton density rises strongly. When X_2 is increased still further, the exciton density remains zero

and the biexciton density falls monotonically to zero in the range $X_2 \gg X_1$. This saturation effect makes the film transparent and this occurs in both channels.

The field amplitudes Y_2 and Y_1 at the output, considered as a function of the input field amplitude X_1 in the exciton part of spectrum when the pump X_2 in the M -band region is fixed, are described by the following equations of state deduced from Eqns (5):

$$X_1 = \sqrt{\frac{X_2 - Y_2}{C_2 Y_2}} (1 + C_1 + Y_2^2), \quad Y_1 = \sqrt{\frac{X_2 - Y_2}{C_2 Y_2}} (1 + Y_2^2). \quad (9)$$

Fig. 3 illustrates the case which is the reverse of that just discussed: the dependencies $Y_1(X_1)$ and $Y_2(X_1)$ are calculated numerically (solid lines) and analytically (dotted curves) on the basis of equations (9) assuming that $X_2 = 20$ and that X_1 varies adiabatically slowly from 0 to 45. It is evident from Fig. 3 that for $X_1 = 0$ the output signal Y_2 is equal to X_2 , whereas in the absence of excitons the incident pulse in the M -band region is transmitted by the film under total transparency conditions. So long as $X_1 < X_2$, all the excitons generated in the TSF are converted into biexcitons. Therefore, as X_1 increased, the amplitude Y_2 falls very slowly, whereas Y_1 rises almost linearly. A further increase in X_1 results in an abrupt jump in the exciton density and a reduction in the biexciton density, the role of saturation becomes much weaker, and the behavior of the output radiation amplitudes is governed solely by transitions in the exciton range of spectrum. In the limit $X_1 \gg X_2$, we obtain $Y_2 = 0$, $Y_1 \approx X_1/(1 + C_1)$.

4. CONCLUSIONS

We shall conclude with estimates of the relevant quantities. In the case of CuCl, we have⁴ $\gamma \sim 10^{11} \text{ s}^{-1}$, $g = 5 \cdot 10^{19} \text{ cgs esu}$, $\sigma = 5 \cdot 10^{10} \text{ cgs esu}$, $\hbar\omega_1 \approx \hbar\omega_2 = 5 \cdot 10^{-12} \text{ erg}$. However, if $L = 10^{-6} \text{ cm}$, we have $C_1 \approx C_2 \sim 10$. These values of the parameters C_1 and C_2 correspond to the critical values of the normalized amplitudes $X_{1c} \approx X_{2c} \approx X_{cr} = 7$. The pump intensities at which resonatorless optical bistability can occur should be of the order of $I = c\gamma X_{cr}^2 / 8\pi\sigma^2 \sim 20 \text{ kW/cm}^2$. Using computer simulations we found that the switching times from one steady state to another no more than 10 ps.

It follows from the above that the TSF can operate efficiently as a bistable integrated-optical switching cell when excitons are generated resonantly in the film and are simultaneously converted into biexcitons by photons from two different pulses. Figures 2 and 3 made it clear that the output of one channel is governed by pumping not only of this channel, but also of the other channel. This presents an opportunity for controlling bistable behavior of the first beam by the second.

5. REFERENCES

1. V. Ben-Aryeh, C. M. Bowden, and J. C. Englund, "Intrinsic optical bistability in collections of spatially distributed two-level atoms," *Phys. Rev. A* **34**(5) (1986) 3917-3928.
2. P. I. Khadzhi, *Kinetics of Exciton and Biexciton Recombination Radiation in Semiconductors*. Știința, Kishinev, 1977.
3. P. I. Khadzhi, *Nonlinear Optical Processes in System of Excitons and Biexcitons in Semiconductors*. Știința, Kishinev, 1984.
4. I. Abram, "Nonlinear optical properties of biexcitons: single-beam propagation," *Phys. Rev. B* **28**(8), 4433-4441 (1983).

Nonlinear transmission of ultrashort light pulses by a thin semiconductor film in the exciton range of spectrum

P. I. Khadzhi and S. L. Gaivan

Institute of Applied Physics, Academy of Sciences of Moldova
Academia Str. 5, Kishinev MD2028, Moldova

ABSTRACT

A study is reported of the influence of the saturation of the dipole momentum of an exciton transition on transient transmission of ultrashort laser pulses by a thin semiconductor film in the exciton range of spectrum. It is shown that when rectangular pulses of resonant laser radiation are incident on the film, a threshold-type qualitative change in the transmission by the film takes place from almost total reflection at low level of excitation to complete bleaching at high values of the incident pulse amplitude. An analogue of the McCall-Hahn area theorem is derived for ultrashort pulses interacting with the film. When the nonlinear parameter is large, the dependence of the area of a pulse transmitted by the film on the area of an incident pulse becomes multivalued.

Keywords: thin films, ultrafast phenomena, excitons

1. HAMILTONIAN AND BASIC EQUATIONS

The interaction of ultrashort light pulses with a thin film consisting of two-level atoms gives rise to a number of interesting effects,^{1,2} which are not typical of bulk resonant media. In particular, a nonlinear relationship between the field of an optical wave transmitted by a film and the optical properties of a resonant medium gives rise to cavityless optical bistability.³ It therefore seems desirable to investigate nonlinear optical properties of thin semiconductor films (TSFs), since semiconductors

We shall report a theoretical investigation of the nonlinear transmission and reflection of ultrashort laser pulses by a thin semiconductor film (TSF) in the exciton range of spectrum taking into account the saturation effect of the exciton dipole momentum and the exciton-photon interaction. An ultrashort laser pulse with electric-field envelope $E_i(t)$ and with a carrier frequency ω , which is in resonance with an exciton self-frequency ω_0 , is assumed to fall normally on a TSF located in vacuum. The TSF thickness L satisfies the inequality $a_0 \ll L \ll \lambda$, where a_0 is the Bohr radius of a free exciton and λ is the wavelength of the incident light. It is assumed that the pulse duration T is shorter than the exciton relaxation time τ_{rel} , but much longer than period of oscillations of the wave ($\omega^{-1} \ll T \ll \tau_{rel}$). Under these conditions the relaxation processes, responsible for the real (dissipative) absorption of light, are too slow to be significance. Coherent photons in the pulse E_i , transmitted by the TSF excite coherent excitons with the same wave vector and phase, and interact with the latter. Radiative recombination of excitons then returns energy to the transmitted pulse, which distorts the pulse envelope. The interaction of the wave field with excitons is described by the Hamiltonian

$$H = -\hbar g(a^+ E^+ + a E^-) + \hbar \mu(a^+ a^+ a E^+ + a^+ a a E^-), \quad (1)$$

where E^+ and E^- are respectively, the positive- and negative-frequency components of the wave field; a is the amplitude of the exciton wave. The constant g describes the linear exciton-photon interaction and the μ represents the influence of saturation of the exciton dipole moment of a transition at high level of excitation. The saturation effect is the result of collective processes of the emission and absorption of light in a high-density system of excitons.

Eqn (1) readily leads to the following Heisenberg equation of motion for the exciton wave amplitude a and to expression for the exciton polarization of the medium P^+

$$i\dot{a} = \omega_0 a - g E^+ + 2\mu a^+ a E^+ + \mu a a E^-, \quad (2)$$

$$P^+ = \hbar(ga - \mu a^+ aa). \quad (3)$$

The set of equations (2) and (3) must be supplemented by electrodynamic relationships between the amplitudes of the incident (E_i^+), transmitted (E^+), and reflected (E_r^+) pulses^{1,2}:

$$E^+ = E_i^+ + i \frac{4\pi\omega L}{c} P^+, \quad E_r^+ = E^+ - E_i^+. \quad (4)$$

Let us represent the amplitudes of the pulses by $E^+ = E_i \exp(-i\omega t)$, $E_i^+ = E_i \exp(-i\omega t)$, $E_r^+ = E_r \exp(-i\omega t)$. The adoption of dimensionless quantities $x = \sqrt{\kappa}u$, $y = \sqrt{\kappa}v$, $\kappa = \mu/g$, $\tau = t/\tau_0$, $\delta = (\omega - \omega_0)\tau_0$, $F_0 = \sqrt{\kappa}g\tau_0 E_i$, $F_t = \sqrt{\kappa}g\tau_0 E_t$, $F_r = \sqrt{\kappa}g\tau_0 E_r$, where

$$\tau_0^{-1} = 2\pi\hbar\omega Lg^2/c, \quad (5)$$

and the use of Eqns (2)-(4) yield a system of equations for determination of the normalized envelopes of the transmitted F_t and reflected F_r pulses for a given pump amplitude F_0 :

$$\begin{aligned} \frac{dx}{d\tau} &= -\delta y - x(1 - x^2 - y^2)^2 + 2xyF_0, \\ \frac{dy}{d\tau} &= \delta x - y(1 - x^2 - y^2)^2 + (1 - 3x^2 - y^2)F_0, \\ F_t &= F_0 - y(1 - x^2 - y^2) + ix(1 - x^2 - y^2), \\ F_r &= -y(1 - x^2 - y^2) + ix(1 - x^2 - y^2). \end{aligned} \quad (6)$$

2. MAIN RESULTS AND DISCUSSION

Let us assume that during a time interval T the film interacts with a pulse of constant amplitude $F_0 = \text{const.}$ At low excitation rates ($F_0 \ll 1$), the solution of the set of equations (6) gives:

$$|F_t| = \frac{F_0}{\sqrt{1 + \delta^2}} (e^{-2\tau} - 2\delta e^{-\tau} \sin \delta\tau + \delta^2)^{1/2}, \quad (7)$$

$$|F_r| = \frac{F_0}{\sqrt{1 + \delta^2}} (e^{-2\tau} - 2e^{-\tau} \cos \delta\tau + 1)^{1/2}. \quad (8)$$

Consequently, if $\delta \neq 0$ the amplitudes $|F_t|$, $|F_r|$ oscillate and decay, approaching asymptotically the steady-state amplitudes $F_0\delta/\sqrt{1 + \delta^2}$ and $F_0/\sqrt{1 + \delta^2}$, respectively. At the exact resonance ($\delta = 0$) the amplitude of the transmitted pulse falls exponentially to zero and the amplitude of the reflected pulse rises correspondingly to F_0 .

We shall now investigate the characteristic features of the interaction of an ultrashort light pulse with a TSF at various excitation levels. If we assume that initially ($\tau = 0$) there are not excitons in the film ($x(0) = y(0) = 0$), then at the exact resonance ($\delta = 0$) it follows from the system (6) that $x \equiv 0$ and this system of equations reduces to:

$$\begin{aligned} \frac{dy}{d\tau} &= (1 - y^2)(F_0 - y + y^3), \\ F_t &= F_0 - y(1 - y^2), \\ F_r &= -y(1 - y^2). \end{aligned} \quad (9)$$

An analysis of the system of equations (9) shows that the transmission by a TSF is of different nature for $F_0 < F_{cr}$ and $F_0 > F_{cr}$, where $F_{cr} = 2\sqrt{3}/9$. The reason for this is that if $F_0 < F_{cr}$, then equation $F_0 - y + y^3 = 0$ has three real roots, but if $F_0 > F_{cr}$ it has only one root and that root is negative.

Therefore, if $F_0 < F_{cr}$, our system evolves in such a way that $y(\tau)$ approaches the smallest positive root of the equation $F_0 - y + y^3 = 0$. For $F_0 < F_{cr}$, the roots of this equation are given by

$$y_1 = -\frac{2}{\sqrt{3}} \cos \frac{2\pi + \varphi}{3}, \quad y_2 = -\frac{2}{\sqrt{3}} \cos \frac{4\pi + \varphi}{3}, \quad y_3 = -\frac{2}{\sqrt{3}} \cos \frac{\varphi}{3}, \quad (10)$$

where $\varphi = \arccos(3\sqrt{3}F_0/2)$, and $y_1 > y_2 > 0 > y_3$. We then readily obtain the implicit dependence $y(\tau)$ for $F_0 < F_{cr}$:

$$F_0\tau = \text{arthy} + C_1 \ln \left(1 - \frac{y}{y_1}\right) + C_2 \ln \left(1 - \frac{y}{y_2}\right) + C_3 \ln \left(1 - \frac{y}{y_3}\right), \quad (11)$$

where

$$C_1 = \frac{y_1}{(y_1 - y_2)(y_1 - y_3)}, \quad C_2 = -\frac{y_2}{(y_1 - y_2)(y_2 - y_3)}, \quad C_3 = \frac{y_3}{(y_1 - y_3)(y_2 - y_3)}. \quad (12)$$

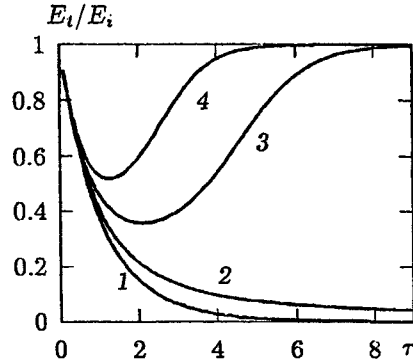


Fig. 1. Evolution of the normalized amplitude E_t/E_i of a transmitted pulse, plotted for different pump amplitudes $F_0 = 0.2$ (1), 0.4 (2), 0.6 (3), and 0.8 (4).

It follows from the above solution that the function $y(\tau)$ rises monotonically and it approaches asymptotically the smallest of the positive roots, i.e. y_2 .

If $F_0 > F_{cr}$ the equation $F_0 - y + y^3 = 0$ has one real (negative) root and two complex roots:

$$y_1 = -\frac{2}{\sqrt{3}} \operatorname{ch} \frac{\varphi}{3}, \quad y_{2,3} = \frac{1}{\sqrt{3}} \operatorname{ch} \frac{\varphi}{3} \pm i \operatorname{sh} \frac{\varphi}{3}, \quad (13)$$

where $\varphi = \operatorname{arch}(3\sqrt{3}F_0/2)$. The solution of the system can then be represented in the form

$$F_0 \tau = \operatorname{arthy} + \frac{1}{3y_1^2 - 1} \left[y_1 \ln \left(1 - \frac{y}{y_1} \right) - \frac{y_2}{2} \ln \left(\frac{y^2 + yy_1 + y_1^2 - 1}{y_1^2 - 1} \right) + \right. \\ \left. + \frac{3y_1^2 - 2}{\sqrt{3y_1^2 - 4}} \left(\operatorname{arctg} \frac{2y + y_1}{\sqrt{3y_1^2 - 4}} - \operatorname{arctg} \frac{y_1}{\sqrt{3y_1^2 - 4}} \right) \right]. \quad (14)$$

It follows from the above solution that the function $y(\tau)$ rises monotonically with time and tends asymptotically to unity.

The evolution of the transmitted and reflected pulses at the exact resonance can be investigated on the basis of Eqns (10)-(14). Fig. 1 gives the time dependencies of the normalized amplitude E_t/E_i of a pulse transmitted by a TSF for various pump amplitudes. We can see, that if $F_0 < F_{cr}$, the envelope of the transmitted pulse decays monotonically with time and vanishes for $\tau \gg 1$. Consequently, the transmission of weak pulses by a TSF ceases rapidly, so that the incident light is almost totally reflected. If $F_0 > F_{cr}$, the amplitude of the transmitted pulse first falls, reaches its minimum, and then rises again, becoming equal to the amplitude of the incident pulse. This means that the TSF becomes totally bleached because of saturation of the dipole moment of the transition. In this bleached state, the incident pulse crosses the TSF as if it were an absolutely transparent medium. The width and depth of a dip in the envelope of the transmitted pulse decrease with increase in the transmitted pulse amplitude.

We can therefore draw the conclusion that when rectangular pulses of resonant laser radiation are incident on a TSF, a threshold-type qualitative change in the transmission by the film takes place from almost total reflection at low amplitudes F_0 to complete bleaching at high values F_0 . Since $E_r = E_i - E_t$, it follows that when the incident pulse amplitude is higher than the critical value, a dome-shaped ultrashort pulse is formed by reflection.

It is not possible to solve with analytic rigor the system of equations (6) for an arbitrary incident pulse profile and a finite detuning from a resonance. Nevertheless, the simplicity of the physical model makes it possible to derive fairly general relationships relating the areas of the incident (θ_i), transmitted (θ_t), and reflected (θ_r) pulses in the case of an inhomogeneously broadened exciton resonance line. The pulse area is defined as $\theta = \sqrt{\kappa g} \int E(t) dt$. Then, in the absence of phase modulation of the envelopes of the fields of the pulses, the adoption of integral quantities in Eqns (2) to (4) gives

$$\theta_i = \theta_t + \beta \left(1 - \frac{5}{6} \tanh^2 \theta_t \right) \tanh \theta_t, \quad (15)$$

$$\theta_i + \theta_r = \theta_t, \quad \beta = \pi \tau_0^{-1} f(0), \quad (16)$$

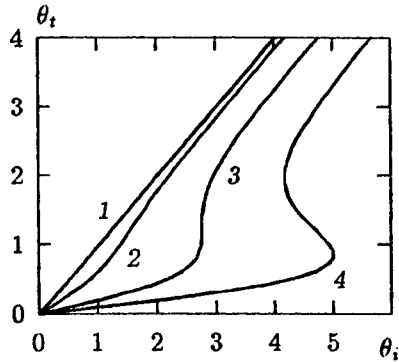


Fig. 2. Dependence of the area θ_t of a pulse transmitted by the film on the area θ_i of an incident pulse, plotted for different values of the nonlinear parameter $\beta = 0.1$ (1), 1.0 (2), 4.44 (3), and 10.0 (4).

where $f(0)$ is the inhomogeneous broadening of the exciton level expressed in terms of $f(\Delta)$ when the detuning is $\Delta = 0$. Expressions (15) and (16) relate the areas of the incident, transmitted, and reflected pulses, and they represent an analogue of McCall-Hahn area theorem⁴ for ultrashort pulses of resonant laser radiation interacting with a TSF in the exciton spectral range. The area θ_t of the transmitted pulse, considered as a function of the area θ_i of the incident pulse, is plotted in Fig. 2. We can see that, if nonlinear parameter β is small, the area θ_t increases almost linearly with θ_i . However, if this parameter is $\beta > 40/9 \approx 4.44$, then in a certain range of values of θ_i the dependence $\theta_t(\theta_i)$ becomes multivalued, i.e. there is an abrupt change in the transmitted pulse area when the incident pulse area is altered. The width of this range of values of θ_i increases as the parameter β increases.

3. CONCLUSIONS

We shall conclude with some numerical estimates obtained for a CuCl crystal. Expression (5) gives the characteristic time τ_0 of the changes in the amplitudes of the transmitted and reflected pulses. If we assume that $\omega = 3.18$ and $g = 5 \cdot 10^{19}$ egs esu,⁵ we find that for a film $L = 4 \cdot 10^{-6}$ cm thick the time is $\tau_0 \sim 10^{-13}$ s. The critical value $F_{cr} = 2\sqrt{3}/9 \approx 0.4$ corresponds to the incident light intensity $I = F_{cr}^2 / 8\pi\kappa g^2 \tau_0^2 \sim 1$ MW/cm². If we assume that the inhomogeneous broadening function $f(\Delta)$ of an exciton level is Gaussian and that its spectral half-width is Δ_0 , we find that the nonlinear parameter is $\beta = \sqrt{\pi} / \Delta_0 \tau_0$. If we assume that $\Delta_0 \sim 1$ meV, we find that $\beta \sim 10$.

4. REFERENCES

1. M. G. Benedict, E. D. Trifonov, "Coherent reflection as superradiation from the boundary of a resonant medium," *Phys. Rev.* **A38**(6), 2854-2861 (1988).
2. M. G. Benedict, V. A. Malyshev, E. D. Trifonov, A. I. Zaitsev, "Reflection and transmission of ultrashort light pulses through a thin resonant medium: Local field effects," *Phys. Rev.* **A43**(7), 3845-3852 (1991).
3. Y. Ben-Aryeh, C. M. Bowden, J. C. Englund, "Intrinsic optical bistability in collections of spatially distributed two-level atoms," *Phys. Rev.* **A34**(5), 3917-3928 (1986).
4. S. L. McCall, E. L. Hahn, "Self-induced transparency," *Phys. Rev.* **183**(2), 457-464 (1969).
5. I. Abram, "Nonlinear optical properties of biexcitons: single-beam propagation," *Phys. Rev.* **B28**(8), 4433-4441 (1983).

Cryptographic mixing transformations for image applications

Adriana Vlad, and Mihai Mitrea

"POLITEHNICA" University of Bucharest, Faculty of Electronics and Telecommunications
1-3 Iuliu Maniu Bvd, 77202, Bucharest-Romania
e-mail: vadriana@vala.elia.pub.ro; mmitrea@helix.elia.pub.ro

ABSTRACT

Several image encryption methods have been recently considered (Opt. Eng. 35, Sept. 1996). This paper presents a new image enciphering method starting from the mixing transformations suggested by C.E. Shannon for natural language.

There are two ways in which images are involved here: first, as a means of visual perception of the mixing transformation features (the very sophisticated *diffusion* and *confusion*); secondly, as the application field itself.

Both the theoretical and experimental aspects pointed out here show the high quality of this method of image enciphering.

The method illustrations were made either for simulated images with different probability laws and autocorrelation functions, or for natural images.

Keywords: image enciphering, cryptographic mixing transformations, diffusion, confusion, simulated random images

1. INTRODUCTION

This paper deals with a new method for image enciphering, which relies on some Shannon's suggestions concerning the usefulness of the mixing transformations in the construction of good practical ciphers.¹ Thus, in his famous work on cryptography, Shannon proposed, for natural language purposes, the following chain of secrecy systems considered to be computationally secure:

$$T_k F S_j F R_i, \quad (1)$$

where T_k, R_i stand for simple ciphers of transposition type, S_j stands for a substitution type cipher, and F is the so called *mixing transformation*. Concerning F , Shannon also suggested a formula:

$$F = L S L S L T, \quad (2)$$

where L, S and T are deterministic transformations, easily to be applied: T is a transposition, S is a substitution, and L is a linear averaging operation described by Eq. (3)

$$y_j = \sum_{i=0}^{P-1} x_{j+i} \bmod q. \quad (3)$$

Eq. (3) means that summing-up P successive pixels from the input image, and then applying $\bmod q$ to this result we obtain a value for the output image. The P value from Eq. (3) represents the mixing transformation parameter.

Note that a key for secrecy system (1) is specified by the group of the three keys (T_k, S_j, R_i) of the respective elementary ciphers.

Relations (1)-(3) show that there are no practical problems when applying the F function; yet, the final effect is remarkable, namely the computational security. This success accomplished by transformation chain (1) is based upon the combination of two concepts: *diffusion* and *confusion*.

Here we applied the same type of enciphering system (1) + (3), but for image purposes. We also developed some variants for the mixing transformations, necessary to this new application field. Besides, the paper presents a study of the meaning of *diffusion* and *confusion* involved in (1) + (3) when applied to images.

Note that *diffusion* and *confusion* are very sophisticated concepts and there are a few details in the literature regarding their operation, even for natural language purposes.² However, Shannon's suggestions concerning the mixing transformations were efficiently turned into practice in developing some very good ciphers (e.g. Data Encryption Standard).

Diffusion spreads the redundancy of the original image over long units of image, involving long combinations of pixels in the enciphered image. *Confusion* leads to a very complicated description of the dependency of the key on the pair message-cryptogram. Finally, these two discourage the cryptanalyst in his trials to get quicker to the solution.

In this paper images are used in two ways: first, as a means of providing a visual perceptions of diffusion and confusion (we developed some procedures with this aim); secondly, as the application field itself. Notice should be done that the visual perception means much more than an objective *per se*, it is a tool to enable the design of this cipher (i.e. to choose the method parameters, to decide how many times to apply LS or LST combinations, whether it is better to use L with a variable P parameter value or not, etc.).

The good quality of this enciphering method is contained within its theoretical basis.^{1,2} There are also some peculiarities regarding the images to be pointed out here.

Method illustrations stand for different original images: we enciphered either simulated images with different probability laws and autocorrelation functions,³ or natural images (i.e. Lena).

2. METHOD ATTRIBUTES: DIFFUSION AND CONFUSION

In this section we shall separately present the two notions, diffusion and confusion. Note that the mixing transformation combine this two notions in its overall action and the separation we do here is only to clarify the explanation.

On the other hand, if diffusion can be revealed on the basis of the mixing transformation (2), confusion is meaningless without the enciphering chain (1).

2.1 Diffusion: analysis and experimental results

It is known that redundancy of the original message source is responsible for the secrecy systems breaking. On the other hand, it is known that source redundancy can not be decreased without compression. The mixing transformation chain (1) \div (3) does not affect the message length (so, there is no compression); yet, it ensures the practical secrecy. Here appears the very role of diffusion: not to decrease the redundancy, but to dissipate it over long combination of pixels in the output image.

In our computer experiments we considered 256×256 pixels, and 32 gray levels images (so, we have considered $q = 32$ in (3)).

Figs. 1 and 2 show diffusion involved only in the L operation from (3); different P parameter values were considered. Certainly, the whole F function from (2) leads to even better results.

In Fig. 1 the original image was a computer generated noise image (Fig. 1a1), having a gamma probability law with 6 degrees of freedom,³ with mean 6 and variance 12. Figs. 1a2 and 1a3 show the autocorrelation function and the gray level histogram for the original message.

Applying the L operation with $P = 10$ to the original from Fig. 1a1 we obtained the output image (Fig. 1b1) with its autocorrelation function (Fig. 1b2) and gray level histogram (Fig. 1b3). Similarly, Figs 1c are obtained when applying the L operation with $P = 25$.

We resumed the experiments, but this time the input was a natural image (Lena, Figs. 2a); Figs. 2b and 2c are the output images obtained when applying the L operation with $P = 10$ and $P = 25$, respectively.

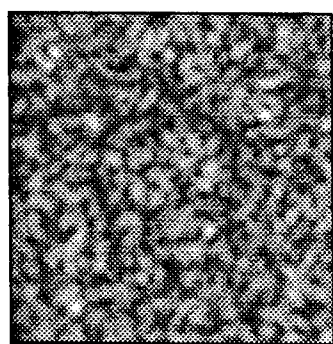
Diffusion is remarkably noticed even when applying only the L operation and even when considering not too large values for P , as it can be seen in Figs. 1 and 2.

For the 2D simulated random signals with prescribed probability laws and autocorrelation functions³ (as in Fig. 1) the diffusion involved in the L operation has the same explanation as for the natural language case:² a direct consequence of the Central Limit Theorem and of the action of the modulo function.

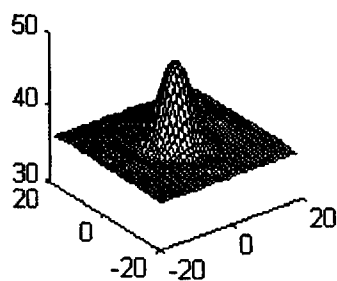
For other images, as the natural ones (Fig. 2) the results regarding diffusion are only experimentally proved. At the limit, for a degenerated 2D random signal, where each sample stands for a constant function (a single gray level assigned to all the pixels in the sample image) the L operation from (3) no longer produces diffusion. In order to obtain diffusion even in this situation, and even more, to improve the chain (1) performances, we developed a variant for the L operation where we successively modified the P parameter value during the L operation (i.e. in (3) we successively modified the sum superscript during the same L operation). For example, using the enciphering transformation (1) with variable P according to the rule: 9,13,19,27,9,13,19,27,9... we got the cryptogram from Fig. 3. These three cryptograms correspond to three different original images: Fig. 3a - a single gray level image; Fig. 3b - the correlated gamma noise image from Fig. 1a1; Fig. 3c - a natural image, namely Lena.

The variant with variable sum superscript in (3) would be utterly useful when the input image contains large single gray level areas (e.g. the background value).

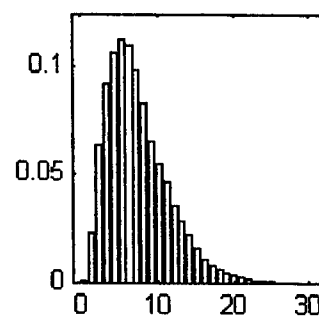
As it can be immediately noticed, the variant we developed for Fig. 3 leads to an improvement in the overall enciphering chain (1) without any difficulty in its software implementation.



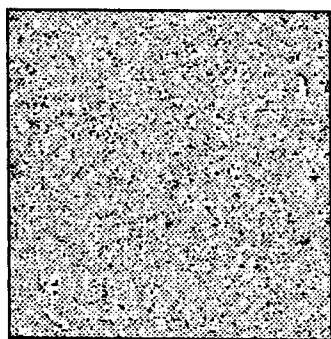
(a1)



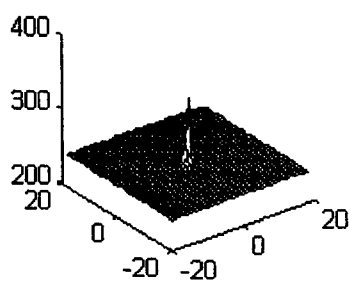
(a2)



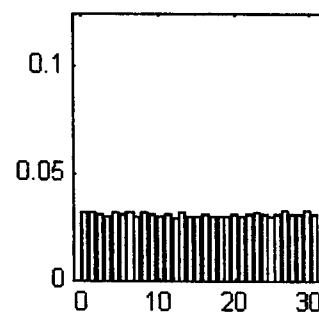
(a3)



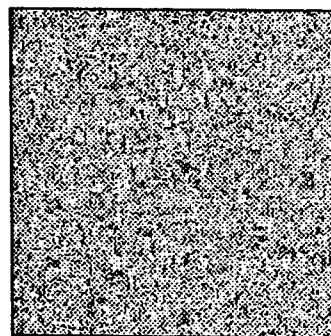
(b1)



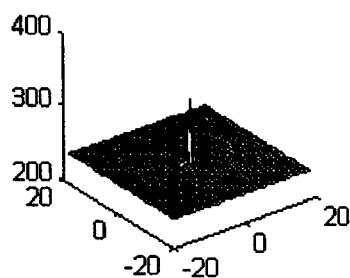
(b2)



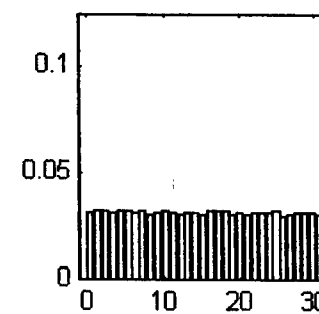
(b3)



(c1)



(c2)

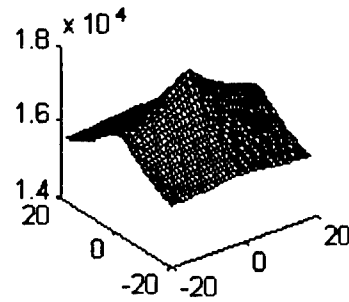


(c3)

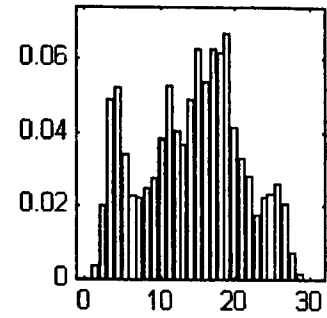
Fig. 1: Diffusion under the L operation. Figs. (a) correspond to the input image: correlated gamma noise image (a1), autocorrelation function (a2), and gray level histogram (a3). Figs. (b) and (c) stand for the corresponding output images obtained when applying the L operation with $P=10$ and $P=25$, respectively.



(a1)



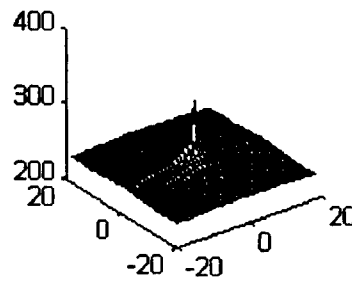
(a2)



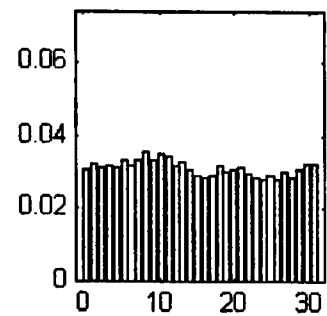
(a3)



(b1)



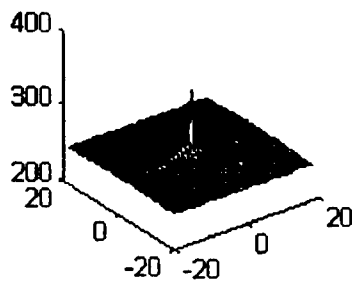
(b2)



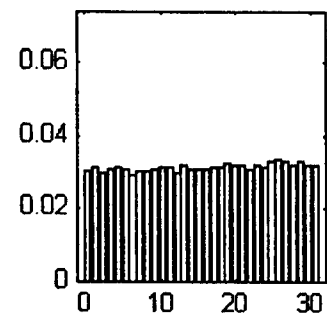
(b3)



(c1)



(c2)



(c3)

Fig. 2: Diffusion under the L operation. Figs. (a) correspond to the input image: Lena image (a1), autocorrelation function (a2), and gray level histogram (a3). Figs. (b) and (c) stand for the corresponding output images obtained when applying the L operation with $P=10$ and $P=25$, respectively.

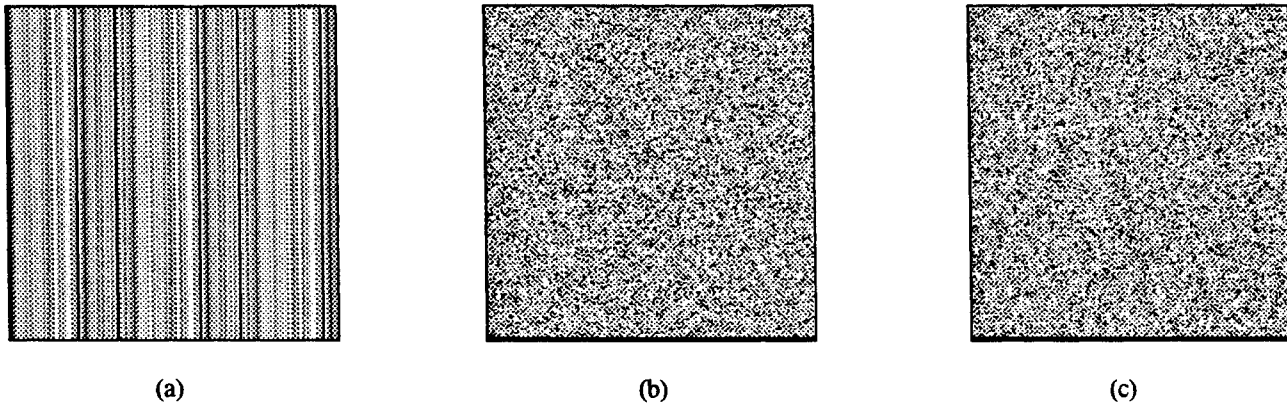


Fig. 3 Cryptograms obtained with the enciphering chain (1) and with variable sum superscript in (3). The original images are: a single gray level image (a), a correlated gamma noise image (b), and Lena (c).

2.2 Confusion: analysis and experimental results

Confusion is a notion even more difficult to be presented than diffusion. As already mentioned, confusion has no meaning in the F mixing transformation only, but in the context of the whole enciphering chain (1).

A secrecy system whose confusion is strong does not allow to find out the key based upon the cryptogram and some fragments from the original message (*chosen text attack*).

For the checking up of the confusion and also for its visual perception we developed two methods. In these methods images are used in two ways: as a tool for confusion perception and also as the application field itself.

a) Method with cryptogram difference image

It is a visual method, based on the fact that any alteration of the key elements (a smallest change in a key) would have led to changes in the whole enciphering image.

In order to notice these effects we have represented the difference of the two enciphered images, obtained from the same original image, but using two keys. Thus, we first chose a key for the secrecy system and then we made the smallest change in it, and then we represented the cryptogram difference image. That is what Fig. 4 shows. In order to reveal the presence/absence of confusion in a cipher, we considered, for comparison, three secrecy systems: first (Fig. 4a) the secrecy system (1) \div (3), then (Fig. 4b) a fixed period transposition cipher, and finally (Fig. 4c) a simple substitution type cipher. Note that in this case a black pixel means no difference between the two enciphered images (the above mentioned) at the respective locations.

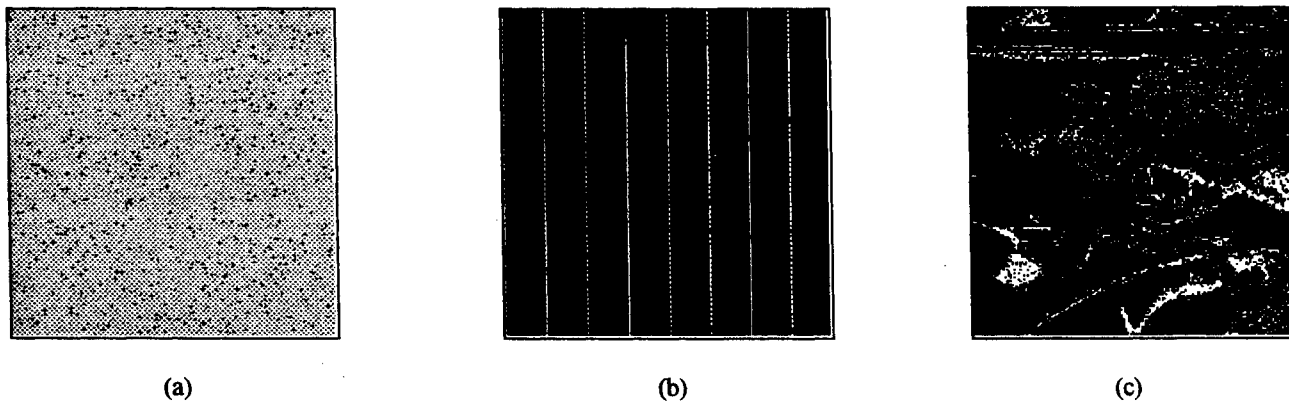


Fig. 4 Confusion perception using difference image. Fig. (a) corresponds to the cryptographic chain (1), Fig. (b) to a fixed period transposition cipher, and Fig. (c) to a simple substitution cipher.

The cryptographic chain (1) is seen to involve the confusion (there are changes in all the locations from Fig. 4a), while the elementary ciphers have nothing to do with the confusion (there are local changes in the cryptograms from Figs. 4b and 4c).

b) Method with evolving cells

This is also a visual method this time intended to point out how different changes in the key can be noticed in a single location of the cryptogram, no matter where that location can be. This is what Fig. 5 illustrates. In this figure, we kept the same input message every time, we chose 9 locations in the cryptogram and we changed 16 elements of the key for the enciphering scheme (1). The local effect of all the 16 alterations of the key was presented as a cell successively growing along 8 axes, in two steps for each axis, according to the confusion strength.

In order to illustrate this idea, we performed all the 16 changes in a (T_k, S_j, R_i) key of the enciphering system (1) in three separate experiments, as follows. First, we successively considered 16 changes only for the R_i elements, preserving unchanged T_k and S_j , Fig. 5a. Then all the 16 changes were applied only for S_j elements, Fig. 5b. Finally, we considered all the 16 changes only for T_k , Fig. 5c.

From Fig. 5 there appears that a proper use of the secrecy system (1) requires, when changing the key, to have at least some changes in the R_i elements.

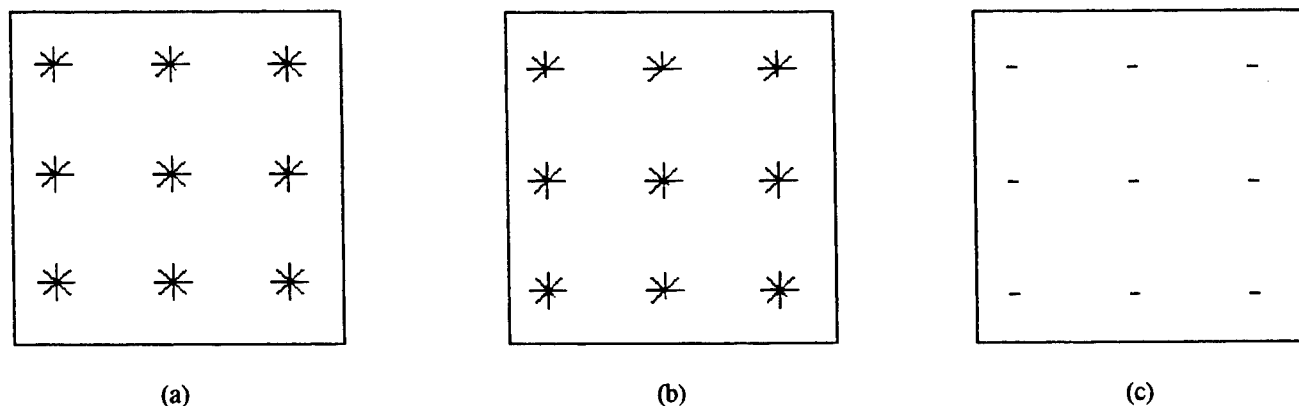


Fig. 5 Confusion perception using evolving cells. 9 location in the cryptograms are considered, and 16 successively changes of the key of cipher (1). All the 16 alterations of the key correspond: to the R_i elements (Fig. a), to the S_j elements (Fig. b), and to the T_k elements (Fig. c).

3. CONCLUSIONS

This paper deals with a new method for image enciphering, starting from some of Shannon's suggestions for natural language. Besides the direct extending of the application field (from natural language to images), there are contributions regarding the visual perception of the two sophisticated notions *diffusion* and *confusion*, the two attributes which ensure the high quality of the cipher (the computational security). This analysis allowed us to develop some variants which improved *diffusion* and *confusion* in image applications.

4. ACKNOWLEDGMENTS

This work was in part supported by a Grant of the National Council for Academic Research.

5. REFERENCES

1. C.E. Shannon, "Communication Theory of Secrecy Systems", *Bell System Technical Journal*, **28**, 656-715, (1949).
2. Adriana Vlad, and M. Mitrea, "Cryptographic Mixing Transformation", *Buletinul Științific al Universității "POLITEHNICA" din Timișoara*, Tom **41**(55), Fasc. 1, 71-76, (1996).
3. Adriana Vlad, M. Ferecatu, and P. Opreșan, "Statistical noise simulation for image processing purposes", *Opt. Eng.* **35**(6), 1590-1599, (1996).

Characterization of the silicon guided-wave optical couplers and Mach-Zehnder interferometers

Niculae N. Puscas, Gabriel Nitulescu, Valentin V. Gherman, Adrian Ducariu

University "Politehnica" Bucharest, Physics Dept., Splaiul Independentei, 313, 77206, Bucharest,
Romania

ABSTRACT

In this paper we report some experimental results concerning the characterization of the silicon guided-wave optical directional couplers and asymmetrical Mach-Zehnder interferometers from the transmitted spectrum in the 1480 - 1620 nm wavelength region.

The experimental results were used for the evaluation of several parameters which define the above mentioned devices, like: the power coupling ratio, the perfect coupling length, the effective interaction length increment and the effective refractive indices, respectively.

First, the experimental data were smoothed and fitted by a fourth order function in the case of waveguide directional couplers and a cosine type function in the case of asymmetrical Mach-Zehnder interferometers, respectively. Then, the evaluation of the above mentioned parameters was performed using the least-square method.

KEYWORDS

silicon waveguide Mach-Zehnder interferometers, power coupling ratio, interaction length

1. INTRODUCTION

The directional coupler is one of the most fundamental element in guided devices. Employing the guided-wave optical directional couplers and Mach-Zehnder interferometers precise data on the coupling characteristics are absolutely necessary to design guided-wave devices, e. g., optical taps, star couplers, wavelength multi/demultiplexers, waveguide light switches/modulators and also in fiber optic and integrated optic technology. In the last years several experimental and theoretical analyses concerning the above mentioned devices were reported^{1,2,3,4}.

Silica-based single-mode waveguides have low propagation losses and also extremely low fiber coupling losses due to the compatibility with single-mode optical fibers. Therefore, silica-based waveguides may be used in various low-loss guided-wave devices for single-mode optical fiber transmission systems or fiber sensor systems.

In this paper we report some theoretical and experimental results concerning the characterization of the silicon guided-wave optical directional couplers with different interaction lengths and asymmetrical Mach-Zehnder interferometers from the transmitted spectrum in the 1480 - 1620 nm wavelength region by using a laser amplifier as a signal source⁵. The evaluation of some parameters which define the above mentioned devices (e. g. the power coupling ratio, the perfect coupling length, the effective interaction length increment and the effective refractive indices, respectively) was performed using the least-square method.

In Sec. 2 we outlined some theoretical considerations concerning the guided-wave optical couplers and asymmetrical Mach-Zehnder interferometers while in Sec. 3 we described the experimental setup used for the measurement of the transmitted spectrum of the above mentioned devices. Sec. 4 is dedicated to the discussion of the obtained results.

2. THEORY

Fig. 1 shows the configuration of the directional couplers investigated, in which the two waveguides were separated by $250 \mu\text{m}$ at the input and output ends using *S*-curved waveguides. The waveguides separation, s , is $50 \mu\text{m}$ and the radius of curvature $50 \mu\text{m}$.

In order to evaluate some parameters which characterize the above mentioned devices, like: the power coupling ratio, the interaction length and the effective interaction length increment the light intensities, I_1, I_2 , from the two output ports were measured on directional couplers with different waveguide and directional parameters: the interaction length, l , radius of curvature, R , waveguides separation, s .

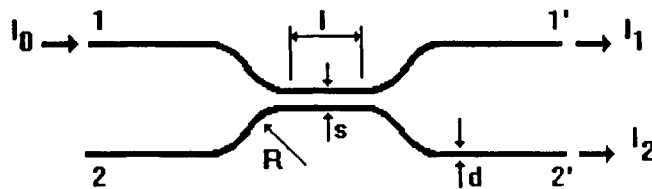


Fig. 1. The configuration of the directional coupler

Taking into account the transmitted light intensities I_1, I_2 from the two output ports of the device the power coupling ratio can be expressed by²:

$$\eta = \frac{I_2}{I_1 + I_2} = \sin^2\left(\frac{\pi l}{2L}\right) \quad (1)$$

where L is the perfect coupling length and l the interaction length.

In the case of the directional coupler structure presented in Fig. 1, the interaction at the *S*-curved waveguides is not negligible and therefore Eq. (1) should be replaced by:

$$\eta = \sin^2\left(\frac{\pi l + \Delta l}{2L}\right) \quad (2)$$

where Δl is the effective interaction length increment due to the *S*-curved waveguides.

In our study we used also the asymmetrical Mach-Zehnder interferometer characterized by two different arm lengths linked by two directional couplers, (ΔL being the difference length), as shown in Fig. 2.

In the above mentioned interferometer (having the length $L = 260 \mu\text{m}$), when the power coupling ratio of each directional coupler is k and the phase shift $\Delta\phi$, the two output powers can be expressed by the following equations:

$$\frac{I_1}{I_0} = (1 - 2k)^2 \cos^2(\Delta\phi / 2) + \sin^2(\Delta\phi / 2) \quad (3)$$

$$\frac{I_2}{I_0} = 4k(1 - k) \cos^2(\Delta\phi / 2). \quad (4)$$

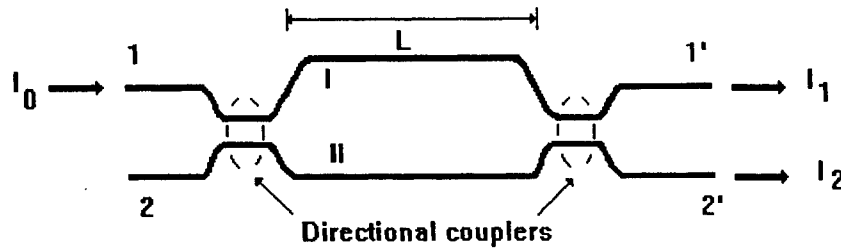


Fig. 2. The schematic representation of the asymmetrical Mach-Zehnder interferometer

If $k = 1/2$ the directional couplers are 3-dB couplers and the interferometer acts as an ideal optical switch with an infinitive extinction ratio.

The transmittance from port 1 to 1' can be expressed by the following equations:

$$T_i = \sin^2(Kv) \quad (5)$$

$$T_c = \cos^2(Kv) \quad (6)$$

where $K = \frac{\pi n \Delta L}{c}$, n is the refractive index of the waveguide, c is the light velocity in vacuum, v is the optical frequency of the coupled light wave and ΔL is the difference length between the two waveguide arms.

When multiplexed lightwaves with optical frequencies of v_1 and v_2 which satisfy $Kv_1 = (m + 1/2)\pi$ and $Kv_2 = m\pi$, (m being integer), are coupled to port 1, $T_i = 1$ for v_1 and $T_c = 1$ for v_2 . The frequency spacing $\Delta v = v_1 - v_2$ between the maximum and minimum of the transmission curve is $\frac{\pi}{2K} = \frac{c}{2n\Delta L}$.

3. EXPERIMENTAL SETUP

The experimental arrangement is shown schematically in Fig. 3⁵. We used a He - Ne laser ($\lambda = 0.63 \mu\text{m}$) for alignment and an optical amplifier (O. A.) in the range 1480 - 1620 nm for the optical signal, coupled together by a 3 dB coupler (C). The transmitted spectra of some silicon optical guided-wave directional couplers (D. C.) having different interaction lengths and asymmetrical Mach-Zehnder interferometers (M-Z) have been measured using an optical spectrum analyser (O. S. A.) and registered

by a computer (CO). The displacement of the above mentioned devices mounted on a support was obtained with an electrostrictive actuator controller. The TE and TM polarizations of the lightwave were selected by the polarization controller (P) and the isolator (I).

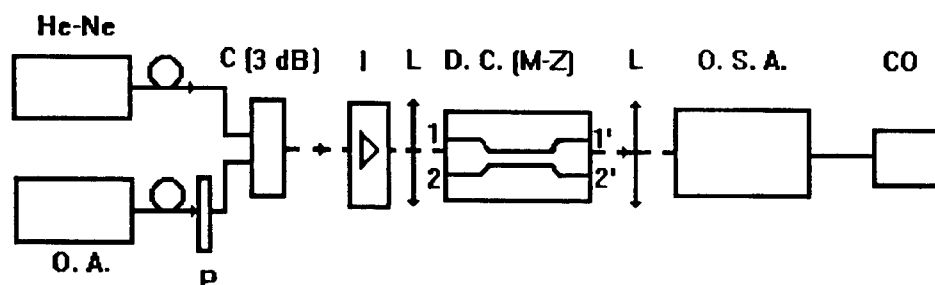


Fig. 3. Schematical experimental setup

The transmitted spectrum TE polarized of a silicon optical guided-wave directional coupler having 2000 μm interaction length, for the ports $1 \rightarrow 1'$ (Fig. 1), in the optical range 1480 - 1620 nm is presented in Fig. 4.

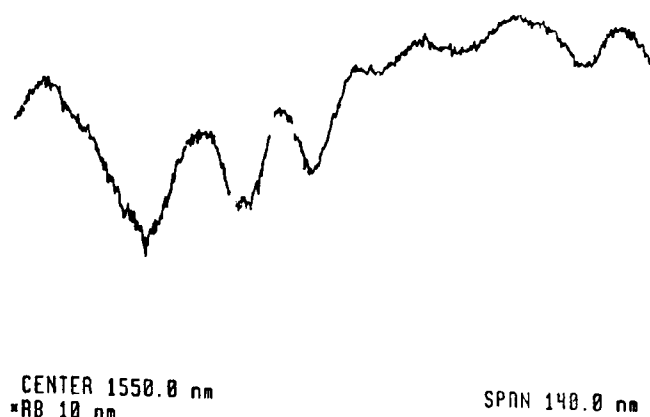


Fig. 4. The transmitted spectrum of the optical guided-wave directional coupler

In Fig. 5 we present the transmitted spectrum for the ports $1 \rightarrow 1'$ (Fig. 2) of the asymmetrical Mach-Zehnder interferometer having the difference length $\Delta L = 29.2 \mu\text{m}$, in the range 1.46 - 1.58 μm .

4. DISCUSSION OF THE RESULTS

We used the experimental data for the evaluation of some parameters which characterize the above mentioned devices.

For the guided-wave optical directional couplers, in the first step, the experimental data were smoothed and fitted by a fourth order function. Then, the evaluation of the perfect coupling length, L , and the effective interaction length increment, Δl , was performed from the dependence of the power coupling ratio, η , on the interaction length, l , using the least-square method². In the case of a radiation having 1530 nm we obtained the following values: $\eta = 0.5285$, $L = 9.99 \mu\text{m}$ and $\Delta l = 9.29 \text{ nm}$.

The experimental transmitted spectrum of the asymmetrical Mach-Zehnder interferometer was fitted by a function of the type:

$$F(i, m, n, p, q) = p \cdot \cos^2(m \cdot \lambda_i + n) + q \quad (7)$$

where i is an integer and m, n, p, q are parameters which determine the best fit.

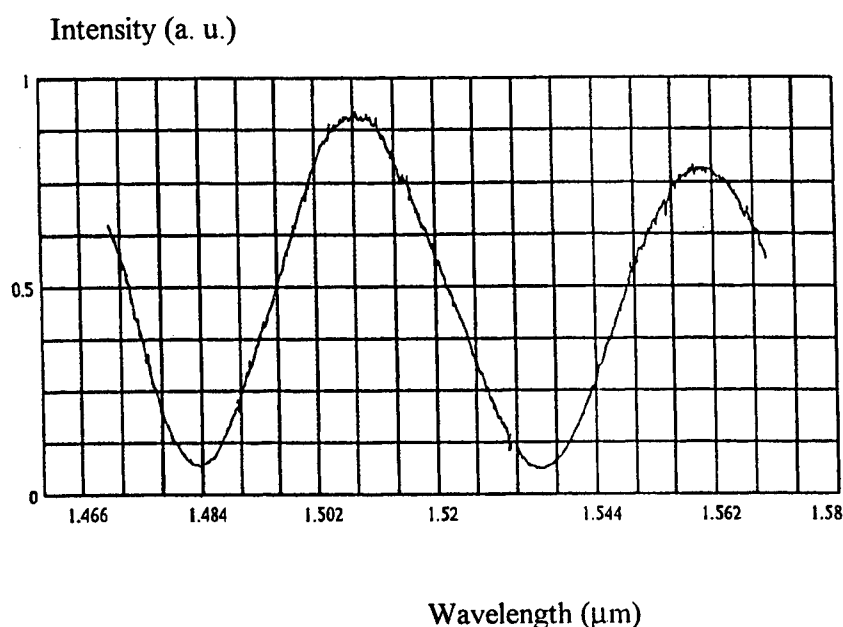


Fig. 5. The transmitted spectrum of the asymmetrical Mach-Zehnder interferometer

After the differentiation of Eq. 7 we have determined the values of the minimum wavelengths of the device $\lambda_1 = 1.48331 \mu\text{m}$ and $\lambda_2 = 1.53549 \mu\text{m}$ and the corresponding effective refractive indices, respectively, $n_{\text{eff}1} = 1.4478$ and $n_{\text{eff}2} = 1.4462$.

5. CONCLUSIONS

Based on the experimental transmitted spectrum in the 1480 - 1620 nm wavelength region for silicon guided-wave optical directional couplers and asymmetrical Mach-Zehnder interferometers in this paper we report the evaluation of some parameters which characterize the above mentioned devices, like: the power coupling ratio, the perfect coupling length, the effective interaction length increment and the effective refractive indices, respectively.

The obtained results can be used in the design of the symmetrical and asymmetrical Mach-Zehnder interferometers which can be applied to a multi/demultiplexer with several gigahertz channel spacing for optical frequency-division-multiplexing transmission systems.

6. ACKNOWLEDGEMENTS

This research was partially performed under contract ERBIC 15 CT 960820 of the European Comission.

7. REFERENCES

1. M. Kawachi, "Silica waveguides on silicon and their applications to integrated-optic components," *Optical and Quantum Electronics*, **22**, 391-416, (1990).
2. N. Takato, K. Jinguji, M. Yasu, H. Toba, and M. Kawachi, "Silica-Based Single-Mode Waveguide on Silicon and their Application to Guided-Wave Optical Interferometers," *J. Light. Technol.* **2** (6), 1003-1010, (1988).
3. H. Porte, J.-P. Goedgebauer, W. Elflein, A. Terras, F. Ledeventec, and N. Butterlin, "Linear Phase Tracking in a Coherence Modulation Electrical Sensor System Using Integrated LiNbO₃ Modulator/Demodulator," *IEEE J. of Selected Topics in Quantum. Electron.* **2** (2), 1-7, (1996).
4. B. Wacogne, M. D. Jackson, N. E. Fisher, A. Podoleanu and D. A. Jackson, "Double Security Level in a Telecommunication System Based on Phase Coding and False Data Transmission," *J. Light. Technol.* **14** (10), 665-670, (1996).
5. N. N. Puscas, D. M. Grobnic, I. M. Popescu, M. Guidi, D. Scarano, G. Perrone, and I. Montrosset, "Characterization of the Er³⁺-doped Ti : LiNbO₃ waveguides: losses, absorption spectra and near field measurements" *Optical Engineering*, **1685**, 1311-1318, (1996).

Holographic interferometry study of interphase mass transfer

Levai Stefan, University of Bucharest-Faculty of Physics

Anicuta Guzun-Stoica, "Polytechnica" University-Bucharest

Mona Kurzeluk, Technical University of Civil Engineering, B-dul Lacul Tei 124, sect. 2., Bucharest-Romania

ABSTRACT

Interfacial turbulence is investigated experimentally by microscope observations and holographic interferometry with double exposure for the system glycerol-acetic acid-n-butyl-acetate. This system exhibits organised interfacial activity upon transfer of acetic acid from glycerol phase to acetate phase. This behaviour was confirmed by the microscope observations in transmitted light. For the holograms obtained the deviation of the fringes between the two exposure times can be related with the changes in the concentration profiles near the interface. Because of the complexity of the phenomenon investigated, the present study is only qualitatively.

Keywords: holographic interferometry, interfacial turbulence.

1. INTRODUCTION

The powerful technique of holographic interferometry has been used in chemical engineering for the accurate measurement of diffusion coefficients^{1,2,3} and for the determination of local mass-transfer⁵ and heat transfer coefficients.⁶

The presence of interfacial turbulence in liquid-liquid systems in which mass transfer is accompanied or not by chemical reaction is a widely studied phenomenon^{7,8,9} and has both scientific interest and practical applications of industrial importance such as the enhancement recovery of crude oil¹⁰ and of metal extraction processes.¹¹ Several optical techniques have been used to investigate the interfacial instability. Observation on cellular convection in systems in which interfacial turbulence occurs were made using: Schlieren optical system^{12,13}, laser-activated photochromic tracer techniques¹⁴, microscopic observations in reflected or transmitted light¹⁰ or microinterferometric and Mach-Zender interferometric methods.¹⁵

The aim of this paper is to extend the applications of holographic interferometry to the study of interfacial turbulence in the system glycerol-acetic acid-n-butylacetate. When interfacial cellular convection accompanying mass transfer occurs the interface becomes unstable and the concentration profile near the interface is altered so that fringes are deviated by modification of refractive ratio. Qualitative observations were also made by microscope in transmitted light for the same system.

2. EXPERIMENTAL TECHNIQUES

The microscope observations of the interfacial instability were made in transmitted light with a NU-2 (Carl-Zeiss Jena) microscope, because the two liquid phases are transparent.

For the holographic experiment with double exposure the optical set-up is illustrated in figure 1. The laser beam (6mW helium-neon) is split by a beam splitter to give a satisfactory ratio of beams intensities. The object beam is passed through a microscope objective and a 20 μm pinhole. The second beam serves as the references beam and illuminates the whole area of the holographic plate. The diffusion cell measured 1cm X 1 cm X 10 cm with glass plates on the two sides to allow the laser light to pass through. The cell was filled through a capillary tube from the bottom to minimise turbulence and mixing. The lighter liquid was put into the cell first. Next, the more dense liquid was admitted slowly from below lifting the first liquid.

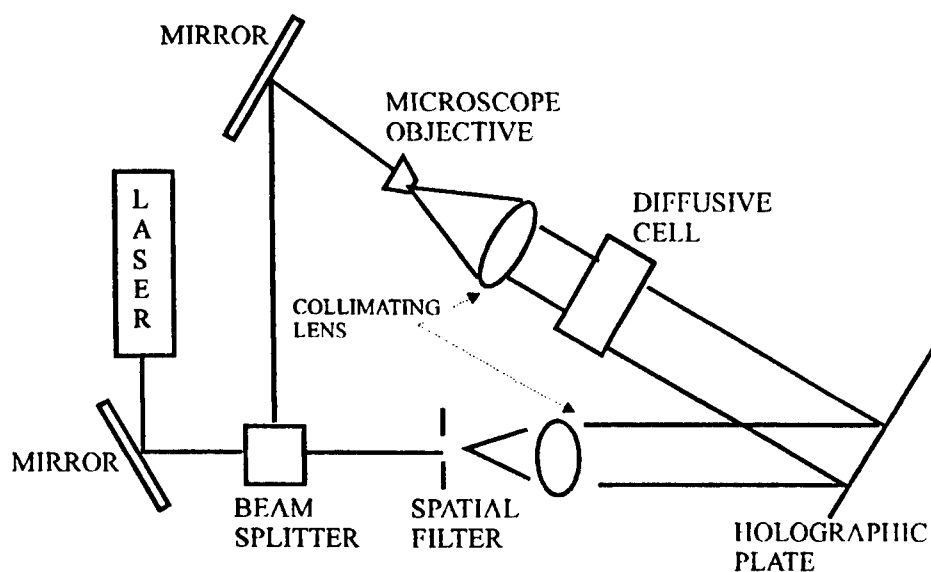


Figure 1 Apparatus for holographic interferometry

3. RESULTS

3.1 Microscope observation on cellular convection

When glycerol containing acetic acid in contact with *n*-butylacetate the interface becomes instantaneously unstable. In figure 2 is presented a photograph in which are visible the regions in the vicinity of the interface with an incipient cellular organisation.



Figure 2 Interfacial turbulence in the system glycerol - acetic acid - *n* butylacetate

The system glycerol- acetic acid -*n*-butylacetate exhibits organised interfacial activity upon transfer of acetic acid from the glycerol phase to the acetate phase. The concentration of acetic acid necessary to observe cellular activity was found to lie between 0.05 and 0.1 wt %. In our experiments we used a 10% wt acetic acid in glycerol. For this concentration Orell and Westwater¹² reported unusually large cells which propagate at relatively low speeds. In figure 3 are presented images of the deformation of the interface as waves which propagate at low speed.



Figure 3 Deformations of the interface in the system glycerol - acetic acid - n butylacetate

3.2 Double exposure holographic interferometry

Holographic interferometry with double exposure compares beams of laser light which have passed through the cell at times t_1 and t_2 . In figure 4 are presented two interferograms obtained for the system glycerol- acetic acid-n-butylacetate system at two different times. In the image is visible the interface formed between n-butylacetate and glycerol containing acetic acid. To observe better the changes in the studied system the vertical fringes were induced by a small rotation of the diffusion cell. Any deviation of the vertical fringes between the two exposure times is due to the modification of the refraction index which can be related with the changes in the concentration profile. In the studied case the overall mass transport is controlled by diffusion and convection due to interfacial turbulence.

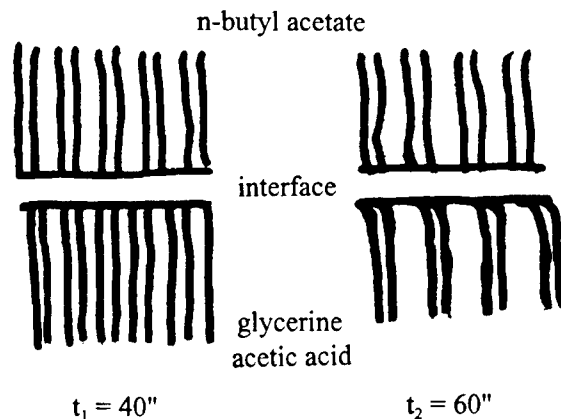


Figure 4 Interference fringes for the system glycerine - acetic acid - n-butylacetate at different times

The fringe shift depends on the change in the refractive index of the two phases near the interface and therefore depends upon mass transport of all species in the system. Because of the complexity of the phenomenon investigated, our observations are only qualitatively.

4. CONCLUSIONS

The main aim of this paper was to extend the holographic interferometry technique for the study of interfacial turbulence in a liquid-liquid system. Microscope observations for the same system glycerol-acetic acid-n-butylacetate were arguments to demonstrate the instability of the interface for a certain value of the acetic acid concentration in glycerol. The fringe shifts observed in the interferograms can be related with the change in the refractive index of the solutions brought into contact but doesn't allow us to determine quantitatively the intensity of the phenomenon. The results can be easily improved in accuracy. However, the present method is quicker and considerably simpler than other optical methods which have been used in interfacial turbulence studies.

5. REFERENCES

1. N.Bochner and J. Pipman, " A simple method of determining diffusion constants by holographic interferometry ", J. Phys. D: Appl. Phys., 9, 1825-1830 (1976).
2. L. Gabelmann-Gray and H. Fenichel, " Holographic interferometry study of liquid diffusion ", Appl. Optics, 18 (3), 343-345 (1979).
3. F.Ruiz-Bevia, J. Fernandez-Sempere and N. Boluda- Botella, " Variation of phosphoric acid diffusion coefficient with concentration", AIChE J., 41(1), 185-189 (1995).
4. T.F. Kosar and R.J. Phillips, " Measurement of protein diffusion in dextrane solution by holographic interferometry ", AIChE J., 41(3), 701-711 (1995).
5. D. N. Kapur and N. Macleod, " The determination of local mass-transfer coefficients by holographic interferometry-I General principles: their application and verification for mass-transfer measurements at a flat plate exposed to a laminar round air-jet ", Int. J. Heat Mass Transfer, 17 (10), 1151-1162 (1994).
6. T.M.Liou and W.B.Wang, Laser holographic interferometry study of developing heat transfer in a duct with a detached rib array", Int. j. Heat Mass Transfer, 38(1), 91-100 (1995).

7. A. Sanfeld and A. Steinchen, "Motion induced by surface- chemical and electrochemical kinetics", Faraday Discuss. Chem. Soc., 77, 169-179(1984).
8. H. Linde, "Time dependent behaviour and regularity of dissipative structures of interfacial dynamic instabilities", Faraday Discuss. Chem. Soc., 77, 181-188, (1984).
9. A. A. Golovin, "Mass transfer under interfacial turbulence: Kinetic regularities", Chem. Engng. Sci., 47 (8), 2069-2080 (1992).
10. J. Rudin and D. T. Wasan, "Interfacial turbulence and spontaneous emulsification in alkali-acidic oil system", Chem. Engng. Sci., 48(12), 2225-2238 (1993).
11. M. A. Mendes-Tassis and E. S. Perez de Ortiz, "Marangoni instabilities in systems with an interfacial chemical reaction", Chem. Engng. Sci., 51(15), 3755-3761 (1996).
12. A. Orell and J. W. Westwater, "Spontaneous interfacial cellular convection accompanying mass transfer: ethylene glycol-acetic acid-ethylacetate", AIChE J., 8(3), 350-356 (1962).
13. C. A. P. Bakker, P. M. van Buytenen and W. J. Beek, "Interfacial phenomena and mass transfer", Chem. Engng. Sci., 21, 1039-1046 (1966).
14. J. D. Thornton, T. J. Anderson, K. H. Javed and S. K. Achwal, "Surface phenomena and mass transfer interactions in liquid-liquid systems", AIChE J., 31(7), 1069-1075 (1985).
15. Y. Nakaike, Y. Tadenuma, T. Sato and K. Fujinawa, "An optical study of interfacial turbulence in a liquid-liquid system, Int. J. Heat Mass Transfer, 14, 1951-1961 (1971).

Nonlinear processes in Laser radiation absorption on metallic surfaces

M. Ursache, V. Calian, M. Socaciu, C. Sarpe-Tudoran

University of Craiova, Department of Physics, 13 A.I.Cuza, Craiova - 1100, Romania
email: violeta@oltenia.ro

ABSTRACT

We performed both experimental and theoretical studies on the laser radiation absorption coefficient of a Copper surface. A theoretical model for the computation of the absorption coefficient was elaborated for two-layer case (metal-oxide), taking into account the nonlinear processes which govern the dynamics of the temperature and of the widths of the layers. The experimental data and the simulation results proved to be in a very good agreement.

Keywords: nonlinear process, laser radiation, absorption coefficient, multiple layer metallic structure.

1. INTRODUCTION

During the heterogeneous chemical reactions stimulating obtained by laser induced heating of a studied substance some thermo - chemical instabilities occur, leading to interference oscillations of the laser radiation absorption coefficient of the metal.

The heating rate of the metal surface strongly depends on the incidence angle of the laser beam on the surface, the laser radiation wavelength, the gaseous medium where the irradiation is performed.

Therefore the possibility of optimum monitoring for these reactions appears by appropriate changing of the laser radiation parameters.

Solving the highly important problem of minimizing the heating expenses is thus made possible for the cases which requires heating of the metal up to a certain temperature, measuring the efficiency of obtaining certain chemical components.

The strong changing of the absorption coefficient may be induced either by the appearance of oxide layers on the metallic surface or by some different type processes.

The laser radiation interaction with the surface is controlled by monitoring the occurrence of the superficial metallic oxides compounds.

2. THEORETICAL MODEL

The laser radiation absorption coefficient of the metallic surface is written ¹ for the case of a system made by (N-1) oxide layers on the metal surface, in oxidant atmosphere, as follows:

$$A(x_1, x_2, \dots, x_{N-1}) = \frac{A_0}{\left[1 + \frac{1}{4} \left(\sum_{j=1}^{N-1} \beta_j x_j / n_j \right)^2 - \frac{1}{4} \left(\sum_{j=1}^{N-1} \beta_j x_j \right)^2 \right]} \quad (1)$$

Here x_j is the width of the j-th oxide layer, $\beta_j = \frac{4\pi}{\lambda} n_j$, n_j is the refraction index of the "j" oxide and A_0 is the laser radiation absorption coefficient of the un-oxidized metallic surface, experimentally determined at the beginning of the measuring processes. It strongly depends on the metallic surface condition.

A rigorous computation of the coefficient "A", for the two oxide cases, had given the following expression:

$$A = \frac{1}{D_1^2 + D_2^2} \left\{ n_1^2 A_0 + 2\kappa_1 K \left[\beta_1 x_1 - \left(K - \sin^2(\beta_2 x_2/2) \right) \sin(\beta_1 x_1) / K \right] + C_1 \right\} \quad (2)$$

where:

$$K = 1 - \left(1 - \frac{n_1^2}{n_2^2} \right) \sin^2(\beta_2 x_2/2) \quad (3)$$

$$C_1 = 2\kappa_2 \left(\frac{n_1}{n_2} \right)^2 \left[\beta_2 x_2 - \left(1 - 2 \frac{\kappa_1 n_2}{\kappa_2 n_1} \sin^2(\beta_1 x_1/2) \right) \sin \beta_2 x_2 \right] \quad (4)$$

$$D_1 = \frac{n_1}{n_2} \sin\left(\frac{\beta_2 x_2}{2}\right) \cos\left(\frac{\beta_1 x_1}{2}\right) + \sin\left(\frac{\beta_1 x_1}{2}\right) \cos\left(\frac{\beta_2 x_2}{2}\right) \quad (5)$$

$$D_2 = n_1 \left(\cos \frac{\beta_2 x_2}{2} \cos \frac{\beta_1 x_1}{2} - \frac{n_1}{n_2} \sin \frac{\beta_2 x_2}{2} \sin \frac{\beta_1 x_1}{2} \right) \quad (6)$$

However, for a laser radiation having $\lambda = 10.6 \mu\text{m}$, we have $\beta_j x_j$ and $\beta_j x_j / n_j \ll 1$, therefore a series expansion is made possible in the expression (1). Using a Cu sample which may have a CuO and CuO₂ oxide layer system, the absorption coefficient becomes²:

$$A(x_1, x_2) = A_0 + \frac{A_0}{4} \left\{ (\beta_1 x_1 + \beta_2 x_2)^2 - (\beta_1 x_1 / n_1 + \beta_2 x_2 / n_2)^2 \right\} \quad (7)$$

The dynamics of the changing in the oxide layers widths is described by the Wagner - Valensi system of equations:

$$\frac{dx_1}{dt} = 2 \cdot \frac{d_1(T)}{x_1} - \frac{d_2(T)}{x_2} \mu \quad (8)$$

$$\frac{dx_2}{dt} = \frac{d_2(T)}{x_2} - \frac{1}{\mu} \cdot \frac{d_1(T)}{x_1} \quad (9)$$

where $\mu = V_1/V_2$ is the ratio of the specific volumes of the two oxides; $d_1(T)$ and $d_2(T)$ are the oxidation "constants" for the two layers having the following temperature dependence which is valid up to the melting temperature of the metal:

$$d_1(T) = d_{10} \exp(-T_{D1}/T) \quad (10a)$$

$$d_2(T) = d_{20} \exp(-T_{D2}/T) \quad (10b)$$

The dynamics of the target temperature changing as a result of the laser irradiation process is described by the equation:

$$\frac{dT}{dt} = \frac{1}{mc} [P \cdot A(x_1, x_2) - P_p] \quad (11)$$

where

$$P_p = S\eta \cdot (T - T_0) + S \cdot \sigma \cdot \sigma_0 \cdot (T^4 - T_0^4) \quad (12)$$

is the power corresponding to convection and radiation losses. S is the total surface, η - the heat transfer coefficient for the convection processes, a characteristic of the experiment. σ - the Boltzmann constant and $\bar{\sigma}_0$ the target emissivity.

We used the following values of the above mentioned parameters:

$$\begin{aligned} A_0 &= 0.015 ; \eta = 14 ; \sigma = 5.66978 \cdot 10^{-8} \text{ W/m}^2 \text{ K}^4 ; m = 80 \cdot 10^{-6} \text{ Kg} ; S = 0.25 \cdot 10^{-4} \text{ m}^2 ; \\ d_{10} &= 10^{-6} \text{ m}^2/\text{s} ; d_{20} = 4 \cdot 10^{-3} \text{ m}^2/\text{s} ; \\ T_{D1} &= 15500 \text{ K} ; T_{D2} = 19900 \text{ K} ; \\ T(t=0) &= 293 \text{ K} ; c(t=0) = 382 \text{ J/kgK} ; \\ x_1(t=0) &= 10^{-11} \text{ m} ; x_2(t=0) = 10^{-11} \text{ m} ; \\ n_1 &= 2.57 ; n_2 = 1.5 . \end{aligned}$$

3. EXPERIMENTAL STUDY AND SIMULATIONS

The samples were irradiated in air by a CO_2 laser having $\lambda = 10.6 \mu\text{m}$ and $P=30\text{W}$, in normal temperature (T_0) and pressure conditions.

The dimensions of the Cu targets were chosen such as to assure the thermal homogeneity.

The target temperature changing in time was recorded using a chromel-alumel thermocouple and a multiple-channel oscilloscope. The input of the oscilloscope received simultaneously the amplified dT/dt signal.

At heating, the signal $(dT/dt)_+$ is given by:

$$\left(\frac{dT}{dt}\right)_+ = \frac{1}{mc} (AP - P_p^+) \quad (13)$$

where P_p^+ is the power loss during the irradiation process.

At target cooling, after the irradiation, the signal $(dT/dt)_-$ is equal to:

$$\left(\frac{dT}{dt}\right)_- = -\frac{P_p^-}{mc} \quad (14)$$

The surface conditions at heating and cooling respectively are different, therefore the values P_p^+, P_p^- are also different for the same sample temperature. This is a measure of the measuring error for the absorption coefficient itself.

If we use the two signals $(dT/dt)_+, (dT/dt)_-$ at the same value of the temperature T_i , we obtain the following expression for the experimental absorption coefficient:

$$A(T_i) = \frac{mc}{P} \left[\left(\frac{dT}{dt}\right)_+ - \left(\frac{dT}{dt}\right)_- \right]_{T_i} \quad (15)$$

Using these signals, the $T(t)$, $A(t)$ and $A(T)$ dependencies were experimentally obtained.

Recording $T(t)$ and $dT/dt=f(t)$ after the end of the target irradiation process we had the possibility to control the heat losses by radiation and convection, thus to control the $P_p=P_p(t)$ and $P_p=P_p(T)$ dependencies.

The emissivity coefficient was supposed to be the one which corresponds to the polished Cu surface at the beginning of the irradiation process ($\bar{\sigma}_0 = 0.018$). During the heating and oxidizing process the $\bar{\sigma}_0$ coefficient was changed progressively up to a 0.78 value which corresponds to the copper oxide.

Solving the differential equations system formed by (8), (9), (11) and using the expressions (7), (10), (12), the numerical solutions for $A(t)$, $T(t)$, $x_1(t)$ and $x_2(t)$ were obtained.

The initial conditions $(T(0), x_1(0), x_2(0))$ were given by the experimental conditions (the copper surface is not oxidized at $t=0$) and we also had taken into account the specific heat dependence on the temperature, $c(T)$, during the $T(t)$ -evolution.

The main innovative parts of our work consist of modelling the absorption coefficient A (see equation (1), given by one of the authors for a simpler case in¹), solving the coupled equation system corresponding to the two oxide layers and changing continuously the emissivity coefficient during the time evolution.

Our theoretical model is valid up to $T_{\max} = 981.56\text{K}$, when $x_1 = 3.6 \cdot 10^{-7}\text{m}$, $x_2 = 42.5 \cdot 10^{-7}\text{m}$ and $A = 0.181319$. For $T > T_{\max}$ the analysis should be modified due to the interference phenomena which appear on the oxide layers.

In Fig.1, the dependencies $A(T)$ are obtained from experimental data (C-curve) and theoretical simulation (A-curve) respectively.

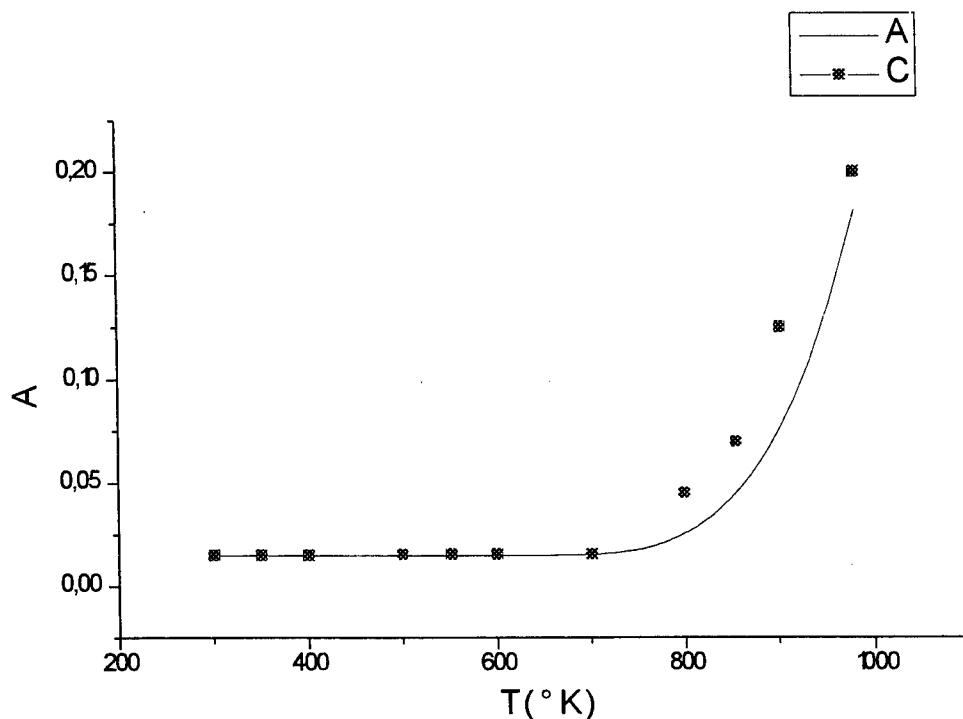


Fig.1

Theoretical (A) and experimental (C) curves for the absorption coefficient dependence on temperature.

For the studied domain the comparison gives us a very good agreement between theory and experiments thus concluding that the proposed model for the absorption coefficient was correctly formulated.

4. REFERENCES

- [1] M. Tutunaru, D. Tatar, I.N. Mihailescu, *Optica Applicata*, Vol.XVI, No. 3, 1986, 209-214
- [2] M. Tutunaru, L. Tatar, I.N. Mihailescu, *Optica Acta*, 1986, vol.33, No. 3, 339-345
- [3] G. Kinsman, W.W. Duley, (1990) *Appl. Phys. Lett.*, Vol. 56, 996

Construction of the first-order stochastic non-linear differential equations in the modelling of the stimulated scattering of optical fields

V. Babin, Maria Grigore, L. Cojocaru, S. Ersen, A. Moldovan
National Institute of Optoelectronics, 1 Atomistilor St, P.O. Box MG-22, 76900 Bucharest, Romania

ABSTRACT

In this work we use a technique inspired by the inverse problem in the scattering theory, that is, the calculation of partial derivatives along the characteristic directions of the D'Alembert solution of the wave equation (Maxwell and Euler). In this way, we construct a system of stochastic non-linear differential equations. The analysis of this system, using algebraic invariants, gives more information in comparison with that given by Ghelfand - Levitan - Marcenko, in the inverse problem in the scattering theory.

Keywords: stimulated light scattering, three-wave resonant interaction, general D'Alembert solution of the nonlinear wave equation, polistochastic process, turbulent media

1. INTRODUCTION

In this work we propose a different approach to the inverse problem in the scattering theory. Instead of solving the Ghelfand - Levitan - Marcenko integral equation, after the calculation of the partial derivatives along the characteristic directions of the general solution of the D'Alembert equation, we obtain a system of stochastic non-linear differential equations, that describes the interaction of the waves involved in the scattering process.

2. THEORY

The scattering of the optical field on acoustic waves had been studied by L. Brillouin¹. The induced scattering process (Mandelstam - Brillouin) was discovered in 1964². Under the irradiation of a crystal (sapphire or quartz in the first experiment) with a strong laser beam with frequency (ω_L), an acoustic field and an optical (scattered) field were generated in the crystal with frequencies ω , $\omega_S = \omega_L - \omega$, respectively.

Both the acoustic and the scattered optical fields propagate on rigorous directions and they exist only when the power of the laser beam exceeds a certain threshold value. The electrical field of the laser radiation incident on the crystal (liquid) induces an alternative variation of the density, as a result of electrostriction, i.e. an acoustic field. The acoustic field modulates the dielectric permittivity of the medium allowing the energy exchange between the two optical fields (the incident laser field and scattered optical field).

The phenomenological dynamics of a stimulated Brillouin scattering (SBS) process may be described in the following way³:

$$\frac{\partial N_S}{\partial t} = A \cdot N_L (N_S + 1) \quad (1)$$

where: N_L is the number of incident photons, N_S is the number of scattered photons; A is "the coupling constant" that defines the magnitude of the scattering process. For $N_L \sim \text{constant}$, the equation (1) becomes linear with the following type of solution:

$$N_S(t) = [N_S(0) + 1] \cdot \exp[A \cdot N_L \cdot t] - 1 \quad (2)$$

where

$$A \cdot N_L \approx g' I_L \cdot v_{LS} \quad (3)$$

Here I_L is the intensity of the incident optical field, g' is the gain of the stimulated diffusion process and v_{LS} is the propagation velocity on the space-time characteristics of the induced scattering process.

Using the wave equation for the electric field intensity (E):

$$\left(\frac{n}{c}\right)^2 \frac{\partial^2 E(z,t)}{\partial t^2} - \frac{\partial^2 E(z,t)}{\partial z^2} = -\frac{n}{c} \cdot \frac{\partial}{\partial t} \left[\alpha \cdot E(z,t) + \frac{4\pi}{nc} \frac{\partial P^{NL}(z,t)}{\partial t} \right] \quad (4)$$

with the Cauchy problem:

$$\begin{aligned} E(z,t) \Big|_{t=0} &= \varphi(z) = 0 \\ \frac{\partial E(z,t)}{\partial t} \Big|_{t=0} &= \psi(z) = 0 \end{aligned} \quad (5)$$

the D'Alembert general solution of (1) becomes:

$$E(z,t) = \frac{c}{2n} \int_0^t d\tau \int_{z-\frac{c}{n}(t-\tau)}^{z+\frac{c}{n}(t-\tau)} F(\xi, \tau) d\xi \quad (6)$$

Calculating the derivatives of (6) along the characteristic directions:

$$\xi_L = \frac{c}{n} \cdot t + z, \quad \xi_S = \frac{c}{n} \cdot t - z \quad (7)$$

we obtain for the two fields (E_L is the incident field, and E_S is the reflected one (Stokes)) :

$$\begin{aligned} \frac{\partial E_L}{\partial \xi_L} &= -\frac{\alpha}{4} E_L - \frac{\pi}{n^2} \frac{\partial}{\partial \xi_L} P^{NL}(E_L, E_S) \\ \frac{\partial E_S}{\partial \xi_S} &= -\frac{\alpha}{4} E_S - \frac{\pi}{n^2} \frac{\partial}{\partial \xi_S} P^{NL}(E_L, E_S) \end{aligned} \quad (8)$$

where the nonlinear interaction between the two fields is described by the nonlinear polarisation (P^{NL}).

Using the same method, one can derive for the acoustic field:

$$\frac{\partial \rho'}{\partial \xi_{1f}} + \left(\frac{4k\omega}{\Gamma_B} \right) \rho' = \frac{\gamma^e \cdot k^3}{8\pi\rho_0\omega\Gamma_B} (E_L + E_S)^2 \quad (9)$$

where $\rho' = \Delta\rho/\rho_0$ is the perturbation of the normal density of the scattering medium, $\xi_{1f} = (\omega/k) t + z'$, $\Gamma_B = 1/\tau$.

$$\text{Putting: } x = \sqrt{\frac{c \cdot n}{8\pi \cdot I_0}} \cdot E_L, \quad y = \sqrt{\frac{c \cdot n}{8\pi \cdot I_0}} \cdot E_S, \quad z = \frac{\pi \gamma^e}{n^2} \left(\frac{\Delta\rho}{\rho_0} \right); \quad A = \frac{2\omega}{\Gamma_B}; \quad \alpha' = \frac{\alpha}{2K_L} \equiv \frac{\alpha}{2K_S} = \frac{\alpha}{K} \quad (10)$$

where I_0 is the maximum value for the intensity of the optical pump field. yields:

$$\begin{aligned}
\frac{\partial x}{\partial \varphi_L} &= -\frac{\alpha'}{2} \cdot x - \frac{\partial}{\partial \varphi_L} (y \cdot z) \\
\frac{\partial y}{\partial \varphi_S} &= -\frac{\alpha'}{2} \cdot y + \frac{\partial}{\partial \varphi_S} (x \cdot z) \\
\frac{\partial z}{\partial \varphi_f} &= -2 \cdot A \cdot z + \frac{\omega_L^2 \gamma^e \pi v I_0}{c^3 n \rho_0 v \Gamma_B 4 \omega} \cdot x \cdot y;
\end{aligned} \tag{11}$$

We define the SBS gain, the interaction length, and the normalised value of the interaction cross-section in the form:

$$g_B^e \left[\frac{\text{cm}}{\text{W}} \right] = \frac{\omega_L^2 \cdot (\gamma^e)^2}{c^3 n \rho_0 v \Gamma_B}, \quad L_B = 4\pi \cdot \frac{v}{\omega}, \quad \sigma = g_B^e \cdot L_B \cdot I_0 = 4\pi g_B^e \cdot \frac{v}{\omega} \cdot I_0 \tag{12}$$

Eqs. (11) become:

$$\begin{aligned}
\frac{\partial x}{\partial \varphi_L} &= -\frac{\alpha'}{2} \cdot x - \frac{\partial}{\partial \varphi_L} (y \cdot z) \\
\frac{\partial y}{\partial \varphi_S} &= -\frac{\alpha'}{2} \cdot y + \frac{\partial}{\partial \varphi_S} (x \cdot z) \\
\frac{\partial z}{\partial \varphi_f} &= -2 \cdot A \cdot z + \sigma \cdot x \cdot y;
\end{aligned} \tag{13}$$

The analysis of the system (13) using algebraic invariants highlights supplementary properties of the scattering process (isentropic and exponential compression, solitons in the Stokes field, etc.).

The system (13) can be written in the compact form as:

$$\begin{aligned}
\frac{dx^i}{d\xi} &= a_j^i x^j + a_{jk}^i x^j x^k \\
i, j, k &= (1, 2)
\end{aligned} \tag{14}$$

where: $x^i = \{E_L, E_S\}$; $\xi = \{\xi_L, \xi_S\}$.

3. RESULTS

Using the algebraic invariants assigned with the system (14), that were deduced by Arongold and Sibirskii, we can build the geometric equivalence classes of the system (14). In this way, we obtain information regarding the distribution and the nature of the singularities from the phase space (delimitation of isentropic compression areas, areas in which solitons exist, etc.).

We define the initial condition for the system (13) in the following way:

$$\begin{aligned}
x'(\varphi_{L0}) &= \cos(\varphi_{L0}) \\
y'(\varphi_{S0}) &= 0 \\
z(\varphi_{f0}) &= 0
\end{aligned} \tag{15}$$

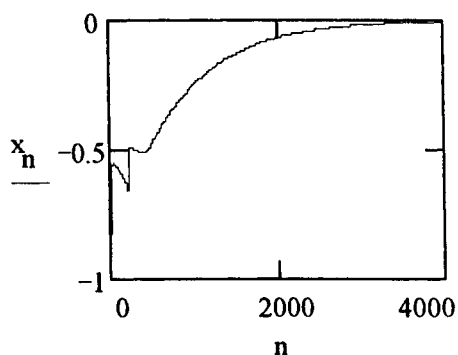


Fig. 1
Amplitude phase dependence of the
pump optical field

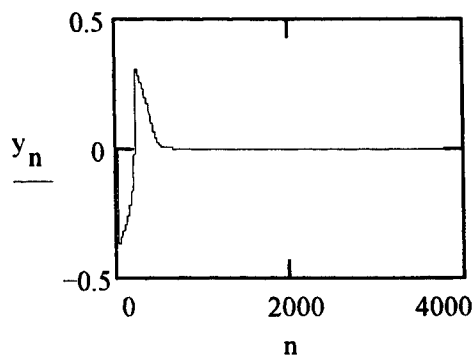


Fig. 2
Amplitude phase dependence of the
scattered optical field

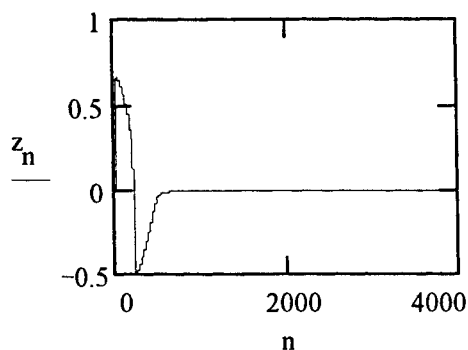


Fig.3
Amplitude phase dependence of the acoustic field

Figures 1- 3 present the evolution of the fields along the characteristics, for an intensity of the pump optical field about ($I_0 \sim 35 \text{ MW/cm}^2$). In this case, one can notice that the oscillation of the three fields does not vanish. This regime takes place in the neighbourhood of the threshold of S.B.S.

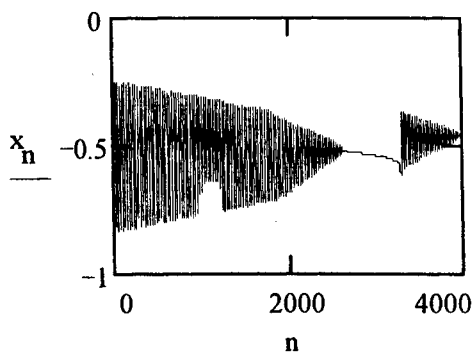


Fig. 4
Amplitude phase dependence of the
pump optical field

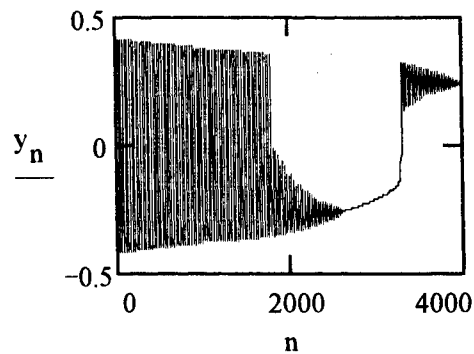


Fig. 5
Amplitude phase dependence of the
scattered optical field

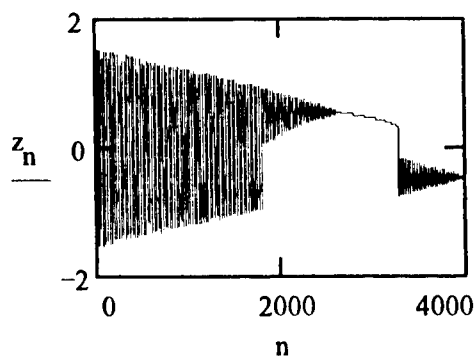


Fig. 6
Amplitude phase dependence of the acoustic field

Figures 4- 6 show the evolution of the three fields along the characteristics for the pump optical field intensity of ($I_0 \sim 150 \text{ MW/cm}^2$). One can notice that the fluctuations affect the oscillation of the three fields. These fluctuations are caused by the big difference between the S.B.S. gain ($\sigma \sim 500$) and the normalised gain of the acoustic field ($A \sim 120$).

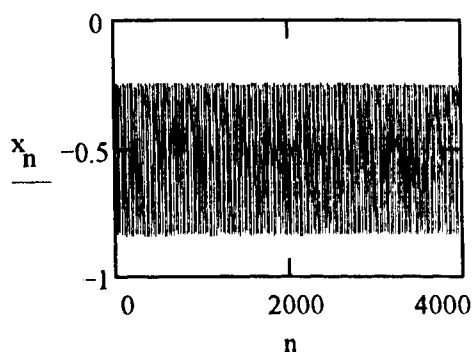


Fig. 7
Amplitude phase dependence of the pump optical field

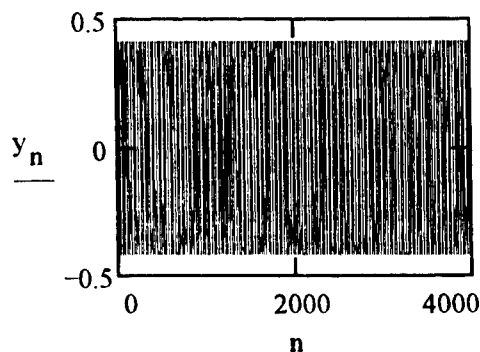


Fig. 8
Amplitude phase dependence of the scattered optical field

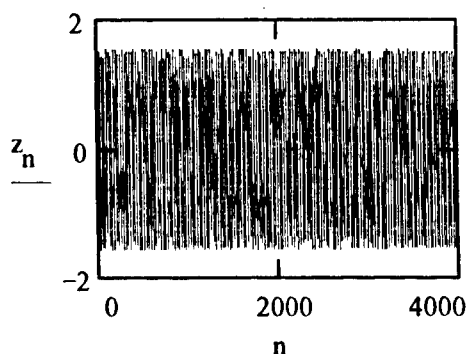


Fig. 9
Amplitude phase dependence of the acoustic field

Figures 7- 9 present the evolution of the three fields along the characteristic directions for the pump optical field intensity of ($I_0 \sim 500 \text{ MW/cm}^2$). One can notice that the oscillating behaviour of the three fields is more homogeneous, the

normalised gain value for S.B.S. ($\sigma \sim 250$) being closer to the normalised gain of the acoustic field ($A \sim 120$). In this case, also, one can notice that fluctuations affect the oscillations of the three fields.

These fluctuations are due, probably, to the poor coherence of the three interacting fields. Figures 1-3 show that the phase correlation between the three fields is good for the phase of the acoustic field (0-200) if we take the coherence time ($\sim \tau$), and the coherence length ($l_c \sim \pi/K$), as defined in the case of the Bragg reflection.

The plots from all figures were obtained by normalising the Eq. 11, using algebraic invariants, as it is shown in ⁴.

4. CONCLUSIONS

In this paper, we used the theory of nonlinear differential equations in order to identify the longitudinal properties of the SBS process. The most important parameter appears to be the interaction length. We developed a polistochastic model for the SBS process, that permitted a complete characterisation of the interaction length, that is a polistochastic probabilistic moment (the spontaneous scattering extinction coefficient). We assumed the absence of dispersion. This presumption permitted the use of characteristic curves and the transforming of the hyperbolic field equations in first order differential equations. In both quasistationary and nonstationary cases, dispersion affects the propagation of the Stokes pulse. The dispersion is induced by the nonlinear effects involved in the SBS process, mainly by the isentropic compression of the nonlinear medium due to the pump optical field.

5. REFERENCES

1. L. Brillouin, *Wave propagation in dielectric structures*, Dover, N.Y., 1953;
2. R. Y. Chiao, C. H. Townes, and B.P. Stoicheff, Stimulated Brillouin scattering and coherent generation of intense hypersonic waves, *Phys. Rev. Lett.*, **12**, 592, 1964;
3. A. Yariv, *Quantum Electronics*, John Wiley and Sons Inc., N.Y., SUA, 1975;
4. V. Babin, *Deterministic and stochastic methods in stimulated Brillouin scattering) and detection of optical radiation*, Ph. D. Thesis, 1997.

SPECTRAL JONES VECTORS AND SPECTRAL COHERENCE MATRICES IN ANALYZING THE MODULATED LIGHT

T. Tudor, I. Vinkler

Faculty of Physics, University of Bucharest, 76900 Bucharest - Magurele
PO Box MG11 ROMANIA

ABSTRACT

In analyzing the polarization spectral structure of the time-varying spinorial fields obtained by light modulation, the notions of spectral Jones vector and spectral coherence matrix are introduced. The KDP longitudinal electrooptic modulator is presented as an example.

Keywords: electro-optic modulator, polarization, coherence

1. INTRODUCTION

One of the most compact description of the states of optical polarization (SOP) of completely polarized light is in terms of Jones vectors¹. As mathematical entities, the Jones vectors are spinors².

The time-varying Jones vectors are often used to describe the output of some lasers^{3,4} or of various modulating devices^{5,6,7,8}, namely when the SOP of this output is a time-varying one. There are also some topics where the spectral structure of such a SOP-time-varying output is touched^{5,6,8,9,10}, with more or less mathematical accuracy.

In fact a time-varying SOP is described by a time-varying Jones vector, by a time-varying spinor, and the spectral analysis of such a SOP reduces to a spinor Fourier analysis. In the following we present such an analysis for the output of one of the most widespread used modulators, that with longitudinal electrooptic effect in crystals of class $\bar{4}2m$ (KDP-like). The notion of *spectral Jones vector* comes naturally to light in such an analysis.

On the other hand, although the Jones vector formalism provides one of the less redundant descriptions of the SOP and of its alteration by interaction of light with optical devices, this description is not yet in terms of optical observables. Measurable entities which describe the SOP are the Stokes vectors¹¹ and the coherence (polarization) matrices¹². Referring only to the completely polarized light, we prefer here the term of polarization matrix instead of coherency matrix. For the SOP description of the modulated light one needs time-varying Stokes vectors, time-varying coherence (polarization) or density matrices.

We apply the Fourier analysis in the field of the time-varying polarization matrices and we introduce the notion of *spectral polarization-matrix*.

For getting a good physical insight into the problem, we present it in the frame of a very concrete situation, namely that of the KDP longitudinal electrooptic modulator.

2. TIME-VARYING JONES VECTORS AND SPECTRAL JONES VECTORS

Let us consider the modulation scheme presented in Fig.1, where K is a KDP longitudinal electro-optic modulator. In the usual arrangement, the incoming light is linearly polarized (OX, Fig.1) at 45° to the electrically induced axes of the crystal (OX', OY') and we are interested in the modulator output polarized parallel or perpendicular to this direction. Therefore it is convenient to do the calculus in the reference system OXY. In this system the operational matrix of the modulator is ⁶:

$$M = \begin{bmatrix} \cos \phi & i \sin \phi \\ i \sin \phi & \cos \phi \end{bmatrix} \quad (1)$$

where 2ϕ is the time-varying phase difference introduced by the modulator between the light components linearly polarized along its induced principal axes. If we apply to the crystal a voltage

$$U = U_0 + U_m \sin \Omega t \quad (2)$$

this phase difference is given by:

$$\phi = \phi_0 + \Gamma \sin \Omega t \quad (3)$$

where:

$$\phi_0 = \frac{\pi}{\lambda_0} n_0^3 r_{63} U_0, \quad \Gamma = \frac{\pi}{\lambda_0} n_0^3 r_{63} U_m \quad (4)$$

with: n_0 - the unperturbed crystalline index of refraction

r_{63} - one of the nonvanishing electrooptic coefficients for crystal of class $\bar{4}2m$

λ_0 - the free-space wavelength of the incident light.

For an unit-intensity incident beam of light polarized at 45° to the induced principal axes of the modulating crystal, the reduced Jones vector of the emergent light is:

$$|\Pi_{out}\rangle = M|\Pi_{in}\rangle = M \begin{bmatrix} 1 \\ 0 \end{bmatrix} = \begin{bmatrix} \cos(\phi_0 + \Gamma \sin \Omega t) \\ i \sin(\phi_0 + \Gamma \sin \Omega t) \end{bmatrix} \quad (5)$$

It is a periodically *time-varying Jones vector*, a *periodically time-varying spinor*, which represents a periodically time-varying SOP.

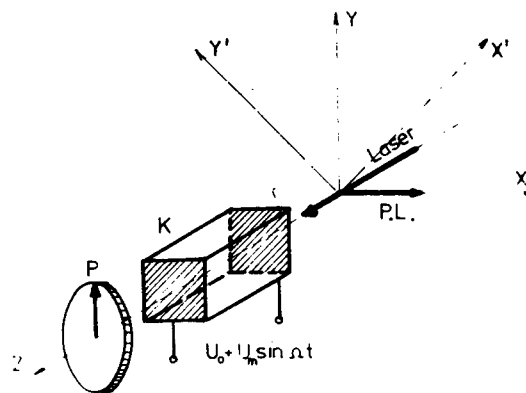


Fig.1 The modulation arrangement. PL-laser polarization, K-modulating crystal, P-output polarizer.

By using ¹³

$$\cos(\Gamma \sin \vartheta) = \sum_{k=-\infty}^{\infty} J_{2k}(\Gamma) e^{i2k\vartheta}$$

$$\sin(\Gamma \sin \vartheta) = -i \sum_{k=-\infty}^{\infty} J_{2k-1}(\Gamma) e^{i(2k-1)\vartheta}$$

(5) may be developed in Fourier series as it follows:

$$|\Pi_{\text{out}}\rangle = \sum_{k=-\infty}^{\infty} J_{2k}(\Gamma) \begin{bmatrix} \cos \phi_0 \\ i \sin \phi_0 \end{bmatrix} e^{i2k\Omega t} + \sum_{k=-\infty}^{\infty} J_{2k-1}(\Gamma) \begin{bmatrix} i \sin \phi_0 \\ \cos \phi_0 \end{bmatrix} e^{i(2k-1)\Omega t} \quad (6)$$

with J-Bessel functions of the first kind.

An entity of the type $\begin{bmatrix} a_{1k} \\ a_{2k} \end{bmatrix}$ with a_{1k} and a_{2k} complex constants, like in each term of (6),

describes completely the SOP of each spectral component of the light emerging from the modulator and may be called *spectral spinor*. Any periodically time-varying spinor can be developed in a series of spectral spinors.

A spectral development of the type (6) is very expressive concerning the SOP analysis of the emergent light. From (6) is straightforward that:

- The SOP of all even components of the emergent light is the same, generally elliptical, right-handed or left-handed. The SOP depends on the value of the d.c. bias applied to the modulator.
- The SOP of all odd components is the same.
- The states of polarization of the odd components and of the even components respectively are orthogonal:

$$\langle \Pi_{\text{odd}} | \Pi_{\text{even}} \rangle = 0 \quad (7)$$

Particularly the handedness of the odd components is opposite to that of the even ones.

3. TIME-VARYING POLARIZATION MATRICES AND SPECTRAL POLARIZATION MATRICES

At the level of observable quantities, all the information concerning the SOP and the intensity characteristics of the emergent light is contained in its polarization matrix:

$$\mathfrak{J}_{\text{out}} = |\Pi_{\text{out}}\rangle \langle \Pi_{\text{out}}| = \begin{bmatrix} \cos \phi \\ i \sin \phi \end{bmatrix} [\cos \phi \quad -i \sin \phi] =$$

$$= \frac{1}{2} \begin{bmatrix} 1 + \cos 2(\phi_0 + \Gamma \sin \Omega t) & -i \sin 2(\phi_0 + \Gamma \sin \Omega t) \\ i \sin 2(\phi_0 + \Gamma \sin \Omega t) & 1 - \cos 2(\phi_0 + \Gamma \sin \Omega t) \end{bmatrix} \quad (8)$$

which is, obviously, a *time-dependent Hermitian matrix*.

$$\begin{aligned}\mathfrak{J}_{out} = & \frac{1}{2} \begin{bmatrix} 1 & 0 \\ 0 & 1 \end{bmatrix} + \frac{1}{2} \begin{bmatrix} \cos 2\phi_0 & -i \sin 2\phi_0 \\ i \sin 2\phi_0 & -\cos 2\phi_0 \end{bmatrix} \cos(2\Gamma \sin \Omega t) + \\ & + \frac{1}{2} \begin{bmatrix} -\sin 2\phi_0 & -i \cos 2\phi_0 \\ i \cos 2\phi_0 & \sin 2\phi_0 \end{bmatrix} \sin(2\Gamma \sin \Omega t)\end{aligned}\quad (9)$$

Making use of ¹³:

$$\cos(2\Gamma \sin \vartheta) = J_0(2\Gamma) + 2 \sum_{n=1}^{\infty} J_{2n}(2\Gamma) \cos 2n\vartheta$$

$$\sin(2\Gamma \sin \vartheta) = 2 \sum_{n=1}^{\infty} J_{2n-1}(2\Gamma) \sin(2n-1)\vartheta$$

a Fourier series expansion of the time-varying polarization matrix is obtained:

$$\begin{aligned}\mathfrak{J}_{out} = & \frac{1}{2} \begin{bmatrix} 1 & 0 \\ 0 & 1 \end{bmatrix} + \frac{1}{2} J_0(2\Gamma) \begin{bmatrix} \cos 2\phi_0 & -i \sin 2\phi_0 \\ i \sin 2\phi_0 & -\cos 2\phi_0 \end{bmatrix} + \\ & + \sum_{n=1}^{\infty} J_{2n}(2\Gamma) \begin{bmatrix} \cos 2\phi_0 & -i \sin 2\phi_0 \\ i \sin 2\phi_0 & -\cos 2\phi_0 \end{bmatrix} \cos(2n\Omega t) + \\ & + \sum_{n=1}^{\infty} J_{2n-1}(2\Gamma) \begin{bmatrix} -\sin 2\phi_0 & -i \cos 2\phi_0 \\ i \cos 2\phi_0 & \sin 2\phi_0 \end{bmatrix} \sin(2n-1)\Omega t\end{aligned}\quad (10)$$

This is the *spectral content of the time-varying polarization matrix* (8) of the modulated light and we shall denominate each spectral component of (8), like, let say

$$\begin{bmatrix} \cos 2\phi_0 & -i \sin 2\phi_0 \\ i \sin 2\phi_0 & -\cos 2\phi_0 \end{bmatrix}\quad (11)$$

as *spectral polarization matrix*.

Once again, this time in terms of observable quantities, the SOP of the modulated light may be analyzed either in its time evolution (8), or, complementary, in its spectral content (10).

From (10) it is seen that, generally, the polarization matrix of the modulated light oscillates both on the odd and on the even multiples of the modulating frequency. All the odd components have the same state of polarization, and all the even components another state, orthogonal to the first.

The most direct information concerning the modulated light in terms of observable quantities is given by the elements of the principal diagonal of the polarization matrices (8) and (10). These elements give the intensities of the modulated light extracted by analyzers parallel respectively perpendicular to the polarization direction of the incident light. To within an irrelevant factor

$$\begin{aligned}
I_{x,y} = I_{\parallel,\perp} &= 1 \pm \cos 2\phi_0 \cos(2\Gamma \sin \Omega t) \mp \sin 2\phi_0 \sin(2\Gamma \sin \Omega t) = \\
&= 1 \pm \cos \phi_0 \sum_{n=0}^{\infty} J_{2n}(2\Gamma) \cos 2n\Omega t \mp \sin 2\phi_0 \sum_{n=0}^{\infty} J_{2n+1}(2\Gamma) \sin(2n+1)\Omega t
\end{aligned} \quad (12)$$

Both the x and y linearly polarized components of the modulated light contain generally odd and even spectral components; they oscillates on the odd as well on the even multiples of the modulating signal frequency.

A detailed experimental confirmation of the result (12) and of some particular cases important from a practical viewpoint is given in ⁶

Fig.2 shows an example of a spectrum analyzer display of the result (12), obtained in the arrangement presented in Fig.1.

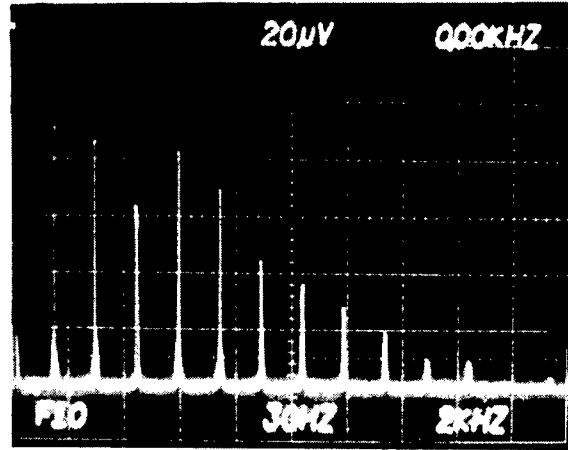


Fig.2 Typical spectrum of the modulator output intensity

4. GENERALIZATION

Let us put now the topic we presented in the previous example, in quite general terms. A whole class of optical modulators is of polarization modulators ¹⁴. Even many intensity modulators perform at an intermediate stage (e.g. before the last polarizer) a modulation of the SOP. The time-varying full Jones vector of the outcoming modulated light in such cases is of the form:

$$|E_{out}(t)\rangle = \begin{bmatrix} A_1(t) \\ A_2(t) \end{bmatrix} e^{i\omega_0 t} \quad (13)$$

where $A_1(t)$ and $A_2(t)$ are two, generally complex, periodic function of time, whose fundamental frequencies are determined by the modulation frequency Ω .

Dropping out the unobservable ^{15, 8} time variation $e^{i\omega_0 t}$, the SOP time-variation of the modulated light is described by the reduced Jones vector:

$$|\Pi_{out}(t)\rangle = \begin{bmatrix} A_1(t) \\ A_2(t) \end{bmatrix} \quad (14)$$

The time-varying spinor (14) describes a generally complicated time-variation of the "polarization form" of the modulated light. We have to point out that the time-variations implied in (14) are already in the diaphason of observable time-variations.

This generally complicated time-variation (14) may be expressed as a series of harmonic oscillations of time-invariant SOPs:

$$|\Pi_{\text{out}}(t)\rangle = \sum_{k=-\infty}^{\infty} C_k \begin{bmatrix} a_{1k} \\ a_{2k} \end{bmatrix} e^{ik\Omega t} \quad (15)$$

where C_k and a_{ik} are constants which depend on the detailed characteristics of the modulation process.

Each elementary time-invariant Jones vector of the series (15), $\begin{bmatrix} a_{1k} \\ a_{2k} \end{bmatrix}$, corresponds to a well defined time-invariant polarization form (SOP), which oscillates as a whole with the frequency $k\Omega$, at the output face of the modulator. The series $\begin{bmatrix} a_{1k} \\ a_{2k} \end{bmatrix}$ defines, together with the amplitudes C_k , the spectral structure of the SOP of the modulated light. The spectral Jones vectors, i.e. the spectral spinors, $\begin{bmatrix} a_{1k} \\ a_{2k} \end{bmatrix}$, are the spectral components of the time-varying Jones vector, i.e. of the time-varying spinor (14), and the complicated time-variation of the polarization form (14) may be conceived as a result of the superposition of these components.

In (15), unlike (14), a separation of the temporal and spinorial variables takes place and each term of (15) may be conceived as a mode of oscillation of the output signal of the modulator.

The reduced Jones vectors describe the completely polarized light with the maximum algebraic brevity, but they are not observable entities. Well-known, observable entities are the Stokes vectors, the coherency (polarization) matrices or the density matrices.

The polarization matrix corresponding to a Jones vector of the general form (13) is:

$$\begin{aligned} \mathfrak{J}_{\text{out}} &= |E_{\text{out}}\rangle \langle E_{\text{out}}| = |\Pi_{\text{out}}\rangle \langle \Pi_{\text{out}}| = \\ &= \begin{bmatrix} A_1(t)A_1^*(t) & A_1(t)A_2^*(t) \\ A_2(t)A_1^*(t) & A_2(t)A_2^*(t) \end{bmatrix} = \begin{bmatrix} \mathcal{J}_{11}(t) & \mathcal{J}_{12}(t) \\ \mathcal{J}_{21}(t) & \mathcal{J}_{22}(t) \end{bmatrix} \end{aligned} \quad (16)$$

This time-varying polarization matrix may be developed in a Fourier series

$$\mathfrak{J}_{\text{out}} = \sum_{n=-\infty}^{\infty} B_n \begin{bmatrix} \mathcal{J}_{11n} & \mathcal{J}_{12n} \\ \mathcal{J}_{21n} & \mathcal{J}_{22n} \end{bmatrix} e^{in\Omega t} \quad (17)$$

The (time-invariant) spectral polarization matrices

$$\begin{bmatrix} \mathcal{J}_{11n} & \mathcal{J}_{12n} \\ \mathcal{J}_{21n} & \mathcal{J}_{22n} \end{bmatrix} \quad (18)$$

together with the coefficients B_n give the spectral content of the global polarization matrix (17) of the output light.

5. REFERENCES

1. S. Huard. *Polarisation de la Lumière*, Chap.1, pp. 14-17, Masson, Paris, 1994.
2. R. W. Schmieder, "Stokes-algebra formalism", *Journ. Opt. Soc. Amer.*, **59** (3), 297-302 (1969).
3. A. D. May, P. Paddon, E. Sjerve, G. Stéphan, "Alternative interpretation of Zeeman and Faraday laser", *Phys. Rev. A*, **53** (4), 2829-2841 (1996).
4. A. P. Voitovich, A. M. Kulminskii, V. N. Severikov, "Nonlinear dynamics of laser system at intracavity modulation of polarization", *Opt. Commun.*, **126**, 152-166 (1996).
5. C. J. Peters, "Optical frequency shifting using two phase modulator in tandem", *Appl. Opt.* **4** (7), 857-861 (1965).
6. T. Tudor, "Harmonic structure of light modulated by longitudinal electrooptic effect in crystals of class $\bar{4}2m$ ", *Journ. Optics*, (Paris), **14** (3), 161-168 (1983).
7. J. Badoz, M.P.Silverman, J.C.Canit, "Wave propagation through a medium with static and dynamic birefringence: theory of the photoelastic modulator", *Journ. Opt. Soc. Amer.*, **A7** (4), 672-681 (1990).
8. J. E. Hopson, "Harmonic structure of modulated light beams", *IEEE Trans. Commun. Syst.*, **C. S. 11**, 464-469 (1963).
9. Robert C. O'Handley, "Modified Jones calculus for the analysis of errors in polarization modulation ellipsometry", *Journ. Opt. Soc. Amer.*, **63** (5), 523-528 (1973).
10. T. Tudor "Polarization waves", *Journ. Opt. Soc. Amer.*, **A14** (8), in press (1997).
11. J. W. Simmons M. J. Guttman, *States, Waves and Photons: A Modern Introduction to Light*, Chap. 4, pp. 77-78, Addison-Wesley, Massachusetts.
12. M. Born, E. Wolf, *Principles of Optics*, Chap. 10, p. 545, Pergamon Press, Oxford, 1986.
13. N. W. McLachlan, *Bessel Functions for Engineers*, Chap. 4, p. 160. Oxford Univ. Press, London, 1941.
14. R. G. Hunsperger, *Integrated Optics. Theory and Technology*, Chap. 8, pp. 133-134, Springer, Berlin, 1995.
15. E. Wolf, "Optics in terms of observable quantities", *Nuovo Cimento* **XII**, 884-888 (1954).

Fidelity evaluation of the conjugated wavefront in photorefractive crystals using direct spatial phase demodulation of optical interferograms

Valentin I. Vlad, Adrian Petris, Angela Jianu

Institute of Atomic Physics - National Institute of Laser, Plasma and Radiation Physics, Lasers Dept.,
P.O. Box MG - 36, R - 76 900 Bucharest, Romania

ABSTRACT

Conjugated wavefront fidelity has been evaluated using an interferometer with a phase conjugate mirror and fringe pattern computer processing. The quantitative interpretation of the fringe patterns is performed using direct spatial phase reconstruction methods (in the space and Fourier domains). A set of algorithms for fast and accurate phase evaluation, by fringe pattern processing, were derived. The result of optical interferograms evaluation appears in terms of different phase representations. These methods have been verified by studies of the optical phase conjugation fidelity in photorefractive crystals.

Keywords: optical phase conjugation fidelity, phase demodulation

1. INTRODUCTION

The phase conjugation is optically characterised by two parameters: the "reflectivity" of the phase conjugate mirror and the fidelity of the conjugated wavefront reconstruction. The fidelity is the key parameter in many important applications of the Optical Phase Conjugation (OPC): image projection by OPC, interferometer with OPC mirrors, adaptive optics, phase distortion compensation in waveguides and in stimulated scattering processes.

The evaluation of the OPC fidelity was done by (i) methods based on measurements of the conjugate wave divergence^{1-6, 10, 11} and (ii) interferometric methods^{7-10, 12}.

Essentially, methods in the first group consist of the computation of the ratio between the conjugate beam energy contained within a given solid angle, and the total energy of this beam, with and without an aberrator in the path of the probe (signal) beam. These methods require simple components and measurements, but they do not provide information about energy distribution within or around the chosen aperture and about wavefront shape changes, when inserting an aberrator.

Interferometric methods involve more complex experimental set-ups, but they are more accurate and provide also information related to the wavefront shape.

In this paper we evaluate the conjugated wavefront fidelity using an interferometer with a phase conjugate mirror and the computer processing of the fringe patterns. The interferometer is used to produce the interference pattern of the incident signal wave with the conjugate wave, in two cases: with and without a phase aberrator inserted in the path of the signal beam. In a perfect conjugation, the interference pattern should not change when the aberrator is inserted. However, if the wavefront reconstruction is not perfect, the fringes are distorted in a way that depends on the type of the inserted phase aberrator. The quantitative interpretation of the fringe patterns is performed using direct spatial phase reconstruction methods (in the space and Fourier domains)^{13, 14}. A set of algorithms for fast and accurate phase evaluation from fringe patterns, by image processing, were derived. The evaluation of optical interferograms appears in terms of different phase representations.

These methods have been verified by studies of the OPC fidelity in photorefractive crystals.

2. EXPERIMENTAL SET-UP

The experimental set-up we built to obtain the conjugate wave and evaluate the conjugated wavefront fidelity is shown in Fig.1. A $\text{Bi}_{12}\text{TiO}_{20}$ (BTO) photorefractive crystal (size $6 \times 8 \times 8 \text{ mm}^3$) is used as non-linear material in a classical four-wave mixing configuration. The He-Ne laser beam ($\lambda = 632.8 \text{ nm}$, $P = 30 \text{ mW}$) is divided (by the beam-splitter BS1) in the signal (S) and pump (P1) beams incident (after reflection on mirrors M2 and M3, respectively) on the BTO crystal. The second pump beam (P2) is obtained from the first, (P1), after passing through the crystal and being reflected by the mirror M4 placed behind the BTO crystal. The conjugated wave (C) is separated by a beam-splitter (BS2) and read by a CCD camera, connected to a TV monitor and to a home-made Image Acquisition and Processing System (IAPS) (which digitizes and stores the images), interfaced to a PC. The beam-splitter (BS3) is introduced in the path of the signal beam to separate a reference beam (R) (identical as wavefront shape with the signal beam) that interferes, after reflection on the mirror M5, with the conjugated beam. An aberrator (AB) is inserted in the path of the signal beam, in order to analyse the changes in the resulting phase conjugated beam. A variable attenuator (VA), introduced in the laser beam can change the intensity of the signal (S) and the pump (P1, P2) beams, varying the response time of the BTO crystal and, consequently, the recording time of the interferograms. The signal, pump, reference and conjugate beams are not expanded. The angle between S and P1 beams is 60° . To compare the "reflection" on the "phase conjugate mirror" with an ordinary one, a plane mirror was introduced instead of the BTO crystal.

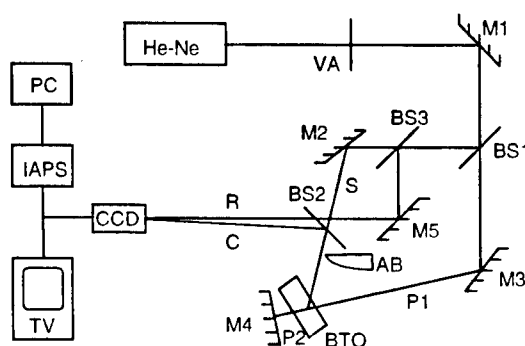


Fig. 1. The experimental set-up for obtaining the conjugated wave and evaluation the conjugated wavefront fidelity.

We used as aberrators a 50 cm focal length lens, a 2° prism and a glass-window with a phase discontinuity shown in Fig 2. Fig. 2 shows the phase map (obtained by DSROP processing of a double-exposure holographic interferogram) of this glass-window.

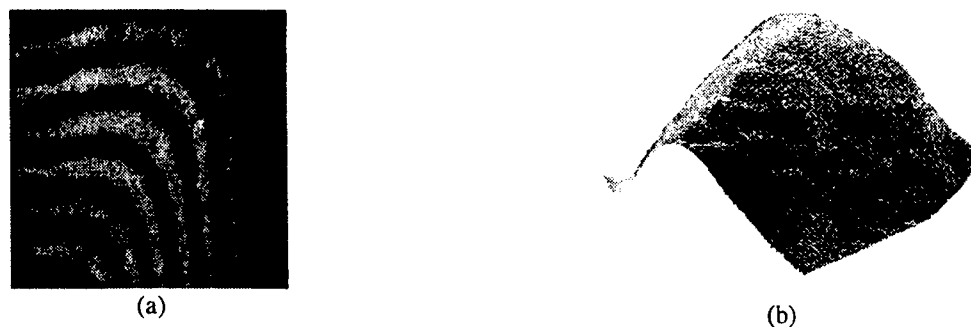


Fig. 2. (a) Double exposure holographic interferogram of a glass-window with a phase discontinuity, used as phase aberrator; (b) the 3D calculated phase distribution.

3. DIRECT SPATIAL PHASE DEMODULATION OF OPTICAL INTERFEROGRAMS

Direct spatial reconstruction of optical phase (DSROP) in the space and Fourier domain uses single pattern analysis being faster than phase shifting methods¹⁴.

A phase-modulated image can be defined as a 2D function:

$$I(x, y) = A(x, y) + B(x, y) \cos [2 \pi u_0 x + \Phi_m(x, y)] \quad (1)$$

$A(x, y)$, $B(x, y)$ - background, respectively, contrast, u_0 -spatial carrier frequency, $\Phi_m(x, y)$ -phase modulation.

In the space domain, phase demodulation can be accomplished by the multiplication of the fringe pattern (FP) with the reference:

$$R(x, y) = \exp (2 i \pi u_0 x). \quad (2)$$

The product $I(x, y) \cdot R(x, y)$ consists of two rapidly-varying functions and one slowly-varying term. By smoothing this pattern over $\Lambda_0 = 1/u_0$, only the slowly-varying term, $Y(x, y)$, is obtained. The spatial phase distribution is given by:

$$\Phi_m(x, y) = -\tan^{-1} \{ \text{Im} [Y(x, y)] / \text{Re}[Y(x, y)] \}. \quad (3)$$

Phase demodulation in the Fourier domain relies on the description of the wavefront recording and reconstruction in holography. Eq. (1) can be written as:

$$I(x, y) = A(x, y) + C(x, y) \exp[i(2\pi u_0 x)] + C^*(x, y) \exp[-i(2\pi u_0 x)] \quad (4)$$

where:
$$C(x, y) = \frac{B(x, y)}{2} \exp[i\Phi_m(x, y)] \quad (5)$$

Taking the Fourier transform of eq. (4):

$$\mathcal{J}(u, v) = \mathcal{J}(u, v) + \mathcal{C}(u - u_0, v) + \mathcal{C}^*(u + u_0, v) \quad (6)$$

After the band-pass filtering of the term $\mathcal{C}(u, v)$ and the computation of the inverse Fourier transform, the phase modulation can be obtained directly, as:

$$\Phi_m(x, y) = -\tan^{-1} \{ \text{Im} [C(x, y)] / \text{Re}[C(x, y)] \} \quad (7)$$

4. RESULTS AND DISCUSSION

Fig. 3 and 4 present interferograms obtained with a "phase conjugate mirror" and an ordinary mirror, respectively, and the corresponding phase maps, calculated using the DSROP algorithms. The phase maps show the measure of the wavefront reconstruction fidelity in optical phase conjugation.

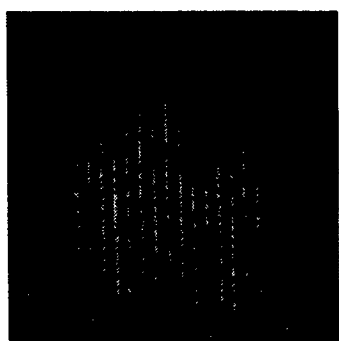
The fringes in Fig. 3 have approximately the same period and orientation independent of the type of the phase aberrator inserted in the path of the signal beam.

The strong dependence of the fringe orientation and shape on the aberrator type can be noticed in Fig. 4, when an ordinary mirror was used.

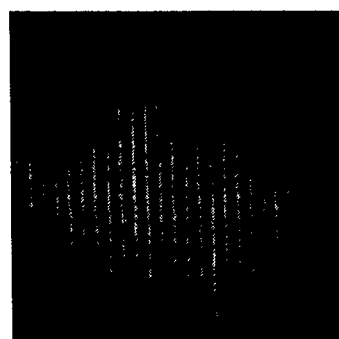
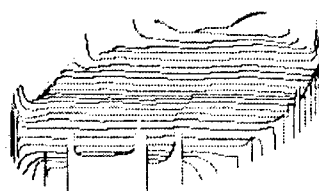
The signal wavefront shape is not varying when changing the aberrator, in the "phase conjugate mirror" case, as in Fig. 3 (b,c,d).

Important differences in this shape can be observed in the ordinary reflection case, as in Fig. 4 (b,c,d).

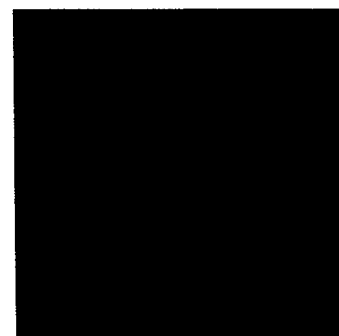
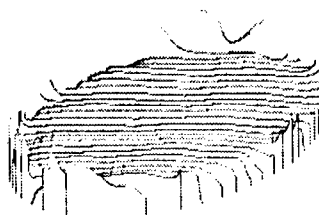
The interferogram generated when using the prism as aberrator could not be obtained with an ordinary mirror, due to the strong deflection produced by the two signal passings through the prism. The "phase conjugate mirror" produces a good correction of this aberration.



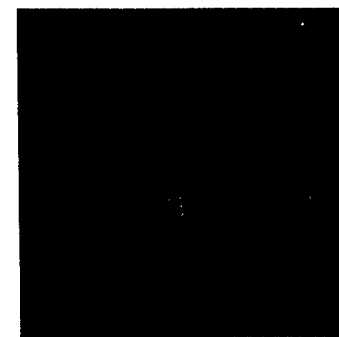
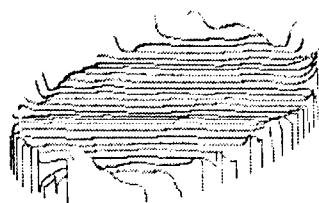
(a)



(b)



(c)



(d)

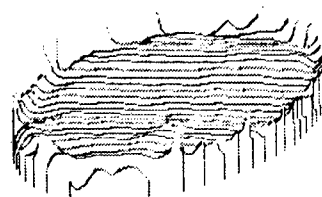
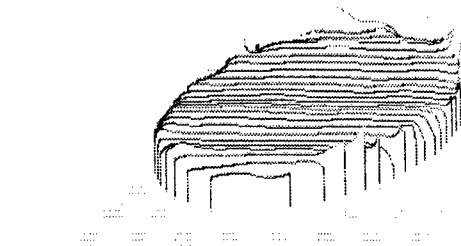
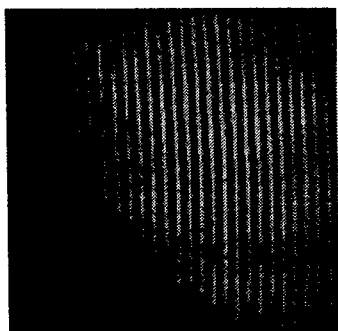
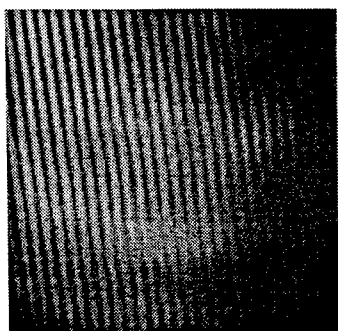
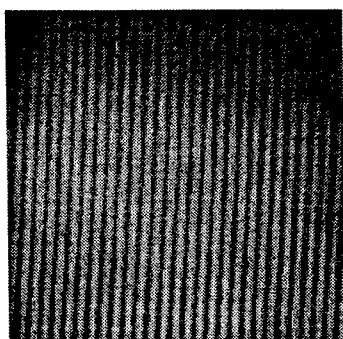
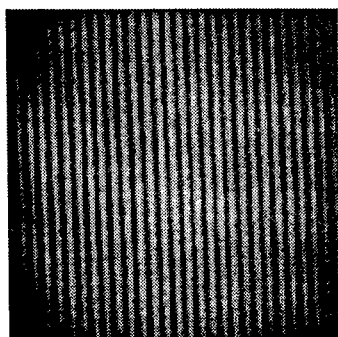
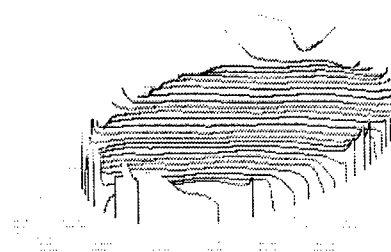


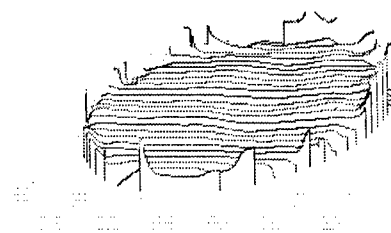
Fig. 3 Interferograms for wavefront reconstruction fidelity evaluation obtained using a BTO crystal as a "phase conjugate mirror" in a 4WM set-up and the corresponding phase maps with no aberrator (a) and the following aberrators: (b) the glass-window with a phase distribution shown in Fig. 2; (c) a 50 cm focal length lens; (d) a 2 deg. prism.



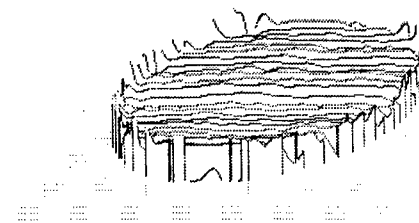
(a)



(b)



(c)



(d)

Fig. 4 Interferograms obtained using an ordinary mirror and the corresponding phase maps with no aberrator (a) and the following aberrators: (b), (c) the glass-window with a phase distribution shown in Fig. 2, in two different positions; (d) a 50 cm focal length lens.

5. CONCLUSIONS

The proposed methods for evaluation of the conjugated wavefront fidelity (yielded by photorefractive crystals) using an interferometer with OPC mirror and a modern evaluation technique of the fringe patterns, were tested with good results. This interferometric method is independent of the non-linear process involved in generating the phase conjugated wavefront in the photorefractive process and could also be applied for phase conjugation studies by stimulated Brillouin scattering.

6. ACKNOWLEDGEMENTS

This research was partially supported by the Romanian Academy under grant 3018 / 1997.

REFERENCES

1. L. P. Schelonka, C. M. Clayton, "Effect of focal intensity on stimulated Brillouin scattering reflectivity and fidelity", *Opt. Lett.*, **13** (1), p. 42-44 (1988)
2. J. J. Ottusch, D. A. Rockwell, "Stimulated Brillouin scattering phase conjugation fidelity fluctuations", *Opt. Lett.*, **16** (6), p. 369-371 (1991)
3. C. B. Dane, V. A. Neuman, L. A. Hackel, "Pulse shape dependence of stimulated Brillouin scattering phase conjugation fidelity for high input energies", *Opt. Lett.*, **17** (18), p. 1271-1273 (1992)
4. I. C. Winkler, R. S. Mandra, "Optical phase conjugation of weak signals by using degenerate four wave mixing", *Opt. Lett.*, **17** (8), p. 568-570 (1992)
5. M. S. Mangir, D. A. Rockwell, "4.5-J Brillouin phase-conjugate mirror producing excellent near- and far-field fidelity", *J. Opt. Soc. Am. B*, **10** (8) p. 1396-1400 (1993)
6. D. L. Naylor, P.W. Tamm, R. W. Hellwarth, "Fidelity of optical phase conjugation by photorefractive degenerate four-wave mixing in barium titanate", *J. Appl. Phys.*, **72** (12), 5840 (1992)
7. J. Munch, R. F. Wuerker, M. J. LeFebvre, "Michelson interferometer with a holographic memory for measuring fidelity of aberrated phase conjugated beams", *Appl. Opt.*, **28** (9), p.1731-1733 (1989)
8. L. P. Schelonka, "The fidelity of stimulated Brillouin scattering with weak aberrations", *Opt. Commun.*, **64** (3), p. 293-296 (1987)
9. B. Fleck, A. Kiessling, L. Wenke, "A simple method for measuring fidelity of phase conjugated beams", *EPS Conference*, Amsterdam, (1990)
10. A. Petris, S. Tibuleac, L. Voicu, "Fidelity measurement methods for phase conjugation by degenerate four wave mixing in photorefractive BTO crystals", *Proc. SPIE* **2108**, p.29-36 (1993)
11. A. Petris, S. Tibuleac, L. Voicu, "Measuring the phase conjugation fidelity by computer image analysis", *Romanian Journal of Physics*, **38** (7), p. 669-673 (1993)
12. A. Petris, S. Tibuleac, L. Voicu, "Interferometric method for phase conjugation fidelity studies", *Romanian Journal of Physics*, **38** (6), p. 633-635 (1993)
13. V.I.Vlad, D. Malacara-Hernandez, A. Petris, "Real-time holographic interferometry using optical phase conjugation in photorefractive materials and direct spatial phase reconstruction", *Optical Engineering*, **35** (5), p. 1383-1388 (1996)
14. V. I. Vlad, D. Malacara, "Direct spatial reconstruction of optical phase from phase-modulated images", *Progress in Optics*, E. Wolf, Ed., Vol.XXXIII, 261 (1994).

Talbot - moiré deflectometry with direct spatial reconstruction of optical phase

Angela Jianu, Adrian Petris, Carmen Popa*, Dragos Popa*, Valentin I. Vlad

Institute of Lasers, Plasma and Radiation Physics, Lasers Dept., PO Box MG-36, R-76900, Bucharest, ROMANIA

* University "Polytechnica", Physics Dept., Bucharest, Romania

ABSTRACT

Improvements in Talbot-moiré deflectometry are presented. A Talbot-moiré interferometer, using a laser diode as light source, a single grating and a CCD camera, placed in one of the Talbot planes, was set-up. The computer yields a moiré pattern by mixing the acquired Talbot image of the first grating with the reference generated by computer or stored as an undisturbed external grating Talbot image. For moiré pattern processing, direct spatial reconstruction of optical phase, in spatial and Fourier domains, implemented in a high-level image processing language (IDL®), was employed. The theoretical limit of the relative error of Talbot-moiré deflectometry was verified by measuring the focal length of a lenticular system with controlled-focal-length.

Keywords: Talbot-moiré deflectometry, fringe pattern processing, optical phase reconstruction

1. INTRODUCTION

Talbot interferometry was introduced by Lohmann and Silva¹, and by Yokozeki and Suzuki² as a method to measure the derivatives of the wavefront transmitted and reflected by an object exploiting the self-imaging property of a grating at integer multiples of the Talbot distance, $z_T = 2\Lambda^2/\lambda$ (Λ - period of the grating, λ - wavelength). Kafri³ developed Talbot-moiré deflectometry using two gratings to obtain a moiré pattern distorted by the object wavefront. Both transparent and reflecting objects were experimentally investigated by moiré deflectometry, showing straightforward interpretation of the fringes, high stability, and measurement accuracy⁴⁻⁶. A simple moiré deflectometer design (the first grating at integer multiples of the Talbot distance from the TV camera and the second grating computer generated and mixed with the direct image on the TV monitor) has been reported⁷.

In this paper, we develop the same structure - one grating located at a distance nz_T from the photosensitive array of a CCD camera and the second grating software-generated and mixed with the acquired image. We have used a digital image processor consisting of a CAMAC unit interfaced to a PC that has been described elsewhere⁸. In computerised Talbot-moiré deflectometry (CTMD) the digital image processor is used for fringe pattern acquisition, processing and interpretation. CTMD experiments have established an ensemble of precise and convenient optical measuring methods in a robust and simple system.

2. CTMD USING ONE GRATING

In moiré deflectometry³, a collimated light beam is deflected by a transparent or reflective object and the deflection angle $\delta(x,y)$ is evaluated by the local displacement of the moiré pattern produced by two identical gratings of Λ period (G_1, G_2), separated by a distance nz_T and slightly rotated by an angle θ [Fig. 1(a)].

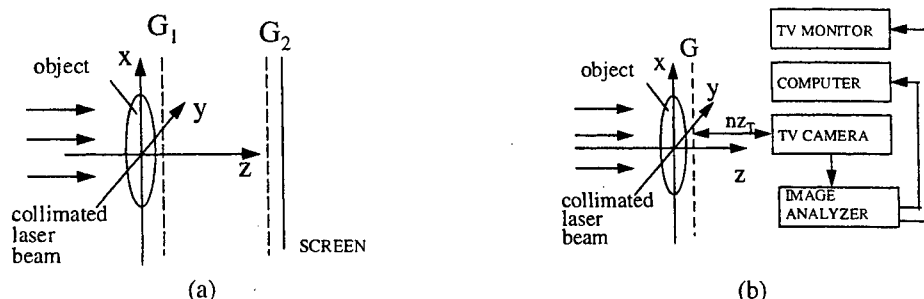


Fig. 1 (a) Talbot - moiré deflectometry; (b) Computerised moiré deflectometry using the Talbot effect.

It is possible to obtain the same results using only one grating (G) at the distance nz_T from the photosensitive array of a TV camera and storing two coded images (states) of the investigated object in the computer-based image processor memory [Fig.1(b)]. The digital mixing of the two images, the display and processing of the moiré deflectogram are performed by computer. There are at least two forms of this double-exposure method: (1) mixing the object image with a stored reference image (with the particular case of the computer-generated reference image) and (2) mixing the current object image with a previously stored object image, i.e., a differential method (with advantages regarding the elimination of optical imperfections and noise).

2.1. Analysis of CTMD with tilted gratings

The rotated (by small θ) grating image, when the phase object is missing, can be written as:

$$I_1 = I_0 \cos^2 \{ (2\pi / \Lambda) \cdot [x \sin(\theta / 2) + y \cos(\theta / 2)] \} \quad (1)$$

Introducing the phase object (as in Fig.1) leads to a small deflection of the illumination beam and to grating shifts along the x-axis, by x_0 , and the y-axis, by y_0 , written as:

$$I_2 = I_0 \cos^2 \{ (2\pi / \Lambda) \cdot [-(x - x_0) \sin(\theta / 2) + (y - y_0) \cos(\theta / 2)] \} \quad (2)$$

Subtracting Eqs. (1) and (2), neglecting the products between the small translations and the angle θ , one obtains:

$$I = I_1 - I_2 \approx I_0 \sin \{ (4\pi / \Lambda) \cdot [x + y_0 / (2 \tan(\theta / 2))] \cdot \sin(\theta / 2) \} \cdot \sin \{ (2\pi / \Lambda) \cdot (y - y_0 / 2) \cdot \cos(\theta / 2) \} \quad (3)$$

Eq. (3) shows that the straight moiré fringes (of period $p = \Lambda / [2 \sin(\theta / 2)]$), perpendicular to the x-axis, appearing when the phase object is absent, are shifted significantly, when introducing the object, only along the x-axis, by:

$$\Delta x = y_0 / (2 \tan(\theta / 2)) \quad (4)$$

If the illuminating beam deflection along the y-axis (in the plane x,y) is denoted by $\delta_y(x,y)$, one can write:

$$\delta_y = y_0 / (nz_T) = [2\Delta x / (nz_T)] \cdot \tan(\theta / 2) \quad (5)$$

This result is identical to Kafri's deflection equation³, demonstrating the full correspondence between moiré deflectometry and single grating CTMD.

By rotating the gratings by 90° , one can similarly obtain the orthogonal deflection angle δ_x .

Considering the case of small θ , Eq. (3) yields:

$$\delta_y \approx [\Delta x / (nz_T)] \cdot \theta = [\Delta x / (nz_T)] \cdot \Lambda / p = [\Delta x / p] \cdot \Lambda / (nz_T) = [\Delta x / p] \cdot \lambda / (2n\Lambda) \quad (6)$$

a relation that shows that CTMD sensitivity can be varied independently by three parameters: the grating period Λ , the grating tilt θ , and the Talbot index n .

2.2 CTMD for transparent objects

Transparent objects are studied by CTMD in the set-up of Fig. 1(b). For small deflections (i.e., small refraction index gradients $\partial n / \partial y$, yielded by a phase object), the deflection angle is:

$$\delta_y(x,y) = (1 / n_0) \int_0^L (\partial n / \partial y)_{x,y} dz \quad (7)$$

where n_0 is the index of the homogeneous medium in which the object of thickness L is immersed. Eq. (7) allows direct calculation of the refractive index gradient from the experimental measured deflection angle. In the case of axis-symmetric objects, the distribution of the refractive index is related to δ_y/y by the Abel transformation.

We remark that, in CTMD without tilting for transparent objects, one can measure and determine quantitatively the second order derivatives of the refractive index. Therefore, CTMD can give, from experiments and simple algorithms, accurate data on the refractive index profiles as well as their first two derivatives in a phase object.

An application of CTMD for transparent objects appears in the measurement of the focal length of lens^{3,4,9}. In this particular case, CTMD with tilted gratings yields straight moiré fringes that, when introducing the lens, are rotated by an angle α from their position in the absence of the lens (Fig. 2).

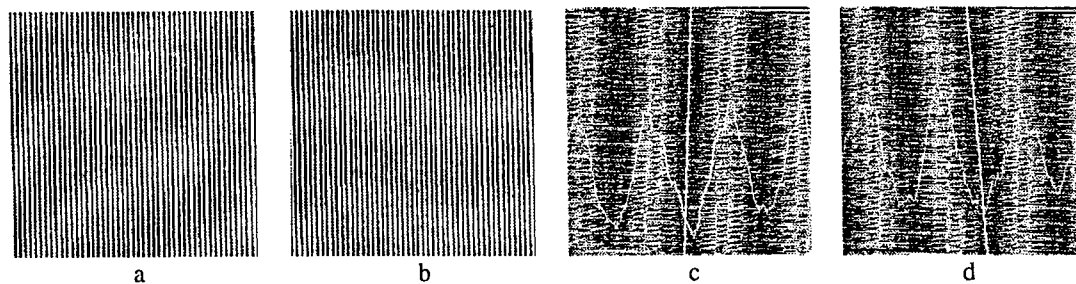


Fig. 2 Fringe and moiré patterns obtained by CTMD in the measurement of lens focal lengths

(a) image of the Ronchi grating ($\Lambda=0.1$ mm); (b) image of a 4m focal length lens "seen" through the Ronchi grating represented in (a); (c) moiré pattern produced by computer-mixing of two tilted (by $\theta \approx 4^\circ$) grating images of the kind represented in (a); (d) moiré pattern produced by computer mixing of the grating image represented in (a) with the lens image, represented in (b), tilted by $\theta \approx 4^\circ$. A rotation (by $\alpha \approx 6^\circ$) of the moiré pattern is produced when introducing the lens [rotation angle between moiré fringes represented in (c) and (d)].

The focal length f of the lens is given by:

$$f = z_T + [z_T / 2 \sin(\theta / 2)] \cdot 1 / \tan \alpha \quad (8)$$

For small θ and α , one can use the simple approximation:

$$f \approx nz_T / (\theta \alpha) \quad (9)$$

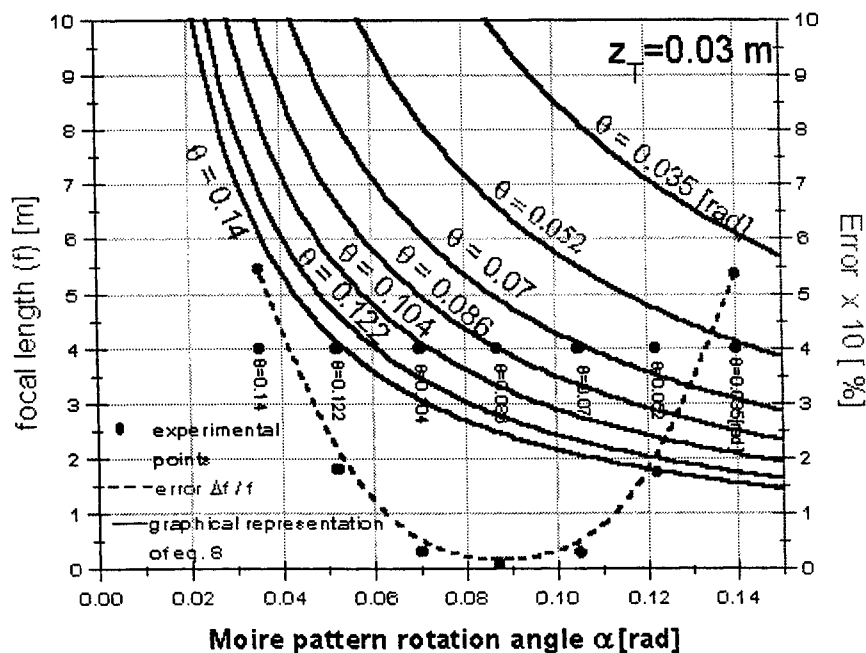


Fig. 3. Graphical representation of Eq. (8) for different θ values, error representation and experimental results

Some graphical representations of Eq. (8) for different θ values together with the experimental results and the error calculations are given in Fig. 3. Considering some limit values in CTMD, $(nz_T)_{\max} \sim 1$ m, $\theta_{\min} \sim 10^{-2}$ rad, and $\alpha_{\min} \sim 10^{-2}$ rad, the maximum focal length that can be measured is $f_{\max} = 10^4$ m. For small f (under a few meters), CTMD can be used but it is in hard competition with other methods.

3. DIRECT SPATIAL RECONSTRUCTION OF OPTICAL PHASE WITH A SHEARED PERIODIC PATTERN

The tested object is "seen" by the TV camera through a grating which is rotated in-plane and around the x-axis by a small angle, $\theta/2$ (Fig. 4). The object yields small deflections of the coherent illumination beam and grating-line shifts along the x-axis, by $x_0 = x_0(x, y)$, and along y-axis, by $y_0 = y_0(x, y)$, so the detected intensity pattern can be written as:

$$\begin{aligned} I(x, y) &= I_0 + I_1 \cos^2 2\pi u_0 \left[-(x - x_0) \sin(\theta/2) - (y - y_0) \cos(\theta/2) \right] = \\ &= A(x, y) + B(x, y) \cos 4\pi u_0 \left[-(x - x_0) \sin(\theta/2) - (y - y_0) \cos(\theta/2) \right] \end{aligned} \quad (10)$$

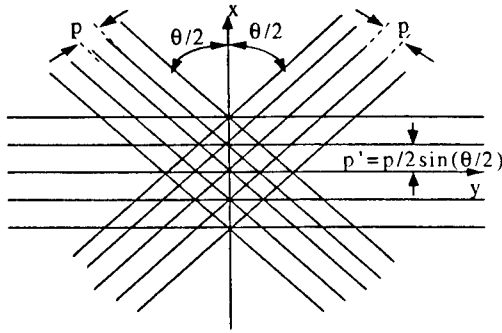


Fig. 4 Rotated carrier (grating) and the corresponding sheared reference used in direct spatial reconstruction of optical phase¹⁰ (DSROP)

If the reference pattern is a grating rotated around the x-axis by the angle $(-\theta/2)$, modulating a 1D carrier along the x-axis, then:

$$R_c(x, y) = \left[\cos 4\pi u_0 (x \sin(\theta/2) + y \sin(\theta/2)) \right] \cos(8\pi u_0 x \sin(\theta/2)) \quad (11)$$

and:

$$\begin{aligned} I \cdot R_c \approx A \cdot R_c + 0.5B \cos \left[8\pi u_0 (y - y_0/2) \cos(\theta/2) \right] \cdot \cos(8\pi u_0 x \sin(\theta/2)) + \\ + 0.5 \cos \left[8\pi u_0 (x + y_0/(2 \tan(\theta/2))) \sin(\theta/2) \right] \cdot \cos(8\pi u_0 x \sin(\theta/2)) \end{aligned} \quad (12)$$

The product moiré pattern phase shift is significant only along the x-axis:

$$\Delta\phi = 4\pi u_0 y_0 / \tan(\theta/2) \quad (13)$$

This phase shift can be obtained from Eq. (12) by a low-pass filtering which will eliminate all terms except:

$$Y_c = \cos(4\pi u_0 y_0 \cos(\theta/2)) \quad (14)$$

By multiplication with a quadrate reference:

$$R_s(x, y) = \left[\cos 4\pi u_0 (x \sin(\theta/2) + y \sin(\theta/2)) \right] \sin(8\pi u_0 x \sin(\theta/2)) \quad (15)$$

and by the same filtering, one can obtain:

$$Y_s = \sin(4\pi u_0 y_0 \cos(\theta/2)) \quad (16)$$

and finally:

$$y_0 = [1 / (4\pi u_0 \cos(\theta/2))] \tan^{-1}(Y_s / Y_c) \quad (17)$$

Similarly, by rotating the external grating and the reference pattern (grating) in the orthogonal position, one can obtain x_0 . The deflection angles can be determined by dividing x_0 and y_0 by $(nz_\tau) / (\sin(\theta/2))$.

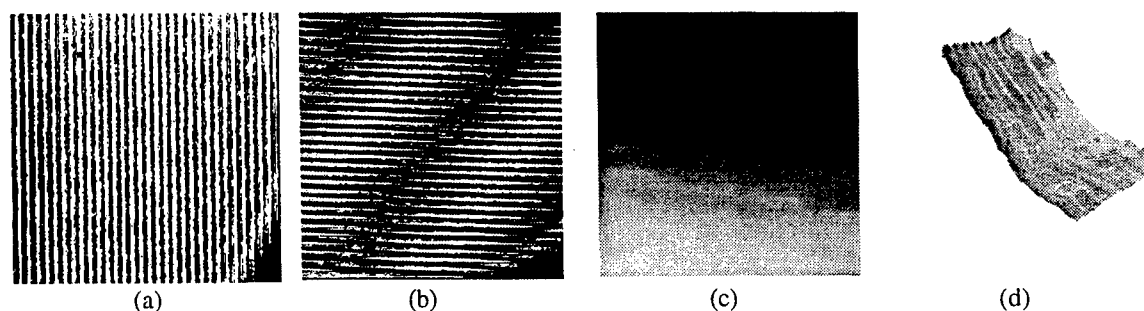


Fig. 5. CTMD for refractive index homogeneity investigation in an ordinary piece of glass (with a phase discontinuity) (a) transparent object "seen" through a Ronchi grating ($\Lambda=0.1$ mm); (b) moiré pattern obtained by computer mixing of the image represented in (a) with a tilted (by $\theta \approx 3^\circ$) reference; (c), (d) 2D, respectively 3D deflection angle maps for the transparent object "seen" in (a)

CTMD, applied to transparent (phase) objects, can replace in many cases the interferometric methods, Schlieren photography ($\theta \neq 0$), and shadowgraphy ($\theta = 0$) due to simple, easy-to-align, and stable optical system as well as to the real-time data acquisition and processing.

4. CONCLUSIONS

CTMD for the measurement of the deflection angles in transparent objects was theoretically and experimentally demonstrated. The optical system that has been used is simple, easy-to-align, and stable. A new algorithm, DSROP with a sheared periodic pattern, implemented using a high-level image processing language (IDL®) was used for CTMD fringe processing. The high sensitivity of CTMD makes it competitive with respect to the conventional interferometric, Schlieren, shadow, and moiré methods.

5. REFERENCES

1. A. W. Lohmann, D. A. Silva, "Talbot interferometer", *J. Opt. Soc. Am.* **61**, 687 (1971)
2. S. Yokozeki, T. Suzuki, "Shearing interferometer using the gratings as beam splitter", *Appl. Opt.* **10**, 1575 (1971).
3. O. Kafri, "Noncoherent method for mapping phase objects", *Opt. Lett.* **5**, 555 (1980)
4. Y. Nakano, K. Murata, *Appl. Opt.* **23**, 2296 (1984)
5. I. Glatt and A. Livnat, *Appl. Opt.* **23**, 2241 (1984)
6. E. Keren, A. Livnat, and I. Glatt, *Opt. Lett.* **10**, 167 (1985)
7. V. I. Vlad, D. Popa, I. Apostol, "Computer moiré deflectometry using the Talbot effect", *Opt. Eng.*, **30**(3), 300-306 (1991).
8. V. I. Vlad, D. Popa, S. Solomon, *Int. Opt. Comp. Conf., Proc. SPIE 700*, 344-351 (1986).
9. L. Horowitz, Y. B. Band, O. Kafri, and D. F. Heller, *Appl. Opt.* **23**, 2229 (1984)
10. V. I. Vlad, D. Malacara, "Direct spatial reconstruction of optical phase from phase-modulated images", *Progress in Optics*, E. Wolf, Ed., Vol. XXXIII, 261 (1994).

SESSION 4

Laser Spectroscopy

Study of the competitive processes in a non isothermal plasma by deconvolution of low intensity spectral lines

I.Iova, Gh. Ilie, M. Băzăvan, C. Biloiu, I. Gruia, I. Chera

*M. Cristea, *T. Constantinescu

University of Bucharest, Faculty of Physics

76900 Bucharest - Măgurele, P.O. Box MG - 11, Romania

* "Politehnica" University of Bucharest, Spl. Independentei 313, 77206 Bucharest, Romania

ABSTRACT

The paper presents a data processing algorithm, based on a deconvolution technique that enables the recovery of the low intensity spectral lines, in connection with the analysis of the radiative mechanisms from the non isothermal plasma of a hollow cathode discharge. This method represents a useful tool in the study of the radiative competitive processes involved in the selective excitation mechanisms for UV and visible spectral line's emission. It permits the evaluation of the second kind collision's weight in conjunction with the concentration of the plasma ions for different discharge parameters.

Keywords: hollow cathode discharge, deconvolution methods, second kind collisions, selective excitations

1. INTRODUCTION

In the hollow cathode discharges the occurrence of second kind collisions processes could induce selective excitations of the plasma atoms and ions. Of practical interest for spectral sources and lasers active media are the line's intensity increasing by selective excitation of the Copper vapor atoms obtained by cathode sputtering under ionic bombardment in pulsed hollow cathode discharge in noble gases' mixtures^{1, 2, 3}. In normal discharge conditions, at relatively low current density (luminescent discharges), the Copper lines of interest are of very low intensity comparing with the noble gases lines, in many cases being covered by the background. Our spectral investigation purpose, is to detect these lines and to identify the radiative mechanisms involved in their emission in order to further tune the experimental conditions (noble gases partial pressures, cathode geometry, current density) to obtain their selective excitation.

2. EXPERIMENTAL CONDITIONS

The hollow cathode discharge was produced in discharge tubes (Fig.1) consisted by a water-cooled Copper cathode with a longitudinal rectangular slot (4÷6 mm depth, 2 mm width, 60÷100 mm length), an anode from a wolfram rod (2 mm diameter) or from a Copper cylinder of small diameter and two quartz windows (Brewster-angled positioned in some experimental cases). The discharge gap was pumped to 10^{-6} torr and was filled with pure noble gases (He, Ne or Kr) or mixture of them (He-Ne, He-Kr, or Ne-Kr) at pressure between 1÷10 torr.

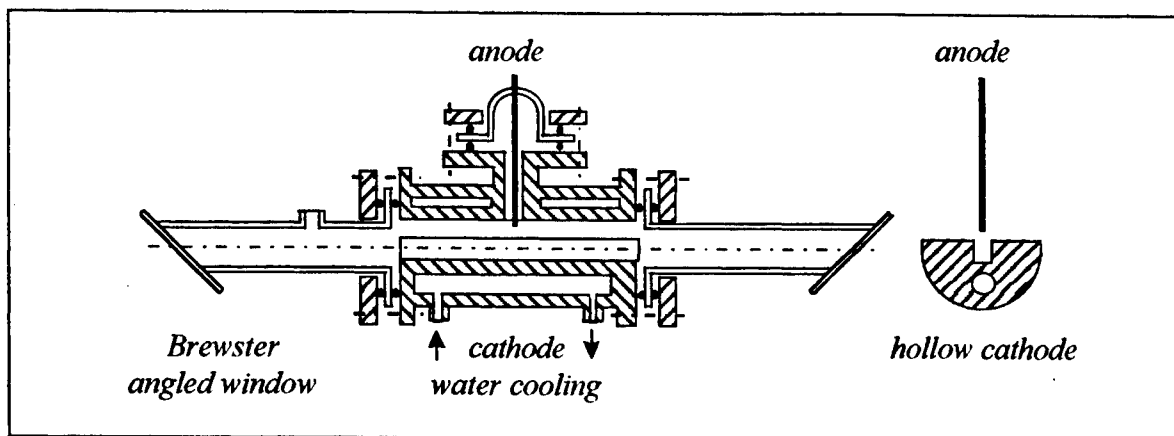


Fig. 1. Hollow cathode discharge tube

The experimental setup for plasma radiation investigations is presented in Fig. 2. It consists from a grating monochromator, on the entrance slit of which the radiation emitted by the hollow cathode discharge is directed through a collimating lens system. A photomultiplier attached to the monochromator exit slit convert the radiation in an electric current that is further amplified and converted in a digital signal by the data acquisition unit and send it to a computer to be stored and processed.

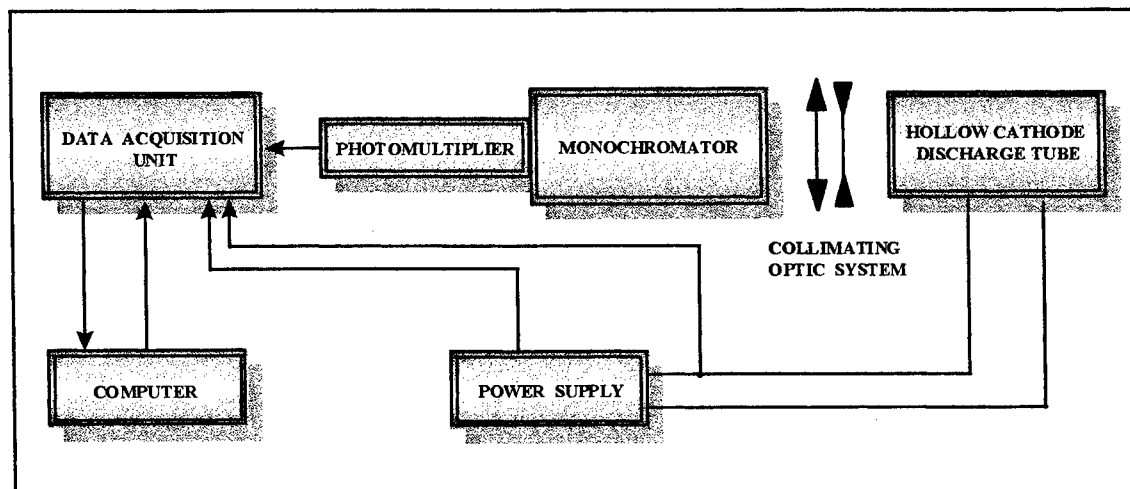


Fig. 2. Block scheme of the experimental setup

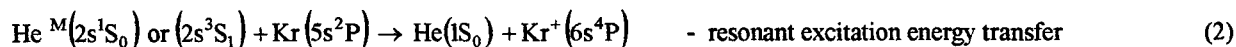
The electric parameters of the discharge are also monitored by the data acquisition unit. The hollow cathode discharge was operated by a power supply that could deliver energy in a DC, pulsed or DC+ pulsed regimes.

3. SELECTIVE EXCITATION PROCESSES

The radiative processes that contribute to the selective excitation of desired energy states include: resonant excitation-energy transfer involving atom-atom, atom-ion, and molecule-molecule reactions, charge transfer, and Penning reactions.

In the conditions of discharge in mixture of He – Kr, in a rectangular geometry of the cathode, the presence of Cu vapors and the collisions of metal atoms and ions with the noble gas atoms will direct to important perturbations in the populations of excited states, with notable effects on the spectral line intensities.

Due to the resonance between the energy levels, in ternary mixtures of noble gases and metal vapors (He – Kr – Cu), there are possible collisional processes of second kind, as is indicated in Fig. 3, that lead to selective excitation of atoms and ions:



The effect of this processes is the increase of concentration of Cu^+ and Kr^+ ions that are very efficient sputtering agents.

A comparison of spectra recorded in pure gases, respectively in mixtures (Fig. 4), shows the remarkable effect produced on the selective excitation of energy states of Cu atoms, produced through the very effective sputtering due to the impact of Kr^+ ions and of self-sputtering of metal ions.

Concerning their role of sputtering agents, a competition will appear between Kr and Cu ions. The symmetrical charge exchange will maintain the kinetic energy of the noble gas ion at low values – the effect being more important at larger partial pressures of the respective component of gas mixture. The role of He ions as sputtering agents is less important; their role is rather to contribute, through the resonant asymmetric charge exchange, to the ionization of metal atoms and to the selective excitation of sputtered metal ions.

Comparing the emitted line spectra (Fig. 4), it is to be observed that, in comparison with the pure gas, where the excitation of Cu is very difficult to be observed, in He – Kr mixture, this is strongly favored.

It is to be mentioned that in conditions of low partial pressures of Kr ($p_{\text{Kr}} = 0.04$ torr, $p_{\text{He+Kr}} = 4.24$ torr) there are established optimal conditions for the excitation of Cu I as well as of Kr II lines.

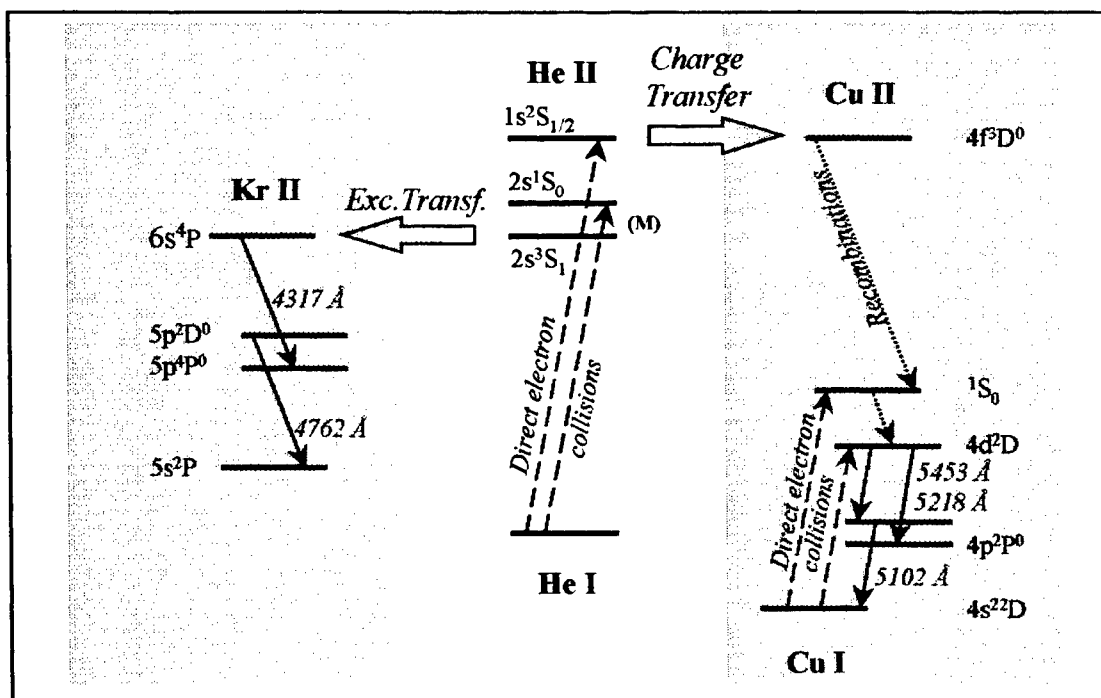


Fig. 3. The diagram of spectral transitions in (He - Cu - Kr)

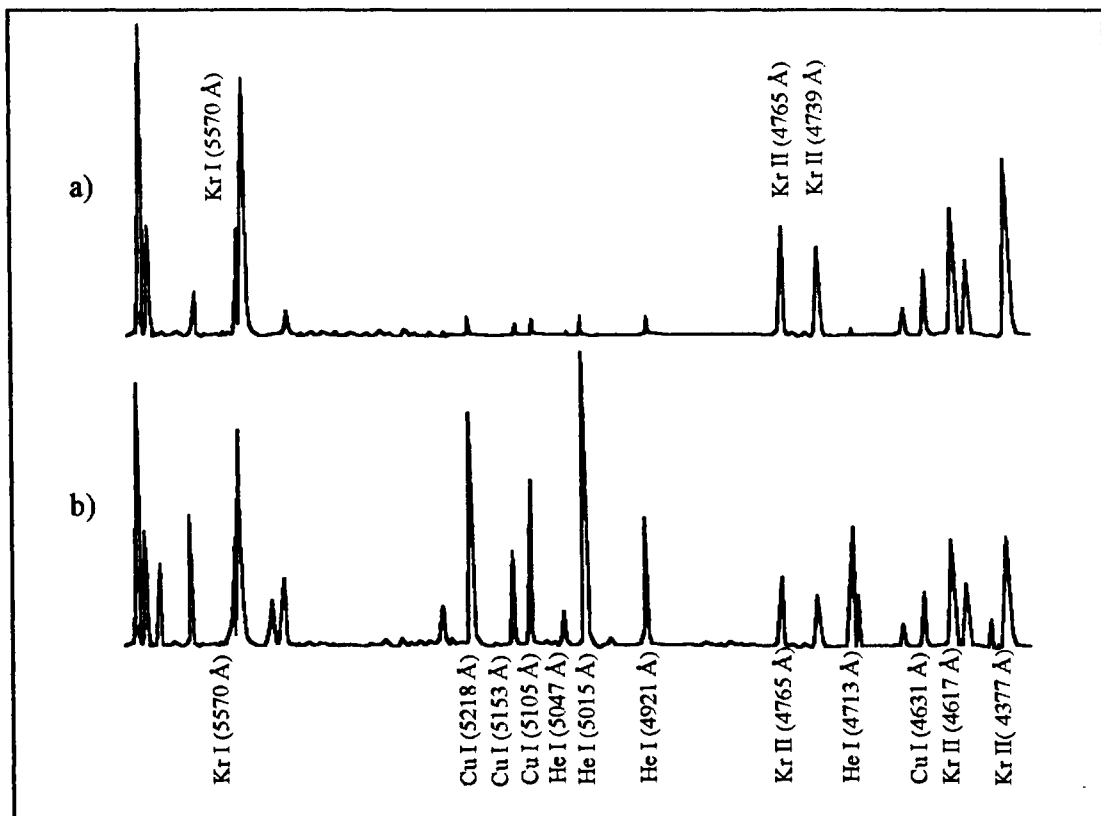


Fig. 4. The line spectra emitted in : a) Kr (1.6 torr);
b) He - Kr mixture (4.2 torr / 0.04 torr)

Another example of radiative process is the asymmetric charge transfer between Ne ions and Cu atoms that appear in the hollow cathode discharge in Ne:



The reactions (1) and (3) represents transfer of excitations processes that leads to the selective excitation of Cu II lines, 5100 Å and respectively 2600 Å, both of laser interest ^{2,3,4}. The detection of these lines in plasma spectrum, even at low intensity, represents important indicators on the radiative processes that take place in plasma, to further perform their amplification by selective excitation.

In many cases the increasing of some particular spectral line intensity require important changes in the design of the tube discharge or in the power supply parameters that imply auxiliary experimental efforts and costs. The analysis of the weak spectral lines by deconvolution, and the identification of the corresponding radiative mechanisms permits a better tuning of the experimental conditions in order to obtain selective excitations.

It was established, by the analysis of the low intensity Cu lines, recovered from the plasma radiation spectrum emitted in a hollow cathode discharge in Ne in DC regime, that in order to increase their selective excitation, higher discharge currents are required. This impose the use of pulsed discharges at high currents. Figure 5 illustrate the role of pulsed discharge on the excitation of Copper spectral lines.

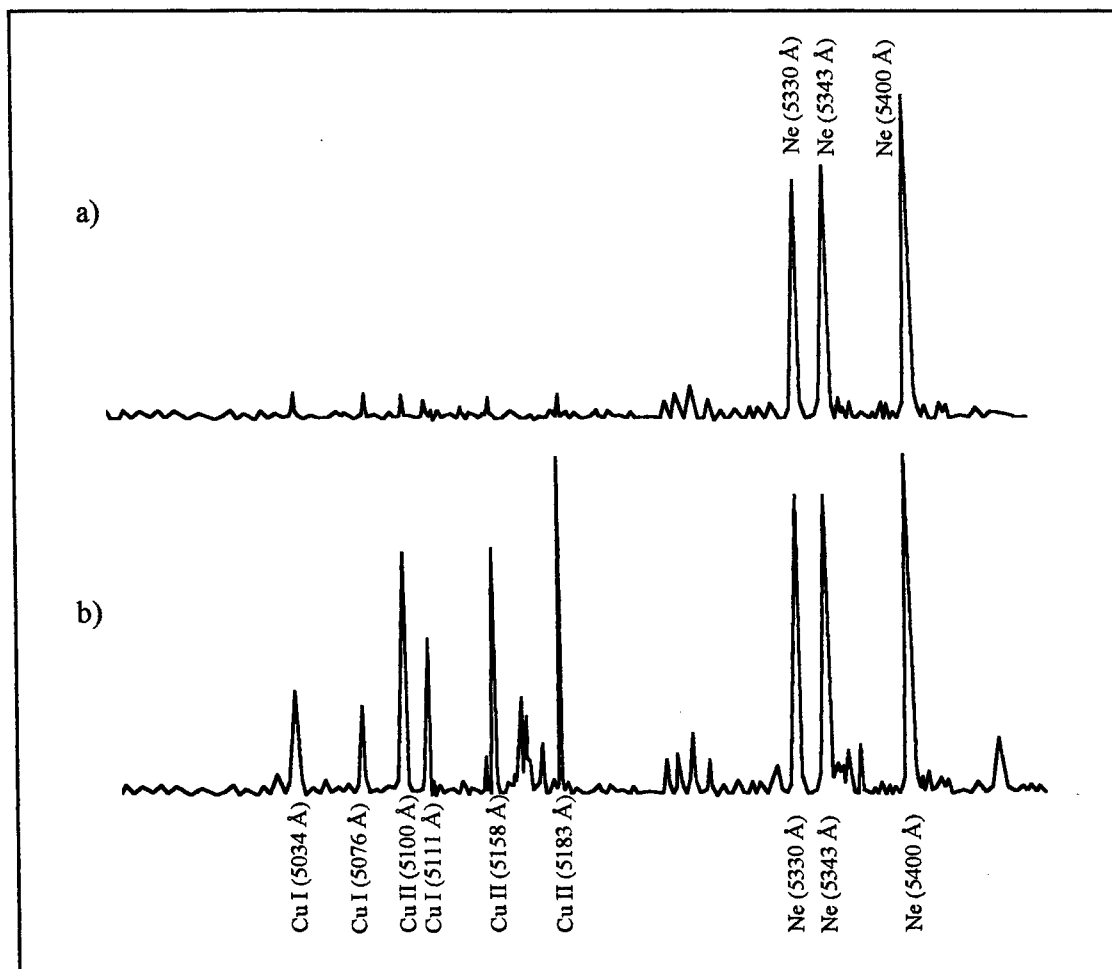


Fig. 5. Role of the pulsed discharge on the excitation of Cu spectral lines:

a) DC regime; b) High current pulses.

4. THE INTENSITY OF SPECTRAL LINES

A characteristic plasma spectrum $I(\nu)$ is a superposition of lines with Voigt profiles with different central frequency ν_m . The Voigt profile f_ν is the result of the convolution between the natural shape of the spectral line and the Doppler and Lorentz collision profiles due to Doppler effect broadening and collisions broadening.

$$I(\nu) = \sum_{m=1}^N I_m \cdot f_{\nu_m}(\nu - \nu_m) = \sum_{m=1}^N I_m \cdot \frac{a_m}{\pi} \cdot \int_{-\infty}^{\infty} \frac{e^{-y^2}}{a_m^2 + (\omega_m - y)^2} dy \quad (4)$$

with:

$$a_m = \frac{\Delta \nu_N + \Delta \nu_C}{\Delta \nu_D} \sqrt{\ln 2} \quad ; \quad \omega_m = \frac{2 \cdot (\nu - \nu_m)}{\Delta \nu_D} \sqrt{\ln 2} \quad (5)$$

I_m is the line intensity and $\Delta \nu_N$, $\Delta \nu_C$, $\Delta \nu_D$ are the line half-width due to natural, collision and respectively Doppler broadening. The parameter a_m depends on the pressure p , temperature T and on the atom or ion spectral line (by C_{m1} , C_{m2} , C_{m3} , C_{m4} , constants):

$$a_m = \frac{C_{m1} + C_{m2}(1 + C_{m3}\sqrt{T}) \cdot p}{C_{m4}\sqrt{T}} \cdot \sqrt{\ln 2} \quad (6)$$

In many cases the Voigt profile could be well approximated by the Gaussian shape of the Doppler profile:

$$f_{\nu_m}(\nu - \nu_m) \rightarrow f_{Dm}(\nu - \nu_m) = 2 \cdot \sqrt{\frac{\ln 2}{\pi}} \cdot \frac{1}{\Delta \nu_D} \cdot e^{-4 \ln 2 \left(\frac{\nu - \nu_m}{\Delta \nu_D} \right)^2} \quad (7)$$

In our numerical simulations we have used spectra generated by formula (4) using different profiles for the spectral lines; most of them are very well approximated by gaussian shapes.

The plasma spectrum obtained with the monochromator and the photomultiplier is recorded on computer through the analog-digital acquisition unit. The digital data form a temporal series $S(t)$, obtained as a result of a convolution process between the spectral intensity $I(\nu)$ and the system transfer function $T(t, \nu)$, according to the following relation:

$$S(t) = \int_{-\infty}^{\infty} I(\nu) \cdot T(t, \nu) d\nu \equiv I(\nu) \otimes T(t, \nu) \quad (8)$$

In general the transfer function is invariant at the frequency translation (for short spectral ranges), and could be approximated with a gaussian. The consequence of the invariance at frequency translation is the transfer function dependence on a single variable, the difference $(t - \nu)$. A univoque correspondence exist between the temporal variable t and the frequency ν (or wavelength λ) as a result of the spectral range scanning by the monochromator ($t \leftrightarrow \nu$).

5. DECONVOLUTION IN THE SIGNAL SPACE

The signal processing require the use of noise filtering, signal smoothing and deconvolution techniques by taking account of the system transfer function $T(t, \nu)$ of the whole experimental chain. Recovery of the real spectral distribution of intensity $I(\nu)$ is made by numerical deconvolution applied to the recorded signal $S(t)$. The commonly used methods are based on the deconvolutions in the frequency space by applying the Fourier transform to the relation (8):

$$\tilde{S}(t) = \tilde{I}(\nu) \cdot \tilde{T}(t, \nu) \Rightarrow \tilde{I}(\nu) = \tilde{S}(t) / \tilde{T}(t, \nu) \quad (9)$$

This method involves the computation of two fast Fourier transforms which impose restrictive conditions on the form of the transfer function and on the value of the signal-to-noise ratio of the experimental chain. The removal of noise effects, is made by cutting off the high frequencies and the low amplitude frequencies from the Fourier spectrum, and determines the elimination of the weak spectral lines.

A deconvolution method that is less sensitive to the transfer function form and to the value of the signal-to-noise ratio is the deconvolution in the signal space. The deconvolution technique developed in what follows is based on the Van Cittert

algorithm⁵, who devised an iterative scheme for recovery of $I(v)$ using operations in the signal space only (as opposed to transform or frequency space). Van Cittert showed that the string I_n , described below, converge to the intensity spectral distribution $I(v)$:

$$I_1 = S(t); I_n = I_{n-1} + [S(t) - I_{n-1} \otimes T(t, v)] \quad (10)$$

$$\Rightarrow I_1, I_2, I_3, \dots, I_n, \dots \xrightarrow{n \rightarrow \infty} I(v)$$

In a previous paper⁸, we have analyzed a modified algorithm developed by Jansson^{6,7}, who introduced a relaxation parameter $\alpha_n(v)$ in the recurrence relation (10), as is indicated in the following relation:

$$I_n = I_{n-1} + \alpha_n(v) \cdot [S(t) - I_{n-1} \otimes T(t, v)] \quad (11)$$

where $y(t)$ represent the amplitude of $I_{n-1}(t)$. The relaxation parameter $\alpha_n(v)$ is dependent on the $I_{n-1}(t)$ value and has the purpose to ensure a better convergence of the I_n string.

As a measure of the convergence speed one use the following function:

$$E_n = \left\{ \frac{1}{N} \sum_{i=1}^N [\alpha_n(v) \cdot (S_i - I_{n-1} \otimes T_i)]^2 \right\}^{\frac{1}{2}} \quad (12)$$

that represent the root mean square of the n -th iteration correction to the previous $(n-1)$ iteration. In the previous relation N represents the total number of points in the temporal series and S_i and T_i are the corresponding values of the signal and transfer function.

6. RESULTS AND DISCUSSIONS

A set of numerical test was completed on spectra generated numerically and on experimental data. We generate numerically transfer functions and spectra combinations that cover a large range of practical situations (lines spectra of different width and shapes, continuous spectra, molecular spectra and superposition of them) and their numerical convolution was performed. After the deconvolution the initial spectra was recovered. The speed of algorithm convergence was analyzed considering its dependence on the relaxation parameter $\alpha_n(v)$, spectrum category $I(v)$ and transfer function form $T(t, v)$.

The function $\alpha_n(v)$ is the key to the success of the deconvolution algorithm. We studied numerically the effect of many $\alpha_n(v)$ functions on the convergence speed of the algorithm. Figure 6 presents some of these functions for which the deconvolution algorithm is rapidly convergent after a small number of iterations. The case c correspond to the algorithm studied by Jansson^{6,7}. We obtain better results using the function presented in Fig. 6, cases a , e and f . The speed of convergence depend on the maximal value α_{max} of the function, increasing with its growth. There are some critical values of α_{max} , over which the algorithm became unstable.

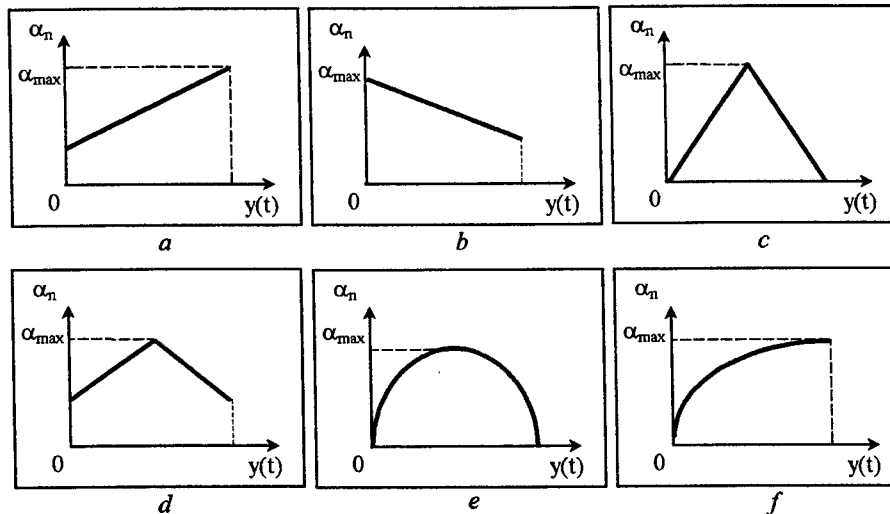


Fig. 6. The parameter of relaxation $\alpha(y)$.

The effect of the spectrum convolution with the transfer function of the experimental chain, involved in the output signal acquisition, is the alteration of the intensity rates between different spectral lines. The deconvolution algorithm presented in this paper restore accurately the original intensities rates between the spectral lines.

Fig. 7 presents the results of a numerical generated signal from an initial spectrum $I(\lambda)$ calculated with relation (4). The signal $S(\lambda)$ was obtained by convolution with a transfer function of gaussian shape with a half-width of 3 Å. The results of the deconvolution after a relatively small number of iterations (80) is shown on Fig. 8. After a higher number of iterations (approximately 300) the deconvoluted spectrum became practically identical with the initial spectrum $I(\lambda)$.

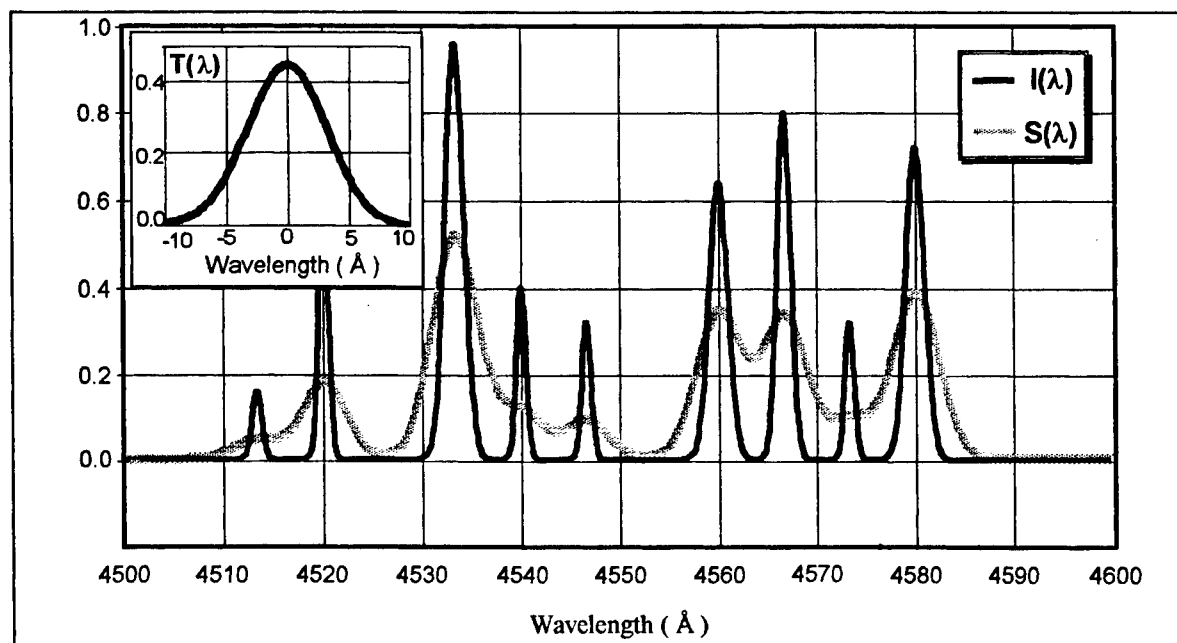


Fig. 7. Numerical simulation results: Input data; $I(\lambda)$ -initial spectrum, $T(\lambda)$ -transfer function, $S(\lambda)$ -convoluted signal

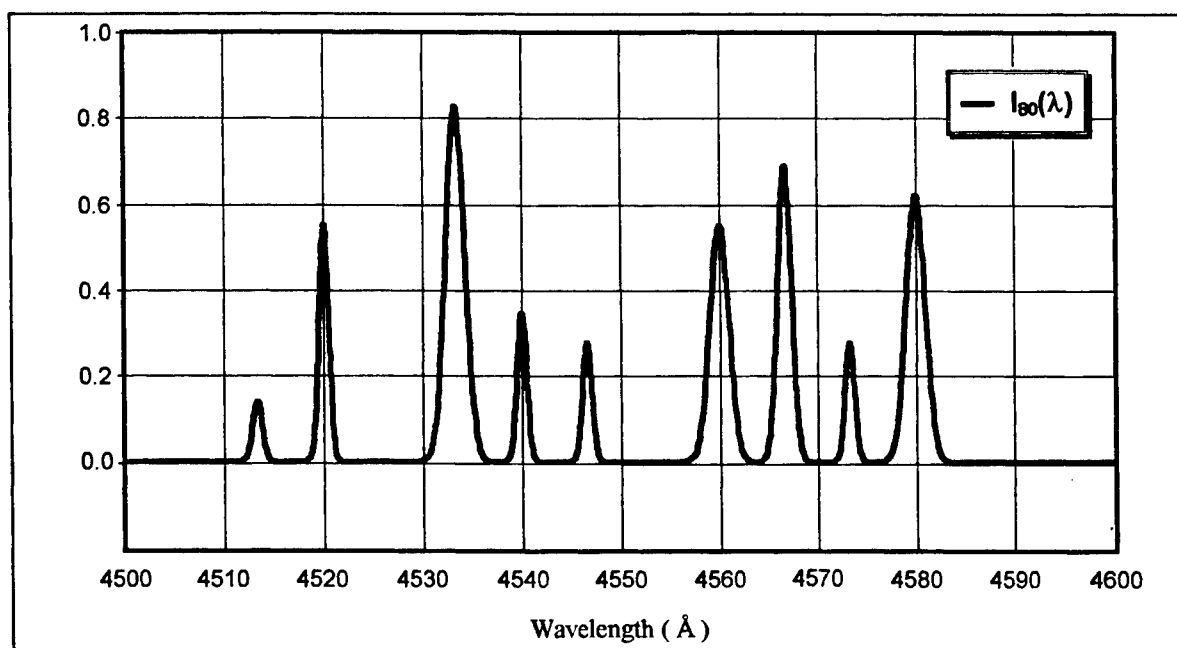


Fig. 8. Deconvolution in process: $I_{80}(\lambda)$ - deconvoluted intensity after 80 iterations

In the case of experimental data processing, the convergence of deconvolution algorithm to real spectra was estimated by comparing the numerical results with the measurements performed on the same spectral source at different resolution of the monochromator grating and at different values of the slit width.

Figure 9 presents the results of the deconvolution of two neighbors spectral lines, one of them being approximately five times weaker in intensity than the other. From the recorded data it is difficult to estimate the presence of a low intensity line in the neighbor of the more intense one. The deconvolution permits also the evaluation of spectral lines half-widths. The transfer function half-width is twice the value of the larger line half-width, so a factor of two in resolution enhancement was achieved.

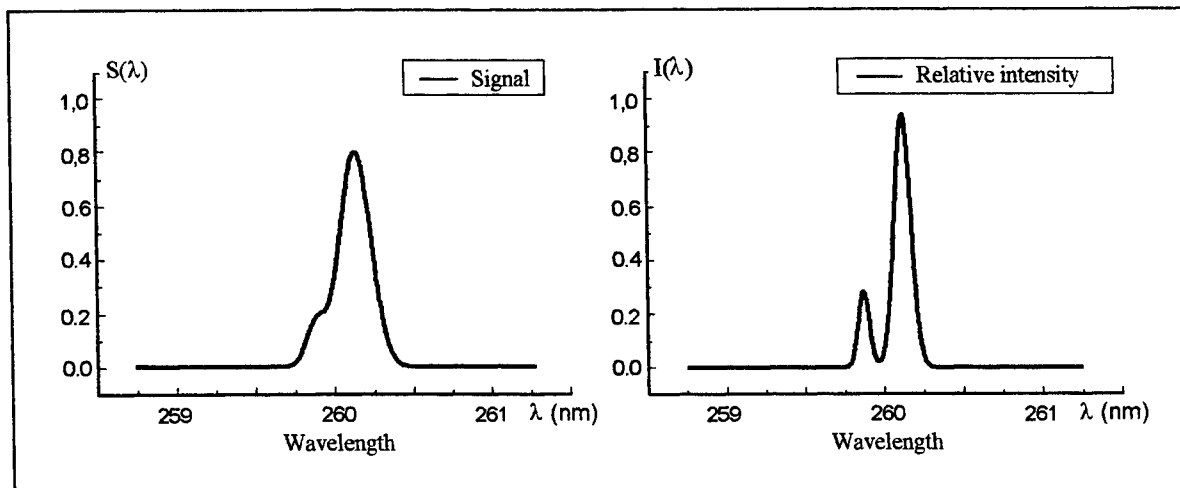


Fig. 9. Deconvolution of two neighbors spectral lines: $S(\lambda)$ -represent the signal recorded from the monochromator; $I(\lambda)$ -represent the relative intensity that results after deconvolution.

The addition of noise to the signal results in limitations of the deconvolution performances under two aspects: first, the final resolution that could be achieved is lower; second, the convergence speed is also lower. Noise effects are diminished by statistical averaging of the signal for every collected data point.

Noise effects were numerically simulated, by summing the signal with randomly generated noise spectra having different values of the signal-to-noise ratio. Results have shown that in order to obtain a 4-5 times enhancement of the resolution by deconvolution is required a signal-to-noise ratio greater than 100. The decrease of signal-to-noise ratio under 100 limits the enhancement of resolution to a factor of 2-2.5 times.

The effect of noise on the deconvolution speed of convergence is shown in Fig. 10.

The algorithm is very efficient for gaussian type transfer functions. Its efficiency become lower for transfer function that differ substantially from gaussian shape. For these situations a modified algorithm have to be used that start with a different initialization of the string I_n .

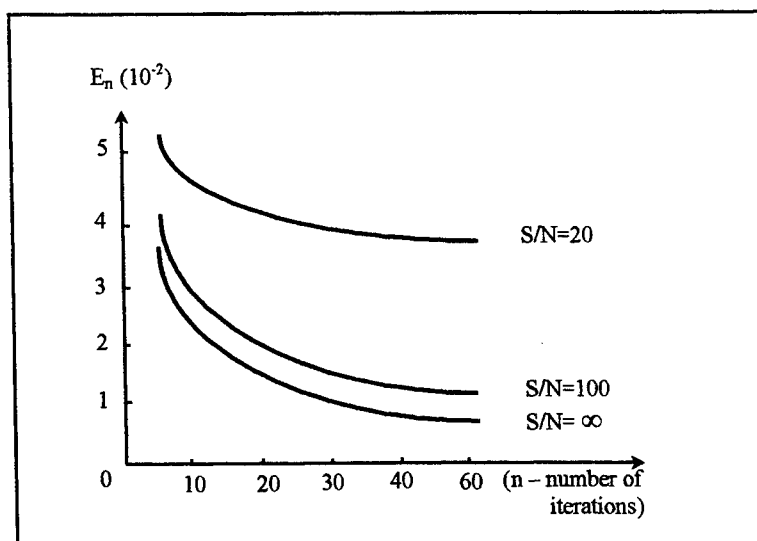


Fig. 10. Root-mean-square correction E_n for different signal-to-noise ratio, as a function of the iteration number.

7. CONCLUSIONS

The enhancement of the spectral lines intensity by selective excitation of atomic and ionic lines of Copper vapor from a hollow cathode discharge require the accomplishment of particular experimental conditions. Their inspection requires experimental efforts and costs. In order to reduce them, experimental investigations tools have to be developed. One of these is the accurate analysis of the spectral data by efficient deconvolution techniques.

We have developed a numerical deconvolution method of the low amplitude spectral lines. In many spectral investigations of plasma radiation the low intensity spectral lines are important indicators on some particular radiative processes like the excitations by second kind collisions (asymmetrical charge transfer and resonant transfer of excitation energy). Their identifications permit the tuning of the discharge parameters to obtain selective excitations of plasma ions. Deconvolution techniques commonly used in plasma spectroscopy require the fast Fourier transform. These impose restrictive conditions on the form of the transfer function and on the value of the signal-to-noise ratio. Removals of the noise effects, performed by cutting off the high and the low frequencies with low amplitudes, induce the elimination of the weak spectral lines. The deconvolution technique developed in this paper is not affected by this inconvenient. It is based on an algorithm developed by Van Cittert and Jansson, who use an iterative schema to recover the spectral lines shape by using operations in the signal space.

The method permits the recovering of the spectral lines half-width and shape, and of the intensity rates between different spectral lines.

The noise that could affect the signal is reduced by statistical average of every recorded point from the emission spectrum. Even if the noise induce limitations in the speed of convergence of the algorithm and in the maximal resolution that could be attained by deconvolution, the method proved to be efficient and versatile.

8. ACKNOWLEDGMENTS

Part of this paper was supported by the National Council of the University Scientific Research by Grant No. 989/1997.

9. REFERENCES

1. I. Iova, I. Chera, M. Băzăvan and I. Gruia; *XX Int. Conf. Ionized Gases*, Pisa, Italy 1991.
2. I. Chera, I. Iova, M. Ganciu-Petcu, I. Gruia and C. Diplășu; *Rev. Roum. Phys.*, Tome 37, No 1, P. 31-39, 1992.
3. I. Iova, I. Chera, I. Gruia, Gh. Ilie and M. Băzăvan; *Romanian Reports in Physics*, Vol. 46, Nos. 7-8, P. 619-626, 1994.
4. I. Iova, Gh. Ilie, M. Băzăvan, C. Duțescu and I. Chera; *Nat. Conf. of Physics*, Iași, 1992.
5. P.H. Van Cittert; *Z. Phys.* 69, 298, 1931.
6. P.A. Jansson; *J. Opt. Soc. Am.* 60, 184, 1970.
7. P.A. Jansson, R.H. Hunt and E. K. Plyler; *J. Opt. Soc. Am.* 60, 596, 1970.
8. I. Iova, S. Levai, Gh. Ilie, M. Băzăvan, I. Gruia, M. Brașoveanu and M. Vlaicu; *Optoelectronica*, Vol. 4, No. 2, P. 69-72, 1996.

Formation of nonlinear optical MQD (Metal Quantum-Dot) in waveguides and modification by high power laser irradiation

G. Battaglin

INFM and Università di Venezia, Dipartimento di Chimica Fisica, Calle Larga Santa Marta 2137, 30123 Venezia, Italy

E. Borsella*, G. De Marchi, F. Gonella, G. Mattei, P. Mazzoldi

INFM and Università di Padova, Dipartimento di Fisica, via Marzolo 8, 35131 Padova, Italy

*permanent address: ENEA, Dip. INN/FIS-SPET, Frascati, Roma, Italy.

A. Quaranta

INFM-Padova and Università di Trento, Dip. di Ingegneria dei Materiali, Via Mesiano 77, 38050 Povo, Trento, Italy

ABSTRACT

Light waveguides were obtained by ion-exchange process in soda-lime glasses. Metal nanoclusters were subsequently formed in waveguides by either low-mass ion irradiation, at energies of 20-2000 keV, or by heating in hydrogen atmosphere at temperatures varying in the range 100-250 °C. Nanoclusters modification induced by pulsed laser irradiation were investigated. The materials were characterized by secondary ion mass spectrometry and nuclear techniques, such as Rutherford backscattering spectrometry, to determine concentration depth-profiles, and by transmission electron microscopy for the nanocluster detection and size evaluation. Optical analyses were performed to evidence linear and nonlinear properties.

keywords: Glass waveguides, nonlinear optical materials, metal quantum-dot composites.

1. INTRODUCTION

Nonlinear optical materials are an essential ingredient of functional photonic devices for optical communication, sensing, and computing¹⁻⁵. Understanding the correlation between material processing and nonlinear optical properties is especially critical for the development of advanced nonlinear optical materials for photonic devices. The main properties of such materials for application in such devices include picosecond or shorter response times, low power switching threshold, wavelength tunability, thermal stability, low two-photon absorption, high threshold for laser-induced damage, and THz recycling frequency.

In the last few years, composite glasses formed by embedding semiconductor or metal nanoclusters in glass have attracted much attention as promising materials for optoelectronics. This interest is strengthened by the general interest in strongly quantum-confined electronic systems which exhibit striking effects deriving from the increased electronic density of states near the conduction-band edges. For metal nanoclusters-doped composites the term *metal quantum-dot composites* (MQDC) has been introduced⁶ in analogy to multiple-quantum-well devices. Glass researchers have employed various ways to prepare metal-doped glasses, namely, sol-gel processes, quenching and heat-treatments, processes which use porous glasses and, more recently, ion implantation⁶. In particular, such technique has attracted a large interest for the possibility to pattern the materials. The material-related aspects of the above mentioned metal colloids, in particular the development of the preparation techniques and the chemical, structural and optical characterization, have been largely studied, but the so-called architecture of systems for optical information processing has been not focused.

In this paper, we present the results obtained in our group, in cooperation with external laboratories, on metal, in particular silver, nanocluster formation by using either low-mass irradiation or annealing in hydrogen atmosphere of light waveguides, prepared by the ion-exchange technique. Such two new methodologies give a promising connection between nonlinear optical material preparation and device developing. Modification induced by pulsed laser irradiation are also presented.

2. NONLINEAR PROPERTIES OF METAL-DOPED GLASSES

Optical nonlinearity of glasses results mainly from three effects: thermal effect, electrostriction and nonlinear polarization⁷. The first two depend on the changes in the density and polarizability due to thermal and electric fields, respectively, while the latter is connected with the nonlinear distortion of the electron orbits. The relative contribution of each effect to the nonlinear response will depend, in turn, on the time scale of the pulse duration of the laser beam. Nonlinearity in glasses is in general quite small, but the nonlinear response may be enhanced of several orders of magnitude by introducing small metal clusters. The nonlinearity in metal-doped glasses is mostly due to third-order processes described by the real part of the third-order electric susceptibility, $\chi^{(3)}$, involving different four-wave mixing processes⁸. A particular four-wave mixing process in which all the frequencies involved are the same is referred to as the optical Kerr effect, which is the most important for the applications in all-optical switching devices¹.

The origin of this nonlinear response may be ascribed, in the case of small metal particles, to the intraband, direct interband and hot electron transitions⁹. The third-order term originated from the conduction electrons is described by the quantum size effect¹⁰. Nonlinear responses in the 5-ps time scale have been observed and described in terms of quantum size effect firstly by Hache and co-workers¹¹. The confinement of the conduction electrons, which can be classically described in terms of limited mean free path, gives rise to an expression for $\chi^{(3)}$ varying roughly as a^{-3} , where a is the radius of the metal sphere. Interband transitions between the d -levels and the conduction band also contribute to the nonlinear response of a metal-doped glass. This process is resonant and size-independent, corresponding to the saturation of the two-level transition between the bands. A third contribution is ascribed to the hot electrons created by the strong absorption near the surface plasmon resonance, which, in turn, depends on the particle size, leading to a modification of the absorption coefficient of d -electrons. In the case of silver the interband contribution is expected to be the major one⁹. In addition, an effective-medium theory approach¹² relates the third-order susceptibility of metal clusters embedded in a linear dielectric medium to the composite effective susceptibility by a local-field enhancement factor.

The nonlinear refractive index n_2 is usually defined by one of the two alternative relations: $n = n_0 + n_2 |E|^2$, $n = n_0 + n_2 I$, where E is the field amplitude, I the intensity averaged over a period and n_0 the linear refractive index. n_2 and n_2^I are related to the real part of $\chi^{(3)}$.

Nonlinear optical materials based on glasses are intrinsically attractive for photonic-device applications owing to their high transparency, ease of fabrication, durability and thermomechanical stability. The MQDC discussed in this paper present two additional factors. One is the increase in oscillator strength near the band edge, characteristic of reduced-dimensional structures and responsible for the lower operating thresholds of optical devices, such as lasers. The second is the inherent compatibility of the materials and fabrication processes with silicon-based electronic materials, with interesting perspectives for hybrid devices. However, realistic correlation of the optical and electronic properties of these materials with the known engineering requirements for photonic and optoelectronic devices is just beginning. The capability of processing light signals without converting them to electronic form should, in principle, allow all-optical devices to operate in a time range inaccessible to electronics. The fastest electronic components now available (GaAs HEMT devices, for example) exhibit switching speeds in the 20-picosecond range at switching rates in the 50-GHz range. The shortest light pulses can be generated in the femtosecond range in the visible to near-IR portions of the spectrum; current pulse repetition frequencies in these devices, however, are only in the 100-MHz range. Furthermore, all-optical switches operating at high pulse-repetition frequencies are the basis for developing optical parallel data processing systems and optical time domain multiplexing transmission systems¹³. High switching speeds, however, must be coupled with low switching energy to allow high packing densities in optoelectronic or photonic devices. Figure 1, adapted from Ref. 14, compares a variety of electronic and photonic materials with respect to the switching energy and switching speed of devices^{6,15}. Nanocluster composites, indicated in the hatched area, show switching speeds faster than any material except PTS, which undergoes a long-term photochemical damage. Where semiconductor quantum dots have non-resonant responses of fractions of a nanosecond, metallic quantum dots have resonant responses of the order of order 10 picoseconds, and may actually be faster. In considering the application potential of glass-based MQDC in optoelectronics, it will also be necessary to evaluate the thermal effects introduced by optical absorption. In a recent paper, Borrelli *et al.*¹⁶ discussed the advantage of non-resonant nonlinear effect over the absorption-based resonant one, in terms of response time. In the first situation, the response time may be determined only by the electronic contribution, and hence can respond at optical frequency rates, while, in resonant situation, is controlled by the lifetimes involved in the transitions, as fast as picoseconds. Also if picosecond time response is adequate for many devices, although not as fast as that of non-resonant situation, the heating and cooling may change the state of the resonant system in a random fashion. These remarks were in context of comparing the high values of $\chi^{(3)}$ obtained in absorption-based resonant systems, such as metal-colloids in glass, with the values (10^{-3} - 10^{-4} times smaller) for non-resonant systems. This is a research area that must be addressed in order to make predictions on device reliability.

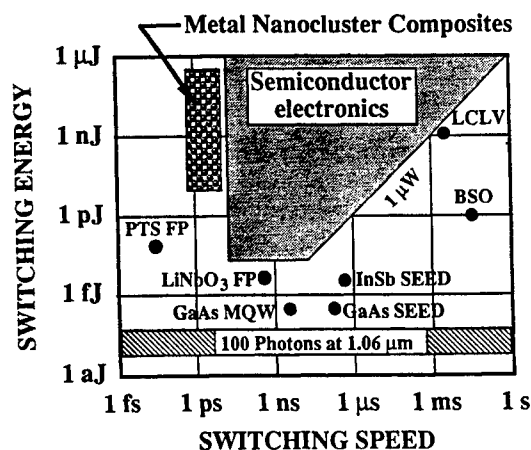


Fig. 1. Chart showing the switching speed and switching energies of various semiconductors and optical materials^{6,15}.

Indeed, the advantages of the high speed of metal quantum dots cannot be realized in device configurations unless substantial reductions in nonlinear threshold energy can be attained, since presently measured switching energies at this speed place the MQDCs above the line which represents the generally accepted limitation on optical switching due to the thermal load on the material at high pulse repetition frequencies¹⁷.

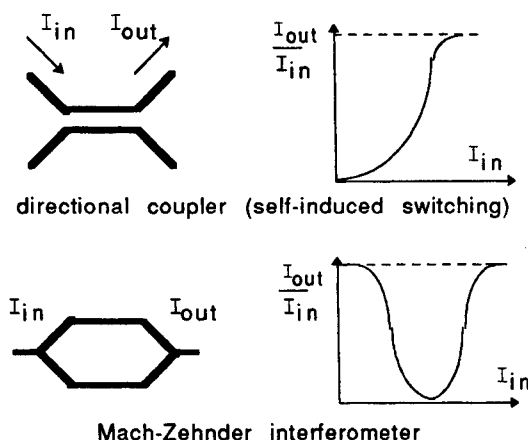


Fig. 2. Two optical switching devices scheme, with the response in the case of linear (dashed lines) and nonlinear (solid lines) materials. The nonlinear behavior correspond to the situation in which one of the two channels is made of nonlinear material.

A rough estimate of $\chi^{(3)}$ required in the case of the Mach-Zehnder interferometer switch gives a value of 10^{-9} esu, assuming a laser beam of 50 mW being launched into a waveguide having 50 mm² cross-sectional area and an effective length of 10 mm to cause a phase change of π in the beam¹⁸.

The large values of $\chi^{(3)}$ achievable in metal nanocluster-doped glasses make them an obvious choice for devices with short path length guides; the non-resonant systems seem to be practicable only for fiber applications. However, these large values are only interesting if constraints on switching energy at high pulse repetition frequencies can be satisfied. The reductions in switching energy to the femtojoule range, reduction of linear optical absorption to the lowest practicable level, and exploitation of quantum size effects can help to make the MQDC more useful in photonics and electro-optics. The reduction to femtojoule levels of the threshold for the nonlinear refractive effects may be achieved by decreasing the amount of inhomogeneous broadening in the composite due to the spread in cluster size, exploiting the enhancement of $\chi^{(3)}$ with decreasing size for intraband transitions, or a combination of both.

Nonlinear switching devices are based on optical waveguiding structures for they provide strong beam confinement in prescribed patterns⁴. In these devices, the intensity of an optical signal is used as the parameter that causes switching

between two output channels that performs logic operations. In Figure 2 two typical examples of all-optical devices are illustrated, together with their response to optical power without (dashed lines) and with (solid lines) nonlinear effect.

3. EXPERIMENTAL

The composition of the glass used in the experiments is (wt%): 69.6 SiO₂, 15.2 Na₂O, 1.8 Al₂O₃, 6.5 CaO, 5.1 MgO, 1.1 K₂O, 0.4 SO₃, 0.2 TiO₂, 0.1 trace-amounts of Fe₂O₃, As₂O₃ and Cs₂O. Glass samples, preheated, were ion-exchanged in a molten salt bath of AgNO₃:NaNO₃ for silver exchange, and of either pure CuCl or CuSO₄:Na₂SO₄ eutectic (46:54 molar ratio) for copper exchange. Exchange temperature of 320 °C was set for silver, while the copper exchange process was carried out at T=585 °C in the case of sulphate bath and at T=550 °C in the case of CuCl. The preheating and the small volume of the samples assured isothermal exchange conditions for short times of treatment. Two different experiments were performed on ion-exchanged samples. Some waveguides were irradiated by He⁺ ions at energies varying from 100 keV to 2 MeV. Other waveguides were heat-treated in a quartz tube, first evacuated to 10⁻⁶ torr pressure, then introduced into a furnace at the working temperature. H₂ flux at a pressure slightly greater than atmospheric pressure was set. Treatments times were between 2 and 12 hrs., with temperatures in the range 120 to 300 °C.

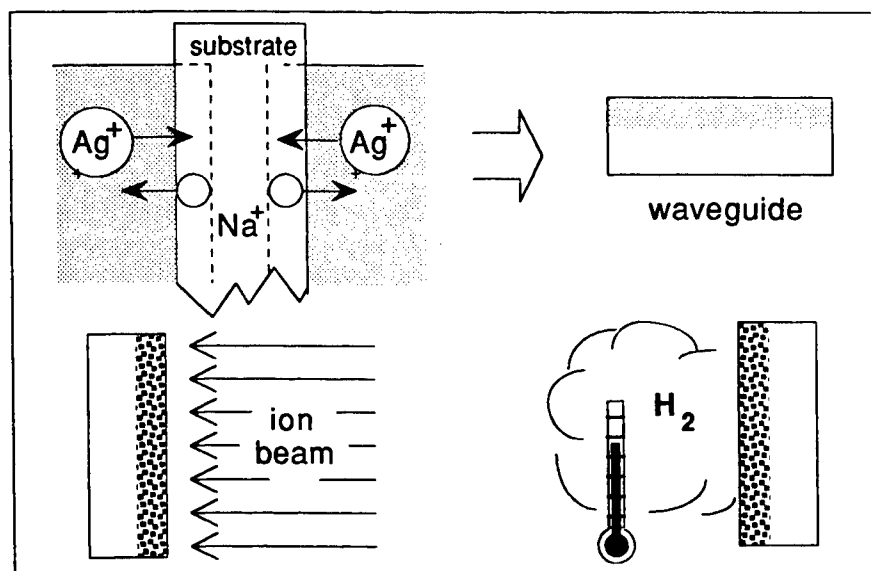


Fig. 3. Two-step methodologies for metal cluster formation in ion-exchanged waveguides.

Some samples, as-exchanged and after He irradiation, were irradiated by a Q-switched Nd:YAG laser operated at both 1064 nm and 532 nm of wavelength. Frequency doubling was obtained using a BBO crystal. The pulse duration was 10±1 ns for both wavelengths. The silver, copper and sodium profiles were determined by Rutherford Backscattering Spectrometry (RBS), while the hydrogen profile was obtained by Elastic Recoil Detection Analysis (ERDA). For both techniques, a ⁴He⁺ beam at the energy of 2.2 MeV was used at National Laboratories INFN-Legnaro. Secondary Ion Mass Spectrometry (SIMS) analyses were also performed with a CAMECA IMS-4f spectrometer. The absolute calibration of the concentration scale was set using the experimental RBS total dose values for silver and the ERDA results for hydrogen. Refractive index profiles were reconstructed by an inverse WKB method from the set of effective indices corresponding to the guided modes¹⁹. The effective indices were determined by m-lines spectroscopy. Optical absorption spectra were determined in the wavelength region from 250 to 600 nm, by a Cary 5 UV-VIS-NIR dual-beam spectrophotometer. Samples for transmission electron microscopy (TEM) were prepared by cutting 3 mm diameter discs from the implanted area with a slurry drill, mechanical grinding of the disc from the backside to a thickness of about 20 µm. The final thinning to the electron transparency was achieved by planar backthinning by ion milling with an Ar gun at 5 keV. To minimize ion damage, samples were cryogenically cooled during ion milling. The prepared samples were examined in a Philips CM30 TEM, operating at 300 kV. Nonlinear refractive index was obtained by Z-scan measurements, made with a mode-locked cavity dumped dye laser pumped by a Nd:YAG laser, for 6 ps pulse duration and in the 560-600 nm wavelength range.

3.1 Cluster formation

The sequential methodologies used to prepare silver or copper cluster-doped glass waveguides following two-step processes are sketched in Fig. 3. With both these methodologies, metal aggregation in nanoclusters is promoted, obtaining waveguides with a significant enhancement of the nonlinear refractive index. Figure 4a shows an example of modal (m-lines) spectroscopy for an $\text{Ag}^+ - \text{Na}^+$ exchanged waveguide supporting 9 modes at 632.8 nm of wavelength. Figure 4b,c gives the corresponding refractive index profile, obtained by a suitable WKB method, and compared to Ag distribution.

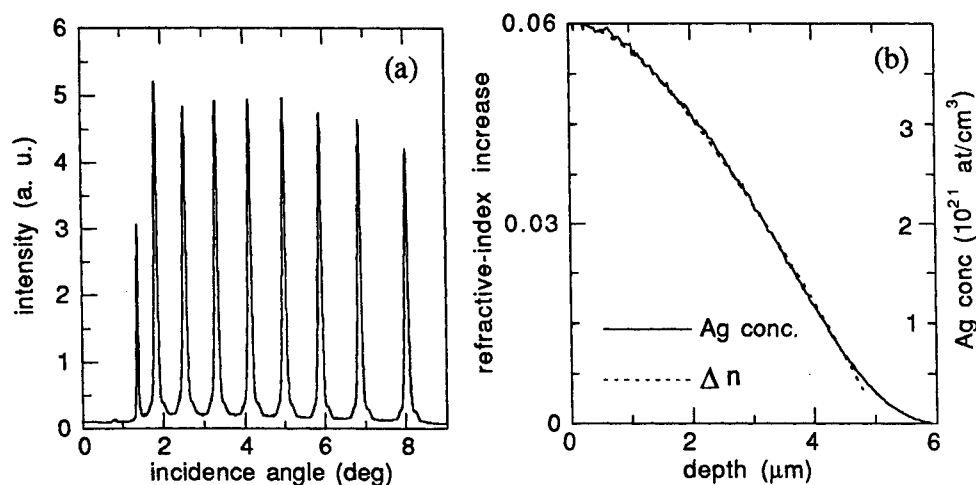


Fig. 4. Guided modes (a) and index (b) and concentration profiles (c) of an Ag-exchanged waveguide.

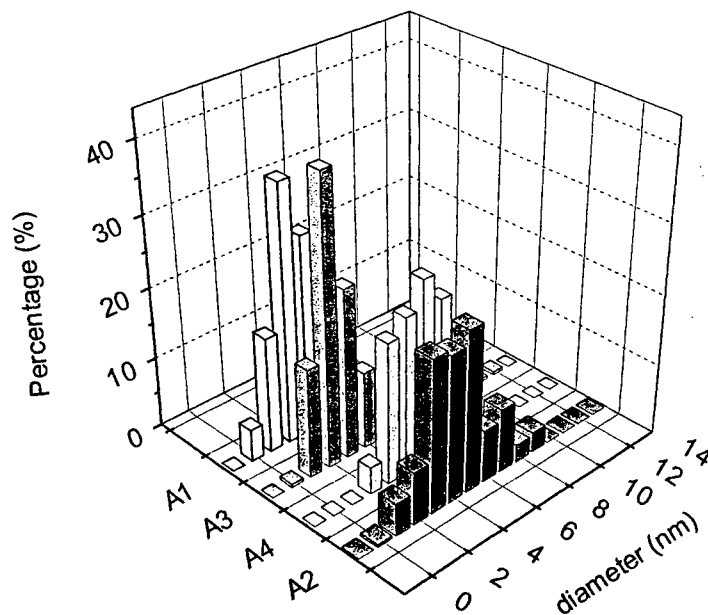


Fig. 5. Size distribution of Ag nanoclusters embedded in ion-exchanged waveguides, for different exchange process conditions, after annealing in hydrogen atmosphere, at the following conditions: samples A1 and A2, 160°C, 5h; sample A3, 180°C, 12h; sample A4, 250°C, 5h. Ag/Na ratio at the surface is 16%, 67%, 19% and 19% for A1, A2, A3 and A4, respectively. The mean diameter of the clusters is 3.2 ± 1.1 , 5.1 ± 1.7 , 3.7 ± 1.5 and 5.5 ± 1.6 for A1, A2, A3 and A4, respectively.

3.2 Annealing in hydrogen atmosphere

Annealing of waveguides in hydrogen atmosphere causes a near-surface precipitation of metallic silver to form nanometer-size clusters with good uniformity in size and spatial distribution, as shown in Fig. 5, where the size distribution of the Ag clusters embedded in glass is reported for different exchange conditions. The ratios between Na and Ag in as-exchanged waveguide are indicated. Clusters, of spheroidal shape, exhibit a fcc structure, are randomly oriented and their diameters are about 2-4 nm for the lowest annealing temperature sample and 4-6 nm for the highest temperature. The samples exhibit an optical absorption band peaked at about 410 nm, typical of absorption of metallic silver nanoclusters due to the surface plasmon resonance (SPR)²⁰. The SPR frequency depends on metal-particle size through the dielectric response function of the metal. This absorption band is consistent with predictions of the Mie theory for silver nanoclusters having radius of the order of a few nanometers.

Hydrogen permeation and ion-exchange between hydrogen and sodium, which remains in the glass matrix after silver for sodium exchange, are steps of the process²¹. A further step is the diffusion of silver towards the surface with an activation energy, 22 kcal/mole, close to that measured for silver-sodium interdiffusion in glasses of comparable composition. Silver migration cannot be simply ascribed to a direct interaction with hydrogen, but rather to a more complex process involving a charge balancing mechanism during hydrogen-sodium ion-exchange. Hydrogen permeation exhibits an activation energy of about 15 kcal/mole. Moreover, the formation of hydroxyl groups is confirmed by the presence of a band at about 3500 cm⁻¹ in the infrared absorption spectra.

3.3 Low-mass ion irradiation

Irradiation of exchanged samples were performed by using He⁺ ion beams. The irradiation current and irradiation time were varied to study the role of deposited energy rate and process time. The irradiation current density is a critical parameter for the precipitation process. The metal diffusivity, the deposited energy distribution and defect migration would play an important role in determining the final concentration distribution of colloids. At present, it is not possible to separate the contributions of the thermal effects, due to local heating, and the radiation-enhanced metal diffusivity to the particles precipitation.

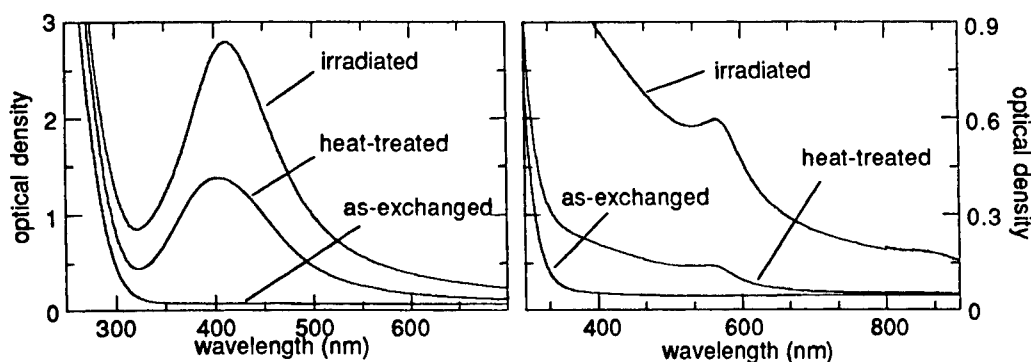


Fig. 6. Optical absorption spectra of silver- and copper-doped waveguides, before and after irradiation with helium beams and before and after treatments in H₂ atmosphere.

Bright-field and dark-field TEM imaging were used to characterize the shape and geometrical structure of nanoclusters. The cluster distribution is uniform throughout the irradiated region up to the projected range of the implanted He⁺ ions. The mean clusters radius in the irradiated region is in the range of 1-3 nm, depending on the irradiation parameters and metal ion type²²⁻²⁴. Figure 6 shows the optical absorption spectra of silver- and copper-doped waveguides, before and after irradiation with helium beams in the MeV energy range and before and after treatments in H₂ atmosphere. Surface plasmon resonance peaks (at 410 nm for Ag and 560 nm for Cu clusters) are evident for both preparation methods, indicating the presence of metallic clusters with radii of a few nanometers.

Measurements of the optical nonlinear features of the samples were performed by the Z-scan technique¹⁵. Third-order susceptibility measurements for metal nanocluster-doped samples gave positive values of the intensity-dependent refractive index n_2 up to 10⁻¹³ m²/W, corresponding to a value of about 6x10⁻⁸ esu. These values are comparable with those reported in literature for silver or copper-implanted silica⁶. It is noted that the n_2 value measured with a pulse duration

of 100 ps is almost two order of magnitude higher than the value measured for 6 ps pulse duration, due to the contribution of thermal effects.

4. CLUSTER MODIFICATION BY LASER-BEAM INTERACTION

Third-order susceptibility measurements for silver nanocluster-doped samples exhibit positive values, that turn into negative values after repeated measurements. This peculiar behavior indicates that, when exposed to high optical power densities, silver tends to modify the chemical environment, possibly changing permanently its oxydation state. Glasses containing silver nanoclusters were laser-treated on larger area, 3 mm in diameter, by using a Q-switched Nd:YAG laser operated at both 1064 and 532 nm of wavelength, with a pulse duration of about 10 ns. After a single pulse irradiation above an energy density threshold value, $E^* = 0.3 \pm 0.1 \text{ J/cm}^2$ for $\lambda = 532 \text{ nm}$ and $E^* = 5 \pm 1 \text{ J/cm}^2$ for $\lambda = 1064 \text{ nm}$, the irradiated region became nearly transparent. The SPR optical absorption peak was dramatically reduced. Cluster-size distribution of a helium irradiated silver-exchanged soda-lime glass sample, subsequently irradiated by a laser pulse at $\lambda = 532 \text{ nm}$ and $E = 0.5 \text{ J/cm}^2$, is reported in Fig. 7 before and after laser irradiation.

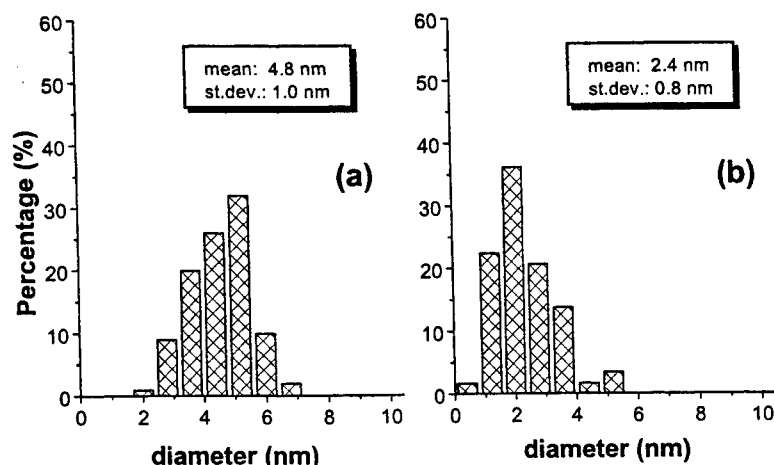


Fig. 7. Size distribution of Ag nanoclusters in an ion-exchanged/ion-irradiated sample before (a) and after (b) laser irradiation with 0.5 J/cm^2 at $\lambda = 532 \text{ nm}$ ²⁵.

A large reduction of the cluster size, from the mean diameter value of about 5 nm before to a mean value of about 2.5 nm after laser irradiation is evident. This is accompanied by a corresponding increase in the number of clusters, being the total silver concentration constant, as determined by RBS analysis. The increasing ratio between the number of surface and bulk atoms with decreasing cluster size favours silver-oxygen with respect to silver-silver bonds, as evidenced by X-ray Photoelectron Spectroscopy (XPS) and X-ray-Excited Auger Electron Spectroscopy (XE-AES) measurements²⁵. After laser treatment the α parameter (binding energy of XPS $\text{Ag}3d_{5/2}$ and kinetic energy of AES $\text{AgM}_{5\text{NN}}$ peak) changed from $720.3 \pm 0.2 \text{ eV}$, close to the value of metallic silver, to $719.1 \pm 0.2 \text{ eV}$, in agreement with the α value of the Ag_2O standard. Besides the fragmentation of the silver clusters formed in the ion-irradiated region, we observed that the laser irradiation is also effective in promoting cluster formation in as-exchanged region, where there are present few small clusters with a mean diameter of about 1.5 nm. In these regions (without low-mass ion irradiation) laser irradiation causes the formation of small nanocluster, about 2.5 nm in diameter. In this case, light induces nucleation and growth depending on different mechanisms. Such results suggest interesting future possibilities for laser patterning of nonlinear waveguide systems.

5. CONCLUSIONS

Metal nanoclusters are formed in soda-lime glasses by different methods. From the point of view of nonlinear optical material fabrication, the investigated techniques promise to be suitable for designing nonlinear devices with performances based on nonlinear metal-doped glasses. More research is necessary to reach a cluster size uniformity and to control the cluster stability during laser irradiation.

6. REFERENCES

1. T. Kobayashi, "Introduction to nonlinear optical materials", *Nonlinear Optics* **1**, 91-117 (1991).
2. E.M. Vogel, "Glasses as nonlinear photonic materials", *J. Am. Ceram. Soc.* **72**, 719-24 (1989).
3. S.R. Friberg and P.W. Smith, "Nonlinear optical glasses for ultrafast optical switches", *IEEE J. Quantum Electron.* **QE-23**, 2089-94 (1987).
4. G.I. Stegeman and R.H. Stolen, "Waveguides and fibers for nonlinear optics", *J. Opt. Soc. Am.* **B6**, 652-62 (1989).
5. K.W. DeLong, A. Gabel, C.T. Seaton and G.I. Stegeman, "Nonlinear transmission, degenerate four-wave mixing, photodarkening, and the effects of carrier-density-dependent nonlinearities in semiconductor-doped glasses", *J. Opt. Soc. Am.* **B6**, 1306-13 (1989).
6. P. Mazzoldi, G.W. Arnold, G. Battaglin, F. Gonella and R.F. Haglund, Jr., "Metal nanocluster formation by implantation in silicate glasses: nonlinear optical applications", *J. Nonlinear Opt. Phys. Mater.* **5**, 285-330 (1996).
7. Gan Fuxi, *Optical and Spectroscopic Properties of Glass*, Springer-Verlag, New York, 1992.
8. P.N. Butcher and D. Cotter, *The Elements of Non-linear Optics*, Cambridge University Press, Cambridge, 1990.
9. F. Hache, D. Ricard, C. Flytzanis and U. Kreibig, "The optical Kerr effect in small metal particles and metal colloids: the case of gold", *Appl. Phys.* **A47**, 347-57 (1986).
10. W.P. Halperin, "Quantum size effects in metal particles", *Rev. Mod. Phys.* **58**, 533-606 (1986).
11. F. Hache, D. Ricard and C. Flytzanis, "Optical nonlinearities of small metal particles: surface-mediated resonance and quantum size effects", *J. Opt. Soc. Am.* **B3**, 1647-55 (1986).
12. J.W. Haus, N. Kalyaniwalla, R. Inguva, M. Bloemer and C.M. Bowden, "Nonlinear-optical properties of conductive spheroidal particle composites", *J. Opt. Soc. Am.* **B6**, 797-807 (1989).
13. W. Nie, "Optical nonlinearity: phenomena, applications, and materials", *Adv. Mater.* **5**, 520-45 (1993).
14. B.E.A. Saleh and M.C. Teich, *Introduction to Photonics*, John Wiley, New York, 1992.
15. R.F. Haglund, Jr., L. Yang, R.H. Magruder, III, C.W. White, R.A. Zuhr, Lena Yang, R. Dorsinville and R.R. Alfano, "Nonlinear optical properties of metal-quantum-dot composites synthesized by ion implantation", *Nucl. Instrum. Meth.* **B91**, 493-504 (1994).
16. N.F. Borrelli, B.G. Aitken and M.A. Newhouse, "Resonant and non-resonant effects in photonic glasses", *J. Non-Cryst. Solids* **185**, 109-122 (1995).
17. P.W. Smith, "Photonic switching: present research and future prospects", *SPIE Proc.* **881**, 30-7 (1988).
18. K. Koizumi, "Nonlinear optics, fiber lasers, and micro optics: novel approach of new glasses for optoelectronics applications", *Proc. XVI International Congress on Glass*, vol. 1, ed. A. Durán and J. M. Fernández Navarro, *Bol. Soc. Esp. Cerám. Vidrio* **31-C**, 45-59 (1992).
19. P.K. Tien, "Integrated optics and new wave phenomena in optical waveguides", *Rev. Mod. Phys.* **49**, 361-420 (1977).
20. U. Kreibig and M. Vollmer, *Optical Properties of Metal Clusters*, Springer, Berlin, 1995.
21. G. De Marchi, F. Caccavale, F. Gonella, G. Mattei, P. Mazzoldi, G. Battaglin and A. Quaranta, "Silver nanoclusters formation in ion-exchanged waveguides by annealing in hydrogen atmosphere", *Appl. Phys. A* **61**, 403-7 (1996).
22. F. Caccavale, G. De Marchi, F. Gonella, P. Mazzoldi, C. Meneghini, A. Quaranta, G.W. Arnold, G. Battaglin and G. Mattei, "Irradiation-induced Ag-colloid formation in ion-exchanged soda-lime glass", *Nucl. Instrum. Meth.* **B96**, 382-6 (1995).
23. G. Battaglin, G. De Marchi, F. Gonella, E.J. Knystautas, P. Mazzoldi and C. Meneghini, "Non-linear glasses by metal cluster formation: synthesis and properties", *J. Non-Cryst. Solids* **196**, 79-83 (1996).
24. F. Gonella, E.J. Knystautas, G. Mattei, P. Mazzoldi, C. Meneghini, E. Cattaruzza, F. Garrido and D.H. Osborne, Jr., "Low-mass ion irradiation of glass waveguides for Cu quantum-dots formation", *Nucl. Instrum. Meth.* **B127/128**, 562-5 (1996).
25. F. Gonella, G. Mattei, P. Mazzoldi, E. Cattaruzza, G.W. Arnold, G. Battaglin, P. Calvelli, R. Polloni, R. Bertoncello and R.F. Haglund, Jr., "Interaction of high-power laser light with silver nanocluster composite glasses", *Appl. Phys. Lett.* **69**, 3101-3 (1996).

Optical pumping via velocity-selective state

N. Leinfellner, L. Windholz

*Institut für Experimentalphysik, Technische Universität Graz,
8010 Graz, Austria*

I. E. Mazets

*Ioffe Institute of Physics and Technology,
194021 St. Petersburg, Russia*

ABSTRACT

We present a new scheme of sub-Doppler laser cooling for atoms used in atomic frequency standards, particularly for ^{40}Ca . We perform calculations concerning optical pumping via a velocity-selective state based upon velocity-selective coherent population trapping. Optical pumping on the Raman transition $4^1S_0 - 4^1P_1 - 3^1D_2$ leads to population of the metastable singlet state followed by a decay into the metastable triplet state $4P_1$. The momentum distribution of atoms in that state (with a half-maximum width of about one corresponding photon recoil momentum) is a direct replica of the distribution of atoms in the $3D_2$ state.

Keywords: Coherent optical effects, multiphoton processes, high resolution spectroscopy

1 INTRODUCTION

The design and setup of an atomic frequency standard (AFS) involves elements having transitions with ultranarrow linewidths. Among a couple of elements calcium has become an attractive candidate. Its most abundant isotope ^{40}Ca provides an intercombination transition ($4^3P_1 - 4^1S_0$) in the visible having a natural line width of only 400 Hz with no hyperfine splitting of the ground state. It has been shown that by the use of this transition the precision of frequency measurements can be considerably improved.¹ Using laser cooled and atoms trapped in a magneto-optical trap (MOT) could lead to even lower frequency uncertainties.² In the last decade velocity selective coherent population trapping has been well known to give subrecoil temperatures. Much efforts have been undertaken to spread the range of atoms relevant to this cooling mechanism more widely. The basic principle of VSCPT relies on the creation of a non-coupled dark state out of two states. It can be explained by a destructive interference of coherent optical excitation of two non-decaying ground states in a lambda system^{3,4} or a superposition of two states within a single cascade⁵ or double cascade.⁶

Recently a couple of different VSCPT cooling schemes involving the intercombination transition itself have been theoretically discussed.⁷ In the work cited, laser cooling by VSCPT has been proposed using the ground state 4^1S_0 and the threefold 4^3P_1 state. One of the disadvantages with the establish-

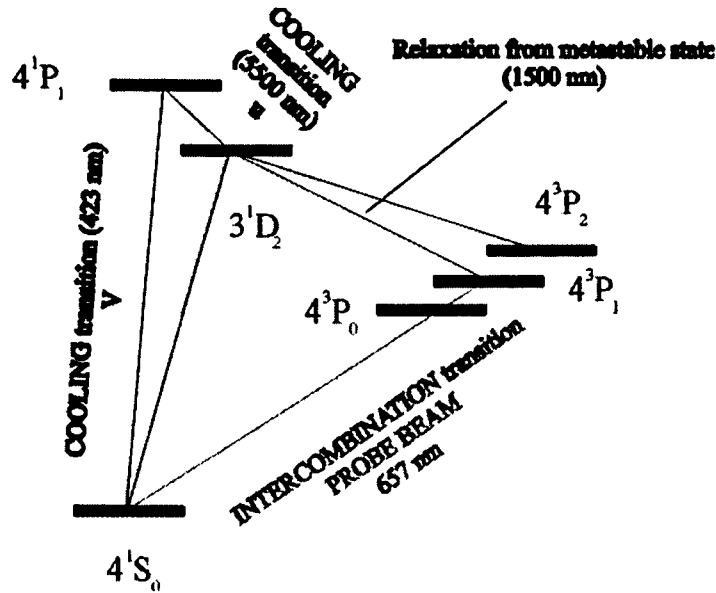


Figure 1: Level scheme of calcium

ment of VSCPT on such a narrow transition as in the case of ^{40}Ca is the slow cooling rate which is proportional to the natural width of the excited state.

The cooling scheme presented in this work is based upon VSCPT on the cascade $4^1S_0 - 3^1D_2 - 4^1P_1$. Numerical simulations show a good confinement of atoms in the momentum space. Final temperatures in the subdoppler range could be achieved.

2 VELOCITY-SELECTIVE PUMPING INTO THE METASTABLE STATE 3^1D_2

Fig.1 shows the relevant energy levels of ^{40}Ca for the cooling mechanism. The level scheme involves the non-degenerated ground state 4^1S_0 , the metastable singlet state 3^1D_2 and an excited state 4^1P_1 . Two possibilities of coherent irradiation can form appropriate dark states: Either two running counterpropagating laser waves having opposite circular polarizations (RW) or standing waves with circular polarization (SW) can create long-living superpositions of states.

It can be easily seen in Fig.2 that the scheme using running waves composes three different VSCPT subsystems. One of them ($m_J = -1, +1 \leftrightarrow m_J = 0$), however, is not populated very much due to small relaxation rates and hence doesn't influence the cooling mechanism.

The transition scheme for irradiation by standing waves is shown in Fig.3. Numerically we restrict ourselves to the case of running waves only. The non-coupled state is the superposition of the states 4^1S_0 and 3^1D_2 . In the RW case the steady-state populations in the cooled fraction of atoms can be

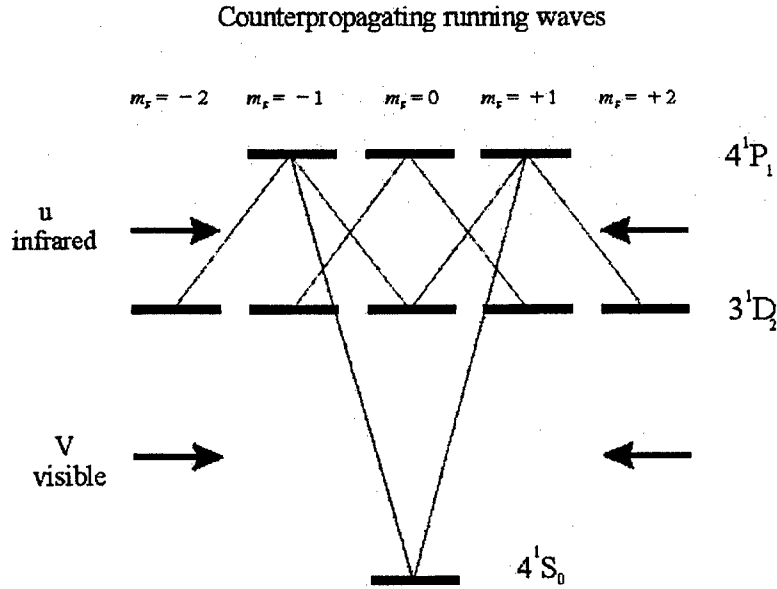


Figure 2: Transition scheme using counterpropagating running waves. In this case there are three VSCPT cooled subsystems present. Two of them are dominating whereas the third one is not significantly populated (see text for explanations). The two pairs of counterpropagating waves are oppositely circular polarized.

written as:

$$\begin{aligned}\Pi(^1S) &= u^2 / (u^2 + V^2) \\ \Pi(^1D) &= 2V^2 / (u^2 + 2V^2)\end{aligned}\tag{1}$$

Here, u denotes the Rabi frequency of the far infrared transition (5500 nm), V is the Rabi frequency for the visible one (423 nm). In the SW case the occurring factors 2 are absent.

In Eq.1 it can be seen that VSCPT can be controlled by the relation between the two Rabi frequencies. As a result atoms can be pumped in either the ground state or in the metastable singlet state.

In the case of $u \gg V$ the 3^1D_2 state is going to be almost depopulated thus filling of the $4^3P_{1,2}$ states is suppressed. Thus it improves the signal to noise ratio of precise frequency measurements using the intercombination transition $\lambda = 657\text{nm}$.

On the other hand, the case $u \ll V$ demonstrates some specific features. In this case atoms are pumped into the metastable singlet state. The 4^1S_0 state is going to be almost depopulated and even a population inversion between the states 4^1S_0 and 4^3P_1 could be achieved. Here, an optical pumping via a velocity selected state takes place since the whole trapping process is a velocity selective one. In principle we expect two peaks arising in the atomic velocity distribution separated by $2\hbar k_{IR1}$. Since k_{IR1} is very small those two peaks overlap in the velocity space. This fact was proved by our numerical calculations. In this work we restrict ourselves to calculations of the velocity distribution in

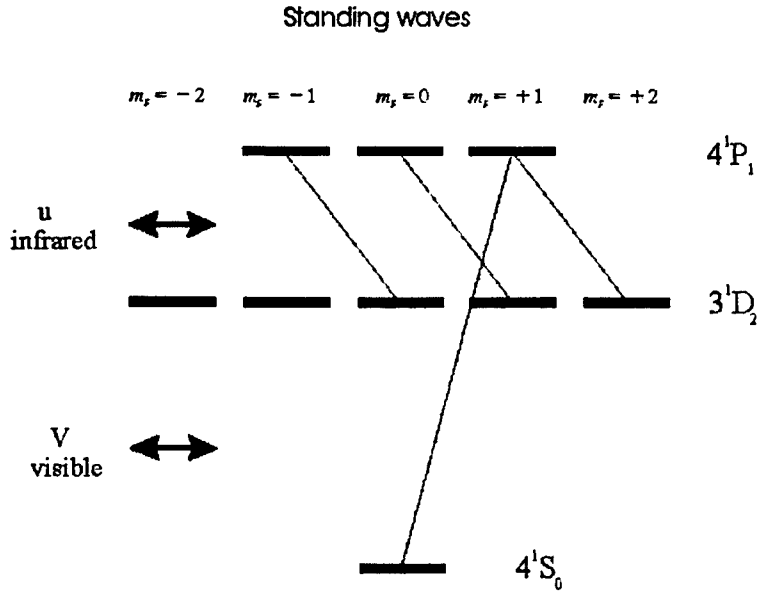


Figure 3: VSCPT cooling scheme using standing waves. The two Zeeman sublevels with $m=-2$ and $m=-1$ are not significantly populated due to very different relaxation rates of the transitions. The polarizations are circular.

the metastable state. Subdoppler cooling can be achieved when the following condition is fulfilled:

$$\Gamma' \gg (\omega_R \gamma)^{1/2} \quad (2)$$

where $\Gamma' \approx \Delta_L + \Delta_{IR}$ (Δ_L , Δ_{IR} are the bandwidths of the visible respectively the infrared laser light), ω_R is the recoil frequency and γ is the spontaneous emission rate of the excited state. Therefore, the coherent light sources must be stabilized as good as a few umpteen of kHz.

From the metastable state atoms can decay to the triplet states. The velocity distribution of atoms in the triplet states is an almost identical image of the distribution in the 3^1D_2 state. However, it differs due to a $k_{IR2} = 1.5\mu m$ photon recoil which smooths the distribution slightly.

We estimate the final atomic temperature as

$$T_{final} = T_1 + T_2 \quad (3)$$

The temperature T_1 is the one achieved by optical pumping. It is of the order of⁶

$$T_1 = \frac{C\Gamma V^2}{\gamma\omega_R^2} T_R \quad (4)$$

where $T_R = 2\hbar\omega_R^2/k_B$ is the recoil temperature and C is a number of the order of 1. The temperature T_2 is due to the IR recoil and can be expressed naturally as

$$k_{IR2}T_2 = \hbar k_{IR2}^2/2M \quad (5)$$

(M ...atomic mass).

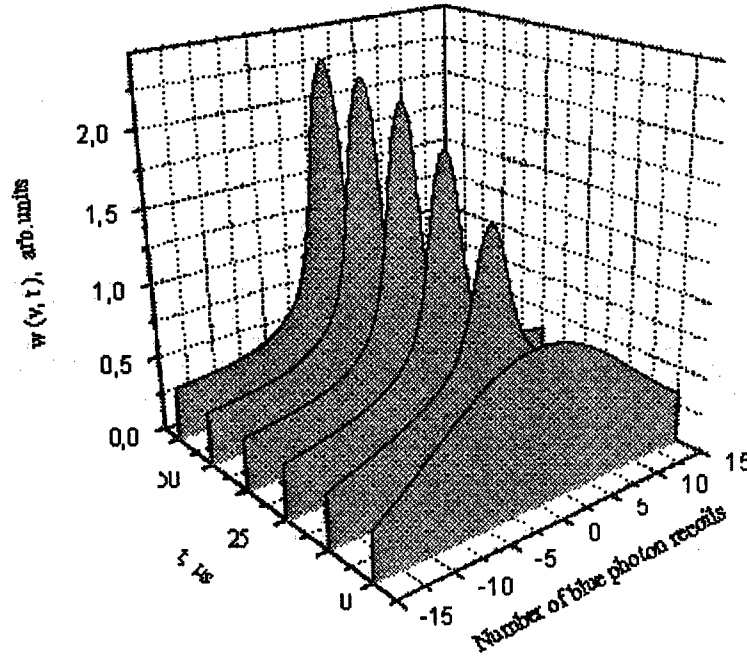


Figure 4: Time evolved velocity distribution with ideal initial conditions. The initial gaussian distribution is assumed to have a FWHM width of 10 times the velocity recoil caused by a single blue photon. In this case the peak area within the borders of ± 15 recoil velocities is almost as large as 100%. After some umpteen microseconds the same number of atoms is confined into a peak characterized by a width of a single photon recoil. For parameters see text. Evolution time as indicated.

3 NUMERICAL CALCULATIONS

We have performed numerical simulations to check the efficiency of the presented cooling mechanism. We have solved the optical Bloch equations (OBE) for the case of running waves. The temporal evolution of the velocity distribution of atoms gives a clear insight into the dynamics of the cooling process. Only velocity distributions of the metastable state are calculated as further relaxation processes are easy to determine (as explained above). The set of parameters for those simulations involve the laser detunings for the visible beam δ_V and the infrared beam δ_u , the Rabi frequencies u and V and the width of any initial velocity distribution which is assumed to possess a gaussian shape. Here we discuss the results of two different cases. The ideal case where the initial distribution is set to an arbitrary (small) value (see Fig.4) and the realistic case where the initial distribution is set to an experimentally achievable value, after precooling in a MOT (see Fig.5). The figures indicate the optimum values for laser detunings and as well as Rabi frequencies. The set of optimum parameters have been found empirically and are given as $\delta_V = \delta_u = -0.2\gamma$, $u = 0.1\gamma$, $V = 0.8\gamma$.

In the ideal case it can be seen that the final temperature of the trapped atoms (indicated by the full velocity width at half peak maximum) undergoes clearly the limit of a single photon recoil velocity. The fraction of ultracold atoms is of the order of more than 50% of all atoms.

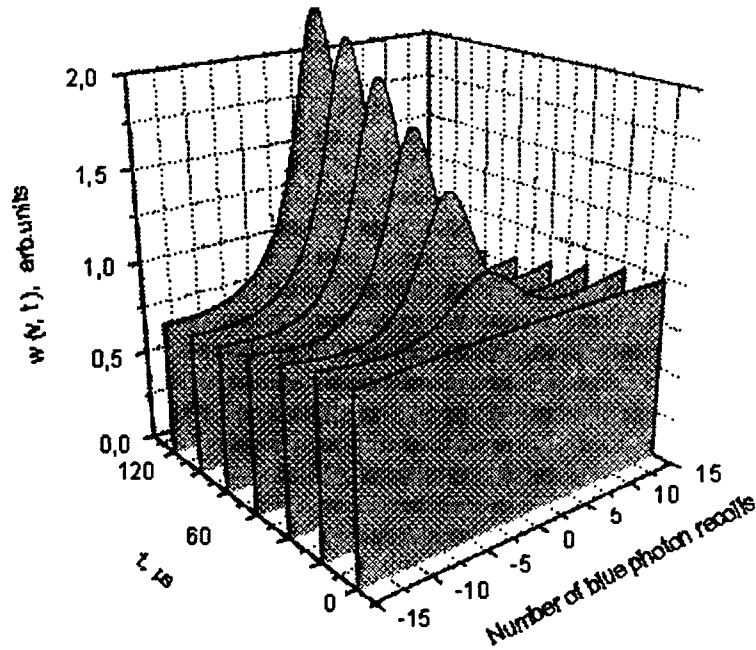


Figure 5: Time evolved velocity distribution with realistic initial conditions. The initial FWHM width is as wide as 80 blue photon recoils which could be achieved in a magneto optical trap. With these realistic conditions a large number of atoms (almost a quarter of initially hot atoms) can be pumped into the VSCPT state(s). The pumping rate however is not faster than hundreds of microseconds which is still smaller than the storage time of the trap. For parameters see text. Evolution time as indicated.

In the realistic case we have set the FWHM width of the initial distribution to values which can be achieved in usual magneto optical traps. However, initially a large number of atoms reside outside the trapping region of usual VSCPT which is some $\hbar k$ wide. In the present scheme, a strong Doppler force assists VSCPT in the early stage of establishment^{6,7}. Therefore, it is still possible to get a considerable number of atoms into the trapping region. In Fig.5 it can be seen that the final distribution of atoms has a width of around a single blue photon. The fraction of cold atoms is about 25% of the number of atoms initially within the depicted range of $-15/+15 \hbar k$.

4 DISCUSSION

The cooling mechanism presented in this work can be considered as a quite simple method to achieve subdoppler temperatures in a MOT storing ^{40}Ca atoms. It is easy to apply because it uses a bichromatic light field only. The availability and good handling of light sources with wavelengths used in this mechanism is another advantage which has to be outlined. We have noted, however, that the demand on frequency stabilisation and on narrow bandwidths of the two independent radiation sources (see Eq.2) are the most difficult steps in a setup arrangement. Nevertheless a couple of examples show that such difficulties could be surmounted.⁸

If the atoms are cooled in a beam then the length of a free flight

$$l \sim v_{beam}\tau \quad (6)$$

is required (v_{beam} is the average velocity of the atomic beam, τ is the lifetime corresponding to the decay $3^1D_2 \rightarrow 4^3P_1$). A laser beam size of order of that used in former experiments on VSCPT in helium³ should provide significant population of the triplet state.

An important problem to be solved is the extension of this method of optical pumping via selected state from an one-dimensional to two- and three-dimensional configurations in calcium as well as to other elements. This task is not trivial since polarization effects and effects related to a finite kinetic momentum corresponding to the IR transition between the P and D singlet states become important here.

5 ACKNOWLEDGMENTS

This work is supported by the Austrian Science Foundation under the grant S 6508. We acknowledge helpful discussions with F. Riehle and E. A. Korsunsky. One of the authors (I.E.M.) is grateful to the Institut für Experimentalphysik, TU Graz, for their hospitality and support.

6 REFERENCES

- [1] H. Schnatz, B. Lipphardt, J. Helmcke, F. Riehle and G. Zinner, "First phase-coherent frequency measurement of visible radiation", *Phys. Rev. Lett.*, **76** (1), 18-21 (1996).
- [2] T. Kisters, K. Zeiske, F. Riehle and J. Helmcke, "High-resolution spectroscopy with laser-cooled and trapped atoms", *Appl. Phys. B* **59**, 89-98 (1994).
- [3] A. Aspect, E. Arimondo, R. Kaiser, N. Vansteenkiste and C. Cohen-Tannoudji, "Laser cooling below the one-photon recoil energy by velocity-selective coherent population trapping", *Phys. Rev. Lett.* **61**, 826 (1988).
- [4] A. Aspect, E. Arimondo, R. Kaiser, N. Vansteenkiste and C. Cohen-Tannoudji, "Laser cooling below the one-photon recoil energy by velocity-selective coherent population trapping: Theoretical analysis", *JOSA B*, **6** (11) 2112-2124 (1989).
- [5] E. Korsunsky and Yu. Roshdestvensky, "Subrecoil laser cooling with coherent population trapping in cascade systems", *Phys. Rev. A*, **52**, 3027 (1995).
- [6] I. E. Mazets, N. Leinfellner, I. A. Grigorenko, B. G. Matisov and L. Windholz : "VSCPT subrecoil laser cooling of atoms with a non-degenerated ($J=0$) ground state", *Zeitschrift für Physik D* **38**, 327-333 (1996).
- [7] N. Leinfellner, I. E. Mazets, E. A. Korsunsky and L. Windholz: "Velocity-selective coherent population trapping on narrow transitions", in *Ultracold Atoms and Bose-Einstein-Condensation*, K. Burnett (ed.), OSA Trends in Optics and Photonics (TOPS) vol 7, 48-52 (1997).
- [8] A. M. Akul'shin, A. A. Celikov, V. L. Velichansky, "Sub-natural absorption resonances on the D_1 -line of rubidium induced by coherent population trapping", *Opt.Commun.*, **84** (3,4), 139-143 (1991).

Linear and nonsaturating effects in atomic multiplets subjected to three strong electromagnetic fields at resonance

F. F. Popescu, F. Marica and G. Radu

University of Bucharest, Faculty of Physics, P.O.Box MG-11,
76900 Bucharest, Magurele-Bucharest, Romania
e-mail address: popf@scut.fizica.unibuc.ro

ABSTRACT

Analytic steady-state solutions of the density-matrix equation are discussed for multilevel spin systems in dilute paramagnetic solids at high temperature and subjected to three frequency-correlated fields at resonance. Unlike the double resonance, in the case of triple resonance, when the three microwave fields are sufficiently strong and the spectroscopic bridge conditions are satisfied, important linear and nonsaturating effects are predicted.

Keywords: quantum amplification and detection, frequency conversion, triple resonance, spectroscopic bridge

1. INTRODUCTION

In usual single or double resonance experiments or maser effects, when the radiation fields are strong, important nonlinear or saturating effects occur^{1,2}. In the case of maser, the better amplification is achieved when the linear effects prevail², so only the pumping field has to be strong, while the emitted field must be weak. When the emitted field is strong too, the nonlinear or saturating effects become limitations that have resulted in a virtual cessation of development in the solid-state maser field³.

Unlike the double resonance, in the case of triple resonance, when the spectroscopic bridge (SB) conditions are fulfilled, high-efficiency microwave generation or detection has recently been predicted^{4,5}. Thus, although the three microwave fields are strong, important linear or nonsaturating effects occur, while the heat absorbed by the lattice per unit time is minimum.

The purpose of the present paper is to analyse the effects mentioned above by means of the analytic steady-state solutions of the density matrix equation. These solutions have been derived considering a formalism suitable for multilevel spin system in dilute paramagnetic solids at high temperature and subjected to several strong fields⁴⁻⁶.

2. STEADY-STATE SOLUTIONS OF THE DENSITY MATRIX EQUATION FOR THREE FREQUENCY-CORRELATED FIELDS AT RESONANCE

In order to obtain the microwave powers absorbed or emitted by a dilute paramagnetic solid subjected to several quasimonochromatic fields at resonance, one can use the analytic steady-state solutions of the density matrix equation for a multilevel spin system⁴⁻⁶:

$$P_{ij} = \int P_{ij}(\omega_{ij}) D_{ij}(\omega) d\omega = 2\hbar\omega_{ij}^0 \Omega_{ij} N \quad (1)$$

If $P_{ij} > 0$ the power is emitted, while if $P_{ij} < 0$ the power is absorbed. $\omega_{ij}^0 = \omega_i^0 - \omega_j^0$, $\omega_i^0 = E_i / \hbar$, with E_i being the exact eigenvalues of the spin Hamiltonian and N the total number of spins. $\omega_{ij} = \omega_{ij}^0 + \delta\omega_{ij}$, where the spectral density $D_{ij}(\omega)$ of a quasimonochromatic field at resonance is nonvanishing as long as $|\delta\omega_{ij}| \ll (T_2^{ij})^{-1}$ where T_2^{ij} is the spin-spin relaxation time corresponding to the pair of spin levels involved.

Let us consider three levels n, σ, m among the levels of a multilevel spin-system. Let us suppose that the number of levels is $n_i > 2$, $E_n > E_\sigma > E_m$ and that the frequencies of the three quasimonochromatic fields are correlated:

$$\omega_{mn} \equiv \omega_{n\sigma} + \omega_{\sigma m} \quad (2)$$

For simplicity, let us suppose that the three fields are at resonance: $|\Delta\omega_{ij}^0| \ll (T_2^{ij})^{-1}$, where $\Delta\omega_{ij}^0$ are the frequency detunings from the resonance of these fields. At resonance, as we have shown in a recent paper⁶, the better efficiency of the frequency conversion is achieved when the coherent mixing of the three fields is negligible. Consequently, let us consider $\delta\omega_{ij} \ll |\Delta\omega_{ij}^0|$ when the overlapping factor could be negligible, and consequently, the coherent mixing term is negligible, too. Then, all the dispersions are vanishing and, if the SB conditions are fulfilled, one obtains the frequency conversion mechanisms discussed in Refs. 4,5. So, although the efficiency of the conversion could be very high, these mechanisms are not parametric processes. In this case, the solutions for the power parameters $\Omega_{ij} = -\Omega_{ji}$ are obtained by solving a system of equation⁴ which in our case becomes:

$$(T_2^{\sigma m} + T_2^{n\sigma} + 2T_1^{mn} + X_{mn})\Omega_{mn} - (T_2^{\sigma m} + 2T_{n\sigma}^{mn})\Omega_{n\sigma} - (T_2^{n\sigma} + 2T_{\sigma m}^{mn})\Omega_{\sigma m} = \rho_{mm}^0 - \rho_{nn}^0 \quad (3)$$

and other two similar equation obtained by circular permutations of mn , $n\sigma$, σm . X_{mn} in Eq. (3) is:

$$X_{mn} = \frac{mn}{mn} \delta_2 T_2^{mn} + \frac{n\sigma}{mn} \delta_2 T_2^{\sigma m} + \frac{\sigma m}{mn} \delta_2 T_2^{n\sigma} \quad (4)$$

$X_{n\sigma}$ and $X_{\sigma m}$ being obtained by circular permutation, and :

$${}^{rs}_{ij} \delta_1 = (T_2^{rs})^{-1} (T_2^{ij})^{-1} \langle p_{ij}^2 \rangle^{-1} \quad ; \quad {}^{rs}_{ij} \delta_2 = \left(\langle p_{rs}^2 \rangle - \langle p_{ij}^2 \rangle \right) \left(\langle p_{ij}^2 \rangle \right)^{-1} \quad (5)$$

ρ_{ii}^0 in Eq. (3) are the thermal equilibrium values of the diagonal elements of the density matrix⁴:

$$\rho_{ii} = (N_i / N) = \rho_{ii}^0 + 2K_{mn}^i \Omega_{ij} + 2K_{n\sigma}^i \Omega_{n\sigma} + 2K_{\sigma m}^i \Omega_{\sigma m} \quad (6)$$

N_i being the population of the level i . p_{ij} are matrix elements (considered to be real) of the time dependent Hamiltonian that represent the interactions of the multilevel system with the three strong fields. They are expressed in \hbar unit and are written in the interaction representation like the off-diagonal elements ρ_{ij} of the density matrix:

$\langle p_{ij}^2 \rangle = \int p_{ij}^2(\omega) D_{ij}(\omega) d\omega$. T_2^{ij} (the spin-spin relaxation times) are given by⁴:

$$(T_2^{ij})^{-1} = (T_2^{ij})_{ss}^{-1} + (1/2) \sum_p [1 - \chi(1 - \delta_{ip})] \omega_{jp} + (1/2) \sum_p [1 - \chi(1 - \delta_{jp})] \omega_{ip} \quad (7)$$

$(T_2^{ij})_{ss}^{-1}$ are the usual contributions to the spin-spin interaction¹ and are dominant at low temperature. The expressions (7) are similar to those given by the usual theories of relaxation (often referred as Redfield Theory¹), the difference being that the contributions of the spin-lattice relaxation rates w_{ij} to the off-diagonal matrix elements of the relaxation matrix have to be multiplied by a narrowing factor χ which is usually one half⁴.

The spin-lattice relaxation parameters K_{ij}^α are obtained by solving the equations:

$$\sum_{\alpha \neq i} (K_{ij}^\alpha w_{\alpha i} - K_{ij}^j w_{i\alpha}) = \sum_{\alpha \neq j} (K_{ij}^j w_{j\alpha} - K_{ij}^\alpha w_{\alpha j}) = 1; \quad \sum_{\alpha \neq \beta} (K_{ij}^\beta w_{\beta\alpha} - K_{ij}^\alpha w_{\alpha\beta}) = 0; \quad \beta \neq i, j \quad (8)$$

K_{ij}^α have the following important properties:

$$\sum_{\alpha} K_{ij}^{\alpha} = 0 ; \quad K_{ij}^{\alpha} = -K_{ji}^{\alpha} ; \quad K_{ij}^{\alpha} = K_{i\beta}^{\alpha} + K_{\beta j}^{\alpha} \quad (9)$$

The spin-lattice relaxation times T_1^{ij} and $T_{ij}^{\alpha i}$ are defined as follows:

$$T_1^{ij} = K_{ij}^{ji} = K_{ij}^j - K_{ij}^i ; \quad T_{ij}^{\alpha i} = K_{ij}^{\alpha i} = K_{ij}^{\alpha} - K_{ij}^i \quad (10)$$

and as a consequence of the Eqs. (9) they exhibit the following properties:

$$T_1^{ij} > T_{ij}^{\alpha i} \quad (\alpha \neq i, j) ; \quad T_1^{ij} = T_{ij}^{\alpha i} + T_{ij}^{j\alpha} \quad (11)$$

At sufficiently high temperatures so that $(E_j - E_i) / kT \gg 1$, $\omega_{ij} / \omega_{ji} \cong 1$. In this case:

$$K_{ij}^{\alpha\beta} \cong K_{\alpha\beta}^{ij} \quad (12)$$

T_1^{ij} represent the spin-lattice relaxation time corresponding to a simple line in usual Electron Paramagnetic Resonance (EPR) experiments¹. The concept of relaxation matrix and consequently Eqs. (3), (7) and (8) remains valid as long as:

$$\langle p_{ij}^2 \rangle / (R_{ks} R_{ij}) \ll 1 \quad (13)$$

$-R_{rs}$ relaxation rates corresponding to the pair of different vibrational states represent the linewidths in infrared (IR) spectra. As $-R_{ij} = (T_2^{ij})^{-1}$ which corresponds to the EPR linewidth is a few Gs (10^{-4} cm^{-1}), the condition (13) is satisfied even for very strong microwave fields, whose magnetic amplitudes do not however exceed a few hundred Gs. Let it be the solutions of the Eqs. (3) of the form:

$$\Omega_{ij} = \Delta_{ij} / \Delta \quad (14)$$

A very important consequence of the properties (9) is that Δ_{ij} and Δ in Eq. (14) do not contain terms independent on X_{ij} . On the contrary, in all the other cases (one field, two fields or three fields whose frequencies are not correlated), the remark mentioned above is not fulfilled. Let us assume that all the three fields are strong enough so that [see Eqs. (5)]:

$$r_{ij}^s \delta_1, r_{ij}^s \delta_2 \ll 1 \quad (15)$$

but not very strong so that the conditions (13) to be satisfied.

3. THE POPULATIONS AND THE HEAT ABSORBED BY THE LATTICE PER UNIT TIME IN STRONG FIELDS

Considering the properties (9) in Eq. (7) one obtains :

$$\chi_i = \rho_{ii} - \rho_{ii}^0 = 2K_{n\sigma}^i \Omega_{mn}^{n\sigma} + 2K_{\sigma m}^i \Omega_{mn}^{\sigma m} \quad (16)$$

where $\Omega_{mn}^{n\sigma} = \Omega_{n\sigma} - \Omega_{mn}$.

The heat absorbed by the lattice per unit time is:

$$P_L = -(P_{mn} + P_{n\sigma} + P_{\sigma m}) = \sum_{\substack{i,j \\ j>i}} (E_j - E_i) (\omega_{ji}\chi_j - \omega_{ij}\chi_i) N ; E_j > E_i \quad (17)$$

Let us assume that all the microwave fields are strong enough so that the conditions (13) and (15) are satisfied simultaneously. In this case as a consequence of the remark made at the end of the previous section, Δ , $\Delta_{mn}^{n\sigma}$ and $\Delta_{mn}^{\sigma m}$ are all proportional to $X = X_{mn} + X_{n\sigma} + X_{\sigma m}$:

$$\Delta \equiv X \left[T_2^{mn} T_2^{n\sigma} + T_2^{mn} T_2^{\sigma m} + T_2^{n\sigma} T_2^{\sigma m} + 2T_1^{mn} T_2^{mn} + 2T_1^{n\sigma} T_2^{n\sigma} + 2T_1^{\sigma m} T_2^{\sigma m} + 4(T_1^{n\sigma} T_1^{\sigma m} - T_1^{\sigma m} T_1^{n\sigma}) \right] = \Delta_{mn} = X \cdot \Lambda \quad (18)$$

$$\Delta_{mn}^{n\sigma} \equiv X \left[(T_2^{mn} + T_2^{n\sigma} + 2T_1^{n\sigma}) (\rho_{nn}^0 - \rho_{\sigma\sigma}^0) + (T_2^{mn} + 2T_1^{\sigma m}) (\rho_{\sigma\sigma}^0 - \rho_{mm}^0) \right] \quad (19)$$

and a similar expression for $\Delta_{mn}^{\sigma m}$ permutating in Eq. (19) $n\sigma$ and σm .

Taking into account Eqs. (14), (18) and (19) in Eqs. (16) and (17) one can observe that the populations ρ_{ii} of the levels and the heat absorbed by the lattice per unit time P_L become independent of X and consequently on the intensities of the three strong microwave fields, and all of them exhibit their extreme values⁴. Thus, although these quantities are saturated, P_L is minimum, and $(\rho_{mm} - \rho_{nn})$ is maximum, while in the usual cases of single or double resonance, when the saturation is reached, P_L is maximum and $(\rho_{mm} - \rho_{nn})$ is vanishing. The minimum value of the heat absorbed by the lattice per unit time is:

$$P_L^{\min} = [T_2^{mn}(E_n - E_m)^2 + T_2^{n\sigma}(E_n - E_\sigma)^2 + T_2^{\sigma m}(E_\sigma - E_m)^2 + 2T_1^{mn}(E_n - E_\sigma)(E_m - E_\sigma) + 2T_1^{n\sigma}(E_n - E_m)(E_\sigma - E_m) + 2T_1^{\sigma m}(E_\sigma - E_n)(E_m - E_n)] \cdot (2N)(NkT\Lambda)^{-1} \quad (20)$$

where we have considered that the temperature is high enough so $\rho_{ii}^0 - \rho_{jj}^0 \equiv (E_j - E_i)/(NkT)$.

At lower temperature, $T_1^{ij} \gg T_2^{ij}$ so the dominant term in Λ defined in Eq. (19) is $(T_1^{n\sigma} T_1^{\sigma m} - T_1^{\sigma m} T_1^{n\sigma})$ which as a consequence of the Eqs. (9) and (11) exhibits the following important property:

$$\Lambda_{\min} = (T_1^{n\sigma m})^2 = (T_1^{n\sigma} T_1^{\sigma m} - T_1^{\sigma m} T_1^{n\sigma}) = (T_1^{mn} T_1^{\sigma m} - T_1^{\sigma m} T_1^{mn}) = (T_1^{mn} T_1^{n\sigma} - T_1^{n\sigma} T_1^{mn}) \quad (21)$$

That is why $T_1^{n\sigma m} (< T_1^{n\sigma}, T_1^{\sigma m}, T_1^{mn})$ may be considered the spin-lattice relaxation times characterising the three spin levels n, σ, m .

4. THE SPECTROSCOPIC BRIDGE

An interesting case is that of the spectroscopic bridge⁴:

$$\langle p_{n\sigma}^2 \rangle = \langle p_{\sigma m}^2 \rangle \quad (22)$$

In this case:

$${}^{n\sigma} \delta_2 = {}^{\sigma m} \delta_2 = 0 \quad (23a); \quad {}^{mn} \delta_2 = {}^{mn} \delta_2 \quad (23b); \quad {}^{n\sigma} \delta_2 = {}^{\sigma m} \delta_2 \quad (23c)$$

$$\left({}^{mn} \delta_2 \right) / \left({}^{n\sigma} \delta_2 \right) = - \left(\left\langle p_{n\sigma}^2 \right\rangle / \left\langle p_{mn}^2 \right\rangle \right) \quad (23d)$$

Let us denote:

$$\delta = {}^{\sigma m} \delta_1 + {}^{mn} \delta_2 = \left[\left\langle p_{mn}^2 \right\rangle - \left\langle p_{n\sigma}^2 \right\rangle + \left(T_2^{\sigma m} \right)^{-1} \left(T_2^{n\sigma} \right)^{-1} \right] \left\langle p_{n\sigma}^2 \right\rangle^{-1} \quad (24)$$

In this case the exact solution for the power parameter Ω_{mn} is:

$$\Omega_{mn} = \frac{(\rho_{mm} - \rho_{nn}) \left\langle p_{n\sigma}^2 \right\rangle T_2^{mn} \delta}{1 + \left(T_2^{n\sigma} \right)^{-1} \left(T_2^{\sigma m} \right)^{-1} \left\langle p_{mn}^2 \right\rangle^{-1} + \left\{ \left[\left(T_2^{mn} \right) / \left(T_2^{\sigma m} \right) \right] + \left[\left(T_2^{mn} \right) / \left(T_2^{n\sigma} \right) \right] \right\} \left\langle p_{n\sigma}^2 \right\rangle \left\langle p_{mn}^2 \right\rangle^{-1}} \quad (25)$$

Let us consider $\left\langle p_{n\sigma}^2 \right\rangle$ constant and $\left\langle p_{mn}^2 \right\rangle$ variable.

A. Nearly balanced bridge

$$\left| {}^{rs} \delta_2 \right| < < {}^{rs} \delta_1 < < 1 \quad (26)$$

consequence of these conditions X_{ij}^a , X^a , Δ_{ij}^a and Δ^a are all proportional to ${}^{rs} \delta_1$. As ${}^{rs} \delta_1$ are all positive and very small, the microwave powers P_{mn} , $P_{n\sigma}$ and $P_{\sigma m}$ are all low and absorbed by the lattice [see the section (a) in Fig. 1]. The populations ρ_{ij} reach their extreme values while $\rho_{mm} - \rho_{nn}$ is maximum and the heat absorbed by the lattice per unit time is minimum (see the previous paragraph and reference 3). In addition, ρ_{ij} and P_L are independent on the microwave field intensities.

B. The strong unbalanced bridge: a high efficient oscillator

$${}^{rs} \delta_1 < < \left| {}^{rs} \delta_2 \right| < < 1 \quad (27)$$

In this case [see Eqs. (23) and (24)]: ${}^{mn} \delta \cong - {}^{n\sigma} \delta_2 \cong \delta$. Consequently, ρ_{ij} and P_L are nearly independent on the fields intensities, $\rho_{mm} - \rho_{nn}$ is nearly maximum and P_L is nearly minimum. We can easily find that $\Omega_{mn}^{n\sigma}$, $\Omega_{mn}^{\sigma m}$ and Δ [see Eqs. (19)] contain terms that are proportional to δ_1 and δ^n ($n \geq 2$) but as a consequence of the properties (9) they do not contain any term proportional to δ . That is why, the populations and the heat absorbed by the lattice per unit time do not depend for small δ on its sign³. On the contrary Δ_{ij} , Ω_{ij} and consequently, P_{ij} contain terms proportional to δ [see for example Eq. (25)]. In the present case we can consider:

$$P_{ij} \cong (c_{ij} \delta) / (a + b \delta^2) \quad (28)$$

where $c_{mn} < 0$, $c_{n\sigma}$, $c_{\sigma m} > 0$ and $a, b > 0$. When $\delta < 0$, $P_{n\sigma}$ and $P_{\sigma m}$ are absorbed and P_{mn} emitted, while for $\delta > 0$, $P_{n\sigma}$, $P_{\sigma m}$ are emitted and P_{mn} is absorbed (see Fig. 1). As we have mentioned above, in this section $\rho_{mm} - \rho_{nn}$ is

nearly maximum and positive. However [see Eq. (25)] , since P_{mn} is also proportional to δ , for $\delta < 0$, although $\rho_{mm} - \rho_{nn} > 0$, P_{mn} is emitted.

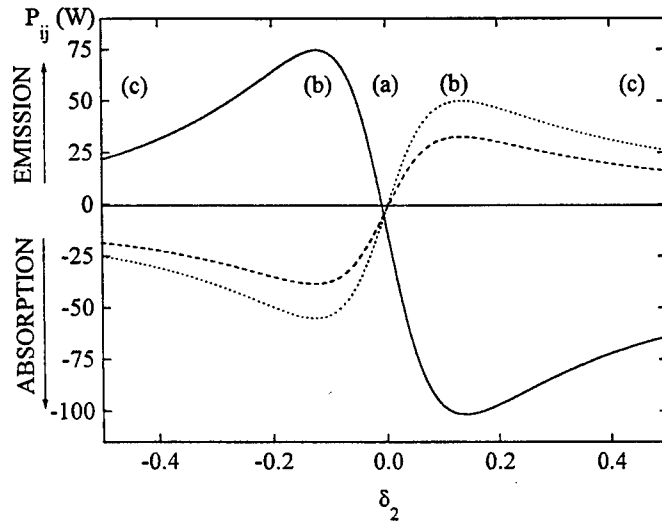


Figure 1. The predicted dependencies (Ref. 12) of the absorbed or emitted powers P_{mn} (full line), $P_{n\sigma}$ (broken line) and $P_{\sigma m}$ (dotted line) on $\delta_2 = \left(\langle p_{mn}^2 \rangle - \langle p_{n\sigma}^2 \rangle \right) / \langle p_{n\sigma}^2 \rangle$, for $\langle p_{n\sigma}^2 \rangle = \langle p_{\sigma m}^2 \rangle = \text{constant}$.

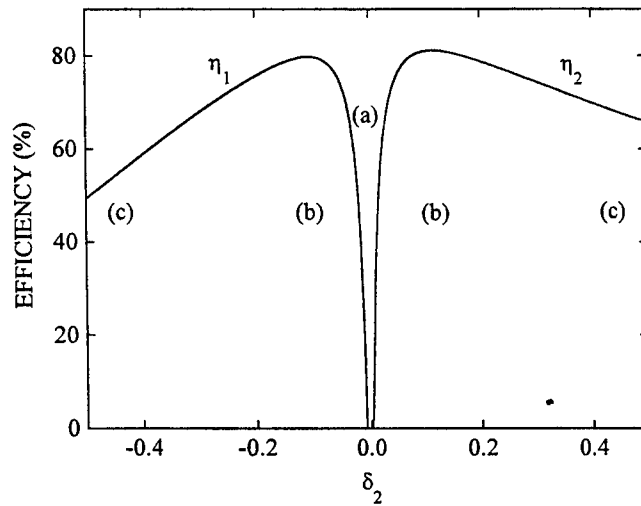


Figure 2. The predicted dependencies (Ref. 12) of the efficiencies of crystal $\eta_1 = -P_{mn} / (P_{n\sigma} + P_{\sigma m})$ and $\eta_2 = -(P_{n\sigma} + P_{\sigma m}) / P_{mn}$ on δ_2 for $\langle p_{n\sigma}^2 \rangle = \langle p_{\sigma m}^2 \rangle = \text{constant}$.

That is why the spectroscopic bridge acts as a maser without inversion³. The powers P_{ij} exhibits extreme values [see Eq. (28) and section (b) in Fig. 1] for $\delta_{ex.} = \pm(a/b)^{1/2}$: $P_{ij}^{max,min} = \pm(c_{ij}) \cdot (ab)^{-1/2}$. Since $c_{ij} \approx \langle p_{n\sigma}^2 \rangle^{-1}$, $a \approx \langle p_{n\sigma}^2 \rangle^{-2}$ and $b \approx \langle p_{n\sigma}^2 \rangle^{-1}$, $P_{ij}^{max,min} \approx \langle p_{n\sigma}^2 \rangle^{1/2}$ and $\delta_{ex.} \approx \langle p_{n\sigma}^2 \rangle^{-1/2}$. The larger $\langle p_{n\sigma}^2 \rangle$ is, the smaller $\delta_{ex.}$ is, and the stronger

emitted powers are . Thus , unlike the usual cases of one or two strong fields, in the case of three strong fields, when the spectroscopic bridge conditions are fulfilled, the emitted and absorbed powers are not saturated . Of course, the three fields may not be however intense , because in this case the condition (13) ceased to be fulfilled.

The efficiency of the crystal (but not of the spectroscopic bridge device) may be defined as $\eta = -P_e / P_a$, where P_e and P_a are power emitted or absorbed. For $\delta < 0$, $\eta_1 = -P_{mn} / (P_{n\sigma} + P_{\sigma m})$, and for $\delta > 0$, $\eta_2 = -(P_{n\sigma} + P_{\sigma m}) / P_{mn}$.

Since in this section the heat absorbed by the lattice is nearly minimum, $\Omega_{mn} \equiv \Omega_{n\sigma} \equiv \Omega_{\sigma m} \gg \Omega_{mn}^{n\sigma}, \Omega_{mn}^{\sigma m}$: $P_{mn} \equiv -(P_{n\sigma} + P_{\sigma m}) \gg P_L$, so unusually high efficiency could be obtained [see section (b) in Fig. 2].

The larger δ_2 / δ_1 is, the stronger emitted powers and efficiencies are. However because δ_1 is positive and never zero: $\eta_1 < \eta_2 < 1$ (see Fig. 2). For given intensities of microwave fields, there are optimum temperature at which the emitted powers and efficiency η have their maximum⁴. These temperatures are relatively high and do not differ too much. The higher field intensities are, the higher optimum temperatures are , but these temperatures do not change strongly⁴.

C. Saturated unbalanced bridge

$$\delta_1 < \delta_2 \leq 1 \quad (29)$$

In Figs. 1 and 2, section c, δ becomes considerable larger, and the contributions of the terms proportional to δ^2 and δ^3 for Δ prevail. In this case $\rho_{mm} - \rho_{nn}$, P_{ij} and η decrease monotonically towards small values, while P_L increases towards its maximum (see Figs. 1 and 2 and reference 4). These small values of P_{ij} and maximum values of P_L become independent on the intensities of the microwave fields , and consequently saturated. Thus, the usual cases of two strong fields [see Figs. 1(c) and 2(c) on the left side of the figures, where $\langle p_{n\sigma}^2 \rangle = \langle p_{\sigma m}^2 \rangle \gg \langle p_{mn}^2 \rangle$], or of a single very strong field [see Figs. 1(c) and 2(c) on the right side of the figures where $\langle p_{mn}^2 \rangle \gg \langle p_{n\sigma}^2 \rangle = \langle p_{\sigma m}^2 \rangle$] could be considered particular cases of three strong fields when one or two among these fields are weak or vanishing.

5. CONCLUDING REMARKS AND OUTLOOK

Our major conclusions are as follows:

The highest efficiency of the frequency conversion could be reached when all the three fields are strong, the corresponding Rabi frequencies are comparable [see the conditions (4)], and the coherent mixing is negligible. This is an unexpected result, since up to now, the maximum efficiency of the frequency conversion was considered to be reached by the parametric processes, when the coherent mixing of the three fields is maximum⁷⁻¹¹.

In the usual cases of single or double resonance, when the electromagnetic fields are strong, important, nonlinear and saturating effects occur, while the heat absorbed by the lattice exhibits its maximum. In the case of triple resonance, when all the spectroscopic bridge conditions are satisfied, very interesting linear or nonsaturating effects could occur , while the heat absorbed by the lattice is saturated at its minimum value. These effects could have two important consequences:

a) Unlike the usual cases of quantum amplifications, when the spectroscopic bridge is balanced, the linear effects allow a more efficiency detection, like the phase-sensitive detection.

b) When the bridge is strongly unbalanced, the saturating effects do not occur, and since the heat absorbed by the lattice is nearly minimum, strong microwave field, emitted with an unusual high efficiency could be possible.

These remarks mentioned above might be valid for any kind of multilevel systems, including the usual cases when the electric field contribution to $\langle p_{ij}^2 \rangle$ is dominant, but only when all the spectroscopic bridge conditions are satisfied.

But before to generalise these conditions to the systems mentioned above, let us make some remarks. Thus, within electric dipole approximation, $p_{mn}p_{n\sigma}p_{\sigma m} = 0$, for the media with a centre of inversion. On the contrary, in the case of magnetic dipole approximation the above quantity is nonvanishing (for example, when two of the microwave fields have magnetic components perpendicular with respect to static magnetic field B , while the third has a magnetic component

parallel to B). Another opportunity is that of solid-state materials, which are in general more rich for the realisation of different energetic configurations, including the cases of media without a centre of inversion . Unfortunately, our treatment is valid on one hand, as long as the concept of relaxation matrix is valid too [see the condition (13)], and on the other hand, the fields are sufficient strongly, so that the condition (15) to be satisfied. As we have justified⁴, because the vibrational states of the paramagnetic impurity are assumed to be more tightly coupled to the lattice than the spin states, it is possible to obtain even in strong fields , the coupled equations (3, 6), characterising the spin-system only. For a multilevel system other than a spin system (corresponding to a well nondegenerate ground state), the two conditions mentioned above might not be simultaneously satisfied.

6. ACKNOWLEDGEMENTS

This work is supported by National Council for University Scientific Research (C.N.C.S.U.) under Contract No. 7009/1997.

7. REFERENCES

1. For reviews, see N. M. Atherton, *Electron Spin Resonance*, Wiley, New York, 1973, and *Multiple Electron Resonance Spectroscopy*, edited by M. M. Dorio and J. K. Freed, Plenum, New York, 1979.
2. N. Bloembergen, *Nonlinear Optics*, Benjamin, New York, 1965.
3. J. W. Orton, D. H. Paxman and J. C. Walling, *The Solid State Maser*, Pergamon, Glasgow, 1970.
4. F. F. Popescu, "Solid-state masers without inversion: Theoretical prediction for high-efficiency oscillators or phase-sensitive detectors," *Phys. Rev. B* **48**, 13569-13572 (1993); F. F. Popescu and F. Marica, "Theoretical analysis of the multiple resonances for many-level spin systems. The four-level spin system of (ns)¹ electron ions subjected to strong microwave fields", *Rom. Rep. Phys.* **46**, 907-943 (1994).
5. F. F. Popescu, "Theory of a type of quantum amplification: phase-sensitive amplification by frequency upconversion", *Phys. Rev. B* **51**, 18007-18010, (1995).
6. F. F. Popescu, and F. Marica, to be published.
7. E. Harris, J. E. Field and A. Imamoglu, "Nonlinear optical processes using electromagnetically induced transparency", *Phys. Rev. Lett.* **64**, 1107-1110, (1990).
8. D. J. Fulton, Sara Shephert, Richard R. Mosely, Bruce D. Sinclair, and M. H. Dunn, "Continuous-wave electromagnetically induced transparency: A comparison of V, Λ , and cascade systems", *Phys. Rev. A* **52**, 2302-2311, (1995).
9. Maneesh Jain, Hui Xia, G. Y. Yin, A. J. Merriam, and S. E. Harris, "Efficient nonlinear frequency conversion with Maximal atomic coherence", *Phys. Rev. Lett.* **77**, 4326-4329 (1996).
10. J. C. Petch, C. H. Keitel, P. L. Knight, and J. P. Marangos, "Role of electromagnetically induced transparency in resonant four-wave-mixing schemes", *Phys. Rev. A* **53**, 543-561 (1996).
11. D. A. Coppeta, P. L. Kelley, P. J. Harshman, and T. K. Gustafson, "Nonperturbative analysis of four-wave mixing in a four-level system with three strong fields", *Phys. Rev. A* **53**, 925-937, (1996).
12. These results correspond to a four level spin-system of Pb^{3+} in calcite (see Refs. 4, 13, 14), where $B=1$ T, $T=90$ K, $m=1$, $\sigma=2$, $n=3$, $\nu_{ng}=19.95$ GHz, $\nu_{om}=30.45$ GHz, and $\nu_{nm}=50.40$ GHz ($\nu = \omega / 2\pi$).
13. F. F. Popescu and V. V. Grecu, "Temperature dependence of Pb^{3+} EPR spectrum in irradiated calcite", *Phys. Stat. Solidi (b)* **68**, 595-601 (1975).
14. F. F. Popescu and V. V. Grecu, "Raman spin-lattice relaxation of Pb^{3+} in calcite: Hyperfine effects", *J. Phys. C* **15**, 1557-1555 (1982).

**Multi-component trace gas analysis with a CO laser based photoacoustic detector;
emission of ethanol, acetaldehyde, ethane and ethylene from fruit**

F.J.M. Harren, J. Oomens, S. Persijn, R.H. Veltman*, H.S.M. de Vries* and D.H. Parker

Department of Molecular and Laser Physics, University of Nijmegen,
Nijmegen, the Netherlands, e-mail: fransh@sci.kun.nl

* Agrotechnological Research Institute, ATO-DLO, Wageningen, the Netherlands

ABSTRACT

A CO laser has been used in combination with photoacoustic detection to monitor traces gases emitted from individual pieces of fruit under changing conditions. Ethanol and acetaldehyde have been detected as indicators of fermentation, ethylene for ripening and ethane for lipid peroxidation during deterioration of cell membranes.

Keywords: trace gas detection, photoacoustic, CO laser, fruit storage, fermentation, lipid peroxidation, ethanol, acetaldehyde, ethylene, ethane.

1. INTRODUCTION

Photoacoustic detection in combination with CO and CO₂ lasers is a sensitive analytical tool to monitor trace gases in the atmosphere ^{1,2,3}. The fingerprint absorption spectra in the infrared of many gaseous molecules allows one to detect a specific specie in a mixture of other gases. The sensitivity, for detection of a gaseous compound at trace gas level, depends on the absorption strength of the molecule, the infrared laser power and efficiency of photoacoustic detection.

Laser-based trace gas detectors are able to monitor gases under normal atmospheric conditions with orders of magnitude better sensitivity compared to current scientific instrumentation; in addition, they are able to monitor non-invasively and on-line under rapidly changing environmental conditions, competing with well established/accepted methods for the detection of molecular trace gases such as gas chromatography and mass spectroscopy.

The first successful application of this technique, using a CO₂ laser, was achieved for the detection of ethylene (C₂H₄; the only gaseous hormone) with a sensitivity of 6 pL/L, allowing on-line measurements of changes in ethylene production in biological tissue ⁴. In cooperation with plant physiologists, studies have been performed on wilting of flowers, water stress of plants, germination, fruit ripening ^{1,2} and nitrogen fixation of bacteria ⁵.

Recently, a CO laser-based trace gas detector suited for detection of a large number of biologically interesting trace gases became operational. With this laser first applications were found in entomology studying the respiration behavior of cockroaches which exhale water vapor, CO₂ and methane ⁶. In this paper we present the application of the technique within agricultural post-harvest research studying fermentation processes during storage of fruit.

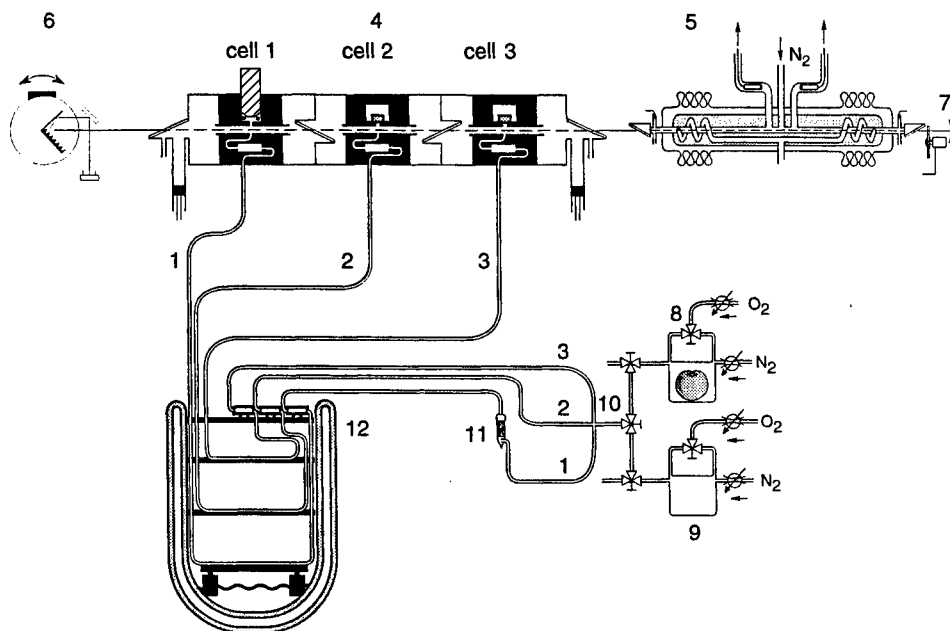


Figure 1: CO laser-based detector: 1, 2 and 3, trace gas flows; 4, triple photoacoustic cell; 5, liquid nitrogen cooled CO laser; 6, grating to select the appropriate transition; 7, chopper; 8, switching valves for (an)aerobic conditions; 9, sampling cuvettes one containing fruit; 10, switching valve to select cuvette; 11, KOH scrubber to remove CO₂; 12, cooling trap.

At present, many fruit varieties are stored at temperatures of -1.5 to 5°C to slow down the metabolic processes inside the fruit delaying ripening and aging. In addition, long term storage of fruit is improved by keeping it under controlled atmosphere (CA), i.e. storage generally under low oxygen concentration and elevated CO₂ levels. However, due to non-optimal storage conditions, worldwide post-harvest losses of crops are estimated between 25 and 40%⁷

Monitoring trace gases released by the crop gives information on biologically changing processes, e.g. on the fermentative state of the crop, ripening phase and damage of cell membranes. The levels of metabolic products may serve as indicators to optimize the CA conditions. If the oxygen level inside a storage chamber is too low, the fruit starts to ferment, emitting ethanol and acetaldehyde (detection limits 3 nL/L and 0.1 nL/L, respectively)^{8,9}. The emission of ethylene, i.e., the gaseous hormone which induces ripening of the fruit decays and the CO₂ level, drops.

During storage one would like to avoid cell membrane damage (lipid peroxidation) of the tissue and subsequent deterioration of fruit. Experiments have been performed on the release of ethane (C₂H₆) by pears due to lipid peroxidation. Cell membranes mainly consist of polyunsaturated fatty acids such as linolenic acid, linoleic acid and arachidonic

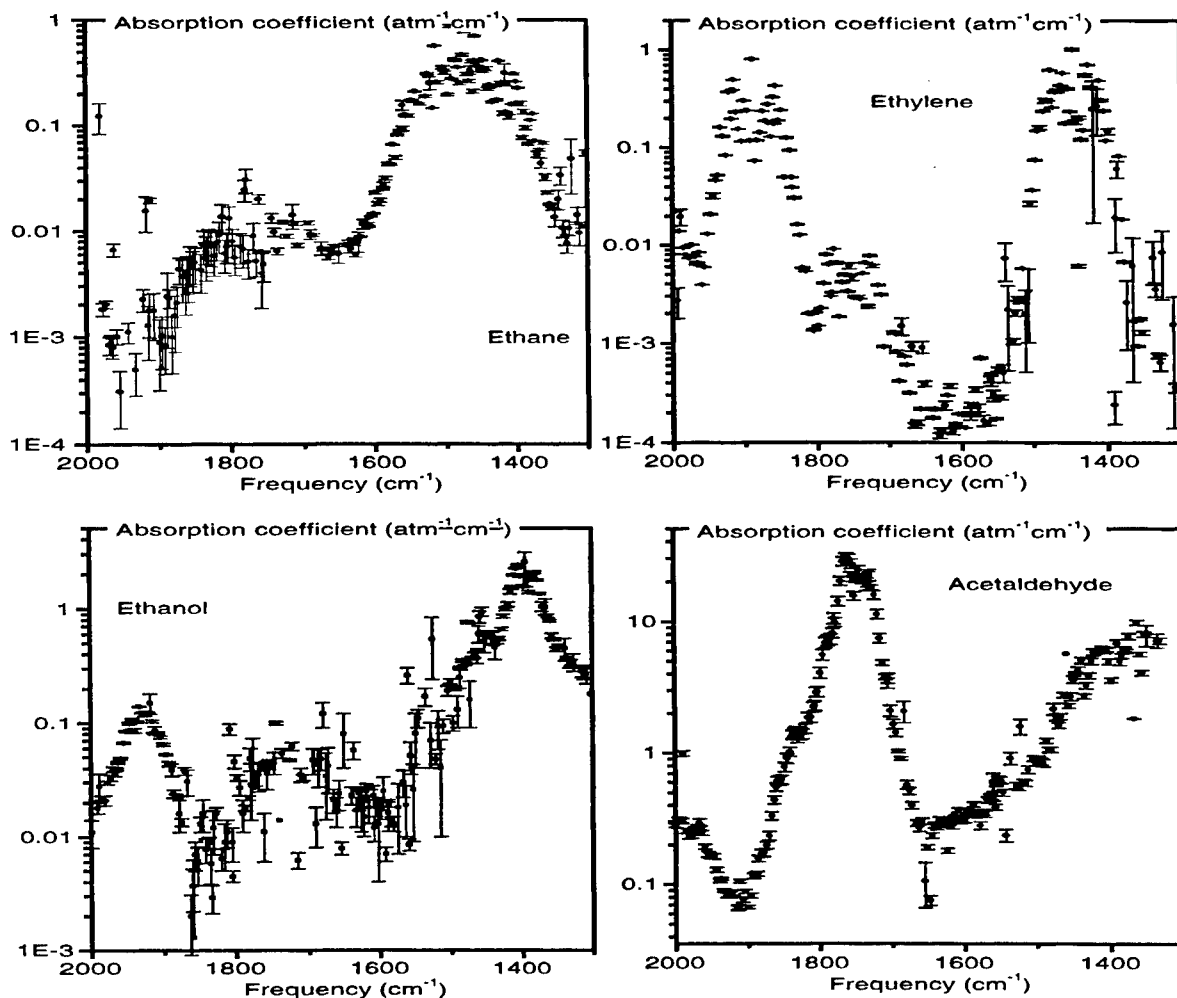


Figure 2: Absorption coefficients of ethane, ethylene, acetaldehyde and ethanol at the CO laser lines. Large error bars indicate either strong interference with water vapor (ethanol) or weak laser lines.

acid. Radicals such as the hydroxy radical cause peroxidation of these fatty acids forming lipid peroxides ¹⁰. Subsequent reactions with iron complexes and β -scission lead to the formation of pentane and ethane. The current detection limit of ethane is 1 nL/L. In the near future, gases like methane, ethane, pentane, carbon dioxide can be detected with much higher sensitivity (30 times) due to the newly developed $\Delta v=2$ CO laser ¹¹.

2. CO-LASER PHOTOACOUSTIC DETECTION

The liquid nitrogen cooled CO laser operates between 1260 and 2000 cm^{-1} on 250 lines with an intracavity laser power up to 40 Watt (Fig. 1)⁶. Multi component measurements involve repeated switching between pre-selected laser lines by tuning the angle of a Littrow-mount grating. Simultaneously with the photoacoustic signal the laser power is

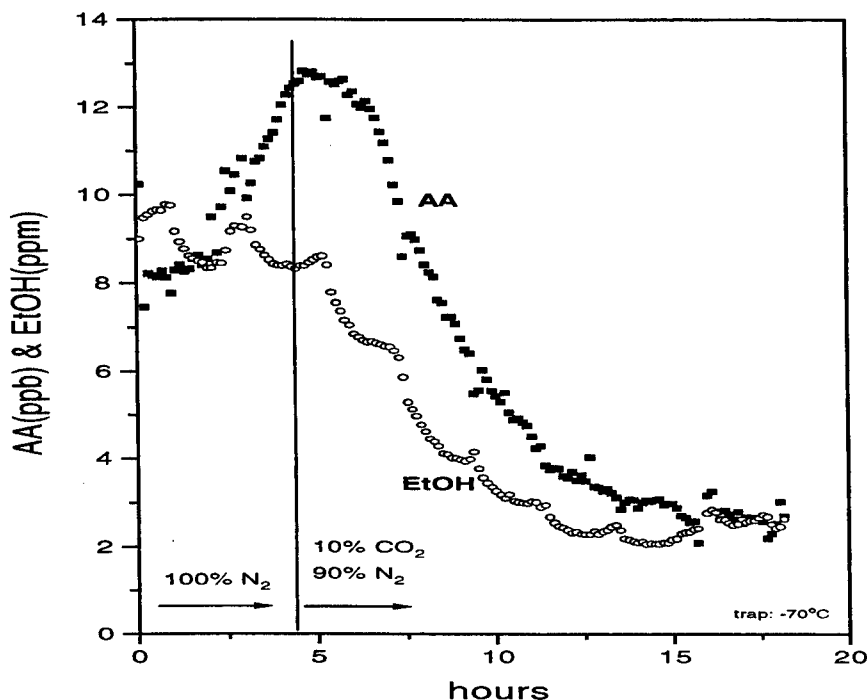


Figure 3: Acetaldehyde (AA) and ethanol (EtOH) emission of a single pear stored at 0°C and anoxic conditions for 3 days. At $t=4$ h high CO_2 levels inhibit the fermentation pathway. The regular pattern on top of the ethanol data are caused by temperature fluctuations inside the cooling trap.

monitored at the zero-order out-coupling of the grating. A mirror with 100 % reflection and a radius of curvature of 5m is used at the opposite end of the cavity.

Three photoacoustic cells are placed in series inside the laser cavity; since the photoacoustic signal is proportional to the laser power it is advantageous to use an intracavity setup. One B&K 4179 microphone and two Knowless EK 3024 microphones are employed for the three resonant photoacoustic cells; the acoustical behavior of the different resonators are described elsewhere ¹².

A single chopper is used and therefore the resonance frequencies of the cells must be equalized. The resonance frequency is strongly affected by the 1 inch membrane of the B&K condenser microphone ¹². To achieve an equal resonance frequency the resonator equipped with this microphone is 8 mm shorter than those of the other two cells. The latter two differed only by 0.3 mm; the remaining differences in resonance frequency are individually corrected by heating each resonator separately using a temperature control unit ($0.5 \text{ K} \propto 1 \text{ Hz}$ frequency change).

Biologically interesting gases can be detected simultaneously in a gas mixture by

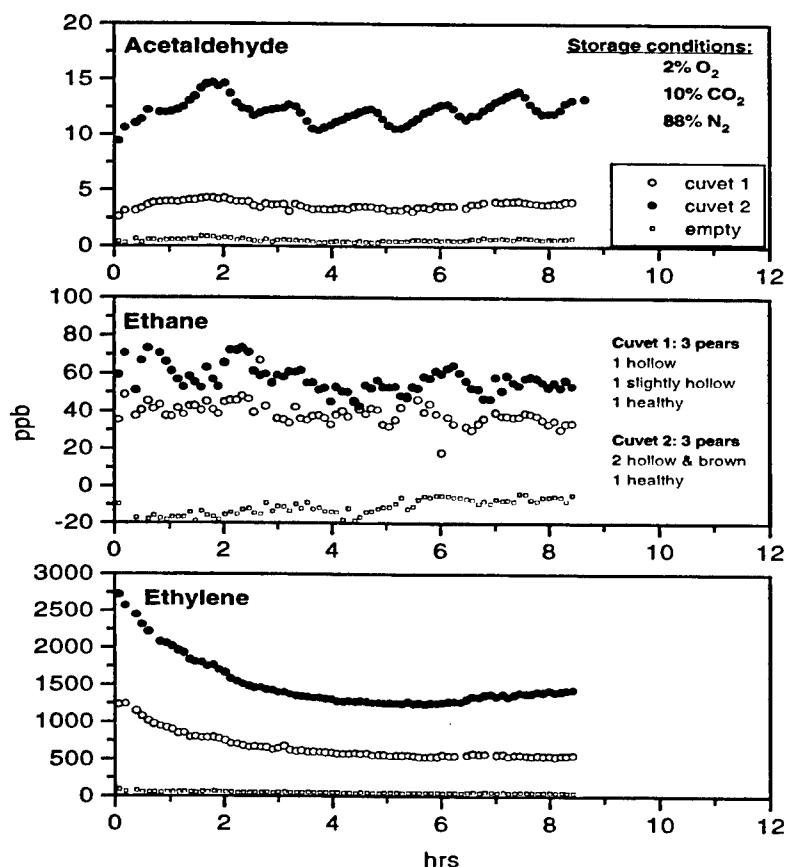


Figure 4: Acetaldehyde, ethane and ethylene emission of 3 pears at 0°C, 10 % CO₂ and 2 % O₂. High CO₂ levels in give rise to cell membrane damage resulting in elevated levels of ethane.

choosing a set of laser lines corresponding to the fingerprint absorption patterns of each of these gases. The selectivity is enhanced by a cold trap kept at temperatures between ambient and liquid nitrogen temperature to selectively freeze out spectrally interfering gases (e.g. water vapor) ¹³. The biological sample is placed in a continuous flow system of a few liters per hour which leads the released gases from the sample cell, via the cold trap to the photoacoustic cell, thus creating an on-line and non-intrusive technique (Fig. 1).

The described set-up was employed to make a survey of the absorption coefficients of biologically interesting gases of ethane, ethylene, acetaldehyde, ethanol on selected CO-laser lines. The absorption spectrum of water vapor is known with high accuracy; because of the ν_2 (moderate) absorption band at 1600 cm⁻¹ and its high concentration compared to other trace gases; it forms the most important source of spectral interference. In Fig.

2 the absorption spectra of ethylene, ethane, acetaldehyde and ethanol are shown. The large error bars on several absorption lines is caused by the strong interference of water absorption at these lines ¹⁴.

For a multi-component analysis of a gas mixture the CO laser is tuned to a number of laser lines. For the analysis it is preferable to obtain an overdetermined system with $G < L$ where G stands for the number of gases and L for the number of laser lines; in this way more information can be obtained from the gas mixture resulting in more accurate results ¹⁵. For practical convenience the signal generated by window absorption and/or resonator wall absorption is added as a fictive gas component, this absorption is significant and cannot be ignored in the calculations. The error in the gas concentrations is mainly determined by the error in the absorption coefficients. The computation of the gas concentrations can suffer from numerical instability. If there are two compounds with almost equal absorption profile, the calculation can fail because a singular matrix would be inverted. Therefore, the method of singular value decomposition ¹⁶ is used to overcome this problem.

3. RESULTS

The acetaldehyde and ethanol emission rate from a single pear stored under anaerobic conditions for three days preceding the experiment are shown in Fig. 3. Acetaldehyde and ethanol emission decrease rapidly after adding 10 % of CO₂ at $t = 4$ h. The elevated levels of CO₂, thus, inhibit the fermentation pathway¹⁷. Long term exposure to elevated CO₂ levels is harmful to pear, revealing either internal browning and cavity formation or only cavity formation. Ethane, acetaldehyde and ethylene emissions have been determined from pear (Fig. 4), immediately after storage at 0.5 % O₂ and 3 % CO₂ for a period of 6 months. From the start of the experiment pears were exposed to 2% O₂ and 10 % CO₂; the latter to exaggerate the effect of CO₂. The degree of internal damage has been inspected after the experiment. the results indicate that acetaldehyde, ethane and ethylene levels are higher for pears at a higher degree of damage. Further research will be conducted to correlate ethane levels acetaldehyde emission.

4. REFERENCES

- [1] F.J.M. Harren and J. Reuss, "Applications in Plant Physiology, Entomology and Microbiology; Gas Exchange Measurements based upon Spectral Selectivity", in *Progress in Photothermal and Photoacoustic Science and Technology*, Eds: A. Mandelis and P. Hess, **3** in the series *Life and Earth Science*, pp. 83-127, SPIE, Bellingham USA, 1997
- [2] F.J.M. Harren and J. Reuss, "Photoacoustic spectroscopy", in *Encyclop. of Appl. Phys.*, **19**, pp. 413-435, VCH publ., Weinheim, 1997
- [3] M.W. Sigrist, *Air monitoring by spectroscopic techniques*, Wiley & Sons, New York, 1994
- [4] F. Harren, F. Bijnen and J. Reuss, L.A.C.J. Voesenek, C.W.P.M. Blom, *Sensitive intracavity photoacoustic measurements with a CO₂ waveguide laser*, *Appl. Phys. B* **50**, pp. 137-144, 1990

- [5] H. Zuckermann, M. Staal, L.J. Stal, J. Reuss, S. te Lintel Hekkert, F.J.M. Harren and D.H. Parker, *On line monitoring of nitrogenase activity in cyanobacteria by sensitive laser photoacoustic detection of ethylene*, Applied and Environmental Microbiology, accepted
- [6] F.G.C. Bijnen, F.J.M. Harren, J.H.P. Hackstein and J. Reuss, *Intracavity CO laser photoacoustic trace gas detection; cyclic CH₄, H₂O and CO₂ emission by cockroaches and scarab beetles*, Appl. Opt. **35**, pp. 5357-5368, 1996
- [7] T.C Lioutas, *Challenges of controlled and modified atmosphere packaging: a food company's perspective*, Food Techn. **42**, pp. 78-86, 1988
- [8] P. Perata and A. Alpi, *Ethanol induced injuries to carrot cells, the role of acetaldehyde*, Plant Physiol. **95**, pp. 748-752, 1991
- [9] H. Zuckermann, F.J.M. Harren, J. Reuss and D.H. Parker, *Dynamics of acetaldehyde production during anoxia and post-anoxia in Red Bell pepper studied by photoacoustical techniques*, Plant Physiol. **113**, pp. 925-932, 1997
- [10] B. Halliwell and J.M.C. Gutteridge, *Free radicals in biology and medicine*, Clarendon press, Oxford, 1985
- [11] E. Bachem, A. Dax, T. Fink, A. Weidenfeller, M. Schneider, W. Urban, *Recent progress with the CO-overtone $\Delta v=2$ laser*, Appl. Phys. B **57**, pp. 185-191, 1993
- [12] F.G.C. Bijnen, F.J.M. Harren and J. Reuss, *Geometrical optimization of a longitudinal resonant photoacoustic cell for sensitive and fast trace gas detection*, Rev. Sci. Instrum. **67**, pp. 2914-2923, 1996
- [13] F.G.C. Bijnen, H. Zuckermann, F.J.M. Harren and J. Reuss, *Multi-component trace gas analysis by three photoacoustic cells intracavity in a CO-laser; observation of anaerobic and post anaerobic emission of acetaldehyde and ethanol in cherry tomatoes*, submitted to Applied Optics
- [14] S. te Lintel Hekkert, M.J. Staal, R.H.M. Nabben, H. Zuckermann, S. Persijn, L.J. Stal, L.A.C.J. Voesenek, F.J.M. Harren, J. Reuss and D.H. Parker, *Laser photoacoustic trace gas detection, an extremely sensitive technique applied in biological research*, submitted to Instrumentation, Science and Technology
- [15] P.L. Meyer and M.W. Sigrist, *Atmospheric pollution monitoring using CO₂-laser photoacoustic spectroscopy and other techniques*, Rev. Sci. Instrum. **61**, 1779-1807, 1990
- [16] W.H. Press, *Numerical Recipes in C*, Cambridge University Press, Cambridge, 1992
- [17] E.L. Kerbel, A.A. Kader and R.J. Romani, *Effects of elevated CO₂ concentrations on glycolysis in intact Bartlett pear fruit*, Plant. Physiol. **86**, 1205-1209, 1988

Spectroscopy of Yb^{3+} co-doped Pr^{3+} : YAG laser crystals

A. Lupei, V. Lupei and A. Petraru

Institute of Atomic Physics, Bucharest, 76900, Romania

ABSTRACT

The sensitisation with Yb^{3+} of other rare earth ions emission is intensively used in the last years for increasing excitation efficiency of infrared (diode laser) pumped solid state lasers. It proved as a good sensitizer for Pr^{3+} emission in various matrices. The spectral investigations for the elucidation of the nature of multisite structure of Pr^{3+} in YAG and of the Yb^{3+} co-doping on Pr^{3+} : YAG are presented in this paper. In Pr^{3+} : YAG two types of multisites have been observed: perturbed Pr^{3+} sites by nonstoichiometric defects and strongly coupled Pr^{3+} - Pr^{3+} near neighbour pairs. Pr^{3+} spectra in Yb^{3+} , Pr^{3+} : YAG show new lines assigned to near neighbour Pr^{3+} - Yb^{3+} pairs and Pr^{3+} - Yb^{3+} - Yb^{3+} triads.

1. INTRODUCTION

In the last years the intense investigation of $\text{Pr}^{3+}(4f^2)$ spectral properties is connected with the possibilities of laser emission of this ion: directly or by up-conversion. It has several metastable multiplets $^3\text{P}_{0,1,2}$, $^1\text{D}_2$, $^1\text{G}_4$ that could present laser action from visible to infrared. Up conversion laser emission from single doped Pr^{3+} or co-doped crystals has been also obtained. Among the co-dopants Yb^{3+} plays a special role. The sensitisation of rare earth emission with Yb^{3+} is intensively used in the last years for increasing excitation efficiency of infrared (laser diode) pumped solid state lasers systems. This sensitisation is based on relatively strong i.r. absorption of Yb^{3+} (900-1000 nm) and efficient migration assisted energy transfer processes to other rare earths ions. Among these an important class is that of the up-conversion systems: the energy transfer from Yb^{3+} populates a metastable level of the rare earth ion from which the excitation could be unconverted either by a subsequent energy transfer from Yb^{3+} or by absorption from an external pump radiation. Another up-conversion could result from a cooperative sensitisation of a high energy level of the active ion by two nearest neighbour (n.n.) Yb^{3+} ions. All these up-conversion processes require high concentrations of Yb^{3+} ions and back transfer processes are also possible. One of interesting matrix for Pr^{3+} emission is yttrium aluminium garnet $\text{Y}_3\text{Al}_5\text{O}_{12}$ (YAG) single crystal.

In order to elucidate the mechanisms involved in these processes, high resolution spectral measurements on single Pr^{3+} doped and Yb^{3+} co-doped YAG samples are necessary. Co-doping can introduce new spectral features connected with pairs, triads, etc. of dopant ions. Previous spectral or up-conversion studies on YAG: Pr^{3+} have revealed many aspects of this system¹⁻⁷, such as the complex problem of electronic structure due to large electron - phonon interferences, various up conversion mechanisms, the multisite structure, etc. The multisite structure problem that could be important in elucidation of luminescence quenching or up- conversion mechanisms has been not definitely solved for YAG: Pr and no references to YAG: Pr, Yb (to our knowledge) are given. Blue up-conversion in YAG: Pr, Yb has been recently reported⁸.

The purpose of this paper is twofold: the elucidation of the nature of multisite structure of Pr^{3+} in YAG and spectral investigation of Yb^{3+} co-doping on Pr^{3+} : YAG. The results of this comparative study of the high resolution spectral data are presented.

2. EXPERIMENT

In order to investigate these problems, YAG crystals single doped with Pr^{3+} (with concentrations from 0.1 to ~ 1at. %) and Yb^{3+} (~ 5at. %) as well as double doped have been grown by Czochralski method. The co-doped samples contain Yb^{3+} from 5at.% up to 20 at.% and Pr^{3+} ~ 1at. %. Pr^{3+} ($4f^3$) being a large ion compared with Y^{3+} or Al^{3+} enters in YAG only in concentrations up to ~ 1at. % and occupies almost exclusively the dodecahedral c- Y^{3+} sites, while Yb^{3+} ($4f^{13}$) replace preponderantly Y^{3+} in c - sites and can be incorporated in large amounts, but part of it can replace also Al^{3+} in octahedral a-sites⁹. High resolution transmission measurements under lamp pumping have been measured with a set-up including computer controlled GDM monochromator, S_{20} or S_1 photomultipliers and a multichannel MCS analyser. Emission data were obtained with an argon laser pumping.

3. HIGH RESOLUTION SPECTRAL DATA ON Pr^{3+} : YAG: AND Pr^{3+} , Yb^{3+} : YAG

3a. Absorption

In order to discuss the experimental data, schematic energy levels diagrams for Pr^{3+} and Yb^{3+} in YAG are presented in Fig. 1.

The excited Yb^{3+} , level $^2\text{F}_{5/2}$ is placed slightly above the $^1\text{G}_4$ Pr^{3+} level and thus a two ion transfer from Yb^{3+} to Pr^{3+} could take place with a low probability for a reverse Pr^{3+} to Yb^{3+} transfer. At the same time, the energy of the crystal field levels of $^3\text{P}_1$ and $^1\text{I}_6$ Pr^{3+} multiplets is twice that of the $^2\text{F}_{5/2}$ Yb^{3+} level, making a three-ion cooperative sensitisation of a Pr^{3+} ion by two Yb^{3+} ions strongly resonant.

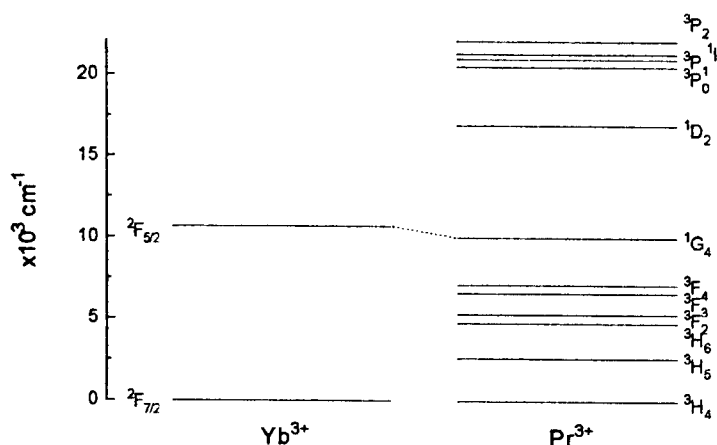


Fig. 1

The Pr^{3+} spectra of single doped YAG contain besides the main lines N corresponding to c-sites, a series of shifted satellite lines, observed in many transitions (Fig. 2)

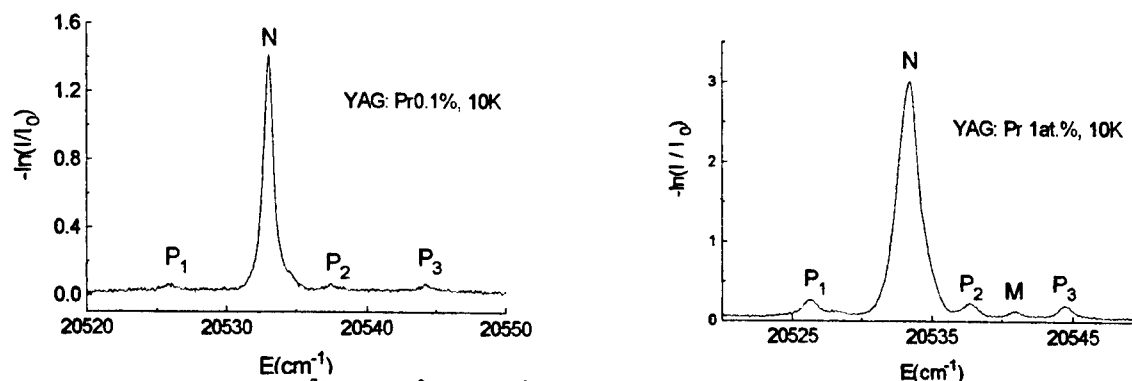


Fig. 2 Absorption spectra of Pr^{3+} : YAG, $^3\text{H}_4(1) \rightarrow ^3\text{P}_0(1)$ transition at 10K for two samples.

In Fig. 2, the high resolution absorption spectra corresponding to $^3H_4(1) \rightarrow ^3P_0(1)$ Pr^{3+} transition at 10K for YAG: Pr^{3+} samples with 0.1at. % and ~ 1at. % are presented (1 denotes the first Stark level of the multiplet). Besides the main Pr^{3+} line N, two types of satellites are observed: P_i with a relative intensity to N independent on Pr^{3+} content and M whose relative intensity grows linearly with it (Fig. 2). This additional structure is observed especially around zero - phonon lines, corresponding to transitions from ground Stark levels of multiplets and should be separated from vibronic satellites that are rather intense for both ions.

The satellite structure has not been observed in the Yb^{3+} absorption spectrum corresponding to $^2F_{7/2}(1) \rightarrow ^2F_{5/2}$ transition at 10K. This could be connected with the fact that our samples have a rather large Yb^{3+} content ~ 5at. % (see the discussion). The complex Yb^{3+} spectral characteristics in YAG, analysed in terms of a strong electron-phonon coupling with the crystal and of the resonant splittings is presented in a different paper⁹. A new energy level diagram for Yb^{3+} in YAG is proposed and the main spectral features are consistently assigned.

The co-doping effects on the spectra of Yb^{3+} and Pr^{3+} ions in YAG have been investigated on YAG samples containing Pr^{3+} ~ 1at. % and variable Yb^{3+} content from 5 to 20at. %. The changes induced by co-doping are evident in the low temperature Pr^{3+} as well as Yb^{3+} spectra. These spectra can be separated into two categories:

(i) At low Yb^{3+} content (~ 5at. %), the lines are still relatively sharp and the single doped Pr^{3+} multisite structure is overlapping with new satellite lines, as shown in Pr^{3+} transmission spectrum ($^3H_4(1) \rightarrow ^3P_0(1)$ transition) of a single doped and a co-doped sample (Fig. 4). A decreasing of P_i and M satellites and the apparition of new lines closer to N is evident. At least three new lines are introduced by co-doping.

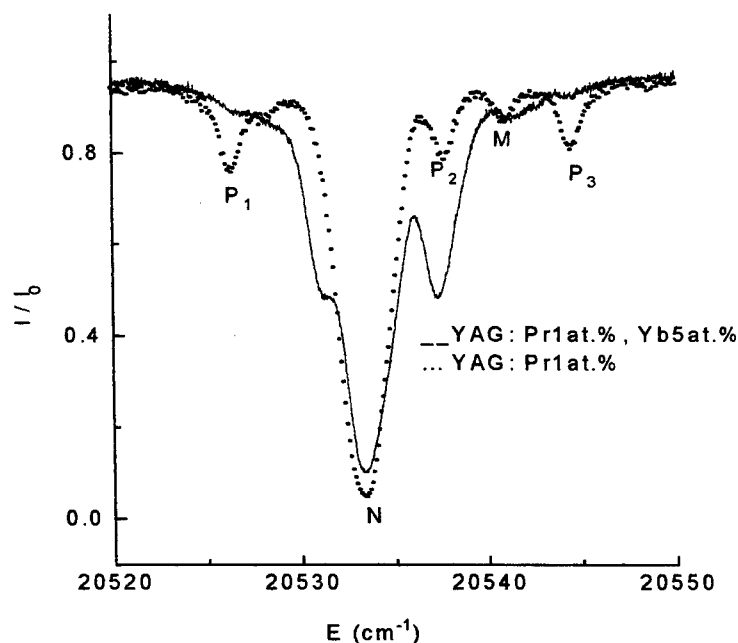
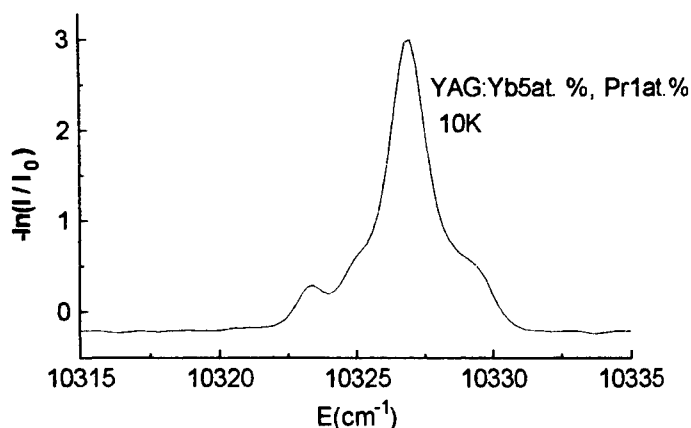


Fig. 3 Transmission spectra of Pr^{3+} ($^3H_4(1) \rightarrow ^3P_0(1)$ transition) in single doped YAG - dotted curve and Yb^{3+} co-doped YAG - continuous line.

The co-doping effects in Yb^{3+} spectra can be also observed in the low temperature spectra of $^2F_{7/2}(1) \rightarrow ^2F_{5/2}(1)$ transition (Fig. 4.). At least three satellites are induced by co-doping.

Fig. 4 Satellite structure of Yb^{3+}
 $^2F_{7/2}(1) \rightarrow ^2F_{5/2}(1)$ transition in Pr 1at.%, Yb
 5at.%, YAG at 10K.



(ii) In the co-doped samples with higher Yb^{3+} content (10 to 20%), P_1 or M Pr^{3+} lines intensities are negligible, the satellites induced by co-doping increase in intensities and new features are apparent. At these concentrations only the most shifted satellites from Pr^{3+} spectra can be resolved. Thus, Fig. 5a shows the $^3H_4 \rightarrow ^3P_1$ Pr^{3+} absorption spectra at 10K for several YAG: Pr^{3+} (~ 1 at. %), Yb^{3+} samples. The most shifted satellites induced by Yb^{3+} are denoted by PY and T. A similar behaviour is clearly observed in other transitions too, such as in $^3H_4 \rightarrow ^1D_2$ (Fig. 5b).

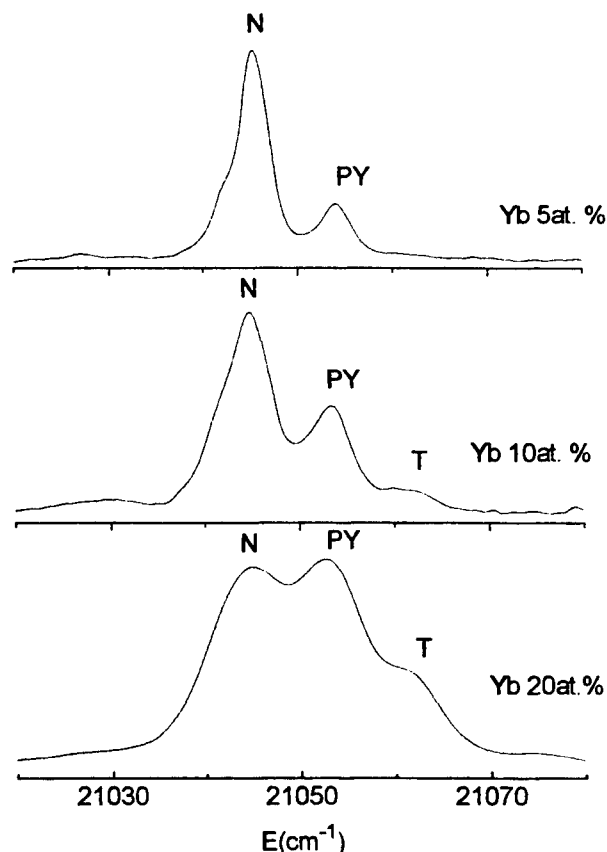


Fig. 5a Satellite structure induced in Pr^{3+} spectra
 $(^3H_4(1) \rightarrow ^3P_1(1))$ by Yb^{3+} co-doping in YAG

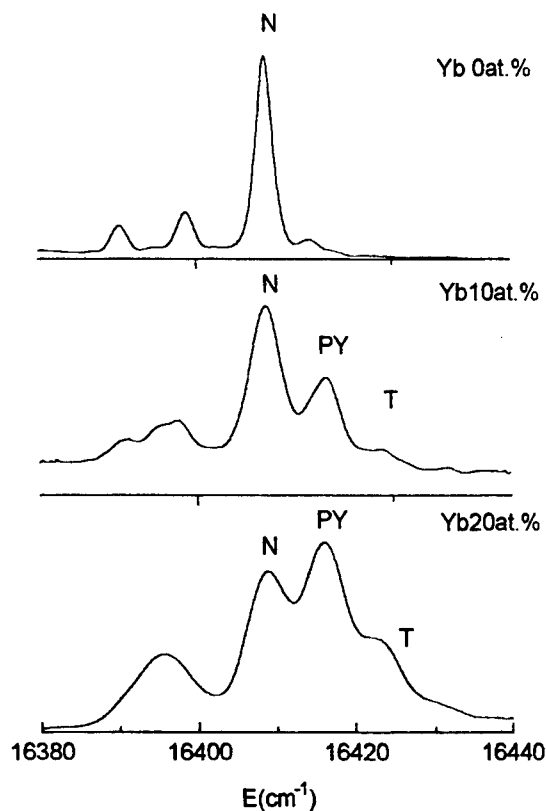


Fig. 5b Modifications induced by Yb co-doping in
 Pr^{3+} absorption spectra observed in $^3H_4(1) \rightarrow ^1D_2$ transition.

3b. Emission spectra

The emission spectra of YAG: Pr³⁺ excited with an argon laser (458nm) in ¹I₆ multiplet present at 77K all the satellite lines corresponding to ³P₀(1) → ³H₄(1) excepting M. (Fig. 6a). It is interesting to observe that all the satellites connected with Yb³⁺ co-doping are missing under this pumping too, as shown in Fig 6b, where the emission spectra of Pr³⁺ in YAG Pr (1at.%), Yb(10at. %) is presented.

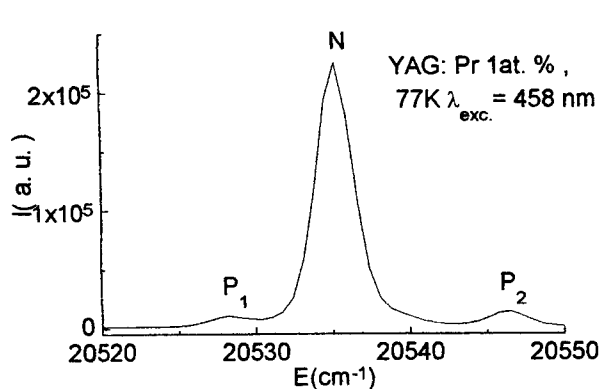


Fig. 6a Emission spectra of Pr³⁺(³P₀(1)→³H₄(1)) in single doped YAG.

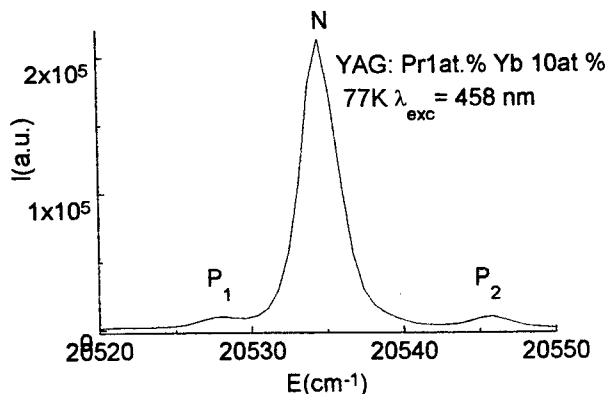


Fig. 6b Emission spectra of Pr³⁺(³P₀(1)→³H₄(1)) in Yb co-doped YAG.

4. DISCUSSION

4.a Multisite structure of Pr³⁺: YAG

the low temperature absorption spectra on Pr³⁺: YAG samples present a clear five lines structure in ³H₄(1)→³P₀(1) transition. The shifts of the satellite lines are of -7, +5, +8, +11 relatively to the main line N. This structure is not so clear in other transitions due to overlapping effects with multisite structure of other N lines; such is the case of transitions to ¹D₂ (where two lowest multiplets are separates with ~ 9cm⁻¹ as given in ref.^{1,3,6}) or to ³P₁ (that overlaps with ¹I₆) multiplets¹⁻⁶. The previous studies¹⁻⁴ on multisite structure of Pr³⁺ in YAG did not give definite assignments for multisites. This could be connected with difficulties to separate the structure in the ³H₄(1) ↔ ¹D₂(1,2) transitions.

Based on spectral data on various Pr³⁺ concentrations, structural data and previous studies on other rare earths ions (see for example^{9,11}) including Pr³⁺: GGG¹², the main observed lines are assigned to: N - unperturbed Pr³⁺(c) centers, P_i - perturbed Pr³⁺(c)-Y³⁺(a) "pairs" and M - Pr³⁺(c)-Pr³⁺(c) pairs. P_i lines, of almost equal intensity are associated with a nonstoichiometric defect, Y³⁺ in octahedral a- sites. The crystal field perturbation produced by this defect Y³⁺(a) at Pr³⁺ c-site is anisotropic, one defect leading to three lines. The relative intensity of P_i/N+ΣP_i is of ~ 2-3%, as measured from the spectra of other rare earth ions in YAG and is characteristic to high temperature grown crystals⁹. Besides M line, another shoulder at about -0.5cm⁻¹ from N presents an increasing with Pr³⁺ concentration, and could be assigned to Pr-Pr pairs from the second coordination sphere. The absence of M₁ line from the emission spectrum suggests a strong quenching, the interaction could be of superexchange type as in case of Nd.

4b. Multisite structure of Yb³⁺: YAG

In the case of single doped Yb³⁺: YAG samples, no multisite structure was observed. This can be determined by the concentration effect (the lowest concentration used is ~ 5at. %). Yb³⁺ has a smaller ionic radius than Y³⁺: 0.81 Å versus 0.97 Å. Thus, since Yb³⁺ can enter in octahedral sites too, it can force out nonstoichiometric excess of Y³⁺. This is experimentally proved in double doped samples. The co-doping of RE: garnets with Cr³⁺, Sc³⁺ remove the P_i satellites f due to Y(a) defects⁹, but they can induce new satellites that depend on that depend on the ionic difference compared with that of Al³⁺(a) and linewidth. For small perturbations and large linewidths, these satellites could be unresolved; this can explain the absence of P_i Yb³⁺ satellites in Yb(5at. %) YAG. On the other hand due to the closeness of Yb³⁺ (0.98 Å) and Y³⁺ (1.02 Å), shifted pair Yb³⁺(c) - Yb³⁺(c) lines are unlikely to be observed since two Yb³⁺ ions in nearest dodecahedral lattice sites are not expected to produce mutual crystal field perturbations leading to resolved satellites.

4c. Multisite structure of Pr³⁺, Yb³⁺: YAG

The Pr³⁺ spectra in co-doped samples present a very complex Yb³⁺ concentration - dependent multisite structure. The analysis of the Pr³⁺ spectra for low Yb³⁺ content (Yb 5at. %), shows that Yb³⁺ co - doping introduces new satellites with rather small shifts from the main line -2.4, +1.2, +4 cm⁻¹ in ³H₄ (1)→ ³P₀(1) transition. It is interesting that similar shifts -3.6, -2, +2.7 cm⁻¹ are observed in the Yb³⁺ spectrum (Fig. 6). It is tempting to assign these lines to Pr (c) -Yb (c) - PY_i pairs from different coordination spheres, the most shifted is most likely connected with nearest neighbour pairs at 3.7 Å. This shift depends, however, on the transition, being as large as 10cm⁻¹ in ³H₄ → ³P₁.

As the Yb³⁺ concentration increases, some of the Pr³⁺ satellites decrease in intensity (P_i and M) and, due to broadening, only the most shifted of the new satellites (PY_i) are observed. This is illustrated in Fig. 6 for ³H₄ (1)→ ³P₁ (1) Pr³⁺ transition. The disappearance of P_i satellites in presence of Yb³⁺ could be explained by the rejection of Y³⁺ ions from octahedral sites by Yb³⁺ as discussed above. Also, since Pr³⁺ ion (ionic radius 1.14 Å) is much larger than Y³⁺ or Yb³⁺, the presence of the last one could prevent the formation of n. n. Pr³⁺ pairs in Pr, Yb: YAG by a dimensional correlation of placement in the lattice sites; this could explain the disappearance of the pair M₁ satellite of Pr³⁺ in the co-doped samples. On the other hand, in the presence of large concentrations of Yb³⁺, the probability of having "isolated" n.n. Pr - Pr pairs is strongly reduced since complex ensembles involving also near Yb ions could be formed. This induces a distribution of a large variety of Pr -Pr pair based satellites which could replace the original M_i satellites by broad or poorly resolved and less intense structures. The analysis of the relative intensities of satellites PY_i allows us to assign some of these lines to near neighbour heterogeneous pairs Pr³⁺(c)-Yb³⁺(c) - PY, or triads Pr³⁺(c)-Yb³⁺(c) - Yb³⁺(c) - T from the first coordination sphere (at 3.7 Å). The distortion of the crystal field at the Pr³⁺ site by one or two Yb³⁺ ions in the first coordination sphere leads to fairly large shifted satellites (up to 10cm⁻¹ for pairs and up to 20cm⁻¹ for triads, depending on transition).

In Table 1 the satellite positions relative to main line N (20533 cm⁻¹) in the Pr³⁺ ³H₄ (1)→ ³P₀(1) transition are presented.

	P ₁	PY ₁	N	PY ₂	PY ₃	P ₂	T	M	P ₃
YAG: Pr	-7	-	0	-	-	5	-	8	11
YAG: Pr, Yb	-	-2.4	0	1.2	4	-	6.7	-	-

The co-doping weakens the P_i (Pr³⁺(c)-Y³⁺(a)) satellites, since Yb³⁺ can reject Y³⁺ from anomalous octahedral sites⁹. The effect of co- doping on Pr³⁺ - Pr³⁺ pairs (lines M) is not so clear due to overlapping effects.

The emission data show a low efficiency for Pr³⁺ - Yb³⁺ pairs or triads. The importance of these new sites in relation with ³P₀ up-conversion emission in these systems shall be analysed in a subsequent paper.

5. REFERENCES

1. O.L.Malta, E. Antic-Financev, M. Lemaitre-Blaise, J. Dexpert Ghys, B. Pirou, *Chem. Phys. Lett.* **129**, 557 -561 (1986)
2. E. Antic-Financev, M. Lemaitre-Blaise, J. C. Krupa, P. Caro, *Czech. J. Phys.* **B38**, 1267 - 1280 (1988)
3. J. B. Gruber, M. E. Hills, R.M. Macfarlane, C. A. Morrison, G. A. Turner, *Chem. Phys.* **134**, 241 (1989)
4. M. Malinowski, P. Szczepanski, W. Wolinski, R. Wolski, Z. Frucacz, *J. Phys.: Cond. Matter*, **5**, 6469-6482 (1993),
5. M. Malinowski, M. F. Joubert, B. Jaquier, *Phys. St. Sol. (a)* **140**, K49-K52 (1993)
6. M. Malinowski, M. F. Joubert, B. Jaquier, *Phys. Rev.* **B59**, 12367- 12374 (1994)
7. M. Malinowski, M. F. Joubert, B. Jaquier, *J. of Luminescence*, **60/61**, 179-182 (1994)
8. M. Malinowski, Z. Frucacz, M. F. Joubert, B. Jaquier, *ILC '96*, P14-153, (1996)
9. V.V. Osiko, Yu. K. Voronko, A. A. Sobol, *Crystal 10*, Springer Verlag, 37 (1984)
10. V. Enaki, A. Lupei, V. Lupei and C. Presura (this conference)
11. V. Lupei, A. Lupei, C. Tiseanu, S. Georgescu, C. Stoicescu, P. M. Nanau
Phys. Rev. B. Condens. Mat. **95**, 8 (1995)
12. A. Lupei, H. Gross, P. Reiche, *J. Phys.: Cond. Matter*, **7**, 5701-5712 (1995),

Effects of resonant electron-phonon interactions for the RE³⁺ ions in laser crystals

V.N. Enaki¹, A. Lupei², V. Lupei², C. Presura², V. E. Ciobu¹

¹Chisinau State University, Moldavian Republic

²Institute of Atomic Physics, Bucharest 76900, Romania

ABSTRACT

This paper presents a theoretical treatment of electron - phonon interaction problem in the case of quasi resonant interaction for rare earths ions in laser crystals. Expressions for the absorption or emission lineshapes (asymmetries or splittings of zero-phonon lines) are obtained. The theory is applied to explain some spectral features of Yb³⁺ transitions in YAG ; it allows also the estimation of the vibronic coupling strengths, phonon energies and the "unsplit" electronic levels. A new electronic energy level scheme of Yb³⁺ in YAG is proposed.

1. INTRODUCTION

The most investigated effects of the electron - phonon interaction in case of the rare earth (RE) ions in crystals are: the multiphonon relaxation, vibronic side bands, temperature line broadening or phonon assistance of non-resonant energy transfer. Since the Stark splittings of the RE ions are of the order of lattice phonons, other effects connected mainly with near resonance processes could appear. If the distance between two Stark levels is in near resonance with peaks in the phonon spectrum, the electron - phonon interaction creates mixed vibronic states, determining modifications of the optical spectral lines (broadening, asymmetries, splittings or shifts)¹⁻¹⁰. In some cases, the vibronic transitions and the resonance effects are so strong that the assignment of the electronic levels is ambiguous. To have intense resonant effects one needs: rather strong electron - phonon coupling and sharp peaks in phonon density in the resonance region. This explains why the experimental reported data on resonance effects in ionic compounds refers especially to Yb³⁺ (4f¹³) ref.^{1,2,5}, Tm³⁺ (4f¹²) ref.⁹ or Tm²⁺ (4f¹³) ref.¹⁰, Pr³⁺ (4f²) ref.^{6,7} or Ce³⁺ (4f¹) ref.⁸ ions; i.e. RE ions at the beginning and the end of lanthanide series that present rather strong electron - phonon interaction^{11,12}.

This paper presents a theoretical treatment of the near resonant effects for RE ions in the case of nondegenerate Stark levels. As an illustration, the analysis of Yb³⁺ spectra in YAG (Y₃Al₅O₁₂) is presented. YAG crystal is known as having sharp peaks in the phonon density¹¹⁻¹³. These investigations are important from fundamental point of view and also since this ion is intensively used as laser activator or sensitizer.

2. THEORY

The problem is to obtain the lineshape function for the absorption or emission of light of frequency Ω between two states of the electron - phonon system in the near resonant conditions. The total Hamiltonian $H = H_L + H_e + V$ contains the electronic Hamiltonian H_e , the vibration Hamiltonian H_L and the electron - phonon interaction Hamiltonian V . The Hamiltonian of interaction may be written in the first order as

$$V = \sum_k (v_k a_k + v_k^* a_k^+); \quad (1)$$

Here $k = (\vec{k}, \mu)$ denotes the phonons, \vec{k} being the phonon impulse and μ its vibration branch; a_k, a_k^+ denote the annihilation and creation operators and v_k the electronic operators.

If $|s\rangle$ and $|p\rangle$ are the eigenfunctions of the *total* Hamiltonian $H = H_L + H_e + V$ and $|s\rangle$ is the initial state, one can write the lineshape function for the absorption of light of frequency Ω as:

$$F(\Omega) = \sum_p |\langle p|d|s\rangle|^2 \delta(\Omega - \Omega_{ps}); \quad (2)$$

where $\Omega_{p,s} = E_p - E_s$ and d is the electronic transition operator.

Using the formula:

$$\delta(\Omega - \Omega_{ps}) = \frac{1}{\pi} \text{Re} \int_0^{+\infty} \exp[i(\Omega_{ps} - \Omega)t - \gamma t] dt \quad (3)$$

where γ is the intrinsic linewidth, the lineshape function becomes:

$$F(\Omega) = \frac{1}{\pi} \text{Re} \int_0^{+\infty} I(t) \exp(-i\Omega t - \gamma t) dt; \quad (4)$$

with

$$I(t) = \sum_p \langle s|d^+|p\rangle e^{i(E_p - E_s)t} \langle p|d|s\rangle. \quad (5)$$

Written as $I(t) = \sum_p \langle s|d^+|p\rangle \langle p|e^{iHt} d e^{-iHt}|s\rangle$ and with notation $d(t) = e^{iHt} d e^{-iHt}$ formula (5) leads to:

$$I(t) = \langle s|d^+ d(t)|s\rangle \quad (6)$$

The unit operator may be written as a sum over the eigenfunctions of the *unperturbed* Hamiltonian $H_0 = H_L + H_e$.

$$I = \sum_{r, n_k} |r, \dots, n_k, \dots\rangle \langle r, \dots, n_k, \dots| \quad (7)$$

where r denotes the electronic states and n_k the occupation number of the phonon k .

If we assume that the initial level is unperturbed by the electron - phonon interaction, the initial state $|s\rangle$ is the eigenfunction of $H_0 = H_L + H_e$ and may be written as $|i, \dots, n_k, \dots\rangle$, where i is the initial electronic state and n_k is the occupation number of phonon k .

In the interaction representation one has,

$$\exp(iHt) = \exp(iH_0 t) U(t) \quad (8)$$

where $U(t)$ is the evolution operator, given by

$$U(t) = \sum_{n=0}^{\infty} \left(\frac{i}{\hbar} \right)^n \frac{1}{n!} \int_0^t \dots \int_0^t T[V(t_1) \dots V(t_n)] dt_1 \dots dt_n \quad (9)$$

and

$$V(t) = \exp(iH_0 t) V \exp(-iH_0 t); \quad (10)$$

Replacing (8) into (6), it follows that

$$I(t) = \sum_{f, P(n_k')} \langle i; \dots n_k \dots | d^+ | f; \dots n_k' \dots \rangle \langle f; \dots n_k' \dots | e^{iH_0 t} U(t) d U^+(t) e^{-iH_0 t} | i; \dots n_k \dots \rangle; \quad (11)$$

Since the electronic operator acts only on the electronic part, one can write

$$I(t) = \sum_f \langle i | d^+ | f \rangle e^{i(E_f - E_i)t} \langle f; \dots n_k \dots | U(t) d U^+(t) | i; \dots n_k \dots \rangle; \quad (12)$$

Since we have assumed that the initial state does not interact with the other states, and using that $U^\dagger = U^{-1}$ it follows that

$$U^+(t) | i; \dots n_k \dots \rangle = | i; \dots n_k \dots \rangle \quad (13)$$

Thus, using (7), one has

$$I(t) = \sum_{f, r} \langle i | d^+ | f \rangle e^{i(E_f - E_i)t} \langle f; \dots n_k \dots | U(t) | r; \dots n_k \dots \rangle \langle r | d | i \rangle \quad (14)$$

Among the terms $\langle f; \dots n_k \dots | U(t) | r; \dots n_k \dots \rangle$, the greatest are the diagonal ones, and thus

$$\langle f; \dots n_k \dots | U(t) | r; \dots n_k \dots \rangle = \delta_{f, r} \langle f; \dots n_k \dots | U(t) | f; \dots n_k \dots \rangle \quad (15)$$

which introduced in (14) and (4) yields to the following form of the lineshape function:

$$F(\Omega) = \frac{1}{\pi} \sum_f |\langle i | d | f \rangle|^2 \operatorname{Re} \int_0^{+\infty} \exp[i(E_f - E_i - \Omega)t - \gamma t] \langle f; \dots n_k \dots | U(t) | f; \dots n_k \dots \rangle; \quad (16)$$

Denoting $U_f = \langle f; \dots n_k \dots | U(t) | f; \dots n_k \dots \rangle$ and using the Laplace transformation

$$\tilde{U}_f(p) = \int_0^{+\infty} U_f(t) \exp(-pt) dt, \quad (17)$$

one reaches a simpler relation:

$$F(\Omega) = \frac{1}{\pi} \sum_f \left| \langle i|d|f \rangle \right|^2 \operatorname{Re} \tilde{U}_f(p); \quad p = i(\Omega + \Omega_{i,f}) + \gamma \quad (18)$$

Since $U(t)$ fulfils the equation

$$U(t) = 1 - \frac{i}{h} \int_0^t dt_1 V(t_1) + \left(\frac{-i}{h} \right)^2 \int_0^t dt_1 \int_0^{t_1} dt_2 V(t_1) V(t_2) U(t_2); \quad (19)$$

one can see that

$$U_f(t) = 1 + \sum_{r, P(n_k)} \left(\frac{-i}{h} \right)^2 \int_0^t dt_1 \int_0^{t_1} dt_2 \langle f; \dots n_k \dots | V(t_1) V(t_2) | r, \dots n_k' \dots \rangle \langle r, \dots n_k \dots | U(t_2) | f; \dots n_k \dots \rangle \quad (20)$$

Using the approximation (15) one has:

$$U_f(t) = 1 + \left(\frac{-i}{h} \right)^2 \int_0^t dt_1 \int_0^{t_1} dt_2 \langle f; \dots n_k \dots | V(t_1) V(t_2) | f; \dots n_k \dots \rangle \langle f; \dots n_k \dots | U(t_2) | f; \dots n_k \dots \rangle \quad (21)$$

The first term of the integral may be easily evaluated using (7), and using again (1) and (10) it becomes:

$$\begin{aligned} \langle f; \dots n_k \dots | V(t_1) V(t_2) | f; \dots n_k \dots \rangle &= \sum_{r,k} \left| \langle f | v_k | r \rangle \right|^2 \{ (n_k + 1) \exp[i(\Delta_{f,r} - \omega_k)(t_1 - t_2)] \\ &\quad + n_k \exp[i(\Delta_{f,r} + \omega_k)(t_1 - t_2)] \} \end{aligned} \quad (22)$$

Differentiating (21) and replacing (22) one reaches the following equation:

$$\begin{aligned} \frac{dU_f(t)}{dt} &= -\frac{1}{h^2} \sum_{r,k} \left| \langle f | v_k | r \rangle \right|^2 \{ (n_k + 1) \int_0^t dt_1 \exp[i(\Delta_{f,r} - \omega_k)(t - t_1)] U_f(t_1) + \\ &\quad + n_k \int_0^t dt_1 \exp[i(\Delta_{f,r} + \omega_k)(t_1 - t_2)] U_f(t_1) \} \end{aligned} \quad (23)$$

Applying the Laplace transformation, one has

$$p\tilde{U}_f(p) - 1 = -\frac{1}{h^2} \sum_{r,k} |\langle f | v_k | r \rangle|^2 \left\{ (n_k + 1) \frac{\tilde{U}_f(p)}{p + i(\Delta_{f,r} - \omega_k)} + n_k \frac{\tilde{U}_f(p)}{p + i(\Delta_{f,r} + \omega_k)} \right\} \quad (24)$$

which has the solution

$$\tilde{U}_f(p) = \left\{ p + \frac{1}{h^2} \sum_{r,k} |\langle f | v_k | r \rangle|^2 \left[\frac{n_k + 1}{p + i(\Delta_{f,r} - \omega_k)} + \frac{n_k}{p + i(\Delta_{f,r} + \omega_k)} \right] \right\}^{-1} \quad (25)$$

Using (25) we can write the final form of the lineshape function (18);

$$F(\Omega) = \frac{1}{\pi} \sum_f |\langle i | d | f \rangle|^2 \frac{\gamma + \Gamma_f(\Omega)}{[\Omega - \Omega_{f,i} - \Sigma_f(\Omega)]^2 + [\gamma + \Gamma_f(\Omega)]^2} \quad (26)$$

Neglecting the intrinsic linewidth γ , one can write:

$$\Gamma_f(\Omega) = \frac{\pi}{h^2} \sum_{r,k} |\langle f | v_k | r \rangle|^2 \left[(n_k + 1) \delta(\Omega - \Omega_{f,i} + \Delta_{f,r} - \omega_k) + n_k \delta(\Omega - \Omega_{f,i} + \Delta_{f,r} + \omega_k) \right] \quad (27)$$

$$\Sigma_f(\Omega) = \frac{1}{h^2} P \sum_{r,k} |\langle f | v_k | r \rangle|^2 \left[\frac{n_k + 1}{\Omega - \Omega_{f,i} + \Delta_{f,r} - \omega_k} + \frac{n_k}{\Omega - \Omega_{f,i} + \Delta_{f,r} + \omega_k} \right] \quad (28)$$

If one transforms the sums into integrals and averages the elements of the interaction matrix over the phonons having the same frequency, one obtains:

$$\Gamma(\Omega) = \frac{\pi}{h^2} \sum_r \int_0^\infty A_r(\omega) \rho(\omega) \left\{ [n(\omega) + 1] \delta(\Omega - \Omega_{f,i} + \Delta_{f,r} - \omega) + n(\omega) \delta(\Omega - \Omega_{f,i} + \Delta_{f,r} + \omega) \right\} d\omega \quad (29)$$

$$\Sigma(\Omega) = \frac{1}{h^2} \sum_r P \int_0^\infty A_r(\omega) \rho(\omega) \left[\frac{n(\omega) + 1}{\Omega - \Omega_{f,i} + \Delta_{f,r} - \omega} + \frac{n(\omega)}{\Omega - \Omega_{f,i} + \Delta_{f,r} + \omega} \right] d\omega \quad (30)$$

where $\rho(\omega)$ denotes the phonon density of states and $A_f(\omega)$ represent the matrix element of electron - phonon interaction averaged over the phonons of frequency ω .

According to (26), $\Gamma(\Omega)$ represents the broadening of the lineshape and $\Sigma(\Omega)$ the shift. The splitting is given by the equation

$$\Omega - \Omega_{f,i} - \Sigma_f(\Omega) = 0 \quad (31)$$

If the resonance involves only one phonon ω_0 (Fig. 1)

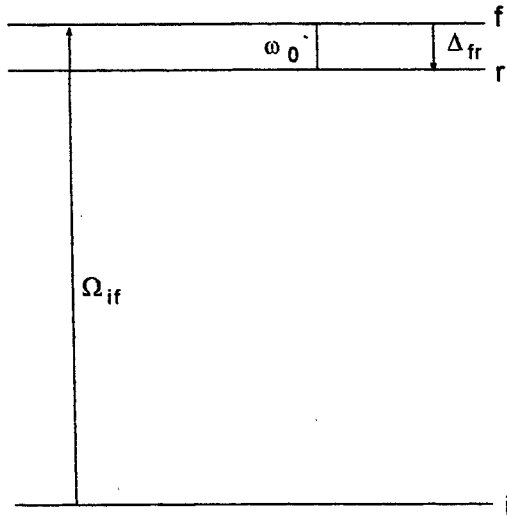


Fig. 1 A schematic model for near resonant effects; $\Delta_{fr} \sim \omega_0$.

and the density of phonons around this peak can be taken as

$$\rho(\omega) = a\delta(\omega - \omega_0) + \rho'(\omega) \quad (32)$$

with a small deviation $\rho'(\omega)$ from a δ function; for $\rho'(\omega)$ negligible one have

$$\Sigma(\Omega) = B \left[\frac{n(\omega_0) + 1}{\Omega - \Omega_{f,i} + \Delta_{f,r} - \omega_0} + \frac{n(\omega_0)}{\Omega - \Omega_{f,i} + \Delta_{f,r} + \omega_0} \right] \quad \text{where } B = \frac{a^* A(\omega_0)}{h^2} \quad (33)$$

At low temperatures, $T=0$ K, it becomes:

$$\Sigma(\Omega) = \frac{B}{\Omega - \Omega_{f,i} + \Delta_{f,r} - \omega_0} \quad (34)$$

Replacing (34) into (31) we obtain the equation for low temperatures:

$$\Omega' - \Delta_{f,r} - \frac{B}{\Omega' - \omega_0} = 0, \quad (35)$$

with $\Omega' = \Omega - \Omega_{r,i}$; i.e. the energy is measured from the intermediate level r . The equation (35) has the solutions:

$$\Omega_{1,2}' = \frac{\Delta_{f,r} + \omega_0}{2} \pm \frac{1}{2} \left[(\Delta_{f,r} - \omega_0)^2 + 4B \right]^{\frac{1}{2}} \quad (36)$$

If the linewidths of the two split components are equal, the ratio of the intensities of the two peaks fulfil the relation:

$$\frac{I_1}{I_2} = \frac{\Omega_2' - \Delta_{f,r}}{\Delta_{f,r} - \Omega_1'} \quad (37)$$

From experimental data Ω_1', Ω_2' and I_1/I_2 one can estimate $\omega_0, \Delta_{f,r}$ and B . The quasisonant problem in the case of more phonons is easily extended. One can consider different shapes of the phonon spectrum near the resonant frequency. It could be taken for example as a Lorentz function². From (29) and (30) the temperature dependencies of zero - phonon linewidth and shifts can be also determined.

3. RESULTS

These results are used to solve the problem of Yb^{3+} energy levels in YAG. The absorption spectra of Yb^{3+} in YAG at various temperatures have been measured with a high resolution system. Since Yb^{3+} ($4f^3$) replace in YAG Y^{3+} dodecahedral sites of D_2 local symmetry, the two multiplets $^2F_{7/2}$ ground and $^2F_{5/2}$ excited, are split in 4 and Stark doublets 3, respectively.

In Fig. 2 the absorption spectrum at 10K, corresponding to $^2F_{7/2} \rightarrow ^2F_{5/2}$ transitions of Yb^{3+} (5at. %) in YAG is presented. It should contain only three zero phonon lines corresponding to Yb^{3+} allowed transitions $^2F_{7/2}(1) \rightarrow ^2F_{5/2}$ in D_2 from the ground Stark component.

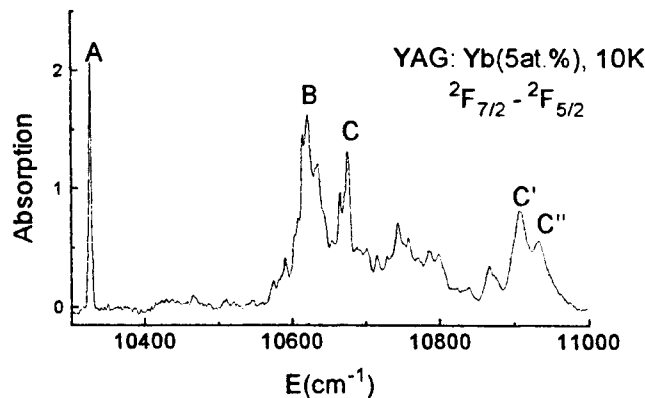


Fig. 2

To explain the spectra we propose the following model: B and C lines are the resonantly split components of the second Stark level E_2 of the excited Yb^{3+} multiplet $^2F_{5/2}$, while C' and C'' lines correspond to the splitting of the third Stark level E_3 . If B and C are resonant splitted components, the fitting with relation (37) gives the position of unsplit electronic level f , i.e. $\Delta_f \sim 323 \text{ cm}^{-1}$ ($E_2 \sim 10650 \text{ cm}^{-1}$), near resonant phonon energy $\omega_1 \sim 327 \text{ cm}^{-1}$ and the interaction parameter $B^{1/2} \sim 26 \text{ cm}^{-1}$. One should mention that the phonon density in YAG has a sharp and intense peak at $\omega_1 \sim 327 \text{ cm}^{-1}$ as observed in sidebands¹³⁻¹⁵ of other ions. The other peaks around B or C are vibronics that present an increasing in intensity, though their position relatively to A (in the limit of experimental errors of previously published data) are unshifted. If C' and C'' lines are considered as resonantly splitted, relation (37) gives $\Delta_f \sim 596 \text{ cm}^{-1}$ ($E_3 \sim 10921 \text{ cm}^{-1}$), $\omega_2 \sim 603 \text{ cm}^{-1}$ (in very good agreement with a sharp phonon peak in YAG¹¹⁻¹²) and $B^{1/2} \sim 13 \text{ cm}^{-1}$. This model gives a new electronic energy level scheme for $^2F_{5/2}$ multiplet of Yb^{3+} in YAG: 10327, 10650 and 10921 cm^{-1} . The proposed energy level diagram for Yb^{3+} in YAG is different from the previous assignments¹⁶⁻²².

4. CONCLUSIONS

The necessity to take into account the near resonant electron - phonon interaction in the analysis of the optical spectra of rare earth ions in inorganic compounds has been remarked by several authors¹⁻¹⁰. It manifests by electronic line splittings or shifts, as well as thermal effects (shifts or broadenings). For some ions, the electron - phonon coupling determine so large interferences of the pure electronic levels with vibronic ones that the elucidation of electronic structure is still a problem. These effects depend strongly on the resonance between Stark levels and peaks in the density of phonons near the resonance and electron - phonon coupling. This last condition makes the effects more efficient for RE³⁺ ions at the beginning or the end of lanthanide series.

Analytical expressions for splitting of an electronic level in resonance with a vibronic level describe well the experimental data of Yb³⁺ in YAG. It is shown that the same near resonant coupling of the first two Stark levels of ²F_{5/2} multiplet with a phonon of $\omega \sim 327\text{cm}^{-1}$ is responsible for the splitting of the second Stark level. The explanation of such large electron - phonon effects for Yb³⁺ is connected with the ion configuration (rather large electron - phonon shifts - up to 35cm^{-1} have been recently estimated¹⁰ for Tm²⁺(4f³) electronic levels in CaF₂ or SrF₂) and the sharp vibration peaks in YAG that could be associated with motion inside or outside AlO₄⁻⁵ tetrahedral group^{13,14}.

Improvements in the crystal field parametric calculations are meaningless in such cases since the shifts induced by electron - phonon coupling could exceed the accuracy of calculations and should be taken into account as outlined recently^{9,10}.

REFERENCES

1. Yu. E Perlin., A. A Kaminskii., V. N Enaki , D. N Vileghanin., *Pisma J. E. T. F.*, **30**, 426 -429 (1979) (in russian)
2. Yu. E Perlin, V. N Enaki, " *Physical processes in semiconductors*", 3-12 (1981) Ed. Stiinta, Chisinau (in russian)
3. V. N Enaki., " *Nonequilibrium processes in multicomponent crystals*", 36 - 42, (1988), Ed. Stiinta, Chisinau (in russian)
4. O L Malta, *J. Phys. Chem. Sol.* **56**, 1053 - 1062 (1995),
5. D. DeLoach L, S A Payne, W L Kway, J B Tassano, S N Dixit, W F Krupke, *J. of Lumines.* **62**, 85 - 94 (1994)
6. P. Caro, O. K. Mouné, E. Antic-Fidancev, M. Lemaitre-Blaise, *J. Less. Common. Metals*, **112**, 153 - 173 (1985)
7. M. Dahl, G. Schaak, *Phys. Rev. Lett.*, **56**, 232- 236 (1986)
8. H. Gerlinger, G. Schaach, *Phys. Rev. B.* **33**, 7438 - 7450 (1986)
9. A. Lupei, V. Lupei, *J. Phys.: Condens. Matter*, **9**, 2807 - 2813 (1997)
10. I. Ignatiev, V. Ovsyankin, *J. of Lumin.* **72-74**, 679 (1997)
11. A. Ellens, H. Andreas, M.L.H. ter Heerdt, R. T. Wegh, A. Meijerink, G. Blasse, *Phys. Rev.* **B55**, 180 - 185 (1997)
12. A. Ellens, H. Andreas, A. Meijerink, G. Blasse, *Phys. Rev.* **B55** (1), 173 -178 (1997)
13. V. M. Markushev, V.I. Tsaryuk, V. F. Zolin, *Opt. i Spectr.* **58**, 583 (1985) (in russian)
14. V. F. Zolin, V. M. Markushev, A. T. Sobolev, V.I. Tsaryuk, *Izv. Akad. Nauk*, **21**, 286 - 290 (1985) (in russian)
15. V. I. Jekov, T. M. Murina, Yu. N. Polivanov, M. N. Popova, A.M. Prohorov, *Sov. Solid St. Phys.* **25**, 1510 (1985) (in russian)
- 16 D. L. Wood, *J. Chem. Phys.* **39**, 1671 (1963)
17. J. A. Koningstein, *Teoret. Chim. Acta*, **3**, 271 (1965)
- 18 R.A. Buchanan, K. A. Wickersheim, J. J. Pearson, G. F. Herrmann, *Phys. Rev.* **159**, 245 (1967)
17. G. A. Bogomolova, D.N. Vylegzhanian, A. A, Kaminskii, *Sov. Phys. JETP*, **69**, 860 - 874 (1975) (in russian)
19. J. J. Pearson, G. F. Herrmann, K. A. Wickersheim, R.A. Buchanan, *Phys. Rev.* **159**, 245 (1967)
20. G. A. Bogomolova, L. A. Bumagina, A. A, Kaminskii, B. Z. Malkin, *Sov. Solid State Phys.* **19**, 1439 - (1977)
21. A. A. Kaminskii, *Laser Crystals*, Springer Verlag, 146 (1981)
22. Yu. E Perlin., A. A Kaminskii., S. I. Klokishner, V. N Enaki, G. A. Bogomolova
D. N Vileghanin, *Phys. Stat. Sol. (a)*, **40**, 643 -653 (1977)

Laser photoacoustic detection of the essential oil vapours of thyme, mint and anise

A. M. El-Kahlout*, M. M. Al-Jourani*, M. I. Abu-Taha* and D.C. Lainé*

* Physics Department, Keele University, Keele, Staffordshire, ST5 5BG, U.K.

+ Physics Department, College of Science and Technology, Al Quds University
Abu Deis, West Bank

Abstract

Photoacoustic studies of the vapours of the essential oils of thyme, mint and anise have been made using a line-tunable waveguide CO₂ laser in conjunction with a heat-pipe type of photoacoustic vapour sample cell operated over the temperature range 20-180°C. Identifying spectral fingerprint features are found in the 9-10 µm spectral region for each of the three essential oils investigated. The principal features of the photoacoustic spectrum of each essential oil are associated with the dominant chemicals present i.e. thymol in thyme oil, menthol in mint and anethole in anise.

Keywords: laser photoacoustics, essential oils, mint oil, thyme oil, anise oil.

1. INTRODUCTION

Essential oils constitute the most important odorous substances found in plants. Their volatility makes them steam distillable from those parts of plants where they are produced. They find wide commercial applications in the production of perfumes, cosmetics, food and beverage flavourings, aromatherapy, pharmaceuticals, insecticides and pesticides and so are of substantial economic value.

The essential oils contain many chemical substances, with as many as 100 or more components. Frequently, the chemical composition of an essential oil is dominated by a single major component, which gives it its characteristic odour. Since plants, from which essential oils are derived, grow under different conditions of climate, rainfall and hours of sunshine, the percentage composition of a given chemical compound can vary greatly, even from the same plant species. Analysis of the chemical composition usually makes use of chromatographic methods, combined with mass spectroscopy and infrared spectroscopy.

With the wider application of laser photoacoustic spectroscopy, the possibility arises of the sensitive monitoring of essential oil vapour emissions from living plants. This could provide a means whereby the potential essential oil yield could be assessed prior to harvesting. The basic requirement is a sufficiently large vapour pressure and an infrared absorption spectrum distinctive of the particular essential oil, or major component of it, which falls within the range of wavelengths covered by the laser used. In this paper, a preliminary study is made of the essential oil vapours of thyme, mint and anise, using a line-tunable CO₂ laser in conjunction with a temperature-variable heat-pipe type of photoacoustic cell.

2. EXPERIMENTAL SYSTEM

A line-tunable waveguide CO₂ laser is used to excite a heat-pipe type of photoacoustic cell, the temperature of which can be varied over the range 5 to 180°C. Nitrogen was used as the carrier gas of the essential oil vapour.

The experimental set-up uses the CO₂ laser to provide highly directional and line-tunable radiation (9.2 - 10.8 µm) which passes into a photoacoustic heat-pipe type of cell¹ which contains the essential oil vapour to be studied. The laser beam is periodically interrupted by means of a rotary chopper (Bentham: Type 218F). A lock-in amplifier (Stanford Research Systems: Type SR510) is used for signal detection, with the reference signal obtained from the chopper control unit. The photoacoustic signal is normalised with respect to laser power by division of the photoacoustic signal by the

laser power measured by an Ophir Model 30A-HP laser power meter. The photoacoustic cell may be operated non-resonantly at 33Hz or at a longitudinal resonance frequency of 550 Hz. The CO₂ laser beam chopper blade is coated with evaporated gold on the laser side. When the chopper blade is set at an appropriate angle to the laser beam axis, the mean laser power can be monitored via a single reflection without any attenuation of laser power entering the photoacoustic cell. The laser power transmitted through the photoacoustic cell serves to operate a CO₂ laser spectrum analyser by which each of the CO₂ ro-vib. laser lines can be identified. The microphone used was of the sub-miniature type (Knowles, Type BT 1754).

The CO₂ waveguide laser used was built in-house. The optical waveguide was made of quartz with an internal diameter 2.6 mm and a plasma discharge length of 45 cm. The laser tube was cooled by circulating water containing antifreeze via a chiller unit, in a closed loop. CO₂ laser line selection was achieved by the use of a rotatable diffraction grating with 150 lines/mm, blazed at 10.6 μ m. The CO₂ laser output coupling mirror was an 80% reflecting germanium mirror, with an antireflection coating on the laser beam exit side. A power output up to 4 watts was obtained on the strongest lines. Laser oscillation was obtained on about 46 ro-vib lines using all 4 branches of the CO₂ laser.

The heat-pipe photoacoustic cell is illustrated in Fig. 1. The central region of the cell is heated electrically by using a resistance wire heater wound around a pyrex tube and the whole wrapped around with thermal insulating tape. A final layer of aluminium foil is added to assist in the even distribution of heat. The cell temperature can be varied between room temperature and 180°C and is measured by thermocouples in contact with the pyrex tube. The microphone is isolated from the region containing hot vapour by placing it beyond one of the pair of cooling jackets. In operation, a liquid sample of the essential oil to be studied is introduced into the centre of the pyrex cell tube, which is then heated to produce a vapour of the volatile chemical components. As the cell is heated, the vapour flows outwards from the centre towards the two water-cooled condensing regions. Condensation of the vapour to the liquid occurs at the position of the water jackets. The liquid is returned via capillary action to the centre of the heat pipe cell by means of a bundle of wires which lie along the bottom of the pyrex tube and act as a metal wick. The vapour/liquid cycle can be maintained indefinitely without condensation of the oil vapour in the microphone, which would impair its sensitivity. The wick consists of a bundle of 25 nickel-chromium wires each 0.2 mm diameter, with a long pitch twist to keep them together. The wick extends the full distance of 25 cm between the two water jacketed cooling regions. The pair of zinc selenide Brewster angle windows which allow the laser beam in and out of the cell are isolated from the photoacoustic cell tube by means of buffer volumes as shown in Fig. 1.

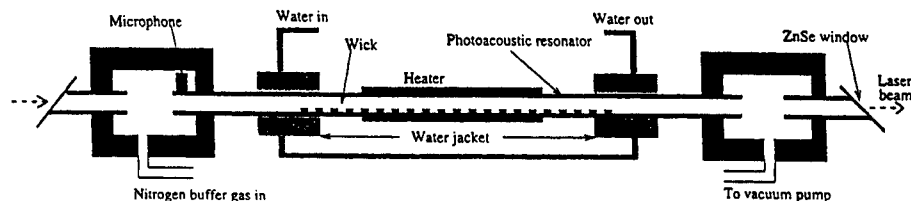


Fig. 1. Sketch of the heat-pipe photoacoustic cell.

3. PHOTOACOUSTIC SPECTRA

3.1 Thyme

The origin, chemical composition and importance of the essential oil of thyme are presented in Table 1. The major component is thymol which has an appreciable vapour pressure at room temperature. The infrared spectrum of thymol vapour lies, in part, within the spectral range of the CO₂ laser. The principal peaks lie at 1088 cm⁻¹, 1060 cm⁻¹, and 945 cm⁻¹ and a further weak peak occurs at 1002 cm⁻¹. The FTIR room temperature spectrum of liquid thyme oil derived from *Thymus vulgaris* L. (thyme red) shows strong peaks at 1088 cm⁻¹, 1060 cm⁻¹, and 944 cm⁻¹. These peaks correspond to the

spectrum of thymol. However, thyme red shows additional but weaker peaks at 1018 cm^{-1} and 995 cm^{-1} which are attributed to carvacrol, (spectral peak at 996 cm^{-1}) and other chemical components.

Table 1: Origin, chemical composition and importance of thyme essential oil².

Origin:	Plant family <i>Lamiaceae</i> ; 350 known species; grown in Europe, East Africa and countries surrounding the Mediterranean. Common examples: <i>Thymus vulgaris</i> L. (thyme red) and <i>Thymus serpyllum</i> L. (thyme wild).			
Extraction	Steam distillation from flowering plant.			
Chemical composition	(e.g. <i>thymus vulgaris</i> L.)			
Major component:	thymol (47 - 86%); C ₁₀ H ₁₄ O	MW 150.2	BP (°C) 232	
Other components:	carvacrol p-cymene α-pinene linalool borneol	bornyl acetate α-terpinene γ-terpinene β-caryophyllene		
Importance:	pharmaceuticals: oral hygiene and dentistry; (antimicrobial properties) perfumery, cosmetics culinary spice; natural food preservative; antioxidant insecticides			

The photoacoustic stick spectrum of the vapour of thyme essential oil (*Thymus vulgaris* L.) within the tuning range of branches of the CO_2 laser is shown in Fig. 2. At 20°C the 10P branch shows a large amplitude photoacoustic signal, with an amplitude peak at the wavelength of the 10P20 CO_2 line (944 cm^{-1}). The 10R branch is somewhat weaker and shows a broad mid-branch dip which persists at higher temperatures (eg 80°C), with a small shift to longer wavelengths. The partial spectrum of the 9P branch is particularly strong. A weak photoacoustic peak is found unexpectedly within this branch at the wavelength of the 9P24 CO_2 laser line at 1043 cm^{-1} which shifts to shorter wavelengths as the temperature of the essential oil is raised. The 9R branch, which is also quite strong, falls in magnitude as the wavelength gets shorter, whereas a dip is expected from the FTIR spectrum. These apparently deviant features may be due to the comb-like photoacoustic spectra sampling going in (or out) of sequence with a fine structure spectrum which possesses a line spacing close to that of the CO_2 laser i.e. $1\text{--}2\text{ cm}^{-1}$.

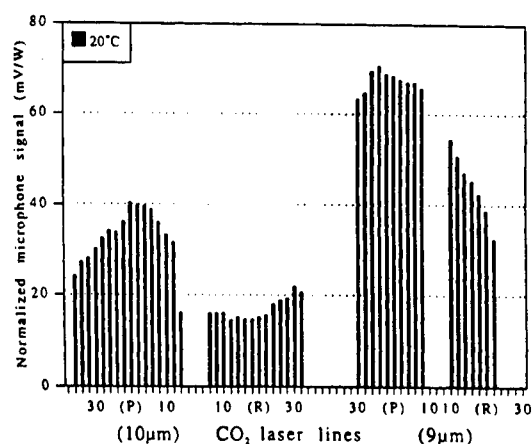


Fig. 2 Room temperature photoacoustic spectrum of the vapour of thyme essential oil from *Thymus vulgaris* L. using the four branches of the CO_2 laser. Buffer gas: nitrogen at one atmosphere pressure.

3.2 Mint

The origin, volatile components and importance^{3,4,5} of the essential oil of peppermint (*Mentha piperita* L.) and Japanese mint (*Mentha arvensis* L. var. *piperascens*) are presented in Table 2.. The principal constituent is menthol which gives plants of the *Mentha* species a minty smell and flavour and gives a cooling sensation when applied to skin and mucosal surfaces⁵. The infrared spectrum of menthol in the spectral region 9.2 - 10.6 μm shows peaks of strong absorption at 1048 cm^{-1} and 1027 cm^{-1} , with much weaker peaks at 992 cm^{-1} and 921 cm^{-1} .

Table 2: Origin, volatile components and importance of mint essential oil.

Origin:	Plant family <i>Labiatae</i> . <i>Mentha arvensis</i> L. indigenous to Japan, introduced to southern California and Brazil. <i>Mentha Piperita</i> L. indigenous to Europe and naturalized in northern USA and Canada.		
Extraction:	Steam distillation of overground parts of plant.		
Chemical composition	(e.g. <i>Mentha arvensis</i> L.)		
Major component:	menthol (70-80%); $\text{C}_{10}\text{H}_{20}\text{O}$	MW 156.3	BP($^{\circ}\text{C}$) 216
Other components:	neomenthol menthyl acetate menthone	pulegone piperitone + others	
Importance:	flavouring of confectionery products pharmaceuticals (coolant, carminative, stimulant, counter-irritant) tooth pastes, chewing gum, mouthwashes cosmetics pesticides		

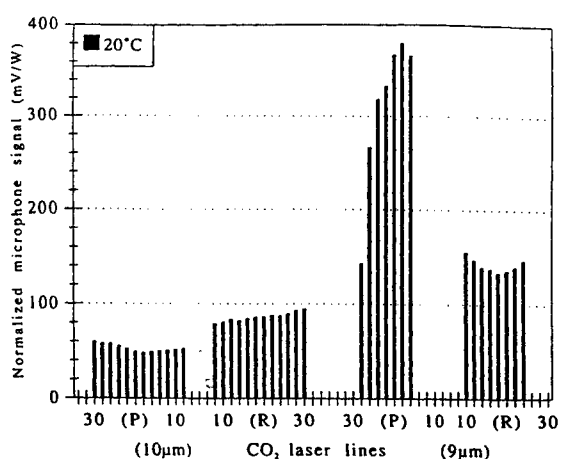


Fig. 3 Photoacoustic stick spectrum for the vapour of Japanese mint essential oil (*Mentha arvensis* L.). Buffer gas: nitrogen at one atmosphere pressure. Vapour at 20°C.

The infrared spectrum of Japanese mint oil closely reproduces these peaks. The photoacoustic spectrum of its oil vapour at 20°C is shown in Fig.3. The 9P branch of the CO_2 laser includes a strong photoacoustic signal peak at 1047 cm^{-1} (9P20 line). Each of the 10P and 9R branches show a broad mid-branch absorption minimum with centres at 10P18 and 9R18 corresponding to 946 cm^{-1} and 1077 cm^{-1} respectively which are in fair agreement with the spectrum of menthol. The 10R branch photoacoustic signal shows a small rise in amplitude for increasing values of wavenumber which corresponds to the correct sign of the slope of the menthol spectrum.

3.3 Anise

The characteristic properties of anise are presented in Table 3. The major chemical component of anise is anethole which may reach 80-90% of the essential from *Pimpinella anisum* L., and a smaller percentage from *Illicium verum* L.

The FTIR spectrum of anethole liquid shows strong absorption peaks at 1037 cm^{-1} , and 965 cm^{-1} , and a weaker peak at 944 cm^{-1} . The FTIR spectrum of anise star essential oil liquid shows essentially the same spectrum as anethole, whereas its vapour spectrum shows a principal absorption peak at 1045 cm^{-1} , and a smaller peak at 962 cm^{-1} , which overlaps with an unresolved line on its long wavelength side. The first of these fits centrally in the CO_2 laser branch 9P which extends from about 1061 cm^{-1} to 1015 cm^{-1} . The second principal peak of anise star essential oil vapour at 962 cm^{-1} lies midway between the 10R and 10P branches. A partially resolved subsidiary peak of anise star liquid (944 cm^{-1}) falls midway within the tuning range of the 10P branch.

The photoacoustic spectrum for anise is shown in Fig. 4. The spectral features of the FTIR anise star vapour spectrum are matched by the photoacoustic results. In particular a strong absorption peak at 1047 cm^{-1} shows a peak situated close to the middle of the 9P branch. The combined photoacoustic spectrum covered by the 10P and 10R laser branches roughly

Table 3: Origin, volatile components, and importance of anise essential oil.

Origin:	Annual herb (<i>Pimpinella anisum</i> L.) indigenous to Asia Minor, Egypt and Greece and cultivated in South America, Germany, Spain, Italy, Southern Russia and Bulgaria. Star anise from Southern China, Vitenam, Japan, the Philippines and Jamaica				
Extraction:	Steam distillation from dried fruit.				
Chemical composition:	Major component; anethole (80-90%) (<i>Pimpinella anisum</i> L.) (1.7 - 6%) (<i>Illicium verum</i> L.)	$\text{C}_{10}\text{H}_{12}\text{O}$	MW 148.2	BP (°C) 234.5	
	Other components:	methyl chavicol anisaldehyde	linalool α -pinene + others		
Importance:	manufacture of liqueurs; food flavouring medicinal: stimulant, carminative and expectorant insecticide				

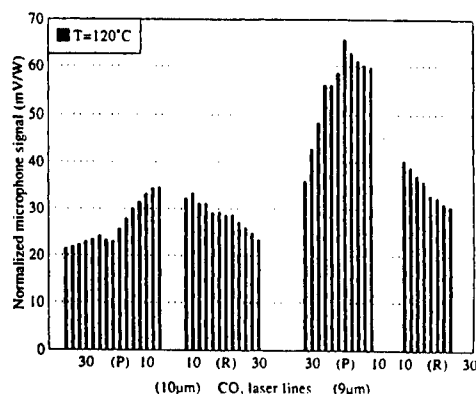


Fig.4 Photoacoustic spectrum of the vapour of essential oil anise (*Illicium verum* L.) for the four branches of the CO_2 laser. Nitrogen buffer gas at one atmosphere pressure. Sample temperature: 120°C .

reproduces the flanks of the second FTIR peak at 962 cm^{-1} , with a subsidiary peak at 939 cm^{-1} . Between this pair of peaks there is a FTIR anise liquid absorption dip in the vicinity of 950 cm^{-1} which lies close to the photoacoustic signal dip in the 10P branch (10P22 i.e. 942 cm^{-1}). This dip is a common feature of all temperatures used for the particular sample of star anise oil vapour studied. The lack of precise agreement between the anise FTIR vapour spectrum and the photoacoustic result may be attributed to spectral sampling of narrowed lines through the dilution effect of nitrogen as a buffer gas. The fingerprint features of the photoacoustic signal for anise are therefore the 9P20 absorption peak, and especially the 10P22 absorption dip.

4. CONCLUSIONS

Strong and distinctive photoacoustic spectra have been obtained for vapours of the three essential oils thyme, mint and anise. Because of the dominance of the principal chemical constituent in each of these oils i.e. thymol, menthol and anethole respectively, the spectra of other oil samples from each plant species are expected to be rather similar to these. However, since some deviations of chemical composition of a given spectra are expected as a result of plant growing conditions and time of harvesting, variation of the magnitude and to a lesser extent the shape of the photoacoustic spectra are expected. Because of the variation of chemical components with hybridized or introgressive plants (eg thyme) it is here that substantial variations of the photoacoustic spectra would be expected from those shown in this paper.

Since the sensitivity of the laser photoacoustic method is very high, it is expected that in many cases a portion of the plant (e.g. a leaf) would produce sufficient of the essential oil for detection without the necessity of resorting to crushing or steam distillation to release the volatile components. In principle this could provide a quick way to determine the optimum yield of the principal chemical component (eg menthol in mint).

Whilst the results presented in this paper are preliminary, distinctive photoacoustic spectra have been shown to be achievable for thyme, mint and anise essential oils. The application of the photoacoustic method should now be explored more fully to check on the effects of the variability of the principal chemical components in the same or related plant species from different sources.

5. ACKNOWLEDGMENTS

The authors would like to thank Mr. H. A. Al-Masri for assistance in extending the range of the photoacoustic spectra. Thanks are also due to Dr. K.M.S.A. Salem of the Biology Department, College of Science and Technology, Al Quds University, West Bank, for suggesting the study of the essential oils reported in this paper. The support of the British Council, East Jerusalem is also gratefully acknowledged.

6. REFERENCES

1. H. Jalink and D. Bicanic, "Concept, design, and use of the photoacoustic heat pipe cell", *Appl. Phys. Lett.* **55** (15) 1507-1509 (1989).
2. W. Letchamo and A. Gosselin, "Effects of HPS supplemental lighting and soil water levels on growth, essential oil content and composition of two thyme (*Thymus vulgaris* L.) clonal selections", *Can. J. of Plant Sci.* **75**(1) 231-238 (1995).
3. S. Perrucci, "Acaricidal activity of some essential oils and their constituents against *Tyrophagus longior*, a mite of stored food", *J. of Food Protection* **58** (5) 560-563 (1995).
4. W. A. Court, R. C. Roy and R. Pocs "Effect of harvest date on the yield and quality of the essential oil of peppermint" *Can. J. Plant Sci.* **73** 815-824 (1993).
5. N. K. Srivastava, R. Luthra and A. Naqvi, "Relationship of photosynthetic carbon assimilation to essential oil accumulation in developing leaves of Japanese Mint", *Photosynthetica* **24** (3), 406-411 (1990).
6. V. E. Tyler, L.R. Brady and J.E. Robbers, "Volatile oils", *Pharmacognosy*, 8th Edn., p.p, 103-143 Lea and Febiger, Philadelphia, 1981.

Coherent Raman scattering on light induced optical gratings prepared by adiabatic population transfer

N. Leinfellner, L. Windholz,
Institut für Experimentalphysik, Technische Universität Graz, Austria
I.E. Mazets,
Ioffe Institute of Physics and Technology, St. Petersburg, Russia

ABSTRACT

We investigate theoretically a process of coherent Raman scattering in a medium where the coherence between two low-energetic levels is prepared by adiabatic population transfer. In the present case the light induced moving optical grating can be formed by a periodical sequence of solitary-type waves (adiabtons). The parameters of this grating (propagation velocity, coefficients of spatial Fourier decomposition) are controlled completely by the amplitudes and phases of the two coupling fields at the medium entrance.

Keywords: Light induced optical grating, adiabtons, low group velocity

1 INTRODUCTION

The existence of a new kind of soliton-like waves has been demonstrated in Ref.¹ Under a certain adiabaticity condition a coherent superposition of low-energy states in a Λ -type three-level medium composes, together with a pair of corresponding resonant electromagnetic fields, an adiabatic invariant. That superposition is responsible for the formation of a bichromatic soliton-like pulse (called adiabaton) and its loss-free and shape-preserving propagation. An experimental evidence of such an object is given by Harris and co-workers.² A number of various theoretical works investigate some aspects of this phenomenon in detail.³⁻⁶ In particular, a four-wave interaction in a double- Λ medium with a co-propagational geometry is a subject of Ref.,⁶ where all four propagating light components show adiabaton-like behaviour.

In the present paper we investigate theoretically a quite different situation. Here, we concentrate on Raman scattering of a probe beam on an optical grating induced in a medium by a periodic sequence of adiabtons. In fact, the adiabaton propagation velocity u is found in¹ to be equal to

$$u = \frac{2\Omega^2/\gamma\kappa}{1 + 2\Omega^2/\gamma\kappa c}. \quad (1)$$

Here γ is the linewidth of the optical transition, κ is the inverse Beer's length of the medium. Ω^2 is the

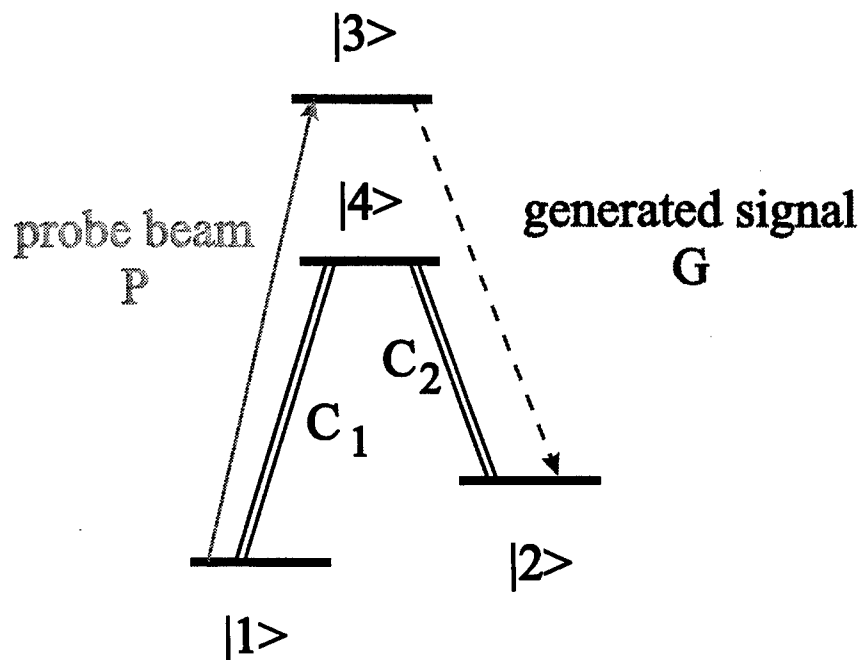


Figure 1: Four level atom under action of two coupling fields C_1 and C_2 and the probe field P . The generated signal is indicated by G .

sum of squares of the Rabi frequencies Ω_1 and Ω_2 associated with the two allowed optical transitions. For an adiabaton-like pulse propagation the input laser pulses should be arranged not only in so-called counterintuitive order but also maintaining Ω constant. One can see from Eq.1 that adiabats can travel with a velocity much less than the vacuum speed of light c . So diffraction of a weak probe beam on a slowly moving optical grating induced in the medium by periodical sequence of adiabats can show some specific features.

2 PROBE LIGHT DIFFRACTION

Let us assume a symmetric Λ -scheme consisting of nearly degenerate levels $|1\rangle$, $|2\rangle$ and the optically excited level $|3\rangle$ (see Fig.1). The wavelength of the microwave transition between $|1\rangle$ and $|2\rangle$ is large enough compared with the size D of the area of wave mixing, but the frequencies of the transitions from a common upper state to these two low-energy states can be discriminated, e.g., by Fabry — Perot interferometer. Any effects which could lead to adiabaton shape distortion^{4,5} are neglected due to a small sample length.

The adiabatic passage signal (in terms of Rabi frequencies) can be written in form of two travelling

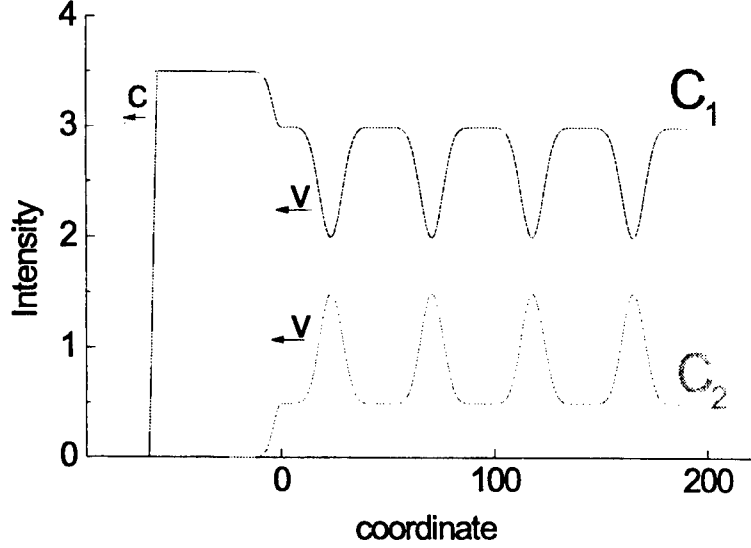


Figure 2: Periodical sequence of pulses composing adiabaton waves. Note that their group velocity v is less than the front propagation velocity c (speed of light).

waves with sinusoide-modulated amplitudes (see Fig.2):

$$\Omega_1(z, t) = \Omega \sin \left[\frac{2\pi}{T} (t - z/u) \right] \exp[i(kz - \omega t)], \quad (2)$$

$$\Omega_2(z, t) = \Omega \cos \left[\frac{2\pi}{T} (t - z/u) \right] \exp[i(kz - \omega t)].$$

The adiabaticity condition¹ requires that $\frac{2\pi}{\Omega T} \ll 1$.

A weak probe signal in the form of a CW travelling wave $V \exp[i(\bar{k}\mathbf{r} - \bar{\omega}t)]$ crosses the region where the adiabaton-induced optical grating is present. The size of this area is denoted by D . The probe beam is in resonance with the transition $|1\rangle - |4\rangle$, where $|4\rangle$ is another excited state characterized by a halfwidth $\bar{\gamma}$. In order to provide adiabaticity in the medium state evolution, the probe field must be sufficiently weak: The rate $V^2/\bar{\gamma}$ of the corresponding optical pumping should be small compared to each of the values Ω , Ω^2/γ , γ .

Now let us examine the nonlinear (third order) polarization that gives rise to the four wave mixing signal. This polarization is proportional to

$$\Omega_1 \Omega_2^* V \propto \sin \left[\frac{4\pi}{T} (t - z/u) \right] \exp[i(\bar{k}\mathbf{r} - \bar{\omega}t)]. \quad (3)$$

Now we apply usual arguments of the optical conjugation theory.⁷ If $\theta \approx uT/D$ is much less than unity then the probe field is diffracted into a narrow cone characterized by angle θ . We note one significant

difference between the present grating formed by slowly varying adiabaton amplitudes (according to Eq.(2)) and the usual case of optical grating with a half-wavelength period formed by carrier oscillations of the two counterpropagating waves. In our case the angle χ between the z -axis and the vector $\bar{\mathbf{k}}$ necessary for a signal formation is not arbitrary but is determined by the following relation:

$$\cos \chi = \frac{u}{c}. \quad (4)$$

Here we neglect terms of the order of $(\omega T)^{-1}$, according to the accepted slowly varying amplitude approximation. The direction of propagation of the diffracted wave (with the frequency of the $|4\rangle - |2\rangle$ transition coincides with $\bar{\mathbf{k}}$.

Eq.(4) can be understood simply when arguing to the Lorenz's transformations. Indeed, in the frame of reference co-moving with the adiabaton-induced grating the new value of the probe field wave vector is

$$\bar{\mathbf{k}}' = \frac{\bar{\mathbf{k}} - \mathbf{e}_z u \omega / c^2}{[1 - (u/c)^2]^{1/2}}. \quad (5)$$

Let us substitute into the latter equation the value of $\bar{\mathbf{k}}$ corresponding to the proper choice of the angle χ given by Eq.(4):

$$\mathbf{k} = \frac{\bar{\omega}}{c} \left(\mathbf{e}_z u / c + \mathbf{e}_{tr} [1 - (u/c)^2]^{1/2} \right),$$

where \mathbf{e}_{tr} is the unit vector perpendicular to the unit vector \mathbf{e}_z of z -axis. From Eq.(5) we get $\bar{\mathbf{k}}' = \frac{\bar{\omega}}{c} \mathbf{e}_{tr}$. So through the whole path of the probe beam the phase of the grating is constant which results in the most effective signal wave generation. If there is a deviation from the proper value of χ (exceeding sufficiently the characteristic angle θ discussed above) then contributions to the signal originating from the optical grating parts mutually cancel due to opposite phases.

Some few words have to be added about the diffraction on periodic non-sinusoidal and quasiperiodic adiabaton-induced gratings, i.e. about cases which are more general than one described by Eq.(2). Firstly, if the grating contains higher harmonics (which can be expanded in Fourier series)

$$\Omega_1 \Omega_2^* \propto \sum_{m=1}^{\infty} a_m \sin \left[\frac{4\pi m}{T} (t - z/u) + \varphi_m \right],$$

where the contribution of the harmonics with very large m is small enough to not violate adiabaticity, then the arguments similar to those used for a pure sinusoid case lead to the same condition Eq.(4). Secondly, the same effect leading to this unique direction relevant for effective four-wave mixing arises in a case of a quasiperiodic grating

$$\Omega_1 \Omega_2^* \propto \int_{q=0}^{\infty} a(q) \sin [q(z - ut) + \varphi(q)],$$

if the spectral components with $q \ll (uT)^{-1}$ are effectively absent. In the latter case the angle of the scattering cone is $\theta \approx (q_{min} D)^{-1}$, where q_{min} is the effective lower cutoff of the grating's wavenumbers.

3 DISCUSSION

Now we should consider the most relevant scheme for experimental observation of the effect being a subject of a preceeding theoretical analysis. It would be best to fix the angle χ between the probe beam

and z-axis. Polarizations of the two light modes forming the periodical adiabaton sequence should be either circular or linear, perpendicular to the probe beam direction. The two electrooptical modulators should be used to split the carrier frequencies to the magnitude of hyperfine splitting between the states $|1\rangle$ and $|2\rangle$. By altering slowly the intensity of adiabaton forming radiation, and, hence, the value of u , one satisfies at the certain power the condition Eq.(4). The signal wave detection should be organized in the following way: The probe beam adopts some admixture of the signal wave after passing the region of nonlinear optical interaction. Their frequencies differ to the lower state hyperfine splitting magnitude and should be discriminated by a mode filter (e.g. Fabry-Perot interferometer). Even if there is no effective four-wave mixing, there is radiation on the $|4\rangle - |2\rangle$ transition.

A gas cell used as a sample should be coated and filled by a buffer gas. Perfect magnetic shielding is strongly required.

Let us assume the following set of parameters: $\gamma = 10^8 \text{ s}^{-1}$, $\kappa = 10^5 \text{ cm}^{-1}$, and $\Omega = 10^9 \text{ s}^{-1}$. Eq.(1) gives $u = 2 \cdot 10^5 \text{ cm/s}$. Also note that the adiabaton amplitude modulation frequency of about 10 MHz provides adiabatic population transfer. The spatial period of the adiabaton-induced optical grating is equal to 0.02 cm. So we can conclude that the probe beam with the diameter of order of 1 cm will be diffracted on this grating providing a divergent signal beam within a cone of some degrees.

4 ACKNOWLEDGMENTS

This work is supported by "Fonds zur Förderung der wissenschaftlichen Forschung" under project S 6508. One of the authors (I. E. M.) is grateful to Institut für Experimentalphysik, TU Graz, for hospitality and support.

5 REFERENCES

- [1] R.Grobe, F.T.Hioe, J.H.Eberly. "Formation of shape-preserving pulses in a nonlinear adiabatically integrable system". *Phys. Rev. Lett.* **73**, No.24, p.3183-3186 (1994).
- [2] A.Kasapi, M.Jain, G.Y.Yin, S.E.Harris. "Electromagnetically induced transparency: Propagation dynamics". *Phys. Rev. Lett.* **74**, No.13, p.2447-2450 (1995).
- [3] J.H.Eberly. "Transmission of dressed states in three-level media". *Quant. Semiclass. Optics* **7**, No.3, p.373-384 (1995).
- [4] I.E.Mazets. "Stimulated Raman processes in optically dense, inhomogeneously broadened media". *Phys. Rev. A* **54**, No.4, p.3539-3545 (1996).
- [5] I.E.Mazets, B.G.Matisov. "Nonlinear wave front sharpening in the adiabatic population transfer regime". *Quant. Semiclass. Optics* **8**, No.4, p.909-913 (1996).
- [6] E.Cerboneschi, E.Arimondo. "Propagation and amplitude correlation of pairs of intense pulses interacting with a double- Λ system". *Phys. Rev. A* **54**, No.6, p.5400-5409 (1996).
- [7] H.J.Eichler, P.Günter, D.W.Pohl. "Laser-induced dynamic gratings", Springer Series in Optical Sciences, vol.50, Springer, Berlin (1986).

Energy transfer processes in Cr^{3+} , Nd^{3+} : YAG

A. Lupei, V. Lupei, A. Petraru and M. Petrache

Institute of Atomic Physics, Bucharest, 76900, Romania

ABSTRACT

The effects of co-doping with Cr^{3+} on the absorption and emission characteristics of double doped Cr^{3+} , Nd^{3+} :YAG (yttrium aluminium garnet) are analysed. The multisite structure due to co-doping (samples with a large range of Cr^{3+} content were used) is separated from that in single doped crystals. At least seven new lines have been separated in high resolution spectra and a tentative assignment in terms of structural data is proposed. These data suggest that the energy transfer data should be analysed in terms of inhomogeneous system. However, the measurements indicate strong migration effects. The global donor and acceptor data at 300K show a linear dependence on donor concentration, but the decays cannot be described in terms of published theoretical models.

1. INTRODUCTION

The pump efficiency of rare earth (RE^{3+}) ions emission in various crystals could be improved by co-doping with Cr^{3+} , due to its strong absorption bands and to the subsequent $\text{Cr}^{3+} \rightarrow \text{RE}^{3+}$ energy transfer. The Cr^{3+} sensitisation processes of RE^{3+} emission have been investigated in many systems, but several aspects are still unclear. Among these we mention: (i) the static spectral modifications due to Cr^{3+} co-doping, (ii) the determination of the nature of Cr^{3+} - RE^{3+} interactions involved in the energy transfer and its connection with static effects, (iii) the investigation of migration on donors and its effect in transfer efficiency. These aspects have not been yet clarified for $\text{Cr}^{3+} \rightarrow \text{Nd}^{3+}$ energy transfer in various crystals¹⁻¹⁰. The presence of an acceptor A close to a donor D determines changes in the spectral properties and the system could appear as a multisite one, each site having its own spectral and dynamic properties. The energy transfer processes are more complex and could involve selective transfer given site as well as the intersite transfer.

This study presents new data relevant to sensitization with Cr^{3+} of Nd^{3+} emission in YAG ($\text{Y}_3\text{Al}_5\text{O}_{12}$).

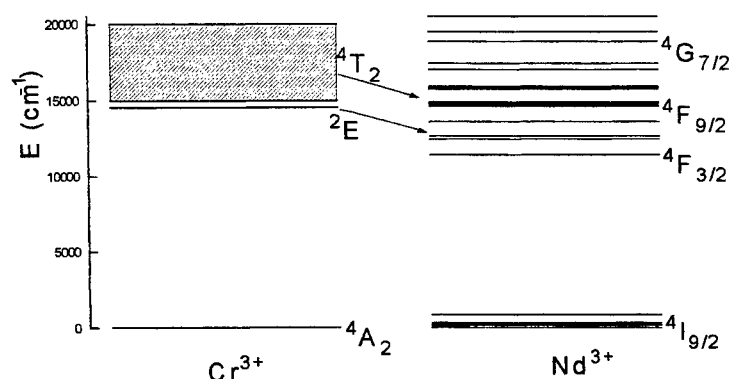


Fig. 1 A global energy level diagram of YAG: Cr,Nd system .

The high resolution spectral data of Cr, Nd: YAG are compared with those of single doped samples Nd: YAG and Cr: YAG. The spectra of Nd^{3+} as well as Cr^{3+} ions show, in high temperature grown YAG, a complex multisite structure. The nature of various sites in single doped crystals has been the subject of many studies^{11, 12} and essentially is elucidated. Nd^{3+} enters in YAG preponderantly in dodecahedral Y^{3+} c-sites (lines N). Besides these lines, shifted lines

due to $\text{Nd}^{3+}(\text{c}) - \text{Nd}^{3+}(\text{c})$ pairs at different distances have been observed (M_i lines), and in high temperature crystals two other types of sites were reported, P_i lines connected with a close nonstoichiometric defect (Y^{3+} in a - octahedral sites) and A lines due probably to Nd^{3+} in octahedral sites. Cr^{3+} enters in octahedral a-positions of YAG and the multisite structure, observed in R lines region in emission (S_i lines) has been assigned to the same nonstoichiometric defect $\text{Y}^{3+}(\text{a})$ ¹³.

The purpose of this paper is to present experimental and analyse the high resolution absorption and emission data Cr^{3+} , Nd^{3+} : YAG in terms of structure of the centers. The luminescence kinetics of both ions, with a stress on the migration effects is also discussed.

2. EXPERIMENT

Cr, Nd: YAG samples with Nd^{3+} content of ~1 at. % and variable Cr^{3+} from 0.1 to 5at. % have been grown by Czochralski method. The transmission spectra with lamp pumping and emission under short pulse laser excitation have been measured with a set-up including a computer controlled GDM monochromator, S_{20} or S_1 photomultipliers and a multichannel MCS analyser. The measurements have been performed at different temperatures. The excitation has been performed with 532nm or a dye laser.

3. RESULTS

3.a Absorption spectra

High resolution transmission spectra at low temperatures have been measured in similar conditions for Cr, Nd: YAG samples as well as for single Nd or Cr -doped crystals. Due to mutual crystal field perturbations of the two ions in co-doped samples an additional multisite structure in Cr, Nd: YAG should be observed in the spectra of both ions. However, in absorption, this structure was analysed only in Nd^{3+} lines, since Cr^{3+} R lines are too weak and broad to detect such effects. Since both ions present a multisite structure in single doped crystals, the new features due to co-doping have been separated by comparison of various co-doped with single doped samples. An example of multisite structure is given in Fig. 2 for the $^4\text{I}_{9/2}(1) \rightarrow ^4\text{F}_{3/2}(1)$ absorption line.

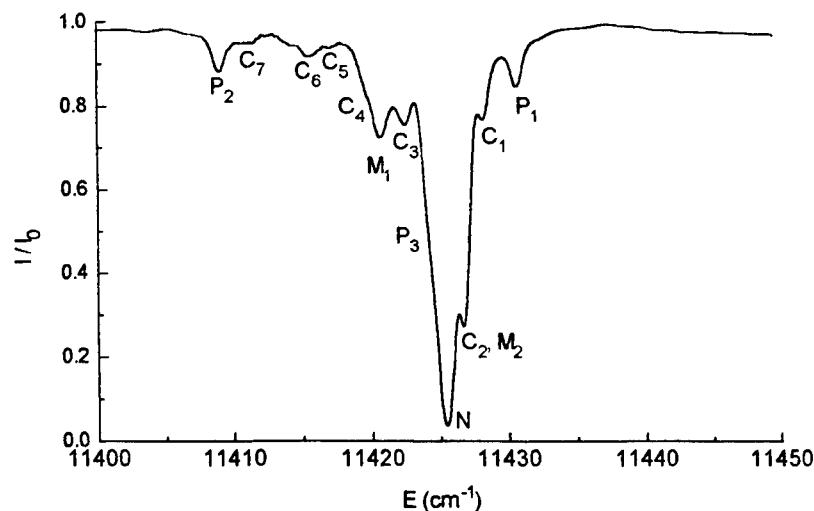


Fig. 2. The transmission spectrum corresponding to $^4\text{I}_{9/2}(1) \rightarrow ^4\text{F}_{3/2}(1)$ Nd^{3+} transition, at 10K, for a Cr (1.25at. %) Nd(1.3at. %):YAG sample.

The new satellites due to Cr^{3+} co-doping are denoted by C_i , while for the others lines representing Nd^{3+} main line and multisite structure in Czochralski grown samples we kept the usual notations (P_i , M_i). Similar complex structure has been observed in other transitions too.

The co-doping with Cr^{3+} determines two effects: the apparition of new lines C_i and changes in the relative concentration of the main line N and other satellite lines; but even at 5at. % Cr^{3+} , the isolated Nd^{3+} lines N are dominant. As the relative intensities of the C_i lines grow with Cr^{3+} content, those of N, P or A (see later) decrease.

3. b. Nd^{3+} emission

We have investigated the Nd^{3+} and Cr^{3+} emission under nonselective pumping with 532nm or a dye laser.

The Nd^{3+} emission spectra under 532nm pumping have been studied since most of the previous data on Cr^{3+} - Nd^{3+} energy transfer have been measured under this excitation, in the assumption that at this wavelength only Cr^{3+} ions are pumped. Fig. 3 presents comparatively part of the $^4\text{F}_{3/2}(1) \rightarrow ^4\text{I}_{9/2}$ emission at 10K under pumping with 532nm in two samples. The spectra were taken in reabsorption conditions, so that the resonant N line ($^4\text{F}_{3/2}(1) \rightarrow ^4\text{I}_{9/2}(1)$ transition), although relatively strong, is practically missing. At low Cr^{3+} content (0.1%) (Fig. 3), the low temperatures emission spectrum is dominated by center A as is the case of single Nd^{3+} doped samples⁹. The Cr^{3+} co-doping brings two changes: the decrease of the relative intensity of A lines comparatively to N and the apparition of new lines denoted by C_i .

At direct nonselective pumping in Cr^{3+} with a dye laser, in the reabsorption conditions, the Nd^{3+} emission is dominated by C_i centers (Fig. 4).

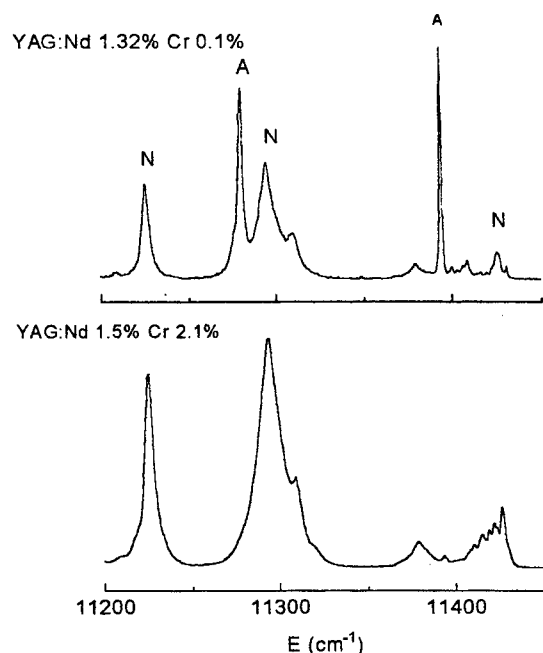


Fig. 3 Part of the $^4\text{F}_{3/2}(1) \rightarrow ^4\text{I}_{9/2}$ emission at 10K under pumping with 532nm in two YAG: Nd, Cr samples.

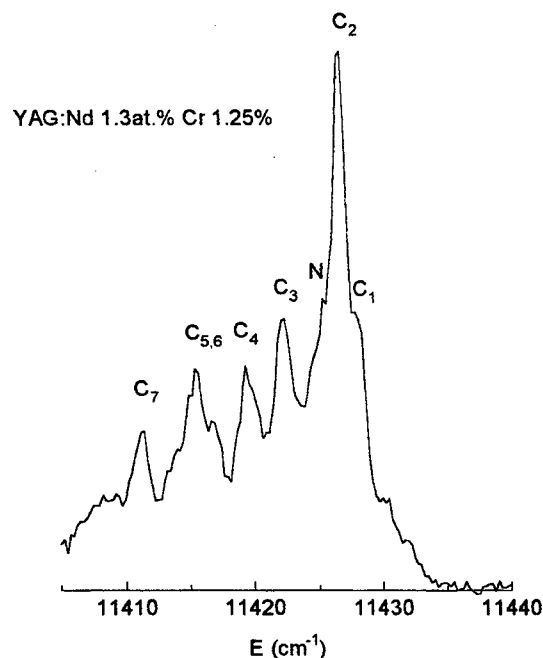


Fig. 4 The emission spectra ($^4\text{F}_{3/2}(1) \rightarrow ^4\text{I}_{9/2}(1)$ transition), taken in reabsorption conditions, of a YAG: Nd, Cr sample at 10K under dye pumping.

The explanation of this behaviour at pumping with 532nm is that, at this wavelength, one excite simultaneously Cr^{3+} ($^4\text{T}_2$) and Nd^{3+} . In Nd^{3+} : YAG crystals at very low temperatures the 532nm radiation is almost resonant with one

of the $^4I_{9/2} \rightarrow ^4F_{9/2}$ absorption lines of a center A and weakly absorbed in a hot band of the absorption spectrum of center N. Thus, at low temperatures, the emission of Nd: YAG, at this pumping, is dominated by center A. At higher temperatures the N center emission in Nd: YAG, at this pumping, becomes prevalent.

In Cr, Nd: YAG with 532nm besides Cr^{3+} (4T_2), a center A of Nd^{3+} is pumped⁹ at low temperatures along with Nd^{3+} N center.. At 300K the competition is between excitation in Nd^{3+} hot band of center N and Cr^{3+} (4T_2). This fact affects the shape of Nd^{3+} decay curves, that will contain contribution of direct pumping too, function of Cr/Nd content and temperature. This is true for other pumpings too, especially at low temperatures, when the transfer efficiency is low and could compete with direct pumping in very small Nd^{3+} lines.

4. LUMINESCENCE KINETICS

4.a Luminescence kinetics at low temperatures

The low temperature decays are very complex and depend strongly on sample and emission wavelength. Since our samples have similar Nd^{3+} content, and a large range of Cr^{3+} concentrations, the kinetics of both ions show clear migration effects even at low temperatures, excepting the samples with a very low Cr^{3+} content.. Though it is difficult to separate all Nd^{3+} centers emission one can present several characteristics of the decays of N and C₁ centers at 10K: (i) for all Cr^{3+} concentrations the decays present risetimes followed by a descending curve with a complex shape; (ii) the risetime decreases as Cr^{3+} content increases and at a given concentration is larger for N and shorter for C₄₋₇ centers. This indicate that at low temperatures the transfer Cr- Nd is rather slow even for perturbed Cr - Nd centers.

4.b Luminescence kinetics at 300K

In order to investigate the energy transfer processes at 300K, the global emission of donor Cr^{3+} (R_1 line) and acceptor ($^4F_{3/2}$ Nd^{3+}) emission decays in various samples have been measured. The intrinsic lifetime τ_0 for Cr^{3+} is strongly dependent on temperature, $\sim 1850\mu s$ at 300K and $\sim 9msec$ at 10K, while the $^4F_{3/2}$ Nd^{3+} decay is practically temperature independent with $\tau_0 \sim 260\mu s$. At Nd^{3+} concentrations used in our co-doped samples, the $^4F_{3/2}$ Nd^{3+} emission is slightly non-exponential, but this is less important for the present discussion. In the co-doped samples both Cr^{3+} and Nd^{3+} resonantly pumped decays are nonexponential and show a strong dependence on the Cr^{3+} content.

4.b.1. Cr^{3+} emission decays in YAG:Cr, Nd

The Cr^{3+} global emission decays in various co-doped samples show a strong increasing of quenching with Cr^{3+} content. Since the acceptor (Nd^{3+}) concentration is around 1at.% in all samples, the observed dependence can be connected to accelerated transfer by migration.

An attempt to describe Cr^{3+} decay curves in terms of energy transfer models¹⁴⁻²⁰ has been made. From the experimental decays the transfer functions defined as

$$-P(t) = \ln\left(\frac{I}{I_0}\right) + \frac{t}{\tau_0}$$

are obtained. For 0.1at% Cr^{3+} the transfer function $P(t)$ can be described, at large times (Fig. 5), by a $t^{1/2}$ dependence, suggesting a direct energy transfer process with a dipole-dipole D - A interaction. A transfer microparameter $C_{DA} \sim 4.5 \cdot 10^{-40} cm^6 s^{-1}$ is estimated; lower than that reported recently³ for a sample with 1at.%Nd 1at.%Cr.

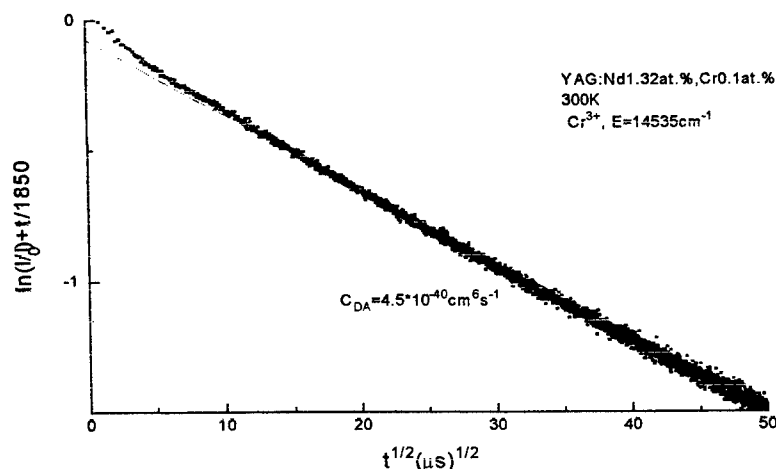


Fig. 5. The transfer function $P(t)$ of the Cr^{3+} emission at 300K for a sample YAG: Nd 1.31at.%, Cr 0.1at. % experimental points and fitting with $t^{1/2}$.

At short times, deviations from this law are observed. The faster parts could be connected with different transfer interactions for closer Cr^{3+} - Nd^{3+} pairs. At larger Cr^{3+} concentrations (even 0.5at. %), the decays are faster suggesting migration accelerated energy transfer. The consideration of migration effects as a linear function of time^{12,13} in $P(t)$ does not give a coherent description of our data, even at large times. For this reason, in order to describe the dependence on donor concentration we use a global effective transfer rate³ W_{tr} defined with the help of an average lifetime as the area under the decay curve, i.e.

$$\tau_{med} = \int I(t) / I_0 dt$$

and the transfer rate

$$W_{tr} = \frac{1}{\tau_{med}} - \frac{1}{\tau_0}$$

where τ_0 is the lifetime of isolated Cr^{3+} ions. The results are presented in Fig. 7. One observes an almost linear dependence on Cr concentrations for the range 0.5-2%, (exception makes 5%). This dependence is a measure of migration.

4.b.2. Nd^{3+} emission

The ${}^4F_{3/2}$ Nd^{3+} emission (at pumping in Cr^{3+} 4T_2 level) presents decays with risetimes and descendent parts depending on the Cr^{3+} content. For an illustration in Fig. 6 comparatively the Nd emission in three samples are presented.

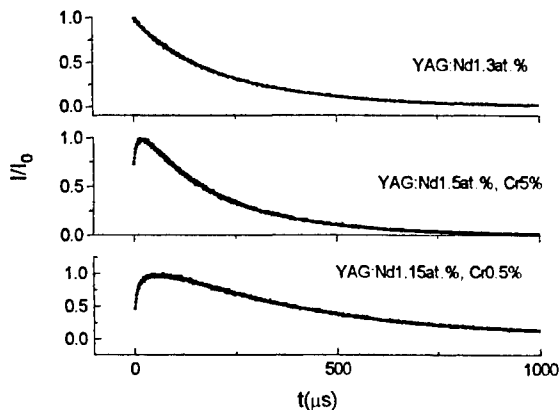


Fig. 6. ${}^4F_{3/2}$ Nd^{3+} decay for a single doped sample (upper curve) and two co-doped samples, pumped in Cr^{3+} .

For 5at. Cr^{3+} the transfer is very fast, so that after $\sim 50\mu s$ Nd^{3+} the decay is similar to that of directly pumped sample (upper curve). For lower Cr^{3+} content (0.5%), the slower transfer from Cr^{3+} is clear on the entire Nd^{3+} decay (lower curve).

No theoretical expressions to describe the acceptor emission in such a case are available. A parameter that could give some information on the global acceptor (Nd^{3+}) emission is the build up time, t_{Amax} . An almost linear dependence of this time on Cr emission is measured at 300K, as shown in Fig. 8.

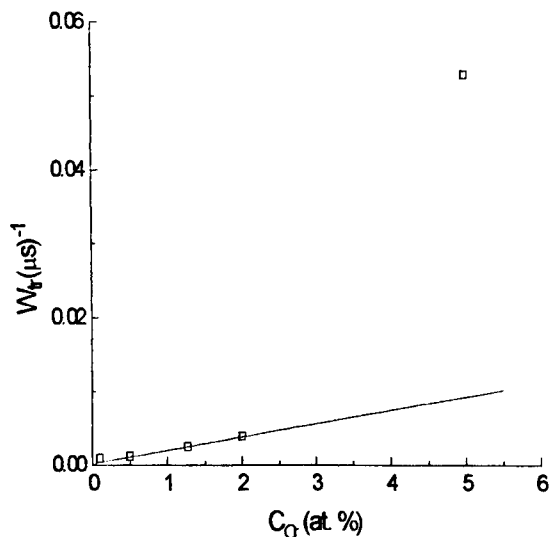


Fig. 7 The dependence of the global Cr - Nd transfer rate on Cr content.

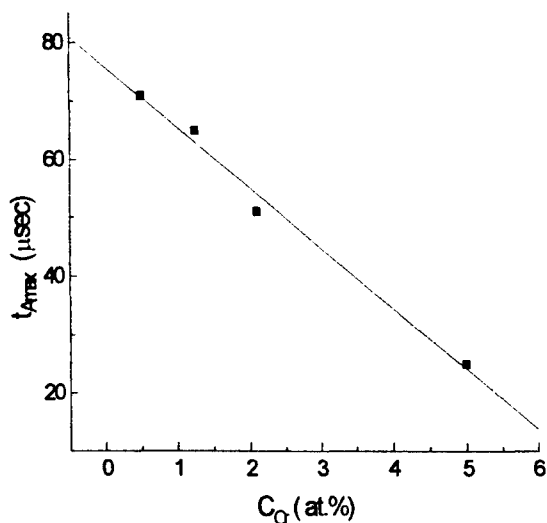


Fig. 8 The dependence of the Nd^{3+} emission building time on the Cr^{3+} concentration .

5. CONCLUSIONS

- The co-doping with Cr^{3+} induce *at least seven new lines* in Nd^{3+} spectra at 10K, but even at 5at. % Cr^{3+} , the isolated Nd^{3+} lines are dominant; the co-doping cannot change laser emission wavelength in this case.

- The positions (in cm^{-1}) of these centers (C_i) in ${}^4F_{3/2}(1) \rightarrow {}^4I_{9/2}(1)$ Nd^{3+} transition relatively to the main line N are given in Table 1. Shifts up to $\sim 14cm^{-1}$ are observed in this transition.

Table 1. Satellite structure induced by Cr^{3+} co-doping in Nd^{3+} spectra.

C_1	C_2	N	C_3	C_4	C_5-C_6	C_7
11428.5	11427	11425.5	11422.2	11419	11415-17	11411.5

- Some of the C_i lines are assigned to $\text{Cr}^{3+}(\text{a})$ - $\text{Nd}^{3+}(\text{c})$ pairs. For nearest neighbours Cr - Nd pairs an anisotropy of the distortion is assumed, i.e. more lines (C_1 , C_3 , C_7) are tentatively assigned to pairs at the minimum distance (3.35 Å). C_2 could be connected with a second order pairs at 5.408 Å. Cr^{3+} replace $\text{Y}^{3+}(\text{a})$ in octahedral sites too. This could bring additional lines in Cr, Nd: YAG.

- Luminescence kinetics of these C_i Nd^{3+} centers at pumping nonselectively in Cr^{3+} show different shapes with risetimes dependent on Cr^{3+} content. This system behaves inhomogeneously and the $\text{Cr} \rightarrow \text{Nd}$ energy transfer is rather slow at low temperatures.

- The fast part at the beginning of Cr^{3+} decay could be connected to another type of interaction and not with correlated distribution; a dipole - quadrupole mechanism is very likely. The ${}^4\text{F}_{3/2}$ Nd^{3+} emission (at pumping in Cr^{3+} ${}^4\text{T}_2$ level) presents decays with risetimes and descendent parts depending on the Cr^{3+} content, unlike the recent results⁸⁻¹⁰ on Cr, Nd: YAlO_3 .

- Two global parameters for migration effects are defined: a global transfer rate W_{tr} (for donors Cr^{3+}) and the build up time, t_{Amax} for global acceptor (Nd^{3+}) emission. An almost linear dependence of these parameters on Cr^{3+} content was obtained. A theoretical treatment to take into account the migration effects in inhomogeneous systems (as in the case of direct transfer) is necessary.

6. REFERENCES

1. J. Mares, W. Nie, G. Boulon, " Multisites and energy transfer in Cr^{3+} - Nd^{3+} codoped YAG and YAlO_3 crystals", *J. Phys.* **51**, 1655-1669 (1990)
2. W. Nie, G. Boulon, A. Monteil, *Opt. and Quantum Electronics*, **22**, S227 (1990),
3. J. Mares, W. Nie, G. Boulon, "Nonradiative energy transfer between Cr^{3+} and Nd^{3+} multisites in YAG laser crystals", *J. Phys.* **11**, 881-899 (1991)
4. J. Mares, W. Nie, G. Boulon, " Energy transfer between various Cr^{3+} and Nd^{3+} multisite in YAG: Nd, Cr", *J. of Lum.* **48/49**, 227- 231 (1991),
5. Y. Guyot, L.E. Bausa, E. Camarillo, J. Garcia Sole, I. Vergara, A. Monteil, R. Moncorge, " Infrared fluorescence spectra of Nd^{3+} sites in GGG: Nd and GGG: Nd, Cr", *J. Appl. Phys.* **72**, 5876- 5880 (1992)
6. T. P.J. Han, M.A. Scott, F. Jaque, H.G. Gallagher, B. Henderson, " Nd^{3+} - Cr^{3+} pairs in GSGG garnet crystals", *Chem. Phys. Lett.* , **208** 63-67 (1993)
7. P. Hong, X.X. Zhang, C. W. Struck, B. di Bartolo, " Luminescence of Cr^{3+} and energy transfer between Cr^{3+} and Nd^{3+} in YAG", *J. Appl. Phys.* **78**, 4659-4667 (1995)
8. S.R. Rotman, E. Luria, N. Yitzhaki, A. Eyal, " Practical models for energy transfer between ions in solids", *Optical Materials* **5**, 1-33 (1996)
9. S.R. Rotman, E. Luria, J. Mares, G. Boulon, A. Brenier, "Time decay of excited chromium and neodymium doped yttrium aluminium perovskite", *J. Appl. Phys.* **80**, 1994-1998, (1996)
10. E. Luria, S.R. Rotman, J. Mares, G. Boulon, A. Brenier, L. Lou, " *J. of Lum.* **72-74**, 951 (1997)
11. V.V. Osiko, Yu. K. Voronko, A. A. Sobol, "Spectroscopic investigations of defect structures and structural transformations in ionic crystals", *Crystal* **10**, Springer Verlag, 37 (1984)
12. V. Lupei, A. Lupei, C. Tiseanu, S. Georgescu, C. Stoicescu, P. M. Nanau, "High resolution optical spectroscopy of Nd in YAG - a test for structural and distribution models", *Phys. Rev. B. Condens. Mat.* **95**, 8 (1995)
13. V. Lupei, L. Lou, G. Boulon, A. Lupei, "On the origin of the satellite structure of luminescent spectra of Cr^{3+} in YAG", *J. Phys. Condens. Mat.* **5**, L 35 (1993)
14. D. L. Dexter, *J. Chem. Phys.* **21**, 836 (1953)
15. M. Inokuti and F. Hirayama, *J. Chem. Phys.* **43**, 1978 (1963)
16. I. S. Golubov and Y. V. Konobeev, *Sov. Phys. Sol. State* **13**, 2679 (1972)
17. A. I. Burnstein, *JETF* **62**, 1695(1972); **73**, 662 (1977)
18. D. L. Huber, *Phys. Rev. B* **20**, 2307 (1977)
19. "Laser Spectroscopy of Solids" Eds. W. M. Yen. P. M. Seltzer, Springer - Verlag (1986)
20. V. Lupei, A. Lupei and G. Boulon, "On the Characteristics of Sensitized Emission in Laser Crystals" *Phys. Rev. B* **53**, 1 (1996)

Infrared Photochemistry of Trichloroethylene in Presence of Oxygen

C.Ungureanu

Institute of Isotopic and Molecular Technology, 3400 Cluj - Napoca 5
P.O.Box 700. Romania

M.Ungureanu

Gh.Lazar College, 2400 Sibiu, Romania

ABSTRACT

Trichloroethylene with added molecular oxygen was photolysed with a TEA CO₂ laser radiation, at ν_4 (933 cm⁻¹) fundamental vibrational band for C₂HCl₃ and at ν_3 (1020 cm⁻¹) fundamental vibrational band for C₂DCl₃. The stable final products in the infrared multiphoton dissociation of trichloroethylene were determined by mass spectrometry in the 0.5-10 Torr pressure range of the gas. After the photodissociation process, the following final products appeared: HCl (or DCl), C₂Cl₂, C₂Cl₄, C₂Cl₄O, CO, CO₂ and C₂O₃. Experimental measurements were also performed to obtain information about the dependence of the specific dissociation rate versus laser pulse energy, for both isotopic species of trichloroethylene.

Keywords: Multiphoton photochemistry; isotopic effects

1.INTRODUCTION

The recent interest in infrared multiphoton dissociation (IRMPD) of the trichloroethylene (TCE) molecule has revealed some questions referring to the first step of the dissociation, to the reactions involving free radicals produced in the dissociation process and to the isotopic selectivity obtained in these conditions. For trichloroethylene recent years have brought considerable progress in relating product state distribution of photoinitiated reactions to detailed features of the potential energy surface and respectively in determination of the transition state structure for products elimination ¹⁻⁴.

A detailed chemical kinetic mechanism for the combustion of C₂HCl₃ under fuel rich and slightly sooting conditions in flames of C₂HCl₃/O₂/Ar has been developed previously by W.D.Chang and S.M.Senken ⁵.

In a recent work we have presented results on the infrared multiphoton absorption of protonated and deuterated TCE ⁶. The dependence of infrared multiple photon cross section and average number of photons absorbed per molecule versus laser fluence and laser frequency, for different pressures of gas, has been investigated by using a TEA CO₂ laser.

In the experiments reported in this paper, we have studied the IRMPD of the TCE in mixture with molecular oxygen (O_2), in order to shed some light on the extent to which non-equilibrium effects may be reflected in overall chemical behavior of the reaction. In the photodissociation of TCE, the primary reaction pathways, such as HCl and Cl elimination, have been observed^{3,4}. The lowest energy dissociation of TCE is the HCl elimination. We have observed that the major final products of pure TCE multiphoton dissociation were HCl, C_2Cl_2 , C_2Cl_4 and C_2 . In the case of mixtures with O_2 the following final products were detected: HCl or/and DCl, C_2Cl_2 , C_2Cl_4 , C_2Cl_4O , CO, CO_2 and C_2O_3 ^{7,9}.

We have carried out the study of reaction induced by multiple infrared photon absorption in TCE/ O_2 mixtures, in order to gain information of use in elucidating the dynamics and detailed mechanism of this process. The attractive feature of this molecule is that while the primary laser-induced process is a simple HCl elimination, there are also competitive channels present (Ex: C-Cl bond cleavage) which provide quantitative tests of model for the dynamics of the process. The formation of reactive radicals induce a complex overall kinetics for secondary reactions.

2.EXPERIMENTAL

The IRMPD experiments were performed using a home built TEA- CO_2 laser, with an output power of 0.7 - 2.5 J/ pulse, with $\pm 5\%$ fluctuations for the rotation lines of the 00^0_1 - 02^0_0 and 00^0_1 - 10^0_0 vibrational bands. The laser beam with a temporal pulse shape beginning with a 250 ns spike followed by an about 1.0 μs tail, was focused in the center of the reaction cell with a 9.5 cm focal length BaF_2 lens. The reaction vessel was a Pyrex cylindrical cell (diameter -2,4 cm, length 10.0 cm), with KCl windows at both ends.

The sample handling has been performed by using a standard vacuum line with pressure monitoring system. The reagents used in this study have been TCE (C_2HCl_3 and/or C_2DCl_3) with a chemical purity better than 99% and O_2 (>99,9%). In some experiments, isotopic mixtures with $\sim 55\%$ C_2HCl_3 and $\sim 45\%$ C_2DCl_3 have been used. The deuterated TCE, with about 3% protonated compound, has been obtained by means of base catalysed aqueous exchange between TCE and D_2O . The purity of the mentioned gases and the analyses of reaction mixtures and of photoreaction products have been carried out by means of a mass spectrometer VARIAN MAT 311. In the case of CO analysis a high resolution system has been necessary to determine unambiguously the peaks for $[CO]^+$ (27,9949 a.m.u.) and $[N_2]^+$ (28,0061 a.m.u.) ions.

In IRMPD experimental measurements, the following laser lines have been used: 10P(34)/931.0 cm^{-1} ; 10P(32)/932.0 cm^{-1} ; 10p(28)/936.8 cm^{-1} ; 10P(24)/940.6 cm^{-1} ; 10P(22)/942.1 cm^{-1} ; 10P(18)/946.0 cm^{-1} ; 10P(12)/951.2 cm^{-1} and 10P(6)/956.2 cm^{-1} for excitation of strong vibrational band ν_4 , (C-Cl bond) /933 cm^{-1} of C_2HCl_3 ⁸. We have used also the laser lines 9P(30)/1037 cm^{-1} and 10R(30)/982.1 cm^{-1} for the excitation of strong vibrational band ν_3 (C-D bond)/1020 cm^{-1} of C_2DCl_3 ^{8,10}.

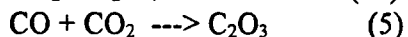
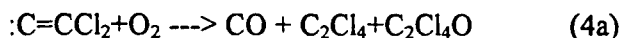
3. RESULTS AND DISCUSSIONS

For the ethylene replacing with Cl one or more H atoms considerably increases the complexity of the system. Yokoyama et al.³ reported the following conceivable reaction channels for the TCE dissociation process, in primary step of the reaction:



In reactions (1a) and (1b) HCl is produced by "three center elimination" and respectively by "four center elimination".³ The difference between the transition state structures, for the two HCl elimination, is presented in the work of Yokoyama et al.³ where it is possible to observe and the contrastive features of the two HCl eliminations. In that paper is presented also the enthalpy diagram for TCE dissociation reaction. The threshold energy (kcal/mol) for reaction (1a) is lower by 5.2 kcal/mol than that for reaction (1b), indicating a possible competition between these reactions. In the photodissociation of TCE the primary reaction pathways, such as HCl and Cl elimination, have been observed. The lowest energy dissociation of TCE is HCl elimination (78.8 kcal/mol). The major final products of pure TCE multiphoton dissociation were HCl, C₂Cl₂, C₂Cl₄ and C₂. The HCl or DCl and C₂ dissociation final products were deposited on the inner wall of the reaction cell. Only C₂Cl₂ and C₂Cl₄ could be analysed by mass spectrometry.

The gas mixtures used in the present experimental measurements were with ratios O₂/TCE between 0.27 and 0.97 at pressures for TCE in the range of 0.5-10 torr. When O₂/TCE mixtures were photolysed and subsequently analysed, the following major products were obtained: HCl or/and DCl, C₂Cl₂, C₂Cl₄, C₂Cl₄O (tetrachloroethylene oxide), CO, CO₂ and C₂O₃. With the exception of HCl or DCl, the other major photoproducts could be analysed by mass spectrometry. The possible reactions which account for the formation of the final products, in the presence of O₂ in a high intensity infrared radiation field, for the case (1a) are the following:



The final products observed in this study are consistent with the C=C bond scission of dichlorovinylidene resulting in the second step of the photodissociation reaction⁸.

Products analysis proves that reaction channel (1a) is dominant in the dissociation process of TCE. In the reaction channel (1b), besides HCl /DCl, is produced CCl≡CCl (dichloroacetylene) that is a relatively stable final product.

The unconverted fraction of TCE, [C₂HCl₃]_n was measured as a function of laser pulse number (n) for three different gas mixtures (O₂/TCE ratios), at the same values for TCE initial pressure P_i, laser radiation frequency ν_L and laser pulse energy E_p. The variation of [C₂HCl₃]_n with n is illustrated in Figure 1. As it can be seen, there are two regions of [C₂HCl₃]_n dependence on

n , for the 0.275 and 0.464 values of O_2/TCE ratio. At $n < 200$ for $O_2/TCE = 0.275$ and at $n < 300$ for $O_2/TCE = 0.464$ there is an exponential decrease of the unconverted fraction of TCE with increasing number of pulses, showing a pseudo-first order kinetics over that range of conversion. At values for n higher than those mentioned before, the dependence of $[C_2HCl_3]_n$ on n shows an approximately constant value with the number of pulses. The plots are nearly parallel to the n -axis, confirming that in this range there is an inhibition of the reaction. In Figure 2 the plot of the unreacted oxygen fraction $[O]_n$ presents a fast decrease for $O_2/TCE = 0.275$ and at $n > 200$ the values of the $[O]_n$ are lower than $5 \cdot 10^{-2}$. The fast decrease of oxygen especially at low values of O_2/TCE ratio may lead to the fact that the conversion of TCE by IRMPD will be insignificant at higher values than those mentioned above for n . In the case of $O_2/TCE = 0.953$, the unconverted fraction $[C_2HCl_3]_n$ as a function of n shows an exponential decrease for the whole range of pulse number values, 0-700 (Fig 1)^{8,9}. Also, from Figure 2 we can see that $[O_2]_n$ shows a monotonous decrease in the mentioned pulse number range. An important conclusion from all experimental results, reported in Figures 1 and 2, is that TCE infrared multiphoton dissociation, in an intense laser radiation field, were carried out under pseudo-first order conditions in a large range of n , only at high values of O_2/TCE ratio for the gas mixture. Final photoproducts analysis proves that reaction channel (1a) is dominant in the dissociation process of TCE.

From Figure 3 one can estimate the formation of CO by $[CO]^+$ ion intensity, represented in arbitrary units (a.u.). As shown in Figure, the slope of $I [CO]^+$ versus n curve decreases as the laser pulse number increases. This is a frequently observed feature in the IRMPD of polyatomic molecules under mildly focusing conditions. The profiles of the curves for the other final stable photoproducts have similar features. The mass spectrometry measurements reveal that CO_2 concentration is close to a factor of 4 lower than that of the CO molecule. The concentration of C_2Cl_2 , C_2Cl_4 , C_2Cl_4O and C_2O_3 molecules are much lower than that of CO molecule.

As shown in Figure 4 there is a complicated dependence of the photoreaction products formation versus E_p . From figure we can observe that CO relative yield increases rapidly with laser pulse energy under 0.75 J/pulse. This means that about 0.75 J/pulse represents the threshold after which there is a saturation in products formation.

TCE excited by IR multiphoton absorption, decomposed by reaction channels exposed in (1a) and (1b) Figure 5, shows the dependence of the specific dissociation rate per pulse,

$$W_d^H = -\frac{1}{n} \ln \left(\frac{[C_2HCl_3]_n}{[C_2HCl_3]_i} \right) \text{ or } W_d^D = -\frac{1}{n} \ln \left(\frac{[C_2DCl_3]_n}{[C_2DCl_3]_i} \right) \quad (6)$$

versus laser pulse energy E_p , at the $\nu_L = 9P(28)/1034 \text{ cm}^{-1}$ and for an isotopic mixture of 54% C_2HCl_3 and 46% C_2DCl_3 . W_d^H is specific dissociation rate for C_2HCl_3 and W_d^D for C_2DCl_3 ^{9,10}. The other experimental conditions are specified in the figure. The 9P(28) laser line is resonant with the intense ν_3 (1020 cm^{-1}) vibrational band of deuterated TCE. From these results one can notice the existence of a low isotopic selectivity in the IRMPD process of the deuterated TCE. Furthermore this behaviour of the system is best interpreted in terms of redistribution of vibrational energy within the molecule, and between molecules, at the same time with the mode specific excitation. Finally we want to determine the fluence dependence of the dissociation probability per laser pulse for deuterated TCE. Figure 6 shows that the decomposition probability

increases rapidly with fluence until near 40 J/cm^2 and saturates near 1.0 after that value of the fluence. A similar behaviour is observed and for C_2HCl_3 .

4. CONCLUSIONS

Our results demonstrate once more the variability of phenomena in IR multiphoton excitation and dissociation of molecules and the fact that they can be understood with profound spectroscopic knowledge. It is necessary to study more rigorously the factors which may influence the IRMPD of TCE and product formation mechanism in the 1-10 Torr interval of pressure. For the experimental conditions exposed in this paper, the $\text{C}=\text{C}$ scission is apparently the dominant mechanism of dissociation in the second step of the reaction process. The presence of O_2 can induce the formation of $\text{C}_2\text{Cl}_4\text{O}$, CO , CO_2 and C_2O_3 molecules as final products, from the dichlorovinylidene fragment.

By means of mass spectrometry analysis both primary and secondary photolysis products were observed. The photoreaction channel (1a) is dominant in the dissociation process of TCE.

It is possible that the elimination of HCl or DCI by an α mechanism^{1,2} determines a low isotopic selectivity in the IRMPD of TCE.

5. REFERENCES

1. A.S.Sudbo, P.A. Schultz, E.R. Grant, Y.R. Shen and Y.T. Lee, "Multiphoton dissociation products from halogenated hydrocarbons" *J.Chem.Phys.*, 68, 1306 (1978).
2. G.R.Long, L.D.Prentice and S.E.Bialkowski, "Chemical reaction following the IRMPD of $\text{C}_2\text{F}_3\text{Cl}$ ", *Appl. Phys.*, B,34,97 (1984).
3. K.Yokoyama, G.Fujisawa and A.Yokoyama, "The mechanism of the unimolecular dissociation of trichloroethylene, $\text{CHCl}=\text{CCl}_2$, in the ground electronic state", *J.Chem. Phys.* 102, 7902 (1995).
4. Y.Huang, Y.Yang, G.He, S.Kashimoto and R.Gordon "State resolved translational energy distributions of Cl and HCl in the ultraviolet photodissociation of chloroethylene", *J.Chem.Phys* 103, 5476 (1995).
5. W.D.Chang and S.M. Seukan, "Detailed Chemical Kinetic Modeling of Fuel-Rich $\text{C}_2\text{HCl}_3/\text{O}_2/\text{Ar}$ Flames.", *Environ. Sci. Technol.* 23,442 (1989).
6. C.Ungureanu, V.Almasan and M.Ungureanu, " Multiphoton absorption of pulsed TEA- CO_2 laser radiation by isotopic species of trichloroethylene " *Infrared Phys. and Techn.* 37,451 (1996).
7. C.Ungureanu " The effects of laser radiation parameters and sample pressure on the multiphoton absorption and dissociation of chlorodifluoromethane- D ", *Rev. Roum. Phys.*,34, 1041 (1989).
8. C.Ungureanu, M.Ungureanu and N.Palibroda "I.R. multiphoton dissociation of protonated trichloroethylene", *Optoelectronica* Vol.4, No3 pag. 13 (1996).
9. C.Ungureanu,, M.Ungureanu, V.Almășan and N.Palibroda, "I.R. multiphoton dissociation of trichloroethylene isotopic species " 7 th International Conference on Multiphoton Processes " Sept 30-Oct 4, 1996, Garmisch-Partenkirchen, Germany.

10. M.Ungureanu and C.Ungureanu "Infrared Photochemistry of trichloroethylene in presence of oxygen", Roum. Jour. Optoelectronics, Vol. 5 No.4 (1997), in press.

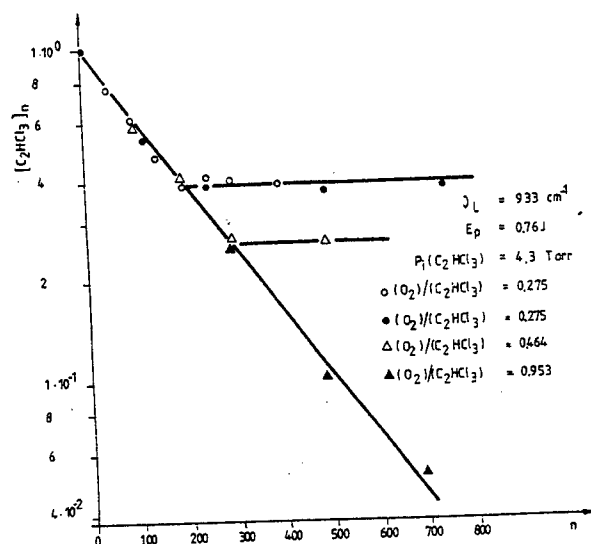


Fig 1. TCE unconverted fraction as a function of laser pulse number for different experimental conditions

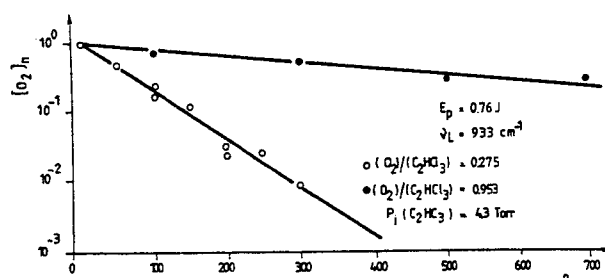


Fig.2 Oxygen unreacted fraction dependence on laser pulse number.

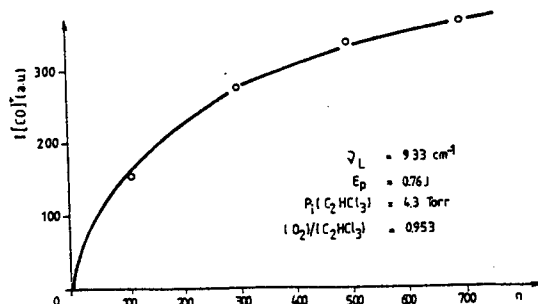


Fig 3. Intensity of the $[CO]^+$ ion peak vs. laser pulse number n , in arbitrary units

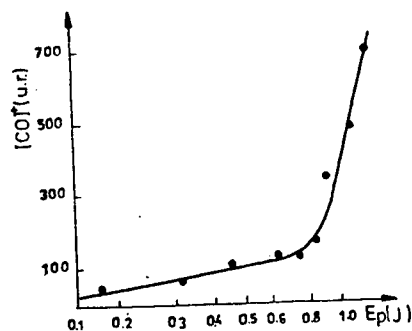


Fig.4. Intensity of the $[\text{CO}]^+$ ion peak vs. laser pulse energy E_p , in arbitrary units.

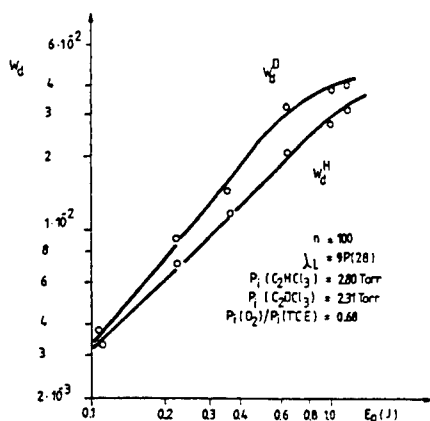


Fig.5. Specific dissociation rate per laser pulse (W_d) vs pulse energy E_p ; W_d^D - C_2DCl_3 and W_d^H - C_2HCl_3

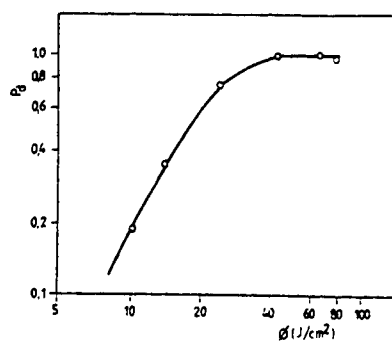


Fig.6. The dissociation probability per pulse (P_d) in function of fluence, (J/cm^2)

Excited xenon($1s_4$) atom detection by modulation laser absorption spectroscopy

Y.Sakai, M.A.Bratescu*, G.Musa*, K.Miyamoto, M.Miclea*

Hokkaido University, Department of Electrical Engineering, Sapporo 060, Hokkaido, Japan

* National Institute for Laser, Plasma and Radiation Physics, Bucharest, PO Box MG-36, Romania

ABSTRACT

A study on the space distribution of the excited xenon atoms on level $1s_4$ in a d.c. discharge in neon-xenon mixture is presented in this paper. The relative density of the excited xenon atoms was measured using diode laser absorption at 828.239 nm, corresponding to the xenon transition between $1s_4$ and $2p_5$ levels. A comparative analysis of the laser absorption signal and corresponding optogalvanic signal, permitted us to define a new parameter, namely optogalvanic effect efficiency, Eff_{OG} , as the size of the optogalvanic signal corresponding to an atom optically pumped by laser.

Keywords: laser plasma spectroscopy, optogalvanic effect, tunable diode laser monitoring of excited Xe species

1. INTRODUCTION

Laser plasma spectroscopy is rapidly becoming a very efficient tool for plasma studies and plasma parameter monitoring^{1,2}. Indeed, due to its precision, the density of atoms in a selected excited state can be observed in both time and space.

A study on the space distribution of the excited xenon atoms on level $1s_4$ in a d.c. discharge in neon-xenon mixture is presented in this paper. The relative density of the excited xenon atoms was measured using diode laser absorption at 828.239 nm, corresponding to the xenon transition between $1s_4$ and $2p_5$ levels.

A comparative analysis of the laser absorption signal and corresponding optogalvanic signal, permitted us to define a new parameter, namely optogalvanic effect efficiency, Eff_{OG} , as the size of the optogalvanic signal corresponding to an atom optically pumped by laser.

The dependencies, experimentally observed, of Eff_{OG} on various working parameters can give useful information on the elementary processes taking place in a discharge.

2. EXPERIMENTAL SET-UP

Two experimental arrangements were used to measure the distribution of the excited xenon atoms on level $1s_4$ and the optogalvanic signal in the interelectrode space of a d.c. discharge, as shown in Fig.1(a) and (b) where:

(a) is a d.c. plasma modulation system for measuring the relative density of excited xenon atoms, and

(b) a diode laser wavelength modulation system for measuring optogalvanic signals.

In these set-ups, the diode laser LT015MDO-Sharp with a wavelength range of 815 nm-845 nm and 30 mW maximum optical power output, is power-supplied and temperature-stabilised with a Melles-Griot Laser Driver 06DLD203. The xenon transition at 828.239 nm ($1s_4 - 2p_5$) can be achieved using a

diode laser current of 102.4mA and a junction temperature of 9.36° C; the optical power density of the laser beam is 3W/cm². The diode laser wavelength scanning over 75GHz range, with 64mHz frequency, is performed by a triangular signal generator and is marked with the interference fringes obtained from a confocal Fabry-Perot etalon (1.5GHz free spectral range). The xenon absorption signal and the marking interference fringes are simultaneously displayed on an oscilloscope screen and stored in a computer memory via GPIB interface.

The d.c. discharge is ignited and maintained between two stainless steel electrodes, 50mm in diameter, mounted inside a large vacuum chamber (200mm in diameter, 270mm high). The chamber is provided with two glass windows, which ensure passage of the laser beam through the gas discharge parallel to the surfaces of the electrodes. One electrode (the cathode) is movable so that the necessary cathode-anode distance can be set.

In the d.c. plasma modulation detection system, the discharge is supplied by a high voltage generator. The current through the discharge is modulated with a controlled frequency in the range of 400Hz-1500Hz, using a working frequency of 465Hz. The plasma is periodically switched *on* and *off* and consequently, the absorption signal has the same frequency as plasma modulation. Fig.2 shows the absorption signal of excited xenon atoms for a 1s₄ - 2p₅ transition as measured by the plasma modulation technique.

The optogalvanic signal is obtained with the experimental set-up shown in Fig.1(b), by using wavelength modulation spectroscopy³. The diode laser modulation frequency is 1.3kHz. The first harmonic signals of xenon transition at 828.239nm are used to carry out the measurement. Fig.3(a) shows the first harmonic optogalvanic signal and Fig.3(b) the corresponding signal in the second harmonic.

3. EXPERIMENTAL RESULTS

As a result of laser light absorption, excited xenon atoms on level 1s₄ change into excited xenon atoms on level 2p₅. From either of these excited states, xenon atoms can be ionised by electron collisions, the corresponding cross sections being $\sigma(1s_4)$ and $\sigma(2p_5)$.

When laser light with a wavelength corresponding to the transition 1s₄ - 2p₅ of xenon atoms is absorbed, the relative value of the laser light absorption signal in plasma modulation absorption method I_{PM} is:

$$I_{PM} = I_0 - I \quad (1)$$

where I_0 is the photodetector signal when plasma is *off* and I the corresponding photodetector signal when plasma is *on*. The value of I_{PM} is directly proportional with the density $[Xe(1s_4)]$ of the excited xenon atoms on level 1s₄:

$$I_{PM} = K \cdot [Xe(1s_4)] \quad (2)$$

where K is a constant.

Absorption of the laser light leads to a population depletion on level 1s₄ and a simultaneous increase in population on level 2p₅. This changes the balance of ions which are generated via electron collisions with the excited xenon atoms on these levels. Consequently, a change in plasma properties, e.g. an increase in or decrease of the electrical conductivity, is observed upon laser light absorption (optogalvanic signal).

In a first approximation, the optogalvanic signal I_{OG} is given by the relation:

$$I_{OG} = k_a n_e [Xe(1s_4)] \cdot [\langle \sigma(2p_5) v \rangle - \langle \sigma(1s_4) v \rangle] + k_b [Xe(1s_4)] \cdot [M] \quad (3)$$

where k_a is a constant, n_e the electron density and $\langle\sigma v\rangle$ the averaged cross-section over electron distribution function¹ (EDF) for the ionisation of excited xenon atoms, while k_b is the rate constant for second kind collisions and $[M]$ is the density of atoms regardless of their nature.

As the optogalvanic signal arises upon optical pumping to upper state of the excited xenon atoms and since the density of these pumped atoms is directly proportional with I_{PM} (see eq.(2)), we may consider the ratio I_{OG}/I_{PM} as the efficiency of the optogalvanic effect Eff_{OG} . So we have

$$Eff_{OG} = \frac{I_{OG}}{I_{PM}} \quad (4)$$

a value proportional with the size of the optogalvanic effect for one absorbed photon.

From eq.(4) we see that this efficiency of the optogalvanic effect can be measured experimentally.

If equations (2) and (3) are taken into account, we obtain:

$$Eff_{OG} = \frac{k_a}{K} n_e [\langle\sigma(2p_5)v\rangle - \langle\sigma(1s_4)v\rangle] + \frac{k_b}{K} [M] \quad (5)$$

which shows the dependence of the optogalvanic efficiency on the elementary processes taking place in the discharge.

Fig.4 gives the values of the optogalvanic signal I_{OG} and absorption signal I_{PM} , as measured in various positions of the incident laser light in the cathode-anode space for the following experimental parameters:

total gas mixture pressures	5 torr; 10 torr
gas mixture	xenon-neon
xenon concentrations	5 %; 10 %; 20 %; 100 %
discharge currents	1 mA; 3 mA; 5 mA

In the case of pure xenon, both the absorption signal and the optogalvanic one have maximum values near the cathode. This maximum moves away from the cathode as neon is added to xenon as can be seen for xenon concentrations of 10% and 20%. On further xenon dilution in the neon-xenon mixture, the maximum of the curve moves back near the cathode as illustrated by the curve corresponding to a xenon concentration of 5%.

In Fig.5, we plotted optogalvanic efficiency (as earlier defined) versus the position of the incident laser beam in the interelectrode space. It is interesting to note that, while for 5% and 100% concentrations of xenon, the efficiency of the optogalvanic effect increases in a practically continuous manner from cathode to anode, in the case of 10% and 20% concentrations of xenon, a minimum value is observed in the middle area of the interelectrode space, with the curves increasing in both directions (to cathode and anode).

4. DISCUSSION OF THE RESULTS

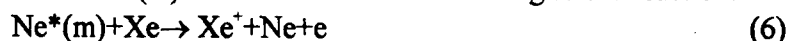
The shape of the experimentally obtained distribution curve of the relative density of the excited xenon atoms $Xe(1s_4)$ along the interelectrode space of a d.c. discharge in pure xenon gas can be accounted for by inelastic electron collisions.

The excitation and ionisation of the atoms are mainly produced by inelastic electron collisions of neutral or excited atoms. Consequently, the density of the excited xenon atoms in the interelectrode space of a d.c. discharge will depend on EDF. As is well known, in the case of luminescent discharges, electron density is maximum in the cathode fall region. As a result, the density of the excited species will have a maximum toward the cathode. Due to the values of the filling gas pressure, which are in the range of 5-10Torr, the excited xenon atoms on state $1s_4$ are coupled by collision with the xenon metastable state

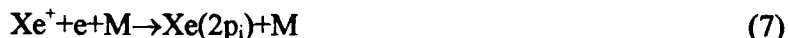
$1s_5$ (energy difference 0.12eV). Consequently, the real lifetime of the excited $Xe(1s_4)$ atoms will be longer than their radiative lifetime, and closer to the one corresponding to a metastable state. This increased lifetime leads to a diffusion of these atoms away from their place of origin before de-excitation. This accounts for the distribution function of the relative density of $Xe(1s_4)$ in the case of measurements on pure xenon discharges.

When neon is added to xenon, the density of xenon atoms decreases 5 up to 10 times, which explains the reduction of the absorption signal (see Fig.4(b)) with the decreased xenon percentage.

Besides this expected reduction of density of the excited xenon atoms, a change in their distribution can also be observed in the interelectrode space, including a shift of the curve maxima away from the cathode. Such a behaviour can be considered the result of second kind Penning collisions between neon atoms in the metastable state $Ne^*(m)$ and xenon neutrals according to the reaction:



Indeed, for the gas mixture used in this experiment, the concentration of the neon atoms is much higher than that of xenon atoms and the density of neon atoms in the metastable state will be accordingly high. Given the lifetime of metastable neon atoms of around 1 sec.⁴ and their density decrease in the proximity of electrodes (wall de-excitation), we may expect a maximum density of the metastable neon atoms in the middle of the interelectrode distance. The xenon ions resulting from reaction (6) can be a source for excited xenon atoms on state $1s_4$ as a result of the radiative recombination of xenon ions and the subsequent reactions:



where M is a heavy particle (Ne or Xe).

Because the process described by eq.(6) depends on the product $[Ne] \cdot [Xe]$, it follows that there must be an optimum Ne-Xe mixture (described by the Xe percentage) for which the shift in distribution function is maximum.

Indeed, Fig.4(b) shows that, as xenon percentages in neon are reduced to 5%, the maximum distribution for $Xe(1s_4)$ moves back toward the cathode.

The dependence of the optogalvanic signal² (OGS) on the position between cathode and anode is different from the density distribution of the excited atoms on level $1s_4$ in spite of the fact that the OGS signal is generated precisely upon $Xe(1s_4)$ optical pumping to the upper state $2p_5$. This proves the change in plasma conductivity due to the increased concentration of excited xenon atoms on level $2p_5$ is not directly proportional with this increase.

This fact is well illustrated when we plot the optogalvanic efficiency dependence on the position in the discharge space. As we can see, the results for 5% xenon in neon (as well as those for 100% xenon) clearly differ in shape from those for xenon concentrations of 20% (and 10%).

The optogalvanic effect depends on a number of elementary processes leading the optically pumped xenon atoms on the upper level $2p_5$ to an ionised state. According to eq.(5), such processes could be electron collisions and heavy particle collisions. The results (see Fig.5) clearly show that in the case of 10% and 20% xenon in neon, the interaction between neon and xenon is the dominant process, while for 100% xenon (where we cannot have any interaction between heavy particles) as well as for 5% xenon in neon, we have electron-collision ionisation as a dominant process.

In the case of pure xenon, it is electron-collision ionisation that is mainly responsible for the ionisation of excited xenon atoms on the upper state. In other words, if we consider eq.(3), it is the first term that is dominant.

By contrast, in the case of a neon-xenon mixture with xenon concentrations of 10%-20%, the main contribution to ion generation will be given by second kind collisions, i.e., the second term in eq.(3).

5. CONCLUSION

The results prove that laser diode absorption spectroscopy can provide the real space distribution of any excited species in a plasma.

The newly defined physical parameter, Eff_{OG} , can give information on the processes taking place in plasma on the atomic and molecular scales. It is important that further studies be conducted on the discharges in neon-xenon mixtures which exhibit, as our experiments have shown, an interesting behaviour in the range of 10%-20% xenon concentration. This interest is particularly related to a potential use of such mixtures to generate uv light.

6. REFERENCES

1. K.Niemax, H.Groll, C.Schnurer-Patschan, *Spectrochimica Acta Rev.*, **15**, 349 (1993)
2. Y.Sakai, M.A.Bratescu, G.Musa, K.Myamoto, *Proceedings ICPIG XXIII*, pp.91-92, Toulouse, France (1997)
3. J.Reid, D.Labrie, *Appl. Phys.* **B26**, 203 (1981)
4. J.L.Delcroix, *Proprietes Physico-Chimique des Gas Simple*, Int.Rept. Universite Paris Sud, LPGP, Paris (1982)

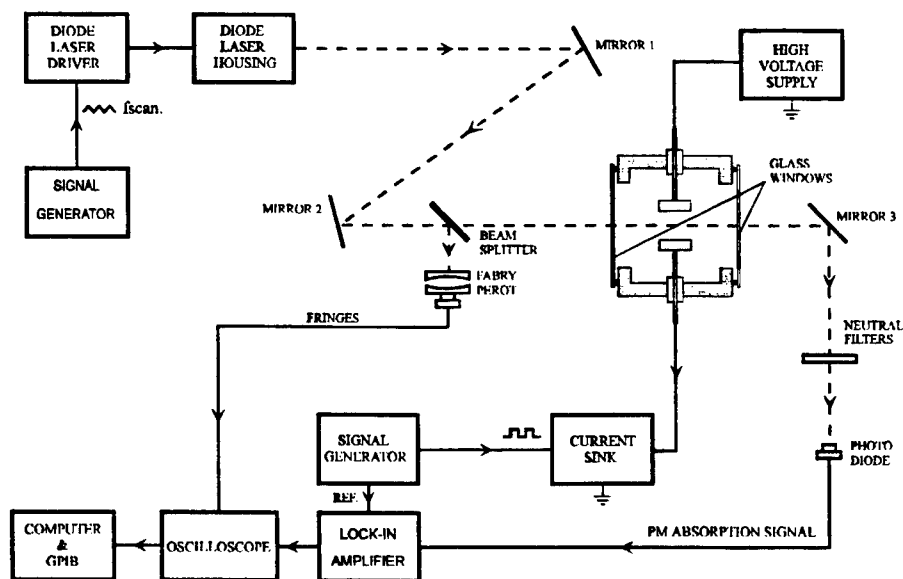


Figure 1(a): Experimental arrangement for d.c. plasma modulation absorption spectroscopy

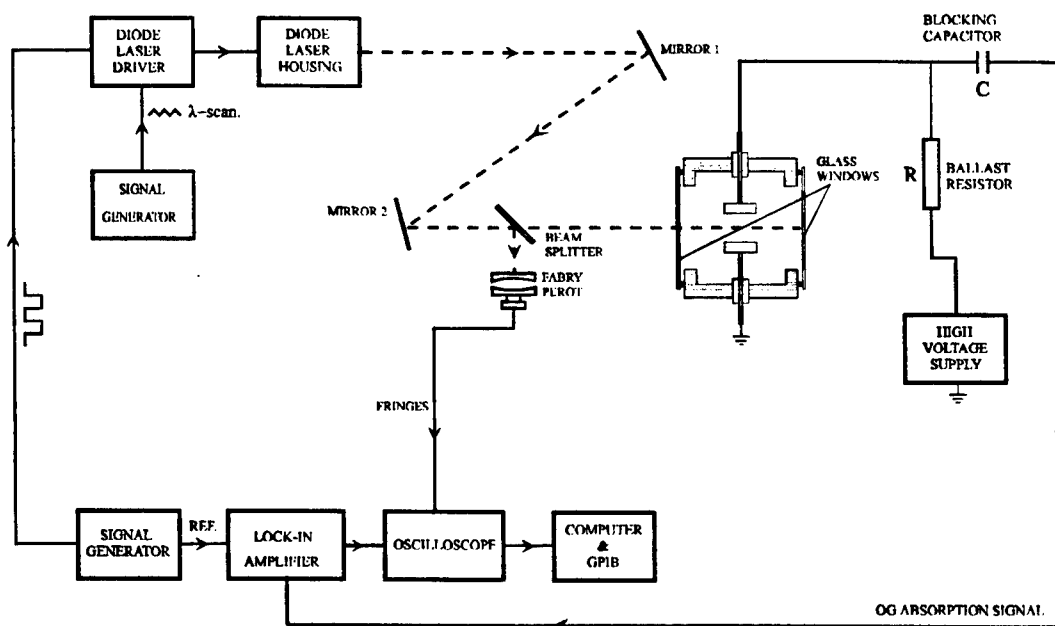


Figure 1(b): Experimental arrangement for optogalvanic spectroscopy

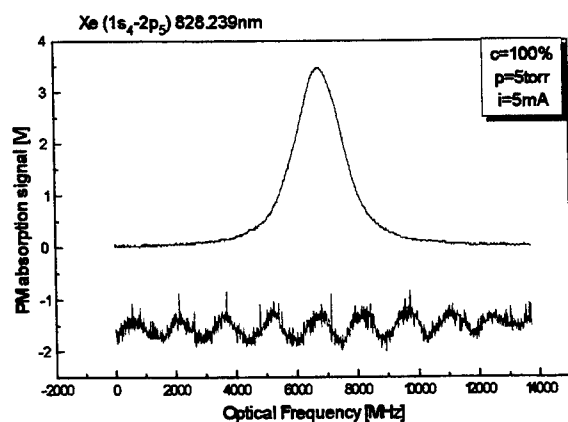


Figure 2: Plasma modulation absorption signal of xenon atoms for $1s_4-2p_5$ transition

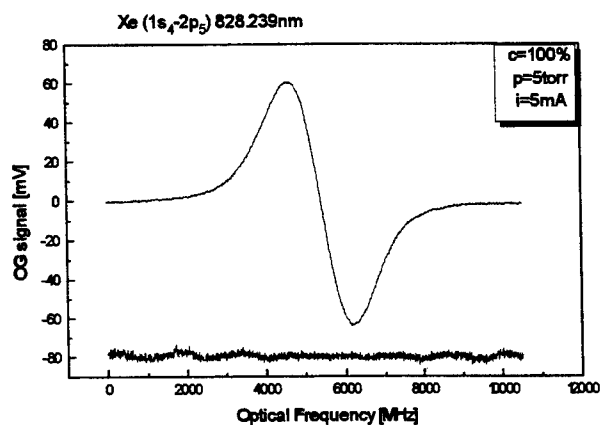


Figure 3(a): First harmonic optogalvanic signal of transition of xenon at $\lambda=828.239\text{nm}$

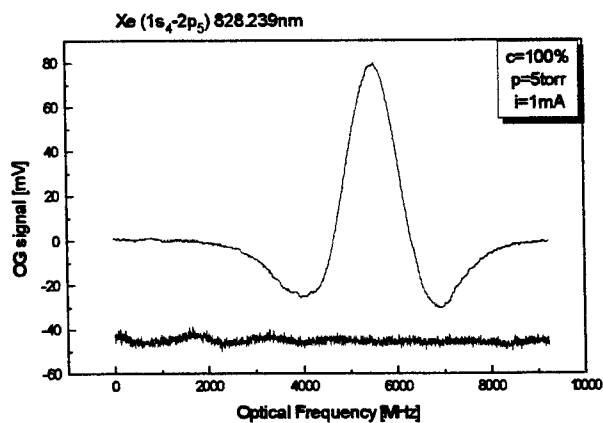
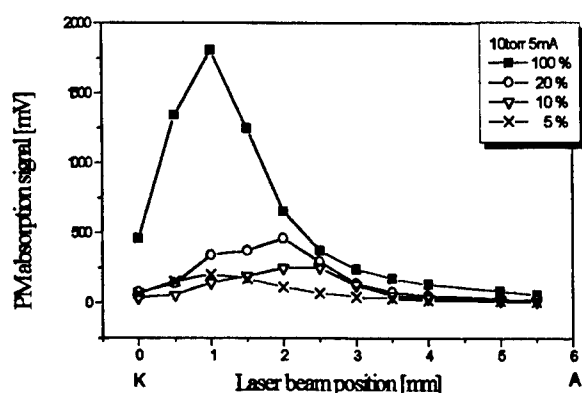
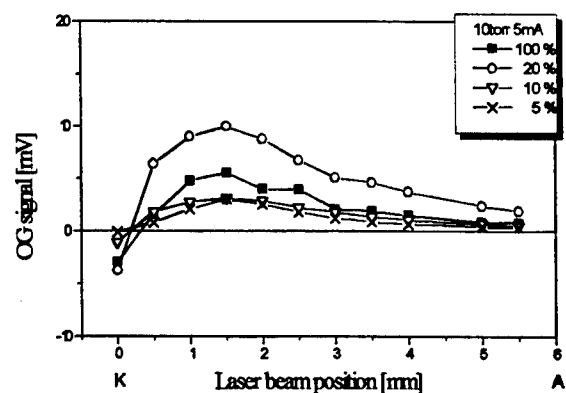
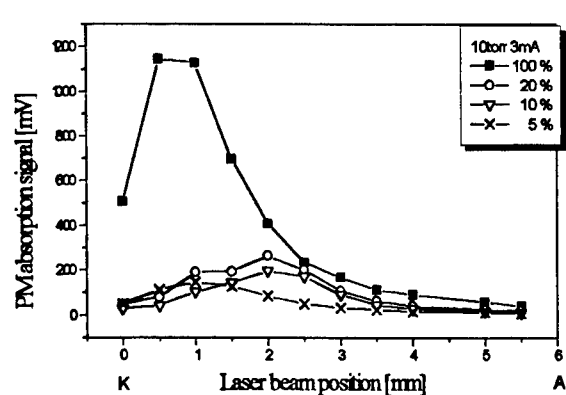
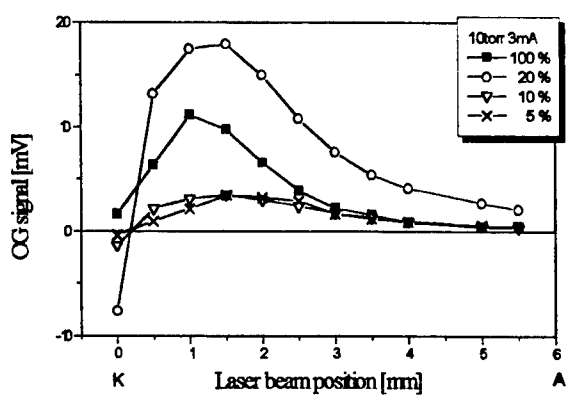
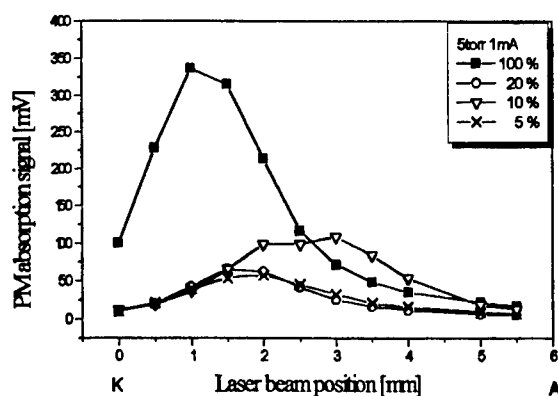
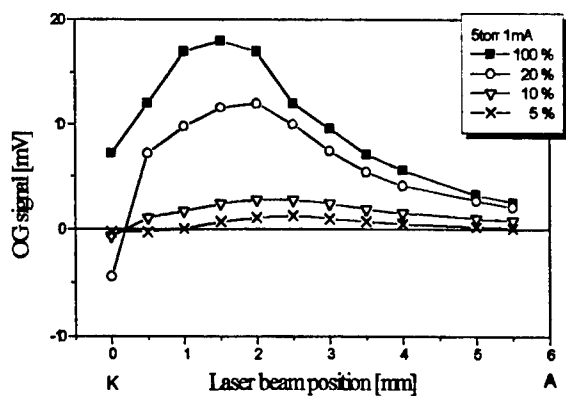


Figure 3(b): Second harmonic optogalvanic signal of transition of xenon at $\lambda=828.239\text{nm}$



(a)

(b)

Figure 4: The values of the optogalvanic signal I_{OG} and of the absorption signal I_{PM} in various positions of incident laser beam between cathode and anode for different experimental conditions

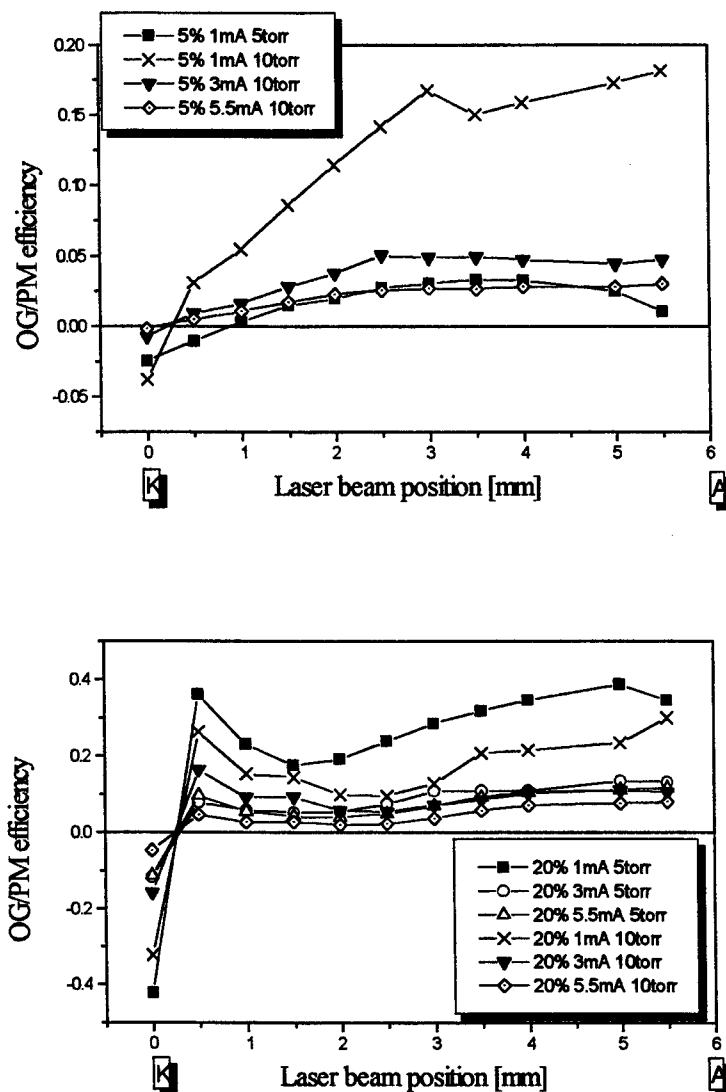


Figure 5: The optogalvanic efficiency versus the position of the incident laser beam in the interelectrode space for different experimental conditions

Multiphonon transitions and heating effects in Er: YAG laser rods

Serban Georgescu and Voicu Lupei

National Institute for Laser, Plasma, and Radiation Physics, Bucharest Romania

ABSTRACT

In this paper we discuss the heat produced by the non-radiative (multiphonon) transitions in Er: YAG laser rods, during the optical pumping, using the mathematical modelling. Three energy transfer processes (up-conversion from $^4I_{15/2}$, up-conversion from $^4I_{13/2}$, and cross-relaxation from $^4S_{3/2}$) are included in the rate equations. The main result of our simulation is that for usual optical pump conditions (Xenon flash-lamp, pumping pulse duration 200 - 300 μ s) more than 50 % of the absorbed energy is lost as heat in the active medium and only a small fraction (~ 1 %) is lost as fluorescent emission.

keywords: mid-infrared laser, Er^{3+}

1. INTRODUCTION

The efficient 3- μ m lasing of concentrated erbium crystals (laser transition $^4I_{11/2} \rightarrow ^4I_{13/2}$) is based on very effective re-circulation of excitation inside the Er^{3+} ions system, due to active energy transfer processes (up-conversion and cross-relaxation)¹⁻³. Both the main up-conversion processes are accompanied by strong multiphonon transitions (degrading part of excitation energy in heat): the up-conversion from the terminal laser level ($^4I_{13/2} \rightarrow ^4I_{15/2}$) + ($^4I_{13/2} \rightarrow ^4I_{15/2}$) is followed by the non-radiative transition $^4I_{9/2} \rightarrow ^4I_{11/2}$, while the up-conversion from the initial one, ($^4I_{11/2} \rightarrow ^4I_{15/2}$) + ($^4I_{11/2} \rightarrow ^4F_{7/2}$), by the chain of non-radiative transitions $^4F_{7/2} \rightarrow ^2H_{11/2} \rightarrow ^4S_{3/2}$. Besides, due to the high cut-off frequency of the phonon spectrum in YAG crystals, all the energy levels involved in the 3- μ m emission (except for $^4I_{13/2}$) decay mainly non-radiatively, generating an appreciable quantity of heat. Therefore, the heat generated in Er: YAG laser rod crystals could represent an important part of the energy absorbed in the laser rod during the optical pumping. Recently⁴, the experimental study of the heating of Er: YAG active medium during optical pumping, was used as an alternative method to the spectroscopic and laser ones, to check the rate equations models and the published spectroscopic data.

The aim of this paper is to use a rate equations model, based exclusively on spectroscopic data, to evaluate the heating effects produced in the Er: YAG laser rods by multiphonon transitions. This study could contribute to the optimisation of the pumping conditions and the efficiency of energy utilisation in 3- μ m erbium lasers.

2. NON-RADIATIVE LOSSES

2. 1. Rate equation model

In concentrated erbium crystals the kinetics of Er^{3+} levels involved in 3- μ m lasing ($^4I_{13/2}$, $^4I_{11/2}$, $^4I_{9/2}$, $^4F_{9/2}$ and $^4S_{3/2}$) is described by the non-linear system of rate equations:

$$\begin{aligned}\frac{dN_5}{dt} &= -(a_{50} + a_{51} + a_{52} + a_{53} + a_{54} + w_{54})N_5 - \omega_{50}N_5N_0 + \omega_{22}N_2^2 + R_{p5}N_0 \\ \frac{dN_4}{dt} &= -(a_{40} + a_{41} + a_{42} + a_{43} + w_{43})N_4 + (a_{54} + w_{54})N_5 + R_{p4}N_0 \\ \frac{dN_3}{dt} &= -(a_{30} + a_{31} + a_{32} + w_{32})N_3 + a_{53}N_5 + (a_{43} + w_{43})N_4 + \omega_{11}N_1^2 + \omega_{50}N_5N_0 + R_{p3}N_0\end{aligned}$$

$$\begin{aligned}\frac{dN_2}{dt} &= -(a_{20} + a_{21} + w_{21})N_2 + a_{52}N_5 + a_{42}N_4 + a_{32}N_3 - 2\omega_{22}N_2^2 + R_{p2}N_0 \\ \frac{dN_1}{dt} &= -a_{10}N_1 + a_{51}N_5 + a_{41}N_4 + a_{31}N_3 + (a_{21} + w_{21})N_2 - 2\omega_{11}N_1^2 + \omega_{50}N_5N_0 + R_{p1}N_0\end{aligned}\quad (1)$$

where N_0 to N_5 are the populations of the $^4I_{15/2}$, $^4I_{13/2}$, $^4I_{11/2}$, $^4I_{9/2}$, $^4F_{9/2}$, and $^4S_{3/2}$ (thermalized, at room temperature, with $^2H_{11/2}$), respectively. The coefficients a_{ij} and w_{ij} are the probabilities of radiative and, respectively, multiphonon ($i \rightarrow j$) transitions (see Fig. 1, Ref. 5). The energy transfer processes are represented in Eqs. (1), by ω_{ij} (for an Er (50 at. %) YAG crystal ^{6,7} $\omega_{11} = 1.3 \times 10^{-15} \text{ cm}^3 \text{ s}^{-1}$, $\omega_{22} = 3.7 \times 10^{-15} \text{ cm}^3 \text{ s}^{-1}$, and $\omega_{50} = 1.06 \times 10^{-21} \text{ cm}^3 \text{ s}^{-1}$). Pumping is allowed in any energy level, i , with the rate R_{pi} .

At low erbium concentrations, when the effect of energy transfer processes could be neglected, the probability of multiphonon transition, w_{ij} , is given by

$$w_{ij} = 1/T_f - a_{ij} \quad (2)$$

where T_f is the measured fluorescence lifetime. The radiative transition probability, a_{ij} , is the sum of electric- and magnetic-dipole transition probabilities. The electric-dipole contribution was evaluated with a modified Judd-Ofelt analysis ⁸.

2. 2. Absorbed energy

In Eqs. (1) optical pumping is allowed in any level i with a pumping rate

$$R_{pi} = \frac{I_0 \sigma_{0i} \kappa_i}{h\nu_i} \quad (3)$$

where I_0 is the incident power density, σ_{0i} is the maximal cross-section of the pump band i , $h\nu_i$ is the average pump quantum, and κ_i is the spectral pump coefficient i. e. the superposition integral of the spectral dependence $g(\lambda)$ of the pump source and the absorption cross-section, of Er^{3+} in YAG, with the spectral dependence $f(\lambda)$:

$$\kappa_i = \int_{\text{abs. band } i} g(\lambda) f(\lambda) d\lambda \quad (4)$$

For monochromatic pump the pumping wavelength is chosen to correspond to the maximum in the function $f(\lambda)$. However, in case of polychromatic pump (such as for flash lamp) we must take into account the contribution of the various pump bands. This can be done by considering the normalised pump coefficients

$$k_{pi} = \frac{\sigma_{0i} \kappa_i}{\sum_i \sigma_{0i} \kappa_i} \quad (5)$$

A rather good approximation of the flash lamp is the black body of 8000 - 12000 K. In Table 1 we give the calculated values of the normalised pumping coefficients k_{pi} for eleven absorption bands of Er^{3+} in YAG, for a 10000 K black body. It is evident that about 78 % of the pump energy is absorbed in the 0.355 - 0.565 μm spectral range. Due to the very rapid multiphonon relaxation of excitation from all the levels placed above $^4S_{3/2}$ on this last level, we can take $R_{p5} \approx 0.78R(t)$ where $R(t)$ is the total pump rate of the system. The value of k_{p5} varies from 0.71 to 0.82 for black body temperatures from 8000 to 12000 K.

Table 1. Spectral pumping coefficients of Er: YAG for pumping with Xenon flash lamp approximated with a black body with T = 10000 K.

Absorption transition	Wavelength range (μm)	k_{pi}
$^4I_{15/2} \rightarrow ^4G_{9/2}, ^2K_{15/2}$	0.355 - 0.375	0.1309
$^4I_{15/2} \rightarrow ^4G_{11/2}$	0.375 - 0.390	0.2940
$^4I_{15/2} \rightarrow ^2H_{9/2}$	0.400 - 0.420	0.0364
$^4I_{15/2} \rightarrow ^4F_{3/2} + ^4F_{5/2}$	0.435 - 0.465	0.0500
$^4I_{15/2} \rightarrow ^4F_{7/2}$	0.480 - 0.505	0.0970
$^4I_{15/2} \rightarrow ^2H_{11/2}$	0.515 - 0.540	0.1473
$^4I_{15/2} \rightarrow ^4S_{3/2}$	0.540 - 0.565	0.0225
$^4I_{15/2} \rightarrow ^4F_{9/2}$	0.640 - 0.680	0.1219
$^4I_{15/2} \rightarrow ^4I_{9/2}$	0.780 - 0.860	0.0167
$^4I_{15/2} \rightarrow ^4I_{11/2}$	0.940 - 1.030	0.0275
$^4I_{15/2} \rightarrow ^4I_{13/2}$	1.440 - 1.580	0.0553

The total energy absorbed effectively by the Er: YAG crystal during the pump duration, Δt , in case of polychromatic pumping is given by

$$E_{abs} = \sum_{i=1}^{11} k_{pi} h\nu_i \int_0^{\Delta t} R(t) dt \quad (6)$$

This equation assumes that the incident pump power density I_0 is the same in all the points of the sample. However, in the case of the strongly absorbing systems, such as concentrated Er crystals, marked departures from the uniform pump picture could take place.

2. 3. Non-radiative losses

In crystals with high phonon energies (such as the oxides) the very efficient electron-phonon interaction leads to an almost complete non-radiative relaxation of excitation between close levels. We can distinguish four main contributions to the non-radiative (multiphonon) losses of the energy absorbed during optical pumping of the laser rod:

(i): The fraction of pump energy lost by multiphonon relaxation from the levels above $^4S_{3/2}$ is given by

$$E_{nrad}^{(1)} = \sum_{i=6}^{11} k_{pi} h\nu_{i5} \int_0^{\Delta t} R(t) N_0(t) dt \quad (7)$$

where $h\nu_{i5}$ (with $i = 6$ to 11) are the photon energies corresponding to the energy difference between the pump level and $^4S_{3/2}$ (pump quantum defects).

(ii) The energy lost in the multiphonon relaxation from the metastable levels 1 to 5:

$$E_{nrad}^{(2)} = \int_0^{\Delta t} \left[\sum_{i=2}^5 N_i(t) w_{i,i-1} h\nu_{i,i-1} \right] dt \quad (8)$$

(iii) The loss due to up-conversion processes ending above the level $^4S_{3/2}$: such a process is the co-operative up-conversion ω_{22} from level $^4I_{11/2}$ (labelled by 2 in our model) which ends up on the level $^4F_{7/2}$ (labelled by 6) from which it relaxes completely on $^4S_{3/2}$:

$$E_{\text{rad}}^{(3)} = \int_0^{\Delta t} \omega_{22} N_2^2(t) h\nu_{65} dt \quad (9)$$

(iv) the energetic balance of the energy transfer processes ending below $^4S_{3/2}$. By using the thermal centres of gravity, defined as

$$E_i^B \equiv \sum_j E_{ij} \frac{\exp[-(E_{ij} - E_{i1}) / k_B T]}{\sum_l \exp[-(E_{il} - E_{i1}) / k_B T]}$$

instead of usual baricenters, we have:

– an energy excess in the up-conversion from $^4I_{13/2}$:

$$\Delta E_e = 2 \times E_B(^4I_{13/2}) - [E_B(^4I_{9/2}) + E_B(^4I_{15/2})] \approx 778 \text{ cm}^{-1}$$

which corresponds to generation of heat;

– an energy deficit in the cross-relaxation from $^4S_{3/2}$:

$$\Delta E_d = [E_B(^4S_{3/2}) + E_B(^4I_{15/2})] - [E_B(^4I_{9/2}) + E_B(^4I_{13/2})] \approx -533 \text{ cm}^{-1}$$

leading to an “absorption” of heat. Thus, we can define another contribution to the non-radiative losses as

$$E_{\text{rad}}^{(4)} = \int_0^{\Delta t} [\omega_{11} N_1^2(t) h\nu_e - \omega_{50} N_0(t) N_5(t) h\nu_d] dt \quad (10)$$

where $h\nu_e$, $h\nu_d$, are, respectively, the excess and deficit energy per act.

The total main non-radiative losses (in J / cm³) are thus

$$E_{\text{rad}} = \sum_{k=1}^4 E_{\text{rad}}^{(k)} \quad (11)$$

It is important to note that $E_{\text{rad}}^{(1)}$ is included in the total losses only during the flash lamp pumping interval, while the other processes act also after the pump pulse.

3. RESULTS AND DISCUSSION

In our simulations we have used square pump pulses of various lengths, Δt . For square pumping pulses we could consider that the variations of temperature, and, as a consequence, the change of the spectral composition of the emission of the flash lamp are not important. The non-radiative losses / cm³, produced during the optical pumping, function of the absorbed energy, are presented in Fig. 1 for monochromatic and flash lamp pumping. For the pump pulse length we have chosen the usual value $\Delta t = 200 \mu\text{s}$. For flash lamp pumping, the non-radiative losses, due to the multiphonon relaxation of the high Er^{3+} energy levels on $^4S_{3/2}$, $E_{\text{rad}}^{(1)}$, were included. Obviously, the losses during the optical pumping are larger for longer pump pulse lengths, and, therefore, shorter pump pulses are preferable. Only small changes in the dependence of the non-radiative losses in rapport with the spectral composition of the pumping light are noted (Fig. 1).

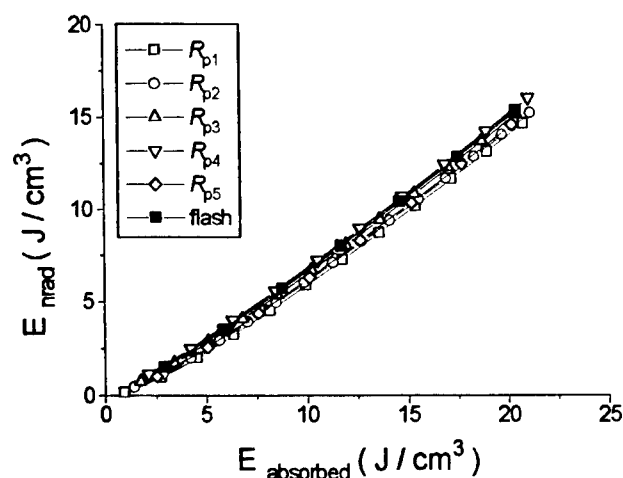


Fig. 1. Non-radiative losses (in J/cm^3), function of absorbed energy, for monochromatic (open symbols) and flash lamp (solid symbols), approximated by a 10000 K black body pumping.

Since the value of the up-conversion parameter ω_{22} is still questionable⁹, it is interesting to appreciate its effect on the non-radiative losses during the optical pumping. This is illustrated in Fig. 2. Thus, for $\omega_{22} = 0$ the heat generated represents approx. 50 % of the absorbed energy, while, for a ratio $\omega_{22} / \omega_{11} = 2.85$ (corresponding to the value given in Table 2, $\omega_{22} = 3.7 \times 10^{-15} \text{ cm}^3 \text{ s}^{-1}$) the heat represents ~ 70 % of the absorbed energy. This can be explained by the important contribution of the multiphonon transition $^4F_{7/2} \rightarrow ^4S_{3/2}$ (Eq. (9)). The radiative losses, estimated with our rate equation model, are inferior to 0.08 % of the absorbed energy.

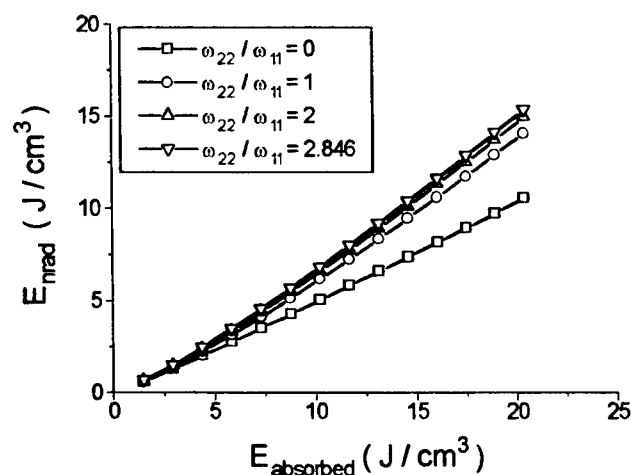


Fig. 2. Non-radiative losses function of the pump energy (flash lamp 10000 K) for various ratios ($\omega_{22} / \omega_{11}$) of the up-conversion parameters.

The energy stored in a cm^3 of active medium at the moment of time t is

$$E_{\text{stored}}(t) = \sum_{i=1}^5 N_i(t) h\nu_i^B \quad (12)$$

where $h\nu_i^B$ corresponds to the thermal centers of gravity, E_i^B . Due to the large non-radiative losses, the efficiency of energy storage (the ratio $\eta_{\text{storage}} = E_{\text{stored}} / E_{\text{absorbed}}$) depends on the pump pulse duration. This is illustrated in Fig. 3, for flash lamp pumping. Though the shortest pump pulses produce the highest efficiency, constructive limitations of the flash lamps and the shift of the spectral composition of the emitted light toward shorter wavelengths (increasing $E_{\text{nrad}}^{(1)}$) for higher current densities, lead to an optimal value of $\sim 200 \mu\text{s}$ for the pump pulse duration.

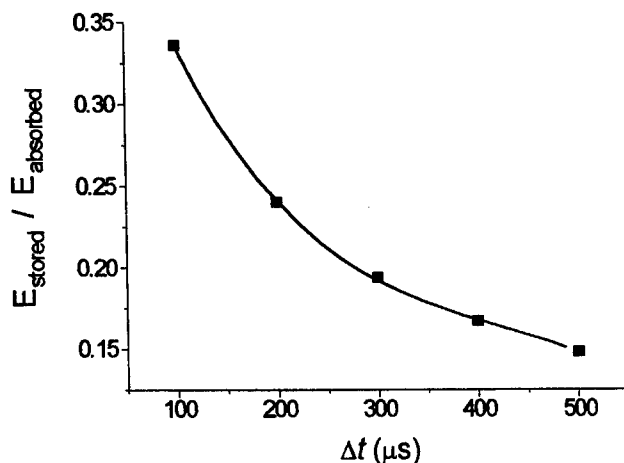


Fig. 3. Efficiency of the energy storage in the active medium function of the pumping pulse duration (flash lamp pumping, square pulses). The pumping rate, $R(t)$ was chosen to have the same absorbed energy (in our example, $20 \text{ J} / \text{cm}^3$) for various pumping pulse duration (100, 200, 300, 400, and $500 \mu\text{s}$). The continuous solid line represents a fitting with a third degree polynom.

4. CONCLUSIONS

The non-radiative losses, associated with various multiphonon transitions and the off-resonance of the energy transfer processes, produced during the optical pumping, are defined and evaluated. Comparatively with non-radiative losses, the radiative ones are negligible. For Er: YAG crystals, with high phonon energies, an important part of the energy absorbed during the optical pump is lost in non-radiative transitions, heating the laser rod and reducing the overall laser efficiency. A major contribution to the heat generation is given by the multiphonon transitions following the up-conversion processes.

5. REFERENCES

1. Kh. S. Bagdasarov, V. I. Zhekov, V. A. Lobachev, T. M. Murina, and A. M. Prokhorov, "Steady-state stimulated emission from $\text{Y}_3\text{Al}_5\text{O}_{12}:\text{Er}^{3+}$ laser ($\lambda = 2.94 \mu\text{m}$, $T = 300 \text{ K}$)," *Kvant. Elektr.*, vol. 10, pp. 452-454, 1983.
2. Kh. S. Bagdasarov, V. I. Zhekov, V. A. Lobachev, A. A. Manenkov, T. M. Murina, and A. M. Prokhorov, "Cross-relaxation YAG: Er^{3+} laser," *Izv. ANSSSR, ser. fiz.*, vol. 48, pp. 1765-1770, 1984.
3. L. G. Van Uitert and L. F. Johnson, "Energy transfer in between rare earth ions," *J. Chem. Phys.*, vol. 44, pp. 3514-3522, 1966.

4. B. Majaron, T. Rupnik, and M. Lukac, "Temperature and gain dynamics in flashlamp pumped Er: YAG," *IEEE J. Quantum Electron.*, vol. 32, pp. 1636-1644, 1996.
5. S. Georgescu, V. Lupei, and C. Hapenciuc, "Q-switch regime of 3- μm erbium lasers", this volume.
6. V. Lupei, S. Georgescu, and V. Florea, "On the dynamics of population inversion for 3 μm Er^{3+} lasers," *IEEE J. Quantum Electronics*, vol. 29, pp. 426-434, 1993.
7. V. I. Zhekov, T. M. Murina, A. M. Prokhorov, M. I. Studenikin, S. Georgescu, A. Lupei, and V. Lupei, "Nonradiative transfer of excitation energy in crystals with the interaction of three optically active centers," *JETP Lett.*, Vol. 52, pp. 670-674, 1991.
8. S. Georgescu, C. Ionescu, I. Voicu, and V. I. Zhekov, "A modified Judd-Ofelt analysis of Er^{3+} in YAG," *Rev. Roum. Phys.*, Vol. 30, pp. 265-276, 1985.
9. S. Georgescu, V. Lupei, T. J. Glynn, and R. Sherlock "Intensity pump effects in the kinetics of $^4\text{I}_{11/2}$ level in ErAG," (will be published).

Determination of phase transitions in liquid crystals by optical absorption spectroscopy

C. Sarpe-Tudoran, M. Socaciu, M. Ursache, J. Neamtu,
G. Bratulescu*, S. Radu*
University of Craiova, Dept. of Physics, *Dept. of Chemistry
13, A. I. CUZA, Craiova 1100, Romania

ABSTRACT

Some interesting experimental results involving new synthesized liquid crystals, derivatives of 4,4'-dihydroxyazobenzene and 4,4'-dihydroxy-azoxybenzene inferred by means of optical absorption spectroscopy are exposed. The absorption spectra dependence on the sample temperature in both heating and cooling processes is investigated. At the same time, the optical density is recorded at a fixed wavelength and it presents significant variations at phase transition temperatures. These data complete the results correlated with mesomorphism, obtained by classical techniques (DTA and microstructural analysis in polarized light).

Keywords: liquid crystals, azo and azoxy derivatives, phase transitions, optical absorption spectroscopy

1. INTRODUCTION

Azo and azoxybenzene with different substituents at the end of the molecule constitute a large group of mesomorphic substances. It is of great interest to investigate the influence of the molecular structure, particularly the nature of terminal groups, on the mesomorphic properties and also on the spectroscopic manifestations.

Etheric and esteric derivatives of the 4,4'-dihydroxyazobenzene and 4,4'-dihydroxyazoxybenzene have been extensively studied due to the fact that some of these substances present mesophases and are deeply colored. The electronic transitions $\pi \rightarrow \pi^*$ determine the appearance of K-bands in the spectra within a range of 340-370nm with relatively increased values for the extinction molar coefficient ϵ .

The azo- and azoxy- type compounds which form liquid crystals can exist in cis- or trans- forms. Azo compounds can be photochemically converted to the cis- form under certain conditions. Only the trans- isomers of these compounds have been found to be mesomorphic.

The aromatic-aliphatic azoethers have been widely presented in literature. However, the research on aromatic-aromatic azoethers is missing at the present stage.

The majority of the liquid crystals consist of one or more aromatic rings. These rings also have the primary contribution to optical properties as absorption and refractive indices of the liquid crystals. In the off resonance region e.g. in the visible spectrum, both scattering and absorption are decreased as follows: the scattering decreases as λ^{-4} and the absorption even more drastically. Consequently, the scattering tends to dominate the transmission losses. In order to obtain an accurate absorption in the visible spectrum, these type of losses must be taken into account in the measuring techniques.

In conventional transmission measurements, the energy conservation law leads to:

$$P_{in} = P_{R_1} + P_S + P_{abs} + P_{R_2} + P_t$$

where: P_{in} is the incident power, P_{R_1} - the reflected power at the front surface, P_{R_2} - the reflected power at the rear surface, P_S - the scattered power due to the liquid crystal, P_{abs} - the absorbed power due to the liquid crystal, P_t - the transmitted power.

The absorption of liquid crystal in the off-resonance region has several important bearings on liquid crystal devices. First, for example, in the electro-optic modulation of high power laser beams, the absorbed energy from laser is transferred to heat and subsequently warms up the molecules. Consequently, the order parameter, viscosity, elastic constant, dielectric anisotropy, etc., are reduced. These changes will influence the performance of the devices in very unpredictable manners. Second, the absorption-induced thermal lensing effect may interfere with other optical field-induced effects. Third, the absorption of short wavelength photons may trigger some inter-molecular chemical reactions leading to degradation and shortening of the lifetime of the devices.

2. EXPERIMENTAL METHOD AND RESULTS

In this section we present our studies concerning the polymorphism and visible absorption spectroscopy of some new synthesized compounds, derivatives of 4,4'-dihydroxyazobenzene and 4,4'-dihydroxyazoxybenzene^{1,2}.

These compounds were prepared using two methods: condensation of sodium salt of 4,4'-dihydroxyazoxybenzene with monochloromethylated derivatives, or by oxidation of the corresponding azobisethers with hydrogen peroxide in the presence of acetic acid. These substances exhibit liquid crystal phases due to the long rigid rod shape of the molecules and to the presence of the azoxy mezojene rigid bond.

Up to present, we have investigated the polymorphism of the above mentioned compounds by microstructural analysis with polarized light and also by differential thermal analysis. Studying the polymorphism of these substances, at heating and cooling, two smectic phases and one nematic phase were observed, as follows: $K \leftrightarrow S_B \leftrightarrow S_A \leftrightarrow N \leftrightarrow I$. The identification of the S_B phase was made only by the DTA plots, for a low heating and cooling speed.

The spectroscopic method was suggested as a way to determinate the temperature dependence of optical transmission in the visible and ultraviolet domains for liquid crystals in different phases, as smectic, nematic and isotropic. We used this method in order to study the phase transitions for the above mentioned compounds.

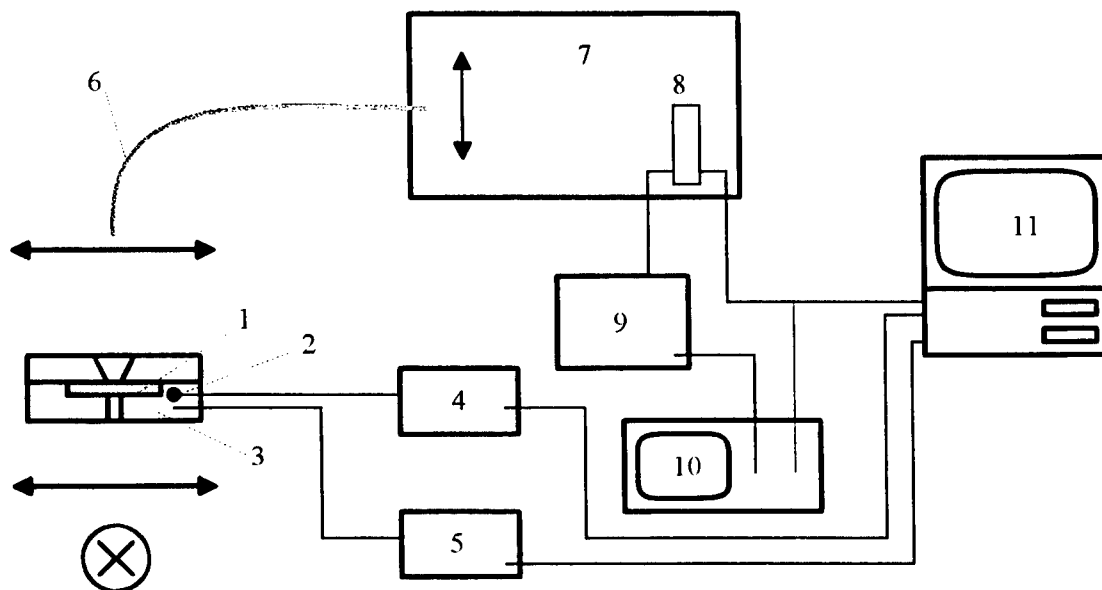


Fig. 1 The experimental set-up.

1) Liquid crystal sample. 2) Termocouple. 3) Electric microscope hot stage. 4) Digital thermometer. 5) Temperature controller. 6) Optical fiber. 7) Holographic grating. 8) Linear CCD detector. 9) Pulse generator. 10) Scope. 11) Computer with A/D and D/A interface.

The samples were conventionally prepared, namely the substance was encapsulated by capillarity in 12 μm thickness cells with parallel plane plates. The cells were thermostated using a special computer-controlled hot stage placed in a MC5-A microscope allowing simultaneous microstructural observations. The temperature was measured with 0.01°C precision, using a KEITHLEY 2000 digital multimeter, a stability around $\pm 0.05^\circ\text{C}$ being obtained by a phase controlled device with a PID algorithm. Using an optical device the light beam was focused on a 1mm-diameter optical fiber and was transmitted to a spectrophotometer equipped with a 1200 grooves/mm holographic grating and a 512 points linear CCD detector. The detector output was connected to the computer through an DAS 1601 Keithley Metrabyte interface in direct memory access mode for a high speed data acquisition. The signal was also monitored on a scope. The exposure time was established by a Tektronics pulse generator in the range of 1 ms - 10 s. For the wavelength calibration of the spectrophotometer, we used ten dichroic filters, the wavelengths being in the 400 - 720 nm interval. The background signal was excluded by numerical processing and the spectral sensibility of the CCD detector was tacked into account.

Using this experimental set-up we have recorded optical transmission spectra in the range 400-850nm, as function of the sample temperature, corresponding to different mesophases. In Fig. 2 we present the results obtained at heating, for 4,4'-bis(4-chlor)benzyloxyazoxybenzene, a representative compound for the entire class of 4,4'-dihydroxyazoxybenzene derivatives. One may see two relatively sharp maxims in the transmission specter, for I, N and

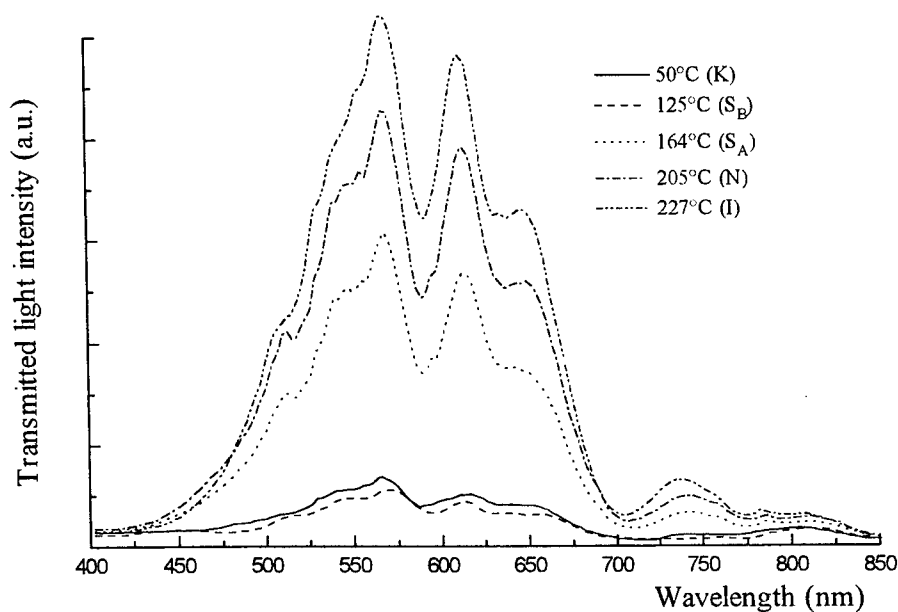


Fig. 2

S_A mesophases, while the maxims which correspond to the solid phase and to S_B mesophase are quite broad. The shape of the spectra is identically reproduced at heating and cooling, for the same mesophases.

For an accurate determination of the phase transition temperature, we recorded the temperature dependence of the transmitted light intensity for the wavelength value which corresponds to the best spectra resolution. These dependencies

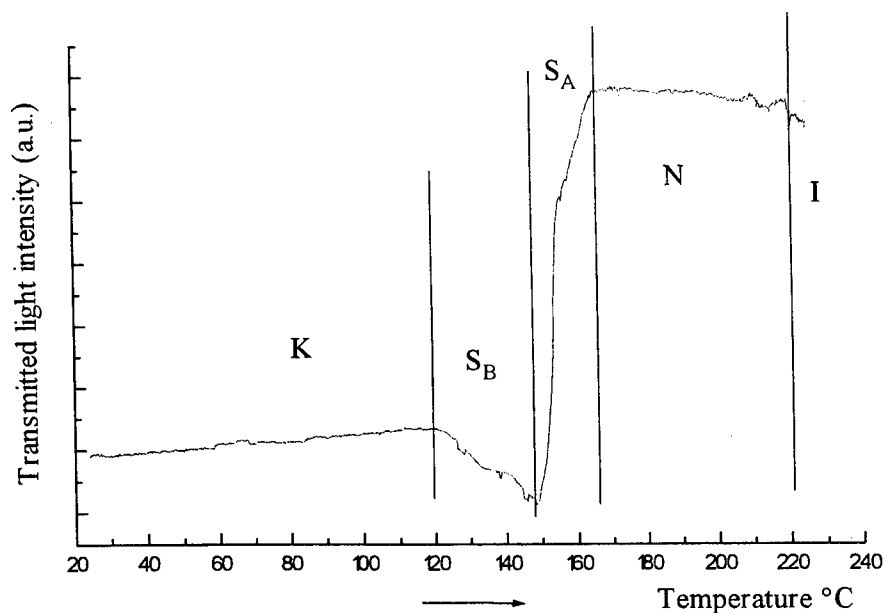


Fig. 3

are shown in Fig 3, 4, for the above mentioned compound, at heating and cooling respectively; studying this curves, one may see that there is an undercooling for the S_A and S_B mesophases. According to microstructural analysis, the minimum from the 200°C point on the cooling curve corresponds to appearance of the schlieren texture, starting from the droplets texture, in nematic mesophase. For the 4,4'-dihydroxyazobenzene derivatives, we may notice that the wavelengths corresponding to the transmission maxims are modified and that they are sharper than the ones obtained for the similar compounds, the 4,4'-dihydroxyazoxybenzene derivatives. Fig. 5 presents the spectra measured for the different phases of

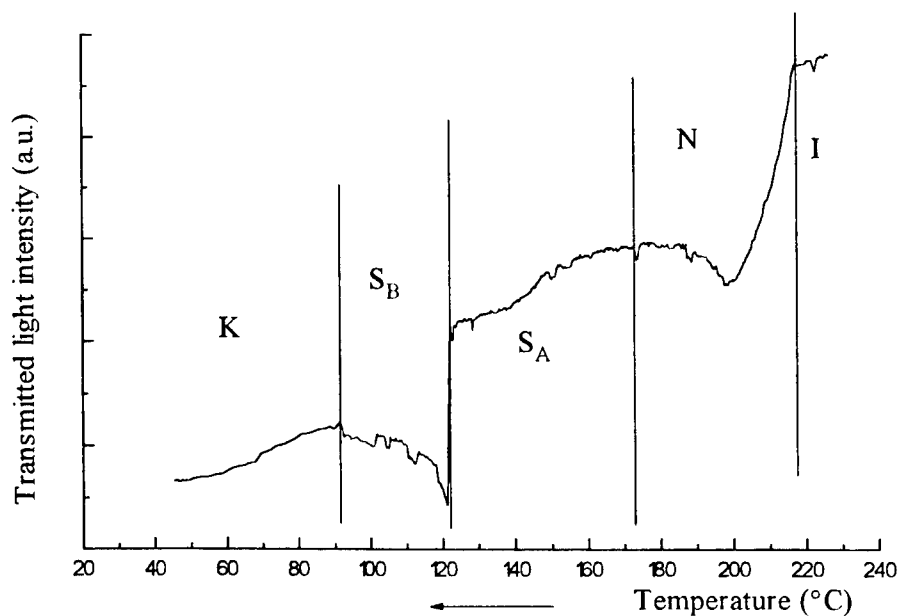


Fig. 4

4,4'-bis-(4-clor)benziloxyazobenzene, at heating. The curves given by the temperature dependence of the transmitted light are similar to the ones obtained for the related azoxy-derivatives.

This way we were able to observe the dependence of the absorption spectra on temperature during heating and

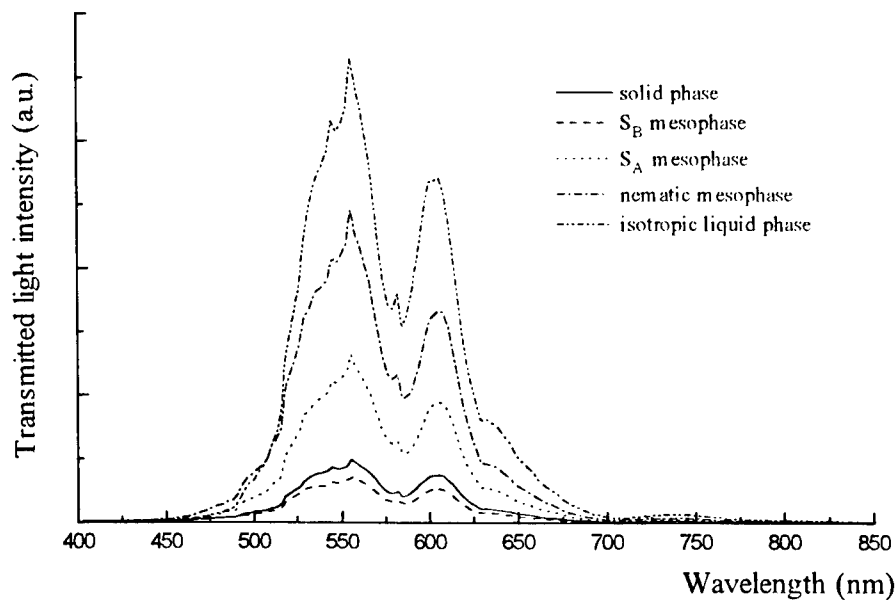


Fig. 5

cooling and the variation of optical density with temperature at a fixed wavelength at the same time. The significant modifications recorded correspond precisely to the phase transition temperatures.

3. REFERENCES

- [1] George Bratulescu, Doctoral Thesis, Institut National Polytechnique de Toulouse, 1996.
- [2] S. Radu, C. Sarpe-Tudoran, to app. in *Afinidad*.
- [3] Grasso, D. *Spectrochim Acta*, 39A, 698.
- [4] Demus, D., Richter, L., *Textures of Liquid Crystals*, Verlag Chemie, 1978.

On the photoluminescence decay in porous silicon films

I.Baltog, M.L.Ciurea, G.Pavelescu, L. Mihut, M.Baibarac

National Institute of Materials Physics
P.O.Box MG 7, Bucharest - Magurele, Romania

ABSTRACT

The photoluminescence (PL) decay measurements were performed on porous silicon films. It was observed that the two components of PL, one of them fast (ns) and the other slow (μ s or ms sometimes) have different contributions to PL signal, depending on the wavelength of the excitation light.

The slow component of PL was in details investigated. Time decay cures for different excitation (337.1 nm, 470 nm and 550nm) and emission (550, 650, 700, 800 and 860 nm) wavelengths and also for different excitation intensities were taken. All decay curves were fitted with a stretched exponential. The slow component of PL was proposed to be attributed to the radiative recombination on surfaces.

Keywords: porous silicon, photoluminescence, decay time

1. INTRODUCTION

The fact that porous silicon (PS) with high porosity can efficiently emit visible light at room temperature has generate enormous interest in this material, for its possible optoelectronical applications¹. Extensive experimental efforts have been carried out to characterize this material and to understand the origin of the visible photoluminescence (PL), using a large variety of measurement techniques. However the origin of the bright visible light emitted from PS is still controversial.

There are some models already accepted that can explain some features of the photoluminescent properties of PS¹⁻³. The most accepted model² considers that the efficient visible PL is due to both, the quantum confinement of the carriers into the Si crystallites with nanometric size and also to the recombination on surface states. It is already accepted, that on the internal surface of PS there are a lot of radiative recombination centers created either by the adsorption of molecules/atoms, or created by the network stress.

In this paper the photoluminescence decay time measurements were carried out on PS films, in the aim to obtain much information about the physical mechanism of visible bright photoluminescence.

2. EXPERIMENTAL

The photoluminescence decay curves at liquid nitrogen temperature (LNT) for different excitation and emission wavelengths, were taken on PS samples. These samples were prepared by anodisation etching from p-type (100) Si wafers with the resistivity of 5--7 Ω cm⁴. Because after the etching the samples have not PL, a PL activation process was made. All sample has the same average porosity of about 72-76%, gravimetrically determined and a thicknesses of about 100 μ m. They were measured after storage in air for more than 3 weeks.

The PL spectra in 90⁰ measurement geometry under pulse excitation were recorded. A nitrogen or dye laser as a pulse excitation source were used. (The pulse duration was 4 ns.). PL decay curves were performed using a Tektronix TD320 oscilloscope. Certain precaution to avoid the photodegradation of samples were carried out by a controlled attenuation of excitation light intensity.

3. RESULTS AND DISCUSSION

It is well known that there are two components of PL, one of them fast (ns) and the other slow (μ s or ms sometimes). The two components have different contributions to PL signal, depending on the wavelength of the excitation light. The slow component contribution increases with the increase of the excitation wavelength from UV to visible spectrum, as it can be seen in Fig.1 for measurements at $\lambda_{\text{emission}} = 760$ nm and $\lambda_{\text{excitation}} = 337.1$ nm, 470 nm and 550 nm.

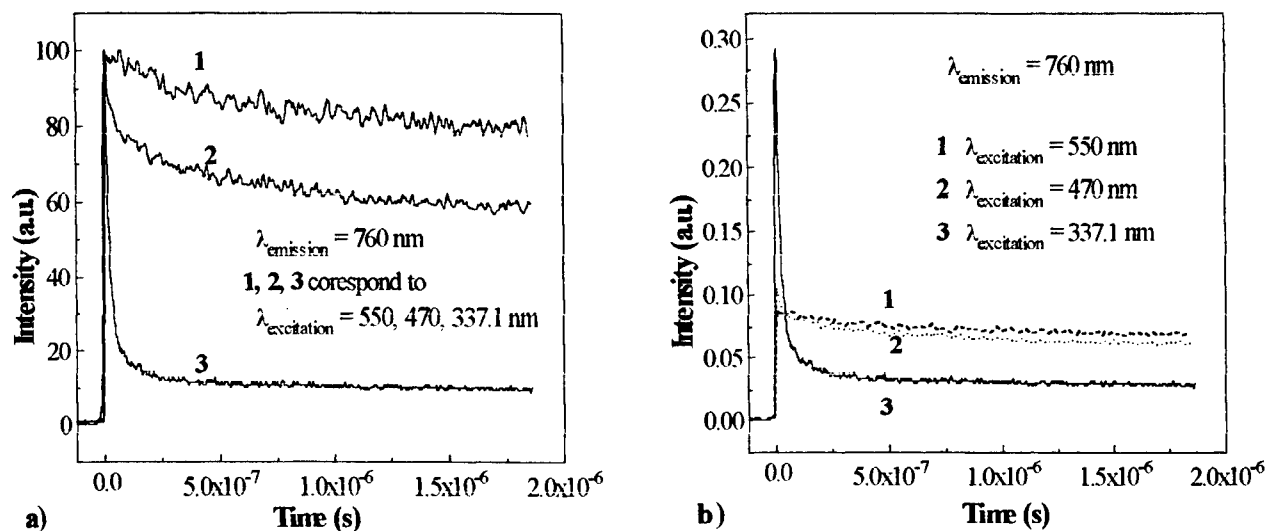


Fig.1 Decay time of PS film (a - normalized and b - unnormalized curves)

The origin and the mechanism that determine the appearance of slow and fast PL components are still discussed. If it is considered that the origin of PL is the radiative recombination inside the Si skeleton (without the participation of trapping centers), a bimolecular process takes place described by the following expression:

$$I(t) = \frac{I_0}{1 + (t/\tau)^2} \quad (1)$$

where $\tau = 1/\alpha n_0$ is a time constant that characterizes the PL decay.

Typical for this process is a fast decay time, whose value decreases with the increase of excitation light intensity (the number of the free carriers n_0 increases).

If the traps participate to this recombination mechanism, the mechanism will become monomolecular and the PL decay will be described by an exponential law:

$$I(t) = I_0 \exp[-(t/\tau_{\text{rad}})] \quad (2)$$

In this case the radiative lifetime τ_{rad} will be a measure of the carriers lifetime on the trapping level.

Unfortunately, any one of the above described processes can not fit the PL decay. A superposition of these two processes fits very well the slow component of the decay curve. Such mechanism occurs with minor probability because the typical dependence of the decay time for bimolecular emission versus the excitation light intensity (the decrease of decay time with the increase of excitation light intensity) was not observed. In Fig.2 the decay curves of PL for three excitation intensities at $\lambda_{\text{excitation}} = 337.1$ nm and $\lambda_{\text{emission}} = 800$ nm are presented.

On the other hand it is normal to suppose the existence of a very large number of localized trapping states, resulting from the behaviour of the radiative lifetime dependence versus the emission and excitation wavelengths (calculated from eq.(2)).

An appropriate fit for our experimental data of the slow component of PL consists of a stretched exponential function:

$$I(t) = I_0 \exp[-(t/\tau)^\beta], \quad 0 < \beta < 1 \quad (3)$$

where τ is the decay time and β is a dispersion factor.

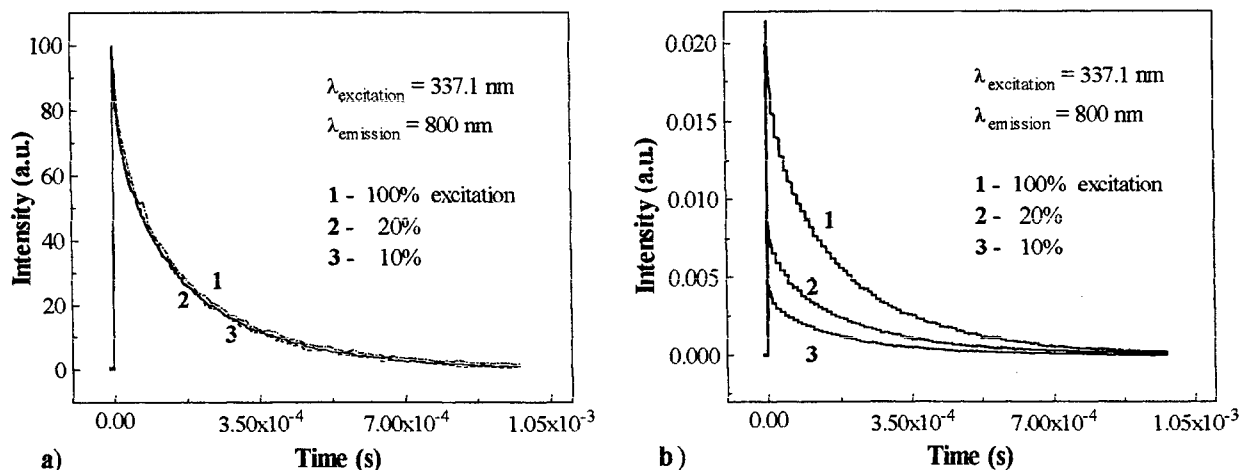


Fig.2 Decay time of PS films for different excitation energy (a - normalized and b - unnormalized)

The wavelength dependence of τ and β parameters are shown in Fig.3. It is observed that decay τ as well as β have different behaviour for the two excitation wavelengths, $\lambda_{\text{excitation}} = 337.1 \text{ nm}$ and 550 nm . For $\lambda_{\text{excitation}} = 550 \text{ nm}$ the values of both parameters decrease with the increase of the energy, in comparison with the behaviour for $\lambda_{\text{excitation}} = 337.1 \text{ nm}$, when approximately constant values obtained between 1.4 eV and 1.6 eV are followed by a decrease when the emission energy increases.

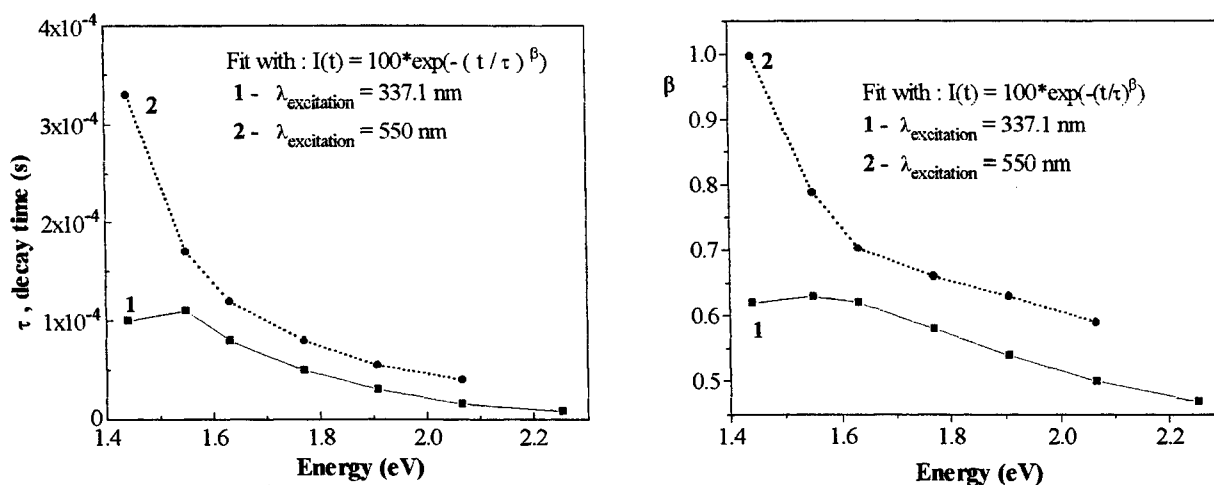


Fig.3 The energy dependence of the decay time and of the dispersion factor

These results could be explained supposing that in the upper layer of PS film where $\lambda_{\text{excitation}} = 337.1 \text{ nm}$

is absorbed there is only one radiative recombination level in (1.4-1.6) eV range. When excitation light penetrates deeper ($\lambda_{\text{excitation}} = 550$ nm), the free electron-hole pairs created by absorption meets also another radiative recombination centers situated deeper in the film, but in the same energetical range. For the emission energy higher than 1.6 eV, an exponential dependence of τ was obtained:

$$\tau \sim \exp(-E_{\text{emis}}/E_0), E_0 - \text{constant} \quad (4)$$

The above supposition is supported by Fig.4 too. In fig. 4a, for $\lambda_{\text{excitation}} = 337.1$ nm the slow component weight is practically the same for curves 2,3 and 4 (corresponding to the (1.43 -1.54) eV) and varies nonuniform for the curves 1 and 5 (following the spectral dependence of PL spectrum). For $\lambda_{\text{excitation}} = 550$ nm, as it can be seen in Fig. 4b, the slow component weight increases with the increase of the emission wavelength.

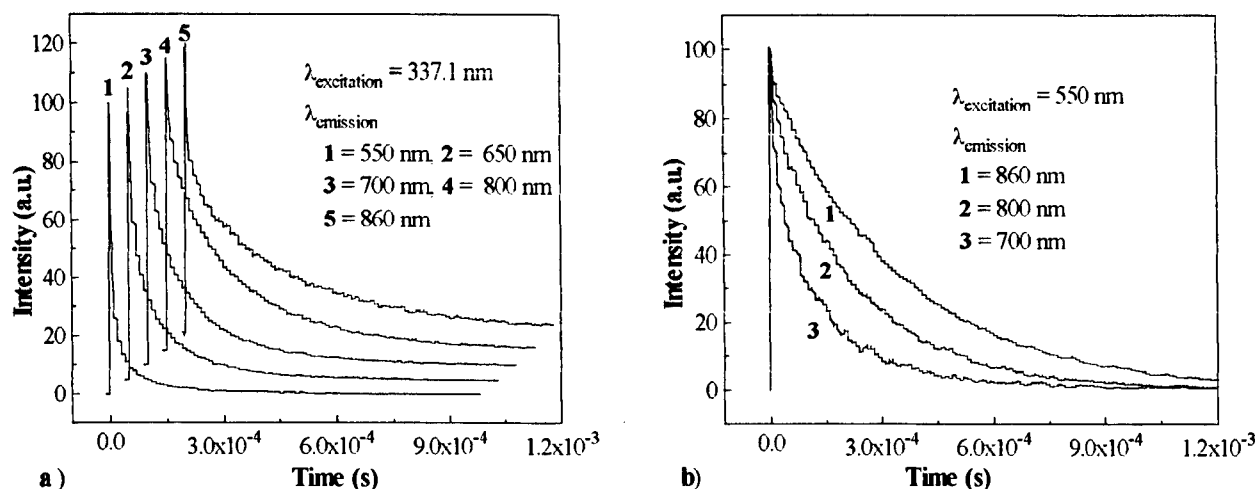


Fig.4 Decay time of PS film for different excitation and emission wavelengths

4. CONCLUSIONS

The origin and the mechanism of slow component of PL are investigated. The slow component is fitted by a stretched exponential function from where the decay time τ and the dispersion factor β are determined. From this analysis we can conclude that this slow component is due to the radiative recombination on some levels situated on the surface: one of them (with energetical position in 1.4 -1.6 eV range) is spatially situated in a top layer corresponding to the penetration depth of $\lambda_{\text{excitation}} = 337.1$ nm and many others deeper in PS films.

5. REFERENCES

1. T.Canham, "Silicon quantum wire array fabrication by electrochemical and chemical dissolution of wavers", *Appl. Phys. Lett.* **57**(10), 1046-1048 (1990).
2. F.Koch, V.Petrova-Koch, T.Muschik, A.Nikolov and V.Gabrilenko, "Some properties on photoluminescence mechanism via surface-confined states of porous Si", *Mater.Res.Soc.Symp.Proc.*, **283**, 197-202 (1993).
3. I. Mihalcescu, J.C.Vial, and R.Romestain, "Carrier localization in porous silicon investigated by time-resolved luminescence analysis", *J. Appl. Phys.* **80**(4), 2404-2411 (1996).
4. M.L.Ciurea, E.Pentia, A.Manea, A.Belu-Marian, and I.Baltog, "Visible Photoluminescence in porous silicon prepared in different conditions", *Phys. Stat. Sol. (b)* **195**, 637-645 (1996)

Photoacoustic detection of ethylene released by biological samples under stress conditions

Simona Cristescu, Dan C. Dumitras and Doru C. A. Dutu

Department of Lasers, National Institute for Laser, Plasma and Radiation Physics
P.O. Box MG-36, R-76900 Magurele, Bucharest, ROMANIA

ABSTRACT

A high sensitive photoacoustic system has been developed to monitor the ethylene released by mature tomatoes and wheat seeds during germination as a response of fast effects of mechanical and thermal stress. Under normal conditions of temperature and pressure, the coronet removal yielded a significant increase of ethylene emission as compared to the local wounding of tomato tissues.

To determine the temperature influence on ethylene emission rates, both tomatoes and germinating wheat seeds were investigated at cold treatment (4°C) and at room temperature (22°C). Early changes in ethylene released after imbibition in connection with the physiological results of germination were also monitored.

The use of the CO₂ laser photoacoustic technique in plant physiological research is discussed.

Keywords: photoacoustic spectroscopy, tunable CO₂ laser, wounding, thermal stress, ethylene

1. INTRODUCTION

In recent years, numerous studies have demonstrated the applicability of CO₂ laser photoacoustic (PA) spectroscopy in several new fields of research like environmental sensing¹, agriculture and biology²⁻⁵. We have applied the PA technique to measure the ethylene (C₂H₄) released by biological samples under stress conditions. The choice of C₂H₄ is motivated by its biological and environmental impact. As a gaseous plant hormone⁶ biosynthesised by plant tissues, it regulates many plant processes and plays an important role in germination, dormancy, growth, ripening and senescence. Physiological disturbances due to "stress" (wounding, thermal etc.) are also followed by changes in C₂H₄ emission⁷. The temporal and local C₂H₄ production released by mechanically wounded tomatoes and the effects of low temperature on C₂H₄ emission both for tomatoes and germinating wheat seeds are presented.

The objectives for the research reported here are: (a) monitoring of fast reaction on tomatoes behaviour following the coronet removal; (b) measuring of ethylene concentration due to the epidermis wounding; (c) temperature influence on C₂H₄ emission released by a mature tomato - ethylene emission for a mature tomato kept at 4°C and warmed up to 22°C; (d) ethylene production from germinating wheat seeds kept at 22°C compared with that measured at 4°C.

2. LASER PA DETECTION SYSTEM

As a radiation source we have used a line tunable and frequency stabilised CO₂ laser, since its emission spectrum overlaps with the absorption fingerprint of C₂H₄. It emits cw radiation with the output power of 2÷8.5 W. The long term frequency stability is better than 3×10⁻⁸ and the power stability is better than 10⁻² for all the transitions in P and R branches of 9÷11 μm range. The PA measurements were performed on 10P(14) laser line (λ=10.532 μm), which is the strongest absorption line for C₂H₄. A scheme of the experimental set-up is shown in Fig. 1.

The cw radiation is amplitude modulated with an optical chopper (C-980 type, DigiRad). After modulation, the focused laser beam passes through the PA resonant cell with H geometry, excited in the first longitudinal mode. The main characteristics of the cell are summarised in Table 1. Acoustic waves produced in the cell are detected with four miniature microphones (Knowles electret, BT-1754 type), connected in series. The PA signal, proportional to the C₂H₄ concentration, is applied to a lock-in amplifier (SR 830 model, Stanford Research System). An original graphical-instrumentation-programming software allows to acquire and process the experimental data into a convenient way.

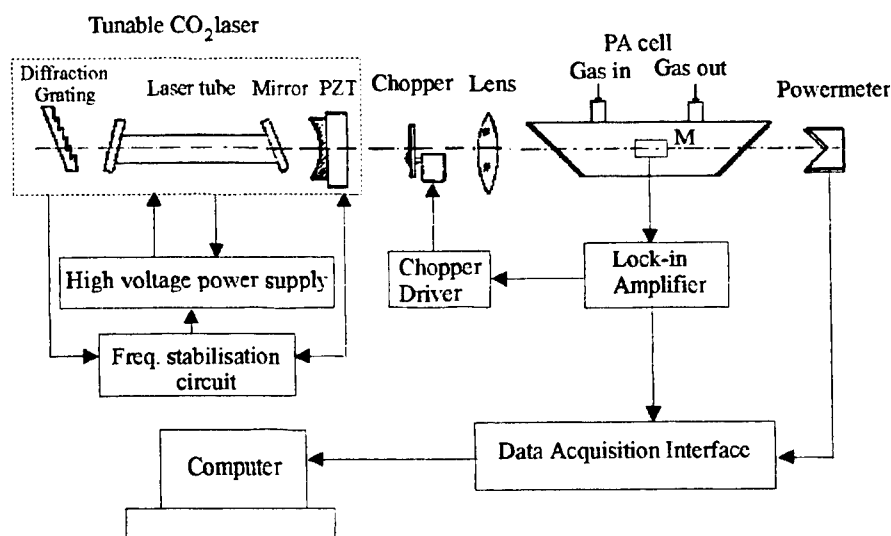


Fig. 1 Schematic of PA detection system

Due to the sensitivity of the tissue even at low C_2H_4 concentration, the gas must be measured in a continuous flow system to prevent the accumulation induced effects. In the PA experiments, we have developed a gas handling and mixing system that allows the preparation of gas mixtures with known ratios and the operation of PA cell in flowing regime in a controlled manner.

The biological samples under investigation are introduced in a small glass cuvette with a volume of 150 cm^3 and flushed with synthetic air (80% N_2 and 20% O_2), at a continuous flow of 2 l/h and at total pressure of 1 atm. The flow was controlled by means of a calibrated flow meter (247 C model, MKS Instruments).

Table 1. Characteristics of the PA cell

Resonator	$\varnothing 6 \times 300\text{ mm}$
Buffers	$\varnothing 57 \times 100\text{ mm}$
Total microphones sensitivity	40 mV/Pa
Q-quality factor	16.5
Cell constant	4600 Pa-cm/W
Responsivity	184 V-cm/W
Resonance frequency (nitrogen)	560 Hz

For the measurement of low C_2H_4 concentrations, it is essential to take measures to reduce CO_2 and water vapours, which introduce undesired supplementary absorption at measuring laser wavelength. To remove CO_2 we have used a special trap with solution of KOH in distilled water of 10% concentration together with a KOH pellets scrubber. An easy way to eliminate water vapour is to introduce a tube filled with P_2O_5 powder in the flow circuit between the sample cuvette and the PA cell.

3. RESULTS AND DISCUSSION

The C_2H_4 measurements were carried out with mature tomatoes which had an individual weight of about 50 g. The wounding effect produced by removal of the coronet (consisting of pedicel and sepals) at the tomato-pedicel junction was investigated. An increase in C_2H_4 emission is observable immediately after removal of the coronet at $t=0$ (Fig.2). The

stimulation of C_2H_4 production by this form of mechanical wounding appears after a delay of 15 minutes and disappears after 2 hours.

Due to its role in ripening and wilting, the exit channels for C_2H_4 may be of special importance. Removal of tomatoes coronet yielded a much pronounced effect as compared to wounding the epidermis region by fold puncturing into the tissue at about 2 mm depth (Fig. 3).

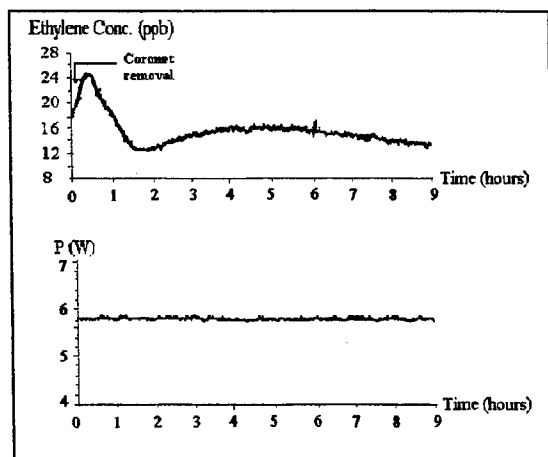


Fig. 2 The ethylene concentration and laser power time dependence for removal of tomato coronet

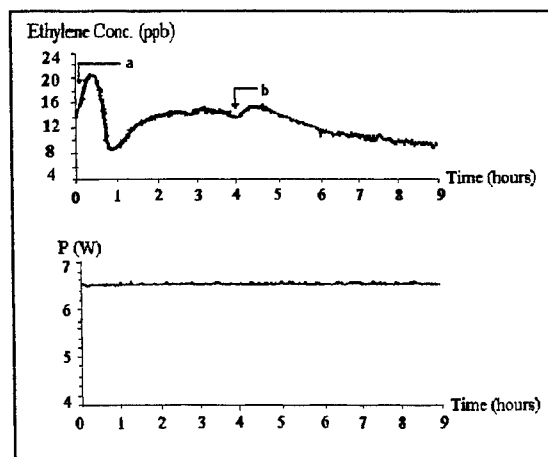


Fig. 3 The ethylene concentration and laser power time dependence in (a) removal coronet case compared with (b) epidermis wounding

These two actions of wounding took place while the tomatoes were flushed with synthetic air and the flow was interrupted momentarily. The temporal aspects concerning the wounded tissue of tomatoes presented in Fig. 2 and Fig. 3 have shown good agreement with data already obtained^{8,9}.

Any organ or part of plant is directly affected by stress, regardless which vegetal tissue was first hurt. The response coordination due to stress and its propagation inside the plant is realised by specific hormones. According to this hypothesis, the tomatoes behavior following wounding is the result of the stimulation of ACC synthase¹⁰ activity, that provides finally an increased C_2H_4 production.

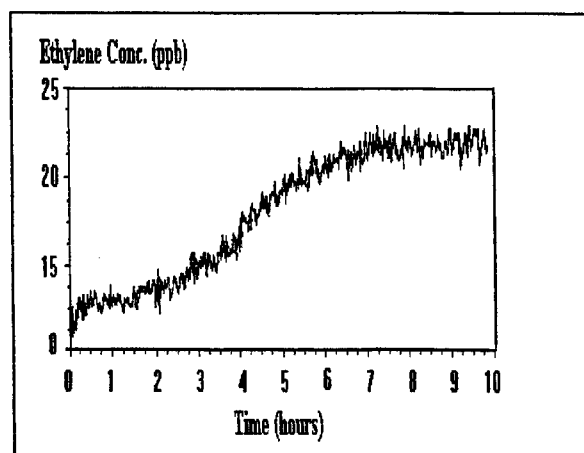


Fig. 4 The ethylene emission for a mature tomato kept at 4°C and warmed up to 22°C

To estimate the effects of thermal stress on C_2H_4 production, we have monitored the ethylene emission for mature tomatoes and germinating wheat seeds. Tomatoes were taken from refrigerator (4°C) and warmed up to the laboratory temperature (22°C). The PA signal, proportional with the C_2H_4 concentration, was monitored during 10 hours (Fig. 4). In order to make a comparison between the tomatoes behaviour under mechanical wounding and thermal stress, attention was paid to evaluate the time dependence of the PA signal after the stress was applied. However, the thermal stress also produces an increase of C_2H_4 emission, but the process has a much slower rate than in coronet removal case. A significant increased PA signal is observed only after 3 hours. About the temperature influence on tomatoes behavior we can note that reduced C_2H_4 emission is obtained at low temperature.

Temperature is one of the most important external factors which influences the seed germination. The germination process needs different values function of the plant species and their adaptation during the genetic evolution. As we mentioned before, C_2H_4 plays a specific role also in germination process. For germinating wheat seeds (*Triticum* Sp.), two types of short PA-ethylene-germination experiments were performed, with seeds kept at $22^\circ C$ as compared to cold treated ($4^\circ C$) seeds.

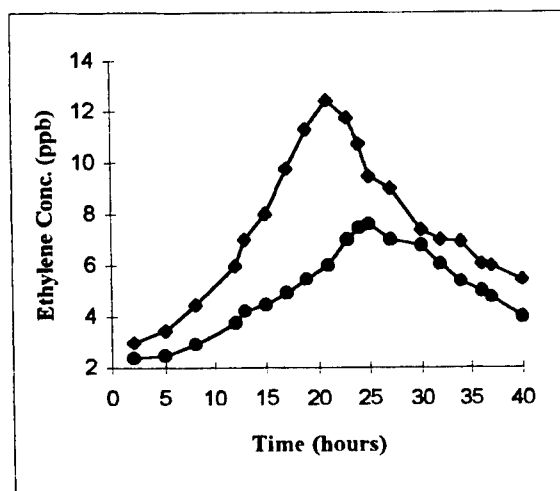


Fig. 5 The ethylene production for wheat seeds kept at $22^\circ C$ (♦) and at $4^\circ C$ (●)

The results presented in Fig. 5 indicate that wheat seeds kept at $22^\circ C$ begin to produce C_2H_4 earlier than at $4^\circ C$. Additionally, the peak in PA signal evolution, associated with visible germination, has a strong rise at $22^\circ C$. The data accords with plant physiology studies that established the optimum temperature needed for wheat seeds germination ($21^\circ C$).

During the growth of embryo, an accumulation of S-adenosyl-methionine inside the seed, which is the direct precursor of C_2H_4 , is produced. When the small shoot appears, the C_2H_4 biosynthesis starts rapidly, being accelerated by the direct absorption of the oxygen at the shoot-cell level. At low temperature, the activity of ACC oxidase is reduced due to delayed permeability of the plasmatic membrane and organelles. In this way the C_2H_4 production is indirectly diminished¹¹.

4. CONCLUSION

PA measurements with biological samples have demonstrated the strong connection between the ethylene emission rate and the stress conditions. The sensitive C_2H_4 detection system allows to observe in detail temporary effects on plant behavior under stress conditions and could offer more information for the plant physiology research.

The studies of wounding and thermal stress effects are very important from agricultural point of view because the fruits and vegetables are often damaged during growth, storage and transport, which can lead to untimely ripening.

5. REFERENCES

1. M. W. Sigrist, *Air monitoring by spectroscopic technique*, John Wiley & Sons Inc., New York, 1994.
2. F. J. M. Harren, J. Reuss, E. J. Woltering and D. D. Bicanic, "Photoacoustic Measurements of Agriculturally Interesting Gases and Detection of C_2H_4 below the PPB Level", *Appl. Spectrosc.*, **44**(9), 1360-1368 (1990).
3. D. Bicanic, F. Harren, J. Reuss, E. Woltering, J. Snel, L. A. C. J. Voosenek, B. Zuidberg, H. Jalink, F. Bijnen, C. W. P. M. Blom, H. Sauren, M. Kooijman, L. van Hove, and W. Tonk, "Trace Detection in Agriculture and Biology", *Photoacoustic, Photothermal and Photochemical Processes in Gases*, P. Hess, Vol. 46, pp. 213-245, Springer-Verlag Berlin Heidelberg, 1989.

4. A. C. Pereira, M. Zerbetto, G. C. Silva, H. Vargas, W. J. da Silva, G. de O Neto, N. Cella and L. C. M. Miranda, "OPC technique for in vivo studies in plant photosynthesis research", *Sci. Technol.*, Vol. 3, pp. 931-934, 1992.
5. F. G. C. Bijnen, H. S. M. de Vries, F. J. M. Harren and J. Reuss, "Cockroaches and tomatoes investigated by laser photoacoustics", *Journal de physique IV*, Vol. 4, pp. 435-443, June 1994.
6. F. B. Abeles, P. W. Morgan, M. E. Jr. Saltveit, *Ethylene in Plant Biology*, 2nd Ed., Academic Press, London, 1992.
7. H. Kende, "Ethylene biosynthesis", *Pann. Rev. Plant Physiol. Plant Mol. Biol.* 44, 283-307 (1993).
8. H. S. M. de Vries, F. J. M. Harren, J. Reuss, *Postharvest Biology and Technology*, 6, 275-285 (1995)
9. H. Kende, T. Boller, "Wound etylene and 1-Aminocyclopropane-1-carboxylate synthase in ripening tomato fruit", *Planta*, 151, 476-481 (1981).
10. S. F. Yang, N. E. Hoffman, "Ethylene biosynthesis and its regulation in higher plants", *Ann. Rev. Plant Physiol.*, 30, 155-189, (1984).
11. S. Yoshida, M. Uemura, "Protein and lipid compositions of isolated plasma membranes from orchard grass (*Dactylis glomerata*) and changes during cold acclimation", *Plant Physiology*, 75, 31-37 (1984).

Luminescence properties of some double activated zinc sulphide-type phosphors

Elisabeth-Jeanne Popovici*, Maria Aneculaese* and Veronica Ursu**

*Institute of Chemistry "Raluca Ripan", str. Fântânele 30, 3400-Cluj-Napoca

**Institute of Physical Chemistry "I.G. Murgulescu" of the Romanian Academy,
Splaiul Independentei 202, Bucuresti, ROMANIA.

ABSTRACT

Silver and copper double activated phosphor samples were synthesised from zinc sulphide prepared by thiosulphate method and with a NaCl-MgCl₂ mixture as flux. The thermal treatment was performed in a protective atmosphere at 900-1100 °C. The samples were characterised by crystalline structure (XRD patterns) and luminescent properties (emission spectra, decay curves). An intensification effect of the copper green fluorescence by silver ions was put in evidence. Conditions for a good green emitting phosphor were established.

Keywords: phosphors, luminescence, zinc sulphide, luminescent substances.

1. INTRODUCTION

The incorporation of silver or copper (activators) and halogenide ions (coactivators) into the crystalline structure of zinc sulphide (host lattice) generates phosphors that show intensive blue or green luminescence when excited by UV radiation, X-rays, α and β radiation or electronic beam. These ZnS-type phosphors with well defined luminescence and morphostructural characteristics are largely used in different devices of importance such as cathode ray tubes for TV-Sets, oscilloscopes or image intensifiers, electroluminescence devices etc.^{1,2}

ZnS-type phosphor preparation takes place by the high temperature calcination of the synthesis mixtures consisting of luminescent grade (l.g.) zinc sulphide, activator salts and alkaline or alkaline-earth halides as flux. According to the literature data, luminescent properties depend on many factors such as flux nature and concentration, activator nature and concentration, thermal synthesis conditions and, to a great extent, on the starting sulphide quality.^{3,4}

The results concerning the conversion of ZnS prepared by thiosulphate method into silver or copper activated phosphors have been presented in some of our previous papers.^{5,6} The aim of the present study is to report some of our results concerning the simultaneous activation of the same ZnS-type with silver and copper ions. The literature data offer rather few information about both this double activation of zinc sulphide and the use of the *thiosulphate route* in phosphor processing.⁷

2. EXPERIMENTAL PART

Luminescent grade (l.g.) ZnS was prepared from highly purified solutions of zinc sulphate and sodium thiosulphate.⁸

ZnS:Cu,Cl, ZnS:Ag,Cl and ZnS:Cu,Ag,Cl phosphor samples were prepared in the usual manner of phosphor synthesis.⁹ The synthesis mixtures consisted of ZnS (l.g.), 2.5 wt % NaCl (l.g) and 2.5 wt % MgCl₂(l.g.) and Cu(NO₃)₂ and/or AgNO₃ in amounts corresponding to $0.47 \div 12.7 \cdot 10^{-3}$ wt % Cu and $0.10 \div 50.0 \cdot 10^{-3}$ wt % Ag.

Two main samples series were prepared in different firing conditions. *Sample series A* was synthesised at 900 °C, in a protective N₂ atmosphere; special quartz ampules were used and open system was achieved. *Sample series B* was prepared at 1100°C, in air; covered alumina crucibles were utilised and closed system was assured. The sample cooling was rapidly performed either in a specially designed device with protective atmosphere, or in air.

The specially conditioned phosphor samples were characterised by crystalline structure (Philips PW 1050 Diffractometer; CuK α) and luminescent characteristics. These ones were estimated on the basis of emission spectra and decay curves which were registered on Perkin Elmer 204 Spectrofluorimeter. The excitation was performed with a 365 nm UV radiation. The registration conditions were different for the two sample series. For *series A*, UG1+UG4/WG1+BG9 filters were used for excitation/emission radiation and Lumilux B₃₁₋₁₀ (Riedel-de-Haen) was used as standard. For *series B*, UG1/WG1 filters were used for excitation/emission radiation and Green Phosphorescent Pigment (Centurion Ltd.Scotland) was the standard.

3. RESULTS AND DISCUSSION

Luminescent grade zinc sulphide used in our experiments possesses a good luminescence ability and is about 90 % cubic in structure.¹⁰ This starting sulphide was converted at 900 °C (N₂-atmosphere) into silver (ZnS:Ag,Cl) and silver copper activated samples (ZnS:Ag,Cu,Cl).

Under 365 nm excitation, the ZnS:Ag(0.01),Cl sample shows an intense blue luminescence whereas the ZnS:Ag,Cu,Cl samples present blue-green to green emissions. The emission spectrum of ZnS:Ag,Cl consists of one large emission band centered at about 445 nm, originated in silver luminescence centres such as $\text{Ag}_{\text{Zn}}^+ - \text{Cl}_\text{s}^-$ (figure 1a). XRD-patterns show that the sample is cubic in structure (~ 100 % sphalerite). These structural and luminescent characteristics confirm that the synthesis conditions were adequate for both a good thermal recrystallisation and silver incorporation.

The addition of copper ions determines the formation of new luminescence centres $\text{Cu}_{\text{Zn}}^+ - \text{Cl}_\text{s}^-$ which generate the development of the Cu-green emission band with a peak at about 525 nm; even at about $4 \cdot 10^{-3}$ % copper, this band is well evidenced. As the Cu concentration increases, the Ag-blue band decreases in intensity and the apparently peak shifts to longer wavelengths. The continuous increase of copper amount results in a continuous increase of the ratio between the two main emission bands (I_{525}/I_{460}) and a slow decrease of the green emission. The latter effect could be correlated with an extinguishing interaction between the luminescence centres (concentration quenching).

The sample series B, prepared at 1100°C (closed system) consist of ZnS:Cu,Cl phosphor in which small silver amounts were gradually added. All samples possess a very well formed hexagonal structure (100 % wurtzite) and under UV excitation exhibit green to blue bright luminescence.

The corresponding emission spectra (figure 1b) consist of two major large bands situated at about 450 nm and 515 nm whose ratio depends on the silver amounts used in phosphor synthesis. For ZnS:Cu,Cl sample prepared in our working conditions, I_{515}/I_{450} is about 2.4. The addition of $1 \cdot 10^{-4}$ % Ag dramatically increases this ratio to a value of 3.8. Larger silver amounts generate a slow decrease of this intensities ratio.

For ZnS:Cu,Ag,Cl prepared with $5 \cdot 10^{-4}$; $1 \cdot 10^{-3}$; $5 \cdot 10^{-3}$; $1 \cdot 10^{-2}$; $5 \cdot 10^{-2}$ % Ag, the I_{515}/I_{450} ratio is equal to 3.8; 3.5; 3.0; 3.0 and 0.4, respectively.

Mention must be made that, in this sample series, the peak position is at shorter wavelengths than in the samples prepared at 900 °C. This is in agreement with the literature data: the change of the crystalline structure of ZnS-type phosphors from cubic to hexagonal generates a shift of the peak position with about 10 nm toward shorter wavelengths.²

The comparison of all emission spectra presented in figure 1 suggests also that, at a certain silver concentration, the Cu-green emission could be intensified by the presence of silver as second activator. This effect could be put in evidence if the relative intensity of phosphor samples is represented versus the silver concentration (figure 2).

Some cub-ZnS:Cu,Ag,Cl samples were prepared at 900°C with $7.5 \cdot 10^{-3}$; $1 \cdot 10^{-2}$ and $1.25 \cdot 10^{-2}$ wt % copper and various silver amounts. In order to avoid concentration quenching, relative small activator quantities were used. In all these cases, a very weak Ag-intensifying effect could be observed. Apparently, this effect takes place when copper and silver are present in almost equal amounts, that means at Ag/Cu atomic ratio of about 0.6 (figure 2a).

The addition of silver ions into the hex-ZnS:Cu,Cl shows a much stronger influence on the Cu-green luminescence (figure 2b). The silver intensifying action takes place within a relatively narrow concentration domain, namely between $5 \cdot 10^{-3}$ and $20 \cdot 10^{-3}$ wt % Ag, corresponding to Ag/Cu ratio between about 0.3 and 1.2. The maximum effect was observed at $1 \cdot 10^{-2}$ wt % Cu and $1 \cdot 10^{-2}$ wt % Ag that is for Ag/Cu ratio of about 0.6.

Mention must be made that hex-ZnS:Ag,Cl sample (prepared without copper) exhibits blue luminescence ($\lambda_{\text{pk}} = 435$ nm) that is very intense at a silver concentration of $1 \cdot 10^{-2}$ wt %. It seems that the Cu-green luminescence in ZnS:Cu,Ag,Cl is very intense when the incorporation degree of silver ions is high and, consequently, when the second activator alone is able to produce a strong blue luminescence. But the emission spectrum of ZnS:Cu,Ag,Cl contains a relatively weak blue band. It is evident that a large part of this emission is used for the effective excitation of the Cu-green luminescence resulting in the observed Ag- intensification action. In the case of ZnS:Cu,Ag,Cl samples, a mechanism of energy transfer is implied into the excitation process.

The silver addition into the ZnS:Cu,Cl samples could also influence on the decay characteristics of the luminescent emission. Figure 3 presents the decay curves registered for the three ZnS:Cu,Ag,Cl samples. The luminescence decay of these samples proceeds in the expected manner: luminescence decreases in time on a mainly hyperbolic decay. The decay becomes faster when larger silver amounts are used beside the copper activator.

The phosphorescence of these samples could be also observed in the dark room (with eyes adapted to darkness). At small silver amounts ($5 \cdot 10^{-4}$ wt %), phosphorescence is slightly improved whereas, at large silver concentrations, a strong diminishing effect is noticed. The sample with $1 \cdot 10^{-2}$ wt % silver exhibits phosphorescence no more.

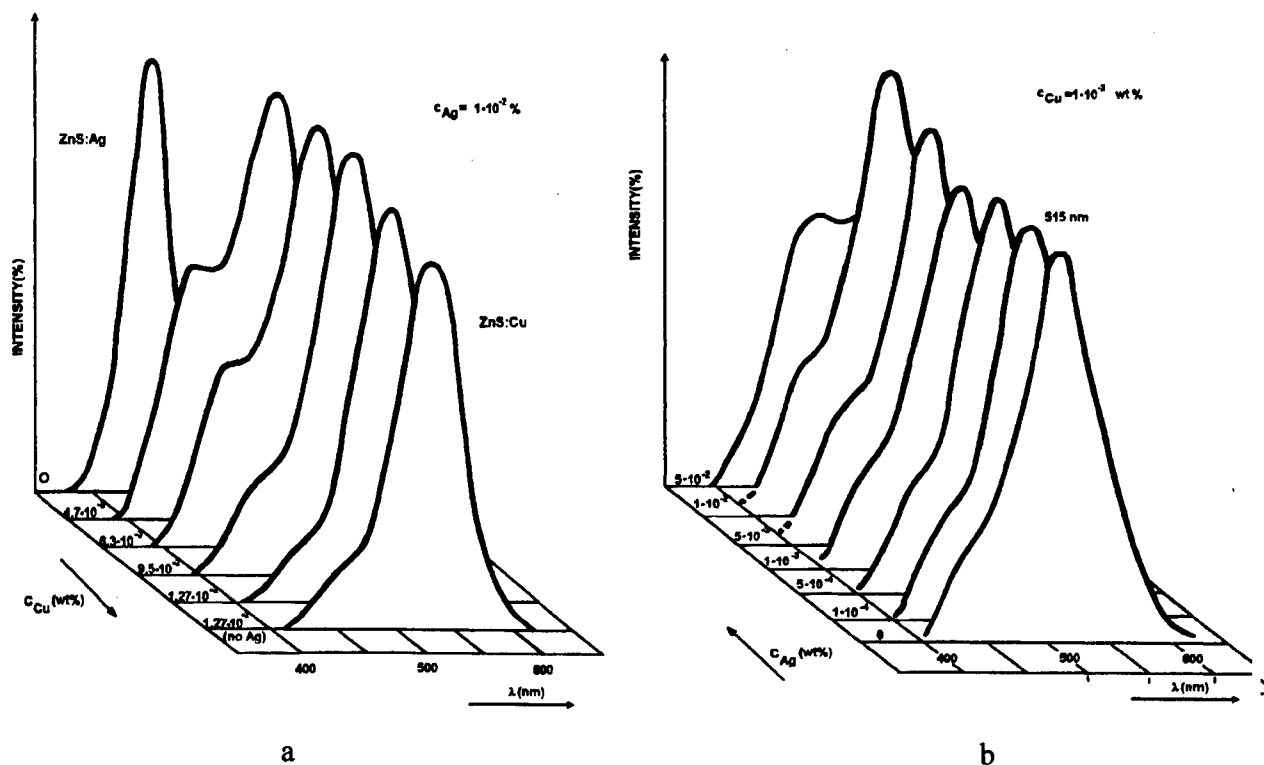


Figure 1. Emission spectra of cub-ZnS:Ag,Cu,Cl (series A; 900°C) and hex-ZnS:Ag,Cu,Cl (series B; 1100°C) prepared with various activator concentrations; (ZnS:Ag, Cl was registered with different sensitivity)

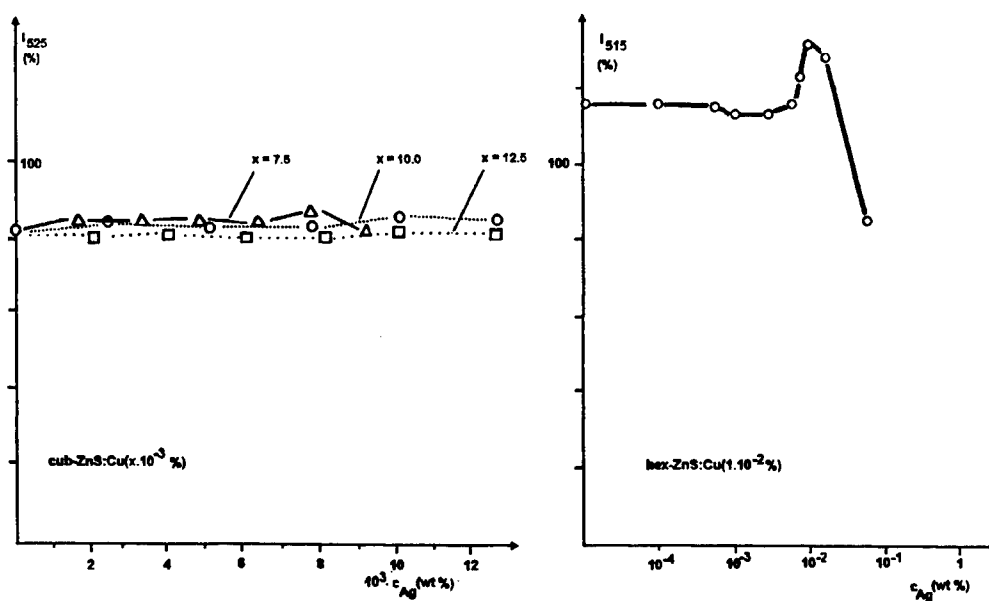


Figure 2. Relative intensity of various cub-ZnS: Cu,Ag,Cl and hex-ZnS: Cu,Ag,Cl samples versus the silver concentration

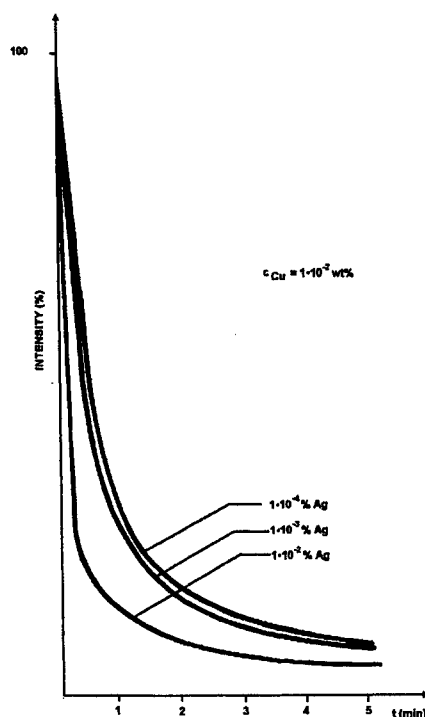


Figure 3. Decay curves for some hex- ZnS:Cu,Ag,Cl phosphors (Sample series B; 1100°C)

4. CONCLUSIONS

Silver addition into the ZnS: Cu,Cl samples generates an intensification of the Cu-green emission band as a result of an energy transfer implying the silver luminescence centres. In our working conditions, for a starting sulphide prepared by thiosulphate route, the maximum effect was obtained at Ag/Cu atomic ratio of about 0.6. It seems that, the silver intensifying action on the Cu-green fluorescence coincides with a silver diminishing effect on the Cu-phosphorescence.

REFERENCES

1. O.N.Kazankin, L.Ya.Markovskii, I.A.Mironov, F.M.Nekerman and L.N.Netoshina, *Neorganicheskie lyuminofovy*, Izd.Himiya, Leningrad, 1975;
2. A.M.Gurvich, *Vvedenie v fizicheskuyu himiyu kristallophosphorov*, Vysch. Schola, Moskva, 1982;
3. E.J.Popovici, V.Ursu and D.Macarovici, "Luminescent - grade zinc sulphide prepared by thiosulphate method. III. Characterization of some phosphor samples prepared by thiosulphate method", *Rev.Roum.Chimie*, **41**(5-6),427-432 (1996);
4. L.A.Smorodina, Z.I.Guretzkaya and A.A.Bundel, "Vlyanie pred'istorii sulfida tzinka na svoistva polychaemykh lyuminoforov", *Neorg. Materialy*, **VI**, 260-261 (1970);
5. E.J.Popovici, M.Aneculaese, V.Ursu and D.Macarovici, "Studies on the synthesis of silver activated zinc sulphide phosphor", *Studia Univ.Babes-Bolyai, Chemia*, **XL** (1-2),55-61 (1995);
6. E.J.Popovici, M.Aneculaese, V.Ursu and D.Macarovici, "Synthesis of zinc sulphide type phosphor with well defined characteristics", *Rom. J.Optoelectronics*, **5**(1), 81-84 (1997);
7. M.I.Tombak, A.V.Popova, O.F.Komar and A.A.Bundel, "O progodonosti tiosulfatogo metoda v poluchenia sulfida tzinka dlya sinteza lyuminoforov", *Izv.A.N.SSSR, ser.Fiz.*, **XXIII**(11), 1363-1369 (1959);
8. E.J.Popovici, M.Aneculaese and D.Macarovici, *Rom.Pat.*, 98116 (1989);
9. E.J.Popovici, M.Aneculaese and D.Macarovici, *Rom.Pat.*, 103769 (1991);
10. E.J.Popovici, V.Ursu and D.Macarovici, "Luminescent - grade zinc sulphide prepared by thiosulphate method.II Some physical properties of different ZnS-types.", *Roum.Chem.Quart.Reviews*, **1**(3), 239-244 (1993);

Correlation of some radiative processes resulting from electronic and vibrational spectra of CN molecule excited in an electric arc discharge

I. Iova, M. Băzavan, C. Biloiu, Gh. Ilie, M. Bulinski

Faculty of Physics, Bucharest University
Bucharest - Magurele, P.O. BOX MG - 11, 76900

ABSTRACT

The molecular vibration temperature of the plasma from an interrupt arc discharge in air at atmospheric pressure and at current intensities in the range of $2 \div 8$ Amperes, using electronic and vibration bands of violet [$B^2\Sigma^+ - X^2\Sigma^+$] and red [$A^2\Pi - X^2\Sigma^+$] systems of the CN molecule was determined. At the equilibrium temperature of 6400 K, 27 lines of Ti, contained as impurity in coal electrode were found. These spectral lines were found in the $247 \div 340$ nm spectral range having the upper levels of the excitation energies in the $3.60 \div 5.69$ eV range, in the neighborhood of the energy of dissociation of the CN molecule on the fundamental electronic state. Some considerations about the vibrational states populations are also made.

Keywords: molecular vibration temperature, vibrational states populations, CN molecule

1. INTRODUCTION

The CN molecule, unstable in common natural conditions, is produced in plasma at sufficiently high temperature, from the electrode's coal and the atmospheric nitrogen. For diagnosis of plasmas used to obtain different chemical compounds or thin film depositions, it is necessary to know the proprieties of the CN molecule which appear as a secondary reaction product.

A fundamental role in the rate of plasma reactions is played by the temperature. Consequently, a method of temperature determination was established^{3,4} using the electronic and the vibration spectra of red [$A^2\Pi - X^2\Sigma^+$] and violet [$B^2\Sigma^+ - X^2\Sigma^+$] systems of the CN molecule. The paper presents also the correlation of this temperature with the ionic Ti lines from the behavior of the relative intensity of the excitation and vibration bands.

2. EXPERIMENTAL

The radiation source was an electric discharge plasma in interrupt arc regime. The power supply was of ORION model. The operating parameters at 4 Amperes current intensity, as peak voltages: + 326 or -330 Volts, profile width of 10 ms, voltage on landing of 50 Volts, repetition frequency of 100, were measured with a TEKTRONICS TDS - 350 oscilloscope³.

The ultraviolet and visible spectra were recorded with an Q - 24 Zeiss spectrograph with sufficiently high linear dispersion and resolution power to resolve vibration structure of electronic spectra of CN molecule. For vibration temperature determination by Boltzmann's diagrams, we used a succession of band-heads with same lower level, e.g. a progression in $v''=2$.

These wavelength were: 4606.0 Å, 4196.1 Å, 3861.2 Å and 3582.6 Å. A heterochromatic correction with the aid of a standard bulb spectra (feeding voltage of 106.7 V corresponding to a color temperature of 2800 K) was performed.

Mathematical relationship used to calculate the molecular vibration temperature from Boltzmann's diagrams was⁵:

$$\ln \left(\frac{I_{v'v''}}{v^4 v'v'' S_{v'v''}} \right) = F \left(\frac{G(v)}{0.6925} \right)$$

which represent a linear dependence of neperian logarithm of relative intensities against values of vibration terms. The relative intensities $I_{v'v''}$ were measured with a microphotometer, the lines strength were taken from² while vibration terms were determined by us using Deslandres's table.

For discharge current intensities of 4, 5, 6 and 8 Amperes we found a vibration temperature which doesn't significantly vary being practically constant at 6400 K. This fact proofs that electronic and vibration levels excitation are produced through direct electronic collisions.

By a complete qualitative spectral analysis of the recorded spectral plates, beside vibration bands of two systems from the CN molecule spectra, in the investigated 247 ÷ 340 nm spectral range, a number of 27 ionic lines of Ti II that is present in coal electrodes like impurities were found⁴. The excitation energies of the upper states are placed in the 3.60÷ 5.69 eV energy range, the upper limit being in the neighborhood of the dissociation energy of CN molecule on the electronic ground states (fig.1)¹.

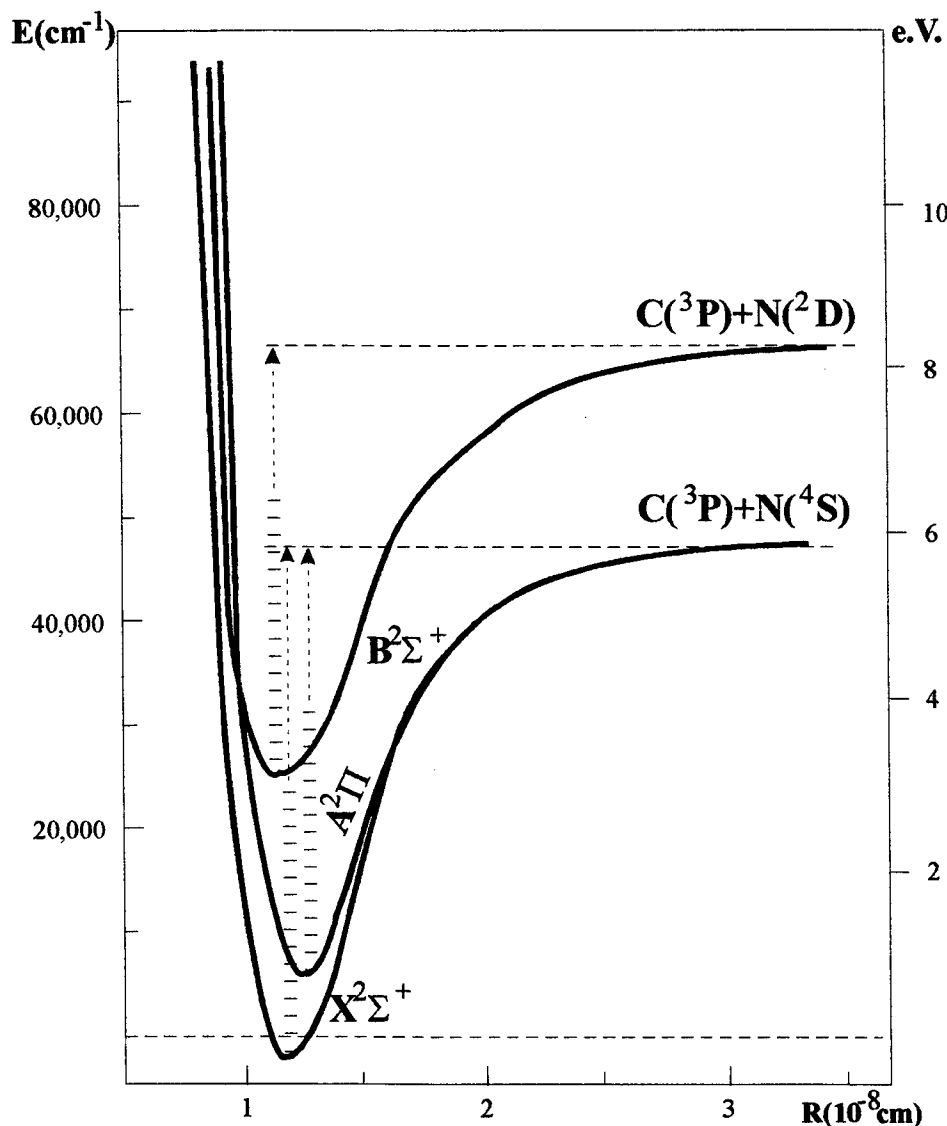


Fig. 1. Potential curves of the electronic states of the CN molecule.

We didn't find neither atomic or ionic lines of isolated N or C atoms originated by the CN molecule dissociation or from other processes. This could be explained by the fact that the temperature is too low to excite these atoms.

The relative intensity distributions for the bands of one of the sequences of the red system excited in the arc plasma at 4 Amperes, measured with a TEKTRONICS TDS - 320 oscilloscope having a band of 100 MHz, a time rise constant of 5 ns and being coupled to an EPSON STYLUS COLOR II DESK JET printer, are represented in the fig. 2.

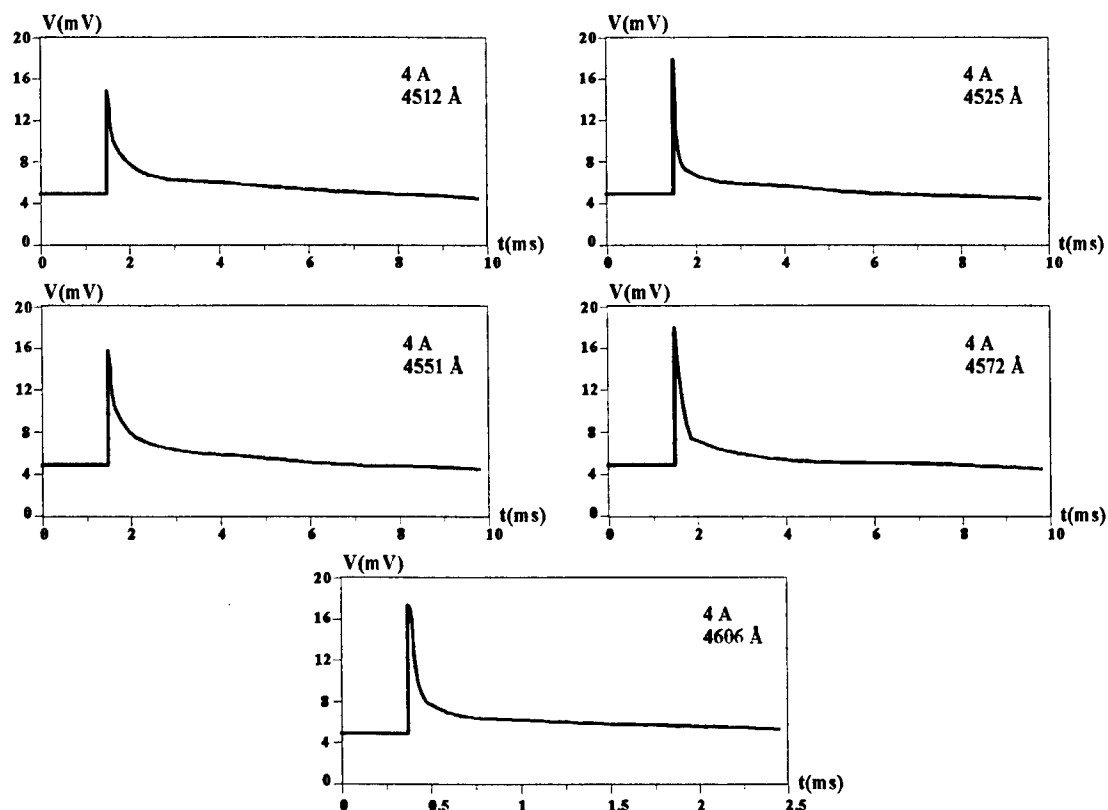


Fig. 2. Relative intensity distributions of the bands with wavelength 4606 Å, 4572 Å, 4551 Å, 4525 Å, 4512 Å, belonging to the red system $[A^2\Pi - X^2\Sigma^+]$ of the CN molecule.

This temporal behavior of the involved band intensities suggests a quasi thermodynamic equilibrium of the plasma radiation in the interrupt arc discharge.

In order to estimate the role of the electron excitation on the electronic and vibration levels of the CN molecule we have had compared the relative intensity distribution of some bands of red $[A^2\Pi - X^2\Sigma^+]$ system excited in arc with the relative intensities of the same system excited in electric spark discharge which, as is known, is not an isothermal spectral source (fig. 3).

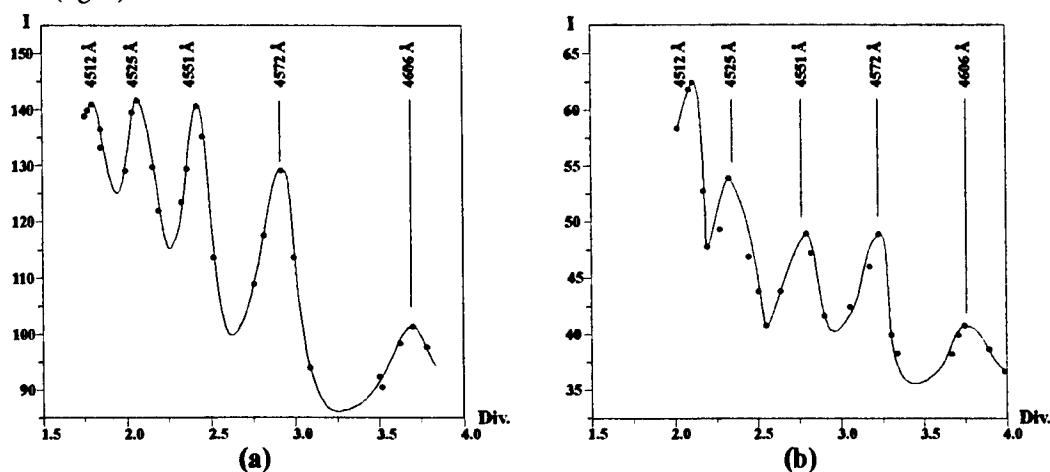


Fig. 3. Relative intensity distributions for one of the sequences of the red system excited in electric arc (a) and in electric spark discharge (b).

In the electric spark discharge the bands coming from higher levels are more intense than in the case of excitation in the electric arc discharge. This is due to an important electronic current component of the plasma spark corresponding to higher energies.

3. CONCLUSIONS

The calculated temperature is compatible with the molecular vibration temperature of the plasma, indicating that the state is in a partial equilibrium not in a total one. These means that exists a difference between molecular vibration and electronic temperatures. The dependency of the vibration bands intensities versus electric current intensity and practical independence of temperature versus the same parameter suggest that the electronic and vibration levels excitation is produced preponderantly through direct electron collisions.

The absence of the dissociation products of the CN molecule and of the other molecules from the free atmosphere, like N_2 , O_2 , H_2 , in the investigated spectral range proof that at the calculated plasma temperature these cannot be enough dissociated and consequently, the electron energies are not sufficiently higher to induce significant dissociation and C and N atoms excitation.

The great number of ionic lines of Ti and the absence of other ionic lines from plasma radiation suggest that global current intensity from the positive column of the arc is fundamentally determined by the Ti ions and electron concentrations, the concentration of the molecules which suffer dissociate ionization in such conditions being less important.

4. ACKNOWLEDGMENTS

Part of this paper was supported by the National Council of the University Scientific Research by Grant 989/1997.

5. REFERENCES

1. G. Herzberg, Molecular spectra and molecular structure, vol. I, D van Nostrand Co. Inc., 1950.
2. L. L. Danylewych and R. W. Nicholls, Proc. R. Soc. Lond., A 360, 557 - 573, 1978.
3. I. Iova, M. Bazavan, C. Biloiu, M. Ganciu, C. Ristorescu, C. Penache and D. Penache, Rom. Rep. Phys., Vol. 49, No. 3-4, 1997 (under press).
4. I. Iova, M. Bazavan, C. Biloiu, Gh. Ilie, The 3rd General Conference of the Balkan Physical Union, abstracts p. 350, 2 - 5 Sept. 1997.
5. I. Iova, I. I. Popescu, E. Toader, Bazele spectroscopiei plasmei, Editura Științifică și Enciclopedică, București, 1987.

Author Index

- Abu-Taha, M. I., 578
Aiftimiei, Cristina, 779, 891
Akimova, Elen A., 790
Al-Jourani, M. M., 578
Albu, Alexandru M., 902, 946
Aldea, E., 831
Alexandrescu, Rodica, 122, 174, 199, 218
Alexe, M., 846
Allott, Ric M., 162
Andrei, A., 182, 199, 831
Andriesh, Andrei M., 258, 385, 1013
Aneculaese, Maria, 632
Anghel, Sorin, 1027
Antipa, Ciprian, 696, 739, 747
Antoniow, Jean S., 1039
Apostol, Dan, 972, 1100
Apostol, Ion G., 702
Apostol, Silvia, 665, 713
Ashurov, Mukhsin Kh., 837
Babin, Vasile, 45, 498, 865, 930
Baibarac, M., 623
Baltateanu, N., 75, 930
Baltog, I., 205, 623
Balucani, M., 762, 784, 831
Barb, D., 311
Barba, N. A., 790
Battaglin, Giancarlo, 533
Băzăvan, M., 524, 636
Beldiceanu, Anca Maria, 1094
Bena, Rodica, 946
Bertinetto, Fabrizio, 990
Bertolotti, Mario, 335
Bicanic, Dane D., 1039
Biloiu, C., 524, 636
Bivol, Valery V., 790
Blanaru, Constantin, 1074, 1100
Boerasu, I., 846
Bondarenko, V., 762, 784
Borsella, E., 533
Bosch, Salvador, 1056, 1120, 1150, 1156
Bota, M., 727
Botez, C. E., 462
Boyd, Ian W., 225, 272
Bradaczek, H., 960
Braescu, Cora Lucia, 779, 891
Bratescu, M. A., 603
Bratulescu, G., 619
Braverman, Ada Livia, 106
Brojbeanu, Gabriela, 692
Bruckner, Ion I., 696, 739
Brynzari, Vladimir, 1032
Buca, D., 233, 267
Bulgaru, M. G., 1013
Bulinski, M., 636
Bunescu, M. C., 225, 272
Bunila, Daniela, 739
Burke, V. M., 39
Bursuc, I. D., 936
Buzdugan, Arthur I., 258
Calian, Violeta, 278, 494
Calin, Mihaela, 727, 733, 801, 860
Carnicer, Arturo, 1150, 1156
Carp, C., 717
Cârstocea, Benone, 665, 713
Chan, H. L., 122
Chartier, Jean-Marie, 990
Chelu, Mariana, 252
Chera, Ionel, 524
Chilibon, Irinela, 813, 883
Chirita, F., 1007
Chirtoc, Mihai, 1039
Chiş, Ioan, 153, 188, 282, 702
Chumash, Valentin N., 446
Cicala, Eugen F., 246, 293, 299
Cimpoca, Valerica, 75
Ciobu, V. E., 570
Ciotaru, D., 727
Cireasa, Raluca, 199
Ciuchita, Tavi, 747
Ciurea, M. L., 205, 623
Cojoc, Dan, 425
Cojocaru, Laurentiu, 498
Cojocaru, S., 199
Constantinescu, B., 311
Constantinescu, T., 524
Copot, Gheorghe, 819, 926
Copot, Rodica, 819
Cordoş, Emil, 1088
Cosereanu, Liviu, 926, 930
Craciun, Doina, 225, 272
Craciun, F., 1194
Craciun, Valentin, 225, 272
Craiu, M., 252
Cristea, M., 524
Cristescu, Constantin P., 65
Cristescu, Simona M., 627
Cristian, Petre, 99
Crunteanu, A., 199
Dabu, Razvan V., 81, 225, 454, 702
Dadarlat, Dorin, 1039
Damaskin, I., 1007
Damian, Victor, 972, 1100
Darvasi, Eugen, 1088
Dascalu, Constanta, 796, 941
Dascalu, Traian, 70, 233, 267, 713
David, Ion, 246, 299

Daviti, Maria, 241
 Defay, Céline, 1106
 de F. Moneo, J. R., 1150, 1156
 De Marchi, Giovanna, 533
 de Vries, Hugo S. M., 556
 Digulescu, Petre P., 825, 999
 Dima, Stefan V., 686
 Dima, Vasile F., 686
 Dincă, Andreea G., 1162, 1173
 Dincă, Mihai P., 1162, 1173
 Dinescu, Gheorghe H., 831
 Dinescu, Maria, 831, 1194
 Dinu, R., 1194
 Dobre, Mara, 722
 Dobroiu, Adrian, 972, 1100
 Dolghier, V., 258
 Dolocan, V., 887
 Dorogan, Valerian, 1007, 1032
 Dragnea, Laurentiu, 912
 Dragoi, V., 846
 Dragulescu, Dumitru, 188
 Ducariu, Adrian, 483
 Dumitras, Dan C., 627, 654
 Dumitrescu, Mihail, 922
 Dumitru, Gabriel, 17, 81, 1083
 Dumitru, Mihaela A., 10
 Dutu, Doru C. A., 627, 654
 Egee, Michel, 1039
 El-Kahlout, A. M., 578
 Elisa, Mihai, 965
 Enaki, Nicolae A., 399
 Enaki, V. N., 570
 Enculescu, Ionut, 262, 897
 Ersen, Simion, 498, 865
 Farcas, Ana-Florica, 45
 Fenic, Constantin G., 81, 252, 454, 702
 Fernández, Xavier, 1056
 Ferrari, A., 762, 784, 831
 Ferré-Borrull, Josep, 1056
 Flory, François, 1106
 Forgaci, Flavia, 288
 Frandas, A., 1039
 Furuhashi, M., 32
 Gafencu, Luiza, 665
 Gafencu, Otilia L., 713
 Gaivan, S. L., 469, 473
 Galeata, G., 205
 Gartner, Mariuca, 887, 1194
 Gasanov, Eldar M., 837
 Georgescu, Geo, 1114, 1132, 1137
 Georgescu, Serban, 2, 112, 612
 Gerardi, C., 1194
 Gherghina, Ion, 930
 Gherman, Valentin V., 483
 Ghica, C., 218, 252, 702, 1137
 Ghica, D., 831
 Ghita, C., 887
 Ghita, R. V., 75
 Giesen, Adolf, 978
 Girardi, R., 24
 Giubileo, Gianfranco, 642
 Gomoiescu, Despina, 1088
 Gonella, Francesco, 533
 Gostian, Doina, 678
 Grigore, Maria, 498
 Grigorescu, Cristiana E. A., 860, 897
 Grigoriu, Constantin, 153, 188, 282
 Groß, Tobias, 17
 Gruia, Ion, 524
 Guina, Mircea, 922
 Guja, Victor B., 439
 Gutu, Iulian, 99, 1114
 Guzun-Stoica, Anicuta, 489
 Gyorgy, Eniko, 182, 218
 Hapenciuc, Claudiu, 2
 Harren, Frans J. M., 556
 Hasegan, Sorin A., 955
 Hening, Alexandru, 218, 678
 Herisanu, Nicolae-Alexandru, 81
 Heumann, E., 51
 Honciuc, Gheorghe, 1178, 1183
 Huber, Guenter, 51
 Hügel, Helmut, 978
 Huq, Syed E., 162
 Hutsanu, V., 887
 Iancu, Ovidiu D., 439, 852
 Ibragimova, E. M., 837
 Iftimia, Nicusor, 865
 Ilie, Gheorghe, 524, 636
 Iliescu, Brandusa, 262, 897
 Ioncea, A., 225, 272
 Ionescu, Elena, 696, 739, 747
 Ionescu-Pallas, Nicholas, 375
 Ioniță, M., 713
 Ioniță-Mânzatu, V., 713
 Iordache, Gh., 81
 Iorga Siman, Ion, 1027
 Iosub, I., 1027
 Iova, Iancu, 524, 636, 1027
 Iovu, Michael S., 258
 Ishimov, B. M., 790
 Ispasoiu, Radu G., 58, 462
 Ivan, R. V., 825
 Ivana, Eugenia, 252
 Jalink, Henk, 1039
 Jeloica, L., 311
 Jiang, Weihua, 153, 188
 Jianu, Angela, 511, 517, 955
 Jipa, V., 930
 Jurba, Mihai, 926, 930
 Juvells, Ignacio P., 1150, 1156
 Kasuchits, N., 762
 Kato, Kiyoshi, 393
 Kennedy, Michael, 1083
 Khadzhi, P. I., 406, 469, 473
 Kim, Nam Seong, 162
 Klein-Douwel, R. J. H., 143
 Kobayashi, Takao, 32

- Koch, P.-J., 960
 Kopica, Mirosław, 756
 Koswig, H. D., 796
 Kosyak, V., 1007, 1032
 Krieger, W., 432
 Kumar, Ashok, 122, 199
 Kurzeluk, Mona, 489
 Labastida, I., 1150, 1156
 Labes, U., 796
 Lăcătușu, Veronica, 252
 Lainé, Derek C., 578
 Laky, Dezideriu, 686
 Lamedica, G., 762, 784, 831
 Lazarescu, Mihail F., 860, 1114
 Leinfellner, N., 541, 584
 Levai, Stefan, 1027
 Lisi, Nicola, 162
 Logofatu, B., 860
 Logofatu, C., 897
 Logofatu, Michaela F., 860
 Lörinczi, A., 960
 Luculescu, C., 81, 454, 702
 Lupei, Aurelia, 563, 570, 589
 Lupei, Voicu, 2, 51, 70, 89, 112, 563, 570, 589, 612, 713, 1162, 1173
 Macovei, M., 399
 Maddison, B. J., 162
 Maksimyak, Peter P., 1022
 Malkov, Sergei A., 1013
 Manaila-Maximean, Doina, 946
 Manea, Stefan A., 860, 897
 Mann, C. M., 162
 Manolescu, G., 1202
 Marcu, A., 153, 188, 282
 Marginean, P., 252
 Marginean, Raluca, 926, 1143
 Marian, A., 233, 267
 Marica, F., 548
 Marin, Gheorghe, 182, 218
 Marom, Emanuel, 363, 418
 Martin, C., 218, 272, 708
 Marzu, Marinica, 1143
 Mästle, Ruediger, 978
 Matei, Consuela-Elena, 654
 Mattei, G., 533
 Mazets, I. E., 541, 584
 Mazzoldi, Paolo, 533
 Medianu, Victor Rares, 85, 99, 1114, 1132, 1137
 Mel'nikov, Igor V., 353
 Mendlovic, David, 363, 418
 Mereutza, Alexandru Z., 462
 Miclea, M., 603
 Miclea, Paul T., 1162
 Micloș, Sorin, 45, 807
 Micluța, Marius, 1189
 Mihailescu, Ion N., 182, 218, 272, 305, 678, 708, 960
 Mihalache, Dumitru, 353
 Mihut, L., 623
 Mincu, Nicolae E., 722, 831
 Mirengi, L., 1194
 Mirzu, Marinica, 926, 930
 Mitrea, Mihai, 477
 Miu, Catalin, 241
 Miu, Dana, 153, 188, 282
 Miyamoto, Kenji, 603
 Mocofanescu, Anca, 45
 Moise, N., 665, 717, 1202
 Moldovan, Adrian, 498, 865
 Moldoveanu, Vladimir, 696
 Montrosset, Ivo, 24, 439, 873
 Moon, S. W., 162
 Morjan, Ion G., 174, 199
 Moroseanu, A., 713
 Motoc, Cornelia, 796, 941
 Motta, Gabriella, 873
 Munteanu, Ion I., 860
 Musa, G., 603
 Muscalu, G. L., 454, 1167
 Nacu, Mihaela, 739
 Nascov, Victor, 972, 1100
 Nastase, N., 1137
 Neamtu, Johnny, 182, 305, 619
 Necsoiu, Teodor, 733
 Negoita, T., 1202
 Nelea, V. D., 218, 708
 Nemes, Miloslava, 288
 Nesheva, D., 960
 Nichici, Alexandru, 246, 293
 Nicola, Marius, 1088
 Ninulescu, V., 10
 Nishiura, K., 153
 Nistor, Leona C., 218, 252, 702
 Nitulescu, Gabriel, 483
 Obst, S., 960
 Oomens, Jos, 556
 Osiac, E., 51, 89
 Oud, J. L., 241
 Panoiu, Nicolae-Coriolan, 353
 Pantelica, D., 182
 Paris, D., 1039
 Parker, David H., 556
 Pascu, Mihai L., 665, 717, 739, 1202, 1215
 Pavel, Nicolaie I., 32, 70
 Pavelescu, Gabriela, 205, 623
 Pentia, E., 205
 Pérez, J., 1150, 1156
 Perrone, Alessio, 130
 Perrone, Guido, 873
 Persijn, S., 556
 Petrache, M., 589
 Petraru, A., 563, 589
 Petre, D., 846
 Petrescu, Emil, 796, 941
 Petris, Adrian, 511, 517
 Petru, Frantisek, 990
 Pintilie, Ioana, 846
 Pintilie, Lucian, 846

Pirc ălăboiu, Daniel, 852, 873
 Piscureanu, Mihai C., 10
 Polychronyadis, E. K., 241
 Popa, Carmen, 517
 Popa, Dragos, 517
 Popescu, Aurelian A., 902
 Popescu, C. R., 174
 Popescu, E., 930
 Popescu, F. F., 548
 Popescu, Gheorghe, 665, 990, 1078
 Popescu, Ion M., 58, 211, 916, 946, 1067
 Popescu, Mihai A., 960
 Popovici, Elisabeth-Jeanne, 288, 632
 Popovici, Maria-Ana, 722
 Poterasu, M., 267
 Poterasu, M., 233
 Preda, A. M., 65, 211
 Preda, Liliana, 65, 211
 Preoteasa, V., 678
 Presura, C., 570
 Prisacari, A. M., 790
 Puscas, Niculae N., 24, 58, 462, 483, 916, 1067
 Puzewicz, Zbigniew, 756
 Quaranta, Alberto, 533
 Radu, G., 548
 Radu, Liliana, 678, 708
 Radu, Mihaela, 727, 733, 801, 860
 Radu, S., 678
 Radu, S., 619
 Răducanu, Dan, 891
 Radulescu, Irina, 678, 708
 Rădvan, Roxana N., 733, 801
 Ralea, Daniel, 926, 1143
 Ricciardelli, A., 784
 Ristau, Detlev, 17, 1083
 Ristici, Iosefina, 85
 Ristici, Marin, 85
 Robea, Bogdan, 807
 Robu, Maria, 801, 813, 883
 Robu, Shtefan V., 790
 Roger, Jean P., 205
 Rogojan, Rodica, 965
 Roman, Miruna, 665, 1215
 Rosu, Constantin, 796, 946
 Rotaru, A. H., 411
 Roundy, Carlos B., 673, 768, 1045
 Rusca, Nicolae, 696
 Rustamov, Igor R., 837
 Rusu, G. I., 951
 Rusu, Ioan I., 936
 Sakai, Yosuke, 603
 Sandroock, T., 51
 Sandu, V., 831, 1194
 Sarpe-Tudoran, Cristian, 278, 494, 619, 1063
 Sava, F., 960
 Savastru, Roxana, 801
 Savi, G., 727
 Scarano, Danilo, 24
 Scarlat, E., 65, 211
 Schiopu, Carmen Liliana, 906
 Schiopu, Paul, 906, 912
 Schmitz, C., 978
 Serbanescu, Ruxandra, 708
 Shabtay, Gal, 418
 Shemer, Amir, 418
 Sibilia, Concita, 335
 Singurel, Gh., 1183
 Smarandache, A., 1202
 Smeu, Emil, 58, 462, 1067
 Socaciu, Margareta, 278, 494, 619, 1063
 Soergel, E., 432
 Sorescu, M., 311
 Sporea, Dan G., 17, 81, 1083
 Staicu, Angela, 1215
 Stamate, Marius D., 951
 Stancalie, Gheorghe, 1220
 Stancalie, V., 39
 Stanciu, Angelia, 241
 Stanciu, Catrinel A., 831, 1194
 Stanciu, George A., 241
 Stefan, Levai, 489
 Stefanescu, Eliade N., 877
 Sterian, Paul E., 10, 825, 877, 965, 999
 Stoian, Razvan, 702
 Stoica, Axente, 891
 Stratan, Aurel, 81, 252, 454, 702
 Stroila, Carmen, 727
 Strzelec, Marek, 756
 Sureau, Alain, 39
 Suruceanu, Grigore I., 58, 462
 Suteanu, S., 692
 Taira, Takunori, 32, 70
 Tanaka, Eiko, 393
 Tchaushev, G., 960
 Teodorescu, Valentin S., 182, 218
 ter Meulen, J. J., 143
 Ticos, C. M., 665
 Timus, Clementina A., 17, 1083, 1132
 Tkachenko, D. V., 406
 Toacsan, M. I., 311
 Tomescu, M., 733
 Țoția, Horațiu, 1189
 Triduh, G. M., 790
 Tronciu, V. Z., 411
 Tsaranu, A., 902
 Tudor, Tiberiu S., 504
 Turcu, I. C. E., 162
 Udrea, M. V., 692
 Ulmeanu, M., 1137
 Ungureanu, Costica, 596, 1039
 Ungureanu, M., 596
 Ursache, Marcela, 278, 494, 619, 1063
 Ursu, Veronica, 288, 632
 Usurelu, Mircea, 747
 Vallmitjana, Santiago R., 1150, 1156
 Varnik, F., 978
 Vascan, Ioan, 936, 951
 Vasile, E., 75, 225, 272, 1132

Vasiliu, Virgil V., 686, 692, 696, 1074, 1137
Vateva, Elena, 960
Veltman, R. H., 556
Verardi, P., 1194
Verlan, Victor I., 1013
Vieru, T., 1007, 1032
Vinkler, Istvan, 504
Vlad, Adriana, 477
Vlad, L. A., 790
Vlad, Valentin I., 375, 432, 511, 517, 955
Vlaiculescu, Mihaela, 696, 739, 747
Voicu, Ion N., 174
Voicu, L., 1202
Volvoreanu, C., 717
Vorozov, N., 762
Wallas, Gordon, 17
Walther, Herbert, 320
Werckmann, J., 218
Windholz, Laurentius, 541, 584
Yakovlev, Vladimir P., 462
Yatsui, Kiyoshi, 153, 188, 282
Yukawa, T., 153, 188, 282
Yuldashev, Bekzad S., 837
Zalevsky, Zeev, 363, 418
Zisu, Tudor, 807
Zoran, Maria, 779, 891
Zsivanov, Delia, 293